PLATE SUBDUCTION AND MINERALIZATION IN EAST AND CENTRAL ASIA

EDITED BY: Kit Lai, Khin Zaw, Sean C. Johnson, Jung-Woo Park and Rui Wang

PUBLISHED IN: Frontiers in Earth Science

frontiers Research Topics

frontiers

ISSN 1664-8714
ISBN 978-2-83250-631-8
DOI 10.3389/978-2-83250-631-8

About Frontiers

Frontiers is more than just an open-access publisher of scholarly articles: it is a pioneering approach to the world of academia, radically improving the way scholarly research is managed. The grand vision of Frontiers is a world where all people have an equal opportunity to seek, share and generate knowledge. Frontiers provides immediate and permanent online open access to all its publications, but this alone is not enough to realize our grand goals.

Frontiers Journal Series

The Frontiers Journal Series is a multi-tier and interdisciplinary set of open-access, online journals, promising a paradigm shift from the current review, selection and dissemination processes in academic publishing. All Frontiers journals are driven by researchers for researchers; therefore, they constitute a service to the scholarly community. At the same time, the Frontiers Journal Series operates on a revolutionary invention, the tiered publishing system, initially addressing specific communities of scholars, and gradually climbing up to broader public understanding, thus serving the interests of the lay society, too.

Dedication to Quality

Each Frontiers article is a landmark of the highest quality, thanks to genuinely collaborative interactions between authors and review editors, who include some of the world's best academicians. Research must be certified by peers before entering a stream of knowledge that may eventually reach the public - and shape society; therefore, Frontiers only applies the most rigorous and unbiased reviews.
Frontiers revolutionizes research publishing by freely delivering the most outstanding research, evaluated with no bias from both the academic and social point of view. By applying the most advanced information technologies, Frontiers is catapulting scholarly publishing into a new generation.

What are Frontiers Research Topics?

Frontiers Research Topics are very popular trademarks of the Frontiers Journals Series: they are collections of at least ten articles, all centered on a particular subject. With their unique mix of varied contributions from Original Research to Review Articles, Frontiers Research Topics unify the most influential researchers, the latest key findings and historical advances in a hot research area! Find out more on how to host your own Frontiers Research Topic or contribute to one as an author by contacting the Frontiers Editorial Office: frontiersin.org/about/contact

PLATE SUBDUCTION AND MINERALIZATION IN EAST AND CENTRAL ASIA

Topic Editors:
Kit Lai, Fortescue Metals Group, Australia
Khin Zaw, University of Tasmania, Australia
Sean C. Johnson, University College Dublin, Ireland
Jung-Woo Park, Seoul National University, South Korea
Rui Wang, China University of Geosciences, China

Citation: Lai, K., Zaw, K., Johnson, S. C., Park, J.-W., Wang, R., eds. (2022). Plate Subduction and Mineralization in East and Central Asia. Lausanne: Frontiers Media SA. doi: 10.3389/978-2-83250-631-8

Table of Contents

frontiers | Frontiers in Earth Science

TYPE Editorial
PUBLISHED 14 October 2022
DOI 10.3389/feart.2022.1057859

OPEN ACCESS

EDITED AND REVIEWED BY
David R. Lentz,
University of New Brunswick
Fredericton, Canada

*CORRESPONDENCE
Chun-Kit Lai,
chunkitl@utas.edu.au

SPECIALTY SECTION
This article was submitted to Economic Geology,
a section of the journal
Frontiers in Earth Science

RECEIVED 30 September 2022
ACCEPTED 04 October 2022
PUBLISHED 14 October 2022

CITATION
Lai C-K, Zaw K, Park J-W, Wang R and Johnson SC (2022), Editorial: Plate subduction and mineralization in East and Central Asia.
Front. Earth Sci. 10:1057859.
doi: 10.3389/feart.2022.1057859

Editorial: Plate subduction and mineralization in East and Central Asia

Chun-Kit Lai[1]*, Khin Zaw[2], Jung-Woo Park[3], Rui Wang[4] and Sean C. Johnson[5]

[1]Global Project Generation and Targeting, Fortescue Metals Group Ltd., Perth, WA, Australia, [2]CODES, Centre for Ore Deposit and Earth Sciences, University of Tasmania, Hobart, TAS, Australia, [3]School of Earth and Environmental Sciences, Seoul National University, Seoul, South Korea, [4]State Key Laboratory of Geological Processes and Mineral Resources, Institute of Earth Sciences, China University of Geosciences, Beijing, China, [5]University College Dublin, Dublin, Ireland

KEYWORDS

ore deposits, subduction, mineralization, East Asia, Central Asia

Editorial on the Research Topic
Plate subduction and mineralization in East and Central Asia

Introduction

Plate subduction has played a pivotal role in shaping the tectonics in East and Central Asia. Since the Paleozoic, the closure of the Paleo-Asian and Tethyan oceans have brought together various continental blocks (e.g., Siberia, Sino-Korea, South China, Indochina and Sibumasu), and many ophiolites and accreted island arc terranes in between to form the present-day tectonic configuration. This generated the Central Asian Orogenic Belt, the world's largest Phanerozoic accretionary orogen, and the Tethyan tectonic domain that extends across much of the southern Central Asia and mainland SE Asia. During this prolonged multiphase subduction process, a number of world-class subduction-related ore deposits within related regional tectonic belts were formed. In the following, we have briefly summarized the key findings of the papers in this Research Topic (Figure 1):

Many ore deposits in East and Central Asia are characterized by multistage metallogeny. By integrating fluid inclusion microthermometry and H-O-S-Pb isotopes on the Haerdaban Pb-Zn deposit (Chinese Western Tianshan Orogen), Xia et al. suggested that the stratiform ores there were sedimentary exhalative (SEDEX)-type formed in the Proterozoic Haerdaban Group meta-carbonate/clastic sequences. Meanwhile, the crosscutting vein-type ores were likely formed by a Late Ordovician-Silurian magmatic-hydrothermal event genetically linked to North Tianshan Ocean subduction. Led by Paleo-Asian Ocean subduction, the Devonian-Carboniferous is a key metallogenic epoch in Central Asia, generating many world-class porphyry Cu deposits in the Balkhash (e.g., Kounrad and Borly; Kazakhstan), Gurvansayhan (e.g., Oyu Tolgoi; Mongolia) and

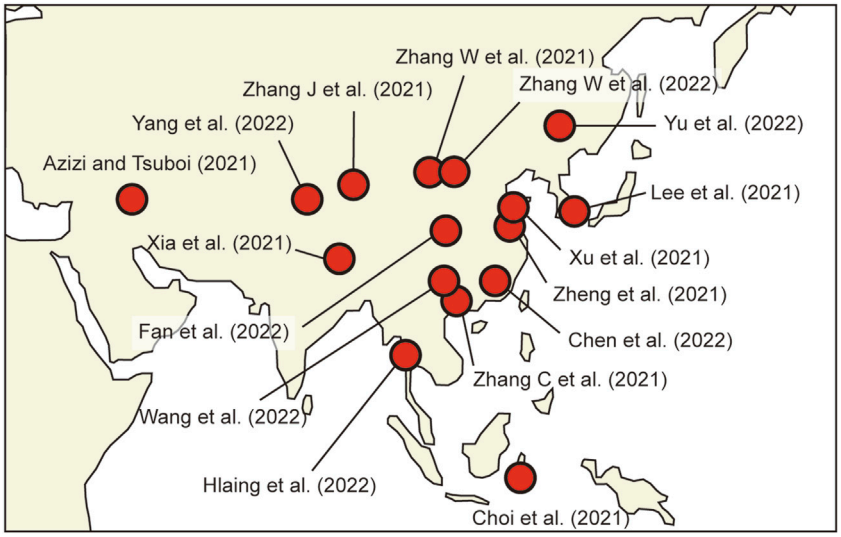

FIGURE 1
Geographic map of East and Central Asia, showing the study area of the 16 papers in this Research Topic.

Chinese Tianshan (Tuwu-Yandong, Xinjiang) regions (e.g., Wainwright et al., 2011; Shen et al., 2017; Mao et al., 2022). Yang et al. reported on the newly discovered Qia'erdunbasixi Fe-Cu skarn deposit in the Zarma-Sawur Cu-Au belt (Kazakhstan-NW China). The ores are hosted along the diorite exocontact by arc-type calc-alkaline andesite and minor basalt and tuff. SHRIMP zircon U-Pb dating of the post-ore syenite (345 ± 2.2 Ma) provided a minimum age for the mineralization.

Despite that fact the Paleo-Asian Ocean was largely closed by the Permian, the influence of subduction may have lasted long after. Zhang et al. presented a new Early Cretaceous age (129.7 Ma) on the dolerite dykes from the Bailingshan Fe deposit (Eastern Tianshan Orogen, NW China). The dolerite has low initial $^{87}Sr/^{86}Sr$ and positive εNd(t) values, indicative of an asthenospheric mantle source. The authors suggested that the mafic magmatism may have occurred in an intraplate extension setting, related to the delamination and sinking of dense, Late Paleozoic subduction-modified lithospheric mantle.

Subduction of the Eastern Paleo-Tethys has been attributed by some authors to contribute to the end-Permian Emeishan Large Igneous Province (LIP) (Xu et al., 2019). The Emeishan LIP has hosted many magmatic Fe-Ti-V oxide and Ni-Cu-PGE sulfide deposits, yet its spatial continuation to the SE (e.g., in Guangxi and NW Vietnam) is still inadequately constrained (Halpin et al., 2016). By studying the Longlin basalt in western Guangxi, Zhang et al. revealed that these basalts (256.7–259.5 Ma) were largely coeval with the Emeishan LIP volcanism and have similar whole-rock geochemical and Sr-Nd isotope features to the Emeishan high-Ti flood basalt sequence. The authors argued that the Emeishan LIP activity had extended to western Guangxi.

In the Kunlun Orogen (Qinghai Province, NW China), Zhang et al. presented new ages on the magmatic Cu–Ni sulfide ore-bearing olivine-pyroxenite (250.8 Ma) and weakly mineralized gabbro (257.3 Ma) from the Xiwanggou complex. These Late Permian ages are much younger than most deposits (Late Silurian–Early Devonian) in this region. Whole-rock Sr–Nd and zircon Hf isotopes suggest that the magma was mainly derived from the metasomatized subcontinental lithospheric mantle (SCLM), and formation of the Xiwanggou complex was likely related to subduction of the Paleo-Tethyan Anemaqen Ocean. The dextral shear of the crustal-scale Wenquan and South Kunlun faults may have served as a major conduit for the magma ascent. Paleo-Tethyan subduction in the Kunlun Orogen was likely completed in the Middle Triassic. Zhang et al. reported new ages and geochemical data on the ore-causative granodiorite porphyry (217.3 Ma) and granite porphyry (217.0 Ma) at the large Harizha Cu polymetallic deposit. The Late Triassic ages of these porphyries fall into the post-collisional magmatic age range of the East Kunlun Orogen, whilst their peraluminous and high-K nature is consistent with a post-collisional petrogenetic setting.

Further west, Neo-Tethyan subduction and post-collisional extension between the Arabian and Eurasian plates has caused the assembly of microcontinents (incl. Taurides–Anatolides and Biston–Avoramanm, Bilitis) along various suture zones, notably the Oshnavieh–Salmas–Khoy ophiolite belt. Through extensive geochemical data compilation and analysis, Azizi and Tsuboi, the newly defined the Van microplate in eastern Turkey-NW Iran was recognized, which drifted from the Arabian plate in the Jurassic and accreted onto the southern Eurasian plate after the closure of northern Neo-Tethyan branch. The process had

generated prolonged multiphase magmatism in the Cretaceous, Eocene, Oligocene-Miocene, and late Miocene-Quaternary.

In the Jurassic-Cretaceous, the Eastern Asian tectono-metallogeny was mainly driven by the Paleo-Pacific subduction, forming the Great Yanshanian Metallogenic Event (Goldfarb, 2021). The event extended from the Russia Far East-NE China-Korea, through the regional Tanlu Fault to South China. In NE and Central China, the metallogeny has formed many world-class porphyry Mo deposits (e.g., Chalukou), as well as numerous intrusion-related, epithermal Cu (-Au-Ag) and skarn Fe (-Cu) deposits. By dating various lamprophyre units from the western Songliao Basin (NE China), Yu et al. found that they were mainly emplaced in the Late Jurassic and Early Cretaceous. Geochemical features suggest that the Early Cretaceous suite was formed at a shallower depth than the Late Jurassic suite. This indicates a probable crustal thickening during 156–132 Ma, prior to the widely reported Early Cretaceous crustal thinning caused by subduction rollback.

In the SE Korean Peninsula, the Paleo-Pacific subduction had formed a series of Cretaceous hydrothermal vein-type Cu deposits in the Gyeongsang basin. Lee et al. analyzed the mineralogy and fluid inclusion geothermometry of the Haman, Gunbuk, and Daejang deposits (Gyeongnam metallogenic belt). The results indicate that Haman was formed at the central-upper part of crystallizing stock under higher P-T conditions than those of typical porphyry Cu deposits, whilst the Gunbuk-Daejang deposits were formed at a shallower peripheral location with partially overlapping P-T conditions with porphyry-style mineralization.

Nonetheless, despite having similarly favorable tectonic triggers (Paleo-Pacific subduction and the Tanlu crustal-scale fault movement) and adakitic-like geochemical signature, some intrusives are Cu-Au ore-forming but others are not. To understand this disparity, Zheng et al. compared the age and geochemistry between the ore-barren adakitic rocks (130–129 Ma, 115.8, and 105.8 Ma) from the Huaibei-Linhuan coalfield with other fertile/barren adakites across Eastern China. They found that the parental magma of the Huaibei-Linhuan adakites may have been considerably more reduced than typical porphyry Cu-Au ore-forming magmas, possibly led by the late assimilation of Carboniferous-Permian coal seams.

In the world-class Jiaodong gold province (east of Tanlu fault, Eastern China), Xu et al. presented a new age on the cataclastic granite ore host (142 Ma) for the Zhaoxian gold deposit, which helps to constrain the maximum mineralization age and is coeval with the regional Yanshanian magmatism. Auriferous pyrite geochemistry and S-He-Ar isotopes suggest that the ore fluids were derived from a crustal-mantle mixed source, with metamorphic and magmatic fluids dominating the early and main ore stages, respectively.

In the Mangling orefield of North Qinling Terrane (west of Tanlu fault, Central China), Fan et al. suggested that the Yaozhuang Mo polymetallic deposits are closely related to the ore-bearing porphyry stocks, which were zircon U-Pb dated to be 157–153 Ma, coeval with the regional magmatic peak. The Yaozhuang stocks were likely formed by the lower crustal delamination in North Qinling.

In South China, the Paleo-Tethys closure (Indosinian orogeny) and Paleo-Pacific subduction has led to major regional tectonic reconfiguration and development of crustal-scale faults, e.g., the Ziyun-Luodian Fault (Wang et al.), as well as the Great Yanshanian Metallogenic Event (Goldfarb et al., 2021), which is well-known to have formed the world-class W-Sn and many rare-metal deposits in the Nanling Range. By studying the ore-forming Jianfengling biotite monzogranite in the Xianghualing orefield (Nanling Range), Ze-Yi et al. suggest that the Jianfengling granite was emplaced in the Late Jurassic (161.3–158.7 Ma), probably sourced from the Mesoproterozoic Cathaysian basement in a lithospheric extensional setting. The Nb-Ta contents increase with fluorine from the porphyritic to equigranular lithofacies of the granite, indicating that the Nb-Ta enrichment may have been caused by the gradual F increase during granitic magma fractionation.

Coincident with the Paleo-Pacific subduction, Neo-Tethys subduction in western SE Asia and the subsequent India-Asia collision had generated many porphyry to epithermal-type Au (-Cu) and Pb-Zn (-Ag) and orogenic gold deposits (Zaw et al., 2014). The latter is well-developed along the 1,300 km long Mogok-Mandalay-Mergui Belt in Central Myanmar. Hlaing et al. presented and compared the geology and genesis of two major gold districts (Modi Taung-Nankwe and Kyaikhto) in the belt. Both gold districts have similar shear zone-hosted ore vein textures and orientation, together with similar ore host of the Carboniferous Mergui Group meta-sediments. They have also similar wallrock alteration styles, ore mineral assemblage and low to medium salinity ore fluids, comparable to typical mesozonal orogenic gold systems.

Further southeast in the Indonesia archipelago, the East Sulawesi Ophiolite, an interpreted Cretaceous-Paleogene oceanic plateau fragment obducted onto the Sundaland margin by the Pacific plate subduction (Kadarusman et al., 2004). The ophiolite at Morowali consists mainly of serpentinized harzburgite and lherzolite, and the extensive weathering formed substantial laterite-type Ni resources. Based on garnierite (main ore mineral) color and XRD/EPMA and whole-rock geochemical analyses, Choi et al. suggested that the garnierite consists of serpentine-like and talc-like phases. The former has high Ni-Fe contents and likely originated from the bedrock, whereas the latter has lower Fe content and a secondary origin, formed by weathering during repeated annual dry and wet cycles.

This Research Topic of 16 articles in the Research Topic does not provide all the new research progress on the tectonic evolution and associated metal mineralization in the region, although tries to cover the wider significant developments in this field. The East and Central Asia region is highly endowed

with a diversity of metallic ore deposits, including porphyry, skarn, epithermal, VHMS, sediment-hosted/orogenic gold, vein-type W-Sn deposits, and critical metal deposits. We envisaged that further work on petrogenetic/metallogenetic studies of these mineral systems, e.g., on the rare-metal enrichments in fractionating magmas, are strategically important for future mineral resource and green energy industry of the region.

Author contributions

All authors listed have made a substantial, direct, and intellectual contribution to the work and approved it for publication.

Acknowledgments

We greatly appreciate the time and effort of the reviewers and authors for their contributions to ensure the papers in this Research Topice are innovative, exclusive and timely. Our special thank goes to the Chief Editor Prof. David R Lentz and staffs from the editorial office, for their help and insightful advice in handling the manuscripts.

Conflict of interest

Author C-KL was employed by the company Fortescue Metals Group Ltd.

The remaining authors declare that the research was conducted in the absence of any commercial or financial relationships that could be construed as a potential conflict of interest.

Publisher's note

References

Goldfarb, R. J., Mao, J.-W., Qiu, K.-F., and Goryachev, N. (2021). The great Yanshanian metallogenic event of eastern Asia: Consequences from one hundred million years of plate margin geodynamics. *Gondwana Res.* 100, 223–250. doi:10.1016/j.gr.2021.02.020

Halpin, J. A., Tran, H. T., Lai, C. K., Meffre, S., Crawford, A. J., and Zaw, K. (2016). U-Pb zircon geochronology and geochemistry from NE Vietnam: A "tectonically disputed" territory between the Indochina and South China blocks. *Gondwana Res.* 34, 254–273. doi:10.1016/j.gr.2015.04.005

Kadarusman, A., Miyashita, S., Maruyama, S., Parkinson, C. D., and Ishikawa, A. (2004). Petrology, geochemistry and paleogeographic reconstruction of the East Sulawesi ophiolite, Indonesia. *Tectonophysics* 392, 55–83. doi:10.1016/j.tecto.2004.04.008

Mao, Q., Xiao, W., Ao, S., Li, R., Wang, H., Tan, Z., et al. (2022). Late Devonian to early Carboniferous roll-back related extension setting for the Tuwu-Yandong porphyry copper metallogenic belt in the Dananhu arc of the eastern Tianshan (NW China) in the southern Altaids. *Ore Geol. Rev.* 149, 105060. doi:10.1016/j.oregeorev.2022.105060

Shen, P., Pan, H., and Seitmuratova, E. (2017). Petrogenesis of the mineralized granitoids from the Kounrad and Borly porphyry Cu deposits and the East Kounrad porphyry Mo deposit in Kazakhstan: Implication for tectonic evolution and mineralization of the Western part of the Central Asian Orogenic Belt. *Lithos* 286–287, 53–74. doi:10.1016/j.lithos.2017.06.006

Wainwright, A. J., Tosdal, R. M., Wooden, J. L., Mazdab, F. K., and Friedman, R. M. (2011). U–Pb (zircon) and geochemical constraints on the age, origin, and evolution of Paleozoic arc magmas in the Oyu Tolgoi porphyry Cu–Au district, southern Mongolia. *Gondwana Res.* 19, 764–787. doi:10.1016/j.gr.2010.11.012

Xu, J., Xia, X. P., Lai, C. K., Zhou, M., and Ma, P. (2019). First identification of late permian Nb-enriched basalts in ailaoshan region (SW yunnan, China): Contribution from emeishan plume to subduction of eastern paleotethys. *Geophys. Res. Lett.* 46, 2511–2523. doi:10.1029/2018GL081687

Zaw, K., Meffre, S., Lai, C.-K., Burrett, C., Santosh, M., Graham, I., et al. (2014). Tectonics and metallogeny of mainland southeast Asia — a review and contribution. *Gondwana Res.* 26, 5–30. doi:10.1016/j.gr.2013.10.010

frontiers in Earth Science

ORIGINAL RESEARCH
published: 29 January 2021
doi: 10.3389/feart.2020.574385

The Van Microplate: A New Microcontinent at the Junction of Iran, Turkey, and Armenia

Hossein Azizi[1]* *and Motohiro Tsuboi*[2]

[1]Department of Mining, Faculty of Engineering, University of Kurdistan, Sanandaj, Iran, [2]Department of Applied Chemistry for Environment, School of Science and Technology, Kwansei Gakuin University, Sanda, Japan

In northwestern Iran, magmatic activity occurred during three main intervals: The Cretaceous, Eocene, and Miocene-Quaternary. The first two phases of magmatic activity are more consistent with arc-type magmatism on an active continental margin; whereas the last phase, which has calc-alkaline and alkaline affinities, shows more similarity to postcollisional magmatism. Magmatic belts are mostly situated in the northern and eastern parts of the Oshnavieh–Salmas–Khoy ophiolite belt (OSK-Ophiolite) in northwestern Iran. The OSK-Ophiolite is known as the Neotethys, an ocean remnant in northwestern Iran, and extends to eastern Turkey and surrounds the Van area. This configuration shows that the Van microplate and surrounding ocean have played an important role in the evolution of magmatic activity in northwestern Iran, eastern Turkey, and the Caucasus since the Cretaceous. The Van microplate is situated among the Arabian plate to the south, northwestern Iran to the east, and Armenia to the north. The subduction of the northern branch of the Neotethys oceanic lithosphere beneath southern Eurasia has been critical in flare-up magmatism in the southern Caucasus since the Late Cretaceous. Considering the Van area as a new microplate makes understanding the geodynamic evolution of this area easier than in the many tectonic models that have been suggested before. When regarding the Van microplate, the main suture zone, which is known as the Bitlis–Zagros zone, should be changed to the Zagros–Khoy–Sevan–Akera suture zone, which extends to the eastern and northern Van microplate and western Iran.

Keywords: Van microplate, neotethys, Jurassic drifting, tethys ophiolites, NW Iran

OPEN ACCESS

Edited by:
Mei-Fu Zhou,
The University of Hong Kong,
Hong Kong

Reviewed by:
Simone Tommasini,
University of Florence, Italy
Justin L. Payne,
University of South Australia, Australia

***Correspondence:**
Hossein Azizi
azizi1345@gmail.com
h.azizi@uok.ac.ir

Specialty section:
This article was submitted to Petrology, a section of the journal Frontiers in Earth Science

Received: *19 June 2020*
Accepted: *21 December 2020*
Published: *29 January 2021*

Citation:
Azizi H and Tsuboi M (2021) The Van Microplate: A New Microcontinent at the Junction of Iran, Turkey, and Armenia. Front. Earth Sci. 8:574385. doi: 10.3389/feart.2020.574385

INTRODUCTION

Most crust in Iran and Turkey is part of the Alpine–Himalaya orogenic belt, which is situated at the junction of Gondwana (in the south) and the Eurasian plate (in the north) (Dewey et al., 1973; An and Harrison, 2000; Göncüoglu, 2010; Prelević and Seghedi, 2013; Tian et al., 2017). This crust includes a number of microcontinents, such as the Taurides–Anatolides and Biston–Avoramanm, Bilitis, and Van microcontinents, with the latter being added by the authors in this research (**Figure 1**). These microcontinents were distributed across the Tethys Ocean in the Mesozoic to early Cenozoic eras but are now surrounded by oceanic-crust remnants (Jassim and Goff, 2006). Nevertheless, there is no well-defined information to confirm that these microcontinents completely drifted from the Arabian plate (Wrobel-Daveau et al., 2010; Azizi et al., 2013; Nouri et al., 2016).

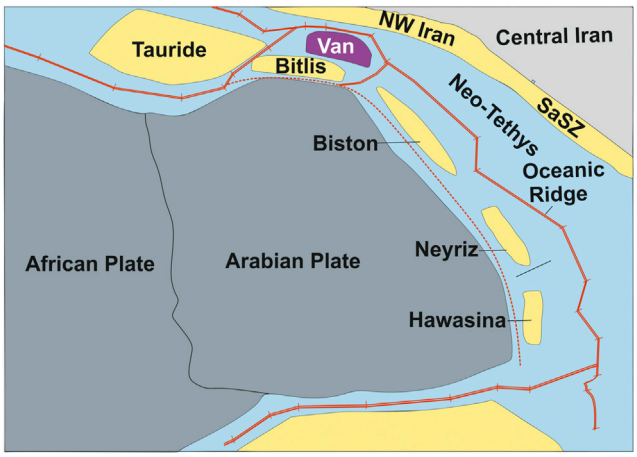

FIGURE 1 | Paleogeographic maps during the Late Jurassic-Early Cretaceous (Jassim and Goff, 2006) show that the Neotethys Ocean surrounded some microcontinents, such as Taurides–Anatolides and Biston–Avoramanm, Bilitis, and Van microcontinents, which were added by the authors in this research.

The northern fossil remnant of oceanic crust is known as the Paleo–Tethys trace, which extends from northern Iran to northern Turkey (Kroner and Romer, 2013; Manafi et al., 2013; Shafaii Moghadam and Stern, 2014). The central and southern parts (**Figure 2**) are known as the Neotethys remnant (Stöcklin and Nabavi, 1973; Golonka, 2004; Ghasemi and Talbot, 2006; Moghadam and Stern, 2015; Hassanzadeh and Wernicke, 2016; Nouri et al., 2019).

Magmatic activity increased in both northwestern Iran and Turkey in the Late Cretaceous and has continued through the Quaternary (Alavi, 1994). Magmatism in both regions was concentrated in four main periods: The Late Cretaceous, Eocene, Miocene, and Quaternary. According to many published research studies, most of the magmatic activity was related to the Tethys (Neotethys) orogeny, which stemmed from the subduction and collision of the Arabian plate with the Turkey and Iran plates, as well as from postcollisional tectonic regimes (Agard et al., 2006; Agard et al., 2011; Ali et al., 2013; Whitechurch et al., 2013; Nouri et al., 2016; Nouri et al., 2017; Nouri et al., 2020; Azizi et al., 2018b; Shabanian et al., 2018). Certainly, in Turkey and the western and central parts of Iran, magmatic rocks show clear similarities to the typical calc-alkaline, magmatic series common to an active continental margin (Parlak et al., 2000; Aldanmaz, 2006; Dilek and Altunkaynak, 2009; Topuz et al., 2004; Topuz et al., 2017).

The focus of this study is on magmatic activity in the region between the Black and Caspian Seas, which includes northwestern Iran, eastern Turkey, Georgia, Armenia, and Azerbaijan (**Figure 2**). This magmatism is of interest, as it has traditionally been considered to be a result of the subduction of oceanic crust of the Neotethys beneath Iran and southern Turkey. The site of this margin is considered to be represented by the

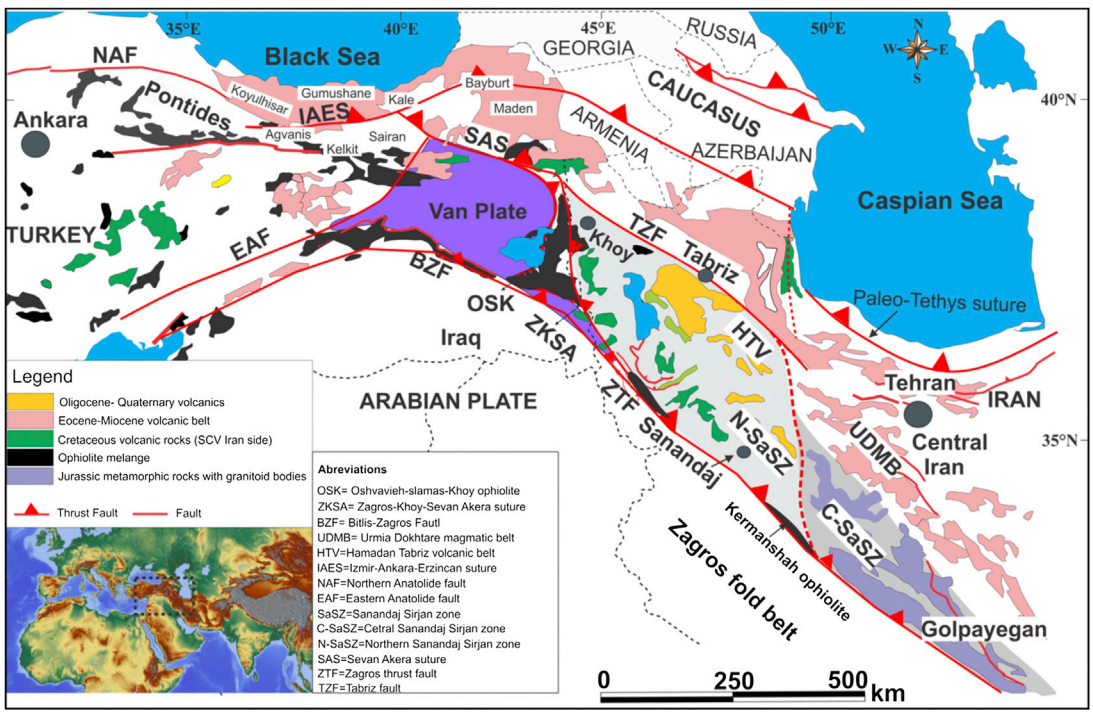

FIGURE 2 | Distribution of the main suture zones and magmatic rocks from the Cretaceous to Quaternary in Turkey and northwestern Iran with the Van-microplate position. Ophiolite members are distributed in the main suture zones that surround the Van microplate (modified from Nouri et al., 2016).

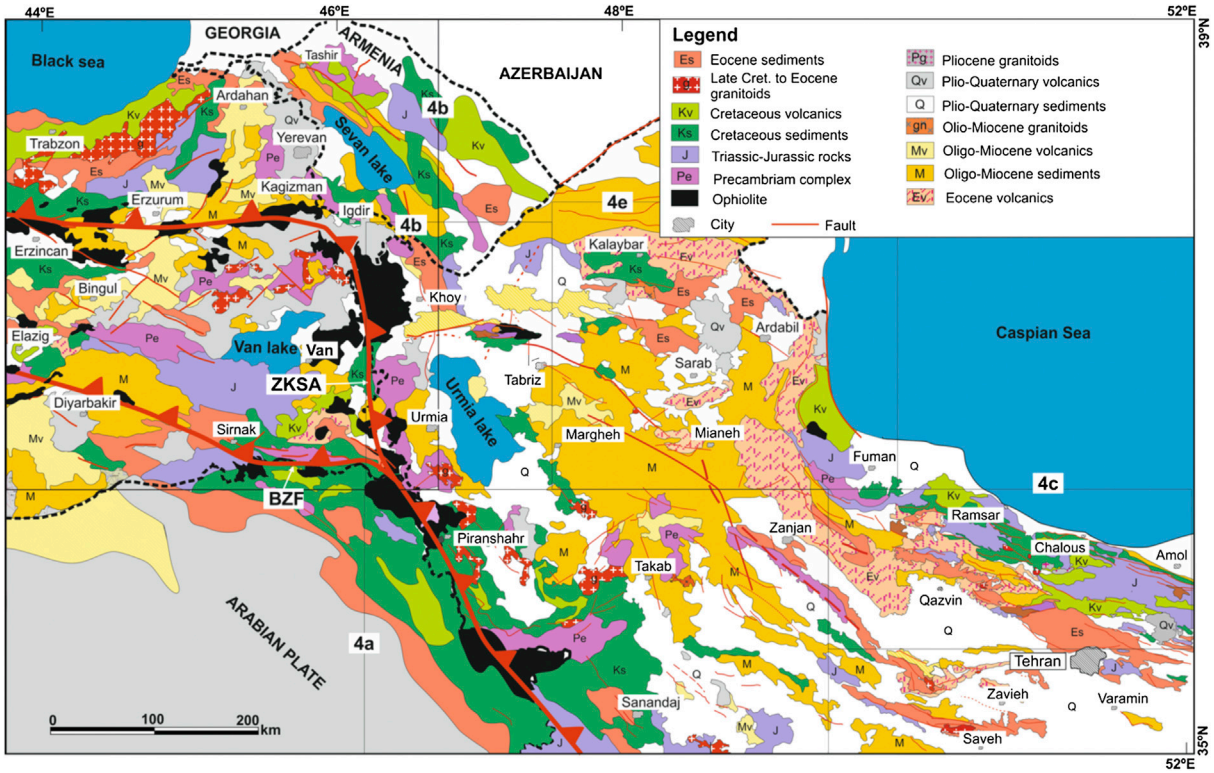

FIGURE 3 | Simplified geology units between the Black and Caspian seas that show the main sutures, ophiolites, and magmatic rocks in more detail. See the **Supplementary S1** for the references. Rectangles show the locations of the detailed geological maps in **Figure 4(A–E)** and the location of the study area examined by researchers.

Bitlis–Zagros–Fault (BZF) suture zone (**Figures 2**, **3**). As the BZF suture zone is distant from the southern and western Caspian Sea (>300 km), it is problematic for the highly, calc-alkaline magmatism to be sourced from subduction coming from that area. Furthermore, the location of the Khoy ophiolite sequence would appear to be inconsistent with subduction focused solely along the BZF. The large size of the Khoy ophiolite and its composition of pelagic sediment, a large thickness of pillow lava, sheeted dikes, both layered and massive gabbro, and cumulate and tectonite peridotites, are highly consistent with typical ophiolite sequences (Hassanipak and Ghazi, 2000; Ghazi et al., 2003; Khalatbari-Jafari et al., 2003) that have been generated in a mature, oceanic basin. These seeming inconsistencies in the geological record led us to propose the existence of a new microcontinent or continental fragment that sits between the BZF suture zone to the south and the Khoy ophiolite sequence to the northeast.

In this study, we introduce a new microplate, the Van microplate, which has an area of approximately 50,000 km^2 and is situated between northwestern and central Iran, the Anatolian block, and the Arabian plate (**Figure 3**). We outline and explain the proposed, microplate boundaries, followed by an explanation of how the northern branch of the Neotethys has controlled the magmatic activity of northwestern Iran and the Caucasus, based on this new microplate, despite the southern branch.

GEOLOGICAL BACKGROUND

Eocene volcanic rocks are widely distributed from the southern Caspian Sea to the southern Black Sea and are almost parallel to the Cretaceous volcanic rocks (**Figures 2**, **3**). **Figures 2**, **3** were compiled based on more than 20 geology maps of Iran and the surrounding area (See the **Supplementary S1** for the map references). Cretaceous volcanic rocks are also extensive, although less so in comparison to the Eocene rocks (**Figures 2**, **3**), and are limited to the south of the Zagros fault in the northern Sanandaj–Sirjan zone (SaSZ). Cretaceous magmatism primarily has calc-alkaline affinity (Azizi and Jahangiri, 2008; Azizi and Moinevaziri, 2009). Ophiolite members, known as Neotethys remnants, are widely distributed along major faults, such as the BZF and Zagros thrust-fault (ZTF) suture in southern Turkey and western Iran. The Bitlis–Zagros, which includes the BZF and ZTF here (**Figures 2**, **3**), is known as a major suture zone between the Arabian and Iranian–Anatolian plates. It was opened in the late Paleozoic Era and closed in the Cenozoic Era (Agard et al., 2011; Alirezaei and Hassanzadeh, 2012; Abdulzahra et al., 2016; Azizi et al., 2019).

Some dismembered mafic and ultramafic rocks are exposed throughout the entire Bitlis-Zagros suture zone in the border between Iran and Iraq along the BZF (**Figures 2**, **3**). Some researchers considered this complex as ophiolites

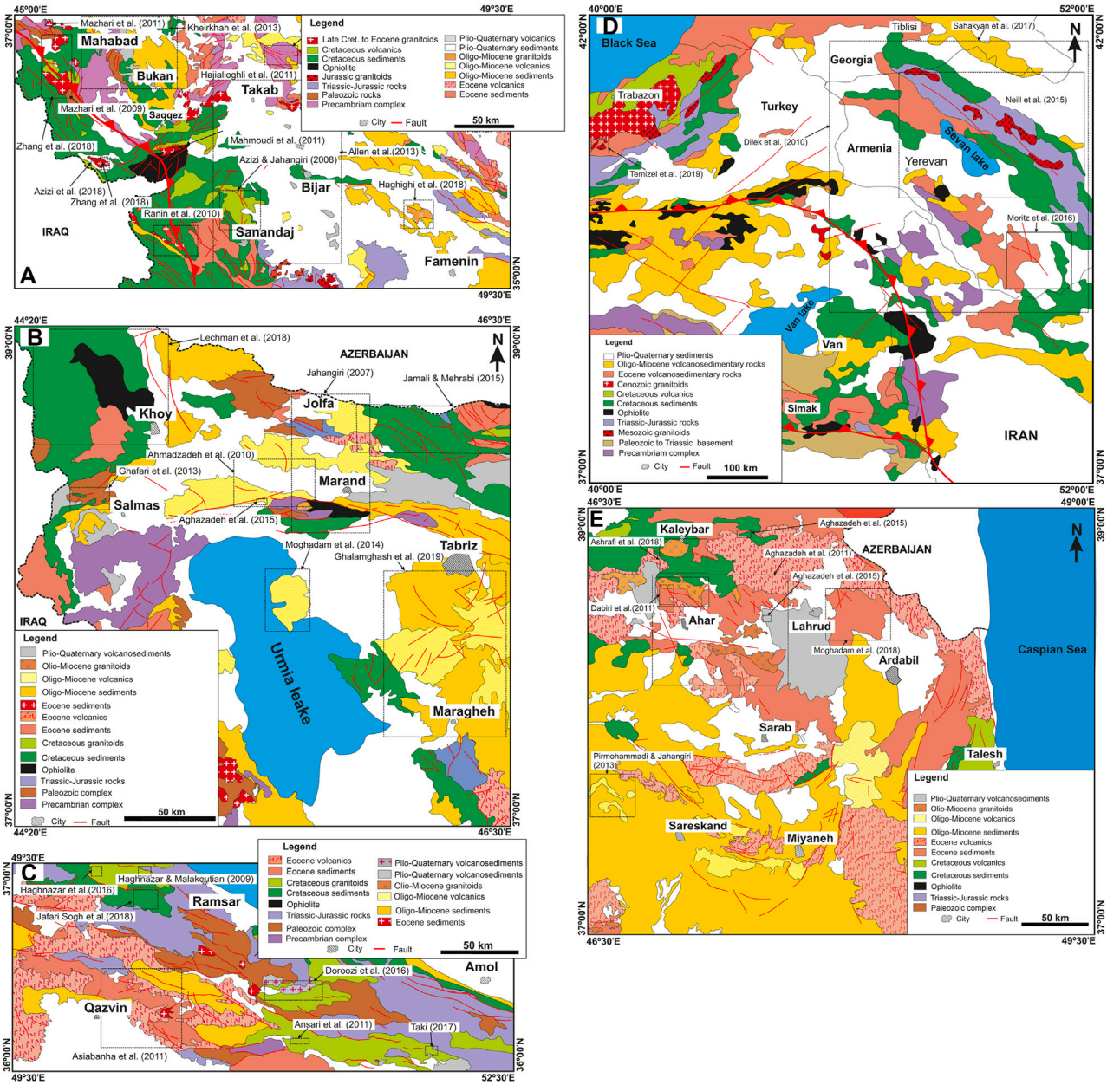

FIGURE 4 | (A–E) Detailed geological maps of the main magmatic units and major faults distributed between the Black and Caspian Seas. The location of collected data and references are shown in the maps. For the location of each map, see **Figure 3**.

(Ismail et al., 2010; Ali et al., 2013; Ali et al., 2016; Mohammad, 2013; Mohammad and Cornell, 2017; Al Humadi et al., 2019) and found that these rocks are more consistent with plume-type magma and barren rifts (Wrobel-Daveau et al., 2010; Azizi et al., 2013; Azizi and Stern, 2019; Karim and Al-Bidry, 2020). In this case, a barren rift between the Van microplate and Arabian plate is more likely than mature oceanic crust. These mafic rocks define the Sanandaj–Sirjan zone (SaSZ) from the Arabian plate in northwestern Iran to southern Turkey. The distribution of the magmatic rocks with the major faults from eastern Turkey to northern Iran is detailed in **Figures 4A–E**.

Azizi and Stern (2019) divided the SaSZ in western Iran (**Figure 2**) into three main parts: northern, central, and southern. In the northern part, which is separated from the Van microplate in this study and the junction, some dismembered ophiolite has been exposed. We call this the Oshnavieh-Salmas-Khoy ophiolite belt (OSK-Ophiolites) here. The OSK-Ophiolites, which has a N-S trend, is the main suture zone between the Van microplate and northwestern Iran block. We describe the OSK-Ophiolites below.

OSK Ophiolites

This dismembered ophiolite belt is exposed in a number of locations. It mainly shows mid-ocean ridge and island-arc, geochemical signatures and is widely exposed in the Khoy area, with some massive-sulfide mineralization and chromite deposits (Zaeimnia et al., 2017). In the Khoy area, the ophiolite members in the east have been classified as the main ultramafic parts of the mantle and comprise dunite and harzburgite (Khalatbari-Jafari et al., 2003). In the west, the members comprise oceanic crust, which consists of deep pelagic sediment, pillow lava, and sheeted dikes, all with a Cretaceous age. This complex was thrust onto the western side of the Van microplate, and the Precambrian basement (Azizi et al., 2011) was thrust onto the ultramafic complex on the eastern side. The entire complex was unconformably covered by Oligocene–Miocene conglomerate and a terrigenous sedimentary layer. The Khoy ophiolite sequences are typical of mid-ocean ridges in mature oceanic crust, such as the recent Pacific oceanic ridge (Sclater et al., 1971; Zhang et al., 2020).

Magmatic Activity

Magmatic activity around the Van microplate is restricted to four main intervals:

Cretaceous, Eocene, Oligocene-Miocene, and late Miocene-Quaternary.

Cretaceous Volcanic Rocks

Cretaceous volcanic rocks surrounding the Van microplate are mostly less exposed, being buried under younger sedimentary and volcanic rocks (**Figures 3**, **4**). Cretaceous volcanic rocks are mainly interbedded with sedimentary layers and are mainly basaltic and andesitic-basaltic rocks (Azizi and Jahangiri, 2008) that have erupted in submarine environments. Due to the high levels of alteration within these rocks, there have been few studies on these rocks. Whole-rock composition confirms that these rocks were formed in an active, continental margin (Azizi and Jahangiri, 2008).

Eocene Volcanic Rocks

This group of rocks is the main volcanic suit and extends from the western Caspian Sea to Armenia, Georgia, and northern Turkey (**Figures 3**, **4**). On the Turkish side, it is divided into two main extensions. The first part extends to the northern IAES fault, and the second extends in a NE-SW direction along the eastern Anatolian fault (EAF), which we consider to be the western edge of the Van microplate (**Figures 2–4**).

Oligocene–Miocene Magmatic Rocks

These volcanic and plutonic rocks are widely distributed, and they cut the Eocene volcanic rocks. Mainly Cu–Mo–Au deposits and Fe mineralization (Azizi et al., 2009; Siani et al., 2015; Mehrabi et al., 2016; Rabiee et al., 2019) occurred during magmatic activity in the western and southern areas of the Caspian Sea.

Late Miocene-Quaternary Rocks

This group of rocks is distributed along the rim of the Van microplate, and they are classified into two main groups. The first group includes adakite and adakitic rocks, and the second includes high-Nb, basaltic rocks (Jahangiri, 2007; Azizi et al., 2014a; Azizi et al., 2014b), which confirms that they were formed in a postcollisional, tectonic regime. In addition, some of the major Pliocene-Quaternary volcanoes, such as Sahand, Sabalan, and Ararat, erupted at this time (Allen et al., 2013a; Chiu et al., 2013; Ghalamghash et al., 2019).

WHOLE-ROCK CHEMISTRY

We have compiled whole-rock, chemical data on 900 volcanic rocks (Agostini et al., 2007; Jahangiri, 2007; Azizi and Jahangiri, 2008; Haghnazar and Malakotian, 2009; Mazhari et al., 2009, 2011; Ahmadzadeh et al., 2010; Dilek et al., 2010; Ranin et al., 2010; Aghazadeh et al., 2011; Aghazadeh et al., 2015; Ansari et al., 2011; Dabiri et al., 2011; Hajialioghli et al., 2011; Mahmoudi et al., 2011; Asiabanha and Foden, 2012; Alishah et al., 2013; Ansari, 2013; Castro et al., 2013; Ghaffari et al., 2013; Kheirkhah et al., 2013; Moghadam et al., 2014; Neill et al., 2015; Doroozi et al., 2016; Haghnazar et al., 2016; Moritz et al., 2016; Sahakyan et al., 2017; Taki, 2017; Ashrafi et al., 2018; Haghighi Bardineh et al., 2018; Jafari Sough et al., 2018; Lechmann et al., 2018; Shafaii Moghadam et al., 2018; Zhang et al., 2018; Azizi et al., 2019; Ghalamghash et al., 2019; Temizel et al., 2019) from Cretaceous to Quaternary magmatism in northwestern Iran, southern Armenia, and eastern Turkey (**Supplementary S2**). The sample locations and references for each area are shown in **Figures 4A–E**.

Cretaceous volcanic rocks include basalt to rhyolite but are mostly classified as andesite. Cretaceous intrusive bodies also show some variation from gabbro to granite, with less exposure compared to volcanic rocks. Whole-rock composition shows that the Cretaceous, magmatic rocks have a large variation in TiO_2 from 0.19 to 3.82 wt% (average = 1.52 wt%, n = 125), Al_2O_3 from 11.2 to 22.7 wt % (average = 15.9 wt%, n = 125), and MgO from 0.03 to 11.8 wt% (average = 5.27 wt%, n = 125). In addition, these rocks have a high concentration of Ba (average = 470 ppm, n = 125), U (average = 2.82 ppm), and Th (average = 8.9 ppm). Eocene–Miocene, magmatic rocks have a large variation in SiO_2 (43–77 wt%), high content of Rb (average = 100 ppm; n = 389), Sr (average = 618 ppm, n = 429), Th (average = 11.7 ppm, n = 331) and U (3.47 ppm, n = 341). The upper Miocene-Quaternary magmatic rocks are mostly categorized into two main groups: adakite, with higher ratios of Sr/Y and La/Yb; and alkali basalts, with a higher content of Nb (average = 27 ppm, n = 328). See **Supplementary S2** for more information about the whole-rock chemistry of each group. For our discussion, the samples are categorized into three main groups: Cretaceous, Eocene-Miocene, and upper Miocene-Quaternary. All of the groups show variances from the basalt to the rhyolites (**Figure 5**) in the $K_2O + Na_2O$ diagrams (Le Bas et al., 1986). Nevertheless, the alkali elements for the Cretaceous and Eocene magmatic rocks largely varied compared to the upper Miocene and Quaternary rocks.

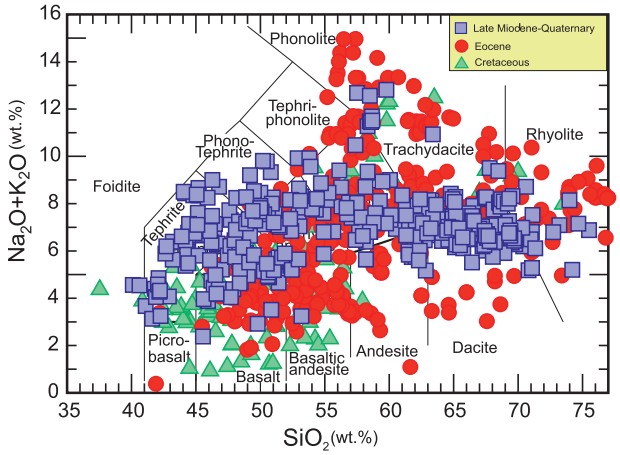

FIGURE 5 | Distribution of the composition of whole rocks, from Cretaceous to Quaternary, for all igneous rocks situated in the southern and western Caspian Sea. For references, see the text and **Supplementary S2**.

TECTONIC SETTING

For understanding tectonic setting, some key and general petrological diagrams are briefly used here. The Ti/V ratio diagram (Shervais, 1982) shows a wide distribution of the Cretaceous volcanic rocks from the arc to extensional basins (**Figure 6A**). Eocene rocks have more affinities for the arc-magma series. The late Miocene-Quaternary arc affinity was decreased and extended to alkaline and within-plate series (**Figure 6A**). The Th/Yb vs. Nb/Yb diagram (Pearce, 2008) shows that most of the mafic rocks plot in the volcanic-arc field because of the higher ratios of Th/Yb (**Figure 6B**). The enrichment of Th occurred during the fluids released from the subduction of the oceanic crust and/or crustal contamination with some assimilation-fractionation and contamination (AFC) processes. The Cretaceous basaltic rocks show a dichotomy for both intraoceanic arc and active continental-tectonic regimes. Eocene basaltic rocks show a clear relation to the typical active continental margin. Upper Miocene-Quaternary basaltic rocks also plot in the volcanic-arc field, with some similarity to oceanic-island basaltic rocks (OIB) near the mantle array, with less effect on crustal components (**Figure 6B**). To avoid the mobility of some trace elements, all Eocene and younger basaltic rocks, other than Cretaceous volcanic rocks because of the wide ranges, were normalized using rare-earth elements (REEs) of the chondrite value (Sun and McDonough, 1989). The normalized pattern shows that both the Eocene and upper Miocene-Quaternary rocks have higher ratios of light REEs than heavy REEs, and negative slopes from LREEs to HREEs (**Figures 7A,B**). Furthermore, the REE_S contained in the upper Miocene-Quaternary rocks are higher than those in the Eocene basaltic rocks (**Figures 7A,B**).

The plotting of the intermediate-to-acidic rocks (SiO_2 > 52 wt%) in FeO/(FeO + MgO) and $Na_2O + K_2O$–CaO vs. SiO_2 (Frost et al., 2001) shows that the lower ratios of FeO/(FeO + MgO) for most of the samples from the three groups plot in the magnesian and/or

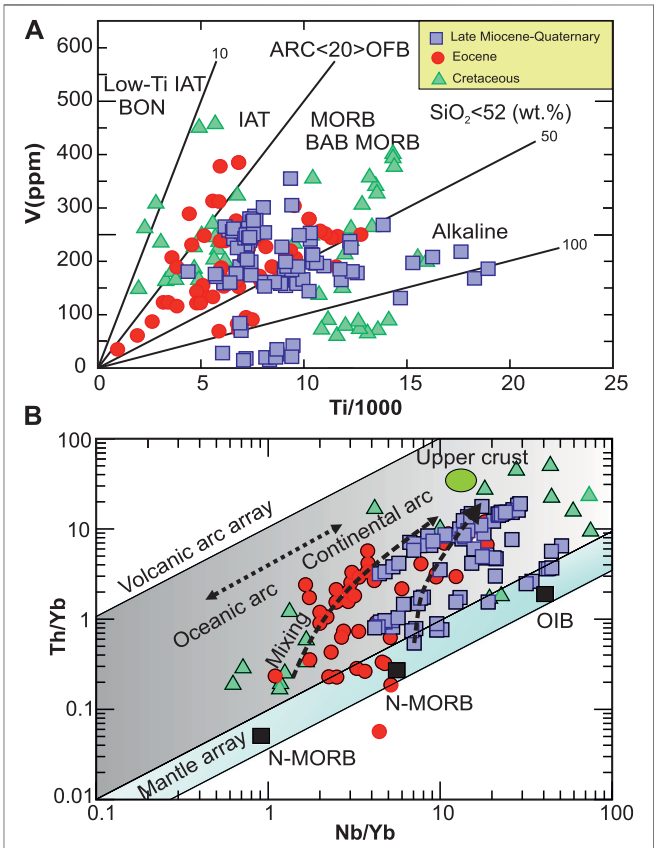

FIGURE 6 | Distribution of basic rocks (SiO_2 less than 52 wt%) from the southern and western Caspian Sea with different ages from the Cretaceous to Quaternary in the Ti–V Diagram (Shervais, 1982) and Th/Yb vs. the Nb/Yb diagrams (Pearce, 2008) in a and b, respectively. The mafic rocks plot near the arc and back-arc fields in the Ti–V diagram, and the higher ratios of the Th/Yb ratios plot in the volcanic-arc field in the Nb/Yb-Th/Yb ratios. See the text for more information and references for the data. For source data, see **Supplementary S2**. *Abbreviations: MORB = Mid-Oceanic Ridge Basalt; BAB = Back Arc Basalt; IAT = Island Arc tholeiite; BON = Boninite.*

I–type granite fields. Some of the Cretaceous and Eocene samples extend to the ferroan granite field. The upper Miocene-Quaternary rocks mainly plot in the magnesian field and/or I-type granite area (**Figure 8A**). In the $Na_2O + K_2O$–CaO vs. SiO_2 (wt%), Cretaceous and Eocene samples are scattered from the calcic to alkalic fields. Nevertheless, most of the samples were concentrated in the alkali-calcic field. The upper Miocene-Quaternary rocks plot in the alkali-calcic field, with less variation than the Cretaceous and Eocene samples (**Figure 8B**).

Intermediate-to-acidic rocks (SiO_2 > 52 wt%) have higher ratios of Rb; lower ratios of Y, Ta, and Nb (**Figures 9A,B**); and almost plot in the active margin to within-plate domains (Pearce et al., 1984). Cretaceous intermediate-to-acidic volcanic rocks mainly plot in the active margin and within-plate tectonic fields. The variation in the Ta/Yb vs. Th/Yb ratios (Pearce, 1982) shows a wide range for the Eocene and Cretaceous intermediate-to-acidic magmatic rocks and more affinity with the upper Miocene-Quaternary for the within-plate granite field (**Figure 9C**).

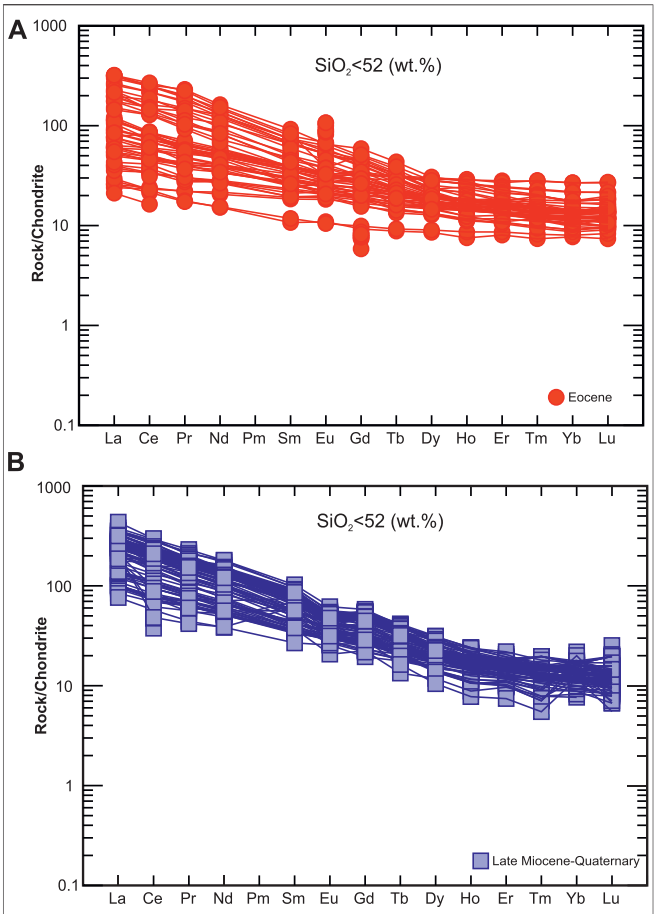

FIGURE 7 | Normalized REE abundances of the Eocene **(A)** and upper Miocene-Quaternary basic rocks (SiO_2<52 wt%) with chondrite values (Sun and McDonough, 1989). The normalized pattern shows that both the Eocene and upper Miocene-Quaternary rocks have higher ratios of light REEs than heavy REEs and negative slopes from LREEs to HREEs.

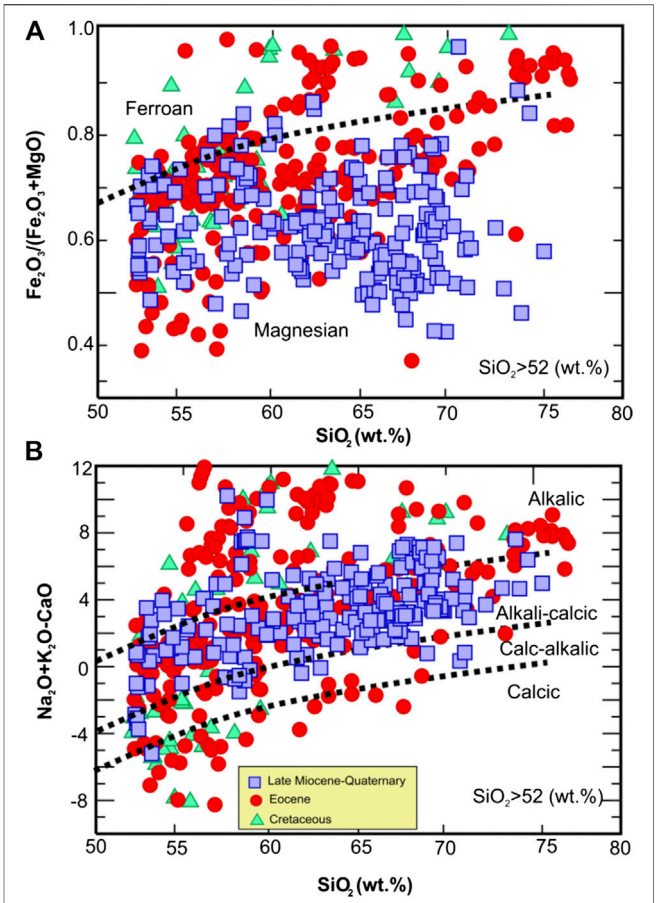

FIGURE 8 | Plotting of the intermediate to acidic rocks in the FeO/(FeO + MgO) vs. SiO_2 **(A)** and $Na_2O + K_2O$-CaO vs. SiO_2 (Frost et al., 2001) diagrams **(B)**, which are used for intermediate and acidic rock classification. See the text for more information.

The scattering of the Cretaceous volcanic rocks probably supports different tectonic regimes during the Cretaceous and requires more detailed work because the Cretaceous volcanic rocks were strongly altered by seawater reactions. Some parts of intermediate-to-acidic rocks have higher ratios of Sr/Y and La/Yb and, based on the adakite key diagrams (Defant and Drummond, 1990), are classified as adakite (**Figure 10A**). The high affinity of the upper Miocene-–Quaternary volcanic rocks for adakite groups, as well as the accompanying high-Nb basaltic rocks, means that there is a correspondence to a postcollisional tectonic regime in northwestern Iran since the Miocene (Azizi et al., 2014a; Asiabanha et al., 2018; Torkian et al., 2019).

Sr-Nd ISOTOPE RATIOS

We plotted 203 sample data points (**Supplementary S2**) in the $^{87}Sr/^{86}Sr$ vs. $^{143}Nd/^{144}Nd$ diagram collected from published works (Alpaslan et al., 2004; Agostini et al., 2007; Haghnazar and Malakotian, 2009; Mazhari et al., 2009, Mazhari et al., 2011; Aghazadeh et al., 2011, Aghazadeh et al., 2015; Dabiri et al., 2011; Allen et al., 2013a, Allen et al., 2013b; Ghaffari et al., 2013; Moghadam et al., 2014; Neill et al., 2015; Sahakyan et al., 2017; Haghighi Bardineh et al., 2018; Lechmann et al., 2018; Shafaii Moghadam et al., 2018; Azizi et al., 2019). Most samples plot near the mantle array with some variation for the Cretaceous and Eocene igneous rocks. Cretaceous samples plot in two main areas: the first group plots near the cross lines of the chondrite uniform reservoir (CHUR) and bulk silicate earth (BSE); and the second group, with lower ratios of $^{143}Nd/^{144}Nd$ and higher ratios of the $^{87}Sr/^{86}Sr$, plots with the combination of both mantle and crustal components for the evolution of these rocks (**Figure 11**).

Eocene igneous rocks mainly plot in the depleted-mantle area and extend to the lower $^{143}Nd/^{144}Nd$ ratio and higher $^{87}Sr/^{86}Sr$ ratio fields, which show heterogeneous sources such as depleted mantle and primitive and metasomatized mantle for the sources of these rocks. Furthermore, the scattering of Eocene samples in the $^{87}Sr/^{86}Sr$-$^{143}Nd/^{144}Nd$ diagram suggests the involvement of both mantle material and crustal components in the magmatic

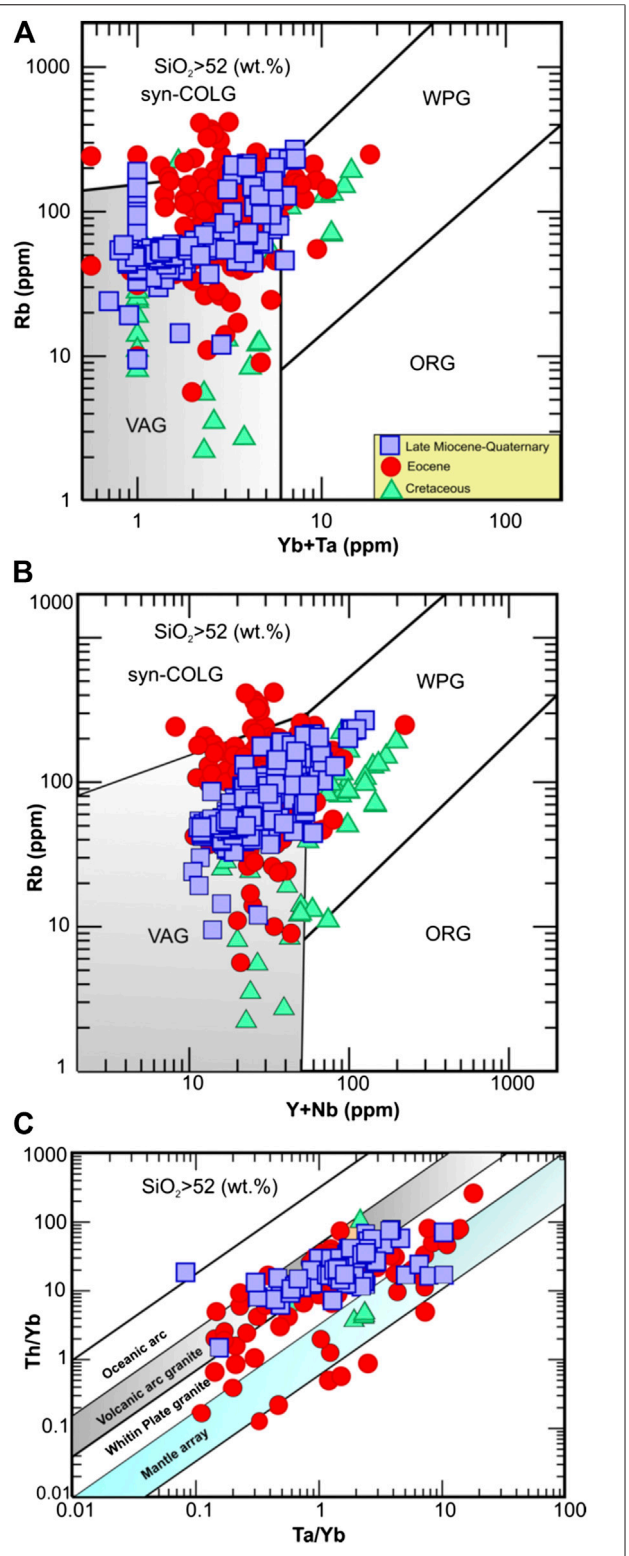

FIGURE 9 | Intermediate to acidic rocks (SiO_2 > 52 wt%) of the Eocene and Miocene mainly plot in the volcanic-arc, tectonic regime, whereas Cretaceous rocks plot in the arc and within-plate fields in the Rb–Yb + Ta **(A)** and Rb–Y + Nb **(B)** diagrams (Pearce et al., 1984). The variation in the Ta/Yb vs. the Th/Yb ratios (Pearce, 1982) shows a wide range for the Eocene (*Continued*)

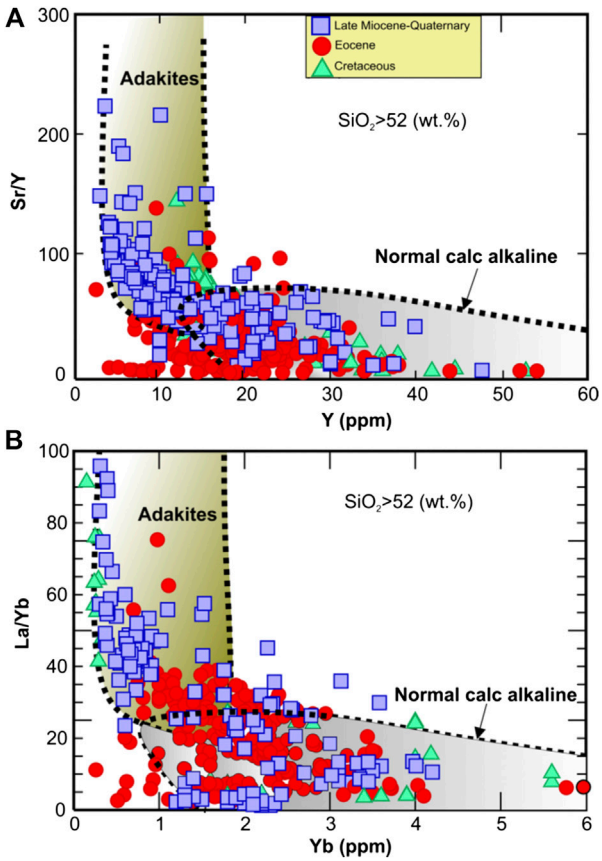

FIGURE 10 | Some intermediate-to-acidic rocks have higher ratios of Sr/Y and La/Yb and are classified as adakite **(A and B)**. See the text for more information. For source data and references, see **Supplementary S2**.

activity during the Eocene. The scattering of the Sr–Nd isotope ratios shows three main trends for the evolution of the Eocene magmatic rocks, which we call EO.1, EO.2, and EO.3 (**Figure 11**). These three trends show depleted mantle with higher ratios of $^{143}Nd/^{144}Nd$ (>0.51290), such as from the subcontinental-lithospheric mantle, as the primary source. During magmatic evolution and/or later, they have been affected by crustal components (EO.2 and EO.3 trend) and/or alteration (EO.1 trend). Due to the wide distribution of Eocene volcanism and the variation in Sr-Nd isotope ratios, metasomatized mantle from the oceanic slab is also the main alternative for the genesis of these rocks, which has been suggested by many researchers for the sources of these rocks.

Upper Miocene to Quaternary samples plot near the mantle array from the depleted mantle to enriched mantle in the $^{87}Sr/$

FIGURE 9 | intermediate-to-acidic rocks and more affinity of the upper Miocene–Quaternary for the within-plate field **(C)**. For source data and references, see **Supplementary S2**. *Abbreviations: MORB = Mid-Oceanic Ridge Basalt; BAB = Back Arc Basalt; IAT = Island Arc tholeiite; BON = Boninite; COLG = Collision Granite; VAG = Volcanic Arc Granite; ORG = Oceanic Ridge Granite; WPG= Within-Plate Granite.*

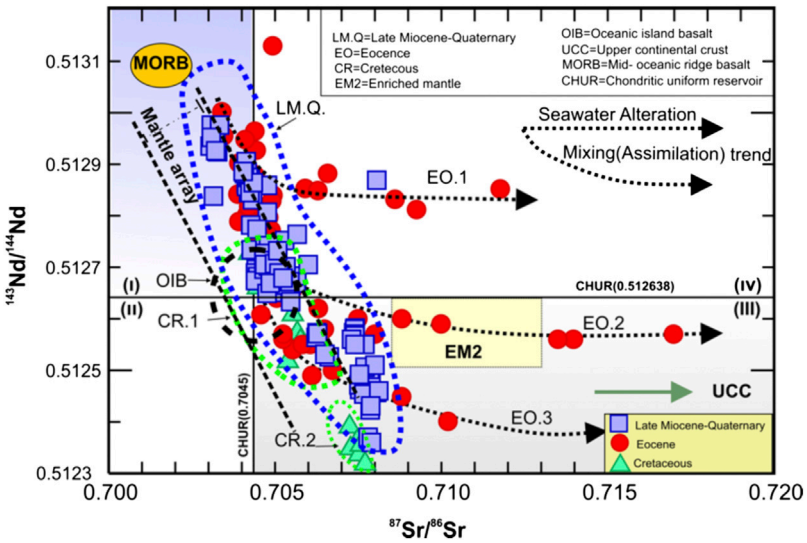

FIGURE 11 | Distribution of $^{87}Sr/^{86}Sr$ vs. $^{143}Nd/^{144}Nd$ ratios shows that the main samples extend along mantle arrays. The Cretaceous samples are plotted in two different fields, CR.1 and CR.2. The Eocene rocks show three different patterns—EO1-EO3—which confirms some seawater alteration and continental-crustal mixing. Upper Miocene-Quaternary samples plot in mantle arrays with less variation. For the sources of the data, see **Supplementary S2**.

^{86}Sr–$^{143}Nd/^{144}Nd$ ratio diagram (**Figure 11**). Most samples are concentrated near the cross line of the CHUR, which mainly shows the combination of depleted ($^{143}Nd/^{144}Nd > 0.512638$) to primitive mantles ($^{143}Nd/^{144}Nd = 0.512638$) as the main sources of these rocks. Crustal-component interactions, for example, assimilation with the magma, are lower than those of the Eocene magmatic rocks (**Figure 11**), which may suggest the thinning of the continental crust after collision. Therefore, depleted mantle, oceanic-island basalt (OIB), source-like, and enriched mantle (EM2) contributed to the genesis of Eocene and upper Miocene-Quaternary magmatic activity, with less contribution from continental crust for the upper Miocene-Quaternary rocks.

DISCUSSION

In most of the traditionally published research, the northern and eastern Bitlis–Zagros suture zone has been considered as an active continental margin since the Jurassic Period (Davoudian et al., 2008; Agard et al., 2011; Hassanzadeh and Wernicke, 2016). Recently published research has confirmed that the initiation of Neotethys subduction beneath the SaSZ (Azizi and Stern, 2019) occurred in the Cretaceous Period, and the collision of the Arabian plate and Van microplate in northwestern Iran occurred in the late Eocene epoch (Azizi et al., 2019). Nevertheless, there are some weak points concerning the relationship of ultramafic rocks to the ophiolite complex in northeastern Iraq within the suture of the Arabian plate and Van microplate. There is also no strong evidence for a typical ophiolite complex here (Azizi et al., 2013). In line with our suggestion, the new OSK zone shows that northwestern Iran-eastern Turkey magmatism was mainly controlled by Neotethys oceanic subduction, which was situated on the northern side of the Van microplate (**Figures 2**, **3**). The Khoy ophiolites mainly occurred during the Late Cretaceous Period (Ghazi et al., 2003; Khalatbari-Jafari et al., 2003, 2004; Moghadam and Stern, 2015) and are in contact with upper Neoproterozoic/lower Paleozoic granites (Azizi et al., 2011) in the east. Additionally, the Precambrian basements mainly include intrusive granite and metamorphic rocks, which were exposed in the Khoy, Urmia (Urmiah), and Tabriz areas. Northwestern Iran was obducted onto the east side of the OSK suture zone (**Figure 3**).

Tertiary volcanism surrounded the Van microplate (**Figures 2**, **3**). Meanwhile, distinct depression basins, such as the Urmia Lake basin (**Figures 2**, **3**), were formed near the OSK suture zone. All evidence shows a typical arc-type tectonic regime here. Nevertheless, our information on the Cretaceous magmatic rocks in northwestern Iran is not sufficient. The Neotethys ophiolite or ophiolite-like belt in northwestern Iran is divided into two branches in the area around Piranshahr (**Figure 3**). The southern (southwestern) branch extends to northeastern Iraq and continues to southern Bitlis, and it is known as the BZF suture zone here. This branch does not show a clear relationship to typical ophiolites, but it has some correlation with plume-type (Azizi et al., 2013) sources with some affinity for immature oceanic crust and/or continental rifts. The second branch is the OSK suture zone, which extends in a NW-SE direction in western Iran and joins the Sevan-Akera suture zone (SAS) in its northern part (**Figures 2**, **3**). The southern branch on the Iran side is named the Kermanshah-Nayriz ophiolites and is exposed along the Zagros fault in western Iran (**Figure 3**).

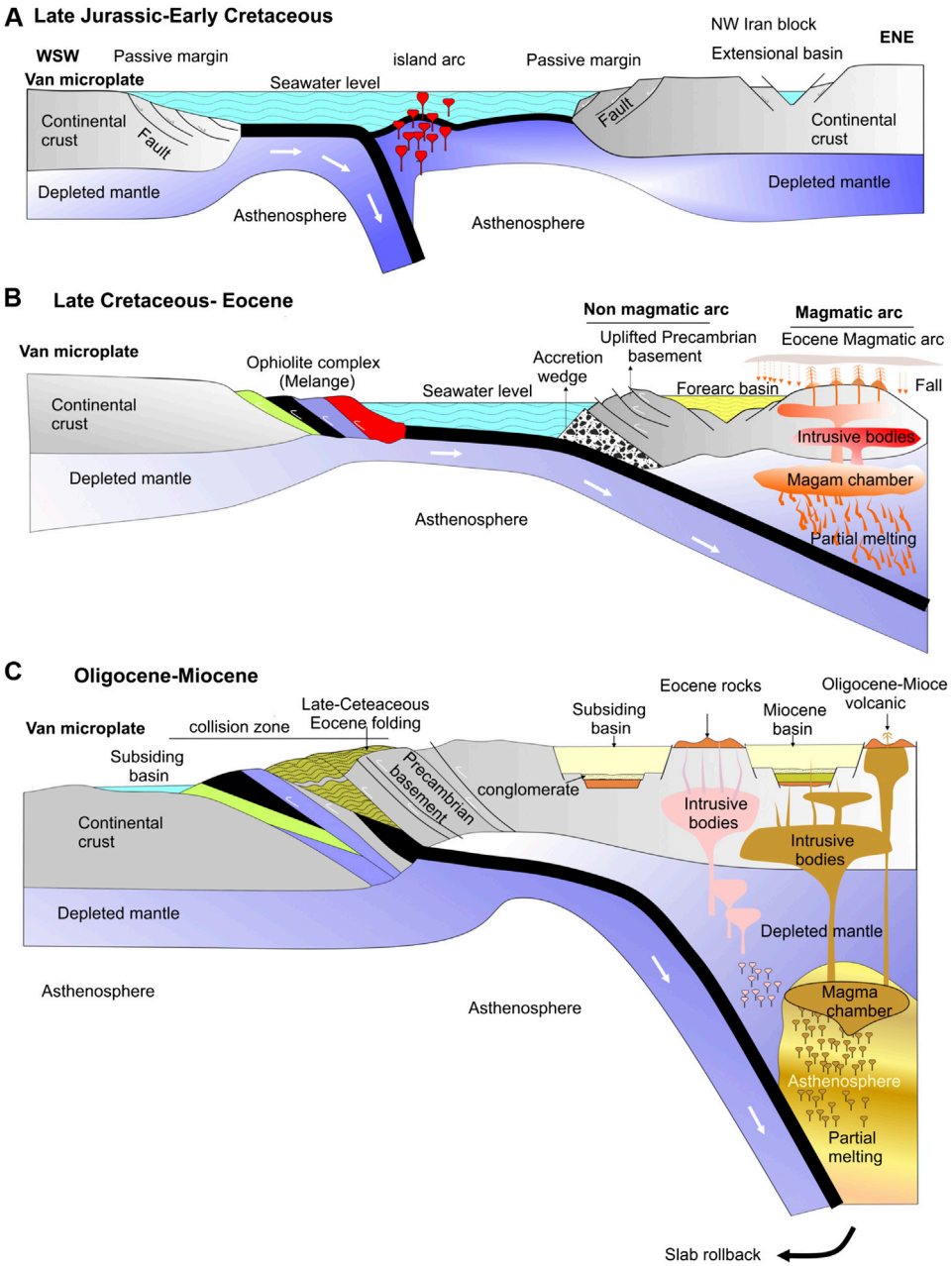

FIGURE 12 | Schematic tectonic model for the development of the magmatic arc from the Jurassic to the Oligocene-Miocene in the northwestern Iran block. **(A)** Development of the intraoceanic arc system in the Late Jurassic-Early Cretaceous periods. **(B)** Obduction of the Piranshahr-Khoy ophiolite complex over the Van microplate passive margin. Subduction of the northern branch of the Neotethys beneath the northern continent in the Late Cretaceous-Eocene led to the development of nonarc and arc magmatism and an Eocene forearc basin. **(C)** Collison of the Van microplate and NWIA, followed by the obduction of the Precambrian basement. Fragmentation of the Eocene magmatic belt, the development of interarc basins, injection, and the eruption of Miocene magmatic rocks. These processes occurred due to oceanic rollback after collision in the Oligocene-Miocene.

Magmatic activity since the Late Cretaceous Period developed in the northern and eastern parts of the Van microplate (**Figure 3**). The northern branches of the Neotethys, which were situated between the Van microplate to the south and the northwestern Iran-Armenia block (NWIA) to the north, were subducted beneath the NWIA block during the middle to Late Cretaceous Period. To consider the magmatic evolution in the southern rim of the NWIA, we suggest the following schematic model for the evolution of magmatic rocks in this belt since the Mesozoic.

Based on our suggested model, Jurassic rocks developed in the Van microplate. NWIA also probably shows the fragmentation of the Van microplate that occurred in the Late Jurassic/Early

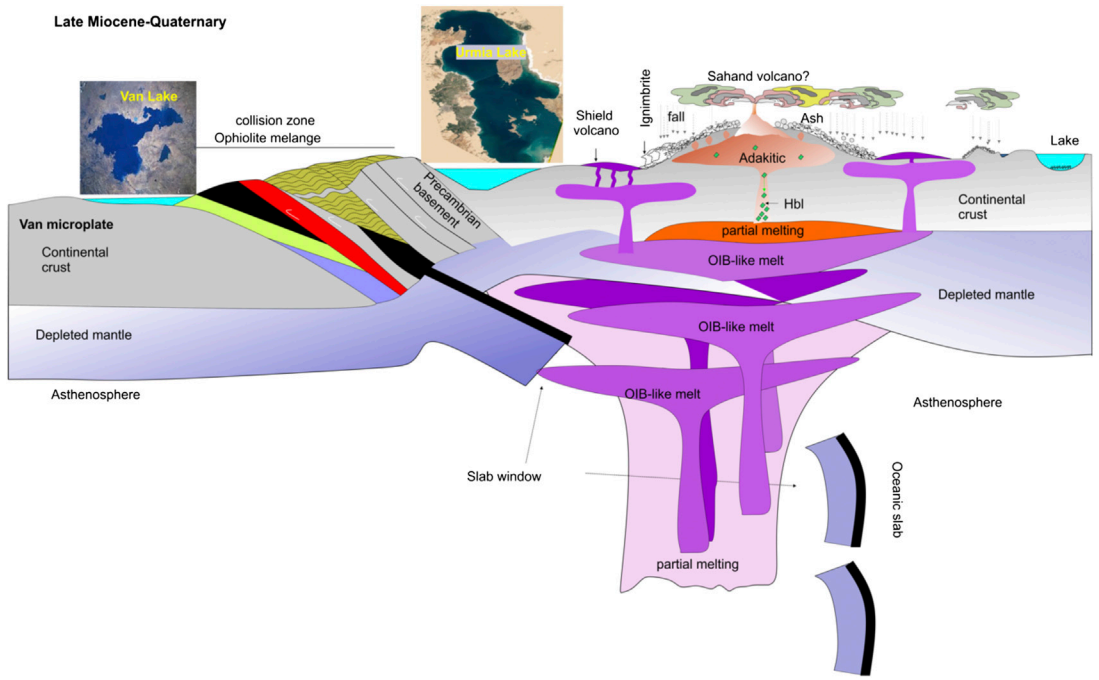

FIGURE 13 | Development of postorogenic basaltic-and-acidic volcanism during the Pliocene-Quaternary in northwestern Iran due to the slab window and injection of hot magma in the base of the lower crust, along with partial melting of earlier calc-alkaline bodies in the hot-root zone. Furthermore, during these processes, Van Lake as a foreland and Urmia Lake as a forearc basin were developed.

Cretaceous periods. Some evidence shows that the Jurassic magmatism was related to the extensional regime and continental rifts in the Khoy area (Khalatbari-Jafari et al., 2003; Lechmann et al., 2018; Miyazaki et al., 2018; Shafaii Moghadam et al., 2019), and they probably confirm the extensional regime or drifting of the Van microplate during the Cimmerian orogeny. This evidence is also consistent with the SaSZ tectonic regime, which had an extensional regime in the Middle-Late Jurassic Period (Azizi et al., 2018a; Badr et al., 2018; Azizi and Stern, 2019).

The OSK ophiolites have been thrust onto the passive margin and are overlaid by Paleocene sedimentary rocks. The ophiolite obduction on the passive margin probably occurred in a continental-arc collision system and, following the Neotethys, it started to subduct beneath the NWIA in the Late Cretaceous (**Figures 12A,B**). During subduction, nonarc magmatism, arc magmatism, and forearc basins developed in an active margin in the NWIA. Precambrian basements were obducted at this time (**Figures 12A,B**), and Upper Cretaceous-Eocene, magmatic rocks were produced during this process.

After colliding with the Van microplate and NWIA in the late Oligocene-Miocene, the oceanic crust experienced rollback, and the NWIA plate was overridden and affected by the extensional regime; some subsiding basins developed among the Eocene fragmented volcanic belt (**Figure 12C**). Deposition in the sedimentary basins started unconformably with a basal conglomerate on top of the Cretaceous-Eocene complex (**Figure 12C**). The extensional regime after the collision, the thinning of the NWIA, and the high-angle subduction connected both the lithospheric and asthenospheric mantle for the genesis of the magmatic rocks in the Miocene Epoch (**Figure 12C**). In the late stage, the oceanic crust was dismembered, and hot magma was injected from the slab window (**Figure 13**). Some parts of the magma erupted directly and made basaltic rocks that had a high similarity to the OIB composition in the HTV belt from Ararat to northern Sanandaj (Kheirkhah et al., 2009; Asiabanha and Foden, 2012; Azizi et al., 2014a; Torkian et al., 2016; Asiabanha et al., 2018). Other parts crystallized inside the lower crust and increased the geothermal gradient in the continental crust. This process was the basis for the partial melting of the lower crust and the production of adakite-like magma in the HTV belt during the Pliocene-Quaternary (Azizi et al., 2014b; Torkian et al., 2019).

CONCLUSION

This research shows that the Van microplate drifted from the Arabian plate in the Jurassic or earlier and is now surrounded by dismembered Neotethys ophiolite. During the closure of the northern branch of the Neotethys and the incorporation of the Van microplate into the southern Eurasian plate, a long period of magmatic activity (from the Late Cretaceous Period to the present) occurred along the southern rim of Eurasia, northwestern Iran, and the Caucasus. Therefore, the main suture is not Bitlis–Zagros, which has been suggested as the

junction of the Arabian and Iran-Armenia plates. Instead, it seems that Zagros–Khoy–Akera is the main suture zone, and it should be considered in future studies. The Zagers–Khoy–Akera suture can explain magmatism in the Caucasus and northwestern Iran more easily than the BZS. Furthermore, the northern SaSZ separated from the Anatolian plate via the Van microplate.

DATA AVAILABILITY STATEMENT

The original contributions presented in the study are included in the article/**Supplementary Material**, further inquiries can be directed to the corresponding author.

AUTHOR CONTRIBUTIONS

All authors listed have made a substantial, direct, and intellectual contribution to the work and approved it for publication.

FUNDING

This research was supported by the Japan Society for the Promotion of Science (JSPS) KAKENHI Grant No. 17H01671.

ACKNOWLEDGMENTS

This paper benefited greatly from previously published works, most of which we referred to in this work. We would like to thank F. Nouri for some technical support. This paper was greatly improved by three anonymous reviewers and the critical comments of the editor, Me-Fu Zhou.

SUPPLEMENTARY MATERIAL

The Supplementary Material for this article can be found online at: https://www.frontiersin.org/articles/10.3389/feart.2020.574385/full#supplementary-material.

REFERENCES

Abdulzahra, I. K., Hadi, A., Asahara, Y., Azizi, H., and Yamamoto, K. (2016). Zircon U–Pb ages and geochemistry of Devonian a-type granites in the Iraqi Zagros Suture Zone (Damamna area): new evidence for magmatic activity related to the Hercynian orogeny. *Lithos.* 264, 360–374. doi:10.1016/j.lithos.2016.09.006

Agard, P., Monié, P., Gerber, W., Omrani, J., Molinaro, M., Meyer, B., et al. (2006). Transient, synobduction exhumation of Zagros blueschists inferred from P–T, deformation, time, and kinematic constraints: implications for Neotethyan wedge dynamics. *J. Geophys. Res. Solid Earth.* 111, 4103. doi:10.1029/2005JB004103

Agard, P., Omrani, J., Jolivet, L., Whithechurch, H., Vrielynck, B., Spakman, W., et al. (2011). Zagros orogeny: a subduction-dominated process. *Geol. Mag.* 148, 692–725. doi:10.1017/S001675681100046X

Aghazadeh, M., Castro, A., Badrzadeh, Z., and Vogt, K. (2011). Post-collisional polycyclic plutonism from the Zagros hinterland: the Shaivar Dagh plutonic complex, Alborz belt, Iran. *Geol. Mag.* 148, 980–1008. doi:10.1017/S0016756811000380

Aghazadeh, M., Prelević, D., Badrzadeh, Z., Braschi, E., van den Bogaard, P., and Conticelli, S. (2015). Geochemistry, Sr–Nd–Pb isotopes and geochronology of amphibole- and mica-bearing lamprophyres in northwestern Iran: implications for mantle wedge heterogeneity in a palaeo-subduction zone. *Lithos.* 216–217, 352–369. doi:10.1016/j.lithos.2015.01.001

Agostini, S., Doglioni, C., Innocenti, F., Manetti, P., Tonarini, S., and Savasçin, M. Y. (2007). *The transition from subduction-related to intraplate Neogene magmatism in the Western Anatolia and Aegean area*. New York, NY: Special Papers-Geological Society of America.

Ahmadzadeh, G., Jahangiri, A., Lentz, D., and Mojtahedi, M. (2010). Petrogenesis of Plio-Quaternary post-collisional ultrapotassic volcanism in NW of Marand, NW Iran. *J. Asian Earth Sci.* 39, 37–50. doi:10.1016/j.jseaes.2010.02.008

Al Humadi, H., Väisänen, M., Ismail, S. A., Kara, J., O'Brien, H., Lahaye, Y., et al. (2019). U–Pb geochronology and Hf isotope data from the Late Cretaceous Mawat ophiolite, NE Iraq. *Heliyon.* 5, e02721. doi:10.1016/j.heliyon.2019.e02721

Alavi, M. (1994). Tectonics of the Zagros orogenic belt of Iran: new data and interpretations. *Tectonophysics* 229, 211–238. doi:10.1016/0040-1951(94)90030-2

Aldanmaz, E. (2006). Mineral-chemical constraints on the Miocene calc-alkaline and shoshonitic volcanic rocks of Western Turkey: disequilibrium phenocryst assemblages as indicators of magma storage and mixing conditions. *Turk. J. Earth Sci.* 15, 47–73. doi:10.5194/se-11-125-2020

Ali, S. A., Buckman, S., Aswad, K. J., Jones, B. G., Ismail, S. A., and Nutman, A. P. (2013). The tectonic evolution of a Neo-Tethyan (Eocene-Oligocene) island-arc (Walash and Naopurdan groups) in the kurdistan region of the northeast Iraqi Zagros suture zone. *Isl. Arc.* 22, 104–125. doi:10.1111/iar.12007

Ali, S. A., Ismail, S. A., Nutman, A. P., Bennett, V. C., Jones, B. G., and Buckman, S. (2016). The intra-oceanic Cretaceous (~108 Ma) Kata-Rash arc fragment in the Kurdistan segment of Iraqi Zagros Suture Zone: implications for Neotethys evolution and closure. *Lithos* 260, 154–163. doi:10.1016/j.lithos.2016.05.027

Alirezaei, S., and Hassanzadeh, J. (2012). Geochemistry and zircon geochronology of the Permian a-type Hasanrobat granite, Sanandaj–Sirjan belt: a new record of the Gondwana break-up in Iran. *Lithos* 151, 122–134. doi:10.1016/j.lithos.2011.11.015

Alishah, F. P., Jahangiri, A., and Branch, S. (2013). Adakitic volcanism in Sahand region, northwest Iran: geochemical and geodynamic implications. *Phys. Sci. Res. Int.* 1, 62–75. doi:10.1155/2013/735498

Allen, M. B., Kheirkhah, M., Neill, I., Emami, M. H., and McLeod, C. L. (2013a). Generation of arc andwithin-plate chemical signatures in collision zone magmatism: quaternary lavas from kurdistan province, Iran. *J. Petrol.* 54, 887–911. doi:10.1093/petrology/egs090

Allen, M. B., Saville, C., Blanc, E. J.-P., Talebian, M., and Nissen, E. (2013b). Orogenic plateau growth: expansion of the Turkish-Iranian Plateau across the Zagros fold-and-thrust belt. *Tectonics* 32, 171–190. doi:10.1002/tect.20025

Alpaslan, M., Frei, R., Boztug, D., Kurt, M. A., and Temel, A. (2004). Geochemical and Pb-Sr-Nd isotopic constraints indicating an enriched-mantle source for late cretaceous to early tertiary volcanism, central anatolia, Turkey. *Int. Geol. Rev.* 46, 1022–1041. doi:10.2747/0020-6814.46.11.1022

An, Y., and Harrison, T. M. (2000). Geologic evolution of the Himalayan-Tibetan orogen. *Annu. Rev. Earth Planet Sci.* 28, 211–280. doi:10.1146/annurev.earth.28.1.211

Ansari, M. R., Abedini, M. V., Zadeh, A. D., Sheikhzakariaee, S. J., and Mirzaee Beni, Z. H. (2011). Geochemical constrain on the Early Cretaceous, OIB-type alkaline volcanic rocks in Kojor volcanic field, Central Alborz Mountain, north of Iran. *Aust. J. Basic Appl. Sci.* 5, 913–925.

Ansari, M. R. (2013). Geochemistry of mid cretaceous alkaline volcanic rocks, member of chaloos formation, Abbas Abad volcanic field, Central Alborz Mountains, North of Iran. *Life Sci. J.* 10, 874–883. doi:10.1155/2013/735498

Ashrafi, N., Jahangiri, A., Hasebe, N., and Eby, G. N. (2018). Petrology, geochemistry and geodynamic setting of Eocene-Oligocene alkaline intrusions from the Alborz-Azerbaijan magmatic belt, NW Iran. *Geochemistry* 78, 432–461. doi:10.1016/j.chemer.2018.10.004

Asiabanha, A., Bardintzeff, J. M., and Veysi, S. (2018). North Qorveh volcanic field, western Iran: eruption styles, petrology and geological setting. *Mineral. Petrol.* 112, 501–520. doi:10.1007/s00710-017-0541-z

Asiabanha, A., and Foden, J. (2012). Post-collisional transition from an extensional volcano-sedimentary basin to a continental arc in the Alborz Ranges, N-Iran. *Lithos* 148, 98–111. doi:10.1016/j.lithos.2012.05.014

Azizi, H., Asahara, Y., and Tsuboi, M. (2014a). Quaternary high-Nb basalts: existence of young oceanic crust under the Sanandaj–Sirjan Zone, NW Iran. *Int. Geol. Rev.* 56, 167–186. doi:10.1080/00206814.2013.821268

Azizi, H., Asahara, Y., Tsuboi, M., Takemura, K., and Razyani, S. (2014b). The role of heterogenetic mantle in the genesis of adakites northeast of Sanandaj, northwestern Iran. *Chemie der Erde - Geochemistry* 74, 87–97. doi:10.1016/j.chemer.2013.09.008

Azizi, H., Chung, S. L., Tanaka, T., and Asahara, Y. (2011). Isotopic dating of the Khoy metamorphic complex (KMC), northwestern Iran: a significant revision of the formation age and magma source. *Precambrian Res.* 185, 87–94. doi:10.1016/j.precamres.2010.12.004

Azizi, H., Hadad, S., Stern, R. J., and Asahara, Y. (2019). Age, geochemistry, and emplacement of the ~40 Ma Baneh granite–appinite complex in a transpressional tectonic regime, Zagros suture zone, northwest Iran. *Int. Geol. Rev.* 61, 195–223. doi:10.1080/00206814.2017.1422394

Azizi, H., Hadi, A., Asahara, Y., and Mohammad, Y. O. Y. (2013). Geochemistry and geodynamics of the Mawat mafic complex in the Zagros Suture zone, northeast Iraq. *Cent. Eur. J. Geosci.* 5, 523–537. doi:10.2478/s13533-012-0151-6

Azizi, H., and Jahangiri, A. (2008). Cretaceous subduction–related volcanism in the northern Sanandaj–Sirjan Zone, Iran. *J. Geodyn.* 45, 178–190. doi:10.1016/j.jog.2007.11.001

Azizi, H., Lucci, F., Stern, R. J., Hasannejad, S., and Asahara, Y. (2018a). The Late Jurassic Panjeh submarine volcano in the northern Sanandaj-Sirjan Zone, northwest Iran: mantle plume or active margin?. *Lithos* 308 (309), 364–380. doi:10.1016/j.lithos.2018.03.019

Azizi, H., Mehrabi, B., and Akbarpour, A. (2009). Genesis of tertiary magnetite-apatite deposits, Southeast of Zanjan, Iran. *Resour. Geol.* 59, 330–341. doi:10.1111/j.1751-3928.2009.00101.x

Azizi, H., and Moinevaziri, H. (2009). Review of the tectonic setting of Cretaceous to Quaternary volcanism in northwestern Iran. *J. Geodyn.* 47, 167–179. doi:10.1016/j.jog.2008.12.002

Azizi, H., Nouri, F., Stern, R. J., Azizi, M., Lucci, F., Asahara, Y., et al. (2018b). New evidence for Jurassic continental rifting in the northern Sanandaj Sirjan Zone, western Iran: the Ghalaylan seamount, southwest Ghorveh. *Int. Geol. Rev.* 68, 142. doi:10.1080/00206814.2018.1535913

Azizi, H., and Stern, R. J. (2019). Jurassic igneous rocks of the central Sanandaj–Sirjan zone (Iran) mark a propagating continental rift, not a magmatic arc. *Terra. Nova.* 31, 415–423. doi:10.1111/ter.12404

Badr, A., Davoudian, A. R., Shabanian, N., Azizi, H., Asahara, Y., Neubauer, F., et al. (2018). A- and I-type metagranites from the north shahrekord metamorphic complex, Iran: evidence for early paleozoic post-collisional magmatism. *Lithos* 300–301, 86–104. doi:10.1016/j.lithos.2017.12.008

Castro, A., Aghazadeh, M., Badrzadeh, Z., and Chichorro, M. (2013). Late Eocene–Oligocene post-collisional monzonitic intrusions from the Alborz magmatic belt, NW Iran. An example of monzonite magma generation from a metasomatized mantle source. *Lithos* 180–181, 109–127. doi:10.1016/j.lithos.2013.08.003

Chiu, H. Y., Chung, S. L., Zarrinkoub, M. H., Mohammadi, S. S., Khatib, M. M., and Iizuka, Y. (2013). Zircon U-Pb age constraints from Iran on the magmatic evolution related to Neotethyan subduction and Zagros orogeny. *Lithos* 162 (163), 70–87. doi:10.1016/j.lithos.2013.01.006

Dabiri, R., Emami, M., Mollaei, H., Chen, B., Abedini, M., Omran, N., et al. (2011). Quaternary post-collision alkaline volcanism NW of Ahar (NW Iran): geochemical constraints of fractional crystallization process. *Geol. Carpathica.* 62, 547–562. doi:10.2478/v10096-011-0039-2

Davoudian, A. R., Genser, J., Dachs, E., and Shabanian, N. (2008). Petrology of eclogites from north of shahrekord, sanandaj-sirjan zone, Iran. *Mineral. Petrol.* 92, 393–413. doi:10.1007/s00710-007-0204-6

Defant, M. J., and Drummond, M. S. (1990). Derivation of some modern arc magmas by melting of young subducted lithosphere. *Nature* 347, 662–665. doi:10.1038/347662a0

Dewey, J. F., Pitman, W. C., Ryan, W. B. F., and Bonnin, J. (1973). Plate tectonics and the evolution of the alpine system. *Geol. Soc. Am. Bull.* 84, 3137. doi:10.1130/0016-7606(1973)84<3137:PTATEO>2.0.CO;2

Dilek, Y., and Altunkaynak, Ş. (2009). Geochemical and temporal evolution of Cenozoic magmatism in Western Turkey: mantle response to collision, slab break-off, and lithospheric tearing in an orogenic belt. *Geol. Soc. Spec. Publ.* 311, 213–233. doi:10.1144/SP311.8

Dilek, Y., Imamverdiyev, N., and Altunkaynak, Ş. (2010). Geochemistry and tectonics of Cenozoic volcanism in the Lesser Caucasus (Azerbaijan) and the peri-Arabian region: collision-induced mantle dynamics and its magmatic fingerprint. *Int. Geol. Rev.* 52, 536–578. doi:10.1080/00206810903360422

Doroozi, R., Vaccaro, C., Masoudi, F., and Petrini, R. (2016). Cretaceous alkaline volcanism in south Marzanabad, northern central Alborz, Iran: geochemistry and petrogenesis. *Geosci. Front.* 7, 937–951. doi:10.1016/j.gsf.2015.11.004

Frost, B. R., Barnes, C. G., Collins, W. J., Arculus, R. J., Ellis, D. J., and Frost, C. D. (2001). A geochemical classification for granitic rocks. *J. Petrol.* 42, 2033–2048. doi:10.1093/petrology/42.11.2033

Göncüoglu, M. C. (2010). *Introduction to the geology of Turkey: geodynamic evolution of the Pre-Alpine and Alpine terrances*. NewYork, NY: Springer, 1–69.

Ghaffari, M., Rashidnejad-Omran, N., Dabiri, R., Chen, B., and Santos, J. F. (2013). Mafic–intermediate plutonic rocks of the Salmas area, northwestern Iran: their source and petrogenesis significance. *Int. Geol. Rev.* 55, 2016–2029. doi:10.1080/00206814.2013.817067

Ghalamghash, J., Schmitt, A. K., and Chaharlang, R. (2019). Age and compositional evolution of Sahand volcano in the context of post-collisional magmatism in northwestern Iran: evidence for time-transgressive magmatism away from the collisional suture. *Lithos* 344–345, 265–279. doi:10.1016/j.lithos.2019.06.031

Ghasemi, A., and Talbot, C. J. (2006). A new tectonic scenario for the Sanandaj-Sirjan Zone (Iran). *J. Asian Earth Sci.* 26, 683–693. doi:10.1016/j.jseaes.2005.01.003

Ghazi, A. M., Pessagno, E. A., Hassanipak, A. A., Kariminia, S. M., Duncan, R. A., and Babaie, H. A. (2003). Biostratigraphic zonation and 40Ar–39Ar ages for the Neotethyan Khoy ophiolite of NW Iran. *Palaeogeogr. Palaeoclimatol. Palaeoecol* 193, 311–323. doi:10.1016/S0031-0182(03)00234-7

Golonka, J. (2004). Plate tectonic evolution of the southern margin of Eurasia in the Mesozoic and Cenozoic. *Tectonophysics* 381, 235–273. doi:10.1016/j.tecto.2002.06.004

Haghighi Bardineh, S. N., Zarei Sahamieh, R., Zamanian, H., and Ahmadi Khalaji, A. (2018). Geochemical, Sr-Nd isotopic investigations and U-Pb zircon chronology of the Takht granodiorite, west Iran: evidence for post-collisional magmatism in the northern part of the Urumieh-Dokhtar magmatic assemblage. *J. Afr. Earth Sci.* 139, 354–366. doi:10.1016/j.jafrearsci.2017.12.030

Haghnazar, S., and Malakotian, S. (2009). Petrography and Geochemistry of the Javaherdasht basalts (east of Guilan Province): the investigation of the role of crystal fractionation and crustal contamination in the magmatic evolution. *Mineral. Iran. J. Crystallogr. Mineral* 88, 253–266. doi:10.1016/0040-1951(94)90030-2

Haghnazar, S., Shafeie, Z., and Sharghy, Z. 2 (2016). Petrogenesis and tectonic setting of an basalt-Trachyte-Rhyolite suite in the Spilli area (south of Siahkal), north of Iran: evidences of continental rift-related bimodal magmatism in Alborz. *Ranian J. Petrol.* 27, 43–60. doi:10.22108/ijp.2016.21017

Hajialioghli, R., Moazzen, M., Jahangiri, A., Oberhänsli, R., Mocek, B., and Altenberger, U. (2011). Petrogenesis and tectonic evolution of metaluminous sub-alkaline granitoids from the Takab complex, NW Iran. *Geol. Mag.* 148, 250–268. doi:10.1017/S0016756810000683

Hassanipak, A. A., and Ghazi, A. M. (2000). Petrology, geochemistry and tectonic setting of the Khoy ophiolite, northwest Iran: implications for Tethyan tectonics. *J. Asian Earth Sci.* 18, 109–121. doi:10.1016/S1367-9120(99)00023-1

Hassanzadeh, J., and Wernicke, B. P. (2016). The Neotethyan Sanandaj-Sirjan zone of Iran as an archetype for passive margin-arc transitions. *Tectonics.* 35, 586–621. doi:10.1002/2015TC003926

Ismail, S. A., Mirza, T. M., and Carr, P. F. (2010). Platinum-group elements geochemistry in podiform chromitites and associated peridotites of the mawat ophiolite , northeastern Iraq. *J. Asian Earth Sci.* 37, 31–41. doi:10.1016/j.jseaes.2009.07.005

Jafari Sough, R., Asiabanha, A., and Nasrabadi, M. (2018). Geochemistry of Cretaceous hydromagmatic lava flows in Separdeh district, NE Qazvin, central Alborz. *Ranian J. Crystallogr. Mineral.* 26, 717–732. http://ijcm.ir/article-1-1154-fa.html.

Jahangiri, A. (2007). Post-collisional Miocene adakitic volcanism in NW Iran: geochemical and geodynamic implications. *J. Asian Earth Sci.* 30, 433–447. doi:10.1016/j.jseaes.2006.11.008

Jassim, S. Z., and Goff, J. C. (2006). *Geology of Iraq. DOLIN, sro, distributed*. London, UK: Geological Society of London.

Karim, K. H., and Al-Bidry, M. (2020). Zagros metamorphic core complex: example from bulfat mountain, qala diza area, kurdistan region, northeast Iraq. *Jordan J. Earth Environ. Sci.* 11, 113–125

Khalatbari-Jafari, M., Juteau, T., Bellon, H., and Emami, H. (2003). Discovery of two ophiolite complexes of different ages in the Khoy area (NW Iran). *Compt. Rendus Geosci.* 335, 917–929. doi:10.1016/S1631-0713(03)00123-8

Khalatbari-Jafari, M., Juteau, T., Bellon, H., Whitechurch, H., Cotten, J., and Emami, H. (2004). New geological, geochronological and geochemical investigations on the Khoy ophiolites and related formations, NW Iran. *J. Asian Earth Sci.* 23, 507–535. doi:10.1016/j.jseaes.2003.07.005

Kheirkhah, M., Allen, M. B., and Emami, M. (2009). Quaternary syn-collision magmatism from the Iran/Turkey borderlands. *J. Volcanol. Geoth. Res.* 182, 1–12. doi:10.1016/j.jvolgeores.2009.01.026

Kheirkhah, M., Neill, I., Allen, M. B., and Ajdari, K. (2013). Small-volume melts of lithospheric mantle during continental collision: late Cenozoic lavas of Mahabad, NW Iran. *J. Asian Earth Sci.* 74, 37–49. doi:10.1016/j.jseaes.2013.06.002

Kroner, U., and Romer, R. L. (2013). Two plates - many subduction zones: the Variscan orogeny reconsidered. *Gondwana Res.* 24, 298–329. doi:10.1016/j.gr.2013.03.001

Le Bas, M., Maitre, R., Streckeisen, A., and Zanettin, B. (1986). A chemical classification of volcanic rocks based on the total alkali-silica diagram. *J. Petrol.* 27, 745–750. doi:10.1093/petrology/27.3.745

Lechmann, A., Burg, J.-P. P., Ulmer, P., Mohammadi, A., Guillong, M., and Faridi, M. (2018). From Jurassic rifting to Cretaceous subduction in NW Iranian Azerbaijan: geochronological and geochemical signals from granitoids. *Contrib. Mineral. Petrol.* 173, 102. doi:10.1007/s00410-018-1532-8

Mahmoudi, S., Corfu, F., Masoudi, F., Mehrabi, B., and Mohajjel, M. (2011). U-Pb dating and emplacement history of granitoid plutons in the northern Sanandaj-Sirjan Zone, Iran. *J. Asian Earth Sci.* 41, 238–249. doi:10.1016/j.jseaes.2011.03.006

Manafi, M., Arian, M., Raeesi, S. H. T., and Solgi, A. (2013). Tethys subduction history in Caucasus region. *Open J. Geol.* 03, 222–232. doi:10.4236/ojg.2013.33026

Mazhari, S. A., Amini, S., Ghalamghash, J., and Bea, F. (2011). Petrogenesis of granitic unit of naqadeh complex, Sanandaj–Sirjan zone, NW Iran. *Arab. J. Geosci.* 4, 59–67. doi:10.1007/s12517-009-0077-6

Mazhari, S. A., Bea, F., Amini, S., Ghalamghash, J., Molina, J. F., Montero, P., et al. (2009). The Eocene bimodal Piranshahr massif of the Sanandaj-Sirjan Zone, NW Iran: a marker of the end of the collision in the Zagros orogen. *J. Geol. Soc. London* 166, 53–69. doi:10.1144/0016-76492008-022

Mehrabi, B., Siani, M. G. M. G., Goldfarb, R., Azizi, H., Ganerod, M., and Marsh, E. E. (2016). Mineral assemblages, fluid evolution, and genesis of polymetallic epithermal veins, Glojeh district, NW Iran. *Ore Geol. Rev.* 78, 41–57. doi:10.1016/j.oregeorev.2016.03.016

Miyazaki, T., Hanyu, T., Kimura, J.-I., Senda, R., Vaglarov, B. S., Chang, Q., et al. (2018). Clinopyroxene and bulk rock Sr–Nd–Hf–Pb isotope compositions of Raivavae ocean island basalts: does clinopyroxene record early stage magma chamber processes?. *Chem. Geol.* 482, 18–31. doi:10.1016/j.chemgeo.2017.12.015

Moghadam, H. S., Ghorbani, G., Khedr, M. Z., Fazlnia, N., Chiaradia, M., Eyuboglu, Y., et al. (2014). Late Miocene K-rich volcanism in the eslamieh peninsula (saray), NW Iran: implications for geodynamic evolution of the Turkish–Iranian high plateau. *Gondwana Res.* 26, 1028–1050. doi:10.1016/j.gr.2013.09.015

Moghadam, H. S., and Stern, R. J. (2015). Ophiolites of Iran: keys to understanding the tectonic evolution of SW Asia: (II) Mesozoic ophiolites. *J. Asian Earth Sci.* 100, 31–59. doi:10.1016/j.jseaes.2014.12.016

Mohammad, Y. O., and Cornell, D. H. (2017). U–Pb zircon geochronology of the Daraban leucogranite, Mawat ophiolite, Northeastern Iraq: a record of the subduction to collision history for the Arabia–Eurasia plates. *Isl. Arc.* 26, e12188. doi:10.1111/iar.12188

Mohammad, Y. O. (2013). P–T evolution of meta-peridotite in the Penjwin ophiolite, northeastern Iraq. *Arab. J. Geosci.* 6, 505–518. doi:10.1007/s12517-011-0372-x

Moritz, R., Rezeau, H., Ovtcharova, M., Tayan, R., Melkonyan, R., Hovakimyan, S., et al. (2016). Long-lived, stationary magmatism and pulsed porphyry systems during Tethyan subduction to post-collision evolution in the southernmost Lesser Caucasus, Armenia and Nakhitchevan. *Gondwana Res.* 37, 465–503. doi:10.1016/j.gr.2015.10.009

Neill, I., Meliksetian, K., Allen, M. B., Navasardyan, G., and Kuiper, K. (2015). Petrogenesis of mafic collision zone magmatism: the Armenian sector of the Turkish-Iranian Plateau. *Chem. Geol.* 403. doi:10.1016/j.chemgeo.2015.03.013

Nouri, F., Asahara, Y., Azizi, H., and Tsuboi, M. (2019). Petrogenesis of the Harsin–Sahneh serpentinized peridotites along the Zagros suture zone, western Iran: new evidence for mantle metasomatism due to oceanic slab flux. *Geol. Mag.* 156, 772–800. doi:10.1017/S0016756818000201

Nouri, F., Asahara, Y., Azizi, H., Yamamoto, K., and Tsuboi, M. (2017). Geochemistry and petrogensis of the Eocene back arc mafic rocks in the Zagros suture zone, northern Noorabad, western Iran. *Chemie der Erde Geochem.* 77, 517–533. doi:10.1016/j.chemer.2017.06.002

Nouri, F., Azizi, H., Asahara, Y., and Stern, R. J. (2020). A new perspective on Cenozoic calc-alkaline and shoshonitic volcanic rocks, eastern Saveh (central Iran). *Int. Geol. Rev.* 17, 185. doi:10.1080/00206814.2020.1718005

Nouri, F., Azizi, H., Golonka, J., Asahara, Y., Orihashi, Y., Yamamoto, K., et al. (2016). Age and petrogenesis of Na-rich felsic rocks in western Iran: evidence for closure of the southern branch of the Neo-Tethys in the Late Cretaceous. *Tectonophysics* 671, 151–172. doi:10.1016/j.tecto.2015.12.014

Parlak, O., HÖck, V., and Delaloye, M. (2000). Suprasubduction zone origin of the pozanti-karsanti ophiolite (southern Turkey) deduced from whole-rock and mineral chemistry of the gabbroic cumulates. *Geol. Soc. London, Spec. Publ.* 173, 219–234. doi:10.1144/GSL.SP.2000.173.01.11

Pearce, J. A. (2008). Geochemical fingerprinting of oceanic basalts with applications to ophiolite classification and the search for Archean oceanic crust. *Lithos* 100, 14–48. doi:10.1016/j.lithos.2007.06.016

Pearce, J. A., Harrison, N. B. W., and Tindel, A. G. (1984). Trace element discrimination diagrams for the tectonic Iinterpretation of granitic rocks. *J. Petrol.* 25, 956–983. doi:10.1093/petrology/25.4.956

Pearce, J. A. (1982). "*Trace element characteristics of lavas from destructive plate boundaries*", in *In andesites: orogenic andesites and related rocks.* (New York, NY: Wiley), 525–548

Prelević, D., and Seghedi, I. (2013). Magmatic response to the post-accretionary orogenesis within Alpine-Himalayan belt-Preface. *Lithos* 180–181, 1–4. doi:10.1016/j.lithos.2013.09.004

Rabiee, A., Rossetti, F., Tecce, F., Asahara, Y., Azizi, H., Glodny, J., et al. (2019). Multiphase magma intrusion, ore-enhancement and hydrothermal carbonatisation in the Siah-Kamar porphyry Mo deposit, Urumieh-Dokhtar magmatic zone, NW Iran. *Ore Geol. Rev.* 110, 102930. doi:10.1016/j.oregeorev.2019.05.016

Ranin, A., Sepahi, A. A., Moein-Vaziri, H., and Aliani, F. (2010). Petrology and geochemistry of the plutonic complexes of the Marivan area, Sanandaj-Sirjan zone (In Farsi with English abstract). *Petrology*, 22, 43–60.

Sahakyan, L., Bosch, D., Sosson, M., Avagyan, A., Galoyan, G., Rolland, Y., et al. (2017). Geochemistry of the Eocene magmatic rocks from the Lesser Caucasus area (Armenia): evidence of a subduction geodynamic environment. *Geol. Soc. London, Spec. Publ.* 428, 73–98. doi:10.1144/SP428.12

Sclater, J. G., Anderson, R. N., and Bell, M. L. (1971). Elevation of ridges and evolution of the central eastern Pacific. *J. Geophys. Res.* 76, 7888–7915. doi:10.1029/jb076i032p07888

Shabanian, N., Davoudian, A. R., Dong, Y., and Liu, X. (2018). U-Pb zircon dating, geochemistry and Sr-Nd-Pb isotopic ratios from Azna-Dorud Cadomian metagranites, Sanandaj-Sirjan Zone of western Iran. *Precambrian Res.* 306, 41–60. doi:10.1016/j.precamres.2017.12.037

Shafaii Moghadam, H., Corfu, F., Stern, R. J., and Lotfi Bakhsh, A. (2019). The eastern Khoy metamorphic complex of NW Iran: a jurassic ophiolite or continuation of the sanandaj–sirjan zone. *J. Geol. Soc. London* 177, 517–529. doi:10.1144/jgs2018-081

Shafaii Moghadam, H., Griffin, W. L., Kirchenbaur, M., Garbe-Schönberg, D., Zakie Khedr, M., Kimura, J.-I., et al. (2018). Roll-back, extension and mantle upwelling triggered Eocene potassic magmatism in NW Iran. *J. Petrol.* 59, 1417–1465. doi:10.1093/petrology/egy067

Shafaii Moghadam, H., and Stern, R. J. (2014). Ophiolites of Iran: keys to understanding the tectonic evolution of SW Asia: (I) Paleozoic ophiolites. *J. Asian Earth Sci.* 91, 19–38. doi:10.1016/j.jseaes.2014.04.008

Shervais, J. W. (1982). Ti-V plots and the petrogenesis of modern and ophiolitic lavas. *Earth Planet Sci. Lett.* 59, 101–118. doi:10.1016/0012-821X(82)90120-0

Siani, M. G., Mehrabi, B., Azizi, H., Wilkinson, C. M., and Ganerod, M. (2015). Geochemistry and geochronology of the volcano-plutonic rocks associated with the Glojeh epithermal gold mineralization, NW Iran. *Open Geosci.* 7. doi:10.1515/geo-2015-0024

Stöcklin, J., and Nabavi, M. H. (1973). *Tectonic map of Iran, scale 1:2,500,000.* Tehran: Geological Survey of Iran.

Sun, S. S., and McDonough, W. F. (1989). Chemical and isotopic systematics of oceanic basalts: implications for mantle composition and processes. *Geol. Soc. London, Spec. Publ.* 42, 313–345. doi:10.1144/GSL.SP.1989.042.01.19

Taki, S. (2017). The role of fractional crystallization in the evolution of magma of the Upper Cretaceous volcanic and subvolcanic rocks from the Nageleh Sar Syncline, south Mahmood Abad, North Iran. *Iran. J. Crystallogr. Mineral.* 25, 50–522. doi:10.1029/2010TC002809

Temizel, İ., Arslan, M., Yücel, C., Yazar, E. A., Kaygusuz, A., and Aslan, Z. (2019). U-Pb geochronology, bulk-rock geochemistry and petrology of Late Cretaceous syenitic plutons in the Gölköy (Ordu) area (NE Turkey): implications for magma generation in a continental arc extension triggered by slab roll-back. *J. Asian Earth Sci.* 171, 305–320. doi:10.1016/j.jseaes.2019.01.004

Tian, S. H., Yang, Z. Sen., Hou, Z. Q., Mo, X. X., Hu, W. J., Zhao, Y., et al. (2017). Subduction of the Indian lower crust beneath southern Tibet revealed by the post-collisional potassic and ultrapotassic rocks in SW Tibet. *Gondwana Res.* 41, 29–50. doi:10.1016/j.gr.2015.09.005

Topuz, G., Altherr, R., Satir, M., and Schwarz, W. H. (2004). Low-grade metamorphic rocks from the Pulur complex, NE Turkey: implications for the pre-Liassic evolution of the Eastern Pontides. *Int. J. Earth Sci.* 93, 72–91. doi:10.1007/s00531-003-0372-5

Topuz, G., Candan, O., Zack, T., and Yılmaz, A. (2017). East Anatolian plateau constructed over a continental basement: no evidence for the East Anatolian accretionary complex. *Geology.* 45, 791–794. doi:10.1130/G39111.1

Torkian, A., Furman, T., Salehi, N., and Veloski, K. (2019). Petrogenesis of adakites from the Sheyda volcano, NW Iran. *J. Afr. Earth Sci.* 150, 194–204. doi:10.1016/j.jafrearsci.2018.11.014

Torkian, A., Salehi, N., and Siebel, W. (2016). Geochemistry and petrology of basaltic lavas from NE-Qorveh, Kurdistan province, Western Iran. *Abhandlungen J. Mineral. Geochem.* 193, 95–128. doi:10.1127/njma/2016/0296

Whitechurch, H., Omrani, J., Agard, P., Humbert, F., Montigny, R., and Jolivet, L. (2013). Evidence for Paleocene-Eocene evolution of the foot of the Eurasian margin (Kermanshah ophiolite, SW Iran) from back-arc to arc: implications for regional geodynamics and obduction. *Lithos.* 182 (183), 11–32. doi:10.1016/j.lithos.2013.07.017

Wrobel-Daveau, J. C., Ringenbach, J. C., Tavakoli, S., Ruiz, G. M. H., Masse, P., and Frizon de Lamotte, D. (2010). Evidence for mantle exhumation along the Arabian margin in the Zagros (Kermanshah area, Iran). *Arab. J. Geosci.* 3, 499–513. doi:10.1007/s12517-010-0209-z

Zaeimnia, F., Arai, S., and Mirmohammadi, M. (2017). Na-rich character of metasomatic/metamorphic fluids inferred from preiswerkite in chromitite pods of the Khoy ophiolite in Iran: role of chromitites as capsules of trapped fluids. *Lithos.* 268–271, 351–363. doi:10.1016/j.lithos.2016.11.021

Zhang, Z., Dong, D., Sun, W., Zhang, G., and Bai, Y. (2020). Investigation of an oceanic plateau formation and rifting initiation model implied by the Caroline Ridge on the Caroline Plate, western Pacific. *Int. Geol. Rev.* 71, 100. doi:10.1080/00206814.2019.1707126

Zhang, Z., Ji, W., Majidifard, M. R., Rezaeian, M., Talebian, M., Xiang, D., et al. (2018). Geochemistry, zircon U-Pb and Hf isotope for granitoids, NW Sanandaj-Sirjan zone, Iran: implications for Mesozoic-Cenozoic episodic magmatism during Neo-Tethyan lithospheric subduction. *Gondwana Res.* 62, 227–245. doi:10.1016/j.gr.2018.04.002

Conflict of Interest: The authors declare that the research was conducted in the absence of any commercial or financial relationships that could be construed as a potential conflict of interest.

frontiers in Earth Science

ORIGINAL RESEARCH
published: 21 April 2021
doi: 10.3389/feart.2021.665610

Petrogenesis of the Cretaceous Intraplate Mafic Intrusions in the Eastern Tianshan Orogen, NW China

Weifeng Zhang[1,2], Xin Deng[1], Bing Tu[1], Lianhong Peng[1] and Xinbiao Jin[2]*

[1] Wuhan Center of China Geological Survey, Wuhan, China, [2] Research Center for Petrogenesis and Mineralization of Granitoids, Wuhan, China

In this study, we conducted zircon U-Pb dating, and whole-rock geochemical and Sr-Nd isotope analyses on the Late Mesozoic dolerite dykes in the Bailingshan Fe deposit (Eastern Tianshan Orogen, NW China) to unravel their petrogenesis and regional tectonic significance. Zircon U-Pb dating on the dolerite yielded an Early Cretaceous age of 129.7 ± 1.4 Ma. The dolerite is calc-alkaline sodic (Na_2O/K_2O = 4.71 to 6.80), and enriched in LILEs (Rb, K, Sr, and Pb) but depleted in HFSEs (Nb, Ta, and Ti). The intermediate Nb/U (16.7 to 18.5) and Ce/Pb (6.33 to 6.90) values, and the presence of xenocrystic zircons in these dolerite dykes suggest crustal assimilation during the magma evolution. Petrological modeling suggests fractionation of olivine, pyroxene, garnet, and spinel. All the dolerite samples have low initial $^{87}Sr/^{86}Sr$ (0.7041 to 0.7043) and positive $\varepsilon_{Nd}(t)$ (+ 4.6 to + 5.1) values, indicative of a depleted asthenospheric mantle source. Partial melting modeling suggests that the melting has occurred in the spinel-garnet stability field. Integrating the data from ore deposit geology, geochronology, geochemistry and Sr-Nd isotopes, we proposed that the Late Cretaceous Eastern Tianshan mafic magmatism was developed in an intraplate extension setting.

Keywords: petrogenesis, asthenospheric melts, within-plate magmatism, late mesozoic, eastern tianshan

OPEN ACCESS

Edited by:
Sean C. Johnson, University College Dublin, Ireland

Reviewed by:
Qiang Ma, China University of Geosciences Wuhan, China
Jinsheng Han, China University of Geosciences Wuhan, China

****Correspondence:***
Xin Deng
cugxd@163.com

Specialty section:
This article was submitted to Petrology, a section of the journal Frontiers in Earth Science

Received: *08 February 2021*
Accepted: *31 March 2021*
Published: *21 April 2021*

Citation:
Zhang W, Deng X, Tu B, Peng L and Jin X (2021) Petrogenesis of the Cretaceous Intraplate Mafic Intrusions in the Eastern Tianshan Orogen, NW China. Front. Earth Sci. 9:665610. doi: 10.3389/feart.2021.665610

INTRODUCTION

The Eastern Tianshan Orogen is located between the Tarim and Junggar blocks (Mao et al., 2005; Han et al., 2010; Wang et al., 2014; Hou et al., 2014). Devonian to Triassic igneous rocks are widely exposed in the orogen, consisting of the Jingerquan granite (376.9 ± 3.1 Ma), Bailingshan granitoids (317 to 307 Ma), Huangshandong mafic-ultramafic intrusions (274 ± 3 Ma), and Donggebi granite porphyry (233.8 ± 2.5 Ma) (Zhou et al., 2010; Deng et al., 2015; Zhang et al., 2015, 2016; Zhao et al., 2019). Since many of these intrusions are related to regional magmatic-hydrothermal mineralization, several studies were conducted to understand their geochronology, petrogenesis, and geodynamic setting (Zhang et al., 2015, 2016; Xiao et al., 2017; Zhao et al., 2019), which suggested that the Devonian-Carboniferous intrusions are arc-related, whereas the Permian-Triassic intrusions are syn- to post-collisional (Wu et al., 2006; Zhou et al., 2010; Wang et al., 2014; Zhao et al., 2019). However, the Late Mesozoic tectonic setting is still poorly constrained due to the lack of robust indicator, which inhibits the reconstruction of the completed geological history for the Eastern Tianshan Orogen.

Geochemistry of basaltic magmas is an effective geodynamic tracer, because basalts from different tectonic settings have distinctive geochemical characteristics (Pearce, 1982, 2014; Wilson, 1989;

Xia and Li, 2019). For instance, oceanic island basalts (OIB) are enriched in light rare earth elements (LREEs) and high field strength elements (HFSEs), whereas arc-related basalts are characterized by low Nb/La ratios and negative Nb, Ta, and Ti anomalies, and mid-ocean ridge basalts (MORB) have high contents of compatible trace elements and depleted isotopic values (Sun and McDonough, 1989; Hofmann, 1997). In the past decades, a large number of tectonic discrimination diagrams were established using basalt geochemistry (Pearce and Norry, 1979, Pearce, 1982, 2008; Wood, 1980; Shervais, 1982; Mullen, 1983; Meschede, 1986; Vermeesch, 2006; Ross and Bedard, 2009; Ishizuka et al., 2014; Saccani, 2015). Recent review studies suggested that intraplate basalts can be distinguished from arc-related ones by Zr-Zr/Y and Th/Yb-Ta/Yb diagrams, whereas OIB and MORB are distinguishable from each other in the ternary 3Tb-Th-2Ta diagram (Xia and Li, 2019).

In this contribution, we describe the newly-discovered Cretaceous dolerite dykes near the Bailingshan deposit in the Eastern Tianshan, and present their whole-rock geochemical and isotopic compositions. These dolerite dykes represent the youngest magmatic rocks in the Eastern Tianshan, and our data provide new petrogenetic insight and improve our understanding in the Late Mesozoic tectonic evolution of the region.

REGIONAL GEOLOGY

The Chinese Eastern Tianshan in NE Xinjiang (NW China) is an important component of the Central Asian Orogenic Belt (CAOB). The prolonged arc magmatism and collisional orogenesis have formed the widespread Paleozoic to Permian magmatic rocks and numerous Fe, Cu-Ni, Au-Ag, Pb-Zn and Mo deposits (Mao et al., 2005; Han et al., 2010; Wang et al., 2014; Hou et al., 2014; Li et al., 2019). From north to south, the Eastern Tianshan comprises four tectonic terranes, including the Dananhu-Tousuquan arc belt, Kanggur shear zone, Aqishan-Yamansu belt and the Central Tianshan block (**Figure 1**; Qin et al., 2002; Mao et al., 2005). These tectonic terranes are bounded by several roughly E-W trending faults, including the Kanggur, Yamansu and Aqikekuduke (Chen and Jahn, 2004; Mao et al., 2005; Xiao et al., 2008; Yang et al., 2009).

The northern Dananhu-Tousuquan island arc belt contains predominantly Silurian to Carboniferous calc-alkaline felsic lavas, mafic volcanic-volcanoclastic rocks and marine clastic sediments (Mao et al., 2005; Zhang et al., 2015). Overlying these sedimentary-volcanic rocks are Permian basalts and Cenozoic sediments. Many Devonian to Carboniferous (ca. 360 – 320 Ma) intrusions were considered to be arc-related (Wu et al., 2006; Zhou et al., 2010; Wang et al., 2014). Several important porphyry copper deposits (PCDs) were discovered along this belt, notably Tuwu, Yandong, Yuhai, and Linglong (Shen et al., 2014; Xiao et al., 2017; Wang et al., 2018). The Kanggur shear zone (about 400 km long and 20 km wide) contains dominantly Carboniferous volcaniclastic rocks, clastic rocks and ophiolite fragments, most of which are ductile deformed (Mao et al., 2005; Li et al., 2006). Abundant Permian mafic-ultramafic intrusions and important Cu-Ni sulfide deposits were formed in the eastern Kanggur shear zone (Han et al., 2010; Zhang et al., 2012; Deng et al., 2015). Besides, some syn- or post-collisional-related

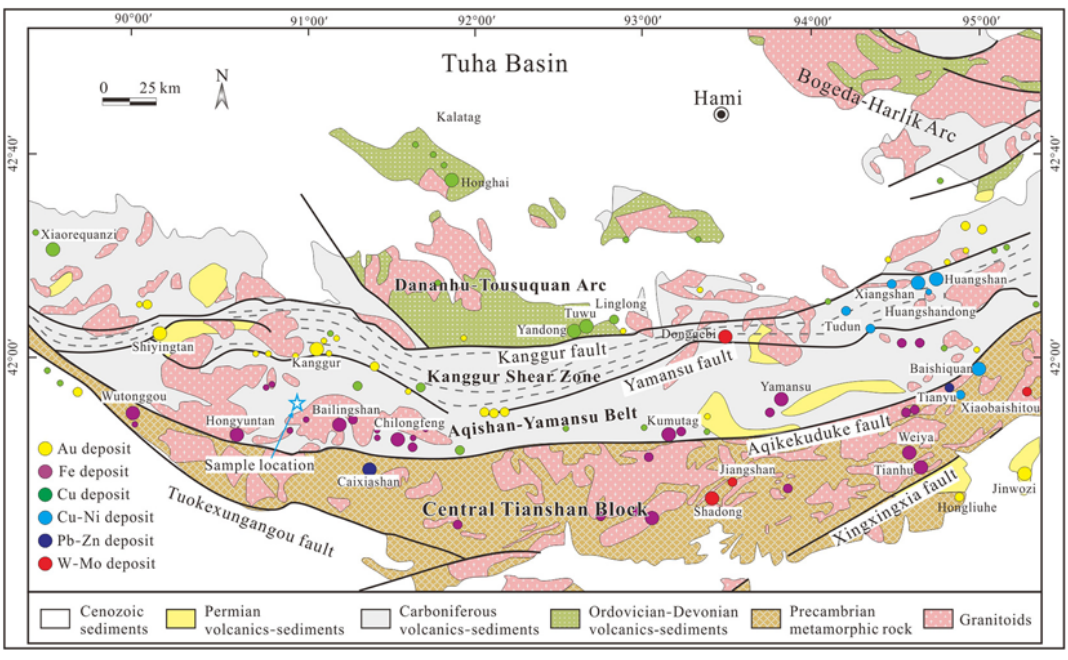

FIGURE 1 | Geologic map of the Chinese Eastern Tianshan Orogen (modified after Mao et al., 2005; Wang et al., 2006).

FIGURE 2 | Representative photographs showing the field relations, mineral assemblages and textural features for the dolerite: **(a)** Dolerite dyke cutting the Late Carboniferous volcaniclastic rocks. **(b)** Mafic rocks with medium- to fine-grained porphyritic texture. **(c)** Groundmasses of the dolerite with doleritic/interstitial texture. Abbreviations: Am = amphibole; Cpx = clinopyroxene; Ep = epidote; Pl = plagioclase.

orogenic Au and porphyry Mo deposits were formed at ca. 280 – 230 Ma (Zhang et al., 2015; Wang and Zhang, 2016; Wu et al., 2017).

The Aqishan-Yamansu belt comprises mainly Carboniferous intermediate-felsic volcanic-volcaniclastic rocks with minor marine sediment interbeds (Zhang et al., 2012; Han et al., 2019). These sequences are widely intruded by Carboniferous-Permian granitoids, which include the Bailingshan intrusive complex, Hongyuntan granodiorite and Xifengshan granite (Zhou et al., 2010; Zhang et al., 2016). Previous studies suggested that the widely-exposed felsic rocks are I-type and arc-related (Luo et al., 2016; Zhang et al., 2016; Zhao et al., 2019; Liu et al., 2020). The Aqishan-Yamansu island arc is well-known for hosting a series of Fe(-Cu) deposits, such as (from west to east) the Hongyuntan, Bailingshan, Yamansu, and Shaquanzi (Mao et al., 2005; Huang et al., 2013; Han et al., 2014; Hou et al., 2014; Jiang et al., 2018; Zhang et al., 2018a,b; Shi et al., 2021). The Central Tianshan Block is mainly consisted of a Precambrian metamorphic basement and Paleozoic active-margin magmatic sequences (Shu et al., 2002). Many skarn-type Fe and Pb-Zn deposits were formed during the Late Carboniferous (Zheng et al., 2015; Lu et al., 2018).

SAMPLING AND ANALYTICAL METHODS

Sampling

Dolerite dyke samples in this study were collected near the Bailingshan Fe deposit (41°48′07″N, 91°11′40″E) in the Aqishan-Yamansu belt, with a sampling interval of about 2 – 5 m from one dyke. In the field, the dolerite dyke (70 – 80 m long, 2 – 3 m wide) was observed to have intruded the Late Carboniferous volcaniclastic rocks (**Figure 2a**), suggesting a younger magmatic event.

TABLE 1 | Zircon U-Pb dating results for the study mafic dykes in the Eastern Tianshan.

Spot No.	Content (ppm)		Th/U	Isotopic ratios						Isotopic ages (Ma)					
	Th	U		$^{207}Pb/^{206}Pb$	1σ	$^{207}Pb/^{235}U$	1σ	$^{206}Pb/^{238}U$	1σ	$^{207}Pb/^{206}Pb$	1σ	$^{207}Pb/^{235}U$	1σ	$^{206}Pb/^{238}U$	1σ
βμ-01	1209	732	1.65	0.0543	0.0024	0.1562	0.0070	0.0209	0.0003	383	100	147	6	133	2
βμ-02	873	744	1.17	0.0535	0.0024	0.1513	0.0067	0.0206	0.0003	354	97	143	6	131	2
βμ-04	139	198	0.70	0.1221	0.0057	0.9643	0.0453	0.0568	0.0009	1987	88	686	23	356	6
βμ-06	132	162	0.82	0.0568	0.0030	0.4477	0.0233	0.0573	0.0011	483	117	376	16	359	7
βμ-07	576	487	1.18	0.0493	0.0033	0.1381	0.0095	0.0206	0.0006	165	157	131	8	132	4
βμ-08	474	350	1.36	0.0516	0.0056	0.1432	0.0165	0.0201	0.0004	333	49	136	15	128	2
βμ-09	143	243	0.59	0.0814	0.0057	0.4603	0.0310	0.0406	0.0006	1231	137	384	22	256	4
βμ-10	512	434	1.18	0.0484	0.0033	0.1350	0.0082	0.0206	0.0003	120	152	129	7	132	2
βμ-11	295	404	0.73	0.0543	0.0034	0.1563	0.0096	0.0209	0.0004	383	139	147	8	134	2
βμ-12	378	748	0.50	0.0615	0.0028	0.3260	0.0141	0.0384	0.0004	657	92	286	11	243	3
βμ-13	547	512	1.07	0.0484	0.0029	0.1355	0.0078	0.0204	0.0003	120	133	129	7	130	2
βμ-14	1735	1082	1.60	0.0526	0.0024	0.1457	0.0066	0.0201	0.0003	322	104	138	6	128	2
βμ-15	2205	1263	1.75	0.0505	0.0022	0.1387	0.0061	0.0197	0.0003	217	100	132	5	126	2
βμ-16	309	360	0.86	0.0558	0.0036	0.1541	0.0096	0.0200	0.0004	443	147	146	8	128	2
βμ-17	1640	1157	1.42	0.0527	0.0022	0.1473	0.0062	0.0202	0.0003	322	94	139	5	129	2
βμ-18	1551	1072	1.45	0.0523	0.0023	0.1448	0.0065	0.0199	0.0003	302	100	137	6	127	2
βμ-19	878	796	1.10	0.0490	0.0023	0.1363	0.0063	0.0200	0.0003	150	107	130	6	128	2
βμ-20	48.5	56.4	0.86	0.1127	0.0039	5.2078	0.1816	0.3344	0.0052	1844	58	1854	30	1860	25
βμ-21	686	519	1.32	0.0570	0.0032	0.1594	0.0087	0.0203	0.0004	500	126	150	8	130	2
βμ-22	473	580	0.82	0.0565	0.0021	0.4551	0.0164	0.0582	0.0008	472	83	381	11	365	5
βμ-23	1279	994	1.29	0.0560	0.0022	0.1631	0.0062	0.0212	0.0004	454	87	153	5	135	2
βμ-24	127	462	0.27	0.0856	0.0077	0.5544	0.0671	0.0416	0.0009	1329	174	448	44	263	6
βμ-25	323	314	1.03	0.0478	0.0037	0.1340	0.0094	0.0206	0.0004	100	161	128	8	132	2

The dolerite samples are dark green, and medium- to fine-grained porphyritic (**Figure 2b**). Euhedral plagioclase is the dominant phenocryst phase and commonly 1 to 3 mm long (**Figure 2b**). The doleritic-/interstitial-textured groundmass is composed mainly of subhedral plagioclase, clinopyroxene and trace Fe-Ti oxides (**Figure 2c**). Minor plagioclase and clinopyroxene grains in the samples are partially altered to epidote and amphibole, respectively. All the sample preparation and laboratory analyses were performed at the Wuhan SampleSolution Analytical Technology Co., Ltd. (WSATCL), China.

Zircon U-Pb Geochronology

After separated with the conventional density and magnetic separation techniques, zircon grains were hand-picked under a binocular microscope. The zircon internal structure was studied via cathodoluminescence (CL) imaging using an Analytical Scanning Electron Microscope (JSM − IT100).

Laser Ablation-Inductively Coupled Plasma-Mass Spectrometry (LA-ICP-MS) zircon U-Pb dating and trace element analysis for the dolerite samples were performed at the WSATCL. The laser ablation used 5 Hz frequency and 24 μm spot size. Each analysis comprises a background acquisition of approximately 20 - 30s, followed by 50s of sample data acquisition. The zircon 91500 and glass NIST610 were used as the external standard, and the Plešovice and GJ-1 zircons as the internal standard. Quantitative calibration for trace element analyses and U-Pb dating were conducted using ICPMSDataCal (Liu et al., 2008). Calculation of weighted mean ages and concordia diagram construction were performed using Isoplot/Ex 3.0 (Ludwig, 2003).

Whole-Rock Major and Trace Element Analyses

All the samples were first powdered to less than 200-mesh, then were placed in an oven at 105°C for drying of 12 h to determine LOI. The major element contents were measured by X-ray fluorescence (XRF) spectrometry (1 g powder for each sample), and the analytical precision is better than 1%. For trace elements (including REEs), 50 mg powder for each sample was dissolved in a mixture of 100ml HNO_3 and 100 ml HF. This solution was then analyzed with an Agilent 7700e ICP-MS, and the analytical precision is better than ± 5%.

Whole-Rock Sr-Nd Isotopes

Whole-rock Sr-Nd isotope analyses were conducted on a Neptune Plus Multi-Collector (MC)-ICP-MS, with the detailed analytical techniques as described by Wang et al. (2019). The $^{87}Rb/^{86}Sr$ and $^{147}Sm/^{144}Nd$ ratios were calculated using the Sr, Rb, Nd and Sm contents obtained by ICP-MS. All the measured Sr and Nd isotope ratios were

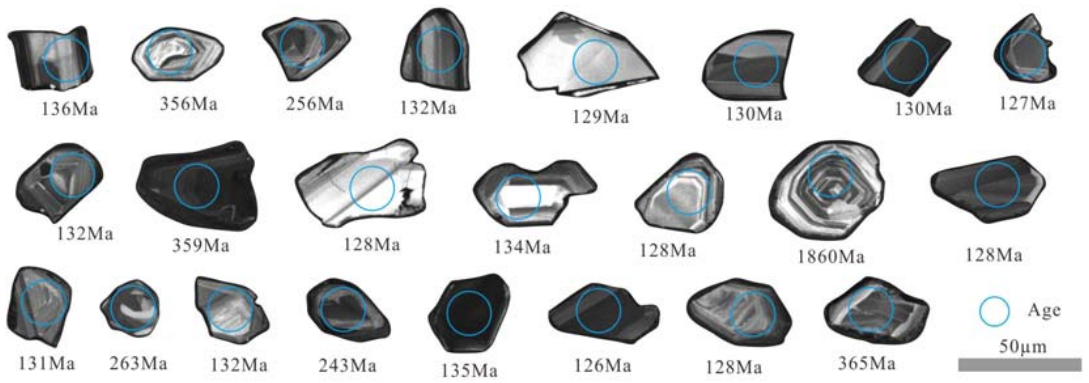

FIGURE 3 | Zircon CL images of the dolerite dyke.

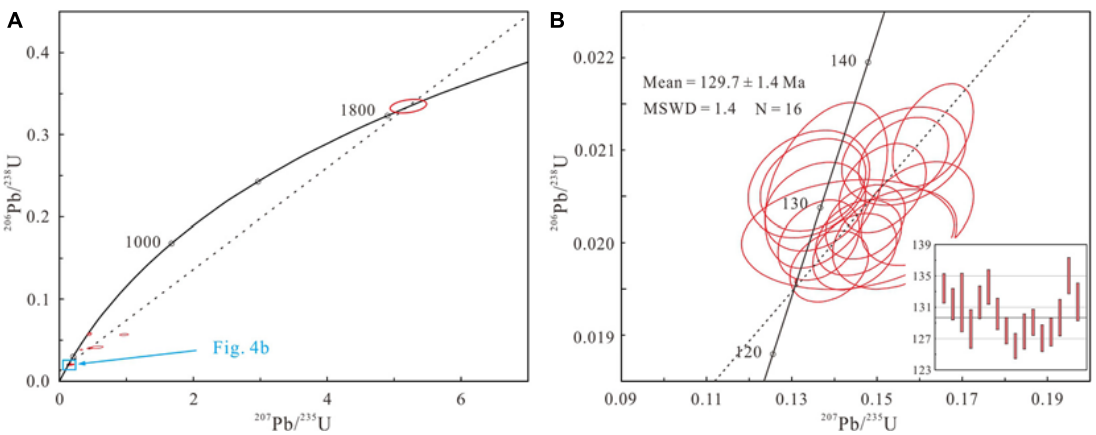

FIGURE 4 | (A) U-Pb concordia diagram of all the analytical zircon grains from the dolerite dyke. **(B)** U-Pb concordia diagram and weighted mean age of the concordant zircons.

normalized with $^{86}Sr/^{88}Sr$ = 0.1194 and $^{146}Nd/^{144}Nd$ = 0.7219, respectively (Lin et al., 2016). Analyses of the standards NIST SRM 987 and JNdi-1 during the measurement period yielded $^{87}Sr/^{86}Sr$ = 0.710244 ± 0.000022 (2σ) and $^{143}Nd/^{144}Nd$ = 0.512118 ± 0.000015 (2σ), similar to the recommended values (Tanaka et al., 2000).

RESULTS

Zircon U-Pb Ages

One sample was dated by zircon U-Pb analysis, and the results are given in **Table 1**. The zircons analyzed have wide ranges of U and Th contents, and all have high Th/U ratios (> 0.4). The zircon grains are transparent and euhedral-subhedral prismatic, indicating a magmatic origin (**Figure 3**; Belousova et al., 2002; Li, 2009). The 23 zircons analyzed show a wide $^{206}Pb/^{238}U$ age range (**Figure 4A**). The concordant zircons (n = 16) range from 136 to 126 Ma, yielding a weighted mean age of 129.7 ± 1.4 Ma (MSWD = 1.4; **Figure 4B**), which likely represents the dolerite crystallization age. Seven inherited/xenocrystic zircons were identified, including a Precambrian (1860 Ma), three Devonian-Carboniferous (365 to 356 Ma), and three Permian-Triassic (263 to 243 Ma) ones.

Whole-Rock Major and Trace Elements

Whole-rock major element and trace element contents of the dolerite dykes are listed in **Table 2**. As our samples are fresh or only slightly altered (e.g., weak epidote alteration in some plagioclase grains), the alteration effect on geochemistry is likely negligible. After normalized to 100 wt.% (anhydrous), the samples contain 49.4 to 50.1 wt.% SiO_2, 19.8 to 20.6 wt.% Al_2O_3, and 6.54 to 6.82 wt.% MgO. They have medium $Fe_2O_3{}^T$ content (8.43 to 8.71 wt.%) with corresponding Mg# (100*Mg/(Mg + Fe)) of 47 – 49. The rocks are sodic (Na_2O/K_2O = 4.71 to 6.80), and fall inside the basalt field in the TAS diagram (**Figure 5**; Wilson, 1989).

All the studied dolerite dykes display uniform chondrite-normalized REE patterns, as characterized by slight LREE enrichments ($(La/Yb)_N$ = 3.63 to 3.77) and subtle Eu anomalies

TABLE 2 | Major oxides (wt.%) and trace elements (ppm) abundances of the doleritic dykes in the Eastern Tianshan.

	β μ -01	β μ -02	β μ -03	β μ -04	β μ -05
Major oxides (wt.%)					
SiO_2	48.34	48.25	48.27	48.75	48.43
TiO_2	0.97	0.97	0.95	0.98	0.99
Al_2O_3	19.43	19.58	19.81	19.42	19.48
$Fe_2O_3^T$	8.44	8.45	8.16	8.52	8.44
FeO	4.90	4.42	4.60	4.38	4.42
MnO	0.13	0.15	0.14	0.13	0.13
MgO	6.60	6.41	6.43	6.39	6.36
CaO	9.68	9.54	9.56	9.87	9.78
Na_2O	2.69	2.75	2.72	2.76	2.76
K_2O	0.56	0.40	0.50	0.58	0.59
P_2O_5	0.25	0.26	0.25	0.26	0.25
Loss	2.52	2.66	2.65	2.39	2.43
Total	99.60	99.42	99.44	100.03	99.63
Trace elements (ppm)					
Sc	22.3	21.8	21.4	22.8	22.3
V	185	184	183	190	190
Cr	149	149	150	144	148
Co	35.6	36.0	35.9	37.1	36.8
Ni	121	113	116	113	112
Cu	75.3	64.4	47.0	72.1	82.3
Zn	57.7	65.9	56.2	57.4	57.7
Ga	17.7	18.2	18.0	18.5	18.2
Rb	19.8	13.5	18.2	25.5	25.3
Sr	541	524	535	552	544
Y	19.4	20.4	19.7	20.6	20.1
Zr	104	99	99	107	106
Nb	4.40	4.31	4.22	4.50	4.52
Cs	0.96	0.84	0.69	1.48	1.42
Ba	153	106	115	158	142
La	9.25	9.20	9.05	9.70	9.48
Ce	22.4	23.0	22.6	24.2	23.4
Pr	3.06	3.07	3.04	3.24	3.17
Nd	13.9	14.0	13.6	14.7	14.2
Sm	3.79	3.73	3.67	3.78	3.74
Eu	1.12	1.20	1.16	1.19	1.18
Gd	3.51	3.48	3.62	3.66	3.56
Tb	0.55	0.56	0.54	0.56	0.55
Dy	3.47	3.44	3.35	3.78	3.54
Ho	0.72	0.69	0.71	0.72	0.72
Er	1.90	1.92	1.86	2.00	1.99
Tm	0.29	0.28	0.27	0.30	0.30
Yb	1.77	1.82	1.75	1.88	1.80
Lu	0.27	0.27	0.26	0.28	0.28
Hf	2.39	2.21	2.35	2.37	2.40
Ta	0.27	0.28	0.26	0.29	0.28
Pb	3.49	3.33	3.30	3.66	3.70
Th	0.66	0.63	0.63	0.65	0.65
U	0.26	0.23	0.24	0.25	0.25
Na_2O/K_2O	4.82	6.80	5.42	4.80	4.71
Mg#	49	48	49	49	47
Nb/U	16.7	18.5	17.9	17.9	18.1
Ce/Pb	6.43	6.90	6.85	6.61	6.33
Sm/Yb	2.14	2.05	2.09	2.01	2.08
Dy/Yb	1.96	1.89	1.91	2.01	1.97
$(La/Yb)_N$	3.75	3.63	3.70	3.70	3.77
Eu/Eu*	0.93	1.01	0.96	0.97	0.97

(Eu/Eu* = 0.93 to 1.01) (**Figure 6A**). In the primitive mantle-normalized multi-element plot (**Figure 6B**), the samples are enriched in large-ion lithophile element (LILE; e.g., Rb, K, Sr, and Pb) and depleted in HFSEs.

Whole-Rock Sr-Nd Isotopes

Whole-rock Sr-Nd isotope compositions of the studied samples are presented in **Table 3**. Initial isotope ratios were back-calculated to the dolerite crystallization age of 130 Ma. The samples have low initial $^{87}Sr/^{86}Sr$ (0.7041 to 0.7043) and positive $\varepsilon_{Nd}(t)$ (+ 4.6 to + 5.1) values, yielding depleted mantle Nd one-stage model ages (T_{DM1}) of 746 – 882 Ma. In the $(^{87}Sr/^{86}Sr)_i$ vs. $(^{143}Nd/^{144}Nd)_i$ diagram (**Figure 7**), all samples plot in the ocean island basalt (OIB) field (Hart, 1985), similar to the Permian Huangshanxi gabbro in the Eastern Tianshan (Zhang et al., 2011; Deng et al., 2015).

DISCUSSION

Fractional Crystallization and Crustal Contamination

The dolerite samples have much lower Mg# (47 – 49), Cr (144 – 150 ppm) and Ni (112 – 121 ppm) contents (**Table 2**) than typical mantle-derived melts (Mg# = 71 – 83, Cr > 1000 ppm and Ni > 400 ppm; Wilson, 1989; Wang et al., 2019), suggesting that their parental magma may have experienced fractional crystallization. Rayleigh fractional crystallization model calculations were conducted to determine the fractionation phase (Wilson, 1989), which shows that all samples plot between the olivine and pyroxene evolution trends in the Cr-Ni diagram (**Figure 8A**). This indicates significant fractionation of olivine and pyroxene. Fractionation of Ti-bearing minerals (e.g., spinel) in the dolerite is evidenced by the negative Nb, Ta and Ti anomalies and the Nb-Ta fractional crystallization model diagram (**Figure 8B**; Saunders et al., 1992; Hawkesworth et al., 1993). The lack of negative Sr and Eu anomalies in the samples suggests limited plagioclase fractionation (**Figure 6**).

Mantle-derived magmas commonly assimilate crustal components during their ascent, which altered their geochemical characteristics (e.g., LREE and LILE enrichments and HFSE depletions; Wilson, 1989; Rudnick and Gao, 2014), as found also in the dolerite dykes (**Figure 6**). This clearly suggests certain degrees of crustal contamination for the doleritic magma. Element pairs (e.g., Nb and U, Ce, and Pb) with similar bulk-solid/melt partition coefficients cannot be significantly

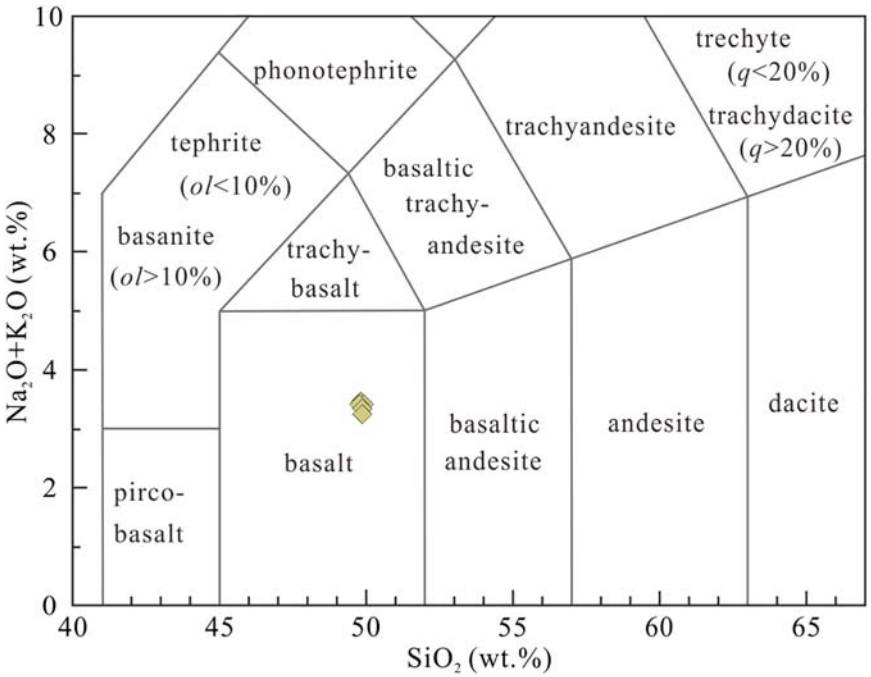

FIGURE 5 | K_2O vs. SiO_2 diagram for the samples (after Peccerillo and Taylor, 1976).

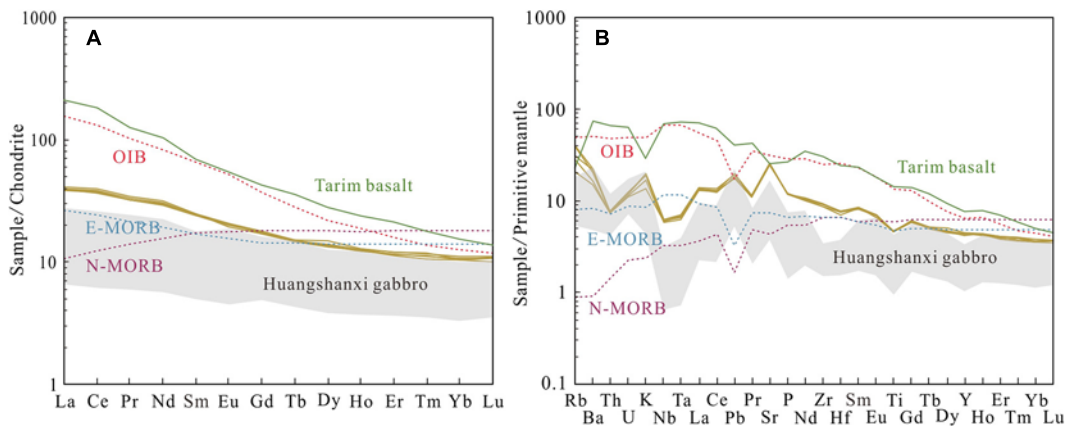

FIGURE 6 | (A) Chondrite-normalized REE patterns; **(B)** Primitive mantle-normalized multi-element diagrams. Data of average primitive mantle, E-MORB, N-MORB and OIB are from Sun and McDonough (1989). Compositions of chondrite, Tarim basalts and Huangshanxi gabbro are from Boynton (1984); Zhou et al. (2009) and Zhang et al. (2011), respectively.

TABLE 3 | Sr and Nd isotopic compositions of doleritic samples from the Eastern Tianshan.

	Rb (ppm)	Sr (ppm)	$^{87}Rb/^{86}Sr$	$^{87}Sr/^{86}Sr$	2σ	$(^{87}Sr/^{86}Sr)_i$	Sm (ppm)	Nd (ppm)	$^{147}Sm/^{144}Nd$	$^{143}Nd/^{144}Nd$	2σ	$(^{143}Nd/^{144}Nd)_i$	$\varepsilon_{Nd}(t)$	TDM_1 (Ga)
βμ-01	19.8	541	0.105745	0.704445	0.0000086	0.7043	3.79	13.9	0.164782	0.512867	0.0000056	0.5127	5.0	0.88
βμ-02	13.5	524	0.074352	0.704215	0.0000085	0.7041	3.73	14.0	0.161012	0.512865	0.0000064	0.5127	5.0	0.82
βμ-03	18.2	535	0.098366	0.704239	0.0000085	0.7041	3.67	13.6	0.162885	0.512872	0.0000078	0.5127	5.1	0.83
βμ-04	25.5	552	0.133849	0.704579	0.0000109	0.7043	3.78	14.7	0.154996	0.512863	0.0000065	0.5127	5.1	0.75
βμ-05	25.3	544	0.134156	0.704471	0.0000116	0.7042	3.74	14.2	0.159375	0.512842	0.0000126	0.5127	4.6	0.86

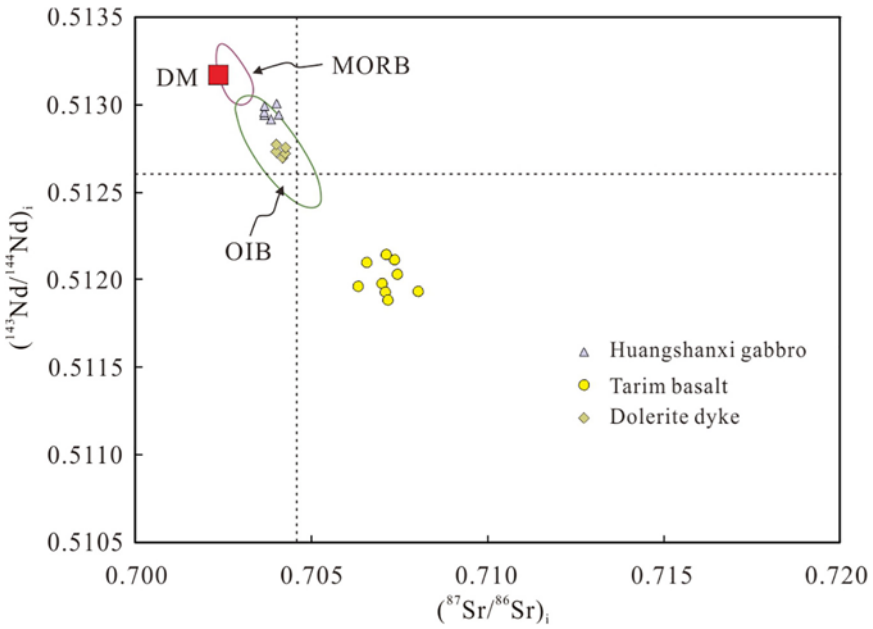

FIGURE 7 | $\varepsilon_{Nd}(t)$ vs. I_{Sr} diagram for the dolerite dyke. All data were calculated to the corresponding zircon U-Pb ages. Data source: Tarim basalts (Zhou et al., 2009); Huangshanxi gabbro (Zhang et al., 2011); DM (Salters and Stracke, 2004). The OIB and MORB fields are after Hart (1985) and Wilson (1989), respectively.

segregated through partial melting or fractional crystallization, and their ratios remain roughly constant and reflect those of the magma source (Hofmann, 1997). The dolerite samples have Nb/U (16.7 to 18.5) and Ce/Pb (6.33 to 6.90) values intermediate between the mantle array (OIB/MORB) and continental crust, also suggesting crustal assimilation (**Figure 9**). Crustal contamination is also evidenced by the presence of xenocrystic zircons in the samples (**Figure 4A**). To summary, both fractional crystallization and crustal contamination occurred during the Cretaceous magma emplacement at/around Bailingshan.

Magma Source

Mafic magmas can be derived from the lithospheric or asthenospheric mantle (Wilson, 1989; Shellnutt, 2014). The lithospheric mantle is generally cooler and isotopically more-enriched due to its interactions with subduction-derived melts and/or fluids and its long isolation from the mantle convection underneath. In contrast, asthenospheric mantle is commonly hotter and isotopically more-depleted (Saunders et al., 1992; Hofmann, 1997). Our dolerite samples have low initial $^{87}Sr/^{86}Sr$ (0.7041 to 0.7043) and positive $\varepsilon_{Nd}(t)$ (+ 4.6 to + 5.1) values, plotting near the MORB field and overlap with typical OIB (**Figure 7**), which suggests an asthenospheric mantle source. This conclusion agrees with published work on the Huangshanxi gabbro, which also pointed to a depleted asthenospheric mantle source beneath the Eastern Tianshan Orogen (Zhang et al., 2011; Deng et al., 2015). As above-discussed, the slight LREE enrichments and distinct negative Nb, Ta and Ti anomalies of the dolerite samples were likely caused by fractional crystallization and crustal assimilation during the magma emplacement.

Since garnet has high partition coefficients for Yb ($D_{garnet/melt}$ = 6.6) relative to Sm ($D_{garnet/melt}$ = 0.25), low-degree partial melting of mantle lherzolite (with garnet residue) would strongly increase the Sm/Yb ratios (Green, 2006; Jung et al., 2006). In contrast, partial melting of mantle spinel lherzolite does not markedly change the Sm/Yb ratios, since spinel has similar partition coefficients for Sm and Yb (McKenzie and O'Nions, 1991; Kelemen et al., 1993). Therefore, mafic magma source can be effectively constrained by fractionation of Sm and Yb (Ellam, 1992; Aldanmaz et al., 2000; Zhang et al., 2015). Our dolerite dykes have slightly elevated Sm/Yb ratios (2.01 to 2.14), and all samples plot near the spinel-garnet lherzolite model curve in the partial melting model diagram (**Figure 10**). This suggests that the parental magma was likely generated by low-degree partial melting of a spinel-garnet lherzolite mantle source at 70 – 80 km depth, which is where the spinel-to-garnet transition is located (McKenzie and O'Nions, 1991).

Tectonic Implications

As discussed above, the dolerite dykes were mainly generated by low-degree partial melting of the asthenospheric mantle. Mafic rocks of similar petrogenesis were proposed to have formed in tectonic events including subducting slab break-off (Davies and von Blanckenburg, 1995; Deng et al., 2015; Zhang et al., 2015), mantle plume upwelling (Campbell and Griffiths, 1990; Bryan and Ernst, 2008; Zhou et al., 2009), continental rifting (Corti, 2009; Thybo and Nielsen, 2009), and lithospheric delamination (Hoernle et al., 2006; McGee and Smith, 2016; Wang et al., 2019).

Slab break-off usually occurs during incipient continent-continent collision (Davies and von Blanckenburg, 1995).

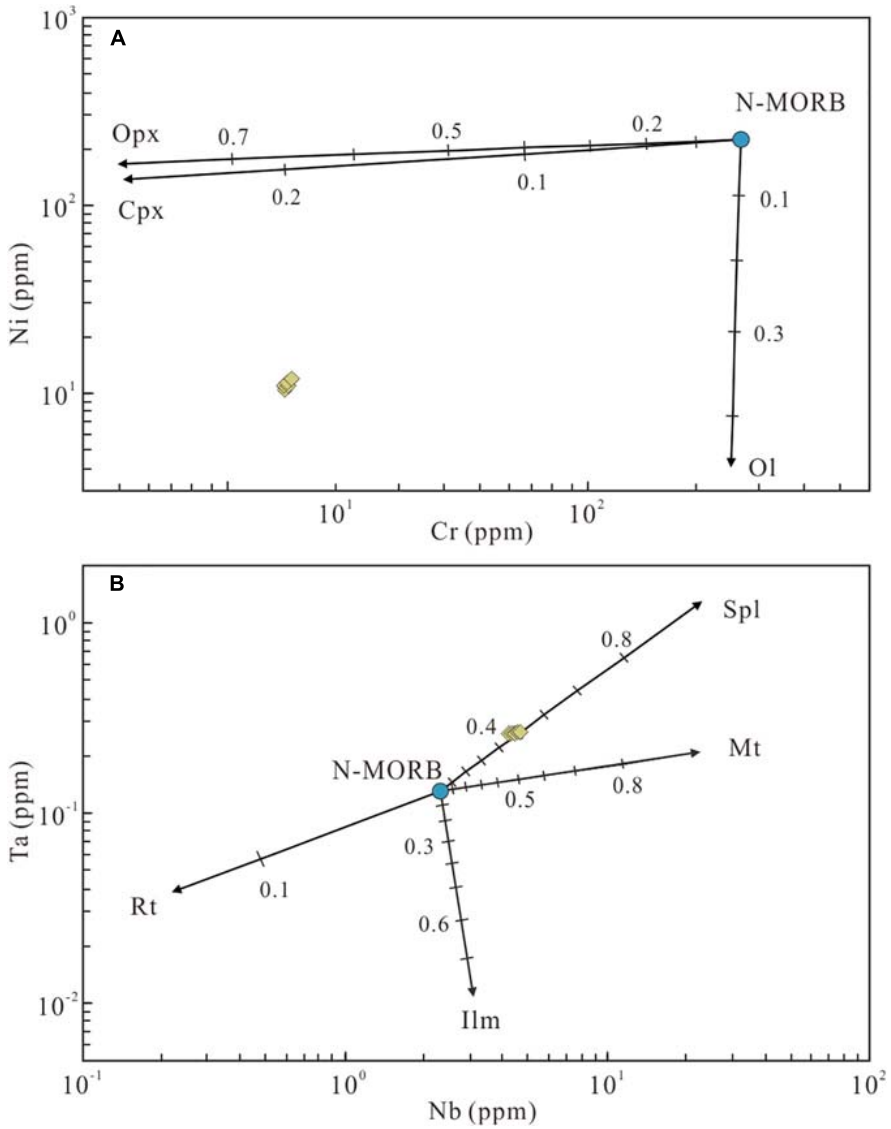

FIGURE 8 | Rayleigh fractionation modal calculations for trace elements **(A)** Cr-Ni, **(B)** Nb-Ta. Partition coefficients (KD) are from http://earthref.org/GERM/, and N-MORB compositions are from Sun and McDonough (1989). Abbreviations: Cpx = clinopyroxene; Ilm = ilmenite; Mt = magnetite; Ol = olivine; Opx = orthopyroxene; Pl = plagioclase; Rt = rutile; Spl = spinel.

Under this setting, the hot asthenospheric mantle would rise through the slab window, and partially melted the overlying metasomatized lithosphere (Rogers et al., 2002; Bonin, 2004; Ferrari, 2004). Therefore, the resulting magmatism would be focused along linear trends (Davies and von Blanckenburg, 1995). In/around our study area, no coeval linear magmatic trends are observed or ever reported, inconsistent with a slab break-off model. Considering the regional tectonic evolution, it is widely considered that the Eastern Tianshan was in a post-collisional setting since the Triassic (Wu et al., 2006; Zhang et al., 2015; Zhao et al., 2019), after the Kanggur Ocean closure and the subsequent Junggar-Central Tianshan collision (Xiao et al., 2008; Wang et al., 2014; Zhang et al., 2016; Zhao et al., 2019). Hence, we suggested that the Cretaceous dolerite was unlikely produced by slab break-off. The dolerite samples display obvious negative Nb, Ta and Ti anomalies, significantly different from typical OIB-like, mantle plume-related Tarim flood basalts (Zhou et al., 2009). The small volume of Cretaceous Eastern Tianshan mafic rocks is also inconsistent with a large igneous province (LIP) origin (Campbell and Griffiths, 1990; Bryan and Ernst, 2008). Furthermore, no geophysical evidence is available to show the presence of mantle plume beneath the Eastern Tianshan. Hence, we considered that the dolerite was unlikely to be mantle plume-related. The continental rift model involves narrow and long tectonic depressions in the lithosphere, leading to partial melting of the upwelling asthenospheric mantle (Corti, 2009; Thybo and Nielsen, 2009).

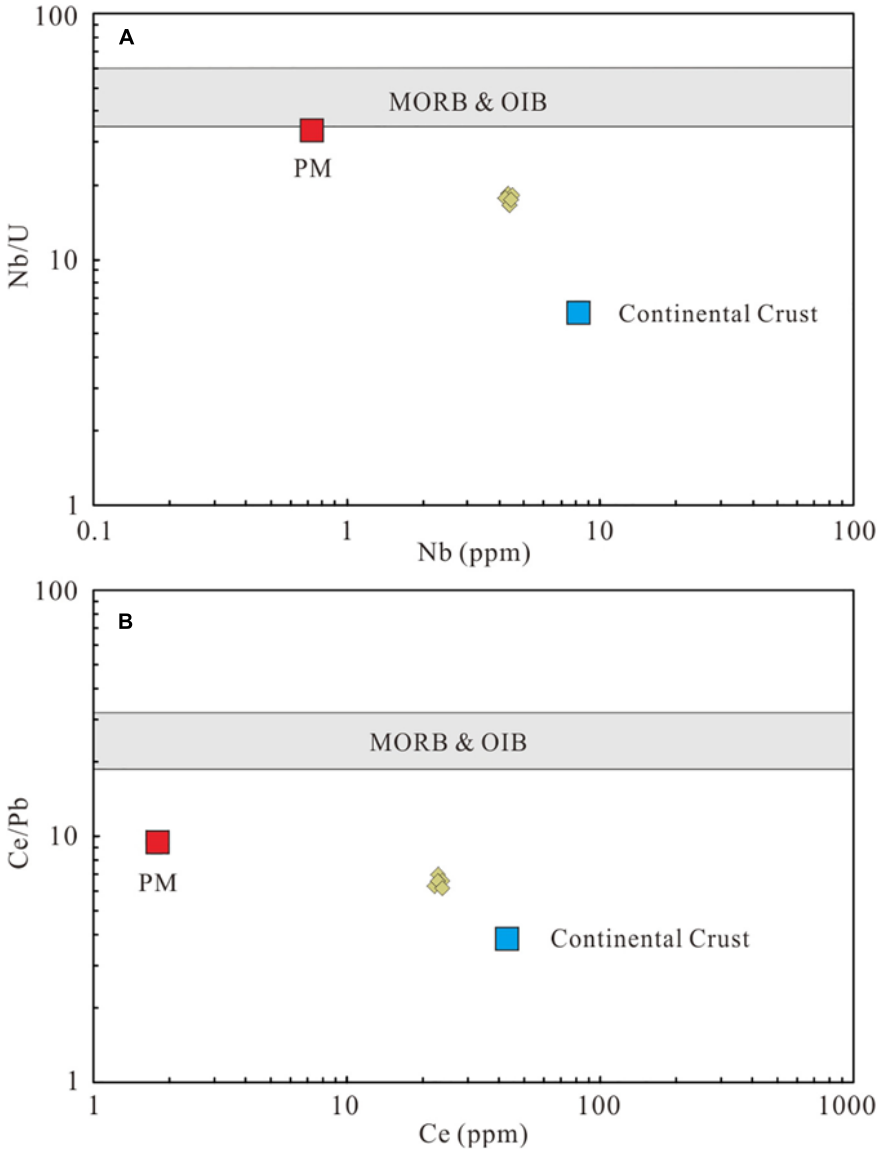

FIGURE 9 | (A) Nb/U vs. Nb; **(B)** Ce/Pb vs. Ce diagrams for the dolerite dyke. Average ratios of Nb/U and Ce/Pb in OIB and MORB are after Hofmann (1997), and data for primitive mantle (Sun and McDonough, 1989) and average continental crust (Rudnick and Gao, 2014) are also shown for comparison.

Key features of this model include an elongated topographic trough and Moho shallowing (Thybo and Nielsen, 2009). However, graben structures are absent in the Eastern Tianshan, suggesting that a continental rift scenario was unlikely either.

Decompression through lithospheric delamination, accompanied by crustal extension, is another possible mechanism to explain the melting of upwelling asthenosphere (Marotta et al., 1998; McGee and Smith, 2016). Jull and Kelemen (2001) reported that the subduction-modified lower lithospheric mantle is denser than the normal upper lithospheric mantle. This makes the lower lithospheric mantle to sink into the underlying asthenosphere, and the latter rises up to take its place (Kay and Kay, 1993; Xu et al., 2002). In the Eastern Tianshan, many recent works documented that Carboniferous arc-related igneous rocks were extensively developed due to the subduction of Kanggur ocean basin (Xiao et al., 2008; Wang et al., 2014; Luo et al., 2016; Zhang et al., 2016; Zhao et al., 2019). This process has likely added oceanic materials into the deep lithospheric mantle beneath the Eastern Tianshan. After that, the high-density lithospheric root was probably removed, resulting in asthenospheric mantle upwelling and the Bailingshan dolerite dyke emplacement. This suggestion is supported by the intraplate tectonic classification in the Zr vs. Zr/Y diagram (**Figure 11**). Zhao et al. (2019) suggested that the Triassic (ca. 235 Ma) felsic magmatism was derived from partial melting of thickened juvenile lower crust, and Zhang et al. (2017) reported that the Duotoushan adakitic dacite porphyry was emplaced via delamination process at around 197 Ma. These

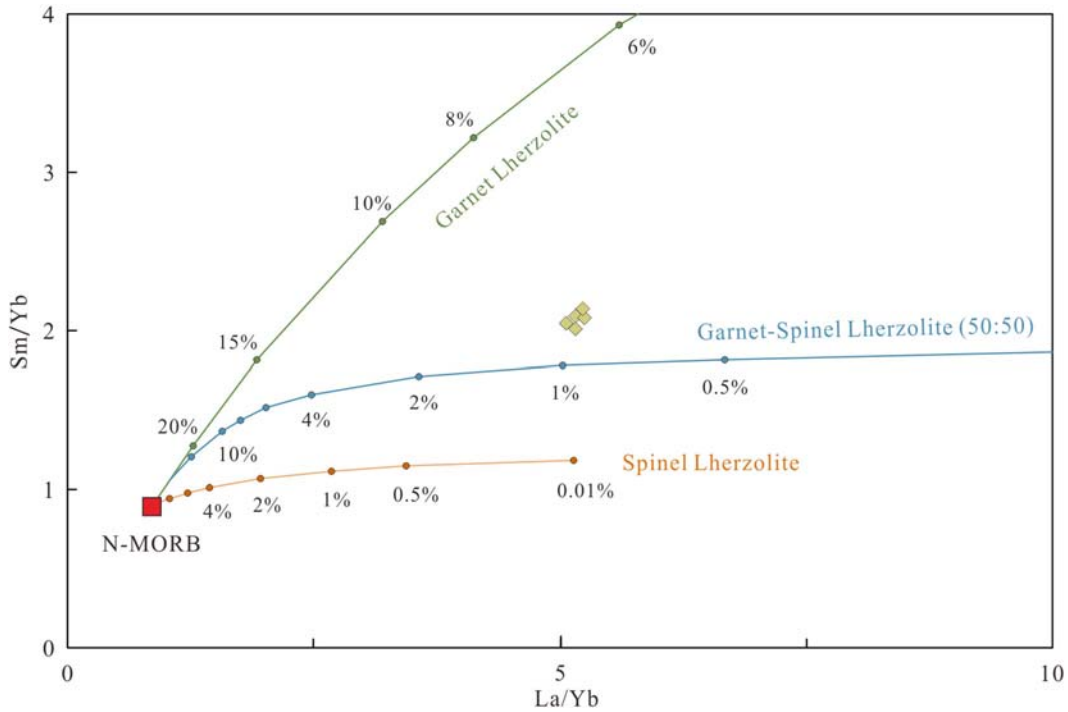

FIGURE 10 | Plots of Sm/Yb vs. La/Yb, showing melting curves obtained with the batch melting equation: $C_1/C_0 = 1/[D + F(1-P)]$ (after Wilson, 1989). C_1: Concentration of a trace element in the melt; C_0: Concentration of the same element in original un-melted source; D: Bulk partition coefficient of the source; P: Proportion of phase entering the melt; F: Melt fraction. Reference curves are the melting trends of spinel lherzolite, garnet lherzolite, and spinel-garnet (50:50) lherzolite. Initial compositions of N-MORB are from Sun and McDonough (1989). Assumed weight fractions of Ol, Opx, Cpx, and Sp in the spinel lherzolite are 0.578, 0.270, 0.119, and 0.033, respectively. Proportions of Ol, Opx, Cpx, and Spl entering the melt are 0.100, 0.270, 0.500, and 0.130, respectively. For garnet lherzolite, the weight fractions of Ol, Opx, Cpx, and Grt in the mineral assemblage are 0.598, 0.211, 0.076, and 0.115, respectively, with melt mode of 0.050, 0.200, 0.300, and 0.450, respectively. Abbreviations: Cpx = clinopyroxene; Grt = garnet; Ol = olivine; Opx = orthopyroxene; Spl = spinel.

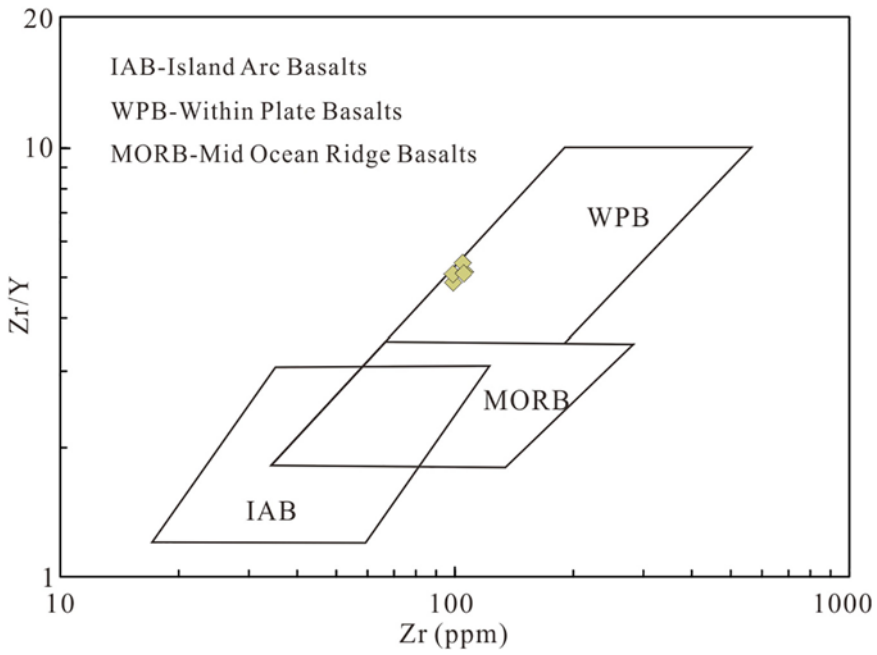

FIGURE 11 | Zr vs. Zr/Y diagram for the dolerite dyke (modified after Pearce and Norry, 1979).

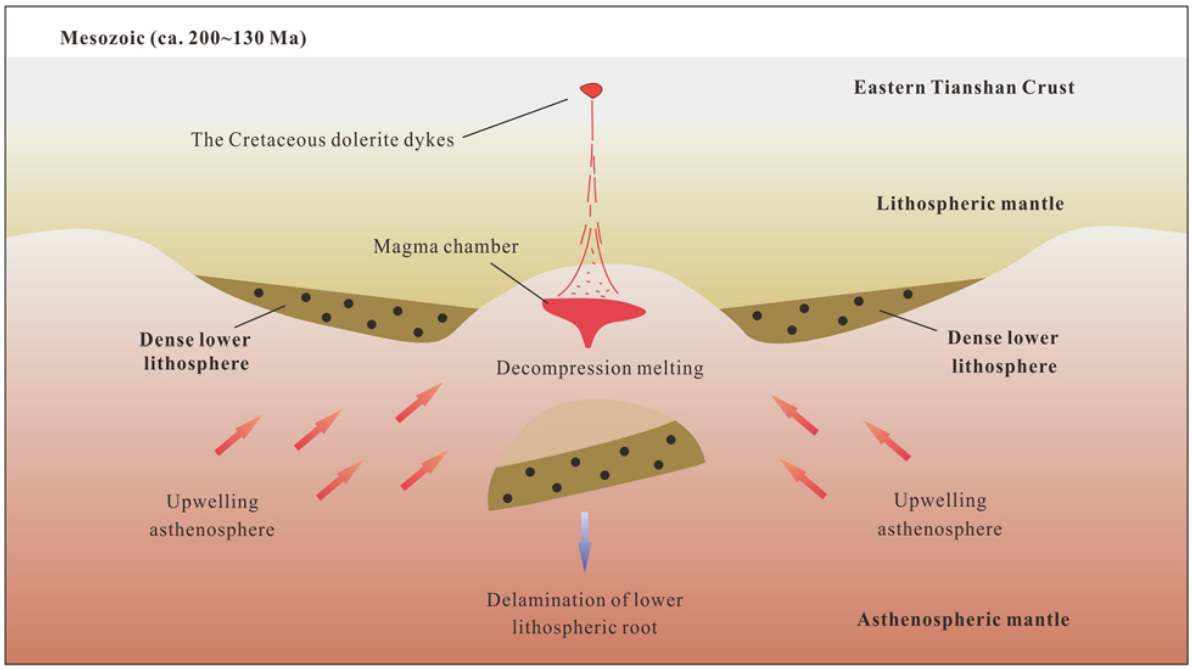

FIGURE 12 | Lithospheric delamination model and the formation of Cretaceous Eastern Tianshan intraplate magmatism (after Wang et al., 2019).

observations indicate an Early Jurassic tectonic transition from post-collisional to intraplate setting in the Eastern Tianshan. Together with our new newly data, we proposed that the removal of the high-density lithospheric root may have continued to the Cretaceous.

To summarize, we have constructed a modified tectonic model to explain the Cretaceous intraplate magmatism in the Eastern Tianshan (**Figure 12**). In our model, the lower lithospheric mantle was modified by oceanic crustal input from the Late Paleozoic subduction, which increased its density. The density imbalance with the less-dense asthenospheric mantle beneath may have caused a small-scale lithospheric root removal. Consequently, the asthenospheric mantle upwelled and partially melted, and formed the parental melt of the Bailingshan dolerite dykes.

CONCLUSION

(1) Zircon U-Pb dating of the Bailingshan dolerite dykes from the Eastern Tianshan yielded an Early Cretaceous age (129.7 ± 1.4 Ma).
(2) Parental magma of the dolerite dykes was likely derived from low-degree partial melting of the asthenospheric mantle in the spinel-garnet stability field, and undergone fractionation and crustal assimilation during its ascent.
(3) Formation of the Cretaceous Eastern Tianshan dolerite dykes was likely in an intraplate extension setting, and related to the sinking of dense, subduction-modified lower lithospheric mantle.

DATA AVAILABILITY STATEMENT

The original contributions presented in the study are included in the article/supplementary material, further inquiries can be directed to the corresponding author/s.

AUTHOR CONTRIBUTIONS

WZ and XD conceived this research. WZ wrotes the manuscript and prepares the figures. BT, LP, and XJ reviews and supervises the manuscript. The co-authors XD are involved in the discussion of the manuscript. All authors finally approved the manuscript and thus agreed to be accountable for this work.

FUNDING

This study was funded by the National Natural Science Foundation of China (41702099) and the China Geological Survey (DD20190050, DD20201121).

ACKNOWLEDGMENTS

We thank Hongfang Chen for helping with the LA-MC-IC-PMS zircon analysis, and Run Zhou and Xianshen Yu for helping with the field work. Special thanks are also due to Editor-in-Chief Prof. David Lentz and Guest Editor Dr. Chun-Kit Lai, as well as two reviewers for their constructive comments and insightful reviews, which significantly enhanced the manuscript.

REFERENCES

Aldanmaz, E., Pearce, J. A., Thirlwall, M. F., and Mitchell, J. G. (2000). Petrogenetic evolution of late Cenozoic, post-collision volcanism in western Anatolia, Turkey. *J. Volcanol. Geotherm. Res.* 102, 67–95. doi: 10.1016/s0377-0273(00)00182-7

Belousova, E., Griffin, W. L., O'Reilly, S. Y., and Fisher, N. L. (2002). Igneous zircon: trace element composition as an indicator of source rock type. *Contrib. Mineral. Petrol.* 143, 602–622. doi: 10.1007/s00410-002-0364-7

Bonin, B. (2004). Do coeval mafic and felsic magmas in post-collisional to within-plate regimes necessarily imply two contrasting, mantle and crustal, sources? A review. *Lithos* 78, 1–24. doi: 10.1016/j.lithos.2004.04.042

Boynton, W. V. (1984). "Geochemistry of the rare earth elements: meteorite studies," in *Rare Earth Element Geochemistry*, ed. P. Henderson (Amsterdam: Elsevier), 63–114. doi: 10.1016/b978-0-444-42148-7.50008-3

Bryan, S. E., and Ernst, R. E. (2008). Revised definition of large igneous provinces (LIPs). *Earth Sci. Rev.* 86, 175–202. doi: 10.1016/j.earscirev.2007.08.008

Campbell, I. H., and Griffiths, R. W. (1990). Implications of mantle plume structure for the evolution of flood basalts. *Earth Planet. Sci. Lett.* 99, 79–93. doi: 10.1016/0012-821x(90)90072-6

Chen, B., and Jahn, B. M. (2004). Genesis of post-collisional granitoids and basement nature of the Junggar Terrane, NW China: Nd-Sr isotope and trace element evidence. *J. Asian Earth Sci.* 23, 691–703. doi: 10.1016/s1367-9120(03)00118-4

Corti, C. (2009). Continental rift evolution: from rift initiation to incipient break-up in the Main Ethiopian Rift, East Africa. *Earth Sci. Rev.* 96, 1–53. doi: 10.1016/j.earscirev.2009.06.005

Davies, J. H., and von Blanckenburg, F. (1995). Slab breakoff: a model of lithospheric detachment and its test in the magmatism and deformation of collisional orogens. *Earth Planet. Sci. Lett.* 129, 85–102. doi: 10.1016/0012-821x(94)00237-s

Deng, Y. F., Song, X. Y., Hollings, P., Zhou, T. F., Yuan, F., Chen, L. M., et al. (2015). Role of asthenosphere and lithosphere in the genesis of the Early Permian Huangshan mafic–ultramafic intrusion in the Northern Tianshan, NW China. *Lithos* 227, 241–254. doi: 10.1016/j.lithos.2015.04.014

Ellam, R. M. (1992). Lithospheric thickness as a control on basalt geochemistry. *Geol.* 20, 153–156. doi: 10.1130/0091-7613(1992)020<0153:ltaaco>2.3.co;2

Ferrari, L. (2004). Slab detachment control on mafic volcanic pulse and mantle heterogeneity in central Mexico. *Geol.* 32, 77–80. doi: 10.1130/g19887.1

Green, N. L. (2006). Influence of slab thermal structure on basalt source regions and melting conditions: REE and HFSE constraints form the Garibaldi volcanic belt, northern Cascadia subduction system. *Lithos.* 87, 23–49. doi: 10.1016/j.lithos.2005.05.003

Han, C. M., Xiao, W. J., Zhao, G. C., Ao, S., Zhang, J., Qu, W., et al. (2010). In-situ U-Pb, Hf and Re-Os isotopic analyses of the Xiangshan Ni-Cu-Co deposit in Eastern Tianshan (Xinjiang), Central Asia Orogenic Belt: constraints on the timing and genesis of the mineralization. *Lithos* 120, 547–562. doi: 10.1016/j.lithos.2010.09.019

Han, C. M., Xiao, W. J., Zhao, G. C., Su, B. X., Sakyi, P. A., Ao, S., et al. (2014). Late Paleozoic metallogenesis and evolution of the east tianshan orogenic belt (NW China, Central Asia Orogenic Belt). *Geol. Ore Deps.* 56, 493–512. doi: 10.1134/s1075701514060075

Han, J. S., Chen, H. Y., Jiang, H. J., Zhao, L. D., Zhang, W. F., and Lai, C. K. (2019). Genesis of the Paleozoic Aqishan-Yamansu arc-basin system and Fe (-Cu) mineralization in the Eastern Tianshan, NW China. *Ore Geol. Rev.* 105, 55–70. doi: 10.1016/j.oregeorev.2018.12.012

Hart, W. K. (1985). Chemical and isotopic evidence for mixing between depleted and enriched mantle, northwestern U.S.A. *Geochim. Cosmochim. Acta.* 49, 131–144. doi: 10.1016/0016-7037(85)90197-8

Hawkesworth, C. J., Gallagher, K., Hergt, J. M., and McDermott, F. (1993). Mantle and Slab contributions in ARC Magmas. *Annu. Rev. Earth Planet. Sci.* 21, 175–204. doi: 10.1146/annurev.ea.21.050193.001135

Hoernle, K., White, J. D. L., Bogaard, P. V. D., Hauff, F., Coombs, D. S., Werner, R., et al. (2006). Cenozoic intraplate volcanism on New Zealand: upwelling induced by lithospheric removal. *Earth Planet. Sci. Lett.* 248, 350–367. doi: 10.1016/j.epsl.2006.06.001

Hofmann, A. W. (1997). Mantle geochemistry: the message from oceanic volcanism. *Nature* 385, 219–229. doi: 10.1038/385219a0

Hou, T., Zhang, Z. C., Santosh, M., Encarnacion, J., Zhu, J., and Luo, W. Q. (2014). Geochronology and geochemistry of submarine volcanic rocks in the Yamansu iron deposit, Eastern Tianshan Mountains, NW China: constraints on the metallogenesis. *Ore Geol. Rev.* 56, 487–502. doi: 10.1016/j.oregeorev.2013.03.008

Huang, X. W., Qi, L., Gao, J. F., and Zhou, M. F. (2013). First reliable Re-Os ages of pyrite and stable Isotope Compositions of Fe (-Cu) deposits in the hami region, eastern tianshan Orogenic Belt, NW China. *Resour. Geol.* 63, 166–187. doi: 10.1111/rge.12003

Ishizuka, O., Tani, K., and Reagan, M. K. (2014). Izu-bonin-mariana forearc crust as a modern ophiolite analogue. *Elements* 10, 115–120. doi: 10.2113/gselements.10.2.115

Jiang, H. J., Han, J. S., Chen, H. Y., Zheng, Y., Zhang, W. F., Lu, W. J., et al. (2018). Hydrothermal alteration, fluid inclusions and stable isotope characteristics of the Shaquanzi Fe–Cu deposit, Eastern Tianshan: implications for deposit type and metallogenesis. *Ore Geol. Rev.* 100, 385–400. doi: 10.1016/j.oregeorev.2016.09.025

Jull, M., and Kelemen, P. B. (2001). On the conditions for lower crustal convective instability. *J. Geophys. Res.* 106, 6423–6446. doi: 10.1029/2000jb900357

Jung, C., Jung, S., Hoffer, E., and Berndt, J. (2006). Petrogenesis of tertiary mafic alkaline magmas in the hocheifel. *Germany. J. Petrol.* 47, 1637–1671. doi: 10.1093/petrology/egl023

Kay, R. W., and Kay, S. M. (1993). Delamination and delamination magmatism. *Tectonophysics* 219, 177–189. doi: 10.1016/0040-1951(93)90295-u

Kelemen, P. B., Shimizu, N., and Dunn, T. (1993). Relative depletion of niobium in some arc magmas and the continental crust: partitioning of K, Nb, La, and Ce during melt/rock reaction in the upper mantle. *Earth Planet. Sci. Lett.* 120, 111–134. doi: 10.1016/0012-821x(93)90234-z

Li, C. M. (2009). A Review on the minerageny and situ microanalytical dating techniques of zircons. *Geol. Surv. Res.* 33, 161–174.

Li, D. D., Wang, Y. W., Shi, Y., Xie, H. J., Wang, J. B., and Lai, C. (2019). Age and geochemistry of the Carboniferous-Permian magmatism and Fe-Ti-V oxide metallogeny in the Eastern Tianshan Orogen, NW China: evidence from the Yaxi mafic-ultramafic complex. *Int. Geol. Rev.* 61, 853–867. doi: 10.1080/00206814.2018.1474499

Li, J. Y., Wang, K. Z., Sun, G. H., Mo, S. G., Li, W. Q., Yang, T. N., et al. (2006). Paleozoic active margin slices in the southern Turfan-Hami basin: geological records of subduction of the Paleo-Asian ocean plate in Central Asian regions. *Acta Petrol. Sin.* 22, 1087–1102.

Lin, J., Liu, Y. S., Yang, Y. H., and Hu, Z. C. (2016). Calibration and correction of LA-ICP-MS and LA-MC-ICP-MS analyses for element contents and isotopic ratios. *Solid Earth Sci.* 1, 5–27. doi: 10.1016/j.sesci.2016.04.002

Liu, B., Wu, J. H., Li, H., Mathur, R., Wu, Q. H., Zheng, H., et al. (2020). Late Paleozoic tectonic evolution of the Kangguer Shear Zone and Yamansu Arc Belt, Eastern Tianshan (NW China): constraints from structure, petrogenesis and geochronology of granitoids. *Lithos* 380–381:105821. doi: 10.1016/j.lithos.2020.105821

Liu, Y. S., Hu, Z. C., Gao, S., Günther, D., Xu, J., Gao, C. G., et al. (2008). In-situ analysis of major and trace elements of anhydrous minerals by LA-ICP-MS without applying an internal standard. *Chem. Geol.* 257, 34–43. doi: 10.1016/j.chemgeo.2008.08.004

Lu, W. J., Zhang, L., Chen, H. Y., Han, J. S., Jiang, H. J., Li, D. F., et al. (2018). Geology, fluid inclusion and isotope geochemistry of the Hongyuan reworked sediment-hosted Zn–Pb deposit: metallogenic implications for Zn–Pb deposits in the Eastern Tianshan, NW China. *Ore Geol. Rev.* 100, 504–533. doi: 10.1016/j.oregeorev.2017.01.004

Ludwig, K. R. (2003). *ISOPLOT 3.00: A Geochronological Toolkit for Microsoft Excel*. Berkeley, CA: Berkeley Geochronology Center.

Luo, T., Liao, Q. A., Zhang, X. H., Chen, J. P., Wang, G. C., and Huang, X. (2016). Geochronology and geochemistry of Carboniferous metabasalts in eastern Tianshan, Central Asia: evidence of a back-arc basin. *Int. Geol. Rev.* 58, 756–772. doi: 10.1080/00206814.2015.1114433

Mao, J. W., Goldfarb, R. J., Wang, Y., Hart, C. J., Wang, Z., and Yang, J. (2005). Late Paleozoic base and precious metal deposits, East Tianshan, Xinjiang, China: characteristics and geodynamic setting. *Episodes* 28, 23–30. doi: 10.18814/epiiugs/2005/v28i1/003

Marotta, A. M., Fernandez, M., and Sabadini, R. (1998). Mantle unrooting in collisional settings. *Tectonophysics* 296, 31–46. doi: 10.1016/s0040-1951(98)00134-6

McGee, L. E., and Smith, I. E. M. (2016). Interpreting chemical compositions of small scale basaltic systems: a review. *J. Volcanol. Geotherm. Res.* 325, 45–60. doi: 10.1016/j.jvolgeores.2016.06.007

McKenzie, D., and O'Nions, R. K. (1991). Partial melt distribution from inversion of rare earth element concentrations. *J. Petrol.* 32, 1021–1091. doi: 10.1093/petrology/32.5.1021

Meschede, M. (1986). A method of discriminating between different types of mid-ocean ridge basalts and continental tholeiites with the Nb-Zr-Y diagram. *Chem. Geol.* 56, 207–218. doi: 10.1016/0009-2541(86)90004-5

Mullen, E. D. (1983). $MnO/TiO_2/P_2O_5$: a minor element discriminant for basaltic rocks of oceanic environments and its implications for petrogenesis. *Earth Planet. Sci. Lett.* 62, 53–62. doi: 10.1016/0012-821x(83)90070-5

Pearce, J. A. (2008). Geochemical fingerprinting of oceanic basalts with applications to ophiolite classification and the search for Archean oceanic crust. *Lithos* 100, 14–48. doi: 10.1016/j.lithos.2007.06.016

Pearce, J. A. (2014). Immobile elements fingerprinting of ophiolites. *Elements* 10, 101–108. doi: 10.2113/gselements.10.2.101

Pearce, J. A., and Norry, M. J. (1979). Petrogenetic implications of Ti, Zr, Y and Nb variations in volcanic rocks. *Contrib. Mineral. Petrol.* 69, 33–47. doi: 10.1007/bf00375192

Pearce, J. A. (1982). "Trace element characteristics of lavas from destructive plate boundaries," in *Andesites: Orogenic Andesites and Related Rocks*, ed. R. S. Thorps (New York, NY: John Wiley and Sons), 525–548.

Peccerillo, A., and Taylor, S. R. (1976). Geochemistry of Eocene calc-alkaline volcanic rocks from the Kastamonu area, northern Turkey. *Contrib. Mineral. Petrol.* 58, 63–81. doi: 10.1007/bf00384745

Qin, K. Z., Fang, T. H., Wang, S. L., Zhu, B. Q., Feng, Y. M., Yu, H. F., et al. (2002). Plate tectonics division, evolution and metallogenic settings in eastern Tianshan Mountains. *NW China. Xinjiang Geol.* 20, 302–308.

Rogers, R. D., Kárason, H., and van der Hilst, R. D. (2002). Epeirogenic uplift above a detached slab in northern Central America. *Geol.* 30, 1031–1034. doi: 10.1130/0091-7613(2002)030<1031:euaads>2.0.co;2

Ross, P. S., and Bedard, J. H. (2009). Magmatic affinity of modern and ancient subalkaline volcanic rocks determined from trace-element discriminant diagrams. *Can. J. Earth Sci.* 46, 823–839. doi: 10.1139/e09-054

Rudnick, R. L., and Gao, S. (2014). Composition of the continental Crust. *Treatise Geochem.* 3, 1–51. doi: 10.1016/b0-08-043751-6/03016-4

Saccani, E. (2015). A new method of discriminating different types of post-Archean ophiolitic basalts and their tectonic significance using Th-Nb and Ce-Dy-Yb systematics. *Geosci. Front.* 6, 481–501. doi: 10.1016/j.gsf.2014.03.006

Salters, V. J., and Stracke, A. (2004). Composition of the depleted mantle. *Geochem. Geophys. Geosyst.* 5:Q05004.

Saunders, A. D., Storey, M., Kent, R. W., and Norry, M. J. (1992). Consequences of plume-lithosphere interactions. *Geol. Soc. Lon., Spec. Publ.* 68, 41–60. doi: 10.1144/gsl.sp.1992.068.01.04

Shellnutt, J. G. (2014). The Emeishan large igneous province: a synthesis. *Geosci. Front.* 5, 369–394. doi: 10.1016/j.gsf.2013.07.003

Shen, P., Pan, H. D., and Dong, L. H. (2014). Yandong porphyry Cu deposit, Xinjiang, China geology, geochemistry and SIMS U-Pb zircon geochronology of host porphyries and associated alteration and mineralization. *J. Asian Earth Sci.* 80, 197–217. doi: 10.1016/j.jseaes.2013.11.006

Shervais, J. W. (1982). Ti-V plots and the petrogenesis of modern and ophiolitic lavas. *Earth Planet. Sci. Lett.* 59, 101–118. doi: 10.1016/0012-821x(82)90120-0

Shi, Y., Wang, Y. W., Wang, J. B., Zhou, G. C., Xie, H. J., Li, D. D., et al. (2021). Formation of the Weiya magmatic Fe–Ti oxide deposit and its ore-hosting layered gabbro intrusion, Eastern Tianshan (Xinjiang, NW China). *Ore Geol. Rev.* 28:104003. doi: 10.1016/j.oregeorev.2021.104003

Shu, L. S., Charvet, J., Lu, H. F., and Laurent-Charvet, S. (2002). Paleozoic accretion-collision events and kinematics of deformation in the eastern part of the Southern-Central Tianshan belt. *China. Acta Petrol. Sin.* 76, 308–323. doi: 10.1111/j.1755-6724.2002.tb00547.x

Sun, S. S., and McDonough, W. F. (1989). "Chemical and isotopic systematics of oceanic basalts: implications for mantle composition and processes," in *Magmatism in the Ocean Basins: Geological Society*, Vol. 42, eds A. D. Saunders and M. J. Norry (London: Special Publications), 313–345. doi: 10.1144/gsl.sp.1989.042.01.19

Tanaka, T., Togashi, S., Kamioka, H., Amakawa, H., Kagami, H., and Hamamoto, T. (2000). Jndi-1: a neodymium isotopic reference in consistency with lajolla neodymium. *Chem. Geol.* 168, 279–281. doi: 10.1016/s0009-2541(00)00198-4

Thybo, H., and Nielsen, C. A. (2009). Magma-compensated crustal thinning in continental rift zones. *Nature* 457, 873–876. doi: 10.1038/nature07688

Vermeesch, P. (2006). Tectonic discrimination diagrams revisited. *Geochem. Geophys. Geosyst* 7:Q06017.

Wang, J., Su, Y. P., Zheng, J. P., Gao, S. L., Dai, H. K., Ping, X. Q., et al. (2019). Geochronology and petrogenesis of Jurassic intraplate alkali basalts in the Junggar terrane, NW China: implication for low-volume basaltic volcanism. *Lithos* 324-325, 202–215. doi: 10.1016/j.lithos.2018.11.002

Wang, J. B., Wang, Y. W., and He, Z. J. (2006). Ore deposits as a guide to the tectonic evolution in the East Tianshan Mountains, NW China. *Geol. China* 33, 461–469.

Wang, Y. F., Chen, H. Y., Xiao, B., Han, J. S., Fang, J., Yang, J. T., et al. (2018). Overprinting mineralization in the Paleozoic Yandong porphyry copper deposit, Eastern Tianshan, NW China—Evidence from geology, fluid inclusions and geochronology. *Ore Geol. Rev.* 100, 148–167. doi: 10.1016/j.oregeorev.2017.04.013

Wang, Y. H., Xue, C. J., Liu, J. J., Wang, J. P., Yang, J. T., Zhang, F. F., et al. (2014). Early Carboniferous adakitic rocks in the area of the Tuwu deposit, eastern Tianshan, NW China: slab melting and implications for porphyry copper mineralization. *J. Asian Earth Sci.* 103, 1–18.

Wang, Y. H., and Zhang, F. F. (2016). Petrogenesis of early Silurian intrusions in the Sanchakou area of Eastern Tianshan, Northwest China, and tectonic implications: geochronological, geochemical, and Hf isotopic evidence. *Int. Geol. Rev.* 58, 1–17.

Wilson, M. (1989). *Igneous Petrogenesis-A Global Tectonic Approach*. London: Unwin Hyman, 466.

Wood, D. A. (1980). The application of a Th-Hf-Ta diagram to problems of tectonomagmatic classification and to establishing the nature of crustal contamination of basaltic lavas of British Tertialy volcanic province. *Earth Planet. Sci. Lett.* 50, 11–30. doi: 10.1016/0012-821x(80)90116-8

Wu, C. Z., Zhang, Z. Z., Zaw, K., Della-Pasque, F., Tang, J. H., Zheng, Y. C., et al. (2006). Geochronology, geochemistry and tectonic significances of the Hongyuntan granitoids in the Qoltag area, Eastern Tianshan. *Acta Petrol. Sin.* 22, 1121–1134.

Wu, Y. S., Zhou, K. F., Li, N., and Chen, Y. J. (2017). Zircon U-Pb dating and Sr-Nd-Pb-Hf isotopes of the ore-associated porphyry at the giant Donggebi Mo deposit, Eastern Tianshan, NW China. *Ore Geol. Rev.* 81, 794–807. doi: 10.1016/j.oregeorev.2016.02.007

Xia, L., and Li, X. (2019). Basalt geochemistry as a diagnostic indicator of tectonic setting. *Gondwana Res.* 65, 43–67. doi: 10.1016/j.gr.2018.08.006

Xiao, B., Chen, H. Y., Hollings, P., Han, J. S., Wang, Y. F., Yang, J. T., et al. (2017). Magmatic evolution of the Tuwu–Yandong porphyry Cu belt, NW China: constraints from geochronology, geochemistry and Sr–Nd–Hf isotopes. *Gondwana Res.* 43, 74–91. doi: 10.1016/j.gr.2015.09.003

Xiao, W. J., Han, C. M., Yuan, C., Sun, M., Lin, S. F., Chen, H. L., et al. (2008). Middle Cambrian to Permian subduction-related accretionary orogenesis of northern Xinjiang, NW China: implications for the tectonic evolution of Central Asia. *J. Asian Earth Sci.* 32, 102–117. doi: 10.1016/j.jseaes.2007.10.008

Xu, J. F., Shinjo, R., Defant, M. J., Wang, Q., and Rapp, R. P. (2002). Origin of Mesozoic adakitic intrusive rocks in the Ningzhen area of east China: partial melting of delaminated lower continental crust? *Geol* 30, 1111–1114. doi: 10.1130/0091-7613(2002)030<1111:oomair>2.0.co;2

Yang, F. Q., Mao, J. W., Bierlein, F. P., Pirajno, F., Zhao, C. S., Ye, H. S., et al. (2009). A review of the geological characteristics and geodynamic mechanisms of Late Paleozoic epithermal gold deposits in North Xinjiang, China. *Ore Geol. Rev.* 35, 217–234. doi: 10.1016/j.oregeorev.2008.09.003

Zhang, D. Y., Zhou, T. F., Yuan, F., Xiao, W. J., White, N. C., Deng, Y. F., et al. (2015). Petrogenesis and mineralization potential of a granite porphyry intrusion beneath the Baishan Mo deposit, Eastern Tianshan, NW China. *J. Asian Earth Sci.* 113, 254–265. doi: 10.1016/j.jseaes.2015.05.002

Zhang, M. G., Li, C., Fu, P., Hu, P., and Ripley, E. M. (2011). The Permian Huangshanxi Cu–Ni deposit in western China: intrusive–extrusive association,

ore genesis, and exploration implications. *Mineral. Deposita* 46, 153–170. doi: 10.1007/s00126-010-0318-3

Zhang, W. F., Chen, H. Y., Han, J. S., Zhao, L. D., Huang, J. H., Yang, J. T., et al. (2016). Geochronology and geochemistry of igneous rocks in the Bailingshan area: implications for the tectonic setting of late Paleozoic magmatism and iron skarn mineralization in the eastern Tianshan, NW China. *Gondwana Res.* 38, 40–59. doi: 10.1016/j.gr.2015.10.011

Zhang, W. F., Chen, H. Y., Jiang, H. J., Lu, W. J., Liang, P., Xu, C., et al. (2017). Geochronology, geochemistry and petrogenesis of granitoids in the Duotoushan Fe-Cu deposit, eastern Tianshan, Xinjiang province: implications on tectonic setting of late Paleozoic magmatism. *Geotech. Metall.* 41, 1171–1191.

Zhang, W. F., Chen, H. Y., Peng, L. H., Zhao, L. D., Huang, J. H., Lu, W. J., et al. (2018a). Discriminating hydrothermal fluid sources using tourmaline boron isotopes: example from Bailingshan Fe deposit in the Eastern Tianshan, NW China. *Ore Geol. Rev.* 98, 28–37. doi: 10.1016/j.oregeorev.2018.05.015

Zhang, W. F., Chen, H. Y., Peng, L. H., Zhao, L. D., Lu, W. J., Zhang, Z. J., et al. (2018b). Ore genesis of the Duotoushan Fe-Cu deposit, Eastern Tianshan, NW China: constraints from ore geology, mineral geochemistry, fluid inclusion and stable isotopes. *Ore Geol. Rev.* 100, 401–421. doi: 10.1016/j.oregeorev.2017.02.021

Zhang, X. H., Huang, X., Chen, J. P., Liao, Q. A., and Duan, X. F. (2012). Stratigraphic sequence of carboniferous marine volcanic-deposit rock and its geological age in Juotage Area, Eastern Tianshan. *Earth Sci.-J. China Univ. Geosci.* 6, 1305–1314.

Zhao, L. D., Chen, H. Y., Hollings, P., and Han, J. S. (2019). Tectonic transition in the Aqishan-Yamansu belt, Eastern Tianshan: constraints from the geochronology and geochemistry of Carboniferous and Triassic igneous rocks. *Lithos* 344-345, 247–264. doi: 10.1016/j.lithos.2019.06.023

Zheng, J. H., Mao, J. W., Yang, F. Q., Liu, F., and Zhu, Y. F. (2015). The post-collisional Cihai iron skarn deposit, eastern Tianshan, Xinjiang, China. *Ore Geol. Rev.* 67, 244–254. doi: 10.1016/j.oregeorev.2014.12.006

Zhou, M. F., Zhao, J. H., Jiang, C. Y., Gao, J. F., Wang, W., and Yang, S. H. (2009). OIB-like, heterogeneous mantle sources of Permian basaltic magmatism in the western Tarim Basin, NW China: implications for a possible Permian large igneous province. *Lithos* 113, 583–594. doi: 10.1016/j.lithos.2009.06.027

Zhou, T. F., Yuan, F., Zhang, D. Y., Fan, Y., Liu, S., Peng, M. X., et al. (2010). Geochronology, tectonic setting and mineralization of granitoids in Jueluotage area, eastern Tianshan, Xinjiang. *Acta Petrol. Sin.* 26, 478–520.

Conflict of Interest: The authors declare that the research was conducted in the absence of any commercial or financial relationships that could be construed as a potential conflict of interest.

The reviewer JH declared a past co-authorship with one of the authors WZ.

frontiers in Earth Science

ORIGINAL RESEARCH
published: 20 May 2021
doi: 10.3389/feart.2021.666967

Geodynamic Setting and Cu-Ni Potential of Late Permian Xiwanggou Mafic-Ultramafic Rocks, East Kunlun Orogenic Belt, NW China

Jiandong Zhang[1,2], Miao Yu[1], Hui Wang[3], Bin Li[1], Chengyou Feng[2], J. M. Dick[1], Jinchao Li[4], Huilei Kong[4] and Zhiyi Zhao[5]*

[1] Key Laboratory of Metallogenic Prediction of Nonferrous Metals and Geological Environment Monitor, Ministry of Education, Central South University, Changsha, China, [2] MNR Key Laboratory of Metallogeny and Mineral Assessment, Institute of Mineral Resources, Chinese Academy of Geological Science, Beijing, China, [3] Laboratory of Mineralization and Dynamics, Chang'an University, Xi'an, China, [4] MLR Key Laboratory for the Study of Focused Magmatism and Giant Ore Deposits, Xi'an Center of Geological Survey, China Geological Survey, Xi'an, China, [5] Qinghai Geological Survey Institute, Xining, China

OPEN ACCESS

Edited by:
Rui Wang,
China University of Geosciences, China

Reviewed by:
Dongyang Zhang,
China University of Geosciences, China
Shengchao Xue,
China University of Geosciences, China

***Correspondence:**
Miao Yu
yumiao1987@csu.edu.cn

Specialty section:
This article was submitted to Geochemistry, a section of the journal Frontiers in Earth Science

Received: *11 February 2021*
Accepted: *01 April 2021*
Published: *20 May 2021*

Citation:
Zhang J, Yu M, Wang H, Li B, Feng C, Dick JM, Li J, Kong H and Zhao Z (2021) Geodynamic Setting and Cu-Ni Potential of Late Permian Xiwanggou Mafic-Ultramafic Rocks, East Kunlun Orogenic Belt, NW China. Front. Earth Sci. 9:666967. doi: 10.3389/feart.2021.666967

Several magmatic Cu–Ni sulfide deposits have recently been explored along the deep Middle Kunlun fault related to the extension of the East Kunlun orogenic belt in Qinghai Province, NW China. The Xiwanggou mafic–ultramafic rocks associated with Cu–Ni sulfide mineralization are first to be dated as late Permian compared to most of the deposits formed during late Silurian–early Devonian in this region. The Xiwanggou complexes located in the junction area between the East Kunlun and West Qinling belts, are composed of gabbros, olivine-gabbros, pyroxenites, olivine-pyroxenites, and peridotites. The Cu–Ni mineralization are mainly hosted in the olivine-pyroxenites and pyroxenites, whereas the sulfide-poor mineralization distributed in gabbros and olivine-gabbros. Zircon LA-ICP-MS U–Pb dating of the gabbro and olivine-pyroxenite revealed their crystallized ages of 250.8 ± 0.8 Ma and 257.3 ± 0.7 Ma, respectively. The trace element characteristics of the Xiwanggou fertile mafic-ultramafic rocks shows the enrichments in Sr, Rb, Th, Ba and light rare earth elements, and depletions in Nb and Ta, which are associated with the slab derived fluid input and dehydration melting of amphiboles. Meanwhile, Sr–Nd and Hf isotopic compositions of the gabbro [$\varepsilon Nd(t)$ = 0.66–1.18; $\varepsilon Hf(t)$ = 5.2–12] and olivine-pyroxenite [$\varepsilon Nd(t)$ = −1.09 – −0.43; $\varepsilon Hf(t)$ = 5.4–17.7] show that the magma was mainly derived from the metasomatized portions of subcontinental lithospheric mantle (SCLM) source in the mantle wedge. The magma primarily experienced dehydration melting processes of amphiboles and subsequently underwent hydrated melting in the overlying mantle wedge and relatively reduced background. The cool subduction process of the Anemaqen oceanic lithosphere maybe trigger large melting in the mantle wedge resulting in a relative low-Ni content in the melt. The transpressional windows formed by the right-lateral strike-slip shearing action of the Wenquan and South Kunlun faults in the South Kunlun forearc belt created a significant conduit for the magma ascending. The thermometer of Fe and Ni exchange between coexisting olivine and sulfide melt indicates the magma were yielded in a temperature range of ca. 1200–1300°C and an oxygen fugacity

range of ca. –10.57 to –8.98 (log unit), which suggested that the parental magma of the Xiwanggou complex derived from a relatively reduced source favoring Ni relative to Fe in the melt. The intermediate sulfide segregation from the melt resulted in a medium tenor potential for the Xiwanggou complex.

Keywords: Xiwanggou, East Kunlun orogen, Cu-Ni sulfide deposit, late Permian, mafic–ultramafic rocks, zircon U–Pb dating, Sr–Nd isotope, Fe–Ni exchange

INTRODUCTION

Several magmatic Cu–Ni sulfide deposits have recently been explored along the deep Middle Kunlun fault paralleled to the extension of the East Kunlun orogenic belt (EKOB), Qinghai Province, NW China (Li et al., 2015; Song et al., 2016; Zhang Z. W. et al., 2016; Li et al., 2018). The Xiariham deposit with reserve of 1.16 Mt averaging grades of 0.65 wt% Ni, 0.14 wt% Cu, and 0.013 wt% Co, and the Shitoukengde deposit with 0.15 Mt averaging grades of 0.32% Ni were explored. And several new middle – small scale deposits, comprising Langmuri, Gayahe, Binggounan, and Xiwanggou mineralized locations have been discovered (**Figure 1A**; Zhang et al., 2015; He et al., 2017; Wang et al., 2020). The Xiwanggou mineralized mafic-ultramafic complex is located in the east of the EKOB, the northern part of the Qinghai-Tibet Plateau (**Figure 1**), which was first outlined by a team from the Xi'an Center, China Geological Survey during field mapping in 2015–2017. Several intrusions outcrop in the Xiwanggou area but only the olivine pyroxenites have been found to contain significant Ni–Cu sulfide mineralization.

Most of the world's large magmatic sulfide deposits are interpreted to have formed in continental rift settings (Maier and Groves, 2011; Naldrett, 2013), where a mantle plume intersects a continental rift, and provides a large volume of magma with high metal content as a result of high degree partial melting (Barnes and Lightfoot, 2005). Moreover, most of the super-large magmatic sulfide deposits often occur in association with small differentiated intrusions, and an open system of protracted-flow magma conduits provides a significant space for ore reservoirs in a extensional environment (Song et al., 2010; Maier and Groves, 2011; Naldrett, 2013; Lightfoot and Evans-Lamswood, 2015; Barnes and Robertson, 2019). However, many magmatic Ni–Cu sulfide deposits have recently been discovered in orogenic settings or subduction-related magmatic arcs (Maier et al., 2008; Sappin et al., 2011), and they have significantly contributed Ni and Cu resources in China and the world. Examples of these include the Early Permian Kalatongke (33 Mt at 0.8 wt% Ni and 1.3 wt% Cu) (Song and Li, 2009; Li C. S. et al., 2012), and Huangshan-Jing'erquan Ni–Cu belt (>50 Mt at an average grade of 0.52 wt% Ni and 0.27 wt% Cu) in North Xinjiang (NW China), and the Early Carboniferous Ni–Cu ore deposits (16 Mt at 0.66 wt% Ni and 0.46% wt% Cu) hosted in the Aguablanca intrusion in Spain (Piña et al., 2006). Therefore, a few significant deposits are associated with the margins of large oceans or with supra-subduction zone environments, possibly reflecting poor preservation potential or, with the latter, limitations on plume interaction with continental lithosphere (Begg et al., 2010).

It is generally accepted that an extension or thinning environment including intracontinental rifting and post collisional extension are optimal for the formation of magmatic sulfide deposits in the EKOB magmatic Cu–Ni–Co mineralization under the Proto- and Paleo-Tethys evolution in the EKOB (Jiang et al., 2015; Zhang Z. W. et al., 2016; Zhang et al., 2021). The mafic-ultramafic complexes show diverse lithofacies with different formation ages, indicating the multiple stages of long-lived Paleozoic mantle-derived magmatism (Song et al., 2011; Wang et al., 2014; Peng et al., 2016), and most identify the ore-forming period as Late Silurian to Early Devonian, such as the Xiariham and Shitoukengde deposits (Wang et al., 2013; Sun et al., 2014; Song et al., 2016). However, the association of the Late Permian Xiwanggou mafic-ultramafic rocks with Cu–Ni sulfide mineralization has significantly broken the previous viewpoints and broadened the prospecting horizon.

The EKOB is generally considered to have been in an oceanic lithosphere subduction environment during late Permian (Zhang et al., 2012; Dong et al., 2018). At this point, we compares contrasting geochemical trends exhibited between fertile and barren late Permian basalts in the EKOB in terms of major and trace elements, Sr–Nd isotopic ratios and zircon Hf isotope to analyze the dynamic setting and ore-forming potential of the Xiwanggou complex. In addition, it is significant to know what the tectonic mechanism controls the conduit formation for the Xiwanggou complexes in a compressional subduction environment.

GEOLOGICAL SETTING

The EKOB is located in the western part of the central orogenic belt (**Figure 1A**), which trends east-west and is approximately 1,500 km long and 50–200 km wide. The EKOB is generally subdivided into four terranes from the north to the south: the North Kunlun, South Kunlun, Muztagh-Anemaqen and Hohxil-Bayanhar Terranes farthest south (**Figure 1A**; Yang et al., 1986; Jiang, 1992; Luo et al., 1999; Yu et al., 2020), which are bounded by the North Kunlun Fault (NKF), Middle Kunlun Fault (MKF), South Kunlun Fault (SKF), and Muztagh-Anemaqen Fault (MAF), respectively, from the north to the south (**Figure 1A**). The orogen is bounded by the Altun Fault to the west and Wenquan Fault to the east (**Figure 1A**). The NW-trending Wenquan fault is the boundary between the EKOB and the West Qinling orogenic belt (WQOB), and crosses the Elashan Mountains (**Figure 1A**). The Elashan Mountain is located in the easternmost segment of the EKOB, and in its eastern part,

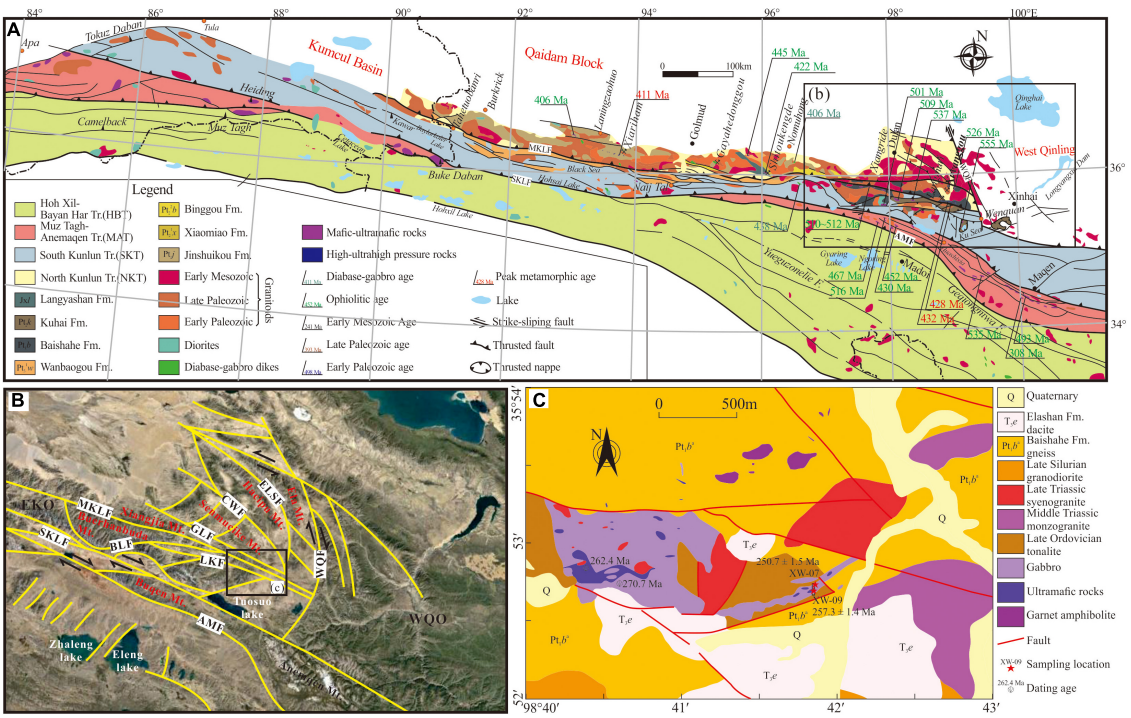

FIGURE 1 | (A) Sketch map showing the distribution of mafic–ultramafic complex and Cu–Ni sulfide mineralization in the East Kunlun Mountains, the northern part of the Qinghai-Tibet Plateau (modified after Dong et al., 2018); LA-ICP MS zircon U–Pb ages from other studies are also shown in Dong et al. (2018) and Yu et al. (2020). **(B)** Satellite map of the Xiwanggou area showing the fault syst. WQF, Wenquan fault; ELSF, Elashan fault; CWF, Chahanwusu fault; GLF, Gouli fault; MKLF, Middle Kunlun fault; BLF, Boluoer fault; LKF, Longwakalu fault; SKLF, South Kunlun fault; AMF, Anemaqen Fault. **(C)** Simplified geological map of the Xiwanggou area showing sample and trench localities. Modified after Kong et al. (2019a).

the metamorphic basement and Pre-Mesozoic sedimentary rocks were uplifted due to the NE-dipping thrust fault systems and the Wenquan dextral strike-slip fault (Jiang et al., 2008). Previous studies suggested that the EKOB and WQOB were part of a unified orogen before the Wenquan fault system developed (Chen et al., 2015; Ren et al., 2016; Shao et al., 2017).

The tectonic evolution of the EKOB are closely associated with the assembling and colliding history of variable terranes in different era. The North Kunlun Terrane (NKT), as an active continental margin, hosted a large amount of Precambrian basement rock of Jinshuikou Group (Liu et al., 2005; He et al., 2016), and late Ordovician-middle Silurian calc-alkaline granitoids (Wu et al., 2012; Qi, 2015; Wang et al., 2016), which are related to the subduction of back arc oceanic lithosphere existed between the NKT and SKT at ca. 460 Ma causing the late Ordovician-middle Silurian magmatism in the NKT and thrusted basement rocks (Dong et al., 2018). The South Kunlun Terrane (SKT), which developed as an inner-oceanic island arc, consisted of the Wanbaogou Group basalts and large amounts of multistage felsic magmatic rocks (Cai and Wei, 2007; Zhang et al., 2010; Kong et al., 2014; Chen et al., 2016; Yu et al., 2020). Xu et al. (2016) got a zircon SIMS dating age of 762 ± 2 Ma for the Wanbaogou basalts, and their geochemical features are similar to those of oceanic island basalt. The Late Silurian to Early Devonian granitoids display either peraluminous or metaluminous features (Zhao et al., 2008; Shi et al., 2016), which were possibly resulted from an transition from collisional to a post-collisional environment between the NKT and SKT during the Late Silurian-Middle Devonian (Long et al., 2006; Zhang D. X. et al., 2016). The Muztagh-Anemaqen Terrane (MAT) developed as a young island arc as a consequence of subduction of Proto-Tethys Oceanic crust, which carried SSZ (supra-subduction zone) type ophiolites (Wu et al., 2005; Li et al., 2017), together with island arc tholeiite (IAT) and TTGs (trondhjemite-tonalite-granodiorites) during the Early Paleozoic (Ren et al., 2012; Qi, 2015; Zhao et al., 2017). The collision between SKT and MAT probably occurred after the middle Devonian, as evidenced from the absence of the upper Devonian strata in the SKT (Ye et al., 2004). A new subduction zone reconstructed along the south of the MAT after the middle Permian, which resulted in extensive development of calc-alkaline granitoids in the NKT, SKT, and MAT (Zhang et al., 2006; Liu et al., 2015; Ma et al., 2015; Dong et al., 2016). The final closure of the Anemaqen Ocean might have occurred in the Late Triassic as indicated by dates from the upper Triassic Babaoshan terrestrial molasse formation (Wu et al., 2017).

The emplacement of mafic-ultramafic magma in the EKOB can be separated into two stages (Yu et al., 2020): (1) the first emplacement stage occurred primarily in the Late Silurian–Early Devonian (ca. 393–427 Ma); (2) the second stage occurred in the Middle-Late Permian. Previous studies indicate that the first stage complexes were probably emplaced

in a post-collisional extensional environment (Wang et al., 2014), and their components are mainly gabbro, pyroxenite, and peridotite facies rocks (Peng et al., 2016). In addition, the first stage intrusions generally developed extensive Cu–Ni sulfide mineralization that are mainly hosted in the pyroxenite and peridotite outcrop in the Xiariham, Binggounan, Shitoukengde, Akchucsai, and Langmuri areas (Sun et al., 2014; Li et al., 2015; Song et al., 2016; He et al., 2017; Zhang et al., 2018). In the second stage, the mafic-ultramafic complexes outcrop mainly in the Jiadang, Bairiqili, and Xiwanggou areas (Xiong et al., 2011a; Kong et al., 2018). In the first two areas, gabbro is the dominant rock type, and no sulfide ore bodies have been found, but the Xiwanggou mafic–ultramafic complex is first discovered containing Cu–Ni sulfide mineralization including chalcopyrite, pyrrhotite, and pentlandite, which predominantly are hosted in the olivine gabbros and olivine pyroxenites.

PETROGRAPHY AND MINERALIZATION

The Xiwanggou mafic–ultramafic complex is mainly composed of gabbro, olivine gabbro, and olivine pyroxenite facies rocks, in which younger mafic gabbroic intrusions emplacing into the older ultramafic bodies (**Figures 1C**, **2A**), both of which show strong differentiation. The complexes underwent extensive alteration by serpentinization and amphibolization. The richest ore bodies are hosted in the ultramafic rocks (**Figures 2D–G**), while some lower grade ones are found in the mafic rocks (**Figures 2B,C**). The olivine gabbro contains a few disseminated sulfides (**Figure 2C**), and is mainly composed of 20–30% olivine, 30–40% clinopyroxene, and 20–30% labradorite, in addition to a few hornblende and secondary chlorite minerals (**Figures 3a,b**). The gabbro has an equigranular texture that is characterized by euhedral pyroxenes and plagioclases (**Figure 2C**), and is predominately composed of 20–30% clinopyroxene, 50–60% plagioclase, and <10% hornblende with accessory apatite and zircon (**Figures 3c,d**). Olivine pyroxenite contains 40–50% olivine and 40% clinopyroxenes, plus hornblende, biotite and sulfide. Pyroxenes commonly occur as large oikocrysts enclosing olivine crystals to form a poikilitic texture (**Figures 3b,d**). The sulfide assemblages including pentlandite, pyrrhotite, and chalcopyrite occur in the interstitial spaces of olivine or pyroxene cumulates (**Figures 2D–G**, **3g,h**). A gabbro vein intruded into the olivine pyroxenite (**Figure 2A**), suggesting that the gabbro formed slightly later than the olivine pyroxenite.

The intrusions were prominently controlled by the NEE and EW fault systems, and extend 1.2 km along the NEE direction with a 100–200 m width. The country rocks hosting the complex are Baishahe Formation and are dominated by Precambrian metamorphic rocks such as biotite schist, quartz-rich schist, quartzite, marble, and gneiss. Small late Ordovician tonalite stocks were cut by the Xiwanggou mafic–ultramafic intrusive rocks in the area (**Figure 1C**). No ages for the granodiorite stocks are currently available, but papers in preparation will give zircon U–Pb ages for the quartz diorite and granodiorite stocks.

The Xiwanggou mafic-ultramafic rocks have undergone variable degrees of post emplacement hydrothermal alteration. Olivine is partially altered to serpentine; clinopyroxene is partially replaced by amphibole and calcite (**Figures 3c,e,f**); plagioclase is partially replaced by chlorite (**Figure 3a**); and secondary magnetite (**Figure 3h**) occurs in the micro-fractures of base-metal sulfides and envelopes the sulfides. In the areas not affected by faulting and deformation, alteration is weak (30% collectively) but pervasive. In the areas affected by faulting and deformation, alteration is far more intensive, up to 100% in places.

SAMPLING AND ANALYTICAL METHOD

All the samples used in this study were collected in the exploratory trench in the central part of the Xiwanggou mafic–ultramafic complexes where the best sulfide mineralization develops (**Figure 1C**). Different types of sulfide mineralization and host rocks were systematically sampled along the trench. Highly altered and deformed outcrops were avoided. Zircon crystals separated from the sulfide-poor gabbro samples (XW-07) and sulfide-rich samples olivine pyroxenite (XW-09) were used for zircon U–Pb dating. Six hand samples are made into polished thin sections to observe the mineral components and be termed. In addition, two samples are made into powder to analyze the chemical and isotopic components.

Zircon LA–ICP–MS U–Pb Dating

Zircon selection and targeting, and transmission and reflected light and cathode luminescence imaging works were conducted at Beijing Zhongxing Meike Technology Co. Ltd. Zircon crystals with various aspect ratios and colors were separated from the samples and inlayed into an epoxy resin target and then polished, cleaned and carbon coated. The cathode luminescence (CL) and back-scatted electron images were photographed to identify zoning patterns in zircons. Some of good patterns were chose for further dating and Hf isotope analysis. The CL images were conducted using a FEI Quanta450 electron microscope, and back-scatted electron images were made with a Gatan MonoCL4, with a voltage of 15 kV.

The U–Pb dating and rare element analyses of zircons was conducted synchronously using laser ablation inductively coupled plasma mass spectrometry (LA-ICP-MS) at the Yanduzhongshi Geological Analysis Laboratories Ltd. Laser Ablation System used was a New Wave UP213, and ICP-MS was a Brooke M90. During the laser ablation process, helium gas was the carrier gas and argon gas was used as the compensation gas to adjust sensitivity, and the two gases were mixed through a homogenizer before entering the ICP-MS. The analysis of each sample point included a blank signal of about 20∼30 s and a sample signal of 50 s. Both a 91500 zircon standard and Plešovice were used as external standards for isotope fractionation correction (Wiedenbeck et al., 1995; Sláma et al., 2008). The actual diameter of LA denudation spots was 25 μm. Concordia diagrams and weighted mean calculations were made using

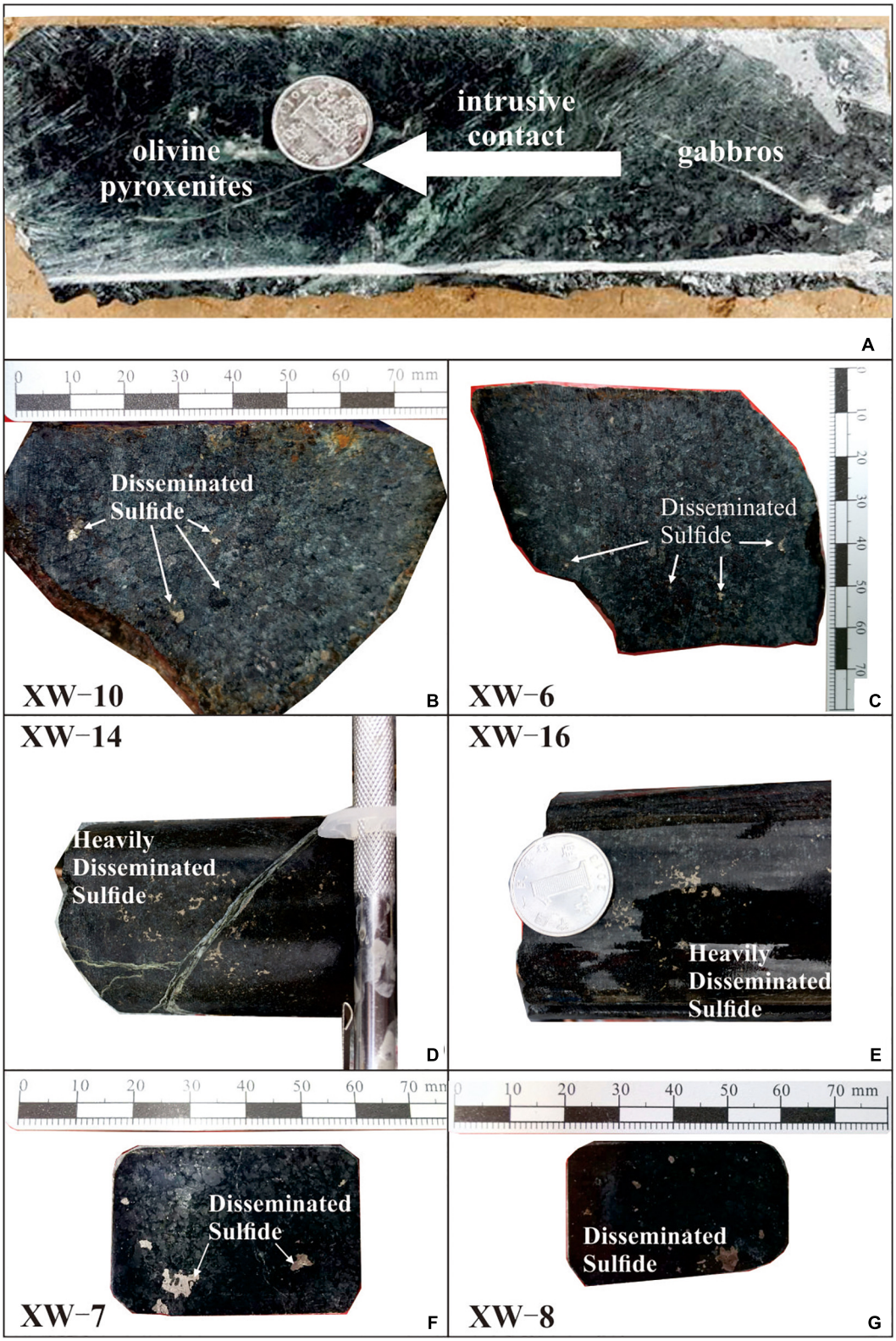

FIGURE 2 | Hand specimen photos of the Xiwanggou mafic-ultramafic rocks. **(A)** The intrusive contact relationship between olivine pyroxenite and gabbro; **(B,C)** Disseminated Cu–Ni sulfide minerals developed in gabbro and olivine gabbro, respectively; **(D–G)** Disseminated Cu–Ni sulfide minerals in olivine pyroxenite.

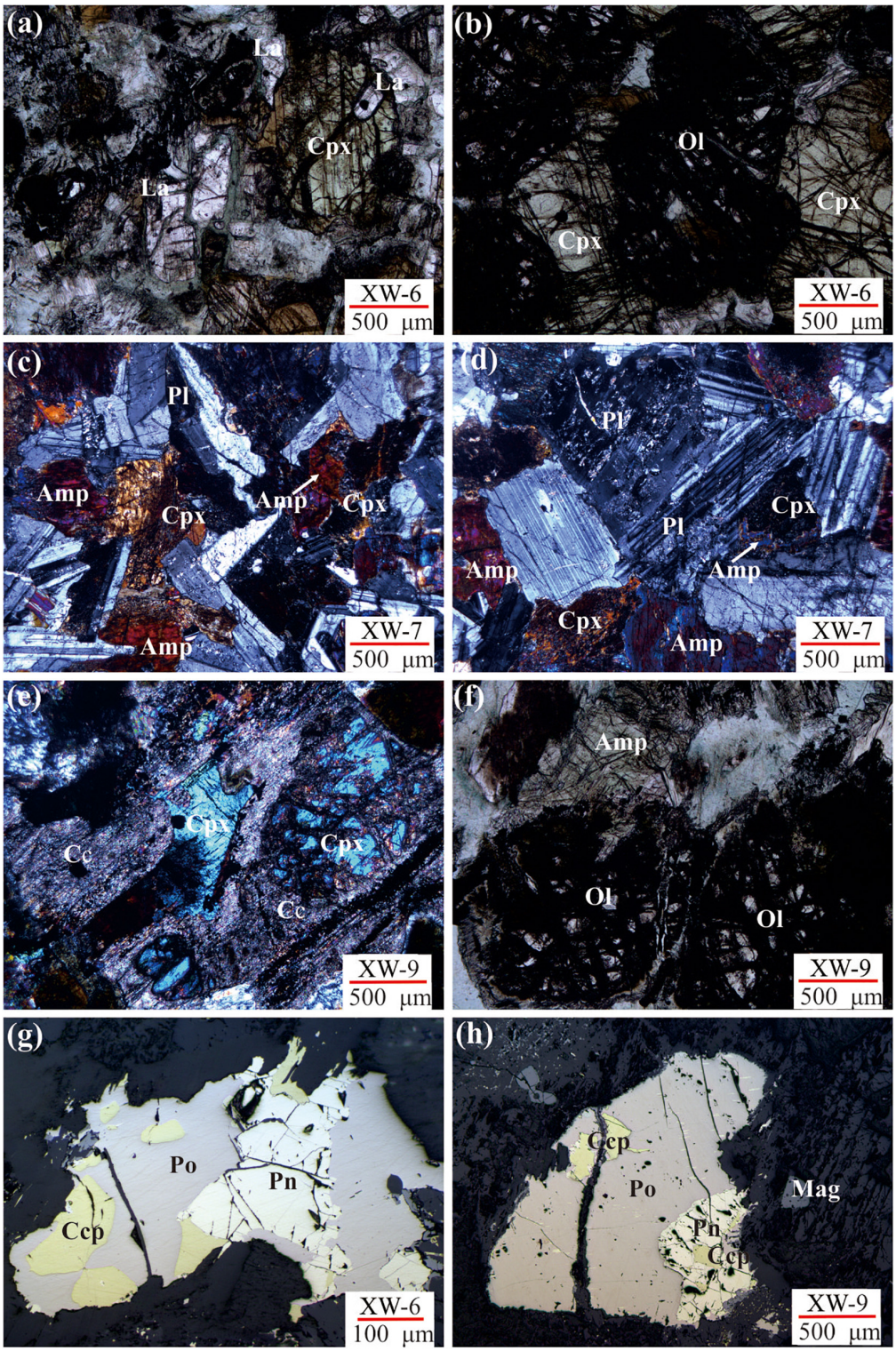

FIGURE 3 | Microphotographs of the Xiwanggou intrusions (**a,b,f**: plain polarized, **c–e**: cross polarized, **g,h**: reflected light). **(a)** some euhedral labradorite clinopyroxene developed in an olivine gabbro sample; **(b)** Medium-grained and severely absorbed olivine surrounded by clinopyroxene in an olivine gabbro sample; **(c,d)** Euhedral clinopyroxene and plagioclase showing equigranular texture filled by fine-grained and interstitial amphibole in a gabbro sample. **(e)** Severe carbonation altered clinopyroxene in a gabbro sample; **(f)** Medium-grained and severely absorbed olivine surrounded by amphibole in an olivine pyroxenite sample; **(g,h)** the pentlandite, pyrrhotite, and chalcopyrite in mineralized olivine gabbros and olivine pyroxenites, respectively; Amp, amphibole; Cpx, clinopyroxene; La, labradorite; Ol, olivine; Pl, plagioclase; Pn, pentlandite; Po, pyrrhotite; Ccp, chalcopyrite; Mag, magnetite.

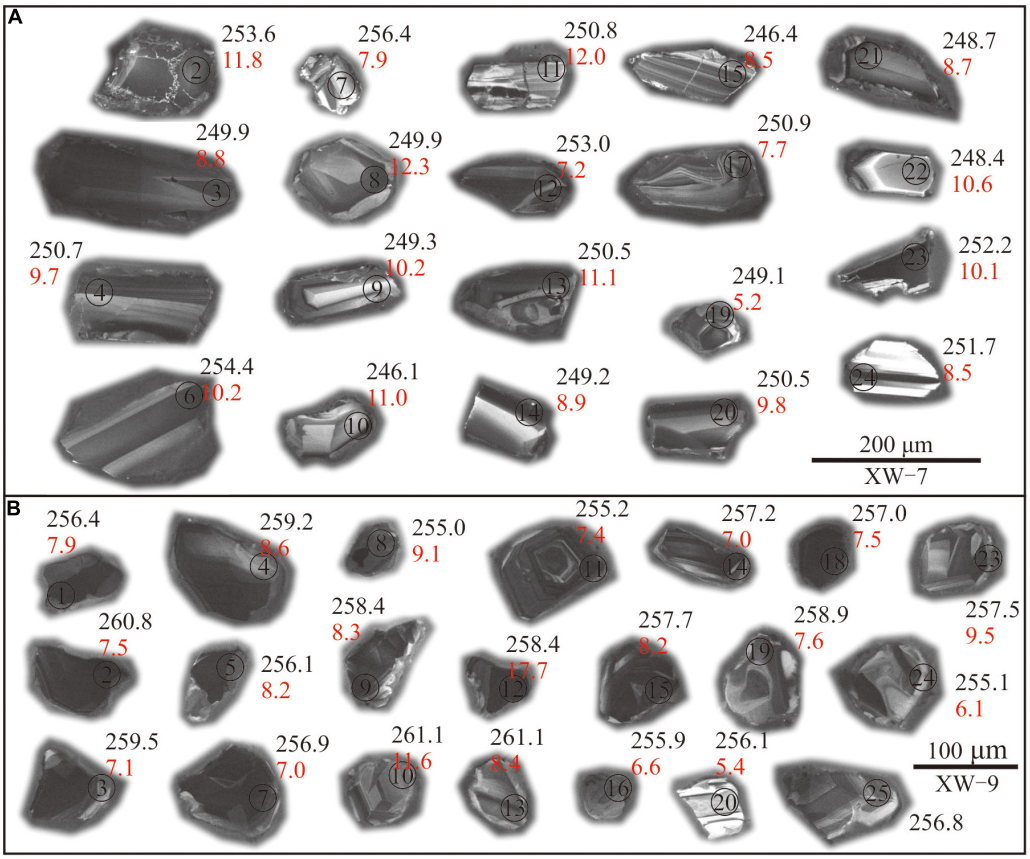

FIGURE 4 | Cathodoluminescence images of selected zircon crystals from the Xiwanggou **(A)** and gabbro **(B)**. Circles are laser beam targets. The black numbers are $^{206}Pb/^{238}U$ ages (Ma), and the red numbers are εHf(*t*) values.

ZSKits authorized by the Yanduzhongshi Geological Analysis Laboratories Ltd.

In situ Hf Isotopic Analyses

In situ zircon Hf isotopic analyses were performed using a Geolas Pro laser ablation system coupled to a Neptune multi-collector ICP-MS at the Key Laboratory for the Study of Focused Magmatism and Giant Ore Deposits, MLR, at the Xi'an Center of Geological Survey, China Geological Survey. The detailed instrumental conditions and data acquisition procedures are similar to those described by Hou et al. (2007). A stationary laser ablation spot with a beam diameter of 30 μm was used for the analyses. The ablated aerosol was carried by helium and combined with argon in a mixing chamber before being introduced to the ICP-MS plasma. All of the Hf analyses were performed on the same spots that underwent U–Pb laser ablation analysis. The GJ-1 zircon standard was used as a reference standard; during this study, it yielded a weighted mean $^{176}Hf/^{177}Hf$ ratio of 0.282030 ± 40 (2SE).

Electron Microprobe Analysis

In this study, olivine, pyroxene and sulfide hosted in the mafic-ultramafic rocks were analyzed. EPMA X-ray elemental analysis were conducted through a 4 WDS detector-equipped Shimadzu EMPA-1720H (Tokyo, Japan) electron microprobe at Key Laboratory of Metallogenic Prediction of Nonferrous Metals and Geological Environment Monitoring (Central South University), Ministry of Education. Operating conditions were 15 kV acceleration, 20 nA beam current, and 5 μm diameter electron beam. Silicon, Ti, Al, Fe, Mn, Mg, Ca, Na, K, Cr, Co, and Ni were analyzed. The back-scatter electronic (BSE) images were photographed under 15 Kv accelerating voltage and 0.5 nA current beam.

Whole-Rock Major and Trace Elements

The major and trace element analysis for the bulk rock samples was mainly performed in the Yanduzhongshi Geological Analysis Laboratories Ltd. Fresh samples were first broken to centimeter sizes; only the fresh pieces were selected, washed with deionized water, dried and then ground to less than 200 mesh (0.5200 ± 0.0001 g) for geochemical analyses. Sample powders were fluxed with Li2B4O7 (1:8) to make homogeneous glass disks at 1250°C using a V8C automatic fusion machine produced by the Analymate Company in China. The bulk rock major elements were analyzed using X-ray fluorescence spectrometry techniques (Zetium, PANalytical). The analytical errors for major elements

TABLE 1 | Concentrations of ^{238}U and ^{232}Th, and U–Pb isotopes of zircon from the Xiwanggou mafic–ultramafic complex.

Sample	U^{238} (μ g/g)	Th^{232} (μ g/g)	U/Th	Pb^{207}/Pb^{206}	1 σ	Pb^{207}/U^{235}	1 σ	Pb^{206}/U^{238}	1 σ	Pb^{206}/U^{238} (Ma)	1 σ
XW-07-02	256	250	1.02	0.05106	0.00164	0.28309	0.00959	0.04012	0.00066	253.6	4.1
XW-07-03	264	120	2.20	0.05165	0.00130	0.28016	0.00666	0.03952	0.00048	249.9	3.0
XW-07-04	663	573	1.16	0.05174	0.00082	0.28329	0.00437	0.03966	0.00039	250.7	2.4
XW-07-06	574	464	1.24	0.05072	0.00122	0.28271	0.00830	0.04025	0.00082	254.4	5.1
XW-07-07	225	95	2.38	0.05041	0.00143	0.28187	0.00772	0.04058	0.00050	256.4	3.1
XW-07-08	488	551	0.88	0.05218	0.00118	0.28319	0.00580	0.03953	0.00054	249.9	3.4
XW-07-09	124	139	0.89	0.05319	0.00203	0.28809	0.01189	0.03943	0.00077	249.3	4.8
XW-07-10	279	228	1.22	0.05063	0.00134	0.27222	0.00922	0.03891	0.00081	246.1	5.0
XW-07-11	156	132	1.18	0.05216	0.00165	0.28288	0.00812	0.03968	0.00065	250.8	4.0
XW-07-12	1231	1054	1.17	0.05128	0.00095	0.28395	0.00759	0.04002	0.00073	253.0	4.5
XW-07-13	517	700	0.74	0.05245	0.00145	0.28737	0.00939	0.03962	0.00068	250.5	4.2
XW-07-14	149	172	0.86	0.05248	0.00212	0.28432	0.01136	0.03942	0.00059	249.2	3.6
XW-07-15	247	350	0.71	0.05100	0.00178	0.27337	0.00986	0.03897	0.00067	246.4	4.1
XW-07-17	306	80	3.81	0.05138	0.00164	0.27926	0.00794	0.03968	0.00056	250.9	3.5
XW-07-19	427	287	1.49	0.05180	0.00108	0.28157	0.00640	0.03939	0.00039	249.1	2.4
XW-07-20	154	163	0.94	0.05163	0.00176	0.28131	0.01001	0.03963	0.00058	250.5	3.6
XW-07-21	475	271	1.75	0.05164	0.00179	0.28123	0.01018	0.03933	0.00058	248.7	3.6
XW-07-22	153	148	1.03	0.05249	0.00162	0.28139	0.00891	0.03929	0.00059	248.4	3.7
XW-07-23	302	193	1.56	0.05060	0.00121	0.27810	0.00684	0.03990	0.00046	252.2	2.8
XW-07-24	188	343	0.55	0.05194	0.00203	0.28378	0.01095	0.03983	0.00054	251.7	3.3
XW-09-01	2893	1674	1.78	0.05259	0.00096	0.29331	0.00530	0.04058	0.00069	256.4	4.3
XW-09-02	1612	0	0.00	0.05093	0.00141	0.28910	0.01086	0.04128	0.00092	260.8	5.7
XW-09-03	1227	884	1.42	0.05084	0.00120	0.28865	0.00627	0.04108	0.00035	259.5	2.2
XW-09-04	401	736	0.55	0.05104	0.00174	0.28848	0.01157	0.04103	0.00077	259.2	4.8
XW-09-05	1557	1483	1.05	0.05187	0.00106	0.28807	0.00592	0.04052	0.00079	256.1	4.9
XW-09-07	2649	1653	1.44	0.05105	0.00086	0.28523	0.00633	0.04065	0.00065	256.9	4.0
XW-09-08	5029	1293	1.76	0.05161	0.00082	0.28721	0.00372	0.04034	0.00035	255.0	2.2
XW-09-09	1616	1631	1.00	0.05150	0.00175	0.28910	0.00902	0.04090	0.00108	258.4	6.7
XW-09-10	560	365	1.58	0.05159	0.00129	0.29361	0.00709	0.04133	0.00047	261.1	2.9
XW-09-11	1739	351	5.23	0.05092	0.00081	0.28324	0.00413	0.04039	0.00046	255.2	2.9
XW-09-12	2101	1394	1.52	0.05165	0.00102	0.29100	0.00626	0.04099	0.00083	258.9	5.1
XW-09-13	488	268	1.92	0.05123	0.00141	0.28755	0.00777	0.04074	0.00039	257.4	2.4
XW-09-14	1890	337	5.69	0.05082	0.00062	0.28490	0.00393	0.04070	0.00050	257.2	3.1
XW-09-15	1445	266	5.55	0.05180	0.00090	0.29131	0.00717	0.04078	0.00075	257.7	4.6
XW-09-16	1260	615	1.48	0.05173	0.00108	0.28790	0.00590	0.04050	0.00071	255.9	4.4
XW-09-18	3083	1423	2.20	0.05116	0.00061	0.28721	0.00453	0.04067	0.00052	257.0	3.2
XW-09-19	262	169	1.56	0.05153	0.00206	0.29095	0.01264	0.04097	0.00076	258.9	4.7
XW-09-20	350	45	9.44	0.05162	0.00161	0.28719	0.00840	0.04052	0.00059	256.1	3.6
XW-09-23	669	816	0.83	0.05075	0.00095	0.28554	0.00603	0.04076	0.00047	257.5	2.9
XW-09-24	846	577	1.72	0.05161	0.00108	0.28775	0.00646	0.04036	0.00052	255.1	3.2
XW-09-25	363	518	0.69	0.05173	0.00148	0.28894	0.00803	0.04064	0.00059	256.8	3.6

were better than 1%. For trace element analysis, sample powders were first dissolved using distilled HF + HNO3 in a screw-top Teflon beaker for 4 days at 100°C. Trace elements of those samples were analyzed by inductively coupled mass spectrometry (ICP-MS) at the Yanduzhongshi Geological Analysis Laboratories Ltd. The analytical uncertainty of the elements examined was better than 5% for ICP-MS analysis, except for a few samples with low trace element content, for which the uncertainty was about 10%. The obtained trace element values in the GSR-2 standard were all consistent with their recommended values.

Sr–Nd Isotope Analysis

Main analysis process is as follows: a 0.25 g sample was placed in a Teflon stewing pot; 0.5 ml HNO_3 and 1.5 ml of HF were added, and the container was closed; the sample underwent heating digestion for 48 h at 190°C; HF was expelled at 160°C, and 3 ml 1:1 HNO_3 was added at 150°C; the container was closed and the temperature was maintained at 150°C for 6 h, and leaving constant mass to 25 g. Extraction of Sr was performed by spinning the appropriate solution in a centrifuge, and drying the

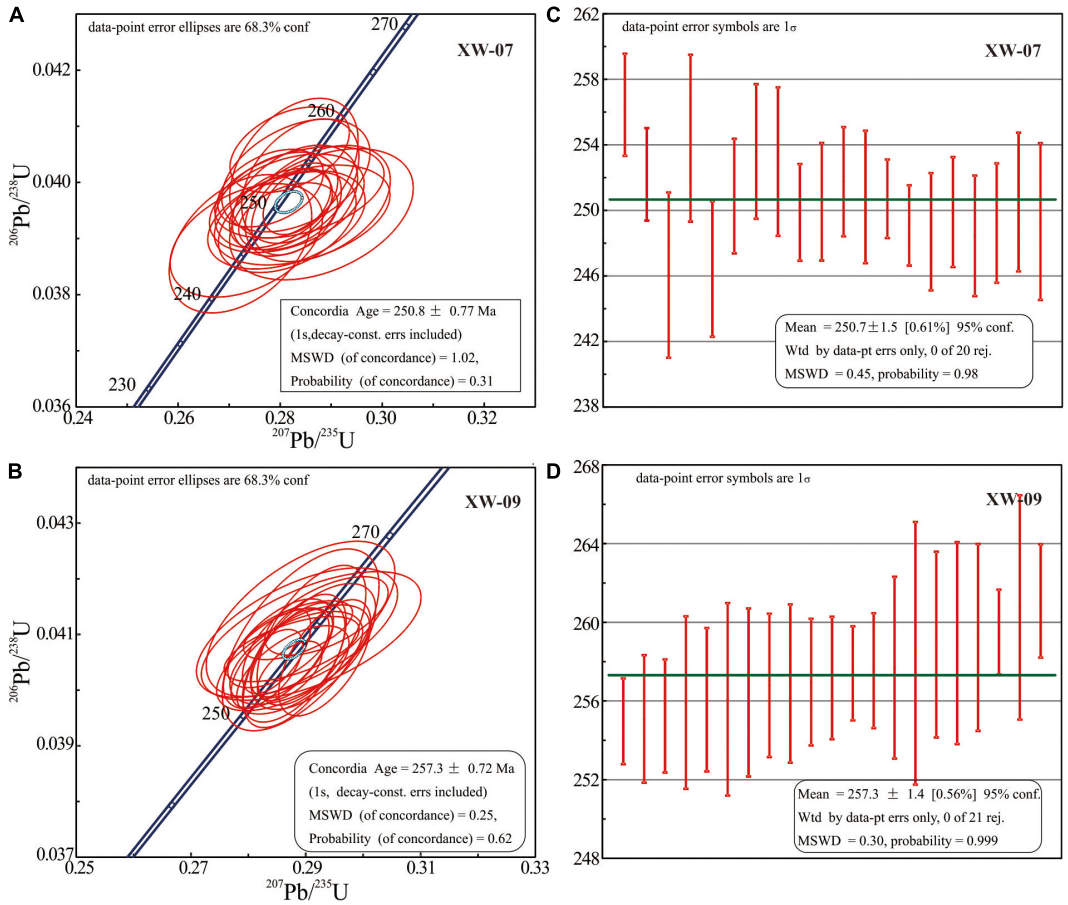

FIGURE 5 | Zircon U–Pb age diagrams of gabbros **(A,C)** and olivine-pyroxenites **(B,D)** in the Xiwanggou mafic–ultramafic complex.

supernatant; the acidity was adjusted; Sr was separated and purified using SR special resin. Extraction of Nd was similar to the extraction of Sr, but LN specific resin was used to separate and purify Nd. The $^{87}Sr/^{86}Sr$ ratios were measured on a Thermo Fisher Scientific multi-receiver ICP-MS and the and $^{143}Nd/^{144}Nd$ ratios were measured on a Neptune Plus Mc-ICP-MS in the Yanduzhongshi Geological Analysis Laboratories Ltd. The measured $^{88}Sr/^{86}Sr$ and $^{143}Nd/^{144}Nd$ ratios were normalized for mass fractionation using $^{88}Sr/^{86}Sr$ = 8.373209 and $^{143}Nd/^{144}Nd$ = 0.7218 respectively.

ANALYTICAL RESULTS

Zircon U–Pb Isotope Age

Cathode luminescence images of the selected zircon crystals from the Xiwanggou sulfide bearing gabbro and olivine-pyroxenite are shown in **Figure 4**. They are mostly wide stubby and columnar with a clear stripped texture at the edge. The long axis of the zircons from XW-07 (gabbro) are variable, from 50 to 250 μm, and those from XW-09 (olivine pyroxenite) range between 50 and 150 μm. The length-width ratios are between 1:1 and 2:1. Most of zircons show oscillatory zoning and inherited cores, but internally a few zircons are texturally homogeneous. These features indicate the selected zircons are of a magmatic origin from the mafic-ultramafic complexes.

The analytical results of the U–Pb isotopic dating are listed in **Table 1**. The zircon grains have 45–1653 μg/g Th, 124–5029 μg/g U, and U/Th ratios of 0.63–9.44. The U/Th ratio of magmatic zircons is generally less than 10; whereas the U/Th of metamorphic zircons is greater than 10 (Rubatto and Gebauer, 2000). This is consistent with our interpretation that all the grains are from magmatic zircons. The concordia plots of the analyses are shown in **Figures 5A,B**, and the average age plots are shown in the **Figures 5C,D**. The concordia plot shows a zircon U–Pb isotope age for the Xiwanggou sulfide-poor garbbo of 250.8 ± 0.77 Ma (**Figure 5A**), and its weighted age is 250.7 ± 1.5 Ma (**Figure 5C**). The concordia plot shows a zircon U–Pb isotope age for the sulfide-rich olivine-pyroxenite of 257.3 ± 0.72 Ma (**Figure 5B**), and its weighted age is 257.3 ± 1.4 Ma (**Figure 5D**). The results show that there is a large age gap of ∼ 7 Ma between the mafic and ultramafic associated with mineralization.

TABLE 2 | MC-ICP-MS zircon Lu–Hf isotopic compositions from the Xiwanggou mafic–ultramafic complex.

Sample	age	$^{176}Yb/^{177}Hf$(corr)	2σ	$^{176}Lu/^{177}Hf$(corr)	2σ	$^{176}Hf/^{177}Hf$(corr)	2σ	eHf (T)	TDM	TDMC	fs
XW-07-02	250.8	0.065209	0.000353	0.001776	0.000011	0.282958	0.000023	11.8	426	525	–0.95
XW-07-03	250.8	0.018209	0.000423	0.000529	0.000011	0.282866	0.000027	8.8	540	719	–0.98
XW-07-04	250.8	0.074527	0.000435	0.002079	0.000010	0.282901	0.000031	9.7	512	656	–0.94
XW-07-06	250.8	0.069588	0.000391	0.001956	0.000017	0.282915	0.000026	10.2	490	624	–0.94
XW-07-07	250.8	0.024615	0.000438	0.000690	0.000014	0.282843	0.000021	7.9	576	774	–0.98
XW-07-08	250.8	0.054090	0.000389	0.001607	0.000009	0.282971	0.000030	12.3	404	492	–0.95
XW-07-09	250.8	0.040387	0.000520	0.001128	0.000011	0.282908	0.000023	10.2	489	630	–0.97
XW-07-10	250.8	0.033413	0.000658	0.000961	0.000015	0.282931	0.000024	11.0	455	577	–0.97
XW-07-11	250.8	0.024161	0.000428	0.000709	0.000008	0.282960	0.000022	12.0	411	509	–0.98
XW-07-12	250.8	0.055200	0.001563	0.001590	0.000041	0.282828	0.000023	7.2	610	816	–0.95
XW-07-13	250.8	0.015963	0.000137	0.000450	0.000002	0.282933	0.000023	11.1	445	566	–0.99
XW-07-14	250.8	0.100246	0.003047	0.002631	0.000088	0.282881	0.000028	8.9	549	707	–0.92
XW-07-15	250.8	0.088039	0.000546	0.002463	0.000014	0.282867	0.000024	8.5	567	737	–0.93
XW-07-17	250.8	0.036838	0.001071	0.001005	0.000028	0.282837	0.000028	7.7	588	789	–0.97
XW-07-19	250.8	0.073293	0.000361	0.002041	0.000009	0.282773	0.000028	5.2	698	946	–0.94
XW-07-20	250.8	0.025506	0.000324	0.000734	0.000010	0.282897	0.000026	9.8	500	652	–0.98
XW-07-21	250.8	0.044156	0.000413	0.001221	0.000012	0.282868	0.000023	8.7	547	721	–0.96
XW-07-22	250.8	0.056651	0.000331	0.001431	0.000009	0.282922	0.000023	10.6	474	603	–0.96
XW-07-23	250.8	0.050193	0.002320	0.001435	0.000065	0.282909	0.000023	10.1	492	631	–0.96
XW-07-24	250.8	0.034403	0.000689	0.000904	0.000012	0.282862	0.000027	8.5	552	733	–0.97
XW-09-01	257.3	0.023660	0.000205	0.000609	0.000006	0.282838	0.000024	7.9	580	779	–0.98
XW-09-02	257.3	0.015845	0.000051	0.000502	0.000002	0.282826	0.000035	7.5	595	805	–0.98
XW-09-03	257.3	0.022233	0.000143	0.000563	0.000003	0.282816	0.000026	7.1	611	830	–0.98
XW-09-04	257.3	0.002906	0.000060	0.000076	0.000002	0.282857	0.000028	8.6	547	731	–1.00
XW-09-05	257.3	0.006253	0.000057	0.000174	0.000001	0.282844	0.000030	8.2	565	760	–0.99
XW-09-07	257.3	0.011385	0.000064	0.000259	0.000002	0.282810	0.000019	7.0	614	839	–0.99
XW-09-08	257.3	0.013233	0.000105	0.000401	0.000004	0.282870	0.000025	9.1	533	705	–0.99
XW-09-09	257.3	0.002606	0.000063	0.000062	0.000001	0.282846	0.000019	8.3	561	755	–1.00
XW-09-10	257.3	0.005199	0.000034	0.000154	0.000002	0.282941	0.000024	11.6	431	542	–1.00
XW-09-11	257.3	0.028089	0.000257	0.000812	0.000008	0.282825	0.000026	7.4	602	810	–0.98
XW-09-12	257.3	0.076114	0.000234	0.002547	0.000007	0.283125	0.000057	17.7	186	149	–0.92
XW-09-13	257.3	0.020316	0.000632	0.000393	0.000012	0.282852	0.000024	8.4	559	747	–0.99
XW-09-14	257.3	0.012864	0.000306	0.000327	0.000012	0.282810	0.000025	7.0	615	839	–0.99
XW-09-15	257.3	0.004513	0.000042	0.000114	0.000001	0.282843	0.000026	8.2	566	762	–1.00
XW-09-16	257.3	0.007368	0.000306	0.000256	0.000010	0.282800	0.000025	6.6	629	863	–0.99
XW-09-18	257.3	0.017092	0.000551	0.000373	0.000010	0.282825	0.000023	7.5	596	807	–0.99
XW-09-19	257.3	0.002477	0.000051	0.000069	0.000002	0.282828	0.000029	7.6	586	796	–1.00
XW-09-20	257.3	0.002330	0.000067	0.000081	0.000003	0.282766	0.000028	5.4	672	937	–1.00
XW-09-23	257.3	0.008891	0.000027	0.000213	0.000002	0.282881	0.000023	9.5	515	679	–0.99
XW-09-24	257.3	0.008955	0.000119	0.000245	0.000003	0.282786	0.000027	6.1	648	894	–0.99

Hf Isotope

The Lu–Hf isotopes of the selected zircon crystals from the Xiwanggou mafic-ultramafic rocks are listed in **Table 2**. The calculated εHf(*t*) values of these zircon crystals are all positive varying from 5.2 to 12 for gabbro and 5.4 to 17.7 for olivine pyroxenite, respectively. A comparison of these values with those for depleted mantle, a potential contaminant, and the Precambrian granitic gneiss which is exposed in the Xiariham and Bokalike areas in the western part of the EKOB (data from Gan, 2014; He et al., 2016) is shown in **Figure 6**.

Mineral Compositions

The compositions of important rock-forming minerals such as olivine and pyroxenes are listed in **Tables 3**, **4**. Olivine occurs as a cumulate phase in olivine gabbro, and commonly encloses chromite with olive crystals and exhibits a reactional rim in contacts with other silicate crystals. Minor amounts of olivine grains are encapsulated by pyroxene with olivine texture and serpentinization. The interiors of subhedral and euhedral olivine grains are often intersected by some serpentine veins. The composition of major elements has little change in the

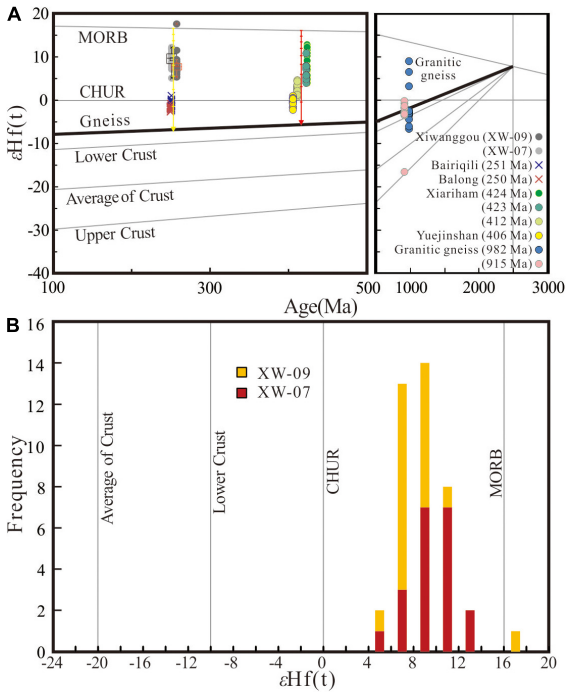

FIGURE 6 | (A) Zircon εHf(*t*) value versus zircon U–Pb isotope age for the Xiwanggou mafic–ultramafic rocks. **(B)** The statistical histogram of zircon εHf(*t*) values from the Xiwanggou complex. The Hf isotope evolution of the Precambrian granitic gneiss from East Kunlun orogen is calculated using the parameters for the upper crust given by Gan (2014) and He et al. (2016). The comparison of the late Silurian-Early Devonian mafic–ultramafic intrusions are based on the data from Xiarihamu and Yuejinshan areas (Liu et al., 2012; Wang et al., 2014; Li et al., 2015; Peng et al., 2016), and the Late Permian Bairiqili gabbro-diabase are based on Xiong et al. (2011b).

samples (**Table 3**) with MgO = 44.34–45.13 wt.%, FeO = 14.61–15.43 wt.%, SiO_2 = 39.36–40.42 wt.%, NiO = 0.12–0.25 wt.%, Cr_2O_3 = 0–0.06 wt.% and a corresponding Fo value of 83.45–84.51 with an average of 84.08, which corresponds to chrysolite (**Figures 7A–F**). The good negative linear relationship between MgO (wt.%) and FeO (wt.%) in olivine indicates that there was a substitution between MgO (wt.%) and FeO (wt.%) (**Figure 7A**). Olivine contains 83.45–84.51 mol% Fo with an average of 84.08 mol% (which is the value for chrysolite), and it is depleted in Mn and Ca.

Pyroxene is mostly euhedral and subhedral grains, from a cumulate phase with olivine or olivine inclusions forming olivine texture. Serpentinization, chloritization, talcification, and fibrillation are common. Pyroxene consists mainly of clinopyroxene with SiO_2 content of 52.38–52.45 wt.%, TiO_2 content of 0.18–0.7 wt.%, Al_2O_3 content of 2.87–3.13 wt.%, FeO content of 4.13–4.26 wt.%, MgO content of 16.85–17wt.%, CaO content of 22.97–23.01 wt.%, Cr_2O_3 content of 1.13–1.34, and NiO content of 0–0.05 (**Figures 7A–F**).

Whole Rock Major and Trace Elements

The concentrations of major and trace elements in the samples from the Xiwanggou mafic–ultramafic intrusions are given as **Supplementary Table 1**. In this study, the Xiwanggou samples can be geochemically divided into two groups based on the variability of SiO_2 and (K_2O + Na_2O) contents: 46.62–49.51 wt.% SiO_2 and 2.46–3.0 wt.% (K_2O + Na_2O) for gabbro; and 41.35–42.49 wt.% SiO_2 and 1.06–1.61 wt.% (K_2O + Na_2O) for olivine pyroxenites. The corresponding $Mg^{\#}$ of two groups are 77.76–82.04 and 88.10–88.22, respectively (**Figure 8**). The TiO_2 contents of all samples are very low, ranging from 0.16 wt.% to 0.74 wt.% (ave. 0.38 wt.%), which is significantly lower than that of oceanic tholeiite (2.63 wt.%), intraplate basalt (2.23 wt.%), but more similar to that of island arc basalt (0.98 wt.%). In summary, the gabbro in the Xiwanggou area is characterized by low Si and Ti, high Mg, and depleted alkali.

Primitive mantle-normalized diagrams for incompatible elements also exhibit nearly identical element concentrations, reflecting a similar abundance and composition for mafic–ultramafic rocks (**Figure 9A**). The abundances of more incompatible large ion lithophile elements (LILE) are greater than those of the high field strength elements (HFSE). This is typical of the mantel magmas proposed to possess a large lithospheric crust component. Other notable features include the depletion of Nb and Ta relative to La and U, enrichment of Sr relative to Pr and Nd, and slight depletion of Ba relative to Rb and Th. Such trace element patterns are clearly similar to those of island arc sulfide-bearing mafic intrusive rocks in the Tati and Selebi-Phikwe belts, eastern Botswana (Maier et al., 2008).

Almost all samples are uniformly enriched in LREE relative to HREE with $(La/Sm)_N$ of 1.43–2.38, and show flat HREE chondrite-normalized patterns with $(Gd/Yb)_N$ = 1.31–1.52 (**Figure 9B**). The gabbro has relatively higher total REE content (ΣREE = 20.46–42.76 ppm) and lower $(La/Yb)_N$ ratios [$(La/Yb)_N$ = 2.82–3.17] than that of olivine pyroxenite [ΣREE = 15.45–24.92 ppm; $(La/Yb)_N$ = 3.63–4.8]. Most of the samples have slightly negative Eu anomalies (Eu/Eu^* = 0.80–0.95).

Sr–Nd Isotopes

The Rb–Sr and Sm–Nd isotope data for the Xiwanggou mafic-ultramafic rocks are given in **Table 5**. The initial isotopic ratios for the olivine pyroxenite and gabbro were calculated using the zircon U–Pb ages of 257.3 and 250.8 Ma for these two different intrusive phases, respectively. The olivine pyroxenite and gabbro samples have distinctive $^{147}Sm/^{144}Nd$ ratio range of 0.15406–0.158684 and 0.170205–0.17175, respectively. The olivine pyroxenites have slightly lower initial $^{143}Nd/^{144}Nd$ ratios varying narrowly between 0.512251 and 0.51285 than that of gabbros varying from 0.512629 to 0.512655. The $(^{87}Sr/^{86}Sr)_i$ ratios of the olivine pyroxenite range from 0.705535 to 0.706133, and the gabbro has a ratio $(^{87}Sr/^{86}Sr)_i$ of 0.705905–0.706620 (**Figure 10A**). In addition, the $(^{87}Sr/^{86}Sr)_i$ values of the Xiwanggou complex almost keep invariable with varying SiO_2 contents (**Figure 10A**). However, the $(^{87}Sr/^{86}Sr)_i$ values of the late Permian Bairiqili non-mineralization gabbro increase with raising SiO_2 contents (**Figure 10A**). The εNd(*t*) values of the olivine pyroxenite and gabbro are from −1.09 to −0.43 and 0.66 to 1.18, respectively (**Figure 10B**).

TABLE 3 | The composition of microprobe analysis of olivine in olivine gabbro from the Xiwanggou deposit.

Sample (wt.%)	X20111	x105.1	x10121	x10101	x109.1	X6011.1	X609.1	X608.3	X603.1	X602.1	X601.3	X902.1	Oli03	Oli	Oli	Oli
SiO_2	40.34	39.82	39.65	39.53	38.84	39.70	39.92	40.40	39.77	40.51	40.37	40.34	40.92	40.66	40.48	40.67
TiO_2	0.02	0.02	0.00	0.00	0.02	0.00	0.00	0.04	0.01	0.05	0.00	0.03	0.00	0.01	0.03	0.03
Al_2O_3	0.01	0.04	0.02	0.01	0.02	0.03	0.02	0.03	0.03	0.01	0.02	0.01	0.01	0.03	0.00	0.00
FeO	15.36	12.92	14.32	15.14	15.26	14.81	14.85	14.59	14.91	14.78	15.08	14.75	14.58	15.25	15.09	15.14
MnO	0.24	0.24	0.23	0.21	0.23	0.25	0.22	0.21	0.23	0.20	0.23	0.21	0.23	0.25	0.24	0.23
MgO	45.22	46.41	45.23	45.15	44.35	45.41	45.12	44.89	44.87	45.31	44.87	45.37	44.13	44.08	44.64	44.40
CaO	0.03	0.05	0.04	0.05	0.04	0.05	0.06	0.06	0.05	0.04	0.06	0.08	0.06	0.05	0.07	0.13
Na_2O	0.01	0.02	0.00	0.01	0.00	0.00	0.02	0.00	0.00	0.00	0.00	0.01	0.00	0.01	0.00	
K_2O	0.01	0.00	0.01	0.01	0.00	0.00	0.02	0.00	0.00	0.00	0.00	0.00	0.00	0.01	0.00	
Cr_2O_3	0.00	0.00	0.00	0.00	0.00	0.02	0.00	0.00	0.00	0.02	0.00	0.00	0.01	0.06	0.00	0.00
NiO	0.12	0.16	0.20	0.23	0.22	0.22	0.21	0.22	0.20	0.24	0.25	0.13	0.18	0.14	0.17	0.15
Total	101.25	99.51	99.50	100.11	98.77	100.25	100.22	100.22	99.87	100.89	100.62	100.81	99.93	100.35	100.54	100.60
Mg × 100/(Mg + Fe)	74.64	78.22	75.96	74.89	74.40	75.41	75.23	75.47	75.05	75.41	74.85	75.47	75.17	74.30	74.73	74.58
Si	1.000	0.995	0.997	0.992	0.989	0.993	0.998	1.007	0.998	1.004	1.005	1.002	1.022	1.015	1.008	1.013
Ti	0.000	0.000	0.000	0.000	0.000	0.000	0.000	0.001	0.000	0.001	0.000	0.001	0.000	0.000	0.001	0.001
Al	0.000	0.001	0.001	0.000	0.001	0.001	0.000	0.001	0.001	0.000	0.001	0.000	0.000	0.001	0.000	0.000
Fe	0.318	0.269	0.300	0.317	0.324	0.309	0.310	0.304	0.312	0.306	0.313	0.306	0.304	0.317	0.314	0.314
Mn	0.005	0.005	0.005	0.005	0.005	0.005	0.005	0.004	0.005	0.004	0.005	0.004	0.005	0.005	0.005	0.005
Mg	1.671	1.729	1.695	1.688	1.684	1.693	1.682	1.669	1.679	1.674	1.665	1.680	1.642	1.640	1.658	1.648
Ca	0.001	0.001	0.001	0.001	0.001	0.001	0.001	0.002	0.001	0.001	0.001	0.002	0.002	0.001	0.002	0.003
Na	0.000	0.001	0.000	0.001	0.000	0.000	0.001	0.000	0.000	0.000	0.000	0.001	0.000	0.000	0.000	0.000
K	0.000	0.000	0.000	0.000	0.000	0.000	0.001	0.000	0.000	0.000	0.000	0.000	0.000	0.000	0.000	0.000
Cr	0.000	0.000	0.000	0.000	0.000	0.000	0.000	0.000	0.000	0.000	0.000	0.000	0.000	0.001	0.000	0.000
Ni	0.002	0.003	0.004	0.005	0.005	0.004	0.004	0.004	0.004	0.005	0.005	0.003	0.004	0.003	0.003	0.003
Mole percent (mol%)																
Forsterite	83.81	86.30	84.74	84.01	83.64	84.34	84.24	84.42	84.11	84.39	83.97	84.42	84.18	83.55	83.88	83.77
Tephroite	0.25	0.25	0.24	0.23	0.25	0.26	0.23	0.23	0.24	0.21	0.24	0.22	0.25	0.27	0.25	0.24
Fayalite	15.94	13.45	15.01	15.77	16.11	15.40	15.52	15.36	15.65	15.40	15.79	15.36	15.57	16.17	15.87	15.98

TABLE 4 | The composition of microprobe analysis of pyroxene in olivine gabbro from the Xiwanggou deposit.

Sample (wt.%)	X6-11.2	X6-9.2	X6-8.2	X6-8.1	X6-7.2	X6-7.1	X6-3.2	X6-1.3	X6-1.2	X6-1.2	X6-1.1
SiO_2	51.33	50.99	50.77	50.82	52.19	51.83	51.53	51.38	51.37	51.90	51.27
TiO_2	0.50	0.41	0.52	0.51	0.53	0.45	0.49	0.55	0.54	0.53	0.51
Al_2O_3	3.65	3.12	3.05	3.37	3.07	3.23	2.83	3.52	3.05	3.01	3.41
FeO	4.06	4.06	4.34	3.91	4.06	4.08	4.70	4.04	4.60	4.23	3.96
MnO	0.11	0.14	0.11	0.10	0.13	0.11	0.13	0.11	0.14	0.14	0.11
MgO	17.00	17.21	17.24	17.74	16.89	16.89	17.07	16.93	17.62	17.41	16.72
CaO	21.35	21.49	21.28	20.54	21.98	21.39	21.02	21.30	20.29	21.07	21.80
Na_2O	0.33	0.36	0.40	0.32	0.41	0.38	0.35	0.35	0.36	0.34	0.37
K_2O	0.00	0.01	0.01	0.01	0.01	0.00	0.00	0.00	0.00	0.00	0.00
Cr_2O_3	1.34	1.20	1.13	1.30	1.29	1.32	1.17	1.34	1.22	1.14	1.32
NiO	0.05	0.02	0.00	0.04	0.03	0.00	0.02	0.01	0.01	0.03	0.01
Total	99.73	99.02	98.86	98.66	100.58	99.70	99.35	99.52	99.20	99.79	99.49
Mg*100/(Fe + Mg)	80.7	80.9	79.9	81.9	80.6	80.6	78.4	80.7	79.3	80.4	80.8
Si	1.903	1.904	1.900	1.900	1.919	1.919	1.919	1.907	1.911	1.917	1.906
Al(IV)	0.062	0.042	0.035	0.048	0.051	0.060	0.043	0.061	0.045	0.048	0.056
Al(VI)	0.097	0.096	0.100	0.100	0.081	0.081	0.081	0.093	0.089	0.083	0.094
Ti	0.014	0.012	0.015	0.014	0.015	0.013	0.014	0.015	0.015	0.015	0.014
Fe^{3+}	0.018	0.020	0.022	0.018	0.022	0.020	0.019	0.019	0.019	0.018	0.020
Fe^{2+}	0.108	0.107	0.114	0.104	0.102	0.106	0.127	0.106	0.124	0.112	0.103
Mn	0.003	0.005	0.004	0.003	0.004	0.003	0.004	0.003	0.004	0.004	0.004
Mg	0.939	0.958	0.962	0.989	0.926	0.933	0.948	0.937	0.978	0.959	0.927
Ca	0.848	0.860	0.853	0.823	0.866	0.849	0.839	0.847	0.809	0.834	0.868
Na	0.006	0.006	0.007	0.006	0.007	0.007	0.006	0.006	0.006	0.006	0.007
K	0.000	0.000	0.000	0.000	0.000	0.000	0.000	0.000	0.000	0.000	0.000
Cr	0.039	0.035	0.033	0.038	0.038	0.039	0.034	0.039	0.036	0.033	0.039
Ni	0.002	0.001	0.000	0.001	0.001	0.000	0.001	0.000	0.000	0.001	0.000
Mol.%											
Enstatite	49.48	49.67	49.77	51.54	48.78	49.33	49.43	49.48	51.07	50.22	48.74
Ferrosilite	5.67	5.54	5.89	5.42	5.38	5.59	6.62	5.60	6.45	5.88	5.41
Wollastonite	44.67	44.56	44.16	42.88	45.62	44.89	43.74	44.74	42.25	43.67	45.66

DISCUSSION

Sources and Geodynamics of Late Permian Mafic–Ultramafic Rocks

The zircon U–Pb ages of gabbro and olivine pyroxenite are 250.8 ± 0.8 Ma and 257.3 ± 0.7 Ma, respectively. These ages are consistent with field observations that mafic gabbro intersected the ultramafic olivine pyroxenite. In addition, the Paleo-Tethyan Anemaqen Ocean in EKOB are considered to begin northward subduction in the Late Permian before 260 Ma, and closed at the Middle Triassic (Mo et al., 2007; Li R. B. et al., 2012; Yang et al., 2013; Chen et al., 2017); and yet other scholars have proposed that the subduction of the Paleo-Tethys Ocean began at the Early Permian (Liu, 2014; Xiong et al., 2014; Chen et al., 2015), and closed in the Middle and Late Triassic as indicated by the deposit of a typical Upper Triassic Babaoshan molasse formation at that time (Wu et al., 2017). Therefore, the Xiwanggou complexes are believed to be formed in a subduction environment from Late Permian to Middle Triassic.

The trace element patterns of the Xiwanggou mafic-ultramafic intrusions are characterized by the depletion of HREE, Nb and Ta, and enrichment of Sr, Rb, Ba, and LREE (**Figure 9**), which are clearly similar to those of island arc sulfide-bearing mafic intrusive rocks in the Tati and Selebi-Phikwe belts, eastern Botswana (Maier et al., 2008). In addition, the Late Permian-Early Triassic gabbroic and dioritic dykes from the EKOB display similar distribution patterns that are enriched in LILEs and depleted in HFSEs (Xiong et al., 2011a; Ding et al., 2014), which generally indicates a metasomatized mantle source in a subduction environment (Jiang et al., 2015; Kong et al., 2018). Therefore, the geochemical and geochronological data of the Xiwanggou complexes, together with the regional considerations, suggest that they record a northward subduction of the Paleo Tethys Ocean during Late Permian to Early Triassic (Mo et al., 2007; Xiong et al., 2011a; Zhang et al., 2012).

The AFC processes tend to obscure the potential distinctions of primary chemical signatures between the fertile and barren basalts. In this study, we calculated the AFC processes involved in the magma evolution controlled by the partition coefficient of minerals. In the conceptual model (**Figures 11A,B**), the geochemical evolution of the middle-late Permian rocks show different paths via two different mechanisms. This further indicates that some of the Late Permian mafic–ultrmafic magma first probably experienced dehydration partial melting controlled

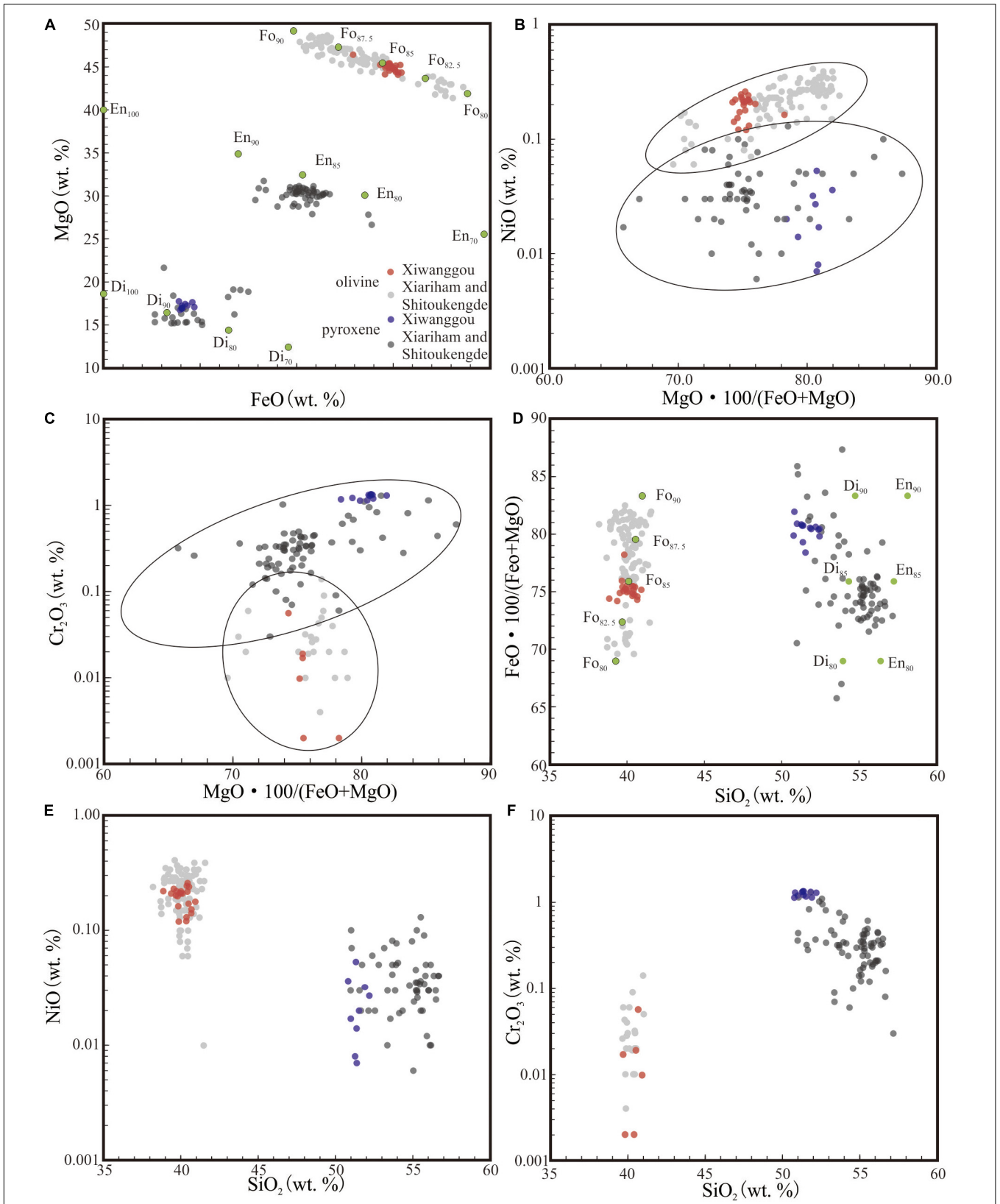

FIGURE 7 | Geochemical diagrams of olivine **(A,B)** and pyroxene **(C–F)** compositions. The blue circles are from the Xiwanggou mafic-ultramafic rocks, and the gray ones from the Xiarihamu and Shitoukengde basic–ultrabasic complexes.

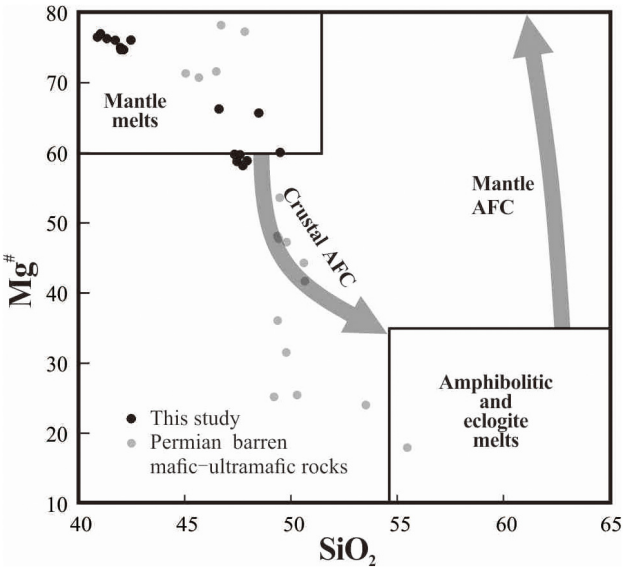

FIGURE 8 | $Mg^{\#}$ vs. SiO_2 plots for the Xiwanggou mafic–ultramafic rocks. Gray circle data for Permian mafic–ultramafic intrusions are from Jiadang and Bairiqili areas (Xiong et al., 2011b; Kong et al., 2018).

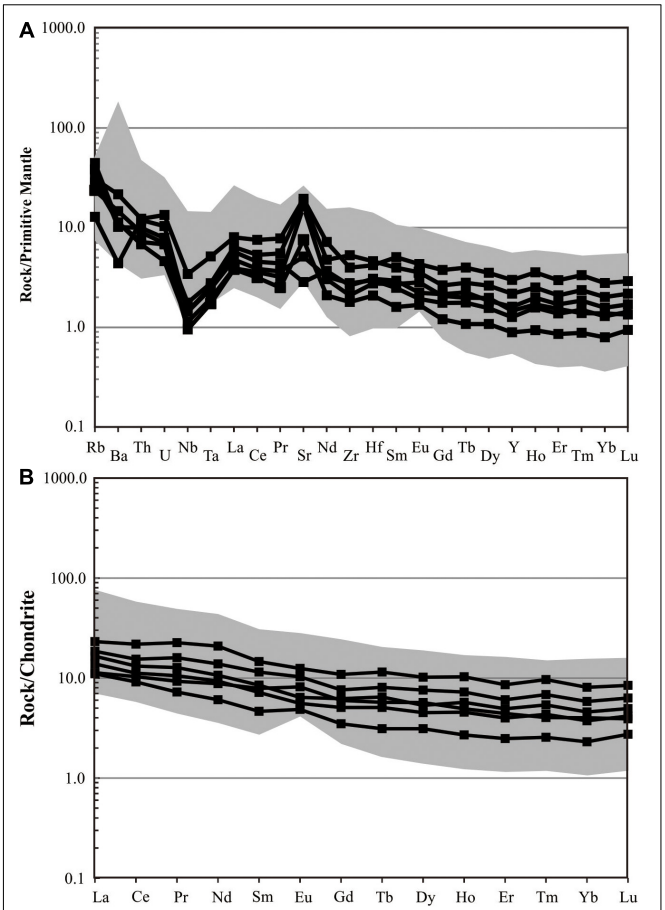

FIGURE 9 | Primitive mantle-normalized trace element patterns **(A)** and chondrite-normalized REE patterns **(B)**. Olivine gabbro normalizing values after Sun and McDonough (1989). The gray shadows show the spectrum of trace and REE elements from the Middle-Late Permian mafic–ultramafic intrusions developed in the East Kunlun Orogen (Xiong et al., 2011a; Kong et al., 2018).

by breakdown of amphibole in the mantle wedge, which usually occurs between ∼825 and 1000°C at pressures between 0.5 and 2.0–2.5 GPa (Peacock et al., 1994). However, some other underwent an assimilation and fractional crystallization (AFC) process jointly controlled by 70% clinopyroxene (Cpx) and 30% garnet (Grt), and tended from lower crust to upper crust composition (**Figures 11A,B**).

The remarkable distinctions between contemporary fertile and barren rocks convey significant information on εNd(t) and $(^{87}Sr/^{86}Sr)_i$ values. The Xiwanggou ore-bearing intrusions with lower contents of SiO_2 and $(^{87}Sr/^{86}Sr)_i$ are believed to be less contaminated by crustal materials (**Figure 10A**; Arndt et al., 2005). However, the Bairiqili barren mafic-ultramafic intrusive rocks with relative high contents of SiO_2 and $(^{87}Sr/^{86}Sr)_i$ maybe indicate a mixing magma source between depleted subcontinental lithospheric mantle (SCLM) and lower crustal materials (**Figure 10A**; Xiong et al., 2011a; Liu et al., 2012). As the mafic microgranular enclaves (MMEs) captured by the Triassic granitoids in EKOB with similar SiO_2 contents and medium $(^{87}Sr/^{86}Sr)_i$ values are generally considered to be sourced from a mixing of subcontinental lithospheric mantle (SCLM) with EMII type mantle as well as felsic magma yielded by the partial melting of lower crust materials (Gao et al., 2015). Furthermore, the late Permian mafic-ultramafic rocks have similar trend paralleling to the EMII (enriched mantle II) features evolved from depleted mantle to lower crustal materials of basement, indicating a partial melting process of intensively depleted lithospheric mantle wedge above subducted slab as a consequence of injection of subduction-related fluid (**Figure 10B**). but the εNd(t) values of the Xiwanggou complex are close to zero and much more depleted than the contemporary barren mafic rocks in the Bairiqili, which may be related to a relatively low assimilation–fractional crystallization (AFC) degree of lower crustal materials. This is consistent with the indication between varying Mg# and SiO_2 values (**Figure 8**). Nevertheless, the εNd(t) values of the contemporary barren mafic rocks show a similar spectrum to those of MMEs (**Figure 10B**), which further indicate that the magma are much more possible yielded by a partial melting process of metasomatized SCLM above subducted slab (Xiong et al., 2011a; Jiang et al., 2015; Peng et al., 2016; Li et al., 2018).

Many recent papers have proposed that the metasomatized portions of the SCLM are enriched in chalcophile and highly siderophile elements, and that partial melting of this part of the mantle are particularly capable of forming magmatic ore deposits (Fiorentini and Beresford, 2008; Richardson and Shirey, 2008; Zhang et al., 2008; Arndt, 2013). The contrasting geochemical signatures between fertile and barren may be attributed not only to the heterogeneity of SCLM sources, but also to the complexity of AFC processes during the interaction between SCLM and overlying crustal materials. The εHf(t) values of zircon crystals

from the Bairiqili and Yuejinshan non-mineralized mafic–ultramafic rocks are also consistent with crustal contamination of the parental magma to various degrees (**Figure 6**; Li et al., 2015, 2018). However, the εHf(*t*) values of the Xiwanggou are all positive between MORB and CHUR (**Figure 6**), which probably indicates a simple depleted mantle source with very slight mix. Apparently, the bulk-rock Nd and zircon Hf isotopes are decoupled in the Xiwanggou complex, in which the discrepancy between the extremely depleted Hf isotopes of zircons and the slight enriched Nd isotopes of bulk rocks demonstrate that zircons do not always capture the full history of magmatic system (Huang et al., 2019). In addition, the participation of amphibole and garnet in the melt producing processes maybe result in isotopic discrepancy between zircon and bulk-rocks (Huang et al., 2017, 2019).

The Xiwanggou fertile melts mainly experienced high degree partial melting of depleted SCLM controlled by amphibole dehydration, which can evolve with time to produce relatively low εNb(*t*) values at a high εHf(*t*) value. In addition, the slight right-dipping REE distribution patterns without obvious Eu anomalies and very low La/Yb ratios of bulk compositions indicates that the Xiwanggou basaltic magma probably experienced amphibole fractionation without garnet incorporation (Çoban, 2007; Dessimoz et al., 2012). Therefore, the favored interpretation may be that the Late Permian basalts was primarily yielded by the dehydration partial melting of amphibole above a subduction zone, and some melts would have directly arisen to a surficial depth along deep faults, e.g., Xiwanggou fertile complex; but some metasomatized melts would be detained at lower crust depth and further produced relatively siliceous magma due to fractional crystallization of Grt and Cpx, e.g., Bairiqili barren diabase-gabbros (**Figure 12**). The garnet-bearing residues after melt extraction were then transformed into juvenile lower crust materials, and evolved with time to produce high εHf(*t*) at a low εNd(*t*) value with elevation of Lu/Hf ratios (Huang et al., 2019).

The experimental petrologic evidence confirmed that the thermal and petrologic evolution of a mantle plume with time shows that the residues after liquidus extraction at the base of the lithosphere will contain garnet peridotite melt, as the following possible garnet-bearing residuum assemblages (Herzberg and O'Hara, 1998). Moreover, the pressure of garnet-bearing assemblages are reported at 1.9 to 2.8 GPa (Kinzler, 1997). Therefore, at pressures in the garnet peridotite stability field, pressure expands the stability field of garnet at the expense of all other crystalline phases, and the Al_2O_3 and HFSE content of magmas is reduced. There is evidence shows that the compositions of liquids produced by progressive equilibrium (batch) partial melting of a fertile mantle peridotite will have a wide range, and the first disappearance of aluminous garnet phase is usually the one leading to subsequent liquid evolution in [Lq + Ol + Opx + Cpx] by advanced melting, from 1 atm to about 3.0 GPa. Therefore, the middle-late Permian rocks record a complete geochemical trace from subduction to modification, indicating that the Middle-Late Permian rocks are much more likely influenced by the subduction environment. Such processes are most similar to that of the arc-related Ural-Alaska type

TABLE 5 | Whole rock Sr–Nd isotopic compositions of the Xiwanggou mafic–ultramafic complex.

Sample	*t*	Rb	Sr	$^{87}Rb/^{86}Sr$	$^{87}Sr/^{86}Sr$	2σ	$(^{87}Sr/^{86}Sr)i$	Sm	Nd	$^{147}Sm/^{144}Nd$	$^{143}Nd/^{144}Nd$	2σ	$(^{143}Nd/^{144}Nd)i$	ε Nd(0)	ε Nd(t)
XW-07-1	250	24.85	373.83	0.192377	0.706589	0.000007	0.705905	1.19	4.17	0.171750	0.512635	0.000015	0.512354	−0.06	0.74
XW-07-2	250	25.58	460.78	0.160606	0.707191	0.000009	0.706620	2.48	8.80	0.170502	0.512629	0.000009	0.512350	−0.18	0.66
XW-07-3	250	19.36	431.70	0.129798	0.706415	0.000008	0.705953	1.79	6.37	0.170205	0.512655	0.000011	0.512376	0.33	1.18
XW-09-1	257	42.03	178.95	0.679569	0.708157	0.000007	0.705672	0.79	3.02	0.158684	0.512524	0.000010	0.512257	−2.22	−0.98
XW-09-2	257	34.73	115.88	0.867154	0.708705	0.000006	0.705535	1.17	4.44	0.159790	0.512520	0.000014	0.512251	−2.30	−1.09
XW-09-3	257	11.35	68.96	0.476477	0.707875	0.000007	0.706133	1.38	5.40	0.154060	0.512544	0.000009	0.512285	−1.83	−0.43

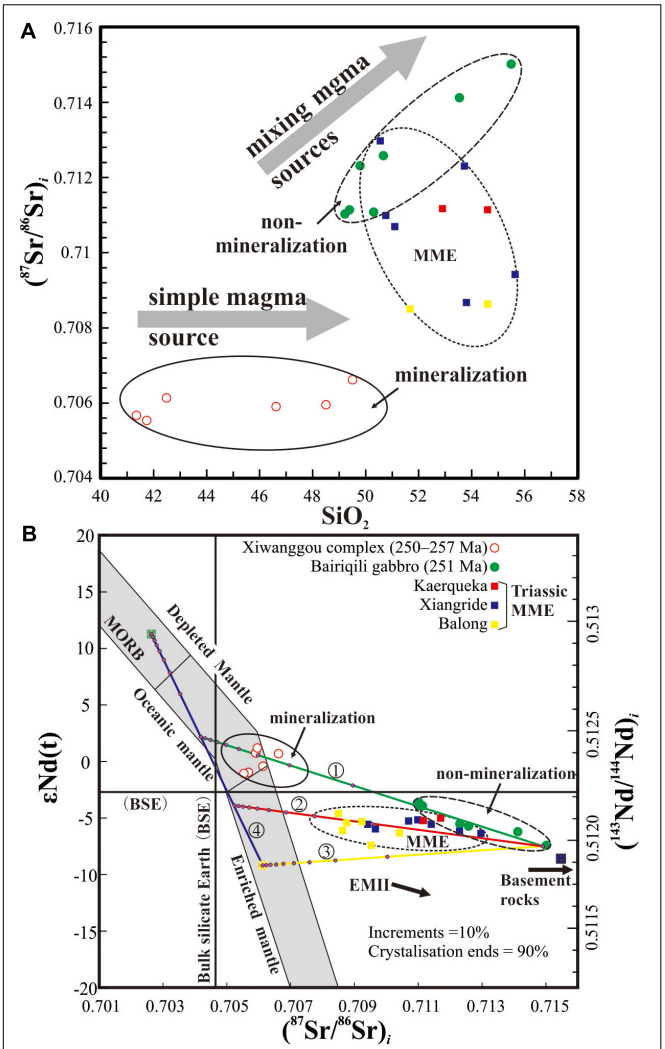

FIGURE 10 | Plots of whole rock $(^{87}Sr/^{86}Sr)_i$ vs. SiO_2 **(A)** andεNd(*t*) vs. $(^{87}Sr/^{86}Sr)_i$ **(B)** for the Xiwanggou mafic-ultramafic rocks. The depleted and oceanic mantle (plume) plots are from White and Hofmann (1982); the Sr–Nd isotope data for enriched mantle (EM) source from Menzies and Murthy (1980); the values of mafic micro enclaves (MME) hosted in the Triassic granitoid intrusions from are Kaerqueka, Xiangride, and Balong, respectively (Zhang et al., 2012; Xiong et al., 2014; Gao et al., 2015). Comparison data from Xiarihamu for Cu-Ni sulfide mineralized mafic-ultramafic complex (Sun et al., 2014; Li et al., 2015; Song et al., 2016; He et al., 2017; Zhang et al., 2018), and barren mafic-ultramafic intrusions from Bairiqili and Yuejinshan (Xiong et al., 2011b; Liu et al., 2012), in the Eastern Kunlun Orogen. The late Permian mafic-ultramafic rocks show similar evolution trends along mixing line from oceanic mantle to lower crustal materials of basement ①; The isotopic components of Triassic MME hosted in the felsic intrusions shows a mixing evolution path ② that lies between a lithospheric mantle source magma and a partial melting of lower crust source (Gao et al., 2015); Evolution path ③ starts at EM with elevating $(^{87}Sr/^{86}Sr)_i$ values, which is a trend similar to the EMII; Mixing line ④ shows an initial mantle evolution from a depleted to an enriched mantle.

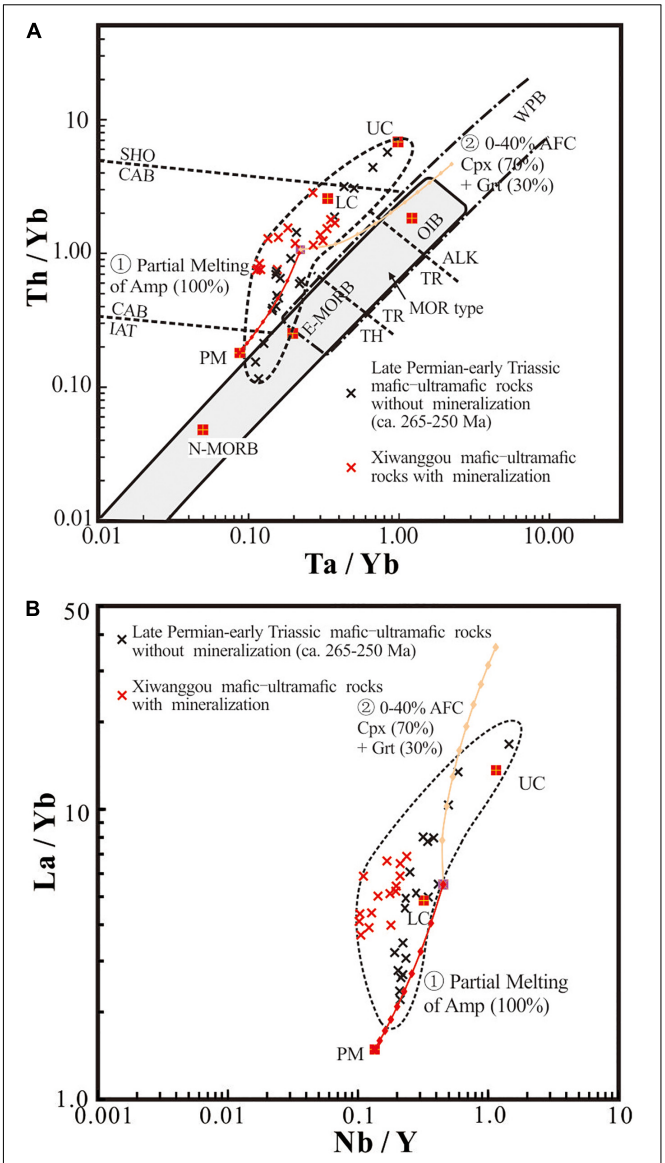

FIGURE 11 | Nb/Y vs. La/Yb **(A)** and Ta/Yb vs. Th/Yb **(B)** diagrams of the middle-late Permian mafic-ultramafic rocks from the East Kunlun Orogen. It plots in the field around primary mantle (PM), lower crust (LC) and upper crust (UC) composition points. AFC, assimilation and fractional crystallization; Amp, amphibole; Bt, biotite; Cpx, clinopyroxene; Grt, garnet. The upper (UC) and lower crustal (LC) components are based on Taylor and Mclennan (1995). The partial melting starting material was an average composition of primary mantle based on Sun and McDonough (1989). The partitioning coefficients for different mafic–ultramafic rock-forming minerals from Keskin (1994) are used in the melting and crystallization fractionation model. Tick marks explain the fraction of partial melting versus various minerals calculated using the petromodeler software (Ersoy, 2013). The data of the Xiwanggou fertile rocks are from this study and Kong et al. (2019b), and those of the barren rocks are from Jiadang (Xiong et al., 2011a; Kong et al., 2018), Bairiqili (Xiong et al., 2011b), and Langmuri (in published) areas.

complexes in Tianshan Orogen, which were produced by a high-degree of differentiation of the SCLM that was metasomatized by melts and/or fluids from the subduction (Su et al., 2012, 2014).

Olivine Fo value can be used as indicator of oxygen fugacity and temperature of hosted melt, which accounts to the activities of metallic Fe controlled by reducing conditions, and ferric

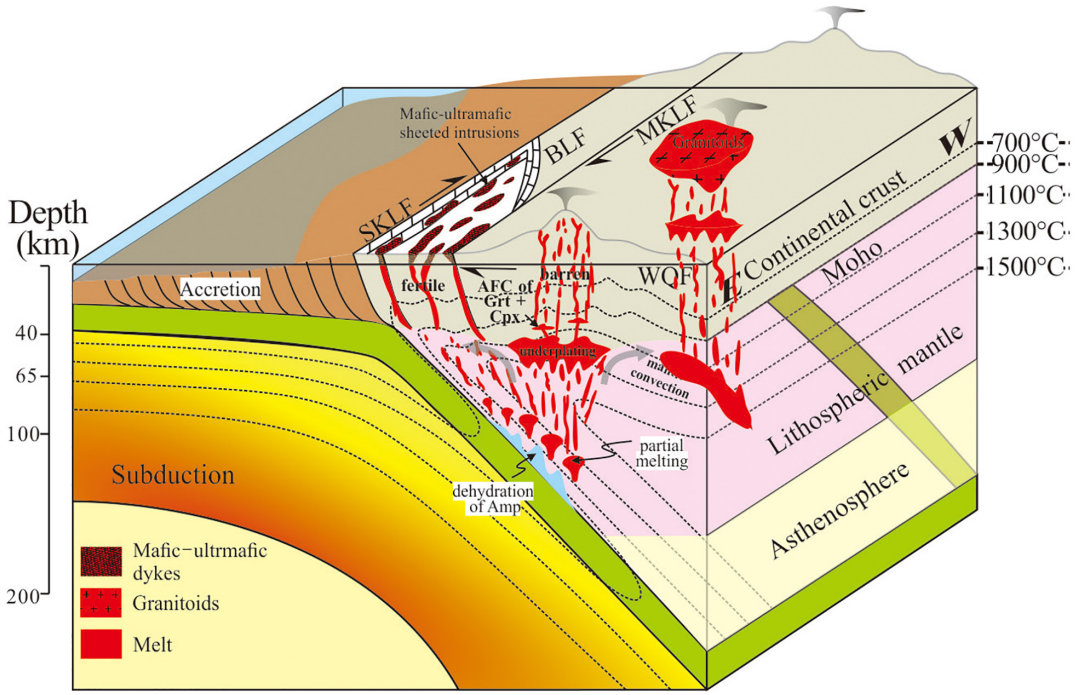

FIGURE 12 | Schematic diagram showing the tectonic evolutionary history of the Permian ultramafic–mafic complex and the corresponding mineralization of the East Kunlun Orogenic Belt. For explanation see text.

iron controlled by oxidizing conditions (Zhou et al., 2018). In addition, the exchange of Fe and Ni between olivine and sulfide melt is significantly controlled by the complex of temperature, sulfur fugacity, oxygen fugacity and nickel contents of sulfide melt (Brenan, 2003; Zhou et al., 2018), which is probably occurred in the deep continental lithosphere as mantle sulfide is likely molten in much of there (Zhou and Hirschmann, 2016). Although compositions of ascending mantle melt will be significantly affected by AFC processes, the Xiwanggou complex is justified to be slightly influenced in this study. Therefore, the olivine compositions from the Xiwanggou complex can be used to estimate the metling conditions of its mantle source. Compilation from previously published olivine-sulfide melt equilibration experiments (Fleet and Macrae, 1988; Gaetani and Grove, 1997; Brenan, 2003; Zhou et al., 2018), olivine Fo values and Ni contents show contrast relationships elevate with decreasing fO_2 at different temperatures (**Figures 13a,b**). On basis of the linear regressions, the moderate Fo values from this study suggests log fO_2 range of −10.57 ± 0.06 to −8.98 ± 0.07 between 1200 and 1300°C (**Figure 13a**), and the Ni contents give a similar logfO_2 range of −10.19 ± 0.28 to −9.02 ± 0.19 at a temperature range of 1200–1300°C (**Figure 13b**). Generally, the temperature of the hottest part of mantle wedge can reach ∼1200–1350°C in continental magmatic arcs; and the crust-mantle boundary are typically at ∼1 GPa and 1100°C (Grove et al., 2012). Moreover, the oxygen fugacity in Earth's mantle decrease with depth, within temperature range of 800–1400°C (Frost et al., 2004; Frost and Mccammon, 2008). Therefore, the parental magma of the Xiwanggou complex derived from a dehydration partial melting of upper mantle wedge (ΔFMQ = −2 – 0 log units) rather than transition zone (ΔIW = 0) or deeper mantle (ΔIW = −1.4 log units and temperature above 1350°C), which was controlled by the breakdown of amphibole between the 1200 and 1300°C isotherms at relative shallow depths of 45–60 km (Peacock et al., 1994; Grove et al., 2012). The relatively reduced source may favor Ni relative to Fe in the melt owing to the great stability of the Ni_3S_2 species with greater metal/anion ratios [(Fe + Ni)/(S + O)] (Brenan and Caciagli, 2000; Kress, 2007).

Ore-Forming Potential of Xiwanggou Mafic–Ultramafic Magma

Several critical aspects for the genesis of the large and super-large magmatic sulfide ore deposits have been identified (Lambert et al., 1998; Naldrett, 1999; Mao et al., 2008; Song et al., 2011), and upgrading concentration and segregation of sulfide liquid from Ni-rich parent magma to an economic level is an imperative precondition (Li and Naldrett, 1999; Li et al., 2007; Mao et al., 2018). Generally, the mechanism of sulfide segregation affect subsolidus Fe–Ni exchange reaction between olivine and a sulfide liquid (Li et al., 2007; Mao et al., 2018). Olivines in contact with sulfide melt would react with sulfides, exchanging Ni and Fe (Li and Naldrett, 1999), which is an important mechanism for producing high Ni sulfide for picritic and basaltic magmas (relatively Ni-rich) (Brenan and Caciagli, 2000; Mao et al., 2018). The Fo values of the olivine from the Xiwanggou complex are covered by those of medium-Ni tenor deposit, and much lower than those from high tenor deposits, such as the Jinchuan and

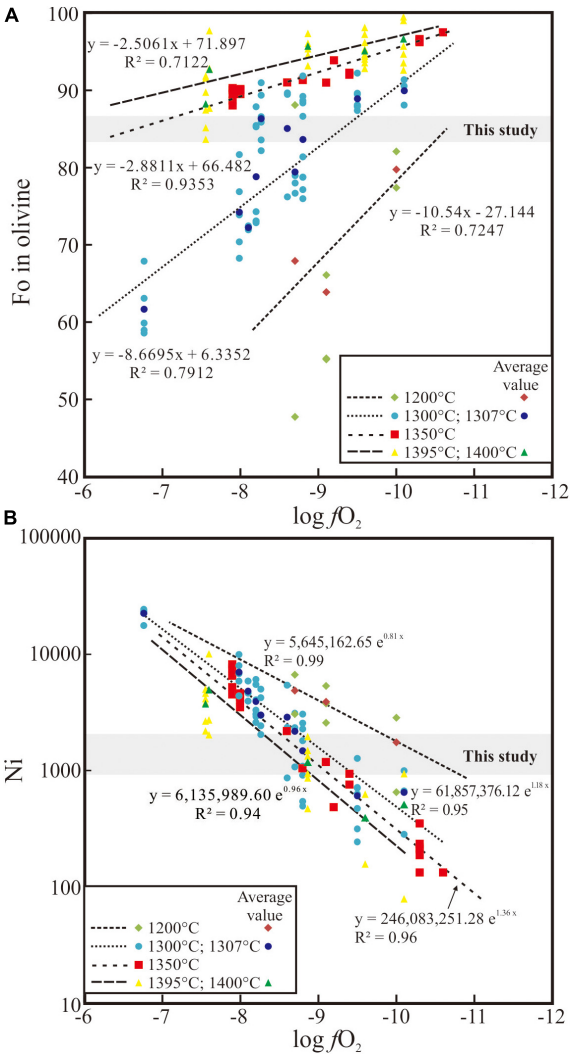

FIGURE 13 | Fo values (mol% MgO/[MgO + FeO]) **(A)** and Ni contents of olivines coexisting with sulfide melts **(B)** show relations to the variable oxygen fugacities and temperatures from various studies. Data sources of different temperatures are: 1200°C from Brenan (2003); 1300°C and 1307°C and from Fleet and Macrae (1988) and Brenan (2003); 1350°C from Gaetani and Grove (1997); 1395°C and 1400°C from Fleet and Macrae (1988) and Zhou et al. (2018).

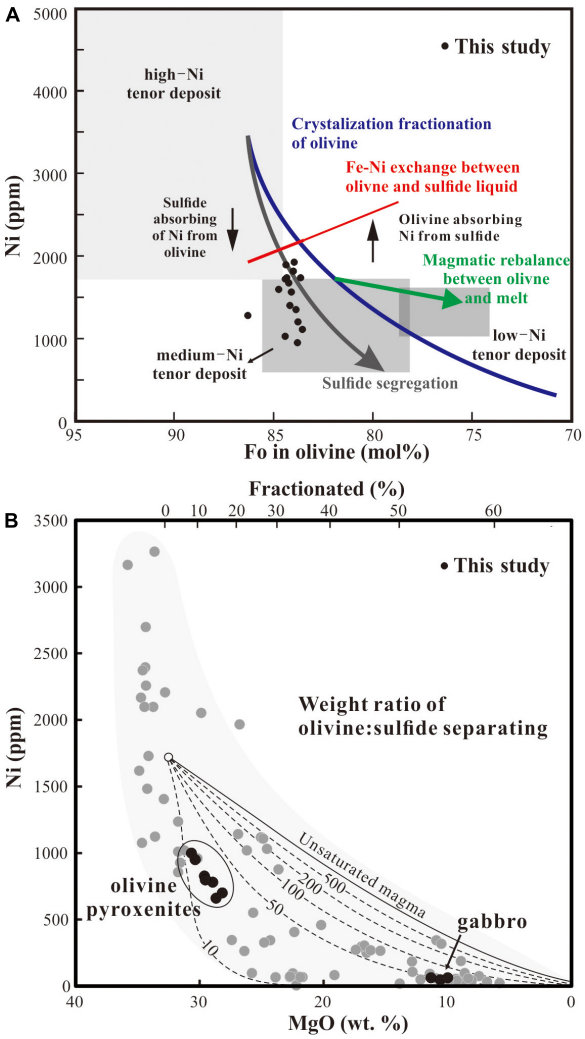

FIGURE 14 | (A) Olivine Ni vs. Fo (mol% MgO/[MgO + FeO]) diagram indicating different processes in forming high-Ni, medium-Ni and low-Ni tenor magmatic Ni–Cu deposits (on basis of Mao et al., 2018); **(B)** MgO (wt.%)-Ni (ppm) diagram of bulk compositions. The curves in the figure are computer simulations of the fractionation of a komatiite magma containing 32 wt% MgO as a consequence of the separation of olivine (unsaturated) or a mixture of different proportions of olivine + sulfide. The numbers indicate the weight ratio between olivine and sulfide segregation.

Xiariham deposits (**Figure 14A**; Zhang Z. W. et al., 2016; Zhou et al., 2016). In addition, the Xiwanggou complex shows a positive Fo-Ni correlation in olivines as a consequence of abundant Ni absorbed by olivine from sulfide and decreasing Fe contents in olivine affected by sulfide segregation (**Figure 14A**). Therefore, a strong sulfide segregation scale resulted in a medium tenor potential of the Xiwanggou deposit, whereas magmatic rebalance between olivine and melt will result in a low-Ni tenor deposit.

Ni and MgO contents in melt are significantly related to the ratios between olivine and sulfide segregation, and decrease with increasing fractionated degrees (**Figure 14B**). The Xiwanggou complex shows very low ratios of olivine and sulfide segregation that are mainly concentrated between 0.1 and 0.5 (**Figure 14B**). The Ni and MgO contents of the Xiwanggou gabbro are obviously lower than the olivine pyroxenites, which accounts to the increasing melt fraction from olivine pyroxenites to gabbro (**Figure 14B**). Clinopyroxenes in the Xiwanggou olivine pyroxenites contain extremely high Cr_2O_3 contents and very low SiO_2 contents, which further indicates that the Xiwanggou complexes underwent relatively low degree fractionation in mantle, and would need more sulfur contents to achieve sulfur saturation (Liu et al., 2007).

The thermal structure of subduction zone was modeled to discuss the ore forming potential of the Xiwanggou mafic–ultramafic magma, as compare to those of the Ural–Alaska

type mafic–ultramafic intrusions in arc environments (Su et al., 2012; **Figure 12**). The subduction of oceanic slab continues from the Middle Permian to early Late Triassic in the EKOB (Yu et al., 2020), in which old and cool oceanic crust (<45 Ma) is subducted with a high angle, representing a rapid convergence (Peacock and Wang, 1999). Yao et al. (2018) suggested that the melting in cooler subduction zones is usually triggered and enhanced by the continuous addition of slab-derived fluids or melts, resulting in a relative low-Ni content in the melt, but warm subduction may produce melts with high Ni abundance. Therefore, we supposed that the Xiwanggou host rocks may reach medium potential for Cu–Ni sulfide mineralization, although its scientific significance are valuable.

Tectonic Control of Magmatic Conduit

Most economic magmatic Ni–Cu–(PGE) deposits have been interpreted to have formed indynamic lava channels or magma conduits (Zhou et al., 2004; Begg et al., 2010), which provide rapid and efficient magma transport to the crust without significant early sulfide segregation (Barnes and Lightfoot, 2005). Therefore, it is important to know the tectonic mechanism of the conduits for middle-late Permian mafic–ultramafic magmas in the EKOB as potential exploration targets.

In addition to the Xiwanggou complex, abundant similar types of the Late Permian- Middle Triassic mafic–ultramafic intrusions have been brought close to the surface as a result of more significant uplifting in the EKOB (Xiong et al., 2011a; Kong et al., 2018). All of these intrusions are located in the junction area between the EKOB and WQOB. Tectonic and geochronological constraints indicates that the subduction of the Paleo Tethys oceanic slab started during the Late Permian along the southern most Anemaqen fault (**Figure 1**), which resulted in large amounts of magmatism formed in the continental arc belt. Although the EKOB was in a suppressed setting as the subduction environment, significant local transpressional windows caused by the right-lateral strike-slip shearing action of the Wenquan (WQF) and South Kunlun faults (SKF) and a series of the secondary faults like the Longwakalu fault and bending Boluoer fault were formed in the South Kunlun forearc belt (**Figure 12**), which provided significant conduits for the large-scale magmatism and related magmatic metallogenesis (Begg et al., 2010). In addition, crustal deep faults have clearly played an important role in providing zones of weakness up which magma has ascended into crustal material. The characteristics of the tectonic setting are similar to those of the Early Permian Huangshan-Jing'erquan Ni–Cu belt in North Xinjiang (NW China), in which the right-lateral wrench tectonics characterized by crustal-scale shear zones most likely controlled and focused the intrusion of parent magmas (Branquet et al., 2012; Wu et al., 2018). It is therefore that the secondary tensional structures formed by large-scale regional shearing stress most likely provide a channel for the ascending of mantle-derived magma and also create a space for the formation of magma chambers in the crust. Furthermore, local transtensional-rifted spaces caused by large scale strike-slip shearing along suture zones provide settings where deep, Moho-penetrating faults are available for reactivation, and accessing any dense mafic underplated material that might be residing at the base of the crust (Lightfoot and Evans-Lamswood, 2015; Barnes et al., 2016).

CONCLUSION

(1) The EKOB is characterized by two-stages of mafic–ultramafic magmatic activities associated with copper–nickel sulfide mineralization in the Late Silurian-Early Devonian and Middle-Late Permian;
(2) The late Permian Xiwanggou Ni–Cu-bearing mafic-ultramafic complexes are sheeted intrusions emplaced by injection of successive mafic-ultramafic magma batches.
(3) The parental magma of the Xiwanggou mafic–ultramafic complex derived from a source of SCLM in a cool subduction zone, which primarily experienced dehydration melting processes of amphiboles and subsequently underwent hydrated melting in the overlying mantle wedge and relatively reduced background.
(4) The Fe–Ni exchange between olivine and melt is significantly associated with the temperature and oxygen fugacity, which indicates that the magma were yielded in a temperature range of ca. 1200–1300°C and an oxygen fugacity range of ca. −10.57 to −8.98 (log unit).
(5) The transpressional windows as a consequence of Late Permian regional scale dextral strike-shearing activities, is considered as a conduit for the syn kinematic sheeted intrusion.

DATA AVAILABILITY STATEMENT

The original contributions presented in the study are included in the article/**Supplementary Material**, further inquiries can be directed to the corresponding author/s.

AUTHOR CONTRIBUTIONS

JZ and MY conceived of the presented idea. MY developed the theory and conducted the all experiments. HW and BL verified the analytical methods. CF, JL, HK, and ZZ helped the field geological survey work. All authors discussed the results and contributed to the final manuscript.

FUNDING

This study was jointly financially supported by the Natural Science Foundation of China (Grant Nos. 41802080, 41873043, 42030809, and 41702073), the Project of Innovation-driven Plan of Central South University (Grant No. 2019CX035), and the Foundation of MNR Key Laboratory of Metallogeny and Mineral Assessment (ZS1914).

ACKNOWLEDGMENTS

We thank Prof. Wang Rui, Zhang Dongyang, and Xue Shengchao for their constructive and thoughtful comments.

SUPPLEMENTARY MATERIAL

The Supplementary Material for this article can be found online at: https://www.frontiersin.org/articles/10.3389/feart.2021.666967/full#supplementary-material

REFERENCES

Arndt, N. (2013). The lithospheric mantle plays no active role in the formation of orthomagmatic ore deposits. *Econ. Geol.* 108, 1953–1970. doi: 10.2113/econgeo.108.8.1953

Arndt, N. T., Lesher, C. M., and Czamanske, G. K. (2005). Mantle-Derived Magmas and Magmatic Ni-Cu-(PGE) Deposits. *Econ. Geol.* 100, 5–24. doi: 10.5382/AV100.02

Barnes, S., and Lightfoot, P. C. (2005). Formation of magmatic nickel-sulfide ore deposits and processses affecting their copper and platinum-group element contents. *Econ. Geol.* 100, 179–213. doi: 10.5382/AV100.08

Barnes, S. J., Cruden, A. R., Arndt, N., and Saumur, B. M. (2016). The mineral system approach applied to magmatic Ni–Cu–PGE sulphide deposits. *Ore Geol. Rev.* 76, 296–316. doi: 10.1016/j.oregeorev.2015.06.012

Barnes, S. J., and Robertson, J. C. (2019). Time scales and length scales in magma flow pathways and the origin of magmatic Ni–Cu–PGE ore deposits. *Geosci. Front.* 10, 77–87. doi: 10.1016/j.gsf.2018.02.00

Begg, G. C., Hronsky, J. A., Arndt, N. T., Griffin, W. L., O'Reilly, S. Y., and Hayward, N. (2010). Lithospheric, cratonic, and geodynamic setting of Ni-Cu-PGE sulfide deposits. *Econ. Geol.* 105, 1057–1070.

Branquet, Y., Gumiaux, C., Sizaret, S., Barbanson, L., Wang, B., Cluzel, D., et al. (2012). Synkinematic mafic/ultramafic sheeted intrusions: emplacement mechanism and strain restoration of the Permian Huangshan Ni–Cu ore belt (Eastern Tianshan, NW China). *J. Asian Earth Sci.* 56, 240–257. doi: 10.2113/econgeo.105.6.1057

Brenan, J. M. (2003). Effects of fO_2, fS_2, temperature, and melt composition on Fe-Ni exchange between olivine and sulfide liquid: implications for natural olivine–sulfide assemblages. *Geochim. Cosmochim. Acta* 67, 2663–2681. doi: 10.1016/j.jseaes.2012.05.021

Brenan, J. M., and Caciagli, N. C. (2000). Fe–Ni exchange between olivine and sulphide liquid: implications for oxygen barometry in sulphide-saturated magmas. *Geochim. Cosmochim. Acta* 64, 307–320. doi: 10.1016/S0016-7037(02)01416-3

Cai, X. F., and Wei, Q. R. (2007). Stratigraphic sequence of oceanic islands and palinspastic reconstruction of the Wanbaogou Group in the eastern Kunlun orogenic belt. *J. Stratigr.* 31, 117–126. doi: 10.1016/S0016-7037(99)00278-1

Chen, G. C., Pei, X. Z., Li, R. B., Li, Z. C., Liu, C. N., Chen, Y. X., et al. (2017). Magma mixing and mingling for Xiangjiananshan granitic batholith at eastern area of the East Kunlun orogenic belt. *Acta Geol. Sin.* 91:63.

Chen, J. J., Fu, L. B., and Wei, J. H. (2016). Geochemical characteristics of late ordovician granodiorite in Gouli area, Eastern Kunlun orogenic belt, Qinghai province: implications on the evolution of Proto-Tethys ocean. *Earth Sci.* 41, 1863–1882. doi: 10.1111/1755-6724.13187

Chen, X. H., Gehrels, G., Yin, A., Zhou, Q., and Huang, P. H. (2015). Geochemical and Nd–Sr–Pb–O isotopic constrains on Permo–Triassic magmatism in eastern Qaidam Basin, northern Qinghai-Tibetan plateau: implications for the evolution of the Paleo-Tethys. *J. Asian Earth Sci.* 114, 674–692.

Çoban, H. (2007). Basalt magma genesis and fractionation in collision-and extension-related provinces: A comparison between eastern, central and western Anatolia. *Earth Sci. Rev.* 80, 219–238. doi: 10.1016/j.jseaes.2014.11.013

Dessimoz, M., Müntener, O., and Ulmer, P. (2012). A case for hornblende dominated fractionation of arc magmas: the Chelan complex (Washington Cascades). *Contrib. Min. Petrol.* 163, 567–589. doi: 10.1016/j.earscirev.2006.08.006

Ding, Q. F., Jiang, S. Y., and Sun, F. Y. (2014). Zircon U–Pb geochronology, geochemical and Sr–Nd–Hf isotopic compositions of the Triassic granite and diorite dikes from the Wulonggou mining area in the Eastern Kunlun Orogen, NW China: petrogenesis and tectonic implications. *Lithos* 205, 266–283. doi: 10.1007/s00410-011-0685-5

Dong, L. Q., Dong, G. C., Huang, H., and Bai, Y. (2016). Geochemical and zircon U-Pb dating characteristics and significance of the Tuluyin granites in the east of East Kunlun orogenic belt. *Geol. China* 43, 1737–1749. doi: 10.1016/j.lithos.2014.07.015

Dong, Y. P., He, D. F., Sun, S. S., Liu, X. M., Zhou, X. H., Zhang, F. F., et al. (2018). Subduction and accretionary tectonics of the East Kunlun orogen, western segment of the Central China Orogenic System. *Earth Sci. Rev.* 186, 231–261.

Ersoy, E. Y. (2013). PETROMODELER (Petrological Modeler): a Microsoft® Excel© spreadsheet program for modelling melting, mixing, crystallization and assimilation processes in magmatic systems. *Turk. J. Earth Sci.* 22, 115–125. doi: 10.1016/j.earscirev.2017.12.006

Fiorentini, M. L., and Beresford, S. W. (2008). Role of volatiles and metasomatized subcontinental lithospheric mantle in the genesis of magmatic Ni–Cu–PGE mineralization: insights from in situ H, Li, B analyses of hydromagmatic phases from the Valmaggia ultramafic pipe, Ivrea-Verbano Zone (NW Italy). *Terra Nova* 20, 333–340.

Fleet, M. E., and Macrae, N. D. (1988). Partition of Ni between olivine and sulfide: equilibria with sulfide-oxide liquids. *Contrib. Min. Petrol.* 100, 462–469. doi: 10.1111/j.1365-3121.2008.00825.x

Frost, D. J., Liebske, C., Langenhorst, F., Mccammon, C. A., Trønnes, R. G., and Rubie, D. C. (2004). Experimental evidence for the existence of iron-rich metal in the Earth's lower mantle. *Nature* 428:409. doi: 10.1007/BF00371375

Frost, D. J., and Mccammon, C. A. (2008). The redox state of Earth's mantle. *Annu. Rev. Earth Planet. Sci.* 36, 389–420. doi: 10.1038/nature02413

Gaetani, G. A., and Grove, T. L. (1997). Partitioning of moderately siderophile elements among olivine, silicate melt, and sulfide melt: constraints on core formation in the Earth and Mars. *Geochim. Cosmochim. Acta* 61, 1829–1846. doi: 10.1146/annurev.earth.36.031207.124322

Gan, C. H. (2014). *Petrology, Geochemistry, U-Pb Dating and Hf Isotopic Composition of Zircons in Igneous Rocks from East Kunlun Orogen, Qinghai*. Beijing: China University of Geosciences. doi: 10.1016/S0016-7037(97)00033-1

Gao, Y. B., Li, K., Qian, B., Li, W. Y., Li, D. S., Su, S. S., et al. (2015). The genesis of granodiorites and dark enclaves from the Kaerqueka deposit in east Kunlun belt: evidence from zircon U-Pb dating, geochemistry and Sr-Nd-Hf isotopic compositions. *Geol. China* 42, 646–662.

Grove, T. L., Till, C. B., and Krawczynski, M. J. (2012). The role of H2O in subduction zone magmatism. *Annu. Rev. Earth Planet. Sci.* 40, 413–439.

He, D. F., Dong, Y. P., Liu, X. M., Yang, Z., Sun, S. S., Cheng, B., et al. (2016). Tectono-thermal events in East Kunlun, Northern Tibetan Plateau: evidence from zircon U–Pb geochronology. *Gondwana Res.* 30, 179–190. doi: 10.1146/annurev-earth-042711-105310

He, S., Sun, F., Li, Y., Li, D., Yu, M., Qian, Y., et al. (2017). Geochemical and geochronological significance of the Binggounan garbbro in the Qiman Tage region, Qinghai province. *Bull. Mineral. Petrol. Geochem.* 36, 582–592. doi: 10.1016/j.jseaes.2016.07.019

Herzberg, C., and O'Hara, M. J. (1998). Phase equilibrium constraints on the origin of basalts, picrites, and komatiites. *Earth Sci. Rev.* 44, 39–79.

Hou, K. J., Li, Y. H., Zou, T. R., Qu, X. M., Shi, Y. R., and Xie, G. Q. (2007). Laser ablation-MC-ICP-MS technique for Hf isotope microanalysis of zircon and its geological applications. *Acta Petrol. Sin.* 23, 2595–2604.

Huang, H., Niu, Y., and Mo, X. (2017). Garnet effect on Nd-Hf isotope decoupling: Evidence from the Jinfosi batholith, Northern Tibetan Plateau. *Lithos* 274–275, 31–38. doi: 10.1016/S0012-8252(98)00021-X

Huang, H., Niu, Y., Teng, F. Z., and Wang, S. J. (2019). Discrepancy between bulk-rock and zircon Hf isotopes accompanying Nd-Hf isotope decoupling. *Geochim. Cosmochim. Acta* 259, 17–36. doi: 10.1016/j.lithos.2016.12.025

Jiang, C. F. (1992). Opening-closing evolution of the Kunlun Mountains. Opening closing tectonics of Kunlun Shan. *Geol. Memoirs Ser.* 5, 205–217. doi: 10.1016/j.gca.2019.05.031

Jiang, C. Y., Ling, J. L., Zhou, W., Du, W., Wang, Z. X., Fan, Y. Z., et al. (2015). Petrogenesis of the Xiarihamu Nibearing layered mafic-ultramafic intrusion, East Kunlun: implications for its extensional island arc environment. *Acta Petrol. Sin.* 31, 1117–1136.

Jiang, R. B., Chen, X. H., Dang, Y. Q., Yin, A., Wang, L. Q., Jiang, W. M., et al. (2008). Apatite fission track evidence for two phases Mesozoic-Cenozoic thrust faulting in eastern Qaidam Basin. *Chin. J. Geophys.* 51, 116–124.

Keskin, M. (1994). *Genesis of Collision-Related Volcanism on the Erzurum-kars Plateau, North Eastern Turkey*. Durham: Durham University.

Kinzler, R. J. (1997). Melting of mantle peridotite at pressures approaching the spinel to garnet transition: application to mid-ocean ridge basalt petrogenesis. *J. Geophys. Res. Solid Earth* 102, 853–874.

Kong, H. L., Li, J. C., Guo, X. Z., Yao, X. G., and Jia, Q. Z. (2019a). The discovery of Early Devonian pyroxene peridotite from the Xiwanggou magmatic Ni-Cu sulfide ore spot in East Kunlun Mountains. *Geol. China* 46, 205–206. doi: 10.1029/96JB00988

Kong, H. L., Li, Y. Z., Li, J. C., Jia, Q. Z., Guo, X. Z., and Zhang, B. (2019b). LA-ICP-MS zircon U-Pb dating and geochemical characteristics of the xiwanggou olivine pyroxenolite in East Kunlun. *J. Geomechan.* 25, 440–452.

Kong, H. L., Li, J. C., Li, Y. Z., Jia, Q. Z., Guo, X. Z., and Zhang, B. (2018). Zircon U-Pb Dating and Geochemistry of the Jiadang Olivine Gabbro in the Eastern Section of East Kunlun,Qinghai Province and Their Geological Significance. *Acta Geol. Sin.* 92, 964–978.

Kong, H. L., Li, J. C., Li, Y. Z., Jia, Q. Z., and Yang, B. R. (2014). Geochemistry and zircon U-Pb geochronology of Annage diorite in the eastern section from East Kunlun in Qinghai province. *Geol. Sci. Technol. Inform.* 33, 11–17.

Kress, V. (2007). Thermochemistry of sulfide liquids III: Ni-bearing liquids at 1 bar. *Contrib. Min. Petrol.* 154, 191–204.

Lambert, D. D., Foster, J. G., Frick, L. R., Ripley, E. M., and Zientek, M. L. (1998). Geodynamics of magmatic Cu-Ni-PGE sulfide deposits; new insights from the Re-Os isotope system. *Econ. Geol.* 93, 121–136. doi: 10.1007/s00410-007-0187-7

Li, C. S., and Naldrett, A. J. (1999). Geology and petrology of the Voisey's Bay intrusion: reaction of olivine with sulfide and silicate liquids. *Lithos* 47, 1–31. doi: 10.2113/gsecongeo.93.2.121

Li, C. S., Naldrett, A. J., and Ripley, E. M. (2007). Controls on the Fo and Ni contents of olivine in sulfide-bearing Mafic/Ultramafic intrusions: principles, modeling, and examples from Voisey's Bay. *Earth Sci. Front.* 14, 177–183. doi: 10.1016/S0024-4937(99)00005-5

Li, C. S., Zhang, M. J., Fu, P., Qian, Z. Z., Hu, P. Q., and Ripley, E. M. (2012). The Kalatongke magmatic Ni–Cu deposits in the central Asian Orogenic Belt, NW China: product of slab window magmatism? *Min. Deposit.* 47, 51–67. doi: 10.1016/S1872-5791(07)60043-8

Li, C. S., Zhang, Z. W., Li, W. Y., Wang, Y. L., Sun, T., and Ripley, E. M. (2015). Geochronology, petrology and Hf–S isotope geochemistry of the newly-discovered Xiarihamu magmatic Ni–Cu sulfide deposit in the Qinghai–Tibet plateau, western China. *Lithos* 216, 224–240. doi: 10.1007/s00126-011-0354-7

Li, L., Sun, F. Y., Li, B. L., Li, S. J., Chen, G. J., Wang, W., et al. (2018). Geochronology, geochemistry and Sr-Nd-Pb-Hf isotopes of No. I complex from the Shitoukengde Ni-Cu sulfide deposit in the Eastern Kunlun Orogen, Western China: implications for the magmatic source, geodynamic setting and genesis. *Acta Geol. Sin.* 92, 106–126. doi: 10.1016/j.lithos.2015.01.003

Li, R. B., Pei, X. Z., Li, Z. C., Liu, Z. Q., Chen, G. C., Chen, Y. X., et al. (2012). Geological characteristics of Late Palaeozoic–Mesozoic unconformities and their response to some significant tectonic events in eastern part of Eastern Kunlun. *Earth Sci. Front.* 19, 244–254. doi: 10.1111/1755-6724.13497

Li, R. B., Pei, X. Z., Li, Z. C., Pei, L., Chen, G. C., Chen, Y. X., et al. (2017). Late cambrian SSZ-type ophiolites in acite zone, East Kunlun Orogen of Northern Tibet plateau: insights from Zircon U-Pb Isotopes and geochemistry of Oceanic Crust rocks. *Acta Geol. Sin.* 91, 66–67. doi: 10.1016/j.gsf.2011.05.005

Lightfoot, P. C., and Evans-Lamswood, D. (2015). Structural controls on the primary distribution of mafic–ultramafic intrusions containing Ni–Cu–Co–(PGE) sulfide mineralization in the roots of large igneous provinces. *Ore Geol. Rev.* 64, 354–386. doi: 10.1111/1755-6724.13189

Liu, B. (2014). *Petrogenesis and Geodynamic Setting of Permian to Triassic Mafic Rocks in the Yushu Area, Central Qinghai-Tibetan Plateau*. Wuhan: China University of Geoscience. doi: 10.1016/j.oregeorev.2014.07.010

Liu, B., Ma, C. Q., Zhang, J. Y., Xiong, F. H., Huang, J., and Jiang, H. A. (2012). Petrogenesis of Early Devonian intrusive rocks in the east part of Eastern Kunlun Orogen and implication for Early Palaeozoic orogenic processes. *Acta Petrol. Sin.* 28, 1785–1807.

Liu, J., Sun, F. Y., Li, L., Zhao, F. F., Wang, Y. D., Wang, S., et al. (2015). Geochronology, geochemistry and Hf isotopes of Gerizhuotuo complex intrusion in west of Anyemaqen suture zone. *Earth Sci. J. China Univ. Geosci.* 40, 965–981.

Liu, Y., Samaha, N., and Baker, D. R. (2007). Sulfur concentration at sulfide saturation (SCSS) in magmatic silicate melts. *Geochim. Cosmochim. Acta* 71, 1783–1799.

Liu, Y. J., Genser, J., Neubauer, F., Jin, W., Ge, X. H., Handler, R., et al. (2005). 40 Ar/39 Ar mineral ages from basement rocks in the Eastern Kunlun Mountains, NW China, and their tectonic implications. *Tectonophysics* 398, 199–224. doi: 10.1016/j.gca.2007.01.004

Long, X. P., Jin, W., Ge, W. C., and Yu, N. (2006). Zircon U-Pb geochronology and geological implications of the granitoids in Jinshuikou, East Kunlun, NW China. *Geochimica* 35, 333–345. doi: 10.1016/j.tecto.2005.02.007

Luo, Z. H., Deng, J. F., Cao, Y. Q., Guo, Z. F., and Mo, X. X. (1999). On late Paleozoic-early Mesozoic volcanism and regional tectonic evolution of Eastern Kunlun, Qinghai Province. *Geoscience* 13, 51–56.

Ma, C. Q., Xiong, F. H., Yin, S., Wang, L. X., and Gao, K. (2015). Intensity and cyclicity of orogenic magmatism: an example from a Paleo-Tethyan granitoid batholith, Eastern Kunlun, northern Qinghai-Tibetan Plateau. *Acta Petrol. Sin.* 31, 3555–3568.

Maier, W. D., Barnes, S., Chinyepi, G., Barton, J. M., Eglington, B., and Setshedi, I. (2008). The composition of magmatic Ni–Cu–(PGE) sulfide deposits in the Tati and Selebi-Phikwe belts of eastern Botswana. *Miner. Deposita* 43, 37–60.

Maier, W. D., and Groves, D. I. (2011). Temporal and spatial controls on the formation of magmatic PGE and Ni–Cu deposits. *Miner. Deposi.* 46, 841–857. doi: 10.1007/s00126-007-0143-5

Mao, J. W., Pirajno, F., Zhang, Z. H., Chai, F. M., Wu, H., Chen, S. P., et al. (2008). A review of the Cu–Ni sulphide deposits in the Chinese Tianshan and Altay orogens (Xinjiang Autonomous Region, NW China): principal characteristics and ore-forming processes. *J. Asian Earth Sci.* 32, 184–203. doi: 10.1007/s00126-011-0339-6

Mao, Y. J., Qin, K. Z., and Tang, D. M. (2018). Characteristics,genetic mechanism,and exploration perspective of Ni-rich sulfide in magmatic Ni-Cu systems. *Acta Petrol. Sin.* 34, 2410–2424. doi: 10.1016/j.jseaes.2007.10.006

Menzies, M., and Murthy, V. R. (1980). Enriched mantle: Nd and Sr isotopes in diopsides from kimberlite nodules. *Nature* 283:634.

Mo, X. X., Luo, Z. H., Deng, J., Yu, X., Liu, C., Yuan, W. M., et al. (2007). Granitoids and crustal growth in the East Kunlun orogenic belt. *Geol. J. China Univ.* 13, 403–414. doi: 10.1016/j.lithos.2006.10.005

Naldrett, A. J. (1999). World-class Ni-Cu-PGE deposits: key factors in their genesis. *Miner. Deposita* 34, 227–240.

Naldrett, A. J. (2013). *Magmatic Sulfide Deposits: Geology, Geochemistry and Exploration*. Berlin: Springer. doi: 10.1007/s001260050200

Peacock, S. M., Rushmer, T., and Thompson, A. B. (1994). Partial melting of subducting oceanic crust. *Earth Planet Sci. Lett.* 121, 227–244.

Peacock, S. M., and Wang, K. (1999). Seismic consequences of warm versus cool subduction metamorphism: Examples from southwest and northeast Japan. *Science* 286, 937–939. doi: 10.1016/0012-821X(94)90042-6

Peng, B., Sun, F., Li, B., Wang, G., Li, S., Zhao, T., et al. (2016). The geochemistry and geochronology of the Xiarihamu II mafic–ultramafic complex, Eastern Kunlun, Qinghai Province, China: implications for the genesis of magmatic Ni–Cu sulfide deposits. *Ore Geol. Rev.* 73, 13–28. doi: 10.1126/science.286.5441.937

Piña, R., Lunar, R., Ortega, L., Gervilla, F., Alapieti, T., and Martínez, C. (2006). Petrology and geochemistry of mafic-ultramafic fragments from the Aguablanca Ni-Cu ore breccia, southwest Spain. *Econ. Geol.* 101, 865–881. doi: 10.1016/j.oregeorev.2015.10.014

Qi, S. S. (2015). *Petrotectonic Assemblages and Tectonic Evolution of the East Kunlun Orogenic Belt in Qinghai Province*. Beijing: China University of Geosciences. doi: 10.2113/gsecongeo.101.4.865

Ren, E. F., Zhang, G. L., Qiu, W., Li, H. X., and Sun, Z. H. (2012). Characteristics of geochemistry and tectonic significance of Caledonian granite in the Maerzheng region in the south area of East Kunlun. *Geoscience* 26, 36–44.

Ren, H. D., Wang, T., Zhang, L., Wang, X. X., Huang, H., Feng, C. Y., et al. (2016). Ages, sources and tectonic settings of the Triassic igneous rocks in the easternmost segment of the East Kunlun orogen, central China. *Acta Geol. Sin.* 90, 641–668.

Richardson, S. H., and Shirey, S. B. (2008). Continental mantle signature of Bushveld magmas and coeval diamonds. *Nature* 453, 910–913. doi: 10.1111/1755-6724.12696

Rubatto, D., and Gebauer, D. (2000). "Use of cathodoluminescence for U-Pb zircon dating by ion microprobe: some examples from the Western Alps," in *Cathodoluminescence in Geosciences*, eds M. Pagel, V. Barbin, P. Blanc, and D. Ohnenstetter (Heidelberg: Springer), 373–400. doi: 10.1038/nature07073

Sappin, A., Constantin, M., and Clark, T. (2011). Origin of magmatic sulfides in a Proterozoic island arc—an example from the Portneuf–Mauricie Domain, Grenville Province, Canada. *Miner. Deposita* 46, 211–237. doi: 10.1007/978-3-662-04086-7_15

Shao, F. L., Niu, Y. L., Liu, Y., Chen, S., Kong, J. J., and Duan, M. (2017). Petrogenesis of Triassic granitoids in the East Kunlun Orogenic Belt, northern Tibetan Plateau and their tectonic implications. *Lithos* 282, 33–44. doi: 10.1007/s00126-010-0321-8

Shi, B., Zhu, Y. H., Zhong, Z. Q., and Jian, K. K. (2016). Petrological, geochemical characteristics and geological significance of the Caledonian peraluminous granites in Heihai region, Eastern Kunlun. *Earth Sci.* 41, 35–54. doi: 10.1016/j.lithos.2017.03.002

Sláma, J., Košler, J., Condon, D. J., Crowley, J. L., Gerdes, A., Hanchar, J. M., et al. (2008). Plešovice zircon — a new natural reference material for U–Pb and Hf isotopic microanalysis. *Chem. Geol.* 249, 1–35.

Song, X., and Li, X. (2009). Geochemistry of the Kalatongke Ni–Cu–(PGE) sulfide deposit, NW China: implications for the formation of magmatic sulfide mineralization in a postcollisional environment. *Miner. Deposita* 44, 303–327. doi: 10.1016/j.chemgeo.2007.11.005

Song, X. Y., Wang, Y. S., and Chen, L. M. (2011). Magmatic Ni-Cu-(PGE) deposits in magma plumbing systems: features, formation and exploration. *Geosci. Front.* 2, 375–384. doi: 10.1007/s00126-008-0219-x

Song, X. Y., Xiao, J. F., Dan, Z., Zhu, W. G., and Chen, L. M. (2010). New insights on the formation of magmatic sulfide deposits in magma conduit system. *Earth Sci. Front.* 17, 153–163. doi: 10.1016/j.gsf.2011.05.005

Song, X. Y., Yi, J. N., Chen, L. M., She, Y. W., Liu, C. Z., Dang, X. Y., et al. (2016). The Giant Xiarihamu Ni-Co sulfide deposit in the East Kunlun Orogenic Belt, Northern Tibet Plateau, China. *Econ. Geol.* 111, 29–55. doi: 10.1007/978-3-662-08444-1

Su, B., Qin, K., Zhou, M., Sakyi, P. A., Thakurta, J., Tang, D., et al. (2014). Petrological, geochemical and geochronological constraints on the origin of the Xiadong Ural–Alaskan type complex in NW China and tectonic implication for the evolution of southern Central Asian Orogenic Belt. *Lithos* 200, 226–240. doi: 10.2113/econgeo.111.1.29

Su, B. X., Qin, K. Z., Sakyi, P. A., Malaviarachchi, S. P., Liu, P. P., Tang, D. M., et al. (2012). Occurrence of an Alaskan-type complex in the Middle Tianshan Massif, Central Asian Orogenic Belt: inferences from petrological and mineralogical studies. *Int. Geol. Rev.* 54, 249–269. doi: 10.1016/j.lithos.2014.05.005

Sun, F. Y., Li, B. L., Li, S. J., Zhao, D. W., Ao, Z., and Yang, Q. A. (2014). Petrography, zircon U-Pb geochronology and geochemistry of the mafic-ultramafic intrusion in Xiarihamu Cu-Ni deposit from East Kunlun, with implications for geodynamic setting. *Earth Sci. Front.* 21, 381–401. doi: 10.1080/00206814.2010.543009

Sun, S. S., and McDonough, W. F. (1989). Chemical and isotopic systematics of oceanic basalts: implications for mantle composition and processes. *Geol. Soc. Lond. Spec. Public.* 42, 313–345. doi: 10.1111/1755-6724.12371_22

Taylor, S. R., and Mclennan, S. M. (1995). The geochemical evolution of the continental crust. *Rev. Geophys.* 33, 241–265. doi: 10.1144/GSL.SP.1989.042.01.19

Wang, C. Y., Zhang, Z. W., Zhang, C. J., Chen, C. H., and Qian, B. (2020). Constraints on sulfide saturation by crustal contamination in the Shitoukengde Cu-Ni deposit, East Kunlun orogenic belt, northern Qinghai-Tibet Plateau, China. *Geosci. J.* 1–15. doi: 10.1029/95RG00262

Wang, G., Sun, F., Bile, L. I., Shijin, L. I., Zhao, J., Cong, A. O., et al. (2014). Petrography, Zircon U-Pb geochronology and geochemistry of the mafic-ultramafic intrusion in Xiarihamu Cu-Ni deposit from East Kunlun, with implications for geodynamic setting. *Acta Geol. Sin.* 88, 318–319. doi: 10.1007/s12303-020-0025-8

Wang, G., Sun, F. Y., Li, B. L., Li, S. J., Zhao, J. W., Qian, Y., et al. (2013). Zircon U-Pb Geochronology and geochemistry of the early devonian syenogranite in the Xiarihamu Ore district from East Kunlun, with Implications for the geodynamic setting. *Geotecton. Metallogen.* 37, 685–697. doi: 10.1111/1755-6724.12371_22

Wang, T., Li, B., Chen, J., Wang, J. S., Li, W. F., and Jin, T. T. (2016). Characteristics of chronology and geochemistry of the early Silurian monzogranite in the Wulonggou area, East Kunlun and its geological significance. *J. Mineral. Petrol.* 36, 62–70.

White, W. M., and Hofmann, A. W. (1982). Sr and Nd isotope geochemistry of oceanic basalts and mantle evolution. *Nature* 296:821. doi: 10.1007/s00410-016-1272-6

Wiedenbeck, M., Alle, P., Corfu, F., Griffin, W. L., Meier, M., Oberli, F. V., et al. (1995). Three natural zircon standards for U-Th-Pb, Lu-Hf, trace element and REE analyses. *Geostand. Newslett.* 19, 1–23. doi: 10.1038/296821a0

Wu, C. Z., Xie, S. W., Gu, L. X., Samson, I. M., Yang, T., Lei, R. X., et al. (2018). Shear zone-controlled post-magmatic ore formation in the Huangshandong Ni–Cu sulfide deposit, NW China. *Ore Geol. Rev.* 100, 545–560. doi: 10.1111/j.1751-908X.1995.tb00147.x

Wu, J., Lan, C. L., and Li, J. L. (2005). Geochemical characteristics and tectonic setting of volcanic rocks in the Muztag ophiolitic mélange, East Kunlun Mountains, Xinjiang, China. *Geol. Bull. China* 24, 1157–1161. doi: 10.1016/j.oregeorev.2017.02.015

Wu, R. C., Gu, X. X., Zhang, Y. M., He, G., Kang, J. Z., Yu, F. C., et al. (2017). The sedimentary geochemical records about the tectonic evolution of the East Kunlun Orogenic Belt from early Paleozoic to early Mesozoic. *Geoscience* 31, 716–733.

Wu, S. F., Chen, L. B., Ren, W. K., Zhang, H. Q., Wang, S. H., and Ding, C. W. (2012). Discovery of rapakivite granite and its geological implication in Qimantage. *J. Qinghai Univ.* 30, 49–54.

Xiong, F. H., Ma, C. Q., Zhang, J. Y., and Liu, B. (2011a). LA-ICP-MS zircon U-Pb dating, elements and Sr-Nd-Hf isotope geochemistry of the Early Mesozoic mafic dyke swarms in East Kunlun orogenic belt. *Acta Petrol. Sin.* 27, 3350–3364.

Xiong, F. H., Ma, C. Q., Zhang, J. Y., Liu, B., Jiang, H. A., and Huang, J. (2011b). Zircon LA-ICP-MS U-Pb dating of Bairiqili gabbro pluton in East Kunlun orogenic belt and its geological significance. *Geol. Bull. China* 30, 1196–1202.

Xiong, F. H., Ma, C. Q., Zhang, J. Y., Liu, B., and Jiang, H. A. (2014). Reworking of old continental lithosphere: an important crustal evolution mechanism in orogenic belts, as evidenced by Triassic I-type granitoids in the East Kunlun orogen, Northern Tibetan Plateau. *J. Geol. Soc. Lond.* 171, 847–863.

Xu, X., Song, S. G., and Su, L. (2016). Formation age and tectonic significance of the Wanbaogou basalts in the middle East Kunlun orogenic belt. *Acta Petrol. Mineral.* 35, 965–980. doi: 10.1144/jgs2013-038

Yang, J. S., Jiang, C. F., Feng, B. G., Zhu, Z. Z., Zhao, M., Shi, X. D., et al. (1986). An outline on the tectonics of the Kunlun region. *Bull. Instit. Geol. Chin. Acad. Geol. Sci.* 2:10.

Yang, Y., Li, B. L., Xu, Q. L., and Zhang, B. S. (2013). Zircon U-Pb ages and its geological significance of the monzonitic granite in the Aikengdelesite, Eastern Kunlun. *Northwestern Geol.* 1, 56–62.

Yao, Z. S., Qin, K. Z., and Mungall, J. E. (2018). Tectonic controls on Ni and Cu contents of primary mantle-derived magmas for the formation of magmatic sulfide deposits. *Am. Miner.* 103, 1545–1567.

Ye, Z. F., Wang, J., Wang, B. Z., Suo, Y. X., Song, T. Z., and Ma, Y. S. (2004). Discovery and primarily research of the Early-Middle Devonian strata in mount Bukedaban district in west-middle section of East Kunlun Mts. *Northwestern Geol.* 37, 13–18. doi: 10.2138/am-2018-6392

Yu, M., Dick, M. J., Feng, C., Li, B., and Wang, H. (2020). The tectonic evolution of the East Kunlun Orogen, northern Tibetan Plateau: a critical review with an integrated geodynamic model. *J. Asian Earth Sci.* 191:104168.

Zhang, A. K., Liu, Y. L., Liu, G. L., Wei, Y. X., Liu, Z. G., Dai, W., et al. (2015). Mineralization types and prospecting potential of Binggounan area in Qimantage metallogenic belt, Qinghai procince. *Northwestern Geol.* 48, 125–140. doi: 10.1016/j.jseaes.2019.104168

Zhang, D. X., Wei, X. L., Zeng, X. P., Wang, W., Yu, X. L., Wang, T., et al. (2016). Geochemical characteristics and tectonic setting analysis of middle devonian intermediate-acid intrusive rock in the Gashundawu area, eastern Kunlun belt. *Miner. Explorat.* 7, 612–623.

Zhang, H. F., Zhang, L., Harris, N., Jin, L. L., and Yuan, H. L. (2006). U–Pb zircon ages, geochemical and isotopic compositions of granitoids in Songpan-Garze fold belt, eastern Tibetan Plateau: constraints on petrogenesis and tectonic evolution of the basement. *Contrib. Miner. Petrol.* 152, 75–88.

Zhang, J. Y., Ma, C. Q., Xiong, F. H., and Liu, B. (2012). Petrogenesis and tectonic significance of the Late Permian–Middle Triassic calc-alkaline granites in the Balong region, eastern Kunlun Orogen, China. *Geol. Mag.* 149, 892–908. doi: 10.1007/s00410-006-0095-2

Zhang, M., Reilly, S. Y. O., Wang, K. L., Hronsky, J., and Griffin, W. L. (2008). Flood basalts and metallogeny: The lithospheric mantle connection. *Earth Sci. Rev.* 86, 145–174. doi: 10.1017/S0016756811001142

Zhang, M. J., Liu, Y. G., Chen, A. P., Liang, K. K., Yang, Y., and Xu, W. (2021). The tectonic links between Palaeozoic eclogites and mafic magmatic Cu-Ni-Co mineralization in East Kunlun orogenic belt, western China. *Int. Geol. Rev.* 6, 1–21. doi: 10.1016/j.earscirev.2007.08.007

Zhang, Y. F., Pei, X. Z., Ding, S. P., Li, R. B., Feng, J. Y., Sun, Y., et al. (2010). LA-ICP-MS zircon U-Pb age of quartz diorite at the Kekesha area of Dulan County, eastern section of the East Kunlun orogenic belt, China and its significance. *Geol. Bull. China* 29, 79–85. doi: 10.1080/00206814.2021.1885504

Zhang, Z., Wang, Y., Qian, B., Liu, Y., Zhang, D., Lü, P., et al. (2018). Metallogeny and tectonomagmatic setting of Ni-Cu magmatic sulfide mineralization, number I Shitoukengde mafic-ultramafic complex, East Kunlun Orogenic Belt, NW China. *Ore Geol. Rev.* 96, 236–246.

Zhang, Z. W., Tang, Q. Y., Li, C. S., Wang, Y. L., and Ripley, E. M. (2016). Sr-Nd-Os-S isotope and PGE geochemistry of the Xiarihamu magmatic sulfide deposit in the Qinghai-Tibet plateau, China. *Miner. Deposita* 52, 51–68. doi: 10.1016/j.oregeorev.2018.04.027

Zhao, F. F., Sun, F. Y., and Liu, J. L. (2017). Zircon U-Pb geochronology and geochemistry of the gneissic granodiorite in Manite area from East Kunlun, with implications for geodynamic setting. *Earth Sci.* 42, 927–1044. doi: 10.1007/s00126-016-0645-0

Zhao, Z. M., Ma, H. D., Wang, B. Z., Bai, Y. S., Li, R. S., and Ji, W. H. (2008). The evidence of intrusive rocks about collision-orogeny during Early Devonian in Eastern Kunlun area. *Geol. Rev.* 54, 1–11.

Zhou, M. F., Lesher, C. M., Yang, Z., Li, J., and Sun, M. (2004). Geochemistry and petrogenesis of 270 Ma Ni–Cu–(PGE) sulfide-bearing mafic intrusions in the Huangshan district, Eastern Xinjiang, Northwest China: implications for the tectonic evolution of the Central Asian orogenic belt. *Chem. Geol.* 209, 233–257.

Zhou, W., Wang, B. Y., Xia, M. Z., Xia, Z. D., Jiang, C. Y., Dong, J., et al. (2016). Mineralogical characteristics of Shitoukengde mafic-ultramafic intrusion and analysis of its metallogenic potential, East Kunlun. *Acta Petrol. Mineral.* 35, 81–96. doi: 10.1016/j.chemgeo.2004.05.005

Zhou, Z., Handt, A. V. D., and Hirschmann, M. M. (2018). An experimental study of Fe–Ni exchange between sulfide melt and olivine at upper mantle conditions: implications for mantle sulfide compositions and phase equilibria. *Contrib. Mineral. Petrol.* 173:19.

Zhou, Z., and Hirschmann, M. M. (2016). Experimental constraints on mantle sulfide melting up to 8 GPa. *Am. Miner.* 101, 181–192. doi: 10.1007/s00410-018-1444-7

Conflict of Interest: The authors declare that the research was conducted in the absence of any commercial or financial relationships that could be construed as a potential conflict of interest.

frontiers in Earth Science

ORIGINAL RESEARCH
published: 03 September 2021
doi: 10.3389/feart.2021.729955

Late Permian High-Ti Basalt in Western Guangxi, SW China and Its Link With the Emeishan Large Igneous Province: Geochronological and Geochemical Perspectives

Chenguang Zhang[1,2], *Renyu Zeng*[2,3,4]*, *Changming Li*[5,6], *Jian Jiang*[6], *Tianguo Wang*[2,3] and *Xingjun Shi*[1]

[1]School of Geographic Sciences, Xinyang Normal University, Xinyang, China, [2]Key Laboratory of Metallogenic Prediction of Nonferrous Metals and Geological Environment Monitoring (Central South University), Ministry of Education, Changsha, China, [3]State Key Laboratory of Nuclear Resources and Environment, East China University of Technology, Nanchang, China, [4]School of Earth Sciences, East China University of Technology, Nanchang, China, [5]China-ASEAN Geosciences Cooperation Center, Nanning, China, [6]Guangxi Institute of Geological Survey, Nanning, China

OPEN ACCESS

Edited by:
Kit Lai,
Universiti Brunei Darussalam, Brunei

Reviewed by:
Weimin Li,
Jilin University, China
Zhiqiang Feng,
Taiyuan University of Technology, China

***Correspondence:**
Renyu Zeng
zengrenyu@126.com

Specialty section:
This article was submitted to Volcanology, a section of the journal Frontiers in Earth Science

Received: 24 June 2021
Accepted: 19 August 2021
Published: 03 September 2021

Citation:
Zhang C, Zeng R, Li C, Jiang J, Wang T and Shi X (2021) Late Permian High-Ti Basalt in Western Guangxi, SW China and Its Link With the Emeishan Large Igneous Province: Geochronological and Geochemical Perspectives. Front. Earth Sci. 9:729955. doi: 10.3389/feart.2021.729955

High-Ti (Ti/Y) flood basalts are widely distributed in the Late Permian Emeishan large igneous province (LIP), SW China, and their spatial distribution and genetic mechanism are important to reveal the role of plume-lithosphere interactions in the LIP origin. Western Guangxi is located on the eastern edge of Emeishan LIP. To explore the genesis of the high-Ti basalt in western Guangxi and any genetic link with the Emeishan LIP, we performed whole-rock geochemical and Sr-Nd isotope and zircon U-Pb-Hf isotope analyses on the Longlin basalts from western Guangxi. The results indicate that the Longlin basalt from Tongdeng area has relatively high SiO_2 but low MgO and TFe_2O_3 contents. The rocks have zircon $\varepsilon Hf(t)$ = –0.42 to 6.41, whole-rock $(^{87}Sr/^{86}Sr)_i$ = 0.707167–0.707345, and $\varepsilon Nd(t)$ = –2.5 to –2.14. In contrast, the Longlin basalt from Zhoudong area has relatively low SiO_2 but high MgO and TFe_2O_3 contents. The rocks have whole-rock $(^{87}Sr/^{86}Sr)_i$ = 0.706181–0.706191 and $\varepsilon Nd(t)$ = –0.57 to 0.69. Four Longlin basalt samples display LREE enrichments and HREE depletions, and with indistinct δEu and δCe anomalies. LA-ICP-MS zircon U-Pb dating on three Longlin basalt samples (from different localities) yielded consistent weighted average age of 257.9 ± 2.6 Ma (MSWD = 0.55), 259.5 ± 0.75 Ma (MSWD = 3.0), and 256.7 ± 2.0 Ma (MSWD = 0.68), indicating a Late Permian emplacement. Considering the similar age and geochemical features between the Longlin basalt and Emeishan flood basalts, we interpret that the former is spatially, and temporally associated with the Emeishan LIP. Geochemical features show that the high-Ti basalts in western Guangxi resemble Deccan-type continental flood basalts (CFBs), which were derived by decompression melting of the mantle plume. Combined with previous geochemical studies, we suggest that the difference in Ti content and Ti/Y ratio in CFBs are related to the depth and melting degree of mantle source, in which high-Ti features may have been linked to low degree of partial melting in the deep mantle.

Keywords: Emeishan large igneous province, late Permian, Sr-Nd-Hf isotopes, basalt geochemistry, western Guangxi (SW China), Plume-lithosphere interaction

INTRODUCTION

Large igneous provinces (LIPs) are formed by voluminous mafic (and minor felsic) rocks emplaced in a short period of time, and are generally considered to be mantle plume-related but not directly related to normal ocean spreading and subduction (Coffin and Eldholm, 1994; Courtillot and Renne, 2003; Acocella, 2021), although recent works suggested that interaction between mantle plumes and subducting/subducted slabs may be plausible (Xu et al., 2019; Xu et al., 2021). LIPs are of great significance for studying of global environmental catastrophes and mass extinctions, mineral resources (esp. magmatic massive Cu-Ni-PGE sulfide and Fe-V-Ti oxide deposits), supercontinent reconstruction, and regional uplift (Wang and Zhou, 2005). Hence, petrogenesis of LIPs, such as the role of plume-lithosphere interaction in the origin of the continental flood basalts (CFB), and the origin of the high-Ti (Ti/Y), and low Ti mafic magmatism, has attracted much research attention (Fodor, 1987; Peate et al., 1999; Lai et al., 2012).

The Emeishan LIP is located in the western margin of the Yangtze craton and the eastern margin of the Tibetan plateau, SW China, and likely related to Late Permian mantle plume processes (Chung and Jahn, 1995; Li et al., 2008; Zhang, 2009). Complex tectonic events in the Sanjiang fold belt had strongly deformed the original distribution of the Emeishan LIP rock units (Xu et al., 2013). Besides, whether the basaltic rocks in the Song Hien

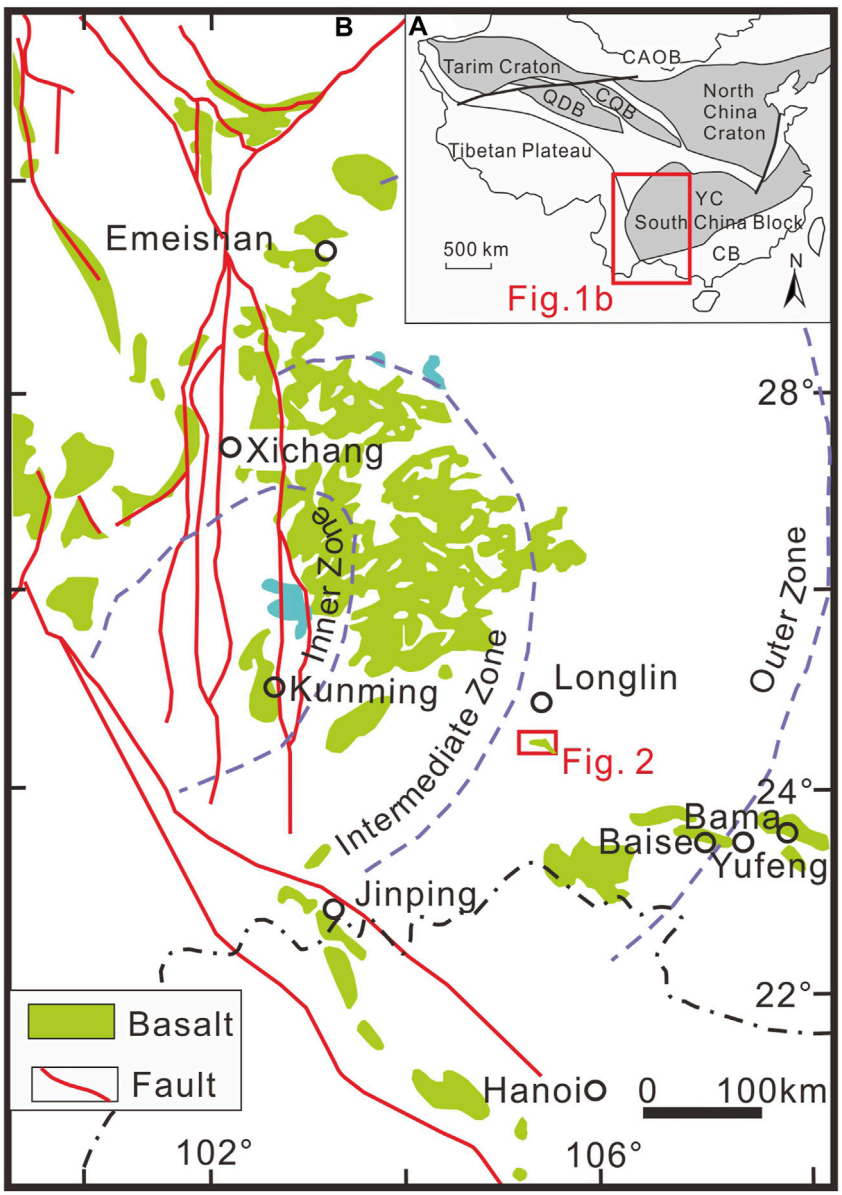

FIGURE 1 | Spatial distribution pattern of the Permian Emeishan flood basalts (outermost purple line denotes the possible extent of the outer zone, after Xu et al., 2001; He et al., 2003). YC–Yangtze Craton; CB–Cathaysia Block; CQB–Central Qilian Block; QDB–Qaidam Block; CAOB–Central Asian Orogenic Belt.

Tectonic Zone (NW Vietnam) are parts of the Emeishan LIP remains disputed (Halpin et al., 2016, and ref. therein). Therefore, it is of great significance to reveal the original spatial extent of CFB magmatism in the Emeishan LIP. Emeishan LIP consists mainly of flood basalts and associated mafic-ultramafic intrusions and (minor) felsic intrusions. The volcanics comprise mainly picrite, basalt and basaltic andesite, and can be divided into a high-Ti and low-Ti suite. This is similar to that in many other LIPs, such as the Siberian and Deccan Traps (Fodor, 1987; Peate et al., 1999; Fan et al., 2008). However, the validity of such Ti-based distinction is still disputed (Xu et al., 2001; Xu et al., 2004; Zhang et al., 2001; Shellnutt, 2014). Xu et al. (2001) considered that these high-Ti basalts were mantle plume-related, and formed by low-degree partial melting in the garnet stability field. However, Li et al. (2008) argued against substantial lithospheric mantle assimilation. Besides, some authors considered that the Emeishan basalts have a continuous TiO_2 range and should not be divided into two suites (Hou et al., 2011). For instance, Zhang (2009) considered that the high-Ti basalts may have formed by fractionation and accumulation of Fe-Ti oxides, whilst Hao et al. (2004) suggested that the high-Ti and low-Ti basalts are different fractionation products of the same parental magma.

Western Guangxi in SW China is located in the southwestern margin of the Yangtze craton (**Figure 1A**). It tectonically lies in the intersection between the Tethyan and Pacific tectonic domains. Mafic magmatism in the region is widespread and closely related to gold mineralization (Huang et al., 2015). Among the many mafic magmatic units, the Late Permian basalts are coeval with the Emeishan CFB, and generally display high-Ti (or high-Ti/Y) characteristics (Fan et al., 2008; Lai et al., 2012; Zhang and Xiao, 2014; Huang et al., 2015). However, petrogenetic setting of this magmatism is variably suggested to be 1) intra-oceanic setting related to the eastern Paleo-Tethys (Wu et al., 1993; Wu et al., 1997); 2) mantle plume related as part of the Emeishan (Liao et al., 2013; Zhang and Xiao, 2014; Huang et al., 2015). Besides, there are various views on the genesis of these rocks, including partial melting of the sub-continental lithospheric mantle (Lai et al., 2012), and mixing of plume-derived magma and continental lithosphere materials (Fan et al., 2008). In order to decipher the genesis and petrogenetic setting of these Late Permian basalts in western Guangxi, we conducted detailed field and petrographic observations on the high-Ti basalts in the Longlin area (western Guangxi), followed by zircon U-Pb-Hf isotope, as well as whole-rock elemental and Sr-Nd isotope analyses. Our findings constrain the formation timing and petrogenetic setting of the Longlin basalts, and explore the spatial distribution of Emeishan LIP and the genesis of high Ti-basaltic magmatism in western Guangxi.

GEOLOGICAL BACKGROUND AND PETROGRAPHIC FEATURES

The study area is located in the northern part of the Nanpanjiang-Youjiang rift basin in western Guangxi (**Figure 1**). Local tectonism is strong, and has undergone the Caledonian (Early Paleozoic), Variscan (Late Paleozoic), Indosinian (Triassic), Yanshanian (Jurassic-Cretaceous), and Himalayan (Cenozoic) tectonic cycles (Xu et al., 2013). The Caledonian orogeny may have closed the early Paleozoic South China ocean basin, forming the folded basement of the region. Afterward, the Indosinian orogeny terminated the pelagic sedimentation in South China, forming the complex tectonic framework of the region.

The study area is mainly covered by pelagic sedimentary rocks of Cambrian and Devonian to Triassic ages (**Figure 2**). The Cambrian rocks (total outcrop size: 60 km^2) comprise mainly carbonates, which are mainly distributed at Shechang and minor at Maxiong, Shuidong, Ganhao, and Poyan of the Xinzhou-Pingban counties (Li et al., 2019). Upper Paleozoic rocks (total outcrop size: 814 km^2) comprise mainly carbonates and minor clastics, of which the carbonate rocks are mainly distributed in the platforms and the limbs of the Shechang anticline, as well as in the northeastern part of the study area (Li et al., 2019). The clastic rocks are mainly distributed in the periphery of the platforms and in the southern limb of the Shechang anticline. Thick Triassic turbidite sequences are widely distributed in the deep-water basins between the carbonate platforms (total outcrop size: 1,005 km^2) (Li et al., 2019).

Magmatic rocks are uncommon in the study area, and consist mainly of mafic volcanic and (minor) plutonic rocks (total outcrop size: 30.75 km^2) in the central and southwestern parts of western Guangxi, e.g., at Nawei, Tongdeng, Boli, and Xiaoren. The basalts occur mainly as interlayers among the Middle Permian Sidazhai Formation and Upper Permian Linghao Formation (**Figure 3A**). Minor tuffaceous rocks were also found, and there is no discernible alteration in the wallrocks. Grain size decreases toward the intrusive margin, and vesicle and almond/pillow structure are uncommon. As shown in **Figure 4**, there are three layers of basalt in the Linghao Formation, with the thickness of 65, 15, and 10 m from bottom to top. The bottom of the first basalt layer consists of the Linghao Formation siltstone, and the top of each layer consists of volcaniclastic rocks. Eight least-altered samples (from Tongdeng, Xiaoren, and Zhoudong) were collected from the Linghao Formation basalt. The rocks are grey-greyish green and porphyritic (**Figure 3B**). Compositionally, the rocks contain mainly pyroxene (40–45%) and plagioclase (47–52%), together with minor biotite, ilmenite, pyrite, and pyrrhotite (**Figure 3C**). The basalts have phenocrysts of pyroxene and plagioclase (grain size: 0.5–1.2 mm). The pyroxene is subhedral-anhedral elongated and partly ilmenite-altered, whilst the plagioclase is elongated and partly epidote-altered. Fine-grained pyroxene, sphene, and serpentine occur as interstitial minerals (**Figure 3D**).

ANALYSIS METHODS

Major oxide concentrations were measured by wave-dispersive X-ray fluorescence (XRF) spectrometry at the

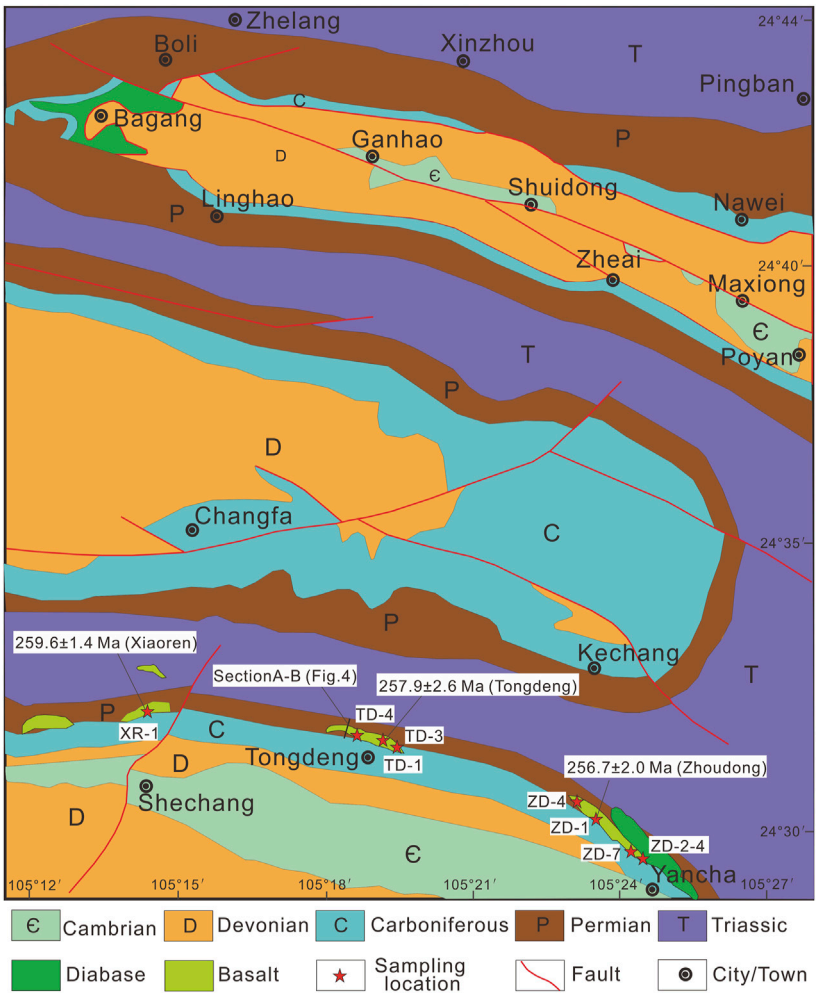

FIGURE 2 | Geologic sketch map of the Longlin area in western Guangxi.

Analytical Chemistry and Testing Services (ALS) Chemex Co. Ltd. (ALS Geochemistry method ME-XRF26). Fused glass disks with lithium borate were used and the analytical precisions were better than ± 0.01%, estimated from repeated analyses of the standards OREAS 146 and SY-4. Trace element concentrations of the samples were determined by a Perkin-Elmer ELAN 6000 inductively coupled plasma mass spectrometry (ICP-MS) after acid digestion in high-pressure Teflon bombs at the GIG-CAS (ALS Geochemistry method ME-MS81). The analytical errors were <5% for rare earth element (REE) and high field strength element (HFSE), and 5–10% for the other elements, based on repetitive analyses of standards NCSDC47009 and SARM-5. Detailed analytical procedures followed those outlined by Zhang et al. (2019).

Whole-rock Sr-Nd isotope analysis was conducted at the Isotope Geochemistry Laboratory, Wuhan Center of Geological Survey (China Geological Survey), using a Triton and MAT 261 thermal ionization mass spectrometer. The chemical analysis was monitored by the GBW04411, GBW04419 and NBS607 procedures, and the equipment conditions by the NBS987, NBS981 and JNDI procedures. Detailed analytical procedures were as described by Wang et al. (2015).

The CL images were performed using the TIMA analysis in the Chengpu Geological Testing Co. Ltd., Langfang, China. LA-ICP-MS zircon U-Pb dating was conducted at the Key Laboratory of Institute Continental Collision and Plateau Uplift, Tibetan Plateau Research (Chinese Academy of Sciences) analysis. The analysis used a UP193 F × 193 nm ArF ablation system coupled with an Agilent 7500a ICP-MS. Analytical conditions include 193 nm wavelength, < 4 ns pulse width, 35 μm spot size. 91,500 zircon was used as the external standard, and was analyzed between every six samples. The sample isotopic and elemental contents were calculated with the Glitter 4.5 software, whilst the Pb isotope calibration and U-Pb age calculation was performed with the ComPbcorr#3_18 (Andersen, 2002), and Isoplot 4.15 (Ludwig, 2003), respectively.

Zircon Lu-Hf isotope analysis was conducted at the State Key Laboratory of Geological Processes and Mineral

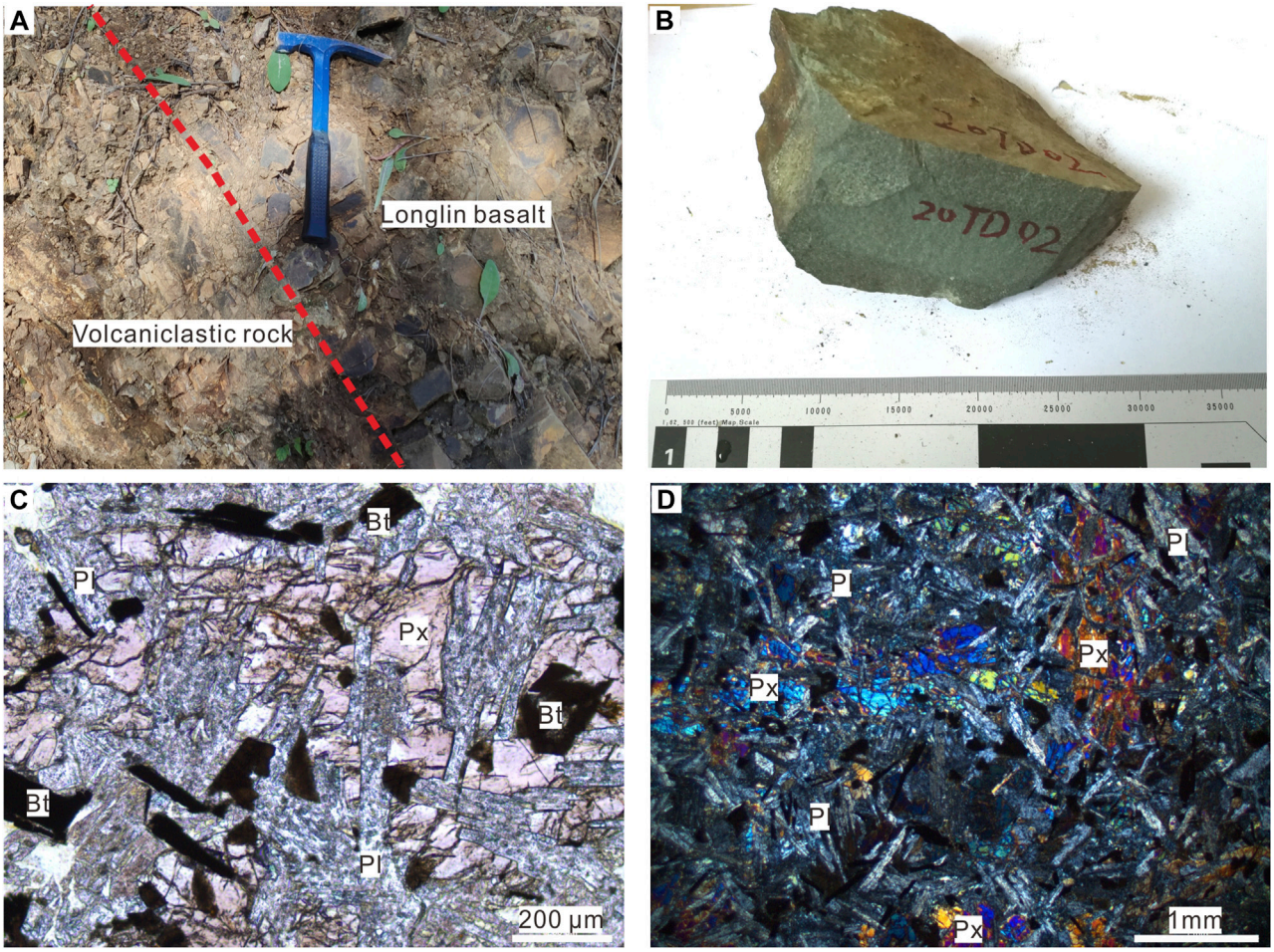

FIGURE 3 | Photos of **(A)** field outcrop, **(B)** hand-specimen, and **(C–D)** thin-section microscopy (c: PPL, d: XPL) of the Longlin basalts.

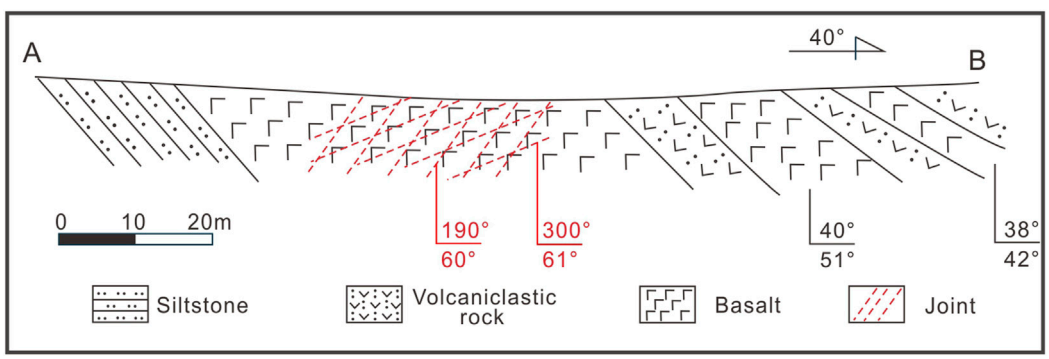

FIGURE 4 | Geological section of Longlin basalt among the Linghao Formation.

Resources [China University of Geosciences (Wuhan)], using a GeoLas 2005 excimer ArF laser ablation system coupled with a Neptune Plus GeoLas 2005 multi-collector (MC)-ICP-MS (Thermo Fisher Scientific). Analytical conditions include 32 μm beam size, 6 Hz frequency with an energy density of ~7 J/cm^2, and helium as the carrier gas. The standards (91,500 and GJ-1 zircon) were analyzed once for every eight zircon samples. Detail procedures for data calibration and processing are as described in Ye et al. (2013).

TABLE 1 | Major element (wt%) and trace element (ppm) compositions for the Longlin basalt samples.

Sample	TD-1	TD-4	ZD-4	ZD-7
wt%				
SiO_2	53.61	51.05	44.96	45.87
Al_2O_3	11.96	12.53	13.89	13.88
MgO	4.42	5.25	5.94	5.74
Na_2O	2.09	1.90	3.32	3.50
K_2O	2.07	2.58	1.27	1.22
P_2O_5	0.38	0.40	0.68	0.69
TiO_2	3.33	3.65	3.72	3.75
CaO	5.16	4.70	7.09	7.39
TFe_2O_3	12.68	13.25	15.92	15.02
MnO	0.18	0.19	0.21	0.22
LOI	3.76	4.09	2.93	2.68
ppm				
Li	12.2	13.6	13.8	12.7
Be	1.79	2.07	1.07	1.14
Sc	24.7	26.8	24.6	25.8
Ti	19,980	21,900	22,320	22,500
V	353	371	452	434
Cr	360	430	30	30
Mn	1250	1280	1410	1480
Co	33.6	37.2	49.2	44.3
Ni	85.6	96.6	43.6	41.4
Cu	98.4	104.5	95.3	86.5
Zn	118	131	120	95
Ga	23.2	24.3	22.4	22.0
As	8.1	9.7	7.9	7.5
Rb	73.7	65.1	19.9	18.2
Sr	1635	1005	484	453
Y	32.2	35.6	31.5	32.4
Zr	310	322	195	203
Nb	41.7	43.2	30.5	30.9
Sn	2.5	2.7	1.6	1.7
Ba	565	607	598	503
La	46.9	49.1	35.4	35.6
Ce	101.5	101.0	81.5	81.3
Pr	13.00	13.70	10.90	10.95
Nd	52.0	56.0	46.0	46.7
Sm	10.40	11.15	9.67	9.65
Eu	2.89	3.10	3.19	3.36
Gd	8.42	9.30	8.31	8.25
Tb	1.20	1.30	1.16	1.20
Dy	6.69	7.06	6.47	6.47
Ho	1.23	1.30	1.20	1.25
Er	3.14	3.40	3.13	3.19
Tm	0.42	0.46	0.44	0.43
Yb	2.54	2.62	2.51	2.61
Lu	0.37	0.40	0.38	0.37
Hf	7.7	7.9	4.8	4.9
Ta	2.43	2.56	1.80	1.88
Pb	7.8	6.9	0.8	0.8
Th	6.39	6.54	3.55	3.66
U	1.15	1.19	0.90	0.89
ΣREE	250.7	259.89	210.26	211.33
LREE	226.69	234.05	186.66	187.56
HREE	24.01	25.84	23.6	23.77
LREE/HREE	9.441482716	9.057662539	7.909322034	7.890618427
La_N/Yb_N	13.24	13.44	10.12	9.78
δEu	0.944166881	0.930692943	1.087929039	1.151256993
δCe	1.01	0.95	1.02	1.01

ANALYSIS RESULTS

Whole-Rock Major and Trace Element Geochemistry

In this study, we analyzed four fresh Longlin basalt samples (two samples from Tongdeng and Zhoudong each) for their whole-rock geochemical compositions (**Table 1**).

The basaltic rocks from Tongdeng and Zhoudong have SiO_2 = 51.05–53.61 wt% and 44.96–45.87 wt% and Al_2O_3 = 11.96–12.53 wt% and 13.88–13.89 wt%, respectively. Basalts from Tongdeng have clearly higher SiO_2 but lower Al_2O_3 contents. The Tongdeng samples have similar Na_2O and K_2O contents, i.e., Na_2O = 1.90–2.09 wt%, K_2O = 2.07–2.58 wt%, and Na_2O/K_2O = 0.74–1.01, whilst the Zhoudong samples have relatively high Na_2O and low K_2O, i.e., Na_2O = 3.32–3.50 wt%, K_2O = 1.22–1.27 wt%, and Na_2O/K_2O = 2.61–2.89. The Tongdeng samples have lower Fe [total iron (TFe_2O_3) = 12.68–13.25 wt%] and Mg (MgO = 4.42–5.25 wt%, Mg# = 41.08–44.21) than the Zhoudong samples (TFe_2O_3 = 15.02–15.92 wt%, MgO = 5.74–5.94 wt%, Mg# = 42.73–43.32). The Tongdeng and Zhoudong samples have TiO_2 = 3.33–3.65 wt% and 3.72–3.75 wt% and Ti/Y = 615–620 and 694–709, respectively, which fall into the high-Ti (Ti/Y) basalt (TiO_2 > 2.8%, Ti/Y > 500) range defined by Xu et al. (2001). In the Zr/TiO_2-Nb/Y and SiO_2-Nb/Y discrimination diagrams (**Figure 5**), all samples fall inside (near) the alkali basalt field.

The Tongdeng and Zhoudong samples have total REE (ΣREE) = 250.70–259.89 ppm and 210.26–211.33 ppm and La_N/Yb_N = 13.24–13.44 and 9.78–10.12, respectively. This indicates that the former has higher ΣREE and LREE/HREE fractionation than the latter. Samples from both Tongdeng and Zhoudong have indistinct Eu and Ce anomalies (**Figure 6A**; Tongdeng: δEu = 0.93–0.94, δCe = 0.95–1.01; Zhoudong: δEu = 1.09–1.15, δCe = 1.01–1.02). In the primitive mantle-normalized multi-element diagram (**Figure 6B**), the Zhoudong samples have distinct positive anomalies for some large ion lithophile elements (LILEs, e.g., Rb, K) and Sr, but negative anomalies in Nb and Y. In comparison, the Tongdeng samples have generally higher LILE contents, and have more distinct negative Sr and Zr-Hf contents than the Zhoudong samples. HREE contents of the Tongdeng and Zhoudong samples are similar.

The Longlin basalt samples have low loss on ignition (LOI = 2.68–4.09 wt%), indicating minimal alteration/weathering, which is consistent with the petrographic observation.

Zircon U-Pb-Hf Isotopes

Tongdeng Samples

Zircons (n = 28) from sample TD-1 show oscillatory zoning in cathodoluminescence (CL) images (**Figure 7A**). Most of them are 80–120 μm long and 60–90 μm wide with length: width ratio of 1.2–1.5. Results of the U-Pb isotopic dating are listed in **Table 2**. The zircons have Th/U = 0.43–0.87 (avg. 0.67). A total of 13 analysis spots clustered together along the U-Pb concordia (**Figure 7B**), yielding a weighted average age of 257.9 ± 2.6 Ma (MSWD = 0.55). 15 inherited zircons were also found, with ages of ca. 460–1811 Ma.

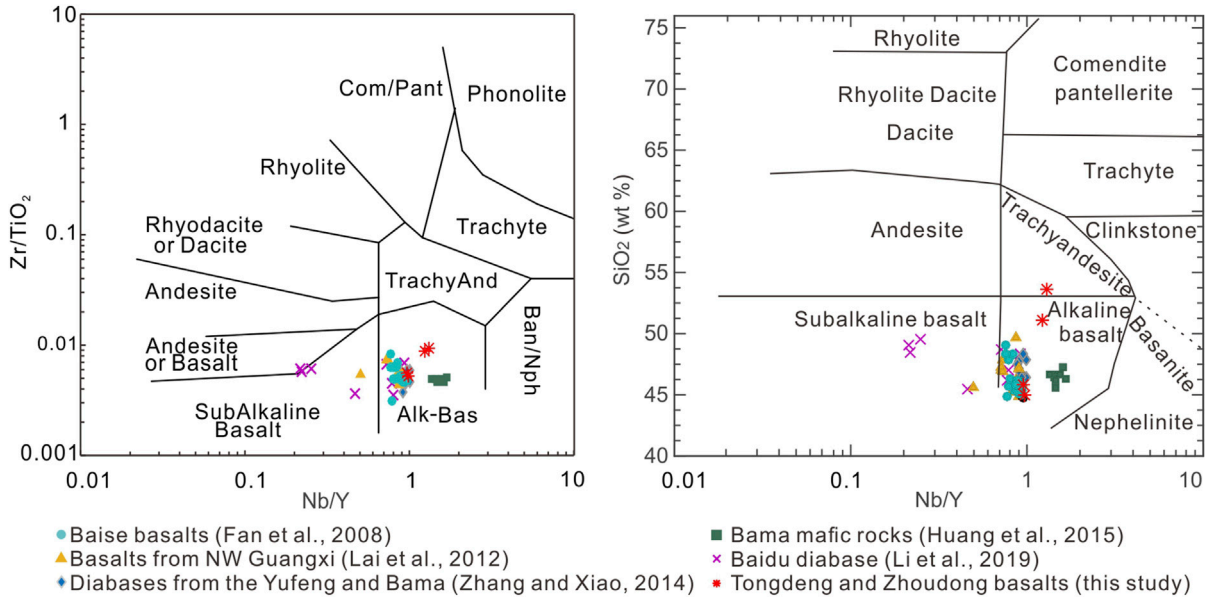

FIGURE 5 | (A) Zr/TiO_2-Nb/Y and **(B)** SiO_2-Nb/Y (Winchester and Floyd, 1977) discrimination diagrams for the mafic rocks from western Guangxi. Published data of other Late Permian mafic magmatic rocks in western Guangxi are also shown for comparison (Baise basalts, Fan et al., 2008; basalts from NW Guangxi, Lai et al., 2012; diabases from the Yufeng, and Bama, Zhang and Xiao, 2014; Bama mafic rocks, Huang et al., 2015; Baidu diabase, Li et al., 2019).

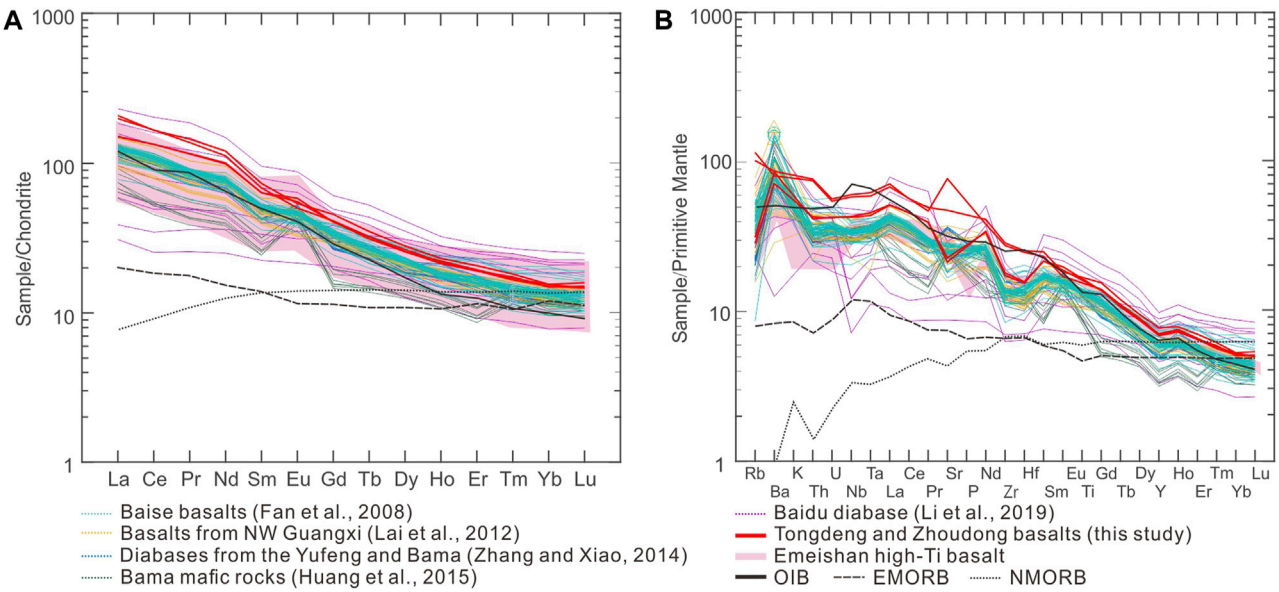

FIGURE 6 | (A) Chondrite-normalized REE and **(B)** primitive mantle normalized multi-element spidergram for the mafic rocks in western Guangxi (normalizing value after Sun and McDonough, 1989).

For the 29 Hf analysis spots (**Table 3**), 13 spots (with weighted average age of 257.9 Ma) yielded $^{176}Hf/^{177}Hf$ = 0.282245–0.282492. Calculated with their respective zircon U-Pb age, the zircons have εHf(t) = −13.22 to −4.15 (avg. −10.20) and one-stage model age (T_{DM1}) = 1,068–1,431 Ma (avg. 1,328 Ma). The remaining 15 analysis spots yielded $^{176}Hf/^{177}Hf$ = 0.281438–0.282658, and calculated εHf(t) = −14.44 to 11.48 and T_{DM} = 868–2,528 Ma.

Xiaoren Samples

Zircons (n = 30) from sample XR-1 show oscillatory zoning in CL images (**Figure 7C**). Most of them are 80–110 μm long and 50–80 μm with length: width ratio of 1.2–1.5. The zircons have high Th/U = 0.45–1.58 (avg. 0.76). All the data points fall on/near the concordia (**Figure 7D**), yielding a weighted average age of 259.6 ± 1.4 Ma (MSWD = 0.22) (**Table 2**). For Hf isotopes

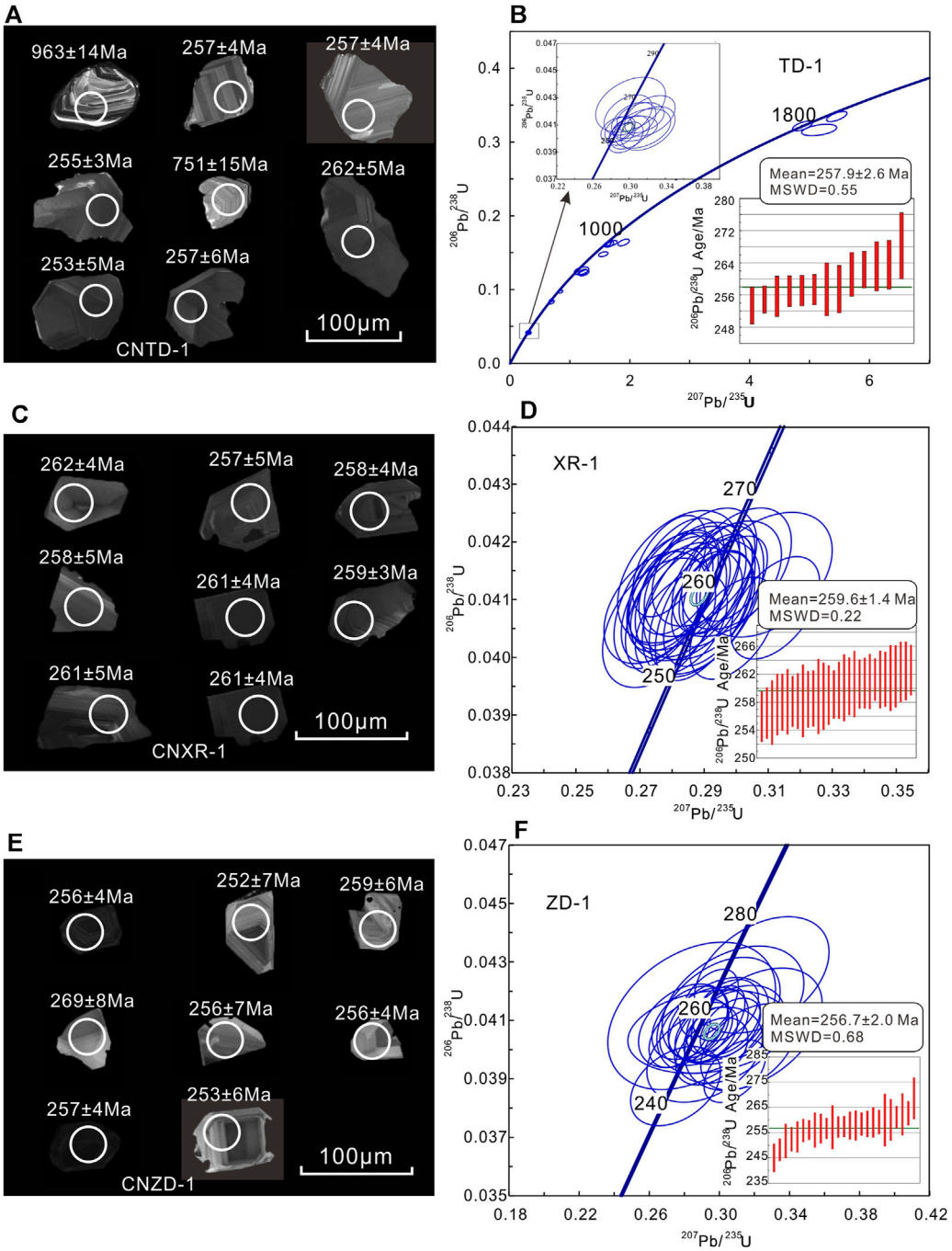

FIGURE 7 | Representative zircon CL image and concordia diagram for the Longlin basalt samples. The hollow ring is the position of analytical spot. Numbers near the analytical spots are the U-Pb ages (Ma).

(**Table 3**), 27 analysis spots yielded $^{176}Hf/^{177}Hf$ = 0.282353–0.282603, εHf(t) = −9.42 to −0.52 (avg. −4.83), and T_{DM1} = 924–1,294 Ma (avg. 1,109 Ma).

Zhoudong Samples

Zircons (*n* = 25) from sample ZD-1 show oscillatory zoning in CL images (**Figure 7E**). Most of them have length = 50–80 μm, width = 40–60 μm, and length: width ratio = 1.1–1.4, and have high Th/U = 0.32–1.87 (avg. 0.72). All the zircons cluster around the concordia and yielded a concordia age of 256.8 ± 1.1 Ma (MSWD = 9.5) (**Figure 7F**), which is similar to the weighted average age of 256.7 ± 2.0 Ma (MSWD = 0.68) (**Table 2**). For Hf isotopes (**Table 3**), 25 analysis spots yielded $^{176}Hf/^{177}Hf$ = 0.282607–0.282825, εHf(t) = −0.42 to 6.41 (avg. 3.10), and T_{DM} = 646–922 Ma (avg. 794 Ma).

TABLE 2 | Zircon La-ICP-MS U-Pb isotopic data for the Longlin basalt samples.

Analysis	Pb	Th	U	$^{207}Pb/^{206}Pb$		$^{207}Pb/^{235}U$		$^{206}Pb/^{238}U$		$^{207}Pb/^{206}Pb$		$^{207}Pb/^{235}U$		$^{206}Pb/^{238}U$	
		ppm		Ratio	1σ	Ratio	1σ	Ratio	1σ	Age (Ma)	1σ	Age (Ma)	1σ	Age (Ma)	1σ
TD-1-01	71	301	321	0.073983	0.001946	1.661195	0.045385	0.161161	0.002537	1043	54	994	17	963	14
TD-1-02	68	138	348	0.072091	0.001658	1.621626	0.039361	0.161001	0.002136	989	46	979	15	962	12
TD-1-03	75	57	193	0.108796	0.002333	4.881075	0.109199	0.321691	0.004352	1789	39	1799	19	1798	21
TD-1-04	17	242	312	0.054132	0.002959	0.306330	0.016354	0.040731	0.000607	376	119	271	13	257	4
TD-1-05	27	271	529	0.050400	0.002001	0.286202	0.011452	0.040664	0.000621	213	91	256	9	257	4
TD-1-06	18	157	362	0.051920	0.002165	0.289863	0.011063	0.040688	0.000616	283	96	258	9	257	4
TD-1-07	33	437	636	0.052019	0.001715	0.292051	0.009584	0.040330	0.000545	287	76	260	8	255	3
TD-1-08	151	153	366	0.116836	0.002303	5.456432	0.113420	0.334623	0.004545	1909	35	1894	18	1861	22
TD-1-09	62	160	310	0.072229	0.001739	1.630263	0.040341	0.161829	0.002242	992	49	982	16	967	12
TD-1-10	15	169	290	0.053942	0.002918	0.305018	0.016190	0.041339	0.000878	369	122	270	13	261	5
TD-1-11	23	142	129	0.071619	0.003122	1.214566	0.052878	0.123474	0.002527	976	89	807	24	751	15
TD-1-12	94	261	814	0.062729	0.001822	0.846737	0.023031	0.097000	0.001319	698	63	623	13	597	8
TD-1-14	38	29	403	0.058780	0.002296	0.686320	0.023430	0.084992	0.001419	567	85	531	14	526	8
TD-1-15	36	109	163	0.083518	0.003035	1.897084	0.063631	0.163738	0.002958	1281	71	1080	22	978	16
TD-1-16	57	189	287	0.075370	0.002619	1.556583	0.052045	0.147889	0.002129	1080	70	953	21	889	12
TD-1-17	34	522	620	0.052799	0.002367	0.300509	0.014478	0.040455	0.000814	320	102	267	11	256	5
TD-1-18	71	80	171	0.115803	0.004142	5.161256	0.192982	0.316251	0.005101	1892	64	1846	32	1771	25
TD-1-19	21	96	119	0.069590	0.004910	1.194028	0.080285	0.125381	0.003519	917	145	798	37	761	20
TD-1-21	24	317	435	0.055305	0.003643	0.314536	0.020712	0.040745	0.000959	433	116	278	16	257	6
TD-1-22	55	141	269	0.074524	0.002622	1.702454	0.057007	0.162877	0.002517	1057	71	1009	21	973	14
TD-1-23	25	266	465	0.056285	0.003486	0.322901	0.018443	0.041669	0.000990	465	137	284	14	263	6
TD-1-24	26	391	450	0.052257	0.003505	0.298829	0.017477	0.041732	0.000982	298	121	265	14	264	6
TD-1-25	28	153	156	0.071778	0.003146	1.235827	0.055249	0.122539	0.002656	989	90	817	25	745	15
TD-1-26	20	259	378	0.054136	0.003198	0.312633	0.017227	0.041529	0.000741	376	133	276	13	262	5
TD-1-27	38	523	707	0.053201	0.002552	0.296136	0.012746	0.040086	0.000746	345	105	263	10	253	5
TD-1-28	14	214	275	0.059202	0.004116	0.320732	0.019868	0.040741	0.001063	576	152	282	15	257	7
TD-1-29	24	90	247	0.059473	0.002428	0.693095	0.029176	0.082947	0.001634	583	89	535	17	514	10
TD-1-30	10	94	188	0.050696	0.004363	0.301635	0.025470	0.042495	0.001335	228	198	268	20	268	8
XR-1-01	19	266	382	0.053735	0.002350	0.309377	0.013623	0.041432	0.000713	361	100	274	11	262	4
XR-1-02	20	250	417	0.049315	0.002211	0.275965	0.011654	0.040597	0.000739	161	106	247	9	257	5
XR-1-03	23	333	443	0.048525	0.001907	0.274737	0.010551	0.040863	0.000640	124	93	246	8	258	4
XR-1-04	20	267	396	0.050880	0.002092	0.289243	0.011974	0.041000	0.000686	235	64	258	9	259	4
XR-1-05	19	258	384	0.050679	0.001821	0.282887	0.009481	0.040585	0.000587	233	81	253	8	256	4
XR-1-06	18	247	354	0.051519	0.001776	0.290333	0.010274	0.040868	0.000837	265	80	259	8	258	5
XR-1-07	20	216	421	0.049522	0.001750	0.282357	0.010448	0.041114	0.000651	172	83	253	8	260	4
XR-1-08	28	357	555	0.050115	0.001719	0.286213	0.009851	0.041316	0.000632	211	80	256	8	261	4
XR-1-09	23	211	487	0.051100	0.001834	0.289357	0.010863	0.040784	0.000707	256	83	258	9	258	4
XR-1-10	28	360	561	0.048900	0.001726	0.277317	0.010207	0.040976	0.000771	143	88	249	8	259	5
XR-1-11	22	275	426	0.049457	0.002235	0.282027	0.012568	0.041396	0.000757	169	106	252	10	261	5
XR-1-12	33	464	648	0.049237	0.001654	0.280739	0.009577	0.041205	0.000660	167	78	251	8	260	4
XR-1-13	23	345	428	0.051208	0.002266	0.289672	0.012517	0.040971	0.000866	250	102	258	10	259	5
XR-1-14	21	214	424	0.049939	0.001951	0.281216	0.010421	0.040850	0.000749	191	91	252	8	258	5
XR-1-15	15	192	308	0.050499	0.002024	0.285813	0.011441	0.041170	0.000770	217	93	255	9	260	5
XR-1-16	41	627	750	0.048329	0.001327	0.279146	0.007588	0.041579	0.000580	122	67	250	6	263	4
XR-1-17	19	183	401	0.049147	0.001658	0.281058	0.010025	0.041256	0.000761	154	80	251	8	261	5
XR-1-18	21	302	409	0.051535	0.001844	0.297106	0.011280	0.041362	0.000661	265	79	264	9	261	4
XR-1-19	12	174	235	0.052164	0.001926	0.300110	0.011310	0.041534	0.000695	300	85	266	9	262	4
XR-1-20	19	410	319	0.050710	0.001961	0.290096	0.010778	0.041561	0.000675	228	61	259	8	263	4
XR-1-21	29	372	568	0.048996	0.001407	0.282051	0.008180	0.041279	0.000581	146	67	252	6	261	4
XR-1-22	26	344	499	0.051325	0.001518	0.292345	0.008267	0.041016	0.000551	254	67	260	6	259	3
XR-1-23	14	204	264	0.049144	0.001694	0.277700	0.008950	0.040903	0.000649	154	81	249	7	258	4
XR-1-24	10	179	188	0.049998	0.001977	0.284489	0.011525	0.040920	0.000645	195	91	254	9	259	4
XR-1-25	41	675	748	0.050857	0.001317	0.294030	0.007823	0.041371	0.000631	235	64	262	6	261	4
XR-1-26	31	460	577	0.051704	0.001299	0.298694	0.007306	0.041361	0.000487	272	57	265	6	261	3
XR-1-27	30	759	480	0.054523	0.001544	0.312213	0.009177	0.040856	0.000585	394	63	276	7	258	4
XR-1-28	33	553	605	0.052665	0.001565	0.298959	0.008869	0.040506	0.000583	322	67	266	7	256	4
XR-1-29	28	482	508	0.051108	0.001290	0.294232	0.007173	0.041259	0.000563	256	57	262	6	261	3
XR-1-30	18	293	328	0.050963	0.001644	0.291304	0.009180	0.040834	0.000652	239	81	260	7	258	4
ZD-1-01	39	306	841	0.055512	0.002205	0.308840	0.011585	0.039262	0.000704	432	89	273	9	248	4
ZD-1-03	12	330	336	0.052805	0.003233	0.195868	0.010996	0.027045	0.000542	320	139	182	9	172	3
ZD-1-05	9	178	176	0.057653	0.003270	0.316499	0.017894	0.040089	0.000973	517	124	279	14	253	6
ZD-1-06	10	128	190	0.049682	0.002468	0.283362	0.014378	0.040918	0.000829	189	119	253	11	259	5
ZD-1-11	12	188	216	0.053998	0.004759	0.307796	0.026723	0.041523	0.001331	372	200	272	21	262	8

(Continued on following page)

TABLE 2 | (*Continued*) Zircon La-ICP-MS U-Pb isotopic data for the Longlin basalt samples.

Analysis	Pb	Th	U	$^{207}Pb/^{206}Pb$		$^{207}Pb/^{235}U$		$^{206}Pb/^{238}U$		$^{207}Pb/^{206}Pb$		$^{207}Pb/^{235}U$		$^{206}Pb/^{238}U$	
		ppm		Ratio	1σ	Ratio	1σ	Ratio	1σ	Age (Ma)	1σ	Age (Ma)	1σ	Age (Ma)	1σ
ZD-1-13	13	302	326	0.052522	0.003997	0.207544	0.015651	0.028673	0.000622	309	174	191	13	182	4
ZD-1-15	42	283	884	0.052178	0.001908	0.295049	0.010140	0.040521	0.000619	300	83	263	8	256	4
ZD-1-19	13	269	222	0.053908	0.004238	0.291651	0.021760	0.039828	0.001074	369	206	260	17	252	7
ZD-1-20	38	259	798	0.053033	0.002719	0.295749	0.013604	0.039940	0.000758	332	117	263	11	252	5
ZD-1-21	3	35	57	0.051343	0.005034	0.284236	0.031571	0.041154	0.001662	257	232	254	25	260	10
ZD-1-24	42	356	850	0.052432	0.002128	0.303630	0.012298	0.041348	0.000694	306	93	269	10	261	4
ZD-1-25	5	57	96	0.056262	0.004866	0.299513	0.023212	0.041173	0.001312	461	193	266	18	260	8
ZD-1-26	5	67	105	0.059686	0.004954	0.319396	0.025931	0.040699	0.001380	591	148	281	20	257	9
ZD-1-27	94	1628	3725	0.050122	0.001399	0.148207	0.004696	0.021115	0.000463	211	32	140	4	135	3
ZD-1-28	29	207	618	0.050826	0.002029	0.288251	0.011320	0.040712	0.000669	232	62	257	9	257	4
ZD-1-29	29	202	619	0.051312	0.001894	0.291135	0.010793	0.040626	0.000655	254	88	259	8	257	4
ZD-1-30	32	237	693	0.052272	0.001958	0.297918	0.011026	0.041031	0.000765	298	90	265	9	259	5
ZD-1-31	43	305	915	0.050757	0.001911	0.294113	0.011006	0.041594	0.000762	232	92	262	9	263	5
ZD-1-32	7	88	137	0.050652	0.003302	0.279244	0.016742	0.040815	0.000944	233	145	250	13	258	6
ZD-1-33	30	198	640	0.054044	0.002119	0.306291	0.011324	0.040748	0.000669	372	87	271	9	257	4
ZD-1-36	7	105	123	0.054228	0.003759	0.299376	0.018899	0.041010	0.000961	389	156	266	15	259	6
ZD-1-38	23	543	369	0.051093	0.004462	0.294296	0.030690	0.040618	0.000942	256	202	262	24	257	6
ZD-1-39	6	67	102	0.060346	0.006044	0.324208	0.025367	0.042553	0.001315	617	218	285	19	269	8
ZD-1-43	17	271	299	0.056477	0.004235	0.305951	0.020844	0.040526	0.001103	472	167	271	16	256	7
ZD-1-44	41	310	849	0.049012	0.002037	0.277313	0.011534	0.040490	0.000725	150	94	249	9	256	4
ZD-1-45	28	459	536	0.051000	0.003011	0.274991	0.016935	0.038751	0.000893	239	137	247	13	245	6
ZD-1-46	43	269	913	0.052999	0.002148	0.303627	0.012999	0.040909	0.000732	328	91	269	10	258	5
ZD-1-47	28	193	593	0.052049	0.003234	0.291269	0.016678	0.040798	0.000881	287	147	260	13	258	5

Note: σ is mean square error.

Whole-Rock Sr-Nd Isotopes

The Tongdeng samples have higher $(^{87}Sr/^{86}Sr)_i$ (0.707167–0.707345) but lower εNd(t) (−2.5 to −2.14) than the Zhoudong samples $(^{87}Sr/^{86}Sr)_i$ = 0.706181–0.706191, εNd(t) = 0.57–0.69 (**Table 4**). The Nd model age for the Tongdeng and Zhoudong samples are 1,227–1,217 Ma and 1,002–1,017 Ma, respectively. In the $(^{87}Sr/^{86}Sr)_i$-εNd(t) discrimination diagram (**Figure 8A**), all the Tongdeng and Zhoudong samples fall close to the MORB field and overlap with the Emeishan high-Ti basalts. In the εNd(t)-εHf(t) discrimination diagram (**Figure 8B**), the Tongdeng samples all fall far below the mantle evolution line, whilst the Zhoudong samples fall on or slightly below it.

DISCUSSION

Permian Mafic Magmatism in Western Guangxi

In this study, our new zircon LA-ICP-MS U–Pb dating results on three Longlin basalt samples yielded weighed mean $^{206}Pb/^{238}U$ age of 257.9 ± 2.6 Ma (Tongdeng), 259.6 ± 1.4 Ma (Xiaoren) and 256.7 ± 2.0 Ma (Zhoudong). Zircons in Longlin basalt are generally characterized by (weak) oscillatory zoning on CL images and high Th/U ratios (0.32–1.87), resembling typical magmatic zircons (Hoskin and Schaltegger, 2003). The Late Permian ages are consistent with the emplacement of these basalts among the Upper Permian Tonglinghao Formation. Therefore, the weighted mean $^{206}Pb/^{238}U$ ages of ca. 257–260 Ma can represent the crystallization age of the Longlin basalts. The older zircons (ca. 460–1811 Ma) in Longlin basalt are likely xenocrystic captured from the intruded wallrocks.

In recent years, many Late Permian magmatic rocks have been discovered in Western Guangxi. Fan et al. (2004) zircon SHRIMP U-Pb dated a basalt sample from Yangxu area and yielded a weighted mean $^{206}Pb/^{238}U$ age of 253.7 ± 6.1 Ma (n = 23, MSWD = 2.8). Fan et al. (2008) reported two zircon SHRIMP U-Pb ages of 259.5 ± 5.2 Ma (n = 14, MSWD = 5.0) and 259.1 ± 4.0 Ma (n = 7, MSWD = 0.85) from two basalts in the Bama area and Baise area. Lai et al. (2012) reported the zircon LA-ICP-MS U-Pb ages of 257 ± 9 Ma (n = 8, MSWD = 2.8) of another basalt sample from Bama area. Recently, Zhang and Xiao (2014) LA-ICP-MS zircon U-Pb dated two diabase sills from Yufeng and Bama and yielded weighted mean $^{206}Pb/^{238}U$ ages of 259.3 ± 0.8 Ma (n = 10, MSWD = 0.35) and $^{206}Pb/^{238}U$ ages of 257 6 ± 2.9 Ma (n = 12, MSWD = 1.06). Integrating these age data, mafic magmatism in the western Guangxi was probably active during ca. 254–260 Ma.

Petrogenesis of the Late Permian Western Guangxi Basalts

Crustal Assimilation

As shown in the $(^{87}Sr/^{86}Sr)_i$-εNd(t) diagram (**Figure 8A**), the samples plot above the evolutionary trend defined by mid-ocean ridge basalt (MORB) and lower or middle continental crust (LCC/MCC). This, and the relatively wide zircon εHf(t) range and linear correlations between MgO, Nb/La, and SiO_2 (**Figure 9**), suggest that parental magma may have experienced crustal assimilation during their ascent. Crustal

TABLE 3 | Zircon Hf isotopic data for the Longlin basalt samples.

Analysis	t (Ma)	$^{176}Yb/^{177}Hf$	$^{176}Lu/^{177}Hf$	$^{176}Hf/^{177}Hf$	1σ	εHf(t)	1σ	TDM1(Hf)	TDM2(Hf)
TD-1-20	240	0.112508	0.003099	0.282322	0.000013	−11.14	0.46	1390	1970
TD-1-27	253	0.097859	0.002856	0.282288	0.00001	−12.05	0.37	1431	2037
TD-1-7	255	0.0853	0.002464	0.282382	0.000013	−8.63	0.45	1279	1823
TD-1-17	256	0.099026	0.002945	0.282439	0.00001	−6.67	0.34	1212	1700
TD-1-5	257	0.110081	0.003339	0.282408	0.000012	−7.79	0.43	1271	1772
TD-1-6	257	0.028456	0.000836	0.282287	0.000009	−11.64	0.33	1356	2016
TD-1-4	257	0.041196	0.001317	0.282285	0.000012	−11.79	0.41	1376	2025
TD-1-28	257	0.03752	0.001152	0.282313	0.00001	−10.79	0.36	1331	1962
TD-1-21	257	0.04143	0.001253	0.282245	0.000011	−13.22	0.39	1430	2115
TD-1-10	261	0.033878	0.001038	0.282254	0.00001	−12.78	0.34	1410	2090
TD-1-26	262	0.035612	0.001093	0.282247	0.000011	−13.01	0.38	1421	2105
TD-1-23	263	0.077877	0.00232	0.282428	0.00001	−6.78	0.34	1206	1713
TD-1-24	264	0.054585	0.001762	0.28227	0.000012	−12.29	0.42	1414	2061
TD-1-30	268	0.021727	0.000756	0.282492	0.000009	−4.15	0.32	1068	1552
TD-1-29	514	0.025869	0.00082	0.282559	0.000008	3.5	0.3	976	1254
TD-1-14	526	0.023621	0.000773	0.282559	0.000009	3.78	0.31	975	1246
TD-1-12	597	0.025355	0.000812	0.282449	0.000016	1.41	0.55	1129	1450
TD-1-25	745	0.050102	0.001767	0.282444	0.00001	4	0.36	1165	1401
TD-1-11	751	0.062281	0.002132	0.282658	0.00001	11.48	0.36	868	932
TD-1-19	761	0.016123	0.000672	0.282002	0.000008	−10.76	0.29	1743	2339
TD-1-16	889	0.037597	0.00114	0.282229	0.000008	−0.22	0.28	1448	1776
TD-1-2	962	0.028373	0.000938	0.282002	0.000012	−6.56	0.44	1755	2228
TD-1-1	963	0.027836	0.001054	0.282308	0.000011	4.24	0.38	1334	1553
TD-1-9	967	0.027851	0.00092	0.282183	0.00001	−0.04	0.35	1504	1824
TD-1-22	973	0.037762	0.001278	0.28214	0.000012	−1.68	0.42	1579	1931
TD-1-15	978	0.015551	0.000544	0.281763	0.000009	−14.44	0.3	2063	2729
TD-1-18	1771	0.017903	0.000601	0.281589	0.000012	−3.09	0.43	2304	2629
TD-1-3	1798	0.038284	0.001358	0.281672	0.000009	−0.46	0.33	2234	2487
TD-1-8	1861	0.028131	0.000892	0.281438	0.000009	−6.83	0.31	2528	2927
XR-1-28	256	0.110715	0.003341	0.282582	0.000021	−1.65	0.75	1010	1383
XR-1-5	256	0.043959	0.001378	0.282432	0.000008	−6.64	0.3	1171	1699
XR-1-2	257	0.045846	0.001429	0.28245	0.00001	−6.01	0.36	1147	1660
XR-1-9	258	0.037287	0.001238	0.282603	0.000009	−0.52	0.31	924	1314
XR-1-30	258	0.052244	0.001626	0.282353	0.000013	−9.42	0.46	1290	1876
XR-1-14	258	0.037546	0.001161	0.282431	0.000009	−6.57	0.32	1165	1697
XR-1-27	258	0.098276	0.003125	0.282572	0.000014	−1.95	0.51	1020	1404
XR-1-3	258	0.076727	0.002297	0.282479	0.000015	−5.1	0.52	1133	1603
XR-1-23	258	0.036711	0.001097	0.282585	0.000012	−1.13	0.44	947	1353
XR-1-24	259	0.030127	0.000965	0.282586	0.000014	−1.08	0.51	942	1349
XR-1-10	259	0.057407	0.00176	0.282423	0.000009	−6.96	0.31	1195	1721
XR-1-4	259	0.051023	0.001579	0.282455	0.000009	−5.78	0.31	1144	1647
XR-1-22	259	0.034962	0.001068	0.282434	0.000012	−6.43	0.43	1158	1689
XR-1-7	260	0.036827	0.001125	0.282446	0.000009	−6.02	0.32	1143	1663
XR-1-15	260	0.038532	0.001242	0.282456	0.000015	−5.68	0.54	1133	1642
XR-1-12	260	0.071761	0.00223	0.282447	0.000012	−6.15	0.44	1176	1671
XR-1-17	261	0.026176	0.000803	0.282442	0.00001	−6.1	0.35	1139	1669
XR-1-29	261	0.083299	0.002381	0.282603	0.000019	−0.65	0.69	953	1323
XR-1-21	261	0.050621	0.001585	0.282473	0.000011	−5.13	0.4	1119	1607
XR-1-8	261	0.048946	0.001499	0.282447	0.000011	−6.02	0.38	1153	1664
XR-1-26	261	0.053506	0.001677	0.282426	0.000013	−6.79	0.45	1188	1712
XR-1-18	261	0.059755	0.001853	0.282562	0.000016	−2	0.57	999	1410
XR-1-25	261	0.080771	0.002498	0.282518	0.000015	−3.68	0.54	1081	1516
XR-1-11	261	0.052477	0.001568	0.282431	0.000009	−6.59	0.31	1178	1700
XR-1-1	262	0.087635	0.002665	0.282583	0.000017	−1.41	0.59	991	1373
XR-1-19	262	0.075995	0.002342	0.282368	0.000012	−8.94	0.42	1294	1848
XR-1-16	263	0.050863	0.001418	0.282447	0.00001	−5.97	0.37	1150	1662
ZD-1-27	135	0.088365	0.002933	0.282319	0.000012	−13.34	0.41	1388	2029
ZD-1-3	172	0.033256	0.001155	0.282295	0.000011	−13.22	0.37	1356	2051
ZD-1-13	182	0.028187	0.001043	0.282347	0.00001	−11.15	0.34	1279	1928
ZD-1-45	245	0.168095	0.004771	0.282825	0.000018	6.51	0.64	672	857
ZD-1-1	248	0.05117	0.001892	0.282633	0.000014	0.22	0.49	898	1259
ZD-1-19	252	0.076251	0.002307	0.282769	0.000018	5.04	0.65	709	955
ZD-1-20	252	0.041787	0.001572	0.282699	0.000027	2.7	0.95	796	1105
ZD-1-5	253	0.06476	0.001964	0.282741	0.000012	4.13	0.44	744	1015

(Continued on following page)

TABLE 3 | (*Continued*) Zircon Hf isotopic data for the Longlin basalt samples.

Analysis	t (Ma)	$^{176}Yb/^{177}Hf$	$^{176}Lu/^{177}Hf$	$^{176}Hf/^{177}Hf$	1σ	εHf(t)	1σ	TDM1(Hf)	TDM2(Hf)
ZD-1-44	256	0.027206	0.00095	0.282639	0.000009	0.77	0.33	866	1230
ZD-1-15	256	0.033752	0.001184	0.28268	0.000009	2.17	0.33	814	1141
ZD-1-43	256	0.101104	0.00298	0.282737	0.000017	3.88	0.61	770	1033
ZD-1-38	257	0.073786	0.002218	0.282734	0.000019	3.93	0.66	758	1030
ZD-1-29	257	0.03739	0.001253	0.282647	0.000011	1.02	0.38	862	1215
ZD-1-26	257	0.033116	0.000993	0.282772	0.000011	5.48	0.38	680	932
ZD-1-28	257	0.038275	0.001372	0.282607	0.000015	–0.42	0.54	922	1307
ZD-1-33	257	0.027671	0.000933	0.282647	0.00001	1.07	0.34	855	1212
ZD-1-47	258	0.042357	0.001492	0.282625	0.00002	0.22	0.69	899	1267
ZD-1-32	258	0.042764	0.001193	0.282757	0.000011	4.93	0.39	705	967
ZD-1-46	258	0.026803	0.000902	0.282634	0.00001	0.65	0.35	872	1240
ZD-1-6	259	0.033849	0.000981	0.28274	0.00001	4.39	0.35	725	1002
ZD-1-36	259	0.037992	0.001101	0.282727	0.000011	3.93	0.38	745	1032
ZD-1-30	259	0.029077	0.000992	0.282659	0.00001	1.53	0.35	840	1184
ZD-1-21	260	0.036689	0.001033	0.282797	0.00001	6.41	0.36	646	874
ZD-1-25	260	0.066052	0.001866	0.282742	0.000012	4.32	0.43	740	1008
ZD-1-24	261	0.048586	0.001851	0.282695	0.000018	2.69	0.64	808	1112
ZD-1-11	262	0.079678	0.002417	0.28272	0.000013	3.5	0.47	783	1062
ZD-1-31	263	0.038586	0.001392	0.282674	0.000012	2.08	0.42	827	1152
ZD-1-39	269	0.045788	0.001428	0.282789	0.000012	6.25	0.42	664	892

Note: For the calculation of εHf(t) values, we have adopted the ^{176}Lu decay constant of 1.867 × 10^{-11} (Söderlund et al., 2004), the present-day chondritic values of $^{176}Lu/^{177}Hf$ = 0.0332 and $^{176}Hf/^{177}Hf$ = 0.282772 (Blichert-Toft and Albarède, 1997). To calculate one-stage model ages (T_{DM1}) relative to a depleted-mantle source, we have adopted the present-day depleted-mantle values of $^{176}Lu/^{177}Hf$ = 0.0384 and $^{176}Hf/^{177}Hf$ = 0.28325 (Vervoort and Blichert-Toft, 1999).

TABLE 4 | Whole-rock Sr and Nd isotopic compositions for the Longlin basalt samples.

Sample	TD-1	TD-3	ZD-1	ZD-2-4
Sr (ppm)	1048	741	959	499
Rb (ppm)	67.9	75.1	64.9	20.5
$^{87}Rb/^{86}Sr$	0.09648	0.2486	0.1603	0.1604
$^{87}Sr/^{86}Sr$	0.7077	0.70808	0.70678	0.70677
2σ	0.00002	0.00002	0.00002	0.00001
$(^{87}Sr/^{86}Sr)_i$	0.7071709	0.7070046	0.706065	0.7063355
Nd (ppm)	66.0	60.6	46.4	47.4
Sm (ppm)	11.72	11.40	10.03	9.96
$^{147}Sm/^{144}Nd$	0.1174	0.1194	0.1223	0.1217
$^{143}Nd/^{144}Nd$	0.512376	0.512398	0.512542	0.512547
2σ	0.000003	0.000003	0.000003	0.000005
$(^{143}Nd/^{144}Nd)_i$	0.512178	0.512196	0.512335	0.512341
$\varepsilon_{Nd}(t)$	–2.167846	–1.949417	0.2974821	0.5097659
T_{DM} (Ma)	1110.948	1148.448	1116.7554	1063.0548
T_{2DM} (Ma)	1205.9407	1188.1823	1004.4052	987.12358

Note: $(^{87}Sr/^{86}Sr)_i$ and $(^{143}Nd/^{144}Nd)_i$ are the initial isotopic ratios of $^{87}Sr/^{86}Sr$ and $^{143}Nd/^{144}Nd$.

assimilation would have increased the Th/Ta ratios (cf. MORB and OIB: Th/Ta < 1.6, Sun and McDonough, 1989), as found in both the Tongdeng (Th/Ta = 2.55–2.63) and Zhoudong (Th/Ta = 1.95–1.97) samples. The Tongdeng samples may have had stronger crustal assimilation influence as their Th/Ta ratios are clearly higher than their Zhoudong counterparts. This conclusion is also supported by the higher SiO_2 and Nb/La, the lower MgO, zircon εHf(t) and whole-rock εNd(t) values, together with the more xenocrystic zircons in the Tongdeng samples.

If the rock formation was influenced by crustal assimilation, the rocks would have $(Th/Ta)_{PM} \approx 1$ and $(La/Nb)_{PM} > 1$ (by lower crustal material); and $(Th/Ta)_{PM} > 2$ and $(La/Nb)_{PM} > 2$ (by upper crustal material) (Peng et al., 1994). The Longlin basalts have $(Th/Ta)_{PM}$ = 0.94–1.27 and $(La/Nb)_{PM}$ = 1.17–1.20, showing mainly lower crustal influence. In the ($^{87}Sr/^{86}Sr)_i$-εNd(t) discrimination diagram (**Figure 8A**), the Longlin basalts plot above the evolutionary trend defined by MORB and LCC/MCC, indicating also lower crustal involvement. Assuming that the Longlin basalts were depleted mantle-derived, zircon Hf isotope calculation indicates that crustal input is of 8% for the Zhoudong samples and 40% for the Tongdeng samples. In the magma mixing modelling, the εHf(t) value of the depleted mantle-derived, ancient crustal-derived, and parental magmas of the Longlin basalts are 16 [depleted mantle εHf(t) value at 259 Ma], −13.22 [minimum measured Longlin basalt εHf(t) value] and −1/−10 [average measured Zhoudong/Tongdeng basalt εHf(t) value], respectively. The assumed Hf contents of the depleted mantle and crustal material are 0.309 μg/g (Taylor et al., 1981) and 4.5 μg/g (Yangtze middle-lower crustal average; Chi and Yan, 2007), respectively. Considering that the mantle-sourced parental magma of the Longlin basalts has lower/equal εHf(t) value than/to that of the depleted mantle, and that the assimilated crustal material has lower εHf(t) value than the lowest εHf(t) value (−13.22) of the samples, the Zhoudong and Tongdeng samples should have their actual degree of crustal assimilation below 8 and 40%, respectively.

The Lu-Hf and Sm-Nd isotopic systems have similar geochemical characteristics, and hence the εHf(t) and εNd(t) values show strongly positive correlation (Vervoort et al., 1999). Nd-Hf decoupling of magmatic rocks are commonly related to residual garnet or zircon enrichment in the magma source region (Patchett et al., 2004; Vervoort et al., 2000; Zeng et al., 2021a), and/or crustal assimilation (Patchett et al., 1984; Carpentier et al., 2009). From **Figure 8B**, it is shown that the Tongdeng samples

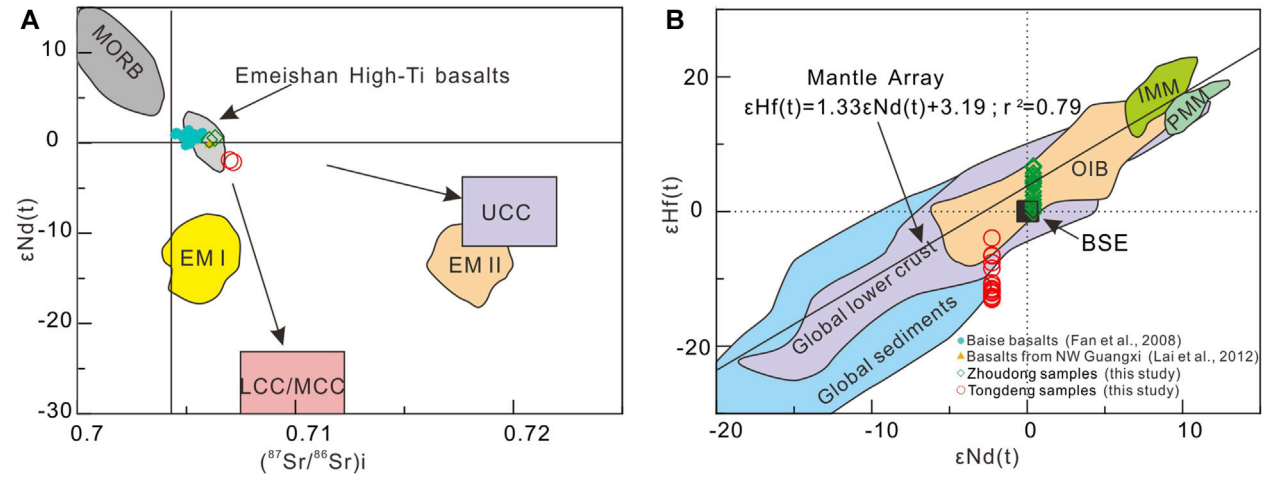

FIGURE 8 | (A) ($^{87}Sr/^{86}Sr)_i$-εNd(t) and **(B)** εHf(t)-εNd(t) (base map after Vervoort et al., 1999 and Zeng et al., 2021a; Zeng et al., 2021b) diagrams for the Longlin basalt samples. MORB, mid-ocean-ridge basalt; EM I and EM II, enriched mantle; HIMU, LCC/MCC, middle to lower continental crust; UC, upper continental crust; IMM, Indian MORB; PMM, Pacific MORB. Data source: the ranges of Emeishan high- and low-Ti basalts are from Xu et al. (2001), Zhou et al. (2006) and Xiao et al. (2003), Xiao et al. (2004)a,b; DM, EM I, and EM II (Zindler and Hart, 2003); LCC, MCC, and UC (Jahn et al., 1999); global sediments from Vervoort et al. (1999); global lower crust from Vervoort et al. (2000); IMM and PMM from Kempton et al. (2012).

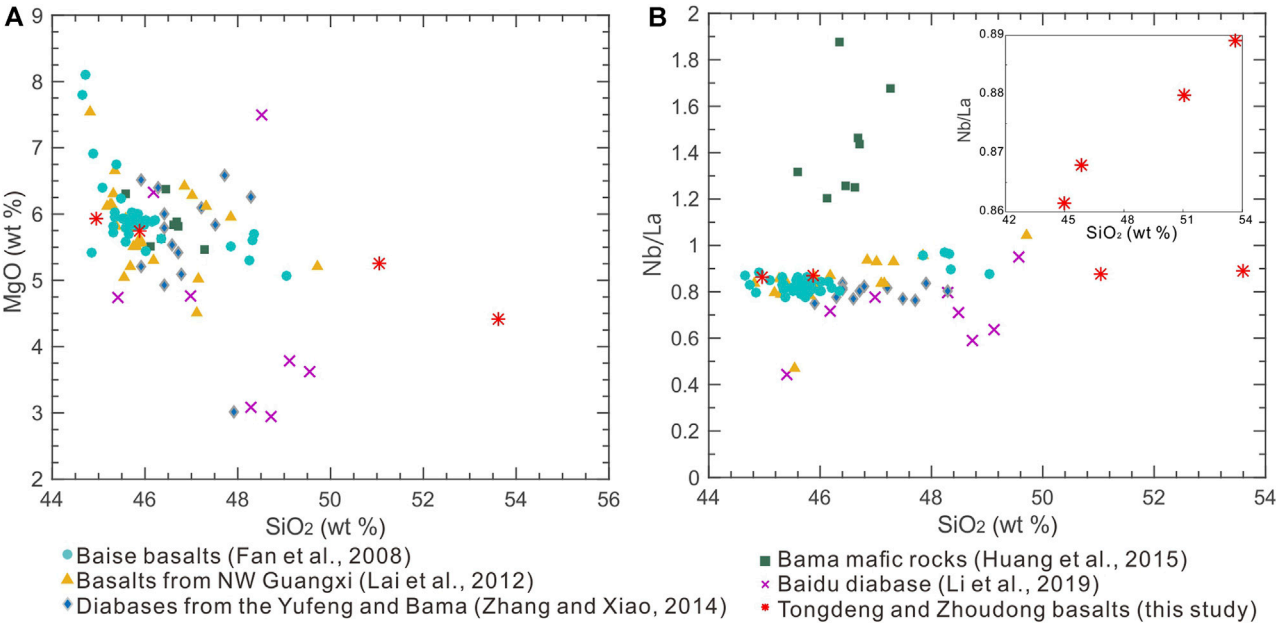

FIGURE 9 | (A) SiO_2-MgO and **(B)** Nb/La-SiO_2 diagrams for the Longlin basalt samples.

have clear Nd-Hf decoupling, whereas for the Zhoudong samples such decoupling is indistinct. Because not all samples of the Longlin basalts show Nd-Hf decoupling, the decoupling is probably unrelated to the mantle source region. As aforementioned, the Zhoudong samples have higher degree of crustal assimilation than the Tongdeng samples, implying that their Hf-Nd isotope decoupling was likely assimilation related. Since Hf^{4+} and Zr^{4+} have similar ionic radii, Hf is commonly enriched in zircon through isomorphism, leading to very low zircon Lu/Hf value (distinct lower than most rock-forming minerals) (Vervoort et al., 2011). After prolonged accumulation, εHf(t) of zircon would be clearly lower than that of other minerals, and thus the sediments or rocks with high zircon contents would have lower εHf(t) than those that lack zircon (e.g., mudstone, shale, or pelagic sediments) (Patchett et al., 1984; Carpentier et al., 2009). Meanwhile, the Sm-Nd

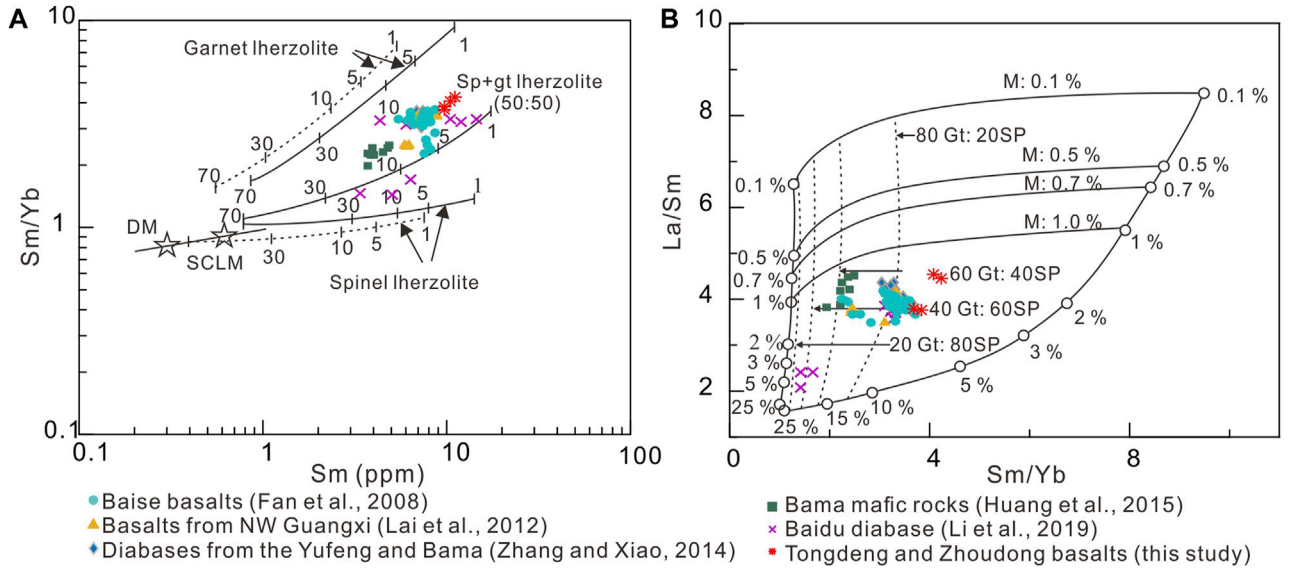

FIGURE 10 | (A) Sm/Yb-Sm diagram (dashed and solid lines are the melting trends for depleted mantle and enriched subcontinental lithospheric mantle, respectively. The numbers beside the lines are degrees of partial melting for a given mantle source); **(B)** La/Sm-Sm/Yb discrimination diagram for the Longlin basalt samples (After Özdemir and Güleç, 2014; M:0.7, M:1, M:2, M:3, and M:5% represents mixing lines between 0.7, 1, 2, 3 and 5% melts of garnet and spinel peridotite. Dashed lines indicate the relative proportions of melts derived from garnet and spinel peridotite mantle sources contributing to the parental magmas). Data from other basalt units in western Guangxi are shown for comparison.

isotope system is unaffected by zircon. Hence, the εHf(t) value of zircon-rich sediments or rocks would deviate negatively from its εNd(t) value with reference to the mantle array, whereas the εHf(t) value of zircon-poor sediments or rocks would deviate positively from its εNd(t) value with reference to the mantle array. The εHf(t) values of the Tongdeng sample are obviously lower than its εNd(t) value, indicating that the crustal materials assimilated by it should be zircon-rich sediments or rocks. The lesser crustal assimilation for the Zhoudong samples may have caused the indistinct Hf-Nd decoupling.

The content of REE in the crust is higher than that in the mantle (Taylor and McLennan, 1985; Sun and McDonough, 1989). Therefore, compared with the Zhoudong samples, the Tongdeng samples experienced stronger crustal contamination, which may be one of the reasons for their higher REE content. In addition, the contents of Zr and Hf in Tongdeng samples are obviously higher than Zhoudong samples, which is consistent with the fact that the crustal materials assimilated by them are rich in zircon.

Fractional Crystallization

It is generally considered that mantle-sourced primitive melts may have had relatively high Ni (> 400 ppm), Cr (> 1,000 ppm) and Mg# (73–81) contents (Mahoney, 1997; Wilson, 1989), which are not found in the Longlin basalts (Tongdeng: Ni = 12–22 ppm, Cr = 20–110 ppm, Mg# = 54–69; Zhoudong: Ni = 111–129 ppm, Cr = 220–280 ppm, Mg# = 58–60). This shows that fractionation of mafic minerals (e.g., olivine and pyroxene) has likely occurred (Frey and Prinz, 1978; Wang et al., 2016; Zeng et al., 2021b). Due to the insufficient element geochemical data, it is hard to determine the fractionated minerals from the Harker-type diagrams. Using the lowest Cr content of mantle-sourced melt (1,000 ppm; Wilson, 1989), calculation suggests that the petrogenesis of the Tongdeng samples requires ~50% olivine or ~20% pyroxene fractionation, whilst that of the Zhoudong samples requires ~30% olivine or ~10% pyroxene fractionation (partition coefficient from GERM website: http://www.earthref.org/). Because crustal assimilation can also reduce the magma Cr content, the degree of crystallization differentiation of mafic minerals in Zhoudong and Tongdeng samples must be lower than the above calculated values, especially the Tongdeng samples with higher degree of crustal contamination. The lack of Eu anomalies in the Longlin basalts indicates insignificant plagioclase fractionation.

Nature of Magma Source

All Longlin basalt samples in this study have lower εHf(t) and εNd(t) values than the depleted mantle, suggesting that the basaltic magma has undergone crustal assimilation during the magma ascent, and/or the magma was sourced from the mantle metasomatized by subducting crustal material, possibly from the altered Paleotethyan slab (Zeng et al., 2018; Xu et al., 2021).

The magma source region can be determined by the most primitive samples of the Longlin basalts (i.e., Zhoudong samples, with the least crustal assimilation and fractionation). Since Yb is more compatible in garnet than in pyroxene and spinel, whilst Sm is incompatible in all these minerals, Sm/Yb can also be used to constrain the mantle source mineralogy (Aldanmaz et al., 2000). In the Sm vs. Sm/Yb diagram (**Figure 10A**), the Zhoudong samples plot between the partial melting curves of garnet lherzolite and spinel-garnet facies (1:1) lherzolite. From the Sm/Yb vs. La/Sm diagram (**Figure 10B**) (Özdemir and Güleç, 2014), the

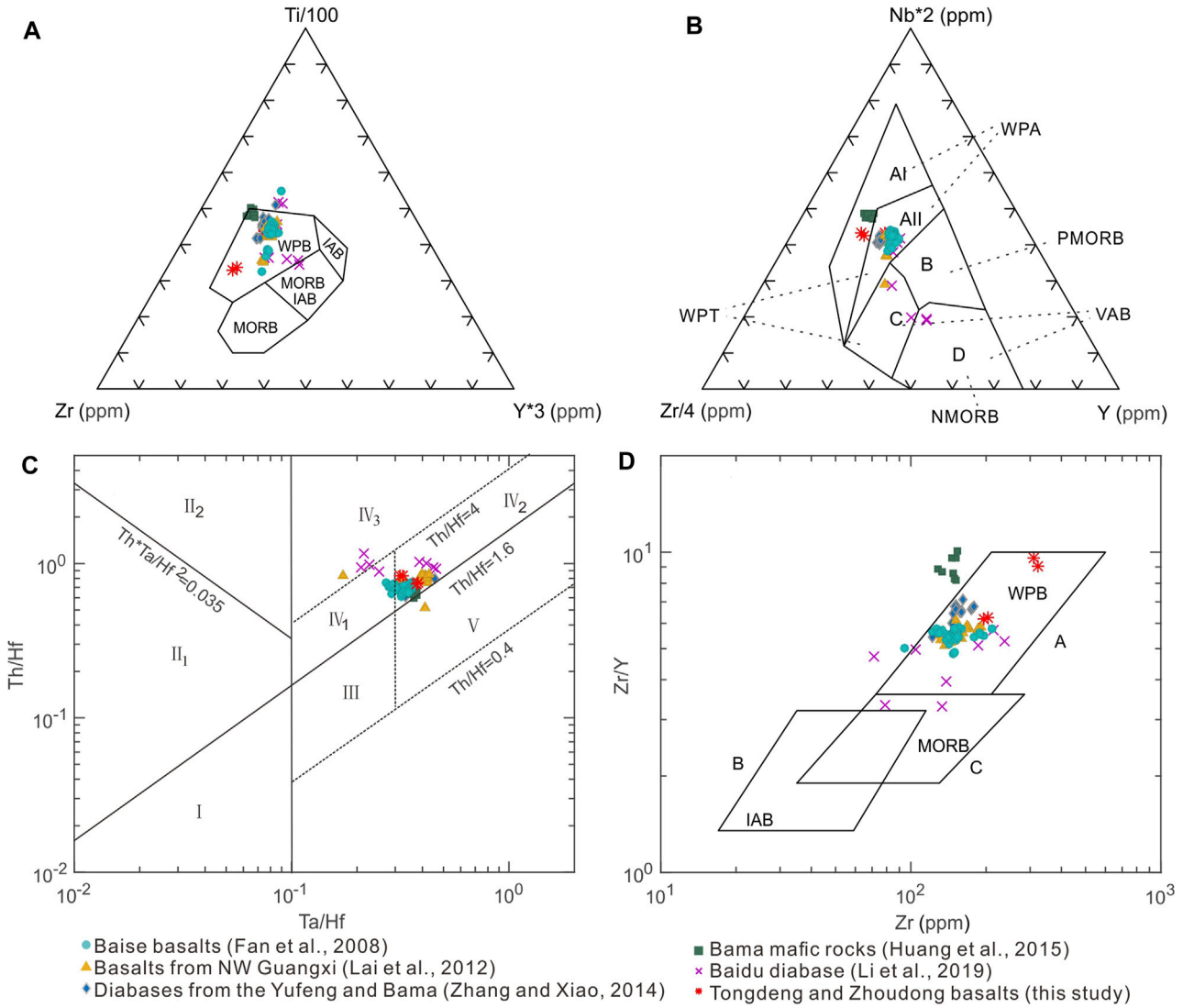

FIGURE 11 | Tectonic discrimination diagrams for the Longlin basalt samples: **(A)** Ti/100-Zr-Y*3 diagram (after Pearce and Cann, 1973); **(B)** Nb*2-Zr/4-Y diagram (after Meschede, 1986); Th/Hf-Ta/Hf diagram (after Wang et al., 2001); Zr/Y-Zr diagram (after Pearce, 1982). Data from other basalt units in western Guangxi are shown for comparison. WPB–within-plate basalt; MORB–mid-ocean ridge basalt; IAB–island-arc basalt; WPA–within-plate alkali basalts; WPT–within-plate tholeiites; VAB–volcanic-arc basalts; PMORB–basalt from plume-influenced regions; NMORB–oceanic basalt from normal mid-ocean ridge environment. **(C)**: I—N-MORB Margin of divergent oceanic plate; II—Margin of convergent plate (II_1—Island are of continental margin; II_2—Volcanic are of continental margin); III—Oceanic intra plate (the oceanic island and seamount, T-MORB, E-MORB); IV—Continental intraplate (IV_1—Continental rift; IV_2— Alkaline basalt zone; IV_3—Tensional zone); V—Mantle plume; **(D)** 1—Continental rift; 2—Continental tensional zone.

compositions of Longlin basalt are consistent with magmas formed by low-degree melting (1.0–2.0%) and >80% garnet lherzolite contribution. It is commonly accepted that the depth of the garnet-spinel stability zone is 75–85 km in the upper mantle (McKenzie and O'Nions, 1991; Klemme and O'Neill, 2000). Therefore, magma for Longlin basalt was likely formed in the spinel–garnet transition zone at 75–85 km depths.

Geodynamic Significance

In many tectonic discrimination diagrams (**Figure 11**), the Longlin basalts fall inside the within-plate basalt field, similar to most mafic rocks from western Guangxi. According to Sun et al. (2007), within-plate basalts have w (Nb)/w (Zr) > 0.04 and w (Th)/w (Nb) > 0.11, of which continental rift-related basalts and continental extension-related basalts have w (Th)/w (Nb) = 0.11–0.27 and >0.27 (generally 0.27–0.67), respectively. The Longlin basalts have their Nb/Zr (0.13–0.16) similar to that of within-plate basalts and their w (Th)/w (Nb) (0.12–0.15) similar to that of continental rift-related basalts of the within-plate basalts. This shows that the Late Permian western Guangxi was located in a continental rifting setting.

Based on ^{40}Ar-^{39}Ar dating, Hou et al. (2006) considered that the Emeishan LIP mafic magmatism occurred at ~258.9 Ma and

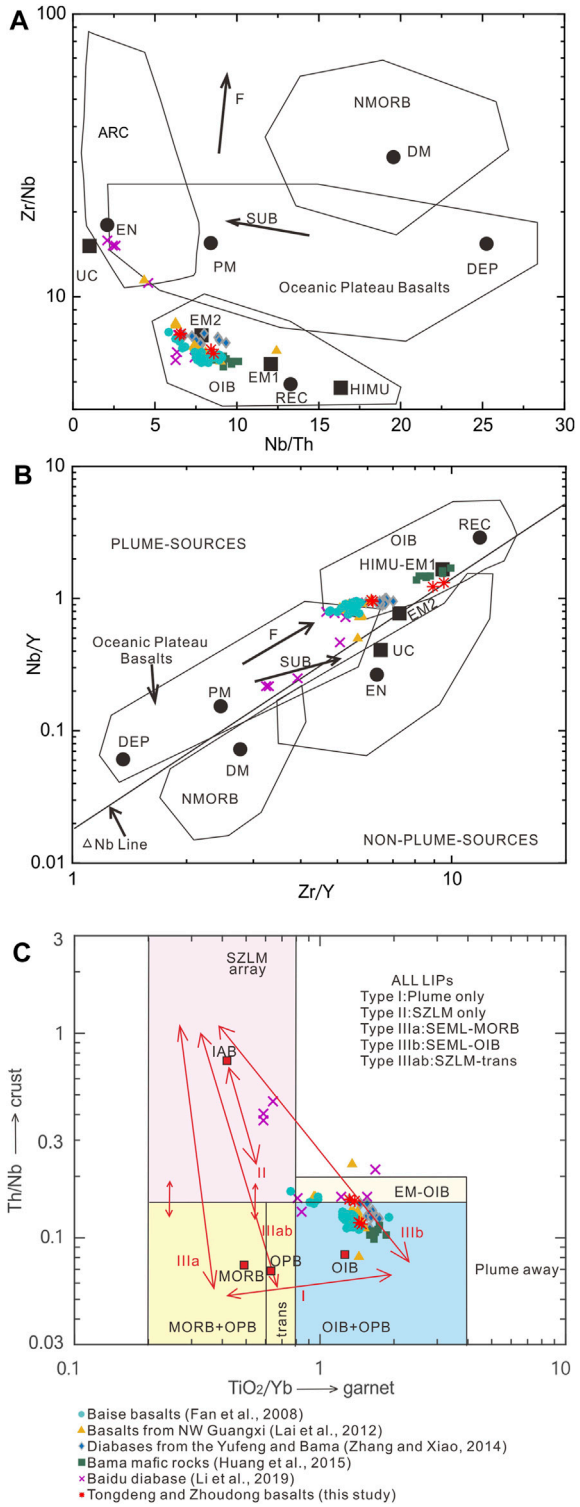

FIGURE 12 | (A) Nb/Th-Zr/Nb diagram (after Condie, 2005); **(B)** Zr/Y-Nb/Y diagram (after Condie, 2005); **(C)** TiO2/Yb-Th/Nb diagram (after Pearce et al., 2021). UC–upper continental crust; PM–primitive mantle; DM–shallow depleted mantle; HIMU–high mu (U/Pb) source; EM1 and EM2—enriched mantle sources; ARC–arc related basalts; NMORB–normal ocean ridge basalt; OIB–oceanic island basalt; DEP–deep depleted mantle; EN–enriched component; REC–recycled component; OPB–oceanic plateau basalt; IAB–island arc basalt.

lasted for less than 3 My. Shellnutt et al. (2008) constrained the timing of the Emeishan LIP plume activity to ~260 Ma. He et al. (2007) dated Xuanwei Formation, silicic ignimbrite and tuff by SHRIMP zircon geochronology, and considered that the activity time of Emeishan basalt is 259–262 Ma. Li (2012) statistically analyzed 70 age data of the Emeishan LIP magmatism, and found that the age was mostly concentrated in 252–265 Ma. As mentioned above, the Late Permian mafic magmatism was also developed in the western Guangxi, and its emplacement age was coeval with the Emeishan LIP magmatism. Moreover, the interpreted intraplate rift setting for the Late Permian mafic magmatism in western Guangxi is consistent with the rift setting of the Emeishan LIP. Previous studies indicate that the intermediate and outer zones of the Emeishan LIP comprise mainly high-Ti basalts (Xu et al., 2004; Cheng et al., 2019). The mafic magmatic rocks in western Guangxi generally have the high Ti-feature (Fan et al., 2008; Lai et al., 2012; Zhang and Xiao, 2014; Huang et al., 2015) and have similar Sr-Nd isotopic composition to the Emeishan high-Ti basalts (**Figure 8A**), which is consistent with its location in the Emeishan LIP margin. Hence, the Late Permian magmatism in western Guangxi is most likely associated with the Emeishan LIP.

Considering the role of mantle plume and lithosphere in the CFB formation, Turner et al. (1996) divided the CFB into two genetic types, i.e., Deccan-type and Parana-type. Deccan-type CFB has geochemical characteristics similar to OIB, which is derived from decompression melting of asthenospheric peridotite in the mantle plume. The Parana-type CFB is rich in incompatible elements, and is formed by partial melting of the lithospheric mantle (driven by mantle plume-derived heating). As shown in **Figure 6**, the Late Permian basalts in western Guangxi are enriched in LILEs and LREEs, with no discernible Nb, Ta and Ti anomalies. The distribution curves are obviously different from NMORB and EMORB, but similar to OIB. In addition, the Late Permian basalt samples in western Guangxi fall mainly in the OIB field (**Figure 12**). Therefore, we suggest that the Late Permian basalt in western Guangxi belongs to the Deccan-type, and its formation is closely related to the decompression melting of a mantle plume. In the Th/Nb-TiO_2/Yb diagram (**Figure 12C**), most of the western Guangxi basalt samples fall near the type-IIIB line (plume-SZLM interactions), which also demonstrates a mantle plume source with lithospheric input. This is consistent with our conclusion that the Longlin mafic magma has experienced crustal assimilation.

Possible formation mechanisms for the Emeishan high-Ti and low-Ti basalts are still under debate, and have been attributed to the different magma source regions, degrees of partial melting, fractional crystallization, and crustal assimilation processes, or a combination of these factors (e.g., Xu et al., 2001; Hao et al., 2004; Li et al., 2008; Zhang, 2009). In this study, formation of the Tongdeng and Zhoudong samples have clearly different degrees of crustal assimilation, yet they all have high-Ti features, which shows no obvious

relation between the high-Ti features and crustal assimilation. Since Fe-Ti oxides commonly fractionated at the late magma evolution stage (when MgO < 4 wt%) (Xu et al., 2013). The Zhoudong basalt samples have MgO > 4.42 wt%, which suggests that the high-Ti features are unlikely to be related to ilmenite fractionation. As afore-discussed, Late Permian basalts from western Guangxi (e.g., Longlin) were mainly sourced from low-degree partial melting of the mantle in the spinel–garnet transition zone, features that may have shaped their high-Ti characters. Since lithospheric thinning is commonly present above the mantle plume axis, partial melting could have extended to shallower depths (e.g., spinel stability field) and become more extensive (i.e., higher-degree partial melting). Conversely, distal from the mantle plume head, the lithospheric mantle is thicker and mantle decompression melting occurred at greater depths (in the spinel–garnet transition zone and garnet stability field) with lower intensity (i.e., low-degree partial melting). Therefore, the location of western Guanxi basalts on the Emeishan LIP margin may explain the high-Ti character of the basalts in this region.

High-Ti and low-Ti basalts also coexist in other LIPs around the world, such as the Paraná, Deccan, and Siberia (Peate et al., 1999; Xia et al., 2012). Fodor (1987) and Arndt et al. (1993) considered that high-Ti and low-Ti basalts are caused by different degrees of melting of the same mantle source, with the degree of partial melting degree for high-Ti basalts being lower than their low-Ti counterparts. McKenzie and Bickle (1988) suggested that the lithospheric mantle thickness is the principal factor that controls the depth and degree of partial melting in the mantle source region. Xia et al. (2012) considered that high-Ti basalts are formed by lower degree of partial melting in the deeper part of the mantle plume (tail), whereas low-Ti basalts are formed by higher degree of partial melting in the shallower part of the mantle plume (head). The above viewpoints are consistent with our conclusion that the difference of mantle source depth and degree of partial melting have caused the significant Ti content variation of magmatic rocks in the Emeishan LIP.

CONCLUSIONS

1) Longlin basalts from different places in western Guangxi yielded similar Late Permian zircon U-Pb ages, i.e., 257.9 ± 2.6 Ma (Tongdeng), 259.5 ± 0.75 Ma (Xiaoren), and 256.7 ± 2.0 Ma (Zhoudong), coeval with the Emeishan flood basalt emplacement.
2) Element and Sr-Nd-Hf isotope geochemistry show that the Longlin basalts were formed from low-degree partial melting in the spinel–garnet transition zone at depths of 75–85 km. The parental magma may have undergone mafic mineral (e.g., olivine and pyroxenes) fractionation and varying degrees of lower crustal assimilation.
3) Late Permian basalts in western Guangxi have similar emplacement age and geochemical features to the Emeishan high-Ti flood basalts. This suggests that the Emeishan LIP activity extended to western Guangxi.
4) Late Permian basalts in western Guangxi have OIB-type geochemical characteristics, and their formation is closely linked to the decompression melting of a mantle plume. The high-Ti features may have caused by the low-degree partial melting in the deep mantle.

DATA AVAILABILITY STATEMENT

The original contributions presented in the study are included in the article, further inquiries can be directed to the corresponding author.

AUTHOR CONTRIBUTIONS

CGZ and RYZ designed the research and drafted the manuscript. CML and JJ collected and processed the data. XJS prepared **Figures 1–12**. TGW contributed to the interpretation of the results.

FUNDING

This research was funded by the National Nature Science Foundation of China (41772349 and 42030809), Open Research Fund Program of State Key Laboratory of Nuclear Resources and Environment (East China University of Technology) (2020NRE13), the research grants from the East China University of Technology (DHBK2017103), Open Research Fund Program of Key Laboratory of Metallogenic Prediction of Nonferrous Metals and Geological Environment Monitoring (Central South University), Ministry of Education (2019YSJS08), the Key Scientific and Technological Research Project of Henan Province, China (192102310268), and the Nanhu Scholars Program for Young Scholars of XYNU.

ACKNOWLEDGMENTS

The authors would like to thank the Chief Editors Profs. David R. Lentz (Economic Geology) and Valerio Acocella (Volcanology), Guest Editor Dr. Chunkit Lai, and two reviewers for their insightful and constructive comments.

REFERENCES

Acocella, V. (2021). *Volcano-Tectonic Processes*. Switzerland: Springer, 1–552. doi:10.1007/978-3-030-65968-4

Aldanmaz, E., Pearce, J. A., Thirlwall, M. F., and Mitchell, J. G. (2000). Petrogenetic Evolution of Late Cenozoic, Post-Collision Volcanism in Western Anatolia, Turkey. *J. Volcanology Geothermal Res.* 102, 67–95. doi:10.1016/S0377-0273(00)00182-7

Andersen, T. (2002). Correction of Common Lead in U–Pb Analyses that Do Not Report 204Pb. *Chem. Geology.* 192 (1), 59–79. doi:10.1016/S0009-2541(02)00195-X

Arndt, N. T., Czamanske, G. K., Wooden, J. L., and Federenko, V. A. (1993). Mantle and Crustal Contributions to Continental Flood Volcanism. *Tectonophysics* 223, 39–52. doi:10.1016/0040-1951(93)90156-E

Blichert-Toft, J., and Albarède, F. (1997). The Lu-Hf Isotope Geochemistry of Chondrites and the Evolution of the Mantle-Crust System. *Earth Planet. Sci. Lett.* 148, 243–258. doi:10.1016/S0012-821X(97)00040-X

Carpentier, M., Chauvel, C., Maury, R. C., and Mattielli, N. (2009). The "Zircon Effect" as Recorded by the Chemical and Hf Isotopic Compositions of Lesser Antilles Forearc Sediments. *Earth Planet. Sci. Lett.* 287 (1-2), 86–99. doi:10.1016/j.epsl.2009.07.043

Cheng, W. B., Dong, S. Y., Jin, C. H., Zhao, B., Zhang, Y., and Wang, C. (2019). Characteristics of Elemental Geochemistry and Petrogenesis Discussion of the Emeishan Basalts in Muchuan Area, Sichuan Province. *J. Mineral. Petrol.* 39 (04), 49–60. (in Chinese). doi:10.19719/j.cnki.1001-6872.2019.04.06

Chi, Q. H., and Yan, M. C. (2007). *Handbook of Elemental Abundance for Applied Geochemistry*. Beijing: Geological Publishing House, 1–148. (in Chinese).

Chung, S.-L., and Jahn, B.-m. (1995). Plume-Lithosphere Interaction in Generation of the Emeishan Flood Basalts at the Permian-Triassic Boundary. *Geol.* 23 (10), 889. doi:10.1130/0091-7613(1995)023<0889:pliigo>2.3.co;2

Coffin, M. F., and Eldholm, O. (1994). Large Igneous Provinces: Crustal Structure, Dimensions, and External Consequences. *Rev. Geophys.* 32 (1), 1–36. doi:10.1029/93RG02508

Courtillot, V. E., and Renne, P. R. (2003). On the Ages of Flood basalt Events. *Comptes Rendus Geosci.* 335 (1), 113–140. doi:10.1016/S1631-0713(03)00006-3

Duggen, S., Hoernle, K., Van Den Bogaard, P., and Garbe-schönberg, D. (2005). Post-Collisional Transition From Subduction- to Intraplate-Type Magmatism in the Westernmost Mediterranean: Evidence for Continental-Edge Delamination of Subcontinental Lithosphere. *J. Petrol.* 46 (6), 1155–1201. doi:10.1093/petrology/egi013

Fan, W., Zhang, C., Wang, Y., Guo, F., and Peng, T. (2008). Geochronology and Geochemistry of Permian Basalts in Western Guangxi Province, Southwest China: Evidence for Plume-Lithosphere Interaction. *Lithos.* 102, 218–236. doi:10.1016/j.lithos.2007.09.019

Fan, W. M., Wang, Y. J., Peng, T. P., Miao, L. C., and Guo, F. (2004). The Ar-Ar and U-Pb Chronology of Late Paleozoic Basalts in Western Guangxi and Their Constraints on the Emeishan Basalt Province Eruption Age. *Chi. Sci. Bull.* 49 (18), 1892–1900. (in Chinese)

Fodor, R. V. (1987). Low- and High-TiO2 Flood Basalts of Southern Brazil: Origin From Picritic Parentage and a Common Mantle Source. *Earth Planet. Sci. Lett.* 84 (4), 423–430. doi:10.1016/0012-821X(87)90007-0

Frey, F. A., and Prinz, M. (1978). Ultramafic Inclusions From San Carlos, Arizona: Petrologic and Geochemical Data Bearing on Their Petrogenesis. *Earth Planet. Sci. Lett.* 38 (1), 129–176. doi:10.1016/0012-821X(78)90130-9

Goldstein, S. L., O'Nions, R. K., and Hamilton, P. J. (1984). A Sm-Nd Isotopic Study of Atmospheric Dusts and Particulates From Major River Systems. *Earth Planet. Sci. Lett.* 70, 221–236. doi:10.1016/0012-821X(84)90007-4

Halpin, J. A., Tran, H. T., Lai, C.-K., Meffre, S., Crawford, A. J., and Zaw, K. (2016). U-pb Zircon Geochronology and Geochemistry from NE Vietnam: A 'Tectonically Disputed' Territory Between the Indochina and South China Blocks. *Gondwana Res.* 34, 254–273. doi:10.1016/j.gr.2015.04.005

Hao, Y. L., Zhang, Z. C., Wang, F. S. M., and Mahoney, J. J. (2004). Petrogenesis of High-Ti and Low-Ti Basalts From the Emeishan Large Igneous Province. *Geol. Rev.* 50 (6), 587–592. (in Chinese). doi:10.16509/j.georeview.2004.06.005

He, B., Xu, Y.-G., Huang, X.-L., Luo, Z.-Y., Shi, Y.-R., Yang, Q.-J., et al. (2007). Age and Duration of the Emeishan Flood Volcanism, SW China: Geochemistry and SHRIMP Zircon U-Pb Dating of Silicic Ignimbrites, Post-Volcanic Xuanwei Formation and clay Tuff at the Chaotian Section. *Earth Planet. Sci. Lett.* 255 (3-4), 306–323. doi:10.1016/j.epsl.2006.12.021

He, B., Xu, Y. G., Chung, S. L., Long, X., and Wang, Y. (2003). Sedimentary Evidence for a Rapid, Kilometer-Scale Crustal Doming Prior to the Eruption of the Emeishan Flood Basalts. *Earth Planet. Sci. Lett.* 213 (3-4), 391–405. doi:10.1016/S0012-821X(03)00323-6

Hoskin, P. W. O., and Schaltegger, U. (2003). 2. The Composition of Zircon and Igneous and Metamorphic Petrogenesis. *Rev. mineralogy Geochem.* 53 (1), 27–62. doi:10.2113/053002710.1515/9781501509322-005

Hou, T., Zhang, Z. C., Kusky, T., Du, Y. S., Liu, J. L., and Zhao, Z. D. (2011). A reappraisal of the high-Ti and low-Ti classification of basalts and petrogenetic linkage between basalts and mafic-ultramafic intrusions in the Emeishan Large Igneous Province, SW China. *Ore Geol. Rev.* 41 (1), 133–143. doi:10.1016/j.oregeorev.2011.07.005

Hou, Z. Q., Chen, W., and Lu, J. R. (2006). The 259Ma Continental Overflow Basalt Eruption Event in Emeishan Large Diagenetic Province, Sichuan, China: Evidence From Laser 40Ar/39Ar Dating. *Acta Geologica Sinica.* 8, 1130, 2006. (in Chinese).

Huang, W. L., Liu, X. J., Shi, Y., Xu, J. F., Liao, S., Guo, L., et al. (2015). Geochemistry of Extreme High Ti/Y Mafic Rocks from Western Guangxi: Implications for the Primitive Magma of High Ti basalt of Emeishan Mantle Plume? *Geol. Bull. China.* 34 (2/3), 474–486. CNKI:SUN:ZQYD. (in Chinese).

Jacobsen, S. B., and Wasserburg, G. J. (1980). Sm-Nd Isotopic Evolution of Chondrites. *Earth Planet. Sci. Lett.* 50, 139–155. doi:10.1016/0012-821X(84)90109-2

Jahn, B. M., Wu, F. Y., Lo, C. H., and Tsai, C. H. (1999). Crust–Mantle Interaction Induced by Deep Subduction of the Continental Crust: Geochemical and Sr–Nd Isotopic Evidence From Post-Collisional Mafic–Ultramafic Intrusions of the Northern Dabie Complex, Central China. *Chem. Geology.* 157 (1–2), 119–146. doi:10.1016/S0009-2541(98)00197-1

Kempton, P. D., Pearce, J. A., Barry, T. L., Fitton, J. G., Langmuir, C., and Christie, D. M. (2002). Sr-Nd-Pb-Hf Isotope Results From ODP Leg 187: Evidence for Mantle Dynamics of the Australian-Antarctic Discordance and Origin of the Indian MORB Source. *Geochem.-Geophys.-Geosyst.* 3 (12), 1–35. doi:10.1029/2002GC000320

Klemme, S., and O'Neill, H. S. (2000). The Near-Solidus Transition From Garnet Lherzolite to Spinel Lherzolite. *Contrib. Mineral. Petrol.* 138 (3), 237–248. doi:10.1007/s004100050560

Lai, S., Qin, J., Li, Y., Li, S., and Santosh, M. (2012). Permian High Ti/Y Basalts From the Eastern Part of the Emeishan Large Igneous Province, Southwestern China: Petrogenesis and Tectonic Implications. *J. Asian Earth Sci.* 47, 216–230. doi:10.1016/j.jseaes.2011.07.010

Li, C. M., Qin, H. F., and Jiang, J. (2019). Regional Geological Survey Report of Longlin (Nanning, China). *Guangxi Geol. Surv. Inst.* 1–336. (in Chinese).

Li, H. B. (2012). Mantle Plume Geodynamic Significances of the Emeishan Large Igneous Province: Evidence from Mafic Dykes, Geochemistry and Stratigraphic Records. *China Univ. Geosciences.*, 1–185. (in Chinese).

Li, J., Xu, J. F., He, B., Xu, Y. G., and Dong, Y. H. (2008). Sr-Nd-Os Isotopic Geochemistry of Permian Picrites From Muliarea, Southeast Tibet. *Acta Petrologica Sinica.* 24 (02), 337–347. CNKI:SUN:YSXB. (in Chinese).

Liao, S., Liu, X. J., Shi, Y., Huang, W. L., and Guo, L. (2013). The Product of Interaction Between Mantle Plume and Island Arc Magma: Evidence From Basic Rocks in Diabase Gold Deposits in Western Guangxi. *Acta Minera Sinica.* 33 (S2), 111–113. (in Chinese). doi:10.16461/j.cnki.1000-4734.2013.s2.493

Liew, T. C., and Hofmann, A. W. (1988). Precambrian Crustal Components, Plutonic Associations, Plate Environment of the Hercynian Fold Belt of Central Europe: Indications From a Nd and Sr Isotopic Study. *Contrib. Mineral. Petrol.* 98, 129–138. doi:10.1007/BF00402106

Long, X., Yigang, X., Jifeng, X., Bin, H., and Franco, P. (2004). Chemostratigraphy of Flood Basalts in the Garzê-Litang Region and Zongza Block: Implications for Western Extension of the Emeishan Large Igneous Province, SW China. *Acta Geologica Sinica - English Edition.* 78, 61–67. doi:10.1111/j.1755-6724.2004.tb00675.x

Ludwig, K. R. (2003). User's Manual for Isoplot /Ex rev.3.00: A Geochronological Toolkit for Microsoft Excel, *Berkeley Geochronology Center.* 4. 1–70.

Lugmair, G. W., and Marti, K. (1978). Lunar Initial 143Nd/144Nd: Differential Evolution of the Lunar Crust and Mantle. *Earth Planet. Sci. Lett.* 39, 349–357. doi:10.1016/0012-821X(78)90021-3

Mahoney, J. J., and Coffin, F. (1997). *Large Igneous Provinces: Continental, Oceanic, and Planetary Flood Volcanism*. Washington, DC: American Geophysical Union, 273–295.

Mckenzie, D., and Bickle, M. J. (1988). The Volume and Composition of Melt Generated by Extension of the Lithosphere. *J. Petrology.* 29, 625–679. doi:10.1093/petrology/29.3.625

McKenzie, D., and O'Nions, R. K. (1991). Partial Melt Distributions From Inversion of Rare Earth Element Concentrations. *J. Petrology.* 32 (5), 1021–1091. doi:10.1093/petrology/32.5.1021

Meschede, M. (1986). A Method of Discriminating Between Different Types of Mid-Ocean Ridge Basalts and Continental Tholeiites With the Nb-Zr-Y Diagram. *Chem. Geology.* 56 (3-4), 207–218. doi:10.1016/0009-2541(86)90004-5

Nebel, O., Scherer, E. E., and Mezger, K. (2011). Evaluation of the 87Rb Decay Constant by Age Comparison Against the U-Pb System. *Earth Planet. Sci. Lett.* 301, 1–8. doi:10.1016/j.epsl.2010.11.004

Nicholas, T. A., Gerald, K. C., Joseph, L. W., and Valeri, A. F. (1993). Mantle and Crustal Contributions to Continental Flood Volcanism. *Tectonophysics.* 223, 39–52. doi:10.1016/0040-1951(93)90156-E

Özdemir, Y., and Güleç, N. (2014). Geological and Geochemical Evolution of the Quaternary Süphan Stratovolcano, Eastern Anatolia, Turkey: Evidence for the Lithosphere-Asthenosphere Interaction in Post-Collisional Volcanism. *J. Petrol.* 55 (1), 37–62. doi:10.1093/petrology/egt060

Patchett, P. J., Vervoort, J. D., Söderlund, U., and Salters, V. J. M. (2004). Lu-Hf and Sm-Nd Isotopic Systematics in Chondrites and Their Constraints on the Lu-Hf Properties of the Earth. *Earth Planet. Sci. Lett.* 222 (1), 29–41. doi:10.1016/j.epsl.2004.02.030

Patchett, P. J., White, W. M., Feldmann, H., Kielinczuk, S., and Hofmann, A. W. (1984). Hafnium/Rare Earth Element Fractionation in the Sedimentary System and Crustal Recycling into the Earth's Mantle. *Earth Planet. Sci. Lett.* 69 (2), 365–378. doi:10.1016/0012-821X(84)90195-X

Pearce, J. A., and Cann, J. R. (1973). Tectonic Setting of Basic Volcanic Rocks Determined Using Trace Element Analyses. *Earth Planet. Sci. Lett.* 19 (2), 290–300. doi:10.1016/0012-821X(73)90129-5

Pearce, J. A., Ernst, R. E., Peate, D. W., and Rogers, C. (2021). LIP Printing: Use of Immobile Element Proxies to Characterize Large Igneous Provinces in the Geologic Record. *Lithos.* 392-393, 106068. doi:10.1016/j.lithos.2021.106068

Pearce, J. A. (1982). Trace Element Characteristics of Lavas From Destructive Plate Boundaries. *John Willey & Sons.* 8, 525–548.

Peate, D. W., Hawkesworth, C. J., Mantovani, M. M. S., Rogers, N. W., and Turner, S. P. (1999). Petrogenesis and Stratigraphy of the High-Ti/Y Urubici Magma Type in the Parana Flood Basalt Province and Implications for the Nature of 'Dupal'-type Mantle in the South Atlantic Region. *J. Petrology.* 40, 451–473. doi:10.1093/petroj/40.3.451

Peng, Z. X., Mahoney, J., Hooper, P., Harris, C., and Beane, J. (1994). A Role for Lower Continental Crust in Flood Basalt Genesis? Isotopic and Incompatible Element Study of the Lower Six Formations of the Western Deccan Traps. *Geochimica et Cosmochimica Acta.* 58 (1), 267–288. doi:10.1016/0016-7037(94)90464-2

Sderlund, U., Patchett, P. J., and Vervoort, J. D. (2004). The 176Lu Decay Constant Determined by Lu–Hf and U–Pb Isotope Systematics of Precambrian Mafic Intrusions. *Earth Planet. Sci. Lett.* 219, 311–324. doi:10.1016/S0012-821X(04)00012-3

Shellnutt, J. G. (2014). The Emeishan Large Igneous Province: A Synthesis. *Geosci. Front.* 5 (3), 369–394. doi:10.1016/j.gsf.2013.07.003

Shellnutt, J. G., Zhou, M.-F., Yan, D.-P., and Wang, Y. (2008). Longevity of the Permian Emeishan Mantle Plume (SW China): 1 Ma, 8 Ma or 18 Ma? *Geol. Mag.* 145 (3), 373–388. doi:10.1017/S0016756808004524

Söderlund, U., Patchett, P. J., Vervoort, J. D., and Isachsen, C. E. (2004). The 176 Lu Decay Constant Determined by Lu–Hf and U–Pb Isotope Systematics of Precambrian Mafic Intrusions. *Earth Planet. Sci. Lett.* 219 (3), 311–324. doi:10.1016/S0012-821X(04)00012-3

Sun, S.-s., and McDonough, W. F. (1989). Chemical and Isotopic Systematics of Oceanic Basalts: Implications for Mantle Composition and Processes. *Geol. Soc. Lond. Spec. Publications.*, 42, 313–345. doi:10.1144/GSL.SP.1989.042.01.19

Sun, S. Q., Zhang, C. J., and Zhao, S. J. (2007). Identification of the Tectonic Settings for Continental Intraplate by Trace Elements. *Geotectonica et Metallogenia.* 31 (01), 104–109. (in Chinese). doi:10.16539/j.ddgzyckx.2007.01.012

Taylor, S. R., and Mclennan, S. M. (1985). The Continental Crust: its Composition and Evolution. *J. Geology.* 94 (4), 57–72.

Taylor, S. R., McLennan, S. M., Armstrong, R. L., and Tarney, J. (1981). The Composition and Evolution of the Continental Crust: Rare Earth Element Evidence From Sedimentary Rocks and Discussion. *Philosophical Trans. R. Soc. B Biol. Sci.* 301 (1461), 398–399. doi:10.1109/WFCS.2015.7160546

Turner, S., Hawkesworth, C., Gallagher, K., Stewart, K., Peate, D., and Mantovani, M. (1996). Mantle Plumes, Flood Basalts, and Thermal Models for Melt Generation Beneath Continents: Assessment of a Conductive Heating Model and Application to the Paraná. *J. Geophys. Res.* 101 (B5), 11503–11518. doi:10.1029/96JB00430

Vervoort, J. D., and Blichert-Toft, J. (1999). Evolution of the Depleted Mantle: Hf Isotope Evidence From Juvenile Rocks Through Time. *Geochimica et Cosmochimica Acta.* 63, 533–556. doi:10.1016/S0016-7037(98)00274-9

Vervoort, J. D., Patchett, P. J., Albarede, F., Blicherttoft, J., Rudnick, R. L., and Downes, H. (2000). Hf-Nd Isotopic Evolution of the Lower Crust. *Earth Planet. Sci. Lett.* 181 (1), 115–129. doi:10.1016/S0012-821X(00)00170-9

Vervoort, J. D., Patchett, P. J., Blichert-Toft, J., and Albarède, F. (1999). Relationships Between Lu–Hf and Sm–Nd Isotopic Systems in the Global Sedimentary System. *Earth Planet. Sci. Lett.* 168 (1–2), 79–99. doi:10.1016/S0012-821X(99)00047-3

Vervoort, J. D., Plank, T., and Prytulak, J. (2011). The Hf-Nd Isotopic Composition of marine Sediments. *Geochimica et Cosmochimica Acta.* 75 (20), 5903–5926. doi:10.1016/j.gca.2011.07.046

Wang, D. Z., and Zhou, J. C. (2005). New Progress in Studying the Large Igneous Provinces. *Geol. J. China Universities.* 11 (1), 1–8. CNKI:SUN:GXDX. (in Chinese)

Wang, L., Jin, X. B., Wang, X. Y., Wu, X. K., Liu, C. F., and Duan, G. L. (2015). Forming Process of Lamprophyre From Luocheng, Northern Guangxi: Constraints from Geochemistry, Geochronology and Sr-Nd-Pb Isotopes. *Geol. Sci. Technology Inf.* 34 (01), 10–19. CNKI:SUN:DZKQ (in Chinese).

Wang, L., Wang, G., Lei, S., Wang, W., Qing, M., Jia, L., et al. (2016). Geochronology, Geochemistry and Sr-Nd-Pb-Hf Isotopes of the Paleoproterozoic Mafic Dykes From the Wulashan Area, North China Craton: Petrogenesis and Geodynamic Implications. *Precambrian Res.* 286, 306–324. doi:10.1016/j.precamres.2016.09.009

Wang, Y. L., Zhang, C. J., and Xiu, S. Z. (2001). Th/Hf-Ta/Hf Identification of Tectonic Setting of Basalts. *Acta Petrologica Sinica.* 17 (3), 413–421. CNKI:SUN:YSXB(in Chinese).

Wang, Y., and Xing, C. M. (2018). Compositions of Clinopyroxenes From the Ertan High-Ti basalt and Baima Layered Intrusion of the Emeishan Large Igneous Province: Implication for a Genetic Link of the High-Ti basalt and Layered Intrusion. *Bull. Mineralogy, Petrology Geochem.* 37 (06), 1019–1034. (in Chinese). doi:10.19658/j.issn.1007-2802.2018.37.113

Wilson, M. (1989). *Igneous Petrogenesis*. London: SpringerHarper Collins Academic, 466.

Wu, H. R., Kuang, G. D., and Wang, Z. C. (1997). Preliminary Study on the Late Paleozoic Tectonic Sedimentary Setting in Guangxi. *Scientia Geologica Sinica.* 32 (1), 11–18. CNKI:SUN:DZKX (in Chinese).

Wu, H. R., Kuang, G. D., and Wang, Z. C. (1993). Reinterpretation of Basic Igneous Rocks in Western Guangxi and its Tectonic Implications. *Scientia Geologica Sinica.* 32 (3), 288–289. CNKI:SUN:DZKX (in Chinese).

Xia, L. Q., Xu, X. Y., Li, X. M., Xia, Z. C., and Ma, Z. P. (2012). Comparison of Three Large Igneous Provinces (Emeishan, Siberia, Deccan) in Asia. *Northwest. Geol.* 45(02), 1–26. (in Chinese)

Xiao, L., Xu, Y.-G., Chung, S.-L., He, B., and Mei, H. (2003). Chemostratigraphic Correlation of Upper Permian Lavas From Yunnan Province, China: Extent of the Emeishan Large Igneous Province. *Int. Geology. Rev.* 45 (6), 753–766. doi:10.2747/0020-6814.45.8.753

Xiao, L., Xu, Y. G., Mei, H. J., Zheng, Y. F., He, B., and Pirajno, F. (2004). Distinct Mantle Sources of Low-Ti and High-Ti Basalts From the Western Emeishan Large Igneous Province, SW China: Implications for Plume-Lithosphere Interaction. *Earth Planet. Sci. Lett.* 228 (3-4), 525–546. doi:10.1016/j.epsl.2004.10.002

Xu, J., Xia, X.-P., Wang, Q., Spencer, C. J., He, B., Lai, C.-K., et al. (2021). Low-δ18O A-Type Granites in SW China: Evidence for the Interaction Between the Subducted Paleotethyan Slab and the Emeishan Mantle Plume. *GSA Bull.* doi:10.1130/B35929.1

Xu, J., Xia, X. P., Lai, C. K., Zhou, M., Ma, P., and Ma, P. F. (2019). First Identification of Late Permian Nb-Enriched Basalts in Ailaoshan Region (SW Yunnan, China): Contribution From Emeishan Plume to Subduction of Eastern Paleotethys. *Geophys. Res. Lett.* 46 (5), 2511–2523. doi:10.1029/2018GL081687

Xu, Y.-G., He, B., Chung, S.-L., Menzies, M. A., and Frey, F. A. (2004). Geologic, Geochemical, and Geophysical Consequences of Plume Involvement in the Emeishan Flood-Basalt Province. *Geol.* 32 (10), 917–920. doi:10.1130/G20602.1

Xu, Y., Chung, S. L., Jahn, B. M., and Wu, G. (2001). Petrologic and Geochemical Constraints on the Petrogenesis of Permian–Triassic Emeishan Flood Basalts in Southwestern China. *Lithos.* 58 (3-4), 145–168. doi:10.1016/S0024-4937(01)00055-X

Xu, Y. G., He, B., Luo, Z. Y., and Liu, H. Q. (2013). Study of Mantle Plumes and Large Igneous Provinces in China: an Overview and Perspectives. *Bull. Mineralogy, Petrology Geochem.* 32 (01), 25–39. CNKI:SUN:KYDH (in Chinese).

Ye, X. F., Zong, K. Q., Zhang, Z. M., He, Z. Y., Liu, Y. S., Hu, Z. C., et al. (2013). Geochemistry of Neoproterozoic Granite in Liuyuan Area of Southern Beishan Orogenic belt and its Geological Significance. *Geol. Bull. China*. 32 (Z1), 307–317. CNKI:SUN:ZQYD (in Chinese).

Zeng, R.-Y., Lai, J.-Q., Mao, X.-C., Yan, J., Zhang, C.-G., and Xiao, W.-Z. (2021a). Geochemistry and Zircon Ages of the Yushigou Diabase in the Longshoushan Area, Alxa Block: Implications for Crust-Mantle Interaction and Tectonic Evolution. *Geol. Mag.* 158 (4), 685–700. doi:10.1017/S0016756820000783

Zeng, R. Y., Lai, J. Q., Mao, X. C., Xiao, W. Z., Yan, J., Zhang, C. G., et al. (2021b). Petrogenesis and Tectonic Significance of the Early Devonian Lamprophyres and Diorites in the Alxa Block, NW China. *Geochemistry.* 81, 125685. doi:10.1016/j.chemer.2020.125685

Zeng, R. Y., Lai, J. Q., Mao, X. C., Li, B., Zhang, J. D., Bayless, R., et al. (2018). Paleoproterozoic Multiple Tectonothermal Events in the Longshoushan Area, Western North China Craton and Their Geological Implication: Evidence from Geochemistry, Zircon U-Pb Geochronology and Hf Isotopes. *Minerals.* 8 (9), 361. doi:10.3390/min8090361

Zhang, B., Guo, F., Zhang, X., Wu, Y., Wang, G., and Zhao, L. (2019). Early Cretaceous Subduction of Paleo-Pacific Ocean in the Coastal Region of SE China: Petrological and Geochemical Constraints from the Mafic Intrusions. *Lithos.* 334-335, 8–24. doi:10.1016/j.lithos.2019.03.010

Zhang, X. J., and Xiao, J. F. (2014). Zircon U-Pb Geochronology, Hf Isotope and Geochemistry Study of the Late Permian Diabase in the Northwest Guangxi Autonomous Region. *Bull. Mineralogy, Petrology Geochem.* 33 (02), 163–176. (in Chinese). doi:10.3969/j.issn.1007-2802.2014.02.003

Zhang, Z. C. (2009). A Discussion on Some Important Problems Concerning the Emeishan Large Igneous Province. *Geology. China.* 36 (3), 634–646. CNKI:SUN:DIZI (in Chinese).

Zhang, Z. C., Wang, F. S., Fan, W. M., Deng, H. L., Xu, Y. G., Xu, J. F., et al. (2001). A Discussion on Some Problems Concerning the Study of the Emeishan Basalts. *Acta Petrologica et Mineralogica.* 20 (3), 239–246. CNKI:SUN:YSKW (in Chinese).

Zhou, M.-F., Zhao, J.-H., Qi, L., Su, W., and Hu, R. (2006). Zircon U-Pb Geochronology and Elemental and Sr-Nd Isotope Geochemistry of Permian Mafic Rocks in the Funing Area, SW China. *Contrib. Mineral. Petrol.* 151 (1), 1–19. doi:10.1007/s00410-005-0030-y

Zindler, A., and Hart, S. (1986). Chemical Geodynamics. *Annu. Rev. Earth Planet. Sci.* 14 (1), 493–571. doi:10.1146/annurev.ea.14.050186.002425

Conflict of Interest: The authors declare that the research was conducted in the absence of any commercial or financial relationships that could be construed as a potential conflict of interest.

Publisher's Note: All claims expressed in this article are solely those of the authors and do not necessarily represent those of their affiliated organizations, or those of the publisher, the editors and the reviewers. Any product that may be evaluated in this article, or claim that may be made by its manufacturer, is not guaranteed or endorsed by the publisher.

frontiers in Earth Science

ORIGINAL RESEARCH
published: 11 October 2021
doi: 10.3389/feart.2021.731233

Genesis of High-Mg Adakites in the Southeastern Margin of North China Craton: Geochemical and U-Pb Geochronological Perspectives

Shuo Zheng[1,2], *Yanfei An*[1]*, *Chunkit Lai*[3], *Hongzhi Wang*[4] and *Yunfeng Li*[4]

[1]School of Resources and Environment Engineering, Anhui University, Hefei, China, [2]Exploration Research Institute, Anhui Provincial Bureau of Coal Geology, Hefei, China, [3]Faculty of Science, University of Brunei Darussalam, Bandar Seri Begawan, Brunei, [4]Third Exploration Team of Anhui Provincial Bureau of Coal Geology, Suzhou, China

OPEN ACCESS

Edited by:
Hassan Mirnejad,
Miami University, United States

Reviewed by:
Wayne Powell,
Brooklyn College (CUNY), United States
Mohsen Rezaei,
Shahid Chamran University of Ahvaz, Iran

***Correspondence:**
Yanfei An
any@ahu.edu.cn

Specialty section:
This article was submitted to Economic Geology, a section of the journal Frontiers in Earth Science

Received: 26 June 2021
Accepted: 21 September 2021
Published: 11 October 2021

Citation:
Zheng S, An Y, Lai C, Wang H and Li Y (2021) Genesis of High-Mg Adakites in the Southeastern Margin of North China Craton: Geochemical and U-Pb Geochronological Perspectives. Front. Earth Sci. 9:731233. doi: 10.3389/feart.2021.731233

In the eastern North China Craton (NCC), Mesozoic tectonics was dominated by the Paleo-Pacific subduction rollback and the Tanlu crustal-scale fault movement. The regional transtension had generated extensive adakitic magmatism, some Cu-Au ore-forming but others not. To establish the geodynamic setting and any metallogenic link for the adakites from the southeastern NCC margin, we analyzed the ore-barren adakitic rocks from underground mines in the Huaibei-Linhuan coalfield (where surface igneous outcrops are scarce), and compared their ages and geochemistry with other mineralized and ore-barren adakites across Eastern China. Zircon U-Pb dating reveals two magmatic episodes in the Huaibei-Linhuan coalfield: 1) early-Early Cretaceous (ca. 130–129 Ma) (quartz-)diorite and granodiorite, and 2) late-Early Cretaceous (ca. 115.8 and 105.8 Ma) microgabbro and dolerite. Whole-rock geochemistry indicates that the (quartz-)diorite and granodiorite are high-Mg adakitic, featured by low K_2O/Na_2O (avg. 0.33), high Sr/La (avg. 44.3), and lack of correlation between SiO_2 (fractionation index) and Sr/Y (avg. 56.55) and MREE/HREE (avg. 1.09), resembling typical adakites derived from oceanic-slab partial melting. Geochronological correlation with the regional tectonic events suggests that the slab-melting may have been caused by the Paleo-Pacific subduction rollback. Further extension and crustal thinning in the late-Early Cretaceous along the southern Tanlu fault may have formed the gabbro-dolerite in the coalfield. Geochemical comparison suggests that parental magma of the Huaibei-Linhuan adakites may have had similar water content [similar zircon 10,000*(Eu/Eu*)/Y and Eu/Eu* ratios] to typical porphyry Cu-Au ore-forming magmas, yet the former may have been considerably more reduced (lower zircon Ce/Nd and whole-rock V/Sc ratios). We considered that the assimilation of Carboniferous-Permian coal seams in the area may have further lowered the magma fO_2 and thus its potential to form Cu-Au mineralization.

Keywords: high-Mg adakites, North China Craton, Paleo-Pacific subduction, Cretaceous, zircon U-Pb dating

INTRODUCTION

The Mesozoic eastern North China craton (NCC) is tectonically complex due to the co-influence of a number of tectonic events, including the North China-South China collision, the Paleo-Pacific subduction and rollback, the gradual NCC decratonization, together with the ~500-km sinistral movement of the regional Tanlu fault zone and the accompanied pull-apart basin formation (e.g., Li et al., 2012, 2017; Hong et al., 2020; Zhang et al., 2020; Sun et al., 2021; Ye et al., 2021). The complex tectonic interactions resulted in the formation of important Cu-Au mineralization across the region, notably the world-class Jiaodong-Liaodong orogenic gold province (e.g., Goldfarb and Santosh, 2014; Zhang Z. et al., 2019; Liu et al., 2019, 2020; Li J. et al., 2020; Deng et al., 2020), and the Cu-Au-Fe polymetallic Middle-Lower Yangtze River Metallogenic Belt (MLYRB) (e.g., Pirajno and Zhou, 2015; Zhou et al., 2015; Zhang Y. et al., 2019; Lü et al., 2021). Many of these deposits are closely related in space-time to adakitic magmatism, yet many adakitic units in the region are also ore-barren (e.g., Liu S.-A. et al., 2010; Li C. et al., 2020; Jiang et al., 2020). Genetic link between adakitic magmatism and Cu-Au mineralization is rather well-established (e.g., Reich et al., 2003; Richards and Kerrich, 2007; Chiaradia et al., 2012), yet understanding why some adakites are ore-barren would also benefit both ore deposit modelling and regional Cu-Au exploration (**Table 1**).

In the southeastern NCC margin (Anhui province) where the North China Alluvial Plain is currently situated, intrusive rocks are rarely exposed and thus less studied. In this study, we collected samples from various underground coal mines across the Huaibei-Linhuan coalfield (**Figure 1**). Through zircon U-Pb dating and whole-rock geochemical analyses, and by comparing geochemically with the coeval Cu-Au mineralized/barren adakites across Eastern China (esp. in the MLYRB and along/near the southern Tanlu fault), we discuss why some adakites are ore-forming and some are not.

TABLE 1 | Summary of ages, intrusions and lithology of major barren and fertile adakite units in Eastern China.

No.	Location	Intrusion	Lithology	Ages (Ma)	Barren or fertile	Source
1	BWGB	Caoshan	Monzogranite	109 ± 3	Au	Li et al. (2020a)
2		Donglushan	Diorite porphyry	113 ± 1		
3		Jiangshan	Altered granite porphyry	117 ± 3		
4		Jiuhuashan	Granodiorite	115 ± 3		
5		Huaiguang	Granodiorite	118 ± 3		Liu et al. (2012)
6		Jingshan	Granodiorite	118 ± 1		
7		Zhuishan	Monzogranite	112 ± 1		
8		Caoshan	Monzogranite	112 ± 2		Yang et al. (2010)
9		Huaiguang	Granodiorite	130 ± 2		
10		Nvshan	Syenogranite	130 ± 3		
11	STLF	Damaocun	Monzonite	128 ± 1	Ore-Barren	Liu et al. (2010a)
12		Fangjiazhuang	Monzonite	129 ± 1		
13		Xiaolizhuang	Quartz monzonite	125 ± 1		
14		Qiaotouji	Monzonite	132 ± 2		
15		Haizi	Diorite	130 ± 2		In this study
16		Taiping	diorite	129 ± 1		
17		Qingdong	Microgabbro	116 ± 1		
18		Yuan-1	dolerite	106 ± 2		
19	MLYRB	Datuanshan	Carbonate	139 ± 3	Cu-Au-Mo	Mao et al. (2006)
20		Tongguanshan	Granodiorite	137 ± 1	Cu-Au	Jiang et al. (2020)
21		Longhushan	Diorite	138 ± 3	Cu-Au-Mo	Sun et al. (2003)
22		Shanxingshan	Granodiorite	138 ± 3	Mo	
23		Xianlinbu	Granodiorite	133 ± 1	Fe-Mo	
24		Yueshan	Quartz diorite	136 ± 2	Cu-Mo	
25		Fengshandong	Granodiorite	144 ± 2	Cu-Mo	Xie et al. (2007)
26		Qianjiawan	Diorite	138 ± 2	Cu-Au	
27		Ruanjiawan	Granodiorite	144 ± 2	W-Cu-Mo	
28		Tongshankou	Granodiorite	142 ± 2	Cu-Mo	
29		Tonglüshan	Granodiorite	138 ± 2	Cu-Fe	
30	DOB	Liujiawa	Gabbronorite	128 ± 1	Ore-Barren	Zhang et al. (2013)
31		Liujiawa	Diorite	127 ± 2		
32		Liguo	Dioritic porphyry	131 ± 3	Fe	Xu et al. (2004)
33		Jiagou	Monzodioritic porphyry	132 ± 4	Ore-Barren	
34		Banjing	Diorite	126 ± 2		Zhou et al. (2019)
35		Banjing	Diorite	127 ± 1		Yang et al. (2008)
36		Fengshan	Monzodiorite porphyry	129 ± 2		
37		Caishan	Quartz diorite	131 ± 1		

**BWGB: Bengbu-Wuhe Gold Belt; STLF: Southern Tan-Lu Fault; MLYRB: Middle-Lower Yangtze River Metallogenic Belt; DOB: Dabie Orogen Belt.*

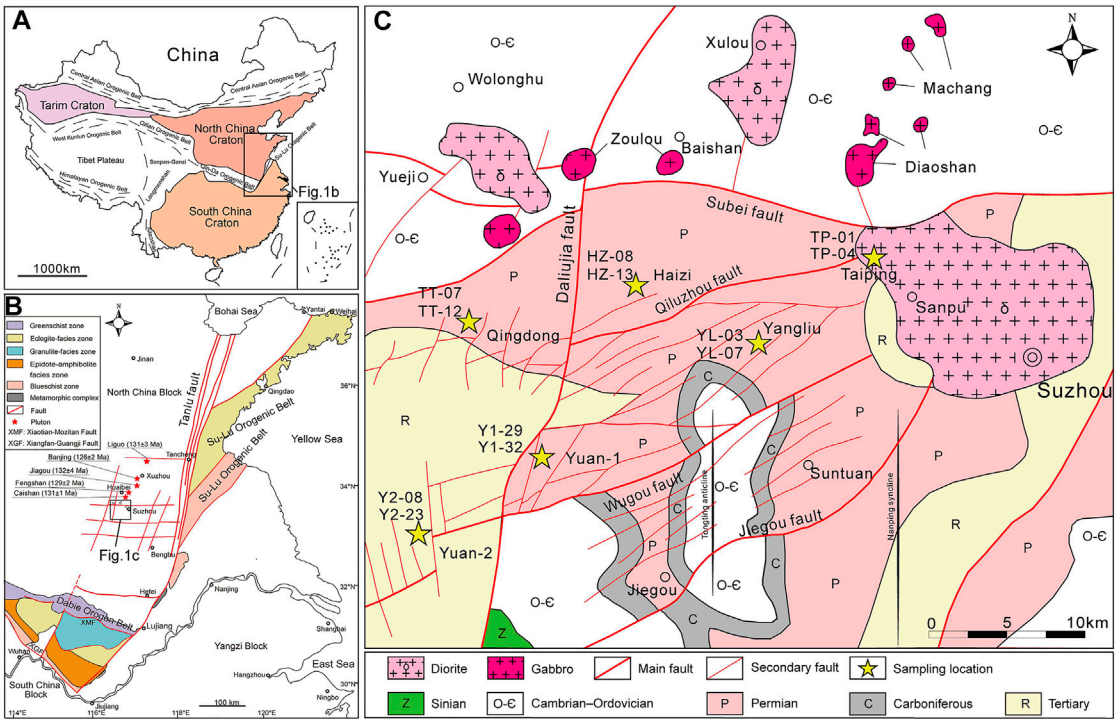

FIGURE 1 | Tectonic maps of China **(A)** and North China **(B)**, and **(C)** geologic map of the Huaibei-Linhuan coalfield, showing the distribution of basement rocks, sampling sites and major structures (modified after Zhao et al., 2016; Zhu et al., 2005, 2009; An et al., 2018).

Geological Background

Archean to Mesozoic geological record is well-preserved in the NCC, except locally in its eastern part due to later decratonization. The craton was largely formed by extensive Archean tonalite-trondhjemite-granodiorite (TTG) emplacement, and remained relatively stable throughout the Paleozoic-Early Triassic. Afterward, the convergence between the Yangtze and North China plates (collided in the Early-Middle Jurassic) had caused widespread Mesozoic magmatism, forming the Cretaceous intermediate-mafic and bimodal (sub-) volcanic rocks in the southern NCC margin (Li et al., 2017). Some intrusive rocks were suggested to have formed by mantle underplating and had a crustal-mantle mixed source. Geochemistry of these rocks implies that the lithospheric mantle beneath the NCC is highly heterogenous (Yang et al., 2008; Zhao et al., 2009; Xia et al., 2013).

Although igneous rock exposure is generally poor in the southeastern NCC margin, many intrusions are encountered in the underground coal mines there, notably those in the Huaibei-Linhuan coalfield. The Huaibei coalfield is located close to the Xuzhou–Suzhou fault system and between the EW-trending Fengpei and Bangpu uplift zones (**Figure 1B**). Faults of various sizes and types were documented in the coalfield, but consist mainly of high-angle normal faults and rare reverse faults. The regional Huangji and Subei faults were interpreted to have formed in the same stage as the regional Carboniferous-Permian folding (which formed the Tongting syncline and Nanping anticline) (**Figure 1C**) (An et al., 2018). The Linhuan coalfield is bounded by the N-S-trending Taihe-Wuhe and Subei faults, and by the E-W-trending Nanping and Fengwo faults, giving a rectangular shape to the coalfield. The Taihe-Wuhe fault is a steeply-dipping normal fault, which connects to the Tanlu fault zone in the east. Secondary faults and interlayer structures are well-developed in the coalfield: the former is mainly NE-trending and less-commonly NW-trending, whilst the latter is developed on both hanging-wall and footwall of the coal seams, which locally damaged the coal seams. Major fault activities likely commenced in the Jurassic (early-stage Yanshanian orogeny), during which the regional stress transition (to NW-SE-trending) may have formed the Xuzhou-Suzhou imbricated structure. Tectonic regime in Eastern China changed again to active extension during the middle- and late-stage Yanshanian orogeny, forming many normal faults and fault-bounded basins. Normal faulting likely reached its peak during the Cenozoic Himalayan orogeny, during which many ancient structures were also reactivated/modified (Yao and Liu, 2012). Intermediate volcanism and plutonism were active during the Yanshanian movement, and were mainly controlled by the NNE-trending and EW-trending faults (Xu et al., 2004; Yang et al., 2010).

Previous geological survey documented that stratigraphy in the Linhuan coalfield comprises Ordovician and Carboniferous-Permian sequences (#3 Exploration Team of Anhui Bureau of Coal Geology, 2007). The coal-bearing sequences include the Upper Carboniferous Benxi and Taiyuan formations, Lower Permian Shanxi Formation, Middle Permian Shihezi

Formation, and the Middle-Upper Permian Shiqianfeng Formation. The Carboniferous sequences comprise mainly greyish mudstone in the lower part, and crystalline limestone and sandy shale-mudstone in the upper part. The Permian sequences comprise mainly sandstone and mudstone (An et al., 2018, and ref. therein). Plutonic emplacement is locally controlled by ancient faults and interlayer fractures, which likely served as magma conduits. Many Jurassic-Cretaceous intermediate-mafic dykes were identified in the Huaibei coalfield, and are controlled mainly by NNE-trending faults and minor by EW-trending and NW-trending ones. Middle Jurassic-Early Cretaceous intermediate-felsic plutons are widespread in the southern NCC margin, and eclogite xenoliths and adakitic rocks were reported in the Xuhuai area as a rectangle tectonic region in the Southern Tan-Lu Fault (STLF) showing in **Figure 1B** (Xu et al., 2006; Xu et al., 2009). Plutonic rocks intruding the coal-bearing sequence in the Huaibei coalfield include mainly diorite porphyry stock, dykes, and sills. All coal mines in the Linhuan coalfield were affected (metamorphosed) by various degrees of plutonism, which intensified toward the Subei and Daliujia faults, e.g., at the Yangliu and Haizi mines (#3 Exploration Team of Anhui Bureau of Coal Geology, 2007; Yangliu Coal Industry Co. Ltd, 2017; Zhao et al., 2019).

Intrusive rock samples in this study were collected from coal mines in the Huaibei-Linhuan coalfield. Plutons are mainly dioritic in the coal mines along the NE-trending Qiluzhou fault (Taiping, Haizi, Yangliu), whilst those in the coal mines along the NS-trending Daliujia fault (Yuandian-1, Yuandian-2, Qingdong) are mainly gabbroic and minor peridotitic.

Sampling and Analysis Methods

In this study, we analyzed igneous rock samples from six mines in the Huaibei-Linhuan coalfield, with the sampling locations shown in **Figure 1C**. Sample lithologies include (quartz-) diorite-granodiorite (n = 6) from Yangliu (YL-03, YL-07), Haizi (HZ-08, HZ-13), and Taiping (TP-01, TP-04), and microgabbro-dolerite (n = 6) from Qingdong (TT-07, TT-12), Yuandian-1 (Y1-29, Y1-32), Yuandian-2 (Y2-08, Y2-23). The rock samples were prepared into petrographic thin sections and rock powder (200 mesh) for microscopic (including SEM) observations and whole-rock geochemical analyses, respectively. Sample preparation and petrographic observation were conducted at the Geological Laboratory of the School of Resources and Environment Engineering, Anhui University. Optical microscopic analysis was performed with an Olympus BX53PLM to identify textural features and rock-forming minerals. Whole-rock major and trace elemental compositions were measured on all samples by X-ray fluorescence (XRF) and inductively coupled plasma mass spectrometry (ICP-MS), respectively.

The XRF analysis follows the Chinese national standard procedure GB/T 14506.28-2010. The powdered samples were dried at 105°C for 2–4 h and then cooled down in a desiccator. For each sample, 0.700 g was weighted and mixed with 5.200 g $Li_2B_4O_7$, 0.400 g LiF, and 0.300 g NH_4NO_3. The mixture was placed in platinum crucibles (95% Pt + 5% Au). Afterward, 1 ml LiBr (1.5%) was added to the crucibles, dried on a hot-plate, and then heat (with lid closed) at 1,200°C for 10 min to form a glass disc.

Solution ICP-MS sample preparation follows the Chinese National Standard Procedure GB/T 30714-2014. Weighted dry sample powder (0.1000 g) was placed in polytetrafluoroethylene (PTFE) bottles, mixed successively with 10 ml HNO_3, 10 ml HF, and 2 ml HCl, and then heated on hot-plate for 2–3 h to completely dissolve the samples. After cooling, the residue was washed with ultra-pure water, dried again, and then redissolved in 2.0 ml aqua reqia and 1.0 ml LH_3BO_3 on hot-plate for around 16 min. The solution was then transferred to 50 ml bottles, diluted with water and then measured (with two blanks) on an Agilent 7700e ICP-MS. The analysis follows the Chinese national standard procedure DZ/T0223-2001.

LA-ICP-MS zircon U-Pb dating was performed at the Wuhan Sample Solution Analytical Technology Co. Ltd. (China) with an Agilent 7900 ICPMS, coupled to a GeoLas HD 193 nm excimer laser ablation system. Zircon 91500 and glass NIST610 were used as external standards for U-Pb dating and trace element calibration, respectively. Each analysis incorporated a background acquisition of approximately 20–30 s followed by 50 s of data acquisition from the sample. An Excel-based software ICPMSDataCal was used to perform off-line selection and integration of background and analyzed signals, time-drift correction and quantitative calibration for trace element analysis and U-Pb dating (Liu et al., 2008; Liu et al., 2010 Y.). Concordia diagrams and weighted mean calculations were made using Isoplot/Ex_ver3 (Ludwig, 2003). Analytical conditions include: 80 mJ laser energy, 5 Hz frequency, and 32 μm laser beam size. The standards were analyzed twice for every six samples. The data processing and concordia plot production were completed with ICPMSDataCal 10.9 and Isoplot 3.0, respectively.

RESULTS

Petrographic Features

Taiping mine: Diorite samples were collected from a dyke (4–6 m thick) at 300 m depth. The rocks are dark-grey, medium-fine-grained, and massive structure. The rocks contain mainly plagioclase (75%) and hornblende (20%) and rare pyroxene (<5%). Some samples are porphyritic and have zoned plagioclase phenocrysts in a dark grey to greyish-green microcrystalline groundmass. The plagioclase grains are largely euhedral-subhedral, whilst hornblende grains are subhedral (**Figures 2A,D**).

Yangliu mine: The diorite-granodiorite samples were collected from a sill at 463–504 m depth (drill-hole 2017-02). The rocks are weakly porphyritic, with subrounded quartz and alkali feldspar phenocrysts and (minor) hornblende phenocrysts set in a dark-grey hornblende groundmass. Feldspar phenocrysts (2 mm) are generally larger than subhedral hornblende phenocrysts (0.5 mm) (**Figures 2C,F**).

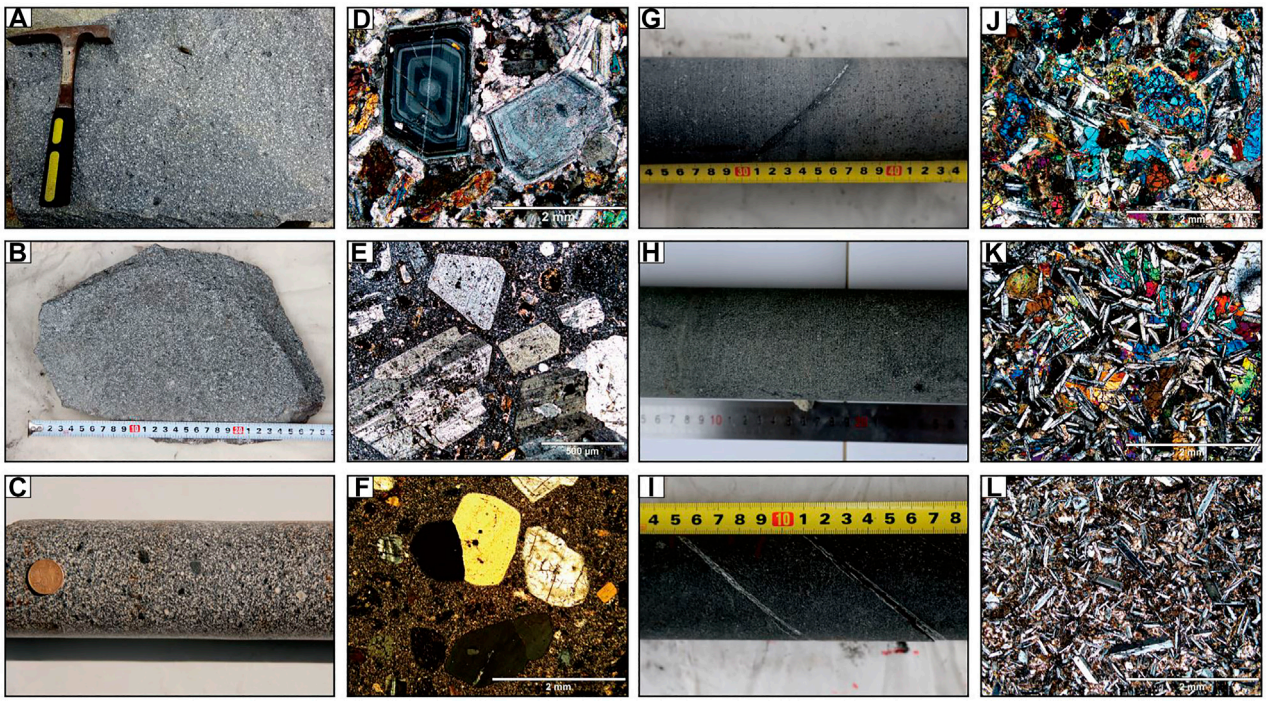

FIGURE 2 | Hand-specimen and thin-section microscopic photos of subvolcanic rocks from the Huaibei-Linhuan coalfield: **(A)** Taiping (TP-01) diorite; **(B)** Haizi (HZ-08) diorite; **(C)** Yangliu (YL-03) diorite; **(D)** Taiping granodiorite with feldspar phenocrysts; **(E)** Haizi porphyritic diorite with altered euhedral feldspar phenocrysts; **(F)** Yangliu granodiorite porphyry with quartz and plagioclase phenocrysts; **(G)** Qingdong (TT-07) microgabbro; **(H)** Yuandian-1 (Y1-29) dolerite; **(I)** Yuandian-2 (Y2-23) dolerite; **(J)** Pyroxene and plagioclase in the Qingdong microgabbro (XPL); **(K)** Plagioclase and pyroxene in the ophitic-textured Yuandian-1 dolerite (XPL); **(L)** Plagioclase and fine-grained Fe-Ti oxides in the Yuandian-2 dolerite (XPL).

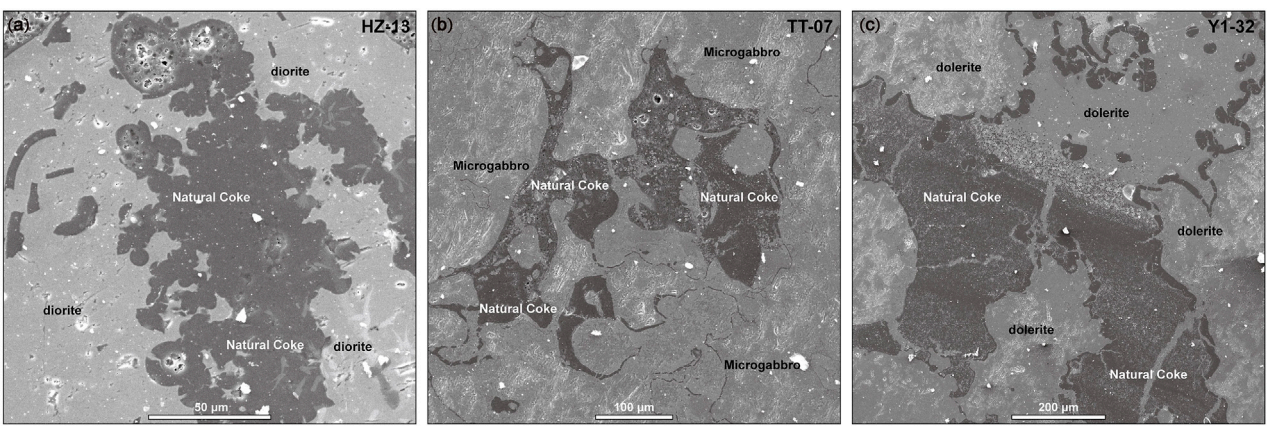

FIGURE 3 | SEM image of plutonic rock samples, showing partially-assimilated porous natural coke inclusions with rounded corroded margin: **(A)** HZ-13; **(B)** TT-07; **(C)** Y1-32.

Haizi mine: The diorite porphyry samples were collected from a dyke (8–10 m thick) at 800 m depth. The rocks are dark grey and medium-fine-grained massive, and contain mainly phenocrysts of plagioclase (60%), hornblende (20%) and pyroxene (<5%), which set in a dark-grey hornblende and (minor) pyrite groundmass (**Figures 2B,E**). Partially assimilated porous and rounded-/irregular-shaped natural coke fragments are included in the diorite (**Figure 3A**).

Qingdong mine: The microgabbro samples were collected from a sill at 478–483 m depth (drill-hole 2016-03). The rocks are greyish-green, fine-grained massive, and contain mainly plagioclase feldspars (55%), pyroxene (35%) and olivine (10%) (**Figures 2G,J**). Partially assimilated natural coke fragments, featured by being porous and rounded/irregular, are observed under SEM in the microgabbro (**Figure 3B**).

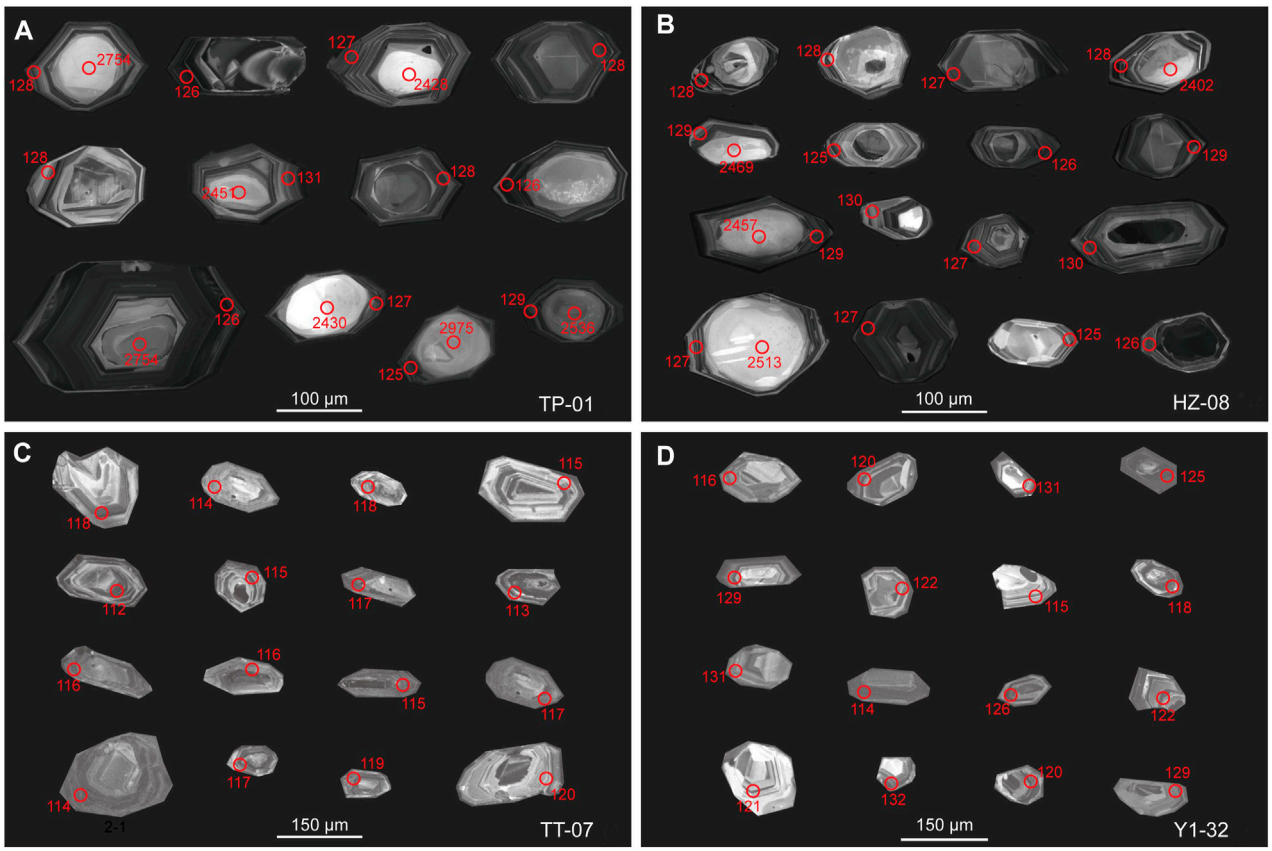

FIGURE 4 | Representative zircon CL images for the Huaibei-Linhuan intrusive rock samples: **(A)** Taiping diorite (TP-01); **(B)** Haizi diorite porphyry (HZ-08); **(C)** Qingdong microgabbro (TT-07); **(D)** Yuandian-1 dolerite (Y1-32).

Yuandian-1 mine: The dolerite samples were collected from a sill at 295–320 m depth (drill-hole 2016-06). The rocks are greyish-green, fine-medium-grained massive (weakly porphyritic), and contain euhedral-subhedral plagioclase (65%) and pyroxene (25%) phenocrysts set in a groundmass (10%) of similar mineral content (**Figures 2H,K**). Some dolerite samples contain partially assimilated natural coke fragments (**Figure 3C**).

Yuandian-2 mine: The dolerite samples were collected from a sill at 278–305 m depth (drill-hole 2016-20). The rocks are greyish-green, fine-medium-grained massive, and weakly porphyritic. The rocks have mainly plagioclase (60%), pyroxene (20%), and minor (10% each) hornblende and Fe-Ti oxides. The pyroxenes are commonly altered to fine-grained amphibole and chlorite (**Figures 2I,L**).

Zircon U-Pb Geochronology and Trace Element Geochemistry

In this study, one Taiping diorite (TP-01) and Haizi diorite porphyry (HZ-08), and one Qingdong microgabbro (TT-07) and Yuandian-1 dolerite (Y1-32) were zircon U-Pb dated. Zircon grains from all rock samples are largely similar in size (50–150 μm, mostly ~100 μm). Zircons from the diorite samples (TP-01 and HZ-08) are featured by rounded, partially resorbed inherited cores (20–120 μm, mostly 25–90 μm) surrounded by oscillatory zoned rims, giving an overall short prismatic or subrounded shape. Most zircon cores have markedly different CL reflectance (darker or brighter) from their growth rims. The cores are mostly unzoned (homogenous) but sector zoning is also found in certain grains. For the microgabbro-dolerite samples (TT-07 and Y1-32), most zircon grains do not have inherited core, and most of them are elongated prismatic (some occur as broken fragments), and are oscillatory- and/or sector-zoned (**Figure 4**).

Zircon samples from the Taiping diorite (TP-01) have high Th/U ratios for both the inherited cores (avg. 0.62) and rims (avg. 0.39), resembling typical igneous zircons (Hoskin and Black, 2000). Most age data (n = 19) from the cores cluster closely around 2,500 Ma, and yielded an upper intercept $^{206}Pb/^{238}U$ age of 2,463 ± 23 Ma (2σ, MSWD = 1.2). Meanwhile, age data (n = 21) from the rims yielded a weighted average $^{206}Pb/^{238}U$ age of 129.2 ± 1.4 Ma (2σ, MSWD = 2.0), which we interpreted to be the diorite emplacement age (**Figures 4A**, **5B**; **Table 2**).

Similarly, zircons from the Haizi diorite porphyry (HZ-08) have high Th/U ratios for both the inherited cores (avg. 0.47) and rims (avg. 0.84), resembling typical igneous zircons (Hoskin and Black, 2000). Age data (n = 19) from the cores also cluster closely around 2,500 Ma, and yielded an upper intercept $^{206}Pb/^{238}U$ age

TABLE 2 | Zircon U-Pb dating results of the plutonic rock samples from the Huaibei-Linhuan coalfield.

Spot No.	Hf	Ti	Th	U	Th/U	Isotopic ratios						Apparent ages (Ma)						Concordance
	ppm					207Pb/206Pb	1σ	207Pb/235U	1σ	206Pb/238U	1σ	207Pb/206Pb	1σ	207Pb/235U	1σ	206Pb/238U	1σ	
HZ-08C																		
HZ-08C-01	9202	11.7	38.1	31.9	1.19	0.1698	0.0056	9.8772	0.3195	0.4218	0.0063	2567	54.9	2423	29.9	2269	28.5	93%
HZ-08C-02	8414	14.0	19.5	38.8	0.50	0.1514	0.0048	9.0596	0.2811	0.4333	0.0067	2361	53.7	2344	28.4	2321	30.0	98%
HZ-08C-03	9685	17.7	1.10	16.2	0.07	0.1555	0.0070	9.3553	0.4266	0.4357	0.0095	2409	77.3	2373	41.9	2331	42.5	98%
HZ-08C-04	8435	9.86	17.4	33.1	0.53	0.1655	0.0063	10.0419	0.3869	0.4392	0.0068	2513	63.9	2439	35.6	2347	30.6	96%
HZ-08C-05	10905	7.35	55.1	76.1	0.72	0.1608	0.0043	9.8848	0.2764	0.4414	0.0058	2465	44.3	2424	25.8	2357	26.1	97%
HZ-08C-06	10007	11.6	2.03	12.0	0.17	0.1777	0.0083	10.7186	0.4708	0.4462	0.0094	2632	77.8	2499	40.8	2378	41.8	95%
HZ-08C-07	9240	14.5	15.1	66.3	0.23	0.1702	0.0047	10.6386	0.2957	0.4517	0.0057	2561	46.3	2492	25.9	2403	25.6	96%
HZ-08C-08	11063	13.4	202	221	0.91	0.1695	0.0048	10.7218	0.3114	0.4563	0.0049	2554	46.8	2499	27.0	2423	21.8	96%
HZ-08C-09	9515	10.6	6.70	6.71	1.00	0.1683	0.0105	10.5411	0.6338	0.4597	0.0114	2543	104.9	2484	55.8	2438	50.2	98%
HZ-08C-10	10489	13.0	9.04	22.0	0.41	0.1674	0.0067	10.4505	0.3924	0.4608	0.0078	2532	67.9	2476	34.8	2443	34.3	98%
HZ-08C-11	8966	68.1	13.5	29.2	0.46	0.1659	0.0129	10.0351	0.7138	0.4623	0.0124	2516	131.3	2438	65.7	2450	54.5	99%
HZ-08C-12	9849	10.8	40.7	28.1	1.45	0.1674	0.0058	10.7327	0.3832	0.4637	0.0068	2532	59.1	2500	33.2	2456	30.0	98%
HZ-08C-13	8861	15.2	16.0	26.5	0.61	0.1638	0.0064	10.5249	0.4005	0.4663	0.0078	2495	65.4	2482	35.3	2467	34.3	99%
HZ-08C-14	10590	15.4	4.95	35.6	0.14	0.1594	0.0052	10.3533	0.3701	0.4686	0.0081	2450	55.6	2467	33.1	2477	35.6	99%
HZ-08C-15	9520	18.4	0.70	4.15	0.17	0.1674	0.0113	10.6939	0.7166	0.4698	0.0158	2531	113.3	2497	62.2	2483	69.5	99%
HZ-08C-16	10230	14.3	6.83	37.7	0.18	0.1640	0.0083	10.3934	0.5197	0.4726	0.0124	2498	85.8	2470	46.3	2495	54.2	99%
HZ-08C-17	9967	16.1	10.1	13.0	0.78	0.1660	0.0080	10.6766	0.4762	0.4780	0.0094	2518	81.6	2495	41.4	2519	41.0	99%
HZ-08C-18	10287	24.9	0.99	8.71	0.11	0.1704	0.0101	10.9619	0.5897	0.4809	0.0116	2561	99.1	2520	50.1	2531	50.5	99%
HZ-08C-19	10707	23.2	102	61.5	1.66	0.1611	0.0043	10.9327	0.2949	0.4893	0.0066	2478	50.2	2517	25.2	2568	28.6	98%
HZ-08E																		
HZ-08E-01	9648	4.51	352	445	0.79	0.0501	0.0035	0.1335	0.0087	0.0202	0.0003	211	161.1	127	7.8	126	2.1	98%
HZ-08E-02	13442	2.96	122	515	0.24	0.0507	0.0034	0.1396	0.0082	0.0201	0.0004	233	157.4	133	7.3	128	2.7	96%
HZ-08E-03	7422	4.62	145	273	0.53	0.0501	0.0040	0.1368	0.0099	0.0199	0.0004	198	-13.9	130	8.9	127	2.4	97%
HZ-08E-04	9026	5.03	185	232	0.80	0.0465	0.0066	0.1365	0.0172	0.0209	0.0005	20.5	311.1	130	15.3	133	3.3	97%
HZ-08E-05	10358	0.93	84.0	245	0.34	0.0497	0.0045	0.1329	0.0113	0.0196	0.0004	189	200.0	127	10.1	125	2.4	98%
HZ-08E-06	9409	4.37	156	386	0.41	0.0514	0.0036	0.1378	0.0090	0.0197	0.0003	257	161.1	131	8.0	126	2.1	95%
HZ-08E-07	8070	4.46	131	154	0.85	0.0472	0.0039	0.1374	0.0102	0.0209	0.0004	61.2	194.4	131	9.1	133	2.7	98%
HZ-08E-08	9950	4.28	206	407	0.51	0.0486	0.0032	0.1296	0.0077	0.0197	0.0003	128	148.1	124	6.9	126	2.1	98%
HZ-08E-09	8842	6.16	232	312	0.75	0.0488	0.0035	0.1410	0.0086	0.0212	0.0004	200	98.1	134	7.6	135	2.2	99%
HZ-08E-10	9824	3.68	282	360	0.78	0.0490	0.0033	0.1345	0.0088	0.0199	0.0003	150	148.1	128	7.9	127	2.1	99%
HZ-08E-11	9396	7.97	164	334	0.49	0.0484	0.0035	0.1373	0.0088	0.0207	0.0004	120	159.2	131	7.9	132	2.2	99%
HZ-08E-12	9953	3.65	173	233	0.74	0.0482	0.0037	0.1334	0.0085	0.0203	0.0005	106	174.0	127	7.6	129	3.0	98%
HZ-08E-13	8972	7.31	84.7	270	0.31	0.0502	0.0043	0.1336	0.0102	0.0199	0.0003	206	185.2	127	9.1	127	2.1	99%
HZ-08E-14	12243	3.34	136	592	0.23	0.0482	0.0025	0.1307	0.0069	0.0199	0.0003	109	118.5	125	6.2	127	1.7	98%
HZ-08E-15	9478	3.49	120	270	0.44	0.0508	0.0041	0.1411	0.0105	0.0204	0.0003	232	187.0	134	9.3	130	2.2	96%
TP-01C																		
TP-01C-01	9812	11.2	54.4	148	0.37	0.1622	0.0040	9.6579	0.2312	0.4273	0.0042	2480	41.7	2403	22.1	2293	19.0	95%
TP-01C-02	11862	46.1	78.0	112	0.70	0.1601	0.0043	9.7043	0.2768	0.4334	0.0061	2457	45.4	2407	26.3	2321	27.6	96%
TP-01C-03	10709	14.7	63.0	43.2	1.46	0.1526	0.0053	9.3034	0.3231	0.4378	0.0062	2376	59.3	2368	31.9	2341	27.8	98%
TP-01C-04	10216	19.2	6.42	12.9	0.50	0.1613	0.0096	9.6874	0.5697	0.4413	0.0116	2469	101.7	2406	54.1	2356	51.7	97%
TP-01C-05	10777	23.0	43.9	59.8	0.74	0.1646	0.0048	10.1085	0.2995	0.4430	0.0054	2506	48.5	2445	27.4	2364	24.3	96%
TP-01C-06	9021	15.0	42.2	50.8	0.83	0.1710	0.0055	10.6793	0.3476	0.4511	0.0055	2569	54.0	2496	30.3	2400	24.5	96%
TP-01C-07	10654	20.9	195	240	0.81	0.1588	0.0041	10.0017	0.2606	0.4526	0.0048	2444	44.0	2435	24.1	2407	21.2	98%
TP-01C-08	10236	12.6	85.7	139	0.61	0.1587	0.0036	10.1313	0.2214	0.4584	0.0043	2442	38.3	2447	20.3	2432	19.2	99%
TP-01C-09	9886	10.1	31.4	30.3	1.04	0.1603	0.0051	10.1053	0.3314	0.4599	0.0087	2461	53.2	2444	30.3	2439	38.6	99%
TP-01C-10	8881	8.33	17.1	26.0	0.66	0.1583	0.0068	9.9209	0.3932	0.4617	0.0081	2439	72.1	2427	36.6	2447	35.7	99%
TP-01C-11	9783	16.7	4.39	18.3	0.24	0.1610	0.0064	10.2574	0.4026	0.4635	0.0083	2466	67.0	2458	36.4	2455	36.6	99%
TP-01C-12	11068	16.8	3.65	13.2	0.28	0.1710	0.0087	10.7429	0.5027	0.4645	0.0097	2568	85.2	2501	43.5	2460	42.9	98%
TP-01C-13	9892	10.4	10.4	31.3	0.33	0.1638	0.0057	10.5364	0.3610	0.4676	0.0077	2495	59.0	2483	31.8	2473	33.8	99%
TP-01C-14	9439	12.0	12.7	19.5	0.65	0.1686	0.0070	10.8547	0.4109	0.4697	0.0077	2544	70.2	2511	35.2	2482	34.0	98%
TP-01C-15	10747	13.8	8.16	17.7	0.46	0.1578	0.0084	9.9969	0.5075	0.4702	0.0087	2432	90.7	2434	46.9	2484	38.2	97%
TP-01C-16	10470	6.92	66.4	40.6	1.63	0.1590	0.0049	10.4772	0.3237	0.4767	0.0082	2456	51.5	2478	28.7	2513	35.8	98%
TP-01C-17	10603	16.3	13.5	20.3	0.66	0.1586	0.0060	10.4191	0.3873	0.4788	0.0088	2443	63.9	2473	34.5	2522	38.2	98%
TP-01C-18	12589	22.5	33.7	50.0	0.67	0.1747	0.0046	11.5898	0.3030	0.4818	0.0061	2603	43.8	2572	24.5	2535	26.5	98%
TP-01C-19	11539	26.4	15.2	35.6	0.43	0.1557	0.0048	10.5203	0.3088	0.4906	0.0070	2410	46.8	2482	27.3	2573	30.3	96%

(Continued on following page)

TABLE 2 | (*Continued*) Zircon U-Pb dating results of the plutonic rock samples from the Huaibei-Linhuan coalfield.

Spot No.	Hf	Ti	Th	U	Th/U	Isotopic ratios						Apparent ages (Ma)						Concordance
	ppm					207Pb/206Pb	1σ	207Pb/235U	1σ	206Pb/238U	1σ	207Pb/206Pb	1σ	207Pb/235U	1σ	206Pb/238U	1σ	
TP-01E																		
TP-01E-01	9517	3.73	82.0	519	0.16	0.0503	0.0032	0.1401	0.0085	0.0204	0.0003	209	146.3	133	7.6	130	1.8	97%
TP-01E-02	11982	0.09	6.14	500	0.01	0.0489	0.0032	0.1374	0.0084	0.0205	0.0003	143	144.4	131	7.5	131	1.9	99%
TP-01E-03	9056	4.81	560	609	0.92	0.0507	0.0025	0.1436	0.0070	0.0204	0.0002	233	119.4	136	6.2	130	1.5	95%
TP-01E-04	10889	1.73	80.3	286	0.28	0.0504	0.0041	0.1428	0.0100	0.0212	0.0004	213	190.7	136	8.9	135	2.5	99%
TP-01E-05	8653	4.54	413	461	0.90	0.0489	0.0027	0.1350	0.0077	0.0200	0.0003	143	163.9	129	6.9	128	2.1	99%
TP-01E-06	9229	2.81	34.0	175	0.19	0.0478	0.0043	0.1382	0.0106	0.0213	0.0005	87.1	200.0	131	9.4	136	2.8	96%
TP-01E-07	8063	3.10	189	222	0.85	0.0532	0.0044	0.1422	0.0102	0.0197	0.0004	345	158.3	135	9.1	126	2.6	93%
TP-01E-08	9676	3.81	97.5	207	0.47	0.0508	0.0047	0.1379	0.0111	0.0201	0.0004	235	212.9	131	9.9	128	2.4	97%
TP-01E-09	9372	2.89	8.32	459	0.02	0.0477	0.0033	0.1272	0.0078	0.0198	0.0003	83.4	159.2	122	7.0	126	2.0	96%
TP-01E-10	9290	5.11	181	255	0.71	0.0501	0.0039	0.1340	0.0085	0.0199	0.0003	198	183.3	128	7.6	127	2.1	99%
TP-01E-11	9236	4.85	71.5	241	0.30	0.0500	0.0042	0.1347	0.0106	0.0200	0.0004	195	181.5	128	9.5	128	2.3	99%
TP-01E-12	10747	1.60	54.6	283	0.19	0.0484	0.0035	0.1315	0.0088	0.0201	0.0004	120	162.9	125	7.9	128	2.4	97%
TP-01E-13	9099	3.96	81.2	211	0.39	0.0523	0.0057	0.1383	0.0120	0.0203	0.0006	298	251.8	132	10.7	129	3.7	98%
TP-01E-14	9069	2.36	97.2	191	0.51	0.0503	0.0053	0.1359	0.0121	0.0205	0.0005	209	225.9	129	10.8	131	3.4	99%
TP-01E-15	10318	3.84	19.1	231	0.08	0.0483	0.0045	0.1340	0.0112	0.0200	0.0006	122	198.1	128	10.0	128	3.6	99%
TP-01E-16	10238	3.92	313	759	0.41	0.0479	0.0023	0.1318	0.0068	0.0198	0.0003	100	105.5	126	6.1	126	1.9	99%
TP-01E-17	10433	5.94	117	693	0.17	0.0480	0.0029	0.1307	0.0082	0.0197	0.0003	98.2	137.0	125	7.3	126	1.8	99%
TP-01E-18	12632	1.52	8.22	134	0.06	0.0507	0.0058	0.1344	0.0136	0.0200	0.0005	228	244.4	128	12.2	127	3.3	99%
TP-01E-19	10076	4.23	246	369	0.67	0.0491	0.0034	0.1291	0.0080	0.0195	0.0004	150	155.5	123	7.2	125	2.4	98%
TP-01E-20	11273	1.38	94.9	316	0.30	0.0502	0.0039	0.1343	0.0097	0.0196	0.0004	206	179.6	128	8.7	125	2.2	97%
TP-01E-21	10201	3.43	252	398	0.63	0.0535	0.0037	0.1462	0.0091	0.0202	0.0004	350	157.4	139	8.1	129	2.3	92%
TT-07																		
TT-07-01	9463	31.9	172	468	0.37	0.0502	0.0061	0.1188	0.0130	0.0175	0.0004	211	250.0	114	11.8	112	2.8	98%
TT-07-02	8566	10.3	220	471	0.47	0.0513	0.0037	0.1262	0.0077	0.0182	0.0003	254	168.5	121	7.0	116	2.1	96%
TT-07-03	9900	4.04	165	522	0.32	0.0536	0.0039	0.1380	0.0091	0.0188	0.0003	354	160.2	131	8.1	120	1.7	91%
TT-07-04	10312	4.36	299	647	0.46	0.0509	0.0026	0.1271	0.0059	0.0182	0.0003	235	112.0	122	5.3	116	1.7	95%
TT-07-05	9656	8.97	291	751	0.39	0.0525	0.0030	0.1316	0.0064	0.0184	0.0004	309	131.5	126	5.7	118	2.4	93%
TT-07-06	9716	2.83	157	535	0.29	0.0506	0.0037	0.1277	0.0083	0.0183	0.0004	233	163.9	122	7.5	117	2.3	95%
TT-07-07	9987	5.55	598	919	0.65	0.0491	0.0028	0.1198	0.0061	0.0177	0.0002	150.1	135.2	115	5.6	113	1.6	98%
TT-07-08	10001	4.85	385	809	0.48	0.0510	0.0043	0.1226	0.0084	0.0179	0.0004	243	196.3	117	7.6	114	2.4	97%
TT-07-09	9697	22.6	136	497	0.27	0.0479	0.0039	0.1187	0.0074	0.0184	0.0003	100	175.9	114	6.7	117	1.9	97%
TT-07-10	10525	4.85	163	567	0.29	0.0502	0.0034	0.1282	0.0076	0.0187	0.0002	206	163.9	123	6.9	119	1.6	97%
TT-07-11	10112	3.49	257	552	0.47	0.0516	0.0027	0.1268	0.0064	0.0179	0.0002	333	123.1	121	5.8	114	1.5	94%
TT-07-12	10407	4.75	303	761	0.40	0.0513	0.0026	0.1311	0.0062	0.0186	0.0002	254	118.5	125	5.6	119	1.6	94%
TT-07-13	9996	10.2	97.2	320	0.30	0.0507	0.0039	0.1258	0.0085	0.0181	0.0003	228	179.6	120	7.7	116	2.1	96%
TT-07-14	10493	671	171	564	0.30	0.0489	0.0057	0.1260	0.0147	0.0185	0.0002	143	251.8	120	13.2	118	1.5	97%
TT-07-15	10030	11.9	257	644	0.40	0.0516	0.0029	0.1267	0.0056	0.0178	0.0002	265	129.6	121	5.0	114	1.5	93%
TT-07-16	9353	2.97	282	258	1.09	0.0499	0.0035	0.1203	0.0076	0.0177	0.0004	187	166.6	115	6.9	113	2.6	97%
TT-07-17	10200	5.49	335	735	0.46	0.0471	0.0026	0.1155	0.0058	0.0178	0.0002	53.8	135.2	111	5.3	114	1.5	97%
TT-07-18	10096	9.84	244	695	0.35	0.0494	0.0033	0.1206	0.0070	0.0176	0.0003	165	157.4	116	6.3	113	1.8	97%
TT-07-19	10278	7.14	431	945	0.46	0.0511	0.0027	0.1289	0.0064	0.0183	0.0002	243	120.4	123	5.7	117	1.5	94%
TT-07-20	9952	5.49	190	484	0.39	0.0504	0.0036	0.1266	0.0082	0.0185	0.0003	213	166.6	121	7.4	118	1.7	97%
TT-07-21	9890	7.05	348	631	0.55	0.0498	0.0048	0.1167	0.0093	0.0173	0.0003	183	214.8	112	8.4	110	2.1	98%
TT-07-22	8864	7.73	434	234	1.86	0.0548	0.0047	0.1344	0.0090	0.0182	0.0004	406	194.4	128	8.0	116	2.7	90%
TT-07-23	10407	3.57	190	577	0.33	0.0503	0.0035	0.1212	0.0074	0.0175	0.0003	206	162.9	116	6.7	112	1.9	96%
TT-07-24	10213	7.26	313	794	0.39	0.0482	0.0026	0.1226	0.0058	0.0184	0.0003	109	122.2	117	5.2	117	1.7	99%
TT-07-25	9131	3.00	123	161	0.77	0.0518	0.0053	0.1274	0.0102	0.0183	0.0004	276	230.5	122	9.2	117	2.8	96%
Y1-32																		
Y1-32-01	9119	6.99	422	409	1.03	0.1471	0.0204	0.3196	0.0332	0.0180	0.0006	2313	239.7	282	25.6	115	3.8	16%
Y1-32-02	9518	9.99	703	581	1.21	0.0481	0.0028	0.1134	0.0059	0.0171	0.0002	106	129.6	109	5.4	109	1.4	99%
Y1-32-03	10079	66.0	375	395	0.95	0.1343	0.0090	0.3408	0.0218	0.0184	0.0003	2155	149.1	298	16.5	117	2.1	12%
Y1-32-04	7902	9.78	210	203	1.03	0.1273	0.0145	0.3210	0.0421	0.0177	0.0005	2061	197.2	283	32.4	113	3.4	14%
Y1-32-05	8864	55.5	273	311	0.88	0.0530	0.0066	0.1168	0.0116	0.0169	0.0004	328	287.0	112	10.6	108	2.6	96%
Y1-32-06	9254	2.26	219	347	0.63	0.0740	0.0146	0.1410	0.0168	0.0163	0.0005	1043	406.0	134	15.0	104	3.2	75%
Y1-32-07	9031	9.98	2493	1702	1.47	0.0765	0.0031	0.1770	0.0070	0.0167	0.0002	1107	76.9	166	6.1	107	1.3	57%
Y1-32-08	10201	7.23	408	544	0.75	0.1012	0.0051	0.2430	0.0114	0.0175	0.0003	1656	92.7	221	9.3	112	1.7	34%

(Continued on following page)

TABLE 2 | (*Continued*) Zircon U-Pb dating results of the plutonic rock samples from the Huaibei-Linhuan coalfield.

Spot No.	Hf	Ti	Th	U	Th/U	Isotopic ratios						Apparent ages (Ma)				Concordance
	ppm					207Pb/206Pb	1σ	207Pb/235U	1σ	206Pb/238U	1σ	207Pb/206Pb	1σ	207Pb/235U	1σ	206Pb/238U	1σ	
Y1-32-09	9542	8.31	201	252	0.79	0.1270	0.0099	0.3267	0.0285	0.0184	0.0004	2057	133.2	287	21.8	117	2.8	16%
Y1-32-10	10928	9.19	909	822	1.11	0.0534	0.0024	0.1209	0.0054	0.0164	0.0002	343	101.8	116	4.9	105	1.3	90%
Y1-32-11	11717	5.67	158	153	1.03	0.1229	0.0119	0.3277	0.0344	0.0188	0.0005	1999	172.4	288	26.3	120	3.3	17%
Y1-32-12	10030	5.01	378	564	0.67	0.0911	0.0064	0.2232	0.0156	0.0178	0.0003	1450	134.1	205	12.9	114	1.8	42%
Y1-32-13	9723	11.6	637	803	0.79	0.1959	0.0108	0.5297	0.0306	0.0195	0.0003	2792	90.4	432	20.3	124	1.9	−11%
Y1-32-14	10295	3.84	391	534	0.73	0.0496	0.0030	0.1178	0.0064	0.0175	0.0002	176	147.2	113	5.8	112	1.6	98%
Y1-32-15	9454	11.1	154	175	0.88	0.0615	0.0061	0.1414	0.0119	0.0175	0.0004	655	212.0	134	10.6	112	2.5	81%

of 2,475 ± 33 Ma (2σ, MSWD = 2.3). Analyses of the zircon rims (n = 15) yielded a weighted average $^{206}Pb/^{238}U$ age of 130.0 ± 2.4 Ma (2σ, MSWD = 2.4), which we interpreted to be the diorite crystallization age (**Figures 4B**, **5A**,C; **Table 2**).

For the Qingdong microgabbro (TT-07), the zircon ages range narrowly from 110.48 to 120.38 Ma and there are no old inherited zircons. The zircons are likely igneous due to their high Th/U ratios (avg. 0.50) and the ubiquitous igneous oscillatory zoning. Twenty-five analyses yielded a weighted average $^{206}Pb/^{238}U$ age of 115.8 ± 1.1 Ma (2σ, MSWD = 2.0), which likely reflects the timing of the microgabbro formation (**Figures 4C**, **5B**,**E**; **Table 2**).

For the Yuandian-1 dolerite (Y1-32), most zircon ages range narrowly from 104.38 to 124.48 Ma. Again, the zircons are likely igneous due to their high Th/U ratios (avg. 0.93) and their igneous oscillatory zoning. Fifteen analyses yielded a weighted average $^{206}Pb/^{238}U$ age of 105.8 ± 1.8 Ma (2σ, MSWD = 2.8), which is largely the same (within error) as the upper intercept $^{206}Pb/^{238}U$ age (106.6 ± 2.4 Ma) and likely represents the dolerite formation age (**Figures 4D**, **5F**; **Table 2**).

Most zircons, regardless of their host-rock types and ages, have similar left-inclining REE patterns and positive Ce anomalies (Ce^{4+}/Ce^{3+} = mostly 0.21–90.78), resembling typical igneous zircons (Belousova et al., 2002). LREE contents are mostly low (often below the detection limit), and the few zircons with abnormally high La content are likely caused by apatite inclusions (Lu et al., 2016). Different rock samples, however, have different zircon Eu anomalies: Zircon rims of samples HZ-08 and TP-01 have no discernible anomalies [δEu: (Eu^*/Eu) = 0.42–0.86], whereas their Neoarchean-Paleoproterozoic cores have distinct negative anomalies (δEu = 0.03–0.48). Varying negative Eu anomalies are present for both samples TT-07 (δEu = 0.03–0.84) and Y1-32 (δEu = 0.12–0.55) (**Figure 6**; **Table 3**).

Whole-Rock Elemental Compositions

For the 12 samples analyzed, their whole-rock major element contents were back-calculated to 100 wt% to remove the volatile influence. A few samples yielded very high LOI (e.g., TT07 = 12.36 wt%, Y2-23 = 10.19 wt%), which we considered to be caused by the natural coke inclusions (instead of alteration/weathering), as demonstrated by the fresh igneous texture and partially-assimilated natural coke fragments observed under the SEM (**Figure 3**). The microgabbro-dolerite samples have SiO_2 = 42.58–50.88 wt%, Al_2O_3 = 12.22–14.55 wt%, MgO = 5.44–8.63 wt%, FeO_T = 6.99–14.68 wt%, and (Na_2O + K_2O) = 2.62–4.08 wt%, whilst the diorite-granodiorite (Haizi, Taiping, and Yangliu) samples have SiO_2 = 57.45–61.27 wt%, Al_2O_3 = 14.53–16.12 wt%, MgO = 2.87–4.63 wt%, FeO_T = 4.0–6.71 wt%, and (Na_2O + K_2O) = 6.45–9.15 wt% (**Table 4**).

In the Total Alkali-Silica (TAS) diagram, the gabbro-dolerite samples fall inside the (olivine-)gabbro fields (some marginally alkali), whilst the diorite-granodiorite samples fall inside the (quartz-)monzonite and syenite fields (**Figure 7A**). Similar results are shown in the immobile Zr/Ti vs. Nb/Y diagram, suggesting that alteration/weathering has no major influence on the major element geochemistry (**Figure 7B**). Both the gabbro-dolerite (ASI = 0.94–1.38) and diorite-granodiorite

(ASI = 1.09–1.42) are peraluminous (**Figure 7C**), with the former being calc-alkaline and latter high-K calc-alkaline (**Figure 7D**). The diorite-granodiorite samples have high Sr (>677.7 ppm) and low Y (<15.48 ppm) (Sr/Y = 49.97–106.95), showing adakitic affinity. In contrast, the gabbro-dolerite samples have lower Sr (<384.2 ppm) and higher Y (>24.13 ppm)(Sr/Y = 15.26–83.19, avg. 47), resembling normal arc magmatic rocks (**Figure 8A**). The gabbro-dolerite and diorite-granodiorite samples have similar total (Σ) REE contents [73.14–193.10 ppm (avg. 112.88) and 50.51–113.45 ppm (avg. 84.99), respectively] and chondrite-normalized REE patterns, which are featured by enrichments in LREE/MREE [$(La/Yb)_N$ = 4.27–17.85 and 8.63–10.62, respectively] and MREE/HREE [$(Dy/Yb)_N$ = 1.76–2.16 and 1.81–1.98, respectively] (**Tables 4**; **Figures 7–8**). In primitive mantle-normalized diagrams, both the gabbro-dolerite and diorite-granodiorite show large ion lithophile element (LILE) over high field strength element (HFSE) enrichments, as well as negative Ta-Nb and Ti anomalies and distinct positive Pb and Sr anomalies.

DISCUSSION

Multiphase Magmatism in the Huaibei-Linhuan Coalfield

Intrusive rocks dated in this study yielded at least two magmatic phases: The Early Cretaceous diorite-granodiorite ages (Haizi: 130.0 ± 2.0 Ma; Taiping: 129.2 ± 1.4 Ma), whilst the microgabbro-dolerite yielded Late Cretaceous ages (Qingdong: 115.8 ± 1.1 Ma; Yuandian-1: 105.8 ± 1.8 Ma). The Early Cretaceous Huaibei-Linhuan diorite-granodiorite are coeval with the high-Mg adakite-like diorite-granodiorite in the Liujiawa pluton (~128 Ma), which is located further southwest in the eastern Dabie Orogen close to the Tanlu fault zone (**Figure 1**) (Jiang et al., 2020). Also along the Tanlu fault, the ore-related Nvshan syenogranite and the Huaiguang granodiorite in the Bengbu-Wuhe goldfield (Anhui Province) were both dated to be ~130 Ma (Li C. et al., 2020). The Huaibei-Linhuan (quartz-)diorite-granodiorite are also of similar age (slightly younger) than the Tongguanshan Cu-Au ore-forming adakites (~136.7 Ma; Tongling orefield), and the ore-barren high-Mg adakitic plutons at Fangjiangzhuang (~129.1 Ma) and Qiaotouji (~131.7 Ma) in the MLYRB (Liu S.-A. et al., 2010; Jiang et al., 2020). This suggests that the emplacement of the Huaibei-Linhuan (quartz-)diorite and granodiorite was part of the extensive Early Cretaceous (high-Mg-)adakitic magmatism, which extended from the along the eastern MLYRB northward along the Tanlu fault. From Eastern China, the Tanlu fault zone likely continues NE-ward across the Bohai sea basin into NE China, although its northeastern-most end is yet to be well identified (Ye et al., 2021). Early Cretaceous adakitic granitoids were documented at Xiuyan (ca. 129–126 Ma) in the Liaodong Peninsula (NE China) (Dong et al., 2020), and Krinichnoye (131.4 Ma) in the southern Sikhote-Alin (SE Russia Far East). As to be discussed in the later section, we attributed this major regional adakitic magmatism as a product of Paleo-Pacific subduction and rollback and/or tearing, facilitated by the reactivation of the Tanlu fault zone movement.

The younger late-Early Cretaceous magmatic phase in Huaibei-Linhuan (Qingdong: 115.8 Ma; Yuandian-1: 105.8 Ma) was also reported elsewhere along the Tanlu fault. For instance, normal-arc-type granite- and diorite porphyries and monzogranite from the Bengbu-Wuhe goldfield were dated at ca. 112–114 Ma, and the associated Bengbu mafic dykes yielded similar Ar-Ar age (plateau: 111.8 ± 0.6 Ma; isochron: 109.6 ± 1.5 Ma) (Liu et al., 2012; Li C. et al., 2020).

Petrogenesis of the Huaibei-Linhuan Magmatic Rocks

In this study, we have identified an earlier adakitic (quartz-) diorite-granodiorite phase and a younger gabbro-dolerite phase for the Early Cretaceous magmatism in Huaibei-Linhuan. For the adakitic (quartz-)diorite-granodiorite, they have relatively high Mg (MgO = 2.87–4.63; Mg# = 0.65–0.76) and low K_2O/Na_2O (0.35–0.54), resembling typical adakites derived from oceanic slab melting. Such features are distinct from the adakites derived from melting of the thickened lower crust, notably those from the Bengbu-Wuhe goldfield situated in the interior of the North China Craton (**Figure 8**) (Li C. et al., 2020). It is not to say that there is no crustal influence in the Huaibei-Linhuan adakitic rocks, as evidence from the presence of Precambrian inherited cores (2,317–2,632 Ma) in the Cretaceous zircons. The weighted average ages of the inherited cores for the (quartz-)diorite-granodiorite samples from Haizi (2,475 ± 33 Ma) and Taiping (2,463 ± 23 Ma) are similar to the relict magmatic zircons in (ca. 2,455 and 2,716 Ma) from the Cenozoic (~1 Ma) Nushan basalts in the southeastern North China Craton (Ping et al., 2019), suggesting clear NCC crustal input for the Huaibei-Linhuan adakite formation. The lack of the clear correlation between the adakitic signature (Sr/Y) and fractional crystallization (SiO_2) suggest that the adakites were not formed by high-pressure fractionation (garnet and/or amphibole) (**Figure 7D**). This conclusion is also supported by the lack of upward-concave MREE-HREE pattern in the chondrite-normalized REE plots (**Figure 9**), or the lack of correlation between MREE/HREE (Dy/Yb) and fractionation (SiO_2), which would be expect for amphibole-garnet fractionation-derived adakites or normal calc-alkaline rocks (such as the Huaibei-Linhuan gabbro-dolerite) (Castillo et al., 1999; Kamvong et al., 2014) (**Figure 10A**). Previous studies suggested that if the adakites were formed by fractional crystallization, substantial amphibole (85%) and garnet (15%) fractionation are needed (Mori et al., 2007). Our (quartz-) diorite-granodiorite samples do not fall on these fractionation trends (**Figures 10A–B**), and no garnet (and very few amphibole) was found in the rocks, suggesting that the adakites were not formed from fractional crystallization. In the Rb/Y vs. Nb/Y and Ba/Th vs. Th discrimination plots, the Huaibei-Linhuan adakite samples fall between the slab-derived and melt-derived enrichment trends, suggesting that the magmas were sourced from both slab-derived fluids and melts (**Figures 10C–D**). The Sr/La ratio has been used to distinguish slab-derived adakites

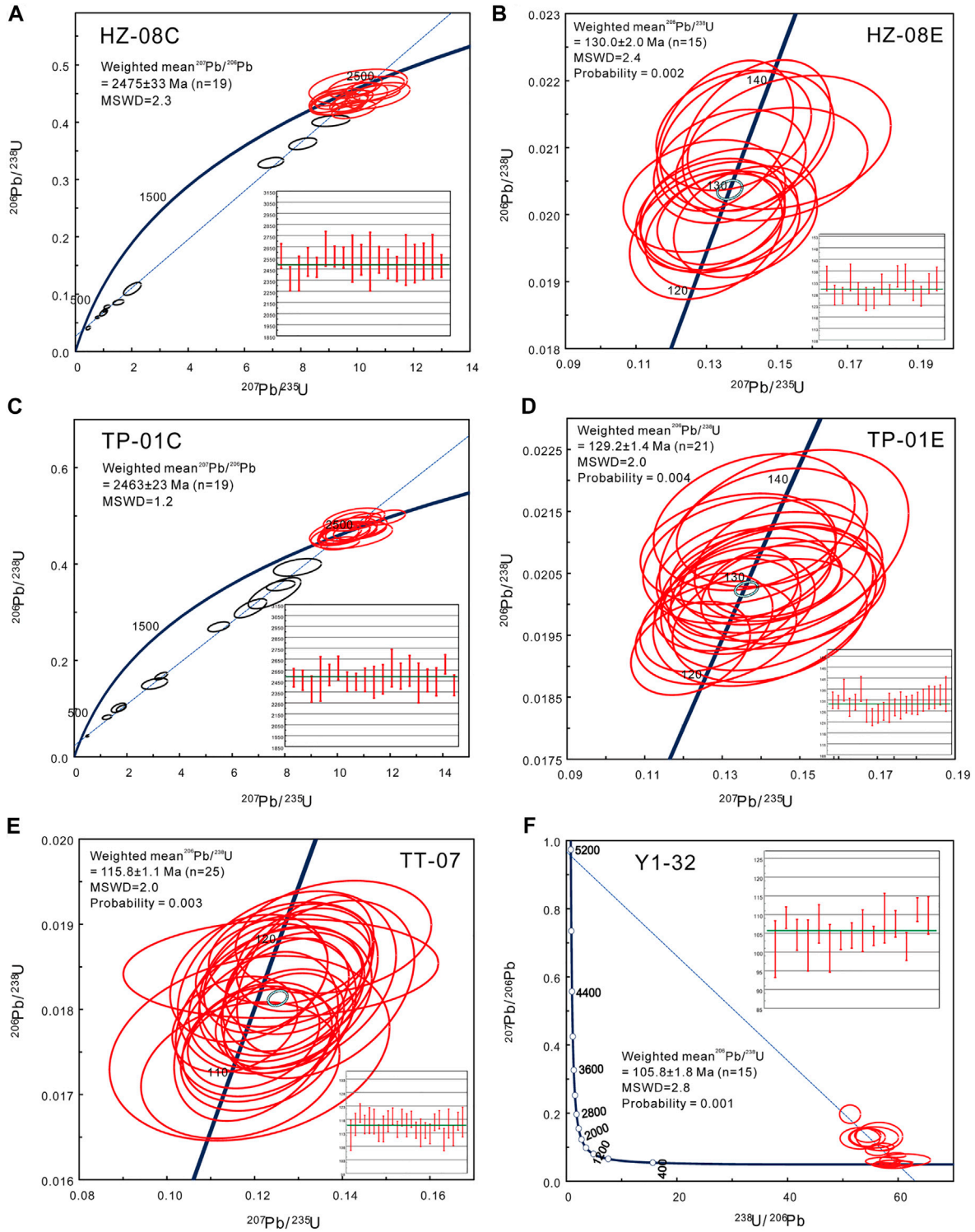

FIGURE 5 | Zircon LA-MC-ICP-MS U-Pb Concordia diagrams of the Huaibei-Linhuan intrusive rock samples: **(A)** inherited zircon cores from Haizi diorite porphyry (HZ-08); **(B)** zircon growth rims from Haizi diorite porphyry (HZ-08); **(C)** inherited zircon cores from Taiping diorite (TP-01); **(D)** zircon growth rims from Taiping diorite (TP-01); **(E)** Qingdong microgabbro (TT-07); **(F)** Yuandian-1 dolerite (Y1-32).

from lower-continental crustal (LCC)-derived ones, because altered oceanic crust (with MORB-type LREE depletion and Sr enrichment by seawater) has much higher Sr/La than the LCC (Liu S.-A. et al., 2010). Our adakitic (quartz-)diorite-granodiorite samples have elevated Sr/La ratios (**Figure 11A**), indicating a slab-derived origin. The slab-derived origin is also supported by

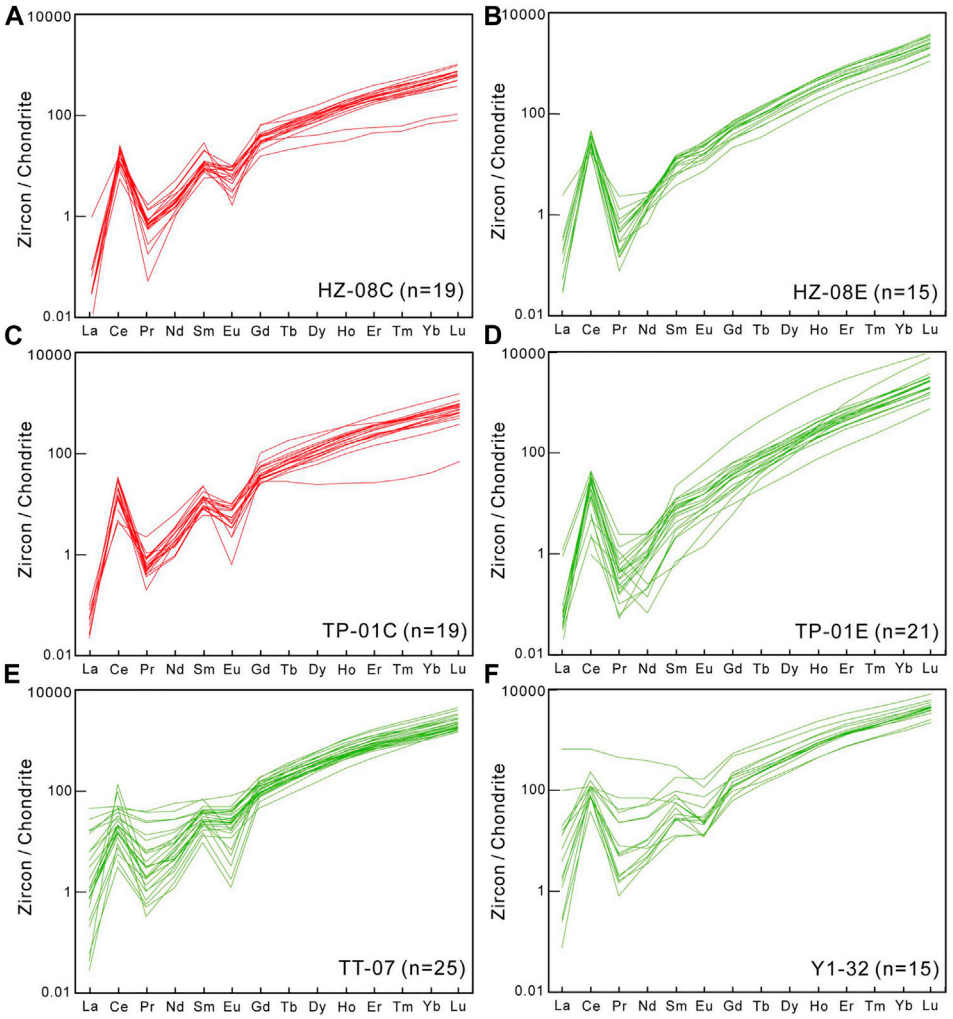

FIGURE 6 | Chondrite-normalized zircon REE patterns for the Huaibei-Linhuan intrusive rock samples: Chondrite normalizing values are from Sun and McDonough (1989).

the zircon trace element compositions. The zircons show in general increasing Yb/Gd with Hf content, which demonstrate a magma cooling and fractionation trend (**Figure 12A**) (Barth and Wooden, 2010). The Cretaceous zircons (or zircon rims) have elevated U/Yb ratio (a proxy of LILE-enrichment), suggesting a more enriched magma source resembling that of typical continental arc (Grimes et al., 2015). This is markedly different from the Precambrian cores, which have lower U/Yb ratio that mimics zircons from typical ocean islands (e.g., Iceland). The Cretaceous and Precambrian zircons have similar Hf and Nb/Yb, showing their host magmas have similar degree of fractionation and alkalinity, respectively (**Figures 12B–C**) (Grimes et al., 2015).

After the magma formation, the lack of distinct Ce or Eu anomalies (some even with weakly positive Eu anomaly), indicates that plagioclase fractionation was insignificant. In the chondrite-normalized REE and primitive mantle-normalized multi-element plots (Sun and McDonough, 1989) (**Figures 9**, **13**), the adakitic (quartz-)diorite-granodiorite and the non-adakitic gabbro-dolerite have generally similar arc-type patterns, e.g., LREE enrichments (between EMORB and OIB), HREE depletions (relative to MORB), negative Nb-Ta-Ti anomalies, and positive Pb-Sr anomalies, suggesting that both rock suites were formed in a subduction-related setting. The only difference between them (apart from the adakitic characters such as the Sr-Y contents), i.e., higher LILE and LREE contents for the (quartz-) diorite-granodiorite, is likely attributed to its more fractionated nature compared with the gabbro-dolerite.

Tectonic Evolution of Cretaceous Eastern China

Cretaceous adakitic magmatism in Eastern China has been variably attributed to the progressive decratonization of North China, and/or the Paleo-Pacific subduction and rollback. As discussed in the previous section, our Huaibei-Linhuan (quartz-)diorite-granodiorite samples show geochemical features typical of oceanic slab melting-derived adakites, but

TABLE 3 | Zircon REE contents of plutonic rock samples from the Huaibei-Linhuan coalfield.

Spot no.	La	Ce	Pr	Nd	Sm	Eu	Gd	Tb	Dy	Ho	Er	Tm	Yb	Lu	Y	ΣREE	LREE	HREE	LREE/HREE	(Dy/Yb)N	δEu	δCe	Ce^{4+}/Ce^{3+}
									Ppm														
HZ-08C																							
HZ-08C-01	—	14.96	0.05	0.92	1.74	0.37	8.65	2.61	29.27	10.76	47.17	9.74	88.77	18.48	329	233.50	18.04	215.45	0.08	0.22	0.24	88.37	159.99
HZ-08C-02	0.01	9.89	0.08	1.21	1.81	0.51	5.76	1.67	18.31	6.40	28.73	6.06	55.51	11.96	205	147.91	13.50	134.40	0.10	0.22	0.44	38.94	65.69
HZ-08C-03	—	6.59	0.08	1.01	1.47	0.25	7.27	2.18	21.93	7.65	31.33	6.29	56.77	11.91	224	154.71	9.39	145.32	0.06	0.26	0.19	26.10	53.13
HZ-08C-04	0.01	10.82	0.03	0.50	0.84	0.35	4.06	1.35	15.40	5.70	26.33	5.54	53.64	12.30	175	136.85	12.54	124.32	0.10	0.19	0.48	120.59	262.27
HZ-08C-05	—	11.37	0.00	0.46	1.33	0.13	5.31	1.74	23.98	9.76	47.00	11.06	105.09	23.71	311	240.94	13.30	227.64	0.06	0.15	0.13	756.26	350.01
HZ-08C-06	0.02	10.22	0.05	0.82	1.59	0.54	7.77	2.45	25.88	9.77	43.67	9.03	83.70	17.81	299	213.33	13.24	200.08	0.07	0.21	0.39	50.38	125.96
HZ-08C-07	0.01	7.26	0.05	0.67	1.28	0.34	5.99	1.80	18.48	7.38	31.69	6.82	65.28	14.29	222	161.35	9.62	151.74	0.06	0.19	0.32	39.88	109.37
HZ-08C-08	0.02	7.36	0.07	1.64	3.06	0.31	5.94	1.30	9.93	2.83	9.16	1.50	14.22	2.57	85	59.93	12.47	47.46	0.26	0.47	0.22	28.28	8.83
HZ-08C-09	—	14.12	0.02	0.60	1.12	0.17	6.27	1.76	20.95	8.03	35.89	7.54	72.85	14.94	247	184.25	16.03	168.23	0.10	0.19	0.15	274.83	268.48
HZ-08C-10	0.01	8.50	0.12	1.59	2.87	0.56	12.34	3.81	38.63	14.25	62.24	12.79	117.57	25.08	413	300.36	13.66	286.70	0.05	0.22	0.24	20.26	46.49
HZ-08C-11	0.22	9.77	0.12	1.28	1.16	0.52	7.98	2.13	22.52	8.27	36.94	7.86	72.38	16.46	249	187.62	13.08	174.54	0.07	0.21	0.39	14.65	87.49
HZ-08C-12	0.01	13.61	0.07	0.83	1.64	0.44	8.77	2.54	27.99	10.54	47.25	10.05	86.84	18.18	318	228.75	16.59	212.16	0.08	0.22	0.28	61.99	163.50
HZ-08C-13	0.01	13.12	0.07	0.88	1.35	0.25	7.37	1.88	20.37	7.11	33.32	6.53	60.01	11.99	224	164.26	15.67	148.59	0.11	0.23	0.19	58.53	131.61
HZ-08C-14	0.01	3.21	0.05	0.73	1.73	0.18	3.06	0.75	6.46	1.70	7.16	1.18	11.18	1.95	54	39.35	5.91	33.44	0.18	0.39	0.24	19.22	11.18
HZ-08C-15	0.01	5.71	0.06	0.70	1.22	0.29	5.60	1.97	23.83	8.90	41.57	9.49	89.14	18.33	260	206.82	7.99	198.83	0.04	0.18	0.28	27.58	105.30
HZ-08C-16	0.01	11.99	0.06	0.86	1.84	0.45	7.53	2.10	24.86	9.06	39.23	8.27	76.72	18.22	263	201.20	15.21	186.00	0.08	0.22	0.32	55.59	130.45
HZ-08C-17	0.01	10.47	0.06	0.98	1.27	0.47	8.12	2.26	26.01	9.06	37.88	8.41	73.52	15.60	270	194.10	13.25	180.85	0.07	0.24	0.34	50.64	111.42
HZ-08C-18	—	4.59	0.06	0.91	1.52	0.44	7.92	2.38	26.53	8.54	39.39	7.57	70.85	15.32	274	186.01	7.52	178.50	0.04	0.25	0.31	24.01	46.26
HZ-08C-19	0.02	6.23	0.15	2.37	4.20	0.09	13.03	2.88	27.12	8.41	31.08	5.72	48.46	9.25	250	159.02	13.07	145.95	0.09	0.37	0.03	12.03	9.14
HZ-08E																							
HZ-08E-01	0.08	27.15	0.08	0.97	2.19	1.41	11.84	3.63	48.45	20.94	103.78	23.33	246.61	60.72	631	551.18	31.88	519.30	0.06	0.13	0.68	77.32	498.35
HZ-08E-02	—	11.10	0.01	0.63	2.10	1.31	15.11	5.47	70.42	29.87	148.97	34.75	348.55	84.36	899	752.63	15.14	737.49	0.02	0.14	0.52	492.82	356.96
HZ-08E-03	—	12.49	0.06	1.11	1.88	1.71	14.69	5.21	66.77	27.02	128.31	28.47	283.75	67.04	824	638.53	17.25	621.28	0.03	0.16	0.70	62.74	222.04
HZ-08E-04	0.07	17.18	0.03	0.31	1.44	0.71	6.97	2.13	28.91	11.90	61.77	14.75	157.21	38.94	376	342.33	19.74	322.58	0.06	0.12	0.56	97.24	901.89
HZ-08E-05	—	9.93	0.01	0.55	0.59	0.43	4.47	1.30	18.19	8.22	44.22	11.21	116.65	30.05	263	245.83	11.51	234.32	0.05	0.10	0.58	235.20	483.15
HZ-08E-06	0.01	14.24	0.02	0.58	0.91	0.79	8.10	2.89	40.53	17.43	91.39	22.06	233.01	56.14	559	488.10	16.55	471.55	0.04	0.12	0.60	230.89	691.29
HZ-08E-07	0.01	15.85	0.04	0.97	1.94	1.12	10.00	3.34	43.14	17.88	88.55	20.94	215.69	54.40	567	473.87	19.94	453.93	0.04	0.13	0.63	105.27	293.95
HZ-08E-08	0.01	27.95	0.03	0.88	2.33	1.62	13.70	4.83	67.90	29.53	148.18	36.09	385.16	93.22	919	811.43	32.81	778.62	0.04	0.12	0.68	287.63	698.73
HZ-08E-09	0.04	23.24	0.12	1.05	1.66	1.13	10.85	3.28	49.14	21.27	107.72	26.09	279.51	70.57	690	595.67	27.24	568.43	0.05	0.12	0.61	53.72	520.38
HZ-08E-10	0.05	29.04	0.04	0.80	2.03	0.94	10.86	3.84	49.51	21.25	107.31	26.15	271.91	66.24	665	589.96	32.89	557.07	0.06	0.12	0.49	147.49	711.11
HZ-08E-11	0.03	22.03	0.04	0.91	2.08	1.48	12.22	4.53	64.09	27.74	143.09	35.08	376.34	98.17	899	787.84	26.57	761.27	0.03	0.11	0.70	133.14	593.65
HZ-08E-12	—	17.78	0.02	0.84	1.00	0.64	6.43	2.18	27.73	12.10	60.73	14.77	158.83	41.53	380	344.58	20.27	324.30	0.06	0.12	0.58	316.26	494.85
HZ-08E-13	0.01	14.60	0.05	0.93	1.55	1.39	13.00	4.77	69.21	30.21	158.13	38.87	402.57	103.70	964	838.99	18.53	820.47	0.02	0.12	0.65	84.31	464.34
HZ-08E-14	0.58	10.86	0.22	1.28	1.01	0.98	6.78	2.65	36.00	16.18	82.51	20.98	212.87	55.03	517	447.93	14.94	432.99	0.03	0.11	0.86	7.45	249.61
HZ-08E-15	—	19.01	0.01	0.67	1.52	0.89	10.52	3.71	52.87	22.64	118.81	29.70	318.51	79.79	744	658.65	22.11	636.54	0.03	0.11	0.50	437.25	723.39
TP-01C																							
TP-01C-01	0.01	20.70	0.05	0.75	1.84	0.53	6.60	1.95	19.00	7.09	32.54	7.55	70.92	16.28	222	185.81	23.88	161.93	0.15	0.18	0.41	122.54	237.39
TP-01C-02	0.02	2.61	0.22	3.01	3.57	0.13	5.88	1.04	6.30	1.49	4.47	0.81	7.17	1.79	45	38.52	9.57	28.95	0.33	0.59	0.09	3.58	0.21
TP-01C-03	—	13.72	0.05	1.02	2.17	0.25	7.43	2.46	25.04	9.49	41.57	8.01	79.76	16.20	279	207.18	17.22	189.96	0.09	0.21	0.17	79.36	111.59
TP-01C-04	0.01	8.68	0.11	0.67	1.45	0.32	6.78	2.01	25.03	8.70	38.35	7.89	67.75	14.38	260	182.13	11.23	170.90	0.07	0.25	0.26	24.54	120.33
TP-01C-05	0.01	8.69	0.06	0.72	1.29	0.20	7.69	2.94	33.30	13.34	58.41	12.00	109.08	20.82	407	268.56	10.98	257.58	0.04	0.20	0.15	43.00	155.30
TP-01C-06	—	9.08	0.09	1.59	2.76	0.58	11.77	3.81	41.41	14.64	62.87	12.59	120.78	24.79	424	306.75	14.10	292.65	0.05	0.23	0.26	32.52	50.90
TP-01C-07	—	4.89	0.08	1.66	3.53	0.13	21.18	6.93	65.06	19.89	68.11	11.82	90.07	16.41	592	309.76	10.29	299.46	0.03	0.48	0.04	19.46	14.49
TP-01C-08	—	21.39	0.04	0.46	1.41	0.28	7.80	2.56	29.80	11.83	53.37	11.79	120.19	24.95	378	285.86	23.58	262.29	0.09	0.17	0.21	161.25	595.28
TP-01C-09	0.01	17.73	0.05	0.89	0.94	0.32	5.34	1.62	15.83	5.68	24.31	4.97	45.21	9.78	180	132.69	19.95	112.74	0.18	0.23	0.35	99.20	190.59
TP-01C-10	—	7.76	0.05	1.28	1.71	0.48	11.50	3.23	38.56	13.26	59.19	11.63	104.44	21.49	392	274.57	11.27	263.29	0.04	0.25	0.24	51.25	63.47
TP-01C-11	0.01	12.66	0.04	0.90	1.41	0.46	7.32	2.46	28.44	10.36	50.12	11.13	109.79	22.48	322	257.57	15.48	242.09	0.06	0.17	0.35	94.91	182.99
TP-01C-12	—	19.47	0.05	1.26	2.22	0.47	13.99	4.74	53.42	20.24	90.77	19.86	187.34	39.23	577	453.06	23.47	429.59	0.05	0.19	0.20	112.50	201.16
TP-01C-13	0.02	8.63	0.04	0.43	1.32	0.32	6.37	1.94	22.39	8.35	39.43	8.29	80.68	17.02	251	195.23	10.76	184.47	0.06	0.19	0.28	58.58	212.06
TP-01C-14	0.01	9.58	0.04	1.30	2.06	0.61	10.84	3.49	38.63	13.90	59.56	12.48	114.53	23.18	394	290.21	13.60	276.60	0.05	0.23	0.32	63.82	74.52
TP-01C-15	0.01	7.80	0.07	1.01	1.95	0.47	9.64	2.97	34.44	12.64	58.15	12.37	115.27	24.26	368	281.05	11.31	269.74	0.04	0.20	0.27	33.86	83.10
TP-01C-16	0.01	20.93	0.06	0.74	1.30	0.43	8.30	2.80	35.33	12.76	62.28	13.45	131.41	28.80	419	318.59	23.47	295.12	0.08	0.18	0.30	106.62	425.88
TP-01C-17	—	20.79	0.08	1.49	2.13	0.24	8.28	2.82	30.27	10.72	48.36	10.50	95.14	19.35	331	250.18	24.73	225.45	0.11	0.21	0.15	77.96	133.56
TP-01C-18	—	12.32	0.02	0.85	1.24	0.20	5.22	1.81	21.51	8.43	37.24	8.46	86.21	18.81	261	202.32	14.63	187.70	0.08	0.17	0.20	195.86	190.20
TP-01C-19	0.01	2.99	0.08	1.28	2.09	0.04	7.30	2.41	24.38	8.71	35.39	7.58	64.48	12.81	245	169.55	6.49	163.06	0.04	0.25	0.03	11.03	16.47
TP-01E																							
TP-01E-01	0.01	8.45	0.02	0.41	1.17	0.92	7.75	2.96	38.04	15.62	79.62	19.52	217.36	52.27	513	444.11	10.98	433.13	0.03	0.12	0.70	98.32	450.76
TP-01E-02	—	1.51	0.01	0.10	0.34	0.41	3.49	1.81	29.66	14.90	90.40	24.20	278.40	71.30	479	516.54	2.37	514.17	0.00	0.07	0.73	79.40	827.96
TP-01E-03	0.29	27.41	0.24	1.15	1.91	1.15	13.08	3.93	46.26	19.09	90.32	21.06	220.26	51.56	597	497.70	32.15	465.55	0.07	0.14	0.52	24.02	394.36
TP-01E-04	—	7.23	0.02	0.38	0.66	0.46	4.82	1.62	23.61	9.11	49.72	11.86	131.24	32.25	307	273.00	8.76	264.24	0.03	0.12	0.57	148.91	456.42

(Continued on following page)

TABLE 3 | (*Continued*) Zircon REE contents of plutonic rock samples from the Huaibei-Linhuan coalfield.

Spot no.	La	Ce	Pr	Nd	Sm	Eu	Gd	Tb	Dy	Ho	Er	Tm	Yb	Lu	Y	ΣREE	LREE	HREE	LREE/HREE	(Dy/Yb)N	δEu	δCe	Ce^{4+}/Ce^{3+}
	Ppm																						
TP-01E-05	—	25.44	0.08	1.10	1.86	1.28	11.15	3.39	42.97	17.47	86.01	20.32	213.40	51.49	559	475.96	29.76	446.20	0.07	0.13	0.66	102.23	401.69
TP-01E-06	—	3.57	0.01	0.10	0.32	0.29	2.00	0.73	9.71	4.34	22.89	6.00	71.07	19.32	137	140.34	4.29	136.05	0.03	0.09	0.84	111.16	957.58
TP-01E-07	0.02	18.58	0.05	0.81	1.00	0.64	6.31	2.12	28.58	11.48	60.21	14.80	158.78	37.07	376	340.45	21.10	319.34	0.07	0.12	0.60	104.54	504.57
TP-01E-08	0.01	15.27	0.04	0.45	0.94	0.65	6.66	2.45	32.63	14.22	71.87	18.62	196.49	50.58	454	410.90	17.37	393.53	0.04	0.11	0.58	101.86	848.91
TP-01E-09	—	0.61	0.00	0.03	0.11	0.08	1.23	1.17	19.93	12.21	83.54	23.80	268.62	69.03	450	480.37	0.84	479.53	0.00	0.05	0.43	—	2247.67
TP-01E-10	0.01	19.41	0.04	0.57	1.48	0.90	9.15	3.59	43.20	19.21	99.52	24.37	263.73	67.00	633	552.18	22.42	529.76	0.04	0.11	0.57	125.10	766.01
TP-01E-11	—	11.44	0.03	0.88	1.68	1.06	9.04	3.78	51.29	23.83	123.14	29.62	321.26	82.53	743	659.58	15.09	644.49	0.02	0.11	0.66	114.25	339.23
TP-01E-12	—	3.93	0.01	0.31	0.49	0.49	3.85	1.72	23.81	11.21	57.56	14.52	156.47	41.60	351	315.97	5.23	310.75	0.02	0.10	0.78	238.75	440.81
TP-01E-13	0.02	12.19	0.06	1.01	1.22	0.70	8.26	3.10	39.20	17.33	93.62	22.86	253.57	68.05	573	521.21	15.21	506.00	0.03	0.10	0.50	55.31	328.47
TP-01E-14	0.01	19.73	0.04	0.52	1.39	0.91	10.06	4.14	49.83	23.01	118.63	30.16	330.56	83.54	750	672.53	22.60	649.93	0.03	0.10	0.54	139.33	990.96
TP-01E-15	0.02	2.98	0.00	0.12	0.09	0.17	2.72	1.50	27.96	19.27	163.01	55.32	730.83	200.29	752	1204.28	3.38	1200.90	0.00	0.03	0.42	126.53	6383.18
TP-01E-16	0.01	17.24	0.03	0.43	1.93	1.70	13.34	4.73	66.01	27.55	137.82	32.27	333.98	78.83	868	715.85	21.33	694.52	0.03	0.13	0.75	148.04	804.19
TP-01E-17	—	11.76	0.02	0.47	3.41	3.64	38.25	16.60	233.73	100.03	493.01	113.97	1138.53	255.97	3,055	2,409.39	19.29	2,390.10	0.01	0.14	0.60	220.89	640.44
TP-01E-18	0.01	1.33	0.00	0.07	0.46	0.39	3.97	2.23	34.36	18.54	106.00	29.86	359.25	95.91	602	652.37	2.25	650.12	0.00	0.06	0.60	135.88	1066.29
TP-01E-19	0.22	20.87	0.13	1.26	1.32	0.90	7.47	2.93	34.83	14.96	74.49	18.37	198.78	48.90	474	425.42	24.69	400.73	0.06	0.12	0.69	29.51	372.00
TP-01E-20	0.02	9.41	0.02	0.30	0.86	0.55	6.46	2.01	27.54	11.83	59.79	15.15	159.20	40.93	369	334.07	11.16	322.91	0.03	0.12	0.51	110.29	695.23
TP-01E-21	0.01	24.22	0.06	1.00	1.22	0.90	9.12	3.08	39.68	16.53	78.95	19.41	199.29	49.60	501	443.07	27.41	415.66	0.07	0.13	0.59	116.92	529.71
TT-07																							
TT-07-01	10.65	30.18	3.56	18.45	10.56	0.93	28.04	9.64	112.47	42.32	192.38	39.78	364.68	72.85	1265	936.49	74.33	862.16	0.09	0.21	0.16	1.20	18.66
TT-07-02	0.28	11.60	0.37	5.44	7.52	2.89	38.34	12.15	138.09	50.76	209.53	40.16	347.81	67.11	1488	932.05	28.11	903.94	0.03	0.27	0.42	7.43	22.32
TT-07-03	0.24	8.74	0.30	2.12	3.02	0.84	15.46	5.52	65.78	24.02	108.55	23.36	199.52	41.27	747	498.74	15.26	483.48	0.03	0.22	0.30	6.83	57.82
TT-07-04	3.91	22.91	2.23	12.71	5.71	1.92	18.74	6.23	67.77	25.74	110.77	21.86	194.99	39.81	772	535.29	49.38	485.91	0.10	0.23	0.51	1.88	19.91
TT-07-05	0.42	12.99	0.64	4.45	5.38	2.30	31.60	10.54	119.36	43.25	188.91	37.71	334.76	67.87	1317	860.18	26.18	834.00	0.03	0.24	0.42	5.02	37.66
TT-07-06	3.83	17.14	1.28	7.94	5.47	1.60	18.06	7.19	79.92	30.01	125.96	27.36	230.26	46.38	899	602.41	37.27	565.14	0.07	0.23	0.45	1.89	26.14
TT-07-07	0.06	4.58	0.10	1.58	3.71	0.40	22.76	9.06	116.53	46.05	208.21	44.78	413.87	85.91	1355	957.59	10.42	947.17	0.01	0.19	0.10	11.70	52.81
TT-07-08	0.99	15.91	0.54	4.21	6.58	2.55	27.94	8.97	95.47	33.78	141.69	27.99	247.71	49.89	1034	664.22	30.79	633.43	0.05	0.26	0.49	5.25	36.14
TT-07-09	0.18	7.21	0.13	2.09	2.55	1.02	16.05	5.82	69.92	27.21	115.05	23.49	213.16	45.10	815	528.97	13.18	515.79	0.03	0.22	0.37	11.16	55.13
TT-07-10	1.48	12.46	0.58	5.28	4.18	1.37	19.31	6.50	71.86	27.91	122.39	25.14	220.66	46.78	839	565.90	25.34	540.56	0.05	0.22	0.39	3.31	30.95
TT-07-11	0.05	3.41	0.17	3.02	6.39	0.30	37.25	13.30	152.77	57.79	254.72	53.19	487.39	101.80	1658	1171.57	13.34	1158.23	0.01	0.21	0.05	5.65	15.36
TT-07-12	0.28	12.53	0.18	1.95	3.70	1.40	21.09	7.37	79.73	29.03	123.14	24.56	225.21	44.12	860	574.30	20.06	554.25	0.04	0.24	0.38	13.11	77.55
TT-07-13	0.01	1.88	0.05	0.55	1.45	0.07	12.42	4.42	59.66	23.93	112.95	25.64	247.00	53.68	719	543.73	4.01	539.71	0.01	0.16	0.03	11.07	76.52
TT-07-14	0.72	8.72	0.28	2.36	3.34	1.27	18.34	5.95	72.56	26.45	120.30	25.04	219.95	46.44	808	551.72	16.70	535.03	0.03	0.22	0.39	4.71	51.14
TT-07-15	6.46	26.78	2.39	12.85	6.25	2.33	27.60	9.05	100.46	37.80	163.16	33.68	284.72	58.16	1154	771.69	57.07	714.62	0.08	0.24	0.46	1.67	25.98
TT-07-16	0.12	59.27	0.10	1.19	3.21	1.09	17.71	6.55	83.66	34.70	173.07	39.37	378.63	82.06	1107	880.73	64.98	815.76	0.08	0.15	0.35	125.59	996.26
TT-07-17	0.01	5.50	0.06	1.41	4.08	0.19	30.51	11.50	150.05	59.77	275.09	59.39	538.56	114.13	1745	1250.25	11.25	1239.00	0.01	0.19	0.04	25.60	75.01
TT-07-18	0.17	9.36	0.18	2.82	4.71	1.50	22.05	7.77	89.85	33.76	145.72	29.24	266.15	54.73	1008	668.01	18.73	649.28	0.03	0.23	0.37	11.84	41.56
TT-07-19	1.46	19.45	0.98	7.04	5.62	2.25	25.01	7.57	87.80	31.06	135.34	27.15	233.51	47.37	960	631.61	36.81	594.80	0.06	0.25	0.49	3.85	30.52
TT-07-20	0.00	2.52	0.05	0.93	2.26	0.10	15.54	5.41	72.71	28.34	135.10	28.02	257.41	55.51	837	603.91	5.87	598.04	0.01	0.19	0.04	14.67	49.21
TT-07-21	3.35	27.20	3.72	26.52	10.14	4.68	25.91	7.79	84.65	30.09	131.21	26.06	230.72	48.04	945	660.08	75.61	584.48	0.13	0.25	0.84	1.67	8.83
TT-07-22	0.01	82.42	0.28	4.07	6.15	2.06	30.87	9.02	98.91	38.17	168.06	35.43	325.58	69.40	1141	870.43	94.98	775.45	0.12	0.20	0.37	90.94	248.14
TT-07-23	0.23	8.47	0.30	2.05	3.72	1.66	16.90	5.84	64.80	23.69	102.01	20.70	179.62	37.32	731	467.32	16.44	450.88	0.04	0.24	0.54	6.61	46.43
TT-07-24	0.18	10.27	0.19	3.41	3.93	1.33	21.18	7.56	90.00	33.82	149.86	31.27	289.42	60.86	1045	703.29	19.31	683.98	0.03	0.21	0.36	12.19	45.83
TT-07-25	—	31.35	0.03	0.71	1.96	0.67	9.40	3.09	37.51	15.61	74.85	17.74	188.52	43.40	498	424.85	34.72	390.12	0.09	0.13	0.40	318.95	794.77
Y1-32																							
Y1-32-01	161.08	416.78	44.06	186.02	46.60	6.78	100.76	27.05	283.89	100.74	422.50	87.14	788.51	162.68	2,890	2,834.58	861.31	1973.27	0.44	0.24	0.29	1.19	9.95
Y1-32-02	0.07	67.75	0.20	2.28	4.00	1.49	25.91	9.17	122.91	51.43	246.01	56.06	542.96	120.67	1581	1250.91	75.79	1175.12	0.06	0.15	0.34	92.52	379.76
Y1-32-03	4.84	73.66	4.09	24.11	15.13	4.43	36.91	10.81	121.66	45.73	231.03	50.71	512.06	111.36	1506	1246.54	126.27	1120.28	0.11	0.16	0.55	3.79	20.44
Y1-32-04	0.06	23.88	0.14	2.15	4.13	1.85	25.24	9.20	112.42	46.58	221.15	45.95	447.76	100.51	1414	1041.03	32.22	1008.81	0.03	0.17	0.43	44.45	121.28
Y1-32-05	0.28	46.96	0.18	2.88	4.50	1.24	26.33	8.71	113.27	46.74	220.69	51.39	514.13	114.11	1466	1151.41	56.04	1095.37	0.05	0.15	0.27	49.21	190.57
Y1-32-06	—	47.65	0.16	1.66	1.85	0.80	15.75	7.11	91.18	41.47	213.38	49.78	507.79	118.28	1319	1096.85	52.11	1044.75	0.05	0.12	0.31	93.81	592.76
Y1-32-07	3.15	146.11	3.53	26.08	28.64	10.01	113.66	34.44	381.02	136.38	573.48	115.30	1031.31	214.52	3,890	2,817.62	217.52	2,600.10	0.08	0.25	0.47	9.46	32.00
Y1-32-08	0.46	45.06	0.48	3.87	7.09	0.71	31.02	10.12	128.59	49.53	223.48	47.67	424.37	88.99	1484	1061.43	57.66	1003.77	0.06	0.20	0.12	21.10	90.78
Y1-32-09	0.96	48.87	0.55	5.04	5.32	1.67	23.69	9.01	108.15	45.51	223.03	50.22	491.74	111.83	1430	1125.59	62.41	1063.18	0.06	0.15	0.38	16.22	110.69
Y1-32-10	3.14	99.25	2.23	13.64	10.99	2.68	41.13	11.84	145.91	57.46	266.53	60.29	593.09	132.37	1746	1440.54	131.93	1308.62	0.10	0.16	0.34	8.83	60.95
Y1-32-11	3.93	44.28	0.77	3.38	2.00	0.78	13.10	4.90	60.46	25.82	127.95	29.27	289.36	66.97	834	672.98	55.14	617.84	0.09	0.14	0.35	5.86	198.41
Y1-32-12	0.38	76.54	0.51	4.85	8.87	1.35	41.55	14.74	186.84	74.20	352.79	73.74	693.09	147.27	2,206	1676.73	92.50	1584.23	0.06	0.18	0.18	36.06	146.58
Y1-32-13	1.69	76.02	2.24	14.35	12.81	1.29	47.24	15.62	189.25	71.07	319.73	66.42	594.76	121.24	2,156	1533.73	108.40	1425.33	0.08	0.21	0.14	8.10	38.23
Y1-32-14	0.02	50.95	0.08	1.79	4.28	0.71	26.08	9.16	122.28	49.43	237.06	52.25	475.26	103.53	1474	1132.88	57.83	1075.05	0.05	0.17	0.16	186.27	309.75
Y1-32-15	24.22	74.34	6.92	33.44	9.00	1.43	20.58	5.55	66.00	25.96	125.12	28.32	260.78	58.05	805	739.71	149.35	590.36	0.25	0.17	0.31	1.39	15.13

*$\delta Eu = (2\times Eu_N)/(Sm_N + Gd_N)$; $\delta Ce = (2\times Ce_N)/(La_N + Pr_N)$.

TABLE 4 | | Major and trace element compositions of plutonic rock samples from the Huaibei-Linhuan coalfield.

Sample no.	TP-01	TP-04	HZ-08	HZ-13	YL-03	YL-07	TT-07	TT-12	Y1-29	Y1-32	Y2-08	Y2-23
Lithology	diorite	diorite porphyry	Diorite	Diorite	diorite porphyry	diorite porphyry	microgabbro	microgabbro	dolerite	dolerite	dolerite	dolerite
SiO2	58.2	61.27	58.81	59.3	60.42	57.45	50.54	50.88	48.06	43.85	48.59	42.58
TiO2	0.61	0.35	0.54	0.53	0.47	0.57	0.77	0.71	1.33	0.9	0.89	0.85
Al2O3	16.12	14.53	14.62	14.53	14.68	14.59	13	12.22	14.25	14.39	14.55	14.23
Fe2O3	6.19	4	6.71	6.67	5.53	6.05	6.99	7.49	14.68	13.72	10.15	10.46
MnO	0.08	0.06	0.06	0.06	0.09	0.09	0.06	0.1	0.19	0.24	0.12	0.12
MgO	4.04	2.87	4.58	4.63	4.2	4.52	6.43	6.73	6.76	8.63	5.69	5.44
CaO	5.6	4.17	5.53	5.52	3.54	3.48	6.78	8.83	7.38	9.55	6.88	11.82
Na2O	4.3	6.8	4.34	4.37	5.11	4.74	2.08	2.63	3.35	2.45	3.16	2.77
K2O	2.33	2.35	2.11	2.2	2.12	2.05	0.57	0.83	0.22	0.17	0.92	0.52
P2O5	0.2	0.12	0.17	0.17	0.14	0.16	0.2	0.19	0.2	0.14	0.29	0.26
LOI	1.87	2.9	1.82	1.54	3.69	5.83	12.36	8.96	3.19	5.71	8.63	10.19
Total	99.53	99.41	99.29	99.52	99.98	99.53	99.77	99.57	99.61	99.73	99.86	99.23
Sc	16.33	10.12	18.68	17.00	15.21	15.54	21.68	20.29	31.91	23.91	20.84	19.13
V	121.2	65.00	128.0	115.9	96.23	102.8	168.0	157.1	211.3	148.7	130.2	119.8
Cr	129.5	137.5	244.4	220.4	194.4	210.0	472.2	467.3	162.6	190.4	192.8	324.2
Co	16.82	11.71	24.38	21.91	17.05	18.09	36.02	35.17	41.84	51.24	39.91	41.36
Ni	49.19	66.20	104.2	93.54	57.45	73.21	200.7	216.2	86.12	144.7	141.9	192.8
Cu	3,365	3,933	7,265	5,984	1768	4,103	1108	1629	76.04	68.44	6516	749.6
Zn	2,132	2,402	4,520	3,720	1095	2,408	687.7	1002	126.60	81.50	4,270	526.1
Ga	21.36	20.43	18.24	18.08	19.10	20.01	17.11	16.40	18.96	17.27	18.55	17.40
Ge	1.36	1.06	1.42	1.32	0.91	1.41	1.81	1.33	1.47	1.39	1.38	2.03
Rb	56.44	48.12	36.97	44.70	50.95	48.62	9.97	14.40	5.89	4.08	16.03	8.49
Sr	773.6	826.5	684.2	1041	680.3	677.7	766.7	975.0	368.2	384.2	740.0	847.7
Zr	120.5	71.52	82.98	83.33	114.4	115.4	87.15	82.57	77.29	53.40	113.1	100.1
Nb	6.06	3.47	3.95	3.52	4.60	5.07	3.98	3.79	4.07	2.87	9.45	8.81
Cs	1.96	2.36	0.91	1.14	0.57	0.63	0.80	0.56	0.32	0.30	0.27	0.20
Ba	1060	1082	955.2	1071	1215	2,264	472.9	641.1	316.6	243.6	749.9	765.6
Hf	3.21	2.15	2.33	2.20	3.09	3.12	2.27	2.16	2.14	1.49	2.56	2.33
Ta	0.35	0.20	0.23	0.21	0.30	0.32	0.24	0.24	0.23	0.16	0.48	0.45
Pb	153.4	237.4	321.2	275.5	113.1	220.5	49.77	70.93	26.14	3.17	285.1	65.93
Th	4.92	2.25	3.54	3.48	4.54	4.97	2.66	2.51	1.57	1.08	7.60	7.16
U	1.36	1.20	1.24	1.21	1.41	1.59	1.00	0.96	0.30	0.22	1.51	1.47
La	22.09	9.54	18.38	15.71	16.76	18.05	13.30	13.07	15.23	11.29	43.59	40.52
Ce	45.13	19.29	36.41	31.07	32.53	35.15	28.42	27.33	31.81	23.53	84.14	77.94
Pr	5.49	2.44	4.47	3.90	3.98	4.25	3.75	3.59	4.00	2.97	9.32	8.66
Nd	22.66	10.24	18.58	16.17	16.03	17.44	16.32	15.54	16.91	12.52	34.02	31.59
Sm	4.43	2.12	3.66	3.22	3.28	3.48	3.45	3.33	3.73	2.81	5.37	4.93
Eu	1.44	0.87	1.19	1.14	1.14	1.50	1.04	1.10	1.23	1.02	1.55	1.46
Gd	4.47	2.17	3.65	3.23	3.30	3.65	3.48	3.31	4.15	3.12	5.99	5.61
Tb	0.57	0.27	0.47	0.41	0.43	0.46	0.46	0.44	0.72	0.54	0.67	0.62
Dy	2.96	1.43	2.46	2.19	2.28	2.45	2.48	2.34	4.58	3.41	3.50	3.26
Ho	0.57	0.28	0.48	0.42	0.44	0.47	0.46	0.44	0.93	0.70	0.68	0.64
Er	1.66	0.83	1.39	1.24	1.30	1.36	1.32	1.24	2.72	2.02	1.99	1.90
Tm	0.23	0.12	0.20	0.18	0.19	0.19	0.18	0.17	0.40	0.29	0.27	0.26
Yb	1.53	0.79	1.24	1.15	1.22	1.28	1.15	1.09	2.56	1.88	1.75	1.66
Lu	0.23	0.12	0.19	0.18	0.19	0.19	0.17	0.16	0.39	0.29	0.26	0.26
Y	15.48	7.73	13.29	11.74	12.19	12.73	12.44	11.72	24.13	18.27	17.78	17.04
ΣREE	113.45	50.51	92.77	80.22	83.05	89.92	75.98	73.14	89.34	66.38	193.1	179.32
LREE	101.23	44.5	82.69	71.22	73.71	79.87	66.28	63.95	72.9	54.14	177.98	165.11
HREE	12.22	6.01	10.08	9	9.34	10.05	9.7	9.18	16.44	12.24	15.11	14.22
LREE/HREE	8.28	7.41	8.21	7.91	7.89	7.95	6.84	6.96	4.44	4.42	11.78	11.61
(La/Yb)N	10.36	8.63	10.62	9.77	9.84	10.13	8.33	8.61	4.27	4.31	17.85	17.5
(Dy/Yb)N	1.93	1.81	1.98	1.9	1.87	1.91	2.16	2.15	1.79	1.81	2	1.96
δEu	0.98	1.23	0.98	1.07	1.05	1.27	0.91	1	0.95	1.05	0.83	0.85
δCe	0.98	0.96	0.96	0.95	0.94	0.95	0.97	0.96	0.98	0.97	0.98	0.97

also contain Precambrian inherited zircon core (Haizi: 2,475 ± 33 Ma; Taiping: 2,463 ± 23 Ma) that reflect NCC crustal inheritance (Cenozoic Nushan basalt: ca. 2,455 and 2,716 Ma) (Ping et al., 2019). An oceanic slab-melting model was also proposed for the adakites (some high-Mg) in the nearby Banjing pluton (Xuhuai area), which is slightly younger (zircon U-Pb: 126.4 ± 2.1 Ma) and has similar structural setting (proximal to the Tanlu fault) to the Huaibei-Linhuan adakites

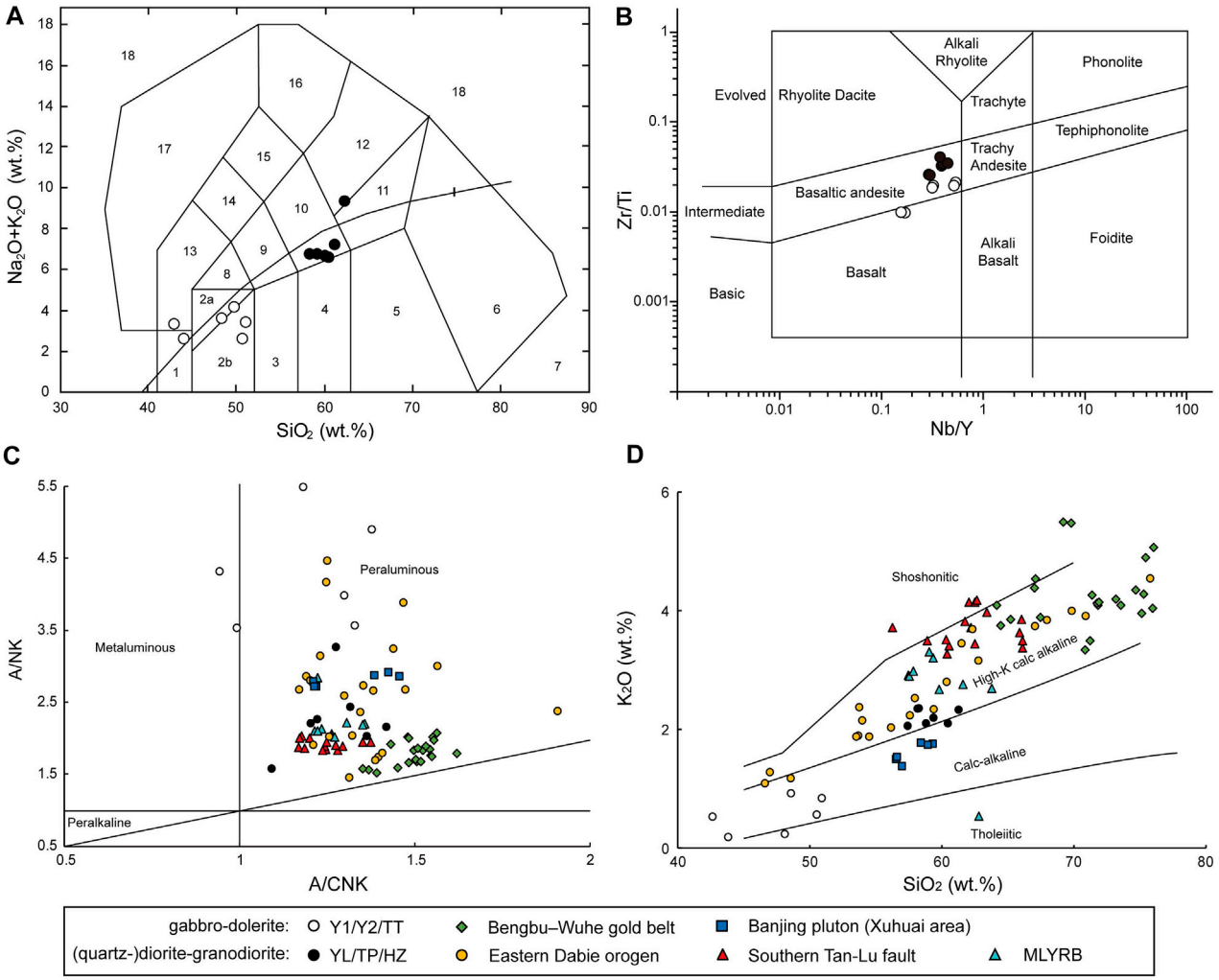

FIGURE 7 | Petrological classification plots for the igneous rock samples from the Huaibei-Linhuan coalfield: **(A)** Total Alkali Silica (TAS) (base map after Middlemost, 1994). The curve denotes the Ir (Irvine) boundary, separating the alkaline (above) and sub-alkaline (below). Number: 1) olivine gabbro; 2a) alkaline gabbro; 2b) sub-alkaline gabbro; 3) gabbroic diorite; 4) diorite; 5) granodiorite; 6) granite; 7) quartzolite; 8) monzogabbro; 9) monzodiorite; 10) monzonite; 11) quartz monzonite; 12) syenite; 13) foid gabbro; 14) foid monzogabbro; 15) foid monzosyenite; 16) foid syenite; 17) foidolite; 18) tawite/urtite/italite; **(B)** Zr/Ti vs. Nb/Y (after Pearce, 1996); **(C)** A/NK vs. A/CNK (base map after Maniar and Piccoli, 1989); **(D)** K_2O vs. SiO_2 (after Peccerillo and Taylor, 1976). For **Figures 5–6**, **9–10**, data from the adakitic rocks in the Bengbu-Wuhe gold belt (Li C. et al., 2020), Banjing pluton (Zhou et al., 2019), Eastern Dabie Orogen (Zhang et al., 2013), Lower Yangtze River Belt (Liu S.-A. et al., 2010) and southern Tanlu fault (Liu S.-A. et al., 2010) are also shown for comparison.

(Zhou et al., 2019). The Huaibei-Linhuan and Banjing are geochemically similar in terms of their low Th content and low Rb/Y and Nb/Y ratios (suggestive of minor crustal melt-derived enrichment), which are in marked contrast with the thickened lower crust-derived Bengbu-Wuhe gold ore-forming granitoids (Liu S.-A. et al., 2010) (**Figures 10C–D**).

Although not without controversies, many studies suggest that the Tanlu fault zone was first formed as a Triassic-Jurassic syn-collisional sinistral fault between the North China and South China (phengite Ar-Ar: ca. 221–210 and 198–181 Ma) (Zhu et al., 2009), and had displaced the Dabie–Sulu UHP metamorphic belt across a ~500 km distance (Zhu et al., 2005). The fault (esp. the southern part where the Huaibei-Linhuan coalfield is located) has likely reactivated several times during the Early Cretaceous (e.g., hornblende Ar-Ar = 143.3 Ma; phengite Ar-Ar = 138.8 Ma) (Zhu et al., 2005). The sinistral movement in the southern Tanlu fault (138.8 Ma; Zhu et al., 2005) was accompanied (or soon followed) by emplacement of granodiorite (~131 Ma), diorite (~130 Ma), and lamprophyre dykes (~128 Ma) of the Guandian intrusive complex (Zhao et al., 2020), whose ages are largely coeval (within error) with the ca. 130–129 Ma ages obtained for the Huaibei-Linhuan (quartz-)diorite-granodiorite. Based on whole-rock geochemical and Sr-Nd isotope geochemical data, Zhao et al. (2020) suggested that these Early Cretaceous intrusive rocks at Guandian were formed in an extensional setting, possibly related to the Paleo-Pacific subduction rollback. Such tectonic setting would fit with our suggestion that the Huaibei-Linhuan high-Mg adakitic (quartz-)diorite-granodiorite was formed by partial melting of the

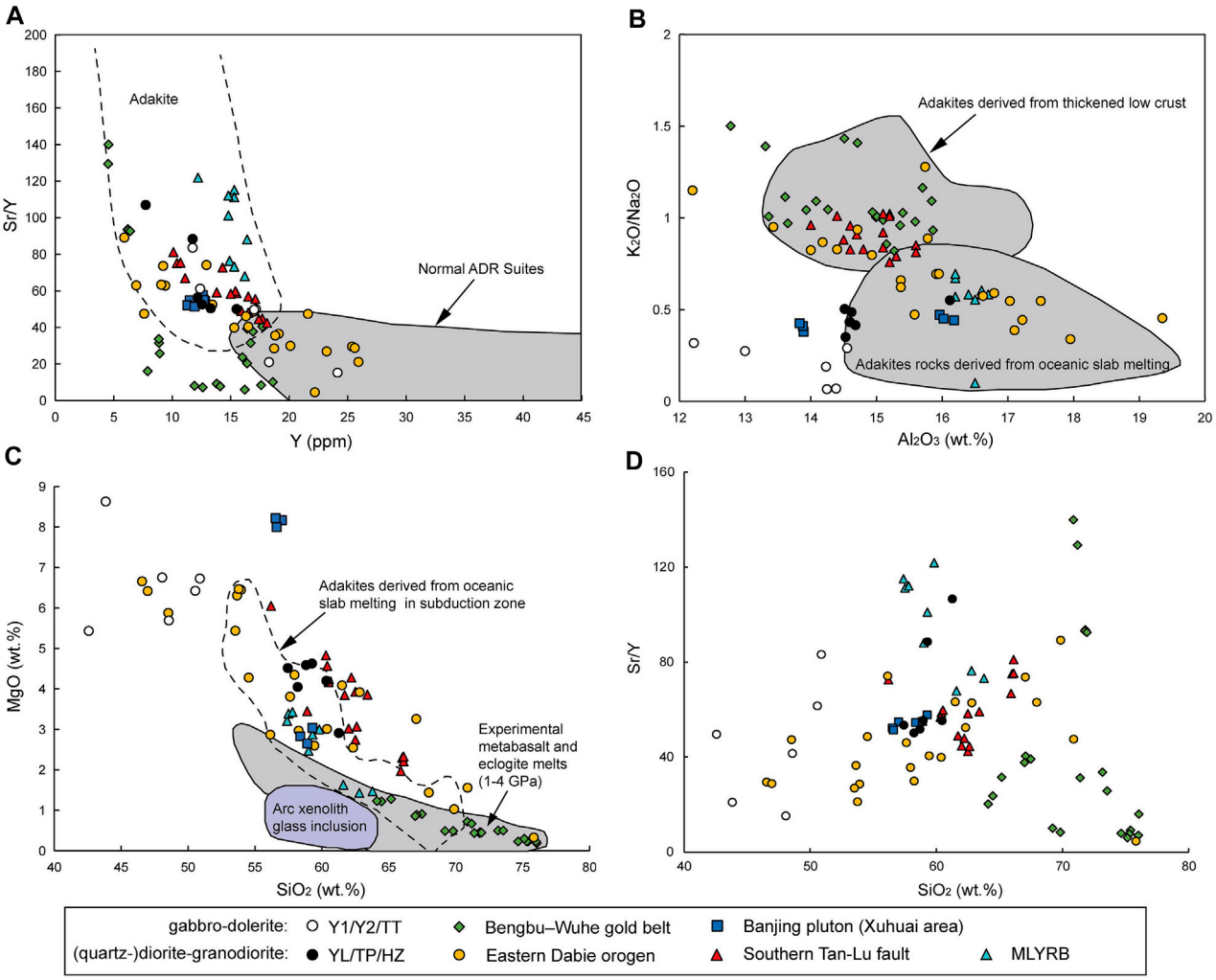

FIGURE 8 | Adakite discrimination plots for the igneous rock samples from the Huaibei-Linhuan coalfield: **(A)** Sr/Y vs. Y (after Defant and Drummond, 1993), andesites, dacites and rhyolites (ADR); **(B)** K_2O/Na_2O vs. Al_2O_3 (after Liu et al., 2010a, and ref. therein); **(C)** MgO vs. SiO_2 (base map after Liu et al., 2010a, and ref. therein); **(D)** Sr/Y vs. SiO_2 (after Richards et al., 2012).

subducted slab. A slab-tearing may also be possible (Zhao et al., 2016) to generate the adakites, although more work will be needed to constrain when and how it actually took place.

A detailed review of the Early Cretaceous tectonics across the North Pacific by Liu et al. (2021) has revealed that the Eastern Eurasia, as facilitated by the Paleo-Pacific subduction rollback (*via* eastward migration of the shallow mantle convection system), has undergone three major extensional events at around 160–145 Ma, 135–120 Ma (peak), and post-120 Ma. These extensional events were accompanied by synextensional magmatism at around 160 Ma, 130–120 Ma (magmatic flare-up), and 100–80 Ma. It is thus clear that the Huaibei-Linhuan high-Mg adakitic magmatism, like many Cu-Au ore-fertile or ore-barren adakitic rocks in the southern Tanlu fault and the LMYRB, were formed during this 130–120 Ma magmatic flare-up during the peak extension episode. Meanwhile, the late-Early Cretaceous gabbro-dolerite magmatism in Huaibei-Linhuan (Qingdong: 115.8 Ma; Yuandian-1: 105.8 Ma) was formed in the post-peak extension. The highly attenuated North China continental crust around the southern Tanlu fault may have enabled higher degree of partial melting with lower degree of crustal assimilation and fractionation, thereby forming more mafic rocks in Huaibei-Linhuan. The presence of highly-attenuated crust is also supported by the complete absence of inherited zircon core or xenocrystic zircon in the Huaibei-Linhuan gabbro-dolerite.

Metallogenic Implications in Fertile *Versus* Barren Adakites

From a metallogenic perspective, it is still unclear on why some Early Cretaceous adakites in Eastern China are Cu-Au ore-fertile (e.g., those in the MLYRB), whereas some others are ore-barren (e.g., those along the southern Tanlu fault). Based on whole-rock elemental and Sr-Nd-Pb isotope data, Liu S.-A. et al. (2010) argued that the ore-fertile MLYRB adakites were formed from partial

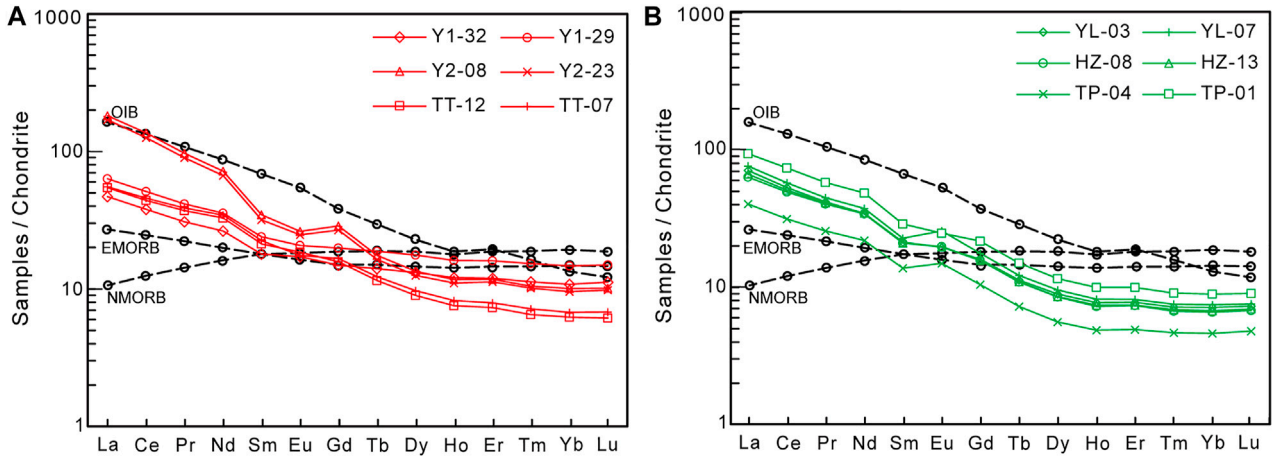

FIGURE 9 | Chondrite-normalized whole-rock REE patterns for the Huaibei-Linhuan intrusive rock samples: **(A)** gabbro-dolerite; **(B)** (quartz-)diorite and granodiorite. Chondrite normalizing values are from Sun and McDonough (1989).

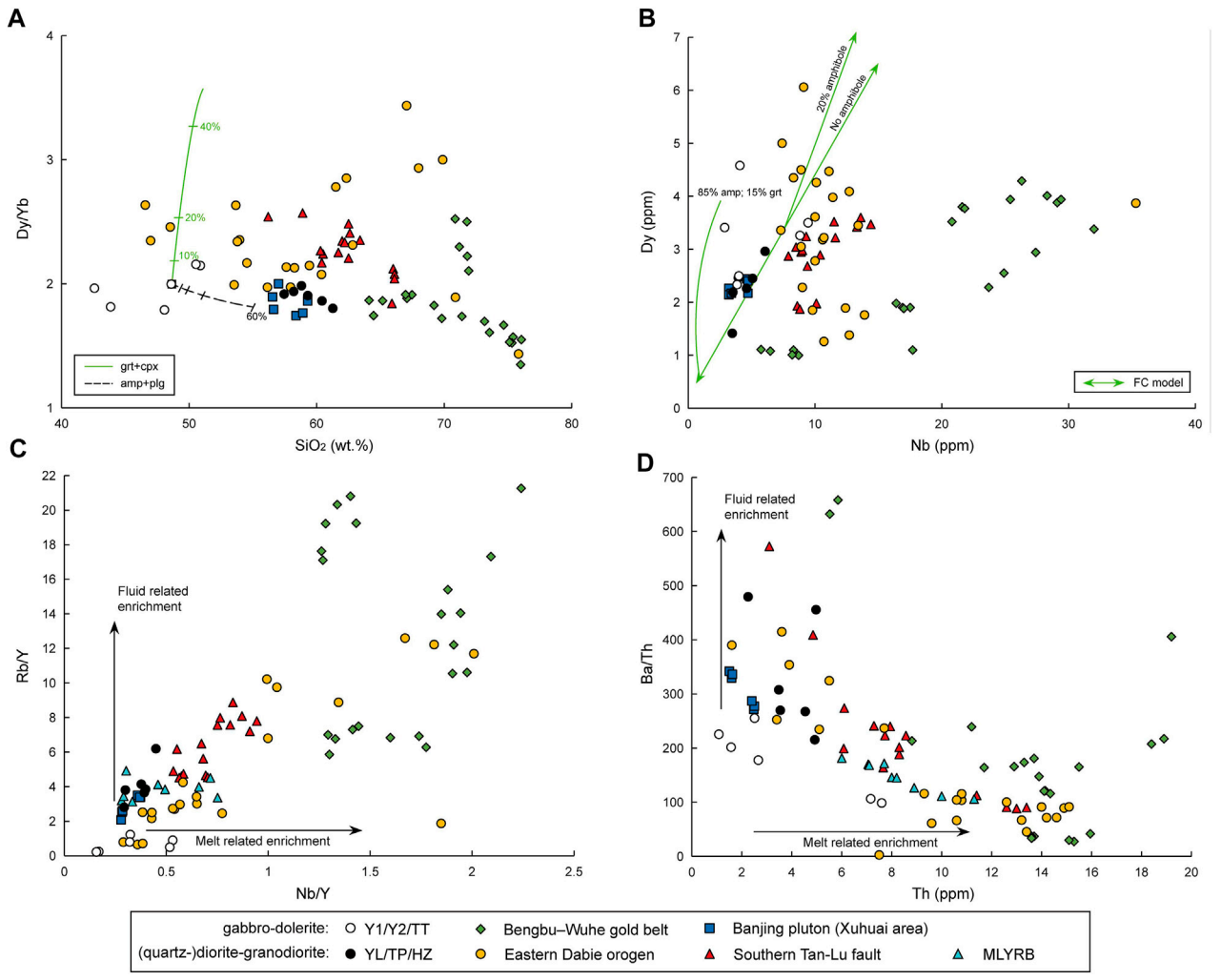

FIGURE 10 | (A–B) Trace element plots for identifying amphibole–garnet fractionation: **(A)** Dy/Yb vs. SiO_2. Model fractionation paths are from Davidson et al. (2007), Macpherson (2008); **(B)** Dy vs. Nb; **(C)** Nb/Ta vs. Nb. Fractional crystallization (FC) and assimilation-fractional crystallization (AFC) trends are from Gómez-Tuena et al. (2007); **(C–D)** Trace element plots for differentiating fluid-related vs. melt-related enrichments (after Zhao et al., 2020): **(C)** Rb/Y vs. Nb/Y; and **(D)** Ba/Th vs. Th. Abbreviations: amp = amphibole; cpx = clinopyroxene; grt = garnet, pl = plagioclase.

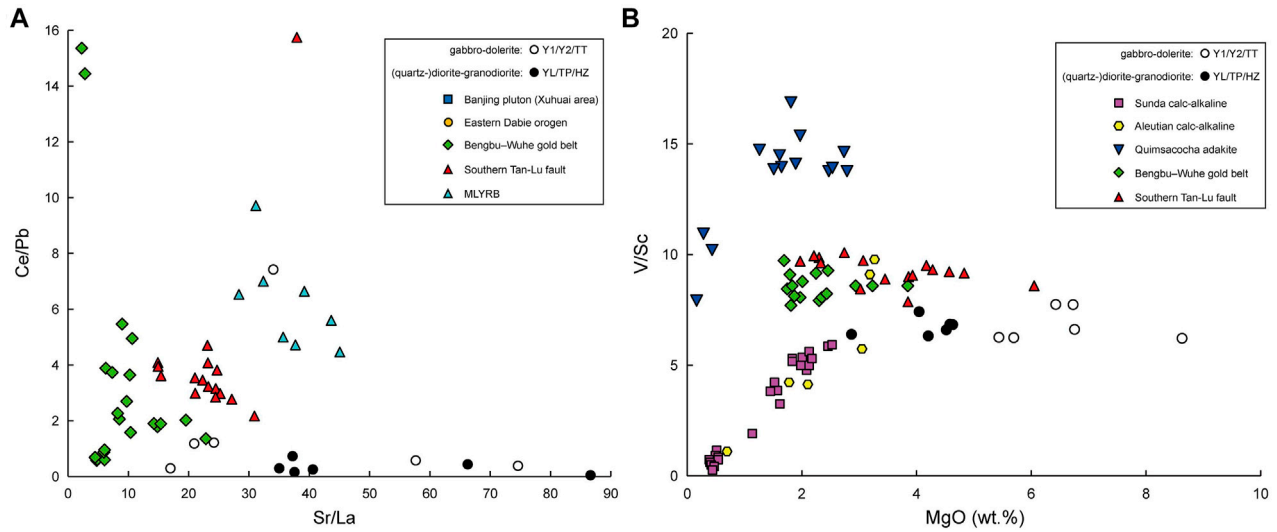

FIGURE 11 | Petrogenetic discrimination plots for the Huaibei-Linhuan intrusive rock samples: **(A)** Ce/Pb vs. Sr/La (after Liu S.-A. et al., 2010); **(B)** V/Sc vs. MgO (after Lee et al., 2005; Kamvong et al., 2014). V/Sc = proxy for fO_2 of parental magma. Data from the ore-related porphyries from Quimsacocha (Ecuador) (Beate et al., 2001) and Dexing (Eastern China) (Wang et al., 2006) and ore-barren calc-alkaline rocks from the Sunda arc (Reubi and Nicholls, 2004) and Aleutian arc (Jicha and Singer, 2006) are also shown for comparison.

melting of the seawater-metasomatized Paleo-Pacific slab, whereas the ore-barren adakites along the southern Tanlu fault were derived from the delaminated North China eclogitic lower continental crust. This explanation, however, is unlikely applicable to the ore-barren Huaibei-Linhuan adakitic (quartz-)diorite-granodiorite, as their formation was likely slab-melting-related similar to the MLYRB adakites. This suggestion is supported by the elevated Sr/La values, which are comparable to the ore-fertile MLYRB adakites but considerably higher than the ore-barren adakites along the southern Tanlu fault (**Figure 12A**).

Porphyry-type Cu-Au fertility is controlled by a number of factors, including the contents of metals, water and sulfur of the magma, the magma oxygen fugacity (fO_2), as well as thickness of the crust into which the magma was emplaced (e.g., Audétat et al., 2008; Richards et al., 2012; Park et al., 2019, 2021). Comparing with our Huaibei-Linhuan samples, both the mineralized adakites in the MLYRB and the barren adakites in the southern Tanlu fault are more fractionated (Liu S.-A. et al., 2010) (**Figure 7D**). The MLYRB adakites have distinctly higher Sr/Y (67.96–121.89) than their barren counterparts in Huaibei-Linhuan (15.26–106.95) and the southern Tanlu fault (42.49–81.19). The "more-adakitic" (higher Sr/Y) character in the MLYRB rocks may have caused by the higher magma water content (i.e., "wetter magma"), which can suppress plagioclase fractionation and promote early amphibole ± garnet fractionation (Richards, 2011, and ref. therein).

Previous studies suggested that elevated zircon Eu/Eu* (>0.3) can reflect elevated magma water content, as widely reported from ore-forming porphyries at El Salvador and Chuquicamata-El Abra (Chile), Yanacocha (Peru), Yerington (Nevada, US), Batu Hijau (Indonesia), Tampakan (Philippines), and Dexing, Qulong, and Jiama (China) (Ballard et al., 2002; Dilles et al., 2015; Lu et al., 2016). Lu et al. (2016) proposed that wet fertile magmas have commonly high 10,000*(Eu/Eu*)/Y and Eu/Eu* ratios, with both ratios being positively correlated with (Ce/Nd)/Y. Zircon Ce/Nd ratio can be used as a proxy of magma fO_2 in replace of Ce^{4+}/Ce^{3+}, which is hard to be accurately determined due to the very low (often below the detection limit) zircon La and Pr contents, and the zircon La content is also susceptible to contamination by minute apatite inclusions (Lu et al., 2016; Loucks et al., 2020). Yttrium is added to the denominator of 10,000*(Eu/Eu*)/Y and (Ce/Nd)/Y because its content is commonly low in fertile magmas, caused probably by early hornblende fractionation (Lu et al., 2016, and ref. therein).

From **Figures 14A–B**, it is seen that the Cretaceous Huaibei-Linhuan adakites have comparable 10,000*(Eu/Eu*)/Y and Eu/Eu* ratios to those of the ore-forming granodiorite porphyries in the MLYRB (Jiurui orefield; Xu et al., 2021), as well as to many other fertile adakitic suites (Lu et al., 2016). Similar to the MLYRB ore-forming porphyries, the zircon 10,000*(Eu/Eu*)/Y and Eu/Eu* ratios of the Huaibei-Linhuan adakites are correlated positively with (Ce/Nd)/Y. This suggests that the Huaibei-Linhuan adakitic magma was not H_2O-poor, as also supported by the considerable amount of hornblende present in our samples (**Figure 14C**).

Therefore, we considered that the cause of Cu-Au infertility for the Huaibei-Linhuan adakites may lie in the lower fO_2 of their parental magma. In **Figure 14**, the Huaibei-Linhuan adakites have generally lower (Ce/Nd)/Y (avg. 0.035) than their MLYRB counterpart (avg. 0.051), suggesting lower fO_2 in the former. For the case of Huaibei-Linhuan, the Ce/Nd ratio can serve as good proxy for the Ce anomaly, as indicated by certain positive correlation (R^2 = 0.29) between the two (**Figure 14D**). The more reducing nature of the Huaibei-Linhuan adakitic magma is further supported by the whole-rock V/Sc content, which serves as a proxy for the original magma fO_2 (Lee et al., 2005). In the V/Sc vs. Mg discrimination plot (**Figure 11B**), the Huaibei-Linhuan adakites have distinctly lower V/Sc values than the Cu-Au ore-related porphyries from Quimsacocha (Ecuador) (Beate et al., 2001) and

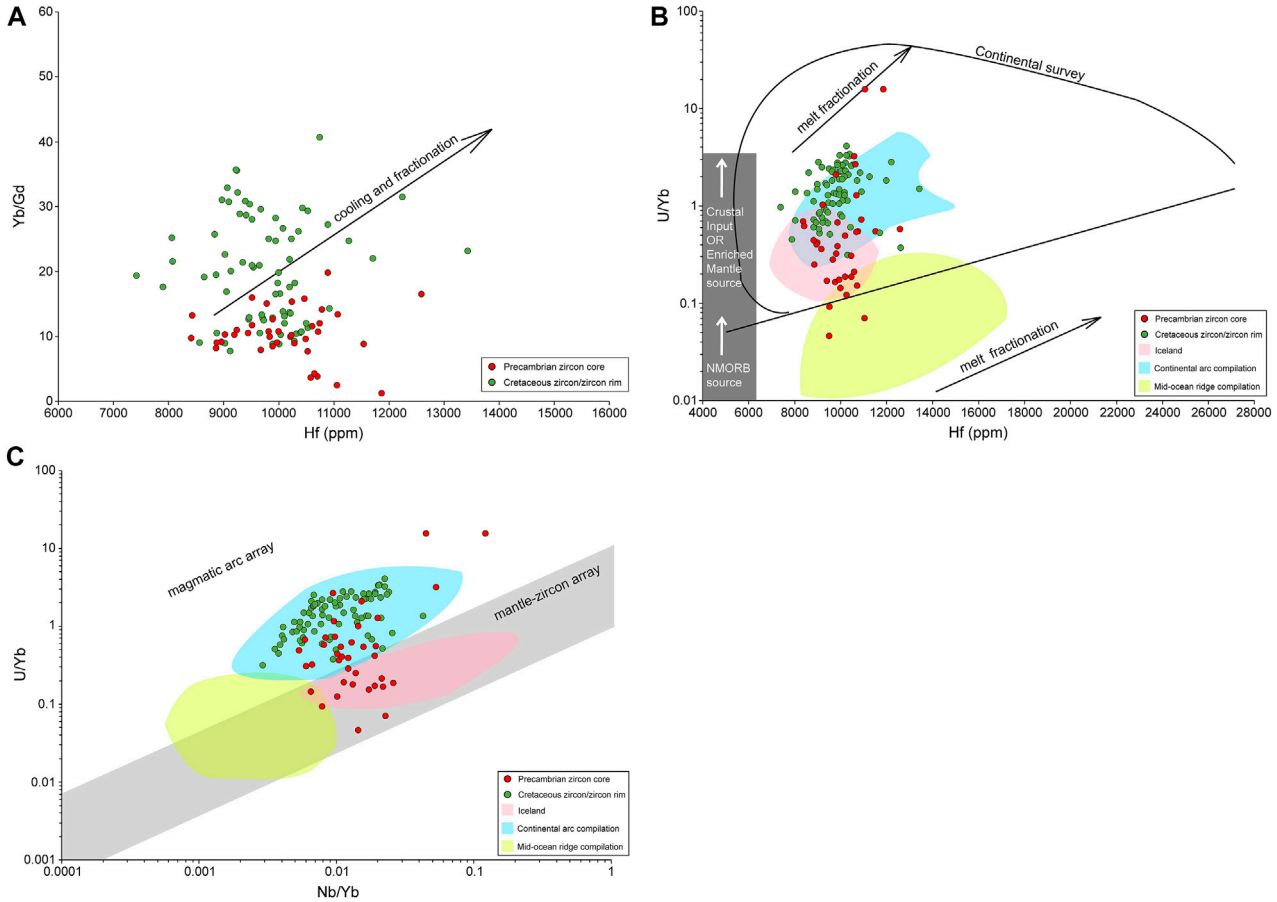

FIGURE 12 | Plots of **(A)** Yb/Gd vs. Hf (base map from Barth and Wooden, 2010), **(B)** U/Yb vs. Hf (base map from Grimes et al., 2015), and **(C)** U/Yb vs. Nb/Yb (base map from Grimes et al., 2015) for zircons from the Huaibei-Linhuan intrusive rock samples.

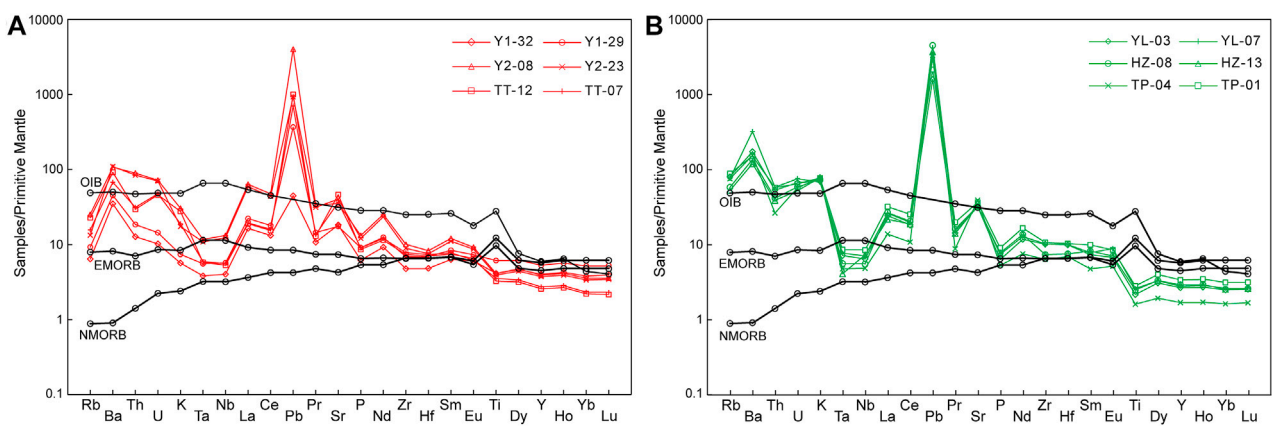

FIGURE 13 | Primitive mantle-normalized spider diagrams for the Huaibei-Linhuan intrusive rock samples: **(A)** gabbro-dolerite; **(B)** (quartz-)diorite and granodiorite. Primitive mantle normalizing values are from Sun and McDonough (1989).

Dexing (Eastern China) (Wang et al., 2006). The V/Sc values remain constant with decreasing MgO, indicating that the V/Sc is not dependent on fractionation. Elevated magma fO_2 has been suggested to be critical in forming porphyry-style Cu-Au mineralization, as it would inhibit early sulfide crystallization and allow chalcophile metals to concentrate in late-stage hydrothermal

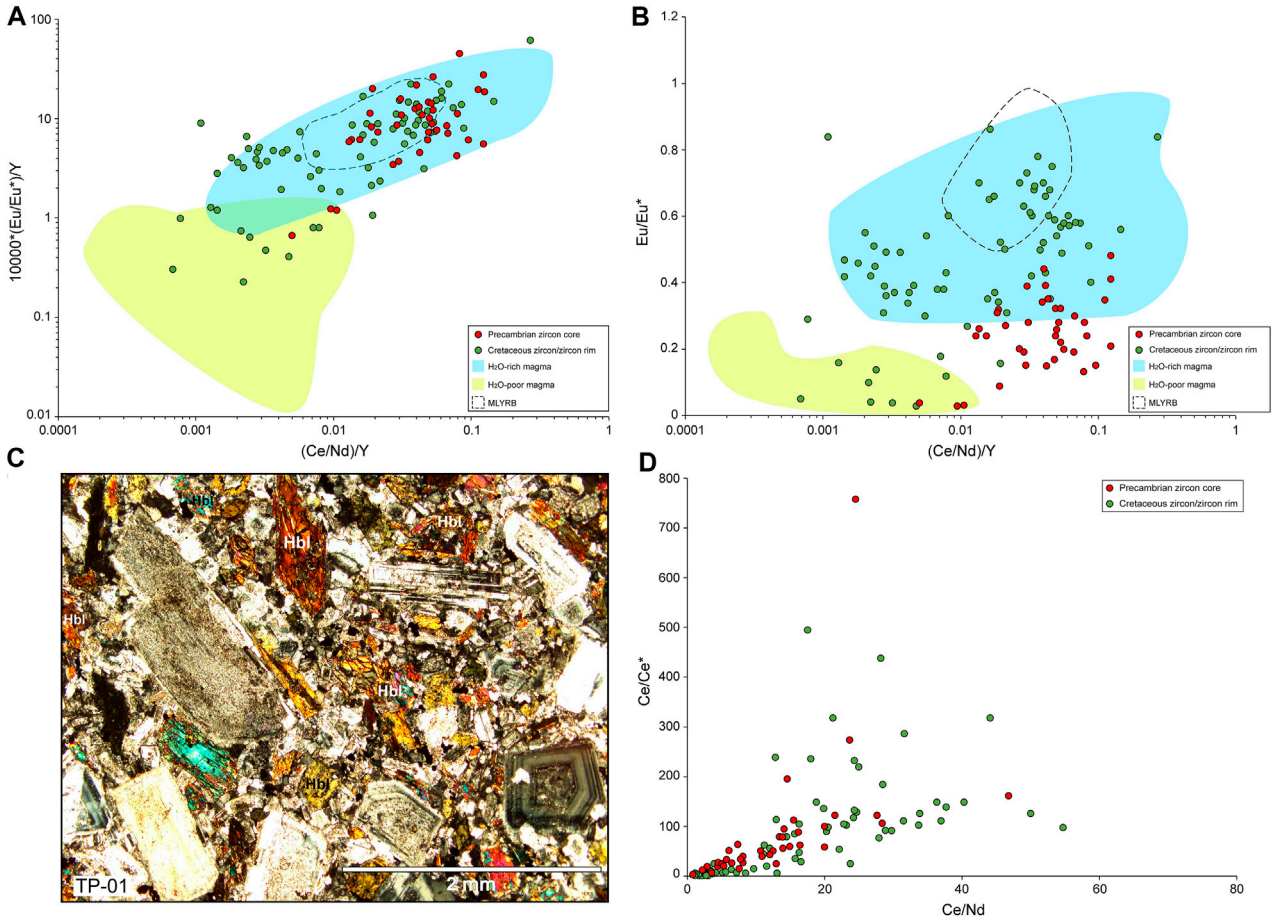

FIGURE 14 | (A) 10000*(Eu/Eu*)/Y vs. (Ce/Nd)/Y and **(B)** (Eu/Eu*)/Y vs. (Ce/Nd)/Y plots for zircons from the Huaibei-Linhuan intrusive rock samples (base map from Lu et al., 2016); **(C)** Thin-section microscopic photos showing the abundance of igneous hornblende in Taiping diorite (TP-01); **(D)** Zircon Ce/Ce* vs. Ce/Nd plot for the Huaibei-Linhuan intrusive rock samples, showing that Ce/Nd is a good proxy for Ce anomalies.

fluids (e.g., Mungall, 2002; Sillitoe, 2010; Zhang et al., 2017). Mungall et al. (2015) further proposed that sulfide liquids can ascend to the shallow crust through attaching with vapor bubbles, rather than only residing in the deep crust as traditionally believed. The reasons why the parental magma of the Huaibei-Linhuan adakites was particularly low-fO_2 (even lower than that of the ore-barren adakites along the southern Tanlu fault) is unclear, but may partly be attributed to the NCC lithospheric heterogeneity, especially along/near the southern Tanlu fault (e.g., Lü, 2019; Wang et al., 2020). In Huaibei-Linhuan, assimilation of the Carboniferous-Permian coal seams (as shown by the partially-assimilated natural coke fragments in our samples; **Figure 3**) would likely further reduce the fO_2 of the intruding dioritic-granodioritic magma, and hence further decrease its potential to form porphyry-style/-related Cu-Au mineralization.

CONCLUSIONS

1) Petrography, zircon U-Pb dating and whole-rock geochemistry suggests that the Huaibei-Linhuan intrusive rocks fall into two types, early-Early Cretaceous (ca. 130–129 Ma) high-Mg adakitic (quartz-)diorite and granodiorite, and late-Early Cretaceous (ca. 115.8 and 105.8 Ma) calc-alkaline microgabbro and dolerite.
2) The Huaibei-Linhuan high-Mg adakitic (quartz-)diorite and granodiorite are featured by low K_2O/Na_2O, high Sr/La, and lack of correlation between SiO_2 (fractionation index) and Sr/Y and MREE/HREE. This suggests that the adakites were not derived from high-pressure garnet-amphibole fractionation or partial melting of the thickened lower crust, but from partial melting of the subducted slab. Age correlation with the regional tectonic events suggests that the slab-melting may have caused by rollback of the subducting Paleo-Pacific slab instead. Further extension and crustal delamination along the southern Tanlu fault may have led to higher-degree partial melting (and lower-degree assimilation-fractionation) that formed the gabbro-dolerite in the Huaibei-Linhuan coalfield.
3) Parental magma of the Huaibei-Linhuan high-Mg adakites was considerably less oxidized than typical porphyry Cu-Au ore-forming magmas, although their water content may have been similarly high. The low magma fO_2 nature is supported

by both the low zircon Ce/Nd and whole-rock V/Sc ratios. The assimilation of the Carboniferous-Permian coal-bearing sequences in the area may have further decreased the magma fO_2, and thus its potential to form Cu-Au mineralization.

DATA AVAILABILITY STATEMENT

The original contributions presented in the study are included in the article/Supplementary Material, further inquiries can be directed to the corresponding author.

AUTHOR CONTRIBUTIONS

SZ: investigation, funding and writing. YA: supervision and writing. CL: data interpretation and writing. HW: analysis and academic support. YL: analysis and academic support. All authors have contributed to the article and approved the submitted version.

FUNDING

The project is jointly funded by the Natural Science Foundation of China (Grant No. 41802244) to the corresponding author.

ACKNOWLEDGMENTS

We sincerely thank Yuangao Sun, Shuai Zhang, and Qiang Fu for their field and logistic support. We would also like to thank Zhongqing Lin and Zheng Liu for assisting with the zircon U-Pb dating and whole-rock geochemical analysis. We are grateful to the Chief Editor Prof. David Lentz, the Handling Editor Prof. Hassan Mirnejad, and two knowledgeable reviewers for their insightful comments.

REFERENCES

Aeolus Lee, C.-T., Leeman, W. P., Canil, D., and Li, Z.-X. A. (2005). Similar V/Sc systematics in MORB and arc basalts: Implications for the oxygen fugacities of their mantle source regions. *J. Petrol.* 46, 2313–2336. doi:10.1093/petrology/egi056

An, Y., Liu, L., Wang, M., Zheng, S., Guo, Y., Zhang, S., et al. (2018). Source and enrichment of toxic elements in coal seams around mafic intrusions: Constraints from pyrites in the Yuandian Coal Mine in Anhui, Eastern China. *Minerals* 8 (4), 164. doi:10.3390/min8040164

Audétat, A., Pettke, T., Heinrich, C. A., and Bodnar, R. J. (2008). Special Paper: The Composition of Magmatic-Hydrothermal Fluids in Barren and Mineralized Intrusions. *Econ. Geology.* 103, 877–908. doi:10.2113/gsecongeo.103.5.877

Ballard, J. R., Palin, M. J., and Campbell, I. H. (2002). Relative oxidation states of magmas inferred from Ce(IV)/Ce(III) in zircon: Application to porphyry copper deposits of northern Chile. *Contrib. Mineral. Petrol.* 144, 347–364. doi:10.1007/s00410–002–0402–5

Barth, A. P., and Wooden, J. L. (2010). Coupled elemental and isotopic analyses of polygenetic zircons from granitic rocks by ion microprobe, with implications for melt evolution and the sources of granitic magmas. *Chem. Geology.* 277, 149–159. doi:10.1016/j.chemgeo.2010.07.017

Beate, B., Monzier, M., Spikings, R., Cotten, J., Silva, J., Bourdon, E., et al. (2001). Mio-Pliocene adakite generation related to flat subduction in southern Ecuador: the Quimsacocha volcanic center. *Earth Planet. Sci. Lett.* 192, 561–570. doi:10.1016/S0012-821X(01)00466–6

Belousova, E., Griffin, W., O'Reilly, S. Y., and Fisher, N. (2002). Igneous zircon: trace element composition as an indicator of source rock type. *Contrib. Mineral. Petrol.* 143, 602–622. doi:10.1007/s00410–002–0364–7

Castillo, P. R., Janney, P. E., and Solidum, R. U. (1999). Petrology and geochemistry of Camiguin Island, southern Philippines: Insights to the source of adakites and other lavas in a complex arc setting. *Contrib. Mineralogy Pet.* 134, 33–51. doi:10.1007/s004100050467

Chiaradia, M., Ulianov, A., Kouzmanov, K., and Beate, B. (2012). Why large porphyry Cu deposits like high Sr/Y magmas. *Sci. Repep* 2, 685. doi:10.1038/srep00685

Davidson, J., Turner, S., Handley, H., Macpherson, C., and Dosseto, A. (2007). Amphibole "sponge" in arc crust. *Geol* 35, 787–790. doi:10.1130/G23637A.110.1130/g23637a.1

Defant, M. J., and Drummond, M. S. (1993). Mount St. Helens: Potential example of the partial melting of the subducted lithosphere in a volcanic arc. *Geol* 21, 547–550. doi:10.1130/0091-7613(1993)021<0547:mshpeo>2.3.co;2

Deng, J., Yang, L.-Q., Groves, D. I., Zhang, L., Qiu, K.-F., and Wang, Q.-F. (2020). An integrated mineral system model for the gold deposits of the giant Jiaodong province, eastern China. *Earth-Science Rev.* 208, 103274. doi:10.1016/j.earscirev.2020.103274

Dilles, J. H., Kent, A. J. R., Wooden, J. L., Tosdal, R. M., Koleszar, A., Lee, R. G., et al. (2015). Zircon Compositional Evidence for Sulfur-degassing from Ore-forming Arc Magmas. *Econ. Geology.* 110, 241–251. doi:10.2113/econgeo.110.1.241

Dong, Y., Liu, J., Zhang, Y., Dou, S., Li, Y., Liu, S., et al. (2020). Early Cretaceous Xiuyan adakitic granitoids in the Liaodong Peninsula, eastern China: petrogenesis and implications for lithospheric thinning of the North China Craton. *Can. J. Earth Sci.* 58, 50–66. doi:10.1139/cjes–2020–0033

Goldfarb, R. J., and Santosh, M. (2014). The dilemma of the Jiaodong gold deposits: Are they unique. *Geosci. Front.* 5, 139–153. doi:10.1016/j.gsf.2013.11.00110.1016/j.gsf.2013.11.001

Gómez-Tuena, A., Langmuir, C. H., Goldstein, S. L., Straub, S. M., and Ortega-Gutiérrez, F. (2007). Geochemical evidence for slab melting in the trans-Mexican volcanic belt. *J. Petrol.* 48, 537–562. doi:10.1093/petrology/egl071

Grimes, C. B., Wooden, J. L., Cheadle, M. J., and John, B. E. (2015). "Fingerprinting" tectono-magmatic provenance using trace elements in igneous zircon. *Contrib. Mineral. Petrol.* 170, 46. doi:10.1007/s00410–015–1199–3

Hong, L., Xu, Y., Zhang, L., Liu, Z., Xia, X., and Kuang, Y. (2020). Oxidized Late Mesozoic subcontinental lithospheric mantle beneath the eastern North China Craton: A clue to understanding cratonic destruction. *Gondwana Res.* 81, 230–239. doi:10.1016/j.gr.2019.11.012

Hoskin, P. W. O., and Black, L. P. (2000). Metamorphic zircon formation by solid-state recrystallization of protolith igneous zircon. *J. Metamorphic Geology.* 18 (4), 423–439. doi:10.1046/j.1525–1314.2000.00266.x

Jiang, X.-Y., Deng, J.-H., Luo, J.-C., Zhang, L.-P., Luo, Z.-B., Yan, H.-B., et al. (2020). Petrogenesis of Early Cretaceous adakites in Tongguanshan Cu-Au polymetallic deposit, Tongling region, Eastern China. *Ore Geology. Rev.* 126, 103717. doi:10.1016/j.oregeorev.2020.103717

Jicha, B. R., and Singer, B. S. (2006). Volcanic history and magmatic evolution of Seguam Island, Aleutian Island arc, Alaska. *Geol. Soc. America Bull.* 118, 805–822. doi:10.1130/B2586110.1130/b25861.1

Kamvong, T., Khin Zaw, K., Meffre, S., Maas, R., Stein, H., and Lai, C.-K. (2014). Adakites in the Truong Son and Loei fold belts, Thailand and Laos: Genesis and implications for geodynamics and metallogeny. *Gondwana Res.* 26, 165–184. doi:10.1016/j.gr.2013.06.011

Li, C., Yan, J., Wang, A.-G., Liu, J.-M., and Li, Z.-S. (2020a). Petrogenesis of Cretaceous granitoids in the Bengbu-Wuhe area, southeastern North China Craton: Implications for gold mineralization. *Ore Geology. Rev.* 126, 103740. doi:10.1016/j.oregeorev.2020.103740

Li, J., Wang, K.-y., Cai, W.-y., Sun, F.-y., Liu, H.-l., Fu, L.-j., et al. (2020b). Triassic gold-silver metallogenesis in Qingchengzi orefield, North China Craton: Perspective from fluid inclusions, REE and H-O-S-Pb isotope systematics. *Ore Geology. Rev.* 121, 103567. doi:10.1016/j.oregeorev.2020.103567

Li, S., Jahn, B.-m., Zhao, S., Dai, L., Li, X., Suo, Y., et al. (2017). Triassic southeastward subduction of North China Block to South China Block: Insights from new geological, geophysical and geochemical data. *Earth-Science Rev.* 166, 270–285. doi:10.1016/j.earscirev.2017.01.009

Li, S., Zhao, G., Dai, L., Liu, X., Zhou, L., Santosh, M., et al. (2012). Mesozoic basins in eastern China and their bearing on the deconstruction of the North China Craton. *J. Asian Earth Sci.* 47, 64–79. doi:10.1016/j.jseaes.2011.06.008

Liu, J., Liu, F.-X., Li, S.-H., and Lai, C.-K. (2019). Formation of the Baiyun gold deposit, Liaodong gold province, NE China: Constraints from zircon U-Pb age, fluid inclusion, and C-H-O-Pb-He isotopes. *Ore Geol. Rev.*, 104. doi:10.1016/j.oregeorev.2018.12.006

Liu, J., Liu, F. X., Li, S. H., and Lai, C. K. (2020). Genesis of the Xiaotongjiapuzi gold deposit of the Liaodong gold province, Northeast China: Fluid inclusion thermometry and S-Pb-H-O-He isotope constraints. *Geol. J.* 55, 1023–1040. doi:10.1002/gj.3454

Liu, J., Ni, J., Chen, X., Craddock, J. P., Zheng, Y., Ji, L., et al. (2021). Early Cretaceous tectonics across the North Pacific: New insights from multiphase tectonic extension in Eastern Eurasia. *Earth-Science Rev.* 217, 103552. doi:10.1016/j.earscirev.2021.103552

Liu, S.-A., Li, S., Guo, S., Hou, Z., and He, Y. (2012). The Cretaceous adakitic-basaltic-granitic magma sequence on south-eastern margin of the North China Craton: Implications for lithospheric thinning mechanism. *Lithos* 134-135 (135), 163–178. doi:10.1016/j.lithos.2011.12.015

Liu, S.-A., Li, S., He, Y., and Huang, F. (2010a). Geochemical contrasts between early Cretaceous ore-bearing and ore-barren high-Mg adakites in central-eastern China: Implications for petrogenesis and Cu-Au mineralization. *Geochimica et Cosmochimica Acta* 74, 7160–7178. doi:10.1016/j.gca.2010.09.003

Liu, Y., Gao, S., Hu, Z., Gao, C., Zong, K., and Wang, D. (2010b). Continental and Oceanic Crust Recycling-induced Melt-Peridotite Interactions in the Trans-North China Orogen: U-Pb Dating, Hf Isotopes and Trace Elements in Zircons from Mantle Xenoliths. *J. Pet.* 51, 537–571. doi:10.1093/petrology/egp082

Liu, Y., Hu, Z., Gao, S., Günther, D., Xu, J., Gao, C., et al. (2008). *In situ* analysis of major and trace elements of anhydrous minerals by LA-ICP-MS without applying an internal standard. *Chem. Geology.* 257, 34–43. doi:10.1016/j.chemgeo.2008.08.004

Loucks, R. R., Fiorentini, M. L., and Henríquez, G. J. (2020). New Magmatic Oxybarometer Using Trace Elements in Zircon. *J. Petrol.*, 61. doi:10.1093/petrology/egaa034

Lü, Q., Meng, G., Zhang, K., Liu, Z., Yan, J., Shi, D., et al. (2021). The lithospheric architecture of the Lower Yangtze Metallogenic Belt, East China: Insights into an extensive Fe-Cu mineral system. *Ore Geology. Rev.* 132, 103989. doi:10.1016/j.oregeorev.2021.103989

Lu, Y.-J., Loucks, R. R., Fiorentini, M., McCuaig, T. C., Evans, N. J., Yang, Z.-M., et al. (2016). Zircon Compositions as a Pathfinder for Porphyry Cu ± Mo ± Au Deposits. *Tectonics Metallog. Tethyan Orog. Belt* 19, 0. doi:10.5382/SP.19.13

Lü, Z. (2019). Uppermost mantle velocity and anisotropy structure beneath the North China Craton and its adjacent regions. *Tectonophysics* 754, 45–55. doi:10.1016/j.tecto.2019.01.014

Ludwig, K. R. (2003). *ISOPLOT 3.00: A Geochronological Toolkit for Microsoft Excel*. Berkeley: Berkeley Geochronology CenterCalifornia.

Macpherson, C. G. (2008). Lithosphere erosion and crustal growth in subduction zones: Insights from initiation of the nascent East Philippine Arc. *Geol* 36, 311–314. doi:10.1130/G24412A.1

Maniar, P. D., and Piccoli, P. M. (1989). Tectonic discrimination of granitoids. *Geol. Soc. Am. Bull.* 101 (5), 635–643. doi:10.1130/0016-7606(1989)101<0635:tdog>2.3.co;2

Mao, J., Wang, Y., Lehmann, B., Yu, J., Du, A., Mei, Y., et al. (2006). Molybdenite Re-Os and albite 40Ar/39Ar dating of Cu-Au-Mo and magnetite porphyry systems in the Yangtze River valley and metallogenic implications. *Ore Geology. Rev.* 29, 307–324. doi:10.1016/j.oregeorev.2005.11.001

Middlemost, E. A. K. (1994). Naming materials in the magma/igneous rock system. *Earth-Science Rev.* 37, 215–224. doi:10.1016/0012–8252(94)90029–9

Mori, L., Gómez-Tuena, A., Cai, Y., and Goldstein, S. L. (2007). Effects of prolonged flat subduction on the Miocene magmatic record of the central Trans-Mexican Volcanic Belt. *Chem. Geology.* 244, 452–473. doi:10.1016/j.chemgeo.2007.07.002

Mungall, J. E., Brenan, J. M., Godel, B., Barnes, S. J., and Gaillard, F. (2015). Transport of metals and sulphur in magmas by flotation of sulphide melt on vapour bubbles. *Nat. Geosci* 8, 216–219. doi:10.1038/ngeo2373

Mungall, J. E. (2002). Roasting the mantle: Slab melting and the genesis of major Au and Au-rich Cu deposits. *Geol* 30, 915–918. doi:10.1130/0091-7613(2002)030<0915:rtmsma>2.0.co;2

Pearce, J. (1996). A user's Guide to basalt discrimination diagrams. *Geol. Assoc. Can. Short Course Notes* 12, 79–113. doi:10.1111/j.1438–8677.1980.tb03374.x10.1093/oq/12.3.83

Peccerillo, A., and Taylor, S. R. (1976). Geochemistry of Eocene Calc-Alkaline Volcanic Rocks from the Kastamonu Area, Northern Turkey. *Contr. Mineral. Petrol.* 58, 63–81. doi:10.1007/BF00384745

Ping, X., Zheng, J., Xiong, Q., Griffin, W. L., Yu, C., and Su, Y. (2019). Downward rejuvenation of the continental lower crust beneath the southeastern North China Craton. *Tectonophysics* 750, 213–228. doi:10.1016/j.tecto.2018.11.012

Pirajno, F., and Zhou, T. (2015). Intracontinental Porphyry and Porphyry-Skarn Mineral Systems in Eastern China: Scrutiny of a Special Case "Made-in-China". *Econ. Geology.* 110, 603–629. doi:10.2113/econgeo.110.3.603

Reich, M., Parada, M. A., Palacios, C., Dietrich, A., Schultz, F., and Lehmann, B. (2003). Adakite-like signature of Late Miocene intrusions at the Los Pelambres giant porphyry copper deposit in the Andes of central Chile: metallogenic implications. *Mineralium Deposita* 38, 876–885. doi:10.1007/s00126–003–0369–9

Reubi, O., and Nicholls, I. A. (2004). Magmatic evolution at Batur volcanic field, Bali, Indonesia: petrological evidence for polybaric fractional crystallization and implications for caldera-forming eruptions. *J. Volcanology Geothermal Res.* 138, 345–369. doi:10.1016/j.jvolgeores.2004.07.009

Richards, J. P. (2011). High Sr/Y Arc Magmas And Porphyry Cu Mo Au Deposits: Just Add Water. *Econ. Geology.* 106, 1075–1081. doi:10.2113/econgeo.106.7.1075

Richards, J. P., and Kerrich, R. (2007). Special Paper: Adakite-Like Rocks: Their Diverse Origins and Questionable Role in Metallogenesis. *Econ. Geology.* 102 (4), 537–576. doi:10.2113/gsecongeo.102.4.537

Richards, J. P., Spell, T., Rameh, E., Razique, A., and Fletcher, T. (2012). High Sr/Y Magmas Reflect Arc Maturity, High Magmatic Water Content, and Porphyry Cu ± Mo ± Au Potential: Examples from the Tethyan Arcs of Central and Eastern Iran and Western Pakistan. *Econ. Geol.* 107, 295–332. doi:10.2113/econgeo.107.2.295

Sillitoe, R. H. (2010). Porphyry copper systems. *Econ. Geology.* 105, 3–41. doi:10.2113/gsecongeo.105.1.3

Sun, P., Guo, P., and Niu, Y. (2021). Eastern China continental lithosphere thinning is a consequence of paleo-Pacific plate subduction: A review and new perspectives. *Earth-Science Rev.* 218, 103680. doi:10.1016/j.earscirev.2021.103680

Sun, S.-s., and McDonough, W. F. (1989). Chemical and isotopic systematics of oceanic basalts: implications for mantle composition and processes. *Geol. Soc. Lond. Spec. Publications* 42, 313–345. doi:10.1144/GSL.SP.1989.042.01.19

Sun, W., Xie, Z., Chen, J., and Zhang, X. (2003). Os-Os dating of copper and molybdenum deposits along the Middle and Lower reaches of the Yangtze River, China. *Econ. Geology.* 98, 175–180. 0361–0128/01/3323/175–610.2113/98.1.175.

Wang, K., Chen, L., Xiong, X., Yan, Z., and Xie, R. (2020). The role of lithospheric heterogeneities in continental rifting: Implications for rift diversity in the North China Craton. *J. Geodynamics* 139, 101765. doi:10.1016/j.jog.2020.101765

Wang, Q., Xu, J.-F., Jian, P., Bao, Z.-W., Zhao, Z.-H., Li, C.-F., et al. (2006). Petrogenesis of Adakitic Porphyries in an Extensional Tectonic Setting, Dexing, South China: Implications for the Genesis of Porphyry Copper Mineralization. *J. Petrol.* 47, 119–144. doi:10.1093/petrology/egi070

Xia, Q.-K., Hao, Y.-T., Liu, S.-C., Gu, X.-Y., and Feng, M. (2013). Water contents of the Cenozoic lithospheric mantle beneath the western part of the North China Craton: Peridotite xenolith constraints. *Gondwana Res.* 23 (1), 108–118. doi:10.1016/j.gr.2012.01.010

Xie, G.-Q., Mao, J.-W., Li, R.-L., Qü, W.-J., Pirajno, F., and Du, A.-D. (2007). Re-Os molybdenite and Ar-Ar phlogopite dating of Cu-Fe-Au-Mo (W) deposits in

southeastern Hubei, China. *Mineralogy Pet.* 90, 249–270. doi:10.1007/s00710–006–0176–y

Xu, W.-L., Gao, S., Yang, D.-B., Pei, F.-P., and Wang, Q.-H. (2009). Geochemistry of eclogite xenoliths in Mesozoic adakitic rocks from Xuzhou-Suzhou area in central China and their tectonic implications. *Lithos* 107 (3), 269–280. doi:10.1016/j.lithos.2008.11.004

Xu, W., Gao, S., Wang, Q., Wang, D., and Liu, Y. (2006). Mesozoic crustal thickening of the eastern North China craton: Evidence from eclogite xenoliths and petrologic implications. *Geol* 34 (9), 721–724. doi:10.1130/G22551.1

Xu, W. L., Wang, Q. H., Liu, X. C., Wang, D. Y., and Guo, J. H. (2004). Chronology and Sources of Mesozoic Intrusive Complexes in the Xuzhou-Huainan Region, Central China: Constraints from SHRIMP Zircon U-Pb Dating. *Acta Geologica Sinica (English Edition)* 78 (1), 96–106. doi:10.1111/j.1755–6724.2004.tb00679.x

Xu, Y.-M., Jiang, S.-Y., and Zhu, J.-X. (2021). Factors controlling the formation of large porphyry Cu deposits: A case study from the Jiurui ore district of Middle-Lower Yangtze River Metallogenic Belt using *in situ* zircon and apatite chemistry from syn-mineralization intrusions. *Ore Geology. Rev.* 133, 104082. doi:10.1016/j.oregeorev.2021.104082

Yang, D.-B., Xu, W.-L., Wang, Q.-H., and Pei, F.-P. (2010). Chronology and geochemistry of Mesozoic granitoids in the Bengbu area, central China: Constraints on the tectonic evolution of the eastern North China Craton. *Lithos* 114 (1-2), 200–216. doi:10.1016/j.lithos.2009.08.009

Yang, J.-H., Wu, F.-Y., Wilde, S. A., Belousova, E., and Griffin, W. L. (2008). Mesozoic decratonization of the North China block. *Geol* 36 (6), 467–470. doi:10.1130/G24518A.1

Yangliu Coal Industry Co. Ltd (2017). Resources verification report on the reserves of Yangliu Coal Mine in Suixi County, Anhui Province. *Huaibei, Anhui*, 62–65.

Yao, Y., and Liu, D. (2012). Effects of igneous intrusions on coal petrology, pore-fracture and coalbed methane characteristics in Hongyang, Handan and Huaibei coalfields, North China. *Int. J. Coal Geology.* 96-97, 72–81. doi:10.1016/j.coal.2012.03.007

Ye, G., Liu, C., Luo, X., Jin, S., Wei, W., Dong, H., et al. (2021). Dynamical significance of the Tanlu Fault Zone in the destruction of the North China Craton: The evidence provided by the three-dimensional Magnetotelluric array study. *Tectonophysics* 813, 228910. doi:10.1016/j.tecto.2021.228910

Zhang, C.-c., Sun, W.-d., Wang, J.-t., Zhang, L.-p., Sun, S.-j., and Wu, K. (2017). Oxygen fugacity and porphyry mineralization: A zircon perspective of Dexing porphyry Cu deposit, China. *Geochimica et Cosmochimica Acta* 206, 343–363. doi:10.1016/j.gca.2017.03.013

Zhang, C., Ma, C., Holtz, F., Koepke, J., Wolff, P. E., and Berndt, J. (2013). Mineralogical and geochemical constraints on contribution of magma mixing and fractional crystallization to high-Mg adakite-like diorites in eastern Dabie orogen, East China. *Lithos* 172-173, 118–138. doi:10.1016/j.lithos.2013.04.011

Zhang, J., Qu, J., Zhang, B., Zhao, H., Niu, P., Zhao, S., et al. (2020). Mesozoic intraplate deformation of the central North China Craton: Mechanism and tectonic setting. *J. Asian Earth Sci.* 192, 104269. doi:10.1016/j.jseaes.2020.104269

Zhang, Y., Cheng, J., Tian, J., Pan, J., Sun, S., Zhang, L., et al. (2019a). Texture and trace element geochemistry of quartz in skarn system: Perspective from Jiguanzui Cu-Au skarn deposit, Eastern China. *Ore Geol. Rev.*, 109. doi:10.1016/j.oregeorev.2019.05.007

Zhang, Z., Wang, Y., Li, D., and Lai, C. (2019b). Lithospheric architecture and metallogenesis in Liaodong peninsula, North China Craton: Insights from zircon Hf-Nd isotope mapping. *Minerals* 9, 179. doi:10.3390/min9030179

Zhao, L., Allen, R. M., Zheng, T., and Hung, S.-H. (2009). Reactivation of an Archean craton: Constraints from P- and S-wave tomography in North China. *Geophys. Res. Lett.* 36 (17), 367–389. doi:10.1029/2009GL039781

Zhao, M., An, Y., Wang, M., Ding, M., and Lai, C. (2019). New Genesis of Natural Coke around Magmatic Intrusion at the Shitai Coalmine of Huaibei City, North China. *Acta Geologica Sinica - English Edition* 93 (4), 1158–1159. doi:10.1111/1755-6724.13827

Zhao, T., Zhu, G., Lin, S., and Wang, H. (2016). Indentation-induced tearing of a subducting continent: Evidence from the Tan-Lu Fault Zone, East China. *Earth-Science Rev.* 152, 14–36. doi:10.1016/j.earscirev.2015.11.003

Zhao, Z., Liang, S., Santosh, M., and Wei, J. (2020). Lithospheric extension associated with slab rollback: Insights from early Cretaceous magmatism in the southern segment of Tan-Lu fault zone, central-eastern China. *Lithos* 362-363, 105487. doi:10.1016/j.lithos.2020.105487

Zhou, H., Shang, D. F., Chan, S. W., and Chen, J. (2019). Zircon U-Pb dating, petrogenesis and geological significance of the Banjing pluton in Xuhuai area. *J. Mineral. Petrol.* 39, 9–16. (in Chinese with English abstract).

Zhou, T., Wang, S., Fan, Y., Yuan, F., Zhang, D., and White, N. C. (2015). A review of the intracontinental porphyry deposits in the Middle-Lower Yangtze River Valley metallogenic belt, Eastern China. *Ore Geology. Rev.* 65, 433–456. doi:10.1016/j.oregeorev.2014.10.002

Zhu, G., Liu, G. S., Niu, M. L., Xie, C. L., Wang, Y. S., and Xiang, B. (2009). Syn-collisional transform faulting of the Tan-Lu fault zone, East China. *Int. J. Earth Sci. (Geol Rundsch)* 98, 135–155. doi:10.1007/s00531–007–0225–8

Zhu, G., Wang, Y., Liu, G., Niu, M., Xie, C., and Li, C. (2005). 40Ar/39Ar dating of strike-slip motion on the Tan-Lu fault zone, East China. *J. Struct. Geology.* 27, 1379–1398. doi:10.1016/j.jsg.2005.04.007

Conflict of Interest: The authors declare that the research was conducted in the absence of any commercial or financial relationships that could be construed as a potential conflict of interest.

Publisher's Note: All claims expressed in this article are solely those of the authors and do not necessarily represent those of their affiliated organizations, or those of the publisher, the editors and the reviewers. Any product that may be evaluated in this article, or claim that may be made by its manufacturer, is not guaranteed or endorsed by the publisher.

frontiers in Earth Science

ORIGINAL RESEARCH
published: 20 October 2021
doi: 10.3389/feart.2021.759328

Multistage Genesis of the Haerdaban Pb-Zn Deposit, West Tianshan: Constraints From Fluid Inclusions and H-O-S-Pb Isotopes

Fang Xia, Shun-Da Li, Chuan Chen, Ling-Ling Gao, Xue-Bing Zhang and Ke-Yong Wang*

Xinjiang Key Laboratory for Geodynamic Processes and Metallogenic Prognosis of the Central Asian Orogenic Belt, College of Geology and Mining Engineering, Xinjiang University, Urumqi, China

The Haerdaban Pb-Zn deposit is located on the western edge of the Chinese Western Tianshan Orogen. This deposit consists of stratiform and veined mineralization hosted in Proterozoic carbonaceous and dolomitic limestone. Three metallogenic stages were recognized: an early sedimentary exhalative stage (stage 1), an intermediate metamorphic remobilization stage (stage 2), and a late magmatic-hydrothermal stage (stage 3). Fluid inclusions (FIs) present in stage 1 are liquid-rich aqueous, with homogenization temperatures of 206–246 C and salinities of 5.9–11.6 wt% NaCl eq. FIs present in stage 2 are also liquid-rich aqueous, with homogenization temperatures of 326–349 C and salinities of 3.4–6.6 wt% NaCl eq. FIs present in stage 3 include halite-bearing, vapor-rich aqueous, and liquid-rich aqueous FIs. Homogenization temperatures for these FIs span a range of 249–316 C. Halite-bearing, vapor-rich aqueous, and liquid-rich aqueous FIs yield salinities of 33.8–38.9, 2.6–3.5, and 4.2–8.1 wt% NaCl eq., respectively. Oxygen and hydrogen isotopic data ($\delta^{18}O_{H2O}$ = 2.6–13.6‰, δD_{H2O} = −94.7 to −40.7‰) indicate that the ore-forming fluids of stages 1–3 were derived from modified seawater, metamorphic water, and magmatic-meteoric mixed water, respectively. Sulfur isotopic data ($\delta^{34}S$ = 2.1–16.3‰) reveal that ore constituents were derived from mixing of marine sulfate and magmatic materials. Lead isotopic data ($^{206}Pb/^{204}Pb$ = 17.002–17.552, $^{207}Pb/^{204}Pb$ = 15.502–15.523, $^{208}Pb/^{204}Pb$ = 37.025–37.503) reveal that ore constituents were derived from a mixed crust-mantle source. We propose that the Haerdaban deposit was a Proterozoic sedimentary exhalative deposit overprinted by later metamorphic remobilization and magmatic-hydrothermal mineralization.

Keywords: fluid inclusions, isotopes, SEDEX, multistage mineraliztion, Haerdaban

OPEN ACCESS

Edited by:
Kit Lai,
Universiti Brunei Darussalam, Brunei

Reviewed by:
Rui Wang,
China University of Geosciences, China
Khin Zaw,
University of Tasmania, Australia

****Correspondence:***
Shun-Da Li
Shunda@xju.edu.cn

Specialty section:
This article was submitted to Economic Geology, a section of the journal Frontiers in Earth Science

Received: *16 August 2021*
Accepted: *06 October 2021*
Published: *20 October 2021*

Citation:
Xia F, Li S-D, Chen C, Gao L-L, Zhang X-B and Wang K-Y (2021) Multistage Genesis of the Haerdaban Pb-Zn Deposit, West Tianshan: Constraints From Fluid Inclusions and H-O-S-Pb Isotopes. Front. Earth Sci. 9:759328. doi: 10.3389/feart.2021.759328

INTRODUCTION

Multistage mineralization is an intricate geological process. Different processes such as sedimentation, volcanism, magmatism and metamorphism, may lead to overprinting of an ore deposit by a late mineralization system, or may provide a material source for the latter. Such processes may thus lead to the formation of a temporally and spatially interweaving polygenetic ore deposit. Deposits with a multistage mineralization history are more likely to be enriched in ore-forming elements than deposits with a single mineralization stage. Indeed, research has shown a

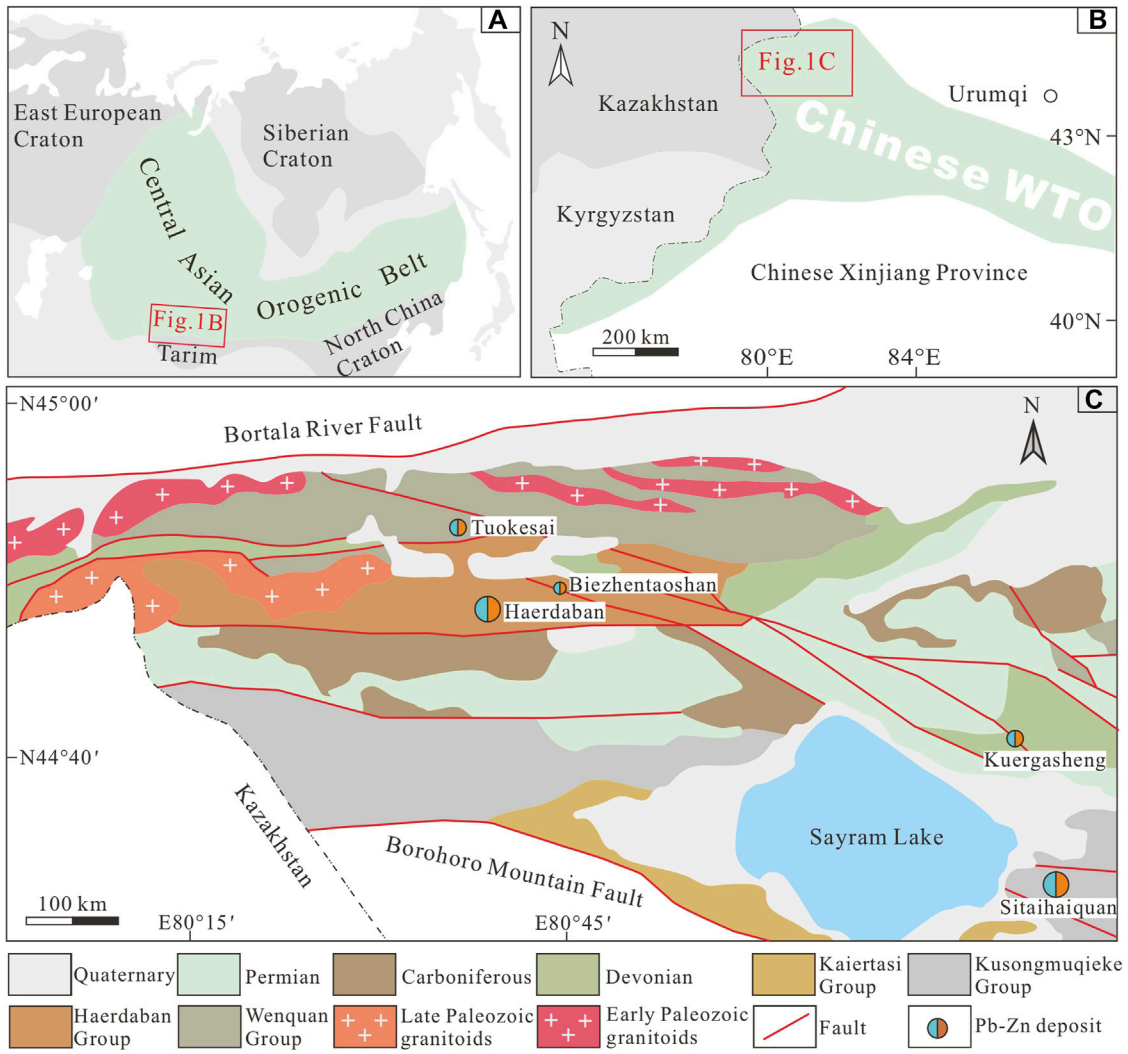

FIGURE 1 | Geological map of the Sayram Lake area (modified after Xue et al., 2014a).

correlation between large and super-large ore deposits and multistage mineralization. Examples showing this correlation are the Sullivan Pb-Zn-Ag deposit in Canada, the Rammelsberg Zn-Pb-Cu deposit in Germany, and the Dongshengmiao Zn-Pb-Cu deposit in China (Taylor, 2004; Muchez and Stassen, 2006; Zhong and Li, 2016).

The Chinese Western Tianshan Orogen (WTO) in Xinjiang province is part of the southern margin of the Central Asian orogenic belt (Şengör et al., 1993; Jahn et al., 2000) (**Figures 1A,B**). It is also located at the gateway of the important Chinese economic development initiative "One Belt and One Road". This region has a unique tectonic configuration, including Proterozoic microcontinent accretion, Paleozoic rifting, and subduction-collision related to the Paleo-Asian Ocean (Kröner et al., 2012; Xiao et al., 2013; Xue et al., 2014b). Its complex geological evolution has made this region a natural laboratory for studying the multistage genesis of ore deposits.

The Haerdaban Pb-Zn deposit is located in the Sayram Lake area of the Chinese WTO (**Figure 1C**). The deposit was discovered by the Xinjiang Nonferrous Geological Exploration Bureau (XNGEB) during regional 1:50,000 stream sediment geochemistry exploration in 2005, and was prospected and evaluated in 2011. To date, over 10,300 m of drill core has been extracted and 13,700 m^3 trenching has been dug. In addition, it has proven reserves of 97,000 t Pb and 549,000 t Zn, with an average grade of 1.09% Pb and 6.19% Zn. Previous studies of the deposit focused their investigations on geological features, as well as geophysical and geochemical exploration. However, the nature, source, and evolution of the ore-forming fluids have not been well constrained in previous research. Moreover, the metallogenic mechanism of this deposit remains subject to considerable debate, and has been interpreted as a sedimentary exhalative (SEDEX) type, a sedimentary-reworking type, and a carbonate-hosted type deposit by different authors (Xue et al., 2014a; Cheng et al., 2015; Wang, 2016). In order to

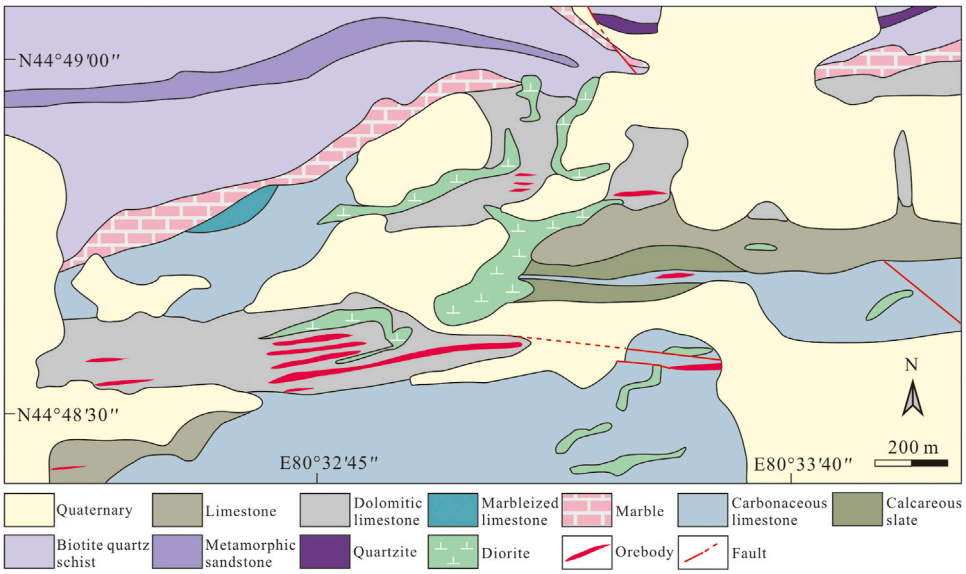

FIGURE 2 | Geological map of the Haerdaban Pb-Zn deposit (modified after Cheng et al., 2015).

facilitate prospection in the area and improve our understanding of the regional metallogeny, it is crucial to gain further insight into the formation of the Haerdaban deposit.

In the present work, we report on the paragenetic relationships between mineralization, petrography, FI microthermometry, and new H-O-S-Pb isotope data. The aim of our research is to 1) document the characteristics of different mineralization stages, 2) determine the nature and source of ore-forming fluids, and 3) present a multistage genetic model for the Haerdaban deposit. Specifically, these datasets shed light on the conflicting interpretations of the Haerdaban deposit, add to a relatively sparse body of literature on the multistage mineralization process, and provide insights for prospection at a regional scale.

REGIONAL AND DEPOSIT GEOLOGY

The Sayram Lake area is located on the western edge of the Chinese WTO, adjoining Kazakhstan to the east, bounded by the Bortala River Fault and the Borohoro Mountain Fault to the north and south, respectively (**Figure 1C**). The rocks exposed in this area comprise a sedimentary succession of Proterozoic, Paleozoic, and Cenozoic units, described as follows. The Paleoproterozoic Wenquan Group is composed of schist, gneiss, and marble. The Mesoproterozoic Haerdaban Group is made up of phyllite, slate, and limestone. The Mesoproterozoic Kusongmuqieke Group contains metasandstone and limestones. The Neoproterozoic Kaiertasi Group is dominated by metasandstone, shale, and carbonate rocks. The Devonian sequence is composed of sandstone and rhyolite. The Carboniferous sequence comprises sandstone and limestone. The Permian sequence is made up of andesite, rhyolite, and tuff. Finally, Quaternary cover is composed of moraine and pluvial-alluvial sediments. In addition, Paleozoic granitoids are widely exposed in the region. Early Paleozoic plutons comprise an assemblage of gneissic diorite, granodiorite, and quartz diorite, with zircon U-Pb ages of 467–447 Ma (Wang et al., 2012; Huang et al., 2013). On the other hand, Late Paleozoic plutons are composed of granodiorite, monzogranite and diorite, yielding zircon U-Pb ages of 398–302 Ma (Zhu et al., 2012; Tang et al., 2010).

The Haerdaban Pb-Zn deposit is located 300 km northwest of Sayram Lake, in the county of Wenquan, covering an area about 2.5 km^2. The strata exposed at the deposit mainly correspond to the Haerdaban Group together with Quaternary sediments (**Figure 2**). The Haerdaban Group, which hosts the ore deposit, is a set of carbonate rocks and low-grade metamorphosed clastics, interpreted as a Mesoproterozoic unit based on its stratigraphy and paleontology (XBGMR, 1993). Sedimentation took place in a shallow marine environment in a passive continental margin rift (Xue et al., 2014b). The strata strike approximately E-W, dipping 65–87° to the south, and can be further divided into lower and upper lithological units. Orebodies are hosted in the upper unit, which outcrop in the southern part of the mine, and consist of metamorphosed limestone, carbonaceous limestone, dolomitic limestone, and calcareous slate. The lower unit is fairly exposed in the northern part of the mine, and consists of biotite quartz schist, quartzite, metamorphic sandstone, and marble. Diorite dikes are widely exposed in the mining area. These dikes are generally 50–300 m long and up to 10 m wide. Several NW-SE trending faults crosscut the orebodies, indicating that the former occurred after mineralization.

GEOLOGY AND MINERALIZATION

Exploration of the Haerdaban deposit has revealed a total of 63 Pb-Zn orebodies, including 43 exposed and 20 concealed

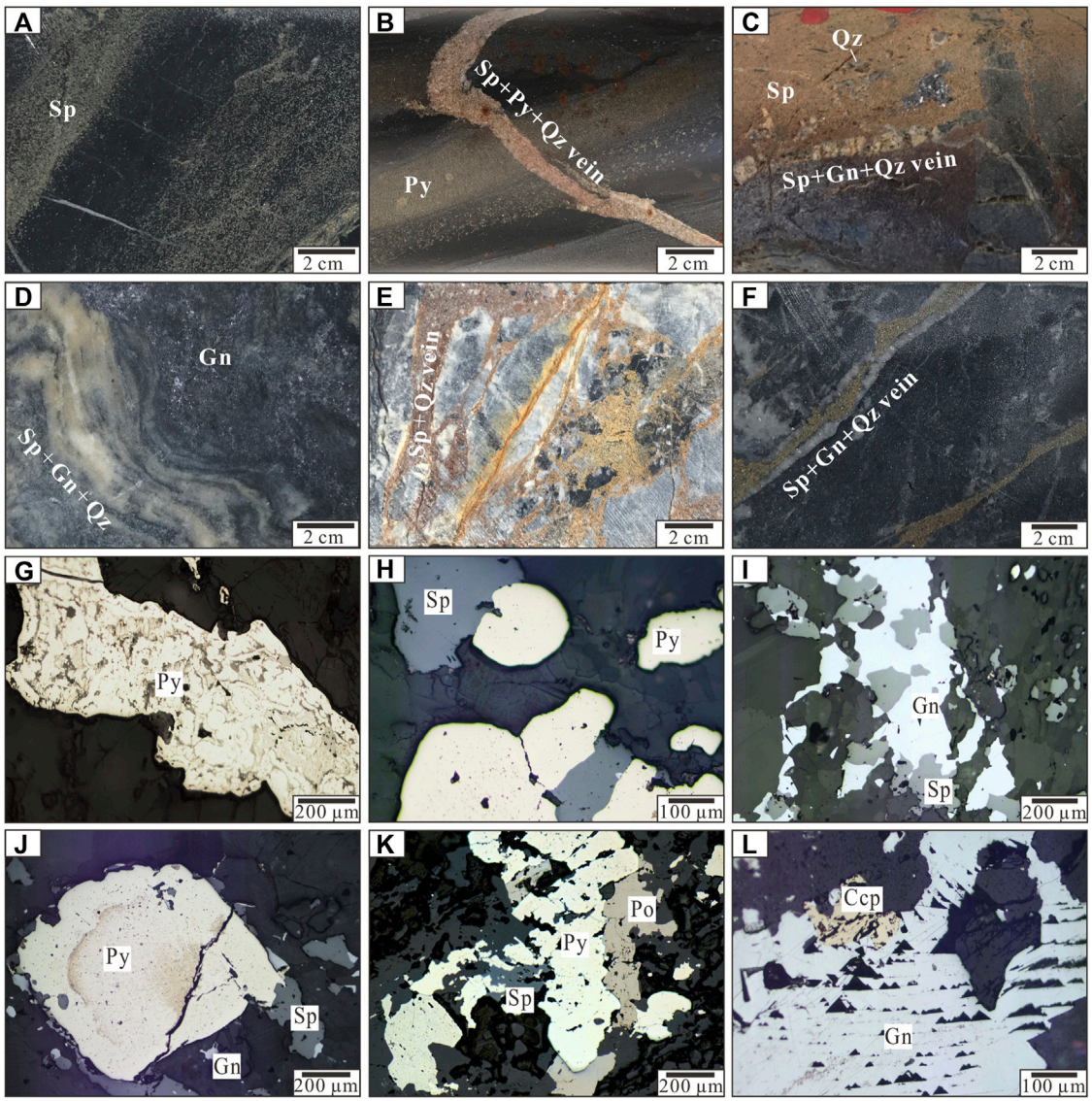

FIGURE 3 | Photographs of ore and mineral assemblages from the Haerdaban Pb-Zn deposit **(A)** Fine-grained sphalerite with laminated structure (stage 1) **(B)** Pyrite-sphalerite-quartz veins (stage 3) crosscutting laminated pyrite of stage 1 **(C)** Sphalerite-galena-quartz veins (stage 3) crosscutting laminated sphalerite and galena of stage 1 **(D)** Sinuous quartz-sulfide veins (stage 2) crosscutting laminated galena of stage 1 **(E–F)** Sphalerite-galena-quartz veins (stage 3) **(G)** Colloidal pyrite crystals of stage 1 **(H)** Pyrite replaced by sphalerite (stage 1) **(I)** Galena replaced by sphalerite (stage 1) **(J)** Pyrite replaced by galena and sphalerite (stage 2) **(K)** Pyrrhotite replaced by pyrite while pyrite replaced by sphalerite (stage 3) **(L)** Chalcopyrite replaced by galena (stage 3). Abbreviations: Py (pyrite); Po (pyrrhotite); Ccp (chalcopyrite); Gn (galena); Sp (sphalerite).

orebodies. Orebodies are hosted in carbonaceous and dolomitic limestone, with stratiform, lenticular, and vein morphologies. These orebodies are 20–800 m long and 1.0–27.5 m thick, generally parallel to wall rocks, and consistently dip 60–80° SE. Ore minerals include galena, sphalerite and pyrite, along with minor chalcopyrite and pyrrhotite (**Figure 3**). Gangue minerals include calcite, quartz, sericite, and barite. Ore structure is mainly massive, laminated, or veined. Drill-hole data show that alteration at the deposit includes carbonation, silicification, sericitization, and chloritization. Carbonation occurs as dolomite and calcite veins and stockworks - which crosscut wall rocks. Silicification is present as fine-to coarse-grained quartz aggregates distributed along ore bodies, with minor quartz veins alongside minor calcite veins. Sericitization occurs as scaly sericite aggregates along the contact zone between Haerdaban Group rocks and diorite. Minor chloritization occurs near the outer edge of the ore bodies. Based on the paragenetic sequence of mineralization and the crosscutting relationships between ore veins, three mineralization stages have been recognized (**Figure 4**): early sedimentary exhalative stage (stage 1), intermediate metamorphic remobilization stage (stage 2), and late magmatic-hydrothermal stage (stage 3).

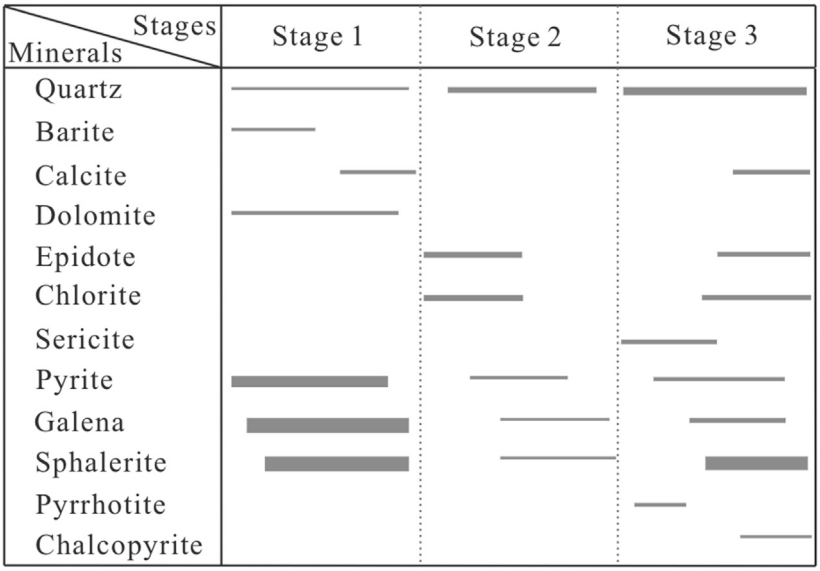

FIGURE 4 | Mineral paragenesis of the Haerdaban Pb-Zn deposit.

Stage 1 is characterized by stratiform mineralization, which accounts for the majority of the Pb-Zn production. Fine-grained (<1 mm) pyrite, sphalerite, and galena are relatively uniform (**Figure 3A**), which is characteristic of rapid deposition (Fan et al., 2007). These sulfides and limestone occur as lamination or interlaminated with each other (**Figure 3B**) and display a syngenetic origin (Leach et al., 2005). Colloidal pyrite crystals were also observed under microscope (**Figure 3G**), indicating their sedimentary origin. The orebodies occurred as stratiform and lenticular, and the ore structure is dominantly massive and laminated. Quartz crystals are rare, embedded within laminated ores (**Figure 3C**), and are considered to be syngenetic with the sulfide minerals.

Stage 2 is characterized by sinuous sulfide-poor metamorphic-hydrothermal quartz veins. Primary stratiform orebodies and wall rocks were asymmetrically folded during this stage, and display visible metamorphism along with shear deformation. Minor galena and sphalerite occur within the aforementioned quartz veins (**Figure 3D**). Widespread low-grade metamorphic rocks exposed in the mining area include biotite quartz schist, quartzite, metamorphic sandstone, and marble. Metamorphic fluids played a key role in the remobilization and redistribution of Zn-Pb sulfides in this stage.

Stage 3 is composed of numerous polymetallic sulfide-quartz veins, and shows obvious epigenetic characteristics. The increase in crystallinity and size of mineral particles indicates a late hydrothermal overprint (Gu et al., 2007; Zheng et al., 2013). Medium-to coarse-grained (1 mm–1 cm) sphalerite, galena, and minor pyrite and pyrrhotite occur in quartz veins (**Figures 3E,H**). These veins have straight boundaries and regular lengths (**Figure 3F**). Some of these epigenetic veins crosscut stratiform orebodies (**Figures 3B,C**). Diorite dikes and veined mineralization commonly occur together, suggesting a genetic correlation between them.

SAMPLES AND ANALYTICAL METHODS

All samples were collected from drill cores and underground galleries. Forty quartz samples from stages 1–3 were collected for FI petrography. Ore-stage quartz occurred in assemblage with galena and sphalerite, indicating their syngenetic property. Four representative quartz samples with abundant FIs were chosen from each mineralization stage - for both FI microthermometry and H-O isotopic analyses. Six stage-1 pyrite and galena samples were chosen for S isotopic analysis - representing stratiform mineralization. Another six pyrite and galena samples from stage 3 were chosen for S isotopic analysis - representing veined mineralization. Only stage-3 galena samples were selected for Pb analysis. Sulfides from stage 2 were not analyzed, since they hold limited economic value and sulfides were not abundant enough to be separated.

Fluid Inclusions

FI petrography and microthermometry analyses were performed at the Geological Fluid Laboratory, Xinjiang University, Urumqi, China. Samples were prepared as doubly polished thin sections to a thickness of 0.20–0.25 mm, soaked in acetone for 3–4 h, rinsed with clean water, and dried thoroughly. Twelve samples with abundant and representative FIs were selected for microthermometry. Petrographic observations were carried out on a Nikon LV-150N microscope. Microthermometric measurements were carried out on a Linkam THMS600 heating/freezing stage with a temperature range of -196–600 C. Heating rates were 1–2 C/min approaching phase transitions. Freezing rates were 0.1–0.2 C/min approaching the final ice melting temperature. Precision was ±0.2 C for freezing measurements and ±2 C for heating measurements.

Microthermometric measurements were calibrated using synthetic FI standards for the freezing points of pure CO_2

(-56.6 C) and pure H_2O (0 C), and for the critical point of pure H_2O (374.3 C). Salinities were calculated using the final melting temperature of ice for aqueous two-phase FIs (Bodnar, 1993), and the final melting temperature of NaCl-crystals for halite-bearing FIs (Hall et al., 1988).

H-O-S-Pb Isotopes

Hydrogen, oxygen, and sulfur isotope analyses were performed using a Finnigan MAT-253 mass spectrometer, and lead isotope analyses were performed using an ISOPROBE-T thermal ionization mass spectrometer at the Analytical Laboratory of the Beijing Research Institute of Uranium Geology. Quartz, pyrite, and sphalerite samples were crushed and sieved to 40–60 mesh and handpicked under a binocular microscope, resulting in a purity above 99%.

Oxygen isotopic analyses were performed using the method of Clayton and Mayeda (1963). Oxygen was extracted from the samples by reaction with BrF_5 and converted to CO_2 on a platinum-coated carbon rod for analysis. The hydrogen isotopic composition of FI water was released from the samples by decrepitation of FIs by heating to ~500 C. The water was then reacted with zinc powder at 410 C for 30 min to generate hydrogen (Friedman, 1953). Results are reported as δD and $\delta^{18}O$ relative to Standard Mean Ocean Water (SMOW) with analytical uncertainties (1σ) of ±2‰ for δD and ±0.2‰ for $\delta^{18}O$. Samples were reacted with Cu_2O until transformation into pure SO_2 for sulfur isotopic analyses (Robinson and Kusakabe, 1975). Results are reported as $\delta^{34}S$ relative to Canyon Diablo Troilite (CDT) with an analytical precision of ±0.2‰. Samples for Pb isotopic analyses were dissolved with concentrated HCl + HNO_3. The two-column AG1-X8 anion resin method was then used to separate and purify the lead. Data obtained were corrected using the ANBS-981 standard for analytical error correction. Analysis accuracy is ±0.005%.

RESULTS

Fluid Inclusion Petrography

Fluid Inclusion Petrography

In order to compare the fluid characteristics of all three mineralization stages, a detailed petrographic analysis of FIs was carried out considering morphology, spatial distribution, vapor/liquid ratios, and genetic types. Based on the criteria of Roedder (1984), both primary, pseudo-secondary, and secondary FIs are present in the Haerdaban deposit. Primary FIs are isolated and randomly distributed, located along growth zones of quartz crystals. Pseudo-secondary FIs occur as short intracrystalline trails. Secondary FIs are arranged along microcracks in grains. We considered the following as individual fluid inclusion assemblages (FIA): groups of FIs occurring along growth bands, and neighboring FIs occurring in microdomains with similar homogenization temperatures (Goldstein and Reynolds, 1994; Chi and Lu, 2008). Three different FI types were identified, based on room temperature phase relationships and phase transitions during heating and freezing: liquid-rich aqueous (LV-type), vapor-rich aqueous (VL-type), and halite-bearing (S-type) FIs (**Figure 5**).

LV-type FIs are biphasic (L_{H2O} + V_{H2O}) at room temperature (**Figure 5A**) and homogenize to the liquid phase when heated. Vapor represents 10–30 vol% of the total FI. FIs have negative quartz crystal or sub-rounded morphologies. The size of FIs measured ranges from 3 to 12 μm. LV-type FIs are present in all mineralization stages and mainly occur as short trails or in clusters within quartz crystals. Some LV-type FIs occur in long trails crosscutting crystal boundaries, which indicate a secondary origin.

VL-type FIs are also biphasic (L_{H2O} + V_{H2O}) at room temperature (**Figure 5B**) and homogenize to vapor when heated. Vapor represents 60–90 vol% of the total FI. FIs have ellipsoidal or amygdaloidal morphologies, and vary in size from 5 to 10 μm. VL-type FIs are isolated or occur as short trails within individual quartz crystals, trapped exclusively during stage 3.

S-type FIs are composed of three phases (L_{H2O} + $V_{H2O+}S_{NaCl}$) at room temperature (**Figure 5C**) and homogenize by salt dissolution followed by vapor disappearance. Vapor represents 10–20 vol%, and halite crystals comprise about 20 vol% of the total FI. FIs occur as negative quartz crystals or as polygonal shapes. The size of measured FIs varies between 8 and 12 μm. S-type FIs are typically isolated and locally clustered within quartz crystals, trapped during stage 3.

Fluid Inclusion Microthermometry

Samples with abundant representative primary FIs were selected for microthermometric measurements. Only primary or pseudo-secondary FIs were examined. Detailed data are listed in **Table 1** and **Figure 6A**.

Stage 1 quartz crystals contain abundant LV-type FIs (**Figure 5D**). Final ice-melting temperatures of LV-type FIs range from −7.9 to −3.6°C, corresponding to salinities of 5.9–11.6 wt% NaCl eq. Total homogenization to the liquid phase occurred at 206–246 C.

Stage 2 quartz crystals contain only LV-type FIs (**Figure 5E**). Final ice-melting temperatures of LV-type FIs occurred between −4.1 and −2.0°C, corresponding to salinities of 3.4–6.6 wt% NaCl eq. Total homogenization to the liquid phase occurred at temperatures of 326–349 C.

Stage 3 quartz veins contain LV-, VL-, and S-type FIs (**Figure 5F**–I). VL- and S-type FIs are scarce and commonly occur in isolation. Individual VL- and S-type FIs within microdomains homogenized at similar temperatures, suggesting they were trapped synchronously, representing a boiling FIA (**Figure 5I**). LV-type FIs occurred in clusters or short trails within crystals and were spatially separated from boiling FIAs. Final ice-melting temperatures of LV-type FIs occurred between −5.2 and −2.5°C, corresponding to salinities of 4.2–8.1 wt% NaCl eq. Total homogenization of LV-type FIs to the liquid phase occurred at temperatures of 249–308 C. Final ice-melting temperatures of VL-type FIs ranged from −2.1 to −1.5°C, corresponding to salinities of 2.6–3.5 wt% NaCl eq. Total homogenization of VL-type FIs to the vapor phase occurred at temperatures of 300–313 C. S-type FIs finally homogenized to a single liquid phase at temperatures of 259–316 C. Halite crystals

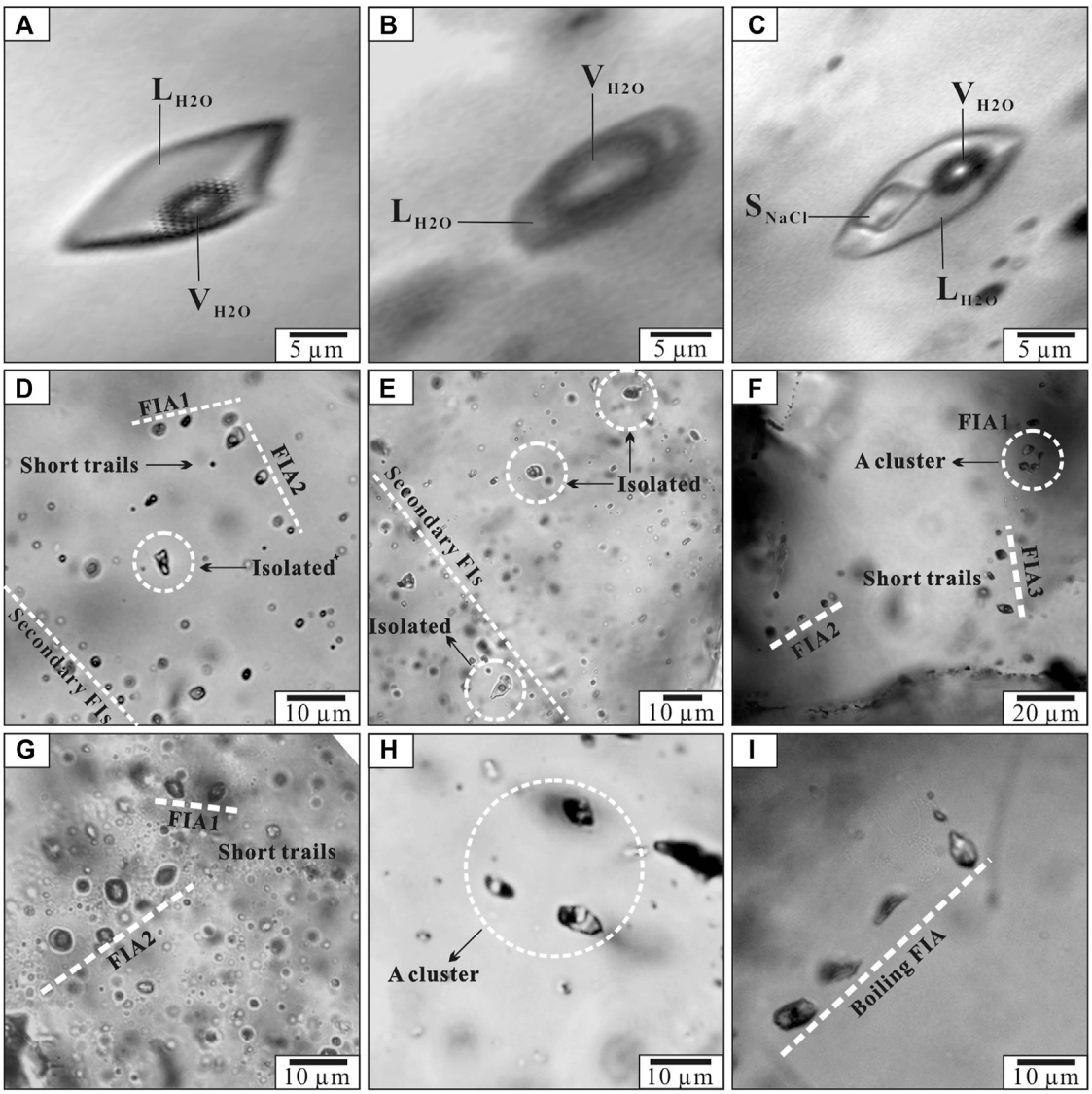

FIGURE 5 | Photomicrographs of FIs in quartz from different stages of the Haerdaban Pb-Zn deposit **(A)** Typical LV-type FI **(B)** Typical VL-type FI **(C)** Typical S-type FI **(D)** Short trails of pseudo-secondary LV-type FIs in stage-1 quartz **(E)** Isolated LV-type FIs in stage-2 quartz **(F)** Short trails of pseudo-secondary LV-type FIs and a cluster of LV-type FIs in stage-3 quartz **(G)** Short trails of VL-type FIs in stage-3 quartz **(H)** A cluster of S-type FIs in stage-3 quartz **(I)** Boiling FIA in stage-3 quartz. Abbreviations: L (liquid phase), V (vapor phase), S (daughter mineral).

within S-type FIs dissolved at temperatures of 235–310 C, corresponding to salinities of 33.8–38.9 wt% NaCl eq.

Oxygen and Hydrogen Isotopes

Isotopic data was obtained for three groups (with four quartz samples in each group) representing three mineralization stages. δD_{H2O} values for stage 1–3 range from −46.5 to −40.7‰, −94.7 to −78.6‰, and −90.3 to −87.8‰, respectively. $\delta^{18}O_{qz}$ values for stage 1–3 vary from 12.8 to 14.6‰, 16.0–19.2‰, and 11.8–13.8‰, respectively. Since our homogenization temperature data plot within a narrow range for each sample, we selected the mean homogenization temperature value as an estimate of the trapping temperature. $\delta^{18}O_{H2O}$ values were calculated using the quartz-H_2O equilibrium equation ($1000\ln\alpha_{qz\text{-}H2O} = 3.38 \times 10^6 \times T^{-2} - 3.40$) of Clayton et al. (1972). Calculated $\delta^{18}O_{H2O}$ values range from 2.6 to 4.4‰, 10.3–13.6‰, and 3.7–7.0‰, respectively. Detailed data are listed in **Table 2**.

Sulfur and Lead Isotopes

Isotopic data was obtained for two groups (with six samples in each group) representing stratiform (stage 1) and veined (stage 3) mineralization, respectively. Stratiform ores record a range of $\delta^{34}S$ values from 8.5 to 16.3‰ (average = 13.7 ± 2.9‰, n = 6). With the exception of sample HR-76 ($\delta^{34}S$ = 8.5), stratiform samples record a narrow range of $\delta^{34}S$ values

TABLE 1 | Microthermometric data from FIAs in hydrothermal quartz of the Haerdaban Pb-Zn deposit.

Sample	Host mineral	FIA	FI type	Number	Gas–liquid ratio	T_m (ice) (°C)	$T_{m\ (NaCl)}$ (°C)	Salinity (NaCl wt%)	T_h (°C)
HR-01	**Quartz from stage 1**	LV	LV	5	10	−7.3 to −4.2	—	6.7–10.8	221–243
		LV	LV	6	10	−7.2 to −4.0	—	6.4–10.7	209–240
HR-03		LV	LV	4	15	−7.5 to −3.9	—	6.3–11.1	215–241
		LV	LV	7	15	−7.7 to −3.6	—	5.9–11.3	206–239
HR-07		LV	LV	3	10	−7.3 to −3.8	—	6.7–10.9	212–246
HR-08		LV	LV	6	10	−7.9 to −4.3	—	6.9–11.6	208–242
HR-11	**Quartz from stage 2**	LV	LV	3	15	−4.1 to −2.1	—	3.5–6.6	326–343
HR-12		LV	LV	7	10	−3.4 to −2.0	—	3.4–5.6	330–348
HR-18		LV	LV	5	15	−4.0 to −2.5	—	4.2–6.4	331–349
		LV	LV	5	15	−3.9 to −2.8	—	4.6–6.3	328–346
HR-21		LV	LV	4	15	−4.1 to −2.9	—	4.8–6.6	334–347
		LV	LV	6	10	−3.9 to −2.6	—	4.3–6.3	328–346
HR-26	**Quartz from stage 3**	S + VL	S	4	20	—	283–310	36.9–38.9	302–315
			VL	3	80	−2.1to −1.5	—	2.6–3.5	300–313
		LV	LV	3	15	−5.2 to −4.5	—	7.2–8.1	296–308
HR-32		LV	LV	5	15	−5.1 to −4.2	—	6.7–8.0	291–305
		S + VL	S	4	20	—	275–309	36.3–38.9	299–316
			VL	2	80	−2.0 to −1.7	—	2.9–3.4	309–313
HR-35		S	S	3	20	—	235–278	33.8–36.5	259–282
		LV	LV	5	15	−4.4 to −3.4	—	5.6–7.0	253–268
HR-37		LV	LV	8	10	−4.2 to −2.8	—	4.6–6.7	255–273
		LV	LV	4	15	−4.3 to −2.5	—	4.2–6.9	249–265

Abbreviations: FIA (fluid inclusion assemblage); LV, VL, and S (fluid inclusion types); Tm (ice) (final ice melting temperature); Tm (NaCl) (final halite crystal dissolving temperatures in inclusions); Th (homogenization temperature).

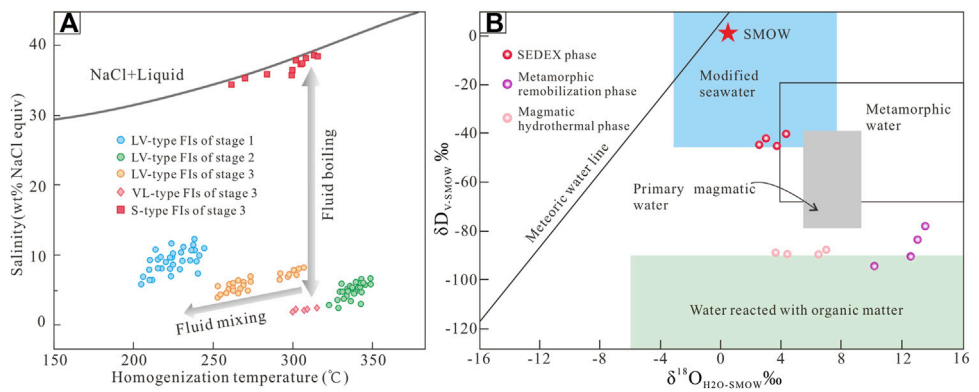

FIGURE 6 | (A) Homogenization temperature vs salinity in the NaCl-H_2O system for FIAs from three stages in the Haerdaban Pb-Zn deposit. Isobars were calculated using the equations of Driesner and Heinrich (2007) **(B)** Diagram showing δD_{H2O} vs $\delta^{18}O_{H2O}$, representing different stages of mineralization in the Haerdaban Pb-Zn deposit. Modified seawater is from Ohmoto and Rye (1979), and Tornos (2006). Fields showing primary magmatic, metamorphic, meteoric waters, and water with organic matter are from Taylor (1974) and Sheppard (1986).

from 13.1 to 16.3‰ (average = 14.8 ± 1.2‰, n = 5). On the other hand, veined samples yield distinct values from 2.1 to 6.2‰ $\delta^{34}S$ (average = 3.4 ± 1.4‰, n = 6), respectively. Stratiform galena samples yield $^{206}Pb/^{204}Pb$ ratios of 17.206–17.552; $^{207}Pb/^{204}Pb$ ratios of 15.518–15.523; and $^{208}Pb/^{204}Pb$ ratios of 37.229–37.503. Veined galena samples yield $^{206}Pb/^{204}Pb$ ratios of 17.002–17.328; $^{207}Pb/^{204}Pb$ ratios of 15.502–15.512; and $^{208}Pb/^{204}Pb$ ratios of 37.025–37.099. Detailed data are listed in **Table 3**.

DISCUSSION

Fluid Sources and Evolution

Fluid inclusions in stage-1 quartz crystals are simple LV-type FIs. Their homogenization temperatures (206–246 C) and salinities (5.9–11.6 wt% NaCl eq.) are widely variable, and they belong to a low temperature and intermediate salinity NaCl-H_2O system. The proportion of vapor phase is relatively consistent (10–15%), indicating that the ore-forming fluid probably did not undergo

TABLE 2 | Oxygen and hydrogen isotope data from quartz and calcite of the Haerdaban Pb-Zn deposit.

Sample	Host minerals	$\delta^{18}O_{qz}$ (‰) SMOW	δD_{H2O} (‰) SMOW	T_h (°C)	$\delta^{18}O_{H2O}$ (‰) SMOW
HR-01	**Quartz from stage 1**	14.6	−40.7	226	4.4
HR-03		14.0	−46.5	225	3.8
HR-07		13.0	−42.5	229	3.0
HR-08		12.8	−45.4	225	2.6
HR-11	**Quartz from stage 2**	18.8	−83.1	335	13.1
HR-12		19.2	−78.6	339	13.6
HR-18		18.2	−90.3	339	12.6
HR-21		16.0	−94.7	338	10.3
HR-26	**Quartz from stage 3**	13.2	−90.3	306	6.5
HR-42		13.8	−87.8	304	7.0
HR-35		11.8	−88.4	268	3.7
HR-37		12.9	−89.2	261	4.4

TABLE 3 | Sulfur and lead isotope data for pyrite and sphalerite from the Haerdaban Pb-Zn deposit.

Sample	Mineral	$\delta^{34}S$ (‰) CDT	$^{206}Pb/^{204}Pb$	$^{207}Pb/^{204}Pb$	$^{208}Pb/^{204}Pb$	Mineralization type
HR-53	Pyrite	13.1	—	—	—	Stratiform
HR-55	Pyrite	15.6	—	—	—	Stratiform
HR-63	Pyrite	16.3	—	—	—	Stratiform
HR-67	Galena	14.3	17.453	15.523	37.207	Stratiform
HR-70	Galena	14.6	17.552	15.518	37.503	Stratiform
HR-76	Galena	8.5	17.206	15.522	37.229	Stratiform
HR-82	Pyrite	2.9	—	—	—	Veined
HR-85	Pyrite	6.2	—	—	—	Veined
HR-88	Pyrite	2.8	—	—	—	Veined
HR-92	Galena	2.6	17.002	15.506	37.099	Veined
HR-95	Galena	3.8	17.195	15.512	37.052	Veined
HR-99	Galena	2.1	17.328	15.502	37.025	Veined

mixing or boiling. The limited range of δD_{H2O} and $\delta^{18}O_{H2O}$ values for stage 1 samples of the Haerdaban Pb-Zn deposit indicates that quartz may have precipitated from a uniform fluid source. The above characteristics resemble other ancient SEDEX deposits (Samson and Russell, 1987; Wang et al., 2008; Rajabi and Canet, 2012). Seawater with δD_{H2O} and $\delta^{18}O_{H2O}$ values close to 0‰ (Ohmoto and Rye, 1979) is considered to be an important fluid source for SEDEX deposits. When plotted on the δD_{H2O} vs $\delta^{18}O_{H2O}$ diagram (**Figure 6B**), isotope data for the Haerdaban deposit fall close to the modified seawater field. Precipitation could result from quenching of metal-bearing submarine hydrothermal solutions in contact with cool seawater, as reported by extensive literature (Sanchez-Espana et al., 2003; Tornos, 2006). The wide range of temperatures and salinities is mainly due to the prolonged period of fluid circulation between submarine hydrothermal solutions and seawater.

Fluid inclusions identified in quartz crystals from stage 2 are also LV-type FIs. Metamorphic fluids are characterized by a NaCl-H_2O system with intermediate temperatures (326–349 C) and low salinities (3.4–6.6 wt% NaCl eq.). Compared to stage 1, FI sizes are smaller, salinities are lower, and the homogenization temperature range is narrower. The difference in fluid nature between the two stages suggests late hydrothermal overprinting. The presence of widespread metamorphic rocks and deformed orebodies and strata gives further evidence of a metamorphic event during mineralization stage 2. Total FI homogenization temperatures were attained in the liquid phase cluster at 326–349 C, which is consistent with lower greenschist facies temperatures (Miu and Ran, 1992). Oxygen isotopes plot well above the field of magmatic water ($\delta^{18}O_{H2O}$ > 9.5‰). Isotope data plot below the metamorphic fluid field, and trend towards the field of water that interacted with organic matter (**Figure 6B**). This indicates that the ore-forming fluid in stage 2 was most likely derived from the dehydration of ^{18}O-enriched metasedimentary rocks during greenschist facies metamorphism and their later interaction with deep-seated carbonaceous slates during fluid migration. The release of δD-depleted organic matter (H_2 and CH_4) from the carbonaceous slate to the metamorphic fluid occurred during regional metamorphism (Ding et al., 2014).

Fluid inclusions identified in quartz crystals from stage 3 are LV-, VL-, and S-type FIs. Vein-type gangue is made up of crystals that formed during hydrothermal overprinting at temperatures of 249–316 C. LV-type FIs are spatially separated from boiling FIAs, indicating they were not trapped synchronously. Boiling FIAs

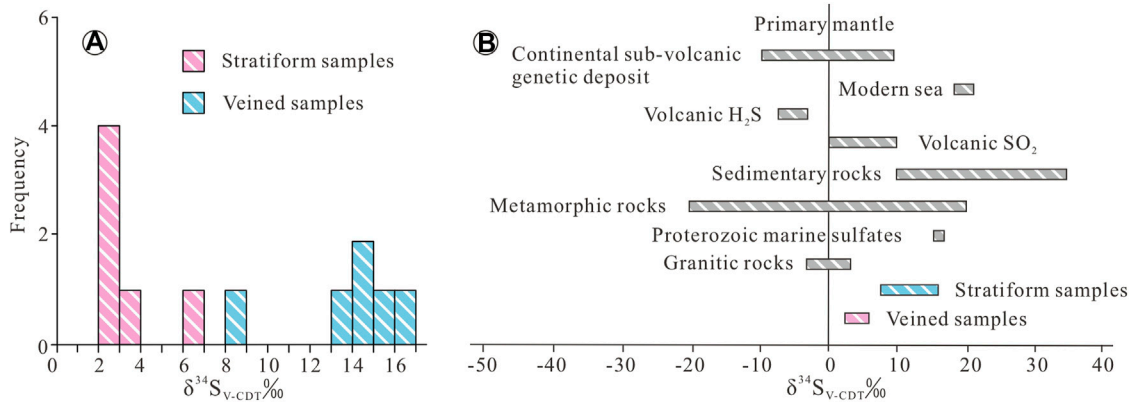

FIGURE 7 | (A) Histogram showing $\delta^{34}S$ values of the Haerdaban Pb-Zn deposit **(B)** $\delta^{34}S$ values from Haerdaban Pb-Zn deposit compared to the values of important geological reservoirs (data from Ohmoto and Rye, 1979; Ohmoto and Goldhaber, 1997; Hoefs, 2009, White, 2013).

most likely originated from the phase separation of magmatic water due to decompression, while LV-type FIs may represent the input of hot extraneous meteoric fluids. When plotted on the δD_{H2O} vs $\delta^{18}O_{H2O}$ diagram (**Figure 6B**), data fall between the magmatic water field and the meteoric water line. Thus, the ore-forming fluids of stage 3 are hybrid in origin–an initial magmatic source with input of meteoric water. The nature of the fluid and its evolution during stage 3 are similar to those of magmatic-hydrothermal deposits (Li et al., 2018, 2021), which typically consist of vein mineralization controlled by magmatism and faults.

In conclusion, our results suggest that FIs and isotopes from the Haerdaban deposit record three different mineralization events: an early SEDEX event, an intermediate metamorphic remobilization event, and late magmatic-hydrothermal overprinting.

Sources of Ore Constituents

Sulfur is one of the most important ore-forming elements in most metal deposits. Sulfur isotope compositions can trace the source of ore constituents and are widely employed to study deposit genesis (Rye and Ohmoto, 1974). In the Haerdaban deposit, there is a tendency towards $\delta^{34}S_{pyrite} > \delta^{34}S_{sphalerite}$, which indicates overall equilibrium of sulfur isotopes among sulfides. Two $\delta^{34}S$ peaks can be observed in the histogram of sulfur isotope data (**Figure 7A**). The $\delta^{34}S$ values of samples from stratiform mineralization range from 8.5 to 16.3‰ (average = 13.7 ± 2.9‰). Such a wide range of $\delta^{34}S$ most likely did not originate from a single source. Except for sample HR-76 ($\delta^{34}S$ = 8.5), other samples are enriched in heavy sulfur isotopes, and have limited $\delta^{34}S$ values of 13.1–16.3‰ (average = 14.8 ± 1.2‰), which is close to the range of Proterozoic marine sulfates (16‰ ~ 17‰, White, 2013) (**Figure 7B**). The sulfide samples from Haerdaban were mostly formed during a submarine exhalative process. On the other hand, sample HR-76 may have been derived from contamination by interaction with deep magmatic materials. This indicates that both ore-hosting limestone and deep magma reservoirs provided the ore constituents for the stratiform mineralization. The $\delta^{34}S$ values of samples from vein mineralization range from 2.1 to 6.2‰ (average = 3.4 ± 1.4‰). Such a limited range indicates a single magmatic source (−3‰ ~ 3‰, Ohmoto and Rye, 1979; Hoefs, 2009) (**Figure 7B**), showing similarities with magmatic-hydrothermal deposits. These sulfide samples precipitated from an epigenetic hydrothermal solution during the magmatic-hydrothermal stage.

Pb isotopic compositions also contribute to understanding the sources of ore constituents (Bierlein and McNaughton, 1998). Pb isotopic data for pyrite and sphalerite samples in the Haerdaban Pb-Zn deposit show values of 17.002–17.552 for $^{206}Pb/^{204}Pb$, 15.502–15.523 for $^{207}Pb/^{204}Pb$, and 37.099–37.503 for $^{208}Pb/^{204}Pb$. Samples plot between the orogenic growth line and the mantle line, or between the orogenic growth line and the lower crust line in the lead isotope compositional diagram (**Figure 8**). These values indicate that the ore-forming material may have originated from a mixed lower crustal and mantle origin (Stacey, 1975; Doe and Zartman, 1979). The high radiogenic end-member is similar to the crustal lead reservoir (Zartman and Doe, 1981), and is possibly represented by host rocks of the Haerdaban deposit. The low radiogenic end-member is similar to the mantle reservoir, which may correspond to the ore-bearing magmatic fluid. Stratiform mineralization may contain a greater proportion of crustal lead components, since corresponding samples display a higher radiogenic lead ratio (^{206}Pb, ^{207}Pb and ^{208}Pb; **Figure 8**).

Genetic Model of the Haerdaban Deposit

The multistage genetic model is discussed in greater detail below.

Firstly, during stage 1, stratiform and laminated mineralization took place in a SEDEX ore-forming system. Being a syngenetic sedimentary deposit, mineralization and diagenesis occurred almost simultaneously. Thus, the age of SEDEX mineralization in the Haerdaban deposit can be estimated as the formation age of the Haerdaban Group, which was determined as Mesoproterozoic (XBGMR, 1993). Moreover, since the mining district is located on the passive continental margin of the Kazakhstan-Yili Plate (Xue et al.,

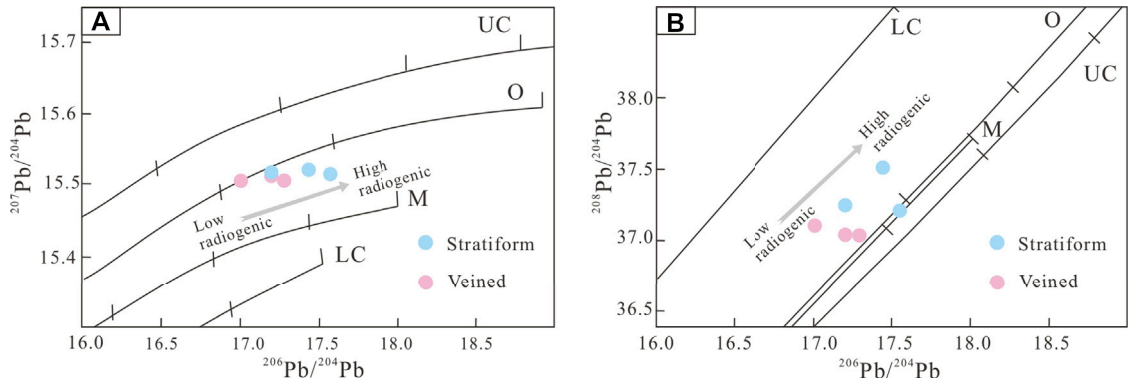

FIGURE 8 | Lead isotope compositions for sulfides of the Haerdaban Pb-Zn deposit **(A)** $^{207}Pb/^{204}Pb$ vs $^{206}Pb/^{204}Pb$ plot **(B)** $^{208}Pb/^{204}Pb$ vs $^{206}Pb/^{204}Pb$ plot. The average growth curve is from Zartman and Doe (1981). Abbreviations: UC-upper crust; LC-lower crust; O-orogenic; M-mantle.

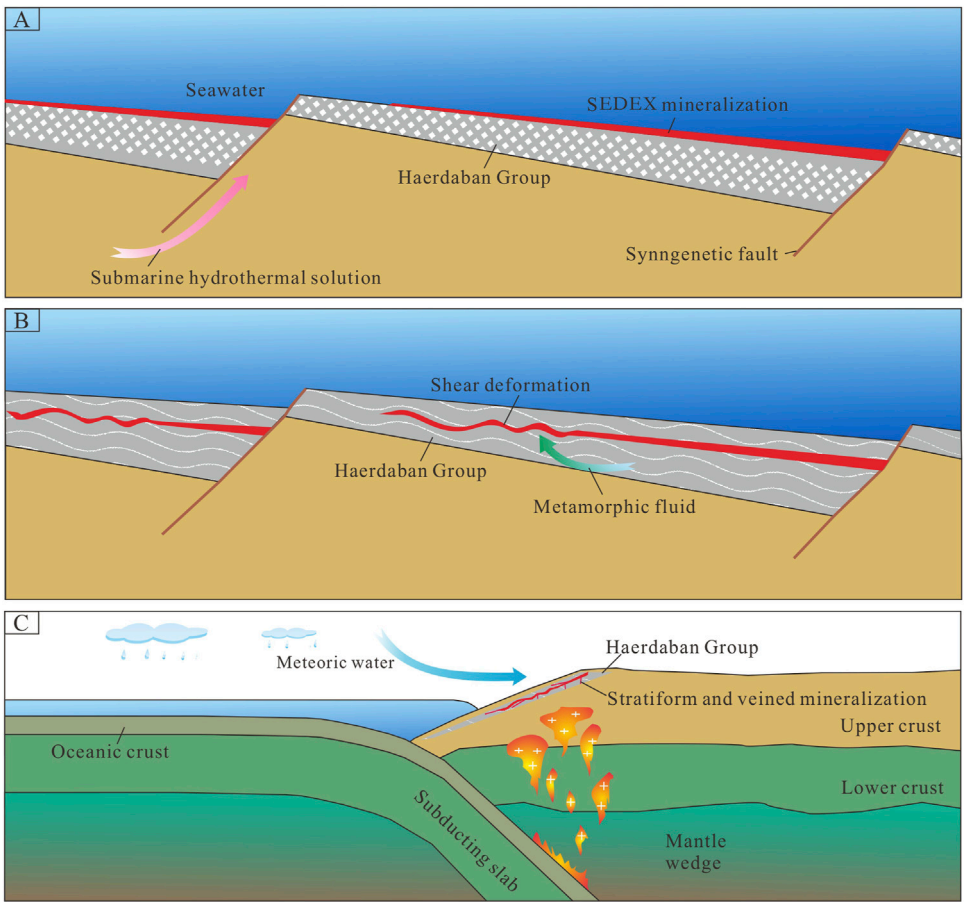

FIGURE 9 | Genetic model of the Haerdaban Pb-Zn deposit.

2014a), its geotectonic location played a crucial role on the occurrence of mineralization. Specifically, upper crustal permeability was enhanced significantly under extensional conditions and resulted in syngenetic faults. These faults provided channels for deep submarine metal-bearing solutions to migrate through, resulting in precipitation by fluid quenching due to contact with cool seawater, which generated the aforementioned stratiform mineralization (**Figure 9A**).

The ore-forming system subsequently underwent metamorphism and shear deformation in stage 2. The ore and

TABLE 4 | Comparison of general features of the Haerdaban and Tekli deposits.

Features	Haerdaban Pb-Zn deposit	Tekli Pb-Zn deposit
Reserves	97, 000 t Pb and 549, 000 t Zn	2,500,000 t Pb and 3,000,000 t Zn
Ore-grade	1.09% Pb and 6.19% Zn	2.8% Pb and 4.19% Zn
Host rocks	Phyllite, slate and limestone of the Mesoproterozoic Haerdaban Group	Slate, limestone and quartz siltstone of the Mesoproterozoic Tekli Group
Occurrence of ore bodies	Stratiform, lenticular, and veined Dipping 60–80° SE	Stratiform and lenticular Dipping 70–75° NW
Ore structure	Massive, laminated, and veined	Massive, laminated, and banded
Ore minerals	Galena, sphalerite, pyrite, chalcopyrite, pyrrhotite, etc.	Galena, sphalerite, pyrite, chalcopyrite, pyrrhotite, boulangerite, tetrahedriteetc.
Alteration of wall rock	Carbonation, silicification, sericitization, and chloritization	Carbonation, silicification, sericitization, and albitization
Geological setting	Extensional setting in passive continental margin	Extensional setting in passive continental margin
Epigenetic enrichment	Metamorphic remobilization and magmatic-hydrothermal overprinting	None
References	This paper	Peng, 1990; Wu et al., 2010

its host rock became folded, and intermediate temperature and low salinity metamorphic fluids were mobilized during this stage (**Figure 9B**). Stratiform mineralization was remobilized with the assistance of metamorphic fluids, forming sinuous quartz-sulfide veins. Low-grade metamorphism took place at a regional scale, and formed assemblages of biotite quartz schist, quartzite, metamorphic sandstone, and marble. The metamorphic fluids were expelled along deep faults, and deformation resulted in quartz sub-grain formation and grain boundary migration. Structural analysis and chronological research (Wang et al., 2018; Xia and Zhang, 2020) show that the region underwent multistage metamorphism-deformation scenarios. The precise timing of the metamorphic remobilization stage in the mining district is difficult to determine.

Finally, stage 3 was triggered by the intrusion of magma, leading to another enrichment in ore-forming elements, and resulting in mineralization as veins crosscutting or overlying the stratiform mineralization. Veined mineralization may have resulted from the emplacement of diorite. Granitoids developed in the region, yielding zircon U-Pb ages of 467–302 Ma (Hu et al., 1999; Tang et al., 2010; Wang et al., 2012; Huang et al., 2013). Large-scale magmatic activity occurred in a two-peak period; in the Late Ordovician and in the Early Carboniferous. In addition, recent Rb-Sr dating of sphalerite yielded an isochron age of 432 ± 45 Ma (Lv, 2016), which places the stage 3 magmatic event in the Late Ordovician. During this period, the metallogenic environment shifted to continental accretion due to subduction of the North Tianshan Ocean beneath the Yili Plate (Kröner et al., 2012; Xiao et al., 2013; Xue et al., 2014b). A later magmatic-hydrothermal fluid percolated through pore spaces and along faults, and metasomatized the original sediments, resulting in the reactivation and enrichment of ore-forming elements. The pre-existing sulfide minerals recrystallized, purifying the grade of the preexisting orebody. Simultaneously, the addition of meteoric water gradually cooled the magmatic-hydrothermal system, and ore minerals precipitated in structural fissures forming veined mineralization (**Figure 9C**).

Comparison With the Tekli Lead-Zinc Deposit

The giant Tekli SEDEX Pb-Zn deposit is located at the southeastern edge of Kazakhstan, close to the Chinese WTO. This deposit has proven reserves of 2,500,000 t Pb and 3,000,000 t Zn, with average grades of 2.8% Pb and 4.19% Zn, respectively (Peng, 1990; Wu et al., 2010). Orebodies are hosted in the Mesoproterozoic Tekli Group of the Riphean Supergroup, and occur as stratiform and lenticular morphologies. The mineralization style of the Tekli deposit is similar to that of the Haerdaban deposit. These two deposits share common features such as the following: 1) ore minerals are predominantly sphalerite and galena; 2) stratiform orebodies occur parallel to host strata; 3) ores display massive and laminated structures; 4) the ore deposits are hosted in Mesoproterozoic sedimentary strata and have a similar geological setting. However, it is worth noting that the Haerdaban mine has evidently undergone epigenetic enrichment and is overlain by later geological processes. A more detailed comparison is shown in **Table 4**.

The Mesoproterozoic is a SEDEX metallogenetic era of global significance (Leach et al., 2010). Recently, Pb-Zn deposits with SEDEX characteristics have been newly discovered in the Chinese WTO, such as the Haerdaban, Tuokesai, and Sitaihaiquan deposits. These deposits are all hosted in carbon-bearing low-grade metamorphosed clastic rocks, and are located on the passive continental margin of the Kazakhstan-Yili Plate in an extensional setting. Based on previous regional geochemical surveys and remote sensing data, we suggest that the Chinese WTO has great prospecting potential to host a series of SEDEX Zn-Pb deposits.

CONCLUSION

1) The metallogenic scheme in the Haerdaban deposit includes early SEDEX formation, intermediate metamorphic remobilization, and late magmatic-hydrothermal overprinting.

2) The ore-forming fluid has multiple origins, including modified seawater, metamorphic water, magmatic water, and meteoric water.
3) Ore constituents were derived from marine sulfates and magmatic materials of mixed crust-mantle origin.

DATA AVAILABILITY STATEMENT

The original contributions presented in the study are included in the article/Supplementary Material, further inquiries can be directed to the corresponding author.

AUTHOR CONTRIBUTIONS

FX, SL, and CC designed the model and wrote the manuscript. FX, LG, KW, and XZ conducted the experiments. SL managed and directed the project. All authors contributed to the article and approved the submitted version.

FUNDING

This work was supported by the Natural Science Foundation of the Xinjiang Uygur Autonomous Region (Project no. 2020D01C075) and Tianchi Doctor Program (Project no. tcbs201930).

ACKNOWLEDGMENTS

We would like to thank the staff of the Xinjiang Nonferrous Geological Exploration Bureau who kindly helped us with sampling and mineral collection at the Haerdaban mine. We are grateful to the managing editor and reviewers for their positive and constructive comments, which significantly improved this paper.

REFERENCES

Bierlein, F. P., and McNaughton, N. J. (1998). Pb Isotope Fingerprinting of Mesothermal Gold Deposits from central Victoria, Australia: Implications for Ore Genesis. *Mineralium Deposita* 33, 633–638. doi:10.1007/s001260050178

Bodnar, R. J. (1993). Revised Equation and Table for Determining the Freezing point Depression of H2O-Nacl Solutions. *Geochimica et Cosmochimica Acta* 57, 683–684. doi:10.1016/0016-7037(93)90378-a

Cheng, Y., Li, Y., Zhu, S. S., and Yablong, Y. (2015). Geological Characteristics and Genesis Analysis of the Haerdaban lead–zinc deposit, Wenquan, Xinjiang. *Mineral. Exploration* 6 (2), 107–114. (in Chinese with English abstract).

Chi, G. X., and Lu, H. Z. (2008). Validation and Representation of Fluid Inclusion Microthermometric Data Using the Fluid Inclusion Assemblage (FIA) Concept. *Acta Petrologica Sinica* 24, 1945–1953. (in Chinese with English abstract).

Clayton, R. N., and Mayeda, T. K. (1963). The Use of Bromine Pentafluoride in the Extraction of Oxygen from Oxides and Silicates for Isotopic Analysis. *Geochimica et Cosmochimica Acta* 27, 43–52. doi:10.1016/0016-7037(63)90071-1

Clayton, R. N., O'Neil, J. R., and Mayeda, T. K. (1972). Oxygen Isotope Exchange between Quartz and Water. *J. Geophys. Res.* 77, 3057–3067. doi:10.1029/jb077i017p03057

Ding, Q.-F., Wu, C.-Z., Santosh, M., Fu, Y., Dong, L.-H., Qu, X., et al. (2014). H-O, S and Pb Isotope Geochemistry of the Awanda Gold deposit in Southern Tianshan, Central Asian Orogenic belt: Implications for Fluid Regime and Metallogeny. *Ore Geology. Rev.* 62, 40–53. doi:10.1016/j.oregeorev.2014.02.017

Doe, B. R., and Zartman, R. E. (1979). "Plumbotectonics, the Phanerozoic," in *Geochemistry of Hydrothermal Ore Deposits*. Editor H. L. Barnes. Second Edition (New York, NY: John Wiley & Sons), 509–567.

Driesner, T., and Heinrich, C. A. (2007). The System H2O-NaCl. Part I: Correlation Formulae for Phase Relations in Temperature-Pressure-Composition Space from 0 to 1000°C, 0 to 5000bar, and 0 to 1 XNaCl. *Geochimica et Cosmochimica Acta* 71, 4880–4901. doi:10.1016/j.gca.2006.01.033

Fan, Y., Zhou, T. F., Yuan, F., Wu, M., Hou, M., and Hu, Q. (2007). Geological Geochemical Features and Geneses of Xiangquan Independent Thallium deposit in Hexian County, Anhui Province. *Miner. Deposits* 6, 597–608. (in Chinese with English abstract).

Friedman, I. (1953). Deuterium Content of Natural Waters and Other Substances. *Geochimica et Cosmochimica Acta* 4, 89–103. doi:10.1016/0016-7037(53)90066-0

Goldstein, R. H., and Reynolds, T. J. (1994). Systematics of Fluid Inclusions in Diagenetic Minerals. *Soc. Sed. Geol. SEPM Short Course* 31, 1–199. doi:10.2110/scn.94.31

Gu, L., Zheng, Y., Tang, X., Zaw, K., Della-Pasque, F., Wu, C., et al. (2007). Copper, Gold and Silver Enrichment in Ore Mylonites within Massive Sulphide Orebodies at Hongtoushan VHMS deposit, N.E. China. *Ore Geology. Rev.* 30, 1–29. doi:10.1016/j.oregeorev.2005.09.001

Hall, D. L., Sterner, S. M., and Bodnar, R. J. (1988). Freezing point Depression of NaCl-KCl-H 2 O Solutions. *Econ. Geol.* 83, 197–202. doi:10.2113/gsecongeo.83.1.197

Hoefs, J. (2009). *Stable Isotope Geochemistry*. 6th ed. Berlin: Springer.

Hu, A. Q., Zhang, G. X., Zhang, Q. F., and Chen, Y. (1999). Basement Age and Crustal Accretion of the Tianshan Orogenic belt, Constrain from Nd Isotopes. *Sci. China (Series D)* 29 (2), 104–112. (in Chinese with English abstract). doi:10.1007/BF02878748

Huang, Z., Long, X., Kröner, A., Yuan, C., Wang, Q., Sun, M., et al. (2013). Geochemistry, Zircon U-Pb Ages and Lu-Hf Isotopes of Early Paleozoic Plutons in the Northwestern Chinese Tianshan: Petrogenesis and Geological Implications. *Lithos* 182-183, 48–66. doi:10.1016/j.lithos.2013.09.009

Jahn, B.-m., Wu, F., and Chen, B. (2000). Massive Granitoid Generation in Central Asia: Nd Isotope Evidence and Implication for continental Growth in the Phanerozoic. *Episodes* 23, 82–92. doi:10.18814/epiiugs/2000/v23i2/001

Kröner, A., Alexeiev, D. V., Hegner, E., Rojas-Agramonte, Y., Corsini, M., Chao, Y., et al. (2012). Zircon and Muscovite Ages, Geochemistry, and Nd-Hf Isotopes for the Aktyuz Metamorphic Terrane: Evidence for an Early Ordovician Collisional belt in the Northern Tianshan of Kyrgyzstan. *Gondwana Res.* 21 (4), 901–927. doi:10.1016/j.gr.2011.05.010

Leach, D. L., Bradley, D. C., Huston, D., Pisarevsky, S. A., Taylor, R. D., and Gardoll, S. J. (2010). Sediment-hosted lead-zinc Deposits in Earth History. *Econ. Geology.* 105 (3), 593–625. doi:10.2113/gsecongeo.105.3.593

Leach, D. L., Sangster, D. F., Kelley, K. D., Large, R. R., Garven, G., Allen, C. R., et al. (2005). Sediment-hosted Lead-Zinc Deposits: a Global Perspective. *Econ. Geol.* 100, 561–608.

Li, S., Chen, C., Gao, L., Xia, F., Zhang, X., Wang, K., et al. (2021). Fluid Evolution in the Beidabate Porphyry Cu-Mo deposit, Xinjiang, Northwest China: Evidence from Fluid Inclusions and H-O-C-S Isotopes. *Ore Geology. Rev.* 135, 104198. doi:10.1016/j.oregeorev.2021.104198

Li, S. D., Zhang, X. B., and Gao, L. L. (2018). Ore Genesis at the Jinchang Gold-Copper deposit in Heilongjiang Province, Northeastern China: Evidence from Geology, Fluid Inclusions, and H-O-S Isotopes. *Minerals* 9, 99.

Lv, C. S. (2016). *Geological Characteristics and Genesis of Haerdaban lead–zinc deposit in West Tianshan, Xingjiang. [master's Thesis]*. [Beijing, China]: China University of Geosciences. (in Chinese with English abstract).

Miu, Y. X., and Ran, C. Y. (1992). Geological and Geochemical Characteristics of Dongshegnmiao Pb-Zn-S deposit of Submarine Exhalative Origin, Inner Mongolia. *Cheochimica* 21, 375–382. (in Chinese with English abstract).

Muchez, P., and Stassen, P. (2006). Multiple Origin of the 'Kniest Feeder Zone' of the Stratiform Zn-Pb-Cu Ore deposit of Rammelsberg, Germany. *Miner Deposita* 41 (1), 46–51. doi:10.1007/s00126-005-0039-1

Ohmoto, H., and Goldhaber, M. (1997). "Sulphur and Carbon Isotopes," in *Geochemistry of Hydrothermal Ore Deposits*. Editor H. L. Barnes (New York, NY: John Wiley & Sons), 517–611.

Ohmoto, H., and Rye, R. (1979). "Isotopes of Sulfur and Carbon," in *Geochemistry of Hydrothermal Ore Deposits*. Editor H. L. Barnes. 2nd ed (New York, NY: John Wiley & Sons), 509–567.

Peng, S. J. (1990). Investigation of the Tekli deposit in the Soviet Union. *Nonferrous Met. Xinjiang* 1990 (3), 51–58. (in Chinese with English abstract).

Rajabi, A., Rastad, E., Alfonso, P., and Canet, C. (2012). Geology, Ore Facies and sulphur Isotopes of the Koushk Vent-Proximal Sedimentary-Exhalative deposit, Posht-E-Badam Block, Central Iran. *Int. Geology. Rev.* 54 (14), 1635–1648. doi:10.1080/00206814.2012.659106

Robinson, B. W., and Kusakabe, M. (1975). Quantitative Preparation of Sulfur Dioxide, for Sulfur-34/sulfur-32 Analyses, from Sulfides by Combustion with Cuprous Oxide. *Anal. Chem.* 47, 1179–1181. doi:10.1021/ac60357a026

Roedder, E. (1984). Fluid Inclusions. *Rev. Mineralogy* 12, 644. doi:10.1515/9781501508271

Rye, R. O., and Ohmoto, H. (1974). Sulfur and Carbon Isotopes and Ore Genesis: a Review. *Econ. Geol.* 69, 826–842. doi:10.2113/gsecongeo.69.6.826

Samson, I. M., and Russell, M. J. (1987). Genesis of the Silvermines zinc-lead-barite deposit, Ireland; Fluid Inclusion and Stable Isotope Evidence. *Econ. Geol.* 82 (2), 371–394. doi:10.2113/gsecongeo.82.2.371

Sánchez-España, J., Velasco, F., Boyce, A. J., and Fallick, A. E. (2003). Source and Evolution of Ore-Forming Hydrothermal Fluids in the Northern Iberian Pyrite Belt Massive Sulphide Deposits (SW Spain): Evidence from Fluid Inclusions and Stable Isotopes. *Miner Deposita* 38, 519–537. doi:10.1007/s00126-002-0326-z

Şengör, A. C., Natal'in, B. A., and Burtman, V. S. (1993). Evolution of the Altaid Tectonic Collage and Palaeozoic Crustal Growth in Eurasia. *Nature* 364, 299–306.

Sheppard, S. M. F. (1986). Chapter 6. CHARACTERIZATION and ISOTOPIC VARIATIONS in NATURAL WATERS. *Mineralogy* 16, 165–184. doi:10.1515/9781501508936-011

Stacey, J. S., and Kramers, J. D. (1975). Approximation of Terrestrial lead Isotope Evolution by a Two-Stage Model. *Earth Planet. Sci. Lett.* 26, 207–221. doi:10.1016/0012-821x(75)90088-6

Tang, G. J., Wang, Q., Wyman, D. A., Sun, M., Li, Z-X., Zhao, Z-H., et al. (2010). Geochronology and Geochemistry of Late Paleozoic Magmatic Rocks in the Lamasu-Dabate Area, Northwestern Tianshan (West China): Evidence for a Tectonic Transition from Arc to post-collisional Setting. *Lithos* 119 (3-4), 393–411. doi:10.1016/j.lithos.2010.07.010

Taylor, B. E. (2004). Biogenic and Thermogenic Sulfate Reduction in the Sullivan Pb-Zn-Ag deposit, British Columbia (Canada): Evidence from Micro-isotopic Analysis of Carbonate and Sulfide in Bedded Ores. *Chem. Geol.* 204 (3–4), 215–236. doi:10.1016/j.chemgeo.2003.11.011

Taylor, H. P. (1974). The Application of Oxygen and Hydrogen Isotope Studies to Problems of Hydrothermal Alteration and Ore Deposition. *Econ. Geol.* 69, 843–883. doi:10.2113/gsecongeo.69.6.843

Tornos, F. (2006). Environment of Formation and Styles of Volcanogenic Massive Sulfides: the Iberian Pyrite Belt. *Ore Geology. Rev.* 28, 259–307. doi:10.1016/j.oregeorev.2004.12.005

Wang, B., Jahn, B.-m., Shu, L., Li, K., Chung, S.-l., and Liu, D. (2012). Middle-Late Ordovician Arc-type Plutonism in the NW Chinese Tianshan: Implication for the Accretion of the Kazakhstan Continent in Central Asia. *J. Asian Earth Sci.* 49, 40–53. doi:10.1016/j.jseaes.2011.11.005

Wang, L. J., Zhu, X. Y., Wang, J. B., Deng, J. N., Wang, Y. W., and Zhu, H. P. (2008). Study on Fluid Inclusions of the Sedimentary-Exhalative System (SEDEX) in Xitieshan lead-zinc deposit. *Acta Petrologica Sinica* 24 (10), 2433–2440. (in Chinese with English abstract).

Wang, S. L., Wang, G. H., Du, J. X., Zhao, J., Chen, Y. X., and Xiu, D. (2018). Petrology and Metamorphic P-T Path of the Garnet Amphibolite in the Wenquan Group, Western North Tianshan, China. *Acta Petrologica Sinica* 34 (12), 3658–3670. (in Chinese with English abstract).

Wang, Y. H. (2016). Geological Characteristics and Genesis Analysis of the Haerdaban Pb-Zn deposit, Wenquan, Xinjiang. *Nonferrous Met. Abstract* 31 (01), 55–56. (in Chinese with English abstract).

White, W. M. (2013). *Geochemistry*. Oxford: John Wiley & Sons, 406–409.

Wu, G., Chen, Y. C., and Chen, Y. J. (2010). Metallogenic Epoch and Tectonic Setting of Epithermal Gold Deposits in the north Eastern Kazakhstan Tianshan. *Acta Petrologica Sinica* 26 (12), 3683–3695. (in Chinese with English abstract).

Xbgmr (Xinjiang Bureau of Geology and Mineral Resources) (1993). *Regional Geology of Xinjiang Uygur Autonomy Region*. Beijing: Geology Publishing House, 841.

Xia, B., and Zhang, L. F. (2020). High T/P Metamorphic Rocks in the Southern Yili Plate: Representative for Precambrian Crystalline Basement or Active continental Margin? *Earth Sci.* 46, (6), 1960–1972. (in Chinese with English abstract). doi:10.3799/dqkx.2020.196

Xiao, W., Windley, B. F., Allen, M. B., and Han, C. (2013). Paleozoic Multiple Accretionary and Collisional Tectonics of the Chinese Tianshan Orogenic Collage. *Gondwana Res.* 23, 1316–1341. doi:10.1016/j.gr.2012.01.012

Xue, C., Chi, G., Li, Z., and Dong, X. (2014b). Geology, Geochemistry and Genesis of the Cretaceous and Paleocene sandstone- and Conglomerate-Hosted Uragen Zn-Pb deposit, Xinjiang, China: A Review. *Ore Geology. Rev.* 63, 328–342. doi:10.1016/j.oregeorev.2014.06.005

Xue, C. J., Zhao, X. B., Mo, X. X., Chen, Y., Nurtaev, B., Dong, L., et al. (2014a). Tectonic-metallogenic Evolution of Western Tianshan Giant Au-Cu-Zn-Pb Metallogenic belt and Prospecting Orientation. *Acta Geologica Sinica* 88 (12), 2490–2531. (in Chinese with English abstract).

Zartman, R. E., and Doe, B. R. (1981). Plumbotectonics-The Model. *Tectonophysics* 75, 135–162. doi:10.1016/0040-1951(81)90213-4

Zheng, Y., Zhang, L., and Guo, Z. L. (2013). Zircon LA-ICP-MS U-Pb and Biotite $^{40}Ar/^{39}Ar$ Geochronology of the Tiemuert Pb-Zn-Cu deposit, Xinjiang: Implications for Ore Genesis. *Acta Petrologica Sinica* 29 (1), 191–204. (in Chinese with English abstract).

Zhong, R., and Li, W. (2016). The Multistage Genesis of the Giant Dongshengmiao Zn-Pb-Cu deposit in Western Inner Mongolia, China: Syngenetic Stratabound Mineralization and Metamorphic Remobilization. *Geosci. Front.* 7 (3), 529–542. doi:10.1016/j.gsf.2015.09.006

Zhu, M., Wu, G., Xie, H., Liu, J., and Mei, M. (2012). Geochronology and Fluid Inclusion Studies of the Lailisigaoer and Lamasu Porphyry-Skarn Cu-Mo Deposits in Northwestern Tianshan, China. *J. Asian Earth Sci.* 49, 116–130. doi:10.1016/j.jseaes.2011.12.013

Conflict of Interest: The authors declare that the research was conducted in the absence of any commercial or financial relationships that could be construed as a potential conflict of interest.

The handling Editor declared a past co-authorship with the authors SL, KW.

frontiers in Earth Science

ORIGINAL RESEARCH
published: 24 November 2021
doi: 10.3389/feart.2021.752908

Magmatic-Hydrothermal Processes of Vein-Type Haman-Gunbuk-Daejang Copper Deposits in the Gyeongnam Metallogenic Belt in South Korea

Tong Ha Lee[1], Jung Hun Seo[1], Bong Chul Yoo[2], Bum Han Lee[2], Seung Hee Han[3], Yun Seok Yang[1,3] and Jun Hee Lee[1]*

[1]Department of Energy Resources and Engineering, Inha University, Incheon, South Korea, [2]Convergence Research Center for Development of Mineral Resources (DMR), Korea Institute of Geosciences and Mineral Resources, Daejeon, South Korea, [3]Korea Polar Research Institute, Incheon, South Korea

Haman, Gunbuk, and Daejang deposits are neighboring vein-type hydrothermal Cu deposits located in the SE part of the Korean Peninsula. These three deposits are formed by magmatic-hydrothermal activity associated with a series of Cretaceous granodioritic intrusions of the Jindong Granitoids, which have created a series of veins and alterations in a hornfelsed shale formation. The copper deposits have common veining and alteration features: 1) a pervasive chlorite-epidote alteration, cut by 2) Cu-Pb-Zn-bearing quartz veins with a tourmaline-biotite alteration, and 3) the latest barren calcite veins. Chalcopyrite, pyrite, and pyrrhotite are common ore minerals in the three deposits. Whereas magnetite is a dominant mineral in the Haman and Gunbuk deposits, no magnetite is present, but sphalerite and galena are abundant in the Daejang deposit. Ore-bearing quartz veins have three types of fluid inclusions: 1) liquid-rich, 2) vapor-rich, and 3) brine inclusions. Hydrothermal temperatures obtained from the brine inclusion assemblages are about 340–600, 250–500, and 320–460°C in the Haman, Gunbuk, and Daejang deposits, respectively. The maximum temperatures (from 460 to 600°C) recorded in the fluid inclusions of the three deposits are higher than those of the Cu ore precipitating temperature of typical porphyry-like deposits (from 300 to 400°C). Raman spectroscopy of vapor inclusions showed the presence of CO_2 and CH_4 in the three deposits, which indicates relatively reduced hydrothermal conditions as compared with typical porphyry deposits. The Rb/Sr ratios and Cs concentrations of brine inclusions suggest that the Daejang deposit was formed by a later and more fractionated magma than the Haman and Gunbuk deposits, and the Daejang deposit has lower Fe/Mn ratios in brine inclusions than the Haman and Gunbuk deposits, which indicates contrasting redox conditions in hydrothermal fluids possibly caused by an interaction with a hosting shale formation. In brines, concentrations of base metals do not change significantly with temperature, which suggests that significant ore mineralization precipitation is unlikely below current exposure levels, especially at the Haman deposit. Ore and alteration mineral petrography and fluid inclusions suggest that the Haman deposit was formed near the top of the deep intrusion center, whereas the Gunbuk deposit was formed at a

OPEN ACCESS

Edited by:
Jung-Woo Park,
Seoul National University, South Korea

Reviewed by:
Khin Zaw,
University of Tasmania, Australia
Pei Ni,
Nanjing University, China

***Correspondence:**
Jung Hun Seo
seo@inha.ac.kr

Specialty section:
This article was submitted to Economic Geology, a section of the journal Frontiers in Earth Science

Received: *03 August 2021*
Accepted: *08 November 2021*
Published: *24 November 2021*

Citation:
Lee TH, Seo JH, Yoo BC, Lee BH, Han SH, Yang YS and Lee JH (2021) Magmatic-Hydrothermal Processes of Vein-Type Haman-Gunbuk-Daejang Copper Deposits in the Gyeongnam Metallogenic Belt in South Korea. Front. Earth Sci. 9:752908. doi: 10.3389/feart.2021.752908

shallower intrusion periphery. The Daejang deposit was formed later at a shallow depth by relatively fractionated magma.

Keywords: haman, gunbuk, daejang, gyeongnam metallogenic belt, hydrothermal alteration, fluid inclusions, LA-ICP-MS

INTRODUCTION

The Haman, Gunbuk, and Daejang deposits occur within the Gyeongnam belt in the southeastern part of the Korean Peninsula, which is a Cu-bearing province in South Korea, and the area has been well investigated for Cu ores (Sillitoe, 1980; Jin et al., 1982; Lee et al., 2003). The Gyeongnam belt hosts numerous hydrothermal vein- and breccia-type copper deposits (Koh et al., 2003; Choi et al., 2006) associated with a porphyritic granodiorite-granite-quartz monzonite resulting from late Cretaceous igneous activities (Bulguksa orogeny: 115–70 Ma) (Min et al., 1982). The Haman, Gunbuk, and Daejang deposits are vein-type Cu deposits in the Gyeongnam metallogenic belt (Choi, 1985; Shin et al., 1987) and are geographically neighboring and hosted in a Cretaceous shale formation (Haman-Jindong shale formations) and Cretaceous granitoids (Jindong Granitoids) (Park et al., 1985; Shin et al., 1987). These three deposits have been studied intensively because the area is regarded to have potential porphyry-style Cu mineralization (Choi, 1985; Park et al., 1985). The Haman and Gunbuk deposits consist of eight orebodies with an ore grade of 1–6 Cu wt% and a tonnage of 1,450 kt (Kim, 1973). The Daejang deposit is located NW of the Haman and Gunbuk deposits and consists of two orebodies and prospects. The ore grades and tonnages of the Daejang deposit have not been reported.

Numerous geologic and geochemical studies have been conducted on the ore deposits in the Haman, Gunbuk, and Daejang deposit areas. Park et al. (1985) reported high metal contents (e.g. Cu, Zn, and Pb) in the Jindong Granitoids as compared with other nearby Cretaceous granitoids. The wide range of salinities (6–68 wt% NaCl equiv.) determined for ore-mineralized fluids in the Haman and Gunbuk deposits (Park et al., 1985) was suggested to have been caused by hydrothermal system changes from an early lithostatic-magmatic fluid into a later meteoric-dominated hydrostatic fluid system (Choi, 1985). Such a hydrothermal evolution in the area was supported by oxygen and hydrogen isotope analysis (Heo et al., 2003). In the Daejang deposit, Shin et al. (1987) presented a range of pressures up to 4.0 kb, which was estimated by FeS analysis on sphalerite, and temperatures of 250–430°C based on AsS analysis on arsenopyrite. Park and Kim (1988) subdivided mineralizations in the Daejang deposit into stages; 1) the earliest base-metal sulfides, 2) Sb-Ag minerals, and 3) the latest barren calcite, and also estimated temperatures (140–280°C) and pressures (fs_2 10^{-13}–10^{-20} bar) of Sb-Ag mineral by fluid inclusion microthermometry. Based on the decreasing trends of the hydrogen-oxygen isotope values observed, Choi (1998) suggested the involvements of meteoric fluids in the later hydrothermal stage in the Daejang deposit.

Whereas individual "deposit-scale" geological features in each of the deposits have been studied, no integrated "district-scale" magmatic-hydrothermal model has been established for the area. Based on systematic field observations and sample petrography studies, we confirmed the alteration patterns and ore mineralogies of the three deposits. After petrography, we performed a fluid inclusion study, which included systematic petrographic observations, microthermometry, laser Raman spectroscopy, and LA-ICP-MS microanalysis. By studying the fluid inclusions in mineralized quartz veins, we obtained information on pressure, temperature, and salinity and on trace element contents of the ore-bearing fluids in the three deposits. Based on the information obtained, we constructed a geologic-geochemical process for magmatic-hydrothermal fluids and ore mineralization in the deposits. Implications regarding mineralization potentials are discussed.

GEOLOGIC SETTINGS AND OVERVIEW OF THE DEPOSITS

Regional Geology

The Gyeongsang basin in the SE of the Korean Peninsula is a Cretaceous sedimentary basin formed in the Precambrian metamorphic basement (**Figure 1**). This basin is a tectonic pull-apart basin formed by northward oblique subduction of an ancient Izanagi oceanic plate into the Eurasian Plate during the Early Cretaceous. Subsequently, in the Late Cretaceous, the subduction angle became northwestward, and orthogonal subduction created an arc volcanism, called a Bulguksa orogeny (Chun and Chough, 1992; Chough et al., 2000; Lee et al., 2003; Ryu et al., 2006; Chough and Sohn, 2010). Bulguksa igneous rocks, generally granodioritic to granitic in composition, intrude into the Gyeongsang sedimentary basin. These are fine to coarse-grained porphyritic rocks mainly comprised of quartz, plagioclase, K-feldspar, biotite, and hornblende, and are classified as I-type magnetite series granitoid (Uchida et al., 2012).

Ryu et al. (2006) divided the Gyeongnam metallogenic belt into five stratigraphic units based on integrated stratigraphy, paleontology, paleomagnetism, geophysics, and age dating of igneous activities. They suggested a process for the formation of the Gyeongsang basin involving igneous activity caused by the direction and angle of subduction of the Izanagi plate. Koh et al. (2003) divided the Gyeongnam metallogenic belt into 3-period groups according to mineralization ages and directions of ore veins and suggested the direction of mineralization in the Gyeongsang basin proceeded from west to east connecting with the three groups with a belt of igneous activities in the SE part of China, the SE part of the Korean Peninsula, and the SW part of Japan.

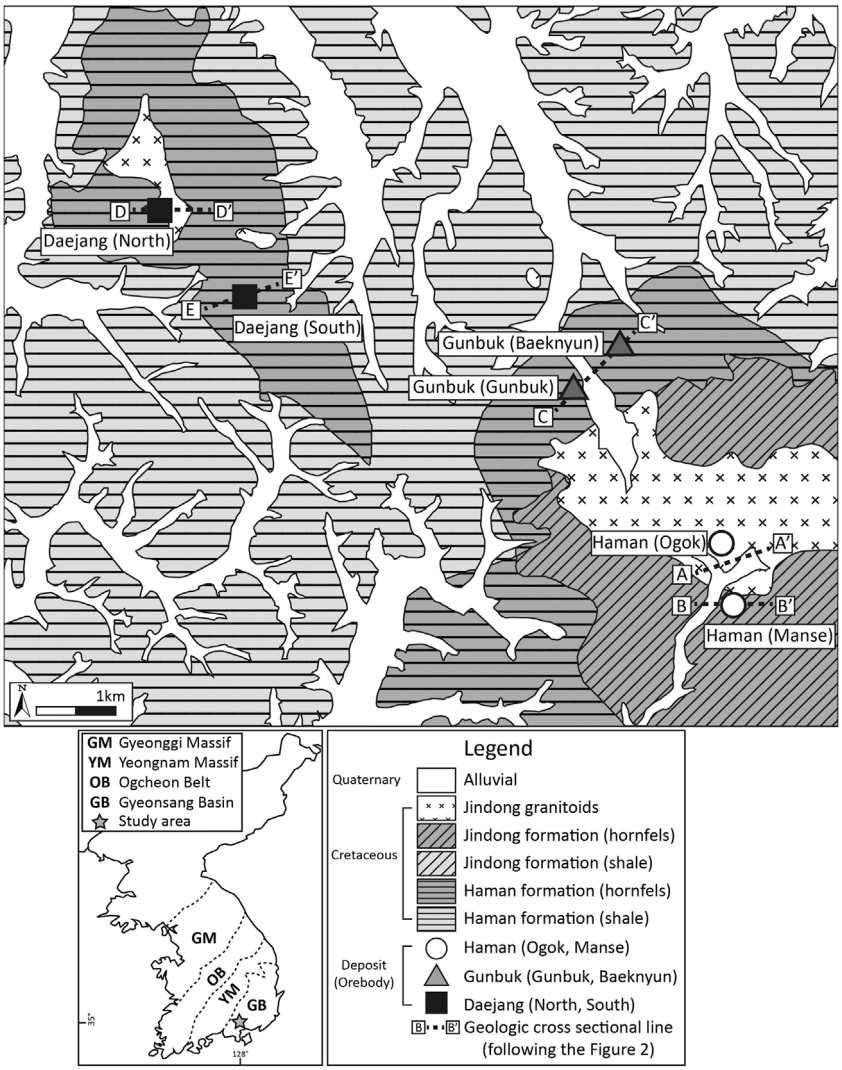

FIGURE 1 | Geological map of the Haman, Gunbuk, and Daejang deposits located in the Gyeongsang basin. The three deposits are hosted in the Cretaceous Haman-Jindong shale formation. The Haman-Jindong formation is widely metamorphosed into hornfels by an intrusion of Jindong granitoids. Geologic cross-sectional maps of the three deposits are shown in **Figure 2**.

The representative vein-type and breccia type deposits in the Gyeongnam metallogenic belt are as follows: vein-type deposits including the Haman-Gunbuk-Daejang deposits (Choi, 1985; Shin et al., 1987), Sambong-Samsan deposits (So et al., 1985), Kuryong-Cheongryong deposits (So et al., 1995), Donjeom deposit (Kim and Kim, 1974), and Keumryung-Gigu deposits (Park and Seol, 1992). The breccia-type deposits include the Ilgwang deposit (Yang and Jang, 2002; Seo, 2016) and Dalsung deposit (Won and Kim, 1966). The Sambong-Samsan, Kuryong-Cheongryong, and Donjeom deposits are hosted in shale-sandstones-conglomerates of the Cretaceous Hayang sedimentary group to an andesitic tuff-tuffaceous conglomerate-welded tuff of the Cretaceous Yuchon volcanoclastic group and show propylitic-potassic-argillic alterations (Kim and Kim, 1974; So et al., 1985; So et al., 1995). The Keumryung-Gigu deposits are hosted in black shale of the Cretaceous Hayang sedimentary group to the rhyolite-andesitic tuff of the Tertiary volcanoclastic group and show propylitic-potassic-argillic alterations (Park and Seol, 1992). The Ilgwang and Dalsung deposits are hosted in andesitic tuff-tuffaceous conglomerate of the Cretaceous Yuchon volcanoclastic group and exhibit a propylitic-sericitic alteration (Won and Kim, 1966; Yang and Jang, 2002; Seo, 2016).

The Haman, Gunbuk, and Daejang deposits in the Gyeongnam metallogenic belt compose an Early to Late Cretaceous Sindong-Hayang sedimentary group, which is intruded by a series of Late Cretaceous Bulguksa magmas called Jindong granitoids (**Figure 1**). The Haman and Jindong shale formations belong to the Sindong-Hayang sedimentary group and are hosted in the Haman, Gunbuk, and Daejang

deposits. The Haman formation consists of conglomerate-sandstone, black sandstone, and reddish mudstone (Chang, 1977; Chang et al., 1998). The Jindong formation, which conformably overlays the Haman formation, consists of black shale, black mudstone, and siltstone (Kim, 1973). The Haman-Jindong shale formations are tilted at a strike of N45 ~ 70 E and a dip of 10 ~ 15 SE (Moon et al., 1970). The Jindong granitoids intrude into both Haman and Jindong formations and are composed of porphyritic-plutonic textured rocks such as granite, granodiorite, and quartz diorite. Granodiorite is the most widely observed igneous rock among the Jindong granitoids. The whole-rock K-Ar (Park et al., 1985; Shin et al., 1987) and zircon U-Pb (Kim et al., 2016a) ages of the Jindong granitoids (granodiorite) have been reported to be 88–97 and 90–91 Ma, respectively. The Jindong granitoid intrusion in the Gyeongsang basin is a magnetite-bearing I-type intrusion, which has been suggested to have caused copper mineralization in the Gyengnam metallogenic belt, including the Haman, Gunbuk, and Daejang deposits (Park et al., 1983; Choi, 1985; Park et al., 1985; Shin et al., 1987; Lee, 1989; Lee et al., 1994; Koh et al., 2003). The Jingdong granitoids have lower Rb and Ba contents and higher Sr contents than the neighboring Pb-Zn related granitoids (Lee and Moon, 1989), which suggests fertile granitoids with higher Cu-Pb-Zn and Cl contents of biotite than barren granitoids (Lee et al., 1994; Lee and Lee, 1994). The shale in the Haman and Jindong formations in studied areas is widely metamorphosed into hornfels by intrusions.

Deposit Overview and Sampling Strategy

The Haman and Gunbuk deposits are neighboring deposits spatially located in a small district (about 25 km^2) in the SW part of the Gyeongnam metallogenic belt (35°13′ 07.9309″N, 128°21′ 41.7172″E ~ 35°11′21.7″N, 128°23′15.1″E) (**Figure 1**). They are hydrothermal vein-type Cu deposits with by-products of Au and Ag (Park et al., 1985; Heo et al., 2003). The estimated reserve of Cu ore in the Haman deposit is about 510 kt with an ore grade of 2–3 wt% of Cu (Kim, 1973). There are six orebodies in the Haman deposit, which are named Manse, Dundeok, Namgok-Bukgok, Deokgok, Gilgok, and Ogok (**Figures 2A,B**). The strike/dip of ore veins in the Manse orebody are N15 ~ 70°W to N80 ~ 85°E and in the Ogok orebody are N20° ~ 30°E to 80° ~ 85°SE (Kim, 1973). The Gunbuk deposit is located 2 km to the NW of the Haman deposit. The estimated reserve of Cu ore in the Gunbuk deposit is about 960 kt (Kim, 1973). Joint and fault systems with a strike of N70°S to N15 ~ 30°W are related to ore distribution in the Gunbuk deposit (Kim, 1973). There are two major orebodies in this deposit, named the Gunbuk and Baeknyun orebodies (**Figure 2C**). The strike/slip of ore veins of the Gunbuk orebody is N5 ~ 20 to N80° ~ 90°W, and ore grades are 5–10 wt% for Cu, 15–20 g/t for Au, and 70–300 g/t for Ag (Kim, 1973). The strike/dip of the veins in the Baeknyun orebody are NS, N15° to S40° ~ 80°W, and the ore grades are 1–2 wt% for Cu, 7 g/t of Au, and 100–260 g/t for Ag (Kim, 1973). The Daejang deposit is a hydrothermal vein-type Cu deposit with minor Au and Ag components (Shin et al., 1987; Choi, 1998) (35°14′ 05.9125″N, 128°18′ 05.4025″E) located 5 km NW of the Gunbuk deposit. There is no record of ore reserves for the Daejang deposit; joint and fault systems with a strike of NS to N20°W are related to ore distribution in this deposit (Kim et al., 2016b). The Daejang deposit has two orebodies, that is, North Cu-Pb-Zn-Au-Ag and South Cu-Au-Ag orebodies (**Figures 2D,E**). The strike/slip of ore veins of the North orebody is N15°W to 65°~ 85°NE, with ore grades of ~0.11 wt% for Cu, 3–7 g/t for Pb, 2–5 g/t for Zn, ~ 0.4 g/t for Au, and 380–770 g/t for Ag (Kim et al., 2016b). The strike/slip of ore veins of the South orebody is N20°W to 80°SW, and ore grades are ~3.5 wt% for Cu, 1.4 g/t for Au, and 10–55 g/t for Ag (Kim et al., 2016b).

In the three deposits, we collected quartz vein samples showing a well-preserved texture of ore-alteration mineralogy and a crosscutting relationship. In the Haman deposit, we collected 31 quartz vein samples from the Manse and Ogok orebodies. In the Gunbuk deposit, we collected nine quartz vein samples from the Gunbuk and Baeknyun orebodies and some granodiorite outcrops. In the Daejang deposit, 10 quartz veins from the North and South orebodies, and some granodiorite outcrops were collected.

PETROGRAPHY

Ore and Alteration Minerals

Hornfels is widely formed (ca. 30°km^2) in the Haman and Jindong formations around Jindong granitoid intrusions (**Figure 1**) and contain disseminated pyrite and magnetite. Magnetic susceptibilities ($\times 10^{-3}$ SI units) of the hornfels and granodiorite of Jindong granitoids in the region are about 50–60 and 17, respectively. The vein-bearing hornfels we studied commonly had pervasive chlorite and epidote alteration (CE alteration) before multiple veining events. In this section, we describe temporal relationships between hydrothermal alterations and paragenesis of ore-gangue mineral assemblages (**Figures 3–6**).

The major ore minerals of the Haman deposit include magnetite, pyrite, pyrrhotite, arsenopyrite, pyrite, and chalcopyrite, and minor ore minerals include scheelite, molybdenite, sphalerite, and galena. Quartz, tourmaline, actinolite, chlorite, and epidotes were observed as gangue minerals. We classified four veining stages in the Haman deposit: the first three quartz veining stages and the latest calcite veining stage. Hornfels in the Haman deposit has an early pervasive CE alteration. The hornfels with CE alteration was crosscut subsequently by a series of quartz veins hosting alterations of albite-actinolite (AA alteration) and tourmaline-biotite (TB alteration) (**Figure 3E**). Quartz veins accompanying an AA alteration are barren. Quartz veins are curvy and have thicknesses of 1–3 cm (**Figure 3E**). Quartz veins with TB alterations contain ore minerals and crosscut the earlier AA alteration (**Figures 3C,D**). These veins have thicknesses of 2–3 cm, but some veinlets are less than 1 cm. We classified two separate stages among the quartz veins with TB alterations. Earlier ones have massive oxide and sulfide ore minerals of magnetite-tourmaline-chalcopyrite-pyrite with disseminated scheelite-molybdenite in the vein. Later ones accompany minor K-feldspar with TB alteration, which has similar mineralogy but is richer in sulfide minerals. The veins show tourmaline-pyrrhotite-chalcopyrite-pyrite-arsenopyrite with

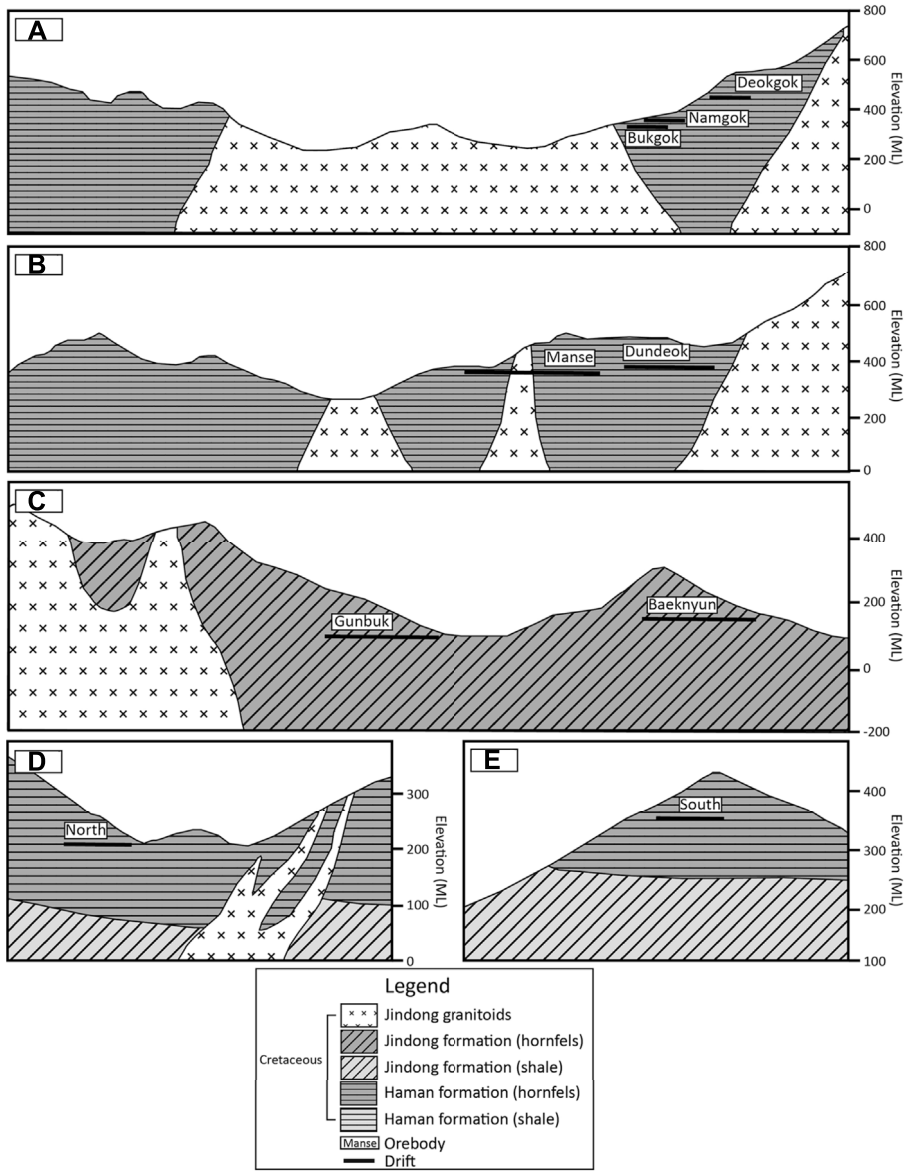

FIGURE 2 | Geologic cross-sections of the Haman, Gunbuk, and Daejang deposits. **(A)** Namgok-Bukgok orebody of the Haman deposit. The Ogok orebody is located near the Namgok-Bukgok orebody surrounded by Jindong granitoids. **(B)** Manse and Dundeok orebody of the Haman deposit. **(C)** Gunbuk-Baeknyun orebody of the Gunbuk deposit. **(D)** North orebody of the Daejang deposit. **(E)** South orebody of the Daejang deposit. The maps are modified versions of those produced by Moon et al. (1986), Kim et al. (2016b).

minors of magnetite-galena-sphalerite (**Figures 3E**, **6A**). No scheelite-molybdenite was observed in the later quartz vein with TB alteration. The latest stage is a calcite vein with disseminated chalcopyrite, and it crosscuts previous quartz veins (**Supplementary Table S1**, **Figures 3**, **6A**).

In the Gunbuk deposit, we observed magnetite, arsenopyrite, pyrrhotite, pyrite, and chalcopyrite as major ore minerals with sphalerite and galena as minor minerals. Quartz, tourmaline, and calcite were observed as gangue minerals. There are two veining stages in the Gunbuk deposit; a mineralized quartz vein and a postdating barren calcite vein. A pervasive CE alteration also appeared in hornfels before the quartz vein with TB alteration (**Figure 4B**). Unlike the Haman deposit, AA alteration was absent in Gunbuk veins. The quartz veins are 1–2 cm thick and have ore minerals including massive magnetite, pyrrhotite, chalcopyrite, pyrite, arsenopyrite, sphalerite, and galena. Unlike the Haman deposit, the oxide-sulfide ores in the quartz veins occur together in the Gunbuk deposit. Sphalerite and galena were more commonly observed in the Gunbuk veins than in the Haman veins. Second stage calcite veins were barren and crosscut previous quartz veins (**Supplementary Table S1** and **Figures 4**, **6B**).

The Daejang deposit, which is geographically removed from the Haman and Gunbuk deposits, contains a distinct ore mineral assemblage. They are Pb-Zn rich and contain no magnetite.

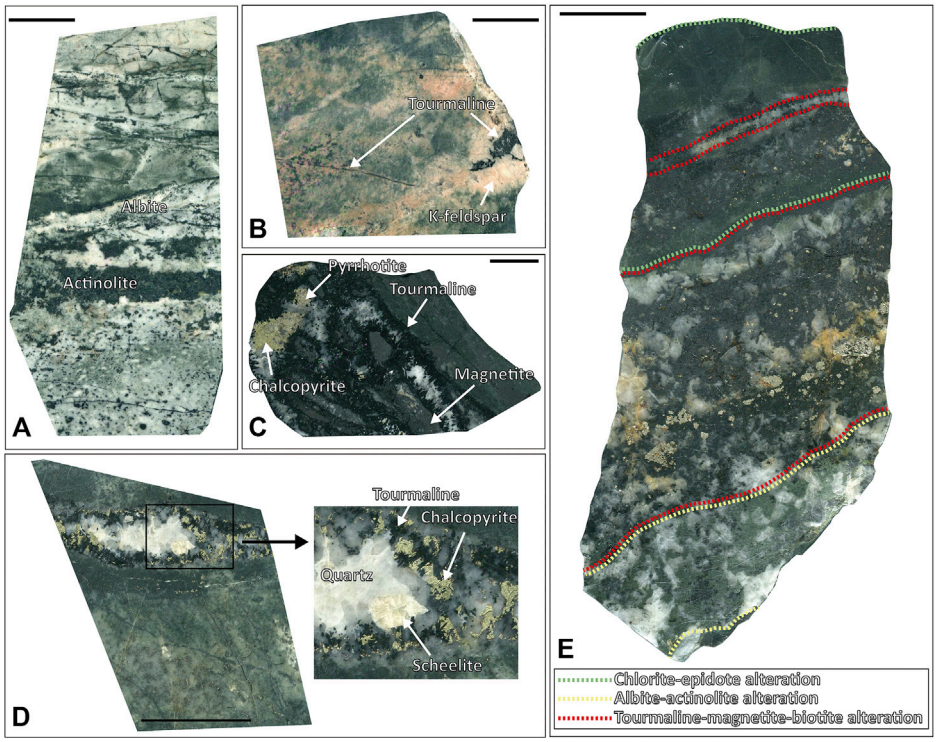

FIGURE 3 | Vein and alteration petrography of the Haman deposit. **(A)** Quartz veins with albite-actinolite alterations. **(B)** Quartz veins with a tourmaline-K-feldspar alteration. **(C)** Quartz veins with tourmaline-magnetite alterations with chalcopyrite and pyrrhotite that cut into chlorite-epidote altered host rock. **(D)** Quartz veins with tourmaline alteration with chalcopyrite and scheelite. **(E)** The chlorite-epidote altered host rock was overprinted by albite-actinolite alterations and cut by quartz veins with a tourmaline-magnetite-biotite alteration. The green dotted lines represent a chlorite-epidote "CE" alteration, the yellow dotted lines represent an albite-actinolite "AA" alteration, and the red dotted lines represent a tourmaline-(magnetite)-biotite "TB" alteration.

Pyrrhotite, arsenopyrite, pyrite, chalcopyrite, sphalerite, and galena were observed as ore minerals, and quartz, and calcite as gangue minerals. Two stages of veins were identified in the Daejang deposit: earlier quartz veins with TB alterations and a later calcite vein stage. A pervasive CE alteration was also observed in hornfels, crosscut by a series of mineralized quartz veins with TB alteration. The quartz veins were 1–3 cm thick and hosted ore mineralization. In the Daejang deposits, TB alterations that developed along quartz veins were generally thinner (<1 cm) than in the Haman and Gunbuk deposits (**Figure 5B**). The quartz veins have massive chalcopyrite-pyrite-sphalerite-galena with minor pyrrhotite-arsenopyrite (**Figure 5C**). Unlike the Haman and Gunbuk deposits, the Daejang deposit hosts massive sphalerite and galena in quartz veins. It has been reported that some Sb-bearing minerals such as gudmundite and boulangerite are also present in the Daejan deposit (Shin et al., 1987; Park and Kim, 1988; Choi, 1998). The latest thin (<1 cm) and barren calcite veins crosscut former quartz veins (**Supplementary Table S1** and **Figure 6C**).

A summary of the mineral and alteration paragenesis in the three deposits is provided in **Figure 6D**. The three deposits show common veining and alteration features: earlier CE alterations in hornfels, crosscutting quartz veins with TB alteration associated with oxide-sulfide mineralization, and the latest calcite veins.

Fluid Inclusion Assemblages

Ore-mineralized main-stage quartz veins were selected to study fluid inclusion. The sizes of the inclusions vary from ~5 to 30 μm in diameter. We petrographically described the pseudosecondary fluid inclusion assemblage (FIA) (**Figure 7**) textual co-genetic group of fluid inclusions (Goldstein and Reynolds, 1994; Bodnar, 2003a), for subsequent microthermometry and microanalysis. We classify three types of fluid inclusions: 1) aqueous liquid-rich "liquid" inclusions (**Figure 7A**, **7D**, **7G**), 2) aqueous vapor-rich "vapor" inclusions (**Figure 7C**, **7F**, **7I**) aqueous halite-bearing "brine" inclusions (**Figure 7B**, **7E**, **7H**). Liquid inclusions had a bubble size of 10–50 vol% (commonly about 20%) and homogenized into a liquid phase. Vapor inclusions had a bubble size of 70–80 vol% and homogenized into a vapor phase. Brine inclusions contained daughter crystals of salts (possibly NaCl and KCl). Some brine inclusions were associated and co-trapped with vapor inclusions in a single assemblage (a boiling assemblage) (**Figure 7J**).

We observed varying distributions and proportions of fluid inclusion types in each deposit and orebody (**Supplementary Table S2**) Brine inclusions predominated in the Haman deposit (ca. > 50%), whereas liquid and vapor inclusions accounted for less than about 20 and 30%, respectively. In the Gunbuk deposit, brine inclusions accounted for ~30%, liquid inclusions ~40% and for ~30% of vapor inclusions. In

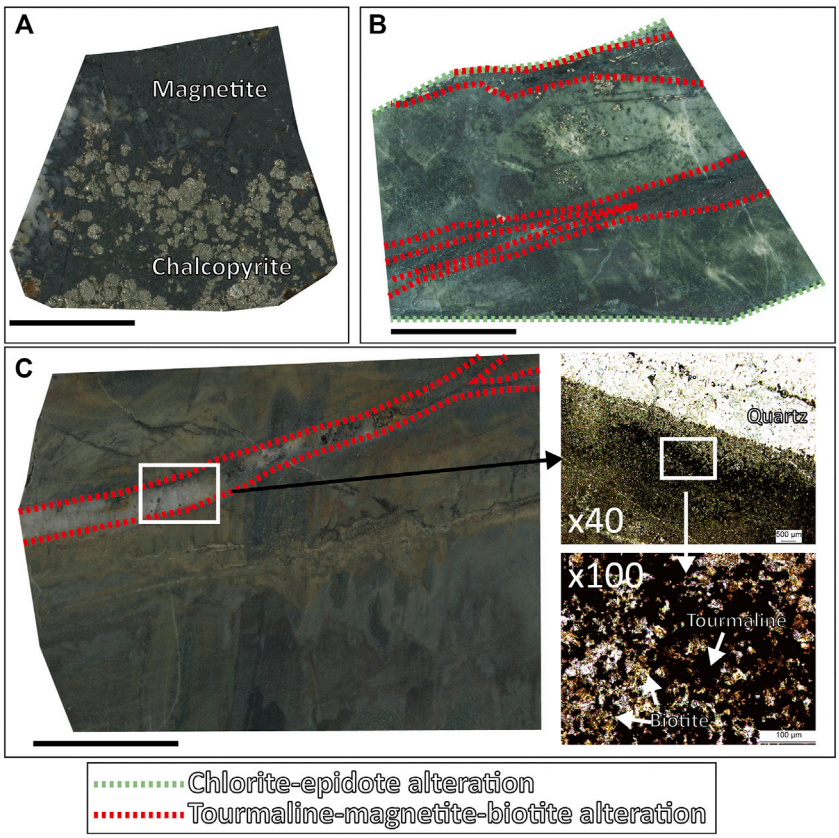

FIGURE 4 | Vein and alterations petrography of the Gunbuk deposit. **(A)** Massive magnetite and chalcopyrite occur in quartz veins with tourmaline alteration. **(B)** The chlorite-epidote altered host rock is crosscut by quartz veins with the tourmaline-magnetite alteration. **(C)** The quartz vein with the tourmaline-biotite alteration. Tourmaline and biotite were confirmed by microscopy. The green dotted lines represent a chlorite-epidote "CE" alteration, and the red dotted lines represent a tourmaline-(magnetite)-biotite "TB" alteration.

the Daejang deposit corresponding values were 40, 30, and 30%, respectively.

METHODS

Fluid Inclusion Microthermometry

Fluid inclusion microthermometry was performed on doubly polished quartz chips from the 13 quartz vein samples obtained from each of the three deposits. A total of 133 FIAs (about 300 single fluid inclusions) were studied, that is, 50 from the Haman deposit, 41 from the Gunbuk deposit, and 42 from the Daejang deposit. Fluid inclusion microthermometry was carried out using a Linkam FTIR 600 heating-freezing stage at Inha University, which was calibrated using synthetic fluid inclusions of H_2O and CO_2-H_2O. The freezing and heating procedures were conducted at accuracies of ±0.1 and ±1°C, respectively. Final ice melting and final halite melting temperatures were measured to calculate apparent salinities (NaCl equivalent wt%) (Bodnar and Vityk, 1994). Calculated salinities and homogenization temperatures (T_h) were combined to calculate a minimum trapping pressure and an isochore using a model NaCl-H_2O system (Driesner and Heinrich, 2007). An average ±1 sigma was calculated for single fluid inclusions in the FIA (**Supplementary Table S3**).

Raman Spectroscopy

Laser Raman spectroscopy was performed on the bubble parts in vapor inclusions to identify gases in the fluids. A LabRAm HR Evolution confocal Raman spectrometer (HORIBA) in Inha University was used, which was equipped with an 1800 g mm^{-1} grating, a 100x confocal lens, and an edge filter. Raman spectra were obtained at a laser excitation wavelength of 532 nm (green laser), a laser power of 2 mW, filtering between 25 and 50%, a beam diameter of 100 μm, an acquisition time of 5 s, accumulation of 3–20 times, and a spectral range of 600–4,200 cm^{-1}. Twelve vapor inclusions from the Haman deposit, 21 from the Gunbuk deposit, and 13 from the Daejang deposit were analyzed.

Laser Ablation-ICP-MS Microanalysis of Fluid Inclusions

LA-ICP-MS microanalysis of brine inclusions in quartz veins was conducted after microthermometry using an LA-ICP-MS system at the Korea Polar Research Institute (KOPRI). The system had a 193 nm ArF Excimer laser (ESI NWR 193 model) connected to a quadruple ICP-MS (iCAP-Q model). 116 single fluid inclusions from 70 FIAs were analyzed. Laser beam sizes were adjusted to the diameters of inclusions to fully evacuate all components in the

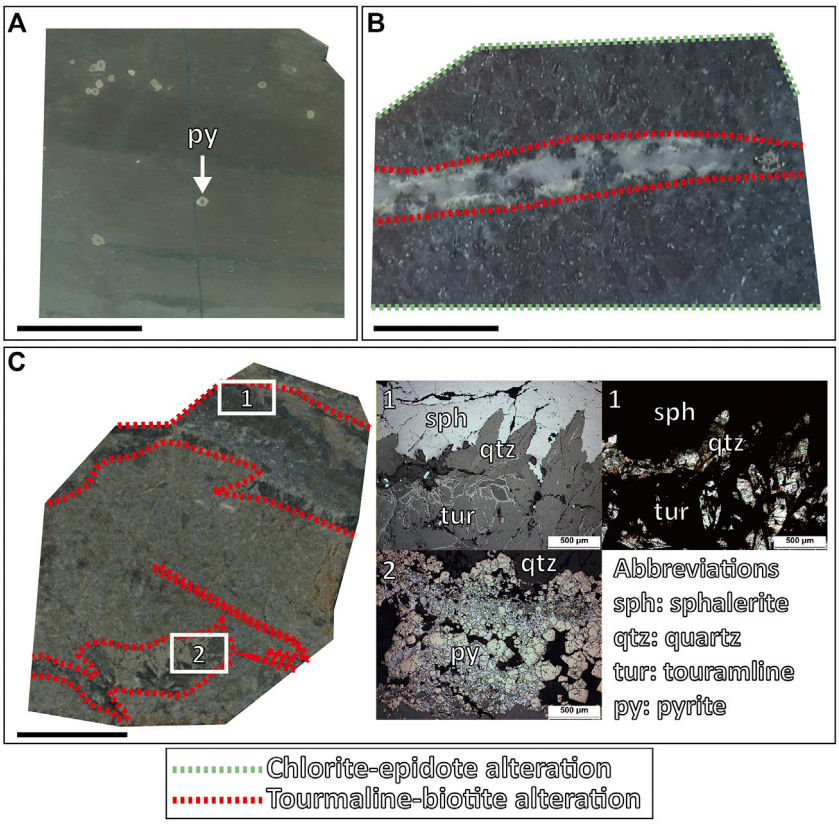

FIGURE 5 | Vein and alterations petrography of the Daejang deposit. **(A)** Pyrite grains are present in hornfels. **(B)** Tourmaline-(K-feldspar)-biotite alterations are shown along the quartz veins cutting the chlorite-epidote altered host rock. **(C)** Tourmaline-biotite alterations formed along the quartz veins. (C-1) Tourmaline, sphalerite, quartz, and (C-2) pyrite images obtained by reflected **(left)** and transmitted light **(right)** microscopy. The green dotted lines represent a chlorite-epidote "CE" alteration, and the red dotted lines represent a tourmaline-(magnetite)-biotite "TB" alteration.

brine inclusions. The laser energy density used was 7–8 J/cm^2 and 3–10 Hz repetition rates were applied. To analyze inclusions and hosting quartz, we used 10 ms dwell times for the following isotopes; ^{11}B, ^{23}Na, ^{27}Al, ^{29}Si, ^{39}K, ^{40}Ca, ^{49}Ti, ^{55}Mn, ^{57}Fe, ^{65}Cu, ^{66}Zn, ^{75}As, ^{85}Rb, ^{88}Sr, ^{133}Cs, and ^{208}Pb. A standard reference material (SRM) of NIST 610 glass was used as an external standard to calculate element ratios. Empirical estimation of Na concentrations from fluid inclusion salinities (Heinrich et al., 2003) was applied as an internal standard. Data reductions and quantifications from convoluted transient signals of fluid inclusions (**Figure 8**) were carried out using SILLS software (Guillong et al., 2008). During the ablations of hosting quartz, trace elements, including Ti and Al, in the quartz were simultaneously analyzed.

RESULTS

Microthermometry and Calculation of Pressure

Ranges of salinities and T_h values obtained from liquid inclusion assemblages were found to be highly overlapping (**Figures 9A**, **10**). T_h values from liquid inclusion assemblages were 96–360°C in the Haman deposit, 200–310°C in the Gunbuk deposit, and 150–290°C in the Daejang deposit. Salinities in liquid inclusion assemblages were 2–19 wt% in the Haman deposit, 3–18 wt% in the Gunbuk deposit, and 6–17 wt% in the Daejang deposit (**Supplementary Table S3**).

T_h values of brine inclusion assemblages were 340–600°C in the Haman deposit, 250–470°C in the Gunbuk deposit, and 320–460°C in the Daejang deposit. Salinities in the brine inclusion assemblages are 33–62 wt% in the Haman deposit, 34–59 wt% in the Gunbuk deposit, and 39–55 wt% in the Daejang deposit. Fluid pressures of each deposit were calculated from salinities and T_h values obtained from brine inclusions. Maximum pressures of the Haman, Gunbuk, and Daejang deposits were 500, 330, and 270 bar, respectively. T_h values and calculated pressures were highest for the Haman deposit and similar for the Gunbuk and Daejang deposits (**Figure 9B**).

Raman Spectroscopy

Gas species were detected in the bubbles of vapor inclusions (**Figure 11**). CO_2 peaks were identified in the Ogok (Haman), Baeknyun (Gunbuk), Gunbuk (Gunbuk), North (Daejang), and outcrop (Daejang) orebodies, and CH_4 peaks were detected in the Gunbuk (Gunbuk) orebody and outcrop (Daejang).

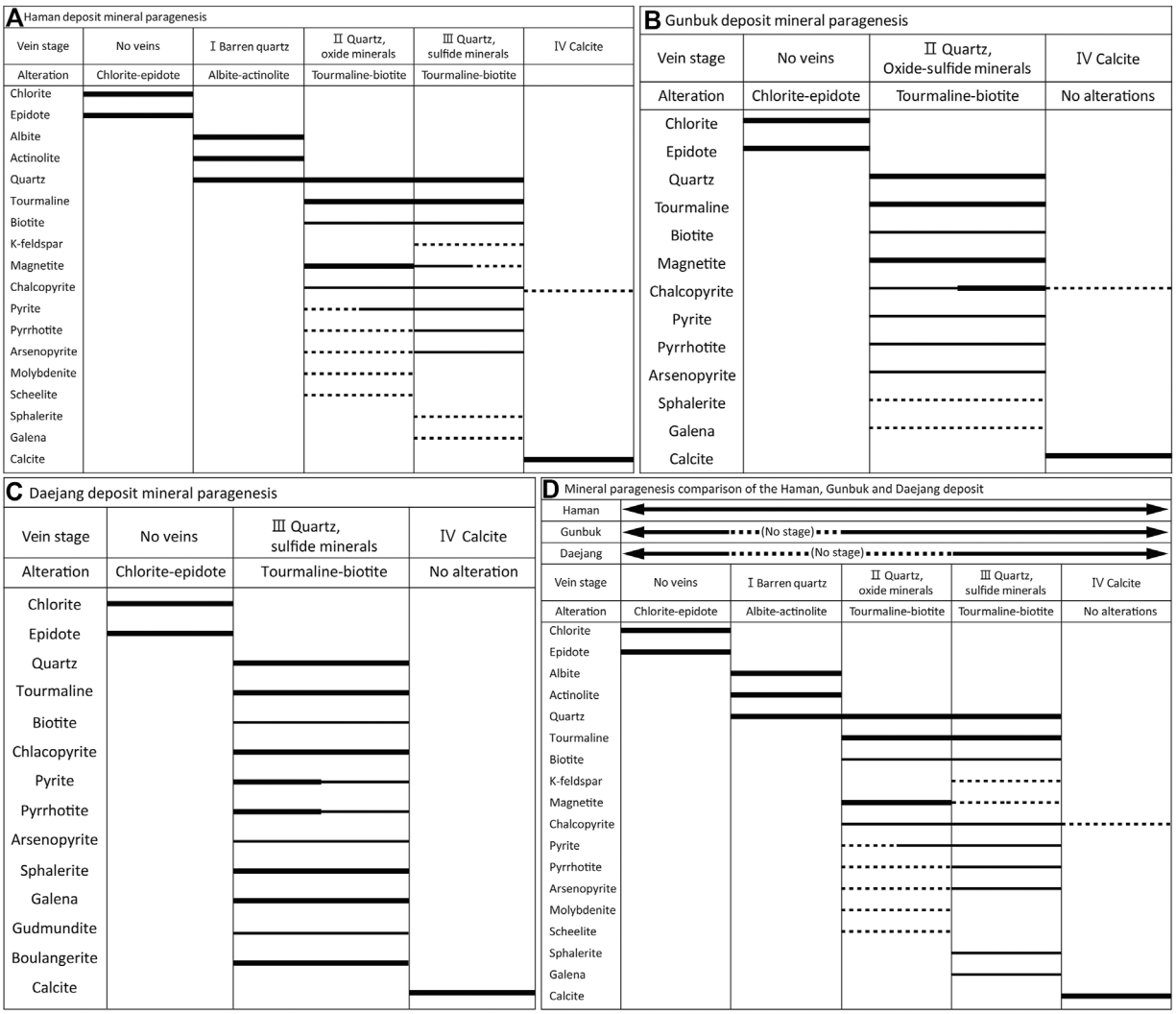

FIGURE 6 | Paragenetic relationships of veins, alterations, and minerals in the **(A)** Haman, **(B)** Gunbuk, and **(C)** Daejang deposits, and **(D)** a summary of the three deposits. Abundances of minerals occurring are represented by line thicknesses. In the three deposits, the chlorite-epidote alteration, tourmaline-biotite alteration with mineralized quartz veins, and the latest calcite veins are observed. Albite-actinolite alterations are observed only in the Haman deposit. In the Daejang deposit, gudmundite and boulangerite have been reported (Shin et al., 1987; Park and Kim, 1988; Choi, 1998), though they were not observed in this study.

Trace Elements in Quartz

Al levels in quartz at the Haman, Gunbuk, and Daejang deposits were 70–510, 40–600, and 30–230 ppm, respectively (**Supplementary Table S4** and **Figure 12A**), and corresponding values for Ti were 12–140, 4–55, and 5–56 ppm (**Supplementary Table S4** and **Figure 12B**).

Trace Elements in Brine Inclusion Assemblages

Rb, Sr, Cs, Mn, Fe, Zn, and Pb signals in brine inclusions were obvious (**Figure 8**), whereas signals of other elements were not clear because of high background levels in gas blanks and quartz matrices. Concentrations of Cs, Mn, Pb, Fe, and Zn, and Rb/Sr and Fe/Mn ratios in brine inclusion assemblages are provided in **Figure 13** and **Supplementary Table S5**. The range of Rb/Sr ratios and Cs concentrations in brine inclusion assemblages of the Haman, Gunbuk, and Daejang deposits were 0.1–1.0 and 10–240 ppm, 0.1–0.8 and 20–340 ppm, and 0.2–16 and 50–1,250 ppm, respectively. The Haman and Gunbuk deposits had similar Cs concentrations and Rb/Sr ratios, whereas the Daejang deposit had higher values. The metal concentrations (ppm) in the brine assemblages of the Haman deposit were 3 ~ 20 k for Mn, 20 ~ 100 k for Fe, 100 ~ 5 k for Zn, and 200 ~ 2 k for Pb, in the Gunbuk deposit were 2 ~ 20 k for Mn, 10 ~ 100 k for Fe, 300 ~ 5 k for Zn, and 100 ~ 2 k for Pb are in the brine assemblages, and in the Daejang deposit were 7 ~ 50 k for Mn, 10 ~ 100 k for Fe, 3 ~ 15 k for Zn, and 2 ~ 10 k for Pb are in the brine assemblages. Mn concentrations and ranges were comparable in all deposits, whereas concentrations of Fe, Zn, and Pb were much higher in the Daejang deposit.

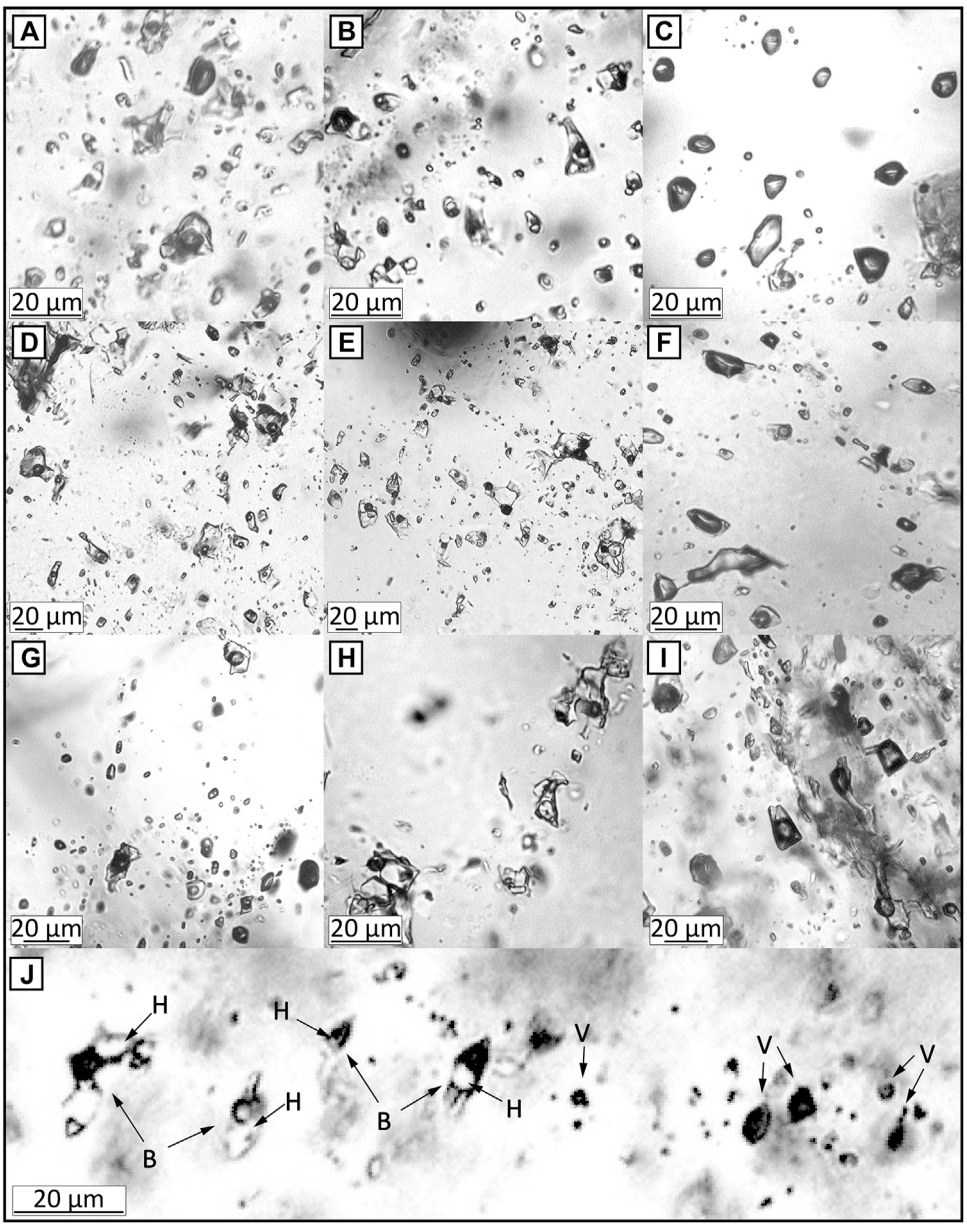

FIGURE 7 | Types of fluid inclusion assemblages in mineralized quartz veins. **(A)** liquid inclusions, **(B)** brine inclusions, and **(C)** vapor inclusions in the Haman deposit. **(D)** liquid inclusions, **(E)** brine inclusions, and **(F)** vapor inclusions in the Gunbuk deposit. **(G)** liquid inclusions, **(H)** brine inclusions, and **(I)** vapor inclusions in the Daejang deposit. **(J)** The brine and vapor inclusions in the boiling assemblage in the Daejang deposit. B, V, and H represent brine inclusion, vapor inclusion, and halite, respectively. Most of the fluid inclusions observed in the studied deposits were either liquid inclusions with a bubble size of around 20 vol% or brine inclusions with a bubble size of 10–30 vol%. Minor vapor inclusions with bubble sizes of 70–80 vol% were also observed.

DISCUSSION

Origin of Alterations and Ore Mineral Assemblages

Based on petrographic features such as vein-cross cutting, alteration, and ore mineral assemblages in the Haman, Gunbuk, and Daejang deposits, we classify their common paragenetic sequences as follows: 1) an early barren pervasive CE alteration overprinting hornfels, 2) main-stage quartz veins of the TB alteration mineralized with chalcopyrite-pyrite-arsenopyrite (±magnetite-pyrrhotite-sphalerite-galena), and 3) the latest barren calcite vein. The main-stage TB alteration was often associated with the AA alteration in the Haman deposit and with K-feldspar in the Haman, Gunbuk, and Daejang deposits.

The Haman-Jindong hornfels was formed by magmatism of the Jindong granitoids (Park et al., 1985; Shin et al., 1987).

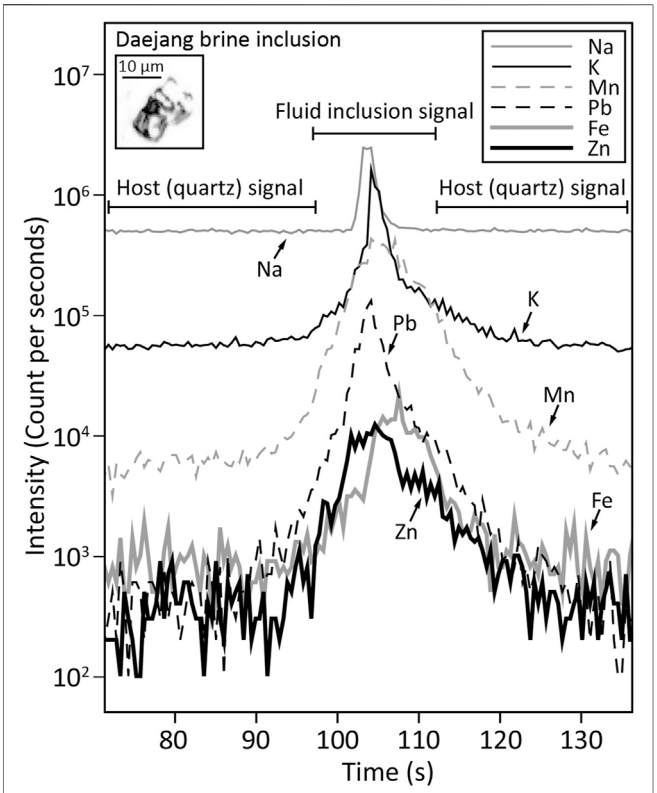

FIGURE 8 | Transient signals of LA-ICP-MS of brine inclusions analysis (Daejang quartz veins) showing signals for Si, Na, Mn, Pb, Fe, and Zn.

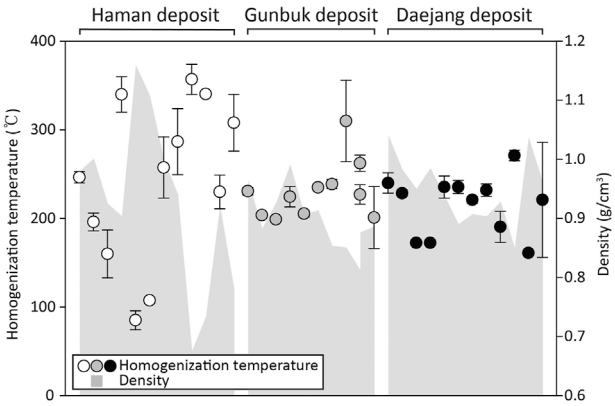

FIGURE 10 | Homogenization temperature and density plots of liquid inclusion assemblages. The Gunubuk and Daejang deposits have similar densities and temperature ranges, whereas the Haman deposit has broader and higher average ranges.

Magnetic susceptibilities (SI unit) in the hornfels were significantly higher (50–60 × 10^{-3}) than in granitoids (granodiorite; 15–17 × 10^{-3} and pegmatite; 2–4 × 10^{-3}). Although we cannot observe under a microscope, we estimated that the hornfels contained disseminated micro-particles of magnetite. Observations of disseminated pyrite in Haman-Jindong hornfels (**Figure 5A**) and unmetamorphosed Haman-Jindong shale (Kim and Paik, 2001; Kim et al., 2018) indicated that the Fe from the Haman-Jindong parent shale was

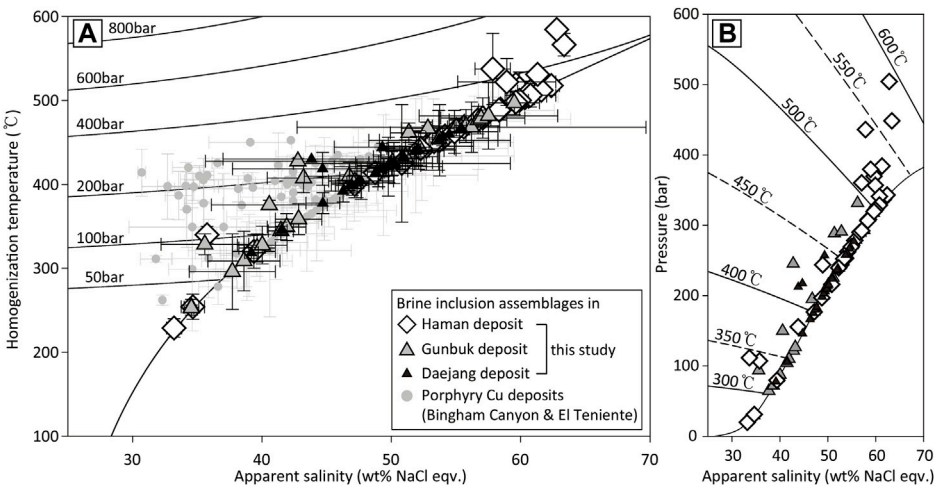

FIGURE 9 | (A) Plots of homogenization temperatures versus apparent salinities (NaCl wt.% equivalents) obtained from brine assemblages of the Haman, Gunbuk, Daejang deposit and porphyry-style deposits (Bingham Canyon & El Teniente deposit) (Klemm et al., 2007; Landtwing et al., 2010). The gray circles represent porphyry deposits, the white diamonds represent the Haman deposit, the gray triangles represent the Gunbuk deposit, and the black triangles represent the Daejang deposit. Ranges of the Gunbuk and Daejang deposits partially overlap with porphyry deposits, maximum temperatures were exceptionally higher in the Haman deposit than in porphyry deposits. **(B)** Plots of salinity versus calculated pressure for brine inclusion assemblages in the three deposits. The circles represent liquid inclusion assemblages, and the rhombus and triangle symbols represent brine inclusion assemblages. White circles and rhombus symbols represent T_h and salinity of the Haman deposit, gray circles and triangles represent T_h and salinity of the Gunbuk deposit, and black circles and triangles represent T_h and salinity of the Daejang deposit.

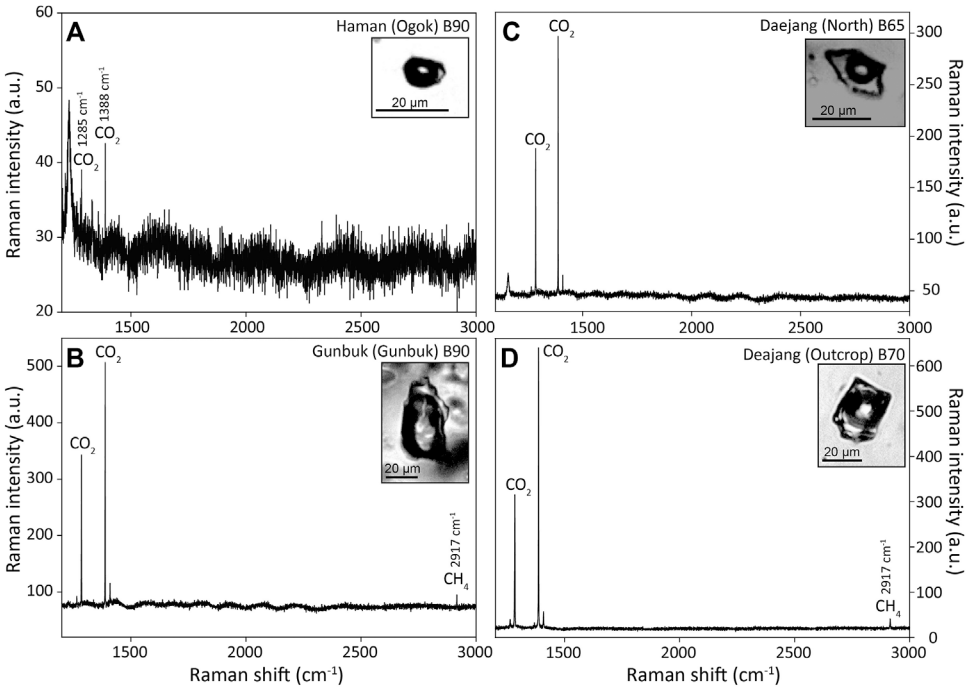

FIGURE 11 | Raman spectra of a bubble part of the vapor-rich inclusions hosted in quartz veins of the **(A)** Haman, **(B)** Gunbuk, and **(C,D)** Daejang deposits. CO_2 (signals at 1,285 and 1,388 cm^{-1}) was detected in the three deposits, whereas CH_4 (signal at 2,917 cm^{-1}) was detected in **(B)** the Gunbuk and **(D)** Daejang deposits.

probably the source of the formation of disseminated magnetite in hornfels. Whereas massive precipitation of magnetite was present in the quartz veins of the Haman and Gunbuk deposits (**Figure 3C** and **Figure 4A**), and magnetite did not precipitate in the Daejang deposit, which may have been due to different temperature and sulfidation conditions of the magmatic-hydrothermal fluids (Einaudi et al., 2003) in the Haman, Gunbuk, and Daejang deposits. The quartz veins with the TB alteration in the Daejang deposit contained massive sulfide minerals such as pyrrhotite, pyrite, galena, and sphalerite, instead of magnetite (**Figure 5C**), whereas Fe concentrations in the brines of all three deposits were comparable (**Supplementary Table S5**). These contrasting Fe mineral precipitations might be due to relatively lower hydrothermal temperatures, which agrees with our fluid inclusion results (**Figures 9**, **10**), and suggests the possibility of higher sulfidation states of magmatic-hydrothermal fluids in the Daejang deposit as compared with the Haman and Gunduk deposits (**Figure 14**) (Einaudi et al., 2003; Reed and Palandri, 2006).

The CE alteration which occurs exclusively along the margin of the Jindong granitoids (Choi, 1998; Heo et al., 2003) indicates that the alteration is strongly associated with the intrusions. A CE alteration can be formed either by a convection of external fluids driven by magmatism (Seedorff et al., 2005; Ayuso et al., 2010; Sillitoe, 2010), or by a cooled magmatic fluids (Orovan et al., 2018; Pacey et al., 2020). The geochemical studies on the alteration minerals (e.g. chlorite, epidote) are required to trace the origin of the alteration and use it as an exploration target in the area (Wilkinson et al., 2020).

An AA alteration (**Figure 3A**) occurs exclusively in the Haman deposit. The AA alteration, which is associated with Na-Ca rich alteration minerals, is often observed in the barren and lower part of Cu ore bodies of porphyry deposits (Carten, 1986; Dilles and Einaudi, 1992; Dilles et al., 2000; Sillitoe, 2010) or in some Iron-Oxide-Copper-Gold (IOCG) deposits (Barton and Johnson, 2004; Williams et al., 2005), in which replacing K-feldspar into Na plagioclase or epidote, and biotite or hornblende into Ca amphibole (actinolite) (Dilles and Einaudi, 1992). The existence of the AA alteration suggests that the Haman deposit may have been formed deeper than the Gunbuk and Daejang deposits, which is in line with our fluid inclusion results. The origins of AA alteration, which can be referred to as a Na-Ca alteration, occurring in some of the magmatic-hydrothermal ore deposits have been suggested to be either externally-derived salty fluids (Dilles and Einaudi, 1992; Barton and Johnson, 1996; Xavier et al., 2008) or magmatically-derived fluids (Oliver, 1996; Pollard et al., 1997a; Mark and Foster, 2000; Perring et al., 2000). In the Haman deposit, pervasive CE alterations occurred after the metamorphism of hornfels due to granitoid intrusions, and quartz veins with AA alterations cut through the CE alternations (**Figure 3A**). The alteration and crosscutting relationship feature in the Haman deposit suggests that the AA alteration might have formed due to a magma-derived fluid from Jindong granitoids, but we cannot rule out the

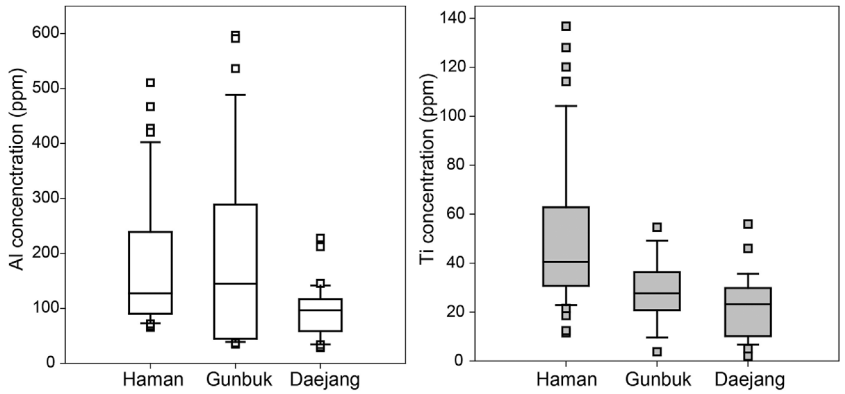

FIGURE 12 | Concentrations and ranges for **(A)** Al and **(B)** Ti concentrations in the quartz veins of the Haman, Gunbuk, and Daejang deposits. Ranges of Al concentrations in the Haman and Gunbuk deposits overlapped, and ranges of Ti concentrations in the Gunbuk and Daejang deposits also overlapped.

possibility of heated externally derived water from pores of the surrounding Haman-Jindong shale formations.

Occurrence of scheelite-molybdenite (**Figure 3D**) in the Ogok orebody of the Haman deposit indicates an elevated W-Mo concentration in magmatic-hydrothermal fluids, which can be related to a significantly fractionated magma (Kooiman et al., 1986; Seedorff et al., 2005; Sinclair, 2007). This differentiated, possibly granitic, magma might be occur at depth, while outcrops of the Jindong granitoids show a rather intermediate magmatic composition ranging from gabbro to granodiorite (Wee et al., 2007).

Like biotite, tourmaline was a commonly observed alteration mineral in the mineralized veins of all deposits (TB alteration: **Figures 3C**, **4C**, **5C**), and the quartz veins associated with tourmaline contained boiling assemblages indicating fluid phase separation (**Supplementary Table S3**). Tourmaline is commonly associated with many alteration types such as Na-Ca, K, and phyllic alterations in porphyry deposits (Sillitoe and Sawkins, 1971; Gustafson and Hunt, 1975; Dilles and Einaudi, 1992). Lynch and Ortega (1997) suggested that the precipitation of tourmaline can be promoted by phase separation of magmatic-hydrothermal fluids rich in boric acid derived from a fractionated B-rich granite. B is abundant in oceanic sediments and in altered oceanic crust and has a relatively high solubility in fluids, which results in B-rich arc magma (Moran et al., 1992; Leeman et al., 1994; Dreyer et al., 2010). Abundant tourmaline in the deposits studied suggests a B-rich causative magma and B-rich magmatic fluids in the area. The Gukjeon Pb-Zn deposit, which is located 55 km NE from the Haman, Gunbuk, and Daejang deposits, contains abundant axinite [$(Ca, Fe, Mn)_3Al_2BO_3Si_4O_{12}(OH)$] as a major skarn mineral, and its B has been suggested to originate from Late Cretaceous arc magma (Kim et al., 2021).

P-T Conditions and the Geochemistry of Hydrothermal Fluids

The presence of boiling assemblages suggests fluid phase separation due to a rapid depressurization, which commonly occurs in magmatic-hydrothermal deposits (Audétat et al., 1998; Heinrich et al., 1999). Many boiling assemblages have been reported in quartz veins in the three deposits, and these could provide the actual P-T conditions of hydrothermal fluids (Roedder and Bodnar, 1980). A density contrast between brine and vapor in boiling assemblages indicates degrees of depressurization during phase separation. Pressures calculated from brine analysis results of boiling assemblages can be converted into paleodepths based on lithostatic (density of 2.7 g/cm^3) or hydrostatic (density of 1.0 g/cm^3) pressure regimes. In the Haman deposit, the apparent paleodepths calculated from lithostatic and hydrostatic pressure regimes were 0.5–2.0 and 1.3–5.4 km, in the Gunbuk deposit were 0.1–1.2 and 0.2–3.2 km, and in the Daejang deposit were 0.3–1.0 and 0.8–2.7 km, respectively (**Supplementary Table S3**).

Since the Fe ($Fe^{2+} \rightarrow Fe^{3+}$) oxidation has a faster reaction rate than Mn ($Mn^{2+} \rightarrow Mn^{4+}$), Fe/Mn ratio can be used as a redox indicator of fluid passing through a fluid-rock buffered system (i.e. the Fe/Mn ratio is lower for an oxidizing fluid) (Boctor, 1985; Naeher et al., 2013). Bottrell and Yardley (1991) reported an increasing trend for Fe/Mn ratio when fluids at equilibrium with chlorite react with the reduced host rock, and Seo et al. (2012) showed a reducing fluid evolution from Cu-stage to Mo-stage in a porphyry deposit when Fe/Mn ratios in brines were increased. Fe/Mn ratios in brine inclusions were found to be lower in the Daejang deposit than in the Haman and Gunbuk deposits (**Figure 13C**), which suggests a relatively oxidizing fluid in the Daejang deposit. CO_2 was detected by Raman spectroscopy in some vapor inclusions (**Figure 11**), whereas clathrate was not observed by fluid inclusion microthermometry. Choi (1985) and Heo et al. (2003) reported that CO_2 was not detected in fluid inclusions of the Haman and Gunbuk deposits, whereas Choi (1998) reported a carbonic liquid phase in fluid inclusions of the Daejang deposit. CO_2 contents in fluids might have increased fluid carbonate activity in the fluids and formed the latest calcite vein (Choi, 1998). CH_4 was detected in fluid inclusions in the Gunbuk and the Daejang deposits by Raman spectroscopy (**Figure 11**). The ratios of mole fractions of CO_2 and CH_4 in fluid inclusions have been used to reconstruct fluid redox conditions (Giggenbach, 1987; Dubessy et al., 1989;

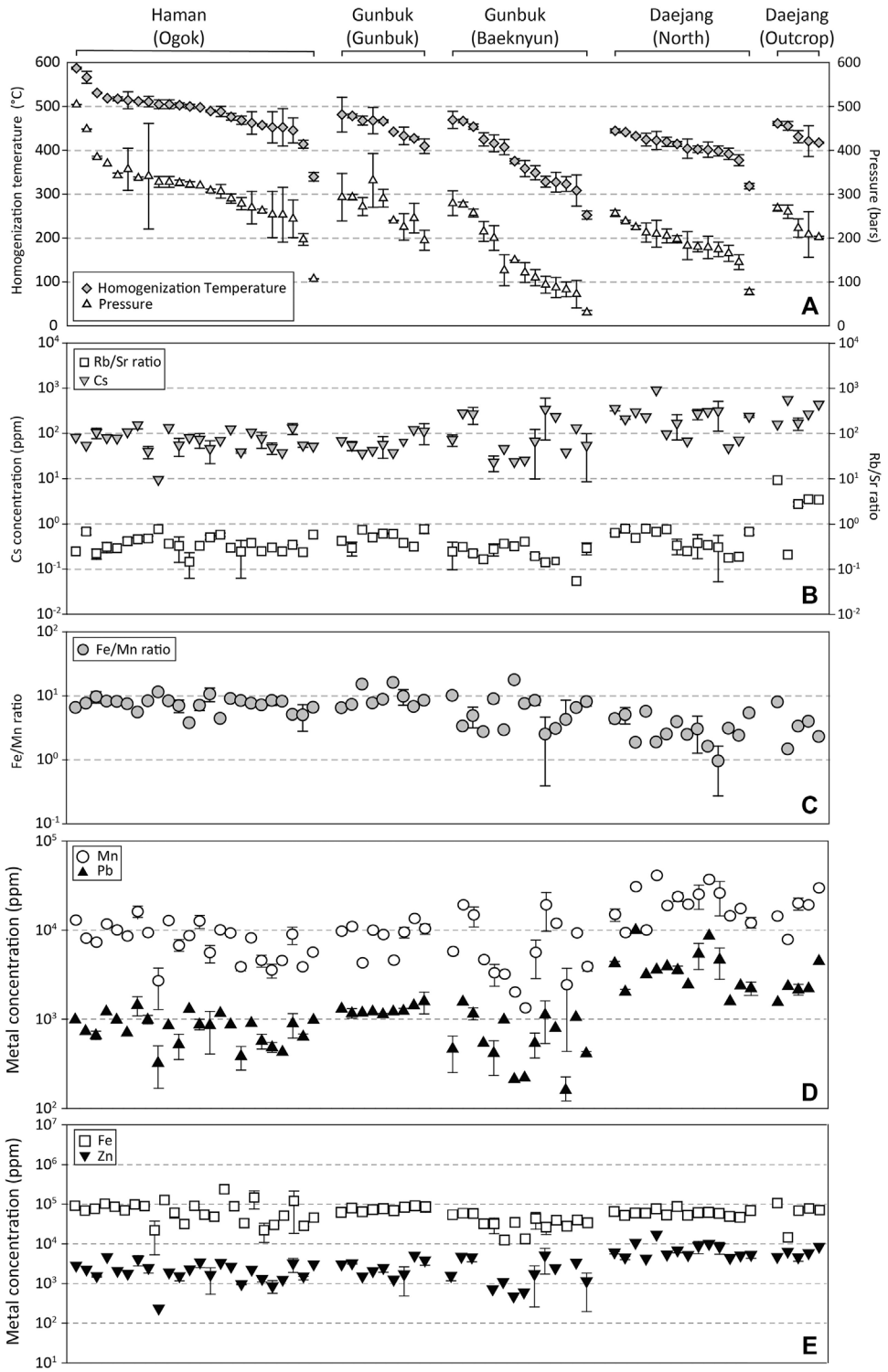

FIGURE 13 | Rb/Sr and Fe/Mn ratio, and concentrations of Cs, Mn, Pb, Fe, and Zn plotted in order of decreasing homogenization temperatures (T_h) of brine inclusion assemblages in orebodies of the Haman, Gunbuk, and Daejang deposits. **(A)** T_h and calculated P of brine inclusion assemblages. **(B)** Rb/Sr ratios and Cs concentrations of brine inclusion assemblages. Rb/Sr ratios and Cs concentrations in the Haman and Gunbuk deposits were lower than in the Daejang deposit. **(C)** Fe/Mn ratios were lower in the Daejang deposit than in the Haman and Gunbuk deposits. **(D)** Concentrations of Mn and Pb, and **(E)** Fe and Zn in brine inclusion assemblages. Mn, Pb, and Zn concentrations in the Daejang deposit were higher than in the Haman and Gunbuk deposits.

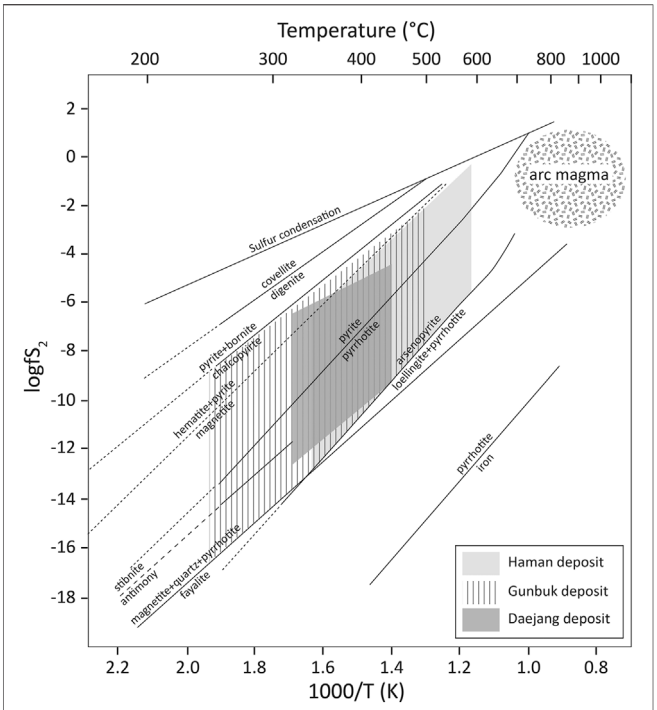

FIGURE 14 | The plot of hydrothermal temperatures versus sulfidation states of ore mineral assemblages, as described by Einaudi (2003) with some modification. Hydrothermal fluids of the Daejang deposit showed a higher sulfidation state (arsenopyrite-pyrrhotite-pyrite-chalcopyrite, no magnetite) and a lower temperature range than the Haman and Gunbuk deposits (arsenopyrite-pyrrhotite-pyrite-chalcopyrite, massive magnetite).

Giggenbach, 1993). Relative redox conditions in deposits can be compared using ratios of their Raman peak heights. The CO_2/CH_4 ratios of Raman peak heights from the Gunbuk and Daejang deposits were 4 and 9, respectively, which suggested more reducing fluid in the Gunbuk deposit. However, CO_2/CH_4 ratios measurements are limited by vapor inclusions, due to a possibility of post-entrapment ion or H_2 diffusion (Li et al., 2009; Zajacz et al., 2009; Seo and Heinrich, 2013) of fluid inclusions in quartz, which could modify gas ratios. The fluids in the three deposits were reduced more than those in typical porphyry-type deposits, comparisons of Fe/Mn ratios in brine inclusions and CO_2/CH_4 ratios in vapor inclusions in the three deposits suggested that fluids in the Daejang deposit were more oxidized than those in the Haman and Gunbuk deposits.

Since the three deposits are hosted within a shale formation (**Figure 1**), which is rich in organic carbon (Kim and Paik, 2001; Kim et al., 2018), differences between the redox states of fluids may have been caused by different degrees of interactions with the hosting shale. It was also noteworthy that, regardless of the redox conditions of the original magmatic ore fluids, fluid-rock interactions would effectively reduce fluids and precipitate ore minerals. Shale formation, therefore, in the study area might prove useful for exploring residual deposits.

Rusk and Reed (2008) suggested hydrothermal fluid acidity controls Al concentrations in quartz, and thus, lower fluid pH values, and that this is highly pronounced in quartz formed at lower temperatures (<350°C) (Rusk and Reed, 2008). Similar Al concentrations in the quartz of Haman and Gunbuk deposits indicated similar pH conditions of ore-forming fluids (**Figure 12A**). The Ti content in quartz has been applied as a Ti-in-quartz geothermometer (Wark and Watson, 2006; Huang and Audétat, 2012) in TiO_2 saturated or rutile-bearing system. Although this geothermometer cannot be applied directly because the activities of TiO_2 in hydrothermal systems may not have achieved equilibrium (Huang and Audétat, 2012), temperature conditions can be compared. The maximum Ti concentration in the Haman deposit was higher than in the Gunbuk and Daejang deposits, which suggests a higher temperature in the Haman deposit and concurs with our microthermometry results (**Figure 12B**). If not in equilibrium, kinetically accumulated Al and Ti in hydrothermal quartz may represent the growth rate of the quartz in hydrothermal fluids (Müller et al., 2002; Huang and Audétat, 2012), which suggests higher growth rates of quartz veins in the Haman deposit than in the Daejang deposit (**Figure 12**).

The Rb/Sr ratios of magmatic-hydrothermal fluids are direct analogs of Rb/Sr ratios in causative magma. Since the Rb/Sr ratios in magma controlled by fractionation of K-feldspar and plagioclase, these ratios indicate a magma source or a degree of magma differentiation (Nockolds and Allen, 1953; Olade and Fletcher, 1975). Cs concentration in magmatic-hydrothermal fluids has been used to determine the fractionation degree of magma (Audétat and Pettke, 2003; Klemm et al., 2008; Lüders et al., 2009). The ranges of Rb/Sr ratios and Cs concentrations observed in brine inclusion assemblages (**Figure 13B**) suggest that magmatic-hydrothermal fluids that formed the Haman and Gunbuk deposits originated from magmas with similar degrees of differentiation, whereas those of the Daejang deposit indicate a more fractionated magma (**Figure 13B**). Relatively higher base metal (Zn and Pb) concentrations in the fluids of the Daejang deposit (**Figures 13D,E**) further support that this deposit may have been formed from a more differentiated magma than the Haman and Gunbuk deposits.

Geological Reconstruction of the Mineralization Processes

Concentrations of metals remain unchanged by changing the P-T conditions of fluids (**Figures 13D,E**), and the temperature ranges of ore-forming fluids are relatively higher than that required for copper mineralization (<350°C) (Ayuso et al., 2010) in magmatic-hydrothermal deposits (**Figure 9**), indicating that a substantial ore at or below the current level of exposure may not be expected (Helgeson, 1969; Ulrich and Günther, 2001; Landtwing et al., 2005). Ore metals in the fluids might have precipitated above the current exposure, but we would expect that most of the economic portions of such deposits might have already been eroded, especially at the Haman deposit where high-temperature alteration minerals such as actinolite and hornblende prevail. The presence of a fluid inclusion

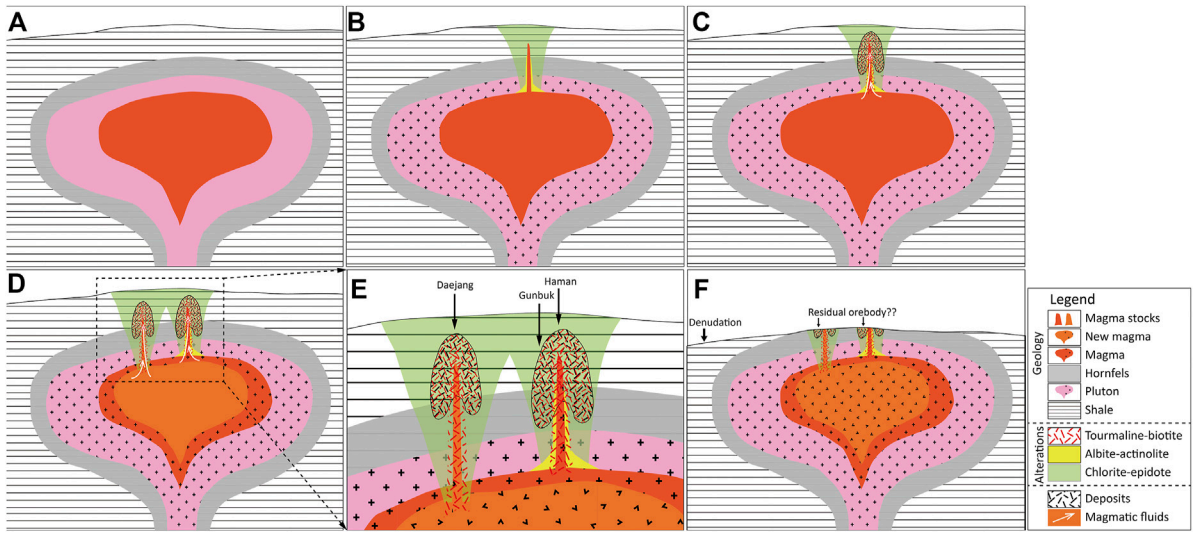

FIGURE 15 | Schematic geological model of the Haman, Gunbuk, and Daejang deposits. **(A)** Cretaceous Jindong granitoid intrusions formed widespread hornfels in Jindong-Haman shale. **(B)** Magma stocks intruded into the hornfels and created a pervasive chlorite-epidote alteration. Albite-actinolite alterations around the deep-center of magma stocks were formed by magmatic-hydrothermal fluid. **(C)** Magmatic fluids derived from stocks formed the quartz veins with a tourmaline-(magnetite)-biotite alteration and main-stage ore-mineralization in the Haman and Gunbuk deposits. **(D)** Possibly later magmatic fluids derived from the stocks of more crystalized magma formed the base metal-rich quartz vein with a tourmaline-biotite alteration in the Daejang deposit. **(E)** The Haman deposit, which was formed under relatively high T-P conditions, was formed near the upper and central part of the magma stock, whereas the Gunbuk deposit was formed at its periphery. The Daejang deposit was formed at a similar T-P to the Gunbuk deposit, but the Daejang deposit may have been formed by a more differentiated and possibly physically separated magma. **(F)** Denudation to the current surface level. If a residual economic orebody remains underground, it might exist in the area around the Gunbuk and the Daejang deposits.

suggests that a deep (hydrostatically >5 km) hot (max. 600°C) magmatic-hydrothermal system exists in the Haman deposit that might be near the upper part of an intrusion center. However, the Gunbuk and Daejang deposits were formed shallower (hydrostatically <3 km) and under cooler conditions in Gunbuk and Daejang deposits (max. 500 and 460°C, respectively) than in the Haman deposit, possibly at the periphery or margin of intrusions.

The fluids in the Haman and Gunbuk deposits were derived from magma of similar level of differentiation, while the fluids in the Daejang deposit were derived from a rather fractionated or physically separated magma. Since the three deposits are neighboring and possibly interacted with an organic-rich shale formation, a varying degree of fluid-rock interaction with the shale could accounts for the different redox states of fluids in the area (i.e. Fe/Mn ratios in **Figure 13C**).

Geological models for the area can therefore be established. 1) The hornfels in the Haman-Jindong shale were formed around the pluton of late Cretaceous Jindong granitoids (**Figure 15A**). 2) A CE alteration in the hornfels was formed pervasively around the Jindong granitoids (**Figure 15B**). 3) External fluids (or magmatic fluids) formed the quartz veins accompanying the AA alteration (only in the Haman deposit) (**Figure 15B**). 4) Magmatic fluids formed the quartz veins accompanying TB alterations with Cu mineralization (**Figure 15C**). The Haman deposit was formed near the upper part of a sub-volcanic magma stock, while the Gunbuk deposit was formed shallower at the periphery (**Figures 15D,E**). In the case of the Daejang deposit, magmatic-hydrothermal fluid is more differentiated than in the Haman-Gunbuk deposits. In the Daejang deposit, the ore precipitated shallower and at the periphery of magma (**Figures 15D,E**). The ore mineralogy in the Daejang deposit indicates a relatively higher sulfidation state than the magnetite-rich Haman and Gunbuk deposits. 5) The deposits were exposed to the current surface level by denudation, and a portion of economic orebodies appeared to have been substantially eroded (**Figure 15F**).

Comparison With Porphyry-Style Deposits and Exploration Potential in the Area

Rock-vein textures, alteration styles, and fluid inclusion types in the Haman, Gunbuk, and Daejang deposits were compared with the key characteristics of porphyry-style deposits. Geologic models of globally representative porphyry-style deposits, including an El Teniente Cu-Mo deposit (Klemm et al., 2007), Bingham Canyon Cu-Mo-Au deposit (Landtwing et al., 2005; Landtwing et al., 2010; Seo et al., 2012), and Ann Mason porphyry Cu deposit (Dilles and Einaudi, 1992), were applied to determine the possibility of a hidden economic ore in the studied area. The CE alteration in the study area corresponds to propylitic alteration of porphyry deposits. The CE alteration was pervasively distributed but only occurs in the hornfels of the Haman-Jindong shale. The CE alteration in hornfels can thus be used to vector the magmatic-hydrothermal or mineralization

center. Economic portions of porphyry deposits are typically associated with K-feldspar-biotite (potassic) and quartz-sericite (phyllic) alterations in deposits (Sillitoe, 2010). Main stage ore-bearing veins in the Haman, Gunbuk, and Daejang deposits are associated with the TB alteration (similar with the potassic alteration). Phyllic alteration was absent in studied deposits possibly because of large formation depths. Our fluid inclusion results show that the TB alteration in the studied deposits formed at a higher temperature than the temperature range of typical potassic alterations in porphyry deposits. T_h and pressure in brine inclusion assemblages in the El Teniente deposit are 320–410°C and max. 300 bar (Klemm et al., 2007), and about 350–410°C and max. 300 bar in the Bingham Canyon deposit (Landtwing et al., 2010). These P-T conditions are somewhat lower than those of the Haman deposit (340–600°C and max. 500 bar) but overlap with those of the Gunbuk (250–500°C and max. 330 bar) and Daejang deposits (320–460°C and max. 270 bar) (**Figure 9A**). The AA alteration that appears in the Haman deposit can be compared with the sodic-calcic alteration (Na-Ca alteration) of some porphyry deposits (Dilles and Einaudi, 1992; Sillitoe, 2010). P-T conditions and alteration styles suggest that the Haman deposit might represent a deep and barren part of a porphyry-style deposit. Although the maximum temperatures are generally higher than the range of porphyry deposits, the Gunbuk and Daejang deposits are closer to the "economic" temperature range. The alteration patterns and range of fluid temperatures observed suggest little possibility of an economic ore in the Haman deposit, but a possibility in the area of the Gunbuk and Daejang deposits. More studies of petrology and geochemistry such as on zircon fertility and stable isotopes in the area are required to fully understand its ore-forming processes and explore hidden economic orebodies.

CONCLUSION

Based on the petrography of the vein-bearing samples and the fluid inclusion studies conducted on Haman, Gunbuk, and Daejang deposits, we derive the following conclusions.

1) In the three deposits, pervasive CE alteration overprinting hornfels, TB alteration with ore mineralized quartz veins, and the latest barren calcite veins commonly occur.
2) The hydrothermal fluids of the Haman and Gunbuk deposits have relatively lower sulfidation and oxidation states than the Daejang deposit.
3) The Daejang deposit appears to have been formed from a relatively later differentiation stage magma than the Haman and Gunbuk deposits, which could result in distinctive ore mineral differences between the Daejang and Haman-Gunbuk deposits.
4) The Haman deposit was formed at the central-upper part of crystalizing magmatic stock under P-T conditions higher than those typical of economic porphyry Cu deposits. The Gunbuk and Daejang deposits were formed at a relatively shallow peripheral location and partially overlapped with the P-T conditions of porphyry deposits.
5) Because of the high fluid pressure and temperature, no large-scale Cu mineralization could be expected underneath the current exposure, especially in the Haman deposit. If there is an orebody remaining underneath, it might be placed in the vicinity of the Gunbuk and Daejang deposits.

DATA AVAILABILITY STATEMENT

The original contributions presented in the study are included in the article/**Supplementary Material**, further inquiries can be directed to the corresponding author.

AUTHOR CONTRIBUTIONS

TL and JS wrote the manuscript. TL, JS, BY, BL, and JL did fieldwork in the area. TL performed petrography of samples and fluid inclusion microthermometry. TL, JS, YY, and SH performed an LA-ICP-MS microanalysis. TL performed laser Raman spectroscopy. All authors discuss the results and correct the manuscript.

FUNDING

This work was supported by the National Research Council of Science and Technology (NST) grant by the Korean government (MSIT) (No. CRC-15-06-KIGAM) and the National Research Foundation (NRF) of Korea Grant funded by the Korea government (MSIT) (No. 2019R1C1C1002588). The LA-ICP-MS analysis was supported by KOPRI Research (PE 21050).

ACKNOWLEDGMENTS

The authors are indebted to professor Khin Zaw, professor Jung-Woo Park, and an reviewer for their constructive and insightful comments and reviews.

SUPPLEMENTARY MATERIAL

The Supplementary Material for this article can be found online at: https://www.frontiersin.org/articles/10.3389/feart.2021.752908/full#supplementary-material

REFERENCES

Audétat, A., Gunther, D., and Heinrich, C. A. (1998). Formation of a Magmatic-Hydrothermal Ore deposit: Insights with LA-ICP-MS Analysis of Fluid Inclusions. *Science* 279, 2091–2094. doi:10.1126/science.279.5359.2091

Audétat, A., and Pettke, T. (2003). The magmatic-hydrothermal evolution of two barren granites: A melt and fluid inlcusion study of the Rito del Medio and Canada Pinabete plutons in northern New Mexico (USA). *Geochimica et Cosmochimica Acta* 67 (1), 91–121. doi:10.1016/s0016-7037(02)01049-9

Ayuso, R. A., Barton, M. D., Blakely, R. J., Bodnar, R. J., Dilles, J. H., Gray, F., et al. (2010). "Porphyry Copper deposit Model: Chapter B of Mineral

deposit Models for Resource Assessment," in *U.S. Geological Survey Scientific Investigations Report 2010-5070-B*. Editor D. A. John (Virginia: U. S. Geological Survey).

Barton, M. D., and Johnson, D. A. (1996). Evaporitic-source Model for Igneous-Related Fe Oxide-(ree-Cu-Au-U) Mineralization. *Geol* 24 (3), 2592. doi:10.1130/0091-7613(1996)024<0259:esmfir>2.3.co;2

Barton, M. D., and Johnson, D. A. (2004). "Footprints of Fe-Oxide (-Cu-Au) Systems," in *SEG 2004: Predictive Mineral Discovery Under Cover*Editors W. A. Perth, J. R. Muhling, and C. M. Knox-Robinson (Centre for Global Metallogeny, the University of Western Australia), 112–116.

Boctor, N. Z. (1985). Rhondonite Solubility and Thermodynamic Properties of Aqueous MnCl2 in the System $MnO^{\square}SiO_2^{\square}HCl^{\square}H_2O$. *Geochimica et Cosmochimica Acta* 49 (2), 565–575. doi:10.1016/0016-7037(85)90048-1

Bodnar, R. J. (2003a). "Introduction to Fluid Inclusions," in *Fluid Inclusions: Analysis and Interpretation*. Editors I. Samson, A. Anderson, and D. Marshall (Quebec City, Canada: Mineralogical Association of Canada Short Course), 1–8.

Bodnar, R. J., and Vityk, M. O. (1994). "Interpretation of Microthermometric Data for H_2O-NaCl Fluid Inclusions," in *Fluid Inclusions in Minerals, Methods and Applications*. Editors B. D. Vivo and M. L. Frezzotti (Blacksburg, VA: Virhinia Tech), 117–130.

Bottrell, S. H., and Yardley, B. W. D. (1991). The Distribution of Fe and Mn between Chlorite and Fluid: Evidence from Fluid Inclusions. *Geochimica et Cosmochimica Acta* 55 (1), 241–244. doi:10.1016/0016-7037(91)90414-Z

Carten, R. B. (1986). Sodium-calcium Metasomatism; Chemical, Temporal, and Spatial Relationships at the Yerington, Nevada, Porphyry Copper deposit. *Econ. Geology*. 81 (6), 1495–1519. doi:10.2113/gsecongeo.81.6.1495

Chang, K. H. (1977). Late Mesozoic Stratigraphy. Sedimentation and Tectonics of southeastern Korea. *J. Geol. Soc. Korea* 13, 76–90.

Chang, K. H., Lee, Y. J., Suzuki, K., and Park, S. O. (1998). Zircon Morphology, CHIME Age and Geological Significance of Kusandong Tuff. *J. Geol. Soc. Korea* 34, 333–343.

Choi, S.-G., Pak, S. J., Kim, C. S., Ryu, I.-C., and Wee, S.-M. (2006). The Origin and Evolution of Mineralizing Fluids in the Cretaceous Gyeongsang Basin, Southeastern Korea. *J. Geochemical Exploration* 89, 61–64. doi:10.1016/j.gexplo.2005.12.009

Choi, S. H. (1998). Geochemical Evolution of Hydrothermal Fluids at the Daejang Cu-Zn-Pb Vein deposit, Korea. *Resource Geology*. 48 (3), 171–182. doi:10.1111/j.1751-3928.1998.tb00015.x

Choi, S. W. (1985). Fluid Inclusion Studies of the Haman-Gunbuk mMining District, Gyeongnam Province. *J. Educ. Res.* 17 (1), 123–146.

Chough, S. K., and Sohn, Y. K. (2010). Tectonic and Sedimentary Evolution of a Cretaceous continental Arc-Backarc System in the Korean peninsula: New View. *Earth-Science Rev.* 101, 225–249. doi:10.1016/j.earscirev.2010.05.004

Chough, S., Kwon, S.-T., Ree, J. H., and Choi, D. K. (2000). Tectonic and Sedimentary Evolution of the Korean Peninsula: A Review and New View. *Earth Sci. Rev.* 52, 175–235. doi:10.1016/s0012-8252(00)00029-5

Chun, S. S., and Chough, S. K. (1992). "Tectonic History of Crataceous Sedimentary Basins in the Southwestern Korean Peninsula and Yellow Sea," in *The Sedimentary Basins in the Korean Peninsula and Adjacent Seas*. Editor S. K. Chough (Hanlimwon, Seoul: Korean Sedimentology Research Group), 60–76.

Dilles, J. H., Barton, M. D., Johnson, D. A., Proffett, J. M., Einaudi, M. T., and Crafford, E. J. (2000). "Part I. Contrasting Styles of Intrusion-Associated Hydrothermal Systems: Part II," in *Geology & Gold Deposits of the Getchell Region* (Littleton, Colorado: Society of Economic Geologists).

Dilles, J. H., and Einaudi, M. T. (1992). Wall-rock Alteration and Hydrothermal Flow Paths about the Ann-Mason Porphyry Copper deposit, Nevada; a 6-km Vertical Reconstruction. *Econ. Geology*. 87 (8), 1963–2001. doi:10.2113/gsecongeo.87.8.1963

Dreyer, B. M., Morris, J. D., and Gill, J. B. (2010). Incorporation of Subducted Slab-Derived Sediment and Fluid in Arc Magmas: B-Be-10Be- Nd Systematics of the Kurile Convergent Margin, Russia. *J. Petrol.* 51 (8), 1761–1782. doi:10.1093/petrology/egq038

Driesner, T., and Heinrich, C. A. (2007). The System H2O-NaCl. Part I: Correlation Formulae for Phase Relations in Temperature-Pressure-Composition Space from 0 to 1000°C, 0 to 5000bar, and 0 to 1 XNaCl. *Geochimica et Cosmochimica Acta* 71 (20), 4880–4901. doi:10.1016/j.gca.2006.01.033

Dubessy, J., Poty, B., and Ramboz, C. (1989). Advances in C-O-H-N-S Fluid Geochemistry Based on Micro-raman Spectrometric Analysis of Fluid Inclusions. *European Journal of Mineralogy* 1, 517–534. doi:10.1127/ejm/1/4/0517

Einaudi, M. T., Hedenquist, J. W., and Inan, E. E. (2003). Sulfidation State of Fluids in Active and Extinct Hydrothermal Systems; Transitions from Porphyry to Epithermal Environments. *Soc. Econ. Geologists Spec. Publ.* 10, 285–313.

Giggenbach, W. F. (1993). Redox Control of Gas Compositions in Philippine Volcanic-Hydrothermal Systems. *Geothermics* 22 (5), 575–587. doi:10.1016/0375-6505(93)90037-N

Giggenbach, W. F. (1987). Redox Processes Governing the Chemistry of Fumarolic Gas Discharges from White Island, New Zealand. *Appl. Geochem.* 2 (2), 143–161. doi:10.1016/0883-2927(87)90030-8

Goldstein, R. H., and Reynolds, T. J. (1994). Systematics of Fluid Inclusions in Diagenetic Minerals. *SEPM Soc. Sediment. Geology. Short Course.*

Guillong, M., Meier, D., Allan, M. M., Heinrich, C. A., and Yardley, B. W. D. (2008). SILLS: a MATLAB-Based Program for the Reduction of Laser Ablation ICP-MS Data of Homogeneous Materials and Inclusions. *Mineralogical Assoc. Can. Short Course* 40, 328–333.

Gustafson, L. B., and Hunt, J. P. (1975). The Porphyry Copper deposit at El Salvador, Chile. *Econ. Geology*. 70 (5), 857–912. doi:10.2113/gsecongeo.70.5.857

Heinrich, C. A., Günther, D., Audétat, A., Ulrich, T., and Frischknecht, R. (1999). Metal Fractionation between Magmatic Brine and Vapor, Determined by Microanalysis of Fluid Inclusions. *Geol* 27 (8), 755–758. doi:10.1130/0091-7613(1999)027<0755:mfbmba>2.3.co;2

Heinrich, C. A., Pettke, T., Halter, W. E., Aigner-Torres, M., Audétat, A., Günther, D., et al. (2003). Quantitative Multi-Element Analysis of Minerals, Fluid and Melt Inclusions by Laser-Ablation Inductively-Coupled-Plasma Mass-Spectrometry. *Geochimica et Cosmochimica Acta* 67 (18), 3473–3497. doi:10.1016/S0016-7037(03)00084-X

Helgeson, H. C. (1969). Thermodynamics of Hydrothermal Systems at Elevated Temperatures and Pressures. *Am. J. Sci.* 267 (7), 729–804. doi:10.2475/ajs.267.7.729

Heo, C. H., Yun, S.-T., Choi, S. H., Choi, S.-G., and So, C.-S. (2003). Copper Mineralization in the Haman-Gunbuk Area, Gyeongsangnamdo-Province: Fluid Inclusion and Stable Isotope Study. *Econ. Environ. Geology.* 36 (2), 75–87.

Huang, R., and Audétat, A. (2012). The Titanium-In-Quartz (TitaniQ) Thermobarometer: a Critical Examination and Re-calibration. *Geochimica et Cosmochimica Acta* 84, 75–89. doi:10.1016/j.gca.2012.01.009

Jin, M. S., Lee, S. M., Lee, J. S., and Kim, S. J. (1982). Lithogeochemistry of the Cretaceous Granitoids with Relation to the Metallic Ore Deposits in Southern Korea. *J. Geol. Soc. Korea* 18 (3), 119–131.

Kim, H. J., Paik, I. S., Kim, S., and Lee, H. (2018). Sedimentary Facies, Paleoenvironments, and Stratigraphy of the Haman Formation (Early Cretaceous) in Sopo-Ri, Haman-Gun, Gyeongsangnam-Do, Korea. *Jgsk* 54 (1), 1–19. doi:10.14770/jgsk.2018.54.1.1

Kim, H. J., and Paik, I. S. (2001). Sedimentary Facies and Environments of the Cretaceous Jindong Formation in Goseong-Gun, Gyeongsangnamdo. *J. Geol. Soc. Korea* 37 (2), 235–256.

Kim, N., Koh, S.-M., You, B.-W., and Lee, B. H. (2021). Mineralogy, Geochemistry, and Age Constraints on the Axinite-Bearing Gukjeon Pb-Zn Skarn Deposit in the Miryang Area, South Korea. *Minerals* 11 (6), 619. doi:10.3390/min11060619

Kim, O. J., and Kim, K. H. (1974). A Study on Red Hill Copper Deposits of the Dongjom Mine. *J. Korean Inst. Mining Geology.* 7 (4), 157–174. doi:10.4097/kjae.1974.7.1.45

Kim, S. U. (1973). A Regional Study for Developments of Kyeongnam Copper Metallogenic Province. *J. Korean Inst. Mining Geology.* 6 (3), 133–170. doi:10.4097/kjae.1973.6.2.247

Kim, S. W., Kwon, S., Park, S.-I., Lee, C., Cho, D.-L., Lee, H.-J., et al. (2016a). SHRIMP U-Pb Dating and Geochemistry of the Cretaceous Plutonic Rocks in the Korean Peninsula: A New Tectonic Model of the Cretaceous Korean Peninsula. *Lithos* 262, 88–106. doi:10.1016/j.lithos.2016.06.027

Kim, Y. H., Hwang, H. G., Baek, G., Seo, J. R., Choi, D. H., Kang, J. N., et al. (2016b). Uiryeong District (Cu) Detailed Investigation Report. *Uiryeong* 117, 127.

Klemm, L. M., Pettke, T., Heinrich, C. A., and Campos, E. (2007). Hydrothermal Evolution of the El Teniente Deposit, Chile: Porphyry Cu-Mo Ore Deposition from Low-Salinity Magmatic Fluids. *Econ. Geology.* 102 (6), 1021–1045. doi:10.2113/gsecongeo.102.6.1021

Klemm, L. M., Pettke, T., and Heinrich, C. A. (2008). Fluid and Source Magma Evolution of the Questa Porphyry Mo deposit, New Mexico, USA. *Miner Deposita* 43 (5), 533–552. doi:10.1007/s00126-008-0181-7

Koh, S.-M., Ryoo, C.-R., and Song, M.-S. (2003). Mineralization Characteristics and Structural Controls of Hydrothermal Deposits in the Gyeongsang Basin, South Korea. *Resource Geology.* 53 (3), 175–192. doi:10.1111/j.1751-3928.2003.tb00168.x

Kooiman, G. J. A., McLeod, M. J., and Sinclair, W. D. (1986). Porphyry Tungsten-Molybdenum Orebodies, Polymetallic Veins and Replacement Bodies, and Tin-Bearing Greisen Zones in the Fire Tower Zone, Mount Pleasant, New Brunswick. *Econ. Geology.* 81 (6), 1356–1373. doi:10.2113/gsecongeo.81.6.1356

Landtwing, M., Pettke, T., Halter, W., Heinrich, C., Redmond, P., Einaudi, M., et al. (2005). Copper Deposition during Quartz Dissolution by Cooling Magmatic-Hydrothermal Fluids: The Bingham Porphyry. *Earth Planet. Sci. Lett.* 235 (1), 229–243. doi:10.1016/j.epsl.2005.02.046

Landtwing, M. R., Furrer, C., Redmond, P. B., Pettke, T., Guillong, M., and Heinrich, C. A. (2010). The Bingham Canyon Porphyry Cu-Mo-Au Deposit. III. Zoned Copper-Gold Ore Deposition by Magmatic Vapor Expansion. *Econ. Geology.* 105, 91–118. doi:10.2113/gsecongeo.105.1.91

Lee, H. K., and Moon, H.-S. (1989). Ore Minerals and the Physicochemical Environments of the Inseong Gold-Silver Deposits, Republic of Korea. *J. Korean Inst. Mining Geology.* 22 (3), 237–252.

Lee, J. K., and Lee, J. Y. (1994). Trace Elements Geochemistry and Copper Mineralization of Jindong Granitic Rocks. *J. Geol. Soc. Korea* 30 (5), 455–466.

Lee, J. Y. (1989). A Geochemical Study on the Chindong and Yucheon-Eonyang Granites in Relation to Mineralization. *J. Korean Inst. Mining Geology.* 22 (1), 21–34.

Lee, J. Y., Lee, J. K., Par, B. J., Lee, I. H., and Kim, S. W. (1994). A Geochemcial Study on Jindong Granites in Relation to Copper Ore Deposits in Gyeongsang basin. *Econ. Environ. Geology.* 27 (2), 161–170.

Lee, S. Y., Choi, S.-G., So, C. H., Ryu, I. C., Wee, S. M., and Heo, C. H. (2003). Base-metal Mineralization in the Cretaceous Gyeongsang Basin and its Genetic Implications, Korea : the Haman-Gunbug-Goseong(-Changwon) Amd the Euiseong Metallogenic Provinces. *Econ. Environ. Geology.* 36 (4), 257–268.

Leeman, W. P., Carr, M. J., and Morris, J. D. (1994). Boron Geochemistry of the Central American Volcanic Arc: Constraints on the Genesis of Subduction-Related Magmas. *Geochimica et Cosmochimica Acta* 58 (1), 149–168. doi:10.1016/0016-7037(94)90453-7

Li, Y., Audétat, A., Lerchbaumer, L., and Xiong, X. L. (2009). Rapid Na, Cu Exchange between Synthetic Fluid Inclusions and External Aqueous Solutions: Evidence from LA-ICP-MS Analysis. *Geofluids* 9 (4), 321–329. doi:10.1111/j.1468-8123.2009.00255.x

Lüders, V., Romer, R. L., Gilg, H. A., Bodnar, R. J., Pettke, T., and Misantoni, D. (2009). A Geochemical Study of the Sweet Home Mine, Colorado Mineral Belt, USA: Hydrothermal Fluid Evolution above a Hypothesized Granite Cupola. *Miner Deposita* 44, 415–434. doi:10.1007/s00126-008-0221-3

Lynch, G., and Ortega, J. (1997). Hydrothermal Alteration and Tourmaline-Albite Equilibria at the Coxheath Porphyry Cu-Mo-Au deposit, Nova Scotia. *Can. Mineral.* 35 (1), 79–94.

Mark, G., and Foster, D. R. W. (2000). Magmatic-hydrothermal Albite-Actinolite-Apatite-Rich Rocks from the Cloncurry District, NW Queensland, Australia. *Lithos* 51, 223–245. doi:10.1016/s0024-4937(99)00069-9

Min, K. D., Kim, O. J., Yun, S. K., Lee, D. S., and Joo, S. W. (1982). Applicability of Plate Tectonics to the post-late Cretaceous Igneous Activities and Mineralization in the Southern Part of South Korea(I). *J. Korean Inst. Mining Geology.* 15 (3), 123–154.

Moon, C. U., Kim, M. W., Lee, J. H., and Chai, C. J. (1986). *Geological Investigation Report of Copper Deposits on the Haman-Gunbuk District*. Wonju, South Korea: Korea resources corporation.

Moon, C. U., Kim, M. W., Lee, J. H., and Choi, C. J. (1970). Geology and Ore Deposits in Haman-Kunbuk Copper Deposit. *J. Korean Inst. Mining Geology.* 3 (2), 55–73.

Moran, A. E., Sisson, V. B., and Leeman, W. P. (1992). Boron Depletion during Progressive Metamorphism: Implications for Subduction Processes. *Earth Planet. Sci. Lett.* 111 (2), 331–349. doi:10.1016/0012-821X(92)90188-2

Müller, A., Kronz, A., and Breiter, K. (2002). Trace Elements and Growth Patterns in Quartz: a Fingerprint of the Evolution of the Subvolcanic Podlesi Granite System (Krusne Hory Mts., Czech Republic). *Bull. Geosciences* 77 (2), 135–145.

Naeher, S., Gilli, A., North, R. P., Hamann, Y., and Schubert, C. J. (2013). Tracing Bottom Water Oxygenation with Sedimentary Mn/Fe Ratios in Lake Zurich, Switzerland. *Chem. Geology.* 352, 125–133. doi:10.1016/j.chemgeo.2013.06.006

Nockolds, S. R., and Allen, R. (1953). The Geochemistry of Some Igneous Rock Series. *Geochimica et Cosmochimica Acta* 4, 105–142. doi:10.1016/0016-7037(53)90055-6

Olade, M. A., and Fletcher, W. K. (1975). Primary Dispersion of Rubidium and Strontium Around Porphyry Copper Deposits, Highland Valley, British Columbia. *Econ. Geology.* 70, 15–21. doi:10.2113/gsecongeo.70.1.15

Oliver, N. H. S. (1996). Review and Classification of Structural Controls on Fluid Flow during Regional Metamorphism. *J. Metamorph Geol.* 14 (4), 477–492. doi:10.1046/j.1525-1314.1996.00347.x

Orovan, E. A., Cooke, D. R., Harris, A. C., Ackerman, B., and Lawlis, E. (2018). Geology and Isotope Geochemistry of the Wainaulo Cu-Au Porphyry Deposit, Namosi District, Fiji. *Econ. Geology.* 113 (1), 133–161. doi:10.5382/econgeo.2018.4546

Pacey, A., Wilkinson, J. J., and Cooke, D. R. (2020). Chlorite and Epidote Mineral Chemistry in Porphyry Ore Systems: A Case Study of the Northparkes District, New South Wales, Australia. *Econ. Geology.* 115 (4), 701–727. doi:10.5382/econgeo.4700

Park, H. I., Choi, S.-W., Chang, H. W., and Chae, D. H. (1985). Copper Mineralization at Haman-Gunbuk Mining District, Kyeongnam Area. *J. Korean Inst. Mining Geology.* 18 (2), 107–124.

Park, H. I., Choi, S. W., Chang, H. W., and Lee, M. S. (1983). Genesis of the Copper Deposits in Goseong District, Gyeongnam Area. *J. Korean Inst. Mining Geology.* 16 (3), 135–147. doi:10.4070/kcj.1983.13.1.135

Park, H. I., and Kim, D. L. (1988). The Mode of Occurrence and Depositional Conditions of Antimony Minerals from North Ore Deposits of the Daejang Mine. *J. Geol. Soc. Korea* 24 (3), 251–266.

Park, H. I., and Seol, Y. K. (1992). The Copper Mineralization of the Keumryeong and Kigu Ore Deposits. *J. Korean Inst. Mining Geology.* 25 (3), 283–296.

Perring, C. S., Pollard, P. J., Dong, G., Nunn, A. J., and Blake, K. L. (2000). The Lightning Creek Sill Complex, Cloncurry District, Northwest Queensland: A Source of Fluids for Fe Oxide Cu-Au Mineralization and Sodic-Calcic Alteration. *Econ. Geology.* 95 (5), 1067–1089. doi:10.2113/gsecongeo.95.5.1067

Pollard, P. J., Blake, K. L., and Dong, G. (1997a). "Proterozoic Cu-Au-Co and Pb-Zn-Ag Mineralization in the Cloncurry District, Eastern Mount Isa Inlier, Australia: Constraints on Fluid Sources from Mineralogical, Fluid Inclusion and Stable Isotope Data," in *Final Report of AMIRA P438*. Editor P. J. Pollard (Cloncurry: Cloncurry base metals and gold).

Reed, M. H., and Palandri, J. (2006). 11. Sulfide Mineral Precipitation from Hydrothermal Fluids. *Rev. Mineralogy Geochem.* 61 (1), 609–632. doi:10.1515/9781501509490-012

Roedder, E., and Bodnar, R. J. (1980). Geologic Pressure Determinations from Fluid Inclusion Studies. *Annu. Rev. Earth Planet. Sci.* 8, 263–301. doi:10.1146/annurev.ea.08.050180.001403

Rusk, B. G., Lowers, H. A., and Reed, M. H. (2008). Trace Elements in Hydrothermal Quartz: Relationships to Cathodoluminescent Textures and Insights into Vein Formation. *Geol* 36 (7), 547–550. doi:10.1130/g24580a.1

Ryu, I. C., Choi, S.-G., and Wee, S. M. (2006). An Inquiry into the Formation and Deformation of the Cretaceous Gyeonsang (Kyeongsang) Basin, Southeastern Korea. *Econ. Environ. Geology.* 39 (2), 129–149.

Seedorff, E., Dilles, J. H., Proffett, J. M., Jr., Einaudi, M. T., Zurcher, L., Stavast, W. J. A., et al. (2005). "Porphyry Deposits: Characteristics and Origin of Hypogene Features," in *One Hundredth Anniversary Volume* (Littleton, Colorado: Society of Economic Geologists).

Seo, J. H., Guillong, M., and Heinrich, C. A. (2012). Separation of Molybdenum and Copper in Porphyry Deposits: The Roles of Sulfur, Redox, and pH in Ore mineral Deposition at Bingham Canyon. *Econ. Geology.* 107, 333–356. doi:10.2113/econgeo.107.2.333

Seo, J. H., and Heinrich, C. A. (2013). Selective Copper Diffusion into Quartz-Hosted Vapor Inclusions: Evidence from Other Host Minerals, Driving Forces, and Consequences for Cu-Au Ore Formation. *Geochimica et Cosmochimica Acta* 113, 60–69. doi:10.1016/j.gca.2013.03.016

Seo, M. (2016). *Cu Mineralization of the Ilkwang Breccua Pipe-type Copper Deposit*. Busan: Master, Pusan National Univerist.

Shin, H. J., Kim, M. Y., and So, C.-S. (1987). Eochemistry and Genetic Environments of the Daejang Vein Deposits. *J. Korean Inst. Mining Geology.* 20 (1), 61–75. doi:10.4097/kjae.1987.20.5.707

Sillitoe, R. H. (1980). Evidence for Porphyry-type Mineralization in Southern Korea. *Mining Geology. Spec. Issue.* 8, 205–214. doi:10.1130/0091-7613(1980)8<11:apcakm>2.0.co;2

Sillitoe, R. H. (2010). Porphyry Copper Systems. *Econ. Geology.* 105, 3–41. doi:10.2113/gsecongeo.105.1.3

Sillitoe, R. H., and Sawkins, F. J. (1971). Geologic, Mineralogic and Fluid Inclusion Studies Relating to the Origin of Copper-Bearing Tourmaline Breccia Pipes, Chile. *Econ. Geology.* 66 (7), 1028–1041. doi:10.2113/gsecongeo.66.7.1028

Sinclair, W. (2007). *Porphyry Deposits*, 223–243.

So, C.-S., Chi, S.-J., Shelton, K. L., and Skinner, B. J. (1985). Copper-bearing Hydrothermal Vein Deposits in the Gyeongsang Basin, Republic of Korea. *Econ. Geology.* 80 (1), 43–56. doi:10.2113/gsecongeo.80.1.43

So, C.-S., Choi, S.-H., and Yun, S.-T. (1995). Geochemistry and Genesis of Hydrothermal Cu Deposits in the Gyeongsang Basin, Korea: Hwacheon-Ri Mineralized Area. *Econ. Environ. Geology.* 28 (4), 337–350.

Uchida, E., Choi, S.-G., Baba, D., and Wakisaka, Y. (2012). Petrogenesis and Solidification Depth of the Jurassic Daebo and Cretaceous Bulguksa Granitic Rocks in South Korea. *Resource Geology.* 62 (3), 281–295. doi:10.1111/j.1751-3928.2012.00195.x

Ulrich, T., Gunther, D., and Heinrich, C. A. (2001). The Evolution of a Porphyry Cu-Au Deposit, Based on LA-ICP-MSAnalysis of Fluid Inclusions: Bajo de la Alumbrera, Argentina. *Econ. Geology.* 96, 1743–1774. doi:10.2113/gsecongeo.96.8.1743

Wark, D. A., and Watson, E. B. (2006). TitaniQ: a Titanium-In-Quartz Geothermometer. *Contrib. Mineral. Petrol.* 152 (6), 743–754. doi:10.1007/s00410-006-0132-1

Wee, S. M., Kim, Y.-J., Choi, S.-G., Park, J. W., and Ryu, I. C. (2007). Adakitic Signatures of the Jindong Granitoids. *Econ. Environ. Geology.* 40 (2), 223–236.

Wilkinson, J. J., Baker, M. J., Cooke, D. R., and Wilkinson, C. C. (2020). Exploration Targeting in Porphyry Cu Systems Using Propylitic Mineral Chemistry: A Case Study of the El Teniente Deposit, Chile. *Econ. Geology.* 115 (4), 771–791. doi:10.5382/econgeo.4738

Williams, P. J., Barton, M. D., Johnson, D. A., Fontbote, L., de Haller, A., Mark, G., et al. (2005). "Iron Oxide Copper-Gold Deposits; Geology, Space-Time Distribution, and Possible Modes of Origin," in *Economic Geology 100th Anniversary Volume*. Editors J. W. Hedenquist, J. F. H. Thompson, R. J. Goldfarb, and J. P. Richards (Littleton CO: Society of Economic Geologists), 371–405.

Won, J. G., and Kim, K. T. (1966). On the Geology and Mineralization in Dalsung Mine Area. *J. Geol. Soc. Korea* 2 (1), 52–69.

Xavier, R. P., Wiedenbeck, M., Trumbull, R. B., Dreher, A. M., Monteiro, L. V. S., Rhede, D., et al. (2008). Tourmaline B-Isotopes Fingerprint marine Evaporites as the Source of High-Salinity Ore Fluids in Iron Oxide Copper-Gold Deposits, Carajás Mineral Province (Brazil). *Geol* 36 (9), 743–746. doi:10.1130/g24841a.1

Yang, K. H., and Jang, J.-Y. (2002). Geochemistry of Tourmaline in the Ilhwang Cu-W Breccia-Pipe deposit, Southeastern Gyeongsang Basin. *J. Petrological Soc. Korea* 11 (3-4), 259–270.

Zajacz, Z., Hanley, J. J., Heinrich, C. A., Halter, W. E., and Guillong, M. (2009). Diffusive Reequilibration of Quartz-Hosted Silicate Melt and Fluid Inclusions: Are All Metal Concentrations Unmodified? *Geochimica et Cosmochimica Acta* 73 (10), 3013–3027. doi:10.1016/j.gca.2009.02.023

Conflict of Interest: The authors declare that the research was conducted in the absence of any commercial or financial relationships that could be construed as a potential conflict of interest.

Publisher's Note: All claims expressed in this article are solely those of the authors and do not necessarily represent those of their affiliated organizations, or those of the publisher, the editors and the reviewers. Any product that may be evaluated in this article, or claim that may be made by its manufacturer, is not guaranteed or endorsed by the publisher.

frontiers in Earth Science

ORIGINAL RESEARCH
published: 25 November 2021
doi: 10.3389/feart.2021.761748

Geochemical and Mineralogical Characteristics of Garnierite From the Morowali Ni-Laterite Deposit in Sulawesi, Indonesia

Yuri Choi[1], *Insung Lee*[1]* *and Inkyeong Moon*[2]

[1]School of Earth and Environmental Sciences, Seoul National University, Seoul, South Korea, [2]Deep-Sea and Seabed Mineral Resources Research Center, Korea Institute of Ocean Science and Technology, Busan, South Korea

The Morowali Ni-laterite deposit is located in the East Sulawesi Ophiolite, which is a large ophiolite belt on Sulawesi Island, Indonesia. The Morowali deposit is developed on a laterite profile due to ophiolite weathering, with saprolite, limonite, and ferruginous cap horizons from the bottom to top. Based on the occurrence of garnierite as the main ore, occurring in the saprolite horizon, it can be classified that the ore deposit is hydrous Mg silicate-type. The Ni ore is classified into different types based on color and XRD and electron probe micro-analyzer analyses. Whole-rock geochemical study was also conducted to understand the mineralization process. The Morowali Ni deposit consists of serpentine-like and talc-like phases. The serpentine-like phase consists of Ni-lizardite and karpinskite (0.76–38.26 wt% NiO) while the talc-like phase is mainly composed of kerolite (4.02–8.02 wt% NiO). The serpentine-like garnierite exhibits high Ni and Fe contents and occurrence similar to that of the serpentine observed in the saprolite horizon, suggesting the serpentine-like garnierite originated from the bedrock, and Mg-Ni cation exchange occurred during laterization. Contrastingly, the lower Fe content of the talc-like phase (0.01–0.05 wt%) than the serpentine-like phase (0.14–7.03 wt%) indicates that the talc-like garnierite is of secondary origin since Fe is immobile during weathering. The Morowali Ni-laterite deposit was mainly formed during laterization. The repetition of dry and wet cycles in each year results in the formation of secondary garnierite.

Keywords: Morowali Ni-laterite deposit, garnierite, Mg-Ni hydrous silicate, ophiolite laterization, Indonesia

OPEN ACCESS

Edited by:
Sean C. Johnson,
University College Dublin, Ireland

Reviewed by:
Mohd Basril Iswadi Basori,
National University of Malaysia, Malaysia
Kit Lai,
Universiti Brunei Darussalam, Brunei

***Correspondence:**
Insung Lee
insung@snu.ac.kr

Specialty section:
This article was submitted to Economic Geology, a section of the journal Frontiers in Earth Science

Received: *20 August 2021*
Accepted: *03 November 2021*
Published: *25 November 2021*

Citation:
Choi Y, Lee I and Moon I (2021) Geochemical and Mineralogical Characteristics of Garnierite From the Morowali Ni-Laterite Deposit in Sulawesi, Indonesia. Front. Earth Sci. 9:761748. doi: 10.3389/feart.2021.761748

INTRODUCTION

Nickel is an important metal that is used to manufacture stainless steel, metal alloys, and rechargeable batteries. Therefore, its demand and production have been constantly increasing since the 20th century (Mudd, 2010; Mudd and Jowitt, 2014). Nickel ores are produced in both magmatic sulfide and laterite-type deposits. The magmatic sulfide deposits occur within the deep crust and are generated by a high degree of partial melting of the mantle that contains Ni-rich sulfide liquids (Barnes and Lightfoot, 2005), while Ni-bearing laterite deposits are developed by the weathering of ultramafic rocks under humid conditions such as tropical or sub-tropical climates (Butt and Cluzel, 2013; Butt, 2016). Although laterite-type Ni deposits account for 60% of the global nickel resources, ~60% of the world nickel production is dependent on sulfide-type ores owing to their convenience in processing (Elias, 2002; Dalvi et al., 2004; Mudd, 2010; Butt and Cluzel, 2013; Mudd and Jowitt,

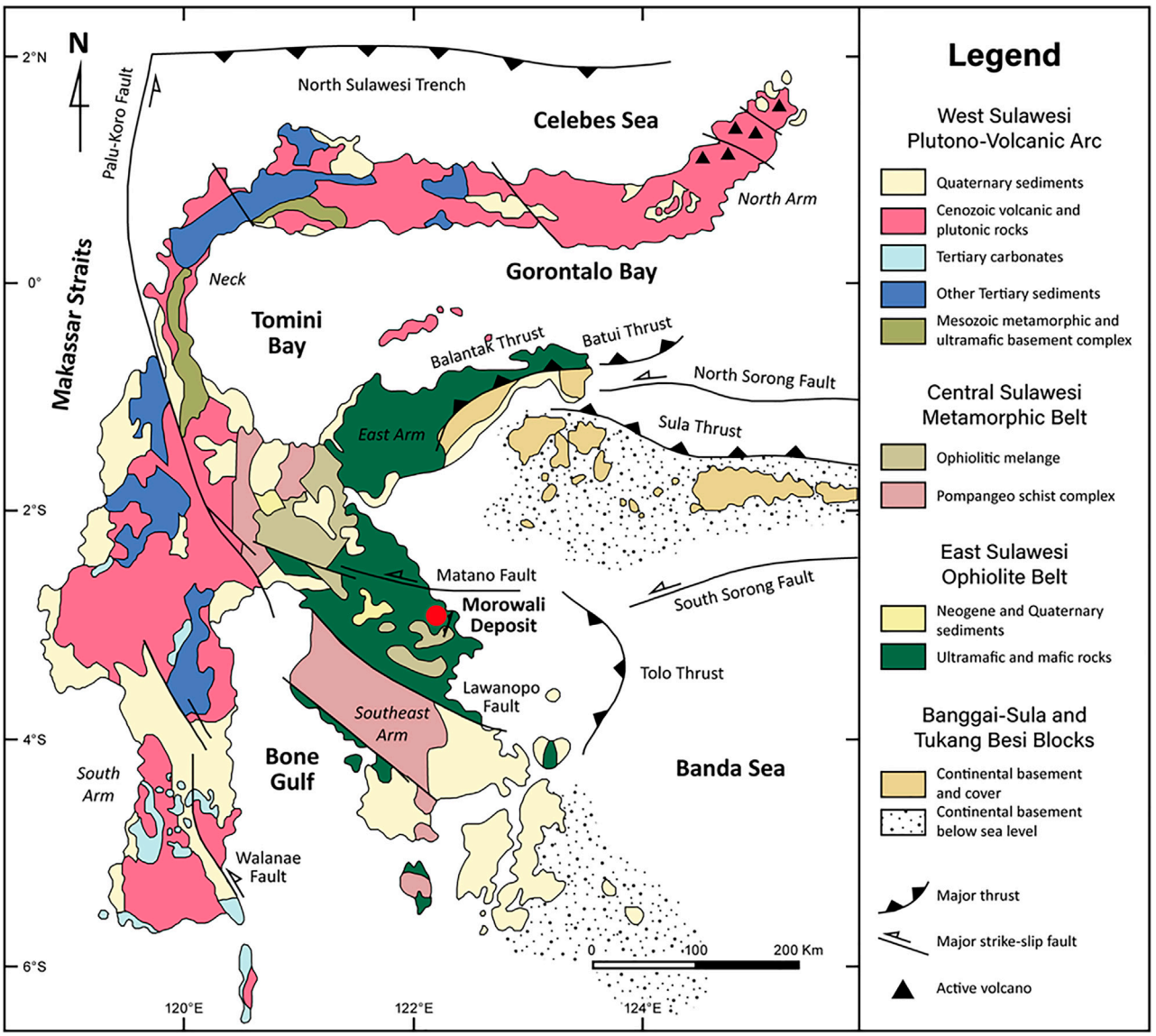

FIGURE 1 | Geological map of Sulawesi island, Indonesia and location of Morowali deposit (modified after Hall and Wilson (2000)). The location of the Morowali deposit is shown in the red circle.

2014). It is believed that there will be a rise in the demand for Ni; lateritic Ni deposits have recently gained attention since they can be utilized to meet this demand.

Lateritic Ni deposits can be classified into three types according to their dominant Ni-bearing mineral groups, i.e., oxide (Fe oxyhydroxides), hydrous Mg-silicate (Ni-rich hydrous silicates), and clay silicate (Ni-rich smectites) deposits (Golightly, 1979; Freyssinet et al., 2005; Butt and Cluzel, 2013). Most laterite-type Ni deposits are distributed in countries that lie within 22°N and S latitudes, such as the Philippines, Indonesia, New Caledonia, Brazil, Dominican Republic, Colombia, and Venezuela (Elias, 2002; Butt and Cluzel, 2013). The Ni-rich hydrous Mg-silicates are the representative Ni ores in the hydrous Mg-silicate deposits and are generally referred to informally as garnierite. Garnierite is a yellowish green to bluish green colored aphanitic mineral containing high Ni concentration, up to 19.9% (Brand, 1998). Although there is still debate on the classification of garnierite because of its origins, it is known that garnierite is a mixture of various hydrous silicates. It is divided into two groups depending on the silicate layer type: 1:1 and 2:1, which are the ratios between tetrahedral and octahedral sheet in hydrous silicates (Brindley and Hang, 1973; Brindley, 1980). The first layer group consists of serpentine minerals, such as lizardite–népouite, chrysotile–pecoraite, and berthierine–brindleyite series; the second layer comprises talc–willemseite, kerolite–pimelite, clinochlore–nimite, and sepiolite–falcondoite series (Brindley, 1980). The most common natural associations for the hydrous

Mg-Ni silicates are with lizardite–nepouite and kerolite–pimelite series (Brindley, 1980). These mineral series are generally referred to as serpentine-like (7 Å-type) garnierite (1:1 group) and talc-like (10 Å-type) garnierite (2:1 group) (Brindley and Hang, 1973; Freyssinet et al., 2005; Butt and Cluzel, 2013; Villanova-de-Benavent et al., 2014; Fu et al., 2018).

In this study, we investigated the Ni-rich laterite deposits in Morowali, Sulawesi, Indonesia to understand garnierite genesis and mineralization during laterization based on mineralogical and geochemical studies. Also, we suggest genetic model of the Morowali Ni laterite deposit.

GEOLOGICAL SETTING

Regional Geological Setting

Sulawesi Island has a complex tectonic setting, which is a result of the collision between the Eurasian, Indian-Australian, and Pacific plates during the Late Cretaceous and Early Tertiary (Katili, 1978; Wilson and Moss, 1999; Hall and Wilson, 2000; Kadarusman et al., 2004). Consequently, the K-shaped Sulawesi island is surrounded by thrusts and has four distinct litho-tectonic belts from west to east: 1) West Sulawesi plutono-volcanic arc, 2) Central Sulawesi metamorphic belt, 3) East Sulawesi ophiolite, and 4) microcontinental blocks of Banggai-Sula and Buton-Tukang Besi (Hall and Wilson, 2000). The study area, Morowali deposit, is located in the East Sulawesi ophiolite belt (**Figure 1**).

According to the tectonic reconstructions of Southeast Asia, the Sulawesi ophiolite was accreted onto the Eurasian plate during subduction of the Indian-Australian plate in the Late Oligocene (Hall, 1997; Parkinson, 1998). The East Sulawesi ophiolite is considered as one of the largest ophiolites in the world, covering more than 15,000 km^2 with a total length of 700 km (Monnier et al., 1995; Kadarusman et al., 2004; Van der Ent et al., 2013). The East Sulawesi ophiolite comprises two lithological units: 1) Neogene and Quaternary sediments; 2) ultramafic and mafic rocks (**Figure 1**). The ophiolite belt is 70% peridotites, composed of lherzolite, harzburgite, and occasional dunite (Kadarusman et al., 2004). The Morowali area principally consists of harzburgite and lherzolite; however, these peridotites are highly altered to serpentinite, making it difficult to identify their original mineral composition and texture. The ophiolitic mélange zone belonging to the Central Sulawesi metamorphic belt is also exposed near the study area along with the active and earthquake-inducing Matano fault (Stevens et al., 1999).

The bedrock lithology, tectonic setting, age of weathering with respect to tectonic activity, climate, and topography control Ni-rich laterite formation (Freyssinet et al., 2005). The Morowali area has a tropical rainforest climate with annual average temperature of 27°C and 2,000 mm of annual precipitation, which makes the area thickly forested with a diverse vegetation in accordance with the elevation. The study area has a moderate relief and gentle slope. Furthermore, the well-developed drainage system of the bedrock promotes Ni-rich laterite profiles in a large area and aids in the formation of high-grade Mg-silicate minerals.

Nickel Laterite Deposit Geology and Sample Description

Geological Characteristics of Ni Laterite Deposit

The Morowali Ni-laterite deposit is located in the southeast arm of the East Sulawesi Ophiolite Belt (**Figure 1**). The Ni-rich laterite profile of the Morowali deposit is developed on top of the bedrock and distinguished into three horizons, from bottom to top: saprolite, limonite, and ferruginous cap (**Figure 2A**). These horizons are classified according to their dominant color, mineralogy, fractures, and texture. The laterite profile of the study area has highly variable thicknesses, ranging 8–19 m, because of the undulatory boundaries of each horizon (**Figures 2A,B**). The part from the top of the saprolite horizon to the ferruginous cap has mostly become soil, making the original form of the top horizon hard to distinguish.

Garnierite usually occurs in the lower saprolite horizon as a coating over the ultramafic rocks with a remarkably distinguishable jade green to grass green color (**Figures 2E–H**). It is aphanitic and fine-grained, showing different shades of green and/or white to yellowish colored grains (**Figures 2H–J**). In addition, some aphanitic garnierite occurs as veins, along the joints. Both the coatings and veins are <1 mm thick. The mineralogical characteristics of each horizon are as follows:

Bedrock

The bedrock in the Morowali area mainly comprises harzburgite and lherzolite (**Figures 2C,D**), usually consisting of serpentine and orthopyroxene as the major phases with minor fine-grained olivine and iddingsite. Although the peridotites in the study area undergo weathering and serpentinization, orthopyroxene occurs as the dominant mineral. The orthopyroxenes are subhedral to euhedral, 1–3 mm in diameter, with exsolution lamellae of clinopyroxene (**Figures 3A,B**). Serpentine occurs as a secondary alteration mineral along joints or cleavages, surrounding or infiltrating the orthopyroxene grains (**Figure 3A**) and/or shows a mesh texture (**Figures 3C,H**). The more weathered orthopyroxenes were altered to clay that occurred as a coating on the orthopyroxene grains (**Figure 3B**). Only a few fine-grained olivines are visible due to their alteration mainly into serpentine with minor iddingsite, which is a reddish- or yellowish-brown colored amorphous mineral (**Figure 3C**).

Saprolite

The saprolite horizon changes color, from yellowish-brown, grayish-yellow, or grayish-green, with respect to the degree of weathering. The thickness of the horizon is 2–7 m, and it is the main ore body in the study area. Most of the horizon consists of fine-grained earthy saprolite and coarse rocky saprolite. The coarse rock fragments partially preserve the original texture of the bedrock. Discontinuous stockwork are developed and garnierite veins or coatings precipitate along this stockwork. Alteration products such as fibrous serpentinite, talc, and clay are also accompanied by the stockwork.

Under microscopic observation, the rocky saprolite has a texture similar to that of the bedrock, but with comparatively more serpentine. The difference between the bedrock and the

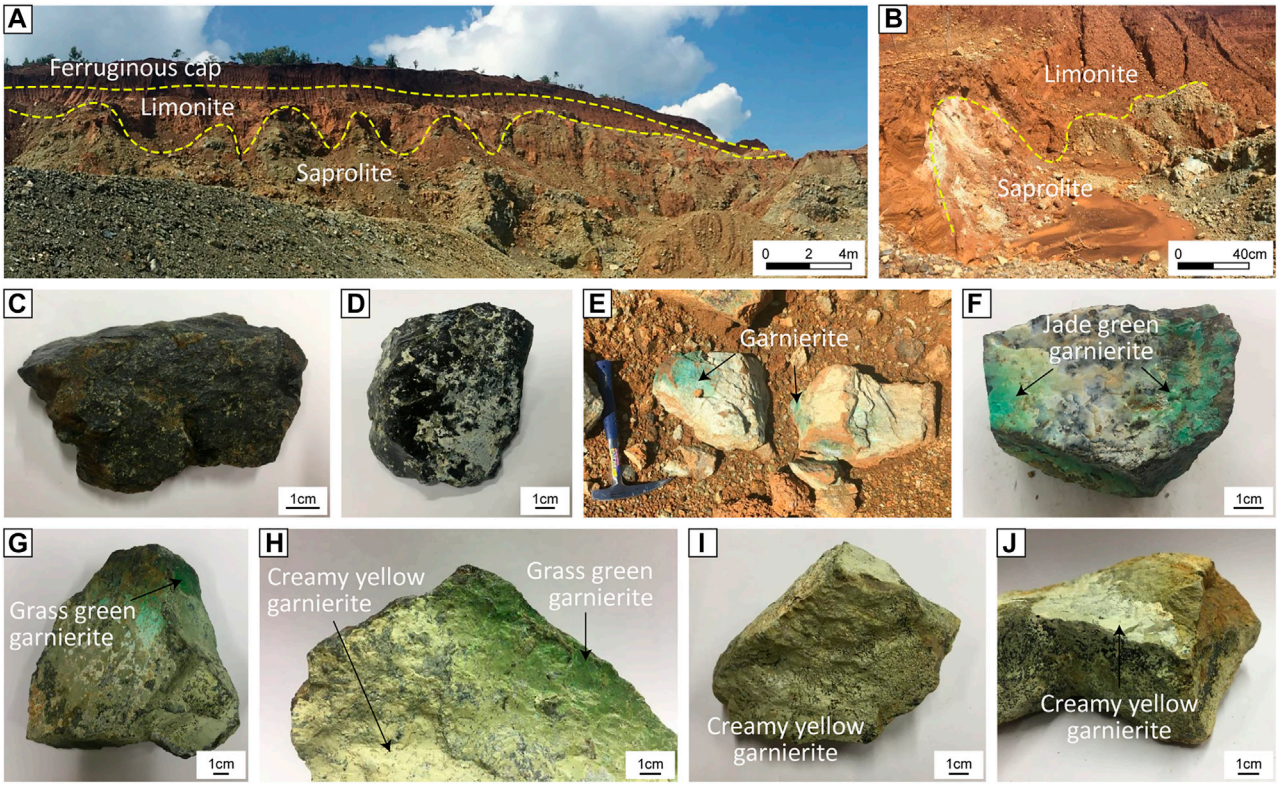

FIGURE 2 | Photographs of lateritic horizons in the Morowali deposit and representative samples from each horizon. Laterite profile **(A)** and undulatory boundary between limonite and saprolite horizon **(B)**. Rock samples from bottom to top **(C)** and **(D)** bedrock **(E)**–**(J)** garnierite samples distinguished by its colors.

saprolite is the presence of mesh-textured serpentine in the saprolite with more secondary minerals such as clay minerals and chromite (**Figures 3C–H**). Serpentine is the most abundant mineral in the saprolite horizon and coexists with orthopyroxene, which is preserved in the bedrock. Almost all the serpentine grains have a tarnished brown or greenish brown color with a mesh texture. A minor form of serpentine was also observed cross-cutting the mesh serpentine and orthopyroxene (**Figures 3D,H**). This serpentine appears as a micro-veinlet and resembles the last stage of serpentine mineralization during weathering. The chrome oxides of <1.2 mm size are surrounded by serpentine and occur as anhedral grains (**Figure 3H**).

Both grass green (**Figure 3E**) and jade green colored (**Figure 3F**) garnierites occur as coatings and show aphanitic character in the macroscopic observation. The grass green colored garnierite contains a dark green Mg-silicate without any remarkable texture, while the jade green colored garnierite contains an ivory colored Mg-silicate with oscillational texture. At the edge of the saprolite and the grass-green garnierite, a ~150 μm thick silicate rim was observed. The vein-type garnierite has a mélange green color in plane-polarized light (**Figure 3G**). Iddingsite and magnetite developed in the vein-type garnierite during its formation.

Limonite

The limonite horizon is a reddish-brown soil consisting of clay minerals. It is 2–7 m thick with a undulating boundary between limonite and saprolite at some places. Two distinct zones are recognized in the limonite horizon, the lower yellow limonite and upper red limonite. Both are composed of goethite and hematite, which make the soil reddish-brown in color due to iron oxidation. However, goethite is the main mineral constituent in the yellow limonite zone, while hematite is the main constituent of the red limonite zone. The original texture of the bedrock is not visible because of the intense weathering in this horizon.

Ferruginous Cap

The ferruginous cap is the top horizon of the Ni-rich laterite profile, which only occurs in the highland area. It is a dark reddish-brown duricrust, rich in ferrous minerals such as hematite. The ferruginous cap is relatively thinner than the lower horizons (1–2 m) (**Figure 2A**). The boundary between the ferruginous cap and the limonite horizon shows a clear distinction. The ferruginous cap could not be observed on the inclined exposures due to erosion (**Figure 2A**).

ANALYTICAL METHODS

Thirteen samples were collected from the bedrock and each of the laterite layers except for the ferruginous cap (Three from bedrock, nine saprolite, and one from limonite) and analyzed by X-ray diffraction (XRD) and X-ray fluorescence spectrometry (XRF) at the National Center for Inter-University Research Facility (NCIRF), Seoul National

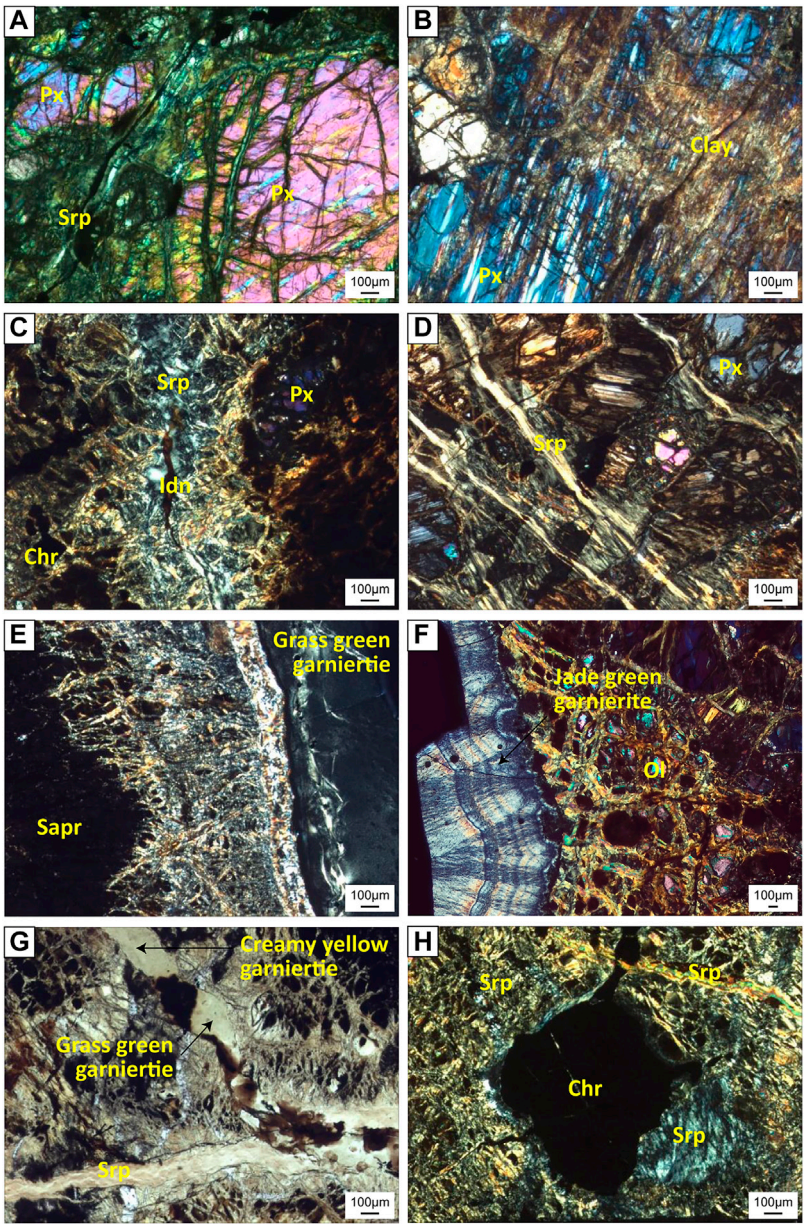

FIGURE 3 | Photomicrographs of the Morowali deposit samples. All photomicrographs except **(G)** were taken under cross-polarized light (XPL). **(A)** phenocrysts of orthopyroxene surrounded by serpentine **(B)** altered orthopyroxene with clinopyroxene exsolutions **(C)** serpentine and development of iddingsite **(D)** serpentine vein crosscutting the bedrock **(E)** and **(F)** development of grass green and jade green garnierite **(G)** veins of serpentine and creamy yellow garnierite **(H)** anhedral chromite phenocryst surrounded by serpentine. Abbreviation: Px = pyroxene, Srp = serpentine, Idn = iddingsite, Chr = chromite, Sapr = saprolite.

University. Mineral chemical analysis was conducted using electron probe micro-analyzer (EPMA) at the Center for Research Facility, Gyeongsang National University and NCIRF, and scanning electron microscopy and energy dispersive spectroscopy (SEM-EDS) was conducted at the School of Earth and Environmental Sciences, Seoul National University.

XRD Analysis

Before the powder XRD analysis, three different colors of garnierite (creamy yellow, grass green, and jade green) were separated from the saprolite samples by handpicking. Each sample was ground into the size of 200 mesh in an agate mortar. XRD analysis was carried out on the garnierite samples using the Rigaku SmartLab with 2θ angles from 5°to 80°, step size of 0.02°, and step duration of 2°s. The mineral phases were indexed using PDXL software and PDF-2 database.

EPMA and SEM Analyses

Six thin sections from the bedrock and saprolite horizon were prepared for EPMA and SEM analyses. Quantitative mineral

TABLE 1 | Summary of the garnierite characteristics from this study.

Sample	Classification	Color	XRD	Structural formula	NiO content from EPMA (wt%)
S1-2, S3-1	Serpentine-like	creamy yellow	7 Å	$(Mg_{2.22\text{-}2.63}Ni_{0.03\text{-}0.33}Fe_{0.17\text{-}0.26})Si_{2.05\text{-}2.14}O_5(OH)_4$	0.76–8.41
S1-2, S1-3, S2-2		grass green	7 + 10 Å	$(Mg_{0.53\text{-}2.65}Ni_{0.03\text{-}1.63}Fe_{0.01\text{-}0.30})Si_{2.02\text{-}2.41}O_5(OH)_4$	0.76–38.26
G-1, G-3	Talc-like	jade green	10 Å	$(Mg_{2.64\text{-}2.80}Ni_{0.22\text{-}0.44})Si_{3.94\text{-}3.99}O_{10}(OH)_2{\cdot}nH_2O$	4.02–8.02

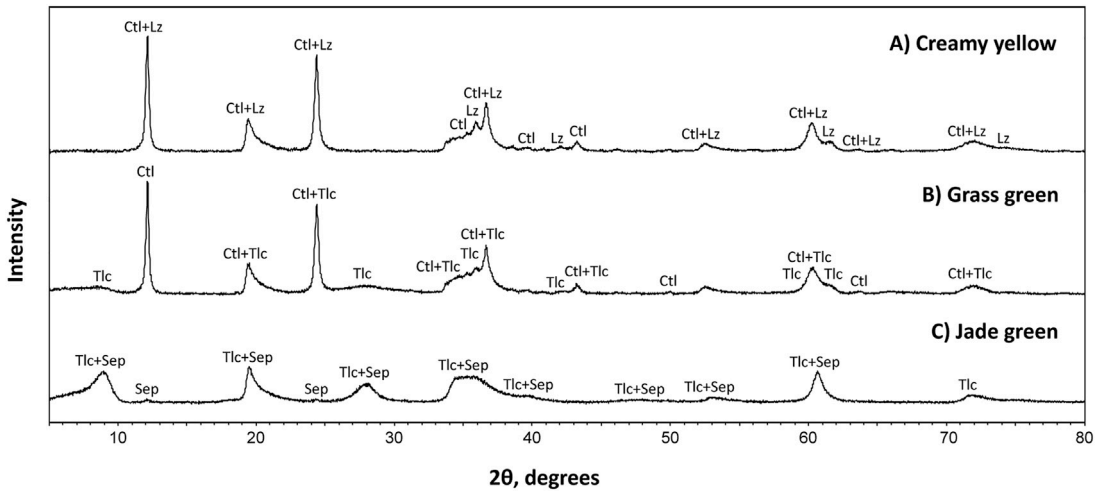

FIGURE 4 | XRD patterns of three garnierite samples from the Morowali deposit distinguished by their colors. Unlike the jade green sample, both the creamy yellow and grass green samples show similar patterns. However, the grass green sample has a mixed pattern between creamy yellow and jade green samples. Abbreviation: Lz = lizardite, Ctl = chrysotile, Tlc = talc, Sep = sepiolite.

analyses were performed using field emission EPMA (JEOL JXA-8530F) and field emission SEM (JEOL JSM-7100F). The field emission EPMA is equipped with five WDS channels and one EDS channel. The applied accelerating voltage was 15 kV, the probe current was 20 nA, and the beam size was 3 μm. Calibration was performed using natural and synthetic standard materials: jadeite (Na), albite (Si), fayalite (Fe), K-feldspar (K), wollastonite (Ca), MgO (Mg), Al_2O_3 (Al), MnO (Mn), TiO_2 (Ti), Cr_2O_3 (Cr), and NiO (Ni). The field emission SEM had an accelerating voltage 15 kV, working distance of 10 mm and an emission current of 53 nA.

XRF Analysis

Twelve samples from the bedrock (B-2, B-3, and G-2), saprolite (G-1, G-3, S1-1, S1-2, S2-1, S2-2, S3-1, and S3-2), and limonite horizon (L-1) were powdered into 200 mesh in an agate mortar for whole rock analysis. Major (SiO_2, Al_2O_3, TiO_2, Fe_2O_3, MgO, CaO, Na_2O, K_2O, MnO, and P_2O_5) and trace elements (NiO and Cr_2O_3), and SO_3 were determined using Shimadzu XRF-1700. Loss on ignition (LOI), which is the weight loss of the sample after burning at 950°C was also measured. Samples were analyzed using lithium tetraborate ($Li_2B_4O_7$) glass beads. The determination limit was better than 10 ppm, and the analytical uncertainties are less than ±2%.

RESULTS

Mineralogical Characteristics of Garnierite

Table 1 summarizes the characteristics of garnierites and their structural formulae. According to XRD and EPMA analyses, garnierite of the Morowali deposit can be distinguished into serpentine- and talc-like. The serpentine-like garnierite occurs in creamy yellow and grass green varieties. XRD pattern of the creamy yellow garnierite (S1-2 and S3-1) shows chrysotile and lizardite phases (**Figure 4A**). The creamy yellow garnierite contains 42.17–44.26 wt% of SiO_2, 30.88–36.83 wt% of MgO, 4.14–6.43 wt% of FeO, and 0.76–8.41 wt% of NiO (**Table 2**). The concentrations of TiO_2, Al_2O_3, Cr_2O_3, MnO, Co, CaO, Na_2O, and K_2O were <0.1 wt%. The general chemical formula of serpentine-like garnierite is $(Mg,Ni)_3Si_2O_5(OH)_4$ (Brindley, 1980; Brand, 1998; Freyssinet et al., 2005), and its structural formulae was calculated using seven oxygens (Brindley and Hang, 1973). Each element concentration is represented in atoms per formula unit (apfu) in **Table 2**. Elements under 0.01 apfu were considered as negligible for the structural formulae calculation. The calculated structural formula for the creamy yellow garnierite is $(Mg_{2.22\text{-}2.63}Ni_{0.03\text{-}0.33}Fe_{0.17\text{-}0.26})Si_{2.05\text{-}2.14}O_5(OH)_4$.

The grass green garnierite (S1-2, S1-3, and S2-2) exhibited mixed XRD patterns with serpentine-like and talc-like structures (**Figure 4B**). The grass green garnierite is composed of

TABLE 2 | EPMA data of serpentine- and talc-like garnierites (in wt%).

Garnierite	Serpentine-like garnierite						
Color	Creamy yellow						
Sample	S1-2						
Spot	1	2	21	22	23	24	25
SiO_2	44.26	42.17	42.66	42.90	43.42	42.91	43.82
TiO_2	0.00	0.01	0.02	0.02	0.01	0.00	0.00
$Al2O_3$	0.02	0.03	0.05	0.04	0.02	0.05	0.00
$Cr2O_3$	0.00	0.00	0.01	0.00	0.00	0.03	0.00
FeO	4.14	4.89	6.43	5.53	5.06	5.36	4.67
MgO	30.88	33.37	35.37	36.76	36.78	36.83	35.69
NiO	8.41	4.57	1.35	1.12	0.76	1.19	1.00
MnO	0.03	0.02	0.07	0.07	0.07	0.04	0.06
CoO	0.00	0.10	—	—	—	—	—
CaO	0.04	0.02	0.03	0.03	0.04	0.04	0.05
Na_2O	0.03	0.00	0.02	0.01	0002E03	0.00	0.05
K_2O	0.08	0.08	0.02	0.01	0.02	0.01	0.03
Total	87.88	85.26	86.03	86.49	86.20	86.47	85.37
Oxygen							
Si	2.14	2.08	2.06	2.05	2.07	2.05	2.10
Ti	0.00	0.00	0.00	0.00	0.00	0.00	0.00
Al	0.00	0.00	0.00	0.00	0.00	0.00	0.00
ΣTetr.	2.14	2.08	2.07	2.06	2.07	2.06	2.10
Cr	0.00	0.00	0.00	0.00	0.00	0.00	0.00
Fe	0.17	0.20	0.26	0.22	0.20	0.21	0.19
Mg	2.22	2.45	2.55	2.62	2.62	2.63	2.56
Ni	0.33	0.18	0.05	0.04	0.03	0.05	0.04
Mn	0.00	0.00	0.00	0.00	0.00	0.00	0.00
Co	0.00	0.00	—	—	—	—	—
Ca	0.00	0.00	0.00	0.00	0.00	0.00	0.01
Na	0.00	0.00	0.00	0.00	0.00	0.00	0.00
K	0.00	0.00	0.00	0.00	0.00	0.00	0.00
ΣOct.	2.73	2.84	2.87	2.89	2.86	2.89	2.80
T/O	0.78	0.73	0.72	0.71	0.73	0.71	0.75
Ni/Mg	0.15	0.07	0.02	0.02	0.01	0.02	0.02

Garnierite	Serpentine-like garnierite																					
Color	Grass green																					
Sample	S1-2	S1-3																				
Spot	3	1	2	3	4	5	6	7	8	9	10	11	12	13	14	15	16	17	18	19	20	21
SiO_2	46.69	48.25	42.39	44.98	41.36	41.60	41.23	42.13	43.06	43.67	46.33	46.35	45.77	45.48	45.78	47.77	44.27	46.78	47.12	43.92	48.23	46.95
TiO_2	0.00	0.02	0.03	0.00	0.00	0.02	0.01	0.00	0.00	0.02	0.00	0.00	0.00	0.00	0.01	0.00	0.01	0.00	0.00	0.01	0.02	0.01
$Al2O_3$	0.00	0.02	0.05	0.00	0.01	0.03	0.02	0.02	0.04	0.02	0.01	0.01	0.00	0.00	0.02	0.01	0.03	0.00	0.02	0.02	0.01	0.02
$Cr2O_3$	0.01	0.03	0.00	0.00	0.00	0.00	0.00	0.00	0.00	0.00	0.00	0.00	0.00	0.00	0.00	0.01	0.00	0.01	0.01	0.00	0.00	0.00
FeO	2.31	2.08	5.67	0.46	6.33	6.30	7.03	5.12	5.48	4.71	0.18	0.25	0.24	0.14	3.47	1.82	3.65	1.08	1.98	3.93	1.40	2.09
MgO	22.06	24.51	36.68	9.08	35.78	27.48	28.45	35.53	37.39	29.68	10.39	7.44	7.19	6.70	25.51	21.92	29.35	19.32	23.40	29.93	20.41	23.68
NiO	16.12	16.65	1.39	35.13	2.22	9.88	8.57	2.72	0.76	8.72	35.83	37.92	37.92	38.26	14.08	17.72	9.65	19.11	16.12	9.18	19.88	16.28
MnO	0.00	0.00	0.03	0.10	0.04	0.02	0.02	0.04	0.04	0.01	0.02	0.06	0.09	0.03	0.03	0.02	0.03	0.02	0.00	0.05	0.02	0.00

(Continued on following page)

TABLE 2 | (*Continued*) EPMA data of serpentine- and talc-like garnierites (in wt%).

Garnierite	Serpentine-like garnierite																					
Color	Grass green																					
Sample	S1-2	S1-3																				
Spot	3	1	2	3	4	5	6	7	8	9	10	11	12	13	14	15	16	17	18	19	20	21
CoO	0.00	0.00	—	—	—	—	—	—	—	—	—	—	—	—	—	—	—	—	—	—	—	—
CaO	0.05	0.08	0.01	0.05	0.01	0.04	0.07	0.05	0.01	0.04	0.08	0.08	0.06	0.09	0.05	0.05	0.03	0.08	0.05	0.03	0.06	0.06
Na_2O	0.00	0.02	0.02	0.05	0.00	0.02	0.03	0.00	0.01	0.03	0.02	0.01	0.03	0.00	0.03	0.03	0.04	0.02	0.02	0.03	0.03	0.04
K_2O	0.18	0.13	0.02	0.08	0.03	0.08	0.04	0.01	0.00	0.05	0.06	0.04	0.06	0.05	0.07	0.08	0.05	0.11	0.08	0.04	0.09	0.05
Total	87.42	91.79	86.28	89.93	85.80	85.47	85.46	85.61	86.80	86.94	92.90	92.16	91.35	90.75	89.05	89.43	87.11	86.53	88.80	87.14	90.15	89.18
Oxygen																						
Si	2.31	2.28	2.04	2.38	2.02	2.12	2.09	2.05	2.05	2.14	2.36	2.41	2.41	2.41	2.23	2.32	2.16	2.36	2.29	2.15	2.34	2.28
Ti	0.00	0.00	0.00	0.00	0.00	0.00	0.00	0.00	0.00	0.00	0.00	0.00	0.00	0.00	0.00	0.00	0.00	0.00	0.00	0.00	0.00	0.00
Al	0.00	0.00	0.00	0.00	0.00	0.00	0.00	0.00	0.00	0.00	0.00	0.00	0.00	0.00	0.00	0.00	0.00	0.00	0.00	0.00	0.00	0.00
ΣTetr.	2.31	2.28	2.04	2.38	2.02	2.12	2.10	2.05	2.05	2.14	2.36	2.41	2.41	2.41	2.23	2.32	2.16	2.36	2.29	2.15	2.34	2.28
Cr	0.00	0.00	0.00	0.00	0.00	0.00	0.00	0.00	0.00	0.00	0.00	0.00	0.00	0.00	0.00	0.00	0.00	0.00	0.00	0.00	0.00	0.00
Fe	0.10	0.08	0.23	0.02	0.26	0.27	0.30	0.21	0.22	0.19	0.01	0.01	0.01	0.01	0.14	0.07	0.15	0.05	0.08	0.16	0.06	0.08
Mg	1.63	1.72	2.63	0.72	2.61	2.08	2.15	2.58	2.65	2.17	0.79	0.58	0.56	0.53	1.85	1.59	2.14	1.45	1.70	2.18	1.48	1.71
Ni	0.64	0.63	0.05	1.49	0.09	0.40	0.35	0.11	0.03	0.34	1.47	1.59	1.60	1.63	0.55	0.69	0.38	0.78	0.63	0.36	0.78	0.64
Mn	0.00	0.00	0.00	0.00	0.00	0.00	0.00	0.00	0.00	0.00	0.00	0.00	0.00	0.00	0.00	0.00	0.00	0.00	0.00	0.00	0.00	0.00
Co	0.00	0.00	—	—	—	—	—	—	—	—	—	—	—	—	—	—	—	—	—	—	—	—
Ca	0.01	0.01	0.00	0.01	0.00	0.00	0.01	0.00	0.00	0.00	0.01	0.01	0.01	0.01	0.01	0.00	0.00	0.01	0.01	0.00	0.01	0.01
Na	0.00	0.00	0.00	0.00	0.00	0.00	0.00	0.00	0.00	0.00	0.00	0.00	0.00	0.00	0.00	0.00	0.00	0.00	0.00	0.00	0.00	0.00
K	0.01	0.01	0.00	0.01	0.00	0.01	0.00	0.00	0.00	0.00	0.00	0.00	0.00	0.00	0.00	0.00	0.00	0.01	0.00	0.00	0.01	0.00
ΣOct.	2.38	2.46	2.92	2.25	2.96	2.77	2.82	2.90	2.90	2.72	2.28	2.19	2.19	2.18	2.55	2.37	2.68	2.29	2.42	2.71	2.32	2.45
T/O	0.97	0.93	0.70	1.06	0.68	0.77	0.74	0.71	0.71	0.79	1.04	1.10	1.10	1.11	0.87	0.98	0.81	1.03	0.95	0.79	1.01	0.93
Ni/Mg	0.39	0.37	0.02	2.09	0.03	0.19	0.16	0.04	0.01	0.16	1.86	2.75	2.85	3.08	0.30	0.44	0.18	0.53	0.37	0.17	0.53	0.37

Garnierite	Talc-like garnierite														
Color	Jade green														
Sample	G1-1														
Spot	1	2	3	4	5	6	7	8	9	10	11	12	13	14	15
SiO_2	56.76	56.96	58.98	58.38	58.10	58.30	57.86	58.88	59.38	58.34	58.32	57.55	59.42	59.26	58.22
TiO_2	0.01	0.01	0.00	0.01	0.00	0.01	0.01	0.00	0.00	0.00	0.00	0.02	0.01	0.02	0.01
Al_2O_3	0.00	0.y00	0.00	0.00	0.00	0.00	0.01	0.00	0.00	0.00	0.00	0.00	0.00	0.00	0.01
Cr_2O_3	0.03	0.00	0.00	0.00	0.00	0.01	0.00	0.01	0.00	0.00	0.00	0.00	0.00	0.03	0.00
FeO	0.05	0.01	0.01	0.01	0.00	0.01	0.02	0.02	0.00	0.01	0.03	0.00	0.02	0.00	0.01
MgO	26.27	26.74	26.44	27.19	25.99	25.99	25.91	26.30	27.09	26.09	26.17	26.09	27.61	27.93	27.63
NiO	6.87	4.75	6.66	5.32	7.84	7.57	7.98	6.68	5.60	7.58	7.19	8.02	4.67	4.02	4.86
MnO	0.02	0.00	0.03	0.00	0.02	0.04	0.01	0.02	0.03	0.02	0.01	0.01	0.02	0.05	0.02
CoO	0.00	0.00	—	—	—	—	—	—	—	—	—	—	—	—	—
CaO	0.03	0.04	0.03	0.03	0.02	0.02	0.02	0.03	0.04	0.03	0.02	0.02	0.02	0.03	0.02
Na_2O	0.06	0.01	0.00	0.03	0.02	0.01	0.02	0.01	0.04	0.00	0.00	0.01	0.00	0.01	0.02
K_2O	0.05	0.07	0.06	0.09	0.05	0.03	0.03	0.04	0.10	0.04	0.04	0.04	0.05	0.07	0.04
Total	90.15	88.58	92.21	91.06	92.05	92.00	91.88	92.00	92.28	92.11	91.79	91.77	91.81	91.42	90.85
Oxygen															
Si	3.94	3.97	3.98	3.97	3.96	3.97	3.96	3.99	3.99	3.97	3.97	3.94	3.99	3.98	3.96
Ti	0.00	0.00	0.00	0.00	0.00	0.00	0.00	0.00	0.00	0.00	0.00	0.00	0.00	0.00	0.00

(Continued on following page)

TABLE 2 | (*Continued*) EPMA data of serpentine- and talc-like garnierites (in wt%).

Garnierite	Talc-like garnierite														
Color	Jade green														
Sample	G1-1														
Spot	1	2	3	4	5	6	7	8	9	10	11	12	13	14	15
Al	0.00	0.00	0.00	0.00	0.00	0.00	0.00	0.00	0.00	0.00	0.00	0.00	0.00	0.00	0.00
ΣTetr	3.94	3.97	3.98	3.97	3.96	3.97	3.96	3.99	3.99	3.97	3.97	3.94	3.99	3.99	3.96
Cr	0.00	0.00	0.00	0.00	0.00	0.00	0.00	0.00	0.00	0.00	0.00	0.00	0.00	0.00	0.00
Fe	0.00	0.00	0.00	0.00	0.00	0.00	0.00	0.00	0.00	0.00	0.00	0.00	0.00	0.00	0.00
Mg	2.72	2.78	2.66	2.76	2.64	2.64	2.64	2.65	2.71	2.64	2.66	2.66	2.76	2.80	2.80
Ni	0.38	0.27	0.36	0.29	0.43	0.41	0.44	0.36	0.30	0.41	0.39	0.44	0.25	0.22	0.27
Mn	0.00	0.00	0.00	0.00	0.00	0.00	0.00	0.00	0.00	0.00	0.00	0.00	0.00	0.00	0.00
Co	0.00	0.00	–	–	–	–	–	–	–	–	–	–	–	–	–
Ca	0.00	0.01	0.00	0.00	0.00	0.00	0.00	0.00	0.01	0.00	0.00	0.00	0.00	0.00	0.00
Na	0.01	0.00	0.00	0.00	0.00	0.00	0.00	0.00	0.01	0.00	0.00	0.00	0.00	0.00	0.00
K	0.00	0.01	0.00	0.01	0.00	0.00	0.00	0.00	0.01	0.00	0.00	0.00	0.00	0.01	0.00
ΣOct	3.13	3.06	3.04	3.06	3.08	3.06	3.09	3.03	3.04	3.07	3.06	3.12	3.02	3.03	3.08
T/O	1.26	1.30	1.31	1.30	1.29	1.30	1.28	1.32	1.31	1.29	1.30	1.27	1.32	1.31	1.29
Ni/Mg	0.14	0.10	0.14	0.11	0.16	0.16	0.17	0.14	0.11	0.16	0.15	0.17	0.09	0.08	0.09

41.23–48.25 wt% of SiO_2, 6.70–37.39 wt% of MgO, 0.14–7.03 wt % of FeO, and a higher amount of NiO (0.76–38.26 wt%) than creamy yellow and talc-like garnierites (**Table 2**). The structural formula of grass green garnierite was also calculated in the same way as that of creamy yellow garnierite. The calculated structural formula for grass green garnierite is $(Mg_{0.53\text{-}2.65}Ni_{0.03\text{-}1.63}Fe_{0.01\text{-}0.30})Si_{2.02\text{-}2.41}O_5(OH)_4$.

The talc-like garnierite (G-1 and G-3) exhibited a jade green color, and consists of comparatively higher concentrations of SiO_2 (56.76–59.42 wt%), MgO (25.91–27.93 wt%), and NiO (4.02–8.02 wt%) while the other elements exist in trace amounts (<0.1 wt%) (**Table 2**). The general chemical formula for talc-like garnierite is $(Mg,Ni)_3Si_4O_{10}(OH)_2{\cdot}nH_2O$ (Brindley, 1980; Brand, 1998; Freyssinet et al., 2005). The structural formulae of talc-like garnierite were calculated on the basis of 11 oxygen atoms (Brindley and Hang, 1973). Mg and Ni were allocated to the octahedral site, while Si was allocated to the tetrahedral site. Due to the trace amounts of Ti, Al, Cr, Fe, Mn, Co., Ca, Na, and K (<0.01 apfu), only Si (3.94–3.99 apfu), Mg (2.64–2.80 apfu), and Ni (0.22–0.44 apfu) were considered for calculation of the structural formulae (**Table 2**). The estimated structural formula is $(Mg_{2.64\text{-}2.80}Ni_{0.22\text{-}0.44})Si_{3.94\text{-}3.99}O_{10}(OH)_2{\cdot}nH_2O$.

Geochemical Characteristics of Bedrock and Saprolite Horizon

Pyroxene and serpentine are abundant minerals in the bedrock saprolite horizon with minor occurrence of chromite. The EPMA data for these minerals are presented in **Table 3**. Pyroxenes in the bedrock and saprolite horizon have similar amounts of SiO_2 (51.35–56.88 wt%), MgO (15.86–33.43 wt%), CaO (0.94–23.2 wt %), FeO (2.32–6.13 wt%), and NiO (0.02–0.15 wt%). The wide ranges of MgO and CaO are probably due to clinopyroxene exsolutions in orthopyroxene (**Figures 3A,B**). Serpentines show a narrow range of SiO_2 (40.12–43.35 wt%) in the bedrock and saprolite samples, while MgO and NiO show a wide variation (27.54–37.1 wt% and 0.97–7.84 wt%, respectively). It was also observed that the NiO content was inversely proportional to the MgO content. This variation indicates a high degree of cation exchange between Ni and Mg at this level. Additionally, chromites with variable Al_2O_3, FeO, and MgO contents were also observed. Such chromites were distinguished into high-Al and low-Al chromites. The high-Al chromites contains relatively lower FeO (16.09–17.37 wt%) and higher MgO (13.76–14.88 wt %) than the low-Al chromites (57.39 wt% FeO and 1.05 wt% MgO).

Whole Rock Geochemistry of Laterite Profile

The major and trace elements concentrations in the bedrock and saprolite horizon are generally similar (**Table 4**). SiO_2, MgO, and Fe_2O_3 were the most abundant in the bedrock and saprolite horizon. SiO_2, MgO, and Fe_2O_3 contents for the bedrock and saprolite horizon vary between 38.79–43.91 wt%, 27.65–36.27 wt

TABLE 3 | EPMA data from minerals in the bedrock and saprolite (in wt%).

Sample	Mineral	Spot	Chemical composition											
			SiO_2	TiO_2	Al_2O_3	Cr_2O_3	FeO	MgO	NiO	MnO	CoO	CaO	Na_2O	K_2O	Total
S2-1	Pyroxene	1	56.88	0.02	2.54	0.71	5.81	33.43	0.06	0.18	0.00	0.96	0.00	0.00	100.58
		2	56.06	0.00	2.71	0.80	5.70	33.11	0.07	0.14	0.25	1.04	0.00	0.01	99.89
		3	52.72	0.06	2.98	1.08	2.32	17.28	0.09	0.14	0.00	23.16	0.01	0.01	99.85
	Olivine	1	40.99	0.04	0.00	0.00	8.75	49.81	0.46	0.18	0.07	0.02	0.00	0.00	100.32
	Serpentine	1	41.85	0.00	1.12	0.47	5.89	27.54	7.84	0.11	0.00	0.04	0.04	0.08	84.99
		2	42.82	0.02	1.45	0.41	7.41	28.84	6.14	0.02	0.00	0.05	0.05	0.10	87.32
	Chromite	1	0.00	0.03	32.65	37.00	16.09	14.88	0.19	0.28	0.07	0.00	0.03	0.00	101.22
		2	0.02	0.03	32.77	35.86	16.84	14.46	0.13	0.25	0.00	0.00	0.00	0.00	100.36
S1-3	Pyroxene	1	55.63	0.13	3.01	0.68	6.12	32.90	0.10	0.12	0.07	0.94	0.03	0.00	99.74
	Serpentine	1	43.35	0.01	0.03	0.00	4.14	32.52	6.10	0.03	0.15	0.04	0.00	0.07	86.45
		2	42.48	0.02	0.11	0.00	4.41	36.61	1.44	0.03	0.00	0.03	0.00	0.02	85.14
S1-2	Pyroxene	1	55.81	0.02	2.39	0.72	5.50	31.98	0.11	0.15	0.00	2.72	0.00	0.00	99.39
	Serpentine	1	41.85	0.00	0.00	0.02	5.31	35.93	1.78	0.07	0.01	0.04	0.04	0.06	85.12
		2	42.72	0.00	0.09	0.02	5.25	36.76	1.15	0.06	0.08	0.01	0.03	0.03	86.20
		3	41.63	0.00	0.45	0.00	5.46	30.96	5.95	0.06	0.00	0.04	0.04	0.07	84.65
		4	40.74	0.00	0.10	0.04	7.34	33.90	2.09	0.06	0.02	0.05	0.04	0.08	84.45
	Chromite	1	0.00	0.01	28.23	41.78	16.19	14.64	0.12	0.27	0.00	0.00	0.00	0.01	101.24
		2	0.00	0.06	29.11	39.29	17.01	14.07	0.16	0.23	0.37	0.00	0.00	0.01	100.31
		3	0.00	0.00	4.32	33.99	57.39	1.05	0.17	0.79	0.00	0.00	0.02	0.00	97.74
G1-1	Pyroxene	1	56.34	0.00	2.24	0.76	5.39	32.92	0.12	0.10	0.03	1.75	0.05	0.01	99.70
		2	56.31	0.04	2.52	0.77	5.82	32.88	0.11	0.19	0.00	1.58	0.00	0.00	100.22
		3	55.95	0.06	2.49	0.74	5.54	32.09	0.15	0.07	0.26	2.62	0.00	0.01	99.97
	Serpentine	1	40.95	0.02	0.00	0.05	4.99	37.10	0.97	0.06	0.00	0.01	0.02	0.00	84.16
		2	40.12	0.00	0.00	0.05	6.92	33.75	2.56	0.04	0.01	0.01	0.00	0.04	83.49
		3	42.49	0.00	0.49	0.00	5.93	35.09	1.72	0.06	0.05	0.02	0.01	0.04	85.88
	Chromite	1	0.01	0.00	27.16	42.71	17.32	14.04	0.12	0.20	0.55	0.00	0.00	0.00	102.10
		2	0.03	0.00	26.36	42.00	17.37	13.76	0.21	0.22	0.61	0.00	0.02	0.01	100.58
B-2	Pyroxene	1	56.13	0.11	3.09	0.83	6.13	32.64	0.10	0.13	0.00	1.02	0.00	0.01	100.18
		2	55.25	0.10	3.60	0.81	5.85	31.21	0.08	0.14	0.08	2.71	0.03	0.00	99.84
		3	55.63	0.13	3.01	0.68	6.12	32.90	0.10	0.12	0.07	0.94	0.03	0.00	99.74
		4	51.35	0.26	4.42	1.24	2.85	15.86	0.02	0.08	0.00	23.20	0.33	0.00	99.60

TABLE 4 | XRF data of bedrock, saprolite, and limonite horizon samples (in wt%).

Sample	Bedrock			Saprolite								Limonite
	B-2	B-3	G-2	G-1	G-3	S1-1	S1-2	S2-1	S2-2	S3-1	S3-2	L-1
SiO_2	42.46	43.91	41.50	42.08	41.86	39.43	39.83	40.09	38.79	38.94	39.80	2.59
Al_2O_3	2.32	2.39	2.02	0.83	1.09	0.84	0.75	0.98	0.92	1.00	1.08	5.92
TiO_2	0.04	0.06	0.05	0.01	0.01	0.00	0.00	0.01	0.01	0.00	0.01	0.05
Fe_2O_3*	8.33	8.50	8.38	8.46	7.60	8.02	8.01	8.85	9.20	10.44	10.36	66.90
MgO	36.27	35.28	36.19	31.04	32.66	35.49	33.89	30.19	30.65	27.65	28.76	0.74
CaO	1.89	2.03	1.78	0.64	0.88	0.67	0.59	0.66	0.31	0.74	0.72	0.02
Na_2O	0.21	0.18	0.16	0.11	0.20	0.14	0.16	0.11	0.13	0.12	0.11	0.09
K_2O	0.011	0.02	0.01	0.01	0.008	0.01	0.006	0.01	0.007	0.008	0.01	0.013
MnO	0.13	0.13	0.12	0.12	0.10	0.11	0.10	0.12	0.11	0.12	0.14	1.22
P_2O_5	0.004	0.004	0.004	0.003	0.004	0.006	0.005	0.003	0.005	0.004	0.003	0.003
NiO	0.45	0.46	0.64	3.14	1.03	0.70	1.46	5.14	3.72	4.03	4.66	1.83
Cr_2O_3	0.58	0.66	0.75	0.57	0.52	0.57	0.32	0.63	0.57	0.72	0.70	3.78
SO_3	n.d	0.06	0.05	n.d	n.d	n.d	n.d	n.d	n.d	n.d	n.d	0.72
L.O.I	7.31	6.35	8.37	12.99	14.04	14.03	14.88	13.19	15.60	16.24	13.63	16.14
Total	100.02	100.03	100.02	100.01	99.99	100.01	99.99	99.98	100.01	100.00	99.99	100.03

L.O.I, loss on ignition; Fe_2O_3, total iron oxide; n.d, not detected.*

%, and 7.6–10.44 wt%, respectively. However, those for the limonite horizon exhibited lower SiO_2 (2.59 wt%) and MgO (0.74 wt%), and higher Fe_2O_3 (66.9 wt%) values. The contents of immobile elements, such as Al_2O_3, Cr_2O_3, and MnO, are below 6 wt% in all the horizons. Minor amounts of CaO (1.89–0.02 wt %) and Na_2O (0.21–0.09 wt%) with extremely low K_2O and P_2O_5 (<0.01%) were also observed. NiO (0.45–5.14 wt%) is abundant in saprolite horizon and depleted in the bedrock.

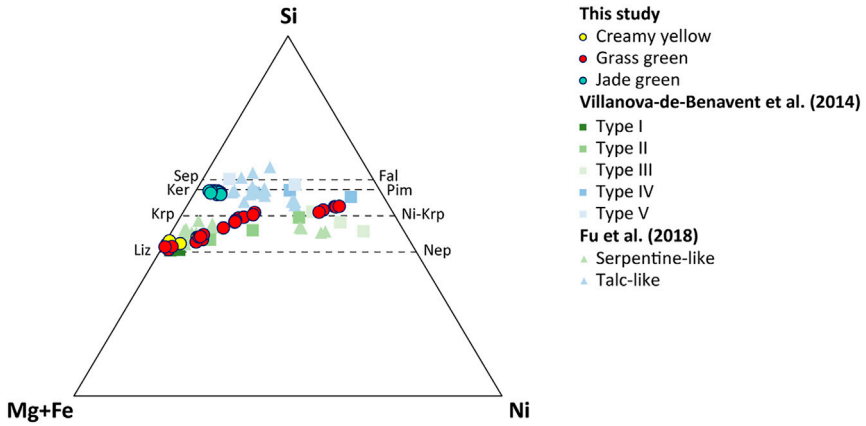

FIGURE 5 | Ternary diagram of Si-Mg + Fe-Ni system showing the garnierite phases in the Morowali deposit and other references. Abbreviation: Sep = sepiolite, Fal = falcondoite, Ker = kerolite, Pim = pimelite, Krp = karpinskite, Liz = lizardite, Nep = népouite.

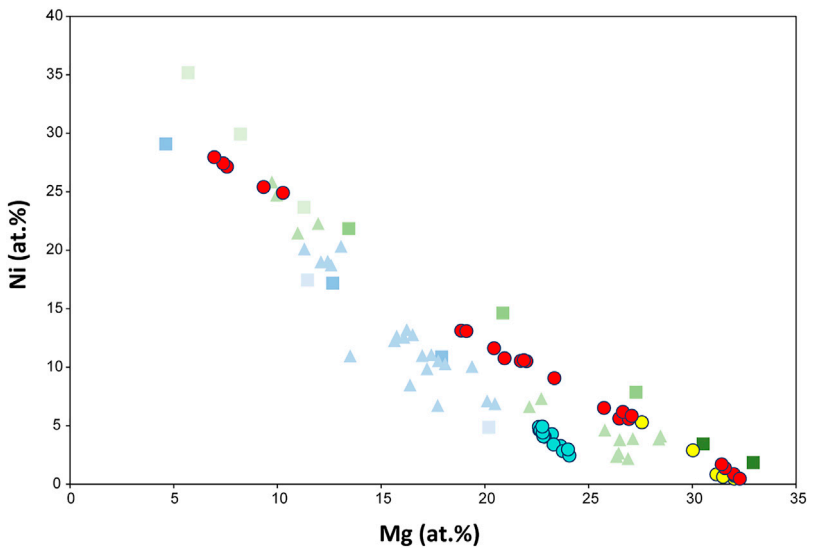

FIGURE 6 | Nickel content of garnierite samples from this study and other references as a function of Mg content in atomic percentage. Type I to V garnierites data are from Villanova-de-Benavent et al. (2014). Serpentine-like and talc-like garnierite data are from Fu et al. (2018). Legend is identical in **Figure 5**.

DISCUSSION

Nature of Garnierite in Morowali Deposit

Precipitation of Garnierite

The term garnierite has been widely used to denote a mixture of serpentine, talc, sepiolite, chlorite, and/or smectite phases due to its poor crystallinity, fine grain size, and ambiguous occurrences (Brindley and Hang, 1973; Springer, 1974). It is generally applied when mineral phases cannot be distinctly demarcated; however, the mineralogical term such as kerolite, which is an end member of the talc series, is sometimes used instead of garnierite when the occurrence of the mineral is known (Cathelineau et al., 2016). Nevertheless, based on the XRD results, where phases such as lizardite, chrysotile, talc, and sepiolite were observed but their origin was not known, we used the term garnierite to denote the Ni-rich phase.

The XRD results of the Morowali garnierite samples display two apparent end members, i.e., serpentine-like and talc-like phases. The creamy yellow and grass green garnierites show similar patterns, and are grouped under serpentine-like phase (**Figures 4A,B**). Even though the grass green garnierite patterns are more similar to the serpentine-like garnierite, some degree of similarity was also observed with the talc-like garnierite, which indicates that the grass green garnierite includes impurities of talc-like phases. These distinctive morphological features of each garnierite are also reflected in their chemical characteristics. Both creamy yellow and grass green serpentine-like garnierites plot between the lizardite-népouite and karpinskite-Ni-karpinskite

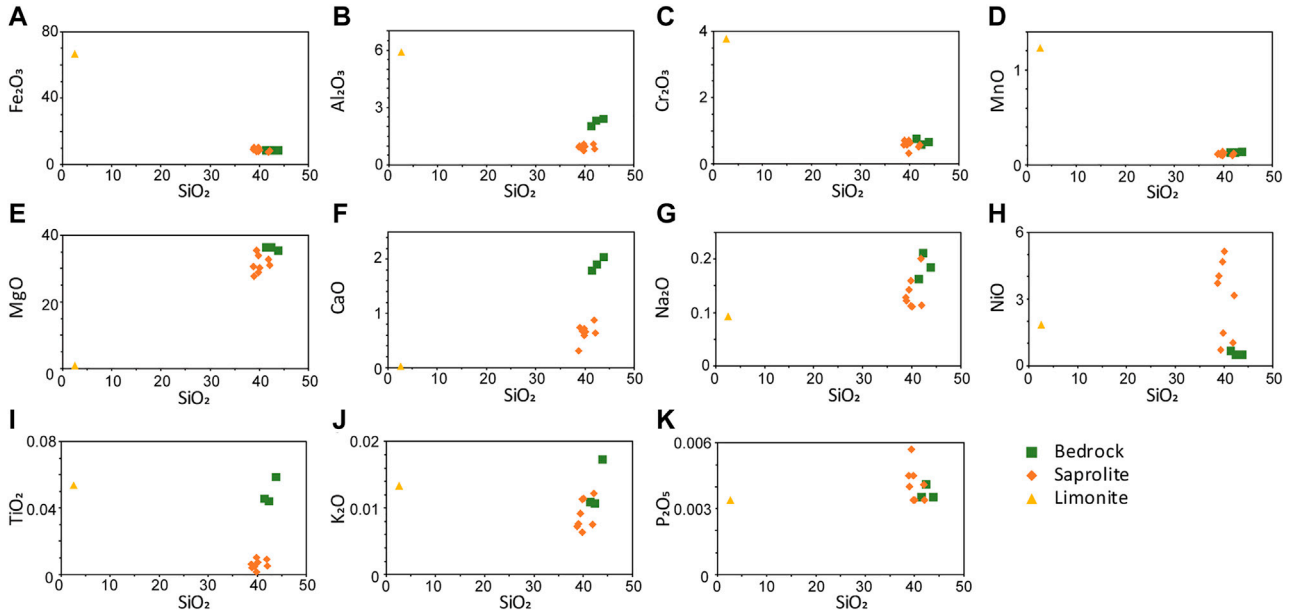

FIGURE 7 | Elemental distribution in bedrock, saprolite, and limonite horizons of the Morowali deposit. With the progress of laterization, a decrease in SiO_2 was observed.

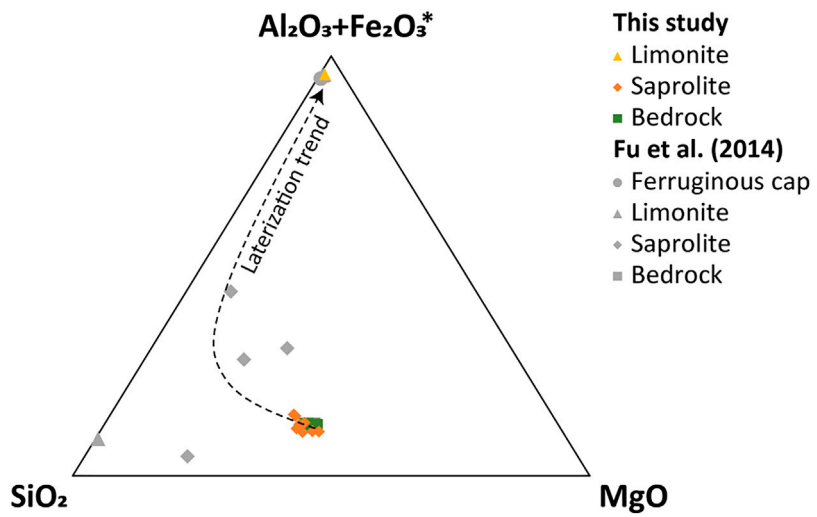

FIGURE 8 | Ternary diagram of Al_2O_3+Fe_2O_3*-SiO_2-MgO system for the laterite horizon in the Morowali deposit. Samples from this study are described in colored symbols and references from Indonesia (Fu et al., 2014) are represented by grey symbols. Fe_2O_3* means total iron oxide.

series (**Figure 5**). Lizardite and népouite are generally well-defined minerals, while karpinskite still lacks mineralogical validity (Fu et al., 2018). Karpinskite ideally maintains a T/O value of 1, and when it is present as an impurity in the serpentine- or talc-like phase, it might allow excess Si in the octahedral site (Tauler et al., 2009).

Three garnierite samples in the Morowali deposit show different physical and chemical characteristics suggesting that they originated from different sources. Iron content has been used as an indicator for determining the sequence of garnierite in many previous studies because of its immobile character during laterization (Villanova-de-Benavent et al., 2014; Fu et al., 2018). The creamy yellow serpentine-like garnierite (**Figure 5**) plots near lizardite and the FeO content (4.14–6.43 wt%) is analogous to that of serpentine in saprolite (4.14–7.41 wt%). This indicates that the creamy yellow garnierite originated from the surrounding serpentine. The grass green garnierite contains a wide range of FeO (0.14–7.03 wt%) and NiO (0.76–38.26 wt%) contents than the creamy yellow garnierite. The XRD pattern of the grass green garnierite exhibits the existence of talc phase

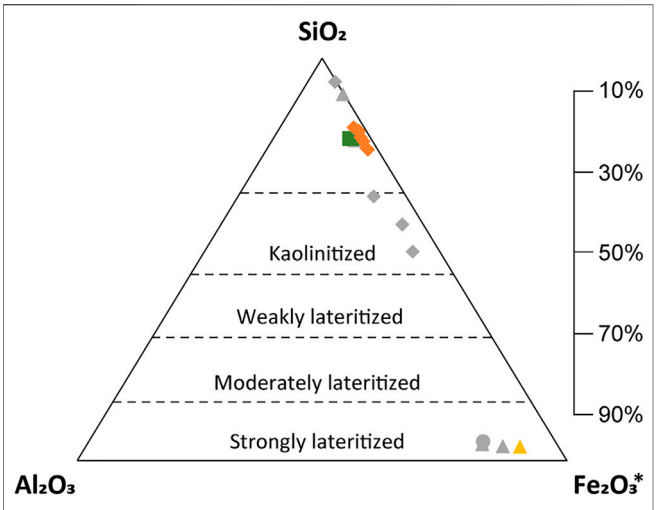

FIGURE 9 | Ternary diagram of SiO_2-Al_2O_3- Fe_2O_3* for the laterite horizon in the Morowali deposit and its index of lateritization (IOL). IOL represents the degree of weathering in the quantitative calculation of chemical composition. The calculation formula of IOL is as follows: IOL = $100x((Al_2O_3+Fe_2O_3^*)/(SiO_2+Al_2O_3+Fe_2O_3^*))$ (Tupaz et al., 2020). Legend is same as in **Figure 8**.

impurity. The NiO content is inversely proportional to the FeO and MgO contents, indicating active ion exchange between Mg and Ni. In addition, grass green garnierite occurs both as coating and as veinlet intruding the creamy yellow garnierite (**Figure 3G**) that covers the surface of the rocky saprolite as coatings. This means that both creamy yellow and grass green garnierites originated from the serpentine in saprolite by Mg-Ni exchange. However, the creamy yellow garnierite is more weathered and has a low Ni content than the grass green garnierite, which continues to interact with the Ni-rich solution passing through the saprolite horizon, precipitating Ni in the micro veins.

According to Manceau and Calas (1985), secondarily precipitated garnierite, which is neoformed garnierite from Ni-bearing solution, has a low iron content (<0.5 wt% FeO) because iron is insoluble during weathering. The iron content of the talc-like Morowali garnierites is < 0.05 wt% (FeO) (**Table 2**), indicating that their origin is secondary in nature. The talc-like garnierite not only shows a low Fe content but also a relatively low Ni content than the grass green serpentine-like garnierite. Their low Ni content suggests that the Ni in them comes from saprolite and not dierctly from the serpentine-like garnierites. Similar signatures were observed by Villanova-de-Benavent et al. (2014). Moreover, the oscillation texture in the talc-like garnierite (**Figure 3F**) indicates that precipitation of talc-like garnierite was accompanied by chemical changes (Fu et al., 2018).

Occurrence of Garnierite From Other Ni-Laterite Deposits

Garnierite occurring in the Morowali laterite can be divided into talc-like and serpentine-like. Such types of garnierites have also been reported from the Sorowako and Kolonodale deposits in Sulawesi (Sufriadin et al., 2011; Fu et al., 2018). These phases have also been discovered globally in New Caledonia (Manceau and Calas, 1985; Cluzel and Vigier, 2008; Wells et al., 2009), Dominican Republic (Proenza et al., 2008; Villanova-de-Benavent et al., 2014), Venezuela (Soler et al., 2008), and Colombia (Gleeson et al., 2004). The garnierite occurring in these countries shows a similar appearance, but their composition differs depending on the host rock and weathering environment. Therefore, for a comparative study, we selected garnierites that were formed in tropical climates and had bedrock compositions analogous to the Morowali samples (**Figures 5**, **6**). Villanova-de-Benavent et al. (2014) classified garnierites in the Falcondo Ni-laterite deposit, Dominican Republic, into five phases from type I to type V by using XRD and EPMA analyses. The Falcondo Ni-laterite deposit formed in a tropical climate and is hosted in partially serpentinized peridotite. It has the same climate conditions and host rock composition as that of the Morowali deposit. Similar to the study area, the Kolonodale deposit in Sulawesi, Indonesia is associated with the same ophiolite (East Sulawesi ophiolite), and has developed under the same climate conditions. The host rock of the Kolonodale deposit is regionally metamorphosed serpentinite (Fu et al., 2014; Fu et al., 2018). Garnierites from Kolonodale deposit are both serpentine- and talc-like.

The XRD patterns of the garnierites in the Morowali deposit show intensities similar to the patterns of the Falcondo deposit. The serpentine-like garnierite in this study corresponds to the type I, type II, and type III garnierite in Villanova-de-Benavent et al. (2014) while the talc-like garnierite from this study coincides with the type IV garnierite from Villanova-de-Benavent et al. (2014). Along with the XRD patterns, the chemical composition also indicates similarity between the Morowali and Falcondo deposits. The Ni and Mg contents (atomic percentage) of the studied garnierite samples (**Figure 6**) suggests that although the classification of Villanova-de-Benavent et al. (2014) is not absolute, garnierites in the Morowali deposit show similar development pathways as those of the Falcondo deposit. Contrastingly, garnierites from the Kolonodale deposit are more heterogeneous in composition than the Morowali deposit; for example, talc-like garnierites plot over serpentine-like garnierite in the Kolonodale deposit, indicating that along with the host rock composition as a primary factor in the formation of Ni-bearing laterite deposits, environmental influence also impacts the Ni enrichment in garnierite. The negative correlation between Mg and Ni implies that the process of garnierite formation is the same everywhere, i.e., by substitution of Mg by Ni. However, the Ni enrichment process in the serpentine- and talc-like phases is not completely understood yet.

Environment of the Morowali Ni-Laterite Deposit

Serpentinization-related extensive water–rock interaction might occur before laterization because most of the laterite deposits that develop on the bedrock are already serpentinized due to chemical reactions with seawater (Golightly, 1981). At low temperatures,

the primary minerals in peridotites, such as olivine and pyroxene, are altered faster than the hydrous phases, such as brucite, serpentine, and talc, because of their instability, and the alteration process continues until equilibrium is reached between the hydrous and primary minerals (Nesbitt and Bricker, 1978). Mesh-like textures are generally formed during serpentinization from seawater by the thermodynamically and kinetically controlled hydration processes (**Figure 3C, E-H**), and indicate olivine weathering (Viti and Mellini, 1998). Olivine hydration results in the formation of brucite and serpentine with minor magnetite (Tupaz et al., 2020). Magnetite formed during serpentinization develops at 200–300°C (Klein et al., 2014; Tupaz et al., 2020). The presence of magnetite associated with serpentine in the studied samples suggests that low-temperature hydration was the primary process that occurred before laterization.

Nickel laterite deposits are mostly developed on accretionary and cratonic terranes (Freyssinet et al., 2005; Butt and Cluzel, 2013). The study area (East Sulawesi ophiolite) is an accretionary terrane. Tectonic uplift plays an important role in the development of Ni-rich laterite profile since it forms faults and joints, which promote physical and chemical weathering along them (Cluzel and Vigier, 2008; Wells et al., 2009; Golightly, 2010; Butt and Cluzel, 2013; Furnes et al., 2014; Villanova-de-Benavent et al., 2014; Tauler et al., 2017). According to field observations, there is a thrust in the vicinity of the study area that uplifts the peridotite. The occurrence of garnierite, both as coatings and veins, along the joints and faults indicates that its precipitation was synchronous with the tectonic uplift. This process of garnierite precipitation is similar to the previous work on the supergene nickel deposit in New Caledonia (Cluzel and Vigier, 2008). Further, serpentine veins that crosscut the pre-existing serpentines and have a higher amount of Ni (**Figures 3D,H**) are a different type of serpentine that were probably formed after the bedrock was exposed to the surface (Tupaz et al., 2020). The occurrence of the crosscutting serpentine veins indicates that the bedrock was constantly weathered since its uplift. In addition, talc-like garnierite was not observed when the degree of weathering was low because the garnierite-forming solution did not become supersaturated (Tupaz et al., 2020b). This suggests that the Morowali Ni-laterite deposit is part of a good drainage system since it shows the presence of talc-like garnierite. The tropical weather of the study area supplies enough water, with an annual rainfall >1800 mm (Butt and Cluzel, 2013; Fu et al., 2014).

These mineralogical and textural characteristics of secondary alteration minerals, and uplifted tectonic setting indicate that the serpentinization had been occurred before uplift, and the uplift influenced the development of the Morowali Ni-laterite deposit.

Development of Laterite Profile

During laterization, water moves downward along the joints and fractures causing fluctuations in the water table, and leaches soluble elements from the host rock causing chemical reactions within the joints and fractures. The enrichment of immobile elements such as Fe, Al, Mn, Cr, and Ti in the limonite horizon is the result of weathering since as the water steadily moves downward, it leaves the immobile elements in the upper horizon (**Figures 7A–D,I**). The main dissolution reactions for element leaching can be explained by the equilibrium between mineral solubility and ion exchange (Golightly, 1981). Olivine dissolves first, followed by pyroxene, serpentine, talc, Ni-bearing minerals (nepouite and kerolite), gibbsite, and goethite (Golightly, 1981; Golightly, 2010). These mineral solubilities are controlled by pH, and increase as pH decreases, except for quartz (Golightly, 2010). Therefore, the degree of weathering can be inferred from the minerals in the horizon. Weathering of the primary minerals cause leaching of soluble alkaline elements (**Figures 7E,F**), and poorly crystalline Fe oxides, mostly goethite, and smectites are precipitated, which contain the Ni released from olivine and serpentine (Humphris and Thompson, 1978; Freyssinet et al., 2005). This observation is reflected in the relatively high NiO of the limonite horizon compared to the bedrock (**Figure 7H**). Alkaline elements prefer to remain in solution rather than precipitate as secondary minerals (Aiuppa et al., 2000), while the relatively immobile Fe and Al replace the element present in the dioctahedral site of smectite (Manceau and Calas, 1985). Continued weathering hydrolyzes the smectites, which causes the enrichment of Fe oxides with Al in the upper horizon (**Figure 8**). Repetition of this process increases porosity, which allows the solution to percolate easily (Freyssinet et al., 2005). This solution might be Ni-rich because during the reprecipitation of Fe oxides in the upper horizon, the Ni contained in goethite is released and incorporated in the garnierite-forming solution.

The garnierite-forming solution percolates downward until it reaches the depth where garnierite can be formed. Formation of garnierite is influenced by the pH; for example, a sudden change in pH from acidic to alkaline oversaturates the garnierite-forming solution causing garnierite precipitation (Golightly, 1979). In this process, Ni replaces Mg in the octahedral site of serpentine or other weathering products of the primary minerals because of their similar ionic radii, leading to Ni enrichment in the saprolite horizon.

The index of lateritization (IOL) was used to verify the degree of laterization (**Figure 9**). The IOL values divide the samples according to the degree of weathering (weak, moderate, and strong). The range of IOL values for the studied bedrock, saprolite, and limonite were 19.87–20.05, 17.18–22.7, and 96.57, respectively. The similar low IOL values of the bedrock and saprolite imply that the Morowali Ni laterite deposit underwent weak weathering in the saprolite horizon. In the Kolonodale deposit, the weathering of the saprolite horizon is also weakly weathered but more evolved than the Morowali deposit. However, high IOL values for the limonite horizon in the two deposits suggest that it is strongly weathered, leading to the formation of a thick limonite horizon and high Ni concentration in the saprolite horizon (Tupaz et al., 2020). In the Morowali Ni-laterite deposit, the saprolite and limonite horizons are 2–7 m thick, and the boundary between the two horizons is undulatory. In the Kolonodale deposit, the high Ni concentrated talc-like garnierite is observed (**Figure 6**), but some limonite is weakly weathered. Therefore, Ni concentration in the

saprolite horizon and the development of garnierite can differ depending on the location and degree of weathering.

Model of Morowali Ni-Laterite Deposit

Several generic evolution models have been proposed for laterite deposits (Golightly (1981); Freyssinet et al. (2005); Butt and Cluzel (2013). More specific models have been suggested based on these models. For example, Cathelineau et al. (2016) and Mongelli et al. (2019) insisted on the redistribution model for garnierite-forming elements in New Caledonia and Iran, respectively, while Fu et al. (2018) suggested a preferential flow model, in which preferential flow is the driving force for the Ni-rich solution. The redistribution model is that the pre-existing elements in the host rock are redistributed and formed nickel ore minerals according to changes in groundwater level or wet-dry season. The preferential flow model is that the precipitation of garnierite occurs mainly along preferential flow pathways, which are the pathways for water preferred to flow such as chemical and geological channels. The formation of the Morowali deposit corresponds to the prevalent models combined with the redistribution model.

Since its tectonic uplift in the Late Oligocene (Hall and Wilson, 2000), the serpentinized eastern Sulawesi ophiolite has undergone weathering because of the tropical climate of Indonesia due to large amount of precipitation, and the primary minerals in the bedrock have altered to smectite group minerals. In the process of laterization, immobile elements (Fe, Al, Mn, Cr, and Ti) remained in the upper horizons, and soluble elements (Mg and Si) were leached from the bedrock. The upper horizon has an oxidizing environment that results in the enrichment of redox-sensitive elements and the formation of Fe oxides (Robb, 2005). The Ni in olivine or serpentine is leached during weathering of the bedrock and reprecipitated in the Fe oxides, mostly goethite (Freyssinet et al., 2005).

As the dry and rainy seasons repeat, the water table fluctuates due to the meteoric water percolating into the bedrock that leads to redistribution of Ni preserved in goethite and formation of garnierite. The acidic meteoric water infiltrates the fractures and joints due to continued uplift. In this process, the Ni adsorbed in goethite, which is in the upper horizon, is leached and migrates downward with the solution (Freyssinet et al., 2005). The transported Ni reacts with the weathering products of ferromagnesian minerals by replacing Mg with Ni and finally producing a serpentine-like garnierite (Freyssinet et al., 2005; Butt, 2016). In the deeper horizon, the garnierite-forming solution percolates along the faults and joints and precipitates secondary talc-like garnierite with low FeO content (<0.5 wt% FeO), occurring as coatings between two blocks of serpentinized bedrock. According to Cathelineau et al. (2016), the talc-like garnierite-forming solution reaches the surface via vertical veins that were synchronous with faulting activity and joints, which contained early formed Ni-rich minerals, thus having high Ni content. However, the talc-like garnierite in this study had a low Ni content, suggesting that the talc-like garnierite-forming solution was a low-Ni-bearing fluid that originated in the saprolite horizon and precipitated garnierite from the outside of the horizontal vein. The garnierite and quartz mineralization occur in the dry season (Cathelineau et al., 2016; Mongelli et al., 2019).

However, the Ni-enriched vertical vein was not observed during the field investigation, which might be due to the frequent erosion of the laterite deposit during the rainy season. Cathelineau et al. (2016) found large Ni-bearing veins in their study area (New Caledonia) during open-pit mining, and they showed that changes in garnierite mineralization occurred within a few months. This means that large Ni-bearing veins can emerge from the Morowali deposit by continuing open-pit mining.

CONCLUSION

1) The Morowali Ni-laterite deposit in Indonesia is developed on the eastern Sulawesi ophiolite, and the host rock is mainly serpentinized harzburgite. The lateritic profile of the deposit is classified into three horizons: saprolite, limonite, and ferruginous cap from bottom to top. The boundaries of each horizon are irregular and undulatory. The main Ni ore is garnierite, which is a hydrous Mg-silicate, and is concentrated in the saprolite horizon. Garnierite is amorphous and exists as veins and coatings.
2) The studied garnierites can be chemically distinguished into serpentine- and talc-like. From the Fe (immobile) content, which is an indicator of the precipitation sequence of garnierite, it was inferred that the serpentine-like garnierite precipitated earlier than the talc-like garnierite. Both creamy yellow and grass green-colored varieties of serpentine-like garnierites originated from the surrounding serpentine. The creamy yellow garnierite was more weathered than the grass green garnierite. The low Ni concentration of talc-like garnierite suggest that they are secondary in nature, originating from saprolite and/or serpentine-like garnierite.
3) The laterite horizon in the Morowali deposit is formed by hydrous weathering. The weathered host rock shows a mesh-like texture resulting from olivine alteration and is composed of secondary minerals such as serpentine and clay minerals. These mineralogical changes caused the enrichment of immobile elements such as Fe, Al, Cr, Mn, and Ti in the limonite horizon, and soluble cations such as Mg are replaced by Ni in the saprolite horizon.
4) The Morowali Ni-laterite deposit is formed by the typical laterization and redistribution process. The tropical climate in the Morowali deposit is a driving force for the dissolution of Mg and Si during the rainy season and the precipitation of garnierite during the dry season. Since the uplift of the eastern Sulawesi ophiolite, chemical reactions occurred within the syntectonic faults and joints during laterization, and serpentine-like garnierite precipitated by replacing the Mg in lizardite with the Ni in solution. After syntectonic faults and joints were formed, meteoric water infiltrated along them to

form talc-like garnierite in the joints within the lower saprolite horizon.

DATA AVAILABILITY STATEMENT

The original contributions presented in the study are included in the article/supplementary material, further inquiries can be directed to the corresponding author.

AUTHOR CONTRIBUTIONS

YC, IL and IM carried out this study. All authors participated in field work. YC conducted analyses, and prepared manuscript and figures. IL and IM supervised all the process and gave advice on the manuscript. All authors reviewed the content of the work and agreed to be accountable for the manuscript.

FUNDING

This research is financially supported by projects 0409-20200243 and 0409-20210067 from National Research Foundation of Korea.

ACKNOWLEDGMENTS

We thank National Center for Inter-University Research Facility (NCIRF) for analyses, and the BK21 program from Seoul National University, Republic of Korea.

REFERENCES

Aiuppa, A., Allard, P., D'Alessandro, W., Michel, A., Parello, F., Treuil, M., et al. (2000). Mobility and Fluxes of Major, Minor and Trace Metals during basalt Weathering and Groundwater Transport at Mt. Etna Volcano (Sicily). *Geochimica et Cosmochimica Acta* 64 (11), 1827–1841. doi:10.1016/s0016-7037(00)00345-8

Barnes, S.-J., and Lightfoot, P. C. (2005). Formation of Magmatic Nickel-Sulfide Ore Deposits and Processses Affecting Their Copper and Platinum-Group Element Contents. *Econ. Geology*. 100th Anniversary volume, 179–213. doi:10.5382/av100.08

Brand, N. (1998). Nickel Laterites: Classification and Features. *AGSO J. Aust. Geol. Geophys.* 17, 81–88

Brindley, G. W., and Hang, P. T. (1973). The Nature of Garnierites-I Structures, Chemical Compositions and Color Characteristics. *Clays and Clay Minerals* 21 (1), 27–40. doi:10.1346/ccmn.1973.0210106

Brindley, G. W. (1980). The Structure and Chemistry of Hydrous Nickel-Containing Silicate and Nickel-Aluminium Hydroxy Minerals. *bulmi* 103 (2), 161–169. doi:10.3406/bulmi.1980.7391

Butt, C. R. M., and Cluzel, D. (2013). Nickel Laterite Ore Deposits: Weathered Serpentinites. *Elements* 9 (2), 123–128. doi:10.2113/gselements.9.2.123

Butt, C. R. M. (2016). The Development of Regolith Exploration Geochemistry in the Tropics and Sub-tropics. *Ore Geology. Rev.* 73, 380–393. doi:10.1016/j.oregeorev.2015.08.018

Cathelineau, M., Quesnel, B., Gautier, P., Boulvais, P., Couteau, C., and Drouillet, M. (2016). Nickel Dispersion and Enrichment at the Bottom of the Regolith: Formation of Pimelite Target-like Ores in Rock Block Joints (Koniambo Ni deposit, New Caledonia). *Miner Deposita* 51 (2), 271–282. doi:10.1007/s00126-015-0607-y

Cluzel, D., and Vigier, B. (2008). Syntectonic Mobility of Supergene Nickel Ores of New Caledonia (Southwest Pacific). Evidence from Garnierite Veins and Faulted Regolith. *Resource Geology.* 58 (2), 161–170. doi:10.1111/j.1751-3928.2008.00053.x

Dalvi, A. D,, Bacon, W. G., and Osborne, R. C. (2004). "The Past and the Future of Nickel Laterites," in *PDAC 2004 International Convention, Trade Show & Investors Exchange: Toronto: the Prospectors and Developers Association of Canada* (Ontario, Canada: Inco Limited), 1–27

Elias, M. (2002). "Nickel Laterite Deposits-Geological Overview, Resources and Exploitation," in *Giant Ore Deposits: Characteristics, Genesis and Exploration* (Chania, Crete, Greece: CODES Special Publication), 4, 205–220

Freyssinet, P., Butt, C., Morris, R., and Piantone, P. (2005). Ore-forming Processes Related to Lateritic Weathering. *Econ. Geology*. 100th Anniversary volume, 681–722. doi:10.5382/av100.21

Fu, W., Yang, J., Yang, M., Pang, B., Liu, X., Niu, H., et al. (2014). Mineralogical and Geochemical Characteristics of a Serpentinite-Derived Laterite Profile from East Sulawesi, Indonesia: Implications for the Lateritization Process and Ni Supergene Enrichment in the Tropical Rainforest. *J. Asian Earth Sci.* 93, 74–88. doi:10.1016/j.jseaes.2014.06.030

Fu, W., Zhang, Y., Pang, C., Zeng, X., Huang, X., Yang, M., et al. (2018). Garnierite Mineralization from a Serpentinite-Derived Lateritic Regolith, Sulawesi Island, Indonesia: Mineralogy, Geochemistry and Link to Hydrologic Flow Regime. *J. Geochemical Exploration* 188, 240–256. doi:10.1016/j.gexplo.2018.01.022

Furnes, H., De Wit, M., and Dilek, Y. (2014). Four Billion Years of Ophiolites Reveal Secular Trends in Oceanic Crust Formation. *Geosci. Front.* 5 (4), 571–603. doi:10.1016/j.gsf.2014.02.002

Gleeson, S. A., Herrington, R. J., Durango, J., Velásquez, C. A., and Koll, G. (2004). The Mineralogy and Geochemistry of the Cerro Matoso S.A. Ni Laterite Deposit, Montelibano, Colombia. *Econ. Geology.* 99 (6), 1197–1213. doi:10.2113/gsecongeo.99.6.1197

Golightly, J. (1981). Nickeliferous Laterite Deposits. *Econ. Geology. 75th Anniversary* 1905-1980, 710–734. doi:10.5382/av75.18

Golightly, J. (1979). "Nickeliferous Laterites: A General Description," in *International Laterite Symposium Proceedings* (New Orleans: Society of Mining Engineers, American Institute of Mining, Metallurgical, and Petroleum Engineers), 38–56

Golightly, J. (2010). Progress in Understanding the Evolution of Nickel Laterites. *The Challenge Finding New Mineral. Resources: Glob. Metallogeny, Innovative Exploration, New Discoveries* 2, 451–475. doi:10.5382/sp.15.2.07

Hall, R. (1997). Cenozoic Plate Tectonic Reconstructions of SE Asia. *Geol. Soc. Lond. Spec. Publications* 126 (1), 11–23. doi:10.1144/gsl.sp.1997.126.01.03

Hall, R., and Wilson, M. E. J. (2000). Neogene Sutures in Eastern Indonesia. *J. Asian Earth Sci.* 18 (6), 781–808. doi:10.1016/s1367-9120(00)00040-7

Humphris, S. E., and Thompson, G. (1978). Trace Element Mobility during Hydrothermal Alteration of Oceanic Basalts. *Geochimica et cosmochimica acta* 42 (1), 127–136. doi:10.1016/0016-7037(78)90222-3

Kadarusman, A., Miyashita, S., Maruyama, S., Parkinson, C. D., and Ishikawa, A. (2004). Petrology, Geochemistry and Paleogeographic Reconstruction of the East Sulawesi Ophiolite, Indonesia. *Tectonophysics* 392 (1-4), 55–83. doi:10.1016/j.tecto.2004.04.008

Katili, J. A. (1978). Past and Present Geotectonic Position of Sulawesi, Indonesia. *Tectonophysics* 45 (4), 289–322. doi:10.1016/0040-1951(78)90166-x

Klein, F., Bach, W., Humphris, S. E., Kahl, W.-A., Jöns, N., Moskowitz, B., et al. (2014). Magnetite in Seafloor Serpentinite--Some like it Hot. *Geology* 42 (2), 135–138. doi:10.1130/g35068.1

Manceau, A., and Calas, G. (1985). Heterogeneous Distribution of Nickel in Hydrous Silicates from New Caledonia Ore Deposits. *Am. Mineral.* 70 (5-6), 549–558

Mongelli, G., Taghipour, B., Sinisi, R., and Khadivar, S. (2019). Mineralization and Element Redistribution in the Chah-Gheib Ni-Laterite Ore Zone, Bavanat, Zagros Belt, Iran. *Ore Geology. Rev.* 111. 102990. doi:10.1016/j.oregeorev.2019.102990

Monnier, C., Girardeau, J., Maury, R. C., and Cotten, J. (1995). Back-arc basin Origin for the East Sulawesi Ophiolite (Eastern Indonesia). *Geol* 23 (9), 851–854. doi:10.1130/0091-7613(1995)023<0851:baboft>2.3.co;2

Mudd, G. M. (2010). Global Trends and Environmental Issues in Nickel Mining: Sulfides versus Laterites. *Ore Geology. Rev.* 38 (1-2), 9–26. doi:10.1016/j.oregeorev.2010.05.003

Mudd, G. M., and Jowitt, S. M. (2014). A Detailed Assessment of Global Nickel Resource Trends and Endowments. *Econ. Geology.* 109 (7), 1813–1841. doi:10.2113/econgeo.109.7.1813

Nesbitt, H. W., and Bricker, O. P. (1978). Low Temperature Alteration Processes Affecting Ultramafic Bodies. *Geochimica et Cosmochimica Acta* 42 (4), 403–409. doi:10.1016/0016-7037(78)90271-5

Parkinson, C. (1998). Emplacement of the East Sulawesi Ophiolite: Evidence from Subophiolite Metamorphic Rocks. *J. Asian Earth Sci.* 16 (1), 13–28. doi:10.1016/s0743-9547(97)00039-1

Proenza, J. A., Lewis, J. F., Galí, S., Tauler, E., Labrador, M., Melgarejo, J., et al. (2008). Garnierite Mineralization from Falcondo Ni-Laterite deposit (Dominican Republic). *Macla* 9, 197–198

Robb, L. J. (2005). *Introduction to Ore-Forming Processes*. United States: Blackwell Publishing

Soler, J. M., Cama, J., Gali, S., Meléndez, W., Ramírez, A., and Estanga, J. (2008). Composition and dissolution kinetics of garnierite from the Loma de Hierro Ni-laterite deposit, Venezuela. *Chem. Geology.* 249 (1-2), 191–202. doi:10.1016/j.chemgeo.2007.12.012

Springer, G. (1974). Compositional and Structural Variations in Garnierites. *Can. Mineral.* 12 (6), 381–388

Stevens, C., McCaffrey, R., Bock, Y., Genrich, J., Endang, C., Subarya, C., et al. (1999). Rapid Rotations about a Vertical axis in a Collisional Setting Revealed by the Palu Fault, Sulawesi, Indonesia. *Geophys. Res. Lett.* 26 (17), 2677–2680. doi:10.1029/1999gl008344

Sufriadin, S., Idrus, A., Pramumijoyo, S., Warmada, I. W., and Imai, A. (2011). Study on Mineralogy and Chemistry of the Saprolitic Nickel Ores from Soroako, Sulawesi, Indonesia: Implication for the Lateritic Ore Processing. *J. Appl. Geology.* 3 (1), 23–33. doi:10.22146/jag.7178

Tauler, E., Lewis, J. F., Villanova-de-Benavent, C., Aiglsperger, T., Proenza, J. A., Domènech, C., et al. (2017). Discovery of Ni-Smectite-Rich Saprolite at Loma Ortega, Falcondo Mining District (Dominican Republic): Geochemistry and Mineralogy of an Unusual Case of "hybrid Hydrous Mg Silicate - clay Silicate" Type Ni-Laterite. *Miner Deposita* 52 (7), 1011–1030. doi:10.1007/s00126-017-0750-8

Tauler, E., Proenza, J. A., Galí, S., Lewis, J. F., Labrador, M., García-Romero, E., et al. (2009). Ni-sepiolite-falcondoite in Garnierite Mineralization from the Falcondo Ni-Laterite deposit, Dominican Republic. *Clay miner.* 44 (4), 435–454. doi:10.1180/claymin.2009.044.4.435

Tupaz, C. A. J., Watanabe, Y., Sanematsu, K., Echigo, T., Arcilla, C., and Ferrer, C. (2020). Ni-Co Mineralization in the Intex Laterite Deposit, Mindoro, Philippines. *Minerals* 10 (7), 579. doi:10.3390/min10070579

Van der Ent, A., Baker, A. J. M., Van Balgooy, M. M. J., and Tjoa, A. (2013). Ultramafic Nickel Laterites in Indonesia (Sulawesi, Halmahera): Mining, Nickel Hyperaccumulators and Opportunities for Phytomining. *J. Geochemical Exploration* 128, 72–79. doi:10.1016/j.gexplo.2013.01.009

Villanova-de-Benavent, C., Proenza, J. A., Galí, S., García-Casco, A., Tauler, E., Lewis, J. F., et al. (2014). Garnierites and Garnierites: Textures, Mineralogy and Geochemistry of Garnierites in the Falcondo Ni-Laterite deposit, Dominican Republic. *Ore Geology. Rev.* 58, 91–109. doi:10.1016/j.oregeorev.2013.10.008

Viti, C., and Mellini, M. (1998). Mesh Textures and Bastites in the Elba Retrograde Serpentinites. *ejm* 10 (6), 1341–1360. doi:10.1127/ejm/10/6/1341

Wells, M. A., Ramanaidou, E. R., Verrall, M., and Tessarolo, C. (2009). Mineralogy and crystal Chemistry of "Garnierites" in the Goro Lateritic Nickel deposit, New Caledonia. *ejm* 21 (2), 467–483. doi:10.1127/0935-1221/2009/0021-1910

Wilson, M. E. J., and Moss, S. J. (1999). Cenozoic Palaeogeographic Evolution of Sulawesi and Borneo. *Palaeogeogr. Palaeoclimatol. Palaeoecol.* 145 (4), 303–337. doi:10.1016/s0031-0182(98)00127-8

Conflict of Interest: The authors declare that the research was conducted in the absence of any commercial or financial relationships that could be construed as a potential conflict of interest.

Publisher's Note: All claims expressed in this article are solely those of the authors and do not necessarily represent those of their affiliated organizations, or those of the publisher, the editors and the reviewers. Any product that may be evaluated in this article, or claim that may be made by its manufacturer, is not guaranteed or endorsed by the publisher.

frontiers in Earth Science

ORIGINAL RESEARCH
published: 07 December 2021
doi: 10.3389/feart.2021.772083

Origin and Characteristics of the Shwetagun Deposit, Modi Taung-Nankwe Gold District and the Kunzeik and Zibyaung Deposits, Kyaikhto Gold District in Mergui Belt, Myanmar: Implications for Fluid Source and Orogenic Gold Mineralization

Myo Kyaw Hlaing[1,2]*, *Kotaro Yonezu*[1], *Khin Zaw*[3], *Aung Zaw Myint*[2], *May Thwe Aye*[2] and *Koichiro Watanabe*[1]

[1]Department of Earth Resources Engineering, Kyushu University, Fukuoka, Japan, [2]Department of Geology, University of Yangon, Yangon, Myanmar, [3]Centre of Ore Deposits and Earth Sciences, School of Natural Sciences, University of Tasmania, Hobart, TAS, Australia

The Mergui Belt of Myanmar is endowed with several important orogenic gold deposits, which have economic significance and exploration potential. The present research is focused on two gold districts, Modi Taung-Nankwe and Kyaikhto in the Mergui Belt comparing their geological setting, ore and alteration mineralogy, fluid inclusion characteristics, and ore-forming processes. Both of the gold districts show similarities in nature and characteristics of gold-bearing quartz veins occurring as sheeted veins, massive veins, stockworks to spider veinlets. These gold deposits are mainly hosted by the mudstone, slaty mudstone, greywacke sandstone, slate, and slaty phyllite of Mergui Group (dominantly of Carboniferous age). The gold-bearing quartz veins generally trend from NNE to N-S, whereas some veins strike NW-SE in all deposits. The gold-bearing quartz veins are mainly occurred within the faults and shear zones throughout the two gold districts. Wall-rock alterations at Shwetagun are mainly silicification, chloritization, and sericitization, whereas in Kyaikhto, silicification, carbonation, as well as chloritization, and sericitization are common. At Shwetagun, the gold occurred as electrum grains in fractures within the veins and sulfides. In Kyaikhto, the quartz-carbonate-sulfide and quartz-sulfide veins appeared to have formed from multiple episodes of gold formation categorizing mainly as free native gold grains in fractures within the veins or invisible native gold and electrum within sulfides. At Shwetagun, the ore minerals in the auriferous quartz veins include pyrite, galena, and sphalerite, with a lesser amount of electrum, chalcopyrite, arsenopyrite, chlorite, and sericite. In Kyaikhto, the common mineralogy associated with gold mineralization is pyrite, chalcopyrite, sphalerite, galena, pyrrhotite, arsenopyrite, marcasite, magnetite, hematite, ankerite, calcite, chlorite, epidote, albite, and sericite.

OPEN ACCESS

Edited by:
David R Lentz,
University of New Brunswick
Fredericton, Canada

Reviewed by:
Mohd Basril Iswadi Basori,
National University of Malaysia,
Malaysia
Thierry Bineli Betsi,
Botswana International University of
Science and Technology, Botswana

***Correspondence:**
Myo Kyaw Hlaing
myokyawhlaing.edu.geol@
gmail.com

Specialty section:
This article was submitted to
Economic Geology,
a section of the journal
Frontiers in Earth Science

Received: *07 September 2021*
Accepted: *16 November 2021*
Published: *07 December 2021*

Citation:
Hlaing MK, Yonezu K, Zaw K, Myint AZ, Aye MT and Watanabe K (2021) Origin and Characteristics of the Shwetagun Deposit, Modi Taung-Nankwe Gold District and the Kunzeik and Zibyaung Deposits, Kyaikhto Gold District in Mergui Belt, Myanmar: Implications for Fluid Source and Orogenic Gold Mineralization. Front. Earth Sci. 9:772083. doi: 10.3389/feart.2021.772083

At Shwetagun, the mineralization occurred at a varying temperature from 250 to 335°C, with a salinity range from 0.2 to 4.6 wt% NaCl equivalent. The Kyaikhto gold district was formed from aqueous–carbonic ore fluids of temperatures between 242 and 376°C, low to medium salinity (<11.8 wt% NaCl equivalent), and low CO_2 content. The ore-forming processes of the Shwetagun deposit in the Modi Taung-Nankwe gold district and the Kyaikhto gold district are remarkably comparable to those of the mesozonal orogenic gold systems.

Keywords: Shwetagun, Kyaikhto, Mergui belt, Mesozonal, Orogenic gold systems

INTRODUCTION

The Mergui Belt (MB) is one of the largest and most economically important gold provinces in Myanmar. This belt has a diverse style of mineralization in Myanmar such as orogenic gold deposits (e.g., Modi Taung), vein-type tin and tungsten deposits (e.g., Hermyingyi), and stratabound antimony deposits (e.g., Kaw Hket–Taunggalay–Htimiwa) (Ye Myint Swe et al., 2017; Khin Zaw, 2017; Mitchell, 2018). The MB was intruded by several granitic rocks of the Central Granite Belt of Myanmar (Khin Zaw, 1990) which extends into peninsular Thailand, and these granites form part of the Western Granite Province of Southeast Asian Tin Belts (Cobbing et al., 1986, 1992). The northern part of MB is characterized by high-grade metamorphic rocks such as gneiss, granitoid gneiss, marble, and calc-silicates associated with Late Proterozoic to Mesozoic sedimentary sequences. The southern part of MB consists of Upper Carboniferous to Lower Permian metasedimentary rocks of predominantly Mergui Group and the rocks are metamorphosed to greenschist facies with small zones of amphibolite facies along the margins of the belt, close to major shear zones and granite intrusions (**Figures 1**, **2**; Cobbing et al., 1986, 1992; Schwartz et al., 1995; Mitchell et al., 1999, Mitchell et al., 2004, Mitchell et al., 2007, 2012; Khin Zaw, 1990; 2017, 2019; Khin Zaw et al., 2014a, 2018; Ye Myint Swe et al., 2017; Mitchell, 2018; Myo Kyaw Hlaing et al., 2019).

Orogenic gold deposits are one of the main groups of gold deposits making up a major source of gold produced worldwide (e.g., Groves et al., 1998; Dubé and Gosselin, 2007). They occur in convergent plate margins in accretionary and collisional orogens, indicating subduction-related metamorphic (thermal events) processes in deep-crustal environments (Barley and Groves, 1992; Groves et al., 1998; Goldfarb et al., 2004, 2005; Bierlein et al., 2006, 2009; Groves and Bierlein, 2007). These gold deposits are typically hosted by rocks of greenschist to amphibolite metamorphic grade, and locally up to granulite facies conditions of various ages, displaying variable degrees of deformation (Groves, 1993; Groves et al., 1998, 2003; Goldfarb et al., 2001, 2005, 2015; Connolly, 2010; Tomkins, 2010). Giant orogenic gold deposits are commonly located in second-order structures linked to shear zones and lithospheric-scale faults, indicating first-order fluid conduits (McCuaig et al., 2010; Groves et al., 2018; Davies et al., 2019).

The occurrences of the orogenic gold deposits in Myanmar have been recorded in the form of gold-quartz veins at the Tatlet, Phayaung Taung, Nankwe, Modi Taung, Shwegyin, Kyaiktho, and Russell Island (Shwekyun) areas within the MB (Ye Myint Swe et al., 2017). The belt has been exploited with a combination of the historical and currently available resources and reserves totaling around 4.92 Mt Au (**Figure 1**; Mitchell et al., 1999, 2004; Ye Myint Swe et al., 2017 and references therein). The Shwetagun deposit in the Modi Taung-Nankwe gold district and the Kunzeik, Zibaung and Meyon deposits in the Kyaikhto gold district are located in central to southern parts of Myanmar along the MB (**Figures 1**, **2**; Mitchell et al., 1999, 2004; Ye Myint Swe et al., 2017).

Previous studies on the gold deposits of the MB have only focused on the general geology of central to southern parts of Myanmar, and there is a lack of systematic studies on the district-scale to local geology, geochemistry, ore mineralogy and genesis, and ore-controlling structures of gold deposits in the interior of the Mergui Belt, which limits our knowledge of gold mineralization and the metallogenic process. Here we compare the nature and setting of gold mineralization of the Shwetagun deposit from the Modi Taung-Nankwe gold district with the Kunzeik, Zibaung and Meyon gold deposits from the Kyaikhto gold district and discuss the conditions of ore formation and metallogenesis in a regional tectonic framework based on geology, ore characteristics, alteration mineralogy, and fluid inclusion studies.

REGIONAL GEOLOGIC SETTING

The gold deposits of Myanmar comprise six major north-south trending geological linkages or tectonic terranes/belts (**Figure 1**). The Mogok-Mandalay-Mergui Belt (MMMB) is exposed in a 1,300 km long belt of 20–100 km in width at the western margin of the Sibumasu (**Figures 1**, **2**; Bender, 1983; Mitchell et al., 2004; Gardiner et al., 2014, 2018; Mitchell, 2018). The southern part of MMMB is defined here as Mergui Belt (MB) and it is also known as Slate Belt in Myanmar. We used the term MB as the Slate Belt is a misnomer due to the presence of abundant other lithologies such as sandstones, carbonaceous siltstones, greywackes, and calcareous mudstones rather than slate unit. These lithologies belong to the Mergui Group, running a distinctly north-south direction from Mandalay towards Dawei (Tavoy) and Myeik (Mergui) and southeastward through Phuket, southern Thailand, and eastern Sumatra to Bangka Island in Indonesia. This belt is made up of interbedded slaty mudstones, slate and pebbly wackes, less abundant quartzites, and rare calcareous beds, and the northern part of the belt extend an additional

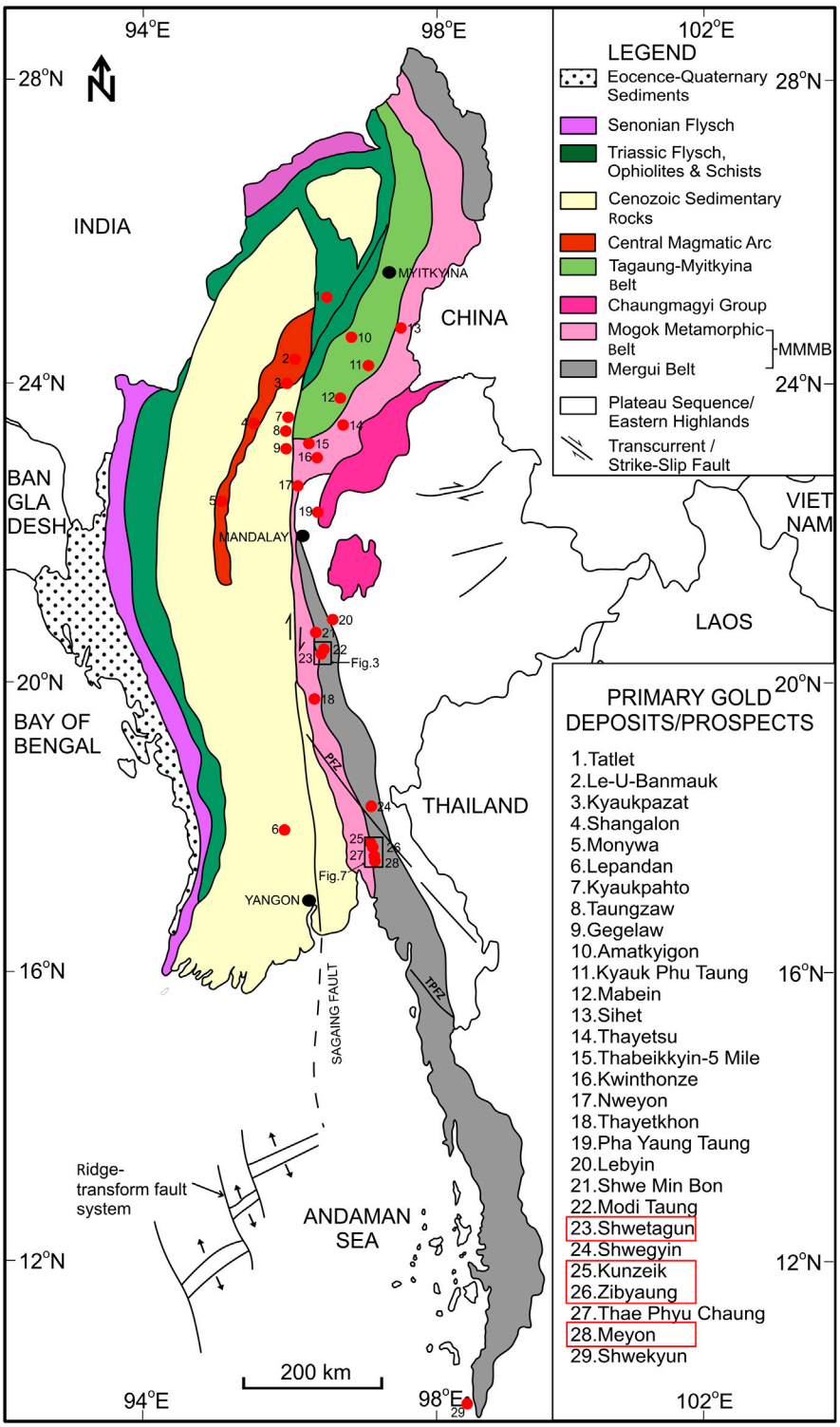

FIGURE 1 | Major structural belts, and gold occurrences in Myanmar (Modified after Mitchell et al., 2004; Ye Min Swe et al., 2017; Myo Kyaw Hlaing et al., 2019), PFZ, Papun Fault Zone; TPFZ, Three Pagodas Pass Fault Zone; MMMB, Mogok-Mandalay-Mergui Belt.

300 km long in the west of the Gaoligong Range in southern China (**Figures 1**, **2**; Mitchell et al., 2004, 2012; Gardiner et al., 2015, 2018; Mitchell, 2018).

The Mogok Metamorphic Belt (MMB) is described as the northern part of the MMMB (**Figures 1**, **2**). Although the local linkages between the MMB and the MB remain an open question

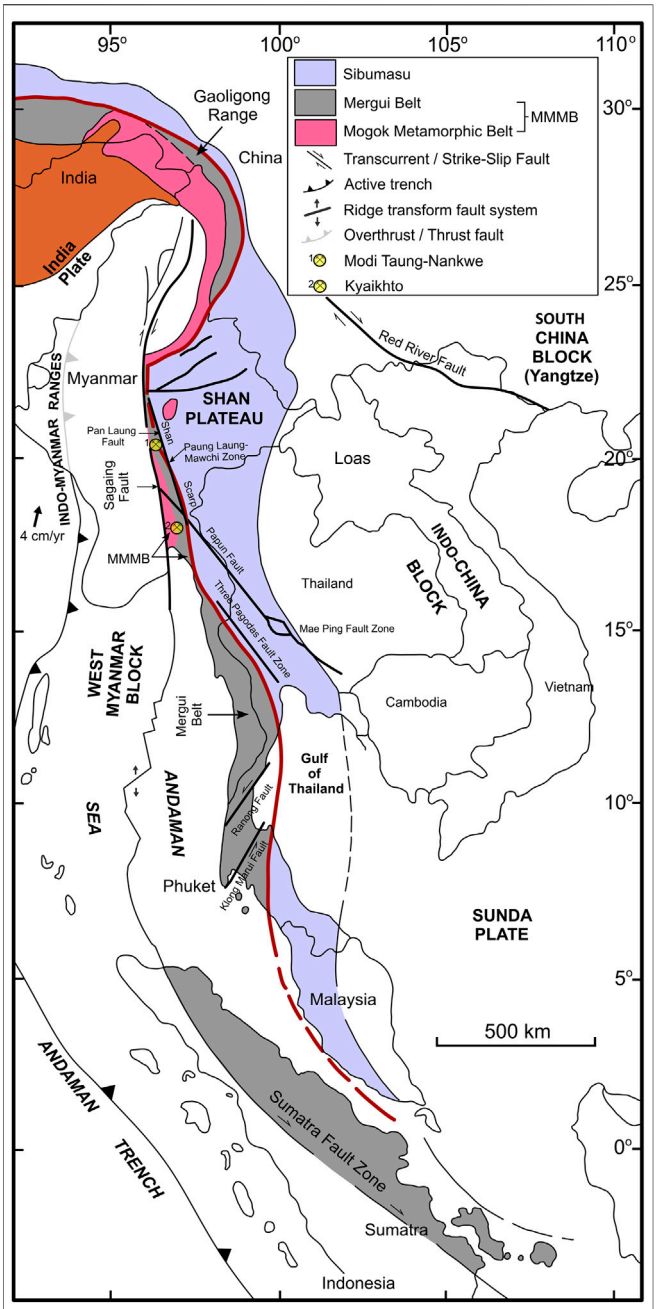

FIGURE 2 | Regional tectonic setting of Myanmar and distribution of Mergui Belt (Gaoligong Range and its southeastward continuation through Thailand into Indonesia). Red line at eastern margin of Mergui Belt is the Medial Myanmar suture zone (Modified after Mitchell, 2018). MMMB, Mogok-Mandalay-Mergui Belt.

(Gardiner et al., 2015), they defined the MB as the southern part of the MMMB. In MMMB, the granites are found in the east of the Sagaing Fault and at the west of the Panlaung-Mawchi Zone, which was located west of the Shan scarps (**Figures 2**, **3**). The MB is bordered on the west by schists, gneisses, marbles, and granites of the MMB (Chhibber, 1934), which are intruded by calc-alkaline dykes and granites (Mitchell et al., 2004). The MB is located along the north-trending zone related to the suturing of the Shan Plateau as part of the Sibumasu (a fragment of Gondwana) and the West Myanmar block, and between the Indo-Myanmar Ranges to the east and the South China block to the south and the Indochina block to the east (**Figures 1**, **2**). The MB consists of several NE-/W-trending faults which are formed within the central to the southern part of Myanmar and are notable for the existence of a large number of orogenic-style gold deposits (**Figures 1**, **2**). Most of the important gold deposits in the MB are associated with the second-order fault, N to NW trending upright folds, 1–6 km long, ductile shear zones, and are best referred to as orogenic gold deposits (e.g., Mitchell et al., 2004). The eastern boundary of the Shwetagun gold deposit in the MB is bordered by the Pan Laung fault, and the eastern margin is represented by the Paung Laung-Mawchi Zone (Shan Scarps) and the strata are dipping steeply to the west from the east of Nankwe to the Sakhanya Taung fault (**Figures 2**, **3**; Mitchell et al., 2004).

The Upper Jurassic rocks of the Paunglaung-Mawchi Zone are overthrusted by the Pan Laung fault along their western margins. The Papun fault lies in the south of the Modi Taung-Nankwe gold district in the MB and MMB, and at the west of the Paunglaung-Mawchi Zone (**Figures 2**, **3**). Gold occurrences in the Kyaikhto area occur close to the NNW–SSE striking Papun fault in the north and the Three Pagodas fault in the south. The Three Pagodas fault is almost parallel to the Papun fault and continuous from the Papun area to the southeast into Thailand, where it is regionally known as the Mae Ping fault or the Wang Chao fault (**Figure 2**; Ridd and Watkinson, 2013). The MB is considered to have formed as a complex fold and thrust belt with the Lower Cretaceous to Middle Miocene of Neo-Tethys accretionary wedge involving major sheared zones (Zaw Naing Oo and Khin Zaw, 2009, 2015, 2017; Khin Zaw et al., 2014a, 2017; Gardiner et al., 2016, 2018). This belt has been reactivated throughout the eastward subduction of continental blocks derived from the India-Asia collision zone to the north and lies north of the active subduction zone of the Sunda-Andaman arc (Mitchell et al., 2004, Zaw Naing Oo et al., 2010; Zaw Naing Oo and Khin Zaw, 2009, 2015, 2017; Khin Zaw et al., 2014a, 2017; Gardiner et al., 2016, 2018).

The MB is originally referred to as the Lower Jurassic regional metamorphic belt of major east-convergence origin that hosts several orogenic gold occurrences (Mitchell et al., 2004, 2012). The gold deposits within the MB are commonly associated with supracrustal rocks or in the vicinity of regional, crustal-scale deformation zones with a brittle to ductile type of deformation (e.g., Mitchell et al., 2004; Mitchell, 2018). The metasedimentary rocks within this belt are intruded by the granitoids of Central Granitoid Belt of Myanmar (or) Western Granite Province of Southeast Asia (**Figures 1**, **2**; Mitchell, 1977; Khin Zaw, 1990; Cobbing et al., 1992; Mitchell et al., 2004, 2012). The MB was also intruded by several generations of granitoid comprising numerous I-type and S-type two-mica granites of Cretaceous-Paleogene age (Khin Zaw, 1990; Cobbing et al., 1992; Barley et al., 2003; Searle et al., 2007; Mitchell et al., 2012; Gardiner et al., 2015, 2018; Aung Zaw Myint et al., 2017). The S-type granites are associated with significant tin-tungsten mineralization (Khin Zaw, 1990, 2017; Gardiner et al., 2014; Aung Zaw Myint et al., 2017; Mitchell, 2018). However, there is no geological evidence of preferential relationships of orogenic-type gold deposits with the

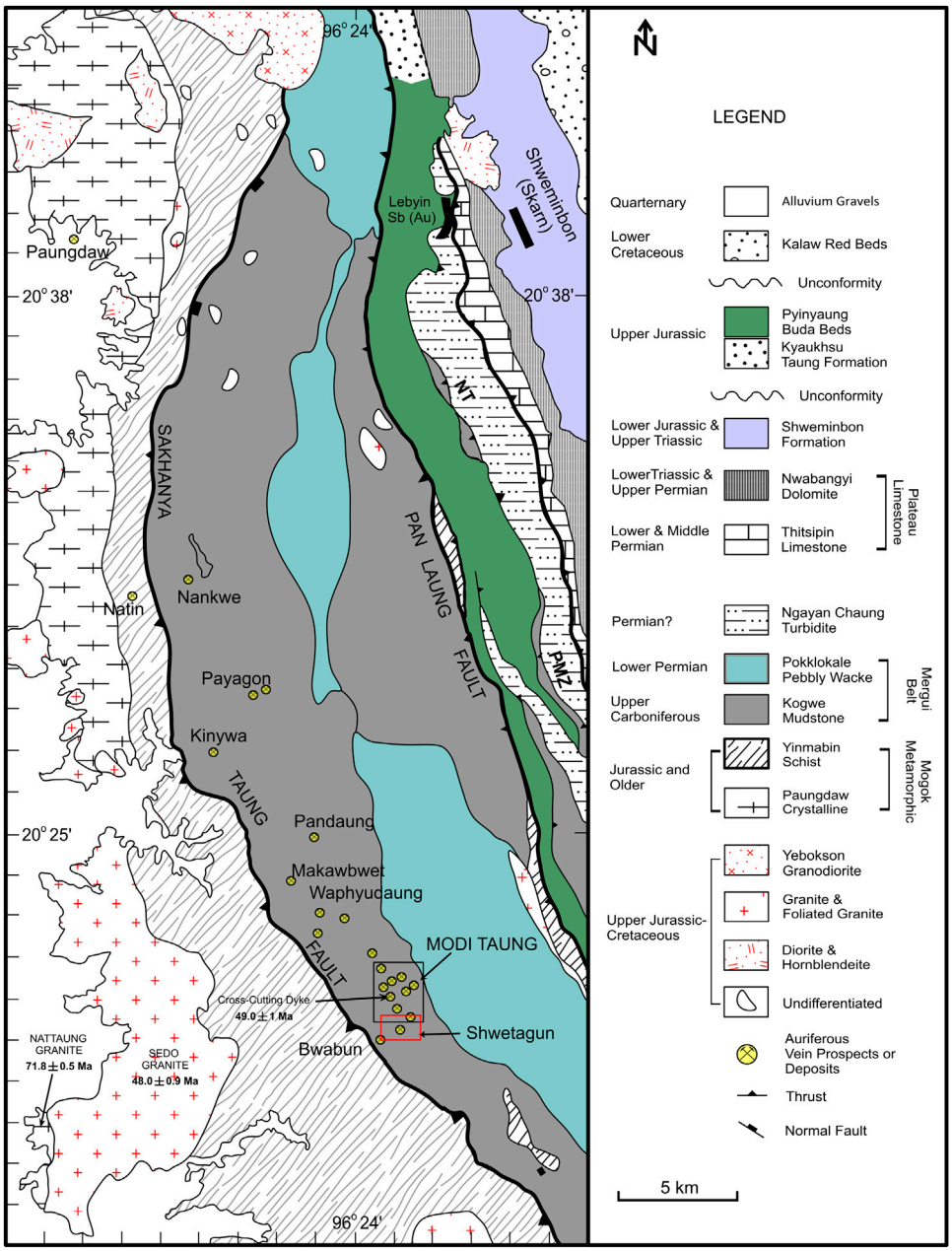

FIGURE 3 | Geological map of the Modi Taung-Nankwe gold district (Modified after Mitchell et al., 2004). NT, Ngapyaw Chaung Thrust; PMZ, Panlaung-Mawchi Zone.

Cretaceous-Eocene granite intrusions (Mitchell et al., 1999, 2004; Gardiner et al., 2014; Mitchell, 2018).

THE GEOLOGY OF GOLD DISTRICTS

Numerous orogenic gold deposits have been discovered in the MB. The Modi Taung-Nankwe and Kyaikhto gold districts lie within the MB from central to southern Myanmar (**Figures 2**, **3**). The geology of the Shwetagun deposit in the southwestern part of the Modi Taung-Nankwe gold district and the Kyaikhto gold district are described below.

Shwetagun Gold Deposit in Modi Taung-Nankwe Gold District

The gold mineralization of the Shwetagun deposit is located about 3 km south of the Modi Taung deposit (**Figures 3**, **4**). The Kogwe mudstone and Poklokkale Pebbly wackestone are mainly exposed at the Shwetagun area (Mitchell et al., 2004; Myo Kyaw Hlaing,

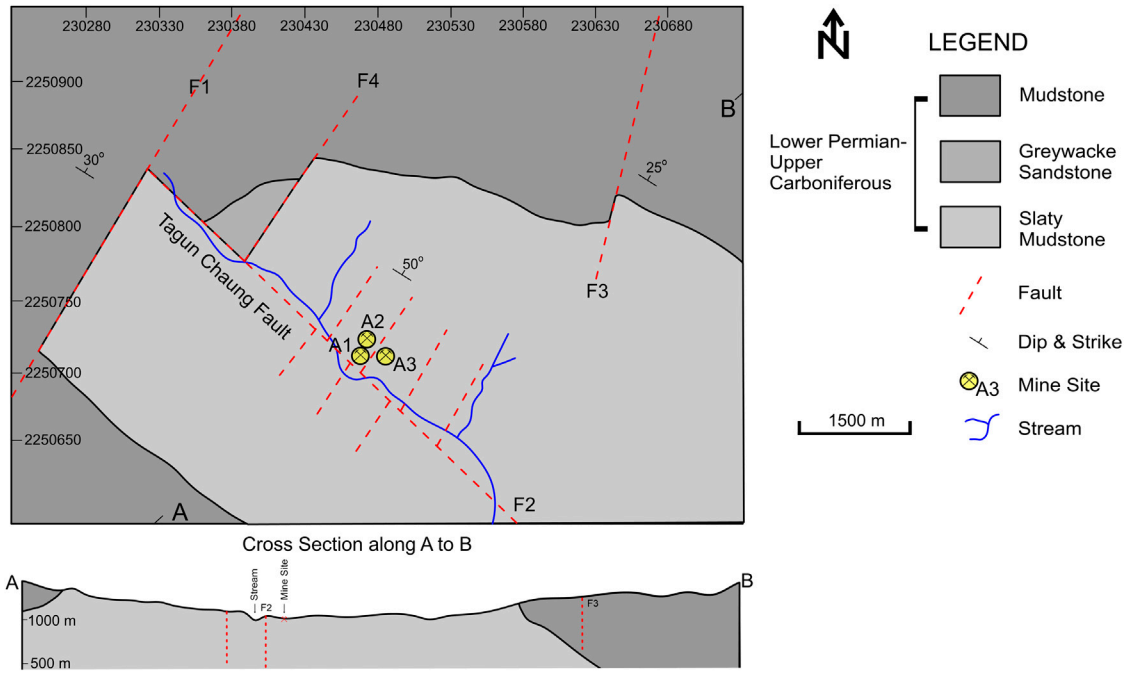

FIGURE 4 | Geological map of the Shwetagun gold deposit, Modi Taung-Nankwe gold district, Myanmar. Abbreviations: A1 = adit-I, A2 = adit-II, A3 = adit-III.

2013; Mitchell, 2018) and the gold mineralized veins are hosted by the Kogwe Mudstone Unit which consists of pebbly mudstone, siltstone and sandstone (Mitchell et al., 2004). Gold-quartz veins are oriented in NE-SW and N-S directions and can be grouped into one of the three vein systems within exploration Adit I, II and III (**Figures 4**, **5A–C**). The Adit I and II are located along the NE-SW strike, whereas Adit III trends north-south. Each vein system consists of either a single vein or multiple parallel veins separated by host rocks. Quartz veins in Adits I and II show stylolitic lamination and sheeted structure (**Figures 5A–C**) which indicate the movement on the shear planes during the formation of gold veins (e.g., Mitchell et al., 2004).

In Adit III, the strong post-vein faulting more or less along the plane of the shear resulted in pinched and swelled structure, and brecciation. F1 and F2 faults are mainly related to the mineralized veins where bedding is usually low angle with southeast-northwest trending fold axes; most veins intersect bedding at a high angle, cut crenulation cleavage where visible, cut the bedding plane, and accompanied by pervasive silicification of the mudstone (**Figures 5A–C**). The general trend of bedding is NE-SW direction paralleling the mineralized veins (**Figure 4**). En-echelon sigmoidal tension gashes filled with barren to weakly auriferous fibrous quartz are widespread in the mudstone sometimes kilometers away from the mineralized veins (**Figures 6A–D**). The tension gash veins in the shear zone imply ductile deformation which is evident for later faulting (**Figure 6C**). The Shwetagun area is structurally complex; there have been at least two or three deformation phases in both small-scale and major structures (e.g., Michell et al., 2004). No igneous rocks have been found at the Shwetagun area, and the nearest igneous rocks to the Modi Taung deposit are the microgranite porphyry at Theingi vein and the late dacite and andesite porphyry dykes which cut across the ore zone at Shwesin vein (Traynor et al., 2015, 2017) and Momi Taung, approximately 3 km northeast of Shwetagun (**Figure 3**).

Kyaikhto Gold District

The Kyaikhto gold district in the southern part of MB consists of several gold deposits and occurrences, including Kunzeik, Zibyaung and Meyon (**Figure 7**). The Kyaikhto gold occurrences are formed as sheeted veins, massive veins, network veinlets, stockworks, and disseminations. The structural setting at the Kyaikhto gold occurrences is dominated by NNE-SSW, and NW-SE striking faults (**Figure 7**). Mineralization in the Kyaikhto gold district is hosted by metasedimentary rocks of sandstone, slate, phyllite, and schist, and associated with the biotite granite and biotite granodiorite (**Figure 7**). The granitic rocks in this area can be correlated to the Mokpalin quartz diorite and the Kyaikhtiyo granite that have yielded the LA-ICP-MS zircon U-Pb ages of 90.8 ± 0.8 Ma and 63.3 ± 0.6 Ma, respectively (**Figure 7**; Mitchell et al., 2012; Myo Kyaw Hlaing et al., 2019). The metamorphic grade of the metasedimentary rocks is greenschist facies, characterized by a mineral assemblage of epidote, biotite, muscovite, and chlorite. Locally, fine-grained pyrite crystals are disseminated in the slate, phyllite, and schist (Myo Kyaw Hlaing et al., 2019).

The quartz vein systems almost invariably appear to be related to regional NNW -SSE trending structures which are commonly recorded along the MB (**Figure 2**). Brecciation and fracturing of the quartz vein contributed favorable sites for supergene gold enrichment processes (Zaw Naing Oo and Khin

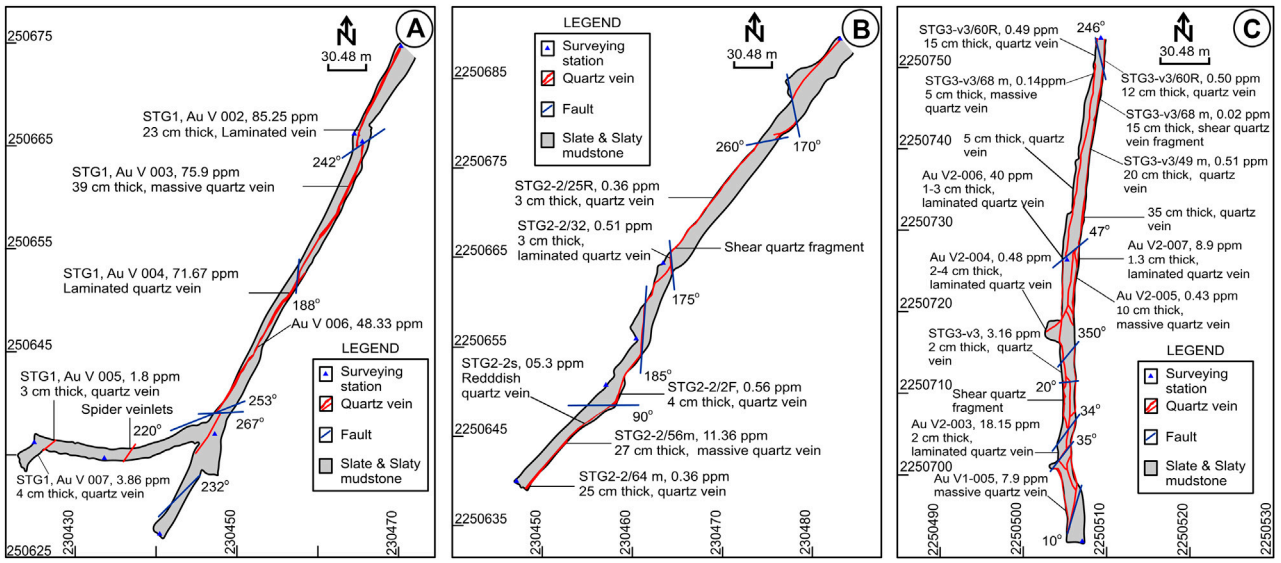

FIGURE 5 | (A) Mineralization map of the adit-I, **(B)** adit-II and **(C)** adit-III at Shwetagun, Modi Taung-Nankwe gold district, Myanmar.

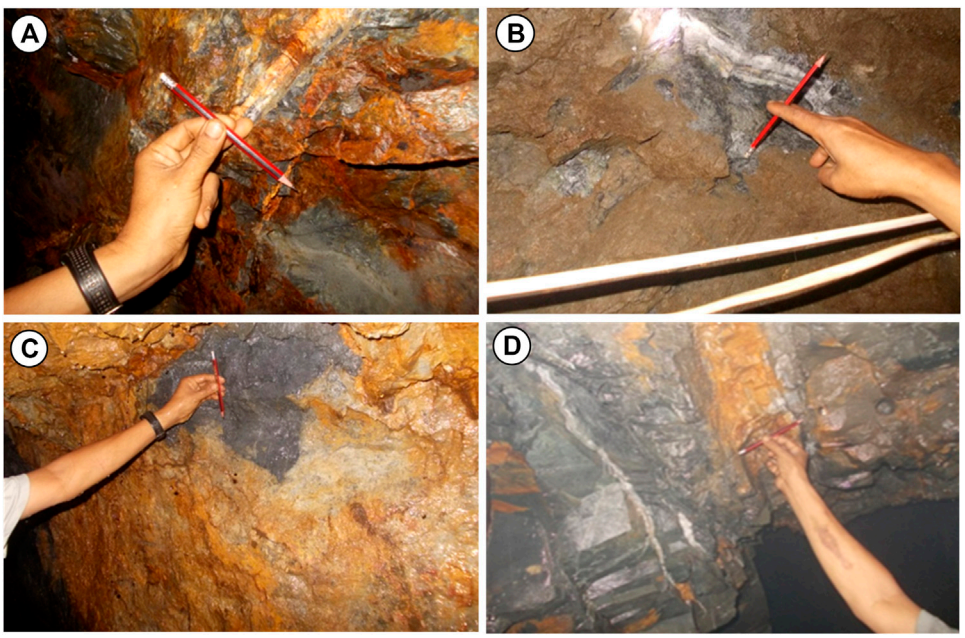

FIGURE 6 | Vein style and texture of the Shwetagun gold deposit. **(A)** Photographs showing auriferous sheeted quartz vein about 10 cm thickness at adit I, **(B)** auriferous sheeted quartz vein about 20 cm thickness at adit I, **(C)** distorted vein by the effects of shear force at adit II and **(D)** nature of auriferous sheeted quartz vein at adit III.

Zaw, 2009; Zaw Naing Oo et al, 2010; Zaw Naing Oo and Khin Zaw, 2015; 2017). The thickness of the tension gash veins and stockwork veins varies from a few 20 cm to 2 m wide. All of these gold deposits feature extensive, steeply dipping, vein systems, usually with multiple stages of vein development. In some deposits, the veins are slightly narrow (1–2 m) and separated, and there may be several parallel veins set within broad structural zones (e.g., Meyon). In other areas, such as at Kunzeik, the multiple vein systems form stockwork structures. At Zibyaung, the mineralized quartz veins are found as white to milky quartz. Mineralization in the Kyaikhto gold district is dominantly related to the deformation of the host rocks and occurred within structurally-controlled dilatant fractures.

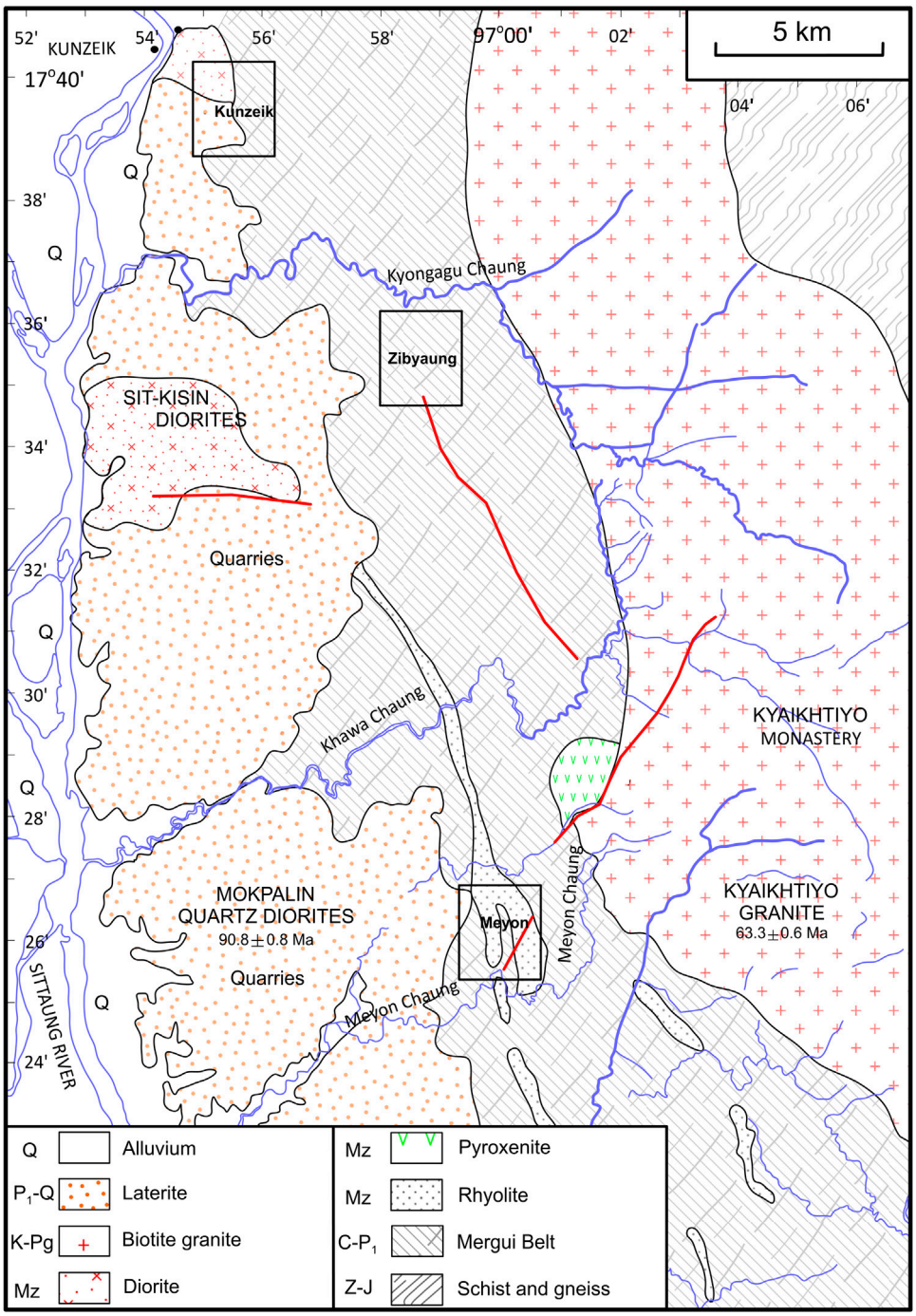

FIGURE 7 | Geological map of the Kyaikhto gold district. Red lines are faults (Modified after Mackenzie et al., 1999; Mitchell et al., 2012; Myo Kyaw Hlaing et al., 2019). Abbreviations: Q = Quaternary, P_1-Q = Lower Pliocene to Quaternary, K-Pg = Cretaceous to Paleogene, Mz = Mesozoic, C-P_1 = Upper Carboniferous to Lower Permian, ZJ = Late Proterozoic to partly Jurassic.

MATERIALS AND ANALYTICAL METHODS

During the years 2012–2018, representative samples of the Shwetagun deposit in the Modi Taung-Nankwe gold district and Kyaikhto gold district were collected from active mining operations. Forty samples were examined using a Rigaku Ultima IV X-ray diffractometer to detect alteration minerals, running at 40 kV and 20 mA with a CuKα varying from 2.0 to 65.0 (2θ).

Forty-five thin sections and seventeen polished sections were prepared for the examination of ore and gangue minerals from

the Shwetagun deposit and Kyaikhto gold occurrences using NIKON ECLIPSE LV100N POL petrographic microscope and the scanning electron microscope (SEM) with energy-dispersive X-ray spectroscopy (EDS) of HITACHI-SU3500 at the Center of Advanced Instrumental Analysis, Kyushu University. SEM-EDS analysis was used to determine the elemental composition of pyrite, chalcopyrite, sphalerite, arsenopyrite, galena, hematite, and other ore minerals, including the Au-Ag ratio of electrum.

Fifteen doubly polished thin sections of mineralized quartz were prepared from the Shwetagun deposit and Kyaikhto gold occurrences for fluid inclusion studies. Microthermometric measurements were conducted at Kyushu University using a Linkam-THMS600 heating-freezing stage equipped on a NIKON ECLIPSE LV100N POL petrographic microscope. The heating/freezing rate was generally 0.2–5.0°C/min but was <0.2°C/min near a phase transition. The uncertainties for the measurements are ±0.5, ±0.2 and ±2.0°C for runs in the range of −120 to −70°C, −70–100°C, and 100–600°C, respectively. The fluid inclusions were classified by the criteria of Roedder (1984). Total salinities of NaCl-H_2O inclusions were calculated from the final melting temperatures of ice using the equation by Bodnar (1993). Salinities of the inclusions of the CO_2-bearing fluid were computed using the melting temperatures of clathrate (Collins, 1979).

RESULTS

Hydrothermal Alteration

Shwetagun Gold Deposit in Modi Taung-Nankwe Gold District

The Shwetagun area comprises several zones of alteration, which occurred in structurally-controlled setting and the general trend is from NS to NE-SW. Two types of hydrothermal alterations are recognized: 1) a regional smectite/illite–chlorite–quartz alteration associated with silicified and slaty mudstone (**Figures 8A–C**); 2) chlorite-sericite-quartz–pyrite alteration associated with gold-quartz veins (**Figures 8A–C**). Chlorite-sericite-quartz–pyrite alteration forms on both sides of the ore veins (**Figures 8A–C**). Petrographic studies and XRD results of alteration mineral assemblages are described schematically in **Table 1**. The smectite/illite–chlorite–quartz alteration zone is dominated by laminated quartz veins with alternating quartz and chlorite-rich layers (**Figures 8A–C**). Smectite/illite–chlorite–quartz alteration forms as the outer zone of chlorite-sericite-quartz–pyrite alteration. The study area is also affected by supergene processes. The chlorite-sericite-quartz–pyrite alteration is overprinted by the secondary minerals (e.g., hematite) that were produced by oxidation process. The three most important hydrothermal alteration processes are silicification, chloritization, and sericitization (**Figures 8B–D**). Silicification occurs as fracture-controlled quartz veins and dense banding and irregular deformation-controlled lenses (**Figure 8D**). The most common alteration process is chloritization, which occurs around gold-bearing quartz veins (**Figure 8C**). There is an orthogonal setting between the intensity of brittle and ductile deformation and the degree of hydrothermal alteration (**Figure 8B**).

Kyaikhto Gold District

The quartz-gold veins in the Kyaikhto gold district are hosted within an intensely deformed sedimentary sequence comprising sandstone and carbonaceous mudstones (Myo Kyaw Hlaing et al., 2019). The host mudstone and phyllite are silicified and hydrothermally altered to assemblages with sericite, chlorite, kaolinite, and pyrite (Myo Kyaw Hlaing et al., 2019). At Kunzeik, the strongly altered rocks adjacent to the auriferous quartz veins are typically enriched in sulfide minerals (e.g., pyrite and chalcopyrite). Silicification and pyritization are easily observable close to the veins. Silicification was followed by sericitization in the felsic host rocks. At Zibyaung, the host phyllite is affected by an earlier (chlorite) alteration and later silicification and sericitization. Chloritization overprinting sericitization becomes more pervasive proximal to the distal parts of ore bodies. At Meyon, hydrothermal alterations are characterized by silicification and chloritization, sericitization, carbonate alteration, kaolinite, and albitic alteration and quartz infill of the metasedimentary rocks and ore breccias are also recorded. Sulfides are sparsely disseminated in the rock and completely altered to limonite (Zaw Naing Oo et al., 2010; Zaw Naing Oo and Khin Zaw, 2015, 2017).

Ore Mineralogy

Microscopically, the ore samples show various mineral assemblages and indications of fracture fillings as well as replacement textures. Based on microscopic observation, there are two types of gold-bearing sulfide ore textures: the disseminated and fracture-filling sulfide types (**Figures 9A,B,D,E**). The electrum occurs as submicron-sized inclusions in the fracture of sulfides at Shwetagun (**Figures 9A,B**). Most of the electrum grains are identified as free grains, but some are intergrown with pyrite, chalcopyrite, galena and sphalerite. Locally, it is concentrated as clumps of irregular electrum grains dispersed in alteration minerals. Some electrum grains are lighter and gradually change to whitish color with very high reflectivity, due to presence of high silver content. The electrum grains at Shwetagun yielded an Au content of 72.9–74.3 atomic %. Sphalerite is one of the major ore minerals and appears in euhedral to subhedral aggregates up to 5 mm in size (**Figure 9C**). The FeS mol% of sphalerite is between 4.02 and 8.41. Chalcopyrite is a primary important hypogene mineral in the ore textures (**Figure 9E**).

Pyrite is the most abundant sulfide mineral at Shwetagun. It occurs as fine-grained, massive aggregate and euhedral to subhedral crystals along the outer margin of the quartz veinlets. The earliest sulfide mineral is invariably pyrite, with deeply fractured sub-euhedral crystals that are locally replaced by other base-metal sulfides (**Figures 9A–E**). A few grains of pyrite are replaced by chalcopyrite along their grain boundaries and microfractures (**Figure 9E**).

At Kunzeik, the quartz-carbonate-sulfide vein consists of chloritized host rock fragments surrounded by irregular to massive aggregates of pyrite, chalcopyrite, and sphalerite

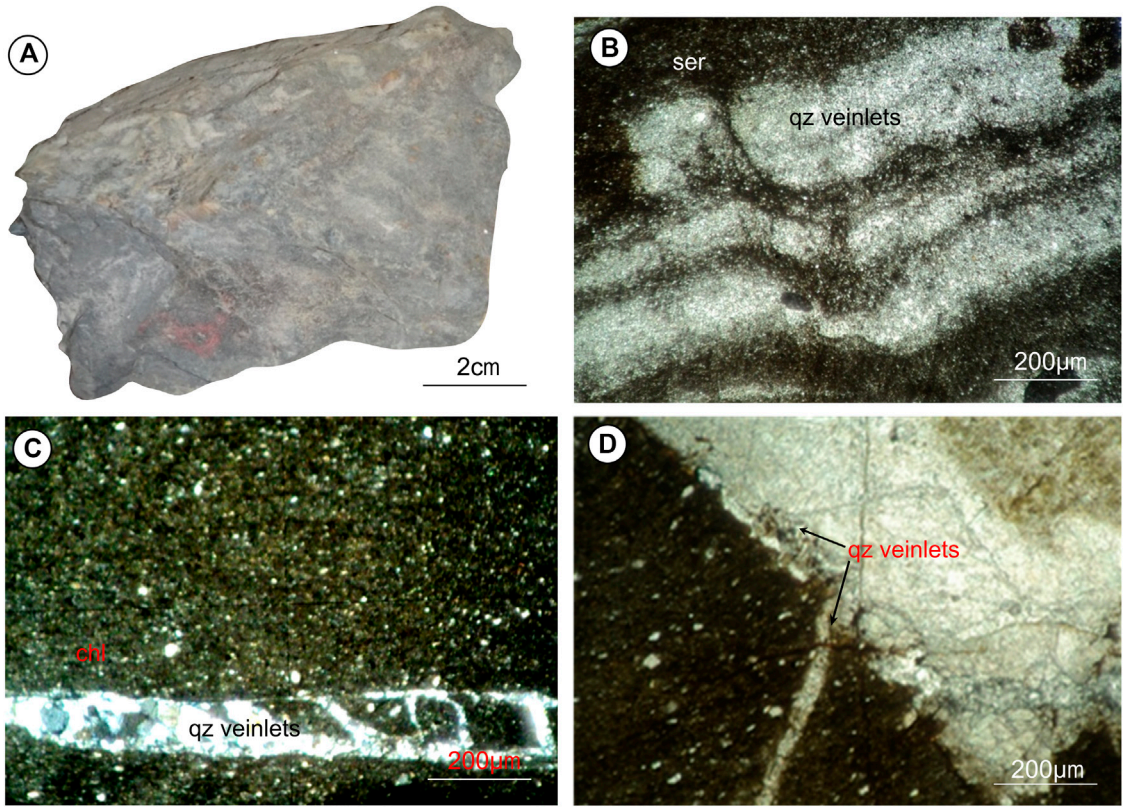

FIGURE 8 | Lithology and microscopic vein texture of the Shwetagun gold deposit. **(A)** Photographs showing slaty mudstone host rock in shear zone from adit I, **(B)** Photomicrographs showing ductile structures with sericite alterations in slaty mudstone from adit II, **(C)** chlorite alterations from adit II and **(D)** Silicification from adit I. Abbreviations: qz = quartz ser = sericite and chl = chlorite.

TABLE 1 | Summary of hydrothermal alteration from orientated samples analyzed by XRD and microscopy.

Deposit Name	Sample No	Rock Name	Kaolinite	Smectite/illite	Sericite	Chlorite	Pyrite
Shwetagun	STG03 (adit-I)	Silicified Mudstone	++	+++	—	+++	—
	STG07 (adit-I)	Greywacke	++	+++	—	+++	—
	STG09 (adit-II)	Slaty Mudstone	++	+++	++	+++	—
	STG10 (adit-II)	Slaty Mudstone	++	+++	—	+++	—
	STG14 (adit-III)	Slate	++	+++	+++	+++	+
Kunzeik	KZ04	Slate	++	+++	+++	++	+
	KZ05	Slate	++	+++	+++	+++	+
Zibyaung	ZB06	Slaty phyllite	++	+++	+++	++	+
	ZB07	Slaty phyllite	++	+++	+++	+	+

Notes: +++ Common, ++ Few, + Rare, - Not Detected.

together with quartz and chlorite (**Figure 9F**; Myo Kyaw Hlaing et al., 2019). Electrum, sphalerite, and galena are mostly found in pyrite at Zibyaung (**Figures 9G,H**; Myo Kyaw Hlaing et al., 2019). Sphalerite forms as a fissure filling mineral within pyrite. Galena occurs as fine-to medium-sized grains filling cracks in pyrite and sphalerite. Electrum grains with an atomic % of 74.5–78.1 Au can be detected as minute grains in pyrite with galena, and sphalerite (**Figure 9F–H**). The FeS mol% of sphalerite ranges from 4.98 to 7.26. At Meyon, chalcopyrite is associated with pyrite and covellite. Covellite occurs as a secondary replacement mineral of chalcopyrite (Myo Kyaw Hlaing et al., 2019). Native gold also develops as free grains in the oxidized zone and fracture fillings within pyrite. Pyrite occurs as two generations, idiomorphic grains intergrown with chlorite aggregates or in contact with massive chalcopyrite, pyrrhotite, arsenopyrite, marcasite, magnetite and hematite (Zaw Naing Oo and Khin Zaw, 2009; Zaw Naing Oo et al, 2010; Zaw Naing Oo and Khin Zaw, 2015; 2017; Myo Kyaw Hlaing et al., 2019).

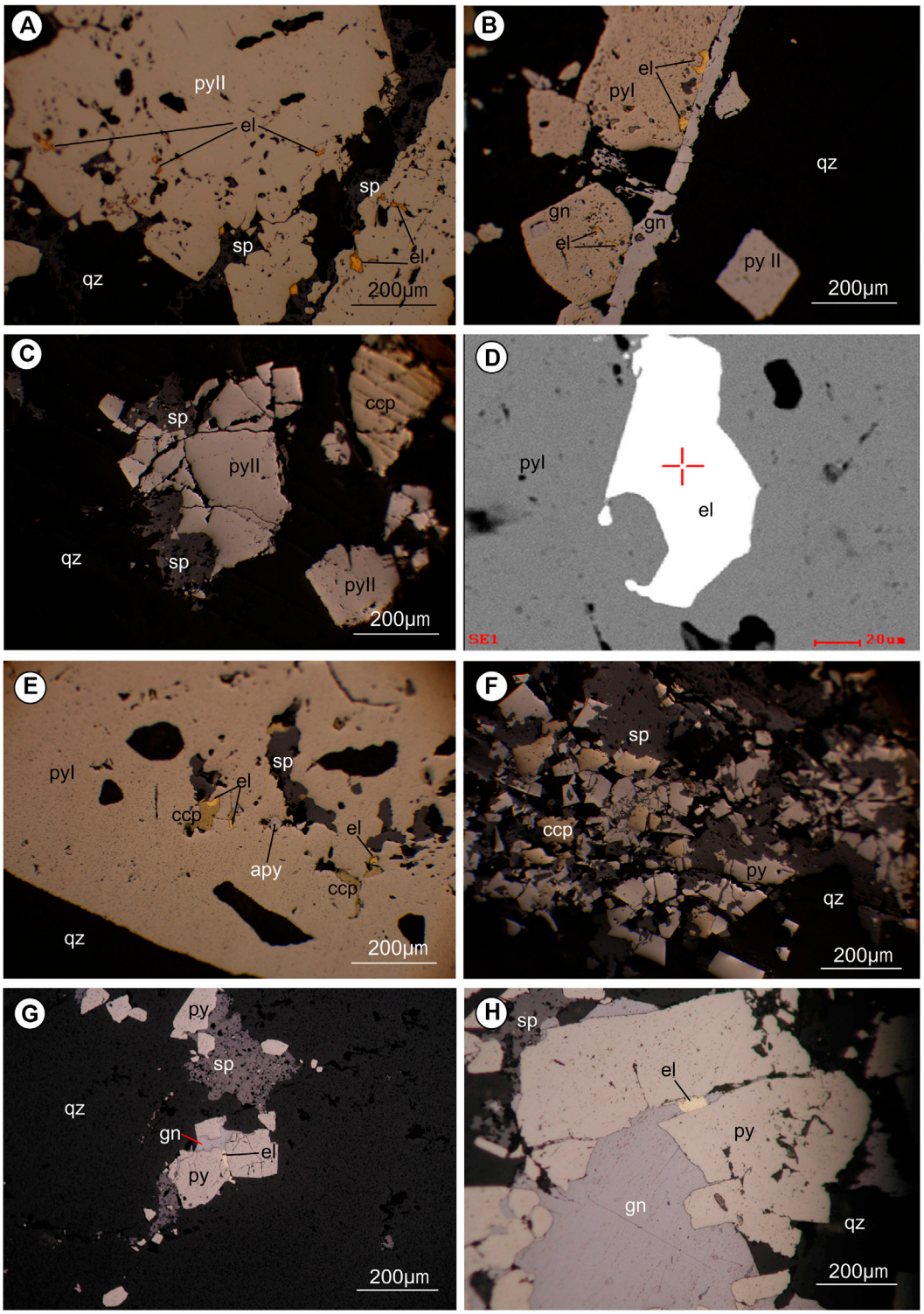

FIGURE 9 | Photomicrographs showing **(A)** electrum inclusion in subhedral pyrite (py II) with sphalerite of the gold-bearing quartz vein in adit-I from Shwetagun, **(B)** fractured electrum filled with euhedral pyrite (py I) and galena, suggesting their chronological relationship of the gold-bearing quartz vein in adit I from Shwetagun, **(C)** euhedral pyrite (py I) associated with sphalerite and chalcopyrite of the gold-bearing quartz vein in adit-III from Shwetagun, **(D)** backscattered electron image with an electrum grain in pyrite from Shwetagun, **(E)** electrum inclusion is surrounded by chalcopyrite, sphalerite and arsenopyrite in pyrite from Shwetagun, **(F)** massive pyrite aggregates with chalcopyrite, and sphalerite of quartz-carbonate-sulfide vein from the Kunzeik, **(G)** and **(H)** fractured electrum filled with euhedral pyrite, galena and sphalerite of quartz-sulfide vein from Zibyaung. Figures (g) and (h) are taken from Myo Kyaw Hlaing et al. (2019). Abbreviations: py = pyrite, gn = galena, ccp = chalcopyrite, sp = sphalerite, apy = arsenopyrite, el = electrum and qz = quartz.

Fluid Inclusion Characteristics

Fluid inclusions studies have been performed in quartz, quartz-sulfide and quartz-carbonate-sulfide veins from the Shwetagun, Kunzeik and Zibyaung deposits (**Figures 10A–D**). At Shwetagun, fluid inclusions were found in quartz in the mineralized veins quartz. There are two types of fluid inclusions: Type A (vapor-rich) and Type B (liquid-rich). Type A (vapor-rich) and Type B (liquid-rich) aqueous fluid inclusions were observed in all quartz samples and occur as isolated groups of primary inclusions as clusters and pseudo-secondary trails. Secondary fluid inclusions (trail-bound) are also present but are extremely small (<2 μm) and have not been studied. Most fluid inclusions were aqueous (H_2O) fluid inclusions. At Kunzeik and Zibyaung, two types of fluid inclusions were found in quartz and calcite of quartz-carbonate-sulfide and quartz-sulfide veins at room temperature (**Figures 11A–H**). Based on the criteria described by Roedder (1984), the fluid inclusions were classified as primary, pseudo-secondary, and secondary, and given below: Type A (aqueous-carbonic) inclusions, Type B (aqueous) inclusions.

Type A (*aqueous-carbonic inclusions*): This type belongs to the H_2O–CO_2–NaCl system and occur in quartz and calcite of the mineralized vein quartz. They are 5–10 μm in size and have bi-phase (liquid and vapor) at room temperature. These inclusions also show presence of three phase (liquid H_2O, liquid CO_2, vapor CO_2) and clathrate during freezing runs. The CO_2: H_2O ratio in these inclusions range from 80: 20 to 50: 20. Occasionally vapor bubbles are moving but no liquid CO_2 is present (**Figures 11C,E–G**).

Type B (*aqueous inclusions*): have been identified in quartz and calcite of the mineralized vein quartz. These inclusions are bi-phase with a vapor bubble and liquid at room temperature (**Figures 11C–F,H**).

Fluid Inclusion Microthermometry

Fluid inclusion characteristics of the gold deposits are summarized in **Table 2** and **Figures 12**, **13**. At Shwetagun, the final ice melting temperatures ($T_{m\text{-}ice}$) for Type A (vapor-rich) aqueous inclusions in quartz range from →0.1 to →2.8 (n = 10) (**Table 2**). The homogenization temperatures of Type A (vapor-rich) aqueous fluid inclusions in quartz of veins vary from 250 to 335 °C (n = 15), with salinities from 0.2 to 4.8 wt% NaCl equivalent (**Table 2**; **Figures 12A,B**). The final ice melting temperatures ($T_{m\text{-}ice}$) of Type B (liquid-rich) aqueous inclusions in quartz of veins studied range from -1.2 to -2.7 (n = 14). The homogenization temperatures of Type B (liquid-rich) aqueous fluid inclusions in quartz were from 261 to 320°C (n = 16), with salinities from 3.1 to 4.5 wt% NaCl equivalent (**Table 2**; **Figures 12A,B**).

At Kunzeik, complete homogenization temperatures (T_h) of (Type A) aqueous-carbonic fluid inclusions in quartz vary between 315°C and 356 °C (n = 21) (**Figure 12C**). Homogenization temperatures (T_h) of the (Type B) aqueous fluid inclusions in quartz of the mineralized vein quartz yielded a range approximately 246°C–376 °C (n = 21) (**Figure 12D**). The melting of CO_2 ($T_{m\ -CO2}$) in (Type A) aqueous-carbonic inclusions in quartz were between → 58.2°C and → 56.8°C (**Table 2**). The CO_2 phases of the (Type A) aqueous-carbonic inclusions in quartz were fully homogenized to the liquid phase at temperatures ($T_{h\text{-}CO2}$) of 25.5°C–30.9°C. The melting temperatures of clathrates in quartz ($T_{m\text{-}cla}$ = 7.6°C–9.2°C) (n = 10) suggest that the salinity of these inclusions is low, around 1.6 to 4.6 wt% NaCl equivalent. The final ice melting temperatures of (Type B) aqueous fluid inclusions in quartz range between → 0.6 and → 7.2°C (n = 14) corresponding to salinities between 1.1 and 10.7 wt% NaCl equivalent.

Total homogenization temperatures (T_h) of (Type A) aqueous-carbonic fluid inclusions in calcite range from 273°C to 318°C (n = 17) (**Figure 12C**). Homogenization temperatures (T_h) of the (Type B) aqueous fluid inclusions in calcite of the vein quartz yielded a range from 248°C to 325 °C (n = 20) (**Figure 12D**). The melting of CO_2 ($T_{m\ -CO2}$) in (Type A) aqueous-carbonic inclusions in calcite took place between → 57.2°C and → 56.8°C (**Table 2**). The CO_2 phases of the (Type A) aqueous-carbonic inclusions in calcite were completely homogenized to the liquid phase at temperatures ($T_{h\text{-}CO2}$) of 21.5°C–29.9°C. The melting temperatures of clathrates in calcite ($T_{m\text{-}cla}$ = 8.6°C–9.2°C) (n = 11) indicates that the salinity of these inclusions are generally low, about 1.6–2.8 wt% NaCl equivalent. The final ice melting temperatures of (Type B) aqueous fluid inclusions in calcite range from → 1.2°C to → 6.8°C (n = 13) corresponding to salinities from 2.1 to 10.2 wt% NaCl equivalent.

At Zibyaung, homogenization temperatures of the (Type A) aqueous-carbonic fluid inclusions in quartz of vein range between 312°C and 348°C (n = 19). The homogenization temperatures of (Type B) aqueous fluid inclusions in quartz of the vein vary between 242°C and 358°C (n = 19). The values of (Type A) aqueous-carbonic inclusions $T_{m\text{-}CO2}$ fall in the range of → 57.3 to → 56.8°C, indicating the only presence of pure CO_2. However, a few inclusions show $T_{m\text{-}CO2}$ values around -60°C, which can be due to the presence of minor other volatile components (Roedder, 1984). The first melting of ice ($T_{m\text{-}ice}$) in most of the (Type A) aqueous-carbonic fluid inclusions in quartz occurred between 20.5 and 30.9°C (n = 8) (**Table 2**). The temperatures of clathrate melting ($T_{m\text{-}cla}$) are between 4.6 and 9.6°C wt% NaCl equivalent (**Table 2**; **Figure 12E**). Final melting of ice ($T_{m\text{-}ice}$) in (Type B) aqueous fluid inclusions in quartz was observed in a temperature range from → 0.5 to → 8.1°C (n = 11) (**Table 2**), suggesting the salinities from 0.9 to 11.8 wt% NaCl equivalent (**Figure 12F**). Box and whisker plots of results from two and three phase fluid inclusions in the two gold districts are shown in **Figures 13A,B**.

DISCUSSION

Comparison With Orogenic Gold Deposits Worldwide

Several geological and geochemical characteristics of the MB gold deposits are comparable with those of the typical orogenic gold deposits worldwide (**Table 3**; e.g., Groves et al., 1998; Hagemann and Cassidy, 2000; Kerrich et al., 2000; Poulsen et al., 2000; Goldfarb et al., 2001; Robert and Poulsen, 2001; Groves et al., 2003; Goldfarb et al., 2005; Robert et al., 2005; Large et al., 2011; Groves et al., 2019). The gold deposits of the MB have a number

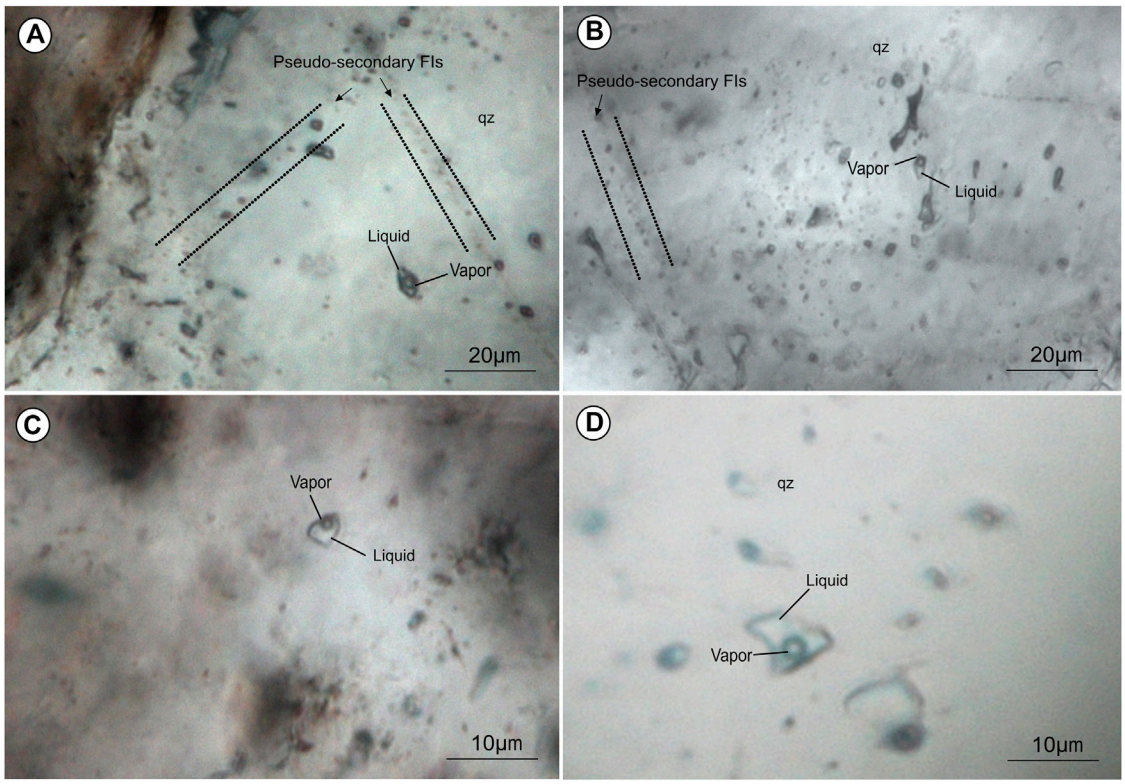

FIGURE 10 | (A) Photomicrographs of fluid inclusions in gold-bearing quartz vein from Shwetagun at room temperature in plane-polarized light. (a) and **(B)** Type A (vapor-rich) and Type B (liquid-rich) fluid inclusions coexisting together within same quartz gain in gold-bearing quartz vein from adit-I, **(C)** Type B (liquid-rich) fluid inclusions in quartz of the gold-bearing quartz vein from adit-I; and **(D)** Type B (liquid-rich) fluid inclusions in quartz of the gold-bearing quartz vein from adit-III. Abbreviations: qz = quartz.

of characteristics that are consistent with an orogenic gold system, including a close association between mineralization and deformation, and mineral assemblages of veins and alteration that are similar to Archean and Paleozoic gold systems (e.g., Groves et al., 1998; Bierlein and Crowe 2000; Hagemann and Cassidy 2000; Large et al., 2007). The orogenic gold systems are formed from the crustal fluids produced during the prograde metamorphism at the greenschist-amphibolite facies transformation and developed at intermediate depths (2–10 km) (Groves et al., 1998, 2003, 2020; Bierlein and Crowe, 2000; Goldfarb et al., 2001, 2005; Phillips and Evans, 2004; Dubé and Gosselin, 2007; Phillips and Powell, 2009, 2010; Tomkins, 2013; Goldfarb and Groves, 2015). Metamorphic fluids are generally regarded to be significant in the formation of orogenic gold deposits (e.g., Groves et al., 1998, 2003). There is still some debate over the appropriate source of orogenic gold ore fluids and the metals they transport (Tomkins, 2013; Goldfarb and Groves, 2015; Wyman et al., 2016; Groves et al., 2020). In comparison, Wyman et al. (2016) explored the presence of magmatic fluids in various orogenic gold deposits worldwide, as well as providing a comprehensive review of mineralizing fluids in orogenic gold systems. The formation of the widespread alteration of albite-silica-chlorite-sericite-carbonate-pyrite associated with the gold-bearing quartz veins in the MB was a major enhancing mineralizing mechanism for many other orogenic gold deposits worldwide (e.g., Phillips, 1993; McCuaig and Kerrich 1998; Goldfarb et al., 2005). The worldwide examples of these structural setting of the orogenic gold deposits are recorded at Golden Mile in Kalgoorlie, Western Australia, Western Lachlan Orogen in Victoria, SE Australia, Buller Terrane in western South Island, New Zealand, Meguma Terrane in Nova Scotia, Canada and Main Divide and Pingfengshan gold mine in Taiwan (**Table 3**; Shackleton et al., 2003; Bierlein et al., 2004; Groves et al., 1998, 2003; Goldfarb et al., 2001, 2005; Craw et al., 2010). Similar structural settings of the gold deposits are found in Myanmar at Phayaung Taung, Modi Taung and Shwegyin (**Table 3**; Mitchell et al., 2004; Win Phyo et al., 2016; May Thwe Aye et al., 2017; Ye Myint Swe et al., 2017).

Fluid Evolution and Depth Estimation

The microthermometric characteristics of fluid inclusions, alteration types, host rocks and tectonic setting related to various stages of vein formation of the mineralized quartz vein systems of Shwetagun (Modi Taung-Nankwe) and the Kyaikhto gold districts are remarkably similar. A majority of orogenic gold deposit studies have reported ore-mineralizing fluids to be of low salinity and aqueous-carbonic in composition (e.g., McCuaig and Kerrich 1998; Ridley and Diamond, 2000; Groves et al., 2003;

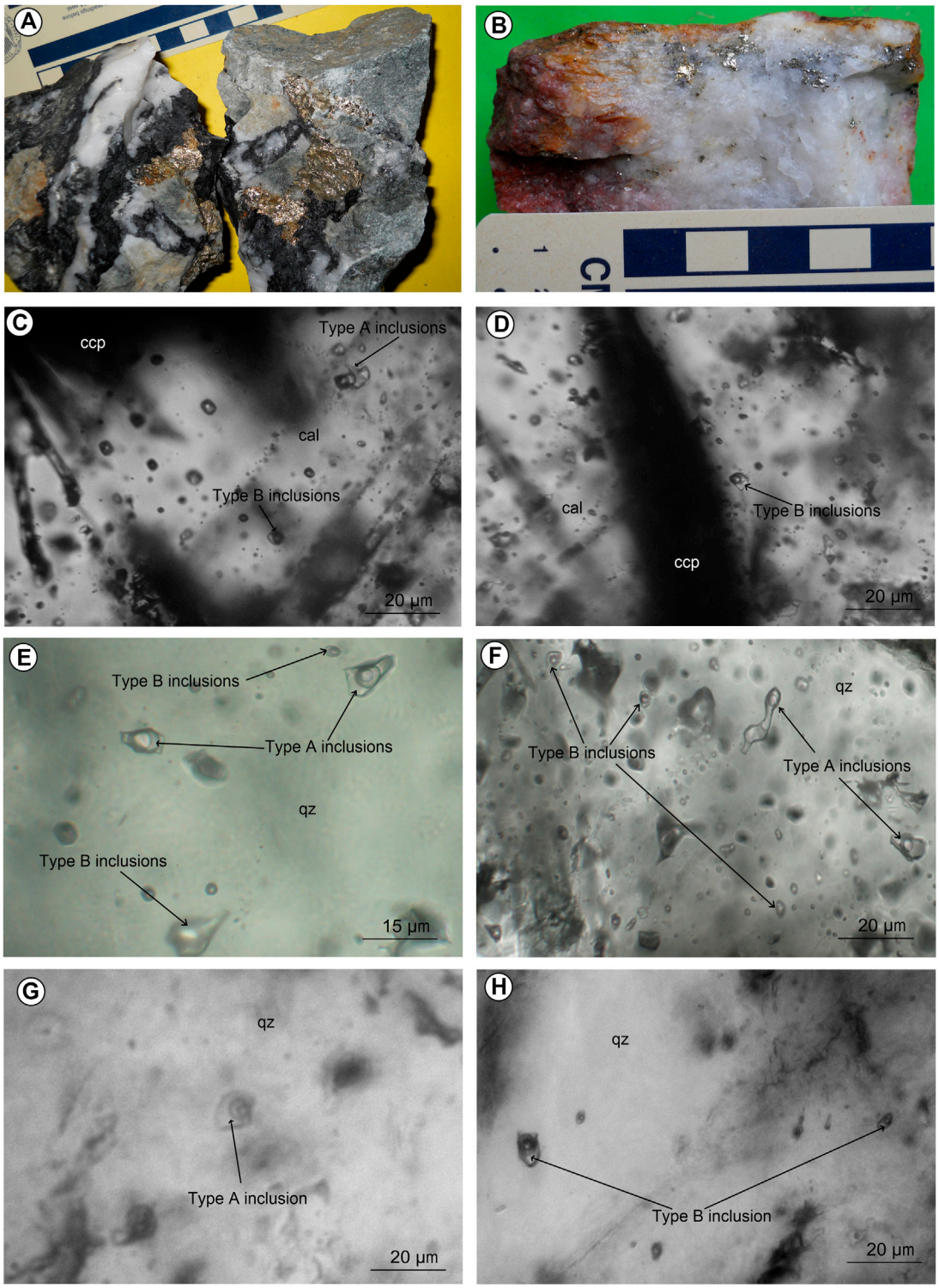

FIGURE 11 | Photographs showing the quartz veins of the deposits. **(A)** quartz-carbonate-sulfide vein from Kunzeik, **(B)** quartz-sulfide vein from Zibyaung, and photomicrographs **(C)** and **(D)** showing Type A (aqueous-carbonic) and Type B (aqueous) fluid inclusions in calcite of the quartz-carbonate-sulfide vein from Kunzeik, **(E)** and **(F)** showing Type A (aqueous-carbonic) and Type B (aqueous) fluid inclusions in quartz of the quartz-carbonate-sulfide vein from Kunzeik, **(G)** and **(H)** Type A (aqueous-carbonic) and Type B (aqueous) fluid inclusions in quartz of the quartz-sulfide vein from Zibyaung. Abbreviations: ccp = chalcopyrite, cal = calcite and qz = quartz.

TABLE 2 | Comparative analyses of fluid inclusion types and microthermometric results of the Shwetagun, Kunzeik and Zibyaung deposits.

Deposit Name	Vein Type	Type	$T_{m\text{-}CO2}$ (°C)	$T_{m\text{-}cla}$ (°C)	$T_{h\text{-}CO2}$ (°C)	T_h (°C)	$T_{m\text{-}ice}$ (°C)	Host mineral	Salinity (wt% NaCl eq.)	CO_2 density g/cm^3	Bulk density g/cm^3	References
Shwetagun	Gold quartz vein	Types A	—	—	—	250 to 335	−0.1 to −2.8	Quartz	0.2 to 4.6	—	0.62 to 0.83	This study
		Type B	—	—	—	261 to 320	−1.8 to−2.7		3.1 to 4.5	—	0.67 to 0.82	
Kunzeik	Quartz-carbonate -sulfide vein	Type A	−58.2 to −56.8	7.6 to 9.2	25.5 to 30.9	315 to 356	—	Quartz	1.6 to 4.6	0.53 to 0.70	—	Myo Kyaw Hlaing et al., 2019
		Type B	—	—	—	246 to 376	−0.6 to −7.2		1.1 to 10.7	—	0.53 to 0.89	This study
		Type A	-57.2 to -56.8	8.6 to 9.2	21.5 to 29.9	273 to 318	—	Calcite	1.6 to 2.8	0.61 to 0.75	—	
		Type B	—	—	—	248 to 325	−1.2 to −6.8		2.1 to 10.2	—	0.67 to 0.89	
Zibyaung	Quartz-sulfide vein	Type A	−57.3 to −56.8	4.6 to 7.6	20.5 to 30.9	312 to 348	—	Quartz	4.6 to 9.6	0.53 to 0.77	—	Myo Kyaw Hlaing et al., 2019
		Type B	—	—	—	242 to 358	−0.5 to −8.1		0.9 to 11.8	—	0.53 to 0.91	This study

Notes: $T_{m\text{-}CO2}$—melting temperature of CO_2; $T_{m\text{-}cla}$—melting temperature of CO_2 clathrate; $T_{h\text{-}CO2}$—partial homogenization temperature of CO_2 inclusions; T_h—total homogenization temperature of inclusions; $T_{m\text{-}ice}$—final ice melting temperature; wt% NaCl eq., weight percent NaCl equivalent.

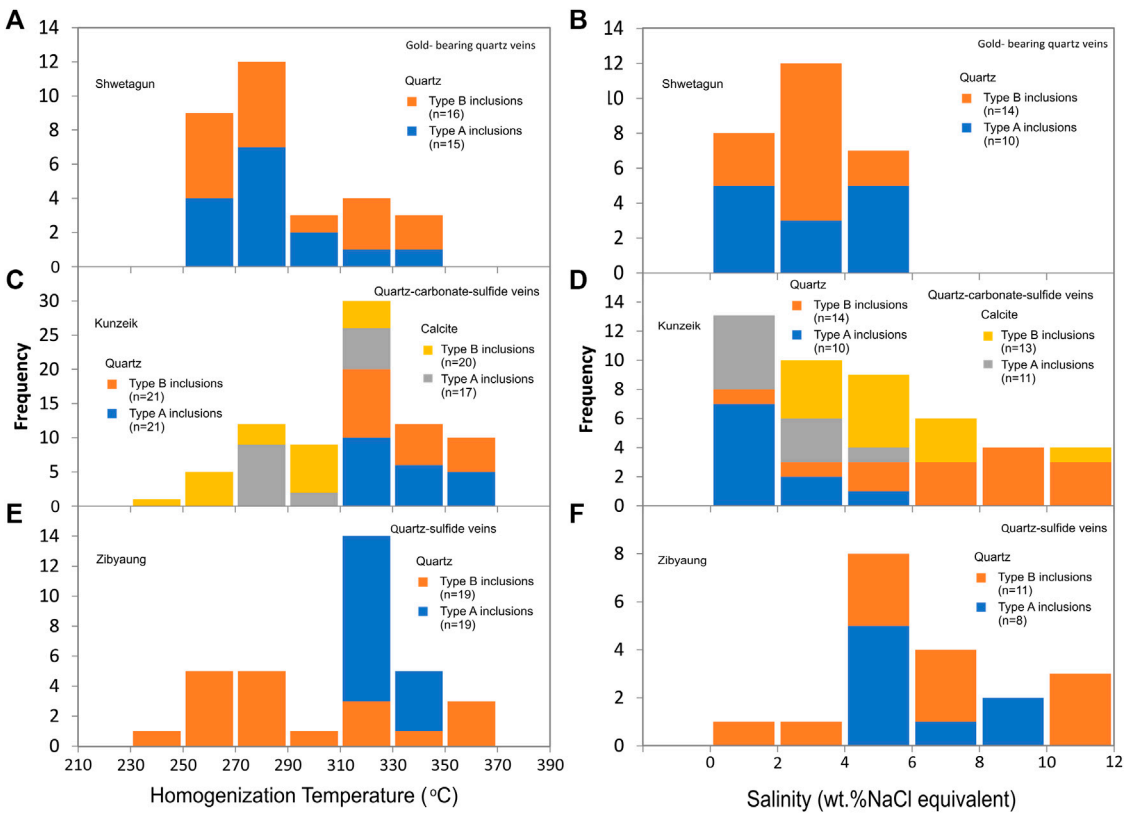

FIGURE 12 | Histograms of total homogenization temperatures (T_h) and salinities of primary fluid inclusions in quartz, quartz-sulfide and quartz-carbonate-sulfide veins from the deposits. **(A)** Histograms of T_h of primary fluid inclusions in gold-bearing quartz veins from the adit-I, II and III at Shwetagun, **(B)** Salinities of fluid inclusions in gold-bearing quartz veins from the adit-I, II and III at Shwetagun, **(C)** Histograms of T_h of primary fluid inclusions in quartz-carbonate-sulfide veins from Kunzeik, **(D)** Salinities of fluid inclusions in quartz-carbonate-sulfide veins from Kunzeik, **(E)** Histograms of T_h of primary fluid inclusions in quartz-sulfide veins from Zibyaung, and **(F)** Salinities of fluid inclusions in quartz-sulfide veins from Zibyaung. Figures **(C)**, **(D)**, **(E)** and **(F)** are adapted from Myo Kyaw Hlaing et al. (2019). Abbreviations: n = number of fluid inclusions.

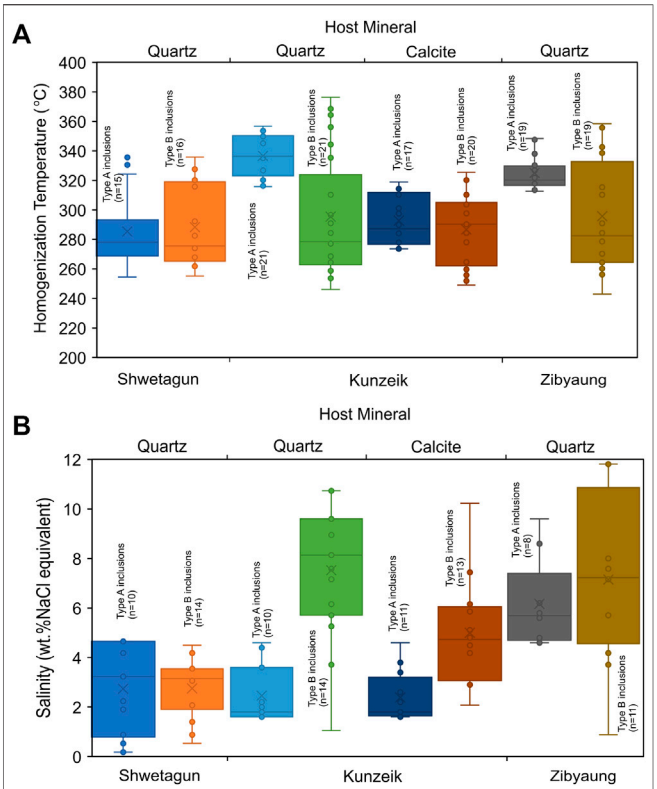

FIGURE 13 | Box and whisker plots showing **(A)** total homogenization temperatures and **(B)** calculated salinity values in two and three phase fluid inclusions from Shwetagun, Kunzeik, and Zibyaung. Abbreviations: n = number of fluid inclusions.

Goldfarb et al., 2005). The abundant aqueous fluid inclusions are similar to gold-related fluids throughout the belt, and typical of orogenic gold deposits elsewhere (e.g., Ridley and Diamond, 2000; Groves et al., 2003).

At Shwetagun, Type A (vapor-rich) inclusions are much less abundant than the Type B (liquid-rich) fluid inclusions, but they were observed as primary and pseudo-secondary inclusions in all samples. The secondary fluid inclusions have similar microthermometric properties to the primary inclusions, indicating that they represent events of vein reactivation in an evolving hydrothermal environment (Roedder, 1984). The ore fluid of Shwetagun ore-forming fluids evolved from a low to medium temperature (250–335°C), low salinity (0.2–4.6 wt% NaCl equivalent).

According to microthermometric results, a drop in salinities is found simultaneously with a decrease in temperature, suggesting that the system is diluted with cooling during the fluid evolution at Shwetagun. The major mechanism of ore and gangue mineral precipitation in veins is temperature drop (**Figure 14**). The absence of CO_2 in the gold-bearing veins at the Shwetagun deposit is in contrast to many ancient orogenic gold deposits, where separate phases of CO_2 are commonly found in fluid inclusions (Groves et al., 1998; McCuaig and Kerrich 1998; Bierlein and Crowe 2000; Goldfarb et al., 2004, 2005; Craw et al., 2010). However, the abundant CO_2 in the fluid is not a prerequisite for orogenic gold mineralization. (e.g., Main Divide and Pingfengshan gold mine in Taiwan; Craw et al., 2010 and references therein). The bulk densities of ore fluids from the Shwetagun deposit range from 0.62 to 0.83 g/cm^3 (**Table 2**). Although no depth estimation of the Shwetagun deposit is possible by fluid inclusion evidence, Mitchell et al. (2004) estimated a depth of 4–7 km based on stratigraphic and structural evidence.

In comparison, fluid inclusions in these deposits at Kunzeik and Zibyaung are dominated by earlier Type A (aqueous-carbonic) and Type B (aqueous) fluids. Histograms of homogenization temperatures and salinities, as well as a diagram of homogenization temperatures versus salinities, show a wide range of homogenization temperatures between 242 and 376°C, and low to medium salinities between 0.9 and 11.8 wt% NaCl equivalent, respectively (**Table 2**; **Figures 12–14**).

According to microthermometric results, the range of total homogenization temperatures (242–376°C) indicate that there may have been more than one episode of CO_2 phase separation during vein formation. The wide range of salinity also indicates a source of fluid, possibly mixed with low-salinity exotic fluid (**Figure 14**). Based on the relative timing of fluid inclusions, Type B (aqueous) fluids formed first, followed by Type A (aqueous-carbonic) fluids (**Figure 14**). The Kunzeik and Zibyaung fluids show two totally identical processes of total homogenization of Type A (aqueous-carbonic) and Type B (aqueous) inclusions within a similar temperature range, indicating that they were trapped together and may represent the same H_2O-CO_2-NaCl system (**Table 2**; **Figures 12–14**).

The coexistence of Type A (aqueous-carbonic) and Type B (aqueous) fluid inclusions allows to estimate the depth of ore formation using the method of intersecting of the isochores based on the CO_2–H_2O–NaCl system. Using the CO_2 density formulae of the state of the isochores of Span and Wagner (1996) and the H_2O density isochores of Steele-MacInnis et al. (2012), and the pressure conditions of Sterner and Pitzer (1994), the bulk composition and density of fluid inclusions of these gold deposits were determined as below. The isochores of the Type A (aqueous-carbonic) and Type B (aqueous) fluid inclusions were plotted using the Roedder and Bodnar (1980) and Bowers and Helgeson (1983) state of equations, respectively (**Figure 15**).

The trapping pressures of fluid inclusions have been determined using CO_2-rich inclusions in quartz veins of the Kunzeik and Zibyaung deposits. The bulk densities vary from 0.53 to 0.91 g/cm^3 and the densities of CO_2 range between 0.53 and 0.77 g/cm^3 (**Table 2**; **Figure 15**). The Types A and B fluid inclusions from the Kunzeik deposit indicate that the deposit was formed at 376–246°C and 54–164 MPa (**Figure 15**), and for Zibyaung, it is estimated to be 358–242°C and 53–156 MPa (**Figure 15**). These data suggest a temperature and pressure variation during the ore-forming process. Depending on the pressure, the depth of mineralization was estimated. Given that studied areas are in a compressive orogenic environment, the formula can be used to estimate the metallogenic depth by lithostatic pressure: $H = P/(\rho \times g)$ (ρ represents average density of rocks, such as 2.70 g/cm^3). These pressures correspond to the

TABLE 3 | Comparative table showing characteristics of the Shwetagun, Kunzeik and Zibyaung deposits with other orogenic gold deposits in Myanmar and worldwide.

Name of Deposit/ Prospect	Location and Geologic Setting	Host Rocks	Mineralization Styles	Alterations	Metal Associations	Ore Fluid Systems, Temperature and Salinity	Regional Peak Metamorphism Events	Age of Host Terranes	References
Golden Mile	Kalgoorlie, Western Australia	Black shale, slate, basalts, and dolerite	Quartz vein and stockwork	Carbonation, Sericitization Sulfidation	Cu, Fe, As, Pb, Zn, Bi, Sb, Mo, Te, Ag, Au	H_2O-CO_2±CH_4-NaCl 200–400 °C (0.5–10 wt% eqiv. NaCl)	Lower greenschist Archean	Archean	Shackleton et al., 2003; Groves et al., 1998, 2003; Goldfarb et al., 2001, 2005
Western Lachlan Orogen	Victoria SE Australia	Slates, massive sandstone	Laminated or ribbon banded quartz vein disseminated–stockwork-breccia systems	Carbonation, Sericitization Sulfidation	Cu, Fe, As, Pb, Zn, Sb, Mo, Ag, Au	H_2O-CO_2±CH_4-NaCl 200–400°C (2–10 wt% eqiv. NaCl)	Zeolite– Lower amphibolite Devonian	Upper Cambrian–Lower Devonian	Groves et al., 1998, 2003; Goldfarb et al., 2001, 2005; Bierlein et al., 2004
Buller Terrane	Western South Island, New Zealand	Massive siltstone and sandstone	Ribbon texture banded vein shear-zone-related quartz lodes gold	Carbonation, Sericitization Sulfidation	Cu, Fe, As, Ag, Au	H_2O-CO_2±CH_4-NaCl 152–293°C (3.5–7.2 wt% eqiv. NaCl)	Lower greenschist Devonian	Upper Cambrian–Middle Ordovician	Bierlein et al., 2004; Groves et al., 1998,2003; Goldfarb et al., 2001, 2005
Meguma Terrane	Nova Scotia, Canada	Slate, argillite or meta-sandstones	Laminated bedding-parallel veins	Carbonate Sericite Chlorite Sulphidation	Cu, Fe, As, Pb, Sn, Ag, Au	H_2O-CO_2±CH_4-NaCl 300–400°C (<10 wt% eqiv. NaCl)	Lower greenschist–Upper amphibolite Devonian	Upper Cambrian–Upper Ordovician	Groves et al., 1998, 2003; Goldfarb et al., 2001, 2005; Bierlein et al., 2004
Main Divide and Pingfengshan	Slate Belt, Taiwan	Mudstones, Siltstones, sandstones and micaceous schists	Chloritic fissure, ankeritic, massive veins	Ankeritic, Chlorite–Calcite	Cu, Fe, As, Pb, Zn, Ag, Au	H_2O-NaCl 172–350°C 0.8–5.4 wt% eqiv.NaCl	Sub-greenschist to Lower greenschist post-Miocene	Eocene–Miocene	Craw et al. (2010)
Phayaung Taung	Mergui Belt, Southern Myanmar	Phyllite, schist, and quartzite	Sulfide quartz vein	Silicification Phyllic/Sericitic, Chloritization Oxidation	Cu, Fe, As, Pb, Zn, Bi, Te, Ag, Au	H_2O-NaCl 243–426°C (0.4–8.4 wt% eqiv. NaCl)	Lower greenschist –Upper Amphibolite Lower Jurassic - Eocene	Upper Carboniferous to Lower Permian	Win Phyo et al., 2016; Ye Myint Swe et al., 2017
Modi Taung	Mergui Belt, Southern Myanmar	Mudstone, graywacke, and slate	Laminated or ribbon banded quartz vein, Sheeted vein	Carbonation, Sericitization Sulfidation	Cu, Fe, As, Pb, Zn, Ag, Au	Unknown	Lower greenschist Lower Jurassic - Eocene	Upper Carboniferous to Lower Permian	Mitchell et al., 2004; Traynor et al., 2015, 2017
Shwetagun	Mergui Belt, Southern Myanmar	Mudstone, graywacke, and slate	Laminated or sheeted quartz vein	Sulfidation Sericitization Chloritization, Silicification	Cu, Fe, As, Pb, Zn, Ag, Au	H_2O-NaCl 250–335°C (0.2–4.6 wt% eqiv. NaCl)	Lower greenschist Lower Jurassic - Eocene	Upper Carboniferous to Lower Permian	This study
Shwegyin	Mergui Belt, Southern Myanmar	Slate, phyllite, schist, and quartzite	Sulfide quartz vein, Sheeted vein	Carbonation, Sericitization Sulfidation	Cu, Fe, As, Pb, Zn, Ag, Au	H_2O-CO_2±CH_4-NaCl 245–411 (1.5–7.0 wt% eqiv. NaCl)	Lower greenschist –Upper Amphibolite Lower Jurassic - Eocene	Upper Carboniferous to Lower Permian	May Thwe Aye et al. (2017)
Kunzeik	Mergui Belt, Southern Myanmar	Slate, biotite granite, granodiorite	Sulfide quartz vein, stockwork	Sulfidation Sericitization	Cu, Fe, Mo, Ag, Au	H_2O ~ CO_2 –NaCl	Lower greenschist Lower Jurassic - Eocene	Upper Carboniferous to Lower Permian	Myo Kyaw Hlaing et al., 2019bib_Kyaw_et_al_2019; This study

(Continued on following page)

TABLE 3 | (*Continued*) Comparative table showing characteristics of the Shwetagun, Kunzeik and Zibyaung deposits with other orogenic gold deposits in Myanmar and worldwide.

Name of Deposit/ Prospect	Location and Geologic Setting	Host Rocks	Mineralization Styles	Alterations	Metal Associations	Ore Fluid Systems, Temperature and Salinity	Regional Peak Metamorphism Events	Age of Host Terranes	References
						*a 273–356°C (1.6–4.6 wt% eqiv. NaCl) *b 246–376°C (1.1–10.7 wt% eqiv. NaCl)			
				Chloritization, Silicification					
Zibyaung	Mergui Belt, Southern Myanmar	Mudstone, Slate and schist	Sulfide quartz vein	Sulfidation	Cu, Fe, Pb, Zn, Ag, Au	H_2O-CO_2-NaCl	Lower greenschist –Upper Amphibolite	Upper Carboniferous to Lower Permian	Myo Kyaw Hlaing et al., 2019; This study
				Sericitization		*a 312–348°C (4.6–9.6 wt% eqiv. NaCl)			
				Chloritization, Silicification		*b 242–358°C (0.9–11.8 wt% eqiv. NaCl)	Lower Jurassic - Eocene		
Meyon	Mergui Belt, Southern Myanmar	Sandstone and carbonaceous mudstones, Slate	Stratabound, Sulfide quartz vein	Carbonation, Sericitization	Cu, Fe, As, Zn, Ag, Au	H_2O-CO_2±CH_4-NaCl 240–370°C (5–12 wt% eqiv. NaCl)	Lower greenschist –Upper Amphibolite	Upper Carboniferous to Lower Permian	Zaw Naing Oo et al. (2010); Zaw Naing Oo and Khin Zaw (2009), Zaw (2015), Zaw (2017)
				Sulfidation			Lower Jurassic - Eocene		
				Albitization					

*Notes: *a = Aqueous-carbonic fluid inclusions, *b = Aqueous fluid inclusions.*

calculated depths of ore formation between 2.0 and 6.1 km under lithostatic conditions. These temperatures, depth and recorded alteration mineralogy in the Kunzeik and Zibyaung deposits are consistent with mesozonal orogenic gold deposits elsewhere (e.g., Groves et al., 1998, 2003; McCuaig and Kerrich 1998; Goldfarb et al., 2001, 2005; Elmer et al., 2006).

Metallogenic Implications

The structural setting of the MB is ideal for generation of orogenic gold deposits as described by Groves et al. (2003), which includes a first-order structure that focuses and channelizes metal-bearing fluids and neighboring second-order and possibly third-order structures that contain fluids, and the major processes comprising the formation of quartz veins and metal deposition around them (e.g., Goldfarb et al., 2001; Groves and Bierlein, 2007). A large number of orogenic or lode gold deposits are structurally-controlled by brittle-ductile shear zones and faults and are distinguished by fault-valve nature (Sibson et al., 1988; Cox et al., 1991; Cox 1995; Robert et al., 1995; Dubé and Gosselin, 2007). In the case of the MB, these structures can be defined by the transcrustal, first-order, the second-order shear zone, and reactivated Papun fault system located in the middle to south of the belt and the third-order structures semi-parallel to the fault zone and hosting the gold mineralization (**Figures 2**, **16**).

The Shwetagun gold-bearing quartz veins and, in particular, the Zibyaung and Khunzeik veins in MB show a structural relationship between the first-order structures, mostly N-S to NNE-NNW oriented, and second order one trending NW–SE. The fault-valve model for orogenic gold deposits represents the cyclic fluctuation in fluid pressures, from lithostatic to hydrostatic, due to episodic shear stress (Sibson et al., 1988; Ridley 1993; Robert et al., 1995; Cox et al., 1995, 2001; Sibson and Scott 1998; Kisters et al., 2000; Oliver and Bons 2001; Groves et al., 2003). The available sulfur isotopic data along MB indicate that the $\delta^{34}S$ values of pyrite range from →2.80–4.43‰ in Meyon, (Zaw Naing Oo and Khin Zaw, 2009) and a range of +1.33–4.75‰ in Modi Taung (Traynor et al., 2015). These data suggest that the sulfur responsible for gold mineralization is likely to have been derived from a dominant magmatic source with a possible other minor fluid such as metamorphic fluid (e.g., Wyman et al., 2016; Groves et al., 2020).

The age of the gold district of Modi Taung-Nankwe was stratigraphically considered between the Upper Permian and the Middle Jurassic (Mitchell et al., 2004). They considered that it was an orogenic style gold, linking its genesis to the crustal fluids generated during the metamorphism of the MMB (Mitchell et al., 2004; Gardiner et al., 2016). This metamorphism was defined as Jurassic in age, contemplating this age for gold mineralization (Mitchell et al., 2004). However, Searle et al. (2007) suggested a much younger age of Paleogene for peak metamorphism in MMB. Here, at Modi Taung, the Theingi vein is cut by a 20 m wide dyke, and the Shwesin and Momi Taung veins are cut by small dykes and sills (Mitchell et al., 2004; Traynor et al., 2015, 2017). LA ICP-MS U-Pb zircon dating of granitoid unit intruding the host sequence of the Modi Taung gold deposit yielded 95 ± 30 Ma and the age of the

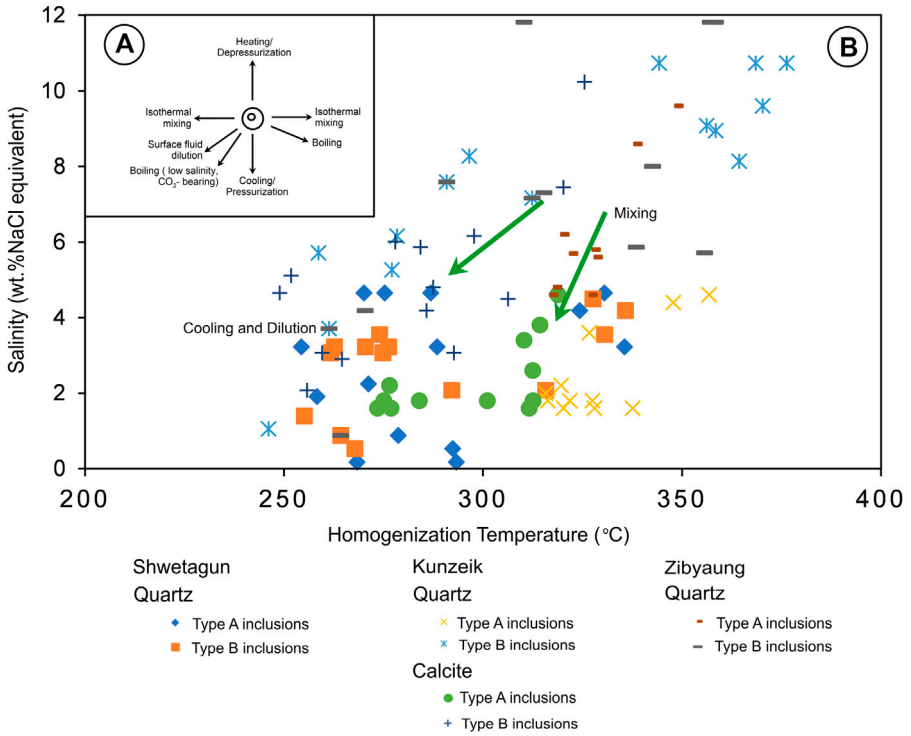

FIGURE 14 | Diagram showing **(A)** typical trends in the T_h (°C)–Salinity space caused by various fluid evolution mechanisms (from Wilkinson, 2001), and **(B)** variations of homogenization temperature and salinity of fluid inclusions with hydrothermal fluid evolution from Shwetagun, Kunzeik, and Zibyaung. The green arrows indicate that both temperature and salinity are decreasing.

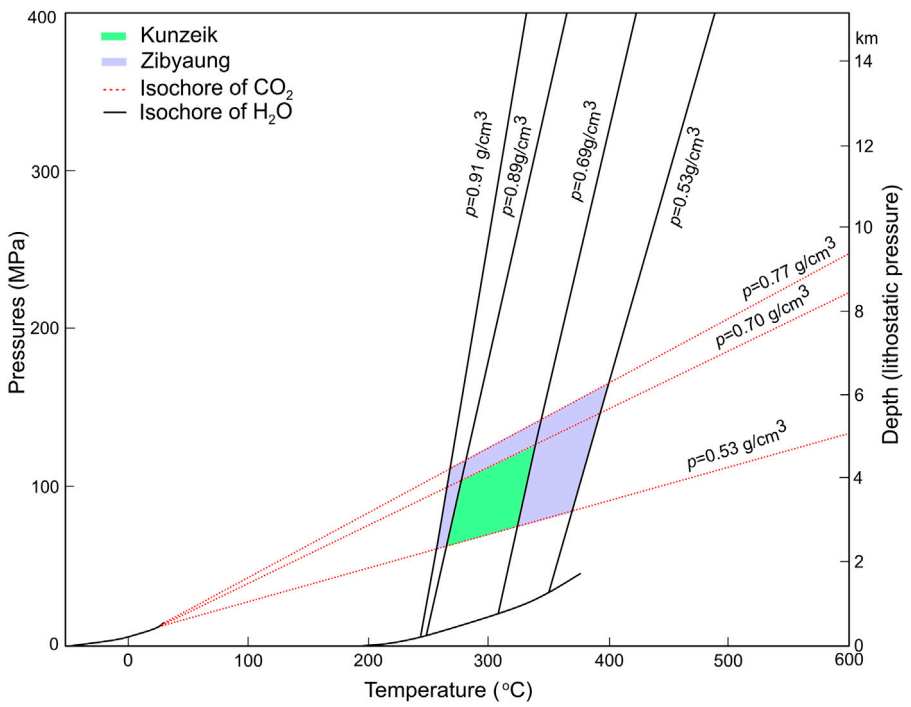

FIGURE 15 | P-T diagram displaying isochores of the minimum and maximum densities of two types of fluid inclusions (modified from Roedder and Bodnar, 1980; Bowers and Helgeson, 1983). Figure indicates the density values (in g/cm^3) for respective inclusions. P-T estimation by intersecting isochores of Type A (aqueous-carbonic) (dashed lines) and Type B (aqueous) (solid lines) inclusions.

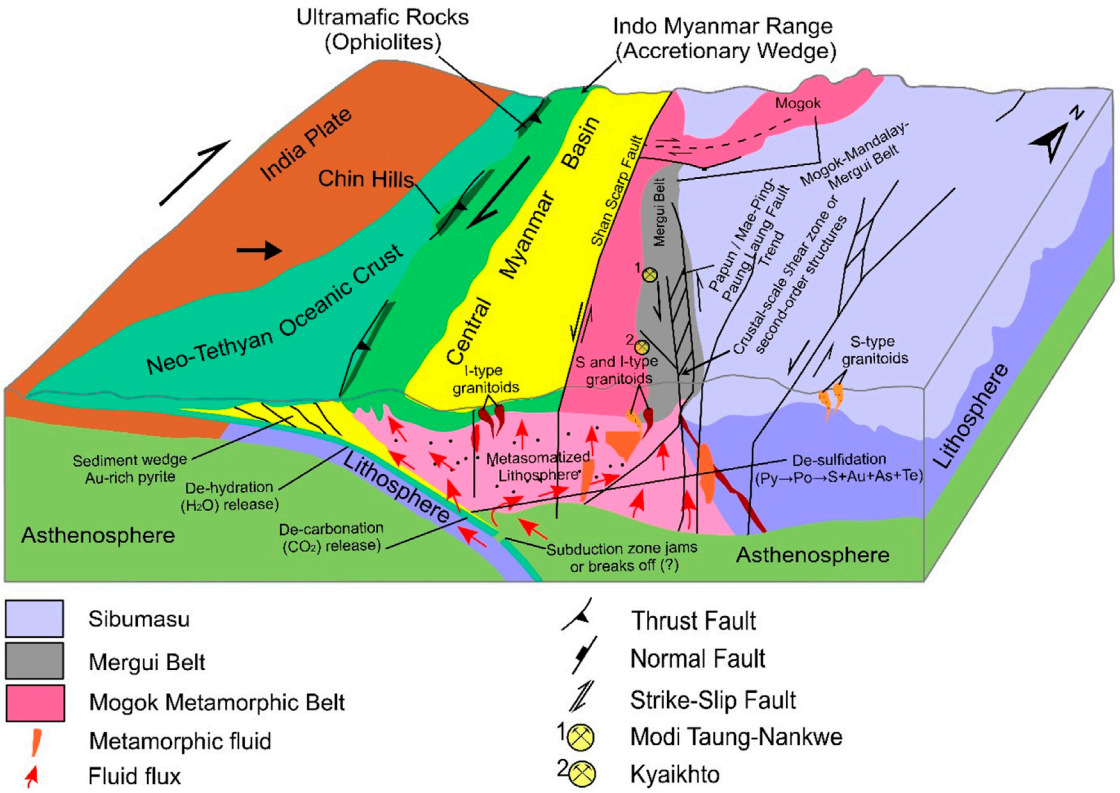

FIGURE 16 | Tectonic setting of Myanmar during Lower Cretaceous to Oligocene depicting formation and evolution of gold mineralization in the framework of subduction and collision-based model for ore-fluid source(s) of the orogenic gold deposits of Mergui Belt (Modified after Gardiner et al., 2016, 2018; Groves et al., 2019, 2020).

andesitic dyke cross-cutting the mineralization by LA ICP-MS U-Pb dating of apatite was determined to be 49 ± 1 Ma (Traynor et al., 2015, 2017). Further work on U-Pb dating of zircon from the cross-cutting dyke is required to ascertain the robust age for the dyke intrusion, the age of the orogenic gold mineralization at the Shwetagun deposit in the Modi Taung-Nankwe gold district appeared that it was formed relatively late. The age of mineralization of the Meyon is proposed to be Lower Cretaceous to Paleogene and may have been consistent with deformation and metamorphism as being structurally-controlled and linked to movement along the Papun Fault Zone (**Figure 16**; Zaw Naing Oo and Khin Zaw, 2009, 2017).

During the Lower Cretaceous to Oligocene, Myanmar was influenced by at least two main orogenic events (Cretaceous and Eocene), which may have contributed to widespread regional metamorphism which is possibly linked to gold mineralization in the MB (e.g., Mitchell et al., 2004; Gardiner et al.,2014; Khin Zaw et al., 2014a; Zaw Naing Oo and Khin Zaw, 2015; Khin Zaw, 2017; Gardiner et al., 2018). Gold veins were formed during the ascent of metamorphic fluids following the uplifting and prograde metamorphism of the entire MMMB. The generation of this high-grade metamorphic process was associated with the subduction and collision of the India-Eurasia Plate (Khin Zaw et al., 2014b). Thus, we suggest that the age of mineralization for the orogenic gold deposits in the MB may have been Lower Cretaceous to Oligocene, and the emplacement of the mineralizing fluids was associated with retrograde metamorphism of the MMMB and dehydration at a depth of 2–12 km (e.g., Mitchell et al., 2004).

All the evidence presented for the orogenic gold deposits of the MB also suggest that the mineralizing fluids were derived from multi-sources and the initial ore-forming fluids were thought to be either due to fluids produced by metamorphic devolatization and/or mixed with magmatic fluid (e.g., Wyman et al., 2016; Groves et al., 2020). These multi-sourced fluids may have been transported from the deep crust to the shallower level via first-order faults during the evolution of the ore fluid, especially in the late stages of ore precipitation (e.g., Kerrich and Fyfe, 1981; Higgins and Kerrich, 1982; Cameron and Hattori, 1987; Phillips and Powell, 1993; Mikucki, 1998; Diamond, 2001; Wilkinson, 2001). The derivation of the ore fluids from the supracrustal rocks below the continental crust is widely accepted for the source (s) of orogenic gold deposits (Phillips and Powell, 2010; Goldfarb and Santosh, 2014), either from the subducted slab, with overlying oceanic sediments, or from the lithosphere below (**Figure 16**; Groves and Santosh, 2015). Dehydration and metamorphism within the oceanic crust and sediments have been well-observed mechanisms for producing abundant aqueous-carbonic and low-salinity fluids, as

documented in orogenic gold deposits from fluid inclusions that induce massive energy and mass transport, culminating in the fractionation of mobile and even immobile elements (Pearce and Peate, 1995; Ridley and Diamond, 2000; Spandler et al., 2003).

In this context, the MB is a tectonic component of the Sibumasu terrane during the Jurassic to Cretaceous when the main tectonic transition from N-S compression to NNE-SSW shearing was progressively occurred. The large-scale circulation of fluids, granitic magmatism and metallogenesis took place during the Lower Cretaceous to Oligocene in the MB, as a result of which the initial ore fluids of the orogenic gold deposits were likely formed by dehydration, decarbonization and desulfidation of the subducting Neo-Tethys slab (**Figure 16**; e.g., Ridley and Diamond 2000; Phillips and Powell, 2010; Goldfarb and Santosh, 2014; Yardley and Bodnar, 2014; Khin Zaw et al., 2014b; Yardley and Cleverley 2015; Groves and Santosh, 2016; Groves et al., 2020).

CONCLUSION

This integrated study provided a framework for the genesis and metallogenic significance of gold mineralization in the Mergui Belt as below:

1. The comparison of the two gold systems in Mergui Belt suggests that the gold deposits are mainly hosted by the mudstone, slaty mudstone, greywacke sandstone, slate, and slaty phyllite of Mergui Group (dominantly of Carboniferous age), and are structurally-controlled by the NNE-NNW trending faults system. Hydrothermal alteration processes of various extents developed along the NNE-NNW trending structures and the alteration process was dominated by chloritization, sericitization, carbonatization, silicification. The most common sulfides are pyrite, sphalerite, chalcopyrite, and galena with native gold and electrum.
2. Comparing the fluid inclusion characteristics, evolution of fluid and depth estimation indicate that the ore fluids are composed of high temperature, low salinity, low CO_2, aqueous–carbonic fluid belonging to a H_2O-CO_2-NaCl system. The ore-bearing fluids are considered to have derived from dominantly of metamorphic with possible magmatic fluid inputs. Intersection of isochores of fluid inclusions in this study suggests that gold deposits were formed under the PT-depth conditions comparable to the global orogenic gold systems as evidenced by temperatures ranging from (242–376°C) to pressure (53–164 MPa) corresponding to a depth at around 2.0 and 6.1 km under lithostatic conditions.
3. The regional tectonic setting provided by comparison of the Shwetagun, Zibyaung and Khunzeik deposits raises the question of the timing of gold mineralization in Mergui Belt. The orogenic gold deposits in the Mergui Belt may have been genetically linked to the deformation and metamorphism of the host Paleozoic sequence at the time of the inferred Cretaceous to Oligocene age of mineralization. This prolonged tectonic and metallogenic event was associated with the subduction of the Neo-Tethys oceanic slab (**Figure 16**).
4. Additional ongoing controversies remain to investigate the origin of the gold deposits of the Mergui Belt in Myanmar whether the source of the gold was derived from deeper mantle or recycling and remobilization of crustal gold syngenetically accumulated in back arc basins of Sinbumasu. Further systematic investigations are required to successfully establish the relative timing of magmatism, metamorphism, and to address the importance of ore-forming processes involved in orogenic gold mineralization and future exploration.

DATA AVAILABILITY STATEMENT

The original contributions presented in the study are included in the article/Supplementary Material, further inquiries can be directed to the corresponding author.

AUTHOR CONTRIBUTIONS

This work is a late result of the first author's Master thesis (Department of Geology, University of Yangon, 2013) combined with some part from Ph. D thesis (Department of Earth Resources Engineering, Kyushu University, 2019). All authors finally endorsed the findings and contributed to the final manuscript.

FUNDING

This study has been financially supported by the Japan International Cooperation Agency (JICA) SHIGEN NO KIZUNA program for the PhD scholarship and the Frontiers Fee Support Grant No. DSC-11032129724PRD).

ACKNOWLEDGMENTS

Special thanks are due to the editor and two reviewers for their insightful suggestions and reviews, which significantly improved the manuscript.

REFERENCES

Aung Zaw Myint., Khin Zaw., Ye Myint Swe., Yonezu, K., Cai, Y., Manaka, T., et al. (2017). "Geochemistry and Geochronology of Granites Hosting the Mawchi Sn-W deposit, Myanmar: Implications for Tectonic Setting and Granite Emplacement," in *Myanmar: Geology, Resources and Tectonics*. Editors A. J.Barber, Khin Zaw, and M. J. Crow (London: The Geological Society, Memoir), 48, 387–402. doi:10.1144/m48.17

Barley, M. E., Doyle, M. G., Khin, Z., Pickard, A. L., and Rak, P. (2003). Jurassic–Miocene Magmatism and Metamorphism in the Mogok Metamorphic Belt and the India-Eurasia Collision in Myanmar. *Tectonics* 22, 1–11. doi:10.1029/2002tc001398

Barley, M. E., and Groves, D. I. (1992). Supercontinent Cycles and the Distribution of Metal Deposits through Time. *Geol* 20, 291–294. doi:10.1130/0091-7613(1992)020<0291:scatdo>2.3.co;2

Bender, F. (1983). *Geology of Burma*. Stuttgart: Gebrüder Borntraeger, 295.

Bierlein, F. P., and Crowe, D. E. (2000). Phanerozoic Orogenic Lode Gold Deposits. *Rev. Econ. Geol.* 13, 103–140. doi:10.5382/Rev.13.03

Bierlein, F. P., Christie, A. B., and Smith, P. K. (2004). A Comparison of Orogenic Gold Mineralisation in central Victoria (AUS), Western South Island (NZ) and Nova Scotia (CAN): Implications for Variations in the Endowment of Palaeozoic Metamorphic Terrains. *Ore Geology. Rev.* 25, 125–168. doi:10.1016/j.oregeorev.2003.09.002

Bierlein, F. P., Groves, D. I., and Cawood, P. A. (2009). Metallogeny of Accretionary Orogens - the Connection between Lithospheric Processes and Metal Endowment. *Ore Geology. Rev.* 36, 282–292. doi:10.1016/j.oregeorev.2009.04.002

Bierlein, F. P., Groves, D. I., Goldfarb, R. J., and Dubé, B. (2006). Lithospheric Controls on the Formation of Provinces Hosting Giant Orogenic Gold Deposits. *Miner Deposita* 40, 874–886. doi:10.1007/s00126-005-0046-2

Bodnar, R. J. (1993). Revised Equation and Table for Determining the Freezing point Depression of H2O-Nacl Solutions. *Geochimica et Cosmochimica Acta* 57, 683–684. doi:10.1016/0016-7037(93)90378-a

Bowers, T. S., and Helgeson, H. C. (1983). Calculation of the Thermodynamic and Geochemical Consequences of Nonideal Mixing in the System H2O-CO2-NaCl on Phase Relations in Geologic Systems: Equation of State for H2O-CO2-NaCl Fluids at High Pressures and Temperatures. *Geochimica et Cosmochimica Acta* 47, 1247–1275. doi:10.1016/0016-7037(83)90066-2

Cameron, E. M., and Hattori, K. (1987). Archean Gold Mineralization and Oxidized Hydrothermal Fluids. *Econ. Geol.* 82, 1177–1191. doi:10.2113/gsecongeo.82.5.1177

Campbell McCuaig, T., and Kerrich, R. (1998). P-T-t-deformation-fluid Characteristics of Lode Gold Deposits: Evidence from Alteration Systematics. *Ore Geology. Rev.* 12, 381–453. doi:10.1016/s0169-1368(98)80002-4

Chhibber, H. L. (1934). *The mineral Resources of Burma*. London: Macmillan.

Cobbing, E. J., Pitfield, P., Darbyshire, D., and Mallick, D. (1992). *The Granites of the Southeast Asian Tin Belt*, 10. London: Overseas Memoirs of the British Geological Survey.

Cobbing, E. J., Mallick, D. I. J., Pitfield, P. E. J., and Teoh, L. H. (1986). The Granites of the Southeast Asian Tin belt. *J. Geol. Soc.* 143, 537–550. doi:10.1144/gsjgs.143.3.0537

Collins, P. L. F. (1979). Gas Hydrates in CO 2 -bearing Fluid Inclusions and the Use of Freezing Data for Estimation of Salinity. *Econ. Geol.* 74, 1435–1444. doi:10.2113/gsecongeo.74.6.1435

Connolly, J. A. D. (2010). The Mechanics of Metamorphic Fluid Expulsion. *Elements* 6 (3), 165–172. doi:10.2113/gselements.6.3.165

Cox, S. F., Knackstedt, M. A., and Braun, J. (2001). "Principles of Structural Control on Permeability and Fluid Flow in Hydrothermal Systems," in *Structural Controls on Ore Genesis*. Editors J. P. Richards and R. M. Tosdal (Littleton, CO: Rev. Econ. Geol.), 14, 1–24. doi:10.5382/Rev.14.01

Cox, S. F., Etheridge, M. A., Cas, R. A. F., and Clifford, B. A. (1991). Deformational Style of the Castlemaine Area, Bendigo-Ballarat Zone: Implications for Evolution of Crustal Structure in central Victoria. *Aust. J. Earth Sci.* 38, 151–170. doi:10.1080/08120099108727963

Cox, S. F. (1995). Faulting Processes at High Fluid Pressures: an Example of Fault Valve Behavior from the Wattle Gully Fault, Victoria, Australia. *J. Geophys. Res.* 100 (B7), 12841–12859. doi:10.1029/95jb00915

Cox, S. F., Sun, S. S., Etheridge, M. A., Wall, V. J., and Potter, T. F. (1995). Structural and Geochemical Controls on the Development of Turbidite-Hosted Gold Quartz Vein Deposits, Wattle Gully Mine, central Victoria, Australia. *Econ. Geol.* 90, 1722–1746. doi:10.2113/gsecongeo.90.6.1722

Craw, D., Upton, P., Yu, B.-S., Horton, T., and Chen, Y.-G. (2010). Young Orogenic Gold Mineralisation in Active Collisional Mountains, Taiwan. *Miner Deposita* 45, 631–646. doi:10.1007/s00126-010-0297-4

Davies, R. S., Groves, D. I., and Standing, J. G. (2019). Litho-structural Controls on Orogenic Gold Deposits within the Sandstone Greenstone belt, Yilgarn Craton, Western Australia: Implications for Exploration Targeting. *Appl. Earth Sci.* 1–10. doi:10.1080/25726838.2019.1674540

Diamond, L. W. (2001). Review of the Systematics of CO2-H2O Fluid Inclusions. *Lithos* 55, 69–99. doi:10.1016/S0024-4937(00)00039-6

Dubé, B., and Gosselin, P. (2007). "Greenstone-hosted Quartz-Carbonate Vein Deposits," in *Mineral Deposits of Canada: A Synthesis of Major Deposit-Types, District Metallogeny, the Evolution of Geological Provinces, and Exploration Methods: Geological Association of Canada, Mineral Deposits*. Editor W. D. Good fellow (India: Division, Spec. Publ.), 5, 49–73.

Elmer, F. L., White, R. W., and Powell, R. (2006). Devolatilization of Metabasic Rocks during Greenschist-Amphibolite Facies Metamorphism. *J. Metamorph. Geol.* 24, 497–513. doi:10.1111/j.1525-1314.2006.00650.x

Gardiner, N. J., Robb, L. J., and Searle, M. P. (2014). The Metallogenic Provinces of Myanmar. *Appl. Earth Sci. (Trans. Inst. Min. Metall. B)* 123, 1. doi:10.1179/1743275814y.0000000049

Gardiner, N. J., Robb, L. J., Morley, C. K., Searle, M. P., Cawood, P. A., Whitehouse, M. J., et al. (2016). The Tectonic and Metallogenic Framework of Myanmar: A Tethyan mineral System. *Ore Geology. Rev.* 79, 26–45. doi:10.1016/j.oregeorev.2016.04.024

Gardiner, N. J., Searle, M. P., Morley, C. K., Robb, L. J., Whitehouse, M. J., Roberts, N. M. W., et al. (2018). The Crustal Architecture of Myanmar Imaged through Zircon U-Pb, Lu-Hf and O Isotopes: Tectonic and Metallogenic Implications. *Gondwana Res.* 62, 27–60. doi:10.1016/j.gr.2018.02.008

Gardiner, N. J., Searle, M. P., Robb, L. J., and Morley, C. K. (2015). Neo-Tethyan Magmatism and Metallogeny in Myanmar - an Andean Analogue? *J. Asian Earth Sci.* 106, 197–215. doi:10.1016/j.jseaes.2015.03.015

Goldfarb, R. J., Ayuso, R., Miller, M. L., Ebert, S. W., Marsh, E. E., Petsel, S. A., et al. (2004). The Late Cretaceous Donlin Creek Gold Deposit, Southwestern Alaska: Controls on Epizonal Ore Formation. *Econ. Geology.* 99, 643–671. doi:10.2113/gsecongeo.99.4.643

Goldfarb, R. J., Baker, T., Dube, B., Groves, D. I., Hart, C. J. R., and Gosselin, P. (2005). "Distribution, Character, and Genesis of Gold Deposits in Metamorphic Terranes," in *Economic Geology 100th Anniversary Volume*. Editors J. W. Hedenquist, J. F. H. Thompson, R. J. Goldfarb, and J. P. Richards (Littleton: Society of Economic Geologists Inc.), 407–450.

Goldfarb, R. J., Groves, D. I., and Gardoll, S. (2001). Orogenic Gold and Geologic Time: a Global Synthesis. *Ore Geol. Rev.* 18 (1-2), 1–75. doi:10.1016/s0169-1368(01)00016-6

Goldfarb, R. J., and Groves, D. I. (2015). Orogenic Gold: Common or Evolving Fluid and Metal Sources through Time. *Lithos* 233, 2–26. doi:10.1016/j.lithos.2015.07.011

Goldfarb, R. J., and Santosh, M. (2014). The Dilemma of the Jiaodong Gold Deposits: Are They Unique? *Geosci. Front.* 5, 139–153. doi:10.1016/j.gsf.2013.11.001

Groves, D. I., and Bierlein, F. P. (2007). Geodynamic Settings of mineral deposit Systems. *J. Geol. Soc.* 164, 19–30. doi:10.1144/0016-76492006-065

Groves, D. I., Goldfarb, R. J., Gebre-Mariam, M., Hagemann, S. G., and Robert, F. (1998). Orogenic Gold Deposits: a Proposed Classification in the Context of Their Crustal Distribution and Relationship to Other Gold deposit Types. *Ore Geology. Rev.* 13, 7–27. doi:10.1016/s0169-1368(97)00012-7

Groves, D. I., Goldfarb, R. J., Robert, F., and Hart, C. J. R., Jr. (2003). Gold Deposits in Metamorphic Belts: Overview of Current Understanding,Outstanding Problems, Future Research, and Exploration Significance. *Econ. Geology.* 98, 1–29. doi:10.2113/gsecongeo.98.1.1

Groves, D. I., Santosh, M., Deng, J., Wang, Q., Yang, L., and Zhang, L. (2019). A Holistic Model for the Origin of Orogenic Gold Deposits and its Implications for Exploration. *Miner Deposita* 55, 275–292. doi:10.1007/s00126-019-00877-5

Groves, D. I., Santosh, M., Goldfarb, R. J., and Zhang, L. (2018). Structural Geometry of Orogenic Gold Deposits: Implications for Exploration of World-Class and Giant Deposits. *Geosci. Front.* 9, 1163–1177. doi:10.1016/j.gsf.2018.01.006

Groves, D. I., and Santosh, M. (2015). Province-scale Commonalities of Some World-Class Gold Deposits: Implications for mineral Exploration. *Geosci. Front.* 6, 389–399. doi:10.1016/j.gsf.2014.12.007

Groves, D. I., and Santosh, M. (2016). The Giant Jiaodong Gold Province: the Key to a Unified Model for Orogenic Gold Deposits? *Geosci. Front.* 7, 409–417. doi:10.1016/j.gsf.2015.08.002

Groves, D. I., Santosh, M., and Zhang, L. (2020). A Scale-Integrated Exploration Model for Orogenic Gold Deposits Based on a mineral System Approach. *Geosci. Front.* 11, 719–738. doi:10.1016/j.gsf.2019.12.007

Groves, D. I. (1993). The Crustal Continuum Model for Late-Archaean Lode-Gold Deposits of the Yilgarn Block, Western Australia. *Mineral. Deposita* 28, 366–374. doi:10.1007/bf02431596

Hagemann, S., and Cassidy, K. (2000). Archean Orogenic Lode Gold Deposits. *Rev. Econ. Geol.* 13, 9–68. doi:10.5382/Rev.13.01

Higgins, N. C., and Kerrich, R. (1982). Progressive 18O Depletion during CO2 Separation from a Carbon Dioxide-Rich Hydrothermal Fluid: Evidence from the Grey River Tungsten deposit, Newfoundland. *Can. J. Earth Sci.* 19, 2247–2257. doi:10.1139/e82-198

Kerrich, R., and Fyfe, W. S. (1981). The Gold-Carbonate Association: Source of CO2, and CO2 Fixation Reactions in Archaean Lode Deposits. *Chem. Geology.* 33, 265–294. doi:10.1016/0009-2541(81)90104-2

Kerrich, R., Goldfarb, R., Groves, D., and Garwin, S. (2000). The Geodynamics of World-Class Gold Deposits: Characteristics, Space–Time Distribution, and Origins. *Rev. Econ. Geol.* 13, 501–551. doi:10.5382/Rev.13.15

Khin Zaw (1990). Geological, Petrogical and Geochemical Characteristics of Granitoid Rocks in Burma: with Special Reference to the Associated WSn Mineralization and Their Tectonic Setting. *J. Southeast Asian Earth Sci.* 4, 293–335. doi:10.1016/0743-9547(90)90004-w

Khin Zaw (2017). "Chapter 24 Overview of Mineralization Styles and Tectonic-Metallogenic Setting in Myanmar," in *Myanmar: Geology, Resources and Tectonics*. Editors A. J. Barber, K. Zaw, and M. J. Crow (London: Geological Society. Memoirs), 48, 531–556. doi:10.1144/M48.24

Khin Zaw (2019). "Tectonic and Metallogenic Significance of Orogenic Gold Deposits in mainland SE Asia" in The Society Of Resource Geology Annual Meeting, Tokyo, Japan, June 26–28, 2019.

Khin Zaw., Meffre, S., Lai, C.-K., Burrett, C., Santosh, M., Graham, I., et al. (2014a). Tectonics and Metallogeny of mainland Southeast Asia - A Review and Contribution. *Gondwana Res.* 26, 5–30. doi:10.1016/j.gr.2013.10.010

Khin Zaw., Santosh, M., and Graham, I. T. (2014b). Tectonics and Metallogeny of mainland SE Asia: Preface. *Gondwana Res.* 26, 1–4. doi:10.1016/j.gr.2014.01.005

Khin Zaw., Makoundi, C., and Hai Thanh Tran. (2018). "Metallogenic Significance of Sediment-Hosted/orogenic Gold Deposits in mainland SE Asia: Keynote Address," in *Geosea XV: Regional Congress on Geology, Mineral and Energy Resources of SE Asia* (Ha Noi, Vietnam), 16–17.

Kisters, A. F. M., Kolb, J., Meyer, F. M., and Hoernes, S. (2000). Hydrologic Segmentation of High-Temperature Shear Zones: Structural, Geochemical and Isotopic Evidence from Auriferous Mylonites of the Renco Mine, Zimbabwe. *J. Struct. Geology.* 22, 811–829. doi:10.1016/s0191-8141(00)00006-7

Large, R. R., Bull, S. W., and Maslennikov, V. V. (2011). A Carbonaceous Sedimentary Source-Rock Model for Carlin-type and Orogenic Gold Deposits. *Econ. Geology.* 106, 331–358. doi:10.2113/econgeo.106.3.331

Large, R. R., Maslennikov, V. V., Robert, F., Danyushevsky, L. V., and Chang, Z. (2007). Multistage Sedimentary and Metamorphic Origin of Pyrite and Gold in the Giant Sukhoi Log deposit, Lena Gold Province, Russia. *Econ. Geology.* 102, 1233–1267. doi:10.2113/gsecongeo.102.7.1233

Mackenzie, M. J. (1999). *Report on the Exploration Progress in Block 3/13 for the Period January 1998 to December 1998*. Myanmar Burma: Palmer Resources Ltd. Myanmar (Burma) Project, 1–67.

May Thwe Aye., Myo Kyaw Hlaing.,Yonezu, K., and Watanabe, K. (2017). Fluid Inclusion Study of Shwegyin Gold deposit, Proceedings of the 7th Asia Africa Mineral Resources Conference, November 20-24, 2017, Bago Region, Myanmar. 157–160.

McCuaig, T. C., Beresford, S., and Hronsky, J. (2010). Translating the mineral Systems Approach into an Effective Exploration Targeting System. *Ore Geology. Rev.* 38, 128–138. doi:10.1016/j.oregeorev.2010.05.008

Mikucki, E. J. (1998). Hydrothermal Transport and Depositional Processes in Archean Lode Goldsystems: a Review. *Ore Geol. Rev.* 13, 307–321. doi:10.1016/S0169-1368(97)00025-5

Mitchell, A., Chung, S.-L., Oo, T., Lin, T.-H., and Hung, C.-H. (2012). Zircon U-Pb Ages in Myanmar: Magmatic-Metamorphic Events and the Closure of a Neo-Tethys Ocean? *J. Asian Earth Sci.* 56, 1–23. doi:10.1016/j.jseaes.2012.04.019

Mitchell, A. H. G. (2018). *Geological Belts, Plate Boundaries, and mineral Deposits in Myanmar*. Oxford: Elsevier, 509. doi:10.1016/B978-0-12-803382-1.01001-4

Mitchell, A. H. G., Nyunt, Htay., Asua, C., Deiparine, L., Aung, Khine., and Po., Sein. (1999). *Geological Settings of Gold Districts in Myanmar*. Berlin: Pacrim Berli Seminar.

Mitchell, A. H. G., Ausa, C. A., Deiparine, L., Hlaing, T., Htay, N., and Khine, A. (2004). The Modi Taung-Nankwe Gold District, Slate Belt, central Myanmar: Mesothermal Veins in a Mesozoic Orogen. *J. Asian Earth Sci.* 23, 321–341. doi:10.1016/S1367-9120(03)00138-X

Mitchell, A. H. G., Htay, M. T., Htun, K. M., Win, M. N., Oo, T., and Hlaing, T. (2007). Myint Thein Htay., Kyaw Min Htun., Myint Naing Win., Thura Oo., and Tin HlaingRock Relationships in the Mogok Metamorphic belt, Tatkon to Mandalay, central Myanmar. *J. Asian Earth Sci.* 29, 891–910. doi:10.1016/j.jseaes.2006.05.009

Mitchell, A. H. G. (1977). Tectonic Settings for Emplacement of Southeast Asian Tin Granites. *Bgsm* 9, 123–140. doi:10.7186/bgsm09197710

Myo Kyaw Hlaing (2013). *Geology and Geochemical Characteristics of Gold Mineralization at Shwetagun Area, Yemethin Township, Mandalay Region*. Myanmar: University of Yangon. M.Sc Thesis.

Myo Kyaw Hlaing., Aung Zaw Myint., Tindell, T., and May Thwe Aye (2019). Gold Mineralization in the Kyaikhto District, Mon State, Southern Myanmar. *Open J. Geol.* 9, 29–42. doi:10.4236/ojg.2019.91003

Oliver, N. H. S., and Bons, P. D. (2001). Mechanisms of Fluid Flow and Fluid-Rock Interaction in Fossil Metamorphic Hydrothermal Systems Inferred from Vein wall Rock Patterns, Geometry and Microstructure. *Geofluids.* 1, 137–162. doi:10.1046/j.1468-8123.2001.00013.x

Pearce, J. A., and Peate, D. W. (1995). Tectonic Implications of the Composition of Volcanic Arc Magmas. *Annu. Rev. Earth Planet. Sci.* 23, 251–285. doi:10.1146/annurev.ea.23.050195.001343

Phillips, G. N. (1993). Metamorphic Fluids and Gold. *Mineral. Mag.* 57 (388), 365–374. doi:10.1180/minmag.1993.057.388.02

Phillips, G. N., and Evans, K. A. (2004). Role of CO2 in the Formation of Gold Deposits. *Nature* 429, 860–863. doi:10.1038/nature02644

Phillips, G. N., and Powell, R. (2010). Formation of Gold Deposits: a Metamorphic Devolatilization Model. *J. Metamorph. Petrol.* 28, 689–718. doi:10.1111/j.1525-1314.2010.00887.x

Phillips, G. N., and Powell, R. (2009). Formation of Gold Deposits: Review and Evaluation of the Continuum Model. *Earth-Science Rev.* 94, 1–21. doi:10.1016/j.earscirev.2009.02.002

Phillips, G. N., and Powell, R. (1993). Link between Gold Provinces. *Econ. Geol.* 88, 1084–1098. doi:10.2113/gsecongeo.88.5.1084

Poulsen, K. H., Robert, F., and Dubé, B. (2000). Geological Classification of Canadian Gold Deposits. *Geol. Surv. Can. Bull.* 540, 106. doi:10.4095/211094

Ridd, M. F., and Watkinson, I. (2013). The Phuket-Slate Belt Terrane: Tectonic Evolution and Strike-Slip Emplacement of a Major Terrane on the Sundaland Margin of Thailand and Myanmar. *Proc. Geologists' Assoc.* 124, 994–1010. doi:10.1016/j.pgeola.2013.01.007

Ridley, J. R., and Diamond, L. W. (2000). "Fluid Chemistry of Lode-Gold Deposits and Implications for Genetic Models," in *Reviews in Economic Geology: Gold in 2000*. Editors S. G. Hagemann and P. Brown (Littleton, Colorado, United States: Society of Economic Geologists), 13, 141–162.

Ridley, J. (1993). The Relations between Mean Rock Stress and Fluid Flow in the Crust: with Reference to Vein- and Lode-Style Gold Deposits. *Ore Geology. Rev.* 8, 23–37. doi:10.1016/0169-1368(93)90026-u

Robert, F., Boullier, A.-M., and Firdaous, K. (1995). Gold–quartz Veins in Metamorphic Terranes and Their Bearing on the Role of Fluids in Faulting. *J. Geophys. Res. Solid Earth* 100 (87), 861–879. doi:10.1029/95jb00190

Robert, F., and Poulsen, K. H. (2001). "Vein Formation and Deformation in Greenstone Gold Deposits," in *Structural Control on Ore Genesis*. Editors J. P. Richards and R. M. Tosdal (Edmonton, AB: Rev. Econ. Geol.), 14, 111–155. doi:10.5382/Rev.14.05

Robert, F., Poulson, H. K., Cassidy, K. F., and Hodgson, J. C. (2005). "Gold Metallogeny of the superior and Yilgarn Cratons," in *Economic Geology 100th Anniversary* (Littleton, Colorado, United States: Society of Economic Geologists), 1001–1033. doi:10.5382/av100.30

Roedder, E., and Bodnar, R. J. (1980). Geologic Pressure Determinations from Fluid Inclusion Studies. *Annu. Rev. Earth Planet. Sci.* 8, 263–301. doi:10.1146/annurev.ea.08.050180.001403

Roedder, E. (1984). Fluid Inclusions. *Rev. Mineralogy* 12, 644pp. doi:10.1515/9781501508271

Schwartz, M. O., Rajah, S. S., Askury, A. K., Putthapiban, P., and Djaswadi, S. (1995). The Southeast Asian Tin belt. *Earth-Science Rev.* 38, 95–293. doi:10.1016/0012-8252(95)00004-t

Searle, M. P., Noble, S. R., Cottle, J. M., Waters, D. J., Mitchell, A. H. G., Tin, Hlaing., et al. (2007). Tectonic Evolution of the Mogok Metamorphic belt, Burma (Myanmar) Constrained by U-Th-Pb Dating of Metamorphic and Magmatic Rocks. *Tectonics* 26. doi:10.1029/2006tc002083

Shackleton, J. M., Spry, P. G., and Bateman, R. (2003). Telluride Mineralogy of the Golden Mile Deposit, Kalgoorlie, Western Australia. *Can. Mineral.* 41, 1503–1524. doi:10.2113/gscanmin.41.6.1503

Sibson, R. H., Robert, F., and Poulsen, K. H. (1988). High-angle Reverse Faults, Fluid-Pressure Cycling, and Mesothermal Gold-Quartz Deposits. *Geol* 16, 551–555. doi:10.1130/0091-7613(1988)016<0551:harffp>2.3.co;2

Sibson, R. H., and Scott, J. (1998). Stress/fault Controls on the Containment and Release of Overpressured Fluids: Examples from Gold-Quartz Vein Systems in Juneau, Alaska; Victoria, Australia and Otago, New Zealand. *Ore Geology. Rev.* 13, 293–306. doi:10.1016/s0169-1368(97)00023-1

Span, R., and Wagner, W. (1996). A New Equation of State for Carbon Dioxide Covering the Fluid Region from the Triple-Point Temperature to 1100 K at Pressures up to 800 MPa. *J. Phys. Chem. Reference Data* 25, 1509–1596. doi:10.1063/1.555991

Spandler, C., Hermann, J. r., Arculus, R., and Mavrogenes, J. (2003). Redistribution of Trace Elements during Prograde Metamorphism from Lawsonite Blueschist to Eclogite Facies; Implications for Deep Subduction-Zone Processes. *Contrib. Mineralogy Petrology* 146 (2), 205–222. doi:10.1007/s00410-003-0495-5

Steele-MacInnis, M., Lecumberri-Sanchez, P., and Bodnar, R. J. (2012). HokieFlincs_H2O-NaCl : A Microsoft Excel Spreadsheet for Interpreting Microthermometric Data from Fluid Inclusions Based on the PVTX Properties of H 2 O-NaCl. *Comput. Geosciences* 49, 334–337. doi:10.1016/j.cageo.2012.01.022

Sterner, S. M., and Pitzer, K. S. (1994). An Equation of State for Carbon Dioxide Valid from Zero to Extreme Pressures. *Contr. Mineral. Petrol.* 117, 362–374. doi:10.1007/bf00307271

Tomkins, A. G. (2013). On the Source of Orogenic Gold. *Geol* 41, 1255–1256. doi:10.1130/focus122013.1

Tomkins, A. G. (2010). Windows of Metamorphic Sulfur Liberation in the Crust: Implications for Gold deposit Genesis. *Geochimica et Cosmochimica Acta* 74 (11), 3246–3259. doi:10.1016/j.gca.2010.03.003

Traynor, J., Eskine, T., Khin ZawLarge, R. R., Makoundi, C., and Knight, J. (2015). Geology and Mineralization Characteristics of the Modi Taung Orogenic Gold deposit, Central Myanmar. Proceedings of the SEG Conference, 27–30 September 2015, Hobart, Australia, CD-ROM.

Traynor, J., Eskine, T., Zaw, K., Large, R. R., Makoundi, C., and Tin Tun (2017). *Geology and Mineralisation Characteristics of the Modi Taung Orogenic Gold deposit, Central Myanmar:* Inaugural Conference On Applied Earth Sciences In Myanmar and Neighboring Regions. Yangon, Myanmar: Myanmar Applied Earth Sciences Association, 118.

Wilkinson, J. J. (2001). Fluid Inclusions in Hydrothermal Ore Deposits. *Lithos* 55, 229–272. doi:10.1016/S0024-4937(00)00047-5

Win Phyo., Yonezu, K., and Watanabe, K. (2016). Ore-forming Conditions of Metasedimentary Rock-Hosted Gold Mineralization, Phayaung Taung Area, Mandalay Region, central Myanmar. *Proc. Int. Symp. Earth Sci. Technology*, 314–319.

Wyman, D. A., Cassidy, K. F., and Hollings, P. (2016). Orogenic Gold and the mineral Systems Approach: Resolving Fact, Fiction and Fantasy. *Ore Geology. Rev.* 78, 322–335. doi:10.1016/j.oregeorev.2016.04.006

Yardley, B. W. D., and Bodnar, R. J. (2014). Fluids in the continental Crust. *Geochemical Perspect.* 3 (1), 123pp. doi:10.7185/geochempersp.3.1

Yardley, B. W. D., and Cleverley, J. S. (2015). "The Role of Metamorphic Fluids in the Formation of Ore Deposits," in *Ore Deposits in an Evolving Earth*. Editors G. R. T. Jenkin, P. A. J. Lusty, I. McDonald, M. P. Smith, A. J. Boyce, and J. J. Wilkinson (London: Geological Soci. Spec. Publ), 393, 117–134. doi:10.1144/sp393.5*Geol. Soc. Lond. Spec. Publications*

Ye Myint Swe., Cho Cho Aye., and Khin Zaw. (2017). "Chapter 25 Gold Deposits of Myanmar," in *Myanmar: Geology, Resources, and Tectonics*. Editors A. J. Barber, K. Zaw, and M. J. Crow (London: The Geological Society, Memoirs, London), 48, 557–572. doi:10.1144/M48.25

Zaw Naing Oo., and Khin Zaw. (2009). Geology and Mineralization Characteristics of Meyon Gold deposit, Mon State, Southern Myanmar. Proceedings of the 11th Regional Congress on Geology, Mineral and Energy resources of Southeast Asia (GEOSEA), 8–10 June, Kuala Lumpur, Malaysia, 32.

Zaw Naing Oo., Khin Zaw., and Mernagh, T. (2010). Geological Setting and Nature of Mineralization at Meyon Gold deposit, Mon State, Myanmar. Proceedings of the 13th quadrennial international association on genesis of ore deposits (IAGOD) symposium, 6–9 April, 2010. CD-ROM, Adelaide.

Zaw Naing Oo., and Khin Zaw. (2015). Geological Setting and Nature of Mineralization at Meyon Gold deposit, Southern Myanmar. Proceedings of the SEG Conference, 27–30 September 2015, Hobart, Australia, CD-ROM.

Zaw Naing Oo., and Khin Zaw. (2017). *Geological Setting and Nature of Mineralization at Meyon Gold Deposit, Southern Myanmar:* Inaugural Conference On Applied Earth Sciences In Myanmar and Neighboring Regions. Yangon, Myanmar: Myanmar Applied Earth Sciences Association, 111.

Conflict of Interest: The authors declare that the research was conducted in the absence of any commercial or financial relationships that could be construed as a potential conflict of interest.

frontiers in Earth Science

ORIGINAL RESEARCH
published: 11 March 2022
doi: 10.3389/feart.2022.830453

Discovery of Yaozhuang Stock and Deep Ore Prospecting Implication for the Western Mangling Orefield in North Qinling Terrane, Central China

Peng Fan[1,2], *Aihua Xi*[1]*, *Bin Zhou*[2], *Xu Chao*[2], *Wenbo Yang*[2], *Jiaxin Sun*[2], *Hongyu Zhu*[2] and *Li Wei*[2]

[1]State Key Laboratory of Oil and Gas Reservoir Geology and Exploitation, Southwest Petroleum University, Chengdu, China, [2]Shaanxi Geological Survey Planning Research Center (Shaanxi Geological Survey Fund Center), Xi'an, China

In the western Mangling orefield, the molybdenum (Mo) polymetallic deposits are closely related to the ore-bearing porphyry stocks (individual outcrop size: <1 km^2). In this study, we have discovered several granitic stocks at Yaozhuang. Systematic petrologic, zircon U-Pb-Hf isotope and whole-rock geochemical studies show that both the granitic stocks of porphyritic granite (157 ± 2 Ma) and the intruding monzogranite dike (153 ± 1 Ma) were emplaced in the Late Jurassic. These granitic stocks are characterized by high SiO_2 (66.83–75.63 wt%), high K_2O (4.15–5.05 wt%), high Al_2O_3 (12.90–16.93 wt%), and low MgO (0.06–0.73 wt%) and are metaluminous to weakly peraluminous, being highly fractionated I-A-type transition granites. The content of the total rare Earth element (ΣREE) of the porphyritic granite (139.6–161.7 ppm) is lower than that of the monzogranite (151.4–253.6 ppm). The porphyritic granite has weakly negative Eu anomalies (Eu/Eu* = 0.77–0.93), whereas the monzogranite has weakly positive Eu anomalies (Eu/Eu* = 0.97–1.21) and are more enriched in light rare Earth elements. Both of them are enriched in large ion lithophile elements (LILEs, e.g., K, Rb, and Ba) but depleted in high-field-strength elements (HFSEs, e.g., Nb, Ta, Ti, Zr, and Hf). The zircon $\varepsilon_{Hf}(t)$ values of all the samples range from −16.1 to −6.9, and the two-stage model ages (t_{DM2}) are 1.78–2.16 Ga. The magma may have originated from partial melting of the lower crust (more than 40 km in depth) caused by mantle-derived magma underwelling. The plutons and stocks were emplaced into the intersection of the early EW-trending faults and the late (Yanshanian) NE-trending faults. The fertile magma with high water content (H_2O > 4%) and high oxygen fugacity (Delta FMQ > 1.5) indicates that the Yaozhuang area has significant potential for porphyry Mo polymetallic ore discovery.

Keywords: Yaozhuang granitic stocks, zircon U-Pb age, late Jurassic granite, western Mangling orefield, North Qinling terrane

OPEN ACCESS

Edited by:
Kit Lai,
Universiti Brunei Darussalam, Brunei

Reviewed by:
Rui Wang,
China University of Geosciences, China
Jian-Jun Fan,
Jilin University, China

***Correspondence:**
Aihua Xi
aihuaxi@163.com

Specialty section:
This article was submitted to Geochemistry, a section of the journal Frontiers in Earth Science

Received: *07 December 2021*
Accepted: *17 January 2022*
Published: *11 March 2022*

Citation:
Fan P, Xi A, Zhou B, Chao X, Yang W, Sun J, Zhu H and Wei L (2022) Discovery of Yaozhuang Stock and Deep Ore Prospecting Implication for the Western Mangling Orefield in North Qinling Terrane, Central China. Front. Earth Sci. 10:830453. doi: 10.3389/feart.2022.830453

Abbreviations: A, A-type granite; FG, differentiated granite; I, S, and M, undifferentiated I, S, and M-type granite; OGT, undifferentiated I, S, and M-type granite.

INTRODUCTION

The Qinling orogen is well-known for its multistage magmatism and orogeny (Mattauer et al., 1985; Kröner et al., 1998; Meng and Zhang, 1999; Liu et al., 2016). The magmatism occurred in four major stages: Neoproterozoic, Paleozoic, Early Mesozoic, and Late Mesozoic (Ratschbacher et al., 2003; Wang et al., 2012; Wang et al., 2015b). Previous works have studied the rock assemblage, magma source, and spatiotemporal evolution of intermediate-felsic plutons in the region and described the multistage orogeny in detail (Zhang et al., 1995; Dong et al., 2012; 2016; Wang et al., 2017; Li N. et al., 2018; Bao et al., 2019).

The western Mangling orefield is one of the deep prospecting hotspots in North Qinling terrane in recent years, and the orefield is also an important component of the Qinling Mo polymetallic ore belt (Fan and Xie, 1999; Mao et al., 2011; Yang et al., 2017). The known deposits in the area include Taoguanping, Xigou, Nantai, Mahe Mo deposits, etc. The Late Jurassic–Early Cretaceous Mangling pluton and the western porphyries are developed in the orefield, and the latter is closely related to the local Mo polymetallic mineralization (Mao et al., 2008, 2010; Zeng et al., 2012; Zhai and Santosh, 2013). In recent years, many workers have studied the age, magma evolution, petrogenesis, and mineralization of the Mangling pluton and Nantai, Taoguanping, and Xigou granitic stocks on the western side of the orefield (Ke et al., 2012a, 2012b; Qin et al., 2012; Yang et al., 2014; Hu et al., 2017), whereas granitic stock in the Yaozhuang area was rarely studied. The 1:50,000 gravity survey in Mangling revealed an oval low Bouguer gravity anomaly at Yaozhuang, and the presence of concealed porphyry bodies was speculated at depth (Yang et al., 2020). In the southwest of the study area, the borehole (Northwest Nonferrous Geological Research Institute Co., Ltd.) drilled porphyry at 380–1,400 m, accompanied by NW-extending Mo polymetallic ore (Yang et al., 2019). In the process of field geological survey, Yaozhuang stock and some monzogranite dikes were found near the gravity anomaly. Therefore, we analyzed the zircon U-Pb geochronology, Lu-Hf isotopes, and whole-rock geochemistry of the Yaozhuang stocks and discussed their petrogenesis and prospecting implications for the western Mangling orefield. This work provides new data for studying the late Mesozoic tectonic–magmatic evolution of the North Qinling terrane.

GEOLOGICAL SETTING

The study area (Yaozhuang, Luonan County) in North Qinling is located in the early Neoproterozoic Kuanping Rift, a narrow EW-trending structure extending along the Luonan–Luanchuan and Qiaorui–Waxuezi deep-seated faults (Zhang S. H. et al., 2019). Among them, there are a large number of NE-trending Yanshanian faults. The intersection of these faults often controls the development of various magmatic deposits (Diwu et al., 2010). Exposed stratigraphy comprises predominantly the Middle-Upper Proterozoic Kuanping Group ($Pt_{2-3}k$), consisting of metamorphosed mafic volcanic rocks, clastic rocks, and carbonate rocks. The Kuanping Group can be divided into the Guangdongping ($Pt_{2-3}gd$), Sichakou ($Pt_{2-3}sc$), and Xiewan ($Pt_{2-3}x$) formations from bottom to top (Li C. D. et al., 2018). The crystalline basement comprises the Qinling Group amphibolite-facies metamorphic rocks, with local granulite- or eclogite-facies rocks (Liu B. X. et al., 2013; Diwu et al., 2014; Zhang et al., 2015). There are a series of Yanshanian (Jurassic–Cretaceous) granitic stocks in the area. The Mangling pluton is a large EW-trending intrusive complex, containing diorite, biotite monzogranite, and moyite. On the western side of the Mangling pluton, shallow granitic stocks (e.g., Taoguanping, Xigou, Nantai, and Panhe) are present with lithology mainly of porphyritic granite, monzogranite, alaskite, and granodiorite (**Figure 1**).

The Yaozhuang granitic stocks intruded the Sichakou Formation biotite-quartz schist and the Guangdongping Formation plagioclase-amphibole schist. The individual stock has an exposed area of $<1\ km^2$ and extends NW or NE (**Figure 2A**). These stocks comprise mainly porphyritic granite and intruding monzogranite dikes (**Figure 2B**).

SAMPLES AND ANALYTICAL METHODS

Sample Descriptions

Ten samples (five porphyritic granite and five monzogranite) in this study were collected from Yaozhuang village, Luonan County. The sampling positions are shown in **Figure 1**.

The porphyritic granite is light gray and massive and composed of phenocrysts (15 vol%) and groundmass (85 vol %). The phenocrysts comprise mainly plagioclase, K-feldspar, and quartz. Plagioclase (size: 1–3 mm) is euhedral–subhedral and polysynthetic twinned. K-feldspar (size: 0.5–4 mm) includes mainly microcline and is euhedral–subhedral and slightly kaolinite altered on the surface. The grain margins are locally rimmed by fine secondary quartz. Quartz (size: 0.8–2 mm) is euhedral granular and colorless. The microcrystalline groundmass is composed mainly of plagioclase, microcline, quartz, and minor biotite. Accessory minerals include apatite and zircon (**Figure 2C**).

The monzogranite is massive; the ores show hypidiomorphic granular texture and contain K-feldspar (35–40 vol%), plagioclase (30–35 vol%), quartz (20–25 vol%), and minor biotite (<5 vol%). K-feldspar (size: 0.5–2 mm) is euhedral–subhedral, dominated by perthite with minor microcline, and weakly kaolinite altered. Plagioclase grains (size: 0.5–3 mm) are subhedral and partially sericite and K-feldspar altered. Quartz (size: 0.7–3 mm) is anhedral granular with wavy extinction. Biotite (size: 0.4–2 mm) is flaky and chloritized locally (**Figure 2D**).

Zircon U-Pb-Hf Isotope Analysis

Zircon grains from one porphyritic granite and one monzogranite sample were separated with conventional heavy liquid and magnetic separation techniques. LA-ICP-MS zircon U-Pb dating was completed at the State Key Laboratory of Continental Dynamics, Northwestern University. The laser ablation system used was a GeoLas 200M from MicroLas

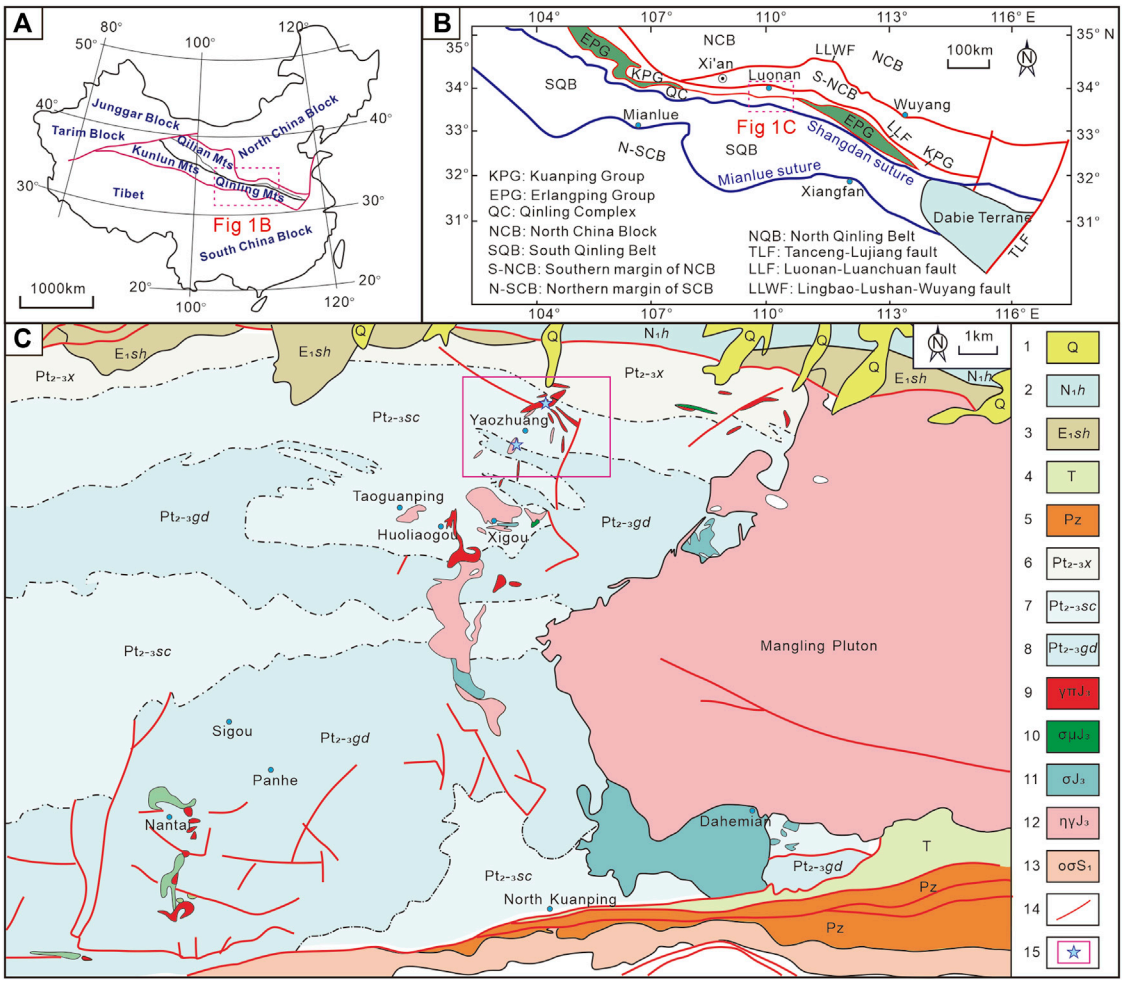

FIGURE 1 | Regional geological map of the western Mangling orefield [**(A)** revised after Ke et al., 2012a; **(B)** after Dong et al., 2011b].

(Germany) with a 30 μm spot size, 10 Hz repetition rate, and 32–36 MJ energy. Ion signal intensities were acquired with a quadrupole Elan 6100 DRC (ICP-MS). The instrument configuration and analytical procedures were as described by Yuan et al. (2003). Zircon GEMOC GJ-1 was used as the external standard to correct elemental fractionation and monitor instrument quality. The zircon U, Th, and Pb contents were calculated by the NIST SRM 610 glass standard (Liu et al., 2010). The method of Andersen (2002) was adopted for common Pb correction, the Glitter program (version 4.0) was used for data processing, and the Isoplot program (version 3.75) was used to calculate the U-Pb age and construct the concordia plot.

The zircon Hf isotope analysis was performed at the Laboratory of Langfang Institute of Regional Geological Survey (China), and the analysis was performed on the U-Pb dating spots. The instrument adopted the GeoLas 200M equipped with a 193 nm ArF excimer system and the Neptune plus multi-receiver plasma mass spectrometry (LA-MC-ICP-MS). The diameter of the laser ablation spot beam is 50 μm, and the denudation depth is 20–40 μm. Helium was used as the carrier gas and mixed with the argon makeup gas. The standard zircon 91500 was used as the external standard to monitor the analytical accuracy. Detailed instrumental conditions and analysis procedures were as described by Yuan et al. (2008). $^{176}Lu/^{175}Lu$ = 0.02655 and $^{176}Yb/^{172}Yb$ = 0.5887 were used for interference correction (Wu et al., 2007a).

Whole-Rock Geochemical Analysis

Whole-rock geochemical compositions were determined at the laboratory of the #203 Institute of Nuclear Industry Geology (Xi'an, China). Major element compositions were measured with an Axios X-ray fluorescence (XRF) spectrometer (Panaco, the Netherlands). The analysis error was less than 5%. After correcting the loss on ignition (LOI), the major element oxide contents were back-calculated to 100%. Meanwhile, the standard curve was established with the GeokitPro program (Lu, 2004). The trace elements and rare Earth elements (REEs) were analyzed by the XSERIES II ICP-MS manufactured by Thermo Fisher (United States) with a precision better than 5%.

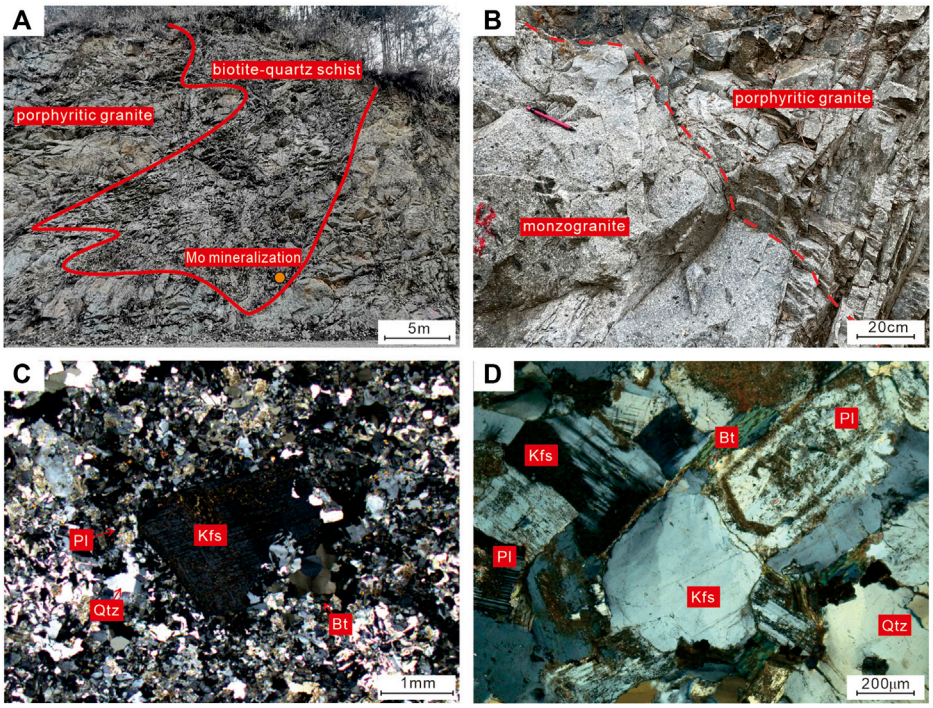

FIGURE 2 | Photos and microstructures of Yaozhuang stock. **(A)** Porphyritic granite intruded into biotite quartz schist; **(B)** monzogranite vein intruded into porphyritic granite; **(C)** porphyritic granite (orthogonal polarization); **(D)** monzogranite (orthogonal polarization); Kfs—K-feldspar, Pl—plagioclase, Qtz—quartz, Bt—biotite; $\gamma\pi J_3$—Late Jurassic porphyritic granite; $\eta\gamma J_3$—Late Jurassic monzogranite; $Pt_{2\text{-}3}sc$—Middle-Upper Proterozoic Sichakou rock formation.

ANALYSIS RESULTS

Zircon U-Pb age

The zircon grains from both samples have lengths of 70–210 μm with aspect ratios of 3:1–3:1 and are mostly transparent and euhedral elongated prismatic. CL images show clear oscillatory zoning (**Figure 3A**), with clear core–mantle–rim structures. The zircons have Th/U = 0.27–2.8, typical of magmatic zircons (Belousova et al., 2002; Wu and Zheng, 2004).

A total of 25 zircons were analyzed for porphyritic granite sample no. D92-1, among which 21 are concordant (>90%) and 17 spots fall on the concordia, yielding a weighted-mean $^{206}Pb/^{238}U$ age of 157 ± 2 Ma (MSWD = 0.15) (**Figure 3B**). A total of 25 zircons were analyzed for monzogranite sample no. D13-8, with 23 spots being concordant and 21 spots falling on the concordia, yielding a weighted-mean $^{206}Pb/^{238}U$ age of 153 ± 1 Ma (MSWD = 0.10) (**Figure 3C**). Two inherited zircons were identified, with the age of 847 ± 7 Ma. Monzogranite is slightly younger than porphyritic granite (4 Ma), consistent with the field observation that the monzogranite dike intruded the porphyritic granite (**Table 1**).

Zircon Hf Isotope Compositions

For our two samples, their $^{176}Lu/^{177}Hf$ ratios are <0.002, indicating negligible radiogenic Hf accumulation after the zircon crystallization, and the sample $^{176}Hf/^{177}Hf$ approximates that of the entire system (Vervoort et al., 1996; Wu et al., 2007a). The samples have $f_{Lu/Hf}$ values of −0.97 to −0.94 (avg. −0.95), and $^{176}Hf/^{177}Hf$ = 0.282301–0.282485 (avg. 0.282367; porphyritic granite) and 0.282225–0.282372 (avg. 0.282317; monzogranite). The samples have $\varepsilon_{Hf}(t)$ values of −13.4 to −6.9 (porphyritic granite) and −16.1 to −11.0 (monzogranite) and two-stage Hf-isotope model ages (t_{DM2}) (representing the age of source material extraction from the depleted mantle) of 1.64–2.05 Ga (porphyritic granite) and 1.89–2.21 Ga (monzogranite) (**Table 2**).

Whole-Rock Geochemistry

The major element oxide compositions of the porphyritic granite and monzogranite are similar, with SiO_2 = 66.83–75.63 wt%, total alkali (Na_2O + K_2O) = 8.09–10.41 wt%, and Al_2O_3 = 12.90–16.93 wt%. The contents of MgO (0.06–0.73 wt%), TFe_2O_3 (0.99–2.23 wt%), and CaO (0.46–1.99 wt%) are generally low. The samples are high-K calc-alkaline (**Figure 4A**) and metaluminous to weakly peraluminous (A/CNK = 0.92–1.09) (**Table 3**; **Figure 4B**).

The monzogranite has a higher total REE (ΣREE = 151.4–253.6 ppm) than that of porphyritic granite (ΣREE = 139.6–161.7 ppm). Both rock types have right-inclining chondrite-normalized REE patterns (**Figure 5A**), with LREE/HREE = 14.4–25.7 and $(La/Yb)_N$ = 16.7–36.4. However, the porphyritic granite has weakly negative Eu anomalies (Eu/Eu* = 0.77–0.93), whereas the monzogranite has weakly positive Eu

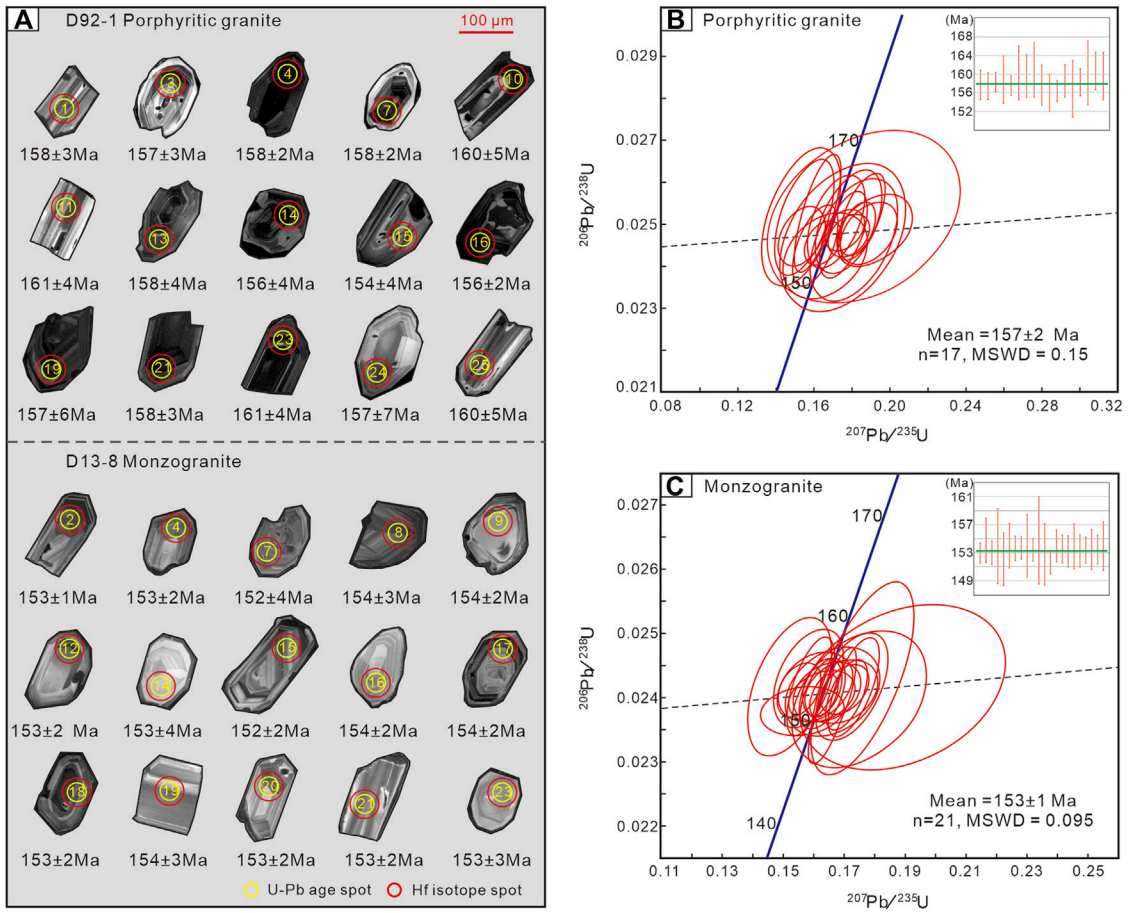

FIGURE 3 | Zircon CL images **(A)** and U-Pb dates **(B,C)** for Yaozhuang stock.

anomalies (Eu/Eu* = 0.97–1.21). In the primitive mantle-normalized spidergram (**Figure 5B**), both rock types are enriched in LILEs (e.g., Rb, K, and Ba) but depleted in HFSEs (e.g., Nb, Ta, Ti, Zr, and Hf) (**Table 3**).

DISCUSSION

Time of the Granitic Stock Emplacement

Late Mesozoic (158–112 Ma) magmatism was extensive in the North Qinling terrane (Wang et al., 2011; Liu R. et al., 2013; Lei et al., 2018; Zhang Y. S. et al., 2019; Wang et al., 2020), as represented by the Muhuguan, Mangling, and Laojunshan plutons and the nearby porphyry stocks. Recent geochronological studies had constrained the magmatic peak to be 158–144 Ma (**Table 4**), which was closely related to the regional Mo polymetallic mineralization (160–150 Ma. Mao et al., 2013, 2017). As shown in **Table 4**, the age of Mangling pluton seems to be slightly later than the stocks in the west, which may be related to the active emplacement controlled by the intersection of faults, or because the late magma in Mangling pluton may not be emplaced to the surface. In this study, the newly obtained zircon U–Pb ages for porphyritic granite (157 ± 2 Ma) and monzogranite (153 ± 1 Ma) fall within the regional magmatic peak. Combined with the available age data and features of granitic rock distribution, it constrains the magmatism of the western Mangling orefield to about 15 My.

Petrogenesis

The Yaozhuang granitic stocks are dominantly high-K calc-alkaline and metaluminous–weakly peraluminous (0.74–1.09). The samples do not contain Al-rich minerals (e.g., garnet and corundum) that are common in S-type granites but contain sphene and apatite that are common in I-type granites. The aluminum content index (A/CNK < 1.1) indicates that they are I-type granites (Wu et al., 2007b). Combined with the data of other stocks near the study area, the Zr-10000Ga/Al diagram shows the sample plot in the I-A-type transition area (**Figure 6A**). The 160–140 Ma period is considered to be the peak period of the transformation mechanism from the paleo-Asia and Tethys tectonic domain to paleo-Pacific tectonic domain (Ding et al., 2011; Dong et al., 2018), accompanied by local crustal compression thickening and later extension. The I-A-type

TABLE 1 | LA-ICP-MS zircon U-Pb ages of Yaozhuang stock.

No.	Element (ppm)		Corrected isotope ratio							Apparent age (Ma)					
	Th	U	Th/U	$^{207}Pb/^{206}Pb$	10	$^{207}Pb/^{235}U$	13	$^{206}Pb/^{238}U$	13	$^{207}Pb/^{206}Pb$	10	$^{207}Pb/^{235}U$	13	$^{206}Pb/^{238}U$	13
D92-1 porphyritic granite															
1	536	743	0.72	0.0554	0.0029	0.1883	0.0102	0.0248	0.0005	428	115	175	9	158	3
2	512	435	1.18	0.0502	0.0032	0.1605	0.0106	0.0231	0.0004	211	145	151	9	147	2
3	2,608	1,495	1.74	0.0449	0.0022	0.1532	0.008	0.0247	0.0005			145	7	157	3
4	1,380	1,566	0.88	0.0514	0.002	0.176	0.0068	0.0249	0.0003	257	87	165	6	158	2
5	667	796	0.84	0.0494	0.0022	0.1944	0.0091	0.0287	0.0008	165	138	180	8	182	5
6	185	162	1.15	0.0686	0.007	0.2313	0.0232	0.0249	0.0008	887	212	211	19	159	5
7	1,712	1,236	1.38	0.0524	0.0023	0.1784	0.007	0.0247	0.0003	306	94	167	6	158	2
8	429	605	0.71	0.0705	0.002	1.5251	0.0433	0.1567	0.0018	943	64	941	17	939	10
9	653	601	1.09	0.0456	0.0027	0.1549	0.0103	0.0252	0.0009			146	9	160	6
10	1,228	957	1.28	0.0495	0.0024	0.1714	0.01	0.0251	0.0007	172	113	161	9	160	5
11	1,334	1,234	1.08	0.048	0.0021	0.1621	0.0081	0.0253	0.0009	98	100	153	7	161	4
12	970	928	1.04	0.0506	0.0044	0.1861	0.0336	0.0252	0.0014	233	202	173	29	160	5
13	619	1,437	0.43	0.0515	0.0021	0.1757	0.0081	0.0247	0.0007	261	94	164	7	158	4
14	2,747	1,338	2.05	0.0483	0.0024	0.1609	0.0076	0.0245	0.0006	122	111	151	7	156	4
15	477	417	1.14	0.0506	0.0044	0.1661	0.0146	0.0243	0.0007	233	202	156	13	154	4
16	2,396	1,673	1.43	0.0487	0.0019	0.1646	0.0063	0.0246	0.0003	200	91	155	6	156	2
17	264	673	0.39	0.1088	0.0024	4.4053	0.116	0.2936	0.0049	1780	41	1,713	22	1,659	24
18	526	371	1.42	0.0561	0.0037	0.1923	0.013	0.0249	0.0006	457	146	179	11	159	3
19	269	985	0.27	0.053	0.0035	0.1811	0.0152	0.0246	0.001	328	150	169	13	157	6
20	986	554	1.78	0.079	0.0091	0.2865	0.0486	0.0247	0.001	1,172	231	256	38	157	6
21	2,876	2,218	1.3	0.0533	0.002	0.1821	0.0067	0.0248	0.0005	339	83	170	6	158	3
22	606	406	1.49	0.0465	0.0046	0.1532	0.0136	0.0252	0.0011	33	222	145	12	160	7
23	2,131	1,907	1.12	0.0535	0.0022	0.1855	0.008	0.0252	0.0006	350	93	173	7	161	4
24	434	285	1.52	0.0496	0.004	0.1753	0.0218	0.0247	0.0012	176	191	164	19	157	7
25	498	457	1.09	0.053	0.0035	0.1784	0.0116	0.0251	0.0008	332	150	167	10	160	5
D13-8 monzogranite															
1	251	422	0.59	0.0701	0.0015	1.43	0.0326	0.1476	0.0016	931	43	902	14	888	9
2	4,102	1,464	2.8	0.0492	0.001	0.1632	0.0031	0.024	0.0002	167	42	153	3	153	1
3	438	960	0.46	0.0491	0.0027	0.1583	0.0076	0.0243	0.0005	154	130	149	7	155	3
4	587	509	1.15	0.0492	0.0022	0.1628	0.0071	0.024	0.0003	167	101	153	6	153	2
5	127	409	0.31	0.0663	0.0013	1.2166	0.0212	0.1331	0.001	817	39	808	10	805	6
6	139	174	0.8	0.0563	0.0052	0.1891	0.0223	0.0242	0.0008	465	202	176	19	154	5
7	398	932	0.43	0.0505	0.0014	0.1662	0.0052	0.0239	0.0006	220	56	156	5	152	4
8	906	507	1.79	0.048	0.0018	0.159	0.0051	0.0242	0.0005	98	87	150	5	154	3
9	773	952	0.81	0.0467	0.0015	0.1551	0.0047	0.0241	0.0003	35	87	146	4	154	2
10	292	869	0.34	0.0513	0.0017	0.1703	0.0052	0.0241	0.0003	254	76	160	4	154	2
11	384	261	1.47	0.0457	0.0026	0.1521	0.0091	0.0242	0.0007			144	8	154	4
12	1,518	1,013	1.5	0.0493	0.0014	0.1635	0.0045	0.0241	0.0003	167	69	154	4	153	2
13	337	1,144	0.3	0.0518	0.0013	0.176	0.0111	0.0243	0.001	280	62	165	10	155	6
14	64	98	0.66	0.0539	0.0049	0.175	0.0146	0.024	0.0007	365	210	164	13	153	4
15	403	319	1.26	0.048	0.0031	0.1561	0.0091	0.0238	0.0003	102	154	147	8	152	2
16	463	394	1.17	0.048	0.0022	0.1605	0.0081	0.0242	0.0004	98	113	151	7	154	2
17	679	1,658	0.41	0.049	0.0012	0.1626	0.0037	0.0241	0.0003	146	56	153	3	154	2
18	2,023	1,840	1.1	0.0516	0.0013	0.1707	0.0045	0.024	0.0004	265	59	160	4	153	2
19	1,617	728	2.22	0.0522	0.0018	0.1731	0.0056	0.0242	0.0005	295	80	162	5	154	3
20	2,631	1,500	1.75	0.0491	0.0012	0.1628	0.0046	0.0241	0.0004	150	55	153	4	153	2
21	1,120	768	1.46	0.05	0.0017	0.1662	0.006	0.0241	0.0003	195	106	156	5	153	2
22	145	534	0.27	0.1625	0.0025	3.9755	0.2317	0.1765	0.0094	2,483	26	1,629	47	1,048	52
23	197	173	1.14	0.05	0.0031	0.1662	0.0104	0.0241	0.0005	195	151	156	9	153	3
24	451	452	1	0.051	0.0023	0.1692	0.0079	0.0241	0.0003	239	106	159	7	153	2
25	1,261	754	1.67	0.052	0.0025	0.1724	0.0079	0.0242	0.0006	287	111	161	7	154	3

transition granites are just the products of this period. The (K_2O + Na_2O)/CaO vs. (Zr + Nb + Ce + Y) diagram shows the features of high-fractionation granites (**Figure 6B**). The occurrence of high-fractionation granites is mainly related to high-temperature magma and rich volatiles, while fractionated crystallization often occurs in emplacement along with extensional structures (Wu et al., 2017). Interestingly, highly fractionated crystallization is of great significance for the enrichment of rare metal minerals (Xu et al., 2021).

Zircon U-Pb age and Hf isotopes can effectively constrain the magma source and crustal evolution (Kinny and Roland, 2003; Xu et al., 2004; Kemp et al., 2007). The similar REEs and trace

TABLE 2 | Zircon Lu-Hf isotope results in Yaozhuang stock.

No.	Age (Ma)	$^{176}Hf/^{177}Hf$	2σ	$^{176}Yb/^{177}Hf$	2σ	$^{176}Lu/^{177}Hf$	2σ	I_{Hf}	εHf	T_{DM} (Ma)	T_{DM2} (Ma)	*fLu/Hf*
D92-1 porphyritic granite												
D92-1-01	158	0.282341	0.00002	0.08896	0.00078	0.00202	0.00002	0.282335	−12	1,321	1,956	−0.94
D92-1-03	157	0.282363	0.00002	0.07857	0.001	0.00187	0.00002	0.282358	−11.2	1,285	1,907	−0.94
D92-1-06	159	0.282485	0.00003	0.08048	0.00197	0.00196	0.00005	0.282479	−6.9	1,112	1,637	−0.94
D92-1-07	158	0.28238	0.00003	0.06288	0.00131	0.00161	0.00002	0.282375	−10.6	1,252	1,868	−0.95
D92-1-13	158	0.282367	0.00002	0.0683	0.00016	0.00172	0	0.282362	−11	1,274	1,898	−0.95
D92-1-14	158	0.282374	0.00002	0.07421	0.00322	0.00168	0.00007	0.282369	−10.8	1,263	1,882	−0.95
D92-1-18	158	0.282413	0.00002	0.08681	0.00013	0.00198	0	0.282407	−9.4	1,217	1,798	−0.94
D92-1-19	157	0.282303	0.00002	0.05378	0.00017	0.00137	0	0.282299	−13.3	1,352	2,036	−0.96
D92-1-21	157	0.282301	0.00002	0.08457	0.00119	0.00182	0.00003	0.282295	−13.4	1,373	2,045	−0.95
D92-1-24	160	0.282345	0.00003	0.08197	0.00257	0.00193	0.00006	0.282339	−11.8	1,313	1,946	−0.94
D13-8 monzogranite												
D13-8-04	153	0.282291	0.00003	0.06485	0.00114	0.00179	0.00002	0.282286	−13.8	1,385	2,068	−0.95
D13-8-07	152	0.282346	0.00002	0.07015	0.00035	0.0018	0.00001	0.282341	−11.9	1,307	1,948	−0.95
D13-8-08	154	0.282372	0.00003	0.06953	0.00451	0.00172	0.00011	0.282367	−11	1,267	1,889	−0.95
D13-8-09	154	0.28231	0.00003	0.06009	0.00194	0.00166	0.00005	0.282306	−13.1	1,353	2,024	−0.95
D13-8-10	154	0.282225	0.00002	0.04428	0.00037	0.00107	0.00001	0.282222	−16.1	1,451	2,209	−0.97
D13-8-12	154	0.282361	0.00003	0.07157	0.00016	0.00186	0.00001	0.282356	−11.3	1,288	1,914	−0.94
D13-8-13	155	0.282288	0.00002	0.06579	0.00059	0.00186	0.00001	0.282282	−13.9	1,392	2,075	−0.94
D13-8-14	153	0.282359	0.00003	0.04588	0.00011	0.00116	0	0.282355	−11.4	1,267	1,915	−0.97
D13-8-16	154	0.282312	0.00002	0.09271	0.00052	0.00199	0.00002	0.282306	−13.1	1,362	2,022	−0.94
D13-8-17	154	0.282301	0.00002	0.06552	0.00022	0.00182	0.00001	0.282296	−13.5	1,372	2,046	−0.95
D13-8-23	153	0.282346	0.00002	0.09296	0.00103	0.0019	0.00003	0.28234	−11.9	1,311	1,948	−0.94
D13-8-24	153	0.282297	0.00002	0.08451	0.00034	0.00187	0.00001	0.282291	−13.7	1,380	2,056	−0.94

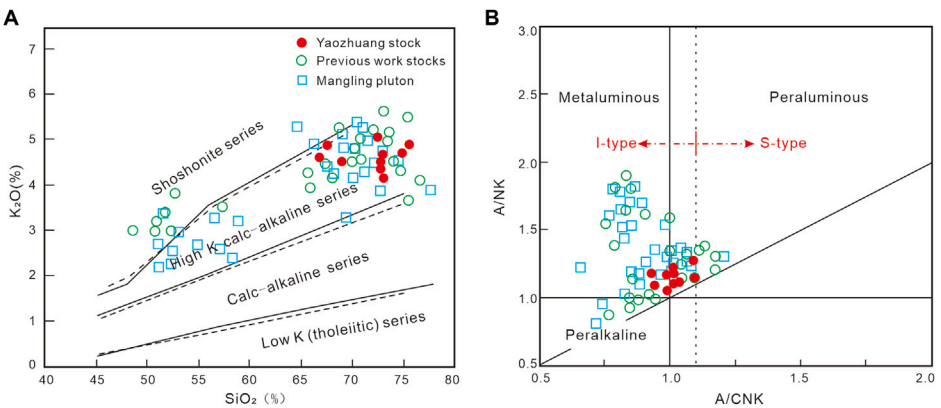

FIGURE 4 | Plots of SiO_2 vs. K_2O [**(A)** after Peccerillo and Taylor, 1976) and A/CNK vs A/NK **(B)** after Maniar and Piccoli, 1989] of the Yaozhuang stock (previous work stocks data after Ke et al., 2012a; Qin et al., 2012; Yang et al., 2014; Hu et al., 2017; Zhang Y. S. et al., 2019).

element patterns (**Figure 5**) and zircon $\varepsilon_{Hf}(t)$ values of the porphyritic granite and monzogranite suggest a common magma source. The $\varepsilon_{Hf}(t)$ values of crystalline zircons range from −16.1 to −6.9, and the sample points are located near the evolution line of the lower crust (**Figures 7A,B**). The $\varepsilon_{Hf}(t)$–t and La–La/Sm diagrams (**Figure 8A**) show the source mainly originates from partial melting of the lower crust. Moreover, Ke et al. (2012b) found that the Xigou stock at the western Mangling pluton had low $\varepsilon_{Hf}(t)$ values (−8.9 to −0.8), which implied that some mantle-derived components may be mixed into the lower crustal melt. A small number of mafic dikes [e.g., lamprophyre dikes of Muhuguan (152 ± 1 Ma) and gabbro dikes of Mokou (145 ± 2 Ma, 132 ± 3 Ma)] also indicates the addition of mantle-derived components (Liu et al., 2013; Liang et al., 2020). The $Mg^{\#}$ [atomic Mg/(Mg + Fe) × 100] values of lower crustal melts are usually below 40, and thus, $Mg^{\#} > 40$ often indicates mantle material involvement (Wilson, 1989; Kelemen, 1995; Smithies and Champion, 2000). The $Mg^{\#}$ values of our samples (33–77, avg. 61) suggest mantle input in the magma source region.

The fractional crystallization of garnet leads to a significant increase in the ratios of $(La/Yb)_N$ and $(Dy/Yb)_N$ (Blundy and Wood, 1994; He et al., 2011). The separation crystallization of garnet (or as a residual phase in the source

TABLE 3 | The major elements (wt%) and trace elements (ppm) of Yaozhuang stock.

Sample	D91-1	D91-2	D92-1	D92-2	D92-3	D13-2	D13-3	D13-5	D13-7	D13-8
Lithology	Porphyritic granite					Monzogranite				
SiO_2	75.63	74.96	72.91	72.89	73.14	67.63	66.83	72.52	73.02	69.03
Al_2O_3	12.90	13.19	13.65	13.64	14.10	16.61	16.93	14.02	13.38	15.19
TFe_2O_3	0.99	1.22	1.61	1.56	1.50	2.03	2.23	1.60	1.84	2.22
MgO	0.06	0.23	0.73	0.52	0.37	0.46	0.59	0.50	0.42	0.73
CaO	0.49	0.63	1.15	1.11	1.09	0.46	1.66	0.60	1.14	1.99
Na_2O	4.17	4.11	4.11	4.21	3.94	5.53	5.33	4.26	4.34	4.80
K_2O	4.89	4.71	4.52	4.35	4.15	4.88	4.61	5.05	4.66	4.52
P_2O_5	0.04	0.02	0.06	0.07	0.07	0.08	0.09	0.06	0.05	0.11
MnO	0.04	0.07	0.08	0.09	0.08	0.05	0.09	0.06	0.04	0.09
TiO_2	0.11	0.16	0.19	0.19	0.18	0.29	0.27	0.21	0.20	0.30
LOI	0.42	0.59	0.68	1.08	1.03	1.58	1.09	1.14	0.87	0.79
Total	99.74	99.89	99.69	99.71	99.65	99.60	99.72	100.02	99.96	99.77
Mg#	33	59	77	68	57	74	69	74	62	68
A/CNK	0.99	1.01	0.99	1.00	1.09	1.09	1.01	1.03	0.94	0.92
La	42.62	38.27	36.49	37.81	44.24	58.25	46.70	39.11	40.43	60.66
Ce	61.37	63.82	63.40	63.37	72.68	131.91	140.52	71.78	67.33	95.32
Pr	7.18	6.90	6.35	6.57	7.41	12.30	13.20	7.33	7.22	9.78
Nd	22.60	21.41	20.27	21.13	23.42	34.97	37.74	23.62	22.90	30.71
Sm	3.59	3.10	3.19	3.34	3.61	3.77	3.85	3.61	3.38	4.13
Eu	0.82	0.89	0.90	0.92	1.00	1.46	1.68	1.17	1.04	1.51
Gd	2.99	3.04	2.77	2.93	3.19	4.48	4.65	3.43	3.16	4.27
Tb	0.41	0.38	0.37	0.38	0.40	0.38	0.41	0.42	0.40	0.48
Dy	2.20	2.11	2.04	2.00	2.10	1.76	1.97	2.49	2.13	2.46
Ho	0.46	0.38	0.43	0.42	0.44	0.34	0.37	0.47	0.41	0.46
Er	1.39	1.33	1.28	1.22	1.33	1.05	1.10	1.37	1.20	1.38
Tm	0.24	0.20	0.22	0.22	0.22	0.17	0.18	0.22	0.20	0.22
Yb	1.65	1.44	1.57	1.45	1.49	1.08	1.12	1.48	1.42	1.55
Lu	0.26	0.24	0.25	0.24	0.24	0.18	0.19	0.24	0.24	0.26
Y	13.11	13.24	12.28	11.70	13.22	10.39	11.78	15.33	13.89	15.90
Rb	177.3	159.7	175.6	168.4	163.5	156.0	138.2	157.2	131.9	144.2
Ba	815.5	1,007.4	1,043.0	984.5	1,054.0	835.4	682.8	940.4	1,120.0	948.5
Th	22.44	19.77	20.61	19.43	20.46	16.02	16.21	19.58	21.23	20.04
U	4.25	3.48	4.21	3.18	2.33	1.47	2.74	2.19	9.46	5.27
Nb	35.45	21.73	24.29	23.06	23.01	11.58	9.67	18.81	20.56	16.71
Ta	2.86	1.75	2.12	2.14	2.14	0.41	0.58	1.48	1.64	1.34
Sr	85.7	106.4	124.7	120.9	128.2	238.0	518.6	166.3	179.3	409.7
Hf	5.05	4.14	4.35	4.62	5.26	8.01	7.50	4.52	4.94	6.43
Zr	113.7	129.4	121.7	121.9	156.2	364.2	351.8	144.3	159.5	250.6
Ga	16.57	17.63	16.71	16.78	17.84	19.80	21.48	18.12	18.07	19.49
Sc	3.81	3.63	4.31	4.24	4.40	3.88	3.73	3.82	3.94	4.65
Cr	13.67	11.02	9.29	9.45	12.50	17.03	19.89	14.75	19.21	16.48
Co	1.04	1.20	1.76	1.61	2.34	3.19	3.19	2.26	2.27	3.81
Ni	3.53	3.08	4.50	4.86	5.35	7.35	8.40	6.46	6.74	6.93
∑REE	147.8	143.5	139.6	142.0	161.7	252.2	253.6	156.7	151.4	213.2
LREE/HREE	14.39	14.74	14.63	15.03	16.19	25.70	24.40	14.49	15.53	18.24
(La/Yb)N	18.52	19.08	16.68	18.70	21.28	36.42	28.14	18.95	20.41	28.09
Eu/Eu*	0.77	0.89	0.93	0.90	0.90	1.09	1.21	1.02	0.97	1.10

area) and the inconspicuous Eu anomaly are usually interpreted as deeper crustal melting (Rudnick and Gao, 2003; Zhang et al., 2018). Yaozhuang stock shows positive correlation on $(La/Yb)_N$ and $(Dy/Yb)_N$ (**Figure 8B**). When the depth of the magma source area is >40 km and the pressure is >1.0–1.2 GPa, garnet will exist as the residual face in the magma source area (Rapp et al., 1999). Therefore, it is speculated that Yaozhuang granitic magma comes from the deep source region >40 km.

Tectonic Implications

The magmatism in the North Qinling terrane is still debated. Some workers suggested that magmatism occurred after the collision of the North China Plate and the Yangtze Plate (Zhu et al., 2009, 2010; Dong et al., 2013), while others inferred that it was caused by the far-field tectonic transition effect of the Paleo-Pacific subduction beneath the Eurasia plate (Wang et al., 2015; Gao and Zhao., 2017; Yang et al., 2021). The Qinling orogen may have undergone continent–continent

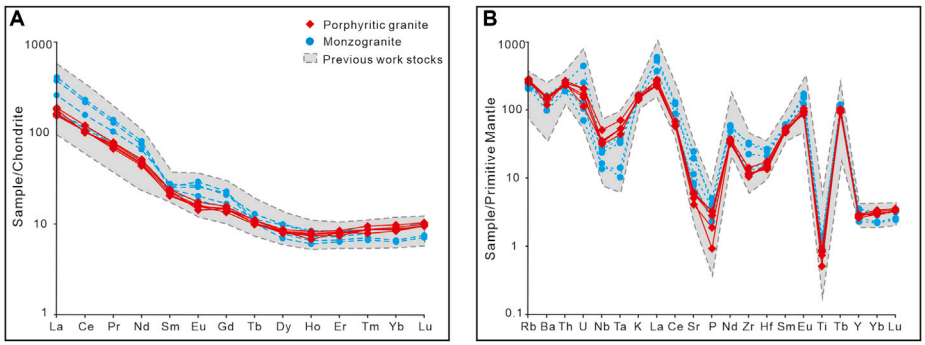

FIGURE 5 | Chondrite-normalized REE patterns **(A)** and primitive mantle-normalized spidergram **(B)** of Yaozhuang stock (normalized values after Sun and McDonough, 1989; previous work stocks data after Ke et al., 2012a; Qin et al., 2012; Yang et al., 2014; Hu et al., 2017; Zhang Y. S. et al., 2019).

TABLE 4 | Age statistics of granitic batholith and stocks in the North Qinling.

Type	Research object	Chronological method	Age (Ma)	Data sources
Stocks	Taoguanping monzogranite	LA-ICP-MS Zircon U-Pb	157±1	Ke et al. (2012)
	Xigou monzogranite	LA-ICP-MS Zircon U-Pb	153±1	Ke et al. (2012)
	Nantai granite porphyry	LA-ICP-MS Zircon U-Pb	151±1	Ke et al. (2014)
	Muhuguan lamprophyre dike	LA-ICP-MS Zircon U-Pb	152±1	Liu R. et al. (2013)
	Mokou lamprophyre dike	LA-ICP-MS Zircon U-Pb	147±3	Liang et al. (2020)
	Yaozhuang porphyroid granite	LA-ICP-MS Zircon U-Pb	157±2	This study
	Yaozhuang monzogranite	LA-ICP-MS Zircon U-Pb	153±1	This study
Plutons	Mangling biotite diorite	LA-ICP-MS Zircon U-Pb	157±1	Yang et al. (2014)
	Mangling porphyroid biotite monzogranite	LA-ICP-MS Zircon U-Pb	148±1	Yang et al. (2014)
	Mangling medium-grained monzogranite	LA-ICP-MS Zircon U-Pb	144±1	Yang et al. (2014)
	Mangling K-feldspar granite	LA-ICP-MS Zircon U-Pb	124±2	Qin et al. (2012)
	Muhuguan monzogranite	LA-ICP-MS Zircon U-Pb	145±3	Zhang Y. S. et al. (2019)
	Muhuguan dark enclaves (MMEs)	LA-ICP-MS Zircon U-Pb	152±1	Liu R. et al. (2013)
	Laojunshan biotite monzogranite	SHRIMP Zircon U-Pb	111±1	Meng et al. (2012)

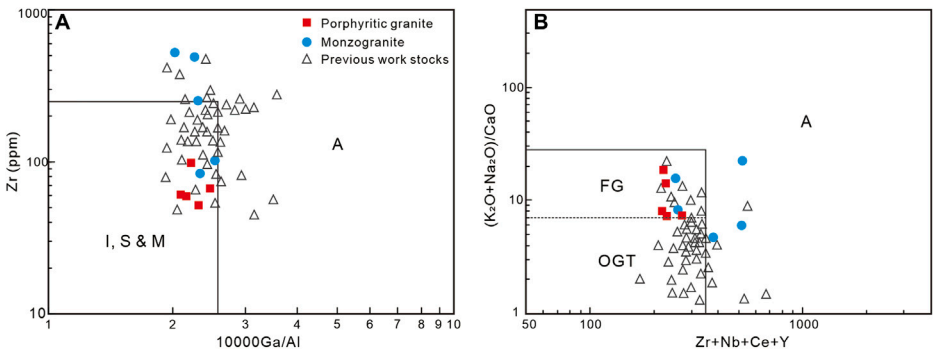

FIGURE 6 | Zr-10000Ga/Al diagram [**(A)** after Joseph et al., 1987] and (K_2O + Na_2O)/CaO-Zr + Nb + Ce + Y diagram [**(B)** after Joseph et al., 1987; previous work stocks data after Ke et al., 2012a; Qin et al., 2012; Yang et al., 2014; Hu et al., 2017; Zhang Y. S. et al., 2019].

collision in the Middle-Late Triassic (242–221 Ma), followed by an intraplate orogenic stage (Bao et al., 2015; Li et al., 2015; Chen et al., 2019). In the Late Triassic (220–195 Ma), it was the late syncollision or post-collision tectonic environment. Some alkaline syenites, rapakivi granites, and I-type granites are developed in the region (Dong et al., 2011a; 2011b; Ding et al., 2011; Wang et al., 2013), followed by tectonic quiescence in the early Middle Jurassic (195–160 Ma) (Li N. et al., 2018). In the Late Jurassic (160–140 Ma), there are some bimodal magmatism, mafic microgranular enclaves, and lamprophyre dikes in the Qinling orogeny (Wang et al., 2008; Liang et al., 2020), implying that

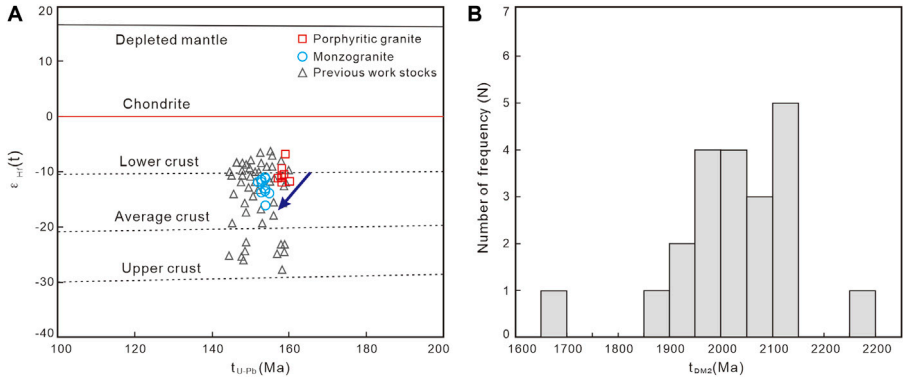

FIGURE 7 | Zircon $\varepsilon_{Hf}(t)$-t diagram of Yaozhuang stock **(A)** and t_{DM2} statistical histogram **(B)** (data after Dong et al., 2011a; Ke et al., 2012b; Liu et al., 2014; Zhao et al., 2021).

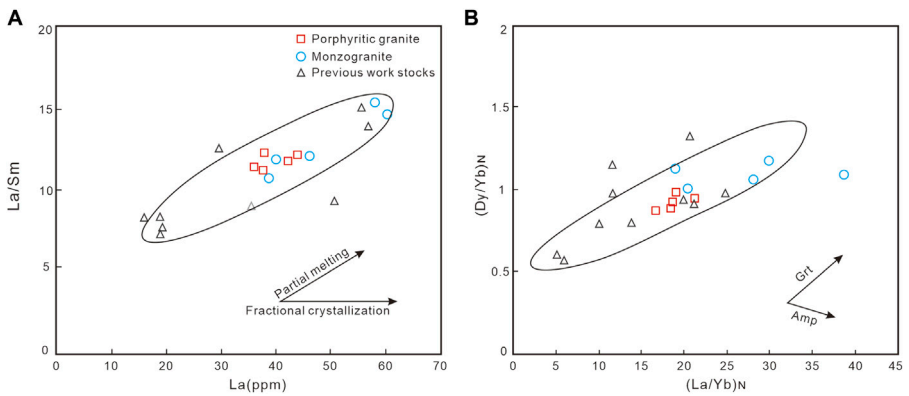

FIGURE 8 | La-La/Sm diagram **(A)** and $(La/Yb)_N$ vs $(Dy/Yb)_N$ diagram **(B)** of Yaozhuang stocks and [**(A,B)** after He et al., 2011; data after Ke et al., 2012a].

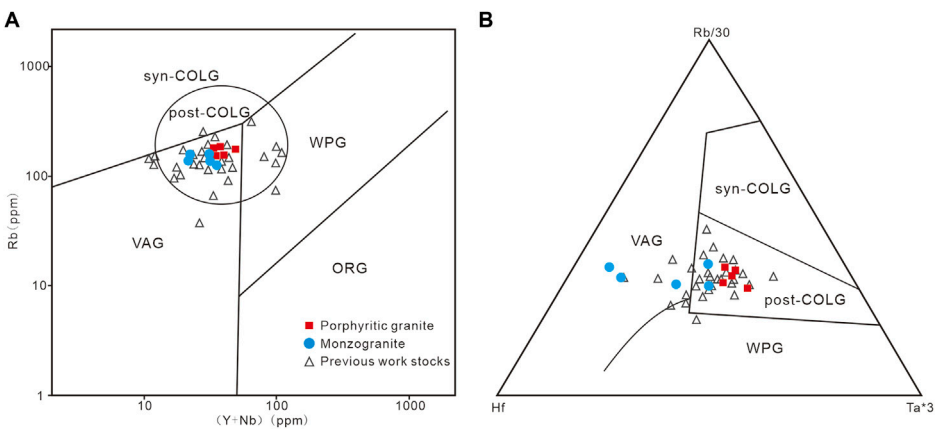

FIGURE 9 | Rb-(Y + Nb) plot [**(A)** after Pearce, 1996] and Hf-Rb/30-Ta*3 plot [**(B)** after Harris et al., 1986] of Yaozhuang stock.

lithospheric extension may have occurred (Liu et al., 2013). Both the Rb vs. (Y + Nb) and Hf-Rb/30-Ta*3 diagrams also revealed post-collisional magmatism (**Figures 9A,B**).

Geophysical data show that there was a WNW-directed uplift in the southern margin of the North China Craton (Xu et al., 2004, 2009; Zhou 2006), which is consistent

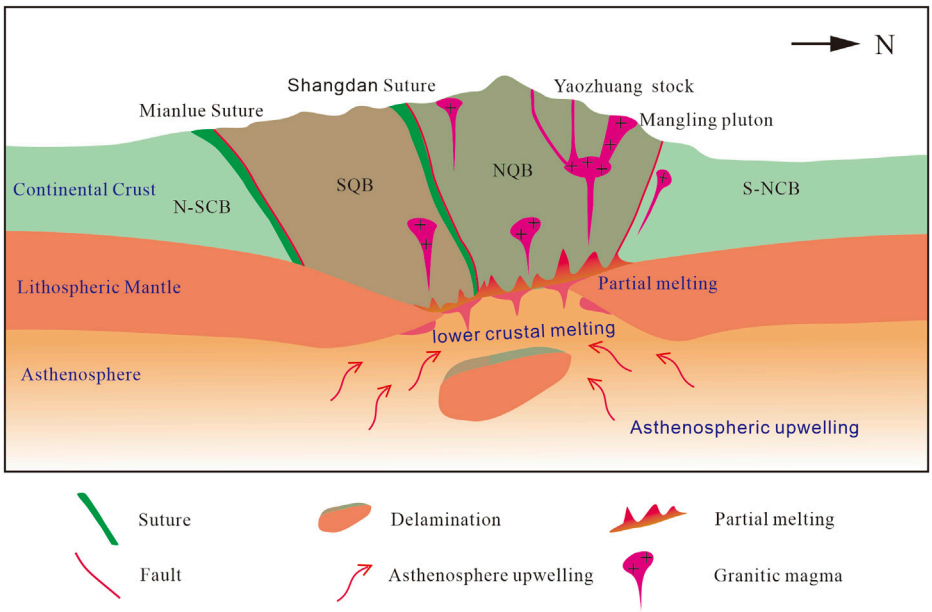

FIGURE 10 | Tectonic magmatic model map of the North Qinling.

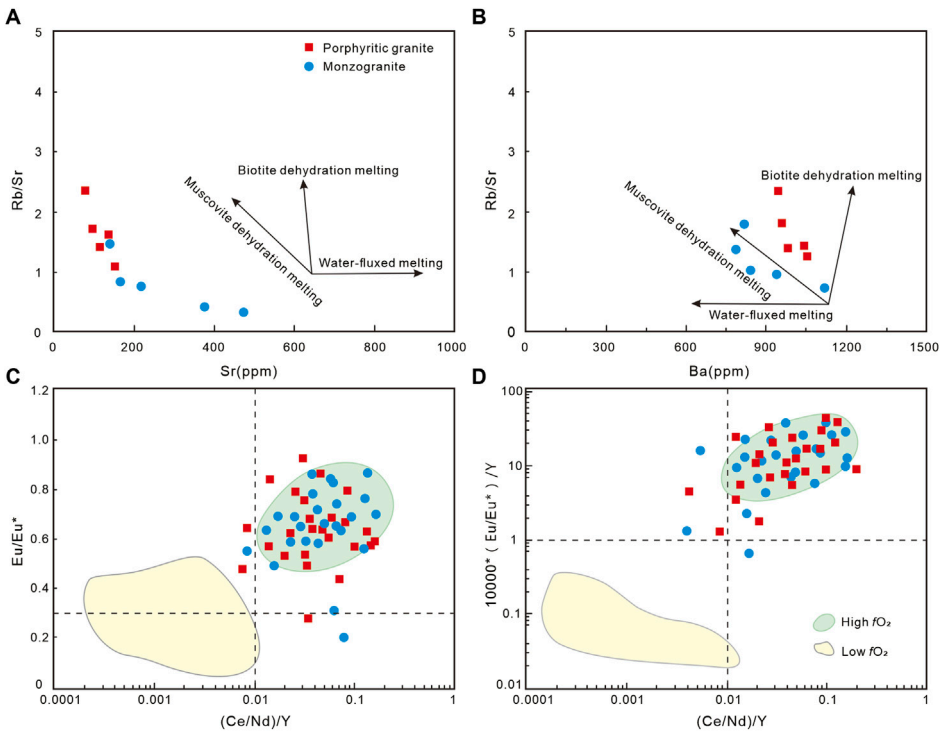

FIGURE 11 | Sr vs. Rb/Sr diagram [**(A)** after Inger and Harris, 1993], Ba vs. Rb/Sr diagram [**(B)** after Inger and Harris, 1993], 10,000*(Eu/Eu*)/Y vs. (Ce/Nd)/Y **(C)**, and (Eu/Eu*)/Y vs. (Ce/Nd)/Y **(D)** plots for zircons from Yaozhuang stock [**(C,D)** after Lu et al., 2016].

with the large Qinling Mo ore belt, regional deep faults and widespread pluton emplacement in the Late Mesozoic. All indicate that the mantle upwelling may occur in the North Qinling terrane. Underplating melting has provided the heat and material for the coeval magmatism.

Some workers suggested a flat-slab subduction model that the Paleo-Pacific subduction could extend up to 1,300 km inland and cause large-scale magmatism in the Late Mesozoic (Li and Li., 2007; Gao and Zhao., 2017). Zhou (2006) argues that the gravity gradient and lithosphere thickness of the Qinling orogen decreases from south to north, but the gravity gradient and lithospheric thickness in eastern China decrease from west to east and cross with the Qinling orogenic belt. If affected by the Paleo-Pacific subduction, the variation of gravity gradient and lithospheric thickness should be consistent in the NE direction, and a large number of NE-trending magmatism should be found. However, the late Mesozoic magmatism in the Qinling area is nearly E–W in direction. We suggest that the Paleo-Pacific subduction has a limited impact on North Qinling, but a significant impact on the decratonization in North China. The study area is about 1,700 km far away from the Paleo-Pacific subduction zone and should have a negligible impact on the subduction. Therefore, regional tectonics may have been controlled mainly by the collision orogeny. We propose that in the North Qinling terrane, the asthenospheric materials may have upwelled and heated the lithospheric mantle to form mantle-derived magma. Subsequently, the magma underplating may have triggered partial melting of the lower crust, and the resultant magma may have then evolved and fractionated. Finally, the highly fractionated granitic magmas may have intruded into the intersection of the older EW-trending faults and the younger NE-trending faults (**Figure 10**).

Implications for Mo Polymetallic Ore Prospecting

The formation of porphyry Mo deposits is controlled by many factors, including the content of water and sulfur in magmatic–hydrothermal solution, oxygen fugacity of magma (Burnham and Berry, 2012), and the migration of metal elements (Sillitoe, 2010; Richards et al., 2012; Park et al., 2021). Porphyry metallogenic magmas not only in subduction settings but also in collision settings have significant water-rich (>4.0%) (Wang et al., 2014a) and high-oxygen fugacity (Delta FMQ > 1.5) (Richards, 2011; Wang et al., 2014b). Previous studies have found that the separation and crystallization of amphibole from the magmatic system require a high water content (4%) (Naney, 1983; Davidson et al., 2007; Ridolfi et al., 2010), but the high water content will inhibit the separation and crystallization of plagioclase (Wang et al., 2021), so that the rare Earth element distribution model of water-rich magma does not show Eu anomaly. The Eu of the studied stock shows no or weakly negative anomalies (Eu/Eu* = 0.77–1.21, avg. 0.98). Moreover, some contemporaneous diorite rocks are found near the study area, containing a large number of amphibole cumulates (Liu et al., 2014; Yang et al., 2014). These characteristics suggest that the original magma has high water content (H_2O > 4%).

Inger and Harris (1993) found that the dehydration and melting of muscovite would lead to the increase of the Rb/Sr ratio and the decrease of Sr and Ba contents in the melt; the trend diagram of dehydration melting and water-fluxed melting was divided (Sylvester, 1998; Meng et al., 2021). From **Figures 11A,B**, it is seen that the Yaozhuang stock shows a good trend of Muscovite dehydration melting; the fluid formed by dehydration melting of water-bearing minerals in the crust leads to further melting of the rock (Weinberg and Hasalová, 2015). Generally, the melt formed by dehydration melting has a higher K/Na ratio, and water-fluxed melting is just the opposite (Douce and McCarthy, 1998). The K/Na ratios of Yaozhuang stock also (0.86–1.19, avg. 1.05) support the above conclusions.

Interestingly, the water of post-collision ore-forming magma may come from additional water supplementation (Wang et al., 2018). One theory is that the water-rich mantle-derived ultra-potassium magma is mixed with the lower crustal magma to provide water (Yang et al., 2015), and the other explains that the subduction of continental crust dehydration releases free fluids into the magma to increase the water content of the magma (Zheng, 2009,; Zheng, 2019).

Researchers previously proposed that 10,000*(Eu/Eu*)/Y and Eu/Eu* ratios are positively correlated with Ce/Nd ratios, which can well indicate the oxygen fugacity of wet fertile magmatic–hydrothermal solution. The best fertility indicators are zircon Eu/Eu* (>0.3), 10,000·(Eu/Eu*)/Y (>1) ratios, and (Ce/Nd)/Y (>0.01) (Lu et al., 2016; Zheng et al., 2021). The above zircon trace element ratios of the Yaozhuang stock plot in the high-oxygen fugacity fertile magma region (**Figures 11C,D**). In addition, the zircon Delta FMQ values of porphyritic granite (avg. +2.7, the calculation method is derived from Li et al., 2019) and monzogranite (avg. + 3.9) in this study are higher than the basic conditions of porphyry mineralization (Delta FMQ > 1.5).

Porphyry-type mineralization is commonly associated with porphyry stocks, where large amounts of ore-forming fluids and materials were focused into the intrusion apex to form disseminated or vein-type ores (Hedenquist and Lowenstern, 1994; Heinrich, 2005; Blundy et al., 2015). Field geological surveys show that the mineralization and alterations are generally developed, such as Mo mineralization and silicic, pyrite, and sericite alterations. The molybdenite filled the wall rock fractures (**Figure 2A**), which indicates that the Yaozhuang area has the potential to prospect porphyry Mo deposits.

CONCLUSION

(1) The newly discovered porphyritic granite and monzogranite in the Yaozhuang area are zircon U-Pb dated to be 157 ± 2 and 153 ± 1 Ma, coeval with the magmatic peak of the region.
(2) The high-K calc-alkaline Yaozhuang I-type granites are metaluminous–weakly peraluminous, with zircon $\varepsilon_{Hf}(t)$ values of −16.1 to −6.9 and t_{DM2} ages of 1.78–2.16 Ga. The granites may have formed from partial melting of the lower crust mixed with some mantle components.
(3) The Yaozhuang granitic stocks were likely formed by the lower crustal delamination in North Qinling. The asthenospheric upwelling may have heated the lithospheric mantle to form mantle-derived magma, which then caused the lower crustal melting and magma mixing. These magmas were finally emplaced into the fault intersections at Yaozhuang.

DATA AVAILABILITY STATEMENT

The original contributions presented in the study are included in the article/Supplementary Material, further inquiries can be directed to the corresponding author.

AUTHOR CONTRIBUTIONS

PF: conceived the research, investigated the literature, and wrote the manuscript. AX, BZ, and XC: provided research funds, supervision, and revision. WY, JS, HZ, and LW: participated in data analysis and academic support. All authors contributed to the article and approved the submitted version.

FUNDING

This study was financially supported by the National Natural Science Foundation of China (No. 41272095), the Geological Exploration Funds of Shaanxi Province (No. 61201908334), and Public Welfare Geological Survey Funds of Shaanxi Province (202112).

ACKNOWLEDGMENTS

We would like to express our sincere thanks to Associate Editor KL and the two reviewers for their valuable comments and suggestions and to Prof. Yunpeng Dong of Northwestern University for his kind assistance on the manuscript.

REFERENCES

Andersen, T. (2002). Correction of Common lead in U-Pb Analyses that Do Not Report 204Pb. *Chem. Geology.* 192, 59–79. doi:10.1016/S0009-2541(02)00195-X

Bao, Z. W., Wang, C. Y., Zeng, L. J., Sun, W. D., and Yao, J. M. (2015). Slab Break-Off Model for the Triassic Syn-Collisional Granites in the Qinling Orogenic belt, Central China: Zircon U-Pb Age and Hf Isotope Constraints. *Int. Geology. Rev.* 57, 492–507. doi:10.1080/00206814.2015.1017777

Bao, Z. W., Xiong, M. F., and Li, Q. (2019). Petrogenesis of Late Mesozoic High-Ba-Sr Granites in the Qiushuwan Cu Mo orefield: Implications for the Distribution of Porphyry Mo Mineralization in the East Qinling Area of Central China. *Lithos* 348-349, 105172–111072. doi:10.1016/j.lithos.2019.105172

Belousova, E., Griffin, W., O'Reilly, S. Y., and Fisher, N. (2002). Igneous Zircon: Trace Element Composition as an Indicator of Source Rock Type. *Contrib. Mineral. Petrol.* 143, 602–622. doi:10.1007/s00410-002-0364-7

Blundy, J., Mavrogenes, J., Tattitch, B., Sparks, S., and Gilmer, A. (2015). Generation of Porphyry Copper Deposits by Gas-Brine Reaction in Volcanic Arcs. *Nat. Geosci* 8, 235–240. doi:10.1038/ngeo2351

Blundy, J., and Wood, B. (1994). Prediction of crystal-melt Partition Coefficients from Elastic Moduli. *Nature* 372, 452–454. doi:10.1038/372452a0

Burnham, A. D., and Berry, A. J. (2012). An Experimental Study of Trace Element Partitioning between Zircon and Melt as a Function of Oxygen Fugacity. *Geochimica et Cosmochimica Acta* 95, 196–212. doi:10.1016/j.gca.2012.07.034

Chen, L., Yan, Z., Guo, X., and Fu, C. (2019). Melting of the Meso-Neoproterozoic Juvenile Crust for the Origin of the Late Triassic Mo Mineralization in South Qinling, central China: Evidence from Geochronology and Geochemistry of the Yangmugou deposit. *J. Asian Earth Sci.* 174, 109–125. doi:10.1016/j.jseaes.2018.11.022

Davidson, J., Turner, S., Handley, H., Macpherson, C., and Dosseto, A. (2007). Amphibole "Sponge" in Arc Crust. *Geol* 35, 787–790. doi:10.1130/G23637A.1

Ding, L. X., Ma, C. Q., Li, J. W., Robinson, P. T., Deng, X. D., Zhang, C., et al. (2011). Timing and Genesis of the Adakitic and Shoshonitic Intrusions in the Laoniushan Complex, Southern Margin of the North China Craton: Implications for post-collisional Magmatism Associated with the Qinling Orogen. *Lithos* 126, 212–232. doi:10.1016/j.lithos.2011.07.008

Diwu, C. R., Sun, Y., Liu, L., Zhang, C. L., and Wang, H. L. (2010). The Disintegration of Kuanping Group in North Qinling Orogenic Belts and Neo-Proterozoic N-MORB. Acta Petrol. *Sin* 26, 2025–2038.

Diwu, C. R., Sun, Y., Zhao, Y., Liu, B. X., and Lai, S. C. (2014). Geochronological, Geochemical, and Nd-Hf Isotopic Studies of the Qinling Complex, central China: Implications for the Evolutionary History of the North Qinling Orogenic Belt. *Geosci. Front.* 5, 499–513. doi:10.1016/10.1016/j.gsf.2014.04.001

Dong, G. C., Santosh, M., Li, S. R., Shen, J. F., Mo, X. X., Scott, S., et al. (2013). Mesozoic Magmatism and Metallogenesis Associated with the Destruction of the North China Craton: Evidence from U-Pb Geochronology and Stable Isotope Geochemistry of the Mujicun Porphyry Cu-Mo deposit. *Ore Geology. Rev.* 53, 434–445. doi:10.1016/j.oregeorev.2013.02.006

Dong, S. W., Zhang, Y. Q., Li, H. L., Shi, W., Xue, H. M., Li, J. H., et al. (2018). The Yanshan Orogeny and Late Mesozoic Multi-Plate Convergence in East Asia-Commemorating 90th Years of the "Yanshan Orogeny". *Sci. China Earth Sci.* 61, 1888–1909. doi:10.1007/s11430-017-9297-y

Dong, Y., Liu, X., Zhang, G., Chen, Q., Zhang, X., Li, W., et al. (2012). Triassic Diorites and Granitoids in the Foping Area: Constraints on the Conversion from Subduction to Collision in the Qinling Orogen, China. *J. Asian Earth Sci.* 47, 123–142. doi:10.1016/j.jseaes.2011.06.005

Dong, Y., Zhang, G., Neubauer, F., Liu, X., Genser, J., and Hauzenberger, C. (2011a). Tectonic Evolution of the Qinling Orogen, China: Review and Synthesis. *J. Asian Earth Sci.* 41, 213–237. doi:10.1016/j.jseaes.2011.03.002

Douce, A. E. P., and McCarthy, T. C. (1998). "Melting of Crustal Rocks during Continental Collision and Subduction," in *When Continents Collide: Geodynamics and Geochemistry of Ultrahigh-Pressure Rocks*. Editors B. R. Hacker and J. G. Liou (Dordrecht: Springer), 27–55. doi:10.1007/978-94-015-9050-1_2*Melting of Crustal Rocks during continental Collision and Subduction*

Fan, H. R., and Xie, Y. H. (1999). Porphyry Type Molybdenum Deposits in the Eastern Qinling Mo belt. *Cent. China. Sci. Geol. Sin* 8, 91–101.

Gao, X., and Zhao, T. (2017). Late Mesozoic Magmatism and Tectonic Evolution in the Southern Margin of the North China Craton. *Sci. China Earth Sci.* 60, 1959–1975. doi:10.1007/s11430-016-9069-0

Harris, N. B. W., Tindle, A. J. A., and Tindle, G. (1986). Geochemical Characteristics of Collision-Zone Magmatism. *Geol. Soc. Lond. Spec. Publications* 19, 67–81. doi:10.1144/gsl.sp.1986.019.01.04

He, Y., Li, S., Hoefs, J., Huang, F., Liu, S.-A., and Hou, Z. (2011). Post-collisional Granitoids from the Dabie Orogen: New Evidence for Partial Melting of a Thickened continental Crust. *Geochimica et Cosmochimica Acta* 75, 3815–3838. doi:10.1016/j.gca.2011.04.011

Hedenquist, J. W., and Lowenstern, J. B. (1994). The Role of Magmas in the Formation of Hydrothermal Ore Deposits. *Nature* 370, 519–527. doi:10.1038/370519a0

Heinrich, C. A. (2005). The Physical and Chemical Evolution of Low-Salinity Magmatic Fluids at the Porphyry to Epithermal Transition: A Thermodynamic Study. *Miner Deposita* 39, 864–889. doi:10.1007/s00126-004-0461-9

Hu, H., Li, J.-W., McFarlane, C. R. M., Luo, Y., and McCarron, T. (2017). Textures, Trace Element Compositions, and U-Pb Ages of Titanite from the Mangling Granitoid Pluton, East Qinling Orogen: Implications for Magma Mixing and Destruction of the North China Craton. *Lithos* 284-285, 50–68. doi:10.1016/j.lithos.2017.03.025

Inger, S., and Harris, N. (1993). Geochemical Constraints on Leucogranite Magmatism in the Langtang Valley, Nepal Himalaya. *J. Petrol.* 34, 345–368. doi:10.1093/petrology/34.2.345

Jingwen, M., Yanbo, C., Maohong, C., and Pirajno, F. (2013). Major Types and Time-Space Distribution of Mesozoic Ore Deposits in South China and Their Geodynamic Settings. *Miner Deposita* 48, 267–294. doi:10.1007/s00126-012-0446-z

Joseph, B. W., Kenneth, L. C., and Bruce, W. C. (1987). A-type Granites: Geochemical Characteristics, Discrimination and Petrogenesis. *Contrib. Mineral. Petrol.* 95, 407–419.

Ke, C. H., Wang, X. X., Li, J. B., and Qi, Q. J. (2012a). Geochronology and Geological Significance of the Granites from the Mahe Mo deposit in the North Qinling. Acta Petrol. *Sin* 28, 267–278.

Ke, C. H., Wang, X. X., Yang, Y., Qi, Q. J., Fan, Z. P., Gao, F., et al. (2012b). *Rock-forming and Ore-Forming Ages of the Nantai Mo Polymetallic deposit in North Qinling Mountains and its Zircon Hf Isotope Composition: Geology. China* 39, 1562–1576

Kelemen, P. B. (1995). Genesis of High Mg# Andesites and the continental Crust. *Contr. Mineral. Petrol.* 120, 1–19. doi:10.1007/BF00311004

Kemp, A. I. S., Hawkesworth, C. J., Foster, G. L., Paterson, B. A., Woodhead, J. D., Hergt, J. M., et al. (2007). Magmatic and Crustal Differentiation History of Granitic Rocks from Hf-O Isotopes in Zircon. *Science* 315, 980–983. doi:10.1126/science.1136154

Kinny, P. D., and Maas, R. (2003). 12. Lu-Hf and Sm-Nd Isotope Systems in Zircon. *Rev. Mineral. Geochem.* 53, 327–342. doi:10.1515/9781501509322-015

Kröner, A., Compston, W., Guo-wei, Z., An-lin, G., and Todt, W. (1988). Age and Tectonic Setting of Late Archean Greenstone-Gneiss Terrain in Henan Province, China, as Revealed by Single-Grain Zircon Dating. *Geol* 16, 211. doi:10.1130/0091-7613(1988)01610.1130/0091-7613(1988)016<0211:aatsol>2.3.co;2

Lei, W., Dai, J., Zhao, T., Zhang, Y., and Tao, N. (2018). Field Geology, Geochronology, and Isotope Geochemistry of the Luyuangou Gold deposit, China: Implications for the Gold Mineralization in the Eastern Qinling Orogen. *Geol. J.* 53, 96–112. doi:10.1002/gj.3064

Li, N., Chen, Y. J., Santosh, M., and Pirajno, F. (2015). Compositional Polarity of Triassic Granitoids in the Qinling Orogen, China: Implication for Termination of the Northernmost Paleo-Tethys. *Gondwana Res.* 27, 244–257. doi:10.1016/j.gr.2013.09.017

Li, W., Cheng, Y., and Yang, Z. (2019). Geo- F O 2 : Integrated Software for Analysis of Magmatic Oxygen Fugacity. *Geochem. Geophys. Geosyst.* 20, 2542–2555. doi:10.1029/2019GC008273

Li, Z. X., and Li, X. H. (2007). Formation of the 1300-km-wide Intracontinental Orogen and Postorogenic Magmatic Province in Mesozoic South China: A Flat-Slab Subduction Model. *Geol* 35, 179. doi:10.1130/G23193A.1

Li, C. D., Zhao, L. G., Xu, Y. W., Chang, Q. S., Wang, S. Y., and Xu, T. (2018). Chronology of Metasedimentary Rocks from Kuanping Group Complex in North Qinling Belt and its Geological Significance. *Geology. China* 45, 992–1010

Li, N., Chen, Y. J., Santosh, M., and Pirajno, F. (2018). Late Mesozoic Granitoids in the Qinling Orogen, Central China, and Tectonic Significance. *Earth-Science Rev.* 182, 141–173. doi:10.1016/j.earscirev.2018.05.004

Liang, T., Li, L.-M., Lu, R., and Xiao, W.-J. (2020). Early Cretaceous Mafic Dikes in the Northern Qinling Orogenic Belt, central China: Implications for Lithosphere Delamination. *J. Asian Earth Sci.* 194, 104142. doi:10.1016/j.jseaes.2019.104142

Liu, B. X., Qi, Y., Wang, W., Siebel, W., Zhu, X. Y., Nie, H., et al. . (2013). Zircon U-Pb Ages and O-Nd Isotopic Composition of Basement Rocks in the North Qinling Terrain, central China: Evidence for Provenance and Evolution. *Int. J. Earth Sci. (Geol Rundsch)* 102, 2153–2173. doi:10.1007/s00531-013-0912-6

Liu, L., Liao, X., Wang, Y., Wang, C., Santosh, M., Yang, M., et al. (2016). Early Paleozoic Tectonic Evolution of the North Qinling Orogenic Belt in Central China: Insights on continental Deep Subduction and Multiphase Exhumation. *Earth-Science Rev.* 159, 58–81. doi:10.1016/j.earscirev.2016.05.005

Liu, R., Chen, M., Tian, X. S., Hu, Y., and Yang, D. P. (2014). Geochemical, Zircon SIMS U-Pb Geochronological and Hf Isotopic Study on Nantian and Muhuguan Plutons in Eastern Qinling, China: Petrogenesis and Tectonic Implications. Acta Miner. *Sin* 34, 469–480

Liu, Y., Hu, Z., Zong, K., Gao, C., Gao, S., Xu, J., et al. (2010). Reappraisement and Refinement of Zircon U-Pb Isotope and Trace Element Analyses by LA-ICP-MS. *Chin. Sci. Bull.* 55, 1535–1546. doi:10.1007/s11434-010-3052-4

Liu, R., Li, J. W., Bi, S. J., Hu, H., and Chen, M. (2013). Magma Mixing Revealed from *In Situ* Zircon U-Pb-Hf Isotope Analysis of the Muhuguan Granitoid Pluton, Eastern Qinling Orogen, China: Implications for Late Mesozoic Tectonic Evolution. *Int. J. Earth Sci. (Geol Rundsch)* 102, 1583–1602. doi:10.1007/s00531-013-0900-x

Lu, Y. F. (2004). GeoKit: A Geochemical Toolkit for Microsoft Excel. *Geochimica* 33, 459–464

Lu, Y. J., Loucks, R. R., Fiorentini, M., McCuaig, T. C., Evans, N. J., Yang, Z. M., et al. (2016). *Zircon Compositions as a Pathfinder for Porphyry Cu ± Mo ± Au Deposits. Tectonics Metallog Tethyan Orog.* doi:10.5382/SP.19.13

Maniar, P. D., and Piccoli, P. M. (1989). Tectonic Discrimination of Granitoids. *Geol. Soc. Am. Bull.* 101, 635–643. doi:10.1130/0016-7606(1989)101<0635:TDOG>2.3.CO;2

Mao, J. W., Xie, G. Q., Pirajno, F., Ye, H. S., Wang, Y. B., Li, Y. F., et al. (2010). Late Jurassic-Early Cretaceous Granitoid Magmatism in Eastern Qinling, central-eastern China: SHRIMP Zircon U-Pb Ages and Tectonic Implications. *Aust. J. Earth Sci.* 57, 51–78. doi:10.1080/08120090903416203

Mao, J. W., Pirajno, F., Xiang, J. F., Gao, J. J., Ye, H. S., Li, Y. F., et al. (2011). Mesozoic Molybdenum Deposits in the East Qinling-Dabie Orogenic belt: Characteristics and Tectonic Settings. *Ore Geology. Rev.* 43, 264–293. doi:10.1016/j.oregeorev.2011.07.009

Mao, J. W., Xie, G. Q., Bierlein, F., Qü, W. J., Du, A. D., Ye, H. S., et al. (2008). Tectonic Implications from Re-os Dating of Mesozoic Molybdenum Deposits in the East Qinling-Dabie Orogenic belt. *Geochimica et Cosmochimica Acta* 72, 4607–4626. doi:10.1016/j.gca.2008.06.027

Mao, J., Xiong, B., Liu, J., Pirajno, F., Cheng, Y., Ye, H., et al. (2017). Molybdenite Re/Os Dating, Zircon U-Pb Age and Geochemistry of Granitoids in the Yangchuling Porphyry W-Mo deposit (Jiangnan Tungsten Ore belt), China: Implications for Petrogenesis, Mineralization and Geodynamic Setting. *Lithos* 286-287, 35–52. doi:10.1016/j.lithos.2017.05.023

Mattauer, M., Matte, P., Malavieille, J., Tapponnier, P., Maluski, H., Qin, X. Z., et al. (1985). Tectonics of the Qinling Belt: Build-Up and Evolution of Eastern Asia. *Nature* 317, 496–500. doi:10.1038/317496a0

Meng, F., Mao, J. W., Ye, H. S., Zhou, K., Gao, Y. L., Li, Y. F., et al. (2012). Zircon SHRIMP U-Pb Dating and Geochemistry of the Laojunshan Intrusion,Western Henan Province. *Geology. China* 39, 1501–1524.

Meng, J., Xia, X., Ma, L., Jiang, Z., Xu, J., Cui, Z., et al. (2021). A H2O-In-Zircon Perspective on the Heterogeneous Water Content of Crust-Derived Magmas in Southern Tibet. *Sci. China Earth Sci.* 64, 1184–1194. doi:10.1007/s11430-020-9790-1

Meng, Q. R., and Zhang, G. W. (1999). Timing of Collision of the North and South China Blocks: Controversy and Reconciliation. *Geology* 27, 1–96. doi:10.1130/0091-7613(1999)0272.3.CO;2

Naney, M. T. (1983). Phase Equilibria of Rock-Forming Ferromagnesian Silicates in Granitic Systems. *Am. J. Sci.* 283, 993–1033. doi:10.2475/ajs.283.10.993

Park, J. W., Campbell, I. H., Chiaradia, M., Hao, H., and Lee, C. T. (2021). Crustal Magmatic Controls on the Formation of Porphyry Copper Deposits. *Nat. Rev. Earth Environ.* 2, 542–557. doi:10.1038/s43017-021-00182-8

Pearce, J. (1996). Sources and Settings of Granitic Rocks. *Episodes* 19, 120–125. doi:10.18814/epiiugs/1996/v19i4/005

Peccerillo, A., and Taylor, S. R. (1976). Geochemistry of Eocene Calc-Alkaline Volcanic Rocks from the Kastamonu Area, Northern Turkey. *Contr. Mineral. Petrol.* 58, 63–81. doi:10.1007/BF00384745

Qin, H. P., Wu, C. L., Wu, X. P., Lei, M., and Hou, Z. H. (2012). LA-ICP-MS Zircon U-Pb Ages and Implications for Tectonic Setting of the Mangling Granitoid Plutons in Qinling Orogen belt. *Geol. Rev.* 58, 783–792.

Rapp, R. P., Shimizu, N., Norman, M. D., and Applegate, G. S. (1999). Reaction between Slab-Derived Melts and Peridotite in the Mantle Wedge: Experimental Constraints at 3.8 GPa. *Chem. Geology.* 160, 335–356. doi:10.1016/S0009-2541(99)00106-0

Ratschbacher, L., Hacker, B. R., Calvert, A., Webb, L. E., Grimmer, J. C., McWilliams, M. O., et al. (2003). Tectonics of the Qinling (Central China): Tectonostratigraphy, Geochronology, and Deformation History. *Tectonophysics* 366, 1–53. doi:10.1016/S0040-1951(03)00053-2

Richards, J. P. (2011). Magmatic to Hydrothermal Metal Fluxes in Convergent and Collided Margins. *Ore Geology. Rev.* 40, 1–26. doi:10.1016/j.oregeorev.2011.05.006

Richards, J. P., Spell, T., Rameh, E., Razique, A., and Fletcher, T. (2012). High Sr/Y Magmas Reflect Arc Maturity, High Magmatic Water Content, and Porphyry Cu ± Mo ± Au Potential: Examples from the Tethyan Arcs of Central and Eastern Iran and Western Pakistan. *Econ. Geol.* 107, 295–332. doi:10.2113/econgeo.107.2.295

Ridolfi, F., Renzulli, A., and Puerini, M. (2010). Stability and Chemical Equilibrium of Amphibole in Calc-Alkaline Magmas: An Overview, New Thermobarometric Formulations and Application to Subduction-Related Volcanoes. *Contrib. Mineral. Petrol.* 160, 45–66. doi:10.1007/s00410-009-0465-7

Rudnick, R. L., and Gao, S. (2003). Composition of the continental Crust. *Treatise Geochem.* 3, 1–64. doi:10.1016/b0-08-043751-6/03016-4

Sillitoe, R. H. (2010). Porphyry Copper Systems. *Econ. Geology.* 105, 3–41. doi:10.2113/gsecongeo.105.1.3

Smithies, R. H., and Champion, D. C. (2000). The Archaean High-Mg Diorite Suite: Links to Tonalite-Trondhjemite-Granodiorite Magmatism and Implications for Early Archaean Crustal Growth. *J. Petrol.* 41, 1653–1671. doi:10.1093/petrology/41.12.1653

Sun, S. S., and McDonough, W. F. (1989). Chemical and Isotopic Systematics of Oceanic Basalts: Implications for Mantle Composition and Processes. *Geol. Soc. Lond. Spec. Publications* 42, 313–345. doi:10.1144/GSL.SP.1989.042.01.19

Sylvester, P. J. (1998). Post-collisional Strongly Peraluminous Granites. *Lithos* 45, 29–44. doi:10.1016/S0024-4937(98)00024-3

Vervoort, J. D., Patchett, P. J., Gehrels, G. E., and Nutman, A. P. (1996). Constraints on Early Earth Differentiation from Hafnium and Neodymium Isotopes. *Nature* 379, 624–627. doi:10.1038/379624a0

Wang, C., Deng, J., Bagas, L., and Wang, Q. (2017). Zircon Hf-Isotopic Mapping for Understanding Crustal Architecture and Metallogenesis in the Eastern Qinling Orogen. *Gondwana Res.* 50, 293–310. doi:10.1016/j.gr.2017.04.008

Wang, R., Luo, C. H., Xia, W. J., Sun, Y. C., Liu, B., and Zhang, J. B. (2021). Progresses in the Study of High Magmatic Water and Oxidation State of Post-Collisional Magmas in the Gangdese Porphyry Deposit Belt. Bull Miner. Petrol. *Geochem* 40, 1061–1077

Wang, R., Richards, J. P., Hou, Z. Q., Yang, Z. Q., Gou, Z. B., and DuFrane, S. A. (2014b). Increasing Magmatic Oxidation State from Paleocene to Miocene in the Eastern Gangdese Belt, Tibet: Implication for Collision-Related Porphyry Cu-Mo Au Mineralization. *Econ. Geology.* 109, 1943–1965. doi:10.2113/econgeo.109.7.1943

Wang, R., Richards, J. P., Hou, Z., Yang, Z., and DuFrane, S. A. (2014a). Increased Magmatic Water Content--The Key to Oligo-Miocene Porphyry Cu-Mo Au Formation in the Eastern Gangdese Belt, Tibet. *Econ. Geology.* 109, 1315–1339. doi:10.2113/econgeo.109.5.1315

Wang, R., Weinberg, R. F., Collins, W. J., Richards, J. P., and Zhu, D.-c. (2018). Origin of Postcollisional Magmas and Formation of Porphyry Cu Deposits in Southern Tibet. *Earth-Science Rev.* 181, 122–143. doi:10.1016/j.earscirev.2018.02.019

Wang, T., Guo, L., Zheng, Y. D., Donskaya, T., Dmirty, G., Zeng, L. S., et al. (2012). Timing and Processes of Late Mesozoic Mid-lower-crustal Extension in continental NE Asia and Implications for the Tectonic Setting of the Destruction of the North China Craton: Mainly Constrained by Zircon U-Pb Ages from Metamorphic Core Complexes. *Lithos* 154, 315–345. doi:10.1016/j.lithos.2012.07.020

Wang, T. H., Mao, J. W., and Wang, Y. B. (2008). Research on SHRIMP Chronology in Xiaoqinling-Xionger'Shan Area: The Evidence of Delamination of Lithosphere in Qinling Orogenic belt. Acta Petrol. *Sin* 24, 1273–1287.

Wang, X. X., Wang, T., Ke, C., Yang, Y., Li, J., Li, Y., et al. (2015a). Nd-Hf Isotopic Mapping of Late Mesozoic Granitoids in the East Qinling Orogen, central China: Constraint on the Basements of Terranes and Distribution of Mo Mineralization. *J. Asian Earth Sci.* 103, 169–183. doi:10.1016/j.jseaes.2014.07.002

Wang, X. X., Wang, T., and Zhang, C. (2015b). Granitoid Magmatism in the Qinling Orogen, Central China and its Bearing on Orogenic Evolution. *Sci. China Earth Sci.* 58, 1497–1512. doi:10.1007/s11430-015-5150-2

Wang, X. X., Wang, T., and Zhang, C. (2013). Neoproterozoic, Paleozoic, and Mesozoic Granitoid Magmatism in the Qinling Orogen, China: Constraints on Orogenic Process. *J. Asian Earth Sci.* 72, 129–151. doi:10.1016/j.jseaes.2012.11.037

Wang, X. X., Wang, T., Qi, Q. J., and Li, S. (2011). Temporal Spatial Variations, Origin and Their Tectonic Significance of the Late Mesozoic Granites in the Qinling, Central China. Acta Petrol. *Sin* 27, 1573–1593.

Wang, Y., Zhang, Y. S., Cheng, H., and Chen, F. (2020). Complex Magma Sources of Late Mesozoic Granites along the Southern Margin of the North China Craton: Constraints from Geochemistry and Geochronology of the Massive Heyu and Lantian Plutons. *Int. Geology. Rev.* 62, 1862–1882. doi:10.1080/00206814.2019.1669078

Weinberg, R. F., and Hasalová, P. (2015). Water-fluxed Melting of the continental Crust: A Review. *Lithos* 212-215, 158–188. doi:10.1016/j.lithos.2014.08.021

Wilson, M. (1989). Igneous Petrogenesis: A Global Tectonic Approach: Boston, MA, Unwin Hyman. *ISBN* 0045520259, 496.

Wu, F. Y., Liu, X. C., Ji, W. Q., Wang, J. M., and Yang, L. (2017). Highly Fractionated Granites: Recognition and Research. *Sci. China Earth Sci.* 60, 1201–1219. doi:10.1007/s11430-016-5139-1

Wu, F. Y., Li, X. H., Yang, J. H., and Zheng, Y. F. (2007b). Discussions on the Petrogenesis of Granites. Acta Petrol. *Sin* 23, 1217–1238.

Wu, F. Y., Li, X. H., Zheng, Y. F., and Gao, S. (2007a). Lu-Hf Isotopic Systematics and Their Applications in Petrology. Acta Petrol. *Sin* 23, 185–220.

Wu, Y. B., and Zheng, Y. F. (2004). Genesis of Zircon and its Constraints on Interpretation of U-Pb Age. *Chin.Sci.Bull.* 49, 1554–1569. doi:10.1007/BF03184122

Xu, P., Wu, F., Xie, L., and Yang, Y. (2004). Hf Isotopic Compositions of the Standard Zircons for U-Pb Dating. *Chin.Sci.Bull.* 49, 1642–1648. doi:10.1360/04wd012810.1007/bf03184136

Xu, Y. G., Ma, J. L., Huang, X. L., Iizuka, Y., Chung, S. L., Wang, Y. B., et al. (2004). Early Cretaceous Gabbroic Complex from Yinan, Shandong Province: Petrogenesis and Mantle Domains beneath the North China Craton. *Int. J. Earth Sci. (Geol Rundsch)* 93, 1025–1041. doi:10.1007/s00531-004-0430-7

Xu, Y. G., Wang, R. C., Wang, C. Y., Linnen, R., and Wu, F. Y. (2021). Highly Fractionated Granites and Rare-Metal Mineralization. *Lithos* 398-399, 106262. doi:10.1016/j.lithos.2021.106262

Xu, Y. G., Li, H. Y., Pang, C. J., and He, B. (2009). On the Timing and Duration of the Destruction of the North China Craton. *Sci. Bull.* 54, 3379–3396. doi:10.1007/s11434-009-0346-5

Yang, H. T., Li, L., Niu, L., He, L., and Bai, X. H. (2019). Report on Survey of Molybdenum Polymetallic Deposits in the Western of Mangling Orefield in Shangzhou District-Luonan County, Xi'an, China. Northwest Nonferrous Geological Research Institute Co., Ltd.

Yang, J. H., Xu, L., Sun, J. F., Zeng, Q., Zhao, Y. N., Wang, H., et al. (2021). Geodynamics of Decratonization and Related Magmatism and Mineralization in the North China Craton. *Sci. China Earth Sci.* 64, 1409–1427. doi:10.1007/s11430-020-9732-6

Yang, Y., Liu, Z. J., and Deng, X. H. (2017). Mineralization Mechanisms in the Shangfanggou Giant Porphyry-Skarn Mo-Fe deposit of the East Qinling, China: Constraints from H-O-C-S-Pb Isotopes. *Ore Geology. Rev.* 81, 535–547. doi:10.1016/j.oregeorev.2016.06.026

Yang, Y., Wang, X. X., Ke, C. H., Li, J. B., Lv, X. Q., Meng, X. Y., et al. (2014). Zircon U-Pb Ages, Geochemistry and Evolution of Mangling Pluton in North Qinling Mountains. *Miner Deposits* 33, 14–36.

Yang, Y., Zhang, L., Xue, S. L., and Wang, S. S. (2020). Report on 1:50,000 Gravity Survey Results in Western Mangling Ore Concentration Area, Xi'an, China. Shaanxi Mineral Geological Survey Center.

Yang, Z. M., Lu, Y. J., Hou, Z. Q., and Chang, Z. S. (2015). High-Mg Diorite from Qulong in Southern Tibet: Implications for the Genesis of Adakite-like Intrusions and Associated Porphyry Cu Deposits in Collisional Orogens. *J. Petrol.* 56, 227–254. doi:10.1093/petrology/egu076

Yuan, H. L., Gao, S., Dai, M. N., Zong, C. L., Günther, D., Fontaine, G. H., et al. (2008). Simultaneous Determinations of U-Pb Age, Hf Isotopes and Trace Element Compositions of Zircon by Excimer Laser-Ablation Quadrupole and Multiple-Collector ICP-MS. *Chem. Geology.* 247, 100–118. doi:10.1016/j.chemgeo.2007.10.003

Yuan, H. L., Wu, F. Y., Gao, S., Liu, X. M., Xu, P., and Sun, D. Y. (2003). Determination of U-Pb Age and Rare Earth Element Concentrations of Zircons from Cenozoic Intrusions in Northeastern China by Laser Ablation ICP-MS. *Chin. Sci. Bull.* 48, 1511–1520.

Zeng, Q. D., Liu, J. M., Chu, S. X., Wang, Y. B., Sun, Y., Duan, X. X., et al. (2012). Mesozoic Molybdenum Deposits in the East Xingmeng Orogenic belt, Northeast China: Characteristics and Tectonic Setting. *Int. Geology. Rev.* 54, 1843–1869. doi:10.1080/00206814.2012.677498

Zhai, M. G., and Santosh, M. (2013). Metallogeny of the North China Craton: Link with Secular Changes in the Evolving Earth. *Gondwana Res.* 24, 275–297. doi:10.1016/j.gr.2013.02.007

Zhang, G. W., Zhang, Z. Q., and Dong, Y. P. (1995). Nature of Main Tectono-Lithostratigraphic Units of the Qinling Orogen: Implications for the Tectonic Evolution. Acta Petrol. *Sin* 11, 101–114.

Zhang, H. F., Yu, H., Zhou, D. W., Zhang, J., Dong, Y. P., and Zhang, G. W. (2015). The Meta-Gabbroic Complex of Fushui in north Qinling Orogen: A Case of Syn-Subduction Mafic Magmatism. *Gondwana Res.* 28, 262–275. doi:10.1016/j.gr.2014.04.010

Zhang, H., Li, S. Q., Fang, B. W., He, J. F., Xue, Y. Y., Siebel, W., et al. (2018). Zircon U-Pb Ages and Geochemistry of Migmatites and Granites in the Foping Dome: Evidence for Late Triassic Crustal Evolution in South Qinling, China. *Lithos* 296-299, 129–141. doi:10.1016/j.lithos.2017.10.024

Zhang, S. H., Han, F. L., Wang, G. B., Wang, B. Y., and Cui, J. T. (2019). *Regional Geology of China Shaanxi Chronicles*. Beijing: Geological Publishing House, 142–186.

Zhang, Y. S., Wolfgang, S., He, S., Wang, Y., and Chen, F. K. (2019). Origin and Genesis of Late Jurassic to Early Cretaceous Granites of the North Qinling Terrane, China. *Lithos* 336-337, 242–257. doi:10.1016/j.lithos.2019.04.008

Zheng, S., An, Y., Lai, C., Wang, H., and Li, Y. (2021). Genesis of High-Mg Adakites in the Southeastern Margin of North China Craton: Geochemical and U-Pb Geochronological Perspectives. *Front. Earth Sci.* 9, 731233. doi:10.3389/feart.2021.731233

Zheng, Y. F. (2009). Fluid Regime in continental Subduction Zones: Petrological Insights from Ultrahigh-Pressure Metamorphic Rocks. *J. Geol. Soc.* 166, 763–782. doi:10.1144/0016-76492008-016R

Zheng, Y. F. (2019). Subduction Zone Geochemistry. *Geosci. Front.* 10, 1223–1254. doi:10.1016/j.gsf.2019.02.003

Zhou, X. H. (2006). Major Transformation of Subcontinental Lithosphere beneath Eastern China in the Cenozoic-Mesozoic: Review and prospect. *Earth Sci. Front.* 13, 50–64.

Zhu, L. M., Zhang, G. W., Guo, B., Lee, B., Gong, H. J., and Wang, F. (2010). Geochemistry of the Jinduicheng Mo-Bearing Porphyry and deposit, and its Implications for the Geodynamic Setting in East Qinling, P.R. China. *Geochemistry* 70, 159–174. doi:10.1016/j.chemer.2009.12.003

Zhu, L. M., Zhang, G. W., Guo, B., and Li, B. (2009). He-Ar Isotopic System of Fluid Inclusions in Pyrite from the Molybdenum Deposits in South Margin of North China Block and its Trace to Metallogenetic and Geodynamic Background. *Chin. Sci. Bull.* 54, 2479–2492. doi:10.1007/s11434-009-0047-0

Conflict of Interest: The authors declare that the research was conducted in the absence of any commercial or financial relationships that could be construed as a potential conflict of interest.

Publisher's Note: All claims expressed in this article are solely those of the authors and do not necessarily represent those of their affiliated organizations, or those of the publisher, the editors and the reviewers. Any product that may be evaluated in this article, or claim that may be made by its manufacturer, is not guaranteed or endorsed by the publisher.

frontiers | Frontiers in Earth Science

DATA REPORT
published: 20 May 2022
doi: 10.3389/feart.2022.886975

Genesis of the Zhaoxian Gold Deposit, Jiaodong Peninsula, China: Insights From *in-situ* Pyrite Geochemistry and S-He-Ar Isotopes, and Zircon U-Pb Geochronology

Yiwen Xu[1], *Guangzhou Mao*[1,2]*, *Xiaotong Liu*[1,3], *Pengrui An*[1], *Yu Wang*[1] *and Mingping Cao*[1]*

[1]*Shandong Provincial Key Laboratory of Depositional Mineralization and Sedimentary Minerals, College of Earth Sciences and Engineering, Shandong University of Science and Technology, Qingdao, China,* [2]*Functional Laboratory of Marine Mineral Resources Evaluation and Detection Technology, Qingdao National Laboratory of Marine Science and Technology, Qingdao, China,* [3]*Agency for Natural Resources of Rongcheng, Weihai, China*

Keywords: pyrite chemistry, isotope geochemistry, Zhaoxian gold deposit, Jiaodong gold province, zircon U-Pb geochronology

OPEN ACCESS

Edited by:
Kit Lai,
Fortescue Metals Group, Australia

Reviewed by:
Guanglai Li,
East China University of Technology, China
Junming Yao,
Xinjiang Institute of Ecology and Geography (CAS), China

****Correspondence:***
Guangzhou Mao
gzmaonjunwu@163.com
Mingping Cao
cmp4688164@163.com

Specialty section:
This article was submitted to Economic Geology, a section of the journal Frontiers in Earth Science

Received: *01 March 2022*
Accepted: *11 April 2022*
Published: *20 May 2022*

Citation:
Xu Y, Mao G, Liu X, An P, Wang Y and Cao M (2022) Genesis of the Zhaoxian Gold Deposit, Jiaodong Peninsula, China: Insights From in-situ Pyrite Geochemistry and S-He-Ar Isotopes, and Zircon U-Pb Geochronology. Front. Earth Sci. 10:886975. doi: 10.3389/feart.2022.886975

INTRODUCTION

The Jiaodong gold province is located in the southeastern margin of the North China plate. The region is composed of a metamorphic basement (Jiaodong Group), multiple generations of magmatic rocks (Linglong and Guojialing plutons), and crosscut by many NE- and NNE-trending faults (**Figure 1B**) (Zhang et al., 2001; Goldfarb and Santosh, 2014; Li et al., 2015; Cheng et al., 2016; Chai et al., 2019). Jiaodong is the most important gold province in China, with three main types of gold mineralization, i.e., altered rock type (Jiaojia-type), quartz vein-type (Linglong-type) and brecciated- and massive type (Pengjiakuang-type), among which the former is more important (>80% of gold reserve in the gold province).

The Zhaoxian is a typical Jiaojia-type gold deposit, and is developed in the cataclastic/altered granite of the Jiaojia fault zone. Drilling shows mineralization at 1,500–2200 m depth, much deeper than most gold deposits (<800 m) in the region. Zhaoxian gold deposit is a typical representative of the Jiaojia type gold deposit. It is of great theoretical and practical significance to study the metallogenic characteristics of Zhaoxian gold deposit in detail, and provide theoretical support for further study of gold deposits in Jiaodong area.

Pyrite contains a wide range of trace elements, and their content/ratio and isotopes can reveal the metallogenesis and the nature/source and evolution of ore-forming fluids (Bi et al., 2004; Zhu et al., 2009; Mao et al., 2013; Reich et al., 2013; Tauson et al., 2013). Application of *in situ* analytical technology can avoid the mixing of different generations pyrite and improve the analysis resolution and speed (Huang et al., 2015; Zhang J. R. et al., 2016). In this study, therefore, we studied the pyrites from different hydrothermal mineralization stages, and analyzed their trace element and sulfur isotope compositions, as well as He-Ar isotopes of fluid inclusions in the pyrite. In addition, we conducted zircon U-Pb dating on the ore-related cataclastic granite to constrain the mineralization age.

GEOLOGICAL BACKGROUND

Regional Geology

The Jiaodong region is located east of the Tancheng-Lujiang fault, in the tectonic intersection between the North China Craton, Yangtze Craton, and the Qinling-Dabie Orogen (**Figure 1A**). The region is

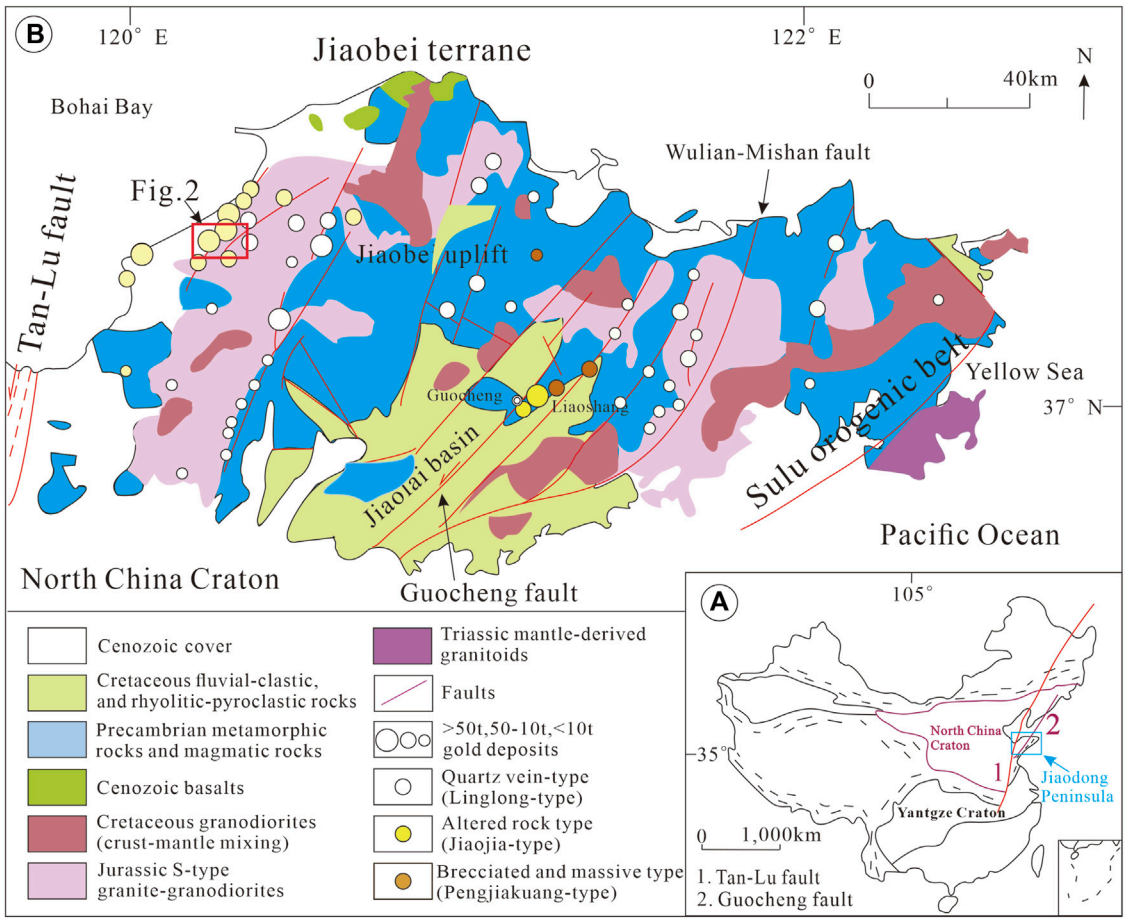

FIGURE 1 | Geologic map of the Jiaodong region **(A)**, showing the distribution of different types of gold deposits **(B)**. (after Deng et al., 2015).

composed of the Jiaobei Uplift in the north, the Jiaolai Basin in the middle, and the Sulu ultrahigh-pressure (UHP) metamorphic belt in the south (**Figure 1B**) (Li et al., 2007; Tan et al., 2012). From the Triassic to the Early Jurassic, the Precambrian North China and Sulu terranes were amalgamated along the NE-trending Wulian-Qingdao-Yantai fault, forming the basic tectonic framework of the Jiaodong gold province (Guo et al., 2017).

The region underwent greenschist-to granulite-facies metamorphism at ~1.9 Ga (Wang et al., 2017). The Sulu terrane is composed of a UHP metamorphic belt, and the basement rocks include mainly granitic gneisses and some mafic rocks (Zhao, 2016; Liu et al., 2018). The late Archean-Neoproterozoic strata are exposed in the region, and the Jurassic-Cretaceous strata are mainly exposed in the Jiaolai Basin (**Figure 1B**). Magmatic rocks are widespread and dominated by Yanshanian (Jurassic-Cretaceous) granites, which intruded the metamorphic basement. These granites are accompanied by Early Cretaceous dykes and volcanic rocks (Zhang, 2011; Zhao, 2016). NE-NNE faults are the main ore-controlling structures in the region, and include (from west to east) the Sanshandao, Jiaojia, Zhaoping, Xilin-Douya, and Jinniushan, in which 90% of the proven reserve in Jiaodong is distributed.

Deposit Geology

Zhaoxian gold deposit is located in the western margin of the Jiaobei Uplift and west of the Jiaojia fault (middle section), and the area is extensively covered by Quaternary sediments (**Figure 2**). Yanshanian intrusive rocks are well developed. Exploration drilling indicates that the Cuizhao Formation (of Linglong Group) is located in the northern and southern parts of the study area, whilst the Luanjiazhai Formation (of Malianzhuang Group) and Xinzhuang Formation (of Qixia Group) are located in the middle section. The deeper part of the mining area is bounded by the Jiaojia fault zone. The upper part of the stratigraphy comprises mainly the Luanjiazhai, Xinzhuang, and Cuizhao formations; whilst the lower part (ore-bearing) comprises the Cuizhao and Shangzhuang formations and locally the Guojialing pluton. Local basement structures include mainly nearly EW-trending ductile shear zones and NE-trending faults. The Jiaojia fault is the main ore-controlling structure, which is 160–500 m wide and W-/NW-dipping (strike: 0–30°). Dip angle of the northern and southern section is 10–26° (avg. 19°) and 12–40° (avg. 27°), respectively. The center of the

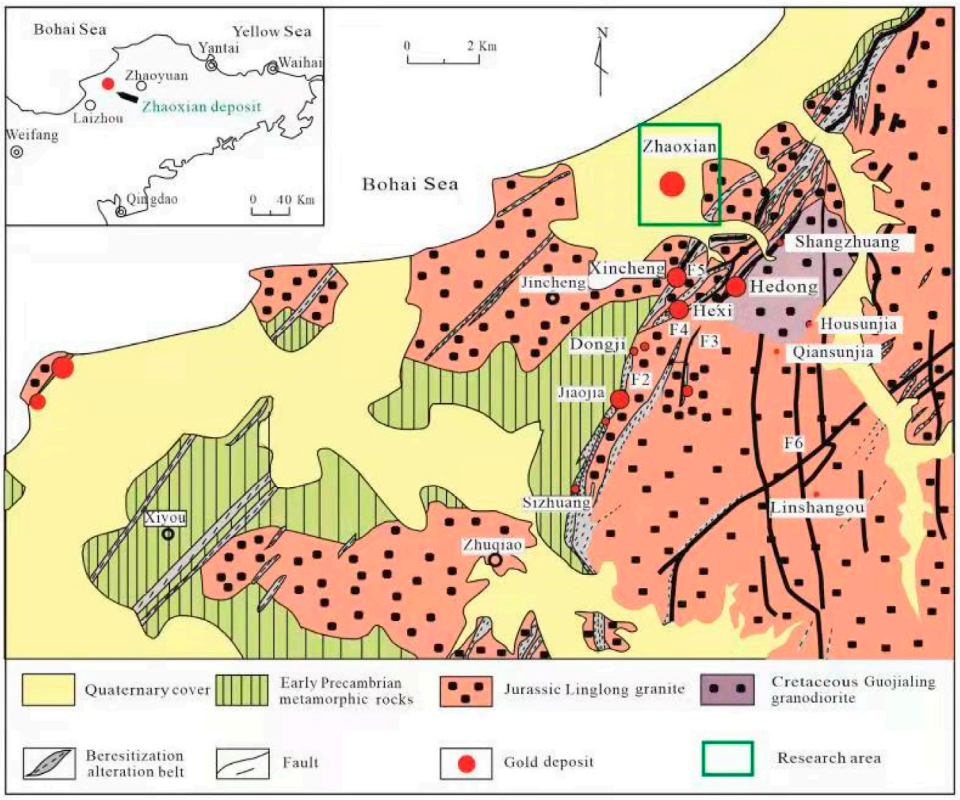

FIGURE 2 | Simplified geological map of the Zhaoxian gold deposit (modified from Li et al., 2015).

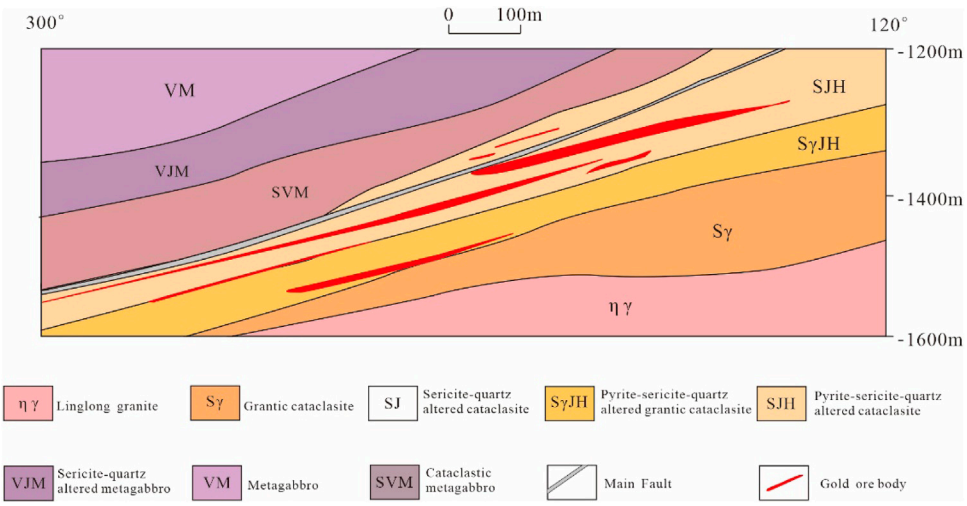

FIGURE 3 | Simplified cross-section of the Zhaoxian gold deposit.

main fault is marked by a dark-gray fault gouge (1–30 cm thick). From inside out, the fault comprises three zones with varying degrees of fragmentation: (1) mylonite and cataclastic zone (average thickness: ~20 m); (2) cataclastic granite and metagabbro (average thickness: ~50 m); (3) sericitized granite and metagabbro (average thickness: ~200 m). The boundaries between these three zones are mostly gradational. The vein/lenticular gold orebodies are mainly distributed in the pyrite-sericite-altered cataclastic rocks, close to the main fracture in the footwall (**Figure 3**).

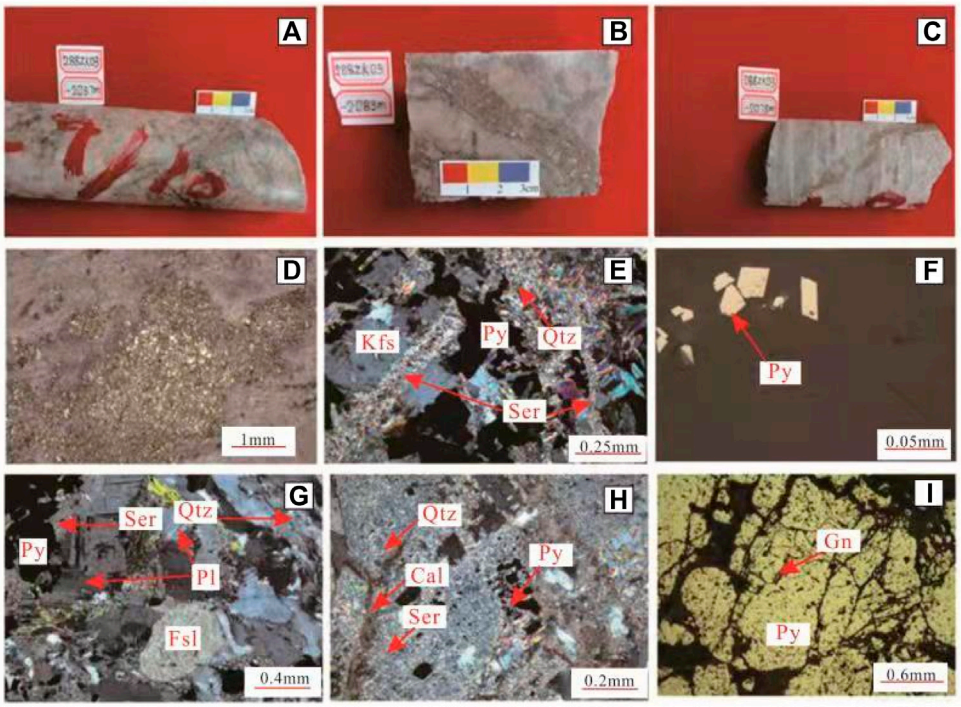

FIGURE 4 | Photos/photomicrographs of the pyrite-sericite-altered cataclastic granitic ore host: **(A–B)** hand-specimen of sericite-altered cataclastic granite and pyrite veins; **(C)** pyrite-sericite-altered cataclastic granite; **(D)** pyrite agglomerates; **(E)** pyrite with quartz, sericite, and altered K-feldspar residue; **(F–G)** granular pyrite with quartz (bent by stress) showing undulatory extinction; **(H)** pyrite metasomatized/corroded along margin, with clear embayment and skeletal structure; **(I)** pyrite broken with galena fracture infill. Kfs- K-feldspar; Qtz- Quartz; Ser- Sericite; Py- Pyrite; Pl- Plagioclase; Fsl-ferriferous augite; Cal- Calcite; Gn- Galena.

A total of 27 gold orebodies are delineated in Zhaoxian mining area, which can be divided into 4 orebody groups, from top to bottom were Ⅳ, Ⅰ, Ⅱ and Ⅲ. Ⅰ-1 and Ⅰ-2 orebodies are the main orebodies in Ⅰ orebody group. The length of Ⅰ-1 orebody is 1985 m, and the maximum dip length is 950 m. The ore body is large vein-like with the characteristics of expansion and contraction, SW- dipping at a dip angle varies from 11.20° to 19.00° and an average dip angle of 15.73°. The thickness of single project is 1.20–12.13 m, the average thickness is 3.55 m, and the variation coefficient is 92.92%. The single sample gold grade is (0.20–10.24) ppm, the average grade is 2.20 ppm, the variation coefficient is 72.79%, belongs to the orebody with uniform distribution of useful components.

Core logging reveals two main types of ore hosts: Pyrite-sericite-altered cataclastic granite (**Figures 4A,B**) and pyrite-sericite-altered cataclasite (**Figure 4C**). Ore structures include mainly disseminated, vein, and agglomerate (**Figures 4A–D**). Metallic minerals include mainly pyrite, followed by chalcopyrite, galena, sphalerite, and native gold (**Figures 4A–F**); whilst non-metallic minerals include quartz, K-feldspar, albite, sericite, chlorite, and calcite (**Figures 4E, G,H**). The ore textures include mainly granular, metasomatic, and cataclastic (**Figure 4I**).

According to the ore crosscutting relation and hydrothermal mineral assemblage, the mineralization of Zhaoxian gold deposit can be roughly divided into four stages. In chronological order, the four stages included (I) Pyrite-quartz-K-feldspar stage, (II) Pyrite-quartz-sericite stage, (III) Polymetallic sulfide-quartz stage and (IV) Quartz-calcite stage (**Table 1**). The first formed minerals often are metasomatism by the later formed minerals, or the late stage veins cut the early stage veins.

(I) Pyrite-quartz-K-feldspar stage: The pyrite grains are relatively coarse-grained (size: 1–6 mm), euhedral, and with relatively clean surface. The pyrite occurs as massive aggregates or veins, with occasional dissolution or fragmentation texture (**Figures 5A–C**). The quartz is coarse-grained, pure white, and deformed with local dynamic recrystallization and undulatory extinction (**Figure 5D**). K-feldspar grains are coarse, granular, and partially altered to sericite (**Figure 5D**). The content of gold in the ore is lower than that in Ⅱ and Ⅲ stages.

(II) Pyrite-quartz-sericite stage: Pyrite is fine-grained (mainly 50–300 μm) and euhedral with local dissolution features. The fine-grained quartz and sericite are altered from early plagioclase. At this stage, gold mainly exists as inclusions or in fissures (**Figures 5E–G**).

(III) Polymetallic sulfide-quartz stage: The fine-grained sulfides at this stage include galena, pyrite, chalcopyrite, and sphalerite (**Figure 5H**), and occur in quartz-sulfide veinlets or disseminations. Besides, fine-grained galena and chalcopyrite also occur as fracture infill in pyrite (**Figures 5I,J**). The quartz grains are fine and smoky-gray, whilst the gold occurs mainly as interstitial among or fracture-infill in galena, chalcopyrite, and pyrite (**Figures 5I,J**).

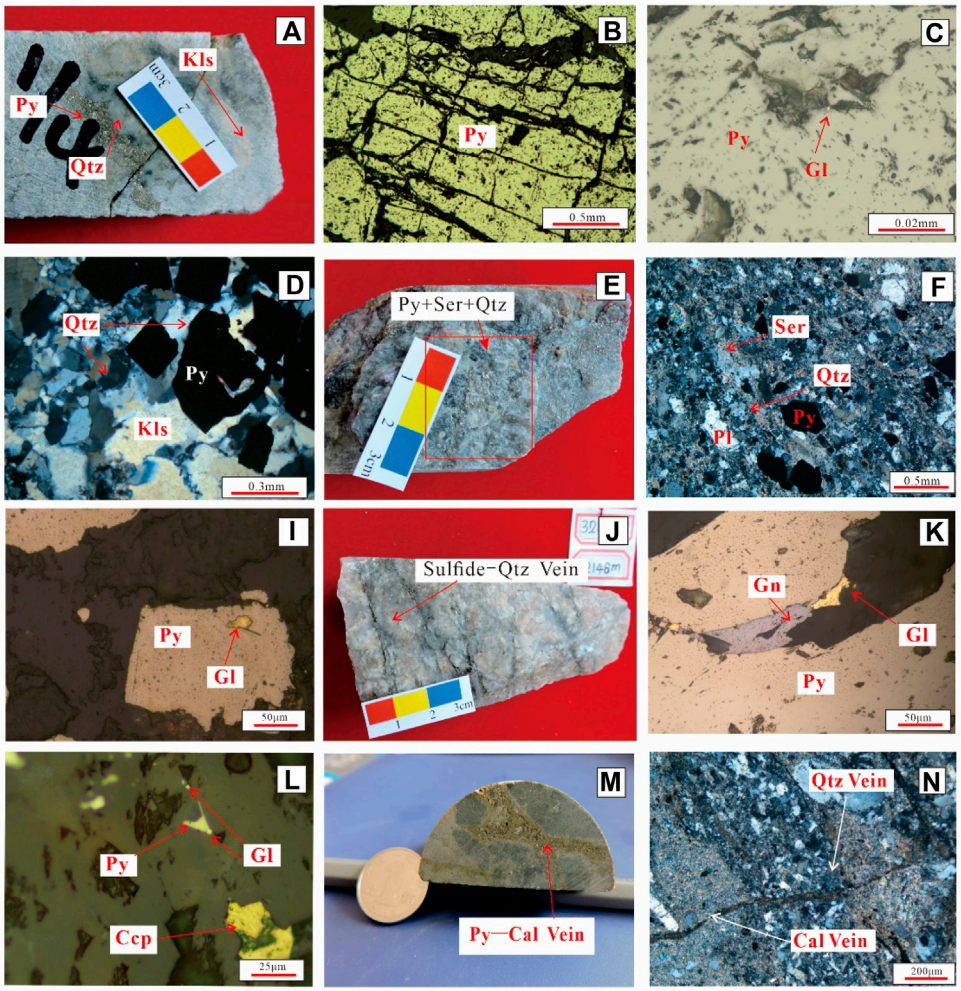

FIGURE 5 | Photos/photomicrographs of rocks and ores from the different mineralization stages of the Zhaoxian gold deposit [hand-specimen **(A,E,H,J,M)**; transmitted light **(D,F,L,N)** and reflected-light **(B,C,G,H,J,L)**]: **(A)** stage I pyrite aggregate; **(B)** stage I broken pyrite; **(C)** gold included in stage I pyrite; **(D)** quartz, K-feldspar (altered), and pyrite; **(E–F)** beresitization with fine mineral grains; **(I)** gold included in stage II pyrite; **(J)** quartz-polymetallic sulfide vein cut disseminated ore; **(K)** gold exists in fissure; **(L)** polymetallic sulfides coexist with gold inclusions; **(M)** coarse-grained stage IV pyrite-carbonate veins; **(N)** stage IV quartz and carbonate veins. Py- Pyrite; Qtz- Quartz; Kfs- K-feldspar; Gl-native gold; Ser- Sericite; Pl- Plagioclase; Gn- Galena; Ccp-Chalcopyrite; Cal- Calcite.

(IV) Quartz-calcite stage: Pyrite grains are coarse (size: up to 10 mm), cubic, and occur in veins/veinlets (**Figure 5K**) with quartz and calcite (**Figure 5L**).

Under the microscope, it is observed that stage II and III are the main gold ore stages, and gold mineralization is closely related to sericitization and silicification. The main gold-bearing minerals are pyrite, chalcopyrite, and galena. Native gold occurs commonly as interstitial or as inclusions or fracture-infill.

ANALYSES

The samples are all taken from drill cores (mainly 2038–2146 m depth). *In-situ* LA-ICP-MS pyrite trace element measurement was completed at the State Key Laboratory of Ore Deposit Geochemistry, Institute of Geochemistry, Chinese Academy of Sciences. The GeoLasPro laser ablation system was used, coupled with an Agilent 7700x ionization mass spectrometer. Analytical conditions include 10Hz pulse frequency, He carrier gas, and 23 μm (for fine-grained pyrite) or 33 μm (for coarse-grained pyrite) spot size. Elemental contents were calibrated against multiple reference materials (GSE-1G, BCR-2G, BIR-1G and BHVO-2G) and internal standardization (Dare et al., 2012). The recommended values of element concentrations for the USGS reference glasses are from the GeoReM database (http://crustal.usgs.gov/geochemical_reference_standards/microanalytical_RM.html). Detailed analytical procedures followed those described by Huang et al. (2016).

In-situ LA-ICPMS pyrite sulfur isotope analysis was completed at the State Key Laboratory of Geological Processes and Mineral Resources, China University of Geosciences (Wuhan). The Geolas2005 laser ablation system and Neptune

TABLE 1 | Mineralization stage and mineral paragenetic sequence.

Mineral	Ore stage			
	I	II	III	IV
K-feldspar				
Quartz				
Sericite				
Pyrite				
Chalcopyrite				
Sphalerite				
Galena				
Gold				
Calcite				

Plus Plasma mass spectrometer were used. Analytical conditions include 33 μm spot size, 10Hz pulse frequency, 50% T energy, 10.1–12.5V acceleration voltage, helium as a carrier gas, and argon as makeup gas. Detailed analytical procedures followed those described by Liu et al. (2008) and Fu et al. (2016).

The He-Ar isotope analysis of pyrite inclusions was completed at the Analytical and Testing Center in the Beijing Institute of Geological Research of Nuclear Industry. The Helix SFT™ Split Flight Tube noble gas mass spectrometer was used, with blank background less than 5×10^{-14} ccSTP, Faraday cup resolution higher than 400, and the ion multiplier resolution higher than 700. Sensitivity of the He and Ar measurements are better than 2×10^{-4} A/Torr and 1×10^{-3}A/Torr, respectively. Four samples (one in stage I, two in stage III, and one in stage IV) were measured. Stage II pyrite is not analyzed due to insufficient sample, and because stage II pyrite is mostly superimposed with pyrites of other stages (and thus prone to contamination). Detailed analytical procedures followed those described by Wang et al. (2016).

LA-ICP-MS zircon U-Pb dating was completed at the State Key Laboratory of Geological Processes and Mineral Resources, China University of Geosciences (Wuhan). Zircons used were all separated from the pyrite-sericite-altered cataclastic granite sample at the Hebei Langfang Keda Mineral Sorting Co. Ltd. The analysis used a GeoLas 2005 laser ablation system coupled with an Agilent 7500a plasma mass spectrometer. Analytical conditions include 24 μm spot size, 20–40 μm denudation depth, and 10Hz frequency. The U-Pb ages are corrected by using srm612 as external standard and 91500 and Plesovice as standard zircons. Detailed analytical procedures followed those described by Yuan et al. (2004).

RESULTS

Pyrite Trace Element Geochemistry

A total of pyrite 35 spots (stage I: 11, stage II: 9, stage III: 9, stage IV: 7) were analyzed, with the results shown in **Table 2**. The pyrite from the four stages has similar Fe (42.33–47.30 wt%) and S (52.19–57.33 wt%) contents, and the average pyrite S:Fe atomic ratios for stage I to IV are 2.08, 2.03, 2.10, and 2.16, respectively, higher than the theoretical value of 2:1, showing that the pyrite sample is Fe-poor, resembling pyrites from the Zhaoxian gold deposits (**Table 3**) and typical deep-level hydrothermal deposits (Cao et al., 2014). The pyrite Fe/(S + As) ratio can also indicate the mineralization depth, i.e., reaching 0.85 for deep-level mineralization and 0.86 for medium-level one, occasionally reaching 0.93 (Zhou et al., 2004; Barker et al., 2009; Cao et al., 2014). The Zhaoxian pyrite samples have Fe/(S + As) = 0.78 to 0.90, with the average value of different ore stages from 0.81 to 0.86. This indicates that the mineralization occurred in medium- to deep-level (more than 5000 m), consistent with the conclusion drawn from the S/Fe ratio.

Stage I pyrite has highest Co (avg. 697.91ppm) and Ni (avg. 46.51ppm) compared with the other three stages. Stage II pyrite has lower Co (avg. 152.391ppm) contents than stage I pyrite. Stage Ⅲ pyrite has lower Co (avg. 61.20 ppm) and Ni (avg. 25.91 ppm) contents than pyrite I and II. Stage Ⅳ pyrite has lowest Co (avg. 0.05 ppm) and Ni (avg. 13.31 ppm) compared with the other three stages.

Under high-temperature conditions, cobalt replaces Fe more readily in pyrite than Ni, leading to higher Co/Ni ratio. The average pyrite Co/Ni values decrease from stage I to IV (55.45, 46.73, 11.37, 1.1, respectively) (**Table 2**), suggesting a decrease of hydrothermal temperature from the early to late stage. Previous studies suggested that Co/Ni << 1 reflects sedimentary/diagenetic pyrite, whereas Co/Ni > 1 reflects magmatic hydrothermal pyrite. The Zhaoxian ore-related pyrite samples have overall Co/Ni ratio >1, suggesting a magmatic hydrothermal origin.

The stage I pyrite Co-Ni data points fall mostly in the hydrothermal field and minor in the magmatic field (**Figure 6**). This shows that early metallogenesis was closely hydrothermal-related with magmatic contribution. The stage II pyrite Co-Ni data points fall mainly (and almost equally) into the hydrothermal and magmatic fields. Compared with stage I

TABLE 2 | Pyrite trace element compositions of the Zhaoxian gold deposit.

No	Stage	S	Fe	Cu	Zn	Pb	Co	Ni	As	Te	Se	Mo	Au	Ag	Sn	Sb	W	Bi	Co/Ni	Au/Ag
A009	I	57.33	42.23	16.04	941.88	105.21	105	6.45	1153.34	1.86	2.33	0.04	0.46	5.62	0.22	1.81	0.01	5.91	16.31	0.08
A019	I	55.00	45.55	3.21	76.39	243.87	244	28.31	582.30	0.10	0.61	0.03	0.078	0.92	0.09	0.50	0.04	0.10	8.61	0.08
A021	I	54.58	47.25	60.12	106.86	410.52	411	4.34	234.68	—	1.04	0.06	0.022	1.47	0.21	1.13	0.07	2.91	94.59	0.02
A052	I	53.57	45.55	46.34	123.23	166.91	167	11.20	4474.43	0.24	—	0.02	1.20	8.92	0.17	1.85	0.004	9.55	14.91	0.13
B008	I	55.29	46.86	39.83	54.61	388.70	389	2.00	34.91	3.16	0.65	0.01	0.025	2.34	0.10	0.20	0.01	16.70	194.20	0.01
B009	I	52.03	44.71	1.25	317.75	304.58	305	3.18	55.50	1.35	0.50	—	0.019	6.95	0.03	—	0.005	17.38	95.88	0.003
A012	I	52.66	46.83	0.24	1.42	3371.26	3371	78.02	168.09	3.73	0.38	0.02	—	0.10	—	—	0.01	6.26	43.21	—
A015	I	50.40	46.65	11.63	131.79	1294.00	1,1294	241.62	297.38	4.75	—	0.07	0.16	3.90	0.11	0.35	0.28	17.65	5.36	0.04
A016	I	54.25	45.15	5.65	9.72	739.12	739	47.45	125.94	3.89	—	—	0.09	3.03	0.10	0.055	0.002	7.33	15.58	0.03
A017	I	55.87	46.33	2.23	8.03	379.23	379	3.21	15.79	1.65	0.56	0.004	0.08	2.35	—	0.032	0.01	2.62	118.15	0.03
A018	I	53.65	45.24	3.65	8.09	272.53	273	85.82	440.32	6.17	0.89	0.035	0.11	0.67	—	0.14	1.45	12.37	3.18	0.16
A019	II	54.05	47.30	28.24	442.59	76.52	76.5	4.11	3076.51	0.74	0.64	0.07	0.96	1.40	0.06	9.86	0.01	3.07	18.61	0.68
B007	II	52.59	46.43	0.93	1.62	619.26	619	236.86	19.39	1.11	1.11	0.01	0.024	0.02	0.08	0.044	0.07	2.13	2.61	1.35
B006	II	54.39	43.78	1.05	1.97	170.23	170	241.06	50.71	3.13	1.67	0.01	0.038	0.13	—	0.059	0.006	8.25	0.71	0.29
A021	II	52.92	46.23	17.15	260.66	232.33	232	140.90	793.12	19.83	0.18	—	1.13	27.8	0.02	0.88	0.002	28.19	1.65	0.04
B038	II	54.88	43.43	27.58	90.63	92.08	92.1	0.37	3532.83	—	—	0.013	0.92	10.9	—	3.42	0.006	4.43	249.43	0.08
B039	II	52.94	44.34	16.45	63.08	10.45	10.4	0.11	1967.86	0.19	0.89	0.005	0.85	7.07	—	4.96	0.01	3.79	92.01	0.12
B040	II	52.33	46.95	8.01	33.39	71.34	71.3	2.48	2277.44	0.18	1.39	—	0.51	2.71	0.09	1.93	0.01	8.19	28.76	0.19
A019	II	54.78	44.92	0.35	10.02	73.69	73.7	32.47	364.26	2.56	1.29	—	0.007	0.15	0.04	0.058	0.005	3.80	2.27	0.05
B037	II	52.19	44.91	14.08	42.46	26.45	26.5	1.08	2411.46	1.49	1.59	0.032	0.33	6.25	0.21	3.709	0.04	2.81	24.54	0.05
A053	III	54.70	43.58	26.58	25.61	106.38	106	3.26	18.02	2.77	0.66	—	0.16	4.85	0.04	0.012	0.003	14.10	32.67	0.03
B030	III	52.67	45.04	1.76	2.93	0.05	0.050	0.03	221.18	0.14	1.22	—	0.03	0.11	—	0.49	—	0.20	1.50	0.30
B031	III	53.45	45.25	0.34	2.22	4.77	4.77	0.09	973.71	0.22	—	0.01	0.001	0.004	0.15	0.006	0.005	0.01	53.49	0.20
A034	III	55.01	43.72	9.16	183.20	185.12	185	126.53	247.28	12.20	—	—	0.68	13.5	0.09	0.07	0.06	25.68	1.46	0.05
A035	III	53.69	45.35	1.44	20.62	112.60	113	39.71	205.13	4.96	0.16	0.02	0.10	0.60	0.20	0.08	0.05	21.55	2.84	0.17
A036	III	56.91	44.88	90.59	29.92	47.18	47.2	41.40	524.72	6.74	0.80	0.01	0.13	1.15	0.01	0.83	0.02	5.24	1.14	0.11
C040	III	55.64	46.24	4.42	12.65	4.84	4.84	2.74	23.05	0.83	0.71	0.005	0.036	0.77	0.05	0.11	—	4.52	1.77	0.05
A048	III	52.86	45.55	10.44	14.42	83.01	83.0	12.94	235.03	0.86	0.58	0.005	—	0.49	0.05	0.23	0.01	4.46	6.42	0.00
B018	III	55.01	47.25	0.19	2.92	6.97	6.97	6.47	516.03	0.31	—	—	0.008	0.02	—	—	—	0.04	1.08	0.38
A028	IV	54.55	45.55	59.46	42.90	0.17	0.17	249.37	1576.01	1.66	0.73	0.07	0.06	2.19	0.30	—	0.74	3.97	1.00	0.03
A031	IV	56.41	46.86	1.12	48.05	—	—	5.10	1.53	—	0.28	0.02	0.014	0.75	—	0.029	0.006	0.21	—	0.018
A032	IV	54.96	44.71	0.02	0.22	0.01	0.014	0.16	0.46	0.25	—	0.07	0.017	0.03	0.16	—	—	0.30	0.09	0.67
A034	IV	54.56	46.83	778.39	118.09	0.17	0.17	0.94	73.80	1.03	0.35	0.05	0.10	7.39	—	0.36	0.10	7.61	0.17	0.01
A091	IV	56.25	46.65	—	0.67	0.00	0.0035	28.07	1.02	—	0.04	0.06	0.027	0.04	—	0.011	0.004	0.63	—	0.72
A094	IV	54.63	45.15	—	0.70	0.02	0.018	33.46	0.07	—	0.64	0.07	0.011	0.06	0.21	0.078	0.01	0.57	—	0.19
A043	IV	54.67	46.33	0.93	5.35	0.06	0.056	3.94	3848.39	3.96	0.45	—	0.54	0.29	0.01	0.23	0.01	5.73	0.01	1.89

N.B. Except for Fe and S, concentrations of the other elements are expressed in ppm; "—": below the detection limit.

TABLE 3 | Atomic number ratio of S and Fe and Fe/(S + As) for the Zhaoxian ore-related pyrite.

Stage I			Stage II			Stage III			Stage IV		
Sample No	S/Fe	Fe/(S + As)	Sample No	S/Fe	Fe/(S + As)	Sample No	S/Fe	Fe/(S + As)	Sample No	S/Fe	Fe/(S + As)
A009	2.36	0.74	A019	2.08	0.84	A053	2.12	0.83	A028	2.13	0.82
A019	2.15	0.81	B007	1.95	0.90	B030	1.95	0.90	A031	2.26	0.77
A021	2.12	0.83	B006	2.09	0.84	B031	2.01	0.87	A032	2.14	0.82
A052	2.04	0.85	A021	1.98	0.88	A034	2.20	0.80	A034	2.11	0.83
B008	2.17	0.81	B038	2.15	0.81	A035	2.03	0.86	A091	2.25	0.78
B009	1.90	0.92	B039	1.98	0.88	A036	2.28	0.77	A094	2.11	0.83
A012	1.96	0.89	B040	1.96	0.89	C040	2.20	0.80	A043	2.13	0.81
A015	1.80	0.97	A019	2.12	0.82	A048	1.97	0.89	—	—	—
A016	2.08	0.84	B037	1.97	0.88	B018	2.14	0.82	—	—	—
A017	2.22	0.79	—	—	—	—	—	—	—	—	—
A018	2.03	0.86	—	—	—	—	—	—	—	—	—
Avg	2.08	0.85	Avg	2.03	0.86	Avg	2.10	0.83	均值	2.16	0.81

N.B. S/Fe (atomic ratio), Fe/(S + As) (concentration ratio).

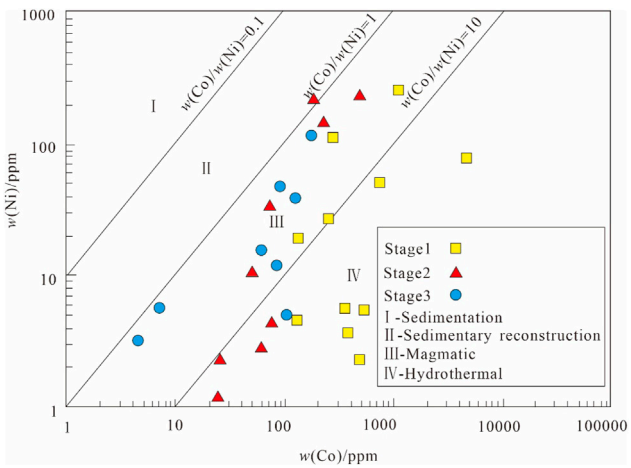

FIGURE 6 | Pyrite Ni-Co diagram for the Zhaoxian gold deposit (after Zhang C. et al., 2014).

pyrite, more pyrite data points of stage II fall into the magmatic field, suggesting more magmatic input. For stage III pyrite, the Co-Ni data points fall mainly into the magmatic field and minor into the hydrothermal field, indicating that the mineralization was closely magmatic-related. The stage IV pyrite Co-Ni data points fall outside the map, and it is a late stage of mineralization, the research significance is not important, so it will not be discussed.

Pyrite Sulfur Isotopes

A total of 31 pyrite sulfur isotope spot analyses were conducted, with the results shown in **Table 4**. The pyrite samples have $\delta^{34}S$ = 4.8–13.1%, with a range of 8.3%. Stage I pyrite (n = 10) has $\delta^{34}S$ = 9.6–13.1‰ (avg. 10.7‰); stage II pyrite (n = 10) has $\delta^{34}S$ = 7.2–10.1‰ (avg. 8.8‰); stage III pyrite (n = 7) has $\delta^{34}S$ = 4.8–6.7‰ (avg. 6.0‰); stage IV pyrite (*n* = 4) has $\delta^{34}S$ = 8.9–9.7‰ (avg. 9.2‰).

TABLE 4 | Pyrite $\delta^{34}S$ values of different hydrothermal stages in the Zhaoxian gold deposit.

No	Stage	$\delta^{34}S$ (‰)	Average $\delta^{34}S$ (‰)
1–2–1	I	13.1	10.7
1–2–3		12.9	
15–1		9.9	
15–2		9.7	
15–3		9.6	
15–4		9.8	
19–2		10.1	
19–4		10.7	
20–1		10.4	
20–2		10.4	
2–2–3	II	7.2	8.8
2–2–4		7.8	
2–2–5		8.8	
5–1		9.3	
5–2		10.1	
5–6		9.6	
9–2		7.6	
9–3		9.7	
11–4		8.8	
11–5		9.5	
1–1	III	6.7	6
1–2		4.8	
5–2		6.7	
9–4		6.6	
9–5		6.7	
12–2		5.0	
12–3		5.5	
3–1	IV	9.0	9.2
3–2		9.1	
3–3		9.7	
3–4		8.9	

The pyrite $\delta^{34}S$ values for the four stages are all positive and higher than the mantle-derived sulfur $\delta^{34}S$ range, suggesting possible multiple sulfur sources (Zhang W. Y. et al., 2014; Zhang R. Z. et al., 2016). **Figure 7** shows that the $\delta^{34}S$ range of the pyrite samples fall into the range of the altered rock-type

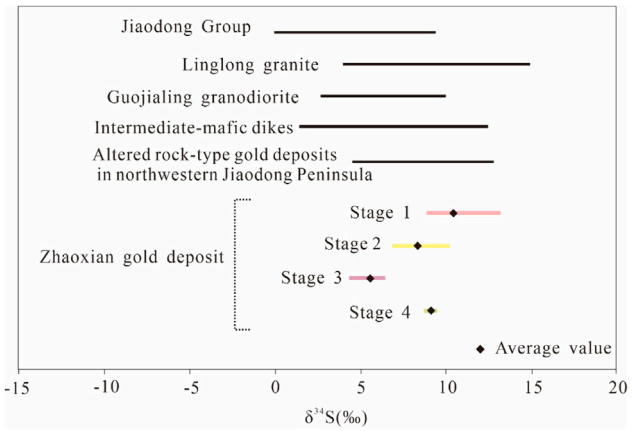

FIGURE 7 | $\delta^{34}S$ diagram of ore-related pyrite in the Zhaoxian gold deposit (modified after Zhang et al., 2014a and Wang, 2016).

gold ores from northwestern Jiaozhou. The higher $\delta^{34}S$ value for the stage I pyrite suggests that the sulfur source may have been the high $\delta^{34}S$ Linglong granite. The pyrite $\delta^{34}S$ value of stage II is slightly lower than that of stage I, suggesting both the Linglong granite and Guojialing granodiorite may have been a sulfur source. Stage III pyrite has the lowest $\delta^{34}S$ value (avg. 6.0‰), close to the average $\delta^{34}S$ value of the Guojialing granodiorite (6.7‰), and thus the latter may have been the sulfur source. During the gold mineralization (stage I to III), the average pyrite $\delta^{34}S$ value decrease from 10.7‰ (stage I) to 6.0‰ (stage III), similar to the trend shown in the neighboring Xincheng deposit (9.7‰ → 8.7‰ → 7.2‰) (Wang, 2016), suggesting similar source change/evolution. The metamorphic Jiaodong Group has $\delta^{34}S$ = 0–9.4‰ (mean 4.99‰) (Zhang C. et al., 2014; Wen et al., 2016), the Linglong granite has $\delta^{34}S$ = 4.0–15‰ (mean 9.5‰) (Li and Yang, 1993; Zhang W. Y. et al., 2014), and the Guojialing granite has $\delta^{34}S$ = 2.7–10.0‰ (mean 6.7‰). This implies that the Zhaoxian ore sulfur may have had similar source to other gold deposits in northwestern Jiaodong, possibly the Jiaodong Group and Mesozoic granites.

The $\delta^{34}S$ content of the Stage IV is higher than Stage II and Stage III, indicating that other fluids may have been mixed in the late stage of mineralization, and ore-forming materials are multi-source.

Fluid Inclusion He-Ar Isotopes

The ^4He content of the four samples is 5.199, 2.259, 2.029, and 3.709 × 10^{-8}ccSTP/g, respectively, whilst their $^3He/^4He$ = 55.4 ppb to 1.46 ppm (R/Ra = 0.04–1.04). The samples have ^{40}Ar = 4.954–11.899 × 10^{-8} and $^{40}Ar/^{36}Ar$ = 928.1–1,217.3 (**Table 5**). The R/Ra value of stage I and stage III is 15–21 times that of average crustal fluids, but lower than the minimum R/Ra of mantle fluids. This implies mantle fluid input during the mineralization. For stage IV samples, their R/Ra falls within the crustal fluid range, showing crustal inheritance. The mantle He content is also an index for evaluating the crust-mantle fluid mixing ratio (Yang et al., 2012; Wen et al., 2016). The proportion of mantle He in fluid inclusions from stage I and III pyrite is 10.02–13.11%, indicating that the coeval ore-forming fluids were mainly crustal-derived with minor mantle input. For stage IV, the proportion of mantle He is only 0.32%, indicating that the fluids were predominantly crustal-derived, consistent with the conclusion drawn from the R/Ra data (**Figure 8A**).

In the R/Ra-$^{40}Ar/^{36}Ar$ plot (**Figure 8B**), data points from stage I and III fall between the mantle and crustal end members, and stage I data points fall distal from the meteoric water field, suggesting legible meteoric water influence. In contrast, stage III data points fall close to the meteoric water field, implying probably meteoric water incursion during late mineralization. Stage IV data points falls inside the crustal fluid end member, consistent with the conclusion drawn from the ^3He-^4He plot.

Zircon U-Pb Age

Representative zircon CL images are shown in **Figure 9**. A total of 30 spots were analyzed, which yielded 20 concordant U-Pb ages. The results are listed in **Table 6**, and the zircon U-Pb age concordia diagram and weighted average age are shown in **Figure 10**.

For the concordant zircons, their U-Pb ages are 133–155 Ma (n = 16) and 190–252 Ma (n = 4). The zircons have 104–963 ppm U and 82–1,212 ppm Th, and their Th/U > 0.4.

DISCUSSION

Ore-Forming Material and Ore-Forming Fluids

Previous studies have suggested that the ore-forming material of gold deposits in northwestern Jiaodong Peninsula were mainly derived from the Jiaodong Group and/or mantle

TABLE 5 | Fluid inclusion He-Ar isotopic compositions of pyrite from the Zhaoxian gold deposit.

Sample	3	9	13	21
Mineral	Pyrite	Pyrite	Pyrite	Pyrite
Stage	IV	III	III	I
$^3He/10^{-14}$	0.017	2.375	3.300	5.723
$^4He/10^{-8}$	3.709	2.029	2.259	5.199
$^3He/^4He$ (R)	55.4 ppb	1.17 ppm	1.46 ppm	1.12 ppm
mantle He (%)	0.32	10.47	13.11	10.02
$^{40}Ar/10^{-8}$	4.954	7.104	7.911	11.899
$^{40}Ar/^{36}Ar$	934.6	940.2	928.1	1,217.3
R/Ra	0.04	0.84	1.04	0.80
$^{40}Ar^*/10^{-8}$	3.39	4.87	5.39	9.00
$^{40}Ar^*$ (%)	68.38	68.57	68.16	75.72
$^{40}Ar^*/^4He$	0.91	2.40	2.39	1.72
F^4He	65477.673	27892.847	27998.81	43689.071

Note: R: sample $^3He/^4He$ ratio; Ra: meteoric $^3He/^4He$ ratio, 1Ra = 1.4 ppm $^{40}Ar^*$ = radiogenic excess Ar after deducting air ^{40}Ar; $F^4He = (^4He/^{36}Ar)_{sample}/(^4He/^{36}Ar)_{air}$, $(^4He/^{36}Ar)_{air}$ = 0.1655; Isotopic content in cc·STP/g.

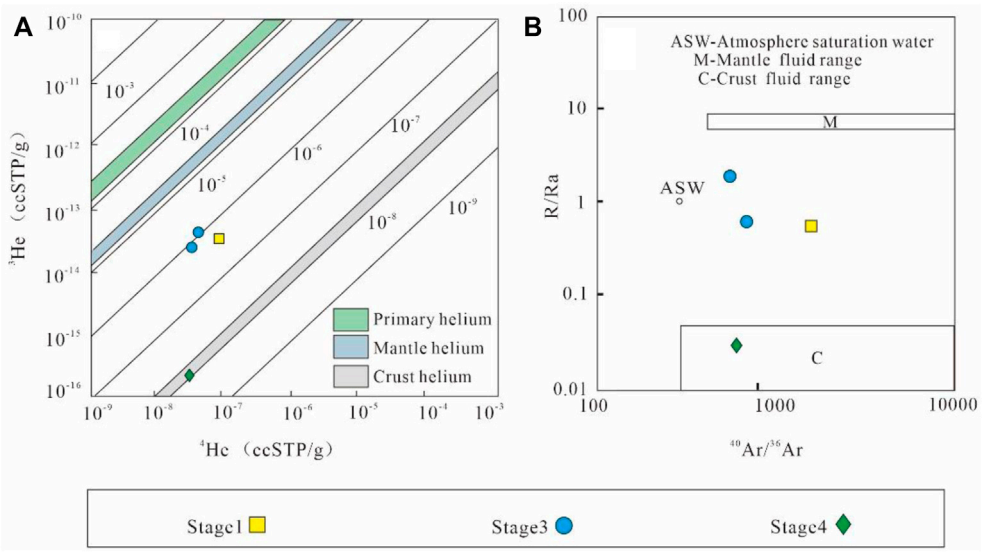

FIGURE 8 | Plots of ^{3}He-^{4}He **(A)**, R/Ra-^{40}Ar/^{36}Ar **(B)** for the inclusions of ore-related pyrite from the Zhaoxian gold deposit (after Winckler et al., 2001; Zhang et al., 2012)

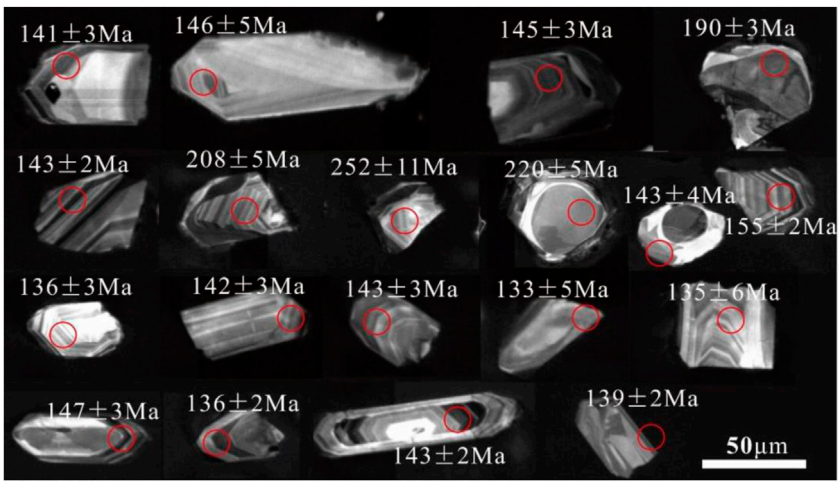

FIGURE 9 | Representative CL images for zircons from the Zhaoxian gold deposit.

(Deng et al., 2004; Li et al., 2007; Guo et al., 2008; Liang et al., 2015). However, the average Au content of the Jiaodong Group (2.47 ppb; Liu, 2016) is lower than the crustal average (4 ppb) (Li, 1976), while that of the Jiaodong Group in the Jiaojia Fault hangingwall at the Zhaoxian deposit is even lower (1.16 ppb). Therefore, it is assumed that the Jiaodong Group had supplied little material for the gold mineralization at Zhaoxian. In contrast, the average Au contents of the Linglong granite (19 ppb) and Guojialing granite (49 ppb) are high (Song et al., 2012), and represent a probably gold source. Previous studies have also suggested an upper-mantle gold source for the Jiaodong gold province (Gui, 2014). The magma may have extracted gold and other ore-forming elements from the upper mantle, and ascended to form the Linglong granite (Deng et al., 2004; Guo et al., 2005).

The pyrite δ^{34}S values are all positive and higher than the mantle-derived sulfur δ^{34}S range, suggesting possible multiple sulfur sources, possibly the Jiaodong Group and Mesozoic granites.

The pyrite trace element data show that the gold mineralization at Zhaoxian is closely related to magmatic-hydrothermal activity, with the ore fluids being magmatic-/metamorphic-sourced with brine input. Fluid inclusion He-Ar isotope compositions of pyrite suggest that the ore fluids

TABLE 6 | LA-ICP-MS zircon dating results for the Zhaoxian gold deposit.

Spot	Total Pb (ppm)	^{232}Th (ppm)	^{238}U (ppm)	Th/U	Isotopic ratio			Isotopic age		
					^{207}Pb/^{206}Pb	^{207}Pb/^{235}U	^{206}Pb/^{238}U	^{207}Pb/^{206}Pb	^{207}Pb/^{235}U	^{206}Pb/^{238}U
z1-1	17.895	332.54	383.24	0.94	0.0520 ± 0.0054	0.1569 ± 0.0165	0.0214 ± 0.0006	287 ± 23	148 ± 14	136 ± 4
z1-7	77.773	1,212.3	1780.8	0.82	0.0527 ± 0.0022	0.1651 ± 0.0067	0.0225 ± 0.0004	316 ± 96	155 ± 6	143 ± 2
z1-14	20.585	377.53	540.12	0.68	0.0457 ± 0.0031	0.1326 ± 0.0085	0.0214 ± 0.0004	153 ± 13	126 ± 7	136 ± 3
z1-39	22.433	251.11	615.25	0.70	0.0479 ± 0.0033	0.1418 ± 0.0085	0.0218 ± 0.0004	100 ± 155	134 ± 7	139 ± 2
z13-3	10.619	22.613	473.45	0.40	0.0533 ± 0.0036	0.2189 ± 0.0143	0.03 ± 0.0006	338 ± 14	200 ± 11	190 ± 3
z13-12	5.4935	2.9472	244.95	0.05	0.0516 ± 0.0034	0.2296 ± 0.0143	0.0329 ± 0.0008	264 ± 149	209 ± 11	208 ± 5
z13-17	5.0681	26.897	105.21	0.01	0.0519 ± 0.0075	0.2834 ± 0.0355	0.0399 ± 0.0019	283 ± 29	253 ± 28	252 ± 11
z13-20	5.2375	11.726	177.67	0.25	0.0556 ± 0.0042	0.2705 ± 0.0209	0.0348 ± 0.0008	438 ± 166	243 ± 16	220 ± 5
z13-6	31.681	277.76	184.2	1.54	0.0503 ± 0.0023	0.1582 ± 0.0078	0.0225 ± 0.0004	209 ± 10	149 ± 6.8	143 ± 2
z13-30	25.208	234.37	963.95	0.19	0.0485 ± 0.0024	0.1658 ± 0.0087	0.0244 ± 0.0005	120 ± 114	155 ± 7.5	155 ± 3
z13-32	15.164	318.8	291.56	0.24	0.0532 ± 0.0052	0.1627 ± 0.014	0.0226 ± 0.0007	338 ± 222	153 ± 12	144 ± 4
z20-1	76.266	314.33	335.46	1.00	0.0507 ± 0.0056	0.1463 ± 0.0142	0.0214 ± 0.0005	227 ± 237	138 ± 12	136 ± 3
z20-17	56.328	121.52	185.36	0.94	0.0510 ± 0.0044	0.1543 ± 0.0123	0.0223 ± 0.0005	242 ± 199	145 ± 10	142 ± 3
z20-20	24.165	258.26	620.31	0.65	0.0551 ± 0.0039	0.1664 ± 0.0109	0.0225 ± 0.0005	416 ± 159	156 ± 9	143 ± 3
z20-21	25.365	263.26	590.66	0.41	0.0551 ± 0.0085	0.1472 ± 0.0201	0.0209 ± 0.0008	416 ± 347	139 ± 17	133 ± 5
z20-23	32.265	296.56	685.26	0.44	0.0521 ± 0.0089	0.1506 ± 0.017	0.0212 ± 0.001	300 ± 342	142 ± 15	135 ± 6
z21-2	5.1737	125.62	123.83	0.43	0.0509 ± 0.0062	0.1491 ± 0.0162	0.0222 ± 0.0006	235 ± 259	141 ± 14	141 ± 3
z21-5	3.9352	82.003	104.27	1.01	0.0498 ± 0.0065	0.145 ± 0.0164	0.023 ± 0.0008	187 ± 277	137 ± 14	146 ± 5
z21-7	6.2455	126.56	182.76	0.78	0.0523 ± 0.0048	0.1588 ± 0.0132	0.0228 ± 0.0006	298 ± 209	149 ± 11	145 ± 3

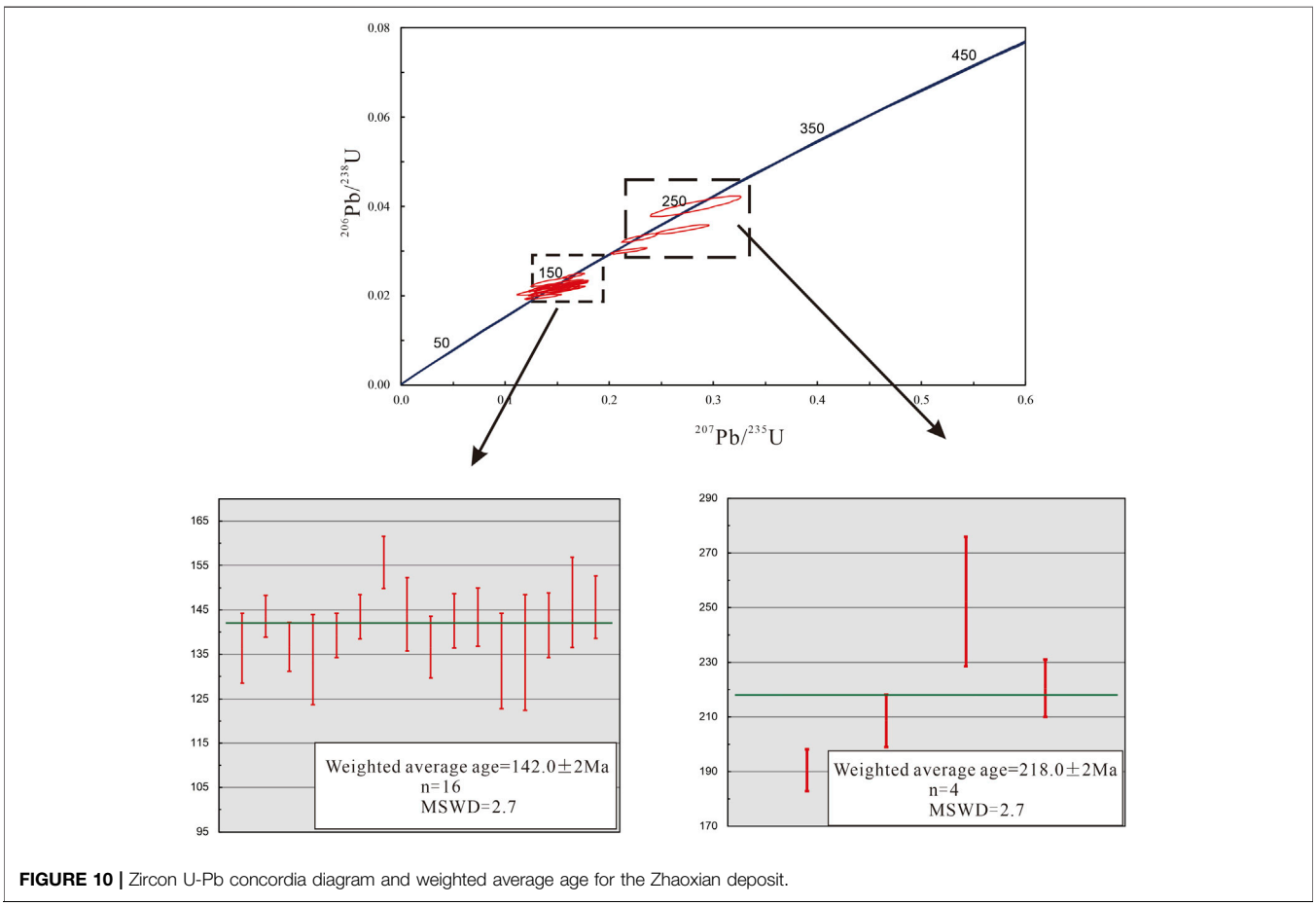

FIGURE 10 | Zircon U-Pb concordia diagram and weighted average age for the Zhaoxian deposit.

were characterized by crust-mantle mixing with minor meteoric water participation. Overall, the Zhaoxian ore-forming fluids were multi-sourced. The early-stage ore fluids were dominantly metamorphic-sourced, together with magmatic and (minor) brine input. Magmatic fluids played a more dominant role in the main-ore stage, in addition to brine and meteoric water contribution. Magmatic activity may have weakened toward the late-ore stage, and the ore fluids were mainly crustal-derived with negligible mantle input.

Therefore, we suggest that the ore-forming material and ore-forming fluids source may have been crust-mantle mixed, i.e., derived directly from the Linglong and Guojialing granites with inheritance from the Jingshan and Jiaodong groups.

Mineralization Age

Mesozoic magmatism in the Jiaodong region was extensive and multi-phase, and the timing was closely related to transformation of tectonic regimes (Deng et al., 2004; Wang et al., 2011). The major tectonic events in the northwestern Jiaojiang gold district were: (1) 240–216 Ma (or 245–220 Ma): the North China and Yangtze plates collided, forming the Dabie-Sulu collisional orogeny and initiating the Tanlu fault movement, accompanied by Indosinian magmatism (Deng et al., 2004; Chen et al., 2015); (2) ~140 Ma, the Paleo-Pacific subduction accelerated, causing large-scale sinistral shearing in the Tanlu fault zone and extensive mantle-derived magmatism (Deng et al., 2004); (3) 130–120 Ma: asthenospheric upwelling occurred due to regional extension, forming extensive magmatism. Pre-existing transpressive faults were transformed to transtensional shear, creating space for gold ore precipitation and concentration (Deng et al., 2004; Chen et al., 2015). At Zhaoxian, since the gold mineralization should occur after the granite ore-host emplacement (142 ± 2 Ma).

The zircon U-Pb ages of Zhaoxian gold deposit are divided into two groups. The first group average age is 243.0 ± 2 Ma, representing the Indosinian collision between the North China Plate and the Yangtze Plate. The other group average age is 142.0 ± 2 Ma, which represents the subduction event of the Pacific plate to the Eurasian plate and the formation time of the Linglong granites. Previous research results suggest that the gold deposit in Jiaodong area was formed in the transition period from extrusion to extension after the collision, later than the plate collision (Deng et al., 2004; Chen et al., 2015). We suggest that the gold mineralization is not earlier than 142 ± 2 Ma. The exact mineralization age would need more precise geochronological work to confirm.

Ore-Forming Processes

During the Late Jurassic (160–140 Ma), crustal delamination occurred in eastern North China, and extensive basement crustal remelting occurred in the northwestern Shandong. The magma may have extracted gold and other ore-forming elements from the upper mantle, and ascended to form the Linglong granite (Deng et al., 2004; Guo et al., 2005). The accelerated Paleo-Pacific subduction (~140 Ma) and collisional orogeny in Jiaodong may have formed a series of NNE-trending faults (e.g., the Zhaoping, Jiaojia, and Sanshandao-Cang Shang) in the Jiaobei Uplift and fractured the rocks along these fault zones, providing the fluid conduits and ore-deposition space. Meanwhile, the ascending magmas may have provided a heat source for the generation/circulation of metamorphic-/magmatic-sourced hydrothermal fluids, which formed the early-ore fluids. As the lithospheric thinning intensified, crust-mantle material mixing and partial melting occurred, and the ore-forming magma/fluids ascended along the deep fracture zones, forming the gold-rich Guojialing granodiorite (Deng et al., 2004; Chen et al., 2005). The subsequent fluid mixing (magmatic hydrothermal, brine, meteoric water) may have triggered ore deposition along structural traps.

CONCLUSION

(1) The Zhaoxian gold deposit comprises four hydrothermal stages, among which the second (pyrite-quartz-sericite-silicic) and third (polymetallic sulfide-quartz) stages are ore-forming. Pyrite is the main gold-bearing minerals, and native gold occurs as interstitial and in fissures and inclusions.

(2) The pyrite trace element and fluid He-Ar isotope characteristics show that the mineralization temperature decreased gradually, and the ore fluids were derived from a crustal-mantle mixed source, with metamorphic and magmatic fluids dominating the early and main ore stage, respectively, plus limited meteoric water input. The pyrite $\delta^{34}S$ values are positive across different hydrothermal stages, and the sulfur may have sourced mainly from the Linglong granite and Guojialing granite.

(3) Zircon U-Pb dating of the cataclastic granite ore host (142 ± 2 Ma) has constrained the maximum age for the Zhaoxian gold mineralization, coeval with the regional Yanshanian magmatism.

DATA AVAILABILITY STATEMENT

The original contributions presented in the study are included in the article/Supplementary Material, further inquiries can be directed to the corresponding authors.

AUTHOR CONTRIBUTIONS

GM is the corresponding author of this paper, responsible for comprehensive technical guidance in the research process, comprehensively analyzed the test data on the basis of comprehensive research, and comprehensively reviewed and finalized the article; YX is the first author of this paper. On the basis of field investigation and sample collection, she has carried out geochemical analysis and testing, and wrote the first draft of the paper; XL carried out the statistical analysis of sample microscopic observation and experimental data, and participated in the revision of the manuscript; PA participated in sample collection and data processing; YW participated in the field investigation and the

revision of the manuscript; MC contributed to the conception and design of the research. All authors contributed to manuscript revision, read, and approved the submitted version.

ACKNOWLEDGMENTS

We acknowledge Prof. Kit Lai and two reviewers for their valuable comments that improved the manuscript greatly. We thank the National Natural Science Foundation of China (42172087, 41572063) and the Key Laboratory of Gold Ore Formation Process and Resource Utilization (Ministry of Land and Resources) (2013003) for financial support of this work. The Guiyang Institute of Geochemistry (Chinese Academy of Sciences), the State Key Laboratory of Geological Processes and Mineral Resources [China University of Geosciences (Wuhan)], and the Beijing Institute of Geological Research of Nuclear Industry are thanked for supporting the laboratory analyses.

REFERENCES

Barker, S. L. L., Hickey, K. A., Cline, J. S., Dipple, G. M., Kilburn, M. R., Vaughan, J. R., et al. (2009). Uncloaking Invisible Gold: Use of Nanosims to Evaluate Gold, Trace Elements, and Sulfur Isotopes in Pyrite from Carlin-type Gold Deposits. *Econ. Geology.* 104 (7), 897–904. doi:10.2113/gsecongeo.104.7.897

Bi, X. W., Hu, R. Z., and Peng, J. T. (2004). REE and HFSE Geochemical Characteristics of Pyrites in Yao'an Gold deposit: Tracing Ore Forming Fluid Signatures. *Bull. Mineralogy, Petrol. Geochem.* 23 (1), 1–4. doi:10.3969/j.issn.1007-2802.2004.01.001

Cao, S. Q., Jia, J. S., and Zhong, Z. Q. (2014). Composition and Sulfur Isotope Characteristics of Auriferous Pyrite from the Shilongtou Gold deposit in Kaihua, Western Zhejiang Province. *Acta Petrologica Et Mineralogica* 33 (5), 937–946.

Chai, P., Zhang, H. R., Dong, L., and Zhang, Z. Y. (2019). Geology and Ore-Forming Fluids of the Dayingezhuang Gold deposit, Jiaodong Peninsula, Eastern China: Implications for mineral Exploration. *J. Geochemical Exploration* 204, 224–239. doi:10.1016/i.gexplo.2019.06.001

Chen, J., Sun, F. Y., and Wang, L. (2015). Zircon U-Pb Geochronology and Petrogeochemistry of Luanjiahe Granite in Jiaodong Region and Their Geological Significance. *Glob. Geology.* 34 (2), 283–295. doi:10.3969/j.issn.1004-5589.2015.02.003

Chen, Y.-J., Pirajno, F., and Qi, J.-P. (2005). Origin of Gold Metallogeny and Sources of Ore-Forming Fluids, Jiaodong Province, Eastern China. *Int. Geology. Rev.* 47 (5), 530–549. doi:10.2747/0020-6814.47.5.530

Cheng, S. B., Liu, Z. J., Wang, Q. F., Wang, F. J., Xue, Y. S., Xu, L., et al. (2016). Mineralization Age and Geodynamic Background for the Shangjiazhuang Mo deposit in the Jiaodong Gold Province, China. *Ore Geology. Rev.* 80, 876–890. doi:10.1016/j.oregeorev.2016.08.018

Dare, S. A. S., Barnes, S.-J., and Beaudoin, G. (2012). Variation in Trace Element Content of Magnetite Crystallized from a Fractionating Sulfide Liquid, Sudbury, Canada: Implications for Provenance Discrimination. *Geochimica et Cosmochimica Acta* 88, 27–50. doi:10.1016/j.gca.2012.04.032

Deng, J., Liu, X., Wang, Q., and Pan, R. (2015). Origin of the Jiaodong-type Xinli Gold deposit, Jiaodong Peninsula, China: Constraints from Fluid Inclusion and C-D-O-S-Sr Isotope Compositions. *Ore Geology. Rev.* 65, 674–686. doi:10.1016/j.oregeorev.2014.04.018

Deng, J., Wang, Q. F., and Yang, L. Q. (2004). The Geological Settings to the Gold Metallogeny in Northwestern Jiaodong Peninsula, Shandong Province. *Earth Sci. Front.* 11 (4), 527–533.

Fu, J. L., Hu, Z. C., Zhang, W., Yang, L., Liu, Y. S., Li, M., et al. (2016). *In Situ* Sulfur Isotopes ($\delta^{34}S$ and $\delta^{33}S$) Analyses in Sulfides and Elemental Sulfur Using High Sensitivity Cones in Combination with the Addition of Nitrogen by Laser Ablation MC-ICP-MS. *Analyt. Chim. Acta* 911 (16), 14–26. doi:10.1016/j.aca.2016.01.026

Goldfarb, R. J., and Santosh, M. (2014). The Dilemma of the Jiaodong Gold Deposits: Are They Unique? *Geosci. Front.* 5 (2), 139–153. doi:10.1016/j.gsf.2013.11.001

Gui, F. (2014). *Mineralization Enrichment Regularity and the Genesis Discussed of Sanshandao Gold deposit Shandong Province Laizhou*. China: Jilin University.

Guo, B., Liu, Z. C., and Li, W. (2008). Geological Features of Sanshan Island Gold Ore Formation and Future of Ore Search. *Mining Eng.* 6 (4), 14–16.

Guo, J. H., Chen, F. K., and Zhang, X. M. (2005). Evolution of Syn-To post-collisional Magmatism from north Sulu UHP belt, Eastern China: Zircon U-Pb Geochronology. *Acta Petrologica Sinica* 21 (4), 1281–1301.

Guo, L.-N., Goldfarb, R. J., Wang, Z.-L., Li, R.-H., Chen, B.-H., and Li, J.-L. (2017). A Comparison of Jiaojia- and Linglong-type Gold deposit Ore-Forming Fluids: Do They Differ? *Ore Geology. Rev.* 88, 511–533. doi:10.1016/j.oregeorev.2016.12.003

Huang, X.-W., Gao, J.-F., Qi, L., Meng, Y.-M., Wang, Y.-C., and Dai, Z.-H. (2016). *In-situ* LA-ICP-MS Trace Elements Analysis of Magnetite: The Fenghuangshan Cu-Fe-Au deposit, Tongling, Eastern China. *Ore Geology. Rev.* 72, 746–759. doi:10.1016/j.oregeorev.2015.09.012

Huang, X.-W., Gao, J.-F., Qi, L., and Zhou, M.-F. (2015). *In-situ* LA-ICP-MS Trace Elemental Analyses of Magnetite and Re-os Dating of Pyrite: The Tianhu Hydrothermally Remobilized Sedimentary Fe deposit, NW China. *Ore Geology. Rev.* 65, 900–916. doi:10.1016/j.oregeorev.2014.07.020

Li, S,X., Liu, C. C., and An, Y. H. (2007). *Geology of Gold Ores in Jiaodong*. Beijing: Geological Publishing House, 27–188.

Li, T. (1976). Earth Abundance of Chemical Elements. *Geochemistry* (3), 167–174.

Li, Y.-J., Li, S.-R., Santosh, M., Liu, S.-A., Zhang, L., Li, W.-T., et al. (2015). Zircon Geochronology, Geochemistry and Stable Isotopes of the Wang'ershan Gold deposit, Jiaodong Peninsula, China. *J. Asian Earth Sci.* 113, 695–710. doi:10.1016/j.jseaes.2015.03.036

Li, Z. L., and Yang, M. Z. (1993). *Geochemistry of Gold Deposits in Jiaodong*. Tianjin: Tianjin Science and Technology Press, 1–300.

Liang, Y. Y., Liu, X. F., and Liu, L. L. (2015). The Micro-geochemical Characteristics of Gold from "Altered Fracture-type" Gold deposit in Jiaodong Peninsula. *Acta Petrologica Sinica* 31 (11), 3441.

Liu, F. X. (2016). *Mineralization Enrichment Regularity and the Genesis Discussion of Xincheng Gold deposit*. China: Laizhou Shandong , Jilin University.

Liu, L. S., Liu, F. L., and Ji, L. (2018). The Polygenetic Meta-Granitic Rocks and Their Geological Significance, within the North Sulu Ultrahigh-Pressure belt. *Acta Petrologica Sinica* 34 (6), 1557–1580.

Liu, Y., Hu, Z., and Gao, S. (2008). *In Situ* Major and Trace Elements of Anhydrous Analysis Minerals LA-ICP-MS without Applying an Internal Standard. *Chem. Geology.* 257 (1-2), 34–43. doi:10.1016/j.chemgeo.2008.08.004

Mao, G., Hua, R., Long, G., and Lu, H. (2013). Rb-Sr Dating of Pyrite and Quartz Fluid Inclusions and Origin of Ore-Forming Materials of the Jinshan Gold Deposit, Northeast Jiangxi Province, South China. *Acta Geologica Sinica - English Edition* 87 (6), 1658–1667. doi:10.1111/1755-6724.12166

Reich, M., Deditius, A., Chryssoulis, S., Li, J.-W., Ma, C.-Q., Parada, M. A., et al. (2013). Pyrite as a Record of Hydrothermal Fluid Evolution in a Porphyry Copper System: A SIMS/EMPA Trace Element Study. *Geochimica et Cosmochimica Acta* 104 (1), 42–62. doi:10.1016/j.gca.2012.11.006

Song, M., Yi, P., Xu, J., Cui, S., Shen, K., Jiang, H., et al. (2012). A Step Metallogenetic Model for Gold Deposits in the Northwestern Shandong Peninsula, China. *Sci. China Earth Sci.* 55, 940–948. doi:10.1007/s11430-012-4366-7

Tan, J., Wei, J., Audétat, A., and Pettke, T. (2012). Source of Metals in the Guocheng Gold deposit, Jiaodong Peninsula, North China Craton: Link to Early Cretaceous Mafic Magmatism Originating from Paleoproterozoic Metasomatized Lithospheric Mantle. *Ore Geology. Rev.* 48 (5), 70–87. doi:10.1016/j.oregeorev.2012.02.008

Tauson, V. L., Babkin, D. N., and Akimov, V. V. (2013). Trace Elements as Indicators of the Physicochemical Conditions of mineral Formation in Hydrothermal Sulfide Systems. *Russ. Geology. Geophys.* (54), 526–543. doi:10.1016/j.rgg.2013.04.005

Wang, F., Lin, J. R., and Hu, Z. H. (2017). Isotopic Characteristics of Metallogenic Fluid and its Genesis in Yunji Uranium deposit of Xiangshan. *World Nucl. Geosci.* 34 (1), 9–13.

Wang, G. Q. (2016). *Mineralization of the Xincheng Gold Deposit, Northwest Jiaodong Peninsula: Multiple Isotope Tracer*. Beijing): China University of Geosciences.

Wang, Q., Deng, J., Liu, X., Zhao, R., and Cai, S. (2016). Provenance of Late Carboniferous bauxite Deposits in the North China Craton: New Constraints on Marginal Arc Construction and Accretion Processes. *Gondwana Res.* 38, 86–98. doi:10.1016/j.gr.2015.10.015

Wang, S. J., Wang, Y. S., and Guo, R. P. (2011). SHRIMP Zircon Dating of Linglong Type (Superunit) Granite in Eastern Shandong Province. *Shandong Land Resour.* 27 (4), 1–7. doi:10.3969/j.issn.1672-6979.2011.04.001

Wen, B.-J., Fan, H.-R., Hu, F.-F., Liu, X., Yang, K.-F., Sun, Z.-F., et al. (2016). Fluid Evolution and Ore Genesis of the Giant Sanshandao Gold deposit, Jiaodong Gold Province, China: Constrains from Geology, Fluid Inclusions and H-O-S-He-Ar Isotopic Compositions. *J. Geochemical Exploration* 171, 96–112. doi:10.1016/j.gexplo.2016.01.007

Winckler, G., Aeschbach-Hertig, W., and Kipfer, R. (2001). Constraints on Origin and Evolution of Red Sea Brines from Helium and Argon Isotopes. *Earth Planet. Sci. Lett.* 184 (3-4), 671–683. doi:10.1016/s0012-821x(00)00345-9

Yang, M., Wang, J. L., and Wang, J. Q. (2012). Helium and Argon Isotopic Tracing of Ore-Forming Fluid from the Wangfeng Gold Deposit in Xinjiang. *Acta Geoscientica Sinica* (5), 794–800. doi:10.3975/cagsb.2012.05.10

Yuan, H., Gao, S., and Liu, X. (2004). Accurate U-Pb Age and Trace Element Determinations of Zircon by Laser Ablation Inductively Coupled Plasma-Mass Spectrometry. *Geostandards Geoanalytical Res.* 28 (3), 357–370. doi:10.1111/j.1751-908x.2004.tb00755.x

Zhang, C., Liu, Y., and Liu, X. D. (2014a). Characteristics of Sulfur Isotope Geochemistry of the Xincheng Gold deposit, Northwest Jiaodong, China. *Acta Petrologica Sinica* 30 (9), 2495–2506.

Zhang, J. (2011). *A Geochemistry Study of Mesozoic Magmatism Rocks in the Sulu Orogeny*. HeFei: University of Science and Technology of China.

Zhang, J. R., Hou, L., and Zhou, Z. C. (2016a). LA-ICP-MS *In Situ* Trace Element Analysis of Auriferous Arsenic Pyrites from the Nibao Gold deposit and its Constraints on the Ore Genesis. *Acta Petrologica et Mineralogica* 35 (3), 493–505. doi:10.1007/s11434-009-0047-0

Zhang, L. C., Zeng, Q. D., and Zhou, W. L. (2001). Deep-seated Geochemistry and Prediction for the Denggezhuang Gold deposit in Jiu Dong. *Geology. Exploration* 37 (1), 27–29. doi:10.3969/j.issn.0495-5331.2001.01.006

Zhang, R. Z., Wang, Z. L., and Wang, S. R. (2016b). Metallogenic Mechanism of Dayingezhuang Gold deposit, Northwestern Jiaodong Peninsula: Geochemistry Constrains from the Gold Bearing Pyrite Typomorph and Sulfur Isotope. *Acta Petrologica Sinica* 32 (8), 2451.

Zhang, W. Y., Wang, C. Z., and Wei, X. C. (2014b). The Implications and Typomorphic Characteristics of Pyrite Chemical Composition in Zijinshan Gold-Copper Deposit. *Adv. Earth Sci.* 29 (8), 974–984. doi:10.11867/j.issn.1001-8166.2014.08.0974

Zhang, X., Li, S. R., and Lu, J. (2012). H-O, He-Ar Isotope Compositions of the Fluid Inclusions for Tracing the Source of Ore-Forming Fluids Jinchiling Gold deposit in Zhaoyuan, Shandong Province. *Bull. Mineralogy, Petrol. Geochem.* 32 (1), 40–47.

Zhao, R. (2016). *Tectonic Evolution and Gold Mineralization in the Jiaodong Peninsula*. Beijing): China University of Geosciences.

Zhou, X. W., Li, S. R., and Lu, L. (2004). Research on the Composition Typomorphism of Pyrite from Longkeng Gold-Silver Mineralization District in Wuyi, Zhejiang Province, China. *Bull. Mineralogy, Petrol. Geochem.* 24 (4), 6–13. doi:10.3969/j.issn.1007-2802.2005.04.006

Zhu, L. M., Zhang, G. W., and Guo, B. (2009). He-Ar Isotopic System of Fluid Inclusions in Pyrite from the Molybdenum Deposits in South Margin of North China Block and its Trace to Metallogenetic and Geodynamic Background. *Chin. Sci Bull* 54, 1725–1735. doi:10.1007/s11434-009-0047-0

Conflict of Interest: The authors declare that the research was conducted in the absence of any commercial or financial relationships that could be construed as a potential conflict of interest.

Publisher's Note: All claims expressed in this article are solely those of the authors and do not necessarily represent those of their affiliated organizations, or those of the publisher, the editors and the reviewers. Any product that may be evaluated in this article, or claim that may be made by its manufacturer, is not guaranteed or endorsed by the publisher.

frontiers | Frontiers in Earth Science

ORIGINAL RESEARCH
published: 09 June 2022
doi: 10.3389/feart.2022.886849

Relationship Between Nb-Ta Enrichments and Highly-Fractionated Granitic Magma Evolution in South China: Geochronological, Zircon Hf Isotopic and Geochemical Evidence From Jianfengling Granite

Chen Ze-Yi[1], *Shao Yong-Jun*[1], *Wei Han-Tao*[2] *and Wang Cheng*[3]*

[1]Key Laboratory of Metallogenic Prediction of Nonferrous Metals and Geological Environment Monitoring, Ministry of Education, School of Geosciences and Info-Physics, Central South University, Changsha, China, [2]MLR Key Laboratory of Metallogeny and Mineral Resource Assessment, Institute of Mineral Resources, Chinese Academy of Geological Sciences, Beijing, China, [3]Guangdong Provincial Key Lab of Geodynamics and Geohazards, School of Earth Sciences and Engineering, Sun Yat-sen University, Guangzhou, China

OPEN ACCESS

Edited by:
Kit Lai,
Fortescue Metals Group, Australia

Reviewed by:
Xiang Fang,
Chinese Academy of Geological Science, China
Shengchao Xue,
China University of Geosciences, China

***Correspondence:**
Wang Cheng
wangcheng6@mail.sysu.edu.cn

Specialty section:
This article was submitted to Economic Geology, a section of the journal Frontiers in Earth Science

Received: *01 March 2022*
Accepted: *16 May 2022*
Published: *09 June 2022*

Citation:
Ze-Yi C, Yong-Jun S, Han-Tao W and Cheng W (2022) Relationship Between Nb-Ta Enrichments and Highly-Fractionated Granitic Magma Evolution in South China: Geochronological, Zircon Hf Isotopic and Geochemical Evidence From Jianfengling Granite. Front. Earth Sci. 10:886849. doi: 10.3389/feart.2022.886849

The Jianfengling granite is an important ore-forming rock unit in the Xianghualing orefield in Nanling region (South China), and its magmatic evolution is vital to understand the regional niobium (Nb)-tantalum (Ta) mineralization. The Jianfengling granite comprises three gradual transitional lithofacies: porphyritic biotite monzogranite (mesophase facies), biotite monzogranite (transition facies) and topaz biotite monzogranite (central facies). All the three biotite monzogranite lithofacies are characterized by being rich in SiO_2 and Al_2O_3, poor in TFe_2O_3, CaO, MgO, TiO_2, MnO and P_2O_5, and are peraluminous high-K calc-alkaline. These rocks are remarkably enriched in Rb, Th, U, Nb and Ta, strongly depleted in Ba and Sr, and slightly depleted in Zr. The LREE/HREE decreases gradually from porphyritic biotite monzogranite, through biotite monzogranite to topaz biotite monzogranite, with increasing convex ("M-type") lanthanide tetrad effect, which similar to the highly-fractionated granite. The high Th-U ($Th_{avg.}$ = 2051.56°ppm; $U_{avg.}$ = 1,498.23°ppm, respectively) and low Th-U ($Th_{avg.}$ = 708.14°ppm; $U_{avg.}$ = 441.57°ppm, respectively) zircon grains from porphyritic biotite monzogranite yielded weighted average $^{206}Pb/^{238}U$ ages of 161.3 ± 1.6 Ma (MSWD = 1.3, *n* = 13) and 158.7 ± 2.0 Ma (MSWD = 1.7, *n* = 13), respectively, consistent with the large-scale magmatic-mineralization event in the Nanling region (ca. 160–150 Ma). The εHf(t) values of the high Th-U (-6.48 to -2.51) and low Th-U (-6.58 to -1.12) zircon grains from the porphyritic biotite monzogranite indicate that the causative magma was formed from partial melting of the Mesoproterozoic Cathaysian basement rocks in a lithospheric extension setting. The Nb and Ta contents increase with fluorine from the porphyritic to topaz biotite monzogranite, indicating that the Nb-Ta enrichment may have caused by the gradual increase of fluxing content (fluorine) during the fractionation of the Jianfengling granitic magma.

Keywords: whole-rock geochemistry, jianfengling, southern hunan, Nb-Ta mineralization, highly-differentiated granite, zircons U-Pb-Hf isotopes

INTRODUCTION

Highly-differentiated granites represent important resource of rare metals, such as Li, Be, Nb, Ta, Rb and Cs, and are also enriched in Sn, Th, Zr, U, Hf and Ga (Černý and Erict, 1985, 1992, 2005, 2012; Simmons and Webber, 2008; Thomas et al., 2011a, 2011b; Kesler et al., 2012; Linnen et al., 2012). This is because rare metals and volatiles are usually enriched in the late-stage differentiated magma (Linnen et al., 2012). In South China (**Figures 1A,B**), the W–Sn–Pb–Zn mineralization in the Nanling region possesses distinct zoning from east to west: the Shizhuyuan and Yaogangxian W deposits (east) → the Furong, Xianghualing and Furong Sn deposits (middle) → the Huangshaping and Baoshan Pb–Zn deposits (west) (**Figure 1C**). The Nanling region is also rich in rare metal resources, including Li, Be, Rb, Ta and Nb in many deposits (e.g., Jianfengling, Laiziling, Xianghualing, Tangguanpu, Changchong and Sanshiliuwan) (**Figure 1D**). The Jianfengling Nb-Ta granite and its genetic link with the Dongshan W-Sn skarn deposit represents an example of

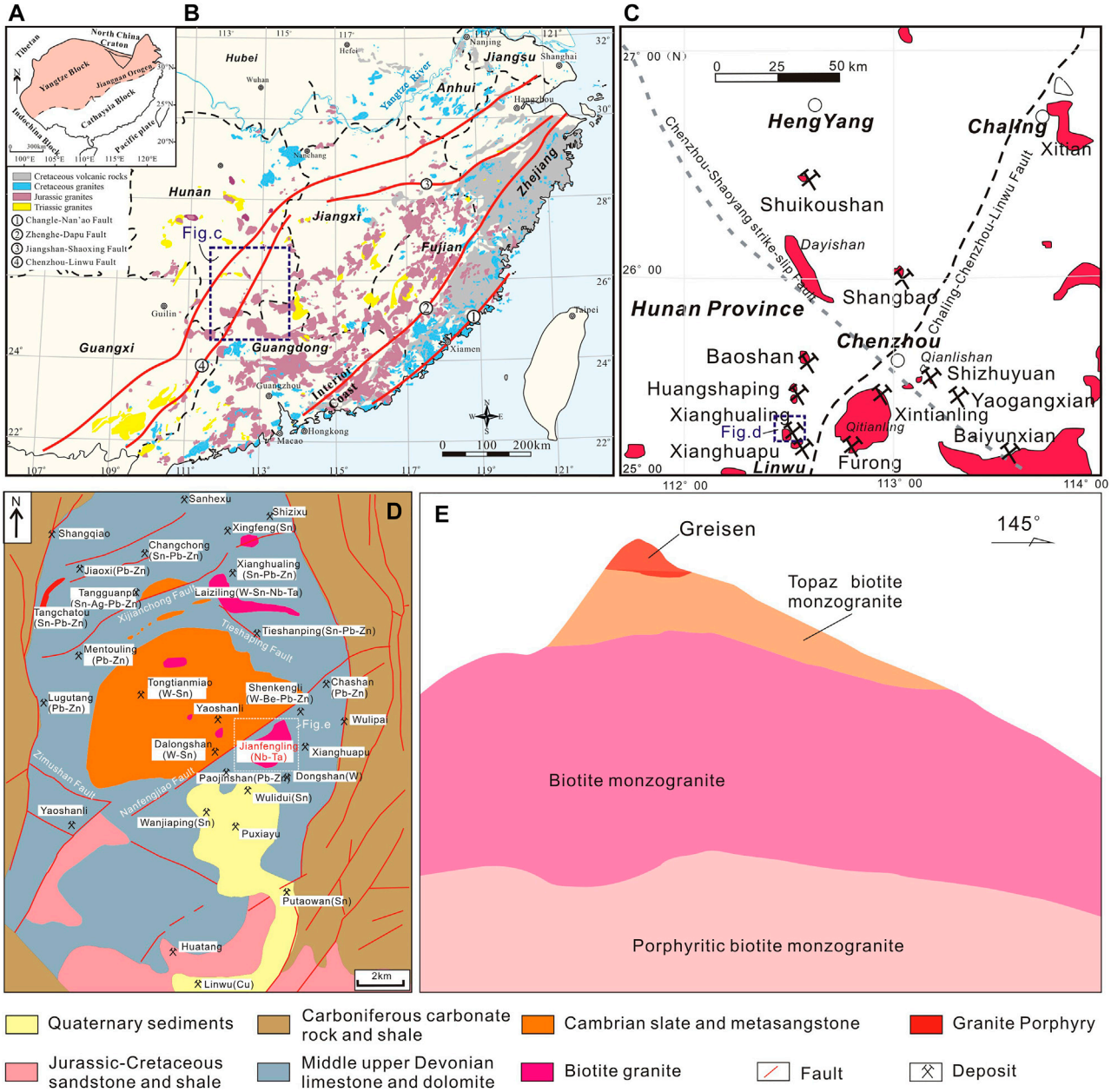

FIGURE 1 | (A,B) Map showing the Jurassic granite distribution in South China (after Wang et al., 2008). **(C)** Jurassic granites and associated W–Sn–Cu–Pb–Zn polymetallic deposits in southern Hunan (after Yao et al., 2007). Simplified geological maps of the **(D)** Xianghualing orefield (after Yang et al., 2013) and **(E)** Jianfengling granitic pluton (after Chen, 2021).

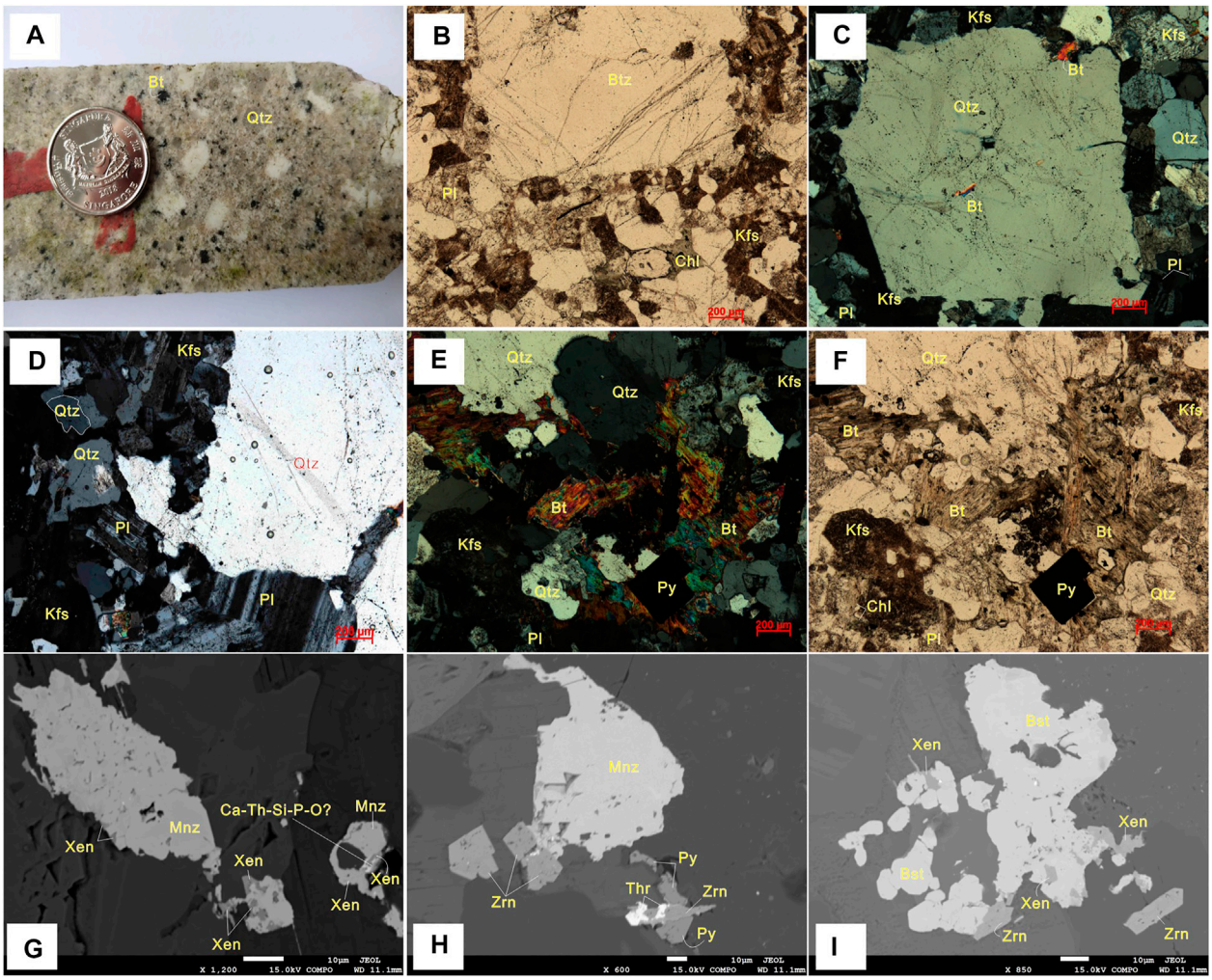

FIGURE 2 | (A) Photograph of the Jianfengling porphyritic biotite monzogranite in the field **(B–F)** Photomicrographs of porphyritic biotite monzogranite; **(G)** Monazite replaced by xenotime; **(H)** Monazite and zircon are co-junction edge structure, and zircon replaced by thorite and late pyrite; **(I)** Bastnasite replaced by xenotime and zircon. Pl, plagioclase; Kfs, K-feldspar; Qtz, quartz; Bt, biotite; Mnz, monazite; Py, pyrite; Zrn, zircon; Bst, bastnasite; Xen, xenotime; Thr, thorite.

the regional W-Sn-rare metal metallogenic system (**Figures 1D,E**; Mo, 1983, Qiu et al., 2003; Chen, 2018; 2021). The Jianfengling granite is highly-differentiated peraluminous high-K calc-alkaline. Many previous studies were focused on the age, magma source and petrogenesis (Qiu and Peng, 1997, 1998, 2002; Lai et al., 2014, 2015; Xuan et al., 2014; Wen et al., 2017; Zhu, 2020). Published zircon U-Pb ages show that the Jianfengling granite was emplaced during ca. 154.4–165.2 Ma (Xuan et al., 2014; Yang et al., 2018; Zhu, 2020). However, it is still unclear why the Jianfengling granite was emplaced over a wide age range. Besides, the K_2O and Na_2O contents of the Jianfengling granites resemble A-type (Xuan et al., 2014; Yang et al., 2018), but the low Zr saturation temperature is inconsistent with typical A-type granite formation (Chen, 2021). Furthermore, how Nb-Ta enrichments was caused by extensive granitic magma fractionation is unclear. To address these issues, we describe the geology of the Jianfengling Nb-Ta rare metal granite, and present new data on its whole-rock geochemistry and *in-situ* zircon U-Pb-Hf isotopes for the different lithofacies of the granite.

REGIONAL GEOLOGY

The Xianghualing orefield is located at the tectonic junction of the EW-trending Nanling metallogenic belt and the NE-trending Qin-Hang belt (**Figure 1B**). Since the Mesozoic, the region has undergone multiple periods of complex tectono-magmatic activities, and developed a series of granitic units and the accompanied W-Sn, Pb-Zn-Cu-Mo, and rare metal (Nb-Ta-Rb) polymetallic deposits

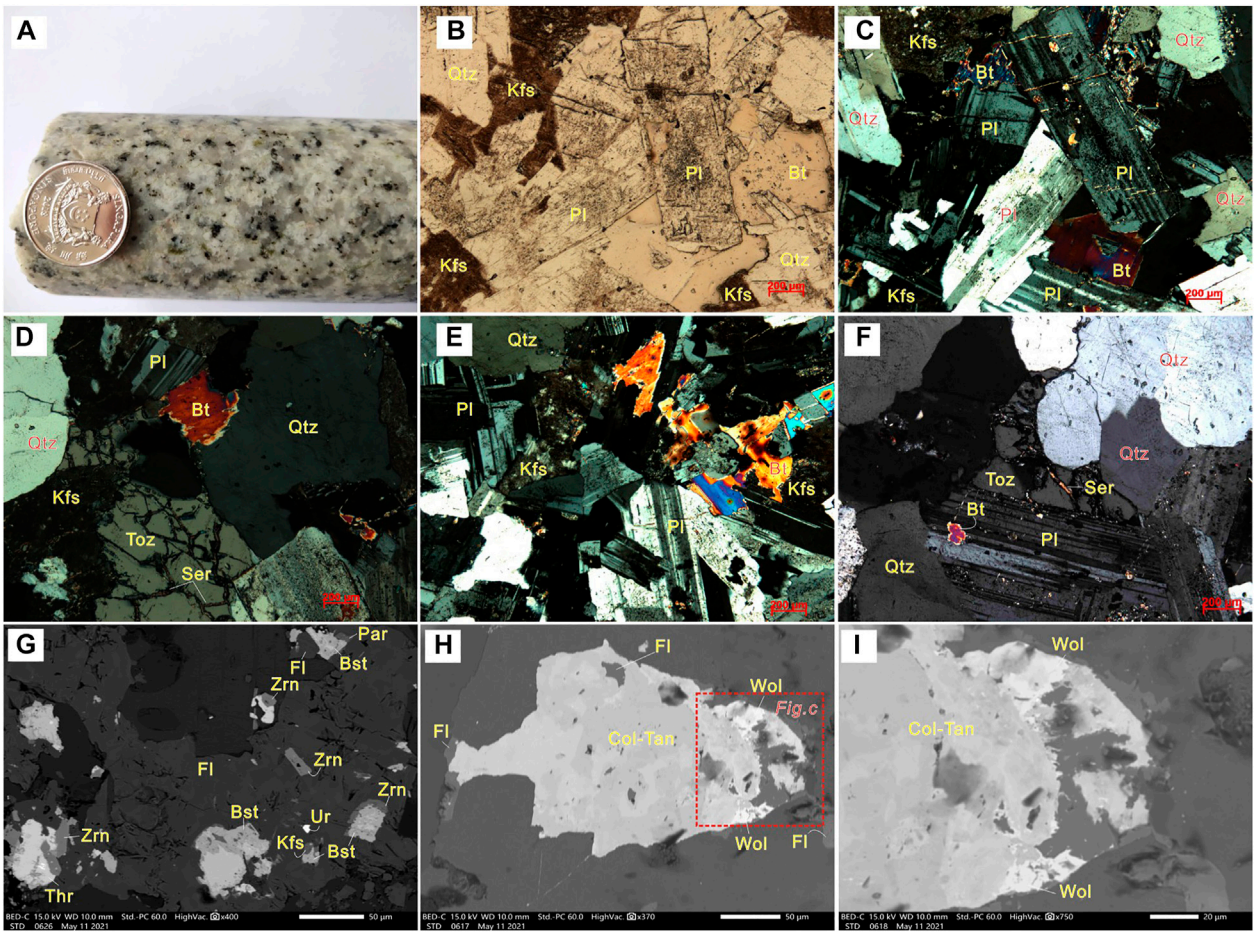

FIGURE 3 | (A) Photograph of the Jianfengling biotite monzogranite in the field **(B–F)** Photomicrographs of biotite monzogranite; **(G)** Zircon, bastnaesite, uraninite, and monazite coexist in fluorite. Bastnaesite replaced monazite, and was then replaced by zircon **(H–I)** Columbite-tantalite replaced by wolframite. Pl, plagioclase; Kfs, K-feldspar; Qtz, quartz; Bt, biotite; Toz, topaz; Mnz, monazite; Py, pyrite; Zrn, zircon; Bst, bastnasite; Xen, xenotime; Thr, thorite; Fl, fluorite; Col-tan, columbite-tantalite; Wol, wolframite.

(**Figure 1C**). The regional structure is dominated by the NS-trending Xianghualing anticline, with NS-trending reverse faults and NNE-trending closed complex linear folds on both limbs. The Tongtianmiao dome is located in the southern part of the anticlinal core. On margin of this dome, there are SW- and SE-trending conjugate tensional and strike-slip faults, NS-trending thrust faults, and NNE-trending thrust. Magmatic rocks and polymetallic mineral occurrences are distributed in/around this dome. The outcropping rocks are composed of the Cambrian to Cretaceous sequences and Quaternary sediments, among which the Devonian Xikuangshan Group and the Upper Devonian Shetianqiao Group are the main ore-host. There are over 180 (15 major) intermediate-felsic plutons in the Xianghualing orefield, covering an outcrop area of about 15 km^2 (X, 1990). Representative plutons include (from north to south) the Tongtianmiao, Yaoshan, Zanziling, Jianfengling, and Qitianling (**Figure 1C**).

JIANFENGLING GRANITE PLUTON

The Jianfengling granite pluton (outcrop area: 4.4 km^2) is located SE of Tongtianmiao anticline in the Xianghualing orefield (**Figures 1D,E**). The pluton has clear vertical/horizontal lithofacies transitional zonation:a) porphyritic biotite monzogranite (mesophase facies), b) biotite monzogranite (transition facies) and c) topaz biotite monzogranite (central facies), combined with 100 m-thick greisenization devolved on top of the Jianfengling granite (**Figure 1E**).

Fresh surface of the porphyritic biotite monzogranite is light fleshy red (**Figure 2**). The rock has massive structure, with feldspar phenocrysts of about 1–10 mm size. The samples contain mainly plagioclase (30%) and alkaline feldspar (25%), quartz (30%) and biotite (10%), as well as accessory zircon, monazite, bastnasite, thorite, xenotime, tantalite, rutile and uraninite. Alteration styles include mainly pyrite, carbonate, fluorite, silicic, argillic, and sericite.

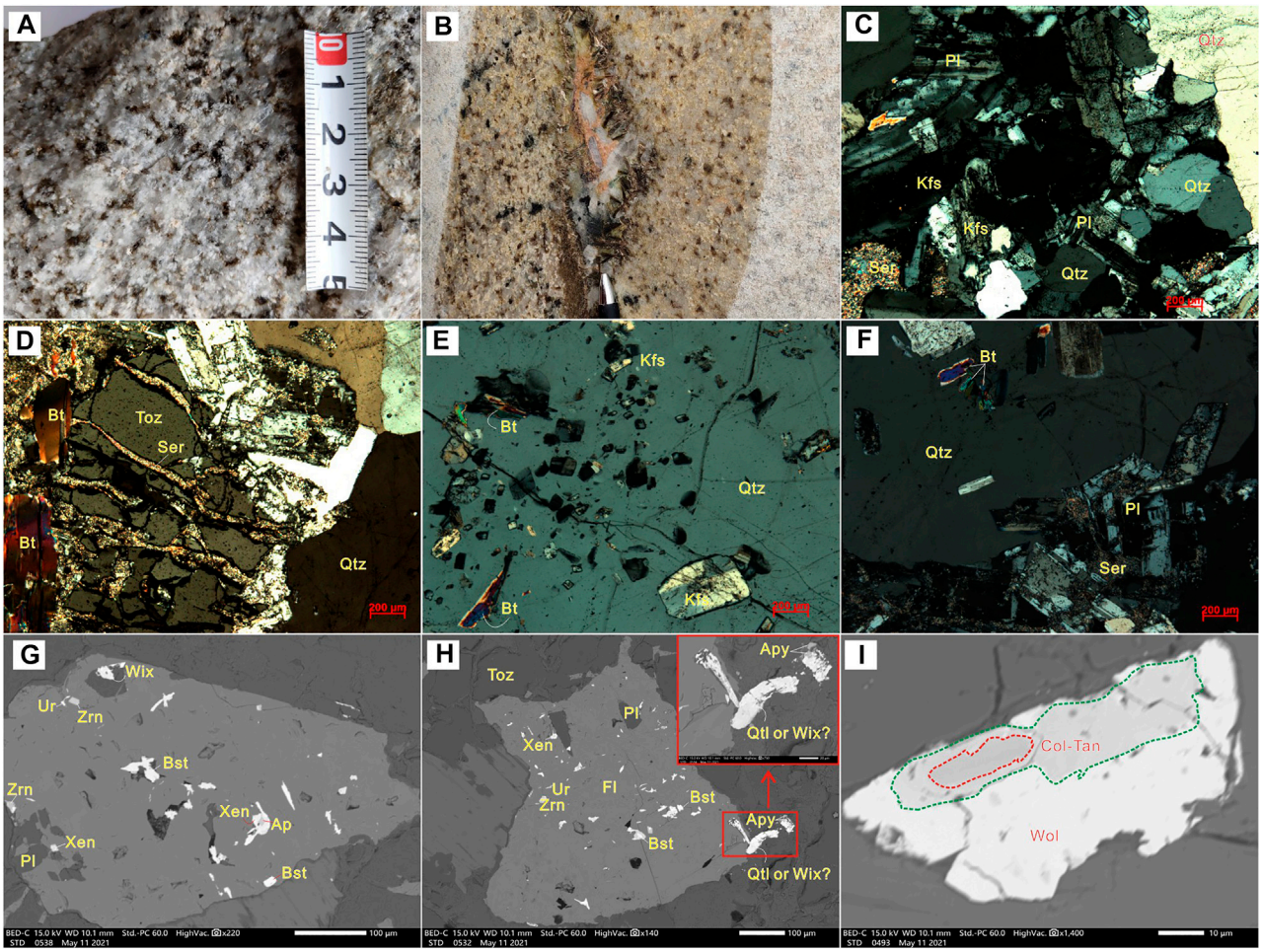

FIGURE 4 | Photographs of **(A)** topaz biotite monzogranite; **(B)** granitic pegmatite in medium-grained biotite monzogranite **(C–F)** Photomicrographs of topaz biotite monzogranite **(G–H)** Zircon, bastnaesite, uraninite, monazite, and arsenopyrite coexist within fluorite; **(I)** Multigenerational zone-banded columbite-tantalite. Pl, plagioclase; Kfs, K-feldspar; Qtz, quartz; Bt, biotite; Toz, topaz; Mnz: monazite; Py, pyrite; Zrn, zircon; Bst, bastnasite; Xen, xenotime; Thr, thorite; Fl, fluorite; Col-tan, columbite-tantalite; Wol, wolframite; Apy, arsenopyrite.

The biotite monzogranite contains mainly alkaline feldspar (25%) and plagioclase (25%), quartz (35%) and biotite (15%) (**Figure 3**). Accessory minerals are similar to its porphyritic counterpart except for the presence of topaz and fluocerite, and their alteration styles are also similar except for the absence of pyritization.

The topaz biotite monzogranite has also massive structure (**Figure 4**). The mineral composition is mainly alkaline feldspar (25%) and plagioclase (25%), quartz (30%), biotite (15%) and topaz (5%). The accessory minerals and alteration styles are both similar to its transition facies counterpart. Compared with the transition facies, the central facies has more and coarser-grained topaz. Granitic pegmatite is developed locally (**Figure 4B**), which contains mainly mica (25%), quartz (40%), K-feldspar (25%), and fluorite (10%).

ANALYTICAL TECHNIQUES

Major and trace elements geochemical analyses were undertaken at the ALS Laboratory (Guangzhou, China). Major oxide concentrations were measured with an X–ray fluorescence (XRF) spectrometer. Fused lithium borate glass disks were used, and the analytical precisions were better than ±0.01%, as estimated based on repeated analyses of the standards GSR–2 and GSR–3. The trace elements concentrations were determined by ICP–MS, using the USGS rock standards of the Columbia River 2 (BCR–2) basalt, Hawaiian Volcanic Observatory 1 (BHVO–1) basalt, and (AGV–1) andesite. The analytical precision and accuracy were better than ±5% for the trace elements studied, and the detailed analytical procedures are as described in Zhou et al. (2014).

Zircon grains were separated using standard heavy liquid and magnetic separation techniques. The selected grains were mounted in epoxy resin, polished, and gold-coated. The zircon internal texture was examined by cathodoluminescence (CL) imaging at the Sun Yat-Sen University (SYSU, Zhuhai). *In-situ* zircon U-Th-Pb dating

TABLE 1 | Whole-rock major and trace element compositions of the Jianfengling pluton.

Sample	45,302-7	45,302-8	45,302-9	45,302-10	45,302-11	45,302-12	45,302-1	45,302-2	45,302-3	45,302-4	45,302-5	45,302-6	45,004-1	45,004-2	45,004-3
	Porphyritic biotite monzogranite								Biotite monzogranite				Topaz biotite monzogranite		
SiO_2	76.67	76.11	76.68	76.08	76.29	75.93	74.56	74.19	75.78	74.78	74.65	75.32	74.77	74.99	75.88
TiO_2	0.063	0.076	0.068	0.07	0.075	0.061	0.041	0.046	0.043	0.048	0.045	0.047	0.028	0.036	0.03
Al_2O_3	12.59	12.7	12.12	12.98	12.49	12.64	13.54	13.89	13.37	13.54	13.83	13.3	13.73	13.5	13.88
TFe_2O_3	0.46	0.68	0.71	0.58	0.77	0.42	1.09	1.2	0.71	1.12	1.01	1.07	0.85	1.02	0.83
FeO	0	0	0	0	0	0	0	0	0	0	0	0	0	0	0
MnO	0.02	0.027	0.026	0.023	0.027	0.02	0.046	0.037	0.04	0.035	0.046	0.033	0.042	0.054	0.044
MgO	0.2	0.21	0.2	0.2	0.2	0.2	0.21	0.24	0.21	0.24	0.22	0.34	0.3	0.27	0.32
CaO	0.84	0.83	0.76	0.85	0.85	0.87	1.22	0.99	0.7	0.69	0.74	0.83	1.28	1.03	1.19
Na_2O	3.41	3.64	3.56	3.77	3.47	3.74	3.46	3.02	3.51	3.15	3.62	2.22	2.91	3.34	3.25
K_2O	4.97	4.52	4.46	4.86	4.68	4.87	4.43	4.83	4.81	4.73	4.38	4.69	3.53	3.48	3.44
P_2O_5	0.032	0.054	0.038	0.034	0.036	0.041	0.033	0.03	0.033	0.039	0.047	0.029	0.029	0.02	0.032
L.O.I	0.56	0.67	0.63	0.72	0.65	0.69	1.04	1.32	0.8	1.13	0.78	1.59	1.81	1.45	0.72
A/CNK	1.37	1.41	1.38	1.37	1.39	1.33	1.49	1.57	1.48	1.58	1.58	1.72	1.78	1.72	1.76
A/NK	1.5	1.56	1.51	1.5	1.53	1.47	1.72	1.77	1.61	1.72	1.73	1.92	2.13	1.98	2.07
Δ	2.09	2.01	1.91	2.25	2	2.25	1.97	1.98	2.11	1.95	2.02	1.48	1.31	1.45	1.36
AR	4.32	4.04	4.3	4.32	4.14	4.51	3.3	3.23	3.89	3.48	3.44	2.91	2.5	2.77	2.6
Rb	845	832	836	883	895	848	1,548	1,504	1,432	1,385	1,309	1,134	741	827	705
Ba	18.3	18.3	11.1	16.7	13.8	12.3	5.61	5.59	12.5	6.22	5.37	5.66	8.71	7.45	9.69
Th	26.7	47.1	38.6	42.1	41.1	31.1	30.6	13.6	33.9	25.7	28.2	11	5.06	6.72	3.4
U	28.1	34.9	36.1	35.9	34.8	33.7	40.7	24.1	40.6	31.5	33.2	22.3	9.46	18	9.2
Ta	8.21	10.8	9.74	9.72	11.6	9.98	15.2	19.5	17.9	19.1	14.8	17.9	15.8	25	20.2
Nb	48.8	62.9	57.1	54.7	65.8	54.7	81.3	80.3	86.2	90.4	74.8	86.3	46.4	75.1	55.6
Sr	12.2	14.1	12	13.6	13.3	12.8	28.9	14.3	25.1	14.9	17.1	15.1	9.58	6.58	8.13
Zr	117	138	146	128	149	117	101	120	117	115	108	110	44.4	83.3	47.4
Hf	6.37	7.79	8.59	7.47	8.39	6.9	7.01	9.09	8.52	7.94	7.49	7.79	3.03	6.87	3.45
F	5,276	4,737	4,937	5,146	5,146	4,856	11,171	9,156	6,253	7,199	8,052	7,110	8,220	7,289	6,936
Li	116	111	139	116	156	109	915	1,028	621	801	668	727	175	334	237
Y	28.9	41.1	40.7	44.2	38.3	31.4	51.4	52	36.6	46.3	38.9	39.5	23.8	26.2	16.9
La	29.5	44.8	34.9	37.7	41.2	28.6	52.7	19.3	42.9	36.4	43.6	15.9	9.13	12.6	6.46
Ce	84.8	122	97.5	102	111	82.3	135	49.1	117	89.6	112	35.8	24.9	35.5	15.8
Pr	6.93	10.7	8.52	9.04	9.96	7.03	13.1	6.42	10.7	9.04	10.6	5.07	2.99	4.28	2.16
Nd	24.2	36.5	30.1	32	34.3	25	44.5	23.8	36.7	31.2	35.8	18.7	10.6	15	7.62
Sm	6.02	8.98	7.83	8.14	8.37	6.36	11.6	7.1	9.23	8.36	9.32	5.48	3.34	4.64	2.47
Eu	0.059	0.077	0.053	0.065	0.07	0.047	0.023	0.018	0.021	0.021	0.017	0.014	0.014	0.012	0.01
Gd	5.63	8.43	7.42	7.64	7.81	6.05	11.6	7.09	9.15	8.17	8.09	5.22	2.95	4.07	2.23
Tb	1.05	1.49	1.38	1.44	1.4	1.14	2.07	1.73	1.69	1.69	1.64	1.31	0.74	0.92	0.59
Dy	6.22	8.58	8.22	8.65	8.13	6.8	12.5	12	10	10.8	9.38	9.15	5.13	6.43	4.35
Ho	1.22	1.64	1.59	1.68	1.56	1.33	2.41	2.48	1.87	2.08	1.78	1.93	1.05	1.37	0.94
Er	3.98	5.27	5.16	5.51	4.98	4.35	8.16	8.45	5.98	6.93	5.85	6.76	3.68	4.9	3.45
Tm	0.59	0.77	0.76	0.82	0.74	0.63	1.26	1.37	0.91	1.1	0.91	1.11	0.64	0.86	0.63
Yb	4.01	5.18	4.95	5.61	4.84	4.29	8.6	9.89	6.08	7.75	6.47	8.12	4.95	6.47	4.8
Lu	0.57	0.73	0.69	0.82	0.7	0.59	1.21	1.47	0.85	1.14	0.95	1.21	0.74	0.98	0.72
ΣREE	642.67	932.6	788.19	840.27	866.24	655.21	1,190.96	746.83	957.35	885.8	944.27	586.9	346.57	469.86	281.59
ΣLREE	439.57	656.4	526.74	558.48	605.38	436.59	773.1	336.96	641.17	531.33	633.28	262.9	160.16	225.54	111.8
ΣHREE	203.09	276.2	261.46	281.78	260.86	218.62	417.86	409.87	316.18	354.47	310.99	324	186.4	244.32	169.79
ΣLREE/ΣHREE	2.16	2.38	2.01	1.98	2.32	2	1.85	0.82	2.03	1.5	2.04	0.81	0.86	0.92	0.66
$(La/Yb)_N$	5.1	6	4.89	4.66	5.9	4.62	4.25	1.35	4.89	3.26	4.67	1.36	1.28	1.35	0.93

(Continued on following page)

TABLE 1 | (*Continued*) Whole-rock major and trace element compositions of the Jianfengling pluton.

Sample	45,302-7	45,302-8	45,302-9	45,302-10	45,302-11	45,302-12	45,302-1	45,302-2	45,302-3	45,302-4	45,302-5	45,302-6	45,004-1	45,004-2	45,004-3
	Porphyritic biotite monzogranite								Biotite monzogranite				Topaz biotite monzogranite		
$(La/Sm)_N$	3.07	3.12	2.79	2.9	3.08	2.81	2.84	1.7	2.91	2.72	2.93	1.81	1.71	1.7	1.64
$(Gd/Yb)_N$	1.4	1.63	1.5	1.36	1.61	1.41	1.35	0.72	1.5	1.05	1.25	0.64	0.6	0.63	0.46
δEu	0.031	0.027	0.021	0.025	0.026	0.023	0.006	0.008	0.007	0.008	0.006	0.008	0.014	0.008	0.013
δCe	1.42	1.34	1.36	1.33	1.31	1.39	1.23	1.06	1.31	1.18	1.25	0.96	1.14	1.16	1.01
$TE_{1,3}$	1.32	1.28	1.29	1.28	1.27	1.31	1.23	1.28	1.30	1.27	1.32	1.22	1.37	1.31	1.29

The lanthanide tetrad effect manifests as a split of the chondrite-normalized REE, patterns into four segments called tetrads (first tetrad La-Ce-Pr-Nd; second tetrad (Pm)-Sm-Eu-Gd; third tetrad, Gd-Tb-Dy-Ho; fourth tetrad, Er-Tm-Yb-Lu) (e.g., fidelis and siekierski, 1966; Peppard et al., 1969). The amount of the lanthanide tetrad effect (e.g., $TE_{1,3}$) in the Jianfengling granite samples was calculated with the method described by Irber (1999).

was undertaken using an iCAP-RQ-ICP-MS coupled with an ArF-193 nm GeolasHD laser-ablation system at the SYSU. A 32 μm spot size with 5 Hz laser repetition rate was used for the ablation. Zircons Plešovice (337 ± 0.4 Ma) and 91,500 (1,065 ± 5 Ma) were used as the external standards and ^{29}Si as the internal standard. Helium carrier gas was used to enhance the transport efficiency of the ablated material. Off-line raw data were processed with the GLITTER program, and the isotopic apparent and weighted mean ages were calculated with the Isoplot program (Ludwig, 2001). Zircon dates with <10% calculated discordance are considered to be valid, and $^{207}Pb/^{206}Pb$ and $^{206}Pb/^{238}U$ apparent ages were used for the older (>1 Ga) and younger (<1 Ga) zircon grains, respectively. Details of the zircon Hf isotope analytical procedures follow those given by Li et al. (2010). The 91,500 standard zircon was used for external standardization, and the resulting data were normalized to $^{176}Hf/^{177}Hf = 0.7325$. The εHf(t) values were calculated using the present-day chondrite values of $^{176}Hf/^{177}Hf = 0.282,772$ and $^{176}Lu/^{177}Hf = 0.0332$ (Blichert-Toft et al., 1997). The Hf model ages (T_{DM1}) were calculated relative to the depleted mantle, using $^{176}Hf/^{177}Hf = 0.283,250$ and $^{176}Lu/^{177}Hf = 0.0384$; whilst the two-stage Hf model ages (T_{DM2}) were calculated with the mean continental crust value of $^{176}Lu/^{177}Hf = 0.015$ (Griffin et al., 2000).

RESULTS

Whole–Rock Geochemistry

The major- and trace-element compositions of the Jianfengling granite are given in **Table 1**. Porphyritic biotite monzogranite, biotite monzogranite, and topaz biotite monzogranite have similarly high SiO_2 and Al_2O_3, but low MgO, CaO, Na_2O and K_2O contents. The samples are classified as sub-alkalic monzogranite in the QAP and SiO_2 vs ($K_2O + Na_2O$) plots (**Figures 5A,B**). The A/CNK values are above 1 (increase from porphyritic to topaz-rich lithofacies), suggesting that the rocks are peraluminous (**Figure 5C**). In addition, the rocks are K_2O-rich and fall into the high-K calc-alkaline field (**Figure 5D**).

Samples from all the three lithofacies have similar chondrite-normalized rare earth element (REE) patterns (**Figure 6A**). Porphyritic and biotite monzogranite have similar total REE content, which is higher than that of the topaz biotite monzogranite (**Table 1**). The LREE/HREE ratio decreases from the porphyritic to topaz-rich lithofacies, whereas the convex lanthanide tetrad effect ($TE_{1,3}$) increase (**Table 1** note). When normalized to primitive mantle, all the biotite monzogranite samples are enriched in Rb, Th, U, Nb, and Ta, strongly depleted in Ba and Sr, and slightly depleted in Zr (**Figure 6B**).

Zircon Trace Element Compositions and U–Pb Geochronology

From the zircon CL images, zircon grains from the porphyritic biotite granite are idiomorphic columnar (ca. 30–200 μm), with the development of oscillatory zoning (**Figures 7A–D**). Zircon grains

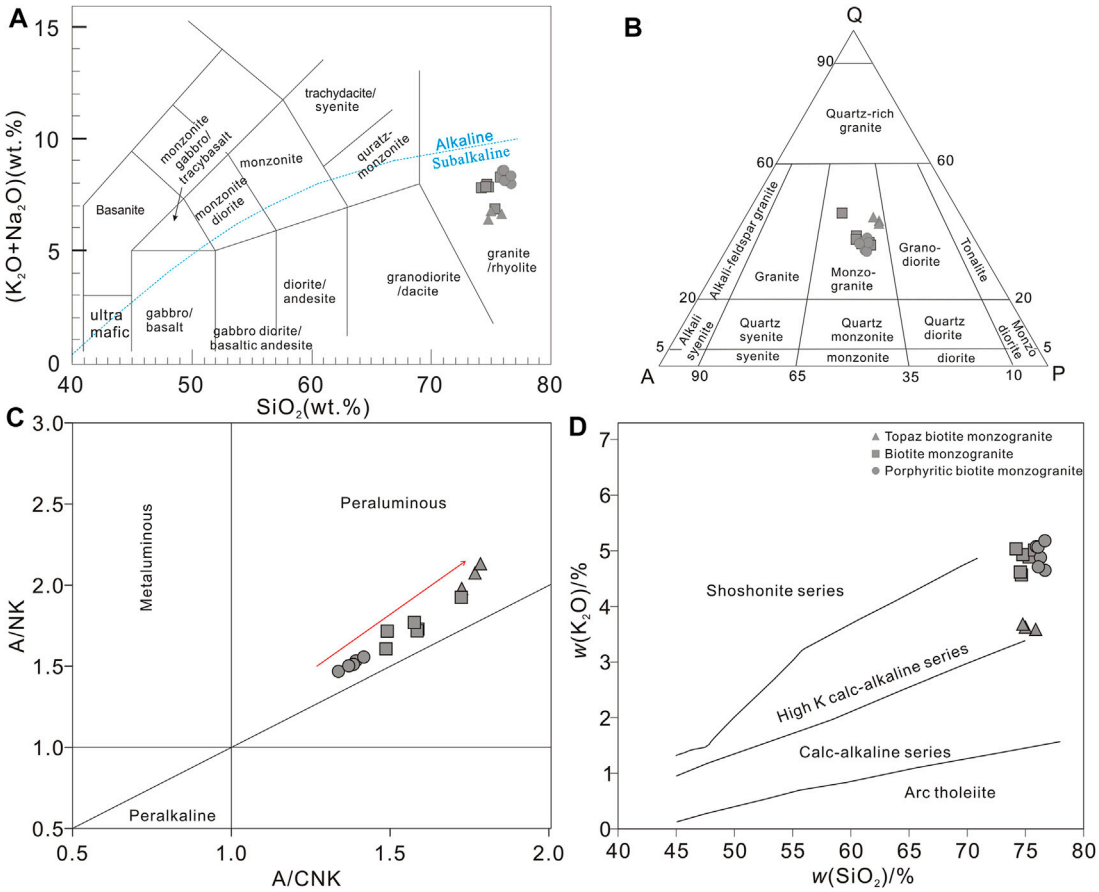

FIGURE 5 | Geochemical discrimination diagrams for the Jianfengling granitic rocks: **(A)** SiO_2 vs. (K_2O + Na_2O) (after Le Maitre, 1989); **(B)** QAP (after Streckeisen and Le Maitre, 1979); **(C)** A/KNC vs A/NK, where A/KNC = molar $Al_2O_3/(K_2O + Na_2O + CaO)$, A/NK = molar $Al_2O_3/(Na_2O + K_2O)$ (after Frost et al., 2001); **(D)** SiO_2 vs K_2O (after Le Maitre, 2002).

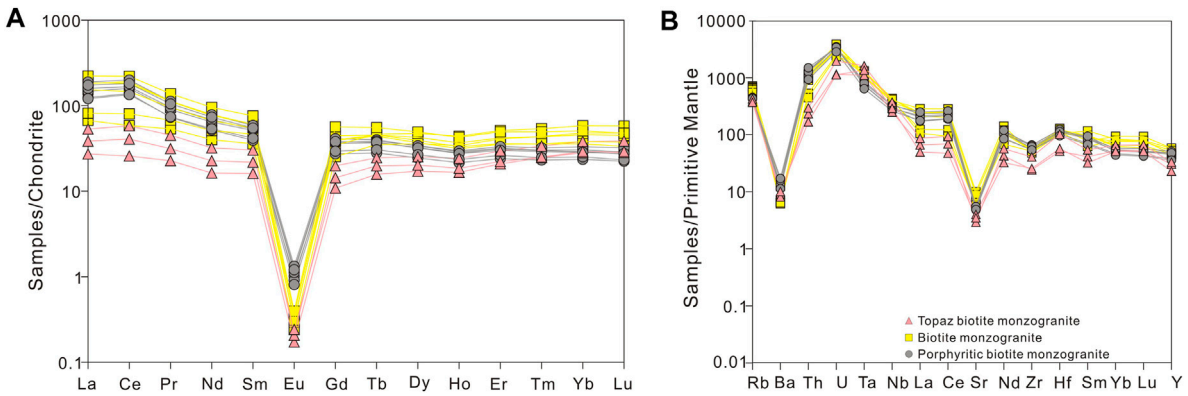

FIGURE 6 | (A) Chondrite-normalized REE patterns and **(B)** primitive mantle-normalized trace element for the Jianfengling pluton. Primitive-mantle and chondrite normalizing values are from Sun and McDonough (1989) and Taylor and McLennan (1985), respectively.

can be divided into two types, those with high CL reflectance (bright, low Th-U; **Figures 7A,B**) and low CL reflectance (dark, high Th-U; **Figures 7C,D**). Furthermore, there are irregular areas with subtle heterogeneous BSE reflectance in the grain margin of zircon from porphyritic biotite granite. Besides, thorite and pores are well-developed in these areas with heterogeneous BSE reflectance

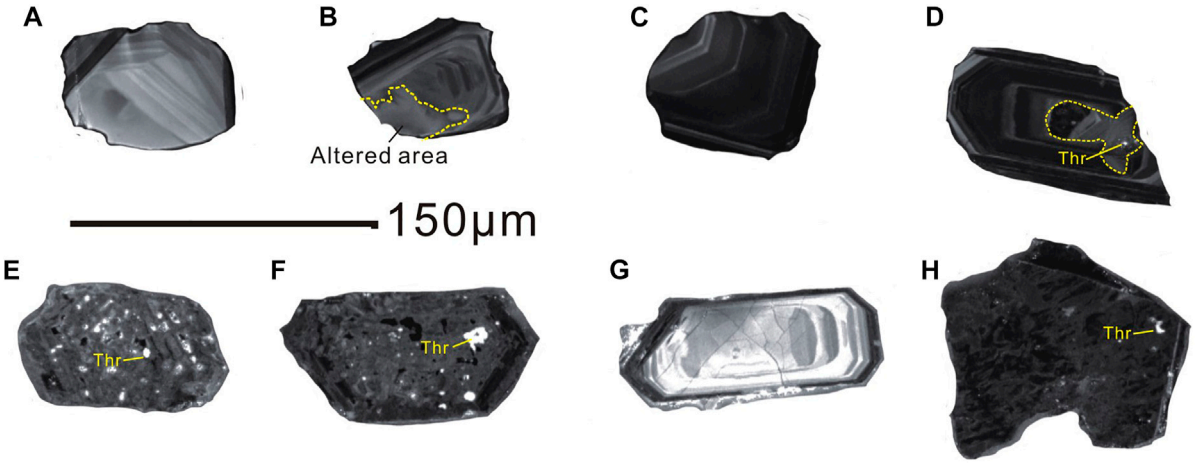

FIGURE 7 | Zircon CL images of the Jianfengling granite **(A–D)** porphyritic biotite monzogranite. Alteration is extensive on the zircon grain margin **(E,F)** medium-fine-grained biotite monzogranite **(G,H)** medium-grained biotite monzogranite. Thr, thorite.

(**Figures 7B,D**). This reflects that zircon grains were substantially fluid-modified through dissolution-reprecipitation (Putnis, 2009). In contrast, metamictization is generally developed in zircon grains from the medium-fine-grained (**Figures 7E,F**) and medium-grained (**Figures 7G,H**) lithofacies. The high Th-U zircons have Th = 454.74–4,085.56 ppm (avg. 2051.56 ppm) (**Table 2**), U = 428.76–7,404.61 ppm (avg. 2,289.82 ppm), and Th/U = 0.8–2.6 (avg. 1.50). The low Th-U zircons have Th = 279.19–1,419.34 ppm (avg. 708.14 ppm), U = 199.04–986.36 ppm (avg. 441.57 ppm), and Th/U = 1.3–2.2 (avg. 1.61). The Th and U contents and Th/U ratio in magmatic zircons are higher (Th/U > 0.5; Hoskin and Black, 2000; Belousova et al., 2002) than those of metamorphic zircons (Th/U < 0.1; Hoskin and Schaltegger, 2003). The high Th/U ratio of both types of zircons from the porphyritic lithofacies indicates a magmatic origin. In addition, chondrite-normalized REE patterns of the two types of zircons are similar to those of typical magmatic origin (**Figure 8A**). Based on the Ti-in-zircon thermometer on the porphyritic lithofacies (**Table 2**), the formation temperatures of primary magmatic- and altered high Th-U zircons are of 619–711°C (avg. 682°C) and 687–811°C (avg. 764°C) (**Figure 8B**), respectively, with the corresponding oxygen fugacity (ΔFMQ) of 0.71–7.47 (avg. 4.70) and from -12.79 to -0.27 (avg. −8.21°C) (**Figure 8C**; **Table 2**). The magmatic- and altered low Th-U zircons were estimated to have formed at 689–756°C (avg. 731°C) and 735–764°C (avg. 747°C), respectively, with their corresponding oxygen fugacity (ΔFMQ) of 1.96–6.92 (avg. 4.62) and -8.50 to -6.58°C (avg. -7.63). Thirteen high Th-U zircons yielded $^{206}Pb/^{238}U$ dates of 156.6 ± 2.4 Ma to 166.6 ± 2.3 Ma, with a weighted average of 161.3 ± 1.6 Ma (n = 13; MSWD = 1.3) (**Figure 8D**; **Table 2**). Thirteen low Th-U zircons yielded $^{206}Pb/^{238}U$ dates of 154.7 ± 2.4 Ma to 164.4 ± 2.9 Ma, with a weighted average of 158.7 ± 2.0 Ma (n = 13; MSWD = 1.7) (**Figure 8E**; **Table 2**).

Zircon Hf Isotope Compositions

The zircon Hf isotope composition data from the Jianfengling porphyritic biotite monzogranite are given in **Table 3**. The εHf(t) values of the high Th-U and low Th-U zircons are largely similar (within error), i.e., high Th-U zircon: εHf(t) = -6.48 to -2.51 (avg. -4.55), corresponding to the second-stage model age (T_{DM2}) of 1364–1613 Ma (avg. 1,492 Ma); Th-U zircon: εHf(t) = -6.58 to -1.12 (avg. -4.32), corresponding to T_{DM2} = 1,276–1,620 Ma (avg. 1,478 Ma).

DISCUSSION

Timing of Jianfengling Granite Emplacement

For the more reliable zircon U-Pb dating technique, the biotite monzogranite yielded U-Pb ages of 154.4–165.2 Ma (Xuan et al., 2014; Yang et al., 2018; Zhu, 2020). However, zircons from the biotite monzogranite are clearly metamict (**Figures 7E–H**), probably leading to the varying U-Pb dates. Zircons from the porphyritic biotite monzogranite have well-developed oscillatory zoning (**Figures 7A–D**), and fall into the dark high Th-U and light low Th-U zircon groups. Similar mineral composition (**Figures 2**–**4**) and whole–rock geochemistry (**Figures 5**, **6**) shows that the three lithofacies are products of the same magmatic evolution system, and thus the crystallization age of porphyritic biotite monzogranite (mesophase facies) can effectively represent the initial emplacement age of the Jianfengling pluton. The weighted average U-Pb age of the high Th-U zircons (161.3 ± 1.6 Ma) is consistent with that of the low Th-U zircons (158.7 ± 2.0 Ma) within error. The timing of the Jianfengling rare-metal granite emplacement is coeval with that of the Middle-Late Jurassic magmatic-metallogenic event across the Nanling region (160–150 Ma; Mao et al., 2004a, b; 2007; Li et al., 2004; Peng et al., 2006; Yuan et al., 2007; 2008; 2011; 2012a, b).

Magma Source

Zircon Hf isotopic compositions are considered to be stable during magma differentiation and hydrothermal alteration

TABLE 2 | Results of LA-ICPMS zircon U–Pb analyses for the porphyritic biotite granite from the Jianfengling pluton.

Sample	—	Th (ppm)	U (ppm)	Th/U	$^{207}Pb/^{206}Pb$	1sigma	$^{207}Pb/^{235}U$	1sigma	$^{206}Pb/^{238}U$	1sigma	$^{208}Pb/^{232}Th$	1sigma	$^{206}Pb/^{238}U$	1sigma
					Ratios		Ratios		Ratios		Ratios		age(Ma)	
302-7–25	High Th-U	2,195	1,002	2.19	0.0486	0.0014	0.1682	0.0049	0.0251	0.0004	0.0082	0.0002	160.0	2.3
302-7–32		869	505	1.72	0.0468	0.0017	0.1655	0.0060	0.0257	0.0004	0.0084	0.0002	163.4	2.5
302-7–36		1964	1907	1.03	0.0504	0.0014	0.1764	0.0050	0.0254	0.0004	0.0082	0.0002	161.6	2.4
302-7–37		1883	958	1.97	0.0478	0.0015	0.1656	0.0053	0.0251	0.0004	0.0075	0.0002	160.0	2.4
302-7–41		4,086	2,746	1.49	0.0491	0.0014	0.1664	0.0050	0.0246	0.0004	0.0076	0.0002	156.6	2.4
302-7–43		931	634	1.47	0.0495	0.0018	0.1691	0.0062	0.0248	0.0004	0.0083	0.0002	157.8	2.5
302-7–7		2,453	1,461	1.68	0.0471	0.0011	0.1699	0.0041	0.0262	0.0004	0.0083	0.0001	166.6	2.3
302-7–10		3,703	2,517	1.47	0.0478	0.0010	0.1685	0.0038	0.0256	0.0004	0.0082	0.0001	162.8	2.2
302-7–14		1893	1,452	1.30	0.0484	0.0012	0.1722	0.0043	0.0258	0.0004	0.0084	0.0002	164.4	2.3
302-7–23		1901	1,424	1.34	0.0503	0.0013	0.1743	0.0046	0.0252	0.0004	0.0083	0.0002	160.1	2.3
302-7–39		1,421	1,075	1.32	0.0485	0.0015	0.1692	0.0053	0.0253	0.0004	0.0082	0.0002	161.3	2.4
302-7–44		2,918	3,526	0.83	0.0882	0.0025	0.3072	0.0090	0.0253	0.0004	0.0251	0.0006	160.9	2.5
302-7–19		455	269	1.69	0.0577	0.0023	0.1990	0.0078	0.0251	0.0004	0.0091	0.0002	159.5	2.5
302-7–11	Low Th-U	1,419	986	1.44	0.0488	0.0013	0.1631	0.0044	0.0243	0.0003	0.0081	0.0002	154.6	2.2
302-7–17		389	254	1.53	0.0526	0.0023	0.1792	0.0076	0.0247	0.0004	0.0084	0.0002	157.4	2.5
302-7–18		480	276	1.74	0.0531	0.0022	0.1839	0.0075	0.0251	0.0004	0.0083	0.0002	160.0	2.5
302-7–20		646	377	1.72	0.0507	0.0019	0.1770	0.0065	0.0254	0.0004	0.0083	0.0002	161.5	2.5
302-7–21		865	533	1.62	0.0487	0.0016	0.1687	0.0057	0.0252	0.0004	0.0083	0.0002	160.2	2.4
302-7–24		696	399	1.74	0.0498	0.0018	0.1760	0.0065	0.0257	0.0004	0.0086	0.0002	163.4	2.5
302-7–26		531	303	1.75	0.0456	0.0019	0.1589	0.0067	0.0253	0.0004	0.0082	0.0002	161.1	2.6
302-7–29		414	270	1.53	0.0515	0.0022	0.1723	0.0075	0.0243	0.0004	0.0080	0.0002	154.6	2.5
302-7–30		878	538	1.63	0.0487	0.0017	0.1656	0.0058	0.0247	0.0004	0.0083	0.0002	157.1	2.4
302-7–31		854	512	1.67	0.0476	0.0017	0.1594	0.0058	0.0243	0.0004	0.0084	0.0002	154.7	2.4
302-7–34		595	444	1.34	0.0506	0.0019	0.1753	0.0066	0.0251	0.0004	0.0086	0.0002	159.9	2.5
302-7–40		279	199	1.40	0.0526	0.0026	0.1871	0.0093	0.0258	0.0005	0.0102	0.0003	164.4	2.9
302-7–46		1,159	649	1.79	0.0496	0.0018	0.1685	0.0063	0.0247	0.0004	0.0080	0.0002	157.1	2.5

process, and can therefore be used to reveal the origin of the magma (Kemp et al., 2007; Lenting et al., 2010). The high Th-U and low Th-U zircon grains from the Jianfengling porphyritic biotite monzogranite have similar $(^{176}Hf/^{177}Hf)_i$ (0.28249–0.28260 and 0.28249 to 0.28264, respectively) and $\varepsilon Hf(t)_{160Ma}$ values (-6.48 to -2.51 and -6.58 to -1.12, respectively) (**Table 3**), which close to the region of lower crustal evolution line (**Figure 9**). The zircon T_{DM2} ages are close to the ages (1,500 Ma) of the Proterozoic meta-sedimentary strata. This inference is further supported by the presence of Proterozoic metamorphic zircons in the granites, which represent residual zircons from the partial melting source

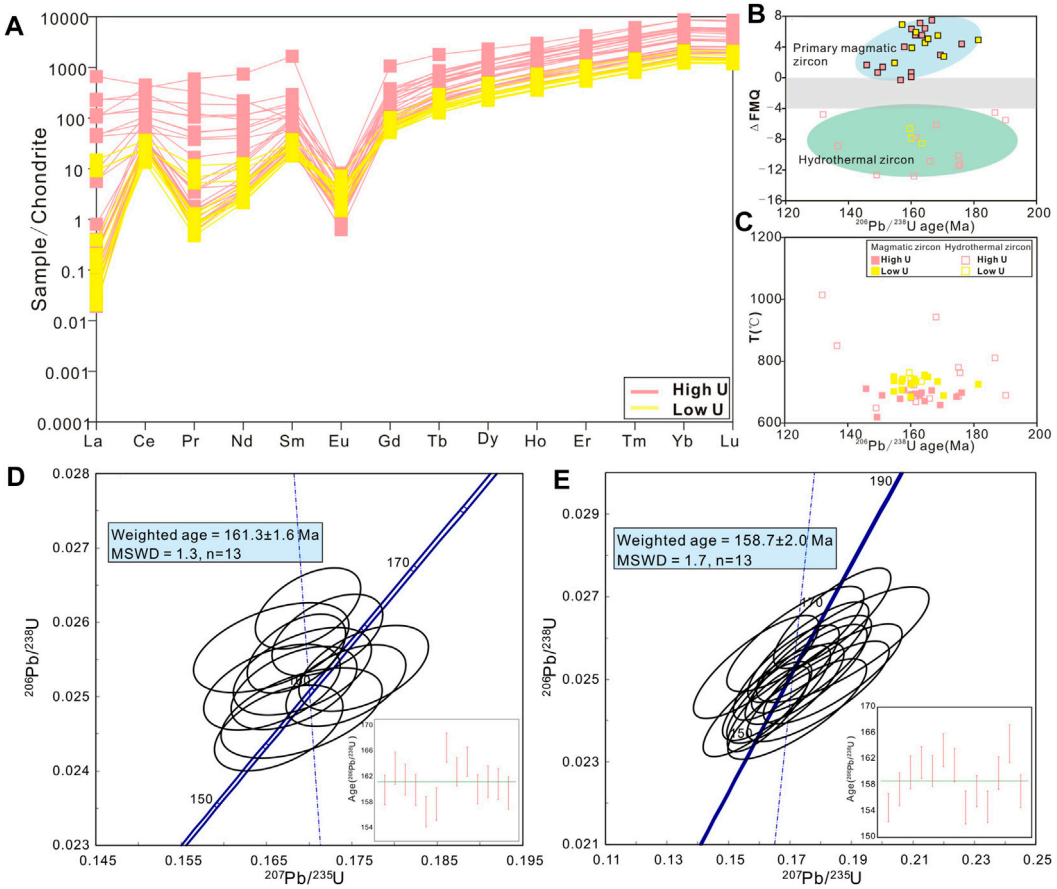

FIGURE 8 | (A) Chondrite-normalized REE patterns of different zircon groups in the Jianfengling porphyritic biotite monzogranite. Chondrite-normalized values from Taylor and McLennan (1985); **(B)** ΔFMQ vs $^{206}Pb/^{238}U$ age. Zircon oxygen fugacity was calculated from the method by Ballard et al. (2002); **(C)** Ti-in-zircon temperature vs $^{206}Pb/^{238}U$ age. The temperature was obtained with the method by Ferry and Watson (2007) **(D,E)** U–Pb concordant plots of different zircon groups in the porphyritic biotite monzogranite.

region (Li et al., 2018). Therefore, it is likely that parental magma of the Jiangfengling granite was derived from partial melting of the lower crust Proterozoic meta-sedimentary strata in South China.

Compared with the transition facies and central facies, the porphyritic lithofacies is the least fractionated (**Section 6.3**), and thus its geochemical composition is closer to the initial magma composition. The CaO/Na_2O ratio is an important index to distinguish the magma source region (Chappell and White, 1992). The CaO/Na_2O < 0.3 for the peraluminous granite formed from argillaceous rock, the CaO/Na_2O > 0.3 for the granitoid formed from psammite. The CaO/Na_2O ratio of the Jianfengling porphyritic biotite monzogranite varies in the range of 0.21–0.25, indicating that the magma was derived from the pelite rocks, such as leucogranite in Himalaya Orogen (Harris and Inger, 1992; Altherret al., 2000). In the $(CaO)/(FeO_t + MgO + TiO_2)$ vs $(CaO + FeO_t + MgO + TiO_2)$ (**Figure 10A**) and $Na_2O + K_2O + FeO_t + MgO + TiO_2$–$(Na_2O + K_2O)/(FeO_t + MgO + TiO_2)$ (**Figure 10B**), Rb/Ba–Rb/Sr (**Figure 10C**), and the Al_2O_3/TiO_2–CaO/Na_2O (**Figure 10D**) plots, the sample data points also fall into the pelite range of the clay-rich source region, indicating that the granitic magma was mainly derived from the partial melting of the meta-pelite of the crust.

Granite Petrogenesis

During the magmatic evolution, the incompatible LILEs and HFSEs would be significantly enriched in highly-fractionated magmas (Deering and Bachmann, 2010; Dostal et al., 2015; Ballouard et al., 2016). The increasing Nb, Ta, Li and Rb contents with decreasing Zr (**Figure 11**) from porphyritic biotite granite to biotite monzogranite, suggesting progressive magma fractionation (Gelman et al., 2014; Lee and Morton, 2015). However, the Nb, Li and Rb contents of the most-evolved topaz biotite monzogranite are very low, which may have been caused by the fractionation of Nb-, Li- and Rb-rich minerals, such as columbite-tantalite, lepidolite and Rb-rich biotite (**Figures 2–4**, Zhu, 2020; Chen, 2021). In the binary plots of Zr versus Zr/Hf, Nb/Ta and Y/Ho (**Figure 11**), the negative correlations from porphyritic biotite granite to topaz biotite monzogranite indicate increasing magma fractionation (Pérez-Soba and Villaseca, 2010; Ballouard et al., 2016). For

TABLE 3 | Zircon Lu-Hf results of the porphyritic biotite granite from the Jianfengling pluton.

Sample	—	$^{176}Lu/^{177}Hf_0$	$^{176}Hf/^{177}Hf_0$	$^{176}Hf/^{177}Hf_i$	εHf(t)	T_{DM} (Ma)	T_{2DM} (Ma)
302-7–1	High Th-U	0.001006	0.282,493	0.282,490	-6.47	1,074	1,613
302-7–6		0.001712	0.282,531	0.282,526	-5.20	1,040	1,533
302-7–8		0.001618	0.282,552	0.282,547	-4.44	1,007	1,485
302-7–25		0.000989	0.282,549	0.282,547	-4.46	994	1,487
302-7–33		0.000972	0.282,492	0.282,490	-6.48	1,073	1,613
302-7–37		0.001181	0.282,513	0.282,510	-5.76	1,050	1,568
302-7–7		0.001033	0.282,596	0.282,593	-2.82	929	1,383
302-7–10		0.001367	0.282,573	0.282,569	-3.67	970	1,437
302-7–12		0.001196	0.282,532	0.282,528	-5.12	1,024	1,528
302-7–14		0.000829	0.282,594	0.282,592	-2.86	927	1,386
302-7–23		0.000809	0.282,604	0.282,602	-2.51	913	1,364
302-7–39		0.000811	0.282,559	0.282,557	-4.09	975	1,463
302-7–44		0.001194	0.282,528	0.282,524	-5.25	1,030	1,536
302-7–5	Low Th-U	0.000767	0.282,541	0.282,539	-4.73	999	1,504
302-7–11		0.000964	0.282,515	0.282,512	-5.68	1,041	1,563
302-7–17		0.000619	0.282,540	0.282,538	-4.75	997	1,505
302-7–18		0.000588	0.282,598	0.282,596	-2.70	915	1,375
302-7–20		0.000618	0.282,551	0.282,549	-4.37	982	1,481
302-7–21		0.000559	0.282,520	0.282,518	-5.46	1,024	1,550
302-7–24		0.000629	0.282,599	0.282,597	-2.69	916	1,375
302-7–26		0.000569	0.282,643	0.282,641	-1.12	853	1,276
302-7–28		0.000527	0.282,573	0.282,571	-3.60	950	1,432
302-7–29		0.000515	0.282,535	0.282,534	-4.91	1,001	1,515
302-7–30		0.000676	0.282,570	0.282,568	-3.71	957	1,439
302-7–31		0.000593	0.282,503	0.282,501	-6.08	1,049	1,588
302-7–34		0.000503	0.282,488	0.282,487	-6.58	1,066	1,620
302-7–40		0.000638	0.282,597	0.282,595	-2.73	918	1,378
302-7–46		0.000624	0.282,513	0.282,511	-5.73	1,035	1,566

T = 160 Ma.

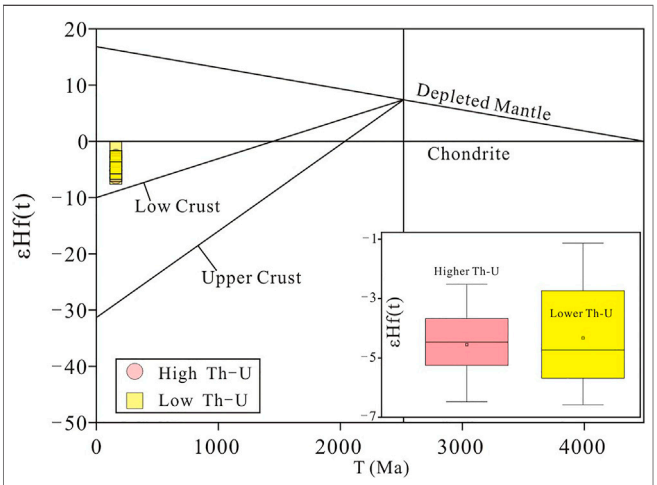

FIGURE 9 | Age vs εHf(t) plots for the Jianfengling granite samples.

granitic magma, Zr/Hf = 26 and Nb/Ta = 5 are proposed to be the boundaries between magmatic to magmatic-hydrothermal states (Bau, 1996; Ballouard et al., 2016). Except for the porphyritic biotite monzogranite, the Nb/Ta ratios of the other two lithofacies (i.e., biotite monzogranite and topaz biotite monzogranite) are all below 5, also indicating that they have experienced strong fractionation (**Figure 11**). During the fractionation of granitic magma, the total REE contents and LREE/HREE ratio would decrease significantly (Gelman et al., 2014). With the increasing Zr content, the total REE and LREE/HREE gradually decrease and the tetrad effects ($TE_{1,3}$) increase significantly (**Figure 12**).

As shown in (Zr + Ce + Y + Nb)-[(Ga/Al) ×10,000] and Zr-[(Ga/Al)×10^4] plots (**Figure 13**; Whalen et al., 1987), the porphyritic biotite monzogranite data points fall into the boundary of highly-fractionated I-, S- and A-type granites, while the biotite monzogranites and the topaz biotite monzogranites fall into the A-type granite field. However, the Zr content of the porphyritic biotite monzogranite (117–149 ppm, avg. 133 ppm), which is much lower than that of typical A-type granite (Zr ≈ 250 ppm). The (Zr + Nb + Y + Ce) content (279.5–364.1 ppm, avg. 327.2 ppm) is also below the minimum value of A-type granite (ca. 350 ppm) (Whalen et al., 1987). In addition, the temperature (from zircon Ti thermometer) for the porphyritic biotite monzogranite (619–811°C) is inconsistent with the high formation temperature of A-type granites. Although the (Ga/Al)×10,000 ratio of the porphyritic biotite monzogranite (2.52–2.72, avg. 2.64) close to the A-type granite range, the porphyritic biotite monzogranitic magma has undergone fractionation and those of highly-differentiated granites have also higher Ga/Al×10,000

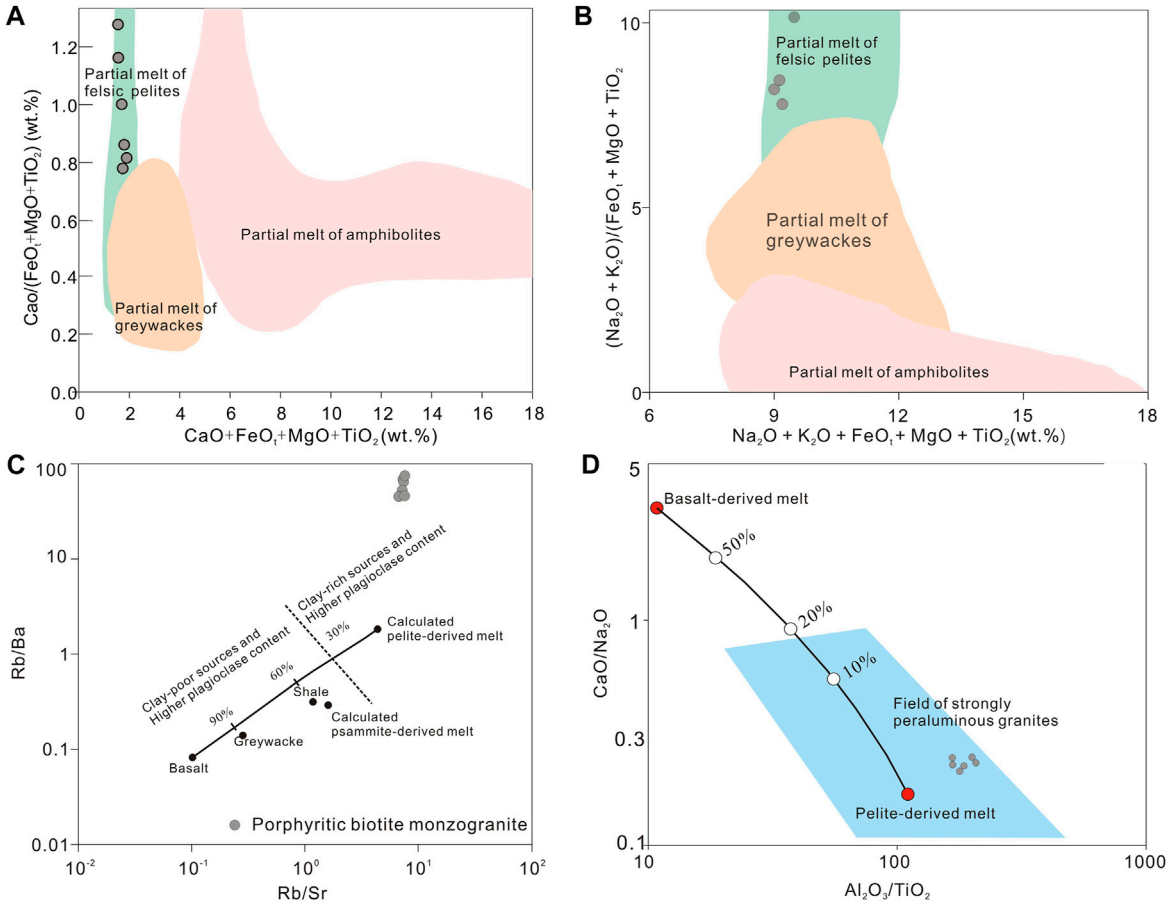

FIGURE 10 | (A) (CaO)/(FeO_t + MgO + TiO_2) vs (CaO + FeO_t + MgO + TiO_2); **(B)** (Na_2O + K_2O)/(FeO_t + MgO + TiO_2) vs (Na_2O + K_2O + FeO_t + MgO + TiO_2). Fields in **(A)** and **(B)** are from Patiño-Douce and Harris. (1999); **(C)** Rb/Ba vs Rb/Sr; **(D)** CaO/Na_2O vs Al_2O_3/TiO_2. The mixing curve between the basalt-and pelite-derived melts in **Figures 11C,D** is from Patiño-Douce and Harris (1998) and Sylvester (1998).

ratio, which is defined as A-type granites (Linnen and Cuney, 2004; Pérez-Soba and Villaseca, 2010; Breiter et al., 2013). As shown in the Zr-[(Ga/Al) × 10,000] plot (**Figure 13B**), the evolution from porphyritic to medium-fine-grained biotite monzogranite is consistent with the evolution trend of highly-differentiated I-/S-type granites. As a highly-fractionated granite, it's inevitable to be plotted in the A-type area, regardless of the Zr + Nb + Y + Ce value. A combination of FeOt/MgO (K_2O + Na_2O)/CaO and Zr + Nd + Y + Ce value is a proper parameter to discuss the highly-fractionated granite (Whalen et al., 1987). In the diagrams of FeO_t/MgO vs Zr + Nd + Y + Ce (**Figure 13C**), and (K_2O + Na_2O)/CaO vs Zr + Nd + Y + Ce (**Figure 13D**), these granites have lower FeO_t/MgO and (K_2O + Na_2O)/CaO than that of typical A-type granite. Some granite sample points do not fall into the high fractionated granite region, however, this does not mean that these are not highly fractionated granites, probably because of biotite (resulting in significantly lower K_2O and FeO_t content) and columbite-tantalite (resulting in a significant reduction in FeO_t contents). In addition, petrography, whole-rocks geochemistry, and REE tetrad effect (>1.1; eg., Irber, 1999) all indicate that these granites are highly fractionated granites. Furthermore, with decreasing Zr content, the P_2O_5, Rb and Th evolution trends (gradually decrease) of the Jianfengling granite are similar to those of highly-differentiated S-type granites (e.g., Chappell and White, 1992; Li et al., 2007, **Figures 13E,F**).

Tectonic Settings

The Early Jurassic (205–180 Ma) marked a relatively calm period for the tectonism and magmatism in South China (Zhou et al., 2006). Maruyama and Seno (1986) and Wan and Zhu (2002) suggested that the Paleo-Pacific block began to move NW and subducted at a low angle beneath Eurasia in the Jurassic. Mao et al. (2011) also inferred that the Paleo-Pacific block subducted NW at a low angle beneath the Eurasia block at ~175 Ma. Due to the NW-dipping Paleo-Pacific subduction, the eastern continental margin of China became an active continental margin, and remelting of the subducting plate occurred along the Qin–Hang paleo-suture zone and Nanling region. Meanwhile, the continental crust may have continued to thicken, and a series of crustal-scale extensional faults were developed in the backarc region (Mao et al., 2011; Wang et al., 2018). The development of bimodal magmatism (158–179 Ma; Chen et al., 2002), A-type

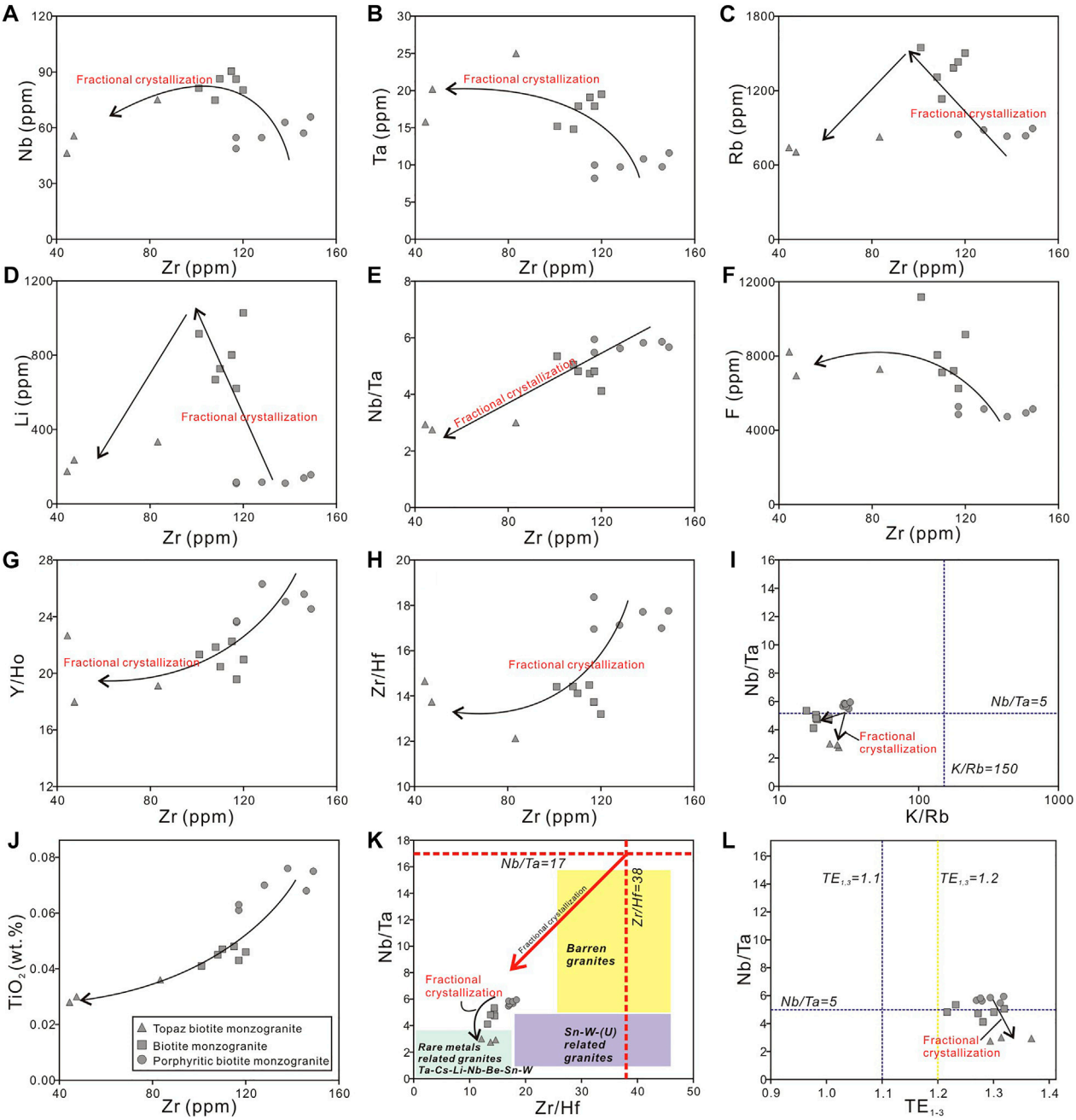

FIGURE 11 | Plots of Zr vs **(A)** Nb, **(B)** Ta, **(C)** Rb, **(D)** Li, **(E)** Nb/Ta, **(F)** F, **(G)** Y/Ho, **(H)** Zr/Hf, and **(I)** Nb/Ta vs K/Rb **(J)** Zr vs TiO_2 **(K)** Nb/Ta vs Zr/Hf **(L)** Nb/Ta vs $TE_{1,3}$ for the different Jianfengling biotite monzogranite lithofacies.

granite and alkaline plutons (165–173 Ma; Li et al., 2003), and the low–t_{DM} and high–εNd granite belt that extends from Hangzhou through Jiangxi and Hunan to Shiwandashan (**Figure 1** in Gilder et al., 1996) all demonstrate that the northeastern Qin–Hang metallogenic belt was under extension in the Middle Jurassic (Gilder et al., 1996). The South China crust may have been extended and thinned in the Mesozoic (Xu, 2012; Wang et al., 2012; Mao et al., 2013; Wang et al., 2017), triggering mantle upwelling and underplating of mantle-derived materials along fractures in the extended continental margin (**Figures 14A,B**). In summary, the ca. 172–145 Ma Nanling granites in the Qin–Hang belt were likely developed in a backarc extensional setting related to the low-angle Paleo-Pacific subduction (Jiang et al., 2006; Mao et al., 2011). In the Y vs Nb and Yb vs Ta plots (**Figures 14C,D**; after Pearce, 1996), the Jianfengling granite sample points both fell into the area of the within-plate granite, also indicating that the magma was formed through lithosphere thinning.

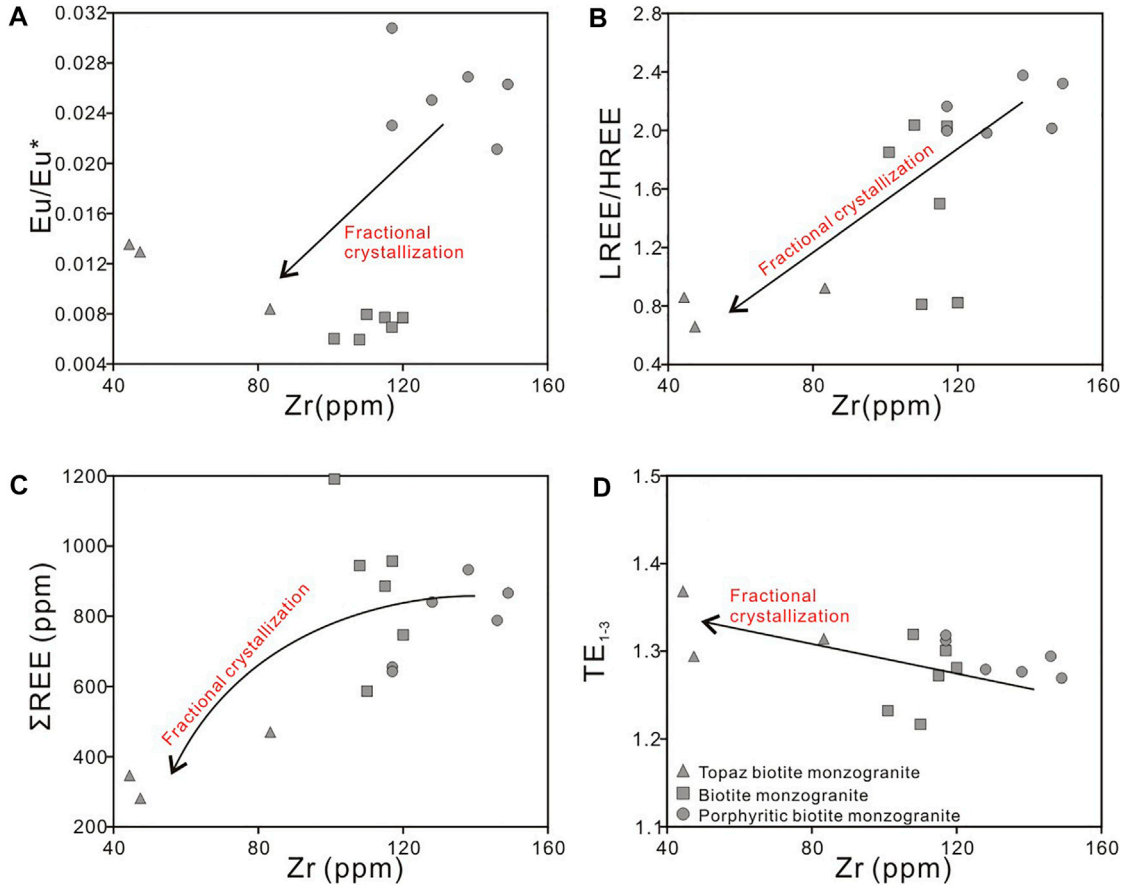

FIGURE 12 | Plots of Zr vs **(A)** Eu/Eu*, **(B)** LREE/HREE, **(C)** ∑REE, and **(D)** $TE_{1,3}$ for the different biotite monzogranite lithofacies from the Jianfengling pluton.

Magma Fractionation and Nb-Ta Enrichments

The Rb-Sr and Ba-Sr plots (**Figures 15A,B**) show fractionation of K-feldspar and plagioclase, consistent with the strong Eu/Eu* depletions of the Jianfengling granite. Granitic magmatic-hydrothermal evolution comprises generally two stages: 1) granite gradually evolved into highly-differentiated pegmatite (Trumbull and Chaussidon, 1999); 2) from granitic magma to magmatic-hydrothermal fluid, which is characterized by widespread greisenization and quartz veins (Roda-Robles et al., 2012; Pirajno, 2013; Breiter et al., 2017, 2019). Pegmatite, greisenization and W-Sn mineralization are developed in the Jianfengling biotite monzogranite, indicating that both stages are present in the evolution of the Jianfengling granitic magma. Compared with the porphyritic biotite monzogranite, tantalum content in the biotite monzogranites and the topaz biotite monzogranites increases significantly, whereas the Nb/Ta ratio decreases (**Figures 11B–E**). The TiO_2 content decreases with increasing Zr, indicating the fractionation of Ti-rich minerals (**Figure 11J**). Biotite is a Ti-rich mineral and their crystallization is conducive to Ta enrichment in the granitic magma (Stepanov and Hermann, 2013; Stepanov et al., 2014). Biotite fractionation would also increase the magma Nb/Ta ratio (Stepanov and Hermann, 2013; Stepanov et al., 2014), however, which is not found in our samples. The compatibility of Nb and Ta in granitic melt depends on the activity of non-bridging oxygen (NBOs) (Van Lichtervelde et al., 2011). The ratio $^{rt/melt}D_{Nb}/D_{Ta}$ is 0.8–1.0 for more silicic melts, remaining <1 for all examined silicate melts (Schmidta et al., 2004). The fractional crystallization of rutile would lead to a significant increase in melt Nb/Ta, contrary to our observations (i.e., **Figure 11E**). Amphibole-rich melts have been proposed to be one such candidate due to the preferential partitioning of Nb over Ta into amphibole, and which, however, is not found in our samples (i.e., **Figures 15A,B**). Moreover, Niobium (Nb), tantalum (Ta), zirconium (Zr) and hafnium (Hf) are moderately incompatible to weakly compatible (Hf at low temperature), with the exception of titanium, which is compatible in the amphibole structure (Nandedkar et al., 2016). Partition coefficient ratios $^{Amph/L}D_{Nb}/^{Amph/L}D_{Ta}$ (0.89–1.41) and $^{Amph/L}D_{Zr}/^{Amph/L}D_{Hf}$ (0.44–0.75) generally

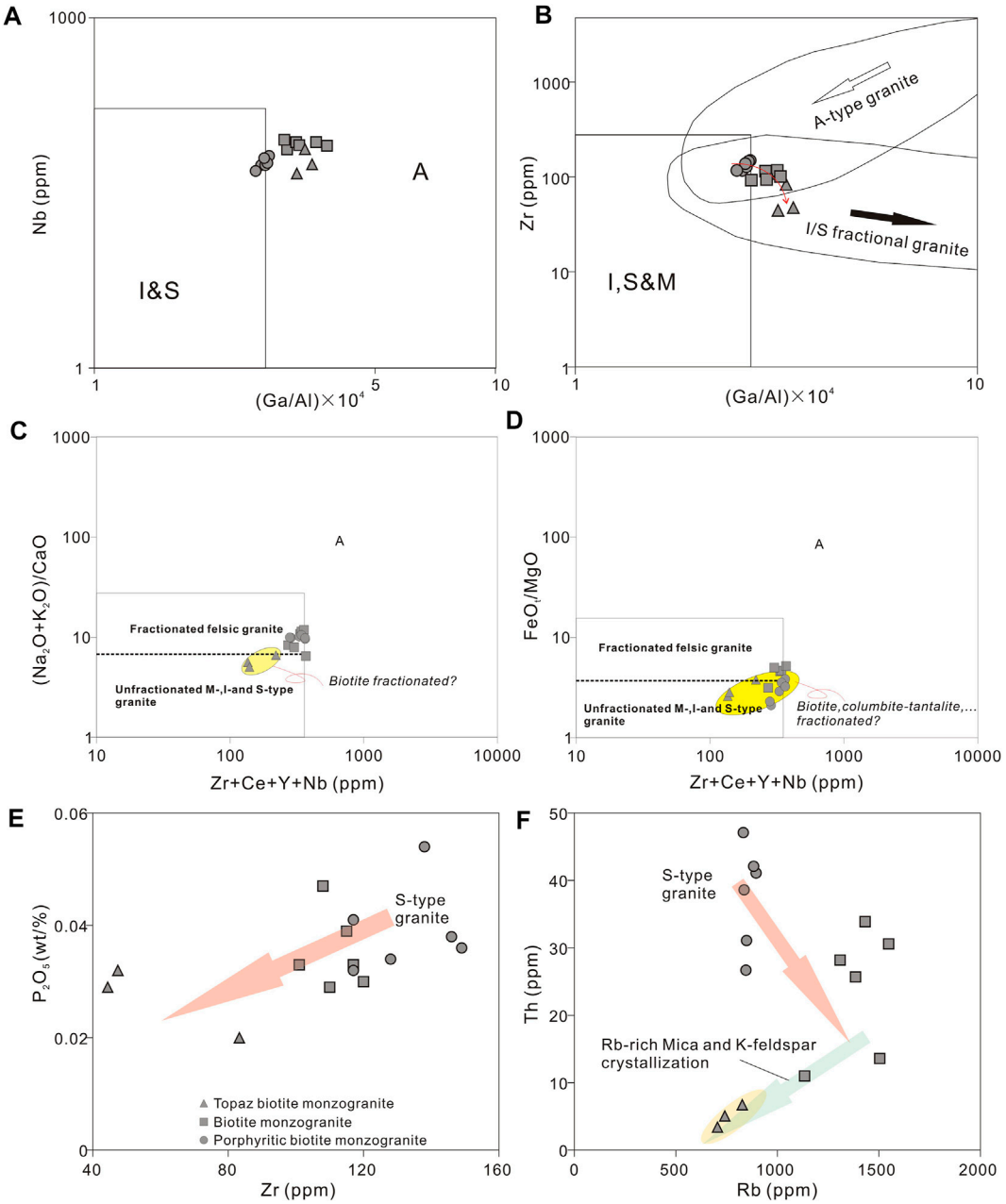

FIGURE 13 | (A) Nb vs (Ga/Al)×10^4; **(B)** Zr vs (Ga/Al) ×10^4; **(C)** (Na_2O + K_2O)/(CaO) vs (Zr + Ce + Y + Nb); **(D)** FeO_t/MgO vs (Zr + Ce + Y + Nb). **(A)**, **(B)**, **(C)** and **(D)** after Whalen et al. (1987) and Wu et al. (2017), respectively; **(E)** P_2O_5 vs Zr; **(F)** Th vs Rb for the different biotite monzogranite lithofacies from the Jianfengling pluton.

increase with decreasing temperature but no systematic trends are evident for the case of Zr and Hf, indicating that other factors are controlling the partition coefficient ratios (Nandedkar et al., 2016). Thus, the fractional crystallization of amphibole would lead to a significant increase in melt Zr/Hf, contrary to our observations (i.e., **Figure 11H**). Fluorine (F) can generally replace O in tetrahedral complex anion $[AlO_2]^-$ in the granitic melt, resulting in the decoupling of $[AlO_2]^-$. Meanwhile, fluorine would complex with Al to form AlF_6^{3-} complex [$3(Na,K)AlSi_3O_8 + 6F - 3O \rightleftharpoons (Na,K)_3AlF_6 + Al_2O_3 + 9SiO_2$; Keppler, 1993], which can significantly increase the magma non-bridging oxygen (NBOs) content. This could neutralize the excess alkali metal ions (Na^+ and K^+), and thus increase the Nb-Ta solubility in the melt (Keppler, 1993; Mysen, 1990). With magma fractionation (**section 6.3**), the contents of F, Nb and Ta in the Jianfengling granitic magma increase gradually (**Figures 15C,D**). This indicates that the F-rich volatile enrichment can significantly

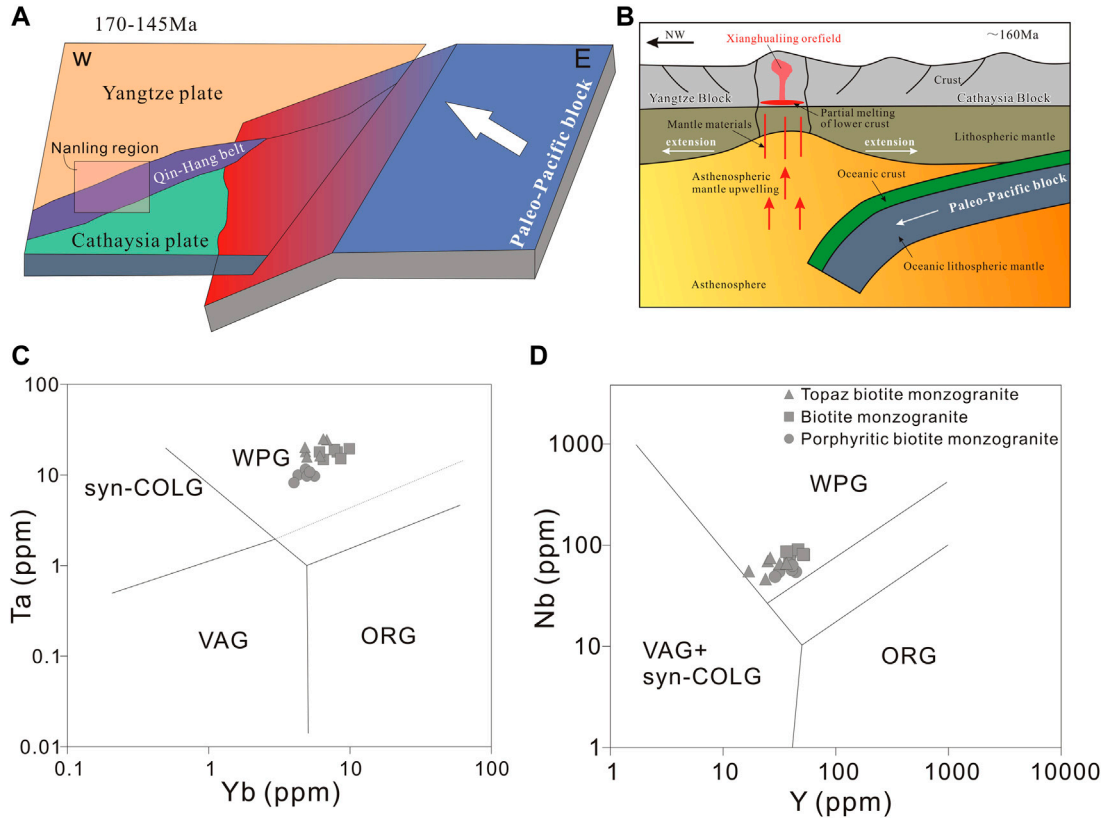

FIGURE 14 | Sketch diagram of the deep dynamic evolution of the Mesozoic metallogenesis of the Xianghualing orefield **(A,B)**. Discrimination diagrams of granite type and tectonic setting for the Jianfengling granitic rocks: **(C)** Y vs Nb; and **(D)** Yb vs Ta. Base maps after Pearce (1996).

increase the Nb-Ta solubility in the melt (Mysen and RyersonVirgo, 1981; London et al., 1993; Xiong et al., 1999).

CONCLUSION

1) The Jianfengling biotite monzogranite pluton comprises three gradual transitional lithofacies: porphyritic (mesophase facies), the biotite monzogranites (transition facies) and the topaz biotite monzogranites (central facies).
2) The high Th-U and low Th-U zircon grains from porphyritic biotite monzogranite yielded weighted average $^{206}Pb/^{238}U$ ages of 161.3 ± 1.6 and 158.7 ± 2.0 Ma, respectively, coeval with the timing of large-scale magmatism-mineralization in the Nanling region (ca. 160–150 Ma). The εHf(t) values of the high Th-U zircons (-6.48 to -2.51) and low Th-U zircons (-6.58 to -1.12) from the porphyritic biotite monzogranite indicate that the parental magma was mainly derived from partial melting of Mesoproterozoic Cathaysian basement rocks under lithospheric extension.
3) The Nb and Ta contents increase with fluorine along with magma fractionation, indicating that the Nb-Ta enrichments was likely resulted from the gradual increase of fluxing content (fluorine) during extensive fractional crystallization of the Jianfengling granitic magma.

DATA AVAILABILITY STATEMENT

The original contributions presented in the study are included in the article/Supplementary Material, further inquiries can be directed to the corresponding author.

AUTHOR CONTRIBUTIONS

CZ-Y, WH-T and W-C conceived this research. CZ-Y wrotes the manuscript and prepares the figures. SY-J and WC reviews and supervises the manuscript. The co-authors XD are involved in the discussion of the manuscript. All authors finally approved the manuscript and thus agreed to be accountable for this work.

FUNDING

This research was supported by the Fundamental Research Funds for the Central Universities, Sun Yat-sen University (2021qntd23) and the Fundamental Research Funds for the Central Universities, Sun Yat-sen University (22qntd2101). This research was supported by the Innovation-driven Plan of Central South University (2018zzts196), National Natural Science

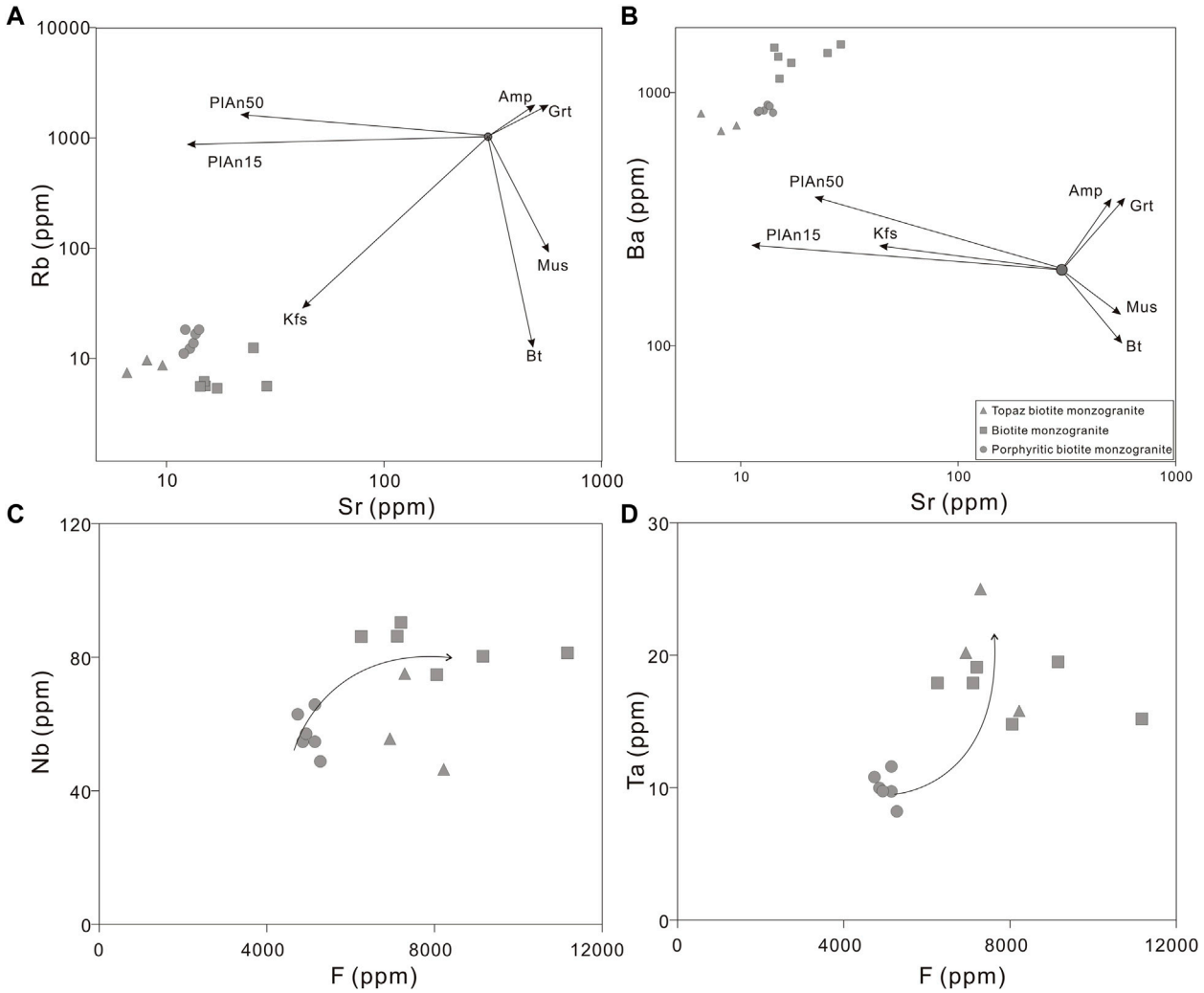

FIGURE 15 | Plots of **(A)** Rb vs Sr; **(B)** Ba vs Sr; **(C)** Nb vs F; **(D)** Ta vs F for the different biotite monzogranite lithofacies from the Jianfengling pluton.

Foundation of China (41702078), Hunan Provincial Geoscientific Research of Land and Resources (2016-04), and General Financial Grant from the China Postdoctoral Science Foundation (2017M622596).

ACKNOWLEDGMENTS

We are grateful to the #416 Brigade of the Hunan BGMR for the field assistance.

REFERENCES

Altherr, R., Holl, A., Hegner, E., Langer, C., and Kreuzer, H. (2000). High-potassium, Calc-Alkaline I-type Plutonism in the European Variscides: Northern Vosges (France) and Northern Schwarzwald (Germany). *Lithos* 50, 51–73. doi:10.1016/s0024-4937(99)00052-3

Ballard, J. R., Palin, M. J., and Campbell, I. H. (2002). Relative Oxidation States of Magmas Inferred from Ce(IV)/Ce(III) in Zircon: Application to Porphyry Copper Deposits of Northern Chile. *Contrib. Mineral. Pet.* 144, 347–364. doi:10.1007/s00410-002-0402-5

Ballouard, C., Poujol, M., Boulvais, P., Branquet, Y., Tartèse, R., and Vigneresse, J.-L. (2016). Nb-Ta Fractionation in Peraluminous Granites: A Marker of the Magmatic-Hydrothermal Transition. *Geology* 44, 231–234. doi:10.1130/g37475.1

Bau, M. (1996). Controls on the Fractionation of Isovalent Trace Elements in Magmatic and Aqueous Systems: Evidence from Y/Ho, Zr/Hf, and Lanthanide Tetrad Effect. *Contributions Mineralogy Petrology* 123, 323–333. doi:10.1007/s004100050159

Belousova, E., Griffin, W., O'Reilly, S. Y., and Fisher, N. (2002). Igneous Zircon: Trace Element Composition as an Indicator of Source Rock Type. *Contrib. Mineral. Pet.* 143, 602–622. doi:10.1007/s00410-002-0364-7

Blichert-Toft, J., Chauvel, C., and Albarède, F. (1997). Separation of Hf and Lu for High-Precision Isotope Analysis of Rock Samples by Magnetic Sector-Multiple Collector ICP-MS. *Contributions Mineralogy Petrology* 127 (3), 248–260. doi:10.1007/s004100050278

Breiter, K., Ďurišová, J., Hrstka, T., Korbelová, Z., Hložková Vaňková, M., Vašinová Galiová, M., et al. (2017). Assessment of Magmatic vs. Metasomatic Processes in Rare-Metal Granites: A Case Study of the Cínovec/Zinnwald Sn-W-Li Deposit, Central Europe. *Lithos* 292-293, 198–217. doi:10.1016/j.lithos.2017.08.015

Breiter, K., Gardenová, N., Kanický, V., and Vaculovič, T. (2013). Gallium and Germanium Geochemistry during Magmatic Fractionation and Post-magmatic Alteration in Different Types of Granitoids: A Case Study from the Bohemian Massif (Czech Republic). *Geol. Carpathica* 64, 171–180b. doi:10.2478/geoca-2013-0018

Breiter, K., Hložková, M., Korbelová, Z., and Galiová, M. V. (2019). Diversity of Lithium Mica Compositions in Mineralized Granite-Greisen System: Cínovec Li-Sn-W Deposit, Erzgebirge. *Ore Geol. Rev.* 106, 12–27. doi:10.1016/j.oregeorev.2019.01.013

Černý, P., and Ercit, T. S. (1985). Some Recent Advances in the Mineralogy and Geochemistry of Nb and Ta in Rare-Element Granitic Pegmatites. *Bull. De. Mineral.* 108, 499. doi:10.3406/bulmi.1985.7846

Černý, P., and Ercit, T. S. (2005). The Classification of Granitic Pegmatites Revisited. *Can. Mineralogist* 43, 2005. doi:10.2113/gscanmin.43.6.2005

Černý, P., Novak, M., and Chapman, R. (1992). Effects of Sillimanite-Grade Metamorphism and Shearing on Nb-Ta Oxide Minerals in Granitic Pegmatites, Marsikov, Northern Moravia, Czechoslovakia. *Can. Mineral.* 30, 699

Černý, P., Corkery, M. T., Halden, N. M., Ferreira, K., Brisbin, W. C., Chackowsky, L. E., and Meintzer, R. E. (2012). Extreme Fractionation and Deformation of the Leucogranite – Pegmatite Suite at Red Cross Lake, Manitoba, canada. Ii. Petrology of the Leucogranites and Pegmatites. *Can. Mineral.* 50, 1793–1806. doi:10.3749/canmin.50.6.1793

Chappell, B. W., and White, A. J. R. (1992). I- and S-type Granites in the Lachlan Fold Belt. *Earth Environ. Sci. Trans. R. Soc. Edinb.* 83, 1–26. doi:10.1017/s0263593300007720

Chen, P., Hua, R., Zhang, B., Lu, J., and Fan, C. (2002). Early Yanshanian Post-orogenic Granitoids in the Nanling Region. *Sci. China Ser. D-Earth Sci.* 45 (8), 755–768. (in Chinese). doi:10.1007/bf02878432

Chen, Z. Y. (2018). Ore-controlling Structure Characteristics and Prospecting Potential of Dongshan Tungsten Deposit. *Mineral Resour. Geol.* 32 (02), 222–226. (in Chinese).

Chen, Z. Y. (2021). *Rock- and Ore-Forming Mechanism of the Jianfengling Rb-Nb-Ta Deposit in Xianghualing Orefield, Hunan Province*. Doctoral Thesis. Changsha: Central South University, 1–186. (in Chinese).

Deering, C. D., and Bachmann, O. (2010). Trace Element Indicators of Crystal Accumulation in Silicic Igneous Rocks. *Earth Planet. Sci. Lett.* 297, 324–331. doi:10.1016/j.epsl.2010.06.034

Dostal, J., Kontak, D. J., Gerel, O., Gregory Shellnutt, J., and Fayek, M. (2015). Cretaceous Ongonites (Topaz-bearing Albite-Rich Microleucogranites) from Ongon Khairkhan, Central Mongolia: Products of Extreme Magmatic Fractionation and Pervasive Metasomatic Fluid: Rock Interaction. *Lithos* 236-237, 173–189. doi:10.1016/j.lithos.2015.08.003

Ferry, J. M., and Watson, E. B. (2007). New Thermodynamic Models and Revised Calibrations for the Ti-In-Zircon and Zr-In-Rutile Thermometers. *Contrib. Mineral. Pet.* 154 (4), 429–437. doi:10.1007/s00410-007-0201-0

Fidelis, I., and Siekierski, S. (1966). The Regularities in Stability Constants of Some Rare Earth Complexes. *J. Inorg. Nucl. Chem.* 28, 185–188. doi:10.1016/0022-1902(66)80243-9

Frost, B. R., Barnes, C. G., Collins, W. J., Arculus, R. J., Ellis, D. J., and Frost, C. D. (2001). A Geochemical Classification for Granitic Rocks. *J. Petrology* 42, 2033–2048. doi:10.1093/petrology/42.11.2033

Gelman, S. E., Deering, C. D., Bachmann, O., Huber, C., and Gutiérrez, F. J. (2014). Identifying the Crystal Graveyards Remaining after Large Silicic Eruptions. *Earth Planet. Sci. Lett.* 403, 299–306. doi:10.1016/j.epsl.2014.07.005

Gilder, S. A., Gill, J., and Coe, R. S. (1996). Isotopic and Paleo–Magmatic Constraints on the Mesozoic Tectonic Evolution of South China. *J. Geophys. Res.* 101 (B7), 13137–16154. doi:10.1029/96jb00662

Griffin, W. L., Pearson, N. J., Belousova, E., Jackson, S. E., van Achterbergh, E., O'Reilly, S. Y., et al. (2000). The Hf Isotope Composition of Cratonic Mantle: LAM-MC-ICPMS Analysis of Zircon Megacrysts in Kimberlites. *Geochimica Cosmochimica Acta* 64 (1), 133–147. doi:10.1016/s0016-7037(99)00343-9

Harris, N. B. W., and Inger, S. (1992). Trace Element Modelling of Pelite-Derived Granites. *Contr. Mineral. Pet.*. 110, 46–56. doi:10.1007/bf00310881

Hoskin, P. W. O., and Schaltegger, U. (2003). 2. The Composition of Zircon and Igneous and Metamorphic Petrogenesis. *Rev. Mineralogy Geochem.* 53, 27–62. doi:10.1515/9781501509322-005

Irber, W. (1999). The Lanthanide Tetrad Effect and its Correlation with K/Rb, Eu/Eu*, Sr/Eu, Y/Ho, and Zr/Hf of Evolving Peraluminous Granite Suites. *Geochimica Cosmochimica Acta* 63, 489–508. doi:10.1016/s0016-7037(99)00027-7

Jiang, Y.-H., Jiang, S.-Y., Zhao, K.-D., and Ling, H.-F. (2006). Petrogenesis of Late Jurassic Qianlishan Granites and Mafic Dykes, Southeast China: Implications for a Back-Arc Extension Setting. *Geol. Mag.* 143, 457–474. doi:10.1017/s0016756805001652

Kemp, A. I. S., Hawkesworth, C. J., Foster, G. L., Paterson, B. A., Woodhead, J. D., Hergt, J. M., et al. (2007). Magmatic and Crustal Differentiation History of Granitic Rocks from Hf-O Isotopes in Zircon. *Science* 315, 980–983. doi:10.1126/science.1136154

Keppler, H. (1993). Influence of Fluorine on the Enrichment of High Field Strength Trace Elements in Granitic Rocks. *Contr. Mineral. Pet.*. 114, 479–488. doi:10.1007/bf00321752

Kesler, S. E., Gruber, P. W., Medina, P. A., Keoleian, G. A., Everson, M. P., and Wallington, T. J. (2012). Global Lithium Resources: Relative Importance of Pegmatite, Brine and Other Deposits. *Ore Geol. Rev.* 48 (5), 55–69. doi:10.1016/j.oregeorev.2012.05.006

Lai, S. H., Chen, R. Y., Zhang, D., Di, Y. J., Gong, Y., Yuan, Y., et al. (2014). Petrogeochemical Features and Zircon LA-ICPMS U-Pb Ages of Granite in the Pantian Iron Ore Deposit, Fujian Province and Their Relationship with Mineralization. *Acta Petrol. Sin.* 030 (006), 1780–1792. (in Chinese).

Lai, S. H. (2015). *Research on Mineralization of the Xianghualing Tin Polymetallic Deposit, Hunan Province, China*. Doctoral Thesis. Beijing: China University of Geosciences Beijing, 1–151. (in Chinese).

Le Maitre, E. W. (2002). *Igneous Rocks: A Classification and Glossary of Terms*. Cambridge: Cambridge University Press, 1

Le Maitre, R. W. (1989). *A Classification of Igneous Rocks and Glossary of Terms: Recommendations of the IUGS Commission on the Systematics of Igneous Rocks*. Cambridge: Oxford Blackwell, 1

Lee, C.-T. A., and Morton, D. M. (2015). High Silica Granites: Terminal Porosity and Crystal Settling in Shallow Magma Chambers. *Earth Planet. Sci. Lett.* 409, 23–31. doi:10.1016/j.epsl.2014.10.040

Lenting, C., Geisler, T., Gerdes, A., Kooijman, E., Scherer, E. E., and Zeh, A. (2010). The Behavior of the Hf Isotope System in Radiation-Damaged Zircon during Experimental Hydrothermal Alteration. *Am. Mineralogist* 95, 1343–1348. doi:10.2138/am.2010.3521

Li, H., Wu, J.-H., Evans, N. J., Jiang, W.-C., and Zhou, Z.-K. (2018). Zircon Geochronology and Geochemistry of the Xianghualing A-type Granitic Rocks: Insights into Multi-Stage Sn-Polymetallic Mineralization in South China. *Lithos* 312-313, 1–20. doi:10.1016/j.lithos.2018.05.001

Li, X. H., Liu, Y., Yang, Y. H., Chen, F. K., Tu, X. L., and Qi, C. S. (2007). Rapid Separation of Lu-Hf and Sm-Nd from a Single Rock Dissolution and Precise Measurement of Hf-Nd Isotopic Ratios for National Rock Standards. *Acta Petrol. Sin.* 23, 221–226. (in Chinese).

Li, X.-H., Chen, Z., Liu, D., and Li, W.-X. (2003). Jurassic Gabbro-Granite-Syenite Suites from Southern Jiangxi Province, SE China: Age, Origin, and Tectonic Significance. *Int. Geol. Rev.* 45, 898–921. doi:10.2747/0020-6814.45.10.898

Li, X.-H., Liu, D., Sun, M., Li, W.-X., Liang, X.-R., and Liu, Y. (2004). Precise Sm-Nd and U-Pb Isotopic Dating of the Supergiant Shizhuyuan Polymetallic Deposit and its Host Granite, SE China. *Geol. Mag.* 141 (2), 225–231. doi:10.1017/s0016756803008823

Li, X.-H., Long, W.-G., Li, Q.-L., Liu, Y., Zheng, Y.-F., Yang, Y.-H., et al. (2010). Penglai Zircon Megacrysts: a Potential New Working Reference Material for Microbeam Determination of Hf-O Isotopes and U-Pb Age. *Geostand. Geoanalytical Res.* 34 (2), 117–134. doi:10.1111/j.1751-908x.2010.00036.x

Linnen, R. L., and Cuney, M. (2004). "Granite-related Rare-Element Deposits and Experimental Constraints on Ta-Nb-W-Sn-Zr-Hf Mineralization," in *Eare-Element Geochemistry and Mineral Deposits*. Editors R. L. Linnen and I. M. Samson (GAC Short Course Notes), 17, 45

Linnen, R. L., Van Lichtervelde, M., and Cerny, P. (2012). Granitic Pegmatites as Sources of Strategic Metals. *Elements* 8 (4), 275–280. doi:10.2113/gselements.8.4.275

London, D., Morgan, G. B., Babb, H. A., and Loomis, J. L. (1993). Behavior and Effects of Phosphorus in the System Na_2O–K_2O–Al_2O_3–SiO_2–P_2O_5–H_2O at 200 MPa(H_2O). *Contr. Mineral. Pet.*. 113 (4), 450–465. doi:10.1007/bf00698315

Ludwig, K. R. (2001). *Using Isoplot/EX, Version 2.49. A Geochronological Toolkit for Microsoft Excel*. San Francisco: Berkeley Geochronological Center Special Publication.

Mao, J. W., Chen, M. H., Yuan, S. D., and Guo, C. L. (2011). Geological Characteristics of the Qinhang (Or Shihang) Metallogenic Belt in South China and Spatial–Temporal Distribution Regularity of Mineral Deposits. *Acta Geol. Sin.* 85 (5), 636–658. (in Chinese).

Mao, J. W., Cheng, Y. B., Chen, M. H., and Pirajno, F. (2013). Major Types and Time-Space Distribution of Mesozoic Ore Deposits in South China and Their Geodynamic Settings. *Miner. Deposita* 48 (3), 267. doi:10.1007/s00126-012-0446-z

Mao, J. W., Li, X. F., Lehmann, B., Chen, W., Lan, X. M., and Wei, S. L. (2004b). ^{40}Ar-^{39}Ar Dating of Tin Ores and Related Granite in Furong Tin Orefield, Hunan Province, and its Geodynamic Significance. *Mineral. Deposits* 22 (2), 164–175. (in Chinese).

Mao, J. W., Stein, H., Du, A. D., Zhou, T. F., Mei, Y. X., Li, Y. F., et al. (2004a). Molybdenite Re-os Precise Dating for Molybdenite from Cu-Au-Mo Deposits in the Middle-Lower Reaches of Yangtze River Belt and its Implication for Mineralization. *Acta Geol. Sin.* 78 (1), 121–132. (in Chinese).

Mao, J. W., Xie, G. Q., Guo, C. L., and Chen, Y. C. (2007). Large-scale Tungsten-Tin Mineralization in the Nanling Region, South China: Metallogenic Ages and Corresponding Geodynamic Process. *Acta Petrol. Sin.* 23 (10), 2329–2338. (in Chinese).

Maruyama, S., and Send, T. (1986). Orogeny and Relative Plate Motions: Example of the Japanese Islands. *Tectonophysics* 127, 305–329. doi:10.1016/0040-1951(86)90067-3

Mo, Z. S. (1983). A Discussion on the Petrogenetic Classification of Granitic Rocks in the Nanling Region. *Geol. Bull. China* 1, 22–26. (in Chinese).

Mysen, B. O., and RyersonVirgo, F. J. D. (1981). The Structural Role of Phosphorus in Silicate Melts. *Am. Mineralogist* 66 (1-2), 106

Mysen, B. (1990). Relationships between Silicate Melt Structure and Petrologic Processes. *Earth-Science Rev.* 27 (4), 281–365. doi:10.1016/0012-8252(90)90055-z

Nandedkar, R. H., Hürlimann, N., Ulmer, P., and Müntener, O. (2016). Amphibole-melt Trace Element Partitioning of Fractionating Calc-Alkaline Magmas in the Lower Crust: an Experimental Study. *Contrib. Mineral. Pet.* 171, 71. doi:10.1007/s00410-016-1278-0

Patino Douce, A. E., and Harris, N. (1998). Experimental Constraints on Himalayan Anatexis. *J. Petrology* 39 (4), 689–710. doi:10.1093/petroj/39.4.689

Pearce, J. (1996). Sources and Settings of Granitic Rocks. *Episodes* 19, 120–125. doi:10.18814/epiiugs/1996/v19i4/005

Peng, J., Zhou, M.-F., Hu, R., Shen, N., Yuan, S., Bi, X., et al. (2006). Precise Molybdenite Re-os and Mica Ar-Ar Dating of the Mesozoic Yaogangxian Tungsten Deposit, Central Nanling District, South China. *Min. Deposita* 41, 661–669. doi:10.1007/s00126-006-0084-4

Peppard, D. F., Mason, G. W., and Lewey, S. (1969). A Tetrad Effect in the Liquid-Liquid Extraction Ordering of Lanthanides(III). *J. Inorg. Nucl. Chem.* 31, 2271–2272. doi:10.1016/0022-1902(69)90044-x

Pérez-Soba, C., and Villaseca, C. (2010). Petrogenesis of Highly Fractionated I-type Peraluminous Granites: La Pedriza Pluton (Spanish Central System). *Geol. Acta* 8, 131. doi:10.1344/105.000001527

Pirajno, F. (2013). "Effects of Metasomatism on Mineral Systems and Their Host Rocks: Alkali Metasomatism, Skarns, Greisens, Tourmalinites, Rodingites, Black-Wall Alteration and Listvenites," in *Metasomatism and the Chemical Transformation of Rock: Lecture Notes in Earth System Sciences*. Editors D. E. Harlov and H. Austrheim (Berlin: Springer Berlin Heidelberg), 203–251. doi:10.1007/978-3-642-28394-9_7

Putnis, A. (2009). 3. Mineral Replacement Reactions. *Rev. Mineral. Geochem* 70, 87–124. doi:10.1515/9781501508462-005

Qiu, R. Z., Deng, J. F., Cai, Z. Y., Zhou, S., Chang, H. L., and Du, S. H. (2002). Material Sources of Granite and Ore in Xianghualing Mult-Metal Orefield, Hunan Province. *Mineral. Deposits* 21 (S1), 1017–1020. (in Chinese).

Qiu, R. Z., Deng, J. F., Cai, Z. Y., Zhou, S., Chang, H. L., and Du, S. H. (2003). Nd Isotopic Characteristics and Genesis of Xianhualing 430 Granitic Body, Hunan Province. *Acta Petrologica Mineralogica* 22 (1), 41–46. (in Chinese).

Qiu, R. Z., and Peng, S. B. (1997). Gensis of Granitic Nb -Ta Deposit in Xianghualing Area and the Role of the Supercritical Fluid in the Process of Rock-Forming and Mineralization. *Hunan Geol.* 16 (2), 92–97. (in Chinese).

Qiu, R. Z., Zhou, S., Chang, H. L., Du, S. H., and Peng, S. B. (1998). The Evolution of Li-Bearing Micas from Xianghualing Granites and Their Ore-Prospecting Significance in Hunan. *J. Guilin Univ. Technol.* 18 (02), 145–153. (in Chinese).

Roda-Robles, E., Pesquera, A., Gil-Crespo, P., and Torres-Ruiz, J. (2012). From granite to highly evolved pegmatite: A case study of the Pinilla de Fermoselle granite-pegmatite system (Zamora, Spain). *Lithos* 153, 192–207. doi:10.1016/j.lithos.2012.04.027

Schmidt, M. W., Dardon, A., Chazot, G., and Vannucci, R. (2004). The Dependence of Nb and Ta Rutile-Melt Partitioning on Melt Composition and Nb/Ta Fractionation during Subduction Processes. *Earth Planet. Sci. Lett.* 226, 415–432. doi:10.1016/j.epsl.2004.08.010

Simmons, W. B. S., and Webber, K. L. (2008). Pegmatite Genesis: State of the Art. *ejm* 20, 421–438. doi:10.1127/0935-1221/2008/0020-1833

Stepanov, A., Mavrogenes, J., Meffre, S., and Davidson, P. (2014). The Key Role of Mica during Igneous Concentration of Tantalum. *Contributions Mineralogy Petrology* 167 (6), 1–8. doi:10.1007/s00410-014-1009-3

Stepanov, A. S., and Hermann, J. (2013). Fractionation of Nb and Ta by Biotite and Phengite: Implications for the "Missing Nb Paradox". *Geology* 41, 303–306. doi:10.1130/g33781.1

Streckeisen, A., and Le Maitre, R. W. (1979). A Chemical Approximation to the Modal QAPF Classification of the Igneous Rocks. *Neues Jahrb. für Mineralogie–Abhandlungen* 136, 169

Sun, S.-s., and McDonough, W. F. (1989). "Chemical and Isotopic Systematics of Oceanic Basalts: Implications for Mantle Composition and Processes,". Editors A. D. Saunder and M. J. Norry (London: Geological Society, London, Special Publications), 42, 313–345. doi:10.1144/gsl.sp.1989.042.01.19*Geol. Soc. Lond. Spec. Publ.*

Sylvester, P. J. (1998). Post-collisional Strongly Peraluminous Granites. *Lithos* 45, 29–44. doi:10.1016/s0024-4937(98)00024-3

Taylor, S. R., and McLennan, S. M. (1985). *The Continental Crust: Its Composition and Evolution*. Oxford: Blackwell Oxford Press, 1

Thomas, R., Davidson, P., and Schmidt, C. (2011b). Extreme Alkali Bicarbonate- and Carbonate-Rich Fluid Inclusions in Granite Pegmatite from the Precambrian Rønne Granite, Bornholm Island, Denmark. *Contributions Mineralogy Petrology* 161 (2), 314–329. doi:10.1007/s00410-010-0533-z

Thomas, R., Davidson, P., and Beurlen, H. (2011a). Tantalite-(Mn) from the Borborema Pegmatite Province, Northeastern Brazil: Conditions of Formation and Melt- and Fluid-Inclusion Constraints on Experimental Studies. *Min. Deposita* 46 (7), 749–759. doi:10.1007/s00126-011-0344-9

Trumbull, R. B., and Chaussidon, M. (1999). Chemical and Boron Isotopic Composition of Magmatic and Hydrothermal Tourmalines from the Sinceni Granite-Pegmatite System in Swaziland. *Chem. Geol.* 153, 125–137. doi:10.1016/s0009-2541(98)00155-7

Van Lichtervelde, M., Holtz, F., Dziony, W., Ludwig, T., and Meyer, H.-P. (2011). Incorporation Mechanisms of Ta and Nb in Zircon and Implications for Pegmatitic Systems. *Am. Mineralogist* 96 (7), 1079–1089. doi:10.2138/am.2011.3650

Wan, T. F., and Zhu, H. (2002). Tectonics and Environment Change of Meso-Cenozoic in China Continent and its Adjacent Areas. *Geoscience* 16 (2), 107–120. (in Chinese). doi:10.1080/12265080208422884

Wang, C., Shao, Y. J., Liu, Z. F., and Zhang, Y. (2017). The Geology and Geochemistry of the Shizitou Molybdenum Deposit, Jiangxi Province, China: Implications for the Geodynamic Setting. *Acta Geol. Sin. Engl. Ed.* 91 (S1), 233–234. doi:10.1111/1755-6724.13271

Wang, C., Shao, Y., Liu, Z., Liu, Q., and Zhang, Y. (2018). Geology and Geochemistry of the Shizitou Molybdenum Deposit, Jiangxi Province: Implications for Geodynamic Setting and Metallogenesis. *Acta Geol. Sin. - Engl. Ed.* 92 (4), 1415–1431. doi:10.1111/1755-6724.13635

Wang, G.-G., Ni, P., Zhao, K.-D., Wang, X.-L., Liu, J.-Q., Jiang, S.-Y., et al. (2012). Petrogenesis of the Middle Jurassic Yinshan Volcanic-Intrusive Complex, SE China: Implications for Tectonic Evolution and Cu-Au Mineralization. *Lithos* 150, 135–154. doi:10.1016/j.lithos.2012.05.030

Wang, Y., Fan, W., Cawood, P. A., and Li, S. (2008). Sr-Nd-Pb Isotopic Constraints on Multiple Mantle Domains for Mesozoic Mafic Rocks

beneath the South China Block Hinterland. *Lithos* 106, 297–308. doi:10.1016/j.lithos.2008.07.019

Wen, C. H., Shao, Y. J., Huang, G. F., Luo, X. Y., and Li, S. M. (2017). Geochemical Features and Mineralization of Jianfengling Rare Metal Granite in Hunan Province. *Mineral. Deposits* (04), 879–892. (in Chinese).

Whalen, J. B., Currie, K. L., and Chappell, B. W. (1987). A-Type Granites: Geochemical Characteristics, Discrimination and Petrogenesis. *Contrib. Mineral. Pet.* 95, 407–419. doi:10.1007/bf00402202

Wu, F., Liu, X., Ji, W., Wang, J., and Yang, L. (2017). Highly Fractionated Granites: Recognition and Research. *Sci. China Earth Sci.* 60, 1201–1219. doi:10.1007/s11430-016-5139-1

Xiong, X. L., Zhao, Z. H., Zhu, J. C., and Rao, B. (1999). Phase Relations in Albite Granite-H_2o-HF System and Their Petro Genetic Applications. *Geochem. J.* 33 (3), 199

Xu, L. (2012). *Multi-stages Structural Deformation and its Influence on the Metallogenesis in the East Part of the Qinzhou –Hangzhou Structural Belt*. Shandong: Ocean University of China, 1–54. (in Chinese).

Xu, Y. K. (1990). *Report of Regional Geological Survey of Hunan Provinc*. Changsha: Hunan Bureau of Geology and Mineral Resources, 90–124. (in Chinese).

Xuan, Y. C., Yuan, S. D., Yuan, Y. B., and Mi, Y. R. (2014). Zircon U-Pb Age. *Geochem. petrogenesis Jianfengling Plut. South. Hunan Prov. Mineral Deposit* 33 (06), 1379–1390. (in Chinese).

Yang, L., Wu, X., Cao, J., Hu, B., Zhang, X., Gong, Y., et al. (2018). Geochronology, Petrology, and Genesis of Two Granitic Plutons of the Xianghualing Ore Field in South Hunan Province: Constraints from Zircon U-Pb Dating, Geochemistry, and Lu-Hf Isotopic Compositions. *Minerals* 8 (5), 213. doi:10.3390/min8050213

Yang, Z., de Fourestier, J., Ding, K., and Li, H. (2013). Li-bearing ferronigerite-2N1S from Xianghualing Tin-Polymetallic orefield,Hunan Province, China. *Can. Mineral.* 51, 913–919. doi:10.3749/canmin.51.6.913

Yao, J., Hua, R., Qu, W., Qi, H., Lin, J., and Du, A. (2007). Re-Os Isotope Dating of Molybdenites in the Huangshaping Pb-Zn-W-Mo Polymetallic Deposit, Hunan Province, South China and its Geological Significance. *Sci. China Ser. D.* 50, 519–526. doi:10.1007/s11430-007-2052-y

Yuan, S. D., Liu, X. F., Wang, X. D., Wu, S. H., Yuan, Y. B., Li, X. K., et al. (2012b). Geological Characteristics and ^{40}Ar-^{39}Ar Geochronology of the Hongqiling Tin Deposit in Southern Hunan Province. *Acta Petrol. Sin.* 28 (12), 3787–3797. (in Chinese). doi:10.1007/s11783-011-0280-z

Yuan, S. D., Pang, J. T., Li, H. M., Shen, N. P., and Zhang, D. L. (2008). *A Precise U-Pb Age on Cassiterite from the Xianghualing Tin-Polyrnetallic deposit(Hunan, South China) Mineralium Deposita* 43, 375–382. doi:10.1007/s00126-007-0166-y

Yuan, S. D., Peng, J. T., Shen, N. P., Hu, R. Z., and Dai, T. M. (2007). ^{40}Ar-^{39}Ar Isotopic Dating of the Xianghualing Sn-Polymetallic Orefield in Southem Hunnan and its Geological Implications. *Acta Geol. sin.* 81 (2), 278

Yuan, S. D., Zhang, D. L., Shuang, Y., Du, A. D., and Qu, W. J. (2012a). Re-Os Dating of Molybdenite from the Xintianling Giant Tungsten-Molybdenum Deposit in Southern Hunan Province, China and its Geological Implications. *Acta Petrol. Sin.* 28 (1), 27. doi:10.1007/s11783-011-0280-z

Yuan, S., Peng, J., Hao, S., Li, H., Geng, J., and Zhang, D. (2011). *In Situ* LA-MC-ICP-MS and ID-TIMS U-Pb Geochronology of Cassiterite in the Giant Furong Tin Deposit, Hunan Province, South China: New Constraints on the Timing of Tin-Polymetallic Mineralization. *Ore Geol. Rev.* 43, 235–242. doi:10.1016/j.oregeorev.2011.08.002

Zhou, L.-G., Xia, Q.-X., Zheng, Y.-F., and Hu, Z. (2014). Polyphase Growth of Garnet in Eclogite from the Hong'an Orogen: Constraints from Garnet Zoning and Phase Equilibrium. *Lithos* 206-207, 79–99. doi:10.1016/j.lithos.2014.06.020

Zhou, X. M., Sun, T., Shen, W. Z., Shu, L. S., and Niu, Y. L. (2006). Petrogenesis of Mesozoic Granitoids and Volcanic Rocks in South China: a Response to Tectonic Evolution. *Episodes* 29, 26––33. doi:10.18814/epiiugs/2006/v29i1/004

Zhu, L. (2020). *Genesis and Rare Metal Enrichment Mechanism of High-Differentiation Granites in Jianfengling, Southern Hunan*. Master Thesis. Changsha: Central South University, 4

Conflict of Interest: The authors declare that the research was conducted in the absence of any commercial or financial relationships that could be construed as a potential conflict of interest.

Publisher's Note: All claims expressed in this article are solely those of the authors and do not necessarily represent those of their affiliated organizations, or those of the publisher, the editors and the reviewers. Any product that may be evaluated in this article, or claim that may be made by its manufacturer, is not guaranteed or endorsed by the publisher.

frontiers | Frontiers in Earth Science

ORIGINAL RESEARCH
published: 13 June 2022
doi: 10.3389/feart.2022.849665

Discovery of the Late Jurassic-Early Cretaceous Lamprophyres in Western Songliao Basin of Northeast China and Their Constraint on Regional Lithospheric Evolution

Taiji Yu[1], *Pujun Wang*[1]*, *Yan Zhang*[1], *Youfeng Gao*[1,2] *and Chongyang Chen*[3]

[1]College of Earth Sciences, Jilin University, Changchun, China, [2]Research Center of Palaeontology and Stratigraphy, Jilin University, Changchun, China, [3]College of Tourism and Geographic Sciences, Jilin Normal University, Siping, China

OPEN ACCESS

Edited by:
Kit Lai,
Fortescue Metals Group, Australia

Reviewed by:
Rui Wang,
China University of Geosciences, China
Chuan-Zhou Liu,
Institute of Geology and Geophysics (CAS), China

***Correspondence:**
Pujun Wang
wangpj@jlu.edu.cn

Specialty section:
This article was submitted to Petrology, a section of the journal Frontiers in Earth Science

Received: *06 January 2022*
Accepted: *18 May 2022*
Published: *13 June 2022*

Citation:
Yu T, Wang P, Zhang Y, Gao Y and Chen C (2022) Discovery of the Late Jurassic-Early Cretaceous Lamprophyres in Western Songliao Basin of Northeast China and Their Constraint on Regional Lithospheric Evolution. Front. Earth Sci. 10:849665. doi: 10.3389/feart.2022.849665

Contrary to the commonly accepted notion that the lithosphere in NE China thinned from the Late Jurassic through to the Early Cretaceous period, we report the discovery of a thickening episode in the backdrop of this long-term thinning. A series of lamprophyre dikes have been recently discovered in the Tuquan Basin of the western Songliao Basin that have been dated to 156.0 ± 2.3 Ma, 132.9 ± 1.2 Ma, and 126.2 ± 2.5 Ma by using the zircon U–Pb technique. These lamprophyres are subdivided into biotite orthoclase lamprophyre (BOL) from the Late Jurassic and quartz magnetite lamprophyre (QML) from the Early Cretaceous. The BOL and QMLs are shoshonite and calc-alkaline in series, are characterized by large amounts of FeO^T, TiO_2, MgO, and Mg#, and are rich in LREEs and LILEs but poor in HREEs and HFSEs. They have high ratios of $(La/Yb)_N$, La/Ta, La/Nb, Th/Y, Ba/Nb, Ba/Ta, and Ba/Th, and low ratios of Zr/Ba, La/Sm, and Nb/Zr. These features collectively point to the derivation of dike magmas from the partial melting of the enriched lithospheric mantle that had been previously metasomatized by subduction-related fluids. The BOL has high ratios of Rb/Sr (0.42) and K/Yb*1000 (28.3), and low ratios of Ba/Rb (13.5) and Dy/Yb (2.35), suggesting the derivation of magma from a high degree of partial melting of the phlogopite-bearing lherzolite mantle in the spinel–garnet transition zone at a depth of about 60 km. The QMLs have low ratios of Rb/Sr (0.02–0.06) and K/Yb*1000 (8.13–19.73), and high ratios of Ba/Rb (17.6–42.6) and Dy/Yb (3.48–4.09), indicating that the magmas were derived from a low degree of partial melting of the lherzolite mantle in the garnet zone at a depth of ca. 85 km. The younger QML (126.2 ± 2.5 Ma) has a lower Dy/Yb ratio (3.48–3.92) than the older QML (132.9 ± 1.2 Ma), with a Dy/Yb ratio of 4.09 implying that the younger magma was formed at a shallower depth of the mantle (<85 km) than the older one. These observations indicate that in 156–132 Ma, the lithosphere thickened by approximately 25 km at a rate of approximately 1.0 km/Myr. This is used to propose a model of geodynamic evolution in three stages.

Keywords: Songliao Basin, Northeast Asia, lamprophyre, geochemistry, lithospheric evolution, Jurassic and Cretaceous

1 INTRODUCTION

Lamprophyres are alkaline/calc-alkaline, mafic, or ultramafic melanocratic hypabyssal igneous rocks characterized by porphyritic textures, with mafic phenocrysts (biotite and/or amphibole) and groundmass mainly consisting of alkali feldspar, plagioclase, feldspathoids, biotite, amphibole, clinopyroxene, and olivine (Rock, 1991). They often occur as dikes (Le Maitre, 2002). Based on the type and content of feldspar and predominant mafic minerals in them, lamprophyres can be categorized into minette, spessartite, and sannaite (Le Maitre, 2002). Distributed widely across the globe, lamprophyres were formed in the Archean (Wyman et al., 2006), the Paleozoic (Rocchi et al., 2009), the Mesozoic (Deng et al., 2017) and the Cenozoic (Li et al., 2002). Lamprophyric magmas are generally thought to have originated from the partial melting of an enriched continental lithospheric mantle (Rock, 1987; Gibson et al., 2006; Choi et al., 2020). Their capacity to record the material composition of the deep lithospheric mantle, mantle–crust interactions, and the process of enrichment of the lithospheric mantle makes lamprophyres an important means of studying the evolution of the continental lithosphere (Rock and Groves, 1988; Stille et al., 1989). Most lamprophyres were formed in extensional tectonic settings (Woolley et al., 1996; Secher et al., 2009) while some have also been identified in convergent settings (Owen, 2008; van der Meer et al., 2016). Lamprophyres are commonly found in collisional orogens, such as southern Tibet and the Sanjiang Belt (Chung et al., 2005; Ding et al., 2007). The mineral and geochemical features of lamprophyres are vital for investigating the properties of the continental lithospheric mantle (Foley et al., 1987; Soder and Romer, 2018) and dynamic processes in the deep Earth (Guo et al., 2004; Ma et al., 2014; Deng et al., 2017).

It is widely believed that the lithosphere in northeast (NE) China thinned significantly from the Late Jurassic through the Early Cretaceous period (Wang et al., 2006; Wu et al., 2011; Zhang et al., 2011). Delamination is the main mechanism of lithospheric thinning (Zhang et al., 2010). However, there are differences in the estimated periods of lithospheric thinning. The estimates include 160–120 Ma (Wang et al., 2006), 162–125 Ma (Zhang et al., 2020), 155–123 Ma (Tang et al., 2015), 136–109 Ma (Zhang et al., 2011), and 135–90 Ma (Ji et al., 2021). Whether thickening occurred during the long period of lithospheric thinning from 162 to 90 Ma, and what the rates of thinning and/or thickening are outstanding questions.

Geodynamic models of lithospheric thinning include the subduction and suture of the Mongol–Okhotsk Ocean from the west (Wang et al., 2006), and the subduction of the Paleo-Pacific Plate from the east (Zhang et al., 2010; Zhang et al., 2011). It is generally recognized that the Mongol–Okhotsk tectonic regime ranges from the Siberian craton in the northwest to the Erguna–Xing'an–Songliao Blocks in the southeast (Tang et al., 2015; Li et al., 2018; Zhang et al., 2020), whereas the Paleo-Pacific tectonic domain ranges from Jiamusi Block in the southeast to the Songliao Block (Zhang et al., 2010; Guo et al., 2015; Wang et al., 2019), and even to the Erguna Block (Ji et al., 2021) in the northwest. This means that the lithospheric thinning and/or thickening of the Songliao Basin and the Great Xing'an Range during 162–90 Ma may have been influenced by the two-sided geodynamics of both the Mongol–Okhotsk Ocean from the west and the Paleo-Pacific Plate from the east. This raises the challenge of identifying the dominant geodynamic factor in a given period in this region that led to the lithospheric changes.

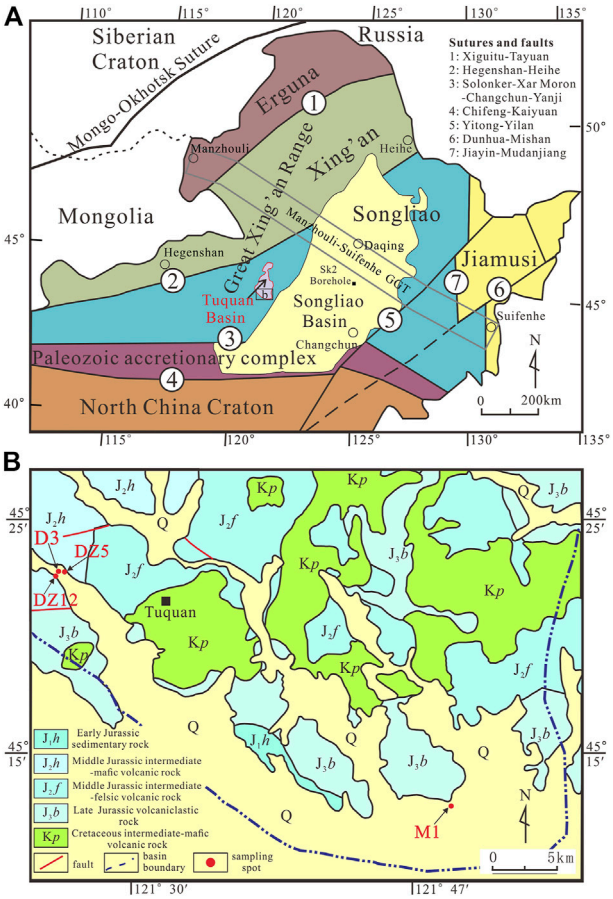

FIGURE 1 | (A) Tectonic subdivisions of northeastern China and the location of the Tuquan Basin (modified after Wu et al., 2011). GGT indicates Global Geosciences Transect. **(B)** Simplified geological map of the Tuquan Basin showing sample locations modified after Inner Jilin Bureau of Geology and Mineral Resources (1977).

We have discovered two types of lamprophyre intrusions—the biotite orthoclase lamprophyre (BOL) and the quartz magnetite lamprophyre (QML)—in the Tuquan Basin along the western margin of the Songliao Basin in northeast China. The BOL showed zircon U–Pb isotopic ages of 156.0 ± 2.3 Ma, whereas the QMLs showed zircon U–Pb isotopic ages of 132.9 ± 1.2 Ma and 126.2 ± 2.5 Ma. The petrologic and geochemical results presented in this paper indicate that the lamprophyres with these three ages recorded three different lithospheric thicknesses and corresponding geodynamic processes. They provide a reasonable constraint on the time limits of the Mongol–Okhotsk oceanic subduction, continental collision, and post-collisional extension, from the Siberian Craton via the Mongol–Okhotsk Suture Zone to the Songliao Block during the Late Jurassic through to the Early Cretaceous.

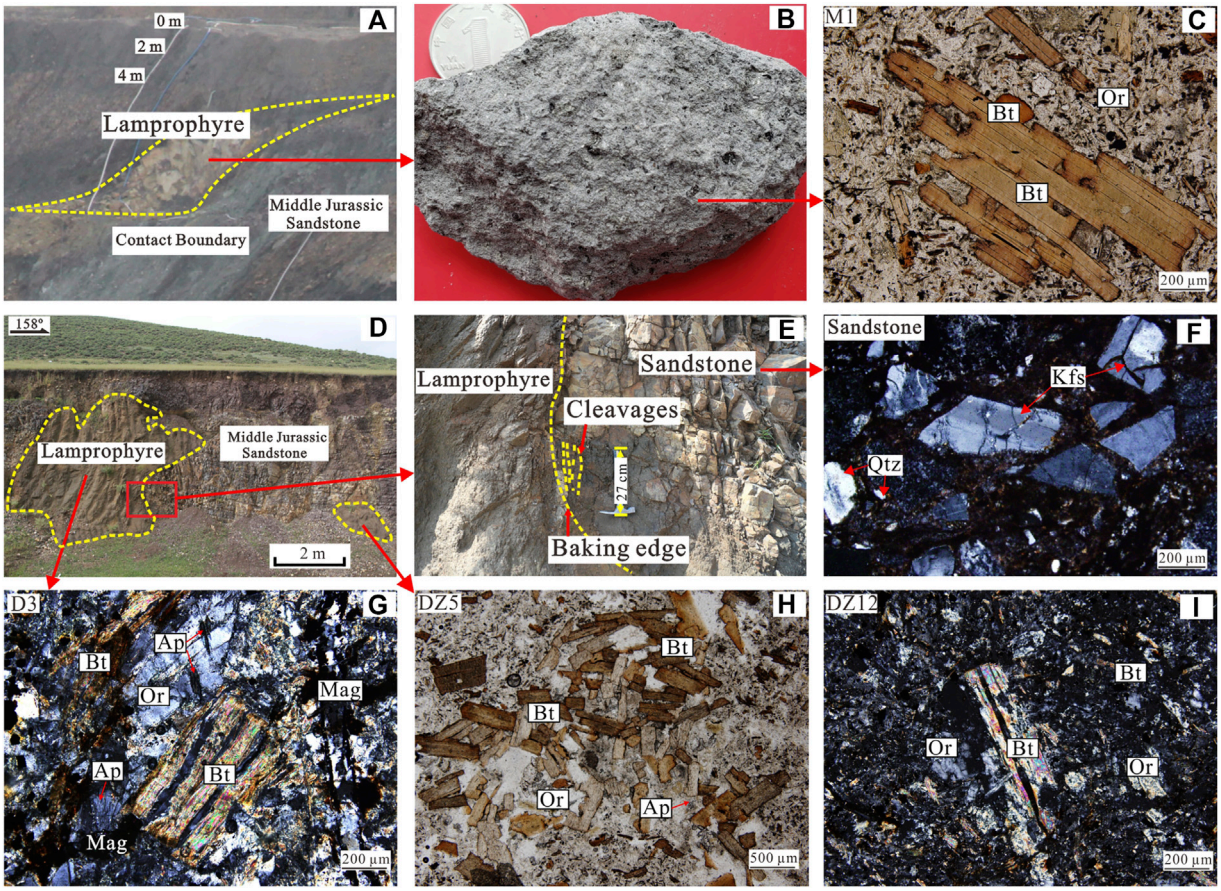

FIGURE 2 | Lamprophyre dikes of the Late Jurassic and the Early Cretaceous intruded in the Middle Jurassic sedimentary sequences. **(A,D)** Photographs of the lamprophyre dikes intruded into the Jurassic sandstone; **(B)** Photograph of the lamprophyre specimen; **(C)** Micro photograph of the Jurassic lamprophyre with typical lamprophyric texture, mainly composed of biotite and orthoclase (named as BOL in this paper); **(E)** The contact between the lamprophyre and the surrounding rock; **(F)** Micro photograph of the Jurassic sandstone intruded by lamprophyres, mainly composed of quartz and feldspar; **(G–I)** Micro photographs of the Cretaceous lamprophyres with typical lamprophyric texture, mainly composed of biotite, orthoclase, magnetite, apatite, and tiny quartz crystals (named as QMLs in this paper). Bt, biotite; Or, orthoclase; Ap, apatite; Mag, magnetite; Pl, plagioclase; Qtz, quartz; Kfs, k-feldspar.

2 GEOLOGICAL SETTINGS AND DESCRIPTION OF SAMPLES

The tectonic components of NE China include the Erguna Block, the Xing'an Block, the Songliao Block, and the Jiamusi Block (from NW to SE). They are separated by suture zones of Xiguitu–Tayuan, Hegenshan–Heihe, and Jiayin–Mudanjiang, respectively (**Figure 1A**; Wu et al., 2011; Liu et al., 2017). The Tuquan Basin of the study area is along the western margin of the Songliao Basin (**Figure 1A**). The outcropping strata in the Tuquan Basin are composed primarily of Jurassic sedimentary rocks and volcanic rocks that were intruded by mafic and intermediate dikes of the Late Jurassic and the Early Cretaceous. The lamprophyre samples examined (M1, D3, DZ5, and DZ12) appeared as a series of small and densely spaced intrusions into the sedimentary sequences from the Middle Jurassic (**Figure 1B**). Appearing in the form of dikes with thicknesses of approximately 2–6 m, the lamprophyres are generally distributed northeast in terms of orientation, with clear contact boundaries with the surrounding Jurassic sandstones (**Figures 2A,D**) that had been baked and cleaved at the contact surface between the lamprophyres and the surrounding rocks (**Figures 2E,F**). All the studied samples, numbered M1, D3, DZ5, and DZ12, were categorized as minette, a type of lamprophyre abundant in biotite and orthoclase, as described in Table 2.9 by Le Maitre (2002). **Table 1** summarizes their mineral composition and characteristics under a microscope, as shown in **Figure 2**.

3 ANALYTICAL METHODS

3.1 Zircon U–Pb Dating

Zircon crystals were extracted from whole-rock samples by combining magnetic and heavy liquid separation, and then handpicking them under a binocular microscope at the Langfang Regional Geological Survey in Hebei Province of China. All zircons were examined under transmitted and

TABLE 1 | Mineral composition and characteristics of lamprophyres under microscope.

Minerals	BOL (M1)			QMLs (D3, DZ5, and DZ12)		
	Content (%)	Grain size (mm)	Characteristic	Content (%)	Grain size (mm)	Characteristic
Biotite	60	0.10–1.50	Lam; Aci	40–50	0.10–1.10	Lam; Cru
Orthoclase	40	0.06–0.12	Mcr	25–35	0.01–0.63	Mcr; Ccr
Magnetite	<1	0.02–0.10	Mgr	10–30	0.02–0.30	Mgr; DDS
Apatite	<1	0.02–0.09	Aci	5	0.01–0.24	Aci; Col
Quartz	None	None	None	<1	0.01–0.05	Ccr; Mcr
Zircon	24 grain/kg	0.06–0.17	Mcr; Col	(34–40) grain/kg	0.05–0.13	Mcr; Col

Lam, lamellar; Aci, acicular; Col, columnar; Ccr, cryptocrystalline; Mcr, microcrystalline; Mgr, microgranular; Cru, crumpled; DDS, dense disseminated structure. Content (%) is area percentage.

reflected light micrographs with an optical microscope. To identify their internal structures, cathodoluminescence (CL) images were obtained using a JEOL scanning electron microscope. Grains of transparent, euhedral, unfractured, and inclusion-free zircons were chosen for isotopic analyses.

Zircon U–Pb analyses with a laser ablation–inductively coupled plasma mass spectrometer (LA–ICP–MS) were performed using an Agilent 7500a ICP–MS equipped with a 193-nm laser at the State Key Laboratory of Geological Processes and Mineral Resources, China University of Geosciences, Wuhan. Zircon 91500 was used as an external standard for age calibration, and NIST SRM 610 silicate glass was applied for instrument optimization. The diameter of the crater was 32 μm during the analyses. The parameters of the instrument and detailed procedures of their use have been described by Yuan et al. (2004). ICPMSDataCal (Ver. 6.7; Liu et al., 2010) and Isoplot (Ver. 3.0; Ludwig, 2003) were used for data reduction. Corrections were made for common Pb following Andersen (2002). Errors in individual LA–ICP–MS analyses were quoted at the 1σ level while errors in the pooled ages were quoted at a 95% (2σ) confidence level.

3.2 Geochemistry of Major and Trace Elements

Samples for geochemical analysis were crushed in an agate mill to a ~200 mesh after the removal of the altered surfaces. The major and trace element concentrations of the lamprophyre samples were determined at the Key Laboratory of Mineral Resources Evaluation in Northeast Asia (Ministry of National Resources of the People's Republic of China, Jilin University, Changchun, China). The major elements were analyzed using X-ray fluorescence (XRF; Rigaku ZSX Primu II) and fused glass disks. We determined the FeO content and the loss on ignition (LOI) values by volumetric and gravimetric methods, respectively. The trace elements were analyzed by using an Agilent 7500a ICP–MS, once the sample powders had been dissolved at high pressure in Teflon bombs. The analytical precisions of identification of the major and trace elements were higher than 1% and 5%, respectively, as determined by repeated analyses according to the USGS BHVO-1, BCR-2, and AGV-1 standards (Rudnick et al., 2004).

4 RESULTS

4.1 Zircon Characteristics and U–Pb Geochronology

Three lamprophyre samples (i.e., M1, D3, and DZ5) were each subjected to a zircon U–Pb dating analysis by using LA–ICP–MS. Colorless and transparent zircon crystals were selected for analysis. Consisting primarily of long and short columnar grains with diameters of 87–142 μm and length/width ratios of 1: 1–3: 1, the zircons displayed a relatively intact morphology with discernible edges and corners, and contained clear oscillatory zones along the edges. With a Th/U ratio greater than 0.2, the zircons were magmatic in origin (Hoskin and Schaltegger, 2003). Samples M1, D3, and DZ5 with older zircons also contained oscillatory growth zoning that was visible in CL imaging, and had Th/U values of 0.20–1.43, indicating that these zircons also had magmatic origins. They were likely to be inherited zircons derived from the subducted crust in the mantle source (Tarney and Jones, 1994). The results of dating are presented in **Table 2**.

A total of 25 zircons retrieved from sample M1 were dated using the U–Pb technique. The results (as shown in **Figure 3A**; **Table 2**) revealed relatively concordant $^{206}Pb/^{238}U$ and $^{207}Pb/^{235}U$ ratios, suggesting that the U–Pb system in the zircons had remained in a closed state and had not lost Pb after formation. Nine of the test points were concentrated near the age of 156 Ma. The $^{206}Pb/^{238}U$–$^{207}Pb/^{235}U$ concordia diagram yielded a concordant age of 156.0 ± 2.3 Ma (mean-squared weighted deviation (MSWD) = 2.1), representing the age of crystallization of the lamprophyre. In other words, the lamprophyre was formed in the Late Jurassic. The other 16 relatively old zircons were likely to have been inherited zircons within the sample.

A total of 27 zircons were tested for sample D3. The results (**Figure 3B**; **Table 2**) revealed relatively concordant $^{206}Pb/^{238}U$ and $^{207}Pb/^{235}U$ ratios, suggesting that the U–Pb system in the zircons had remained in a closed state and had not lost Pb after formation. Specifically, 13 test points were concentrated near 133 Ma. The $^{206}Pb/^{238}U$–$^{207}Pb/^{235}U$ concordia diagram yielded a concordant age of 132.9 ± 1.2 Ma (MSWD = 1.2), representing the age of crystallization of the lamprophyre and indicating that it had been formed in the Early Cretaceous. The other 14 relatively old zircons were likely to have been inherited zircons within the sample.

TABLE 2 | LA–ICP–MS U–Pb isotopic data for zircons from the lamprophyres in the Tuquan Basin.

Spot	Th/U	Contents ($\times10^{-6}$)			$^{207}Pb/^{206}Pb$		$^{207}Pb/^{235}U$		$^{206}Pb/^{238}U$		$^{207}Pb/^{206}Pb$		$^{207}Pb/^{235}U$		$^{206}Pb/^{238}U$	
		Pb	Th	U	Ratio	1σ	Ratio	1σ	Ratio	1σ	Age (Ma)	1σ	Age (Ma)	1σ	Age (Ma)	1σ
M1																
M1-1	0.70	20.26	130.28	186.31	0.051	0.0032	0.2062	0.0113	0.0301	0.0004	238.96	150.91	190.35	9.52	191.32	2.78
M1-2	0.65	11.98	73.19	111.98	0.0516	0.0033	0.2327	0.0133	0.0333	0.0006	333.39	143.50	212.46	10.92	211.42	3.63
M1-3	0.61	16.70	115.18	188.85	0.1187	0.0774	0.1736	0.024	0.0264	0.0006	1936.73	857.41	162.52	20.74	167.85	4.00
M1-4	0.35	11.08	71.96	207.11	0.0485	0.0026	0.1626	0.0081	0.0247	0.0004	120.46	122.20	152.96	7.09	157.16	2.44
M1-5	0.61	36.62	293.88	482.57	0.0501	0.0024	0.1655	0.0078	0.0242	0.0003	198.23	111.10	155.47	6.78	153.99	1.75
M1-6	0.56	22.84	163.89	293.33	0.0488	0.0023	0.1613	0.007	0.0243	0.0003	200.08	111.10	151.88	6.11	154.63	1.95
M1-7	1.12	50.32	170.89	153.26	0.0579	0.0033	0.4795	0.0278	0.0597	0.0007	524.11	130.54	397.71	19.05	373.67	4.29
M1-8	0.43	32.25	147.70	345.18	0.0515	0.0021	0.2496	0.0102	0.0351	0.0004	261.18	94.43	226.27	8.29	222.60	2.43
M1-9	0.37	2.02	10.82	29.02	0.0565	0.0087	0.1805	0.0256	0.0263	0.0009	472.27	347.02	168.53	22.01	167.50	5.78
M1-10	0.40	36.37	245.73	619.08	0.0499	0.0026	0.1639	0.0068	0.0244	0.0003	190.82	120.35	154.09	5.96	155.39	1.92
M1-11	0.20	30.25	108.94	553.56	0.0499	0.0019	0.2273	0.0093	0.0334	0.0007	190.82	88.88	208.01	7.70	211.79	4.38
M1-12	0.53	43.69	154.42	294.10	0.0529	0.0018	0.3632	0.0122	0.0499	0.0005	324.13	112.03	314.58	9.08	314.00	2.92
M1-13	0.03	9.08	11.86	421.22	0.0493	0.002	0.1859	0.0072	0.0275	0.0003	161.20	94.43	173.13	6.17	174.58	1.74
M1-14	0.43	110.24	472.25	1091.46	0.0509	0.0012	0.2764	0.0065	0.0393	0.0003	235.25	55.55	247.78	5.16	248.62	1.97
M1-15	0.53	17.03	131.87	250.79	0.0504	0.0029	0.1651	0.0085	0.0244	0.0004	213.04	131.46	155.14	7.40	155.48	2.25
M1-16	0.54	53.87	161.27	297.57	0.0486	0.0021	0.3256	0.015	0.0481	0.0005	127.87	103.69	286.20	11.48	303.11	3.21
M1-17	0.08	20.07	21.90	278.04	0.0134	0.0183	0.1709	0.0539	0.0251	0.0006	none	none	160.24	46.72	160.11	3.55
M1-18	0.83	91.92	244.21	294.54	0.0546	0.0021	0.5186	0.0188	0.0693	0.0007	394.50	87.03	424.25	12.61	432.21	4.04
M1-19	0.70	27.23	131.36	188.10	0.0524	0.0032	0.3001	0.0175	0.0421	0.0005	301.91	134.24	266.48	13.64	265.63	3.27
M1-20	0.37	29.39	128.96	344.69	0.0513	0.002	0.2565	0.0098	0.0365	0.0003	253.77	90.73	231.85	7.93	230.82	2.16
M1-21	0.60	31.46	133.65	222.80	0.0524	0.0023	0.3056	0.0129	0.0425	0.0004	305.62	127.76	270.80	10.05	268.31	2.76
M1-22	0.24	45.94	261.22	1097.77	0.0489	0.0014	0.1647	0.0047	0.0244	0.0002	146.38	68.51	154.84	4.09	155.42	1.30
M1-23	0.83	156.76	447.72	539.76	0.0552	0.0012	0.5363	0.012	0.0703	0.0006	420.42	54.63	436.01	7.93	438.24	3.54
M1-24	0.68	28.13	162.39	237.90	0.051	0.0026	0.2347	0.0121	0.0337	0.0005	238.96	118.50	214.08	9.96	213.90	3.40
M1-25	0.51	101.79	452.60	895.04	0.0884	0.0033	0.328	0.0099	0.0273	0.0004	1391.67	70.84	288.00	7.56	173.49	2.37
D3																
D3-1	0.86	68.63	636.62	757.93	0.0528	0.0019	0.156	0.0054	0.0213	0.0002	320.43	79.62	147.20	4.77	135.99	1.43
D3-2	0.37	3.52	33.65	90.23	0.0507	0.0058	0.1385	0.0131	0.0208	0.0005	233.40	244.42	131.72	11.64	133.02	3.24
D3-3	0.65	57.30	541.00	835.28	0.0494	0.0019	0.1379	0.0052	0.0203	0.0002	168.60	88.88	131.16	4.66	129.86	1.22
D3-4	0.73	25.46	232.75	335.33	0.0495	0.0025	0.1381	0.0064	0.0207	0.0003	172.31	115.73	131.32	5.73	131.97	1.66
D3-5	0.60	10.89	92.41	150.49	0.0506	0.0039	0.146	0.0093	0.0211	0.0004	220.44	179.61	138.34	8.20	134.56	2.24
D3-6	0.82	26.21	125.94	156.67	0.0571	0.0033	0.3116	0.0167	0.0399	0.0006	494.49	127.76	275.39	12.90	252.40	3.59
D3-7	0.47	21.20	131.67	282.82	0.0502	0.0024	0.1742	0.0073	0.0255	0.0003	205.63	104.62	163.06	6.31	162.02	2.08
D3-8	0.80	45.72	226.71	282.10	0.0521	0.0021	0.2821	0.0109	0.0396	0.0005	287.10	90.73	252.34	8.66	250.14	2.93
D3-9	0.63	30.40	145.84	230.39	0.0513	0.0024	0.2731	0.0121	0.0391	0.0005	253.77	109.24	245.20	9.62	247.35	2.86
D3-10	0.83	16.31	108.60	129.38	0.0515	0.0035	0.2023	0.0121	0.0292	0.0005	264.88	155.54	187.06	10.20	185.74	3.21
D3-11	0.38	65.39	273.01	601.07	0.0523	0.0049	0.2642	0.024	0.0395	0.001	298.21	208.31	238.03	19.25	250.03	6.46
D3-12	0.52	16.43	143.41	279.15	0.0499	0.0024	0.1435	0.0065	0.0209	0.0003	190.82	112.95	136.20	5.81	133.59	1.73
D3-13	0.41	9.36	73.33	176.07	0.0493	0.0032	0.1428	0.0085	0.0213	0.0003	161.20	148.13	135.51	7.52	135.64	2.18
D3-14	0.27	30.92	42.28	158.59	0.0607	0.002	0.8199	0.0266	0.098	0.001	627.80	72.21	607.97	14.85	602.75	5.77
D3-15	0.56	34.04	287.91	514.18	0.05	0.0022	0.1428	0.0058	0.0208	0.0002	194.53	99.99	135.52	5.19	132.87	1.45
D3-16	0.28	29.39	154.73	544.91	0.0499	0.0025	0.1845	0.009	0.0268	0.0003	190.82	113.87	171.90	7.72	170.65	2.02
D3-17	0.64	22.49	202.78	316.11	0.0487	0.0031	0.1408	0.0089	0.0209	0.0003	200.08	79.62	133.74	7.93	133.30	1.82
D3-18	0.75	24.95	125.97	177.65	0.0518	0.0027	0.2705	0.0133	0.0375	0.0005	275.99	120.35	243.08	10.67	237.20	2.90
D3-19	0.45	12.68	102.84	225.08	0.0495	0.0034	0.1392	0.0086	0.0206	0.0003	168.60	155.53	132.36	7.68	131.73	1.96
D3-20	0.45	35.01	103.41	260.37	0.0555	0.0022	0.4129	0.0157	0.0538	0.0006	435.23	88.88	350.96	11.30	338.11	3.58
D3-21	1.13	109.12	359.28	317.72	0.0624	0.0022	0.5186	0.0166	0.0601	0.0006	688.59	74.07	424.24	11.12	376.22	3.45
D3-22	0.85	71.82	657.08	793.46	0.0504	0.003	0.1437	0.0077	0.0209	0.0004	213.04	134.24	136.38	6.85	133.31	2.51
D3-23	0.48	9.43	73.41	152.82	0.0489	0.0035	0.1423	0.0094	0.021	0.0003	142.68	162.94	135.05	8.39	134.04	2.08
D3-24	0.41	63.75	143.97	353.19	0.0588	0.0017	0.5962	0.0171	0.0734	0.0007	566.70	60.18	474.81	10.89	456.58	4.46
D3-25	1.24	56.88	209.01	165.83	0.0563	0.0026	0.4051	0.0174	0.0529	0.0007	464.86	99.07	345.34	12.57	332.09	3.99
D3-26	1.43	88.34	914.13	636.22	0.0486	0.0022	0.1383	0.0061	0.0207	0.0002	127.87	109.24	131.52	5.41	132.34	1.44
D3-27	0.89	101.26	534.54	601.79	0.0511	0.0015	0.2627	0.0075	0.0371	0.0003	255.62	73.14	236.85	6.05	234.98	1.93
DZ5																
DZ5-1	0.60	10.89	92.41	150.49	0.0545	0.0013	0.3064	0.0084	0.0408	0.0011	392.00	50.39	271.40	6.50	257.70	6.51
DZ5-2	0.56	58.84	356.68	424.94	0.0663	0.0021	1.2407	0.0411	0.1358	0.0038	814.20	64.23	819.20	18.61	821.10	21.64

(Continued on following page)

TABLE 2 | (*Continued*) LA–ICP–MS U–Pb isotopic data for zircons from the lamprophyres in the Tuquan Basin.

Spot	Th/U	Contents (×10^{-6})			^{207}Pb/^{206}Pb		^{207}Pb/^{235}U		^{206}Pb/^{238}U		^{207}Pb/^{206}Pb		^{207}Pb/^{235}U		^{206}Pb/^{238}U	
		Pb	Th	U	Ratio	1σ	Ratio	1σ	Ratio	1σ	Age (Ma)	1σ	Age (Ma)	1σ	Age (Ma)	1σ
DZ5-3	0.60	10.89	92.41	150.49	0.0513	0.0017	0.1333	0.0047	0.0188	0.0005	255.10	74.48	127.10	4.18	120.30	3.31
DZ5-4	0.82	26.21	125.94	156.67	0.0559	0.0013	0.3124	0.0086	0.0405	0.0011	449.40	50.18	276.00	6.63	255.90	6.53
DZ5-5	0.63	30.40	145.84	230.39	0.054	0.0018	0.2855	0.0098	0.0384	0.0011	369.00	71.41	255.00	7.75	242.70	6.67
DZ5-6	0.83	16.31	108.60	129.38	0.0521	0.0017	0.1935	0.0066	0.0269	0.0008	290.60	71.90	179.60	5.63	171.20	4.72
DZ5-7	0.44	34.78	101.06	166.29	0.0515	0.0013	0.2307	0.0067	0.0325	0.0009	264.60	57.11	210.80	5.55	206.00	5.41
DZ5-8	0.52	16.43	143.41	279.15	0.051	0.0017	0.1466	0.0051	0.0208	0.0006	240.50	74.99	138.90	4.55	133.00	3.73
DZ5-9	0.41	9.36	73.33	176.07	0.053	0.0015	0.2593	0.0082	0.0355	0.001	328.30	64.22	234.10	6.62	224.80	6.08
DZ5–10	0.27	30.92	42.28	158.59	0.0561	0.0014	0.3749	0.0109	0.0484	0.0013	456.60	55.16	323.30	8.05	304.90	8.00
DZ5-11	0.56	34.04	287.91	514.18	0.0583	0.0014	0.3783	0.0107	0.047	0.0013	542.60	51.58	325.80	7.86	296.20	7.72
DZ5-12	0.28	29.39	154.73	544.91	0.0517	0.0017	0.1628	0.0058	0.0228	0.0007	273.10	75.33	153.10	5.03	145.50	4.10
DZ5-13	0.64	22.49	202.78	316.11	0.0521	0.0016	0.1986	0.0066	0.0277	0.0008	287.60	69.51	184.00	5.63	176.00	4.87
DZ5-14	0.45	12.68	102.84	225.08	0.0555	0.0016	0.3694	0.0116	0.0483	0.0013	430.00	62.15	319.20	8.62	304.20	8.23
DZ5-15	0.45	35.01	103.41	260.37	0.0506	0.0016	0.1748	0.0059	0.025	0.0007	224.20	71.77	163.60	5.12	159.40	4.45
DZ5-16	1.13	109.12	359.28	317.72	0.0495	0.0014	0.1626	0.0052	0.0238	0.0007	170.20	65.97	153.00	4.52	151.90	4.16
DZ5-17	0.85	71.82	657.08	793.46	0.0573	0.0015	0.6534	0.0191	0.0828	0.0023	501.10	55.38	510.60	11.72	512.50	13.41
DZ5-18	0.60	15.59	114.24	192.90	0.0491	0.0018	0.1323	0.005	0.0196	0.0006	151.50	82.58	126.20	4.47	124.90	3.59
DZ5-19	0.48	9.43	73.41	152.82	0.0487	0.0021	0.1314	0.0057	0.0196	0.0006	133.70	97.92	125.40	5.09	124.90	3.79
DZ5-20	0.41	63.75	143.97	353.19	0.051	0.0012	0.2802	0.008	0.0399	0.0011	238.30	55.26	250.80	6.37	252.20	6.67
DZ5-21	1.43	88.34	914.13	636.22	0.0524	0.0016	0.2372	0.0079	0.0328	0.0009	304.10	68.50	216.20	6.47	208.20	5.82
DZ5-22	0.62	65.73	128.75	205.98	0.1115	0.0029	4.9949	0.1446	0.325	0.0092	1823.70	45.71	1818.50	24.49	1814.30	44.72
DZ5-23	0.89	101.26	534.54	601.79	0.044	0.0024	0.1194	0.0063	0.0197	0.0007	0.10	17.80	114.50	5.74	125.60	4.12
DZ5-24	0.65	57.30	541.00	835.28	0.0526	0.0022	0.1649	0.0070	0.0227	0.0006	312.8	91.84	155	6.06	144.9	3.61
DZ5-25	0.73	25.46	232.75	335.33	0.0587	0.0019	0.1665	0.0056	0.0206	0.0005	555.7	68.41	156.4	4.85	131.3	3.17
DZ5-26	0.38	65.39	273.01	601.07	0.0571	0.0021	0.1580	0.0058	0.0201	0.0006	492.8	77.92	148.9	5.1	128.2	3.7
DZ5-27	0.80	45.72	226.71	282.10	0.0551	0.0022	0.1719	0.0070	0.0226	0.0007	415.1	87.56	161.1	6.06	144.3	4.26
DZ5-28	0.65	57.30	541.00	835.28	0.0587	0.0021	0.1543	0.0056	0.0191	0.0006	555.8	75.26	145.7	4.93	121.8	3.46

A total of 28 zircons were tested for sample DZ5. The results revealed relatively concordant ^{206}Pb/^{238}U and ^{207}Pb/^{235}U ratios, suggesting that the U–Pb system in the zircons had remained in a closed state and had not lost Pb after formation. The analysis of eight test points yielded a weighted mean age of 126.2 ± 2.5 Ma (MSWD = 1.6), representing the age of crystallization of the lamprophyre (**Figure 3C**; **Table 2**). The other 20, relatively old, zircons were likely to have been inherited zircons within the sample.

4.2 Major and Trace Element Contents

The results of the major and trace element analyses are listed in **Table 3**. The major element contents were normalized to 100% on an LOI-free basis before plotting them in diagrams. The petrography of these samples (as described above), combined with these geochemical data, enabled the division of the lamprophyre intrusions into two types. The Late Jurassic lamprophyre was found to consist primarily of biotite and orthoclase, and was thus referred to as the biotite orthoclase lamprophyre (BOL), while the Early Cretaceous lamprophyre was determined to predominantly comprise quartz and magnetite as accessory minerals, in addition to biotite and orthoclase, and was thus called the quartz magnetite lamprophyre (QML). For the BOL, three samples were collected from the dike with thicknesses of approximately 4–6 m (**Figure 2A**). All three samples were distributed northeast in terms of orientation, and had the same petrographic characteristics (**Table 1**). We selected M1 to represent the BOL for the major and trace element analyses.

4.2.1 Late Jurassic Lamprophyre (BOL)

The BOL (sample M1) had 56.06 wt.% of SiO_2 and a high content of total alkalis (Na_2O + K_2O) of 7.89 wt.%. It was classified as trachyandesite (Middlemost, 1994) (**Figure 4A**). In addition, its K_2O content was 5.54 wt.%, and it had a high K_2O/Na_2O ratio of 2.36. Because of this, it was plotted in the shoshonitic series (**Figure 4B**). The BOL had low contents of P_2O_5 (0.69 wt.%), CaO (1.78 wt.%), and F_2O_3 (1.72 wt.%), and high contents of MgO (4.81 wt.%), Na_2O (2.35 wt.%), FeO (4.43 wt.%), FeO^T (5.98 wt.%), Al_2O_3 (16.25 wt.%), and TiO_2 (1.51 wt.%). It had a Ti/Y ratio of 488 and an Mg# value of 58.92.

In the chondrite-normalized rare Earth element (REE) pattern (**Figure 5A**), the BOL was rich in light rare Earth elements (LREEs) [$(La/Yb)_N$ = 11.1] relative to heavy rare Earth elements (HREEs). No Eu anomaly was noted (Eu/Eu* = 1.00), and the ∑REE content was 173 ppm. In the primitive mantle-normalized spider diagram (**Figure 5B**), the BOL was rich in large-ion lithophile elements (LILEs; e.g., Ba, K, and Pb) and depleted in elements with a high field strength (HFSEs; e.g., Nb, Ta, and Ti).

4.2.2 Early Cretaceous Lamprophyres (QMLs)

The QML samples (D3, DZ5, and DZ12) had SiO_2 contents of 57.13–62.57 wt.% and high total alkali (Na_2O + K_2O) contents of 7.10–8.48 wt.%. They were classified as ranging from trachyandesite to trachyte (**Figure 4A**). They had K_2O contents of 1.93–4.88 wt.% and low K_2O/Na_2O ratios ranging from 0.37 to 1.60, which led to them being plotted in the shoshonitic to the high-K calc-alkaline and

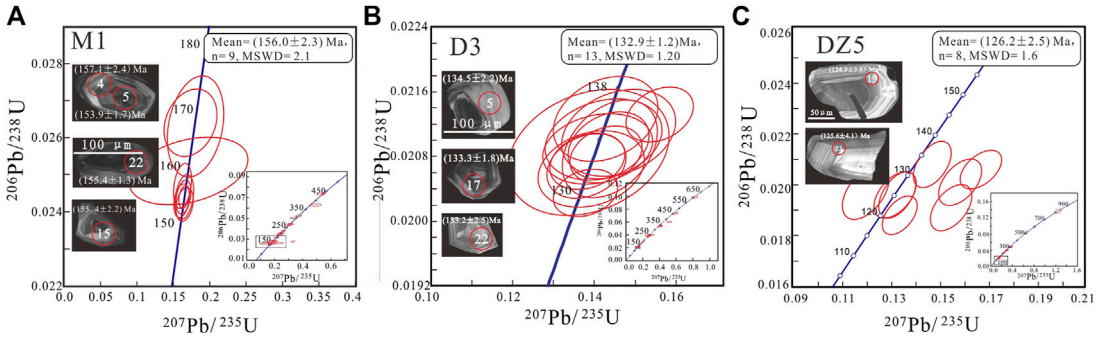

FIGURE 3 | LA–ICP–MS zircon U–Pb concordia diagrams for lamprophyres **(A)** M1, **(B)** D3, and **(C)** DZ5 in the Tuquan Basin. The insets show typical CL images of zircons with U–Pb ages.

calc-alkaline series (**Figure 4B**). The QMLs had low contents of P_2O_5 (0.56–1.09 wt.%), CaO (0.49–2.38 wt.%), and FeO (0.92–1.15 wt.%), and high contents of MgO (1.50–4.23 wt.%), Na_2O (3.05–5.17 wt.%), F_2O_3 (6.41–7.20 wt.%), FeO^T (6.92–7.40 wt.%), TiO_2 (1.34–1.53 wt.%), and Al_2O_3 (13.21–13.99 wt.%). They had a Ti/Y ratio of 203–349 and Mg# values of 27–52.

In the chondrite-normalized REE pattern (**Figure 5A**), the QML samples were rich in LREEs [$(La/Yb)_N$ = 34.4–39.0] relative to HREEs, featured Eu anomalies (Eu/Eu* = 0.88–0.93), and their ∑REE contents ranged from 361 to 694 ppm. In the primitive mantle-normalized spider diagram (**Figure 5B**), the QMLs were rich in LILEs (e.g., Ba, K, and Pb) and strongly depleted in HFSEs (e.g., Nb, Ta, and Ti).

5 DISCUSSION

5.1 Timing of Formation of the Lamprophyres

Zircons from the Late Jurassic lamprophyre (BOL) and Early Cretaceous lamprophyres (QMLs) exhibited striped absorption that was visible in the CL images, and is characteristic of zircons derived from mafic magmas. This magmatic origin is also supported by their relatively high Th/U ratios (0.2–1.43; Hoskin and Schaltegger, 2003). The U-Pb dating of these zircons should therefore yield the time of formation of the lamprophyres. The BOL (sample M1) yielded the youngest age of 156.0 ± 2.3 Ma, representing their time of formation. The QMLs (D3 and DZ5) yielded the youngest $^{206}Pb/^{238}U$ ages of 132.9 ± 1.2 and 126.2 ± 2.5 Ma, respectively, indicating the timing of formation of the lamprophyres. The Late Jurassic–Early Cretaceous ages were similar to those of the U-Pb dating (164–130 Ma) of high-K volcanic rocks in the Erguna–Xing'an–Songliao Blocks (Tang et al., 2015; Ji et al., 2021). They are also consistent with the results of U–Pb dating of Mesozoic intrusions and basalts in northeast China (Wang et al., 2006; Zhang et al., 2010; Wu et al., 2011; Zhang et al., 2011; Xu et al., 2013). The time of formation of the lamprophyres in the western Songliao Basin is therefore consistent with a widespread Late Jurassic–Early Cretaceous magmatic event that occurred in northeast China (**Figure 6**).

5.2 Petrogenesis

5.2.1 Alteration Effects

Before any inference can be made regarding the characteristics of the parental magma source of the lamprophyres, it is necessary to assess the possible effects of alteration on the whole-rock geochemical composition. The lamprophyre samples were characterized by variably high LOI values (2.58–4.60 wt.%), which indicates that they might have undergone low-grade metamorphism or variable degrees of alteration.

Because Zr and Th are considered to be the most immobile elements during low-grade alteration and metamorphism, they are preferred as an alteration-independent index of geochemical variation in igneous rocks. We used this to evaluate the mobility of other elements during alteration. The contents of HFSEs (such as Nb and Ta), LILEs (e.g., K and Rb), LREEs (e.g., La, Ce, and Nd), HREEs (such as Yb), and U were strongly correlated with Zr and Th (**Figure 7**) in the lamprophyre samples, which indicates that these elements were also essentially immobile during post-magmatic processes. The lamprophyre samples were characterized by subparallel patterns of elemental concentrations on chondrite- and primitive mantle-normalized trace element diagrams (**Figure 5**), which demonstrates the relative immobility of most elements at a whole-rock scale. Moreover, fresh lamprophyres may also have high LOI values (Rock, 1991). We conclude that post-magmatic processes had only minor effects on the chemical compositions of the studied samples, and high LOI values were intrinsic to the lamprophyres.

5.2.2 Effect of Continental Crustal Contamination

Before trying to assess the characteristics of the mantle source of these mafic dikes, it is important to consider the effects of crustal contamination that is also common in the generation of mantle-derived rocks. Evidence suggests that crustal contamination did not play a significant role in the petrogenesis of the lamprophyres. Such evidence includes the following: 1) The lamprophyres occurred as dike swarms, suggesting a rapid ascent through the crust. 2) The minerals in the lamprophyres were euhedral crystals, such as biotite and orthoclase. 3) The lamprophyres had incompatible elemental concentrations—for instance those of Sr (173–1506 ppm), Ba (616–1787 ppm), K_2O (1.93–5.54 wt.%), and Nd (30.2–137.4 ppm)—that were higher than those of the bulk

TABLE 3 | Major (wt.%) and trace element (ppm) compositions of the lamprophyres.

Lithology	BOL	QMLs		
Sample	M1	D3	DZ5	DZ12
Major element (wt.%)				
SiO_2	56.06	57.13	62.08	62.57
TiO_2	1.51	1.34	1.53	1.52
Al_2O_3	16.25	13.99	13.21	13.98
Fe_2O_3	1.72	6.41	7.20	6.63
FeO	4.43	1.15	0.92	1.08
FeO^T	5.98	6.92	7.40	7.05
MnO	0.06	0.11	0.10	0.14
MgO	4.81	4.23	2.16	1.50
CaO	1.78	2.38	1.17	0.49
Na_2O	2.35	3.05	5.17	4.91
K_2O	5.54	4.88	1.93	3.57
P_2O_5	0.69	1.09	0.95	0.56
LOI	4.60	3.90	3.17	2.58
Total	99.81	99.66	99.60	99.53
Mg#	58.92	52.13	34.23	27.51
$K_2O + Na_2O$	7.89	7.93	7.10	8.48
K_2O/Na_2O	2.36	1.60	0.37	0.73
Trace element (ppm)				
La	26.4	127.1	97.7	76.9
Ce	65.9	280.3	211.3	132.3
Pr	7.6	34.7	25.5	18.9
Nd	30.2	137.4	98.3	70.5
Sm	6.14	25.47	18.68	12.90
Eu	1.96	7.20	5.02	3.46
Gd	5.64	20.55	15.11	9.84
Tb	0.79	2.27	1.77	1.18
Dy	4.00	9.57	7.97	5.40
Ho	0.76	1.50	1.26	0.89
Er	1.98	3.45	2.97	2.08
Tm	0.28	0.44	0.35	0.25
Yb	1.70	2.34	2.03	1.55
Lu	0.27	0.36	0.29	0.22
Rb	73.4	101.3	14.5	28.3
Ba	991	1787	616	1167
Th	7.55	21.03	20.64	15.71
U	2.39	4.86	5.45	4.57
Nb	19.6	19.8	22.9	23.2
Ta	1.36	1.54	0.83	0.83
K	45.765	40.313	15.943	29.491
Pb	11.64	28.91	39.68	31.07
Sr	173	1506	501	599
P	3012	4757	4146	2444
Zr	455	503	580	593
Hf	14.18	14.07	15.11	15.30
Sc	10.88	15.27	14.29	12.62
V	160.0	162.7	170.6	163.8
Cr	166.5	126.1	31.2	23.8
Co	22.5	23.9	17.7	15.5
Ni	94.1	54.8	23.7	19.8
Ga	20.0	22.0	19.5	17.5
Y	19.6	41.9	38.2	25.4
Cs	1.00	3.59	2.20	3.41
δEu	1.00	0.93	0.88	0.90
$(La/Yb)_N$	11.15	39.01	34.48	35.59
∑REE	173.15	694.54	526.35	361.73
Rb/Sr	0.42	0.06	0.02	0.04

(Continued in next column)

TABLE 3 | (*Continued*) Major (wt.%) and trace element (ppm) compositions of the lamprophyres.

Lithology	BOL	QMLs		
Sample	M1	D3	DZ5	DZ12
Ba/Rb	13.5	17.6	42.6	41.2
Dy/Yb	2.35	4.09	3.92	3.48
K/Yb*1000	28.3	17.9	8.13	19.63

Note: *FeO^T = FeO+0.8998*Fe_2O_3. LOI, loss on ignition. Mg# = 100× molar Mg/(Mg + Fe^T). δEu = $Eu_N/(Sm_N \times Gd_N)^{0.5}$. REE, rare earth elements.*

continental crust (average abundances of Sr, Ba, K_2O, and Nd in the crust were 320 ppm, 456 ppm, 1.81 wt.%, and 20 ppm, respectively; Rudnick and Gao, 2003). 4) The lamprophyres had Nb/Ta (12.8–27.4) and Zr/Hf (32.1–38.7) ratios similar to those of the primitive mantle (17.5 ± 0.2 and 36.27 ± 2.0, Taylor and McLennan, 1985), and much higher than those of the continental crust (11 and 33, Taylor and McLennan, 1985). 5) The Lu/Yb ratios are considered to be an indicator of crustal contamination. The continental crust was characterized by high Lu/Yb (0.16–0.18) ratios while mantle-derived magmas had low Lu/Yb (0.14–0.15) ratios (Sun and McDonough, 1989). The low Lu/Yb (0.14–0.15) ratios of the lamprophyres were similar to those of the mantle-derived magmas, thus ruling out the prospect of noticeable crustal contamination. 6) Fifty-four concordant analyses of the rocks of the walls, e.g., the Jurassic sedimentary rocks. yielded two age populations at 160.0–185.4 Ma (n = 47) and 222.1–274 Ma (n = 7) (unpublished LA–ICP–MS U-Pb data). Eighty concordant analyses of the lamprophyres yielded six age populations at 120.3–144.9 Ma (n = 23), 145.5–160.1 Ma (n = 10), 162.0–185.5 Ma (n = 9), 191.3–296.2 Ma (n = 23), 303.1–376.2 Ma (n = 8), and 432–1832.7 Ma (n = 7). The youngest analyses yielded ages of the lamprophyres lower than those of the Jurassic sedimentary rocks. In addition, nine analyses of the lamprophyres yielded ages of 162.0–185.5 Ma, much lower than those of the Jurassic sedimentary rocks, which yielded ages of 160.0–185.4 Ma over 47 analyses. These results suggests that the youngest ages of the lamprophyres can represent their age of formation, and crustal contamination did not play a major role in this process.

5.2.3 Magma Sources and the Nature of the Lamprophyre

Mafic rocks are generally considered to be mantle-derived melts. In particular, lamprophyres are considered to be the products of the partial, low-degree melting of the enriched subcontinental lithosphere mantle (Rock, 1987; Gibson et al., 2006; Choi et al., 2020). The lamprophyres in the Tuquan Basin are characterized by high contents of FeO^T, MgO, and TiO_2, high Mg# values, strong fractionation between LREEs and heavy (H) REEs, LILE enrichment, and HFSE depletion. These geochemical signatures are similar to those of contemporaneous arc-like mafic rocks for which the magmas were interpreted to have originated from the lithospheric mantle source (Tang et al., 2015; Zhang et al., 2020; Ji et al., 2021). Moreover, the Lu/Yb ratios of the BOL and QML

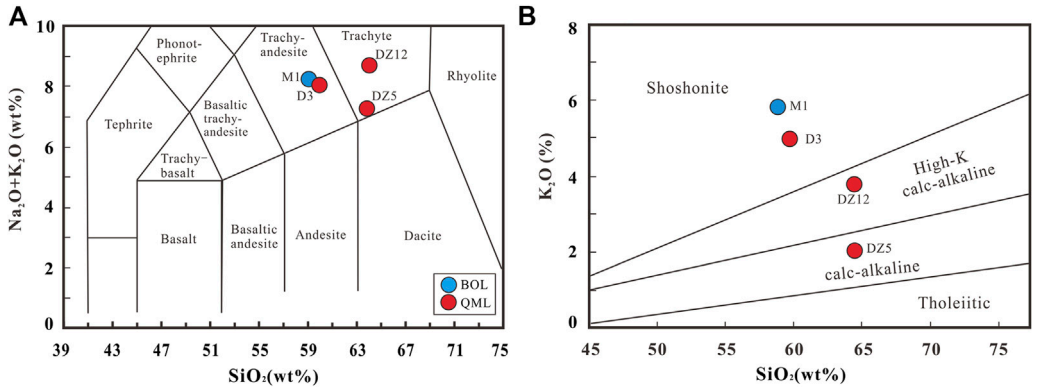

FIGURE 4 | (A) SiO_2 vs. ($Na_2O + K_2O$) classification diagram (modified after Middlemost, 1994). **(B)** SiO_2 vs. K_2O Diagram (after Peccerillo and Taylor, 1976) of the lamprophyres in the Tuquan Basin.

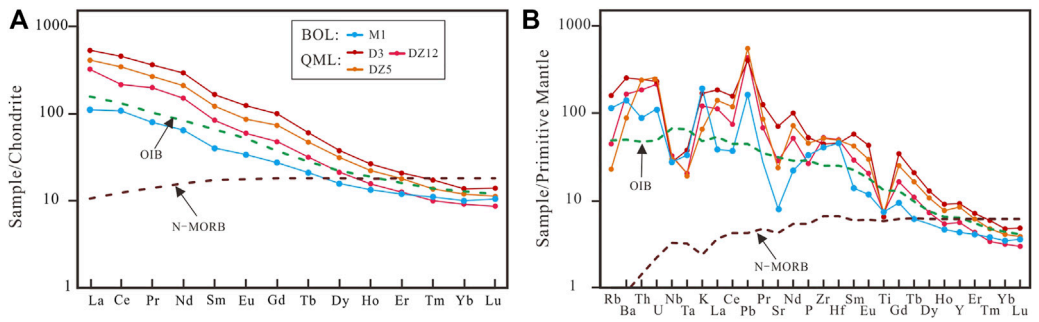

FIGURE 5 | (A) chondrite-normalized REE pattern and **(B)** primitive mantle-normalized spider-diagram of the lamprophyres in the Tuquan Basin. Data sources: chondrite (Sun and McDonough, 1989), primitive mantle (Sun and McDonough, 1989), N-MORB, and OIB (Sun and McDonough, 1989).

samples, ranging from 0.14 to 0.15, were similar to the range for mantle magmas (0.14–0.15, Sun and McDonough, 1989) rather than the continental crust (0.16–0.18, Sun and McDonough, 1989). The BOL and QML samples exhibited low ratios of Zr/Ba (0.28–0.94), and high ratios of La/Ta and La/Nb (9.33–117.26 and 1.34–6.43, respectively), close to the ratios of the region of the lithospheric magma source (Thompson and Morrison, 1988; Menzies et al., 1991). The BOL and QML samples had high Sr contents (173–1506 ppm) and lacked significant Eu anomalies ($Eu/Eu^* = 0.88–1.00$), indicating that they had originated from a mantle source (Rapp and Watson, 1995). In addition, the high LREE/HREE ratios of the lamprophyre samples are often assumed to be caused by the partial melting of a metasomatized lithospheric mantle (Guo et al., 2004). Furthermore, the trace element compositions of the lamprophyres were neither Mid-Ocean Ridge Basalt (MORB) like nor Ocean Island Basalt (OIB) like, indicating that the lamprophyres had not derived from MORB- or OIB-type sources within the asthenospheric mantle (Sun and McDonough, 1989).

In terms of the pattern of distribution of the trace elements, the BOL and QML samples were rich in LREEs and LILEs and depleted in HREEs and HFSEs (Nb, Ta, and Ti), suggesting that the magmas had derived from an enriched lithospheric mantle that had previously been modified by interaction with subducted slab material (Tarney and Jones, 1994). The BOL and QML samples exhibited relatively high ratios of Ba/Nb, Ba/Ta, and Ba/Th (26.93–90.43, 726.46–1398.27, and 29.84–84.97, respectively), and a low ratio of La/Sm (4.99–5.95), suggesting that a subduction-modified continental lithospheric mantle had been involved in the magma source for the lamprophyres (Fitton et al., 1988; Genç and Tüysüz, 2010).

The characteristics of the trace element of the samples in **Figure 8** show that the sources of the lithospheric mantle of the BOL and QMLs were formed at an active continental margin, and had been previously metasomatized by subduction-related fluids. The Ba/Nb vs. La/Nb diagram in **Figure 8A** indicates that the lamprophyres showed lithologic affiliation to the volcanic arc. The Th/Yb vs. Ta/Yb diagram in **Figure 8B** shows the characteristics of the lamprophyres formed at an active continental margin. The Th/Y vs. Sm/Th diagram in **Figure 8C** shows that the BOL and QML lamprophyres originated from an enriched lithospheric mantle. Slab-

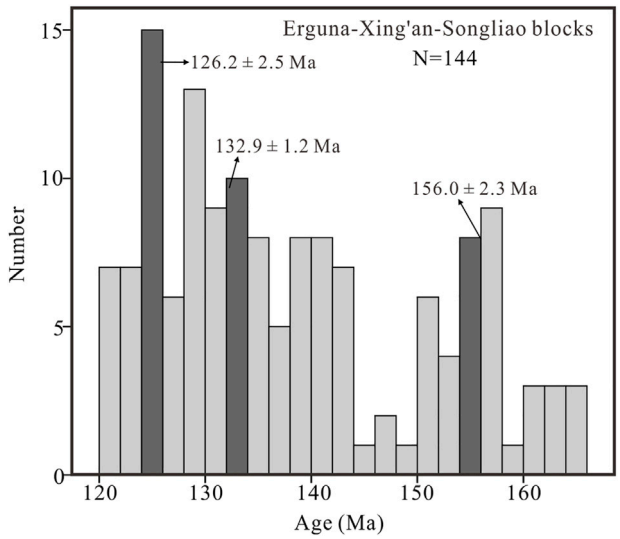

FIGURE 6 | Histogram of the U–Pb ages of zircons from Mesozoic igneous rocks in the Erguna-Xing'an-Songliao Blocks. Age data sources: Wang et al., 2006; Zhang et al., 2010; Wu et al., 2011; Tang et al., 2015; Li et al., 2018; Ji et al., 2020, 2021 and this study.

released fluids or melts would have metasomatized the overlying lithospheric mantle and led to them being rich in LILE elements, such as K, Sr, and Pb. As shown in **Figure 8D**, the BOL and QML samples exhibited Nb/U ratios of 8.2 and 4.0–5.0, respectively. These values are significantly lower than those of the MORB (47 ± 10, Hofmann et al., 1986) and the OIB (47 ± 10, Hofmann et al., 1986). They are also lower than the values of the upper crust (9, Taylor and McLennan, 1985) and the lower crust (21, Taylor and McLennan, 1985). However, the Nb/U values of the lamprophyres were similar to those of the subduction zone-related hydrous fluids and the global average for subducted sediments (Nb/U = 5, Plank and Langmuir, 1998). These results suggest that the lamprophyres recorded the fluid-related metasomatism of the region of their lithospheric mantle source as a result of subduction (Hofmann, 1997). The Ba/Th vs. La/Sm diagram in **Figure 8E** shows that the mantle source was primarily influenced by slab dehydration (Genç and Tüysüz, 2010). Some HFSEs signatures can be used to distinguish between the roles of fluids and melts as metasomatizing agents (Polat and Hofmann, 2003). The BOL and QMLs had low ratios of Th/Zr (0.01–0.04) and Nb/Zr (0.03–0.04) (**Figure 8F**), indicating that the magma source had been affected by the metasomatism of the fluid.

5.2.4 Source Mineralogy and Depth

The Late Jurassic BOL and Early Cretaceous QML samples had high K_2O contents and were rich in LILEs. The volatility-enriched minerals, such as amphiboles and phlogopites, were the primary host minerals for K and LILEs in the lithospheric mantle (Foley et al., 1996; Ionov et al., 1997). Melts in equilibrium with amphibole in the source were expected to have a significantly low Rb/Sr ratio (0.1) and a high Ba/Rb ratio (>20), whereas melts from a phlogopite-containing source region had a relatively high Rb/Sr ratio (>0.1) and a low Ba/Rb ratio (<20) (Furman and Graham, 1999; Ma et al., 2014). The BOL exhibited a high Rb/Sr ratio of 0.42 (>0.1) and a low Ba/Rb ratio of 13.5 (<20), indicating that it had involved a magma source of phlogopite-containing, enriched lithospheric mantle (**Figure 9**). The QML samples had a low Rb/Sr ratio of 0.02–0.06 (<0.1) and a high Ba/Rb ratio of 17.6–42.6 (on average, 33.8), indicating a magma source from an amphibole-containing and enriched lithospheric mantle (**Figure 9**).

The K/Yb vs. Dy/Yb diagram can be used to constrain regions of the magma source and the degree of partial melting, and to distinguish between partial melting in the spinel and the garnet stability fields of a phlogopite- and/or amphibole-bearing lherzolite (Duggen et al., 2005). Melts formed from partial melting had relatively high and low Dy/Yb ratios (>2.5 and <1.5, respectively) in the stable areas for garnet and spinel, respectively (Duggen et al., 2005). The K/Yb ratio corresponds to the degree of partial melting. The BOL sample had a Dy/Yb ratio of 2.35 and a K/Yb*1000 ratio of 28.3. The projected point of the BOL sample fell between the curves of partial melting of garnet-facies phlogopite lherzolite and spinel-facies lherzolite, corresponding to a degree of melting of 10% (**Figure 10A**) and implying that the partial melting had likely occurred in the spinel–garnet transition zone. In the REE melting model for mantle peridotites (**Figure 10B**), the projected point of the BOL sample was found to fall on the curve of a mixture of garnet peridotite and spinel peridotite at a ratio of 7:3. The QML samples exhibited Dy/Yb ratios of 3.48–4.09 and K/Yb*1000 ratios of 8.13–19.63. Their projected points fell between curves of partial melting of garnet-facies lherzolite and garnet-facies amphibole lherzolite, corresponding to degrees of melting of 1%–3.5% (**Figure 10A**). In the REE melting model for mantle peridotites (**Figure 10B**), the projected points of the QML samples were found to fall on the curves for garnet peridotite and spinel peridotite mixed at different ratios (proportion of garnet >90%).

What is the mechanism driving the melting of the mantle at different depths? The upwelling of the asthenosphere triggers the decompression-induced melting of the mantle (McKenzie and Bickle, 1988). Conditions for the contemporaneous partial melting of the mantle at different depths can be satisfied if the top of the asthenosphere window reaches a certain depth (Luo et al., 2006). The thickness of the lithosphere controls this depth, and thus limits the extent of decompression-induced melting and equilibrium pressure/depth of the melt extraction, i.e., the lid effect (Ellam, 1992; Niu, 2021). Experiments have shown that the minimum pressure at which garnet is stable on the anhydrous solidus of fertile peridotite is 2.8 GPa, corresponding to a depth of about 85 km (Robinson and Wood, 1998). The maximum depth of the spinel–garnet transition zone is 60–70 km (McKenzie and O'Nions, 1991; Klemme and O'Neill, 2000). The above analyses were used to plot the melting curves of the BOL and the QML samples for lherzolite (**Figure 10B**). They have relatively low and high garnet/spinel ratios (<2.3 and >9, respectively). We suggest that the BOL (156.0 ± 2.3 Ma) was likely derived from the high-degree partial melting of the phlogopite-bearing lherzolite mantle

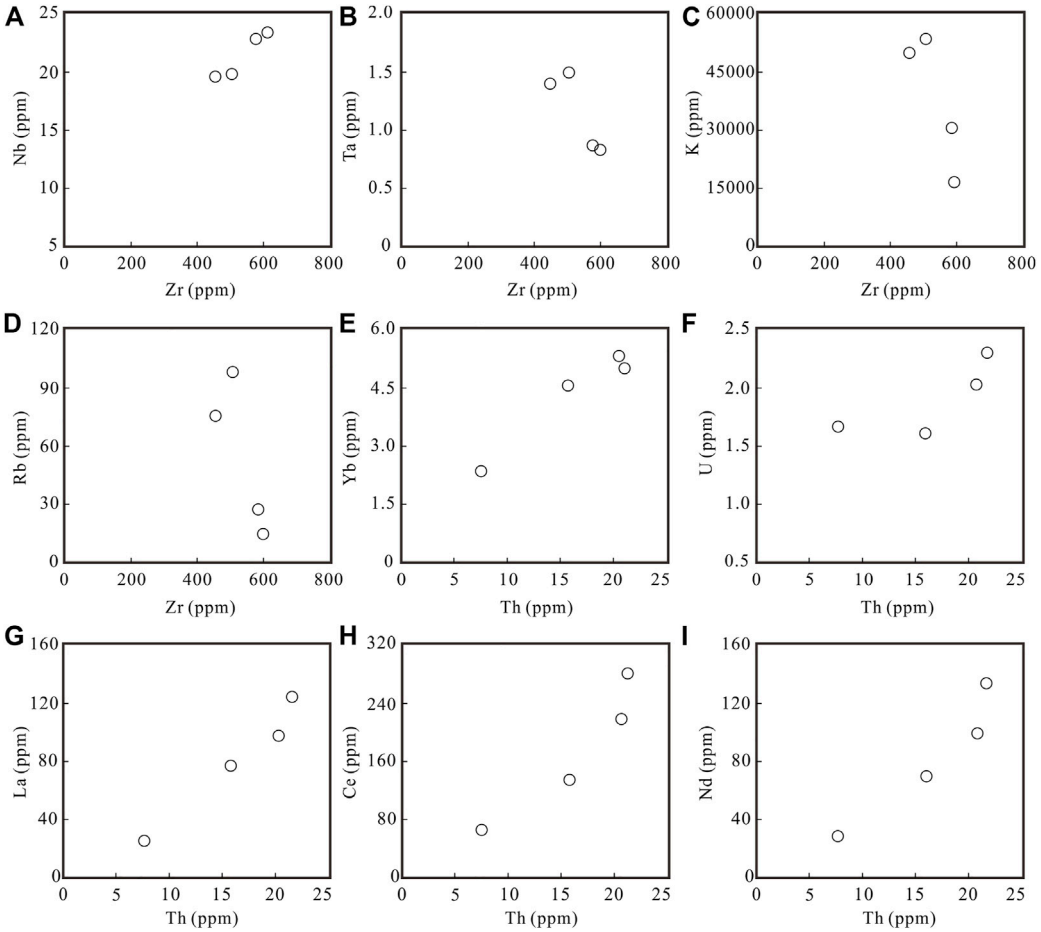

FIGURE 7 | Diagrams showing variations of selected elements **(A)** Nb, **(B)** Ta, **(C)** K, **(D)** Rb vs. Zr and **(E)** Yb, **(F)** U, **(G)** La, **(H)** Ce, **(I)** Nd vs. Th in the lamprophyre samples to check for element mobility during post-magmatic alteration.

in the spinel–garnet transition zone at a depth of about 60 km. The older QML (132.9 ± 1.2 Ma) was likely derived from the low-degree partial melting of the lherzolite mantle in the garnet zone at a depth of ca. 85 km. The younger QML (126.2 ± 2.5 Ma) had lower Dy/Yb ratios (3.48–3.92) than the older QML (132.9 ± 1.2 Ma), with a Dy/Yb ratio of 4.09 implying that the younger magma had been produced at a shallower depth of the mantle (<85 km) than the older one. Thus, from 156 Ma to 132 Ma, the lithosphere in the study area thickened by approximately 25 km at a rate of approximately 1.0 km/Myr.

5.3 Geodynamics

5.3.1 Changes in the Thickness of the Lithosphere

The Manzhouli–Suifenhe geoscience transect in northeast China, which is part of the Global Geoscience Transect (GGT) Project, extends from Manzhouli in the west to Suifenhe in the east over a distance of 1300 km, and passes through the Great Xing'an Range and the Songliao Basin (see **Figure 1**).

Data on deep seismic reflections, and gravitational and magnetic data of the GGT (Yang et al., 1996) shows that the crust and lithosphere in NE China are 30–40 and 55–110 km thick at present, respectively. The thickness of the lithosphere in the Songliao Basin ranges from 55 km (in Daqing and Anda at the center of the basin) to 110 km (at the eastern margin of the basin in Shangzhi). The lithosphere in the Great Xing'an Range is 76–90 km thick, and is 80 km thick in the Tuquan Basin (**Figure 11**).

The depths at which the magmas of the BOL and QMLs originated in the Tuquan Basin, as calculated in this study, show that the lithospheric thickness in NE China thickened from 156.0 ± 2.3 Ma to 132.9 ± 1.2 Ma and then thinned from 132.9 ± 1.2 Ma to 126.2 ± 2.5 Ma (**Figure 12**). The thickness of the lithosphere in this period fluctuated within a range of magnitude that it has at present.

5.3.2 Cause of the Thickening of the Lithosphere

During the Late Mesozoic, the tectonics of the study area were involved in both the subduction of the Paleo-Pacific plate beneath the Eurasian continental margin (Guo et al., 2015; Wang et al., 2019) and tectonic events related to the Mongol–Okhotsk Suture Zone (Tang et al., 2015; Liu et al., 2018).

In the Erguna and Xing'an Blocks volcanic rocks from the Early-to-Middle Jurassic (193–164 Ma) are thought to have

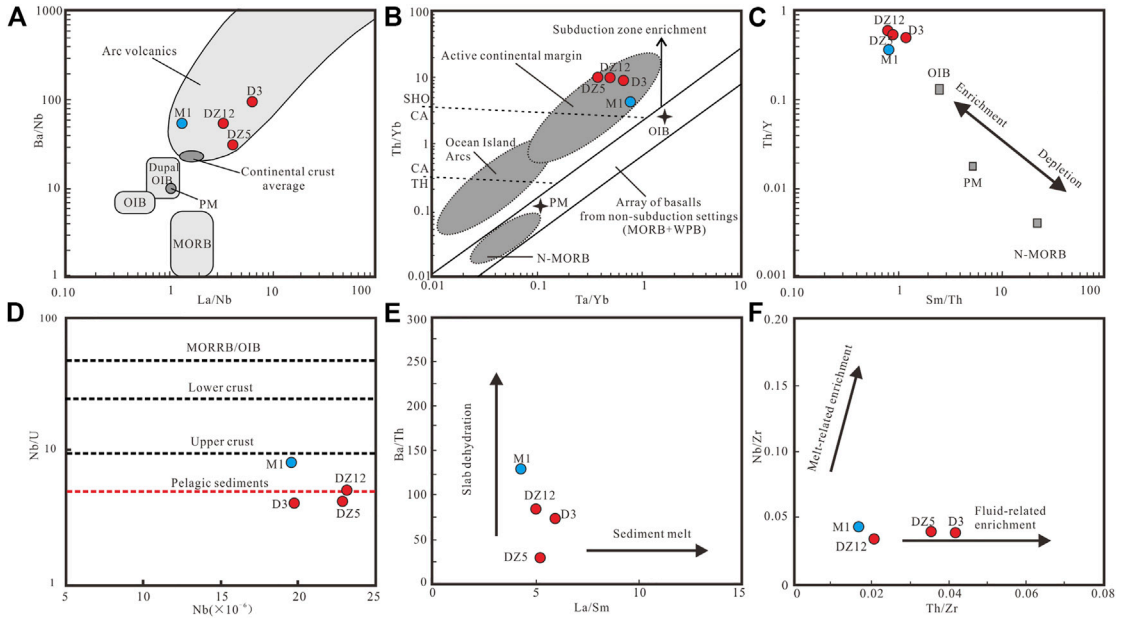

FIGURE 8 | Plot of **(A)** Ba/Nb vs. La/Nb (after Niu et al., 2017). **(B)** Th/Yb vs. Ta/Yb (after Pearce, 1983). **(C)** Th/Y vs. Sm/Th (after Su et al., 2012), the reference fields for primitive mantle (PM), OIB, and N-MORB are from Sun and McDonough (1989). **(D)** Nb/U vs. Nb diagram for the lamprophyres in the Tuquan Basin. Data sources: MORB and OIB (Hofmann et al., 1986), lower and upper crust (Taylor and McLennan, 1985), pelagic sediments (Plank and Langmuir, 1998). **(E)** Ba/Th vs. La/Sm (after Labanieh et al., 2012). **(F)** Nb/Zr vs. Th/Zr (after Kepezhinskas et al., 1997). Abbreviations are as follows: WPB, within-plate basalts; N-MORB, normal mid-ocean ridge basalts; OIB, ocean island basalts; MORB, mid-ocean ridge basalts; PM, primitive mantle; TH, tholeiitic; CA, calc-alkaline; SHO, shoshonitic.

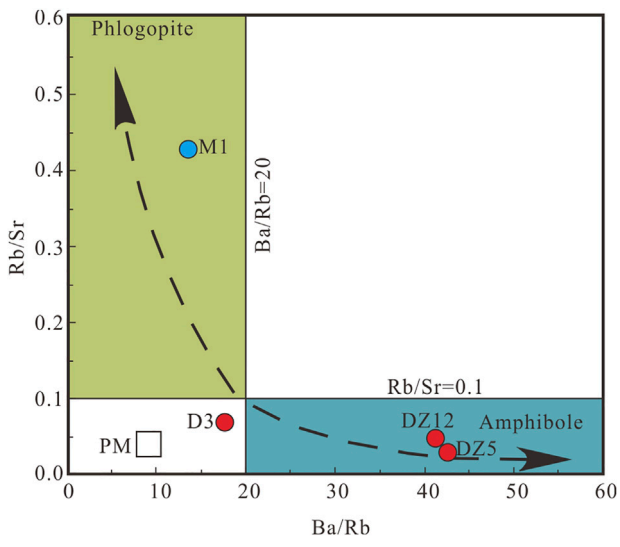

FIGURE 9 | Rb/Sr vs. Ba/Rb diagram (see e.g., Furman and Graham, 1999).

been formed in an active continental margin setting related to the southward subduction of the Mongol–Okhotsk Oceanic plate (Xu et al., 2013; Wang et al., 2015). In the Jiamusi and Songliao Blocks, volcanic rocks from the Early-to-Middle Jurassic (194–174 Ma) have been thought to have formed in an intraplate extensional setting related to the westward subduction of the Paleo-Pacific plate (Guo et al., 2015; Huang et al., 2021). There was a remarkable reduction in magmatic activity during the Late Jurassic and the Early Cretaceous (173–133 Ma) in the Jiamusi and Songliao Blocks (Xu et al., 2013; Ji et al., 2019), suggesting that subduction-related igneous activities in the Paleo-Pacific plate were waning in this period. By contrast in the Erguna and Xing'an Blocks, volcanic rocks from the Late Jurassic and the Early Cretaceous (164–124 Ma) are widely distributed (Zhang et al., 2010; Ji et al., 2021). They are related to the combined effects of the Paleo-Pacific and Mongol–Okhotsk tectonic regimes (Ouyang et al., 2015; Li et al., 2018). The question is: which of them in this region was dominant in terms of geodynamics during the Late Jurassic and the Early Cretaceous?

Based on the results of this study, we propose that the Mongol–Okhotsk tectonic regime was most likely responsible for the generation of the lamprophyres, in that space and time were coupled between the formation of lamprophyre and the tectonic event of the Mongol–Okhotsk Suture Zone. The study area is located less than 500 km from the Mongol–Okhotsk Suture (**Figure 1A**), and the closure of the Mongol–Okhotsk Ocean occurred mainly during the Jurassic and ended during the Early Cretaceous (Cogné et al., 2005; Metelkin et al., 2010). The BOL from the Late Jurassic and the QMLs from the Early Cretaceous are shoshonite and calc-alkaline in series, and were formed in an active continental margin and derived from the partial melting of an enriched lithospheric mantle that had been previously metasomatized by subduction-related fluids. In addition, these lamprophyres were coeval with the Late Jurassic and the Early Cretaceous volcanic rocks in the Erguna

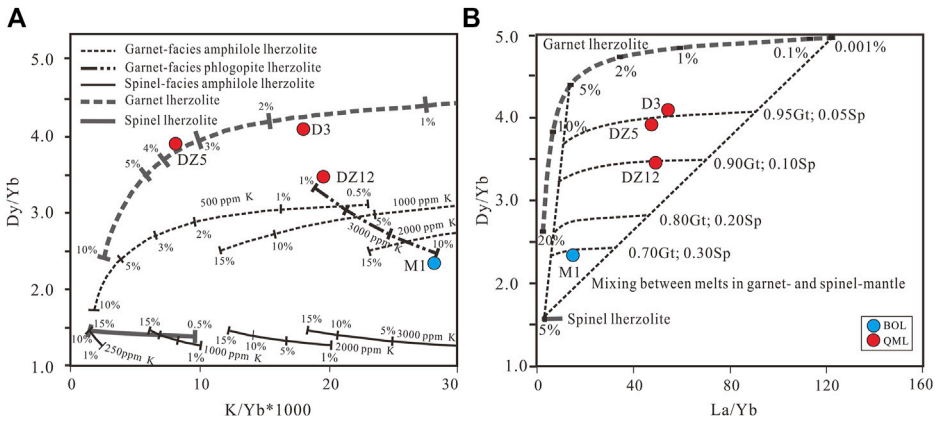

FIGURE 10 | (A) Plot of K/Yb vs. Dy/Yb for lamprophyres in the Tuquan Basin. Melting curves for garnet lherzolite, spinel lherzolite, garnet-facies phlogopite lherzolite, garnet-facies amphibole lherzolite and spinel-facies amphibole lherzolite are taken from Duggen et al. (2005). **(B)** La/Yb vs. Dy/Yb in lherzolite REE melting model is from Thirlwall et al. (1994), partition coefficients are from McKenzie and O'Nions (1991).

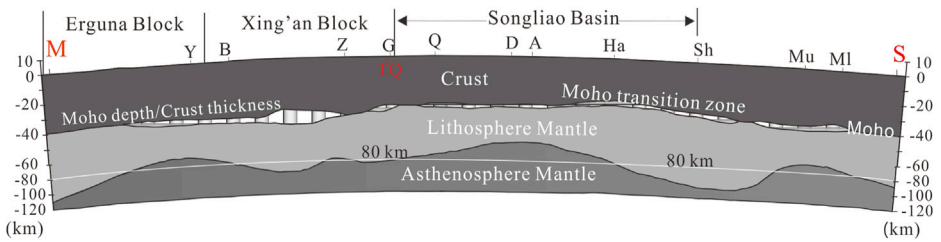

FIGURE 11 | Underlying crust and lithospheric and asthenospheric mantle of the Songliao Basin along the GGT (according to Wang et al., 2016). Cities: M, Manzhouli; Y, Yakeshi; B, Boketu; Z, Zhalantun; TQ, Tuquan; G, Gannan; Q, Qiqihaer; D, Daqing; A, Anda; Ha, Harbin; Sh, Shangzhi; Mu, Mudanjiang; Ml, Muling; S, Suifenhe.

and Xing'an Blocks, which are thought to be related to the Mongol–Okhotsk tectonic regime (Xu et al., 2013; Tang et al., 2015). The collision associated with the closure of the Mongol–Okhotsk Ocean could have caused lithospheric thickening between the Siberia and the Mongolia-China Blocks (Metelkin et al., 2010). The BOL (156.0 ± 2.3 Ma) recorded the lithospheric thickness at about 60 km and the QML (132.9 ± 1.2 Ma) recorded it at 85 km. Thus, in the period 156–132 Ma, the lithosphere in the study area thickened by approximately 25 km (**Figure 12**). It is widely believed that the delamination of a thickened lithosphere could have caused the lithosphere thinning in NE China (Wang et al., 2006; Zhang et al., 2010; Wu et al., 2011). The younger QML (126.2 ± 2.5 Ma) recorded a thinner lithosphere (< 85 km), suggesting that the lithosphere in NE China thinned from 132.9 ± 1.2 Ma to 126.2 ± 2.5 Ma.

We used the results of this study to create a three-stage model of geodynamic evolution in NE China from 156 Ma to 126 Ma, as shown in **Figure 13**. Stage A: This consisted of the southeastward subduction of the Mongol–Okhotsk oceanic crust under the counterpart continental crust, and suturing, between the Siberian craton in the northwest and the Erguna–Xing'an–Songliao Blocks in the southeast, in the Kimmeridgian and Tithonian. Stage B: This consisted of the closure of the Mongol–Okhotsk Ocean, eventually leading to continental collision between the Siberian craton and

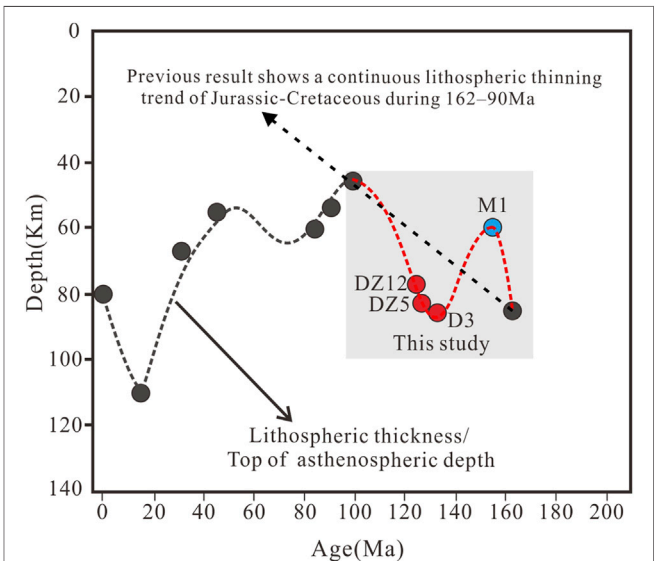

FIGURE 12 | Variation in lithospheric thickness in Northeast China (200 Ma-0 Ma). 170 Ma from Lu et al. (1996) and Huang et al. (2021); 100 Ma from Xu et al. (1994); 88 Ma from Wang et al. (2009); 92 Ma, 31 Ma, and 15 Ma from Zhang et al. (2006); 45 Ma from Zhou (2006); 0 Ma from Wang et al. (2016).

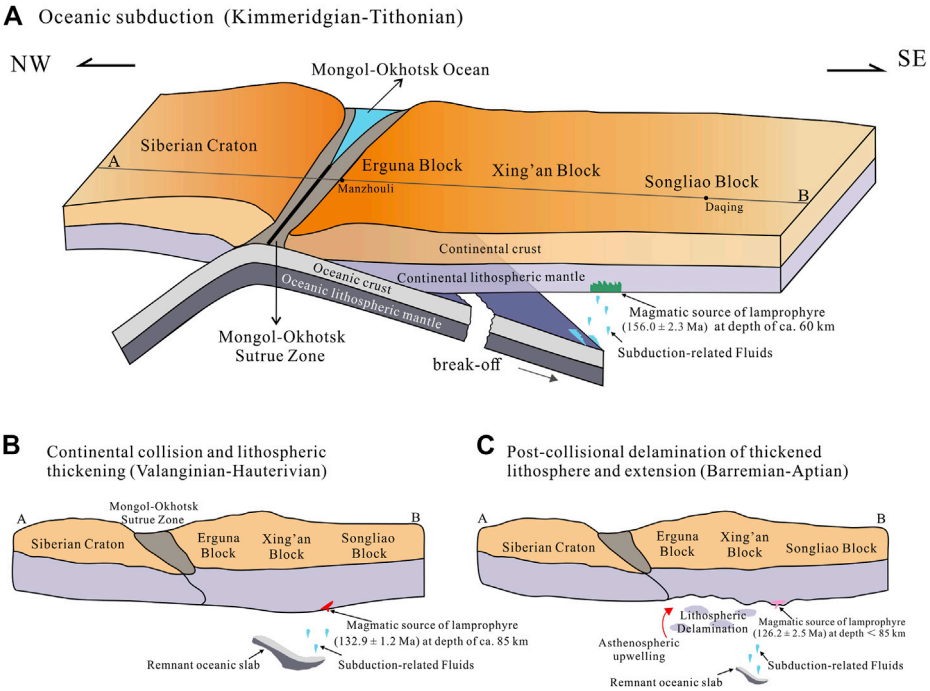

FIGURE 13 | The cartoon illustrations showing the Late Jurassic to the Early Cretaceous tectonic evolution of NE China. **(A)** the southeastward subduction of the Mongol–Okhotsk oceanic crust that resulted in the suture between the Siberian craton and the Erguna–Xing'an–Songliao Blocks in the Kimmeridgian and Tithonian; **(B)** continental collision of the related Blocks and the following lithospheric thickening near the suture zone in the Valanginian and the Hauterivian; **(C)** post-collisional delamination of the thickened lithosphere and its extension during the Barremian up to the Aptian.

Erguna–Xing'an–Songliao Blocks. The collision caused lithospheric thickening in the Valanginian and the Hauterivian. Stage C: This consisted of the post-collisional delamination of the thickened lithosphere and extension, resulting in lithospheric thinning in the Barremian and Aptian.

6 CONCLUSION

(1) The lamprophyres found along the western margin of the Songliao Basin can be categorized into two types: namely, the biotite orthoclase lamprophyre (BOL) and the quartz magnetite lamprophyre (QML). Zircon U–Pb dating yielded an age of 156.0 ± 2.3 Ma for the BOL, and ages of 132.9 ± 1.2 and 126.2 ± 2.5 Ma for the QMLs, suggesting that they had been formed in the Late Jurassic and the Early Cretaceous, respectively.

(2) The lamprophyres originated from the partial melting of enriched lithospheric mantle that had been previously metasomatized by subduction-related fluids.

(3) The Late Jurassic lamprophyre BOL (156.0 ± 2.3 Ma) originated in the high-degree partial melting of the phlogopite-bearing lherzolite mantle in the spinel–garnet transition zone at a depth of about 60 km. One of the two Early Cretaceous QMLs (132.9 ± 1.2 Ma) was derived by the low-degree partial melting of garnet-facies lherzolite mantle at a depth of ca. 85 km. The other (126.2 ± 2.5 Ma) was produced from the low-degree partial melting of amphibole-bearing lherzolite mantle in the garnet zone at a shallower depth <85 km. Thus, from 156 to 132 Ma, the lithosphere in the study area thickened by approximately 25 km at a rate of approximately 1.0 km/Myr.

(4) The lithospheric scale of tectonic evolution, ranging from the Siberian craton *via* the Mongol–Okhotsk Suture Zone to the Songliao Block during the Kimmeridgian and the Aptian, involved three pulsed stages: the southeastward subduction of the Mongol–Okhotsk oceanic crust that resulted in the suture between the Siberian craton and the Erguna–Xing'an–Songliao Blocks in the Kimmeridgian and Tithonian, the continental collision and lithospheric thickening in the Valanginian and the Hauterivian, and the post-collisional delamination of the thickened lithosphere and its extension during the Barremian up to the Aptian.

DATA AVAILABILITY STATEMENT

The original contributions presented in the study are included in the article/supplementary material, further inquiries can be directed to the corresponding author.

AUTHOR CONTRIBUTIONS

TY: Geological context and introduction, field mapping and field relationships, geochemical and LA–ICP–MS U–Pb isotope data

processing, data documentation, petrography, discussion, and interpretations. PW: Fieldwork, geodynamic evolution model, discussion, and interpretation. YZ, YG, and CC: Fieldwork, sample collection, some petrography and data processing, parts of the analytical methods section. All authors contributed to the article and approved the submitted version.

FUNDING

This study was supported by the National Natural Science Foundation of China (NSFC No. 41790453), the National Key Research & Development Program of China (2019YFC0605402), and NSFC (Nos. 41472304, 42102129, and 41972313).

ACKNOWLEDGMENTS

We would like to thank working group of Volcanic Reservoirs and their Exploration, Jilin University, Changchun, China for their helps with field work and zircon U-Pb analyses. We also thank the two reviewers and Editors Kit Lai and Sean C. Johnson for the constructive reviews that significantly improved the manuscript.

REFERENCES

Andersen, T. (2002). Correction of Common Lead in U–Pb Analyses that Do Not Report ^{204}Pb. *Chem. Geol.* 192, 59–79. doi:10.1016/S0009-2541(02)00195-X

Choi, E., Fiorentini, M. L., Giuliani, A., Foley, S. F., Maas, R., and Taylor, W. R. (2020). Subduction-related Petrogenesis of Late Archean Calc-Alkaline Lamprophyres in the Yilgarn Craton (Western Australia). *Precambrian Res.* 338, 105550. doi:10.1016/j.precamres.2019.105550

Chung, S.-L., Chu, M.-F., Zhang, Y., Xie, Y., Lo, C.-H., Lee, T.-Y., et al. (2005). Tibetan Tectonic Evolution Inferred from Spatial and Temporal Variations in Post-collisional Magmatism. *Earth-Sci. Rev.* 68, 173–196. doi:10.1016/j.earscirev.2004.05.001

Cogné, J.-P., Kravchinsky, V. A., Halim, N., and Hankard, F. (2005). Late Jurassic-Early Cretaceous Closure of the Mongol-Okhotsk Ocean Demonstrated by New Mesozoic Paleomagnetic Results from the Trans-Baikal Area (SE Siberia). *Geophys. J. Int.* 163, 813–832. doi:10.1111/j.1365-246X.2005.02782.x

Deng, J., Liu, X., Wang, Q., Dilek, Y., and Liang, Y. (2017). Isotopic Characterization and Petrogenetic Modeling of Early Cretaceous Mafic Diking—Lithospheric Extension in the North China Craton, Eastern Asia. *GSA Bull.* 129, 1379–1407. doi:10.1130/B31609.1

Ding, L., Kapp, P., Yue, Y., and Lai, Q. (2007). Postcollisional Calc-Alkaline Lavas and Xenoliths from the Southern Qiangtang Terrane, Central Tibet. *Earth Planet. Sci. Lett.* 254, 28–38. doi:10.1016/j.epsl.2006.11.019

Duggen, S., Hoernle, K., Van Den Bogaard, P., and Garbe-schönberg, D. (2005). Post-Collisional Transition from Subduction to Intraplate-type Magmatism in the Westernmost Mediterranean: Evidence for Continental-Edge Delamination of Subcontinental Lithosphere. *J. Petrol.* 46, 1155–1201. doi:10.1093/petrology/egi013

Ellam, R. M. (1992). Lithospheric Thickness as a Control on Basalt Geochemistry. *Geology* 20, 153–156. doi:10.1130/0091-7613(1992)020<0153:ltaaco>2.3.co;2

Fitton, J. G., James, D., Kempton, P. D., Ormerod, D. S., and Leeman, W. P. (1988). The Role of Lithospheric Mantle in the Generation of Late Cenozoic Basic Magmas in the Western United States. *J. Petrol.* Special_Volume, 331–349. doi:10.1093/petrology/Special_Volume.1.331

Foley, S. F., Venturelli, G., Green, D. H., and Toscani, L. (1987). The Ultrapotassic Rocks: Characteristics, Classification, and Constraints for Petrogenetic Models. *Earth-Sci. Rev.* 24, 81–134. doi:10.1016/0012-8252(87)90001-8

Foley, S. F., Jackson, S. E., Fryer, B. J., Greenouch, J. D., and Jenner, G. A. (1996). Trace Element Partition Coefficients for Clinopyroxene and Phlogopite in an Alkaline Lamprophyre from Newfoundland by LAM-ICP-MS. *Geochim. Cosmochim. Acta* 60, 629–638. doi:10.1016/0016-7037(95)00422-X

Furman, T., and Graham, D. (1999). Erosion of Lithospheric Mantle beneath the East African Rift System: Geochemical Evidence from the Kivu Volcanic Province. *Lithos* 48, 237–262. doi:10.1016/S0024-4937(99)00031-6

Genç, Ş. C., and Tüysüz, O. (2010). Tectonic Setting of the Jurassic Bimodal Magmatism in the Sakarya Zone (Central and Western Pontides), Northern Turkey: A Geochemical and Isotopic Approach. *Lithos* 118, 95–111. doi:10.1016/j.lithos.2010.03.017

Gibson, S. A., Thompson, R. N., and Day, J. A. (2006). Timescales and Mechanisms of Plume–Lithosphere Interactions: ^{40}Ar/^{39}Ar Geochronology and Geochemistry of Alkaline Igneous Rocks from the Paraná–Etendeka Large Igneous Province. *Earth Planet. Sci. Lett.* 251, 1–17. doi:10.1016/j.epsl.2006.08.004

Guo, F., Fan, W., Wang, Y., and Zhang, M. (2004). Origin of Early Cretaceous Calc-Alkaline Lamprophyres from the Sulu Orogen in Eastern China: Implications for Enrichment Processes beneath Continental Collisional Belt. *Lithos* 78, 291–305. doi:10.1016/j.lithos.2004.05.001

Guo, F., Li, H., Fan, W., Li, J., Zhao, L., Huang, M., et al. (2015). Early Jurassic Subduction of the Paleo-Pacific Ocean in NE China: Petrologic and Geochemical Evidence from the Tumen Mafic Intrusive Complex. *Lithos* 224-225, 46–60. doi:10.1016/j.lithos.2015.02.014

Hofmann, A. W., Jochum, K. P., Seufert, M., and White, W. M. (1986). Nb and Pb in Oceanic Basalts: New Constraints on Mantle Evolution. *Earth Planet. Sci. Lett.* 79, 33–45. doi:10.1016/0012-821X(86)90038-5

Hofmann, A. W. (1997). Mantle Geochemistry: the Message from Oceanic Volcanism. *Nature* 385, 219–229. doi:10.1038/385219a0

Hoskin, P. W. O., and Schaltegger, U. (2003). The Composition of Zircon and Igneous and Metamorphic Petrogenesis. *Rev. Mineral. Geochem.* 53, 27–62. doi:10.2113/0530027

Huang, F., Zhang, Z., Xu, J., Li, X., Zeng, Y., Xu, R., et al. (2021). Lithospheric Extension in Response to Subduction of the Paleo-Pacific Plate: Insights from Early Jurassic Intraplate Volcanic Rocks in the Sk2 Borehole, Songliao Basin, NE China. *Lithos* 380-381, 105871. doi:10.1016/j.lithos.2020.105871

IJBGMR (Inner Jilin Bureau of Geology and Mineral Resources) (1977). *Report of 1:200,000 Regional Geological Research*. (Tuquan Sheet). Beijing: Geological Publishing House, 142. (in Chinese).

Ionov, D. A., Griffin, W. L., and O'Reilly, S. Y. (1997). Volatile-bearing Minerals and Lithophile Trace Elements in the Upper Mantle. *Chem. Geol.* 141, 153–184. doi:10.1016/S0009-2541(97)00061-2

Ji, Z., Meng, Q.-a., Wan, C.-b., Ge, W.-C., Yang, H., Zhang, Y.-l., et al. (2019). Early Cretaceous Adakitic Lavas and A-type Rhyolites in the Songliao Basin, NE China: Implications for the Mechanism of Lithospheric Extension. *Gondwana Res.* 71, 28–48. doi:10.1016/j.gr.2019.01.014

Ji, Z., Wan, C. B., Meng, Q. A., Zhu, D. F., Ge, W. C., Zhang, Y. L., et al. (2020). Chronostratigraphic Framework of Late Mesozoic Terrestrial Strata in the Hailar–Tamtsag Basin, Northeast China, and its Geodynamic Implication. *Geol. J.* 55, 5197–5215. doi:10.1002/gj.3731

Ji, Z., Zhang, Y.-L., Wan, C.-B., Ge, W.-C., Yang, H., Dong, Y., et al. (2021). Recycling of Crustal Materials and Implications for Lithospheric Thinning: Evidence from Mesozoic Volcanic Rocks in the Hailar-Tamtsag Basin, NE China. *Geosci. Front.* 12, 101184. doi:10.1016/j.gsf.2021.101184

Kepezhinskas, P., McDermott, F., Defant, M. J., Hochstaedter, A., Drummond, M. S., Hawkesworth, C. J., et al. (1997). Trace Element and Sr-Nd-Pb Isotopic Constraints on a Three-Component Model of Kamchatka Arc Petrogenesis. *Geochim. Cosmochim. Acta* 61, 577–600. doi:10.1016/S0016-7037(96)00349-3

Klemme, S., and O'Neill, H. S. (2000). The Near-Solidus Transition from Garnet Lherzolite to Spinel Lherzolite. *Contrib. Mineral. Petrol.* 138, 237–248. doi:10.1007/s004100050560

Labanieh, S., Chauvel, C., Germa, A., and Quidelleur, X. (2012). Martinique: a Clear Case for Sediment Melting and Slab Dehydration as a Function of Distance to the Trench. *J. Petrol.* 53, 2441–2464. doi:10.1093/petrology/egs055

Le Maitre, R. W. (2002). *Igneous Rocks: A Classification and Glossary of Terms*. second ed. Cambridge: Cambridge University Press, 236. doi:10.1017/CBO9780511535581

Li, X. H., Zhou, H. W., Wei, G. J., Liu, Y., Zhong, S. L., Luo, Q. H., et al. (2002). Geochemistry and Sr-Nd Isotopes of Cenozoic Ultrapotassic Lamprophyres in Western Yunnan: Constraints on the Composition of Sub-continental Lithospheric Mantle. *Geochimica* 31, 26–34. (in Chinese with English abstract). doi:10.19700/j.0379-1726.2002.01.005

Li, Y., Xu, W.-L., Tang, J., Pei, F.-P., Wang, F., and Sun, C.-Y. (2018). Geochronology and Geochemistry of Mesozoic Intrusive Rocks in the Xing'an Massif of NE China: Implications for the Evolution and Spatial Extent of the Mongol-Okhotsk Tectonic Regime. *Lithos* 304-307, 57–73. doi:10.1016/j.lithos.2018.02.001

Liu, Y., Gao, S., Hu, Z., Gao, C., Zong, K., and Wang, D. (2010). Continental and Oceanic Crust Recycling-Induced Melt–Peridotite Interactions in the Trans-North China Orogen: U–Pb Dating, Hf Isotopes and Trace Elements in Zircons from Mantle Xenoliths. *J. Petrol.* 51, 537–571. doi:10.1093/petrology/egp082

Liu, Y., Li, W., Feng, Z., Wen, Q., Neubauer, F., and Liang, C. (2017). A Review of the Paleozoic Tectonics in the Eastern Part of Central Asian Orogenic Belt. *Gondwana Res.* 43, 123–148. doi:10.1016/j.gr.2016.03.013

Liu, H., Li, Y., He, H., Huangfu, P., and Liu, Y. (2018). Two-phase Southward Subduction of the Mongol-Okhotsk Oceanic Plate Constrained by Permian-Jurassic Granitoids in the Erguna and Xing'an Massifs (NE China). *Lithos* 304-307, 347–361. doi:10.1016/j.lithos.2018.01.016

Lu, F. X., Zhu, Q. W., Xie, Y. H., and Zheng, J. P. (1996). Discovery of High Pressure Pyroxene Megacrystal in Dacite and Their Signficance. *Earth Sci.* 21, 541–545. (in Chinese with English abstract).

Ludwig, K. R. (2003). *ISOPLOT 3.0: A Geochronological Toolkit for Microsoft Excel*, 74. Berkeley: Berkeley Geochronology Center Special Publication.

Luo, Z. H., Wei, Y., Xin, H. T., Zhan, H. M., Ke, S., and Li, W. T. (2006). Petrogenesis of the Post-orogenic Dike Complex - Constraints to Lithosphere Delamination. *Acta Petrol. Sin.* 22, 1672–1684. (in Chinese with English abstract). doi:10.3969/j.issn.1000-0569.2006.06.024

Ma, L., Jiang, S.-Y., Hofmann, A. W., Dai, B.-Z., Hou, M.-L., Zhao, K.-D., et al. (2014). Lithospheric and Asthenospheric Sources of Lamprophyres in the Jiaodong Peninsula: A Consequence of Rapid Lithospheric Thinning beneath the North China Craton? *Geochim. Cosmochim. Acta* 124, 250–271. doi:10.1016/j.gca.2013.09.035

McKenzie, D., and Bickle, M. J. (1988). The Volume and Composition of Melt Generated by Extension of the Lithosphere. *J. Petrol.* 29, 625–679. doi:10.1093/petrology/29.3.625

McKenzie, D., and O'Nions, R. K. (1991). Partial Melt Distributions from Inversion of Rare Earth Element Concentrations. *J. Petrol.* 32, 1021–1091. doi:10.1093/petrology/32.5.1021

Menzies, M. A., Kyle, P. R., Jones, M., and Ingram, G. (1991). Enriched and Depleted Source Components for Tholeiitic and Alkaline Lavas from Zuni-Bandera, New Mexico: Inferences about Intraplate Processes and Stratified Lithosphere. *J. Geophys. Res.* 96, 13645–13671. doi:10.1029/91JB00556

Metelkin, D. V., Vernikovsky, V. A., Kazansky, A. Y., and Wingate, M. T. D. (2010). Late Mesozoic Tectonics of Central Asia Based on Paleomagnetic Evidence. *Gondwana Res.* 18, 400–419. doi:10.1016/j.gr.2009.12.008

Middlemost, E. A. K. (1994). Naming Materials in the Magma/igneous Rock System. *Earth-Sci. Rev.* 37, 215–224. doi:10.1016/0012-8252(94)90029-9

Niu, X., Chen, B., Feng, G., Liu, F., and Yang, J. (2017). Origin of Lamprophyres from the Northern Margin of the North China Craton: Implications for Mantle Metasomatism. *J. Geol. Soc.* 174, 353–364. doi:10.1144/jgs2016-044

Niu, Y. (2021). Lithosphere Thickness Controls the Extent of Mantle Melting, Depth of Melt Extraction and Basalt Compositions in All Tectonic Settings on Earth – A Review and New Perspectives. *Earth-Sci. Rev.* 217, 103614. doi:10.1016/j.earscirev.2021.103614

Ouyang, H., Mao, J., Zhou, Z., and Su, H. (2015). Late Mesozoic Metallogeny and Intracontinental Magmatism, Southern Great Xing'an Range, Northeastern China. *Gondwana Res.* 27, 1153–1172. doi:10.1016/j.gr.2014.08.010

Owen, J. P. (2008). Geochemistry of Lamprophyres from the Western Alps, Italy: Implications for the Origin of an Enriched Isotopic Component in the Italian Mantle. *Contrib. Mineral. Petrol.* 155, 341–362. doi:10.1007/s00410-007-0246-0

Pearce, J. (1983). "Role of Sub-continental Lithosphere in Magma Genesis at Destructive Plate Margins," in *Continental Basalts and Mantle Xenoliths*. Editors C. J. Hawkesworth and M. J. Norry (Nantwich: Shiva Publishing), 158–185.

Peccerillo, A., and Taylor, S. R. (1976). Geochemistry of Eocene Calc-Alkaline Volcanic Rocks from the Kastamonu Area, Northern Turkey. *Contr. Mineral. Petrol.* 58, 63–81. doi:10.1007/BF00384745

Plank, T., and Langmuir, C. H. (1998). The Chemical Composition of Subducting Sediment and its Consequences for the Crust and Mantle. *Chem. Geol.* 145, 325–394. doi:10.1016/S0009-2541(97)00150-2

Polat, A., and Hofmann, A. W. (2003). Alteration and Geochemical Patterns in the 3.7–3.8 Ga Isua Greenstone Belt, West Greenland. *Precambrian Res.* 126, 197–218. doi:10.1016/S0301-9268(03)00095-0

Rapp, R. P., and Watson, E. B. (1995). Dehydration Melting of Metabasalt at 8–32 Kbar: Implications for Continental Growth and Crust-Mantle Recycling. *J. Petrol.* 36, 891–931. doi:10.1093/petrology/36.4.891

Robinson, J. A. C., and Wood, B. J. (1998). The Depth of the Spinel to Garnet Transition at the Peridotite Solidus. *Earth Planet. Sci. Lett.* 164, 277–284. doi:10.1016/S0012-821X(98)00213-1

Rocchi, S., Di Vincenzo, G., Ghezzo, C., and Nardini, I. (2009). Granite-amprophyre Connection in the Latest Stages of the Early Paleozoic Ross Orogeny (Victoria Land, Antarctica). *Geol. Soc. Am. Bull.* 121, 801–819. doi:10.1130/B26342.1

Rock, N. M. S., and Groves, D. I. (1988). Can Lamprophyres Resolve the Genetic Controversy over Mesothermal Gold Deposits? *Geology* 16, 538–541. doi:10.1130/0091-7613(1988)016<0538:clrtgc>2.3.co;2

Rock, N. M. S. (1987). "The Nature and Origin of Lamprophyres: an Overview," in *Alkaline Igneous Rocks*. Editors J. G. Fitton and B. G. J. Upton (London: Geological Society Special Publications), 30, 191–226. doi:10.1144/gsl.sp.1987.030.01.09

Rock, N. M. S. (1991). *Lamprophyres*. London: Blackie, 225.

Rudnick, R. L., and Gao, S. (2003). "Composition of the Continental Crust," in *Treatise on Geochemistry*. Editors H. D. Holland and K. K. Turekian (Oxford: Pergamon), 1–64. doi:10.1016/b0-08-043751-6/03016-4

Rudnick, R. L., Gao, S., Ling, W.-l., Liu, Y.-s., and McDonough, W. F. (2004). Petrology and Geochemistry of Spinel Peridotite Xenoliths from Hannuoba and Qixia, North China Craton. *Lithos* 77, 609–637. doi:10.1016/j.lithos.2004.03.033

Secher, K., Heaman, L. M., Nielsen, T. F. D., Jensen, S. M., Schjøth, F., and Creaser, R. A. (2009). Timing of Kimberlite, Carbonatite, and Ultramafic Lamprophyre Emplacement in the Alkaline Province Located 64°–67° N in Southern West Greenland. *Lithos* 112, 400–406. doi:10.1016/j.lithos.2009.04.035

Soder, C. G., and Romer, R. L. (2018). Post-Collisional Potassic–Ultrapotassic Magmatism of the Variscan Orogen: Implications for Mantle Metasomatism during Continental Cubduction. *J. Petrol.* 59, 1007–1034. doi:10.1093/petrology/egy053

Stille, P., Oberhänsli, R., and Wenger-Schenk, K. (1989). Hf-Nd Isotopic and Trace Element Constraints on the Genesis of Alkaline and Calc-Alkaline Lamprophyres. *Earth Planet. Sci. Lett.* 96, 209–219. doi:10.1016/0012-821X(89)90133-7

Su, Y., Zheng, J., Griffin, W. L., Zhao, J., Tang, H., Ma, Q., et al. (2012). Geochemistry and Geochronology of Carboniferous Volcanic Rocks in the Eastern Junggar Terrane, NW China: Implication for a Tectonic Transition. *Gondwana Res.* 22, 1009–1029. doi:10.1016/j.gr.2012.01.004

Sun, S.-s., and McDonough, W. F. (1989). "Chemical and Isotopic Systematics of Oceanic Basalts: Implications for Mantle Composition and Processes," in *Magmatism Ocean Basins*. Editors A. D. Saunders and M. J. Norry (London: Special Publications), 42, 313–345. doi:10.1144/gsl.sp.1989.042.01.19

Tang, J., Xu, W.-L., Wang, F., Zhao, S., and Li, Y. (2015). Geochronology, Geochemistry, and Deformation History of Late Jurassic–Early Cretaceous Intrusive Rocks in the Erguna Massif, NE China: Constraints on the Late Mesozoic Tectonic Evolution of the Mongol-Okhotsk Orogenic Belt. *Tectonophysics* 658, 91–110. doi:10.1016/j.tecto.2015.07.012

Tarney, J., and Jones, C. E. (1994). Trace Element Geochemistry of Orogenic Igneous Rocks and Crustal Growth Models. *J. Geol. Soc.* 151, 855–868. doi:10.1144/gsjgs.151.5.0855

Taylor, S. R., and McLennan, S. M. (1985). *The Continental Crust: Its Composition and Evolution*. Oxford: Blackwell Scientific, 312.

Thirlwall, M. F., Smith, T. E., Graham, A. M., Theodorou, N., Hollings, P., Davidson, J. P., et al. (1994). High Field Strength Element Anomalies in Arc Lavas: Source or Process? *J. Petrol.* 35, 819–838. doi:10.1093/petrology/35.3.819

Thompson, R. N., and Morrison, M. A. (1988). Asthenospheric and Lower-Lithospheric Mantle Contributions to Continental Extensional Magmatism:

An Example from the British Tertiary Province. *Chem. Geol.* 68, 1–15. doi:10.1016/0009-2541(88)90082-4

van der Meer, Q. H. A., Storey, M., Scott, J. M., and Waight, T. E. (2016). Abrupt Spatial and Geochemical Changes in Lamprophyre Magmatism Related to Gondwana Fragmentation Prior, during and after Opening of the Tasman Sea. *Gondwana Res.* 36, 142–156. doi:10.1016/j.gr.2016.04.004

Wang, F., Zhou, X.-H., Zhang, L.-C., Ying, J.-F., Zhang, Y.-T., Wu, F.-Y., et al. (2006). Late Mesozoic Volcanism in the Great Xing'an Range (NE China): Timing and Implications for the Dynamic Setting of NE Asia. *Earth Planet. Sci. Lett.* 251, 179–198. doi:10.1016/j.epsl.2006.09.007

Wang, P. J., Gao, Y. F., Ren, Y. G., Liu, W. Z., and Zhang, J. G. (2009). $^{40}Ar/^{39}Ar$ Age and Geochemical Features of Mugearite from the Qingshankou Formation; Significances for Basin Formation, Hydrocarbon Generation and Petroleum Accumulation of the Songliao Basin in Cretaceous. *Acta Petrol. Sin.* 25, 1178–1190. (in Chinese with English abstract).

Wang, W., Tang, J., Xu, W.-L., and Wang, F. (2015). Geochronology and Geochemistry of Early Jurassic Volcanic Rocks in the Erguna Massif, Northeast China: Petrogenesis and Implications for the Tectonic Evolution of the Mongol–Okhotsk Suture Belt. *Lithos* 218-219, 73–86. doi:10.1016/j.lithos.2015.01.012

Wang, P.-J., Mattern, F., Didenko, N. A., Zhu, D.-F., Singer, B., and Sun, X.-M. (2016). Tectonics and Cycle System of the Cretaceous Songliao Basin: An Inverted Active Continental Margin Basin. *Earth-Sci. Rev.* 159, 82–102. doi:10.1016/j.earscirev.2016.05.004

Wang, F., Xu, W. L., Xing, K. C., Wang, Y. N., Zhang, H. H., Wu, W., et al. (2019). Final Closure of the Paleo-Asian Ocean and Onset of Subduction of Paleo-Pacific Ocean: Constraints from Early Mesozoic Magmatism in Central Southern Jilin Province, NE China. *J. Geophys. Res. Solid Earth* 124, 2601–2622. doi:10.1029/2018JB016709

Woolley, A. R., Bergman, S. C., Edgar, A. D., Le Bas, M. J., Mitchell, R. H., Rock, N. M. S., et al. (1996). Classification of Lamprophyres, Lamproites, Kimberlites, and the Kalsilitic, Melilitic, and Leucitic Rocks. *Can. Mineral.* 34, 175–186.

Wu, F.-Y., Sun, D.-Y., Ge, W.-C., Zhang, Y.-B., Grant, M. L., Wilde, S. A., et al. (2011). Geochronology of the Phanerozoic Granitoids in Northeastern China. *J. Asian Earth Sci.* 41, 1–30. doi:10.1016/j.jseaes.2010.11.014

Wyman, D. A., Ayer, J. A., Conceição, R. V., and Sage, R. P. (2006). Mantle Processes in an Archean Orogen: Evidence from 2.67 Ga Diamond-Bearing Lamprophyres and Xenoliths. *Lithos* 89, 300–328. doi:10.1016/j.lithos.2005.12.005

Xu, W. L., Sun, D. Y., and Zhou, Y. (1994). *Manzhouli-Suifenhe Geoscience Transect Magmatism and Crust Structure*. Beijing: Geological Publishing House, 94. (in Chinese).

Xu, W.-L., Pei, F.-P., Wang, F., Meng, E., Ji, W.-Q., Yang, D.-B., et al. (2013). Spatial-temporal Relationships of Mesozoic Volcanic Rocks in NE China: Constraints on Tectonic Overprinting and Transformations between Multiple Tectonic Regimes. *J. Asian Earth Sci.* 74, 167–193. doi:10.1016/j.jseaes.2013.04.003

Yang, B. J., Mu, S. M., Jin, X., and Liu, C. (1996). Synthesized Study on the Geophysics of Manzhouli-Suifenhe Geoscience Transect, China. *Acta geophys. Sin.* 39, 772–782. (in Chinese with English abstract).

Yuan, H., Gao, S., Liu, X., Li, H., Günther, D., and Wu, F. (2004). Accurate U-Pb Age and Trace Element Determinations of Zircon by Laser Ablation-Inductively Coupled Plasma-Mass Spectrometry. *Geostand. Geoanalyt Res.* 28, 353–370. doi:10.1111/j.1751-908X.2004.tb00755.x

Zhang, H. H., Xu, Y. G., Ge, W. C., and Ma, J. L. (2006). Geochemistry of Late Mesozoic-Cenozoic Basalts in Yitong-Datun Area, Jilin Province and its Implication. *Acta Petrol. Sin.* 22, 1579–1596. (in Chinese with English abstract).

Zhang, J.-H., Gao, S., Ge, W.-C., Wu, F.-Y., Yang, J.-H., Wilde, S. A., et al. (2010). Geochronology of the Mesozoic Volcanic Rocks in the Great Xing'an Range, Northeastern China: Implications for Subduction-Induced Delamination. *Chem. Geol.* 276, 144–165. doi:10.1016/j.chemgeo.2010.05.013

Zhang, F. Q., Chen, H. L., Yu, X., Dong, C. W., Yang, S. F., Pang, Y. M., et al. (2011). Early Cretaceous Volcanism in the Northern Songliao Basin, NE China, and its Geodynamic Implication. *Gondwana Res.* 19, 163–176. doi:10.1016/j.gr.2010.03.011

Zhang, C., Quan, J.-Y., Zhang, Y.-J., Liu, Z.-H., Li, W., Wang, Y., et al. (2020). Late Mesozoic Tectonic Evolution of the Southern Great Xing'an Range, NE China: Evidence from Whole-Rock Geochemistry, and Zircon U-Pb Ages and Hf Isotopes from Volcanic Rocks. *Lithos* 362-363, 105409. doi:10.1016/j.lithos.2020.105409

Zhou, X. H. (2006). Major Transformation of Subcontinental Lithosphere beneath Eastern China in the Cenozoic-Mesozoic: Review and Prospect. *Earth Sci. Front.* 13, 50–64. (in Chinese with English abstract).

Conflict of Interest: The authors declare that the research was conducted in the absence of any commercial or financial relationships that could be construed as a potential conflict of interest.

frontiers | Frontiers in Earth Science

ORIGINAL RESEARCH
published: 24 June 2022
doi: 10.3389/feart.2022.852261

Qia'erdunbasixi Fe–Cu Deposit in Sawur, Xinjiang: A Case Study of Skarn Deposit Hosted by Volcanic Rock

Shuang Yang[1], *Qiu-Shi Zhou*[1], *Rui Wang*[1]* *and Yongfeng Zhu*[2]*

[1]State Key Laboratory of Geological Processes and Mineral Resources, and Institute of Earth Sciences, China University of Geosciences, Beijing, China, [2]The Key Laboratory of Orogenic Belts and Crustal Evolution, Ministry of Education, School of Earth and Space Science, Peking University, Beijing, China

The Sawur Cu–Au belt, northern Xinjiang, China, is the eastward extension of the Zarma–Sawur Cu–Au belt in Kazakhstan, where Late Paleozoic volcanic rocks and intrusions are highly developed. The Qia'erdunbasixi Fe–Cu deposit in Sawur is a recently discovered deposit and is still under exploration. The intrusive rocks are syenite and diorite, and the wall rocks consist of andesite and minor basalt, lamprophyre, and tuff. The U–Pb SHRIMP zircon age of the Qia'erdunbasixi syenite intruding into the volcanic rocks is 345 ± 2.2 Ma (MSWD = 1.3), presenting as the lower limit of skarn Fe mineralization. The intrusives belong to the calc–alkaline to high-K calc-alkaline series with large ion lithophile element (LILE) enrichment, high LREE/HREE fractionation, and high field strength element (HFSE) depletion. The initial $^{87}Sr/^{86}Sr$ ratios of the Qia'erdunbasixi syenite range from 0.70403 to 0.70420, and the $\varepsilon_{Nd}(t)$ values are from +5.5 to +6.8, which are the typical characteristics of island arc igneous rocks. Diorites having similar REE features with syenite should share the same magma source. Magnetite and copper mineralization develop mostly along the contact zones of syenite and diorite, respectively. Fe mineralization develops along the contact zone of syenite, with typical skarn zonation. The metallogenesis event can be divided into the prograde skarn stage (diopside–augite–andradite–magnetite–calcite–quartz), retrograde skarn stage (epidote–chlorite–actinolite–K-feldspar–calcite–magnetite–quartz), and quartz–sulfide stage (quartz–magnetite–K-feldspar–calcite–sercite–chlorite–actinolite–prehnite–chalcopyrite–pyrite). The early–mid-stage magnetite with certain amounts of Ti and V was crystallized from magma, while the late-stage magnetite has the typical characteristics of hydrothermal calcic skarn magnetite. The temperature of mineralization is between 350 and 450°C based on mineral assemblages and phase diagrams. Copper mineralization is concentrated along the outer contact zone of the diorite. Paragenesis sequences of the four stages of mineralization could be identified for copper mineralization: 1) albite–quartz; 2) chalcopyrite–pyrite–gold–seriate–quartz; 3) chalcopyrite–pyrite–epidotic–reunite; and 4) sphalerite–galena–quartz–calcite. Qia'erdunbasixi is a composite deposit with skarn-type Fe mineralization and mesothermal Cu mineralization and has a genetic relationship with magmatism in an island arc setting.

Keywords: skarn, magnetite, syenite, Sawur, island arc, Fe–Cu deposit

OPEN ACCESS

Edited by:
Hassan Mirnejad,
Miami University, United States

Reviewed by:
Xiao-Ping Xia,
Guangzhou Institute of Geochemistry (CAS), China
Lejun Zhang,
University of Tasmania, Australia

***Correspondence:**
Rui Wang
rw@cugb.edu.cn
Yongfeng Zhu
yfzhu@pku.edu.cn

Specialty section:
This article was submitted to Economic Geology, a section of the journal Frontiers in Earth Science

Received: *11 January 2022*
Accepted: *11 May 2022*
Published: *24 June 2022*

Citation:
Yang S, Zhou Q-S, Wang R and Zhu Y (2022) Qia'erdunbasixi Fe–Cu Deposit in Sawur, Xinjiang: A Case Study of Skarn Deposit Hosted by Volcanic Rock. Front. Earth Sci. 10:852261. doi: 10.3389/feart.2022.852261

INTRODUCTION

Skarn deposits occur in both the contact zone with carbonate rocks and the contact zone with volcanic–sedimentary rocks, such as volcanic sedimentary tuff and andesite. Einaudi (1981) suggested that skarn deposits hosted in volcanic rocks should belong to the metasomatic skarn deposit. Zhao et al. (1990) classified this type into the skarn deposit related to volcanic gas and fluid. Such atypical skarn deposits mainly present as calcic iron skarn deposits, which are usually found in island arcs. The intrusive rocks are generally dioritic, sometimes also syenitic (Einaudi, 1981). British Columbia contains at least 147 recorded iron skarn deposits, wherein over 90% are hosted by Late Triassic limestone and volcanic rocks (Ray, 1995). Skarn minerals such as garnet and pyroxene hosted in volcanic rocks are different in their element compositions from those hosted in carbonate rocks (Meinert, 1984). Wall rock lithology plays an important role in the metallogenesis of skarn deposits. Carbonate rocks, such as limestone, dolomitic limestone, and dolomite are easily replaced because they are chemically active, brittle, easy to penetrate, and enriched in Ca. In contrast, volcanic rocks are less vulnerable to modification, but are richer in iron and mobile elements, such as K and Na. These atypical deposits hosted by volcanic rocks are petrologically and geochemically unique, and detailed studies are needed to understand their genesis in comparison with typical skarn deposits.

The Sawur Cu–Au belt, an eastward extension of the Zarma–Sawur Au–Cu belt in Kazakhstan, is in the Sawur Mountains along the northwestern margin of the Junggar Basin, northern Xinjiang, China. A considerable quantity of gold and copper deposits is hosted in the volcanic rocks of the Sawur area (Yuan et al., 2015; Zhang, 2016; Xia et al., 2022). The Qia'erdunbasixi Fe–Cu deposit in Sawur is a newly discovered deposit (Wang and Zhu, 2007, 2010; Xia et al., 2022). The wall rocks mainly consist of andesite with minor basalt, lamprophyre, and tuff, intruded by syenite and diorite. Magnetite and chalcopyrite mineralization develops along the contact zone between intrusives (syenite and diorite) and andesite.

In this article, we report our studies of the Qia'erdunbasixi deposit with respect to deposit geology. We have conducted zircon U–Pb dating of syenite to better constrain the age of mineralization, and determine the whole major and trace elements, and radiogenic isotopes (Sr, Nd) of intrusions, and ore mineral geochemistry to constrain the origin of intrusions and the nature of the ore-forming fluid. ig. This study reveals the genesis of the volcanic hosted Fe–Cu deposit and their controlling factors, and the proposed genetic model could be used to guide the exploration of potential Fe–Cu deposits in the Sawur area.

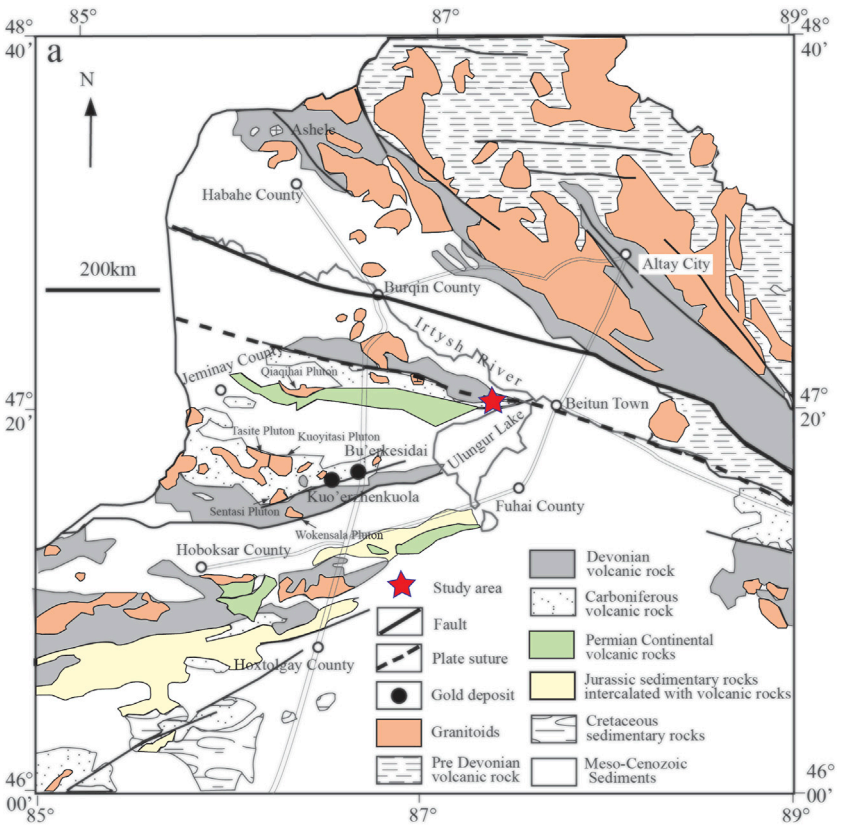

FIGURE 1 | Regional geological map of Sawur and adjacent regions (modified after He et al., 2005).

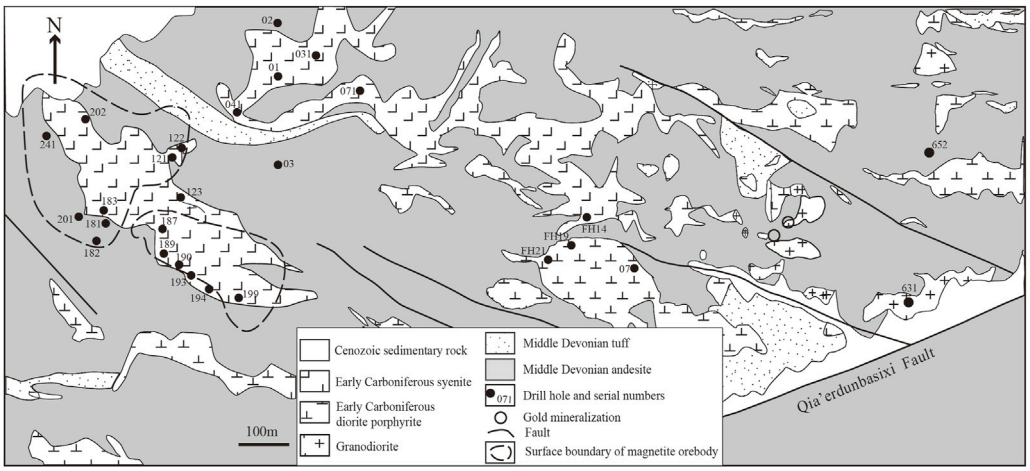

FIGURE 2 | Geological map of the Qia'erdunbasixi deposit (modified after Wang and Zhu, 2010 and Xia et al., 2022).

REGIONAL GEOLOGY

The Zharma–Sawur volcanic arc is separated by the Irtysh–Zaysan suture zone from the Altai orogen in the north (**Figure 1**). The NW–SE trending Irtysh–Zaysan suture zone is the product of a collision between the Altai and Kazakhstan blocks (e.g., Windley et al., 2007; Vladimirov et al., 2008; Chen et al., 2010; Zhu et al., 2016). In East Kazakhstan, abundant Late Devonian–Early Carboniferous conodonts and radiolarians were discovered in the silicic rocks of the Char ophiolite within the Irtysh–Zaysan suture zone (Iwata et al., 1994, 1997).

The Sawur region, an eastward extension of the Zarma-Sawur island arc belt in Kazakhstan, is located along the northwestern margin of the Junggar Basin (He et al., 1995; Windley et al., 2002; Zhu et al., 2013; 2015). The strata outcropping in the Sawur region consist of a Devonian–Carboniferous marine volcanic-sedimentary sequence, a Permian continental volcanic–sedimentary sequence, and Cenozoic sediments (Bureau of Geology and Mineral Resources of Xinjiang Uygur Autonomous Region, 1993). The Middle Devonian Sawur Formation, as the oldest in the Sawur district, mainly consists of volcanic rocks. The Burqin Formation in the later period of the Middle Devonian is a series of marine intermediate–basic volcanic clastic rocks and sedimentary clastic rocks. Upper Devonian Taerbahata is a set of volcanic flysch. The Lower Carboniferous Formations include the Heishantou, Halabayi, and Nalinkala Formations. The Heishantou Formation, hosting Buerkesidai and Kuoerzhenkuola gold deposits, consists of a succession of volcanic rocks and volcanic clastic rocks with an intercalation of limestone and siltstone, representing a typical island arc volcanic assemblage (Shen et al., 2007; Chen et al., 2017). The Rb–Sr isochron age of andesite in the Heishantou Formation is 342 Ma, and 325 Ma for sillite (He et al., 1994). The Upper Carboniferous sequences consist of the Sarbulake and Qiaqihai Formations. The Permian strata are made of volcanic–sedimentary rocks. The Harjiao Formation features continental volcanic rocks, and the overlying Kalagang Formation, as volcanic rocks, has a typical bimodal characteristic (Zhou et al., 2006). The $^{40}Ar/^{39}Ar$ age of the volcanic rocks in the Kalagang Formation is between 283 and 280 Ma (Tan et al., 2007).

Granitic intrusions are widespread in the Sawur region. Based on previous work (Yuan et al., 2006; Zhou et al., 2006, 2008; Chen et al., 2010), these granitic intrusions can be subdivided into I-type granites (Tasite, Sentasi, Wokensala, and Kaerjia plutons) and A-type granites (Kuoyitasi and Qiaqihai plutons). The I-type granite consists of granite, granodiorite, and the A-type granite is mostly alkali granite. The SHRIMP U–Pb dating results indicate that the I-type granites were formed between 337 Ma and 302.6 Ma, and the A-type between 297.9 Ma and 290.7 Ma. From the oldest to the youngest granite, compositions vary from calc–alkaline to high-K calc-alkaline, to alkali series (Zhou et al., 2008).

Many gold deposits and other mineral occurrences are hosted in the volcanic rocks of the Sawur area, and together they define the EW-trending gold belt (Zhu et al., 2014; Xia et al., 2022). The Kuoerzhenkuola and Buerkesidai volcanogenic hydrothermal gold deposits are the two largest deposits in the belt (Shen et al., 2007), wherein gold mineralization is genetically associated with mantle-derived materials (Shen et al., 2008; Xia et al., 2022).

DEPOSIT GEOLOGY

The Qia'erdunbasixi Fe skarn is located along the contact between syenite and Middle Devonian volcanic rocks, which are andesite interbedded with basalt, lamprophyre, and tuff as displayed in the Qia'erdunbasixi deposit (**Figure 2**). In the mining area, the NE-trending Qia'erdunbasixi fault and several NW-trending branch faults (**Figure 2**) are developed. The mineralization is featured by development in the contact zone between plutons and volcanic wall rocks. Magnetite mineralization is mainly developed in the internal and external contact zones of syenite; copper

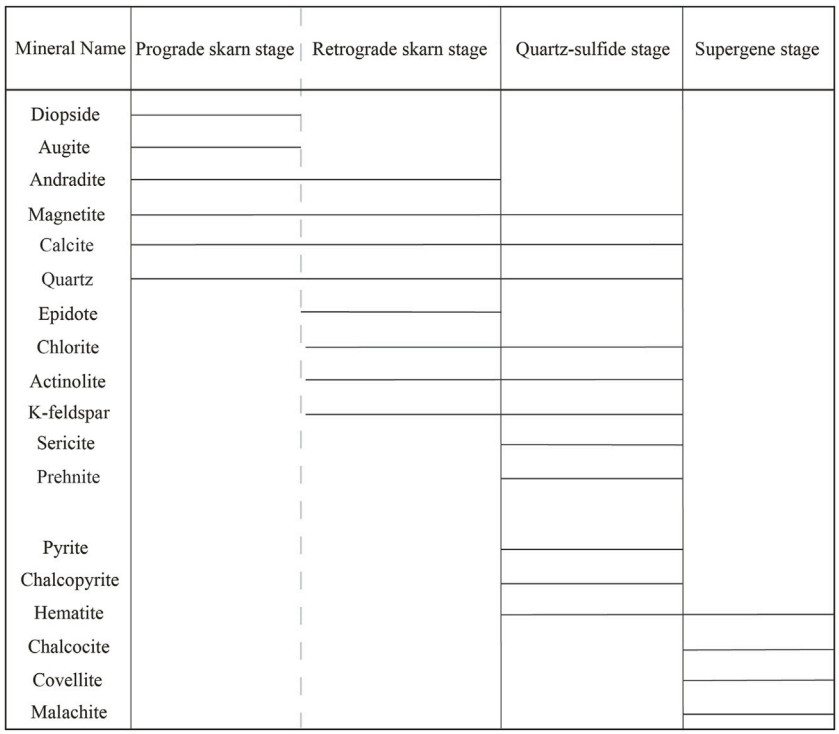

FIGURE 3 | Paragenetic sequence for the four stages of the Fe–Cu mineralizationin Qiaer'dunbasixi deposit (modified from Wang and Zhu, 2010).

mineralization is mainly developed in the external contact zone of diorite, and gold mineralization is closely related to granodiorite porphyry. In the Qia'erdunbasixi area, the volcanic rock is in the second part of the Burqin Formation. This part comprises of dacite, rhyolite, tuffaceous breccia, and tuff, interbedding amygdaloid andesite, basalt, and minor lamprophyre. Andesite with minor basalt, tuff and rhyolite are the main wall rocks. Andesite develops a clear amygdaloidal structure and hyalopilitic texture, as well as minor pyrite–epidote veins. Amphiboles and minor plagioclases are the main phenocrysts in andesite, some amphiboles are replaced by epidotes and chlorites, as well as a minor development of quartz–calcite veins. The amygdule minerals include quartz, calcite, albite, epidote, and chlorite. Basalt, as a minor phase in the volcanic wall rocks, can be classified into two categories depending on their mineralogical features: 1) megacryst basalt is characterized by clinopyroxene megacrysts (5–10 mm) with a hyalopilitic texture, where albite microcrysts are also present. 2) Amphibole basalt is characterized by clinopyroxene and amphibole phenocrysts of 0.5–1.5 mm. The tuffs are highly brecciated andesite or diorite. There are quartz phenocrysts and minor fragments of plagioclase in rhyolite. Both tuff and rhyolite are highly developed with quartz and epidote veins.

The syenite consists of clinopyroxene, plagioclase, and minor apatite (~5 vol%), and magnetite (~5 vol%). Primary basic plagioclase is replaced initially by albite, calcite, and sericite, and then enclosed by K–feldspar. Some clinopyroxene rims are surrounded by large quantities of magnetite. There are two groups of magnetite, the former type is characterized by a larger size (1 mm), abundant cracks, round shape, and cloudy face, indicating xenocrysts. The latter type is clean, euhedral, and small (<0.3 mm), and usually intergrown with chlorite and epidote.

Mineralization

Magnetite, copper, and gold mineralizations are well developed in the Qia'erdunbasixi deposit. The late Paleozoic basalt, andesite, tuff, and volcanic breccia exposed in a large area in the Qia'erdunbasixi mining area are intruded by diorite and syenite.

Copper mineralization is concentrated mainly in the outer contact zone of diorite, and most of the copper mineralization is filled in hydrothermal breccia, featuring a mesothermal hydrothermal vein copper deposit. Ore minerals mainly include pyrite, chalcopyrite, galena, and sphalerite, and Gangue minerals mainly include quartz, calcite, epidote, sericite, prehnite, chlorite, K-feldspar, albite, and pumpellyite. The ore structure is mainly disseminated veinlet and breccia structures. Diorite ore has a disseminated veinlet structure, while the andesite and tuff ores are mainly filled with chalcopyrite veinlets and pores. The main wall rock alteration types include sericite, epidote, K-feldspar, chlorite, quartz, and calcite alteration. Epidote and sericite alterations are closely related to chalcopyrite mineralization. Tuff and andesite are widely subjected to epidote and pyrite alteration, and the late quartz alteration is closely related to galena and sphalerite mineralization. Magnetite mineralization develops along the contact zone between syenite and volcanic rocks (dominated by andesite). There are two magnetite ore bodies shown in **Figure 2**. Ore types include massive and disseminated

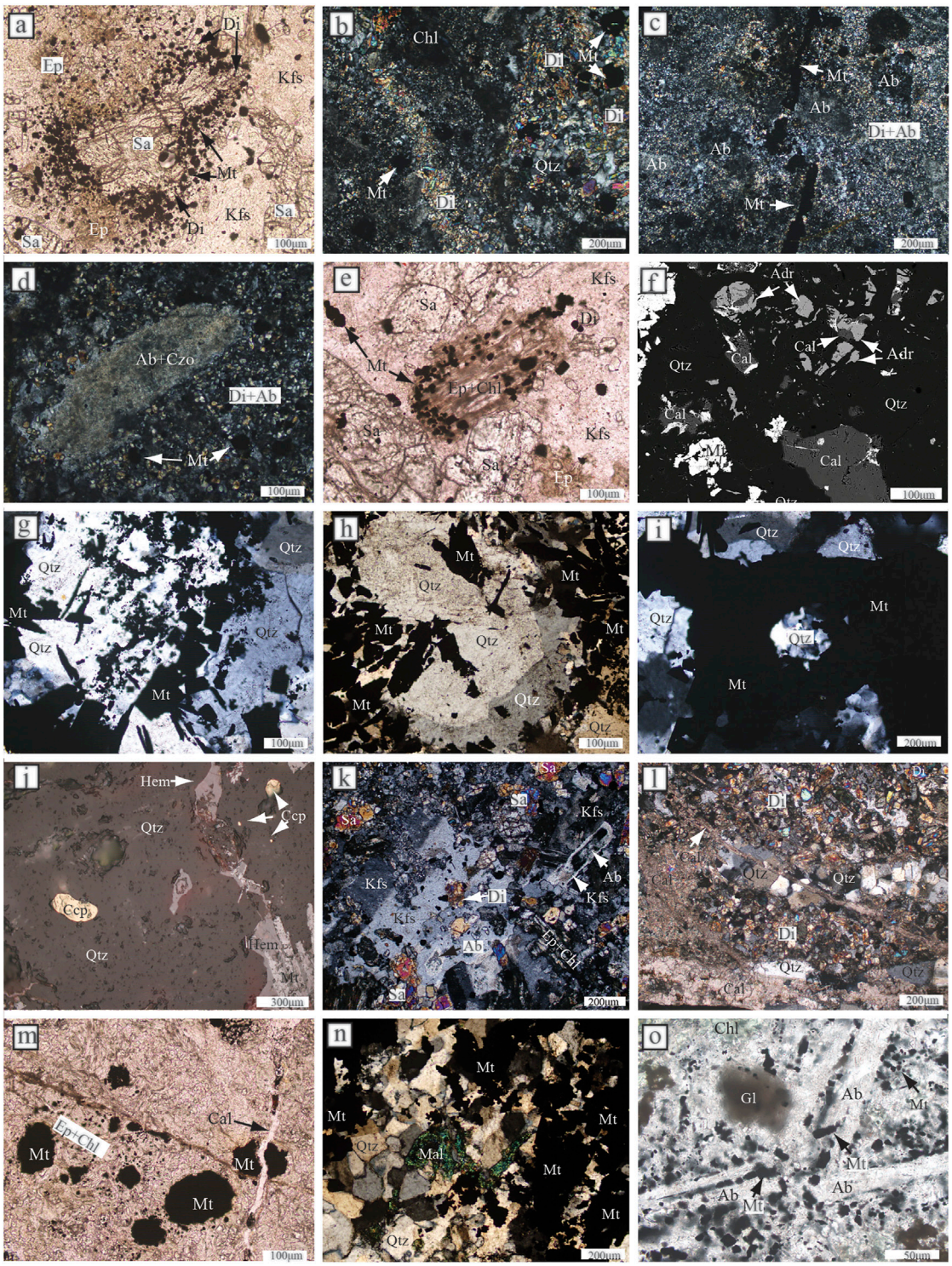

FIGURE 4 | (A) Clinopyroxene is densely disseminated or presents as veinlets near the contact zone; **(B)** Magnetite is sparsely disseminated; **(C)** Magnetite veinlets; **(D)** Clinopyroxene is metasomatized by epidote + chlorite + magnetite, and epidotization and chloritization in the outer contact zone are well developed; **(E,I)** Alterations of quartz + magnetite + K-feldspar + calcite + sericite + chlorite + prehnite + actinolite + chalcopyrite + pyrite are developed in the hydrothermal stage; **(F,G)** The quartz–magnetite vein with a width of about 2–10 cm, where magnetite accounts for as much as 40 vol% of the vein volume; **(J)** Chalcopyrite is disseminated and magnetite is metasomatized by hematite; **(K,L)** Coarse K-feldspar grain, with inclusions of diopside formed in the early stage; **(M)** The calcite vein formed in the latest stage cuts through the early-stage magnetite; **(N)** Malachite in the magnetite–quartz vein; **(O)** Wall rock of andesite is intensely mineralized with magnetite. Plane polarized light **(A,E,M, and O)**, cross polarized light **(B–D,G–I, K,L, and N)**, reflected light **(J)**, and the BSE image **(F)**. Ab—albite; Adr—andradite; Cal—calcite; Ccp—chalcopyrite; Chl—chlorite; Czo—clinozoisite; Di—diopside; Ep—epidote; Gl—glass; Hem—hematite; Mal—malachite; Mt—magnetite; Kfs—K-feldspar; Qtz—quartz; Sa—salite; Ser—sericite (modified after Wang and Zhu, 2010).

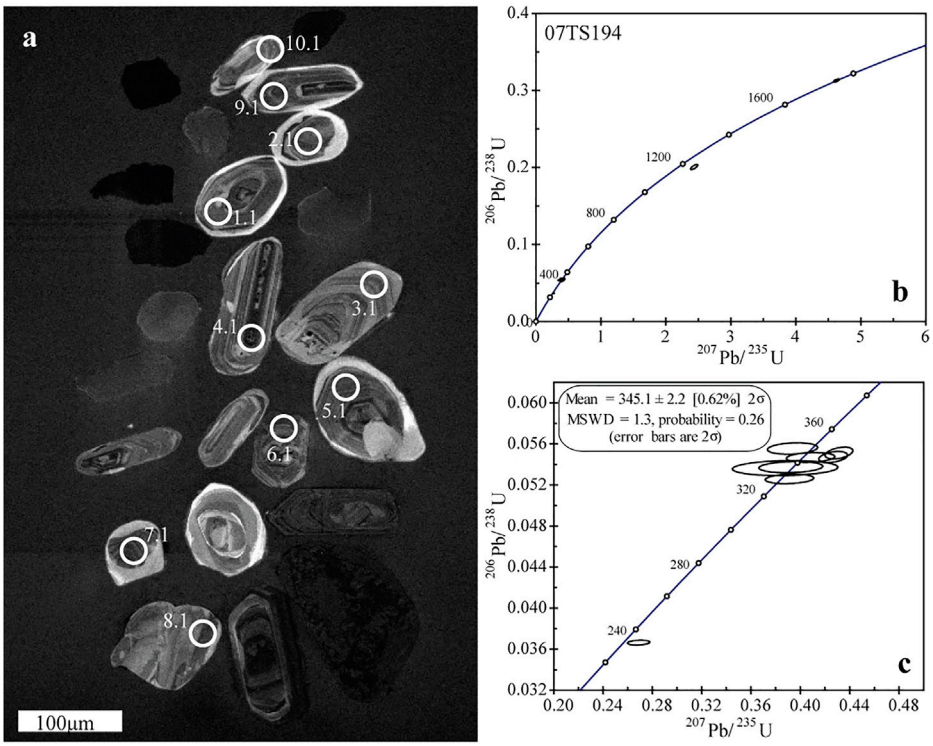

FIGURE 5 | (A) Cathodoluminescence (CL) image of zircons from Fuhai syenites; **(B,C)** U–Pb concordia diagrams showing the SHRIMP dating results for Fuhai syenites.

magnetite ore. The main ore minerals are magnetite and chalcopyrite, and the gangue minerals include pyrite, quartz, diopside, epidote, chlorite, actinolite, calcite, sericite, and andradite. The wall rock alteration is mainly skarn, quartz, chlorite, calcite, and sericite alterations.

Magnetite mineralization has distinctive zoning features. Through sampling from the interior of a syenitic intrusion to the andesitic host rock, each 5 m thick, it is revealed that the types of altered minerals and the content of magnetite vary greatly. The typical alteration features of the Qia'erdunbasixi iron deposit are the pervasive development of diopside with minor andradite. The grain sizes of clinopyroxene and feldspar phenocrysts of syenite decrease significantly near the contact zone of the syenite pluton, indicative of quenching. Magnetite mineralization mainly develops in magnetite-–quartz veins in the outer contact zone of syenite.

Alteration Stages

Based on field and microscopic observations, the magnetite mineralization can be divided into the skarn, quartz–sulfide, and supergene stages (**Figure 3**). The skarn stage includes the prograde and retrograde skarn stages. The minerals in the prograde skarn stage are composed of diopside + augite + andradite + magnetite + calcite + quartz. In the internal contact zone between syenite and intermediate–basic volcanic rocks, abundant fine-grained diopside and magnetite develop around the primary salite. These clinopyroxenes are densely disseminated or are present as veinlets near the contact zone (**Figure 4A**), whereas magnetite is sparsely disseminated or in veinlets (**Figures 4B, C**). Andradite has been substituted by chlorite through pseudomorphism in the later stage.

The minerals in the retrograde skarn stage are composed of epidote + chlorite + actinolite + K–feldspar + calcite + magnetite + quartz + andradite, which are developed both in the internal and external contact zone. Clinopyroxene is commonly metasomatized by epidote + chlorite + magnetite, and epidote and chlorite alterations in the outer contact zone are well developed (**Figure 4D**). At this stage, abundant magnetite develops in the outer contact zone in a densely disseminated manner, becoming the main ore. Alteration of quartz + magnetite + K–feldspar + calcite + sericite + chlorite + prehnite + actinolite + chalcopyrite + pyrite is developed in the quartz–sulfide stage (**Figures 4E–I**). A quartz–magnetite vein with a width of about 2–10 cm is the typical feature of this stage, where magnetite accounts for as much as 40 vol% of the vein volume (**Figures 4F, G**). Chalcopyrite is disseminated and magnetite is metasomatized by hematite, and reflected light (**Figure 4J**). Minerals of the hydrothermal period are developed both in the internal and external contact zones. The grain size of K–feldspar is coarse, with inclusions of diopside formed in the early stage (**Figures 4K–L**). The calcite vein formed in the latest stage cuts through the early-stage magnetite (**Figure 4M**). Malachite is also developed in

TABLE 1 | Zircon SHRIMP dating results for the Qia'erdunbasixi syenites.

	$^{206}Pb_c$	U	Th	$^{232}Th/^{238}U$	$^{206}Pb^*$	$^{206}Pb/^{238}U$		$^{207}Pb/^{206}Pb$		Total $^{238}U/^{206}Pb$	Error	Total $^{207}Pb/^{206}$ b	Error	$^{238}U/^{206}Pb$	Error	$^{207}Pb/^{206}Pb^*$	Error	$^{207}Pb^*/^{235}U$	Error	$^{206}Pb^*/^{238}U$	Error	Correlation
	%	ppm	ppm			Age, Ma	Ma	Age, Ma	Ma		%		%		%		%		%		%	
1.1	0	271	137	0.52	12.8	343.5	2.2			18.27	0.65	0.05654	1.7	18.27	0.65	0.05654	1.7	0.4266	1.8	0.05472	0.65	0.365
2.1	0.71	314	178	0.59	14.6	337.5	2.2			18.47	0.61	0.05868	1.5	18.61	0.67	0.0529	4.3	0.392	4.3	0.05375	0.67	0.154
3.1	0.03	668	222	0.34	180			1751.5	7.9	3.193	0.39	0.10737	0.43	3.194	0.39	0.10715	0.43	4.626	0.58	0.31310	0.39	0.674
4.1	0.32	305	243	0.82	14.6	348.5	2.2			17.94	0.63	0.05401	1.6	18	0.66	0.0514	3.3	0.394	3.4	0.05556	0.66	0.194
5.1	0.13	365	185	0.52	16.5	330.5	1.9			18.99	0.55	0.05502	1.4	19.01	0.58	0.0539	3.3	0.391	3.3	0.05260	0.58	0.177
6.1	0.31	902	226	0.26	28.5	232.0	0.97			27.2	0.41	0.05570	1.1	27.29	0.42	0.0532	2.1	0.2689	2.2	0.03665	0.42	0.194
7.1	0.24	393	232	0.61	18.5	343.2	1.9			18.242	0.54	0.05610	1.3	18.29	0.58	0.0542	3.1	0.408	3.2	0.05469	0.58	0.182
8.1	--	191	266	1.44	32.8			1,383	18	4.988	1.10	0.08749	0.8	4.985	1.1	0.08801	0.95	2.434	1.4	0.20060	1.10	0.752
9.1	--	296	160	0.56	14	345.9	2.3			18.14	0.69	0.05672	1.6	18.14	0.69	0.05676	1.6	0.4313	1.7	0.05512	0.69	0.403
10.1	0.98	189	99	0.54	8.82	336.9	2.9			18.46	0.79	0.06030	2.9	18.64	0.89	0.0524	7.2	0.388	7.3	0.05365	0.89	0.123

the magnetite–quartz vein (**Figure 4N**), showing the overprint of secondary oxidation. The wall rock of andesite is intensely mineralized with magnetite (**Figure 4O**).

SAMPLING AND ANALYTICAL METHODS

In this study, Sr–Nd isotopic analysis and electron microprobe analysis of the main minerals were carried out for syenite and diorite in the study area, as well as U–Pb dating of zircon in syenite. All samples numbered 07TS187, 07TS189, 07TS190, 07TS193, 07TS194, 07TS199, FH14, FH19, FH21, FH26, and ZK07–33 were collected from the drill holes shown in **Figure 2**, and sampling depths were between 20 and 40 m. Ten U–Pb ages of zircon from syenite in drill hole 194 were analyzed. The Sr–Nd isotopic analysis was carried out on five syenite and four diorite samples from different drill holes. Minerals such as andradite, epidote, chlorite, sericite, and prehnite were analyzed by EPMA.

Zircon was selected under a microscope and Cathodoluminescence (CL) images were taken of it using a CAMECA SX–50 microprobe. The zircon was dated using the SHRIMP II in Curtin University of Technology at the Beijing SHRIMP Center using the SHRIMP Remote Operation System, and the data correction was based on Williams (1998).

Major element compositions of minerals were measured by an electron probe microanalysis (EPMA) on a JEOL Superprobe JXA 8100 at Peking University. Operating conditions include an accelerating voltage of 15 kV, beam current 1×10^{-8} A, and spot diameter of 1 μm. Counting times were 20s on the background position and peaked for each element. Standard specimens used natural minerals (albite for NaKα, orthoclase for KKα, wollastonite for SiKα and CaKα, hematite for FeKα, rhodonite for MnKα, and rutile for TiKα) and synthetic oxides (Al_2O_3 for AlKα, MgO for MgKα, Cr_2O_3 for CrKα, and NiO for NiKα).

An Sr–Nd isotopic analysis was conducted at the Isotope Geology Lab, Chinese Academy of Geological Science (Beijing). Sr and Nd isotopic measurements were carried out using a MC–ICP–MS (MAT-262). NBS987 ratio of $^{87}Sr/^{86}Sr$ = 0.71024 ± 2 (2c); the measurement accuracy of the Rb/Sr ratio was better than 0.1%, the mass fractionation of Sr isotopes was corrected using $^{88}Sr/^{86}Sr$ = 8.37521; Jndi-1 ratio of $^{143}Nd/^{144}Nd$ = 0.511,126 ± 6 (2c), measurement accuracy of the Sm/Nd ratio was better than 0.1%, and the mass fractionation of Nd isotopes was corrected using $^{146}Nd/^{144}Nd$ = 0.7219.

ANALYTICAL RESULTS

SHRIMP U–Pb Ages

The strata mainly comprised of basalt, andesite, tuff, and breccia volcanic rock outcrops in Qia'erdunbasixi belonging to Part II of the Burjin group, which were intruded by syeniteic and dioritic plutons. The zircons separated from syenite show sector texture or core–mantle texture on CL images (**Figure 5A**). The oldest apparent age is 1751.5 Ma (spot 3.1, Th/U = 0.34, see **Table 1**), and one zircon sample exhibited an extremely young age (spot

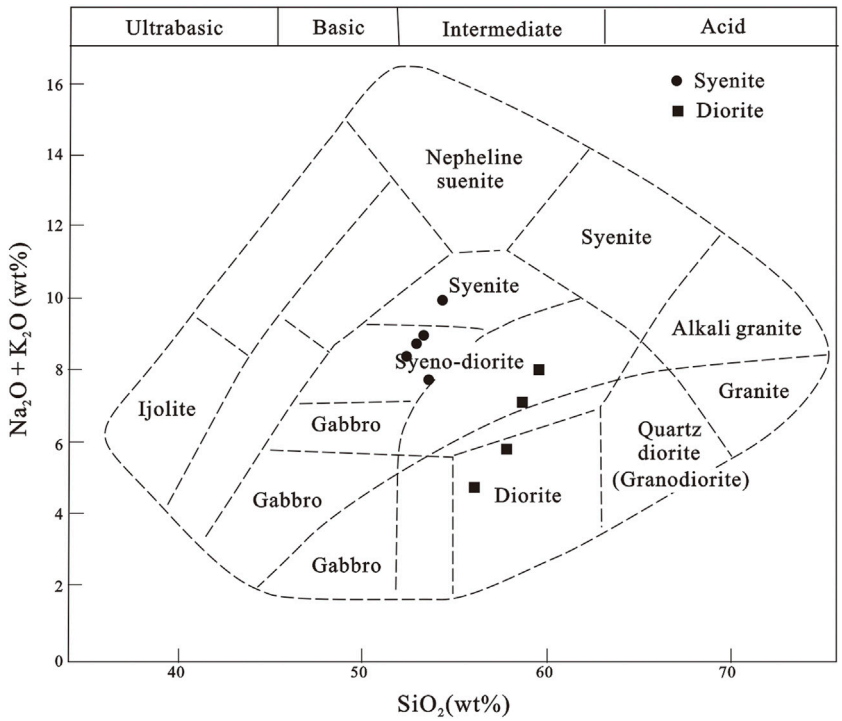

FIGURE 6 | TAS diagram of syenite and diorite, data from Wang and Zhu (2010).

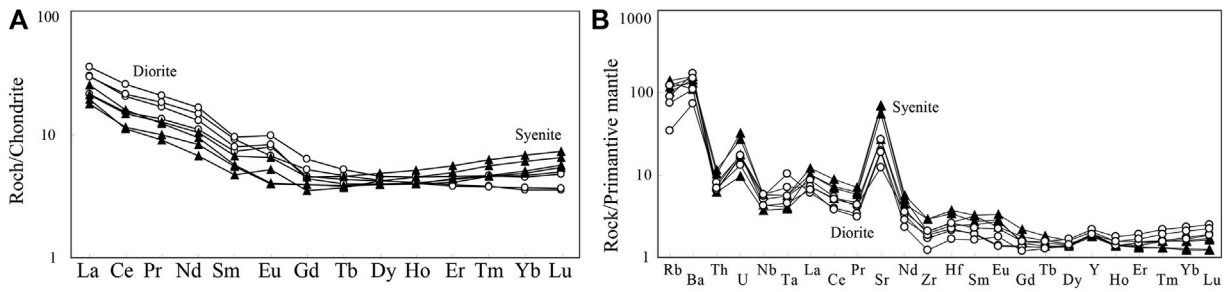

FIGURE 7 | Chondrite-normalized REE patterns **(A)** and the primitive mantle-normalized multi-element plots **(B)** for syenites and diorites in the Qiaer'dunbasixi deposit (modified from Wang and Zhu, 2010). Normalized values after Sun et al., 1989.

6.1, 232 Ma, see **Table 1**). Most zircons constitute a concordant age and give a weighted mean age of 345 ± 2.2 Ma (MSWD = 1.3, **Figure 5C**) with Th/U ratios of 0.52–0.82 (**Table 1**).

Whole Rock Sr–Nd Isotopic Result

Whole rock major and trace element compositions of syenite and diorite have been reported in Wang and Zhu (2010). They have similar SiO_2 contents, but syenites have higher Na_2O + K_2O contents (**Figure 6**). They belong to the calc-alkaline to high-K calc-alkaline series. Syenites enrich LILE such as Rb, Ba, and Sr, and deplete HFSE such as Th, Nb, Ta, Zr, Hf, and HREE (**Figure 7**). Furthermore, a Ce-negative anomaly and Eu-positive anomaly are present. The $\varepsilon_{Nd(345Ma)}$ varies from 5.5 to 6.8, with a weighted average value of 6.14 (n = 5). The ratios of $(^{87}Sr/^{86}Sr)_i$ are between 0.704,034–0.704,197.

Diorites enrich LILE such as Rb, Ba, and Sr, and deplete HFSE such as Th, Nb, Ta, Zr, Hf, and HREE. Furthermore, a Ce-negative anomaly is present and an Eu anomaly varies (**Figure 7**). The $\varepsilon_{Nd(345Ma)}$ varies from 4.6 to 5.0 with a weighted average value of 4.8 (n = 4). The ratios of $(^{87}Sr/^{86}Sr)_i$ are between 0.704,086–0.704,114.

Skarn and Ore Mineral Chemistry

The EPMA data of main minerals during magnetite mineralization are shown in **Table 2**; **Table 3**. Minerals formed in the prograde skarn stage of the Qia'erdunbasixi

TABLE 2 | Major element abundances (wt%) of andradite, epidote, chlorite, sericite, and prehnite.

Comment	Andradite	Epidote	Epidote	Chlorite	Chlorite	Chlorite	Sericite	Prehnite
SiO_2	35.77	37.58	37.94	28.36	28.82	30.12	49.09	43.07
Al_2O_3	0.01	25.33	26.63	14.64	15.26	17.29	30.56	23.37
FeO_t	27.15	9.68	7.36	20.34	19.70	20.05	1.85	2.11
CaO	33.17	22.97	22.55	0.09	0.07	0.37	0.05	26.77
MgO	0.05	0.01	0.05	22.67	22.10	16.67	1.59	0.36
K_2O	0	0.01	0	0	0	0.57	10.84	0.01
Na_2O	0.01	0.03	0.06	0	0.03	0.04	0.30	0
MnO	0.16	0.61	0.56	1.00	0.95	0.64	0	0.06
TiO_2	0.02	0.04	0.04	0.25	0.20	1.21	0.03	0
Total	96.43	96.26	95.19	87.59	87.25	87.09	94.31	95.76
	O = 12	O = 12.5	O = 12.6	O = 14	O = 14	O = 14	O = 22	O = 11
Si	3.03	2.99	3.02	2.95	2.99	3.11	6.61	2.97
Al^{IV}	0	0.01	0	1.05	1.01	0.89	1.39	0.03
Al^{VI}	0	2.37	2.50	0.75	0.85	1.22	3.46	1.87
Ti	0	0	0	0.02	0.02	0.09	0	0
Fe^{3+}	1.93	0.64	0.49	0	0	0	0	0.12
Mg	0.01	0	0	3.52	3.41	2.57	0.32	0.04
Fe^{2+}	0	0	0.01	1.77	1.71	1.73	0.21	0
Mn	0.01	0.03	0.03	0.07	0.07	0.04	0	0
Ca	3.02	1.96	1.92	0.01	0.01	0.04	0.01	1.98
K	0	0	0	0	0	0	1.86	0
Na	0	0	0.01	0	0	0.01	0.08	0
Sum	8.00	8.00	7.98	10.13	10.07	9.71	13.93	7.02

deposit mainly include diopside + augite + andradite + magnetite + calcite + quartz. Andradite has a low SiO_2 content (35.77 wt%) and nearly no Al_2O_3 content (0.01 wt%) as well as MnO content (0.16 wt%). Epidotes formed in the retrograde skarn stage have SiO_2 contents of 37.58–37.94 wt%. The Al_2O_3 and MnO contents of the epidotes are within in25.33–26.63 wt% and 0.56–0.61 wt%, respectively. Chlorite belongs to pycnochlorite based on their Si–Fe contents (SiO_2 = 28.36–30.12 wt%, FeOt = 19.70–20.34 wt%). Sericite has Al_2O_3 of 30.56 wt% with Si/Al^{IV} ratio of 4.76, classifying it as phengite. Prehnite with CaO of 26.77 wt% is mainly formed in the quartz–sulfide stage. Magnetite in the mining area contains certain amounts of V and Ti, and can be divided into three generations: magnetite in the clinopyroxene phenocryst (**Figures 4A, B**), magnetite in th syenite matrix (**Figures 4C, D**), and magnetite in the hydrothermal vein (**Figures 4F, G**). The magnetite inclusion in clinopyroxene has $Fe^{3+}/\sum Fe$ of 0.53–0.65, with a little Al_2O_3 (0.07–0.31 wt%). From the core to the rim of clinopyroxene, the TiO_2 of magnetite inclusions decreases from 12.78 wt% to 0.21 wt%, and $Fe^{3+}/\sum Fe$ ratios increase from 0.53 to 0.60, indicating that the oxygen fugacity gradually increases with the crystallization evolution of magma. Some magnetite inclusions in clinopyroxene contain up to 12.78 wt% TiO_2 (**Table 3**). The magnetite in the matrix contains low Ti, with $Fe^{3+}/\sum Fe$ ratios being 0.64–0.66. Magnetite in the quartz vein contains nearly no Ti. The content of Ti is a sensitive indicator of the origin of magnetite: magnetite of magmatic origin normally has the highest content of Ti and often forms titanomagnetite, whose TiO_2 composition can be 12–16%. The content of Ti in its composition decreases significantly when contacting metasomatic or hydrothermal origin magnetite. For magnetites of the sedimentary metamorphic origin, the content of Ti is the lowest. In this study, the magnetite in clinopyroxene contains up to 12.78 wt % TiO_2, indicating a magmatic origin. This is also evidenced in **Figure 8** where they generally fall within the area of magmatic magnetite. Magnetite in the magnetite–quartz vein falls into the "skarn type" (**Figure 8B**) and "hydrothermal type" (**Figure 8C**) of the "contact metasomatic magnetite area" (**Figure 8A**), showing the characteristic of the skarn type. At last, magnetite in the syenite matrix is relatively complex and generally belongs to magmatic magnetite (**Figure 8**).

DISCUSSION

Geochronology

Magnetite mineralization occurs in both the internal and external contact zones of syenite, and therefore is closely associated with the emplacement of the syenite pluton. We suggest that the crystallization age of the syenite pluton corresponds to the metallogenic age of the Qia'erdunbasixi iron deposit. Zircons from syenite generally have typical magmatic oscillatory zoning. Some zircons show a fan-shaped structure and a few zircons have a core–mantle structure. The apparent age of the oldest zircon is 1751.5 Ma (measuring point three.1, Th/U = 0.34), and the other zircon exhibits the age of Mesoproterozoic (1,383 Ma, measuring point 8.1, Th/U = 1.44). On the contrary, point 6.1 indicates an abnormally young zircon (232 Ma, Th/U = 0.26). In addition to these three measuring points, the other seven zircons give a relatively consistent concordia age, with a weighted average of 345 ± 2.2 Ma (MSWD = 1.3, **Figure 5**). The variation of zircon Th/U ratios is also relatively limited (0.52–0.82). We suggest that this mean age (345 ± 2.2 Ma) represents the crystallization age of

TABLE 3 | Major element abundances (wt%) of magnetites (c: core; r: rim).

Sample	187-5	187-6	187-11	187-7	187-8	187-9	187-10	187-1	187-2	187-3	187-4	FH26-1	FH26-2	FH26-3	FH26-4
Location	Cpx	Cpx	Cpx	Cpx	Mantle	matrix	matrix	matrix	matrix	matrix	matrix	vein	vein	vein	vein
Position	r	r	c	r	-	-	-	-	-	-	-	-	-	-	-
SiO_2	0.01	0	0.02	0.08	0.08	0.04	0.03	0.07	0.06	0.06	0.07	0.07	0.06	0.11	0.02
TiO_2	0.39	0.21	12.78	4.28	2.15	0.10	0.09	0.08	0.07	0.11	0	0.01	0	0.01	0.02
Al_2O_3	0.26	0.07	0.09	0.31	0.28	0	0	0.02	0.01	0	0	0	0	0	0
Cr_2O_3	4.39	4.47	1.72	2.27	1.94	1.99	1.34	5.26	5.64	6.32	6.20	0	0.08	0.21	0.17
FeO_t	88.54	91.57	78.50	86.61	85.54	87.71	92.15	91.79	90.50	90.48	90.67	91.57	91.01	89.38	90.02
MnO	0	0.16	0.20	0	0.02	0.16	0.09	0.01	0	0	0.07	0	0.06	0	0.02
MgO	0.02	0.07	0.25	0.03	0.02	0.01	0	0.03	0.03	0.02	0.02	0	0.05	0.10	0.13
CaO	0	0	0.01	0.15	0.26	0.16	0	0.04	0.05	0.07	0.16	0	0.20	0.61	0.48
O = 32															
Si	0	0	0.01	0.02	0.03	0.01	0.01	0.02	0.02	0.02	0.02	0.02	0.02	0.03	0.01
Ti	0.09	0.05	2.98	0.99	0.51	0.02	0.02	0.02	0.02	0.02	0	0	0	0	0
Al	0.09	0.02	0.03	0.11	0.11	0	0	0.01	0	0	0	0	0	0	0
Cr	1.07	1.05	0.42	0.55	0.49	0.50	0.32	1.23	1.33	1.48	1.45	0	0.02	0.05	0.04
Fe^{3+}	14.65	14.83	9.56	13.31	14.33	15.43	15.62	14.69	14.60	14.43	14.51	15.95	15.94	15.87	15.94
Fe^{2+}	8.08	7.98	10.82	8.95	8.44	7.93	8.01	8.01	8.00	8.01	7.94	8.02	7.91	7.78	7.78
Mn	0	0.04	0.05	0	0.01	0.04	0.02	0	0	0	0.02	0	0.02	0	0.01
Mg	0.01	0.03	0.12	0.01	0.01	0	0	0.01	0.01	0.01	0.01	0	0.02	0.05	0.06
Ca	0	0	0	0.05	0.09	0.05	0	0.01	0.02	0.02	0.05	0	0.07	0.21	0.16
$Fe^{3+}/(Fe^{3+}+Fe^{2+})$	0.64	0.65	0.53	0.60	0.63	0.66	0.66	0.65	0.65	0.64	0.65	0.67	0.67	0.67	0.67

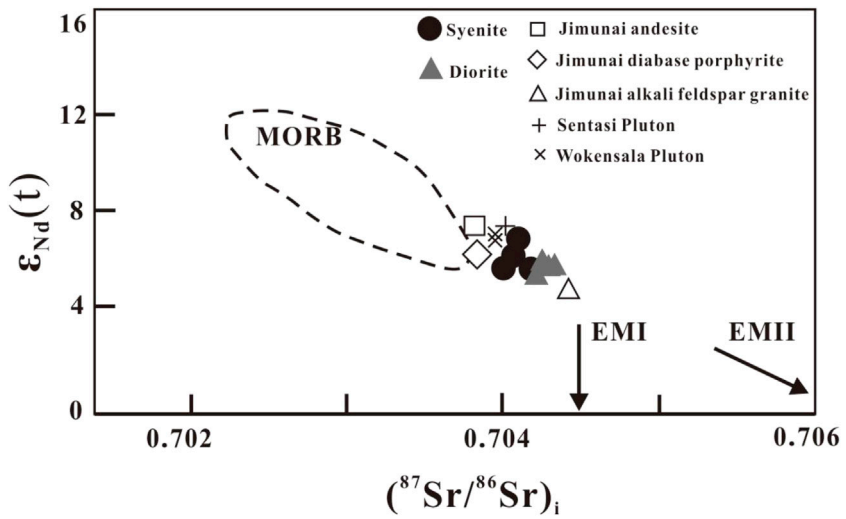

FIGURE 8 | $\varepsilon_{Nd(t)}$ vs. $(^{87}Sr/^{86}Sr)_i$ plot for syenite and diorite in Qiaer'dunbasixi deposit. The field for MORB is from Zou et al. (2000) and Barry and Kent (1998), EMI and EMII are from Zindler and Hart (1986). Jimunai andesite, sillite and alkali–feldspar granite are from He et al. (1994), Sentasi and Wokensala intrusions are from Yuan et al. (2006).

syenite, and Proterozoic zircon should be the residue of magma source material. The young age (232 Ma) obtained at point 6.1 is significantly different from other early Carboniferous zircons by its abnormally low Th/U ratio. We estimate that there is no geological significance, but it is possibly the result of the destruction of magmatic zircon by metallogenic hydrothermal fluid, which is similar to zircon in granite transformed by a ductile shear zone (Zhu and Song, 2006).

Petrogenesis and Geodynamic Setting

The intrusive rocks in the Qia'erdunbasixi mining area are syenite, diorite, and granodiorite. They have calc–alkaline island arc–like compositions with a distinctive light and heavy rare earth differentiation, and are enriched in large ion lithophile elements and depleted in high field strength elements such as Nb, Ta, Zr, and Hf (Wang and Zhu, 2010). Syenite has high ε_{Nd} (t) (+5.5–+6.8) and relatively low $(^{87}Sr/^{86}Sr)_i$

TABLE 4 | Sr–Nd isotopic composition for the intrusive rocks in the Qia'erdunbasixi deposit.

Sample	07TS187	07TS190	07TS193	FH14	07TS189	07TS199	FH21	FH19	ZK07-33
Lithology	Syenite	Syenite	Syenite	Syenite	Syenite	Diorite	Diorite	Diorite	Diorite
$^{87}Rb/^{86}Sr$	N.A	0.179695	0.161246	0.166444	N.A	0.235611	0.253706	N.A	0.315731
$^{87}Sr/^{86}Sr$	N.A	0.705,079	0.704,885	0.704,851	N.A	0.705,396	0.70589	N.A	0.705,893
(2σ)	N.A	0.000021	0.000012	0.00001	N.A	0.00001	0.000012	N.A	0.00001
$(^{87}Sr/^{86}Sr)_i$		0.704197	0.704093	0.704034		0.704109	0.704086		0.704114
$^{147}Sm/^{144}Nd$	0.116,442	0.105983	0.108047	0.106275	0.115034	0.123978	0.115478	0.125954	0.126571
$^{143}Nd/^{144}Nd$	0.512,794	0.512731	0.512747	0.512717	0.5128	0.512711	0.51271	0.512715	0.512737
(2σ)	0.000010	0.000013	0.000012	0.000013	0.000013	0.000014	0.000013	0.000012	0.000012
$\varepsilon_{Nd(345Ma)}$	6.6	5.8	6	5.5	6.8	4.6	5	4.6	5

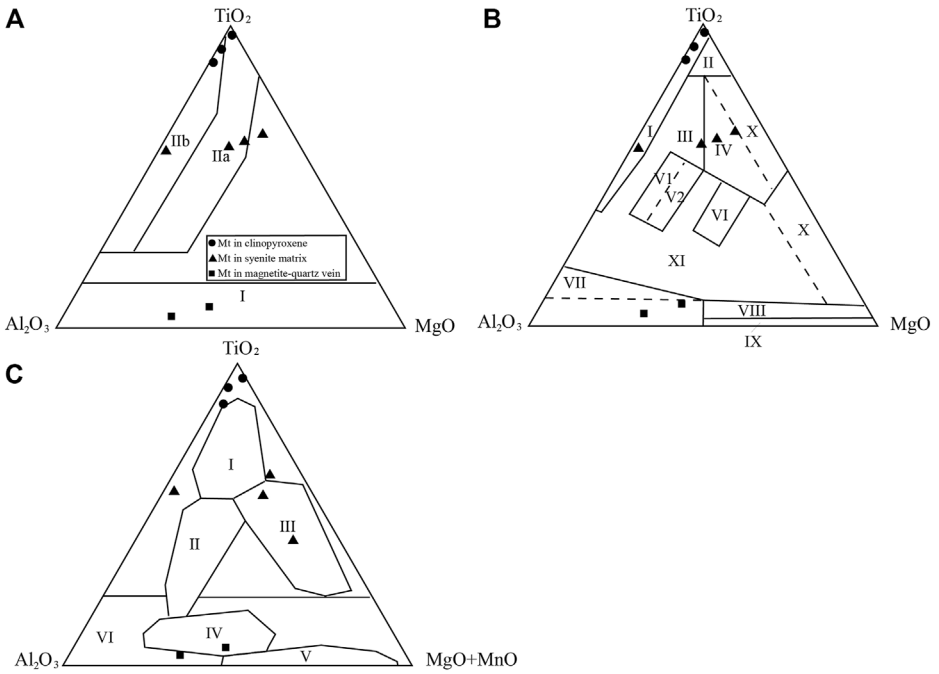

FIGURE 9 | Genetic diagram of magnetite: **(A)** I. sedimentary metamorphism-contact metasomatic magnetite, IIa. ultrabasic–basic–neutral magmatic magnetite, IIb, acid–alkaline magmatic magnetite (based on Chen et al., 1987); **(B)** I–VI. Magma type, VII. Hydrothermal and calcic skarn type (hydrothermal type under dash line, calcic type below dash line); **(C)** I. Accessory mineral type, II. Magma immiscible separation titanium magnetite type, III. Volcanic type, IV. Hydrothermal type, V. Skarn type, VI. Metasendimentary (based on Chen et al., 1987).

(0.7040–0.7042) as shown in the $(^{87}Sr/^{86}Sr)_i$–$\varepsilon_{Nd}(t)$ diagram (**Table 4**; **Figure 9**), which generally indicates a mantle source with a certain amount of assimilation of crustal materials. A previous Sr–Nd isotopic analysis of the magmatic rocks in the Sawur area shows that they all have low $(^{87}Sr/^{86}Sr)_i$ and high $\varepsilon_{Nd\ (t)}$ and are relatively uniform ($(^{87}Sr/^{86}Sr)_i$ = 0.7035–0.7046, $\varepsilon_{Nd\ (t)}$ = +5.7–+8.0) (He, 1994; Yuan et al., 2006; Zhou et al., 2006). Their depleted model ages are concentrated between 500 and 700 Ma with small variations, indicating a young magma source. All these lines of evidence suggest that the Sawur area was an island arc setting in at least the Early Carboniferous.

Microfossils in silicic rocks in the Char ophiolite confirm the existence of the Ertix–Zhaisang ocean between Altay and Kazakhstan from the Devonian to Early Carboniferous (Iwata et al., 1994, 1997; Zheng et al., 2021), and therefore the Zarma–Sawur volcanic arc on the northeast edge of the Kazakhstan plate is thought to be the product of southward subduction of the Ertix–Zhaisang ocean (Demidenko & Morozov, 1999; Vladimirov et al., 2008; Chen et al., 2019; Duan et al., 2019). The intrusions near the Sawur Mountain in the Early Carboniferous may represent the island arc magmatism triggered by the southward subduction of the Ertix–Zhaisang ocean, which is a part of the Zarma–Sawur Island arc (Chen et al., 2010). Calc–alkaline andesitic lavas, andesitic breccias, pyroclastic rocks, and subvolcanic rocks are widely exposed in the Kuoerzhenkuola and Buerkesidai mining areas in the Sawur area. The age of the andesite measured by the Rb–Sr method is 347–343 Ma (Liu et al., 2003). Both gold deposits are in the same volcanic system, belonging to the Lower Carboniferous Heishantou

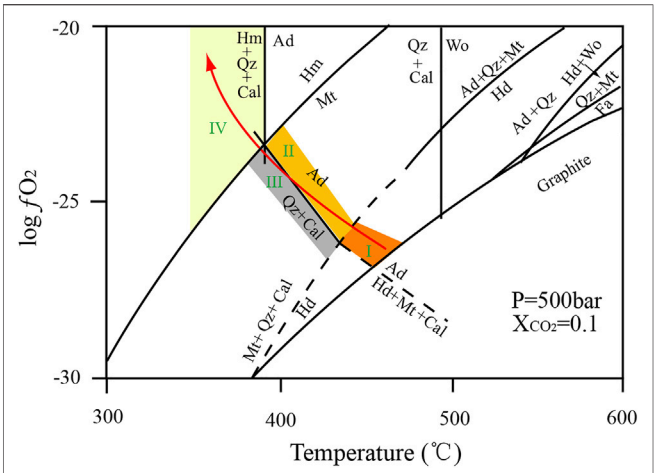

FIGURE 10 | Temperature–log f_{O2} diagram at 500 bar and X_{CO2} = 0.1 for the system Ca–Fe–Si–C–O–H (modified after Einaudi, 1981). The arrow shows the T-log f_{O2} path of magnetite mineralization in the Qia'erdunbasixi deposit (modified from Wang and Zhu, 2010). Ab—Albite; Ad—Andradite; Cal—Calcite; Di—Diopside; Fa—Fayalite; Hm—Hematite; Hd—Hedenbergit; Mt—Magnetite; Qtz—Quartz; Wo—Wollastonite.

Formation. A geochemical analysis of this set of volcanic rock also corresponds with the island arc setting (Shen et al., 2005, 2007).

Skarn Evolution and Mineralization

In the prograde skarn stage, the salite in the syenite was altered into diopside and magnetite (**Figure 10**) (**formula 1**). There are two generations of andradite. The andradite in the early stage coexists with hedenbergite and calcite, with a temperature range of 450–500 ℃ (**Figure 10**). Then, the hedenbergite breaks into andradite, quartz, and magnetite, suggesting an increase in the oxygen fugacity and a decrease in temperature of the metallogenetic environment (**Figure 10**) (**formula 2**). In the retrograde skarn stage, the salite was metasomatized by epidote and chlorite, and fine-grained magnetite was precipitated resulting in actinolite. Chou and Eugster (1977) suggested that iron circulates in the form of ferrous chloride ($FeCl_2$) in supercritical fluid with an absence of S and the presence of Cl (**Formula 3**). The hydrochloric acid generated from the reaction dissolves the precipitated magnetite, and to drive the reaction in the direction of magnetite formation, conditions which neutralize hydrochloric acid must exist. The sericitization of feldspar in syenite is developed mostly in the early stage; sericitization of feldspar can consume H^+ and promote the formation of magnetites (**formula 4**). A large quantity of magnetite and quartz forms veins which constitute the main ore body. The magnetite at this stage is highly euhedral, and lath-shaped, accounting for about 50 vol% of the veins (**Figures 4F, G**), and the formation temperature is below 400 ℃ (**Figure 10**). This process mainly occurs in the quartz–sulfide stage, and is accompanied by a strong potassic alteration.

$$15Ca(Mg_{0.8}Fe_{0.2})Si_2O_6 + H_2O + 15CO_2 = 12CaMgSi_2O_6 + Fe_3O_4 + 3CaCO_3 + 6SiO_2 + H_2 \quad (1)$$

$$9CaFe(Si_2O_6) + 2O_2 = 3Ca_3Fe_2(SiO_4)_3 + 9SiO_2 + Fe_3O_4 \quad (2)$$

$$3FeCl_2^{fluid} + 4H_2o^{fluid} = Fe_3o_4^{mt} + 6HCl^{fluid} + H_2^{fluid} \quad (3)$$

$$3AlSi_3O_8^- + 2H^+ = Al_2[AlSi_3O_{10}](OH)_2^- + 6SiO_2 \quad (4)$$

Comparisons With Other Skarn Deposits

A comparison between the Qia'erdunbasixi Fe deposit and a typical skarn deposit is listed in **Table 5**. In contrast to typical skarn deposits, the Qia'erdunbasixi deposit has weak skarn mineralization and small reserves. In the island arc setting, mafic magma pools and interacts with crustal rock in the MASH zone, with the generation of less dense, hybrid, andesitic–dacitic magma that associates with Cu mineralization. Consequently, the relatively mafic magmas ascend and trigger the Fe skarn mineralization in the Sawur volcanic rocks (**Figure 11**). Einaudi et al. (1981) proposed that skarn with volcanic rocks as the wall rocks belongs to the metasomatic skarn, which is the result of large-scale magmatic hydrothermal fluid infiltrates which react with volcanic rocks. The properties of hydrothermal fluid are the major controlling factor (Einaudi et al., 1981). Zhao et al. (1990) referred to these deposits as skarn deposits related to volcanic gas–liquid interaction,

TABLE 5 | Comparison between the Qia'erdunbasixi Fe deposit and a typical skarn deposit (Meinert et al., 2005; Chang et al., 2019).

	Typical skarn Deposit	Qia'erdunbasixi Fe Deposit
Country rock	Limestone, dolomitic limestone, dolomite, and other carbonate rocks	Andesite and tuff
Grade and reserves	High grade and large reserves	Rich ore and reserve unknown
Lithosome	Calcareous alkaline series: granite-granodiorite porphyry-quartz diorite-diorite; Alkaline series: alkaline syenite - granite syenite - quartz monzonite - monzonite	Syenite
Alteration	Calcium skarn: garnet, pyroxene, epidote, and actinolite; Magnesium skarn: magnesium olivine, diopside, spinel, wollastonite, serpentine, phlogopiteetc.	Calcium skarn: pyroxene, garnet, epidote, chloriteetc
Mineralization	Internal and external contact zones of rock mass and bedding of country rock	Internal and external contact zone of intrusion
Orebody	Layer-like, lenticular, nest-like, columnar, vein-like, etc	Irregular veins, beaded and fine veins formed by filling and metasomatism
Ore structure	Massive, disseminated, banded, and miarolitic structure	Massive and veined, etc.
Metal	W、Cu、Fe、Mo and Zn	Fe,Cu, and Au
Tectonic environment	Oceanic island arc, continental margin, orogenic belt	Island arc
Representative deposit	Sayak, Kazakhstan, Hanxing Iron Mine, and Shouwangfen Copper Mine	Similar: Monku, Xinjiang, Merry Widow, Iron Hill, Canada

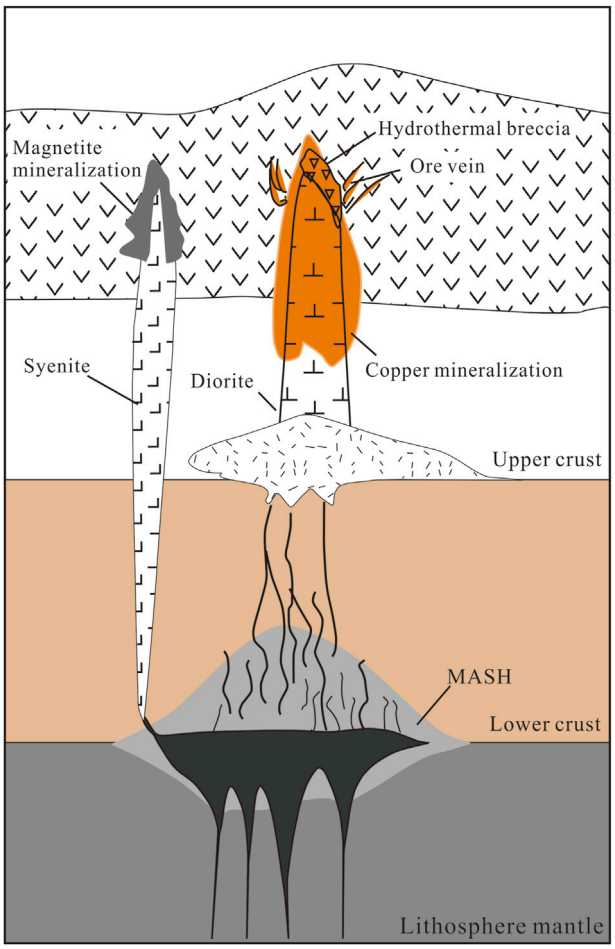

FIGURE 11 | Visualization of the MASH zone at the base of the crust, where hot, dense, mafic magmas pool and interact with crustal rocks to generate less dense, hybrid, andesitic–dacitic magmas, minor mafic magma will ascend, then exist in the form of syenites with an intense skarn alteration and magnetite mineralization. Andesitic–dacitic magma after MASH will enhance copper mineralization.

which were formed mostly by contact metasomatism by an ore-bearing volcanic gas–liquid. Skarn deposits related to volcanic wall rock are mainly calcic iron skarn deposits, which normally develop in an island arc or post-collisional environment, such as seen in Canada, China, the United States, Cuba, and Japan (Einaudi et al., 1981; Wang et al., 2020; Sun et al., 2022). The intrusions are typically diorite or syenite, both rich in iron (Ray et al., 1995), and the wall rock includes limestone and intermediate–basic volcanic rocks (Einaudi et al., 1981).

The main minerals of calcic iron skarn deposits are garnet and pyroxene, as well as minor epidote, ilvaite, and actinolite, all of which are iron-rich (Prutov et al., 1989). In addition to endoskarn alteration, intrusive rocks also extensively develop albite, K-feldspar, and scapolite (Meinert et al., 2005). There are many iron skarn deposits occurring in Triassic limestone and volcanic wall rocks reported in western Canada (Ray et al., 1995). For example, the wall rocks of Iron Hill, Iron Crown, and Merry Widow iron deposits are limestone and volcanic rock, causing different types of skarn alterations. Generally, the skarn in limestone is more iron-rich, and the representative skarn minerals such as garnet and monoclinic pyroxene are very different. Garnet in volcanic rocks contains more Al, Mn, Mg, Ti, and V, and pyroxene also contains more Al and V, implicating significant interaction with volcanic rocks (Meinert et al., 1981). To make a comparison, further studies on the mineral chemistry of the Qia'erdunbasixi deposit are required in the future.

CONCLUSION

The Qia'erdunbasixi Fe–Cu deposit in Sawur is hosted by Devonian and Carboniferous volcanic rocks in an island arc setting. The ore-causative intrusions are syenite and diorite, and the SHRIMP U–Pb age of syenite is 345 ± 2.2Ma (MSWD = 1.3). Their Sr–Nd isotopic compositions ($(^{87}Sr/^{86}Sr)_i$ = 0.70403 to 0.70420 and $\varepsilon_{Nd(t)}$ = +5.5 to +6.8) as well as their REE and PM patterns all exhibit arc magma characteristics with a certain amount of crustal contamination. Magnetite and copper mineralization developed mostly along the contact zones of syenite and diorite, respectively. Magnetite mineralization shows the typical characteristics of skarn alteration, which can be divided into prograde skarn, retrograde skarn, and Quartz–sulfide stages. In contrast to the typical skarn deposits, the Qia'erdunbasixi deposit has weak skarn mineralization and small reserves. Copper mineralization is concentrated along the outer contact zone of diorite, and has four stages of albite–quartz (1), chalcopyrite–pyrite–gold–seriate–quartz (2), chalcopyrite–pyrite–epidote–prehnite (3), and sphalerite–galena–quartz–calcite (4). Many magnetite, gold, and copper deposits and other mineral occurrences have been discovered in the volcanic rocks of the Sawur area, suggesting that the Devonian and Carboniferous volcanic rocks are highly susceptible to Fe, Cu, and Au mineralization.

DATA AVAILABILITY STATEMENT

The original contributions presented in the study are included in the article/Supplementary Material; further inquiries can be directed to the corresponding authors.

AUTHOR CONTRIBUTIONS

SY and RW interpreted the data and wrote the manuscript, and YZ designed the experiment and participated in the writing. Q–SZ processed the data and participated the writing.

FUNDING

Financial support was provided by the Chinese National Natural Science Foundation (Grant Nos. 92162104, 41973037, 40821002, 40572033, and 42072077).

REFERENCES

Barry, T. L., and Kent, R. W. (1998). "Cenozoic Magmatism in Mongolia and the Origin of Central and East Asian Basalts, "in *Mantle Dynamics and Plate Interactions in East Asia, American Geophysical Union*. Editor M. F. J. Flower, S. L. Chung, C. H. Lo, and T. Y. Lee Geodynamics 27, 347–364.

Bureau of Geology and Mineral Resources of Xinjiang Uygur Autonomous Region (1993). *Regional Geology of Xinjiang Uygur Autonomous Region*. Beijing: Geological Publishing House. in Chinese.

Chen, G. Y. (1987). *Genetic and Prospecting Mineralogy* Chongqing: Chongqing Publishing House. In Chinese.

Chen, J.-F., Han, B.-F., Ji, J.-Q., Zhang, L., Xu, Z., He, G.-Q., et al. (2010). Zircon U-Pb Ages and Tectonic Implications of Paleozoic Plutons in Northern West Junggar, North Xinjiang, China. *Lithos* 115, 137–152. doi:10.1016/j.lithos.2009.11.014

Chen, J. F., Ma, X., Simon, A., Du, H. Y., and Liu, B. (2019). Late Ordovician to Early Silurian Calc–Alkaline Magmatism in the Xiemisitai Mountains, Northern West Junggar: a Response to the Subduction of the Junggar–Balkhash Ocean. *Int. Geol. Rev.* 61, 2000–2020. doi:10.1080/00206814.2019.1576148

Chen, S. S., Li, P., Guo, X. J., Liu, X. F., Zhang, B., and Du, X. W. (2017). Zircon U–Pb Geochronology and Geochemistry of Monzonite in the Heishantou Gold Deposit in Sawuer Region, West Junggar and Prospecting Potential. *Geotect. Metallogenia* 41, 865–878. in Chinese.

Chou, I.-M., and Eugster, H. P. (1977). Solubility of Magnetite in Supercritical Chloride Solutions. *Am. J. Sci.* 277, 1296–1314. doi:10.2475/ajs.277.10.1296

Demidenko, A. N., and Morozov, O. L. (1999). Geology and Paleomagnetism of Middle–Upper Paleozoic Rocks of the Saur Ridge. *Geotectonics* 4 (4), 64–80. in Russian with English abstract.

Duan, F., Li, Y., Zhi, Q., Yang, G., and Gao, J. (2019). Petrogenesis and Geodynamic Implications of Late Carboniferous Sanukitic Dikes from the Bieluagaxi Area of West Junggar, NW China. *J. Asian Earth Sci.* 175, 158–177. doi:10.1016/j.jseaes.2019.01.013

Einaudi, M. T., Meinert, L. D., and Newberry, R. J. (1981). Skarn Deposits. *Econ. Geol.* 75, 317–391. doi:10.5382/av75.11

He, G. Q., Cheng, S. D., Xu, X., Li, J. Y., and Hao, J. (2005). *Geotectonic Map of Xinjiang and its Neighboring Areas, China 1:1500000*. Beijing: Geological Publishing House.

He, B. C., Tan, K. R., and Wu, Q. H. (1994). Ages and Sr, Nd Isotopic Evidences of Mantle Source Magmatite in the Bu's Gold Deposit, Jimunai County, Northern Xinjiang. *Geotect. Metallogenia* 18, 219–228.

He, G. Q., Liu, D. Q., Li, M. S., Tang, Y. L., and Zhou, R. H. (1995). The Five-Stage Model of Crustal Evolution and Metallogenic Series of Chief Orogenic Belts in Xinjiang. *Xinjiang Geol.* 13, 99–180.

Iwata, K., Obut, O. T., and Buslov, M. M. (1997). Devonian and Lower Carboniferous Radiolarian from the Chara Ophiolite Belt, East Kazakhstan. *News Osaka Micropaleontol.* 10, 27–32.

Iwata, K., Watanabe, T., Akiyama, M., Dobretsov, N. L., and Belyaev, S. Y. (1994). Paleozoic Microfossils from the Chara Belt (Eastern Kazakhstan). *Russ. Geol. Geophys.* 35, 145–151.

Liu, G. R., Long, Z. N., Chen, Q. Z., and Zhou, C. (2003). The Formation Age and Geochemical Characteristics of the Volcanic Rock of Kuo'erzhenkuola's Gold Mine in Xinjiang. *Xinjiang Geol.* 21, 177–180.

Meinert, L. D., Dipple, G. M., and Nicolescu, S. (2005). World Skarn Deposits. *Econ. Geol.* 100, 299–336. doi:10.5382/av100.11

Meinert, L. D. (1984). Mineralogy and Petrology of Iron Skarns in Western British Columbia, Canada. *Econ. Geol.* 79, 869–882. doi:10.2113/gsecongeo.79.5.869

Meinert, L. D. (1981). Skarns and Skarn Deposits. *Geosci. Can.* 19, 145–162.

Purtov, V. K., Kholodnov, V. V., Anfilogov, V. N., and Nechkin, G. S. (1989). The Role of Chlorine in the Formation of Magnetite Skarns. *Int. Geol. Rev.* 31, 63–71. doi:10.1080/00206818909465861

Ray, G. E., Webster, I. C. L., and Ettlinger, A. D. (1995). The Distribution of Skarns in British Columbia and the Chemistry and Ages of Their Related Plutonic Rocks. *Econ. Geol.* 90, 920–937. doi:10.2113/gsecongeo.90.4.920

Shen, P., Shen, Y. C., Liu, T. B., Li, G. M., and Zeng, Q. D. (2005). Geochemistry of Ore-Forming Fluid and its Significance in Kuo'erzhenkuola Gold Field, Xinjiang. *Sci. China (Series D).* 35, 862–869.

Shen, P., Shen, Y., Liu, T., Li, G., and Zeng, Q. (2007). Genesis of Volcanic-Hosted Gold Deposits in the Sawur Gold Belt, Northern Xinjiang, China: Evidence from REE, Stable Isotopes, and Noble Gas Isotopes. *Ore Geol. Rev.* 32, 207–226. doi:10.1016/j.oregeorev.2006.10.005

Shen, P., Shen, Y., Liu, T., Li, G., and Zeng, Q. (2008). Geology and Geochemistry of the Early Carboniferous Eastern Sawur Caldera Complex and Associated Gold Epithermal Mineralization, Sawur Mountains, Xinjiang, China. *J. Asian Earth Sci.* 32, 259–279. doi:10.1016/j.jseaes.2007.10.004

Sun, F., Zhang, J. B., Wang, R., Zhou, L. M., Jeon, H., Li, Y. Y., et al. (2022). Magmatic Evolution and Formation of the Giant Jiama Porphyry-Skarn Deposit in Southern Tibet. *Ore Geol. Rev.* 145. doi:10.1016/j.oregeorev.2022.104889

Sun, S. S., and McDonough, W. F. (1989). *Chemical and Isotopic Study of Oceanic Basalts: Implications For Mantle Composition and Processes*. Geological Society of London, Special Publication 42, 313–345.

Tan, L. G., Zhou, T. F., Yuan, F., Fan, Y., and Yue, S. C. (2007). ^{40}Ar-^{39}Ar Age of the Kalagang Formation Volcanic Rocks in Western Junggar. *Xinjiang* 42, 579–586. in Chinese.

Vladimirov, A. G., Kruk, N. N., Khromykh, S. V., Polyansky, O. P., Chervov, V. V., Vladimirov, V. G., et al. (2008). Permian Magmatism and Lithospheric Deformation in the Altai Caused by Crustal and Mantle Thermal Processes. *Russ. Geol. Geophys.* 49, 468–479. doi:10.1016/j.rgg.2008.06.006

Wang, R., Zhu, D., Wang, Q., Hou, Z., Yang, Z., Zhao, Z., et al. (2020). Porphyry Mineralization in the Tethyan Orogen. *Sci. China Earth Sci.* 63, 2042–2067. doi:10.1007/s11430-019-9609-0

Wang, R., and Zhu, Y. F. (2010). Geology and Geochemistry of Qia'erdunbasixi Fe–Cu–Au Deposit in Sawur, Northern Xinjiang. *Mineral. Deposits* 29, 229–242.

Wang, R., and Zhu, Y. F. (2007). Geology of the Baobei Gold Deposit in Western Juggar and Zircon SHRIMP Age of its Wall-Rocks, Western Juggar (Xinjiang,NW China). *Geol. J. China Univ.* 13, 590–602.

Williams, J. S. (1998). "U–Th–Pb Geochronology by ion Microprobe," in *Application of Microanalytical Techniques to Understanding Mineralizing Processes* 7. doi:10.5382/Rev.07.01

Windley, B. F., Alexeiev, D., Xiao, W., Kröner, A., and Badarch, G. (2007). Tectonic Models for Accretion of the Central Asian Orogenic Belt. *J. Geol. Soc.* 164. 31–47. doi:10.1144/0016-76492006-022

Windley, B. F., Kröner, A., Guo, J., Qu, G., Li, Y., and Zhang, C. (2002). Neoproterozoic to Paleozoic Geology of the Altai Orogen, NW China: New Zircon Age Data and Tectonic Evolution. *J. Geol.* 110, 719–737. doi:10.1086/342866

Xia, W. J., Wang, R., and Zhu, Y. F. (2022). Petrogenesis of Lamprophyre in Sawur, Northern Xinjiang, China: Implication for Volcanic Hosted Gold Deposits. *Ore Geol. Rev.* 144. doi:10.1016/j.oregeorev.2022.104856

Yuan, F., Zhou, T. F., Deng, Y. F., Guo, X. J., Zhang, D. Y., Xu, C., et al. (2015). Ore-forming Type and Regional Metallogenic Regularity in the Sawuer region,West Junggar, Xinjiang. *Acta Petrol. Sin.* 31, 388–400. in Chinese.

Yuan, F., Zhou, T. F., Tan, L. G., Fan, Y., Yang, W. P., He, L. X., et al. (2006). Isotopic Ages of the I Type Granites in West Junggar Sawuer Region. *Acta Petrol.* 22, 1238–1248.

Zhang, R. (2016). *Geological and Genesis of Volcanic Hydrothermal Type Copper (Gold) Deposits (Points) in Taerbahatai–Sawuer Area*. West Junggar: Hefei: Hefei University of Technology. Dissertation/Master's thesis.

Zhao, Y. M., and Shen, W. B. (1990). *Skarn Deposits in China*. Beijing: Geological Publishing House. in Chinese.

Zheng, Q., Xu, X., Zhang, W., Zheng, Y., Liu, Y., Kuang, X., et al. (2021). A Fossil Paleozoic Subduction-Dominated Trench–Arc–Basin System Revealed by Airborne Magnetic-Gravity Imaging in the Western Junggar, NW China. *Front. Earth Sci.* 9, 1076. doi:10.3389/feart.2021.760305

Zhou, T., Yuan, F., Fan, Y., Zhang, D., Cooke, D., and Zhao, G. (2008). Granites in the Sawuer Region of the West Junggar, Xinjiang Province, China: Geochronological and Geochemical Characteristics and Their Geodynamic Significance. *Lithos* 106, 191–206. doi:10.1016/j.lithos.2008.06.014

Zhou, T., Yuan, F., Tan, L., Fan, Y., and Yue, S. (2006). Geodynamic Significance of the A-type Granites in the Sawuer Region in West Junggar, Xinjiang: Rock Geochemistry and SHRIMP Zircon Age Evidence. *Sci. China Ser. D.* 49, 113–123. doi:10.1007/s11430-005-0121-7

Zhu, Y., An, F., Feng, W., and Zhang, H. (2016). Geological Evolution and Huge Ore-Forming Belts in the Core Part of the Central Asian Metallogenic Region. *J. Earth Sci.* 27, 491–506. doi:10.1007/s12583-016-0673-7

Zhu, Y., Chen, B., and Qiu, T. (2015). Geology and Geochemistry of the Baijiantan-Baikouquan Ophiolitic Mélanges: Implications for Geological Evolution of West Junggar, Xinjiang, NW China. *Geol. Mag.* 152, 41–69. doi:10.1017/s0016756814000168

Zhu, Y., Chen, B., Xu, X., Qiu, T., and An, F. (2013). A New Geological Map of the Western Junggar, North Xinjiang (NW China): Implications for Paleoenvironmental Reconstruction. *Episodes* 36, 205–220. doi:10.18814/epiiugs/2013/v36i3/003

Zhu, Y. F., and Song, B. (2006). Petrology and SHRIMP Chronology of Mylonitized Tianger Granite, Xinjiang: Also about the Dating on Hydrothermal Zircon Rim in Granite. *Acta Petrol. Sin.* 22, 135–144.

Zhu, Y. F., Xu, X., Luo, Z. H., Shen, P., Ma, H. D., Chen, X. H., et al. (2014). *Geological Evolution and Ore-Formation in the Core Part of Central Asian Metallogenic Region*. Beijing: Geological Publishing House, 1–202. in Chinese.

Zindler, A., and Hart, S. R. (1986). Chemical geodynamics. *Ann. Rev. Earth Planet.* 14, 493–571.

Zou, H. B., Zindler, A., Xu, X. S., and Qi, Q. (2000). Mgjor, Trace Element, and Nd, Sr and Pb Isotope Studies of Cenozoic Basalts in SE China: Mantle Sources, Regional Variations and Tectonic Significance. *Chem. Geol.* 171, 33–47.

Conflict of Interest: The authors declare that the research was conducted in the absence of any commercial or financial relationships that could be construed as a potential conflict of interest.

frontiers | Frontiers in Earth Science

TYPE Correction
PUBLISHED 04 August 2022
DOI 10.3389/feart.2022.981906

OPEN ACCESS

EDITED AND REVIEWED BY
Hassan Mirnejad,
Miami University, United States

*CORRESPONDENCE
Rui Wang,
rw@cugb.edu.cn
Yongfeng Zhu,
yfzhu@pku.edu.cn

SPECIALTY SECTION
This article was submitted to Economic Geology, a section of the journal Frontiers in Earth Science

RECEIVED 29 June 2022
ACCEPTED 04 July 2022
PUBLISHED 04 August 2022

CITATION
Yang S, Zhou Q-S, Wang R and Zhu Y (2022), Corrigendum: Qia'erdunbasixi Fe-Cu deposit in Sawur, Xinjiang: A case study of skarn deposit hosted by volcanic rock.
Front. Earth Sci. 10:981906.
doi: 10.3389/feart.2022.981906

Corrigendum: Qia'erdunbasixi Fe-Cu deposit in Sawur, Xinjiang: A case study of skarn deposit hosted by volcanic rock

Shuang Yang[1], Qiu-Shi Zhou[1], Rui Wang[1]* and Yongfeng Zhu[2]*

[1]State Key Laboratory of Geological Processes and Mineral Resources, and Institute of Earth Sciences, China University of Geosciences, Beijing, China, [2]The Key Laboratory of Orogenic Belts and Crustal Evolution, Ministry of Education, School of Earth and Space Science, Peking University, Beijing, China

KEYWORDS

skarn, magnetite, syenite, Sawur, island arc, Fe-Cu deposit

A Corrigendum on
Qia'erdunbasixi Fe-Cu deposit in Sawur, Xinjiang: A case study of skarn deposit hosted by volcanic rock

by Yang S, Zhou Q-S, Wang R and Zhu Y (2022). Front. Earth Sci. 10:852261. doi: 10.3389/feart.2022.852261

In the published article, a citation of "Wang and Zhu, 2010" was erroneously missed. The citation has now been added in the caption of Figure 4. The updated caption can be seen below.

"**FIGURE 4 | (A)** Clinopyroxene is densely disseminated or presents as veinlets near the contact zone; **(B)** Magnetite is sparsely disseminated; **(C)** Magnetite veinlets; **(D)** Clinopyroxene is metasomatized by epidote + chlorite + magnetite, and epidotization and chloritization in the outer contact zone are well developed; **(E–I)** Alteration of quartz + magnetite + K-feldspar + calcite + sericite + chlorite + prehnite + actinolite + chalcopyrite + pyrite are developed in the hydrothermal stage; **(F,G)** Quartz-magnetite vein with a width of about 2~10 cm, where magnetite accounts for as much as 40 vol.% of the vein volume; **(J)** Chalcopyrite is disseminated and magnetite is metasomatized by hematite; **(K,L)** Coarse K-feldspar grain, with inclusions of diopside formed in the early stage; **(M)** The calcite vein formed in the latest stage cuts through the early-stage magnetite; **(N)** Malachite in magnetite-quartz vein; **(O)** Wall rock of andesite is intensely mineralized with magnetite. Plane polarized light

(A,E, M,O), cross polarized light **(B–D,G–I,K,L,N)**, reflected light **(J)**, BSE image **(F)**. Ab—albite; Adr—andradite; Cal—calcite; Ccp—chalcopyrite; Chl—chlorite; Czo—clinozoisite; Di—diopside; Ep—epidote; Gl—glass; Hem—hematite; Mal—malachite; Mt—magnetite; Kfs—K-feldspar; Qtz—quartz; Sa—salite; Ser—sericite (modified after **Wang and Zhu, 2010**)."

The authors apologize for this error and state that this does not change the scientific conclusions of the article in any way. The original article has been updated.

Publisher's note

frontiers | Frontiers in Earth Science

TYPE Original Research
PUBLISHED 17 August 2022
DOI 10.3389/feart.2022.970944

OPEN ACCESS

EDITED BY
Kit Lai,
Fortescue Metals Group, Australia

REVIEWED BY
Chao Wang,
The University of Hong Kong, Hong Kong, SAR China
Kai Liu,
China University of Geosciences, China

*CORRESPONDENCE
Wei Du,
duweiletian@126.com

SPECIALTY SECTION
This article was submitted to Economic Geology,
a section of the journal
Frontiers in Earth Science

RECEIVED 16 June 2022
ACCEPTED 25 July 2022
PUBLISHED 17 August 2022

CITATION
Wang Y, Du W, Wang Y, Lin R, Zhang D, Zhao F, Sun Z, Chen Y and Wang Y (2022), Meso-cenozoic tectonic evolution of the ziyun-luodian fault in SW China.
Front. Earth Sci. 10:970944.
doi: 10.3389/feart.2022.970944

Meso-cenozoic tectonic evolution of the ziyun-luodian fault in SW China

Yi Wang[1], Wei Du[2,3]*, Yuyang Wang[1,2], Ruiqin Lin[2,3], Daquan Zhang[2,3], Fuping Zhao[2,3], Zhao Sun[2,3], Yi Chen[2,3] and Yang Wang[1]

[1]Guangdong Provincial Key Laboratory of Geodynamics and Geohazards, School of Earth Sciences and Engineering, Sun Yat-Sen University, Guangzhou, China, [2]Key Laboratory of Unconventional Natural Gas Evaluation and Development in Complex Tectonic Areas, Ministry of Natural Resources, Guiyang, China, [3]Guizhou Engineering Research Institute of Oil and Gas Exploration and Development, Department of Natural Resources of Guizhou Province, Guiyang, China

Regional-scale fault systems are important in adjusting intracontinental deformation. Closure of the Paleo-Tethys, Paleo-Pacific subduction, and India-continent-continent collision have all interacted to shape the Meso-Cenozoic tectonics of South China. The Ziyun-Luodian fault (ZLF) straddles across the Guizhou region in southwestern China. New petrographic and structural studies were conducted to reveal the structural evolution of the ZLF and regional deformation. At least three distinct deformation events are identified within the fault zone: During the Indosinian orogeny, dextral thrusting occurred along the ZLF, accompanied by moderate regional uplift in Guizhou, as evidenced by the Upper Triassic-Lower Jurassic disconformity. The main tectonic framework across Guizhou was established during the Yanshanian orogeny. Driven by the west-dipping Paleo-Pacific subduction (Middle Jurassic-Early Cretaceous), sinistral transpression occurred along the ZLF and NE-to N-S-trending fold belts in central-eastern Guizhou, and the NW-striking folds west of the ZLF were developed in under nearly E-W-directed compression. In the late Cenozoic, the ZLF may have undergone sinistral strike-slip movement, similar to the sinistral Ailaoshan-Red River shear zone. The Ziyun-Luodian fault plays an important role in accommodating the Meso-Cenozoic regional deformation in SW South China.

KEYWORDS

South China, ziyun-luodian fault (ZLF), structural analysis, tectonic evolution, meso-cenozoic

1 Introduction

The South China Block (SCB) has experienced multiphase tectono-magmatic events, in response to the Phanerozoic convergence, subduction, and collision of tectonic terranes, making the SCB a natural laboratory for understanding intracontinental orogeny (e.g., Li, 2000; Zhou et al., 2006; Zhang and Cai, 2009; Wang et al., 2013; Li et al., 2014). The Mesozoic is a key period for the tectonic

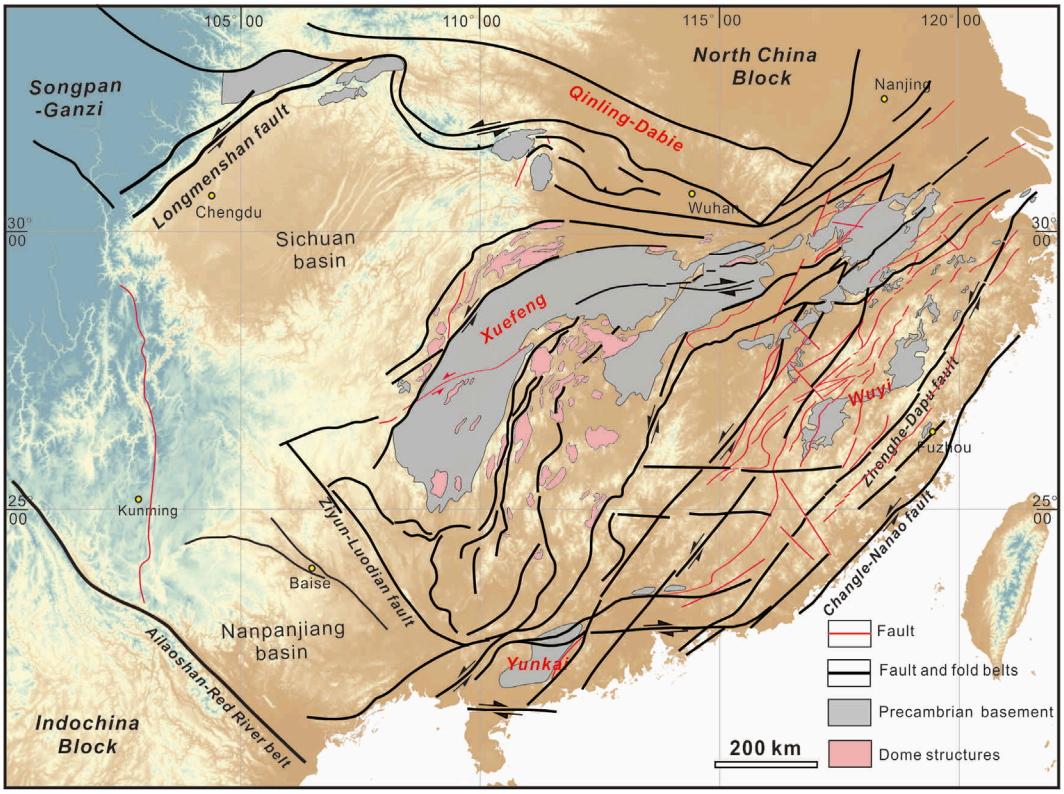

FIGURE 1
Tectonic framework of the South China Block with major fold and fault systems (after Zhang et al., 2013). The SCB was squeezed by the North China Block and Indochina Block, and subsequently affected by the Pacific subduction-accretion.

evolution of South China, including the Triassic (Indosinian) and Jurassic-Cretaceous (Yanshanian) orogenesis, during which spatially prevalent fault systems and fold belts were developed to accommodate crustal deformation (Wang et al., 2013 and references therein). In the Cenozoic, the India-Eurasia continental collision has driven the growth of the Tibetan Plateau and extended the deformation into the SCB (e.g., Yin & Harrison, 2000; Tapponnier et al., 2001), and existing structural features were tectonically reworked/reactivated in response to its far-field impact (e.g., Li et al., 2005; Shen et al., 2012; Wang et al., 2020). Therefore, the Meso-Cenozoic tectonic evolution is recorded in these large fault and fold systems/belts, which provide insights into the regional deformation patterns and geodynamics.

Comprehensive structural, petrological, geochronological, and geochemical studies have been conducted in the past decades and achieved great advancements in understanding the tectonics and dynamics of the SCB (e.g., Jahn et al., 1990; Charvet et al., 1994; Shu et al., 1998, Shu et al., 2009; Wang et al., 2005, Wang et al., 2013 and references therein). The SCB is connected with the Qinling-Dabie orogenic belt to the north, which were characterized by intense fold-and-thrust belts and HP-UHP metamorphic zone (e.g., Zhang et al., 2013). Its western boundary is the Longmenshan thrust fault, which was formed by the Triassic convergence between the Songpan-Ganze and Yangtze Blocks (e.g., Liu et al., 1995). The SCB is separated from the Indochina Block by the Ailaoshan-Red River shear zone along its southwestern margin (Figure 1; e.g., Zhong, 2000). The Ziyun-Luodian fault (ZLF) is an important tectonic boundary separating the Nanpanjiang basin and Xuefengshan domain in SW China (Zhang et al., 2013). It straddles over several hundreds of kilometers, and is parallel to the well-studied Ailaoshan-Red River shear zone (Figure 1; Wang et al., 2016, Wang et al., 2020). However, little is known regarding its geometry, kinematics, and deformation sequences, especially those in the Meso-Cenozoic.

Here, we report new petrologic and structural observations from field investigations along the ZLF. Based on these data, we examine the geometric features and kinematics of the ZLF and determine its deformation sequence. We also analyze the regional structural features in the Guizhou. Our results contribute to understanding the Meso-Cenozoic tectonic evolution of Guizhou and the role of the ZLF in accommodating regional deformation.

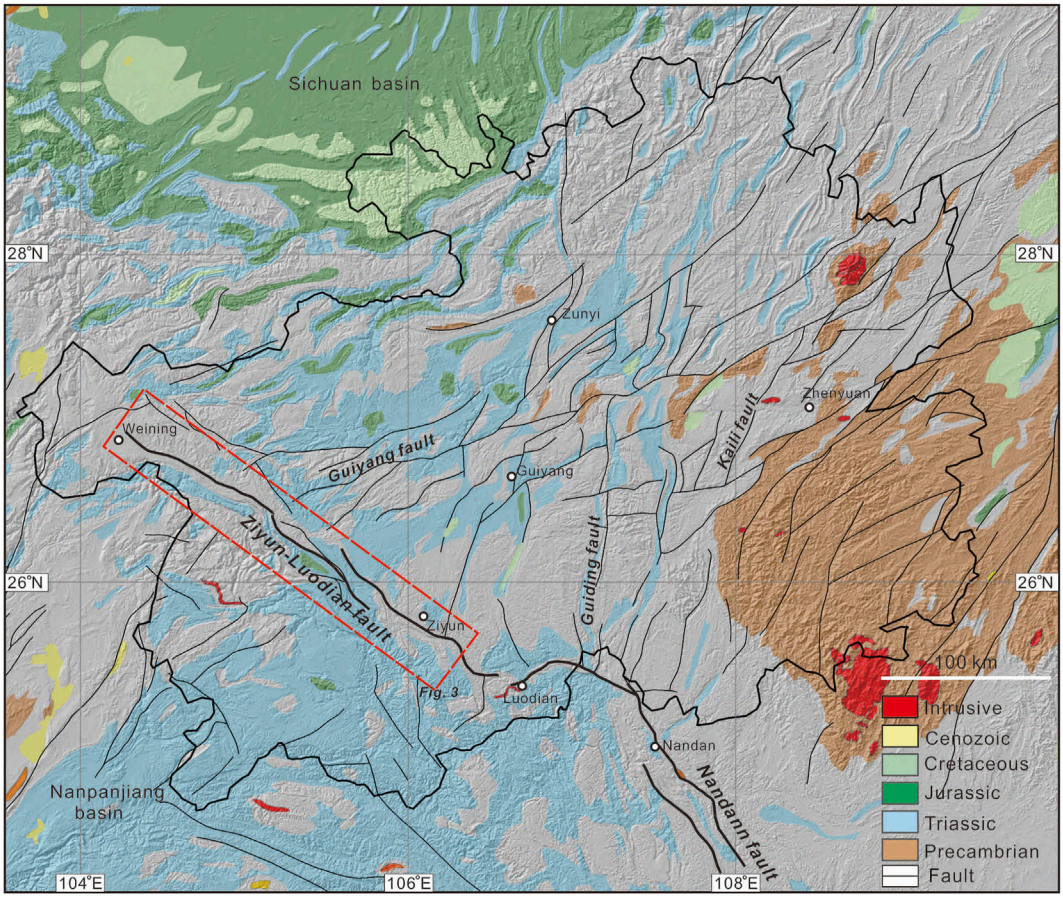

FIGURE 2
Geological map of the Guizhou Province and adjacent regions. The Guizhou Province is tectonically located in the SW margin of the Yangtze Block, adjacent to the Jiangnan orogen to the east, the Sichuan Basin to the north, the Sanjiang orogenic belt to the west, and the Nanpanjiang basin to the southwest. The NW-trending Ziyun-Luodian fault runs across the Yunnan, Guizhou, and Guangxi Provinces in SW China.

2 Geological setting

The SCB consists of the Yangtze Block in the northwest and the Cathaysia Block in the southeast, which are characterized by different basements (e.g., Wang et al., 2007, Wang et al., 2013; Yu et al., 2010). These two blocks were likely amalgamated before ~820 Ma, forming the Jiangnan orogenic belt. The ophiolite mélange was situated along the Jiangshan-Shaoxing fault (e.g., Charvet et al., 1996; Shu and Charvet, 1996; Wang et al., 2013). The SCB may have experienced three main regional tectono-thermal events in the early Paleozoic, early Mesozoic, and late Mesozoic, as evidenced by the regional unconformities and Ar-Ar ages of syn-kinematic minerals from major deformation zones (with three age clusters at 440–410 Ma, 240–200 Ma, and 145–95 Ma; Wang et al., 2013 and references therein). Most early Paleozoic structures are tectonically reworked (Wang et al., 2005). Charvet et al. (2010) documented Ordovician flower structure in the Wuyi Mountains, recording the early Paleozoic crustal deformation.

The SCB collided with the North China and Indochina block to the north and south in the Triassic, respectively, establishing the main tectonic framework of the SCB (Wang et al., 2013). The N-S-directed shortening may have occurred in the early Triassic (~250–225 Ma), and may have resulted in dextral thrusting along a series of the WNW-/W-trending fault and fold systems (Figure 1; Wang et al., 2021). Sinistral transpression may have occurred along the NE-trending fold and fault belts in the SCB interior (ca. 230–190 Ma; Figure 1; Wang et al., 2021). Affected by the west-dipping Paleo-Pacific subduction and subsequent rollback, these NE-trending structures were reactivated and experienced multiple stages of deformation in the late Mesozoic (e.g., Wang et al., 2013, Wang et al., 2021; Li et al., 2014). Furthermore, widespread extensional (half-)grabens with red bed sedimentation, dome structures, and magmatism were developed in the Cretaceous,

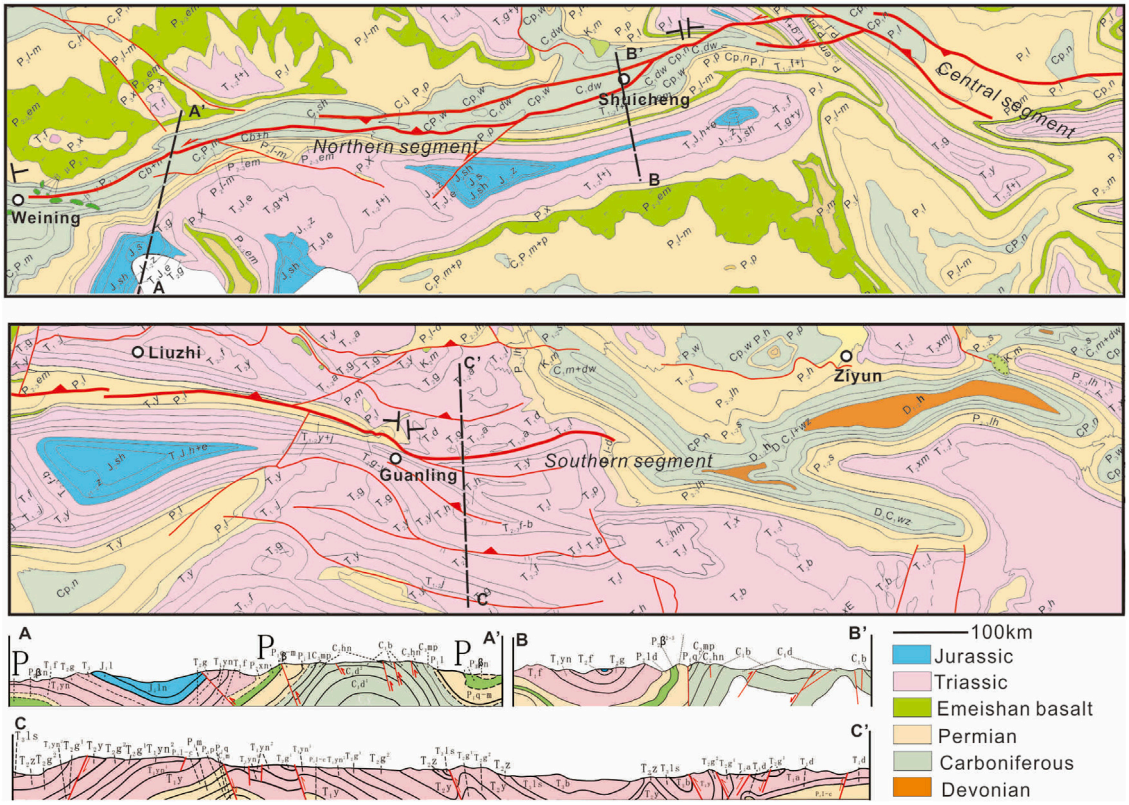

FIGURE 3
Geological map and cross-sections of the Ziyun-Luodian fault and adjacent regions.

reflecting regional extension (e.g., Faure et al., 1996; Shu et al., 1998; Zhou et al., 2006; Shu et al., 2009; Chu et al., 2019). Due to the far-field effect of the India-Asia continental convergence, compressional deformation and accelerated regional exhumation were identified across the SCB in the late Oligocene to early Miocene (Wang et al., 2020 and references therein).

The Guizhou region is tectonically located in the SW margin of the Yangtze Block, and is bounded by the Jiangnan orogen to the east, the Sichuan Basin to the north, the Sanjiang orogenic belt to the west, and the Nanpanjiang basin to the southwest (Figure 2). Fold and fault systems are widespread with different kinematic and geometric characteristics, indicating multistage structural superimposition and overprinting (e.g., Li, 2012). The NW-trending ZLF extends across the Yunnan, Guizhou, and Guangxi Provinces in SW China (from Weining to Ziyun for ~350 km in Guizhou) and joins the Nandan fault in the southeast (Figure 2; Zhang et al., 2013). The ZLF may be originated from a late Paleozoic continental rift, and was reactivated in the Meso-Cenozoic (e.g., Wang and Yin, 2009; Han, 2010; Wu et al., 2012).

3 Stratigraphy

Upper Paleozoic to Mesozoic strata are exposed along the ZLF, albeit being variably deformed by fault movements (Figures 3, 4). Devonian strata are exposed in the southeastern fault segment, including the Huohong, Liujiang, Wuzhishan formations ($D_{1\text{-}2}h$, D_3l, and D_3C_1wz; Figure 4). They are mainly gray-black mudstone intercalated with fine-grained quartz sandstone, thin-medium-bedded chert interlayered with thick limestone. Carboniferous rocks are mainly composed of the Xiangbai (C_1x), Jiusi (C_1j), Shangsi (C_1sh), Weining (CP_1w), Nandan (CP_1n), Baizuo (Cb), Huanglong (C_2h) formations (Figure 4). They are mainly gray-black thin-medium-bedded limestone and dolomite interlayered with mudstone (Cb), black shale with silty mudstone (C_1dw), fine-grained sandstone and quartz sandstone (C_1x), medium-thick-bedded limestone, argillaceous limestone and dolomite (e.g., the Nandang, Jiusi, and Shangsi formations). The Permian strata in the southeastern fault segment comprise mudstone, carbonaceous shale, limestone, chert, and clastic rocks (e.g., the Sidazhai and Linghao formations).

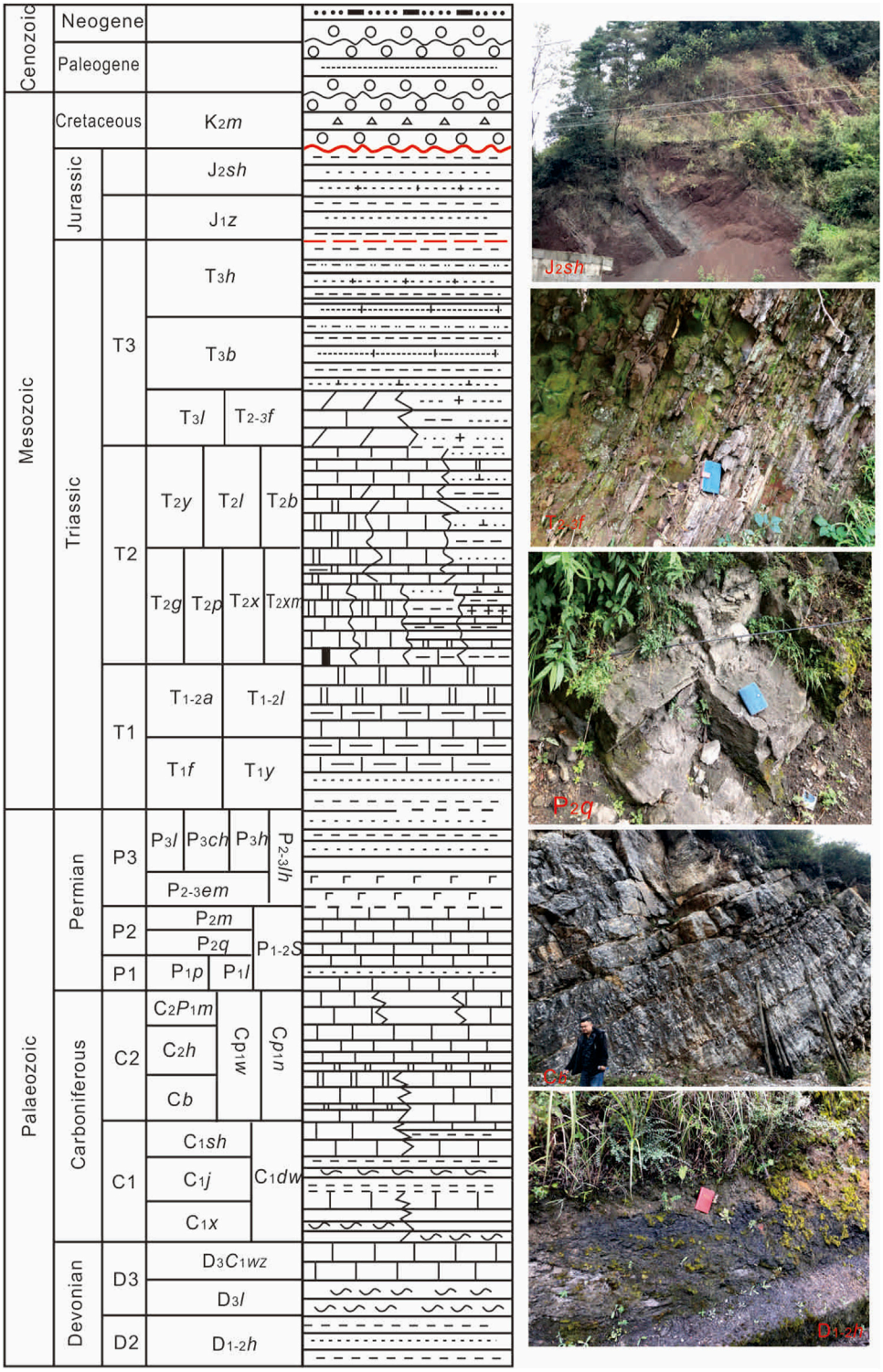

FIGURE 4
Stratigraphic column and typical photos of rock units outcropped along the Ziyun-Luodian fault.

In the northwestern segment, the Permian rocks comprise mainly medium-thick limestone and dolomite intercalated with mudstone (e.g., Qixia and Maokou formations), and Emeishan basalt (Figures 3, 4). Triassic strata (e.g., Luolou, Xuman, Feixianguan, and Guanling formations) are widely distributed along the fault zone, including mainly terrigenous clastic rocks (thin mudstone, silty mudstone, and sandstone) and carbonate rocks (grey dolomite, limestone, and marl). The Jurassic strata are locally distributed along strike (Figure 3). It is mainly composed of fluvial and lacustrine silty mudstone and fine sandstone, with minor lacustrine limestone and marl. They are in disconformity contact with the underlying Triassic strata (Figure 4). The Cretaceous rocks (e.g., Maotai Formation, K_2m) do not outcrop along the ZLF, and are locally documented in Guizhou. The Maotai Formation is a set of alluvial red conglomerate, gravel-bearing sandstone and mudstone. The gravel is mainly composed of Carboniferous and Permian limestone (Figure 4).

4 Structural analysis

4.1 Geometry

The NW-striking ZLF can be traced from Weining to the east of Ziyun in the Guizhou region (Figure 2), and is confined by several NE-trending faults at its northeastern end. The fault becomes difficult to trace toward the southeast near Ziyun (Figure 3). Based on the different geometric features along strike, the ZLF can be subdivided into the Weining-Shuicheng, Shuicheng-Guanling, Guanling-Ziyun segments (Figure 3). The northwestern segment (Weining-Shuicheng) strikes 290–320° and consists of several parallel, closely-spaced branches. Most fault branches were developed in the anticlinal core of the Carboniferous limestone (Figure 3). Fault planes dip toward the NE or SW at various angles, forming back-thrust structures. In the middle segment, it branches southeastward into two strands west of Shuicheng. The general strike of the fault zone changes to N20°W, and then turns to N40-60°W west of Liuzhi. Most faults dip toward the NE at high angles. At the intersection with the Guiyang fault, dozens of WNW-trending faults were developed at various scales, which crosscut or confined the ZLF (Figure 2). The ZLF is mainly developed in the anticlinal core of the Permian limestone between Liuzhi and Guanling (Figure 3). In the southeastern segment, several sub-parallel faults were developed southeast of Guanling, mostly dipping toward NE at high angles (Figure 3). Further southeast, although highly fractured bedrock outcrops are identified, we cannot delineate a continuous fault structure.

4.2 Deformation sequence

In order to explore the kinematics and deformation sequence of the ZLF, we present new structural observations along the fault zone. At least three distinct deformation events are identified, dextral thrusting (D_1), sinistral transpression (D_2), and sinistral shear (D_3).

4.2.1 Dextral thrusting (D_1)

The deformation fabrics preserved in these upper Paleozoic to Triassic rocks reflect the kinematics from upper-middle structural levels. D_1 deformation is best expressed by shortening and transpression structures. Thrust faults were mainly developed within the Carboniferous and Permian strata, e.g., two thrust faults in the Carboniferous limestone (Figure 5A; C_{1d} Datang Formation). The limestone contains medium-thick layer with interbedded mudstone and shows an occurrence of 56°∠60°. A NE-dipping fault damage zone (~1 m thick) was developed along F1. The limestone wallrock was strongly sheared to form penetrative cleavages dipping toward N55°E at 54°, exhibiting S-C fabrics. Together with asymmetric folds of calcite veins in the fault zone, they all indicate top-to-the-SW thrusting (Figure 5A). In addition, the calcite veins were sheared to form asymmetric boudins in the Y-Z plane, pointing to a dextral strike-slip component. F2 is located >10 m southwest of F1. It was developed along a mudstone layer in the limestone. Penetrative cleavages, asymmetric folds and veins are also identified within the fault zone, indicating the same kinematics. In the northwestern segment, the Emeishan basalt is in fault contact with the overlying Permian Qixia Formation limestone. The fault dips toward the NE at 43–60° (Figure 5B). The Permian limestone and Emeishan basalt are intensely fractured on both sides, and the original bedding is difficult to distinguish. Fault gouge (up to 0.5 m thick) was identified adjacent to the fault plane, and contains clasts of various sizes in a greyish-green rock-powder matrix. NW-plunging slickensides were developed on the fault plane, indicating dextral thrusting of the NE wall (Permian limestone) over the SW wall (Emeishan basalt).

4.2.2 Sinistral thrusting (D_2)

D_2 is also characterized by crustal shortening, but with a clear component of sinistral shearing. For example, a thrust fault was found in the Baizuo Formation limestone, with the NE wall thrust over the SW wall (orientation of F1: 25°∠37°). The bedrock is highly fractured, and fault breccia with (sub)angular limestone clasts is identified in the core of fault zone. The clast alignments indicate thrust faulting. The slickensides are SE-plunging, indicating sinistral shearing. It is worth noting that F1 is cut by the steeply-dipping F2 which strikes N70°W. Sub-horizontal striations and steps are observed on the F2 plane, indicating later sinistral shearing. The former SE-plunging striations are also tectonically reworked (Figure 5C). A sinistral thrust fault is identified in the Permian Qixia Formation. The fault plane is steeply ENE-dipping, and the wallrocks are highly fractured. SE-plunging striations indicate sinistral thrusting of the ENE wall over the WSW wall (Figure 5D).

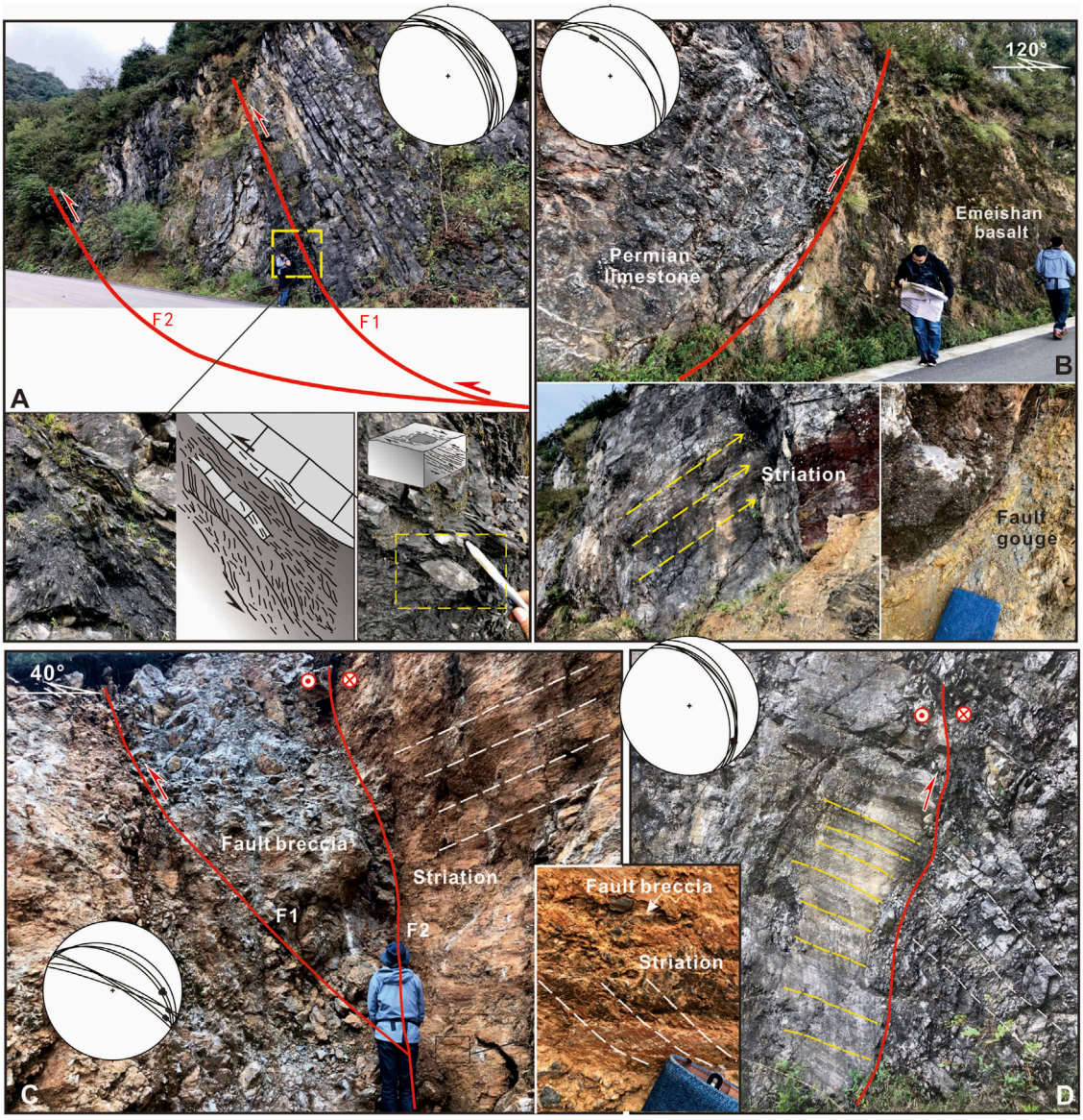

FIGURE 5
Typical deformation associated with dextral thrusting and sinistral transpression. **(A)** A series of thrust faults developed in the Carboniferous limestone. Deformation fabrics indicate a top-to-the-SW sense of thrusting with a component of dextral strike-slip motion. **(B)** The Permian limestone was thrust over the Emeishan basalt. **(C)** A thrust fault developed in the limestone of the Baizuo Formation, which is cross-cut by a steeply-dipping F2. **(D)** The northeast wall was thrust over the southwest wall in the Triassic dolomite.

4.2.3 Sinistral strike-slip faulting (D_3)

D_3 deformation formed penetrative and steeply-dipping planar fabrics, sub-horizontal striations, and linear geomorphic features. For example, in the central fault segment, Permian and Triassic strata are sinistrally displaced 6–7 km along two NW-trending fault branches (Figure 6A). A linear valley and prominent fault cliffs were developed along strike (Figure 6B). Penetrative fault cleavages were formed in a ~10 m-wide cataclastic zone (Figure 6C). Sub-horizontal fault striations and steps indicate sinistral strike-slip movement (Figure 6D). In the northern fault segment, a linear valley is identified on the satellite and DEM images, which strikes WNW. A fault zone was found to develop in the Carboniferous Baizuo Formation limestone (*Cb*), with an orientation of 47°∠71°. The main fault plane strikes N30°W and dips steeply to the NE (Figure 7A). The fault core zone consists of fault gouge and partially-cohesive breccia. The fault gouge is 10–20 cm thick and weakly foliated. The breccia flanking the fault gouge is mainly composed of angular to subangular clasts. The sub-horizontal striations and steps are observed, indicating sinistral strike-slip

FIGURE 6
Offset geological units and typical deformation fabrics associated with sinistral strike-slip shearing. **(A)** Permian and Triassic strata are sinistrally displaced by 6–7 km along two NW-striking fault branches. **(B)** A linear valley and prominent fault cliffs developed along strike. **(C)** Penetrative fault cleavages formed in the cataclastic zone with a width of ~10 m. **(D)** Sub-horizontal striations and steps on the fault plane indicate sinistral strike-slip movement.

faulting (Figure 7A). The cataclastic zone consists of strongly deformed limestone with extensive fractures and cleavages. Adjacent to Weining, the thick Baizuo Formation limestone are gently dipping, and are cut-through by a series of strike-slip faults. Multiple branch faults bifurcate upward, striking N20-30°W and dipping to NE or SW steeply. They also show a component of normal faulting, forming a negative flower structure (Figure 7B).

5 Regional deformation patterns

Field investigation and structural analysis of 1:20,000 and 1: 50,000 geologic map reveal various types of folds, faults, and strain zones across Guizhou. The most striking features in northeastern Guizhou are a series of Jura-type folds, which exhibit narrow synclines together with open and gentle anticlines (Figure 2). These linear folds mostly strike N-S or NNE (Figure 8). Triassic or Jurassic rocks formed tight synclinal cores (several km wide) and extend for over a hundred kilometers. The limbs dip steeply on both sides. The box-like anticlines are composed of Paleozoic rocks. The strata in the fold core are mostly horizontal or gently dipping. These fold belts are accompanied with numerous sub-parallel thrust faults, which generally dip toward the east (Figure 8). In the southeastern Guizhou, Alpine-type folds were developed in the Precambrian units. These folds mostly strike NE to NNE, with their axial planes being nearly vertical or slightly west-dipping. A series of thrusts also extend NNE parallelly. Linear fold belts are also identified in central Guizhou, which are NNE- or N-S-trending. Along or adjacent to the ZLF, Mesozoic to upper Paleozoic strata formed anticline-syncline pairs, which generally strike NW. The strata on limbs are gently or moderately dipping, and are locally offset by the thrust

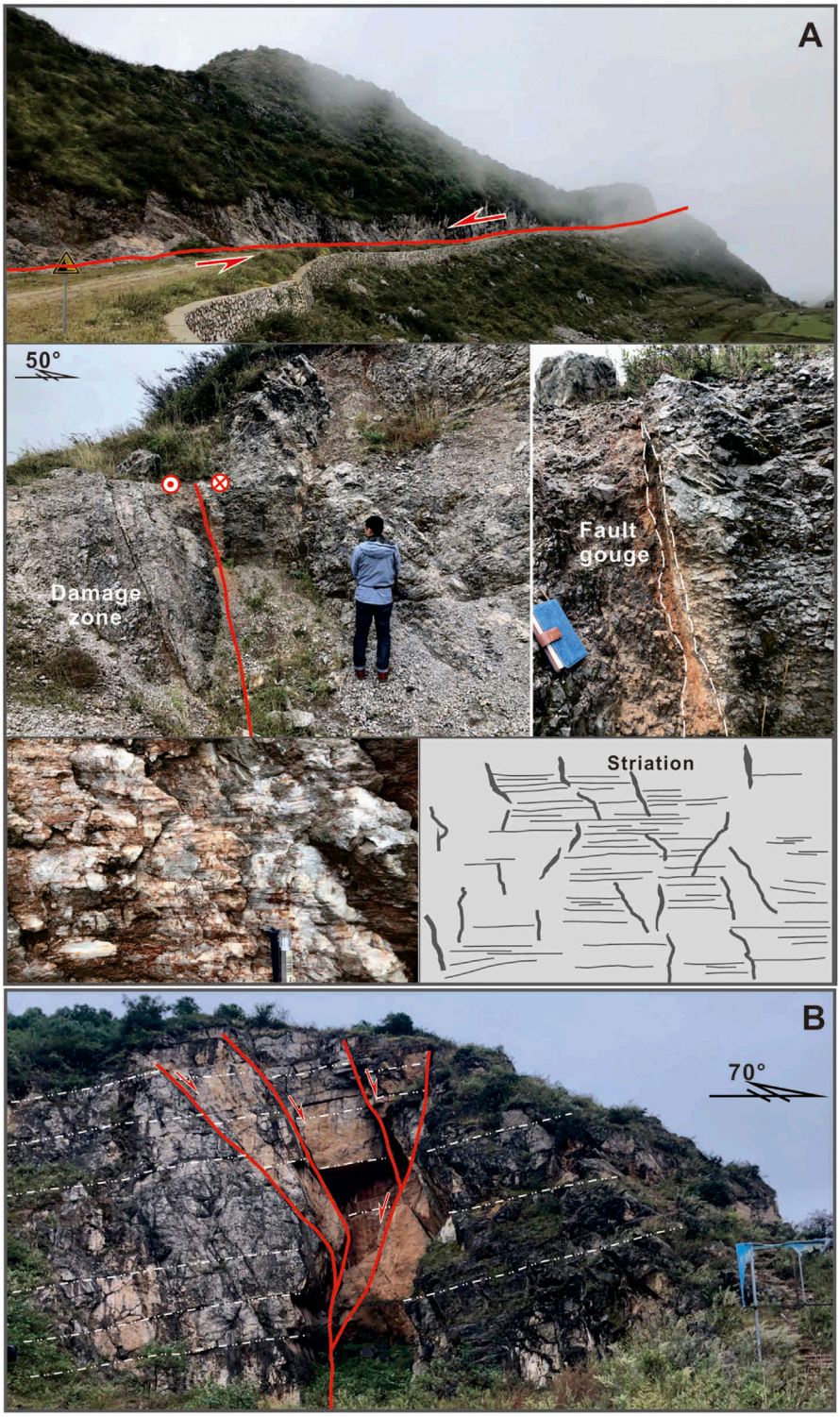

FIGURE 7
Typical deformation fabrics associated with sinistral strike-slip shearing. **(A)** Steeply dipping fault planes, sub-horizontals striations, and linear valleys indicate sinistral strike-slip movement. **(B)** A negative flower structure developed in the thick Carboniferous limestone of the Baizuo Formation.

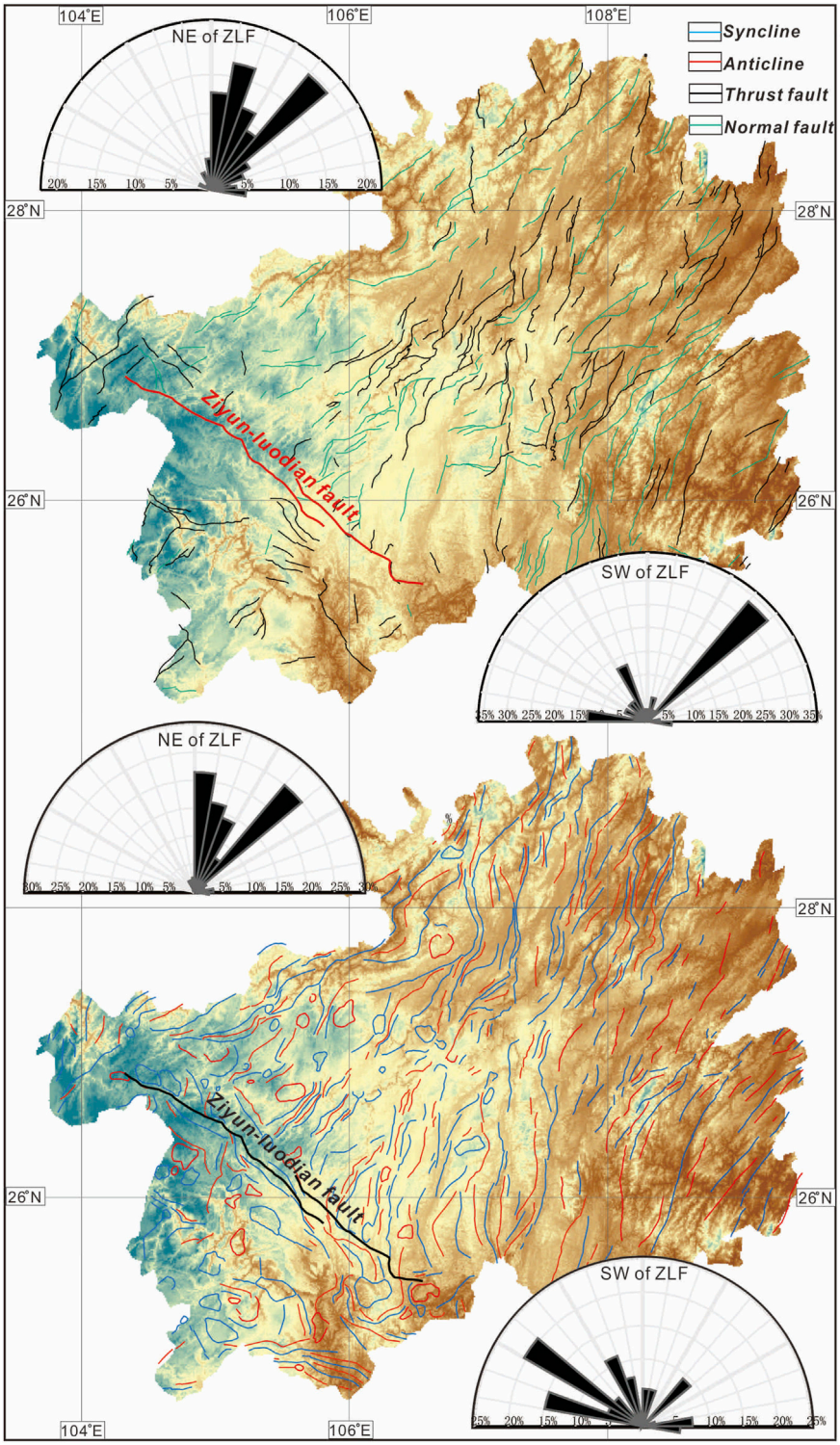

FIGURE 8
Structural pattern of the Guizhou Province.

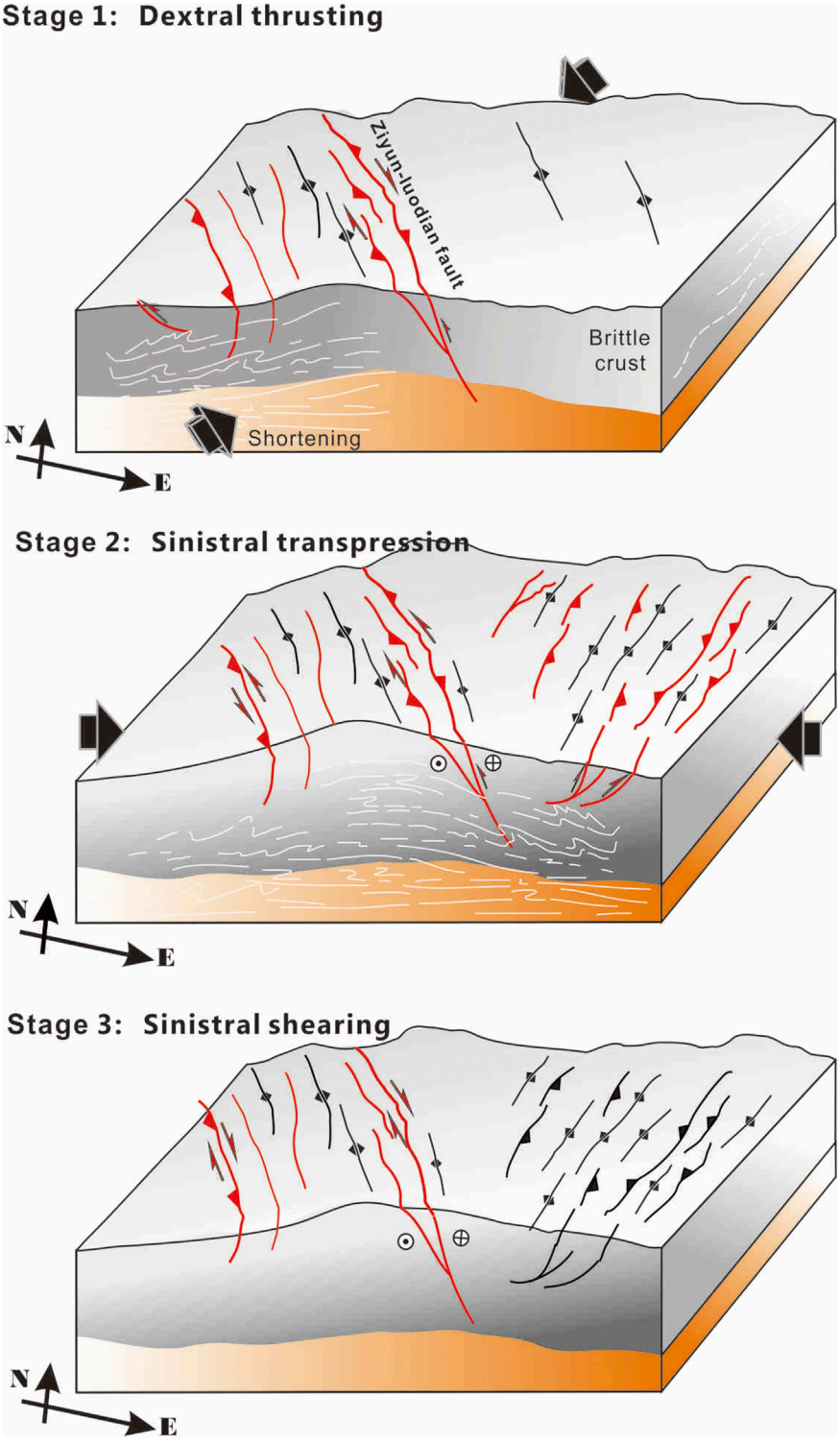

FIGURE 9
Tectonic model of the Ziyun-Luodian fault and the Guizhou Province during the Meso-Cenozoic. At least three stages of deformation including dextral thrusting, sinistral transpression, and sinistral strike-slip movement have been recognized along the ZLF in the Meso-Cenozoic.

faults. In addition, dome-shaped folds were developed on both sides of the ZLF. The youngest strata in these folds are Jurassic (Figure 4). Their long axis strikes NW to the west of the ZLF, but mostly strikes NE to the east. The regional fault systems (incl. thrust and normal faults with strike-slip components) are distributed across Guizhou, and displaced or cut the upper Paleozoic to Mesozoic strata. Thrusts are generally NE-to NNE-striking to the east of the ZLF, but change to NW-trending to the southwest, parallel to regional fold belts (Figure 8). The normal faults are developed mainly east of the ZLF, extending parallel to the thrust fault systems and fold bels. This indicates crustal extension after shortening and thickening.

6 Tectonic evolution

Three distinct episodes of deformation in the Meso-Cenozoic including dextral thrusting, sinistral transpression, and sinistral strike-slip movement have been recognized along the NW-trending Ziyun-Luodian fault, respectively. The deformation sequence of the ZLF is compatible with the regional structural framework. Therefore, in the following part, we integrate existing structural, stratigraphical, and chorological data to constrain the timing of the Meso-Cenozoic tectonic evolution of the ZLF and Guizhou region.

D_1 dextral thrusting is inferred to occur in the Triassic, which may be related to a broader tectono-thermal event in South China. The major tectonic framework of South China may have been established in the Indosinian orogeny (e.g., Zhang et al., 2013; Wang et al., 2013 and references therein). Closure of the Paleo-Tethyan and continental collision with the North China Block may have caused the nearly N-S-directed crustal shortening across the SCB (Wang et al., 2021). Accordingly, Wang et al., 2013, Wang et al., 2021 proposed that WNW-/W-striking fault systems (e.g., Hechi-Liucheng, Turong-Jianyang, Nanling, Luoyuan-Mingxi, Xianyou-Zhangping, Fogang-Fengliang, Gaoyao-Huilai and Changjiang-Qionghai) and fold-and-thrust belts (e.g., Shimen-Linxiang, Anhua-Liuyang, Longshan-Liling, Jiuling, Wugongshan, Wudianmei and Guposhan-Huashan) may have developed since the Early Triassic across the SCB, based on petrographic, structural, and $^{40}Ar/^{39}Ar$ geochronologic evidence. The ZLF may have also been affected by the northward convergence of the Indochina Block in the Triassic. The dextral thrusting along the fault zone may have occurred in response to the N-S-directed compression. In addition, the Triassic and Jurassic strata are in conformable or disconformable contact across the Guizhou region. Therefore, regional uplift and moderate deformation likely occurred during the Indosinian orogeny (Figure 9).

D_2 sinistral transpression is inferred to occur in the Yanshanian orogeny. NE-/NNE-striking ductile shear zones, thrusts, and fold belts have long been recognized across the SCB, and are attributed to the Paleo-Pacific subduction (e.g., Li and Li, 2007; Zhang and Cai, 2009; Wang et al., 2013, Wang et al., 2021; Li et al., 2014). Older WNW-/W-striking structures were also reactivated. The ZLF may have experienced sinistral transpression under a nearly E-W-directed shortening (Figure 9). The NNE- or N-S-trending Jura-type fold belts and linear anticline-syncline pairs east of the ZLF also indicate ESE-to E-W-directed compression. The youngest strata in the fold belts are the Middle-Upper Jurassic rocks. The Upper Jurassic and Lower Cretaceous strata are mostly absent across Guizhou. The Upper Cretaceous rocks are locally distributed, and are in angular unconformity with the underlying deformed Jurassic and Triassic strata. Therefore, the sinistral transpression along the ZLF and formation of extensive fold belts may have occurred coevally in the Late Jurassic to Early Cretaceous.

It is worth noting that the fold geometry changes spatially across Guizhou. The linear fold belts (Jura- or Alpine type) were mostly developed in the central and eastern Guizhou, and generally change to dome-shaped folds in the western part. The similar deformed strata in these folds suggest that they may have formed at the same stage. However, such geometric variance suggests that the driving force may have originated from the eastern side. Furthermore, the fold long axis is mostly NE-/N-trending and NW-trending in the eastern and western side of the ZLF, respectively (Figure 8). The anticline-syncline pairs are mostly gentle folds in or near the ZLF, except for some locations affected by fault movements. Despite different geometry, we argue that these NW-striking folds were developed coevally with NE-to N-trending folds, since the Middle Jurassic rocks were also involved into the folding. Those observations suggest that the ZLF played an important role in accommodating regional strain during the Yanshanian orogeny.

D_3 sinistral strike-slip faulting may have occurred in the late Cenozoic because (Figure 9): 1) subvertical fault planes, sub-horizontal striations, and geomorphic features (such as linear valleys and fault scarps) are present in the fault zone, indicating strike-slip movement. Combined with crosscutting relationship, sinistral shearing represents another deformation episode which is distinct from the early sinistral transpression featured by shortening structures and NW- or SE-plunging striations; 2) to the southwest of the ZLF, several large-scale fault zones were developed sub-parallelly in Yunnan, such as the Ailaoshan-Red River, Chuxiong-Qujiang, Wuliangshan, and Lancang-Genma faults (e.g., Wang et al., 2014, Wang et al., 2022; Li et al., 2020). Published structural analysis and geochronologic data indicate that sinistral strike-slip shearing may have occurred along these faults in the early Oligocene to early Miocene (e.g., Leloup et al., 2001; Liu et al., 2012; Zhang et al., 2014; Wang et al., 2016, Wang et al., 2020, Wang et al., 2022). Based on the similar geometry and kinematics, we infer that the ZLF and the regional NW-trending faults were formed under a uniform tectonic regime to

accommodate the SE extrusion of the Indochina block. Therefore, we infer that the sinistral motion along the ZLF likely commenced since the early Oligocene. Interestingly, these NW-striking fault systems mostly experienced kinematic reversal (from sinistral to dextral) since the late Miocene (Wang et al., 2017, Wang et al., 2020, Wang et al., 2022). We cannot determine if dextral motion also occurred along the ZLF due to the limited information, but we deem that possible since modern stress field (derived from oil and gas exploration) adjacent to the fault zone point to N-S-directed maximum horizontal principal stress (Cao et al., 2020).

7 Conclusion

Based on our investigations of the geometry and kinematics of the Ziyun-Luodian fault and regional structural analysis, we conclude that:

(1) At least three Meso-Cenozoic deformation stages, including dextral thrusting, sinistral transpression, and sinistral strike-slip movement occurred along the ZLF.
(2) The Guizhou region may have experienced regional uplift during the Indosinian orogeny. Extensive crustal shortening occurred in a nearly E-W-directed compressional regime in the Late Jurassic and Early Cretaceous, forming Jura-/Alpine-type and dome-shaped folds.
(3) The main tectonic framework in Guizhou was established during the Yanshanian orogeny. The ZLF is a key structure accommodating regional strain and separates different tectonic domains.
(4) The ZLF is characterized by sinistral strike-slip shearing in the late Cenozoic, similar to the NW-trending fault systems in the SE Tibetan Plateau.

Data availability statement

The original contributions presented in the study are included in the article/Supplementary Material, further inquiries can be directed to the corresponding author.

Author contributions

WD and YaW designed the project. YiW, YyW, RL, DZ, FZ, ZS, and YC carried out the field work and collected the samples. YiW, WD, and YaW wrote the manuscript with input of the rest authors.

Funding

This work is supported by the Natural Science Foundation of Guangdong Province (2021A1515011631, 202102020490) and Guizhou Geological Exploration Foundation (208-9912-JBN-L1D7).

Acknowledgments

We sincerely thank Guest Editor Kit Lai for editorial handling and constructive comments and the reviewers for their thorough and critical reviews. All the data used in this study are listed in the references and available in the figures. This work is supported by the Guizhou Geological Exploration Foundation (208–9912-JBN-L1D7) and the Natural Science Foundation of Guangdong Province (2021A1515011631, 202102020490). We appreciate the fruitful discussion with Yang Bing.

Conflict of interest

The authors declare that the research was conducted in the absence of any commercial or financial relationships that could be construed as a potential conflict of interest.

Publisher's note

References

Cao, H., Sun, D. S., Yuan, K., Li, A. W., and Z, G. H. (2020). *In-situ* stress determination of 3 km oil-gas deep hole and analysis of the tectonic stress field in the southern Guizhou. *Geol. China* 47, 88–98. (in Chinese with English abstract).

Charvet, J., Lapierre, H., and Yu, Y. W. (1994). Geodynamic significance of the Mesozoic volcanism of southeastern China. *J. Southeast Asian Earth Sci.* 9, 387–396. doi:10.1016/0743-9547(94)90050-7

Charvet, J. L., Shu, S., Faure, M., Choulet, F., Wang, B., Lu, H. F., et al. (2010). Structural development of the lower paleozoic belt of South China: Genesis of an intracontinental orogen. *J. Asian Earth Sci.* 39 (4), 309–330. doi:10.1016/j.jseaes.2010.03.006

Charvet, J. L., Shu, S., Shi, Y. S., Guo, L. Z., and Faure, M. (1996). The building of South China: Collision of yangzi and Cathaysia blocks, problems and tentative answers. *J. Southeast Asian Earth Sci.* 13 (3–5), 223–235. doi:10.1016/0743-9547(96)00029-3

Chu, Y., Lin, W., Faure, M., Xue, Z. H., Ji, W. B., and Feng, Z. T. (2019). Cretaceous episodic extension in the south China block, east asia: Evidence from the yuechengling massif of central south China. *Tectonics* 38, 3675–3702. doi:10.1029/2019tc005516

Faure, M., Sun, Y., Shu, L., Monie', P., and Charvet, J. (1996). Extensional tectonics within a subduction-type orogen: The case study of the wugongshan dome

(jiangxi province, southeastern China). *Tectonophysics* 263, 77–106. doi:10.1016/s0040-1951(97)81487-4

Han, W. (2010). *The tectonic evolution and geological significance of the Ziyun-Luodian-Nandan rift zone*. Kirkland, WA: Northwest University. (in Chinese with English abstract).

Jahn, B. M., Zhou, X. H., and Li, J. L. (1990). formation and tectonic evolution of southeastern China and taiwan: Isotopic and geochemical constraints. *Tectonophysics* 183, 145–160. doi:10.1016/0040-1951(90)90413-3

Leloup, P. H., Arnaud, N., Lacassin, R., Kienast, J. R., Harrison, T. M., Trong, P. T. T., et al. (2001). New constraints on the structure, thermochronology, and timing of the Ailao Shan-Red River shear zone, SE Asia. *J. Geophys. Res.* 106 (B4), 6683–6732. doi:10.1029/2000jb900322

Li, J., Zhang, Y., Dong, S., and Johnston, S. T. (2014). Cretaceous tectonic evolution of South China: A preliminary synthesis. *Earth-Science Rev.* 134, 98–136. doi:10.1016/j.earscirev.2014.03.008

Li, X. H. (2000). Cretaceous magmatism and lithospheric extension in Southeast China. *J. Asian Earth Sci.* 18 (3), 293–305. doi:10.1016/s1367-9120(99)00060-7

Li, X. (2012). *Mesozoic structural deformation characteristics and superposition pattern in Southwest Guizhou, China*. Urban: China University of Geosciences. (in Chinese with English abstract).

Li, X. M., Wang, Y. J., Tan, K. X., and Peng, T. P. (2005). Meso-cenozoic uplifting and exhumation on yunkaidashan: Evidence from fission track thermochronology. *Chin. Sci. Bull.* 50 (9), 903–909. doi:10.1360/04wd0040

Li, Z., Wang, Y., Gan, W., Fang, L., Zhou, R., Seagren, E. G., et al. (2020). Diffuse deformation in the SE Tibetan plateau: New insights from geodetic observations. *J. Geophys. Res. Solid Earth* 125. doi:10.1029/2020jb019383

Li, Z. X., and Li, X. H. (2007). Formation of the 1300-km-wide intracontinental orogen and postorogenic magmatic province in mesozoic south China: A flat-slab subduction model. *Geol.* 35, 179–182. doi:10.1130/g23193a.1

Liu, J. L., Tang, Y., Tran, M. D., Cao, S. Y., Zhao, L., Zhang, Z. C., et al. (2012). The nature of the Ailao Shan-Red River (ASRR) shear zone: Constraints from structural, microstructural and fabric analyses of metamorphic rocks from the Diancang Shan, Ailao Shan and Day Nui Con Voi massifs. *J. Asian Earth Sci.* 47, 231–251. doi:10.1016/j.jseaes.2011.10.020

Liu, S. G., Luo, L. Z., and Dai, S. L. (1995). Dennis, Arne. C.J.L. Wilson. The uplift of the Longmenshan thrust belt and subsidence of the Western Sichuan foreland basin. *Acta Geol. Sin.* 1995 (03), 205–214. (in Chinese with English abstract).

Shen, C. B., Mei, L. F., Min, K., Jonckheere, R., Ratschbacher, L., Yang, Z., et al. (2012). Multichronometric dating of the huarong granitoids from the middle Yangtze craton: Implications for the tectonic evolution of eastern China. *J. Asian Earth Sci.* 52, 73–87. doi:10.1016/j.jseaes.2012.02.013

Shu, L. S., and Charvet, J. (1996). Kinematics and geochronology of the proterozoic dongxiang-shexian ductile shear zone: With HP metamorphism and ophiolitic melange (jiangnan region, south China). *Tectonophysics* 267 (1–4), 291–302. doi:10.1016/s0040-1951(96)00104-7

Shu, L. S., Sun, Y., Wang, D. Z., Faure, M., Monie, P., and Charvet, J. (1998). Mesozoic doming extensional tectonics of Wugongshan, South China. *Sci. China Ser. D-Earth. Sci.* 41 (6), 601–608. doi:10.1007/bf02878742

Shu, L. S., Zhou, X. M., Deng, P., Wang, B., Jiang, S. Y., Yu, J. H., et al. (2009). Mesozoic tectonic evolution of the southeast China block: New insights from basin analysis. *J. Asian Earth Sci.* 34 (3), 376–391. doi:10.1016/j.jseaes.2008.06.004

Tapponnier, P., Xu, Z. Q., Roger, F., Meyer, B., Arnaud, N., Wittlinger, G., et al. (2001). Geology: Oblique stepwise rise and growth of the tibet plateau. *Science* 294 (5547), 1671–1677. doi:10.1126/science.105978

Wang, E. Q., and Yin, J. Y. (2009). Cenozoic multi-stage deformation occurred in southwest Sichuan: Cause for the dismemberment of the proto-Sichuan Basin. *J. Northwest Univ.* 39 (03), 359–367. (in Chinese with English abstract).

Wang, X. L., Zhou, J. C., Griffin, W. L., Wang, R. C., Qiu, J. S., O'Reilly, S. Y., et al. (2007). Detrital zircon geochronology of precambrian basement sequences in the jiangnan orogen: Dating the assembly of the Yangtze and Cathaysia blocks. *Precambrian Res.* 159 (1–2), 117–131. doi:10.1016/j.precamres.2007.06.005

Wang, Y. J., Fan, W. M., Zhang, G. W., and Zhang, Y. H. (2013). Phanerozoic tectonics of the south China block, key observations and controversies. *Gondwana Res.* 23 (4), 1273–1305. doi:10.1016/j.gr.2012.02.019

Wang, Y. J., Wang, Y., Zhang, Y. Z., Cawood, P. A., Qian, X., Gan, C. S., et al. (2021). Triassic two-stage intra-continental orogenesis of the South China Block, driven by Paleotethyan closure and interactions with adjoining blocks. *J. Asian Earth Sci.* 206, 1367–9120.

Wang, Y. J., Zhang, Y. H., Fan, W. M., and Peng, T. P. (2005). Structural signatures and 40Ar/39Ar geochronology of the indosinian xuefengshan tectonic belt, south China block. *J. Struct. Geol.* 27 (7), 985–998. doi:10.1016/j.jsg.2005.04.004

Wang, Y., Schoenbohm, L. M., Zhang, B., Granger, D., Zhou, R. J., Zhang, J. J., et al. (2017). Late Cenozoic landscape evolution along the Ailao Shan Shear Zone, SE Tibetan Plateau: Evidence from fluvial longitudinal profiles and cosmogenic erosion rates. *Earth Planet. Sci. Lett.* 472, 323–333. doi:10.1016/j.epsl.2017.05.030

Wang, Y., Wang, Y. J., Schoenbohm, L. M., Zhang, P. Z., Zhang, B., Sobel, E. R., et al. (2020). Cenozoic exhumation of the Ailaoshan-Red River shear zone: New insights from low-temperature thermochronology. *Tectonics* 39, 06151. doi:10.1029/2020tc006151

Wang, Y., Wang, Y. J., Zhang, P. Z., Zhang, J. J., Zhang, B., Zeng, J. L., et al. (2022). Cenozoic tectonic evolution of regional fault systems in the SE Tibetan Plateau. *Sci. China Earth Sci.* 65, 601–623. doi:10.1007/s11430-021-9880-3

Wang, Y., Zhang, B., Hou, J. J., and Xu, X. W. (2014). Structure and tectonic geomorphology of the Qujiang fault at the intersection of the Ailao Shan-Red River fault and the Xianshuihe-Xiaojiang fault system, China. *Tectonophysics* 634, 156–170. doi:10.1016/j.tecto.2014.07.031

Wang, Y., Zhang, B., Schoenbohm, L. M., Zhang, J., Zhou, R., Hou, J., et al. (2016). Late Cenozoic tectonic evolution of the Ailao Shan-Red River fault (SE Tibet): Implications for kinematic change during plateau growth. *Tectonics* 35, 1969–1988. doi:10.1002/2016tc004229

Wu, G. Y., Wang, W. F., and Chi, H. X. (2012). Basin evolution and later reformation of marine sediments in southern Guizhou Depression and neighboring areas. *J. Palaeogeogr.* 14 (04), 507–521. (in Chinese with English abstract).

Yin, A., and Harrison, T. M. (2000). Geologic evolution of the himalayan-Tibetan orogen. *Annu. Rev. Earth Planet. Sci.* 28 (1), 211–280. doi:10.1146/annurev.earth.28.1.211

Yu, J. H., O'Reilly, S. Y., Wang, L. J., Griffin, W. L., Zhou, M. F., Zhang, M., et al. (2010). Components and episodic growth of precambrian crust in the Cathaysia block, south China: Evidence from U-Pb ages and Hf isotopes of zircons in neoproterozoic sediments. *Precambrian Res.* 181 (1-4), 97–114. doi:10.1016/j.precamres.2010.05.016

Zhang, B., Zhang, J. J., Liu, J., Wang, Y., Yin, C. Y., Guo, L., et al. (2014). The Xuelongshan high strain zone: Cenozoic structural evolution and implications for fault linkages and deformation along the Ailao Shan-Red River shear zone. *J. Struct. Geol.* 69, 209–233. doi:10.1016/j.jsg.2014.10.008

Zhang, G. W., Guo, A. L., Wang, Y. J., Li, S. Z., Dong, Y. P., Liu, S. F., et al. (2013). Tectonics of South China continent and its implications. *Sci. China Earth Sci.* 56, 1804–1828. doi:10.1007/s11430-013-4679-1

Zhang, K. J., and Cai, J. X. (2009). NE–SW-trending hepu-hetai dextral shear zone in southern China: Penetration of the yunkai promontory of South China into Indochina. *J. Struct. Geol.* 31 (7), 737–748. doi:10.1016/j.jsg.2009.04.012

Zhong, D. L. (2000). *Paleotethyan orogenic belts in yunnan and western sichuan*. Beijing: Science Press, 230–240.

Zhou, X. M., Sun, T., Shen, W. Z., Shu, L. S., and Niu, Y. L. (2006). *Petrogenesis of Mesozoic granitoids and volcanic rocks in South China: a response to tectonic evolution Episode*, 29, 26–33.

frontiers | Frontiers in Earth Science

TYPE Original Research
PUBLISHED 25 August 2022
DOI 10.3389/feart.2022.963351

OPEN ACCESS

EDITED BY
Kit Lai,
Fortescue Metals Group, Australia

REVIEWED BY
Shiwei Wang,
Hefei University of Technology, China
Jing Chen,
Qinghai Normal University, China

*CORRESPONDENCE
Chulin Xia,
xiachulin@163.com

SPECIALTY SECTION
This article was submitted to Geochemistry, a section of the journal Frontiers in Earth Science

RECEIVED 07 June 2022
ACCEPTED 14 July 2022
PUBLISHED 25 August 2022

CITATION
Zhang W, Xia C, Zhen S, Quan C, Du Y and Han Z (2022), Geochronology and geochemistry of Late Triassic granitoids in Harizha Cu polymetallic deposit (East Kunlun Orogen) and their metallogenic constraints.
Front. Earth Sci. 10:963351.
doi: 10.3389/feart.2022.963351

Geochronology and geochemistry of Late Triassic granitoids in Harizha Cu polymetallic deposit (East Kunlun Orogen) and their metallogenic constraints

Wenzhao Zhang[1], Chulin Xia[1,2]*, Shikun Zhen[1], Chang'en Quan[1], Yu Du[1] and Zhihong Han[1]

[1]Qinghai University, Xining, Qinghai, China, [2]Key Laboratory of Cenozoic Resource and Environment in North Margin of the Tibetan Plateau, Xining, Qinghai, China

The large Harizha copper (Cu) polymetallic deposit is located in the eastern section of East Kunlun Orogen. The ore-related lithologies include mainly the granodiorite, monzogranite, and their porphyries. Zircon U-Pb dating of the ore-bearing granodiorite porphyry and granite porphyry yielded Late Triassic age of 217 Ma. The rocks are characterized by being rich in SiO_2 (68.44–78.13 wt%) and high alkali (4.03–8.33 wt%) and peraluminous (A/CNK = 1.02–1.68). In general, the granite samples are peraluminous and high-K calc-alkaline. The rocks are significantly enriched in light rare earth elements (LREE), large ion lithophile elements (e.g., K, Rb, Ba) and other incompatible elements (e.g., U, Th), but are depleted in heavy rare earth elements (HREEs), with weakly negative Eu and Ce anomalies, resembling I-S transitional granite. The zircons have ε_{Hf} (t) = -8 to -4, and the corresponding zircon two-stage Hf model age (T_{DM2}) from 1.5 to 1.8 Ga. We speculated that the ore-forming materials in the mining area were mainly from partial remelting of crustal materials, and that the tectonic regime was post-collisional extension.

KEYWORDS

granodiorite-porphyry, zircon U-Pb dating, geochemistry, the Harizha Cu polymetallic deposit, East Kunlun metallogenic belt

1 Introduction

Porphyry copper deposit is the world's most important copper deposit type, and is characterized by being large-scale, low-grade (Zhai et al., 2011; Park et al., 2021). Porphyry copper deposits in the region were mainly formed in the late Mesozoic (Yanshanian) and Cenozoic (Himalayan), when the Indian plate subducted northward and collided with Eurasia, resulting in multiphase tectonism and magmatism that provided favorable metallogenic conditions (Tang et al., 2010; Liu et al., 2019).

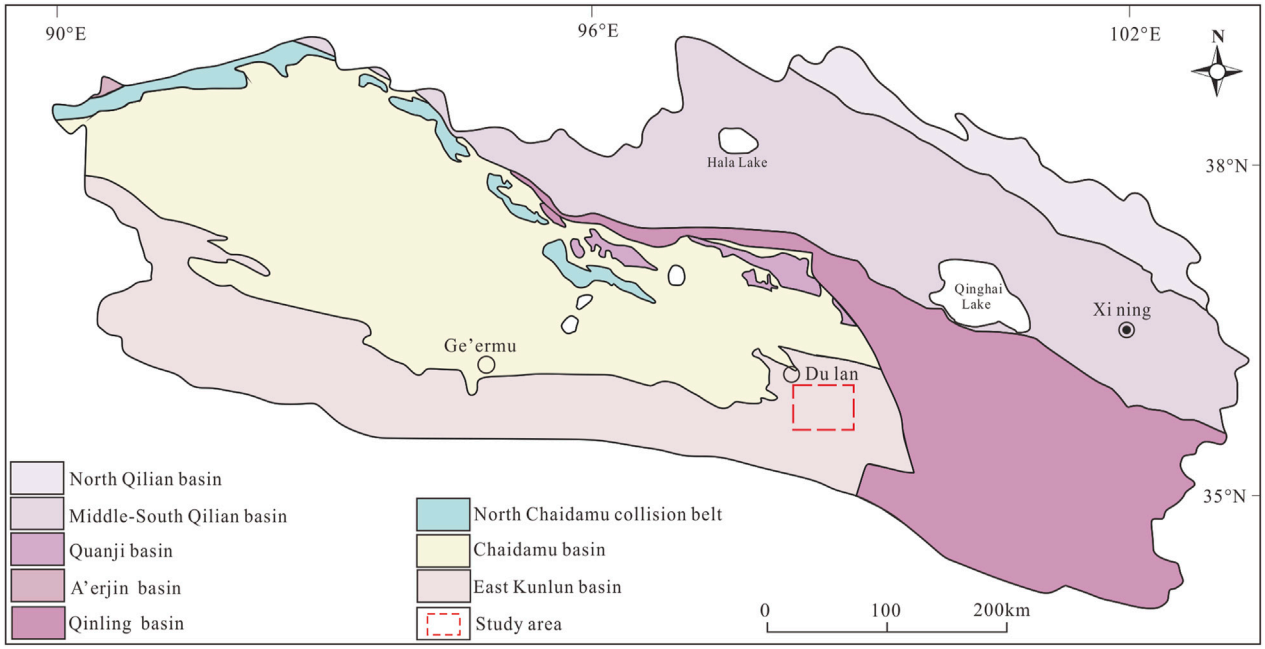

FIGURE 1
Geotectonic location map of the eastern East Kunlun Orogen (modified after Yang et al., 2017).

Typical porphyry Cu deposits include the Aktogai in Kazakhstan (Chen et al., 2010), the Escondida porphyry copper deposit and Collahuasi porphyry Cu-Mo in northern Chile (Urqueta et al., 2009; Karl et al., 2021), Saindak and Rekodiq in Pakistan (Yao et al., 2013; Lv et al., 2017), and Zhunuo in Tibet, China (Sun et al., 2021).

The large Harizha Cu-polymetallic deposit is located in the East Kunlun metallogenic belt, with estimated ore resource of 505 kt. Ore deposits in the district include those of porphyry, skarn, and medium-low temperature hydrothermal-altered rock types (Song et al., 2013; Sun et al., 2016; Yan, 2019). In recent years, the Harizha mining district has attracted much research attention. Previous studies were mainly focused on the geological-metallogenic conditions and the ages of the ore-related magmatic rocks. Tectonism at Harizha is relatively complex: NW-trending faults are the main structures, while the NE trending faults are secondary structures. Previous works have zircon U-Pb dated the ore-bearing granodiorite porphyry (234.5 ± 4.8 Ma; Song et al., 2013) and the quartz diorite (239.3 ± 2.2 Ma; Guo et al., 2016) at Harizha to be Middle Triassic (Indosinian Orogeny). However, some workers have reported older magmatic ages (diorite: 424.7 ± 4.8 Ma; granite porphyry: 242.6 ± 2.6 Ma) at Harizha, and proposed multi-stage mineralization and a diorite and/or granite porphyry ore-material source (Wang et al., 2017). In terms of metallogenesis, geochemical analysis shows that the northern Harizha mining area in Qinghai contains mainly porphyry-hydrothermal vein-skarn polymetallic deposits (Ma et al., 2016). Lithogeochemistry research and its relationship with the Cu-polymetallic mineralization is largely inadequate, and the mineralization age remains controversial. In this study, we conducted LA-ICP-MS zircon U-Pb dating and whole-rock geochemical analysis on the Harizha deposit, and discuss the ore genesis and tectonic setting.

2 Geological background

2.1 Geologic setting

The East Kunlun Orogen is a key metallogenic belt in China, and is located in the tectonically active belt of the northern Qinghai-Tibetan Plateau. The belt is located in the southern margin of the Chaidam basin and the northern margin of the Paleo-Tethys tectonic domain (Qian et al., 2000; Pan et al., 2009; Shao et al., 2017; Wu et al., 2020). The strong magmatism has led to the formation of a giant granite belt and many sizeable hydrothermal deposits (Figure 1) (Li, 2010; Du et al., 2012; Wang, 2014), including those of shallow low-temperature hydrothermal, orogenic, and hydrothermal-sedimentary types. Many metal and non-metallic minerals with development value had been discovered. It is one of the most important Mo-polymetallic metallogenic belts in Qinghai Province (Qi, 2015;

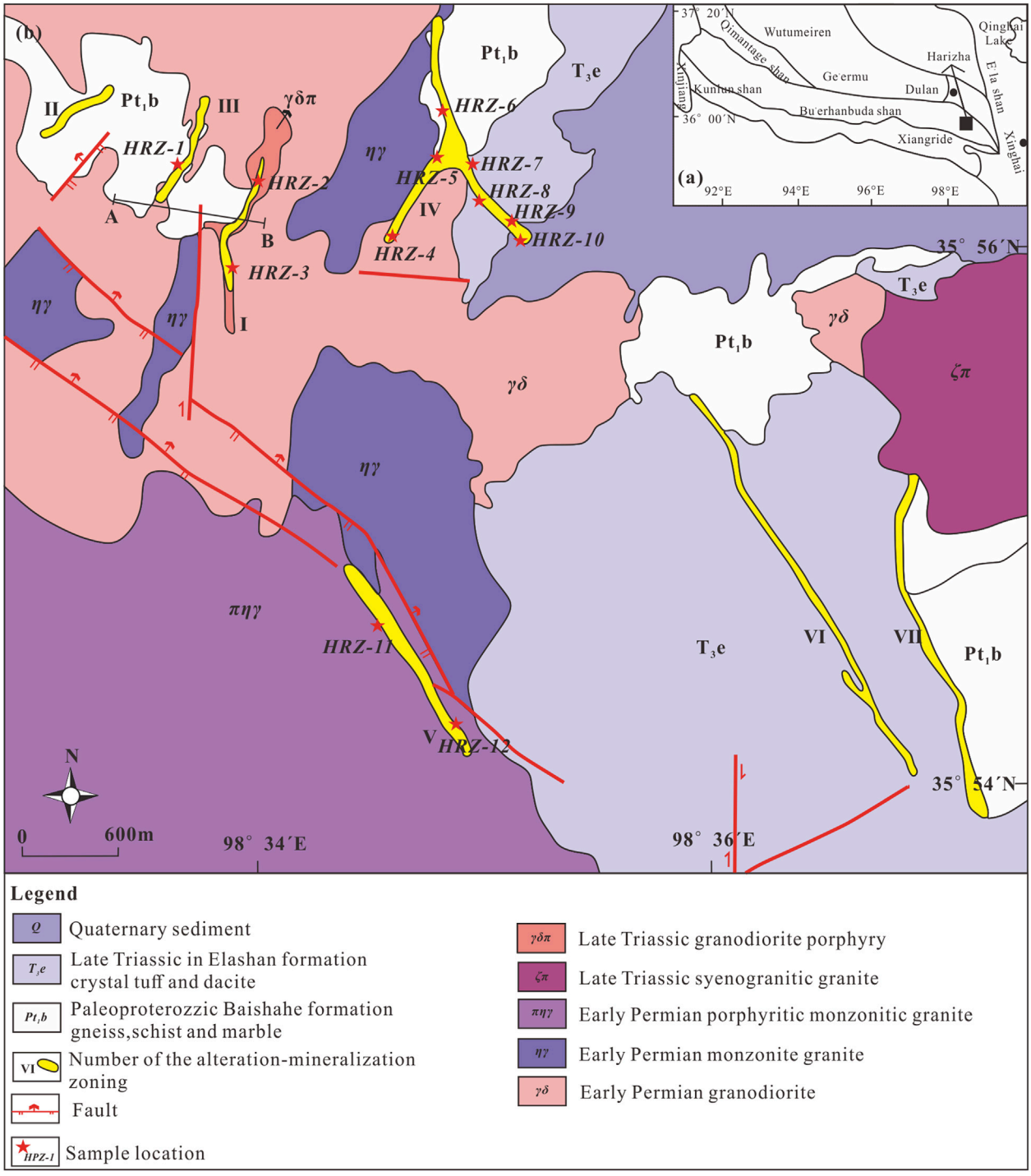

FIGURE 2
(A) Geotectonic map of Harizha; **(B)** Geological map of the Harizha deposit, showing the sampling locations (modified after Ma et al., 2016).

Han J. J. et al., 2020; Lei et al., 2020; Li Y. J. et al., 2020). Under the influence of Elashan collision-extensional orogeny, the intermediate-felsic magma in the eastern East Kunlun ore belt may have ascent along the regional NW-trending deep faults, and produce strong dissolution to surrounding strata, forming the widely-distributed intermediate-felsic plutonic and volcanic rocks. During this period, granitic magma may have formed by partial melting of crustal material under intraplate extension.

During the late Indosinian to early Yanshanian orogeny (227–205 Ma), the intermediate-felsic magma may have formed the granite-granodiorite porphyries of various sizes (Wang K. et al., 2020; Zhang et al., 2020; Zhou et al., 2020). At present, the porphyry deposits are mainly concentrated in the western part of the belt, with the Harizha deposit being a rare exception in the eastern part of the belt.

At Harizha (Dulan County, Qinghai Province), the main tectonic-magmatic activities occurred mainly in the Caledonian-Yanshanian (Yang et al., 2015; Feng et al., 2017). The deposit is 7.8 km long, 7.1 km wide, 4,200 m in elevation (max 4,767 m) (Zhong, 2018; Zhang et al., 2019). Exposed strata include mainly the Paleoproterozoic Baishahe Formation, Upper Triassic Elashan Formation, Neogene Youshashan Formation, and Quaternary sediments (Figure 2). The ore-related lithologies include mainly the granodiorite, monzogranite, and their porphyries. The wallrocks have undergone varying degrees of alteration, including mainly chlorite, epidote, sericite, and silicic.

The deposit is located between the northern Kunlun fault and central Kunlun fault, and has recorded multi-stage of tectonic-magmatic activities in the Early Paleozoic (Caledonian), Late Paleozoic (Variscan), and Triassic (Indosinian). Structures are well-developed and complex, and are dominated by compressional/transpressional faults with rare folds. The faults are NE-, NW-, and EW-trending, among which the NE- and NW-trending ones are ore-hosting (Ma et al., 2013).

Magmatic rocks are multiphase and widely distributed. Intrusive rocks include mainly gabbro, granodiorite (porphyry) and monzogranite (porphyry). The volcanic rocks include mainly the Elashan Formation dacite crystal tuff and (minor) dacite. Our study focused mainly on the ore-related granodiorite porphyry and granodiorite porphyry, whose petrographic features are described below:

Granodiorite porphyry (Figure 3A) is grayish-white (Figure 3B) and massive, and comprises phenocrysts (~40 vol %) and groundmass (~60 vol%). The phenocrysts (size: 0.1–3.5 mm) include mainly quartz, plagioclase, and biotite, and minor muscovite, hornblende, and K-feldspar. The phenocrysts are randomly distributed and euhedral-subhedral. The groundmass is composed mainly of plagioclase and quartz, with minor dark minerals. Secondary minerals include kaolinite, calcite and sericite.

The granite porphyry (Figure 3C) is grayish-white/pink (Figure 3D) and massive, and comprises phenocrysts (~25 vol %) and groundmass (~75 vol%). The phenocrysts (size: 0.2–2.5 mm) include plagioclase, K-feldspar, quartz, and biotite. The phenocrysts are randomly distributed. The groundmass is composed of quartz and feldspar laths with minor biotite. Secondary minerals include mainly sericite and kaolinite.

2.1.1 Mineralization

A total of seven mineralization belts (zone I-VII) have been identified (Figure 1). Mineralization belt I occurs in the granodiorite porphyry, and the alteration styles include mainly silicic, sericite, K-feldspar, propylitic, and kaolinite. Mineralization belt II occurs in the biotite plagioclase gneiss, and the alteration style is mainly silicic. Mineralization belt III is hosted in the granodiorite and the biotite plagioclase gneiss. Mineralization belt IV is located in the northeast tectonic fracture zone. Mineralization belt V and VI occur in the altered fracture zone and crystal tuff, respectively. Ore minerals include mainly chalcopyrite, pyrite, and malachite. Ore minerals include mainly chalcopyrite, pyrite, and malachite. (Xia, 2018; Guo et al., 2019; Li, 2019).

The copper ore samples have vein-disseminated structure (Figure 3E) and are semi-automorphic-heteromorphic granular. The ores (Figure 3F) contain mainly pyrite (25 vol%), galena (10 vol%), and chalcopyrite (1 vol%), together with non-metallic minerals (55 vol%) of plagioclase, quartz, and biotite.

The lead ore samples have also vein-disseminated structure (Figure 3G) and are semi-automorphic-heteromorphic granular. The ores (Figure 3H) have mainly galena (30 vol%), pyrite (15 vol %), sphalerite (2 vol%), arsenopyrite (8 vol%), and chalcopyrite (1 vol%), and non-metallic minerals (about 38 vol%) of plagioclase, quartz, and calcite. Lead mineralization occurs mainly in zones VI to VI.

2.1.2 Alteration

The wallrock alterations include silicic, sericite, potassic, kaolinite, chlorite and carbonate. Among which the former two are closely ore-related and widely developed. Quartz veins are relatively well-developed (Figure 4A), and often accompanied by pyritization (Figure 4B). Secondly, kaolinization, potassium and chloritization are developed (Figure 4D). Malachite (Figure 4C) and limonite supergene ores are developed on/near the surface. Therefore, the alteration zoning can be divided into: K-felsparization-sericitization-propylitization (Figure 5). The main orebodies are located in the outer part of the potassic zone and the sericite zone, similar to typical porphyry copper deposits (Lv et al., 2017).

3 Samples and methods

The sampling locations are shown in Figure 2. The samples were collected for thin-section petrography, LA-ICP-MS zircon U-Pb dating, and whole-rock geochemical analysis. The ore-related granodiorite porphyry and monzogranite porphyry were zircon U-Pb dated, whilst samples analyzed for whole-rock geochemistry include monzogranite, (altered/mineralized) granodiorite porphyry, and syenogranite porphyry.

3.1 Zircon U-Pb dating

The selected zircon was mounted with epoxy resin, and is then polished into half the thickness. LA-ICP-MS zircon U-Pb

10.3389/feart.2022.963351

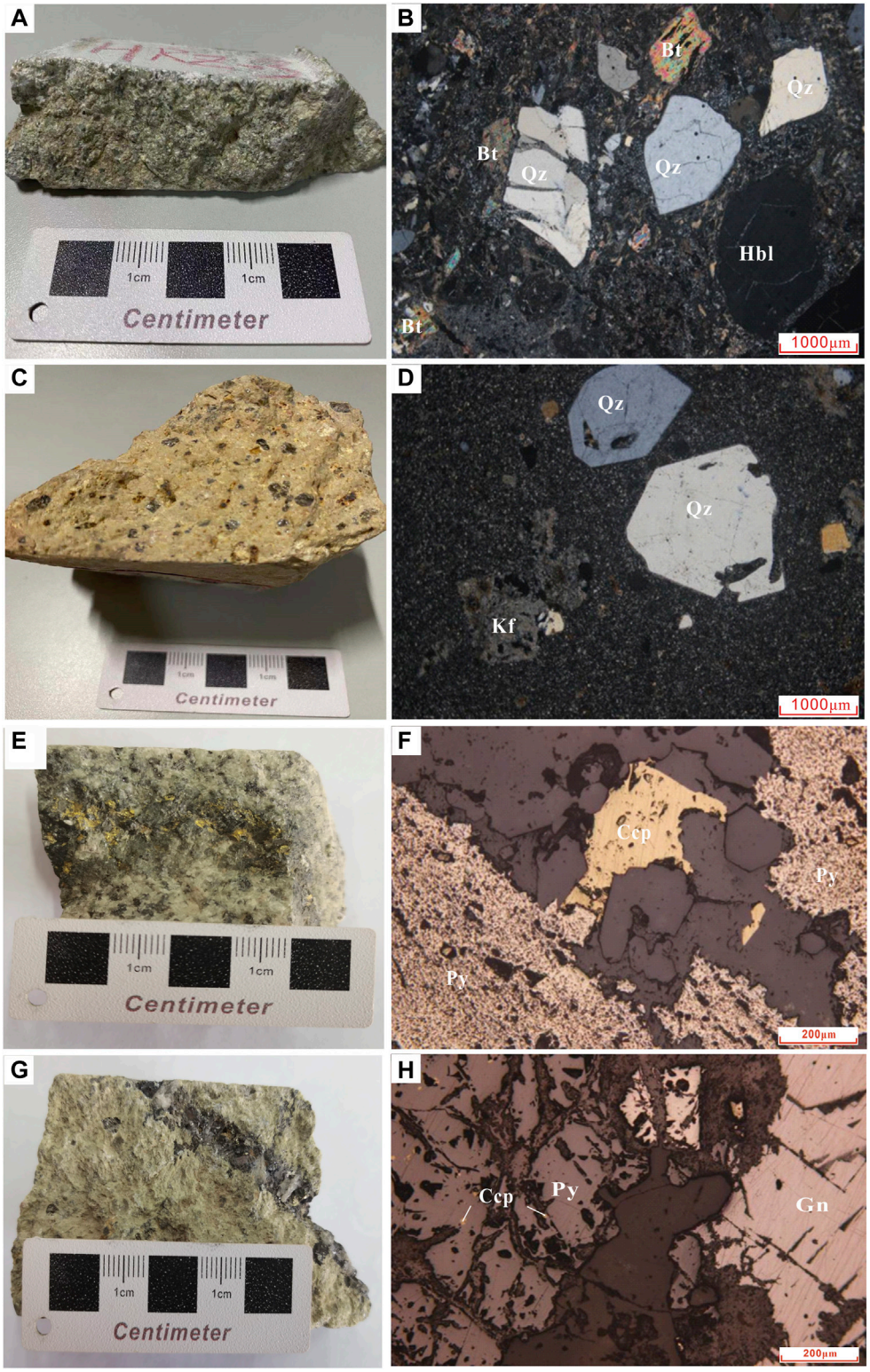

FIGURE 3
Representative photographs of rock and ore samples and corresponding micrographs of major mineral assemblages of the Harizha Cu deposit **(A)**. granodiorite porphyry; **(B)**. porphyritic texture; **(C)**. granite porphyry; **(D)**. porphyritic-matrix microcrystalline texture; **(E)**. copper ore samples; **(F)**. microscopic image of copper ore; **(G)**. lead ore samples;**(H)** microscopic image of lead ore; Pl-Plagioclase; Kfs-K-feldspar; Qz-Quartz; Bt-Biotite; Hbl-Hornblende; Py-Pyrite; Gn-Galena; Ccp-Chalcopyrite).

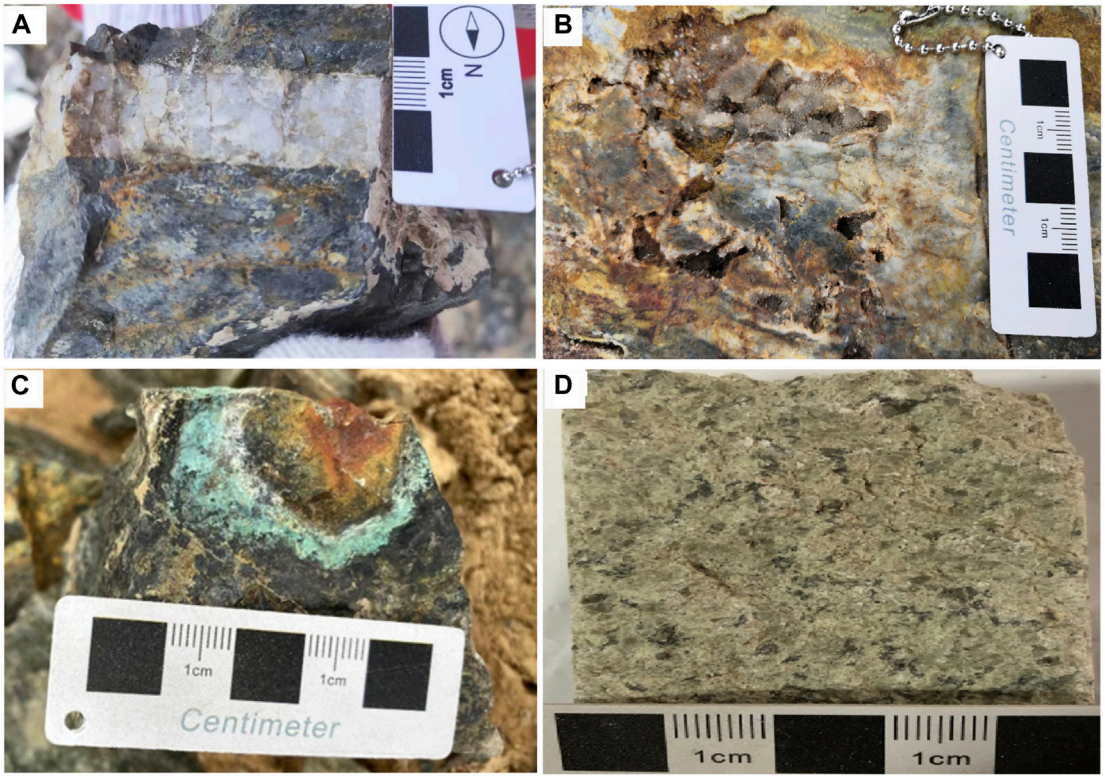

FIGURE 4
Photos showing the characteristics of ores and wallrock alteration at the Harizha deposit: **(A)**. Quartz veins; **(B)**. Pyrite associated with quartz veins; **(C)**. Malachite; **(D)**. Chloritization.

dating used an Agilent 7500 ICP-MS, a Geo Las 200 M optical system, and a Com Pex 102 ArF excimer laser. Helium was used as the carrier gas. 91500 were used as the external standards, and each standard was measured once every six samples. GJ-1 zircon standard sample was analyzed as an unknown to monitor the stability of the test process. NIST610 is used as an external standard to calculate the content of U and Th in zircon to ensure the accuracy of the test process. NIST610 and GJ-1 were measured once every 20 samples. Detailed analytical procedures are as described in Horn, Rudnick, and McDonough (2000) and Yuan et al. (2003). The data were processed using the Glitter program, and the age calculation and concordia plotting were conducted using Isoplot 3 (2006).

3.2 Zircon Hf isotope analysis

Based on zircon U-Pb dating, LA-MC-ICP-MS Hf isotope analysis was performed on the same or nearby zircon spots on the granodiorite porphyry and granite porphyry. This study was performed using a GeoLas Pro laser-ablation system coupled to a Neptune multiple-collector ICP-MS. A stationary laser ablation spot with a beam diameter of 32 μm was used for the analyses. The ablated aerosol was carried by helium and then combined with argon in a mixing chamber before being introduced to the ICP-MS plasma. A total of 10 spots were analyzed for each sample, and the raw data were processed with the Hfllow macro program.

3.3 Whole-rock geochemical analysis

Whole-rock major element contents were measured with an Axiosmax X-ray fluorescence (XRF) spectrometer. First, 500–1,000 mg samples were place in an oven for 200 min. After cooling to room temperature, the samples were weighed and the loss on ignition was calculated. Then, 600 mg of the sample was added with Li_3BO_3 and cosolvent, and the mixture was fully mixed and fused into a glass disc at high temperature. After cooling, the sample was analyzed by X-ray fluorescence spectrometer. The analysis accuracy is better than 1%. The trace element compositions were analyzed with an X Series 2 ICP-MS. HNO_3, HF, and $HClO_4$ were added to 50 mg sample to dissolve it completely, and then the solution was analyzed after cooling and dilution. The analysis accuracy is better than 5–10%. The ambient temperature of chemical analysis was 18–27 °C, with relative humidity of 25–50%.

10.3389/feart.2022.963351

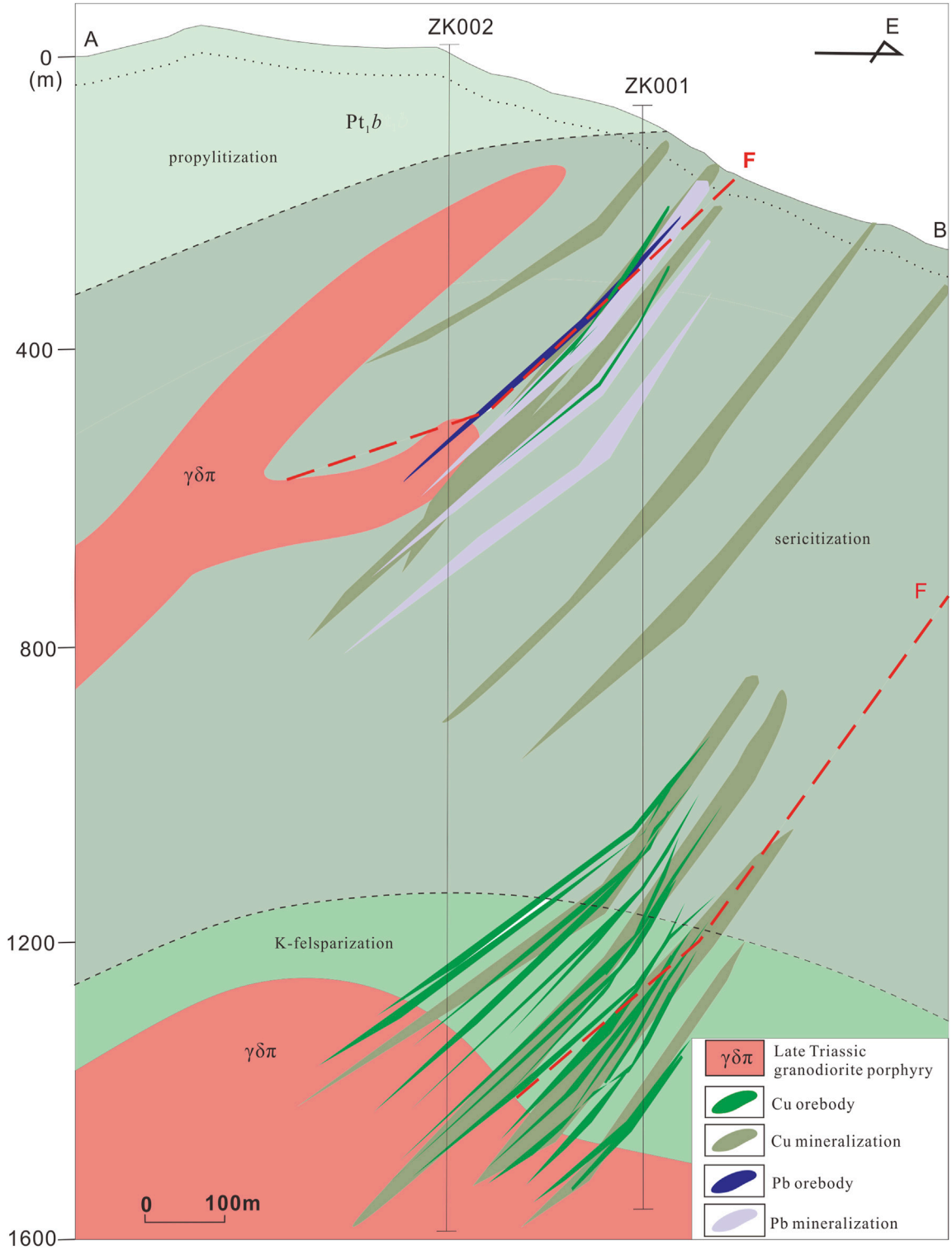

FIGURE 5
Geological profile of the Harizha mineralization zone I and orebodies.

TABLE 1 LA-MC-ICP-MS zircon U-Pb isotope dating results for the Harizha.

Sample and point number	Isotopic content/ppm			Isotope ratio						Isotopic age/Ma					
	Th	U	Th/U	$^{207}Pb/^{206}Pb$	2σ	$^{207}Pb/^{235}U$	2σ	$^{206}Pb/^{238}U$	2σ	$^{207}Pb/^{206}Pb$	2σ	$^{207}Pb/^{235}U$	2σ	$^{206}Pb/^{238}U$	2σ
HRZ-03															
1	225	414	0.5	0.0517	0.00222	0.2384	0.01029	0.0335	0.0008	270.4	95.6	217.1	8.4	212.3	5.0
2	246	647	0.4	0.0504	0.00126	0.2397	0.00631	0.0345	0.00077	213.2	56.8	218.2	5.2	218.7	4.8
3	358	664	0.5	0.0516	0.00127	0.2443	0.00635	0.0343	0.00077	268.9	55.4	222	5.2	217.6	4.8
4	326	741	0.4	0.0513	0.0014	0.2396	0.00683	0.0339	0.00076	252.6	61.7	218.1	5.6	214.9	4.8
5	504	471	1.1	0.0502	0.00144	0.2332	0.00691	0.0337	0.00076	204.1	65.2	212.8	5.7	213.6	4.7
6	428	744	0.6	0.0510	0.0014	0.2435	0.00693	0.0347	0.00078	239.3	62.0	221.3	5.7	219.6	4.9
7	320	558	0.6	0.0557	0.00141	0.2620	0.00693	0.0341	0.00076	440.9	55.0	236.3	5.6	216.2	4.8
8	117	177	0.7	0.0523	0.00235	0.2492	0.01118	0.0346	0.00083	299.7	99.3	225.9	9.1	218.9	5.2
9	430	780	0.6	0.0550	0.00209	0.2625	0.01002	0.0346	0.00081	411.7	82.1	236.7	8.1	219.4	5.0
10	211	285	0.7	0.0523	0.0025	0.2465	0.01172	0.0342	0.00083	298	105.5	223.7	9.6	216.7	5.2
11	400	478	0.8	0.0506	0.00131	0.2406	0.0065	0.0345	0.00077	221.5	58.9	218.9	5.3	218.6	4.8
12	324	525	0.6	0.0504	0.00149	0.2382	0.00724	0.0343	0.00077	211.9	67.2	216.9	5.9	217.3	4.8
13	278	657	0.4	0.0499	0.00131	0.2386	0.00651	0.0347	0.00077	188.4	60.0	217.3	5.3	219.9	4.8
14	422	886	0.5	0.0543	0.00144	0.2566	0.00706	0.0343	0.00076	382.1	58.5	231.9	5.7	217.3	4.7
15	282	774	0.4	0.0514	0.00119	0.2425	0.00591	0.0342	0.00075	259.3	52.3	220.5	4.8	216.8	4.7
16	373	850	0.4	0.0516	0.00177	0.2471	0.00857	0.0347	0.00079	268.4	76.7	224.2	7.0	219.9	4.9
17	356	618	0.6	0.0516	0.00147	0.2445	0.00715	0.0343	0.00076	268.6	64.1	222.1	5.8	217.6	4.8
18	174	621	0.3	0.0505	0.00163	0.2373	0.00775	0.0340	0.00077	219.4	72.9	216.2	6.4	215.7	4.8
19	216	353	0.6	0.0520	0.00267	0.2396	0.0122	0.0334	0.00081	283.9	113.5	218.1	10.0	211.9	5.1
20	219	522	0.4	0.0487	0.00129	0.2306	0.00633	0.0344	0.00076	131.4	61.4	210.7	5.2	217.7	4.7
21	202	562	0.4	0.0491	0.00123	0.2322	0.00606	0.0343	0.00075	151.5	57.9	212	5.0	217.3	4.7
22	228	562	0.4	0.0494	0.00135	0.2318	0.00653	0.0340	0.00075	164.3	62.9	211.6	5.4	215.7	4.7
23	222	541	0.4	0.0488	0.00144	0.2308	0.00704	0.0343	0.00077	140.1	67.9	210.8	5.8	217.2	4.8
24	174	656	0.3	0.0517	0.0013	0.2449	0.00648	0.0343	0.00077	273.6	56.5	222.4	5.3	217.5	4.8
25	610	1,417	0.4	0.0503	0.00169	0.2381	0.00816	0.0343	0.00079	208	76.1	216.9	6.7	217.6	4.9
26	160	430	0.4	0.0524	0.00147	0.2454	0.00718	0.0340	0.00077	302.1	62.8	222.9	5.9	215.4	4.8
27	210	512	0.4	0.0527	0.00141	0.2511	0.00701	0.0346	0.00078	314.9	59.5	227.4	5.7	219	4.8
28	159	243	0.7	0.0522	0.00391	0.2474	0.01829	0.0344	0.00095	292.7	162.5	224.5	14.9	217.9	5.9
29	253	816	0.3	0.0511	0.00123	0.2396	0.00613	0.0340	0.00076	243.5	54.6	218.1	5.0	215.7	4.7
30	431	858	0.5	0.0517	0.00197	0.2460	0.00951	0.0345	0.00081	270.3	85.3	223.3	7.8	218.8	5.0
31	233	562	0.4	0.0492	0.00136	0.2342	0.00675	0.0345	0.00078	155.1	63.4	213.6	5.6	218.9	4.9

(Continued on following page)

10.3389/feart.2022.963351

TABLE 1 (*Continued*) LA-MC-ICP-MS zircon U-Pb isotope dating results for the Harizha.

Sample and point number	Isotopic content/ppm			Isotope ratio						Isotopic age/Ma					
	Th	U	Th/U	$^{207}Pb/^{206}Pb$	2σ	$^{207}Pb/^{235}U$	2σ	$^{206}Pb/^{238}U$	2σ	$^{207}Pb/^{206}Pb$	2σ	$^{207}Pb/^{235}U$	2σ	$^{206}Pb/^{238}U$	2σ
32	256	552	0.5	0.0489	0.00129	0.2327	0.00646	0.0345	0.00078	144.8	60.8	212.5	5.3	218.5	4.8
33	579	593	1.0	0.0502	0.00139	0.2380	0.00686	0.0344	0.00078	204	62.9	216.7	5.6	217.8	4.8
HRZ-12															
1	131	203	0.6	0.0519	0.00215	0.2466	0.01031	0.0345	0.00083	278.7	92.1	223.8	8.4	218.6	5.1
2	353	316	1.1	0.0496	0.00152	0.2340	0.00741	0.0342	0.00079	176	69.8	213.5	6.1	216.9	4.9
3	171	236	0.7	0.0511	0.00221	0.2447	0.01064	0.0348	0.00084	242.9	96.6	222.2	8.7	220.3	5.2
4	222	520	0.4	0.0501	0.00163	0.2342	0.00785	0.0339	0.00079	197.8	74.0	213.6	6.5	215.1	4.9
5	218	407	0.5	0.0494	0.00158	0.2348	0.00773	0.0345	0.0008	164.8	73.0	214.1	6.4	218.6	5.0
6	120	211	0.6	0.0520	0.0041	0.2402	0.01864	0.0335	0.00096	284.8	170.5	218.6	15.3	212.5	6.0
7	449	804	0.6	0.0523	0.00164	0.2412	0.00782	0.0334	0.00077	300.4	69.9	219.4	6.4	211.9	4.8
8	332	616	0.5	0.0541	0.00268	0.2661	0.01316	0.0357	0.00089	375.6	107.2	239.6	10.6	225.9	5.5
9	157	385	0.4	0.0493	0.00202	0.2297	0.00951	0.0338	0.00081	164.1	93.0	209.9	7.9	214	5.0
10	127	198	0.6	0.0484	0.00268	0.2331	0.01287	0.0349	0.00088	120.3	125.7	212.7	10.6	221.1	5.5
11	234	298	0.8	0.0504	0.00168	0.2417	0.00828	0.0348	0.00081	213.1	75.5	219.8	6.8	220.4	5.0
12	178	215	0.8	0.0498	0.00169	0.2372	0.00825	0.0345	0.0008	186.3	77.1	216.1	6.8	218.8	5.0
13	123	252	0.5	0.0512	0.00198	0.2426	0.00952	0.0344	0.00081	250.2	86.7	220.5	7.8	217.7	5.1
14	200	328	0.6	0.0511	0.0017	0.2432	0.00829	0.0345	0.0008	245.9	74.6	221	6.8	218.7	5.0
15	196	317	0.6	0.0503	0.00163	0.2414	0.00804	0.0348	0.00081	210.5	73.2	219.6	6.6	220.4	5.0
16	99	179	0.6	0.0519	0.0018	0.2438	0.00866	0.0341	0.0008	280.5	77.4	221.5	7.1	216	5.0
17	155	279	0.6	0.0517	0.00176	0.2463	0.00858	0.0346	0.00081	272.5	75.9	223.6	7.0	219	5.0
18	140	267	0.5	0.0503	0.00155	0.2402	0.00766	0.0347	0.0008	207.6	69.8	218.6	6.3	219.6	5.0
19	158	283	0.6	0.0525	0.0025	0.2429	0.01158	0.0336	0.00083	307.2	104.9	220.8	9.5	212.7	5.2
20	94	181	0.5	0.0528	0.00237	0.2492	0.01126	0.0342	0.00083	318.9	99.0	225.9	9.2	217.1	5.2
21	239	271	0.9	0.0506	0.00152	0.2422	0.00756	0.0347	0.0008	222.2	67.9	220.2	6.2	220	5.0
22	636	573	1.1	0.0522	0.00141	0.2494	0.00711	0.0347	0.00079	293.6	60.6	226.1	5.8	219.7	4.9
23	160	192	0.8	0.0480	0.0019	0.2245	0.00895	0.0339	0.00079	99	92.2	205.7	7.4	214.9	4.9
24	348	665	0.5	0.0501	0.00124	0.2344	0.00608	0.0339	0.00075	201.2	56.3	213.8	5.0	214.9	4.7
25	277	345	0.8	0.0506	0.00157	0.2376	0.00754	0.0341	0.00077	221.5	70.1	216.5	6.2	216	4.8
26	141	275	0.5	0.0517	0.00172	0.2412	0.00819	0.0339	0.00077	270	74.7	219.4	6.7	214.7	4.8
27	76	141	0.5	0.0481	0.00294	0.2246	0.01358	0.0339	0.00086	104.5	138.4	205.7	11.3	214.6	5.4
28	303	499	0.6	0.0505	0.00141	0.2352	0.00682	0.0338	0.00076	215.9	63.5	214.5	5.6	214.3	4.7

(Continued on following page)

10.3389/feart.2022.963351

10.3389/feart.2022.963351

TABLE 1 (*Continued*) LA-MC-ICP-MS zircon U-Pb isotope dating results for the Harizha.

Sample and point number	Isotopic content/ppm			Isotope ratio						Isotopic age/Ma					
	Th	U	Th/U	$^{207}Pb/^{206}Pb$	2σ	$^{207}Pb/^{235}U$	2σ	$^{206}Pb/^{238}U$	2σ	$^{207}Pb/^{206}Pb$	2σ	$^{207}Pb/^{235}U$	2σ	$^{206}Pb/^{238}U$	2σ
29	215	354	0.6	0.0503	0.0015	0.2377	0.0073	0.0343	0.00077	207.9	67.8	216.5	6.0	217.3	4.8
30	190	331	0.6	0.0485	0.00153	0.2301	0.00743	0.0344	0.00078	123.3	72.6	210.3	6.1	218.1	4.9
31	93	178	0.5	0.0494	0.00181	0.2291	0.0085	0.0336	0.00077	168.1	83.3	209.4	7.0	213.1	4.8
32	175	240	0.7	0.0502	0.00164	0.2362	0.00789	0.0341	0.00078	202.4	74.1	215.3	6.5	216.4	4.9
33	241	390	0.6	0.0511	0.00154	0.2403	0.00746	0.0341	0.00077	247	68.1	218.6	6.1	215.9	4.8

4 Results

4.1 LA-ICP-MS zircon U-Pb dating

Zircon U-Pb dating was carried out on two samples from Harizha. The data are presented in Table 1, whilst representative zircon cathodoluminescence (CL) images and analytical spots are shown in Figure 6. The analyzed zircons are euhedral long columnar and (minor) short columnar, with aspect ratios of 1:1 to 3:1. Oscillatory zoning is well developed, and the high Th/U values (0.3–1.1) resemble typical magmatic zircons. Therefore, the U-Pb age can reflect the rock crystallization age (Hoskin and Schaltegger 2003; Wang et al., 2014; Yang et al., 2020).

A total of 33 spots were measured for the granodiorite porphyry (HRZ-3) (Table 1). The zircons have Th = 116.99–610.14 ppm, U = 177.49–1,416.97 ppm, Th/U = 0.20–1.27, and $^{206}Pb/^{238}U$ = 211.9–219.9 Ma. All the 33 zircon spots are concordant and plot on/near the concordia (Figures 7A, B). The weighted average age (217.3 ± 1.8 Ma; MSWD = 0.17) likely represents the crystallization age of the granodiorite porphyry.

A total of 33 spots were measured for the granite porphyry (HRZ-12) (Table 1). The zircons have Th = 75.54–635.59 ppm, U = 140.56–804.24 ppm, Th/U = 0.52–0.79, and $^{206}Pb/^{238}U$ = 211.9–225.9 Ma. All the 33 zircon spots are concordant and plot on/near the concordia (Figure 7C, D). The weighted average age (217.0 ± 1.7 Ma; MSWD = 0.35) likely represents the crystallization age of the granite porphyry.

4.2 Zircon Hf isotopes

The study performed 40 Hf isotope spot analyses on the granodiorite porphyry and granite porphyry (20 spots each) (Table 2). Twenty analyses on the granodiorite porphyry yielded $^{176}Lu/^{177}Hf$ = 0.000611–0.001957, $^{176}Hf/^{177}Hf$ = 0.282,417–0.282,510, and $\varepsilon_{Hf}(t)$ = -7.98 to -4.58, $f_{Lu/Hf}$ = -0.98 to -0.94. Calculated zircon two-stage Hf model age (T_{DM2}) = 1.5 to 1.8 Ga. Twenty analyses on the granite porphyry yielded $^{176}Lu/^{177}Hf$ = 0.000585–0.001118, $^{176}Hf/^{177}Hf$ = 0.282,442–0.282,509, and $\varepsilon_{Hf}(t)$ = -6.89 to -4.65, $f_{Lu/Hf}$ = -0.98 to -0.97. Calculated zircon two-stage Hf model age (T_{DM2}) = 1.5 to 1.7 Ga.

4.3 Whole-rock geochemical compositions

The rock samples have SiO_2 = 68.44–78.13 wt% (avg. 73.06 wt%), K_2O = 0.75–5.46 wt% (avg. 4.22 wt%), total alkali (K_2O+Na_2O) = 4.03–8.33 wt% (avg. 7.09 wt%), Al_2O_3 = 12.22–15.17 wt% (avg. 13.86 wt%), CaO = 0.44–3.65 wt% (avg. 1.50 wt%), and A/CNK = 1.02–1.68 (avg. 1.18) (Table 3).

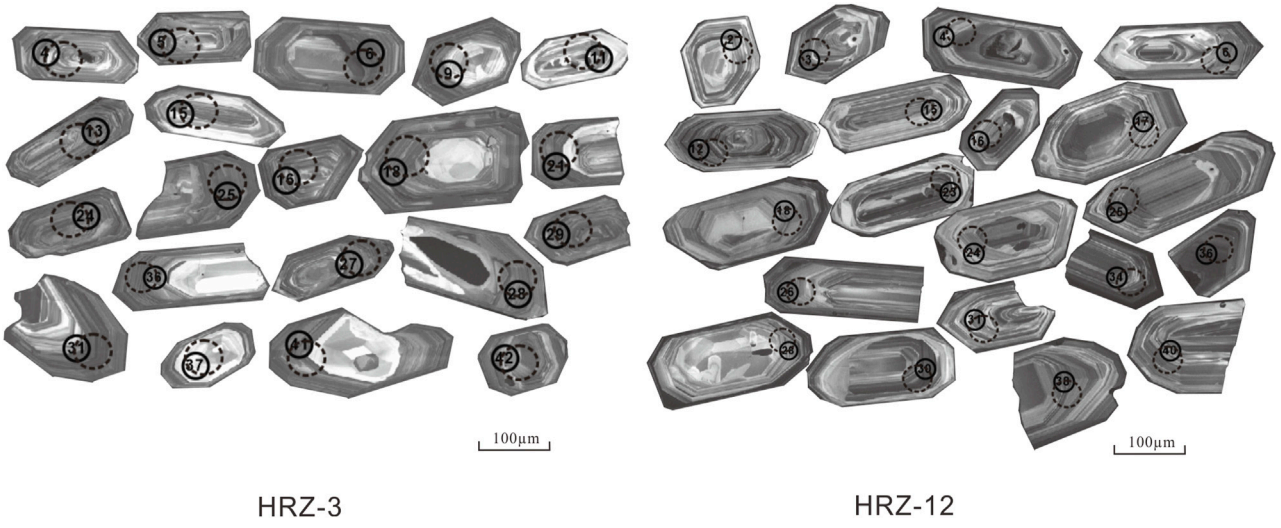

FIGURE 6
Representative zircon CL images of the Harizha granitoids. Solid-line and dotted-line circles denote the locations of U–Pb and Hf isotopic analysis spots, respectively.

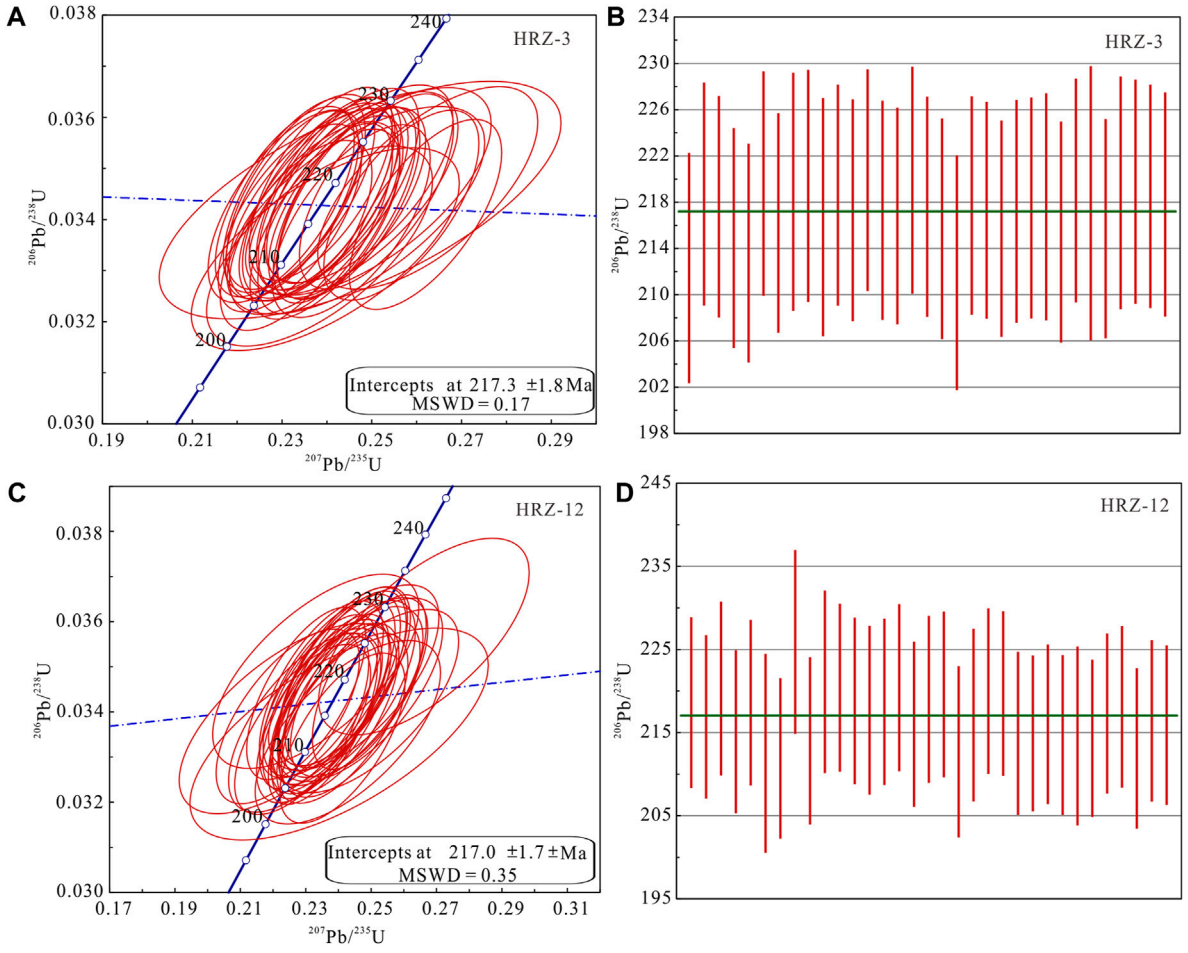

FIGURE 7
Zircon U–Pb concordia age and weighted mean age diagrams of the Harizha granitoids. **(A–D)** MSWD, mean square weighted deviation.

TABLE 2 Results of LA-ICP-MS Hf isotopes of zircon from the Harizha.

Point number	t (Ma)	$^{176}Yb/^{177}Hf$	$^{176}Lu/^{177}Hf$	$^{176}Hf/^{177}Hf$	$\varepsilon_{Hf}(0)$	±1σ	$\varepsilon_{Hf}(t)$	±1σ	$T_{DM1}(Hf)$ (Ma)	$T_{DM2}(Hf)$ (Ma)	$f_{Lu/Hf}$
HRZ-03											
4	219	0.023409	0.000823	0.282,475	-10.44	0.74	-5.83	0.74	1,095	1,620	-0.98
5	218	0.029516	0.000948	0.282,437	-11.79	0.58	-7.21	0.58	1,152	1706	-0.97
6	215	0.025840	0.000823	0.282,440	-11.67	0.59	-7.14	0.59	1,143	1,699	-0.98
9	220	0.027370	0.000989	0.282,510	-9.19	0.51	-4.58	0.51	1,050	1,541	-0.97
11	219	0.039069	0.001378	0.282,430	-12.01	0.63	-7.48	0.63	1,174	1724	-0.96
13	219	0.030174	0.001048	0.282,495	-9.72	0.71	-5.14	0.71	1,073	1,576	-0.97
15	217	0.034530	0.001229	0.282,470	-10.61	0.86	-6.10	0.86	1,114	1,635	-0.96
16	219	0.059911	0.001957	0.282,419	-12.43	0.73	-7.98	0.73	1,209	1755	-0.94
18	217	0.018640	0.000611	0.282,417	-12.49	0.62	-7.89	0.62	1,169	1748	-0.98
21	217	0.021716	0.000736	0.282,425	-12.20	0.60	-7.61	0.60	1,162	1731	-0.98
24	218	0.031473	0.001046	0.282,453	-11.22	0.53	-6.66	0.53	1,132	1,671	-0.97
25	216	0.021050	0.000746	0.282,445	-11.50	0.56	-6.94	0.56	1,134	1,687	-0.98
27	218	0.026999	0.000921	0.282,473	-10.50	0.53	-5.93	0.53	1,100	1,625	-0.97
28	217	0.020878	0.000700	0.282,439	-11.72	0.56	-7.13	0.56	1,142	1700	-0.98
29	216	0.024017	0.000850	0.282,500	-9.56	0.61	-5.01	0.61	1,061	1,566	-0.97
31	217	0.030312	0.001023	0.282,458	-11.03	0.65	-6.49	0.65	1,124	1,660	-0.97
36	219	0.021892	0.000754	0.282,438	-11.75	0.51	-7.13	0.51	1,145	1702	-0.98
37	218	0.029066	0.001031	0.282,479	-10.29	0.79	-5.73	0.79	1,095	1,613	-0.97
41	219	0.023010	0.000823	0.282,461	-10.92	0.56	-6.31	0.56	1,114	1,650	-0.98
42	218	0.031473	0.001046	0.282,453	-11.22	0.53	-6.66	0.53	1,132	1,671	-0.97
HRZ-12											
2	219	0.026083	0.000964	0.282,493	-9.80	0.66	-5.21	0.66	1,074	1,580	-0.97
3	217	0.023014	0.000823	0.282,487	-10.00	0.72	-5.43	0.72	1,078	1,593	-0.98
4	220	0.022979	0.000763	0.282,492	-9.83	0.62	-5.19	0.62	1,069	1,580	-0.98
6	219	0.022265	0.000813	0.282,472	-10.56	0.68	-5.94	0.68	1,099	1,627	-0.98
12	226	0.025410	0.000972	0.282,442	-11.61	0.86	-6.87	0.86	1,146	1,691	-0.97
15	221	0.022072	0.000810	0.282,493	-9.80	0.65	-5.14	0.65	1,069	1,578	-0.98
16	220	0.029311	0.000998	0.282,490	-9.90	0.67	-5.29	0.67	1,079	1,586	-0.97
17	219	0.020417	0.000723	0.282,465	-10.78	0.62	-6.15	0.62	1,105	1,640	-0.98
18	218	0.017553	0.000604	0.282,481	-10.22	0.59	-5.60	0.59	1,080	1,604	-0.98
23	220	0.025253	0.000892	0.282,462	-10.90	0.67	-6.28	0.67	1,115	1,649	-0.97
24	216	0.018425	0.000617	0.282,469	-10.64	0.60	-6.07	0.60	1,097	1,632	-0.98
25	219	0.016809	0.000585	0.282,507	-9.30	0.66	-4.65	0.66	1,043	1,545	-0.98
26	220	0.019302	0.000681	0.282,498	-9.60	0.54	-4.95	0.54	1,058	1,565	-0.98
28	217	0.027198	0.000931	0.282,479	-10.27	0.62	-5.72	0.62	1,091	1,611	-0.97
30	220	0.033061	0.001118	0.282,448	-11.38	0.63	-6.78	0.63	1,141	1,681	-0.97
31	215	0.023751	0.000868	0.282,454	-11.17	0.59	-6.65	0.59	1,125	1,668	-0.97
34	215	0.029260	0.000972	0.282,448	-11.40	0.53	-6.89	0.53	1,137	1,684	-0.97
36	214	0.024548	0.000843	0.282,509	-9.24	0.63	-4.74	0.63	1,048	1,547	-0.97
38	218	0.017713	0.000625	0.282,459	-11.00	0.61	-6.38	0.61	1,111	1,653	-0.98
40	216	0.022412	0.000781	0.282,459	-11.01	0.66	-6.46	0.66	1,116	1,657	-0.98

In the total alkali-silica (TAS) classification diagram (Figure 8A), the rock samples plot in the subalkaline granite field. In the A/NK-A/CNK (Figure 8B) and SiO_2-K_2O (Figure 8C) diagrams, the rocks are classified as peraluminous and high-K calc-alkaline. In the (Na_2O+K_2O-CaO)/SiO_2 diagram (Figure 8D), the data points fall into the calc-alkaline field.

The rocks have total rare earth element (REE) contents of 46.13–211.16 ppm (avg. 132.05 ppm), and negative Eu anomalies

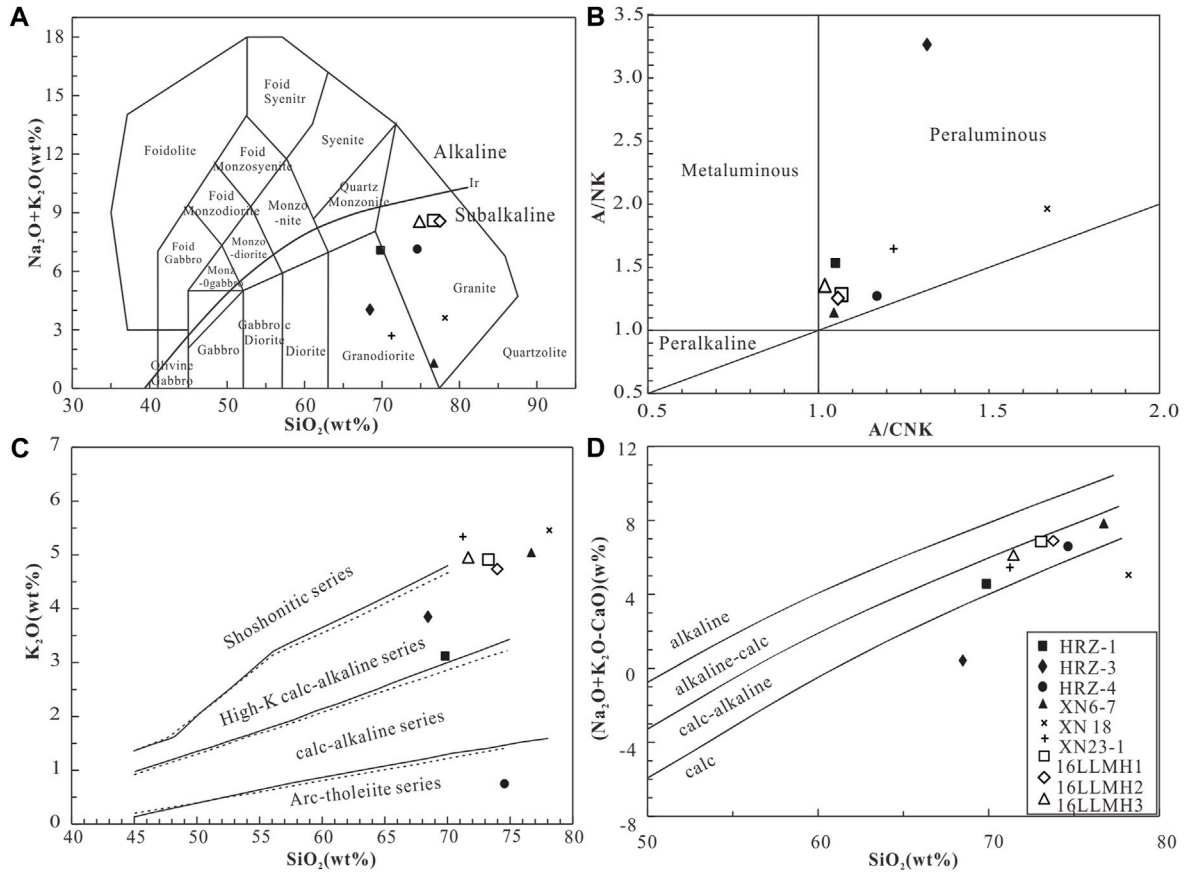

FIGURE 8
Geochemical classification diagrams for the Harizha granitoids: **(A)** TAS (after Middlemost and Sun 1985); **(B)** $Al_2O_3/(Na_2O+K_2O)$ versus $Al_2O_3/(CaO+Na_2O+K_2O)$ (Maniar and Piccoli, 1989); **(C)** K_2O versus SiO_2 (after Middlemost 1985); **(D)** (Na_2O+K_2O-CaO) versus SiO_2 (Frost et al., 2001).

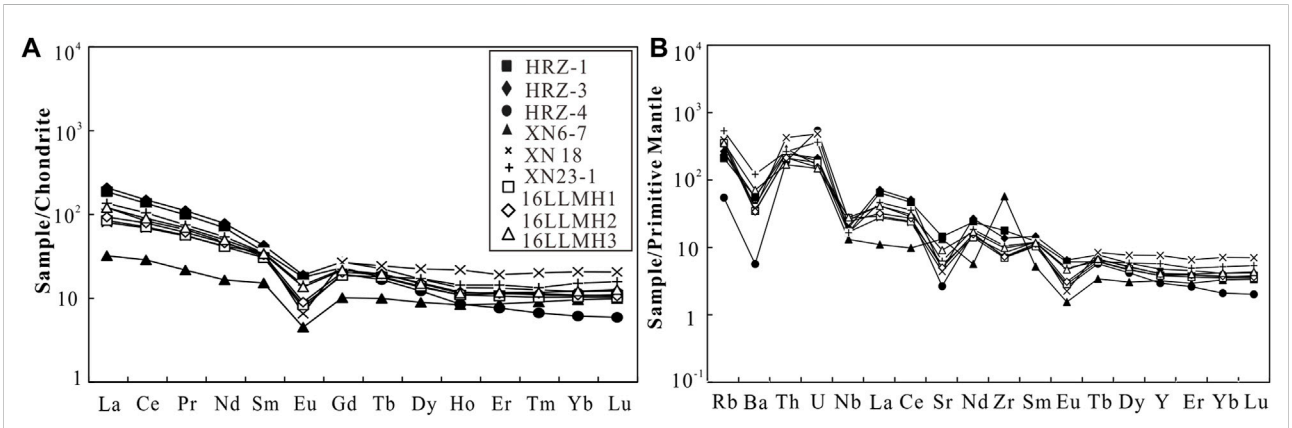

FIGURE 9
(A) Chondrite-normalized REE patterns; **(B)** Primitive mantle-normalized trace element patterns. Chondrite and primitive-mantle normalizing values are from Sun and McDonough (1989) and Rudnick and Gao (2004), respectively.

(δEu = 0.21–0.60, avg. 0.41). In the chondrite-normalized REE plot (Figure 9A), the rocks show right-inclining patterns (LREE/HREE enrichment), with LREE/HREE = 4.30–12.82, $(La/Yb)_N$ = 3.34–19.67, indicating significant fractionation (Han Z. H. et al., 2020). The rocks have slightly negative Ce anomalies (δCe = 0.89–1.07, avg. 0.98), indicating that the oxidized conditions were relatively stable during the magmatic evolution (Wang P. X. et al., 2020). In the primitive mantle-normalized multi-element spider diagram (Figure 9B), the element distribution curves of the different rock samples are similar, and are featured by enrichments in large ion lithophile elements (LILE; e.g., Rb, K), other incompatible elements (e.g., Th and U), and depletions in high field strength elements (HFSE; e.g., Nb, Th) (Table 3).

5 Discussion

5.1 Petrogenesis and magma source

-From the diagram of Zr+Nb+Ce+Y–(K_2O+Na_2O)/CaO (Figure 10A), it can be seen that most of the samples fall into the I-,S- and M-type regions of the undifferentiation granite. In the diagram of SiO_2–Zr (Figure 10B), most of the samples fall into the S-type region. In general, A/CNK = 1.1 is the threshold for distinguishing I- from S-type granite (Sylvester, 1998). The aluminum saturation index of Harizha samples is between 1.02 and 1.68 (avg. 1.18). Therefore, we speculated that the Harizha samples have the characteristics of I- to S-type transitional granite.

When discussing the magma source region, previous studies suggested that Rb/Sr > 0.5 and Nd/Th ≈ 3 indicate likely crustal material remelting during orogenic process (Gibbs, 1986; McDonough and Sun 1995; Xiao et al., 2002), similar to our samples (Rb/Sr = 0.44–2.69 (avg. 1.53); Nd/Th = 0.31–1.72 (avg. 1.15)), which indicates a crustal source for the Harizha granitoids. Meanwhile, the rocks have low Sr (56.20–306.50 ppm) but high Y (13.50–34.70 ppm) and Yb (1.04–3.51 ppm), consistent with the content of mafic rocks in the crust. The high SiO_2 and K_2O but low MgO contents, and the LREE/HREE enrichment again support a crustal magma source (Gao and Sun, 2021).

The zircon Lu-Hf isotope system has high closure temperature, and can reflect the Hf isotopes during petrogenesis (Wu et al., 2007). In this study, the $^{176}Lu/^{177}Hf$ ratios of the two samples were <0.002, and the variation range is very small. It shows that Hf isotopes are rarely accumulated after zircon formation, which can represent Hf isotopic composition of magmatic system during zircon formation (Zhang et al., 2020). The $f_{Lu/Hf}$ ratios are significantly lower than the average continental crust (-0.55) (Griffin et al., 2000). Thus, its two Hf model ages (T_{DM2}) can better reflect the average crustal retention age of the source material (Huang et al., 2016). In the Age-ε_{Hf} (t) diagram (Figure 11), the granodiorite porphyry and granite porphyry samples from Harizha fall below the meteorite evolution line. The ε_{Hf} (t) value is mainly distributed between -8 and -4, and the corresponding T_{DM2} is mainly concentrated between 1.5 and 1.8 Ga. In this study, the ε_{Hf} (t) values of granodiorite porphyry and granite porphyry are negative, indicating that the ancient crustal material was remelted.

5.2 Tectonic setting

Previous studies have shown that tectonic evolution of the East Kunlun Orogen mainly involved four stages: 1) ocean

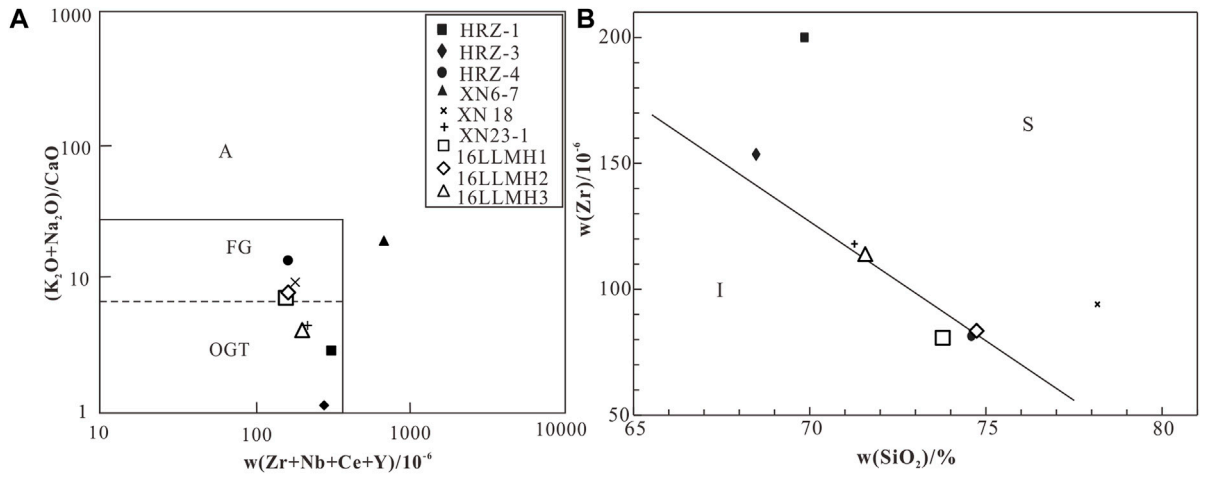

FIGURE 10
(Zr+Nb+Ce+Y) versus (K_2O+Na_2O)/CaO diagrams of Harizha (A—A-type granite; FG—Fractionated I, S, M-type granite; OGT—Non-fractionated I, S, M-type granite; I—I-type granite). **(A,B)** S-S-type granite.

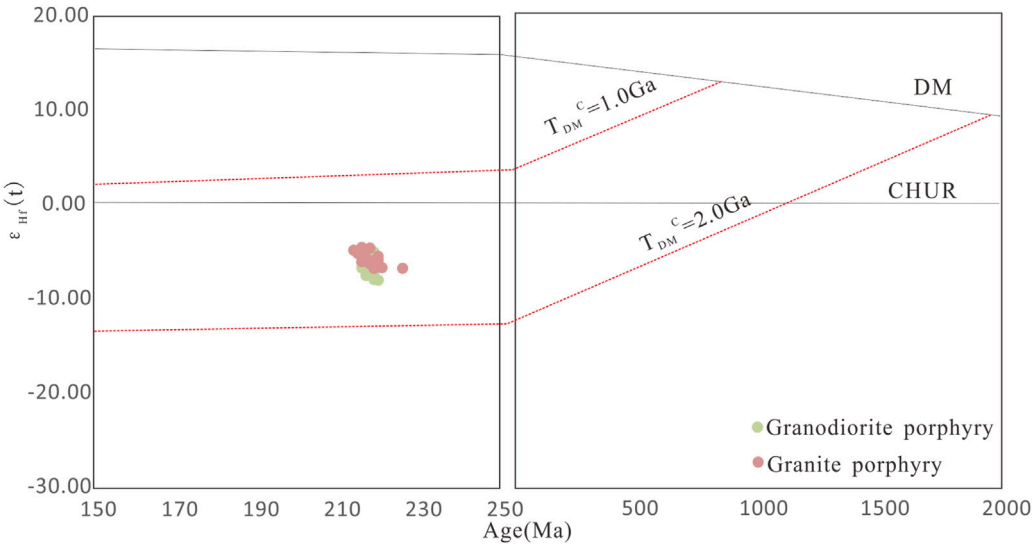

FIGURE 11
U–Pb age versus $\varepsilon_{Hf}(t)$ diagram of Lu-Hf isotopic evolution of zircon from the Harizha (Belousova et al., 2010)

basin opening and expansion (Neoarchean–Proterozoic), 2) ocean basin subduction (Early Paleozoic), 3) continent-continent collision (Late Paleozoic-Early Mesozoic), and 4) post-collisional extension (Cenozoic-Mesozoic) (Liu et al., 2013; Zhang et al., 2016). The Late Paleozoic-Early Mesozoic was the Paleo-Tethys orogenic period and was the main granite emplacement period in the East Kunlun (Xia et al., 2014; Feng et al., 2017; Xu et al., 2021). Some workers proposed that the Late Carboniferous-Late Permian (309–260 Ma) was the ocean-ridge formation and expansion stage. The Late Permian-Middle Triassic (260–230 Ma) was the ocean subduction stage. The Middle Triassic-Early Jurassic (230–190 Ma) was the intraplate orogenic stage (Guo and Deng, 1998; Li X. R. et al., 2020; Li et al., 2021). It is widely accepted that the Paleotethys have begun subduction in the East Kunlun in the Late Permian, and have changed from a subduction to a collision setting in the Middle Triassic (Guo et al., 2016; Wang K. et al., 2020; Xu et al., 2020). During the tectonic evolution, regional mantle-derived magma underplating, accompanied by partial melting of crustal rocks, may have formed voluminous calc-alkaline magmas

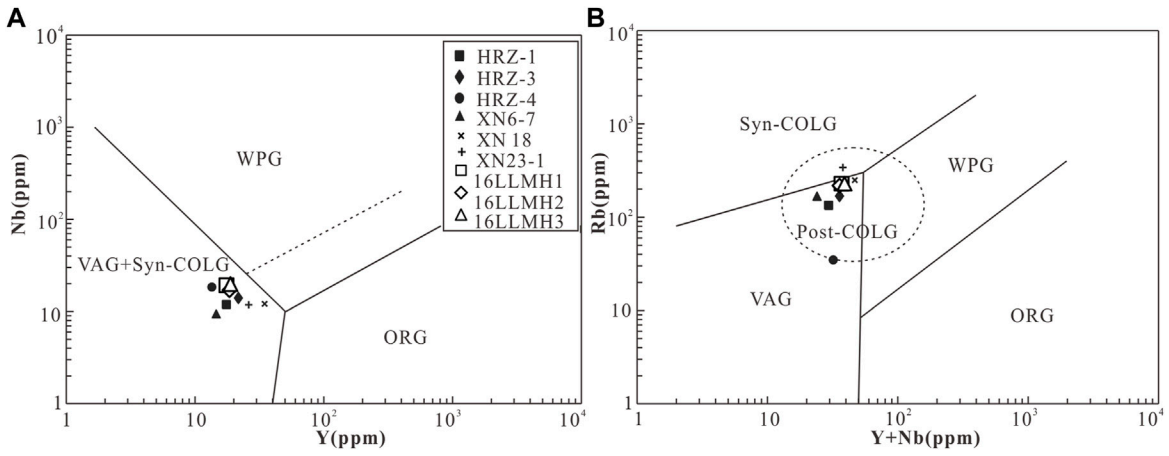

FIGURE 12
Tectonic discrimination diagrams for the Harizha granitoids: **(A)** Nb versus Y (Pearce, Harris, and Tindle, 1984); **(B)** Rb versus (Y + Nb) (Pearce, Harris, and Tindle, 1984). Abbreviations: Syn-COLG, syn-collisional granites; Post-COLG, post-collisional granites; WPG, within-plate granites. VAG, volcanic arc granites; ORG, ocean ridge granites.

TABLE 3 Major and trace element data for the Harizha.

Sample No.	HRZ-1	HRZ-3	HRZ-4	XN6-7	XN18	XN23-1	16LLMH1	16LLMH2	16LLMH3
	Monzogranite	Granodiorite porphyry	Granodiorite	Granite porphyry	Syenogranite porphyry	Mineralized Granite porphyry	Granodiorite	Granodiorite	Granodiorite
SiO_2	69.81	68.44	74.55	76.69	78.13	71.23	73.28	74.18	71.21
Al_2O_3	15.17	14.70	14.39	12.22	12.26	14.25	13.77	13.48	14.46
TiO_2	0.40	0.39	0.18	0.08	0.11	0.28	0.16	0.14	0.29
Fe_2O_3	0.41	0.40	0.22	1.25	2.54	3.06	0.53	0.33	0.44
FeO	1.95	1.50	0.79	0.82	0.37	1.49	1.03	0.92	1.44
CaO	2.49	3.65	0.53	0.44	0.61	1.62	1.13	1.03	1.97
MgO	0.96	0.97	1.04	0.16	0.31	0.86	0.53	0.39	0.62
K_2O	3.12	3.85	0.75	5.04	5.46	5.34	4.88	4.65	4.93
Na_2O	3.96	0.18	6.39	3.29	0.17	1.76	3.33	3.51	3.20
MnO	0.07	0.04	0.01	0.02	0.01	0.06	0.03	0.03	0.04
P_2O_5	0.12	0.10	0.10	0.01	0.02	0.06	0.07	0.07	0.19
LOI	1.21	5.52	0.95	-	-	-	1.21	1.23	1.22
$K_2O+ Na_2O$	7.08	4.03	7.14	8.33	5.63	7.10	8.21	8.16	8.13
Na_2O/K_2O	1.27	0.05	8.47	0.65	0.03	0.33	0.68	0.75	0.65
A/KNC	1.05	1.32	1.17	1.05	1.68	1.22	1.07	1.06	1.02
La	44.30	49.20	28.60	7.60	19.00	32.00	20.00	22.10	28.50
Ce	83.00	91.20	50.90	17.50	42.10	63.70	43.30	48.20	54.90
Pr	9.39	10.50	6.24	2.05	5.26	7.10	5.34	5.79	6.57
Nd	32.30	36.40	21.80	7.70	19.60	25.20	19.20	21.30	23.10
Sm	5.50	6.50	4.75	2.32	5.35	5.31	4.64	5.04	5.18
Eu	1.03	1.09	0.44	0.26	0.38	0.83	0.48	0.52	0.79
Gd	4.74	5.55	3.99	2.08	5.50	4.56	3.83	4.16	4.41
Tb	0.66	0.84	0.62	0.37	0.91	0.67	0.67	0.72	0.73
Dy	3.42	4.30	3.10	2.26	5.65	4.33	3.51	3.86	3.78
Ho	0.62	0.75	0.48	0.47	1.23	0.81	0.62	0.67	0.65
Er	1.88	2.18	1.26	1.41	3.16	2.38	1.75	1.87	1.93
Tm	0.28	0.32	0.17	0.23	0.51	0.34	0.26	0.29	0.30
Yb	1.81	2.04	1.04	1.63	3.51	2.56	1.75	1.85	2.06
Lu	0.28	0.31	0.15	0.25	0.52	0.40	0.26	0.27	0.32
Y	17.50	21.70	13.50	14.60	34.70	26.10	17.40	18.40	18.70
Rb	134.17	168.84	34.85	167.50	250.00	342.00	225.00	215.00	225.00

(Continued on following page)

10.3389/feart.2022.963351

TABLE 3 (*Continued*) Major and trace element data for the Harizha.

Sample No.	HRZ-1	HRZ-3	HRZ-4	XN6-7	XN18	XN23-1	16LLMH1	16LLMH2	16LLMH3
	Monzogranite	Granodiorite porphyry	Granodiorite	Granite porphyry	Syenogranite porphyry	Mineralized Granite porphyry	Granodiorite	Granodiorite	Granodiorite
Ba	391.45	294.08	39.79	389.00	269.00	852.00	245.00	238.00	499.00
Th	21.46	21.12	16.17	24.60	36.20	22.50	18.00	18.30	14.40
U	4.09	4.46	11.33	3.52	10.20	7.66	3.81	3.26	3.13
Nb	11.89	14.01	18.43	9.40	12.10	11.80	19.50	17.20	20.00
Sr	306.50	98.92	56.15	282.00	93.00	132.00	118.00	106.00	193.00
Zr	199.78	153.68	81.50	640.00	94.00	118.00	78.80	81.40	110.00
∑REE	189.26	211.16	123.57	46.13	112.68	150.19	105.61	116.64	133.22
LREE/HREE	12.82	11.96	10.43	4.30	4.37	8.36	7.35	7.52	8.39
(La/Yb)N	17.54	17.27	19.67	3.34	3.88	8.97	8.20	8.57	9.92
δEu	0.60	0.54	0.30	0.35	0.21	0.50	0.34	0.34	0.49
δCe	0.95	0.94	0.89	1.07	1.02	0.99	1.01	1.02	0.95
Rb/Sr	0.44	1.71	0.62	0.59	2.69	2.59	1.91	2.03	1.17
Nd/Th	1.51	1.72	1.35	0.31	0.54	1.12	1.07	1.16	1.60
Y+Nb	29.44	35.70	31.96	24.00	46.80	37.90	36.90	35.60	38.70

Note: XN6-7, XN18, XN23-1 are from Ma et al. (2016); 16LLMH1, 16LLMH2, 16LLMH3 are from Guo et al. (2019); Other samples are from this study.

10.3389/feart.2022.963351

(Figures 8C,D), and also many mafic rock units (Xin et al., 2019). In Yanshanian period, plate collision was close to the late stage, and the magmatism was mainly driven by crustal delamination in an extensional environment (Yang et al., 2010). The ore-bearing rocks in the East Kunlun Orogen were mainly formed in the Early-Middle Triassic subduction-continental collision stage (235–248 Ma), but a few of them were also formed in the Late Triassic post-collisional stage (204–219 Ma). For example, the Jiangjunmu ore-bearing granodiorite porphyry in the eastern East Kunlun was dated at 218 Ma (Yu et al., 2020), whilst the Huanglonggou granodiorite (also in eastern East Kunlun) was dated at 220 Ma (Zhang et al., 2017). In this study, emplacement of the ore-related Harizha granodiorite porphyry (217.3 ± 1.8 Ma) and granite porphyry (217.0 ± 1.7 Ma) was coeval with the post-collision stage in the East Kunlun Orogen (Gao et al., 2017). In addition, the samples plot in the volcanic arc-collisional granites field in the Nb-Y discrimination plot (Figure 12A) and in the post-collisional granites field in the Y+Nb-Rb discrimination plot (Figure 12B)), which also suggests that the Harizha granites were formed in a post-collisional extension environment (Han J. J. et al., 2020).

Data availability statement

The original contributions presented in the study are included in the article/supplementary material further inquiries can be directed to the corresponding author.

Author contributions

All authors contributed to the study conception and design. Material preparation, data collection and analysis were performed by WZ and CX. The first draft of the manuscript was written by WZ. CX, WZ, and ZH made field investigation and collected samples; SZ and CQ took part in the experiments; CX and WZ interpreted all the data and finished the original draft of the manuscript.

Funding

This study was supported by the Application Basic Research Project of Qinghai Science and Technology Plan (2020-ZJ-762).

Acknowledgments

We thank the Laboratory of the Hebei Institute of Regional Geology and Mineral Resources Survey, the State Key Laboratory of Continental Dynamics (Northwest University), and the Department of Geological Engineering (Qinghai University) for providing technical and platform support for the analyses in this study.

Conflict of interest

The authors declare that the research was conducted in the absence of any commercial or financial relationships that could be construed as a potential conflict of interest.

Publisher's note

All claims expressed in this article are solely those of the authors and do not necessarily represent those of their affiliated organizations, or those of the publisher, the editors and the reviewers. Any product that may be evaluated in this article, or claim that may be made by its manufacturer, is not guaranteed or endorsed by the publisher.

References

Belousova, E. A., Kostitsyn, Y. A., Griffin, W. L., Begg, G. C., O'Reilly, S. Y., Pearson, N. J., et al. (2010). The growth of the continental crust: Constraints from zircon Hf-isotope data. *Lithos* (119), 457–466. doi:10.1016/j.lithos.2010.07.024

Chen, X. H., Yang, N., Chen, Z. L., Han, S. Q., Wang, Z. H., and Ye, B. Y. (2010). Geological characteristics and metallogenic model of super-large porphyry copper deposit in Aktogai ore field, Kazakhstan. *J. Geomechanics* 16 (4), 325–339. (in Chinese with English abstract). doi:10.3969/j.issn.1006-6616.2010.04.001

Du, Y. L., Jia, Q. Z., and Han, S. F. (2012). Mesozoic tectono-magmatic-mineralization and copper-gold polymetallic ore prospecting research in east Kunlun metallogenic belt in Qinghai. *Northwest. Geol.* 45 (4), 69–75. (in Chinese with English abstract).

Feng, Y. L., Yuan, W. M., Tian, Y. T., Feng, X., Hao, N. N., Zhang, L., et al. (2017). Preservation and exhumation history of the harizha-halongxiuma mining area in the east Kunlun range, northeastern Tibetan plateau, China. *Ore Geol. Rev.* 90, 1018–1031. doi:10.1016/j.oregeorev.2016.12.029

Frost, B. R., Barnes, C. G., Collins, W. J., Arculus, R. J., Ellis, D. J., Frost, C. D., et al. (2001). A geochemical classification for granitic rocks. *J. Petrology* 42 (11), 2033–2048. doi:10.1093/petrology/42.11.2033

Gao, H. C., and Sun, F. Y. (2001). Middle to late triassic granitic magmatism in the East Kunlun Orogenic Belt, NW China: Petrogenesis and implications for a transition from subduction to post-collision setting of the Palaeo-Tethys Ocean. *Geol. J.* 56 (6), 3378–3395. doi:10.1002/gj.4104

Gao, Y. B., Li, W. Y., Li, K., and Qian, B. (2017). Magmatism and mineralization during early mesozoic continental accretion process in qimantag, East Kunlun mountains. *Mineral. Deposits* 36 (2), 463–482. (in Chinese with English abstract). doi:10.16111/j.0258-7106.2017.02.013

Gibbs, A. K. (1986). *The continental crust: Its Composition and evolution*. Stuart ross taylor , scott M. McLennan. *J. Geol.* 94 (4), 632–633. doi:10.1086/629067

Griffin, W. L., Pearson, N. J., Belousova, E., Jackson, S. E., O'Reilly, S. Y., and Shee, S. R. (2000). The Hf isotope composition of cratonic mantle: LAM-MC-ICPMS analysis of zircon megacrysts in kimberlites. *Geochimica Cosmochimica Acta* 64 (1), 133–147. doi:10.1016/S0016-7037(99)00343-9

Guo, F. Z., and Deng, J. F. (1998). Late Paleozoic-Mesozoic intracontinental orogenic process and intermediate-acidic igneous rocks from the Eastern Kunlun Mountains of Northwestern China. *Geoscience* 12 (3), 344–352. (in Chinese with English abstract).

Guo, X. Z., Jia, Q. Z., Kong, H. L., Li, Y. Z., Li, J. C., and Wang, Y. (2016). Zircon U-Pb geochronology and geochemistry of Harizha quartz diorite in the eastern section from East Kunlun. *Geol. Sci. Technol. Inf.* 35 (5), 18–26. (in Chinese with English abstract). doi:10.3969/j.issn.0001-5717.2016.10.019

Guo, X. Z., Jia, Q. Z., Li, J. C., Kong, H. L., Yao, X. G., and Ma, Z. Y. (2019). The forming age and geochemistry characteristics of the granodiorites in Harizha, East Kunlun and its tectonic significance. *J. Geomechanics* 25 (2), 286–300. (in Chinese with English abstract). doi:10.12090/j.issn.1006-6616.2019.25.02.027

Han, J. J., Li, Y. D., Song, C. Z., He, J., Han, X., and He, X. L. (2020). Zircon U- Pb dating and geochemistry of granite in the Reshui area of Dulan County, eastern section of east Kunlun orogen and its tectonic implications. *Acta Geol. Sin.* 94 (3), 768–781. (in Chinese with English abstract).

Han, Z. H., Sun, F. Y., Tian, N., Gao, H. C., Li, L., and Zhao, T. F. (2020). Zircon U-Pb geochronology, geochemistry and geological implications of the early Paleozoic Wulanwuzhuer granites in the Qimantag, East Kunlun, China. *Earth Sci.*, 1–27. (in Chinese with English abstract).

Horn, I., Rudnick, R. L., and McDonough, W. F. (2000). Precise elemental and isotope ratio determination by simultaneous solution nebulization and laser ablation-ICP-MS: Application to U-Pb geochronology. *Chem. Geol.* 164, 281–301. doi:10.1016/S0009-2541(99)00168-0

Hoskin, P. W. O., and Schaltegger, U. (2003). The composition of zircon and igneous and metamorphic petrogenesis. *Rev. Mineralogy Geochem.* 53 (1), 27–62. doi:10.2113/0530027

Huang, D. M., Wan, Y. S., Zhang, D. H., Dong, C. Y., and Zhao, Y. Y. (2016). Paleoproterozoic tectono—thermal events in the xiatang area, lushan county, southern margin of the north China craton—evidence from geochemical features, zircon SHRIMP dating and Hf isotopic analysis. *Geol. Rev.* 62 (6), 1439–1461. doi:10.16509/j.georeview.2016.06.006

Karl, R. J., Eduardo, C., Jamie, J. W., Clara, C. W., Anton, K., Miranda-Diaz, G., et al. (2021). Hydrothermal fluid evolution in the Escondida porphyry copper deposit, northern Chile: Evidence from SEM-CL imaging of quartz veins and LA-ICP-MS of fluid inclusions. *Min. Depos.* 57, 279–300. doi:10.1007/S00126-021-01058-Z

Lei, Y., Shu, Y. D., Zhi, C. L., Zhao, C., Pang, Z., Yu, X., et al. (2020). Origin of the late permian gabbros and middle triassic granodiorites and their mafic microgranular enclaves from the eastern Kunlun orogen belt: Implications for the subduction of the palaeo-tethys ocean and continent-continent collision. *Geol. J.* 55 (1), 147–172. doi:10.1002/gj.3340

Li, H. P. (2010). *Metallogenic geological characteristics and Metallogenic prediction of Qimantage iron and polymetallic deposit of East Kunlun Mountains*, Doctoral Dissertation. Beijing): China University of Geosciences, 1–168.

Li, J. Q., Zhang, X. L., Wang, T., Li, Q., Wang, T. S., and Xue, W. W. (2021). Zircon U-Pb dating and geochemical characteristics of granite porphyry in Zhanhongshan area, East Kunlun. *Northwest. Geol.* 54 (1), 30–40. (in Chinese with English abstract). doi:10.19751/j.cnki.61-1149/p.2021.01.003

Li, Q. (2019). *Study on the Geological characteristics and enrichment regularities of mineralization of Harizha Ag-Cu polymetallic deposit in Eastern Kunlun orogenic belt, Qinghai Province*. Master Dissertation. Jilin: Jilin University, 1–80.

Li, X. R., Wan, Y. L., and Wang, J. (2020). Petrogeochemical characteristics, zircon U-Pb ages and Hf isotopic composition of Baicuo granites in central Qiangtang Basin, and its tectonic significance. *Geol. Rev.* 66 (5), 1172–1185. (in Chinese with English abstract). doi:10.16509/j.georeview.2020.05.007

Li, Y. J., Wei, J. H., Santosh, M., Li, H., Liu, H., Niu, M., et al. (2020). Anisian granodiorites and mafic microgranular enclaves in the eastern Kunlun Orogen, NW China: Insights into closure of the eastern Paleo-Tethys. *Geol. J.* 55 (9), 6487–6507. doi:10.1002/gj.3814

Liu, B., Ma, C. Q., Jiang, H. A., Guo, P., Zhang, J. Y., and Xiong, F. H. (2013). Early Paleozoic tectonic transition from ocean subduction to collisional orogeny in the Eastern Kunlun region: Evidence from Huxiaoqin mafic rocks. *Acta Petrol. Sin.* 29 (6), 2093–2106. (in Chinese with English abstract).

Liu, J., Huang, B., Yang, T., Xu, W. J., Liu, M., and Cao, Q. C. (2019). Analysis on the super-large porphyry copper deposits in the world. *Geol. Resour.* 28 (4), 345–349+400. (in Chinese with English abstract). doi:10.13686/j.cnki.dzyzy.2019.04.006

Lv, P. R., Yao, W. G., Zhang, H. D., Tian, H. H., and Yang, B. (2017). Geological characteristics of the Saindak porphyry Cu-Au deposit in Pakistan and its main ore-controlling factor. *Geol. Sci. Technol. Inf.* 36 (2), 206–214. doi:10.19509/j.cnki.dzkq.2017.0227

Ma, Z. Y., Li, L. J., Zhou, Q. L., Ma, C. X., and Zhao, J. P. (2013). The characteristics of the porphyry copper deposit and its formation in the East Kunlun Harizha area. *J. Qinghai Univ. Nat. Sci. Ed.* 31 (3), 69–75. (in Chinese with English abstract). doi:10.13901/j.cnki.qhwxxbzk.2013.03.012

Ma, Z. Y., Sun, F. F., Hao, N. N., Ma, C. X., Zhu, C. B., and Cao, J. H. (2016). Geochemical characteristics and metallogenic environment of granite in the Harizha copper polymetallic deposit area, Qinghai. *Mineral. Explor.* 7 (6), 929–937. (in Chinese with English abstract). doi:10.3969/j.issn.1674-7801.2016.06.006

Maniar, P. D., and Piccoli, P. M. (1989). Tectonic discrimination of granitoids. *Geol. Soc. Am. Bull.* 101 (5), 635–643. doi:10.1130/0016-7606(1989)101<0635:tdog>2.3.co;2

McDonough, W. F., and Sun, S. S. (1995). The composition of the Earth. *Chem. Geol.* 120 (3/4), 223–253. doi:10.1016/0009-2541(94)00140-4

Middlemost, E. A. K. (1985). *Magmas and magmatic rocks*. London: Longman, 1–266.

Pan, G. T., Xiao, Q. H., Lu, S. N., Deng, J. F., Feng, Y. M., and Feng, Y. F. (2009). Subdivision of tectonic units in China. *Geol. China* 36 (1), 1. 16+255+17-28. (in Chinese with English abstract).

Park, J. W., Campbell, I. H., Chiaradia, M., Hao, H. D., and Lee, C. T. (2021). Crustal magmatic controls on the formation of porphyry copper deposits. *Nat. Rev. Earth Environ.* 8 (2), 542–557. doi:10.1038/s43017-021-00182-8

Pearce, J. A., Harris, N. B. W., and Tindle, A. G. (1984). Trace element discrimination diagrams for the tectonic interpretation of granitic rocks. *J. Petrology* 25, 956–983. doi:10.1093/petrology/25.4.956

Qi, S. S. (2015). *Petrotectonic assemblages and tectonic evolution of the East Kunlun orogenic belt in Qinghai Province*. Doctoral Dissertation. Beijing: China University of Geosciences, 1–343.

Qian, Z. Z., Hu, Z. G., Liu, J. Q., and Li, H. M. (2000). Active continental margin and regional metallogenesis of the paleo-tethys in the east Kunlun mountains. *Geotect. Metallogenia* (2), 134–139.

Rudnick, R., , and Gao, S. (2004). *Treatise on geochemistry*. Elsevier Science, Holland and Turekian Composition of the Continental Crust3, 1–64.

Shao, F. L., Niu, Y. L., Liu, Y., Chen, S., Kong, J. J., Duan, M., et al. (2017). Petrogenesis of triassic granitoids in the east Kunlun orogenic belt, northern Tibetan plateau and their tectonic implications. *Lithos* 282, 33–44. doi:10.1016/j.lithos.2017.03.002

Song, B. Z., Zhang, Y. L., Chen, X. Y., Jiang, L., Li, D. S., and Kong, H. L. (2013). Geochemical characteristics of Harizha granite diorite-porphyry in East Kunlun and their geological implications. *Mineral. Deposits* 32 (1), 157–168. (in Chinese with English abstract). doi:10.3969/j.issn.0258-7106.2013.01.011

Sun, F. F., Zhu, C. B., Yuan, W. M., Zhang, A. K., Ma, Z. Y., and Feng, Y. L. (2016). Apatite fission track analysis of tectonic activity in Harizha polymetallic ore district, Dulan county, Qinghai province. *Nucl. Tech.* 39 (12), 41–48. (in Chinese with English abstract). doi:10.11889/j.0253-3219.2016.hjs.39.120501

Sun, S. S., and McDonough, W. F. (1989). "Chemical and isotopic systematics of oceanic basalts: Implications for mantle composition and processes,". Editors A. D. Saunders, and M. J. Norry (Geological Society London Special Publications), 42, 313–345.*Magmatism ocean basins*. doi:10.1144/gsl.sp.1989.042.01.19

Sun, X., Hollings, P., and Lu, Y. J. (2021). Geology and origin of the Zhunuo porphyry copper deposit, Gangdese belt, southern Tibet. *Min. Depos.* 3 (56), 457–480. doi:10.1007/s00126-020-00970-0

Sylvester, P. J. (1998). Post-collisional strongly peraluminous granites. *Lithos* 45 (1/4), 29–44. doi:10.1016/S0024-4937(98)00024-3

Tang, J. X., Wang, D. H., Wang, X. W., Zhong, K. H., Ying, L. J., and Tang, X. Q. (2010). Geological features and metallogenic model of the jiama copper-polymetallic deposit in Tibet. *Acta Geosci. Sin.* 31 (4), 495–506.

Urqueta, E., Kurt, K. T., Clark, A. H., Stanley, C. R., and Oates, C. J. (2009). Lithogeochemistry of the Collahuasi porphyry Cu–Mo and epithermal Cu–Ag (–Au) cluster, northern Chile: Pearce element ratio vectors to ore. *Geochem. Explor. Environ. Anal.* 9 (1), 9–17. doi:10.1144/1467-7873/07-169

Wang, G. (2014). *Metallogenesis of nickel deposits in eastern Kunlun orogenic belt, Qinghai Province. Doctoral dissertation*. Jilin: Jilin University, 1–214.

Wang, G., Sun, F. Y., Li, B. L., Li, S. J., Zhao, J. W., and Yang, Q. A. (2014). Petrography, zircon U-Pb geochronology and geochemistry of the mafic-ultramafic intrusion in Xiarihamu Cu-Ni deposit from East Kunlun, with implications for geodynamic setting. *Earth Sci. Front.* 21 (6), 381–401. (in Chinese with English abstract). doi:10.13745/j.esf.2014.06.036

Wang, K., Wang, L. X., Ma, C. Q., Zhu, Y. X., and Gao, L. Y. (2020). Petrogenesis and geological implications of the middle Triassic garnet-bearing two-mica granite

from Jialuhe Region, East Kunlun. *Earth Sci.* 45 (2), 400–418. (in Chinese with English abstract). doi:10.3799/dqkx.2018.393

Wang, P. X., Guo, F., and Wang, Z. N. (2020). Zircon U-Pb geochronology, geochemistry and geological significance of granitoids in the Yazigou, Qimantage area of East Kunlun Mountains. *Geoscience*, 1–14. (in Chinese with English abstract). doi:10.19657/j.geoscience.1000-8527.2020.026

Wang, X. L., Yuan, W. M., Feng, X., Feng, Y. L., and Cheng, X. Q. (2017). LA-ICP-MS zircon U-Pb age and geological significance of granite porphyry and diorite in the Harizha polymetallic ore district, East Kunlun Mountains. *Geol. Bull. China* 36 (7), 1158–1168.

Wu, D. Q., Sun, F. Y., Pan, Z. C., and Tian, Nan. (2020). Geochronology, geochemistry, and Hf isotopic compositions of triassic igneous rocks in the easternmost segment of the east Kunlun orogenic belt, NW China: Implications for magmatism and tectonic evolution. *Int. Geol. Rev.* 63, 1011–1029. doi:10.1080/00206814.2020.1740895

Wu, F. Y., Li, X. H., Zheng, Y. F., and Gao, S. (2007). Lu-Hf isotopic systematics and their applications in petrology. *A cta Petrol. Sin.* 23 (02), 185–220. doi:10.3321/j.issn:1000-0569.2007.02.001

Xia, C. L. (2018). *Research on the copper-lead-zinc-silver polymetallic metallogenic system related to magma-volcano hydrothermal in the eastern part of East Kunlun*, Doctoral Dissertation. Beijing: China University of Geosciences, 1–174.

Xia, R., Wang, C. M., Deng, J., Carranza, E. J. M., Li, W. L., Qing, M., et al. (2014). Crustal thickening prior to 220 Ma in the east Kunlun orogenic belt: Insights from the late triassic granitoids in the xiao-nuomuhong pluton. *J. Asian Earth Sci.* 93, 193–210. doi:10.1016/j.jseaes.2014.07.013

Xiao, Q. H., Deng, J. F., and Ma, D. Q. (2002). *Thinking and method of granite research*. Beijing: Geological Publishing House, 1–294.

Xin, W., Sun, F. Y., Zhang, Y. T., Fan, X. Z., Wang, Y. C., Li, L., et al. (2019). Mafic–intermediate igneous rocks in the East Kunlun Orogenic Belt, northwestern China: Petrogenesis and implications for regional geodynamic evolution during the Triassic. *Lithos* 346-347, 105159. doi:10.1016/j.lithos.2019.105159

Xu, B., Wang, C. Y., Liu, J. D., Wei, L. Q., Ji, M. J., and Li, X. (2020). The petrogenesis of the late triassic granites heergetou area, East Kunlun: Constraints from geochronology, geochemistry and Sr-Nd-Pb isotopes. *Acta Geol. Sin.* 94 (12), 3643–3656. (in Chinese with English abstract). doi:10.19762/j.cnki.dizhixuebao.2020284

Xu, X. B., Wang, L. X., Ma, C. Q., Zhu, Y. X., and Wang, K. (2021). Petrogenesis and geological implications of the yangfengou intermediate-felsic dykes in the balong area within the eastern Kunlun orogen. *Bull. Mineralogy, Petrology Geochem.*, 1–24. (in Chinese with English abstract). doi:10.19658/j.issn.1007-2802.2021.40.021

Yan, Z. J. (2019). *Genesis of silver polymetallic deposit in Harizha area Qinghai Province. Master dissertation*. Jilin: Jilin University, 1–62.

Yang, H. Y., Ma, W. M., and Wang, G. Z. (2015). The prospecting sign of copper polymetallic deposit in Harizha area, Qinghai. *Mod. Min.* 31 (10), 140–143. (in Chinese with English abstract). doi:10.3969/j.issn.1674-6082.2015.10.045

Yang, P., Pei, S. J., Chen, L. J., Tang, J., and Zhao, H. X. (2010). Characteristic of copper-bearing porphyry and analysis on the Prospecting potential in Harizha of Qinghai. *J. Qinghai Univ. Nat. Sci.* 28 (06), 62–68. (in Chinese with English abstract). doi:10.13901/j.cnki.qhwxxbzk.2010.06.009

Yang, T., Zhou, H. B., Zheng, Z. H., Liu, H., Li, J., Li, M. T., and Wang, Y. (2017). Geological characteristics and genetic type of the Nagengkangqieer silver polymetallic deposit in East Kunlun. *Northwest. Geol.* 50 (04), 186–199. (in Chinese with English abstract). doi:10.19751/j.cnki.61-1149/p.2017.04.020

Yang, Z. L., Hu, X. J., Wang, S. Q., Xin, H. T., Li, C. D., Liu, W. G., et al. (2020). Geochronology, geochemistry and geological significance of early paleozoic volcanic rocks in northern east ujimqin banner, inner Mongolia. *Acta Petrol. Sin.* 36 (4), 1107–1126. (in Chinese with English abstract). doi:10.3969/j.issn.1000-8845.2006.02.021

Yao, W. G., Hong, J., Yang, B., and Lv, P. R. (2013). Types and characteristics of main copper deposits in Pakistan. *Acta Mineral. Sin.* 33 (S2), 1076–1077. (in Chinese with English abstract). doi:10.16461/j.cnki.1000-4734.2013.s2.092

Yu, J. Z., Zheng, Y. Y., Xu, R. K., Hou, W. D., and Cai, P. J. (2020). Zircon U-Pb chronology, geochemistry of Jiangjunmu ore-bearing pluton, eastern part of East Kunlun and their geological significance. *Earth Sci.* 45 (04), 1151–1167. (in Chinese with English abstract). doi:10.3799/dqkx.2019.134

Yuan, H. L., Wu, F. Y., Gao, S., Liu, X. M., Xu, P., and Sun, D. Y. (2003). Zircon laser probe U-Pb dating and REE composition analysis of Cenozoic intrusions in Northeast China. *Chin. Sci. Bull.* 48 (14), 1511–1520. (in Chinese with English abstract).

Zhong, M. F. (2018). *Discussion on the application of integrated geophysical methods in the exploration of the Harizha polymetallic ore in Dulan County, Qinghai Province*. Master Dissertation. Jilin: Jilin University, 1–57.

Zhai, Y. S., Yao, S. Z., and Cai, K. Q. (2011). *Mineral deposits*. Beijing: Geological Publishing House.

Zhang, B., Guo, F., and Zhang, X. B. (2020). Petrogenesis of granitic rocks in the Pingtan Island, Fujian Province: Constraints from zircon U▪Pb dating, O▪Hf isotopes and biotite mineral chemistry. *Acta Petrol. Sin.* 36 (4), 995–1014. doi:10.18654/1000-0569/2020.04.02

Zhang, B., Kong, H. L., Li, Z. M., Li, J. C., Yang, T., and Wang, Y. (2016). Zircon U-Pb dating, geochemical and geological significance of the tonalites from the Harizha lead-zinc polymetallic mine in East Kunlun Mountains. *Geol. Sci. Technol. Inf.* 35 (5), 9–17. (in Chinese with English abstract).

Zhang, J. Y., Ma, C. Q., Li, J. W., and Pan, Y. M. (2017). A possible genetic relationship between orogenic gold mineralization and postcollisional magmatism in the eastern Kunlun Orogen, Western China. *Ore Geol. Rev.* 81, 342–357. doi:10.1016/j.oregeorev.2016.11.003

Zhang, Z. W., Wang, Y. L., Wang, C. Y., Qian, B., Li, W. Y., Zhang, J. W., et al. (2019). Mafic-ultramafic magma activity and metallogeny during paleozoic in the eastern Kunlun orogenic belt, Qinghai province, China. *China Geol.* 2 (4), 1–11. doi:10.31035/cg2018124

Zhou, H. Z., Zhang, D. H., Wei, J. H., Wang, D. Z., Santosh, M., Shi, W. J., et al. (2020). Petrogenesis of Late Triassic mafic enclaves and host granodiorite in the Eastern Kunlun Orogenic Belt, China: Implications for the reworking of juvenile crust by delamination-induced asthenosphere upwelling. *Gondwana Res.* 84, 52–70. doi:10.1016/j.gr.2020.02.012

Advantages of publishing in Frontiers

OPEN ACCESS
Articles are free to read for greatest visibility and readership

FAST PUBLICATION
Around 90 days from submission to decision

HIGH QUALITY PEER-REVIEW
Rigorous, collaborative, and constructive peer-review

TRANSPARENT PEER-REVIEW
Editors and reviewers acknowledged by name on published articles

Frontiers
Avenue du Tribunal-Fédéral 34
1005 Lausanne | Switzerland

Visit us: www.frontiersin.org
Contact us: frontiersin.org/about/contact

REPRODUCIBILITY OF RESEARCH
Support open data and methods to enhance research reproducibility

DIGITAL PUBLISHING
Articles designed for optimal readership across devices

FOLLOW US
@frontiersin

IMPACT METRICS
Advanced article metrics track visibility across digital media

EXTENSIVE PROMOTION
Marketing and promotion of impactful research

LOOP RESEARCH NETWORK
Our network increases your article's readership